ABSTRACT

Title of dissertation: ANATEXIS AND CRUSTAL DIFFERENTIATION: INSIGHTS FROM THE FOSDICK MIGMATITE–GRANITE COMPLEX, WEST ANTARCTICA

Christopher John Anthony Yakymchuk, Doctor of Philosophy, 2014

Dissertation directed by: Professor Michael Brown
Department of Geology

In the Fosdick migmatite–granite complex of West Antarctica, U–Pb geochronology of monazite in migmatites and zircon in granites records two episodes of high-temperature metamorphism, one in the Devonian–Carboniferous and another in the Cretaceous. For the older lower-grade event, whole-rock and zircon isotope geochemistry of granites within the Fosdick complex are interpreted to record crustal reworking during metamorphism associated with continental arc magmatism along the East Gondwana convergent plate margin. By contrast, the geochemistry of correlative granites suites from along and across the same margin indicates a greater proportion of crustal growth. This

suggests prominent arc-parallel and arc-normal variations in the mechanisms of crustal reworking versus growth in continental arc systems.

Based on garnet Lu–Hf ages, the timing of peak metamorphism in the younger higher-grade event has been determined as *c*. 116–111 Ma. U–Pb ages of monazite from migmatites and zircon from anatectic granites suggest that exhumation of the complex as a gneiss dome occurred during the interval *c*. 107–100 Ma. Contemporaneous exhumation of high-grade metamorphic rocks in the Western Province of New Zealand suggests that intracontinental extension preceded the final breakup of New Zealand from West Antarctica by *c*. 25 Myr.

Melt migration through and emplacement within the Fosdick complex during Cretaceous metamorphism was accomplished via a self-organized melt network controlled by the regional stress field and anisotropy of the host rocks. Granites within this network and in sills at shallower crustal levels have microstructures and chemistry consistent with a cumulate origin, and are interpreted to record fractional crystallization during magma ascent and doming related to exhumation.

Phase equilibria modeling of open system melting during prograde metamorphism is used to quantify the reduced fertility of source rocks during high-temperature exhumation and later overprinting orogenic events. Quantitative modelling of the dissolution of zircon and monazite during prograde melting demonstrates that accessory minerals are expected to be partially to completely consumed up to the metamorphic peak. New growth of these minerals in migmatite melanosomes is predicted to be limited during cooling, whereas leucosomes and anatectic granites are predicted to contain new zircon and monazite growth.

ANATEXIS AND CRUSTAL DIFFERENTIATION: INSIGHTS FROM THE FOSDICK MIGMATITE–GRANITE COMPLEX, WEST ANTARCTICA

by

Christopher John Anthony Yakymchuk

Dissertation submitted to the Faculty of the Graduate School of the
University of Maryland, College Park, in partial fulfillment
of the requirements for the degree of
Doctor of Philosophy
2014

Advisory Committee:

Professor Michael Brown, Chair
Professor George Helz
Professor Sarah Penniston-Dorland
Dr Philip Piccoli
Professor Christine Siddoway

Letter of Certification

UNIVERSITY OF MARYLAND

DEPARTMENT OF GEOLOGY

Geology Building
University of Maryland
College Park, Maryland 20742-4211 USA
301.405.4365 TEL 301.314.9661 FAX
www.geol.umd.edu

July 9, 2014

Dr. Charles Caramello
Associate Provost for Academic Affairs & Dean of the Graduate School
2123 Lee Building
Campus

Dear Dr Caramello

This letter certifies that the examining committee for my dissertation has determined that I made a substantial contribution to work included in this dissertation that was co-authored with faculty members and colleagues. The inclusion of this co-authored work has the approval of Dr Michael Brown as my dissertation advisor and Dr William McDonough as Director of Graduate Studies in Geology.

Yours sincerely,

Chris Yakymchuk

Foreword

A significant portion of the research presented in this dissertation was previously published or is in review in the form of peer-reviewed journal articles. I made substantial contributions to the relevant aspects of the jointly authored work included in this dissertation. Following is a list of Chapters in review or published with a summary of the contributions made by me to each.

Chapter 3

C.R. Brown, C. Yakymchuk, M. Brown, C.M. Fanning, F.J. Korhonen, P.M. Piccoli, and C.S. Siddoway. In Review. Are cumulate granites characteristic of migmatite–gneiss domes? An example from the Fosdick Mountains of Marie Byrd Land, West Antarctica. Journal of Petrology.

I collected samples from the field with several of the joint authors, acquired and interpreted zircon U–Pb, Hf and O isotope data (under the direction of C.M. Fanning, Australian National University), collected and interpreted the initial LA-ICP-MS U–Pb isotope data with C.R. Brown (under the direction of Mark Pecha, University of Arizona), conducted the phase equilibria and isotope mixture modeling, created the figures (with the exception of Figs 3.9–3.13), and co-wrote the first draft of the manuscript with the lead author prior to review by the remaining joint authors.

Chapter 4

Yakymchuk, C., Brown, M., Brown, C., Siddoway, C.S., Fanning, C.M., Korhonen, F.J. In Review. Paleozoic evolution of western Marie Byrd Land, Antarctica. Geological Society of America Bulletin.

I collected the samples from the field with several of the joint authors (except for several additional samples provided by C. Siddoway and F.J. Korhonen), acquired and interpreted zircon U–Pb, Lu–Hf, and O isotope data (under the direction of C.M. Fanning, Australian National University), collected and interpreted U–Pb and Lu–Hf isotope data from detrital zircons (under the direction of Mark Pecha, University of Arizona), except for U–Pb data from four samples that was provided by C. Siddoway, created the tables and figures (unless otherwise specified in the figure caption), and wrote the first draft of the manuscript prior to review by the joint authors.

Chapter 5

Yakymchuk, C. and Brown, M. 2014. Behaviour of zircon and monazite during crustal melting. Journal of the Geological Society, London, 171 (4).

I conducted the phase equilibria modeling, created the tables and figures, and wrote the first draft of the manuscript prior to review by the second author.

Chapter 6

Yakymchuk, C. and Brown, M. 2014. Consequences of open system melting in tectonics. Journal of the Geological Society of London, 171: 21–40.

I conducted the phase equilibria modeling, created the tables and figures, and wrote the first draft of the manuscript prior to review by the second author.

Chapter 7

Yakymchuk, C., Brown, M., Ivanic, T.J. and Korhonen, F.J., 2013. Leucosome distribution in migmatitic paragneisses and orthogneisses: A record of self-organized melt migration and entrapment in a heterogeneous partially-molten crust. Tectonophysics, 603: 136–154.

I collected field data with the joint authors, conducted and interpreted the statistical and phase equilibria modeling, created the figures and tables, and wrote the first draft of the manuscript prior to review by the joint authors.

Chapter 8

Yakymchuk, C., Siddoway, C.S., Fanning, C.M., McFadden, R., Brown, M., and Korhonen, F.J. 2013. Anatectic reworking and differentiation of continental crust along the active margin of Gondwana: a zircon Hf-O perspective from West Antarctica. Geological Society of London Special Publications, 383: 169–210.

This study was based on a dataset of zircon isotope analyses that was collected over several years by C.M. Fanning and C. Siddoway. I collated and interpreted the data, conducted the isotope mixture modeling, compiled a regional isotope dataset (a portion of which was generously contributed by A.I.S. Kemp, University of Western Australia), created the tables and figures (unless otherwise specified in the figure caption) and wrote the first draft of the manuscript prior to review by the joint authors.

Acknowledgements

First and foremost, I thank Mike Brown for his support, patience and providing me with opportunities to travel around the world for fieldwork, conferences and to collaborate and network with internationally renowned researchers. I have thoroughly enjoyed working with Mike and I am grateful for the many discussions on academia and the philosophy of science that will guide me through the next phase of my career. I thank Phil Piccoli for providing me with much needed advice and encouragement along the way. Christine Siddoway is thanked for introducing me to Antarctica and always providing me with a positive outlook. Fawna Korhonen is a mentor, colleague and friend who has provided endless moral support and guidance. I thank Sarah Penniston-Dorland and George Helz for acting as members of my dissertation advisory committee.

This project has been supported by: a Post Graduate Scholarship from the National Science and Engineering Research Council of Canada, the National Science Foundation (ANT0944615 to M. Brown at the University of Maryland; OPP-0338279 and OPP-0944600 to C. Siddoway at Colorado College), a graduate student grant from the Geological Society of America and a supplementary grant from the division of Mineralogy, Geochemistry, Petrology, and Volcanology; an Exploration and Field Research Grant from the Explorers Club Washington Group; a scholarship from the American Federation of Mineralogical Societies. I acknowledge support for travel to conferences from the Geochemical Society, the Geological Society of America, the

National Science Foundation, the Byrd Polar Research Center and the University of Maryland.

I thank Rich Taylor and Chris Clark at Curtin University for assistance with monazite U–Pb SHRIMP geochronology; Mark Pecha, Nicky Giesler and Mauricio Ibanez-Mejia for assistance with data collection at the Arizona LaserChron Center; Mark Fanning and Bin Fu for assistance with sample preparation and analytical work at the Australian National University and Brenda Armstrong for logistical support; Dianne Wilford, Chris Fisher, Charles Knaack and Jeff Vervoort for assistance with garnet Lu–Hf geochronology at Washington State University; Richard Ash and Igor Putchel for assistance with trace element analysis in the Isotope Geochemistry Laboratory at the University of Maryland. I acknowledge the NanoCenter and the NISP-Lab at the University of Maryland, which are supported by the NSF as a MRSEC Shared Experimental Facility.

Critical reviews of published chapters were provided by: Dave Kelsey (Chapter 5), Nigel Kelly and Johann Diener (Chapter 6), Elena Druguet and Olivier Vanderhaeghe (Chapter 7), Michael Flowerdew, Tony Kemp, Evgeny Mikhalsky and an anonymous reviewer (Chapter 8). In addition to the people listed above, this project has benefited from input by Mark Caddick, Rich Gaschnig, Victor Guevara, Ian Main, Aaron Martin, Samuel Morfin, Ed Sawyer and Richard Walker.

Fieldwork in Antarctica was made possible and successful by the 109th Airlift Wing of the New York Air National Guard, the pilots and aircraft engineers of Kenn Borek Air, the staff at the Byrd Field Center and McMurdo station, all the folks at Siple

Dome camp (Drew and Silver in 2011–2012; Sal, Eric, Tony and Brendon in 2010–2011), and the mountaineers of project G-097: Tim Burton, Kevin Emery and Danny Uhlmann. In particular, I thank Tim Burton for keeping me safe and sane, asking tough geological questions, and his uncanny ability to prepare a gourmet meal and tailor a formal wardrobe under any circumstances. Tim Ivanic is thanked for his enthusiastic collaboration during our second field season and for the many jam sessions in between SHRIMP sessions in WA.

Caitlin Brown is thanked for her moral support and collaboration on this project. I thank my fellow graduate students and the entire faculty in the Geology department for their encouragement and thoughtful discussions. I also thank Dorothy Brown, Todd Karwoski, Suzanne Martin, Michelle Montero, Joanna Patterson and Sandy Romeo for the administrative and technical support that keeps the department functioning. I thank the library staff responsible for interlibrary loan services, which has saved me many hours of searching the stacks.

Finally, I thank my wife, Kristen, for her limitless support and encouragement over these last four years. This would not have been possible without you.

Table of Contents

List of Tables

List of Figures

Chapter 1: Introduction

1.1 Anatexis, crustal differentiation and the Fosdick migmatite–granite complex

The generation and segregation of granitic melt by anatexis in the deep continental crust followed by extraction, ascent and emplacement into the upper crust is an important process by which the continents have become differentiated into a depleted lower portion and a complementary enriched upper portion (Sawyer et al., 2011; Brown, 2013). Crustal reworking by this process plays a major role in the redistribution of mass and energy within the continental crust (Brown, 2010a).

In the absence of H_2O-rich fluid infiltration, partial melting commences at the wet solidus, although very little melt is produced due to the limited amount of grain boundary H_2O (e.g. Yardley, 2009), and continues with increasing temperature via hydrate-breakdown melting reactions according to protolith composition and ultimately by the consumption of any remaining feldspar(s) and quartz (White et al., 2001; Clemens, 2006, Brown and Korhonen, 2009; Brown, 2013). With increasing melt fraction, melt becomes segregated from the initial sites of melt accumulation—along grain boundaries—into lower pressure sites where melt may accumulate (e.g. strain shadows associated with peritectic minerals, deformation bands) prior to extraction via ascent conduits that feed plutons at shallower structural levels (Brown, 2010b). Evidence of melt drainage in migmatites and residual granulites includes chemical depletion of these rocks in a granitic component relative to protolith compositions (Korhonen et al., 2010b), preservation of peritectic minerals and lack of extensive retrogression (White et al., 2004), and the formation of collapse structures (Brown et al., 1999; Bons et al., 2008). During melt extraction and ascent, peritectic mineral entrainment (Clemens et al., 2011; Clemens and

Stevens, 2012), fractional crystallization (Sawyer, 1987; Morfin et al., 2014) and wall rock stoping and assimilation (e.g. Clarke, 2007) may modify the composition of the magma prior to emplacement.

This dissertation explores the processes and timescales of high-temperature metamorphism, partial melting, melt transport and granite genesis in the deep crust and the mechanisms that focus melt movement throughout the crust and modify its composition en route. Particular topics that I address include: (1) constraining the pressure–temperature–time (*P–T–t*) evolution of migmatites and granulites that underwent two superimposed episodes of high-temperature metamorphism and melt drainage (Chapters 2 and 6), (2) exploring the range of compositions of leucosome and granite in migmatite–granite complexes and their relationship to primary melt compositions (Chapter 3), (3) evaluating the behavior of zircon and monazite during crustal melting and the geological significance of U–Pb ages obtained from them (Chapter 5), (4) investigating the role of protolith composition and imposed tectonic stresses on the development of melt-transport networks in migmatites at intermediate levels in the continental crust (Chapter 7), (5) using Hf and O isotopes in zircon from granites emplaced in the shallow crust to investigate the relative contributions of crustal reworking to crustal growth (Chapters 4 and 8).

Related exposures of high-temperature metamorphic rocks, their low-grade equivalents and associated anatectic granites are rare, in part because the former generally represent deeper crustal levels relative to the latter two that represent shallower crustal levels. One exception occurs in the Ford Ranges of West Antarctica. Here, in the Fosdick Mountains, Cretaceous extensional deformation has exposed a migmatite–granite

complex in a dome structure. The Fosdick complex is composed predominately of anatectic granites and the high-grade metamorphosed equivalents of a Cambrian–Ordovician metaturbidite sequence and a calc-alkaline Devonian–Carboniferous granodiorite suite that crop out in the surrounding Ford Ranges. Based on U–Pb ages of monazite, two metamorphic events have been documented in the Fosdick migmatite–granite complex, one in the Devonian–Carboniferous and, based on the results of quantitative phase equilibria modelling, a higher-grade overprint in the Cretaceous (Korhonen et al., 2010b, 2012; Chapter 2). The presence of two chemically and isotopically distinct protoliths, their high-grade metamorphosed equivalents, associated anatectic granites and a polyphase metamorphic history make the Fosdick complex in West Antarctica a suitable location to investigate high-temperature metamorphism, crustal anatexis, melt loss and granite petrogenesis.

1.2. Exploration and fieldwork in the Ford Ranges

"Polar Exploration is at once the cleanest and most isolated way of having a bad time which has been devised*" – A. Cherry-Garrard. The Worst Journey in the World.*

The Edsel Ford Ranges of western Marie Byrd Land, West Antarctica were named after the former president and CEO of the Ford Motor Company (1919–1943), and the son of Henry Ford, by Admiral Richard Byrd in December of 1929 during an aerial survey of previously unexplored territory. A four-man sledge party, led by Paul A. Siple (biologist) and including F. Alton Wade (geologist), conducted the first inland expedition in the Ford Ranges over 39 days in the Antarctic summer of 1934–1935. This team explored and sampled scattered outcrops across the Ford Ranges. Wade produced the first geological map of the region, which was published in the Bulletin of the Geological

Society of America (Wade, 1937). During this expedition, Siple and one companion split off from the remainder of the party and headed towards the Raymond Fosdick Mountains—named after the former president of the Rockefeller Foundation (1936–1948). They visited 'Volcano 116' (formally named Vulcan Nunatak in 1970) in the southeastern part of the range and collected olivine fourchite samples that are described in detail by Fenner (1938).

The first geological work in the Fosdick Mountains was conducted in October of 1940 by a party of biologists led by J.E. Perkins and included: Dr. E.E. Lockhart, H.H. Richardson, and L. Colombo. The results of this expedition, as well as a comprehensive account of the geology of the Ford Ranges, were summarized in Warner (1945). Subsequent expeditions to the Ford Ranges, including the Fosdick Mountains, were aided by aircraft that had the ability to land on and—perhaps most importantly—take off from the ice. These expeditions included teams from: Texas Technology College (1966–1969), University of California Santa Barbara (1989–1991; NSF–OPP 8817615), University of California Santa Barbara and Colorado College (1998–2001; NSF–OPP 9615282), Colorado College and University of Minnesota (2005–2007; NSF–OPP 0338279), University of Maryland (2006–2008; NSF–OPP 0631324), and the University of Maryland and Colorado College (2010–2012; NSF–OPP 0734505). This dissertation is based in part on data and samples collected over two field seasons in West Antarctica in 2010–2011 and 2011–2012.

Western Marie Byrd Land is one of the most difficult areas in which to work in Antarctica. Isolated outcrop coupled with unpredictable weather results in few days that are safe for air travel. Unfortunately, our first field season (Nov. 2010–Jan. 2011)

consisted of 35 days at Siple Dome camp (Nov. 15 through Dec. 21) in the middle of the West Antarctic ice sheet. In principle, Siple Dome camp is a refueling stop or a temporary stop over en route to the Fosdick Mountains. However, a combination of weather and scarce availability of air support left our team stuck at Siple Dome camp and, after several weeks delay, putting a tent camp into the Fosdick Mountains for the short time that remained was impracticable. As a consequence of these events, on only four of the 35 days in Siple Dome camp was fieldwork possible via a Twin Otter aircraft, including one day in the Ford Ranges (Dec. 4) and three days in the Fosdick Mountains (Dec. 5, 9 and 17). During our stay at Siple Dome camp, a separate research project based on thermodynamic modeling of processes during crustal melting was conceived that developed into Chapters 5 and 6 of this dissertation.

Our second field season (Oct. 2011– Jan. 2012) was more successful. We spent 61 days in the Fosdick Mountains (Nov. 5 through Jan. 6) on roughly half of which fieldwork was possible, with setting up and breaking down camps, relocation, resupply via aircraft support and storms accounting for the other half. Data from samples collected during this period contributed to Chapters 2–4 and field measurements during this period contributed to Chapter 7 of this dissertation. The final two weeks of this field season (Jan. 6–21) were allocated for close-support work by Twin Otter Aircraft (Kenn Borek Air). Fieldwork was only possible on 3 of these days (Jan. 18–20), during which samples were collected from isolated peaks across the Ford Ranges. Data from samples collected during these 3 days contributed to portions of Chapters 2–4 in this dissertation. For a detailed account of the second field season, the interested reader is referred to the G-097 team blog <http://g097-mbl.blogspot.com>.

1.3 Outline of this dissertation

This dissertation is divided into nine chapters. Chapters 2 through 8 comprise the original research component and are in reverse chronological order with the most recently completed research first. Each of these chapters represents a stand-alone manuscript that has been published, is in review for publication, or will be submitted to a peer-reviewed journal. Chapter 9 summarizes the work presented herein and discusses several outstanding questions and directions for future research. The appendices (A through E) contain detailed analytical methods, tabulated data and supplementary information for Chapters 2–4, and, 7 and 8. In Appendix F, I list the latitude and longitude of all samples collected during the two field seasons in the Ford Ranges of West Antarctica.

Chapter 2: Decoding polyphase migmatites using geochronology and phase equilibria modelling

2.1 Abstract

Retrieving the *P–T* conditions of overprinting metamorphic events imposed on deep crustal rocks requires the use of multiple high-temperature geochronometers integrated with careful petrography and robust quantitative phase equilibria modelling. As an example, *in situ* U–Pb monazite ages and Lu–Hf garnet geochronology are used to distinguish mineral parageneses in polyphase migmatitic paragneisses and orthogneisses from the Fosdick migmatite–granite complex in West Antarctica. Inverse and forward phase equilibria modelling are then used to quantify the *P–T* conditions for each event. U–Pb monazite ages define dominant populations at 365–300 Ma (cores of polychronic grains, dominantly from deeper structural levels in the central and western sectors of the complex) and 120–100 Ma (rims of polychronic grains, dominantly from the central and western sectors of the complex, and from monochronic grains mostly at shallower structural levels in the eastern sector of the complex) that record two separate high-grade metamorphic events. For five paragneiss and two orthogneiss samples, Lu–Hf garnet ages range from 116 to 111 Ma, *c*. 10–15 Ma older than published Sm–Nd garnet ages of 102–99 Ma from three of the same samples. Although individual garnet grains have flat Sm zoning patterns consistent with high-temperature diffusive resetting, Lu zoning is variable with most grains having Lu-enriched rims relative to Lu-depleted cores. Lutetium enrichment of garnet rims is interpreted to record the breakdown of a Lu-rich

accessory mineral during the final stage of garnet growth immediately prior to peak *P–T* and/or the preferential retention of Lu as cordierite replaced garnet in the presence of melt during the initial stages of exhumation. Therefore, garnet is interpreted to be part of the overprinting Cretaceous mineral paragenesis and the Lu–Hf garnet ages are interpreted to record the approximate timing of peak metamorphism for this event. For the older (Devonian–Carboniferous) metamorphism, phase equilibria modelling of the metasedimentary protoliths to the paragneisses and a diatexite interpreted to be a product of Devonian–Carboniferous anatexis restrict the peak *P–T* conditions for this event to 720–800°C at 0.45–1.0 GPa. For the younger (Cretaceous) metamorphism, phase equilibria modelling of residual paragneiss and orthogneiss compositions constrain *P–T* conditions of the solidus phase assemblage after decompression to 850–880°C at 0.65–0.80 GPa. This younger metamorphic event is dominant throughout the Fosdick complex and has extensively reworked or obliterated evidence of the Devonian–Carboniferous metamorphism, especially at shallow structural levels. During the initial stages of exhumation after peak *P–T*, garnet breakdown to cordierite and biotite in the presence of melt is recorded by Y-enriched rims in monazite that yield ages of *c.* 106–100 Ma. In a wider context, this time frame coincides with the exhumation of high-grade rocks in the western Province of New Zealand, which formed part of the East Gondwana active plate margin at this time, and indicates that regional extension enabling exhumation preceded the final breakup of Gondwana by *c.* 25 Myr.

2.2 Introduction

Linking ages obtained from isotope geochronology with estimates of metamorphic pressures and temperatures provides a powerful tool to elucidate the *P–T–t* paths experienced by metamorphic rocks during the buildup and collapse of mountain belts (Rubatto, 2002; Pyle and Spear, 2003; Baldwin and Brown, 2008; Kelsey *et al.*, 2008; Reno *et al.*, 2011; Korhonen *et al.*, 2013). Although the U–Pb ages retrieved from accessory minerals are commonly precise, the geological significance of these ages may be ambiguous unless they are linked to the growth and consumption of major rock-forming minerals by trace element chemistry (Rubatto, 2002; Clark *et al.*, 2009; Reno *et al.*, 2011). The interpretation of these ages may be even more difficult in metamorphic rocks that have experienced multiple overprinting high-temperature metamorphic events, particularly where crustal melting is involved (e.g. Korhonen *et al.*, 2012).

In principle, direct dating of metamorphic minerals such as garnet avoids this ambiguity in interpretation as long as the isotope systems considered have closure temperatures above those achieved at the peak of metamorphism (e.g. Scherer *et al.*, 2000; Zirakparvar *et al.*, 2010; Sousa *et al*., 2013; Smit *et al.*, 2013). Importantly, Lu–Hf garnet geochronology commonly yield ages older than those obtained from Sm–Nd garnet geochronology (Scherer *et al.*, 2000; Kylander-Clark *et al.*, 2007; Smit *et al.*, 2010; Cheng *et al.*, 2010), which suggests a higher closure temperature for the Lu–Hf system as compared to the Sm–Nd system in garnet. Therefore, the Lu–Hf isotope system has the potential to preserve evidence of the timing of garnet growth in high-grade metamorphic rocks in circumstances where other isotope geochronometers may be

difficult to link to growth of the major rock-forming minerals or may have been reset (e.g. Scherer *et al.*, 2002; Albarède, 2003; Kohn, 2009; Smit *et al.*, 2013).

In the Fosdick migmatite–granite complex of West Antarctica, U–Pb zircon ages of granites and U–Pb monazite ages of migmatitic paragneisses and orthogneisses record two orogenic events, one in the Devonian–Carboniferous and the other in the Cretaceous (Korhonen *et al.*, 2010b; 2012; Brown *et al*., 2014; Yakymchuk *et al*., 2014). The relatively well-constrained Cretaceous orogenic event is characterized by garnet- and cordierite-bearing assemblages in migmatitic paragneisses. For this event, Korhonen *et al.* (2010a; 2012) calculated pressures of 0.60–0.75 GPa at temperatures of 830–870°C for the solidus phase assemblage in these rocks. However, the *P–T* conditions for the Devonian–Carboniferous orogenic event were poorly constrained due to uncertainty over whether any garnet growth occurred during this earlier period of metamorphism. The ambiguity was created by U–Pb geochronology on monazite inclusions in garnet that showed Devonian–Carboniferous age cores but Cretaceous age rims (Korhonen *et al.*, 2012). Moreover, the garnet itself yielded Cretaceous Sm–Nd model ages that were interpreted to represent diffusional resetting of the Sm–Nd isotope system in Devonian–Carboniferous garnet during the Cretaceous (Korhonen *et al.*, 2012).

In this contribution, Lu–Hf garnet geochronology is used to argue that garnet growth occurred during the Cretaceous and that garnet was not part of the Devonian–Carboniferous mineral paragenesis. With the ambiguity over the age of garnet growth resolved, we determine the maximum *P–T* conditions likely to have prevailed during the Devonian–Carboniferous orogenic event. Then we integrate quantitative phase equilibria modelling with additional *in situ* U–Pb monazite geochronology, the garnet

geochronology and published *in situ* U–Pb monazite geochronology to determine the Cretaceous *P–T–t* evolution of the migmatitic paragneisses and orthogneisses in the Fosdick complex. The techniques and results presented in this study provide an example of how to decode multiple episodes of metamorphism and anatexis in deep crustal rocks that should be widely applicable to other polyorogenic high-grade metamorphic terrains.

2.3 Geological setting

2.3.1 Regional Geology

In the Phanerozoic, Marie Byrd Land in West Antarctica, together with parts of New Zealand (Zealandia) and further east (present co-ordinates) Australia, formed part of the active continental margin of East Gondwana (Fig. 2.1; Boger, 2011; Veevers, 2012). One of the few exposures of bedrock in western Marie Byrd Land occurs in the Ford Ranges, which lie along the eastern side of the Ross Sea (Fig. 2.1).

The oldest exposed unit in the Ford Ranges is the Cambrian–Ordovician Swanson Formation, which comprises folded and cleaved metagreywackes and slates of sub-greenschist to greenschist facies due to deformation and regional metamorphism dated at *c*. 450 Ma (Adams, 1986). Detrital zircon age profiles indicate derivation from granite protoliths in the Ross–Delamerian orogen and largely unexposed Proterozoic basement to the south (Pankhurst *et al*., 1998; Yakymchuk *et al.*, 2014).

The Swanson Formation was intruded by the Devonian–Carboniferous calc-alkaline Ford Granodiorite suite (Adams, 1987; Weaver *et al.*, 1991; Pankhurst *et al*., 1998; Yakymchuk *et al.*, 2014). This episode of magmatism is widely recognized along the East Gondwana margin (Muir *et al*., 1996; Mukasa and Dalziel, 2000; Siddoway and Fanning, 2009) and has been attributed to subduction (Borg *et al*., 1987; Weaver *et al*.,

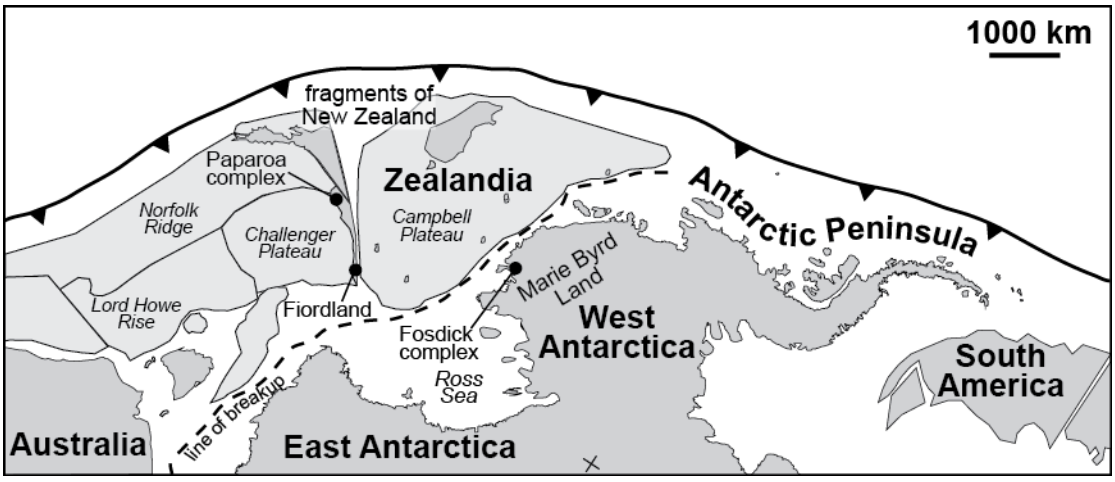

Fig. 2.1. Geometrical reconstruction of the East Gondwana active convergent margin (modified from Veevers, 2012, fig. 4).

1991) or back-arc extension (Muir *et al*., 1996; Siddoway and Fanning, 2009; Tulloch *et al*., 2009).

A diachronous transition from oblique convergence to oblique divergence between 115 and 109 Ma in the Ford Ranges facilitated the exhumation and doming of a migmatite–granite complex exposed in the Fosdick Mountains (Siddoway *et al.*, 2004; McFadden *et al.*, 2010a, b). The rapid transition to divergence has been attributed to ridge–trench interaction (Bradshaw, 1989; Luyendyk, 1995), the presence of a mantle plume (Weaver *et al.*, 1994; Storey *et al.*, 1999), or intracontinental extension that preceded the breakup of the East Gondwana continental margin at *c.* 83 Ma (Siddoway, 2008).

2.3.2 Fosdick migmatite–granite complex

2.3.2.1 Geological overview

In the Fosdick Mountains, Cretaceous extensional deformation has exposed a migmatite–granite complex as an elongate dome approximately 80 km long and 15 km wide (Fig. 2.2). The Fosdick complex is bounded to the north by the inferred Balchen Glacier fault, a steep dextral strike-slip fault (Siddoway *et al*., 2004, 2005), and to the south by the South Fosdick detachment, a south-dipping, dextral oblique detachment zone (McFadden *et al*., 2010a).

The complex comprises layered sequences of migmatitic paragneisses and orthogneisses, and associated granites that are all crosscut by mafic dykes (Richard *et al.*, 1994; Siddoway *et al.*, 2004; Saito *et al*., 2013). Based on whole-rock geochemistry and a similar distribution of detrital zircon age populations, the paragneisses are inferred to be

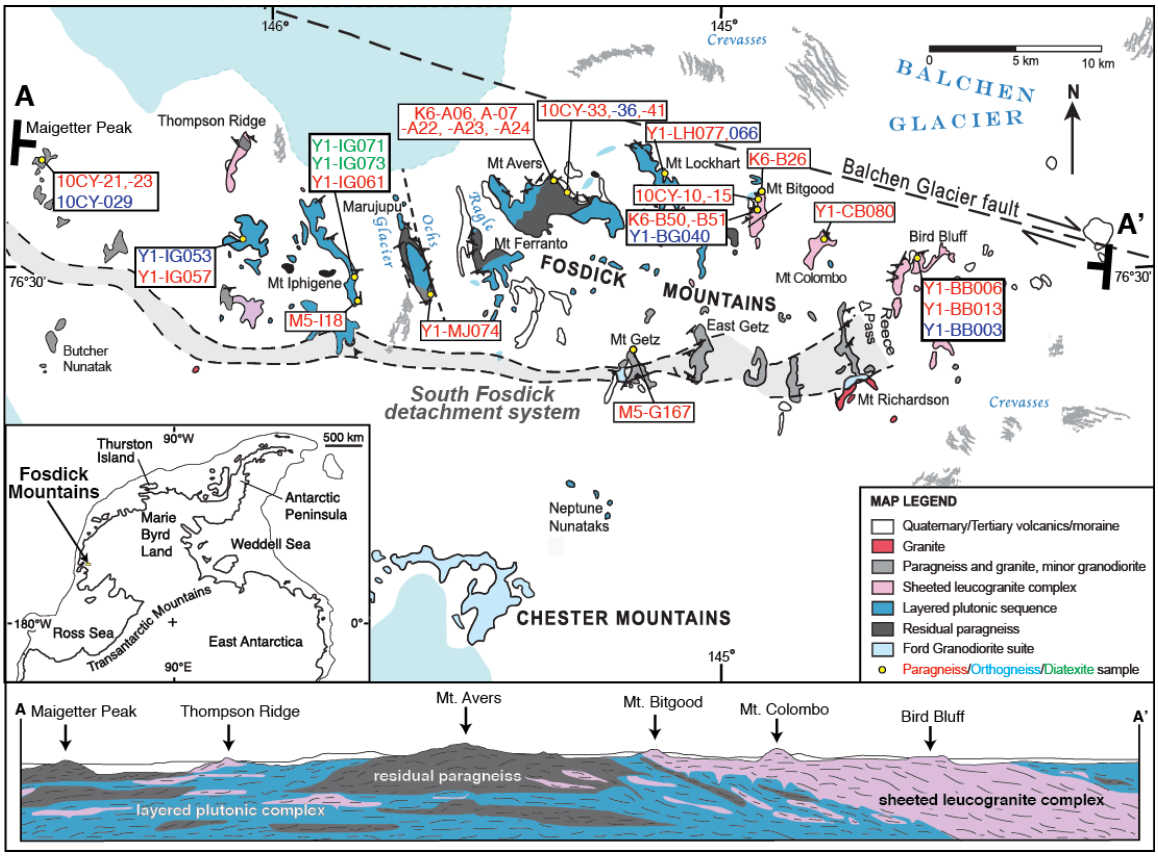

Fig. 2.2. Geological map and schematic cross-section of the Fosdick migmatite–granite complex. Sampling locations of migmatitic paragneisses, orthogneisses and diatexites are labelled.

the high-grade metamorphosed equivalents of the Swanson Formation (Korhonen *et al.*, 2010b; Yakymchuk *et al.*, 2013a, 2014; Brown *et al.*, 2014). Orthogneisses contain zircons that yield U–Pb ages that overlap those for the Ford Granodiorite suite and have whole-rock compositions, including εNd and $^{87}Sr/^{86}Sr$ values, and zircon Hf and O isotope compositions compatible with a Ford Granodiorite suite protolith (Siddoway *et al.*, 2004; Korhonen *et al*., 2010b; Yakymchuk *et al.,* 2013a, Brown *et al*., 2014).

The Fosdick complex comprises several lithological units that consist of similar rock types but in different proportions. In the western and central Fosdick Mountains, at deeper structural levels in the complex, a layered plutonic sequence dominates much of the outcrop from Mt Iphigene to Mt Lockhart (Fig. 2.2). This unit is composed of 10 m- to 100 m-thick sheets of migmatitic orthogneiss and m- to dam-thick sheets of granite, granodiorite and diorite, with minor m- to 10 m-thick layers of migmatitic paragneiss. At Maigetter Peak in the extreme west of the study area (Fig. 2.2) and around Mt Avers in the centre, a thick unit of residual paragneiss dominates the outcrops and orthogneisses are rare (Korhonen *et al.*, 2010*a*; McFadden *et al*., 2010*a*; Yakymchuk *et al.*, 2013*b*). In these locations, thick concordant granite sheets are rare and discordant granite bodies of variable thickness are common. In the eastern Fosdick Mountains, at shallower structural levels, a sheeted leucogranite complex dominates the outcrop from Mt Bitgood to Bird Bluff (Fig. 2.2). This unit is composed of up to 100 m-thick subhorizontal leucogranites interlayered with 1–10 m-thick migmatitic paragneiss and orthogneiss horizons. Cretaceous mafic dykes in this unit are generally folded and boudinaged (Siddoway *et al*., 2005; McFadden *et al*., 2010*b*; Saito *et al.*, 2013).

2.3.2.2 Metamorphism

Based on U–Pb zircon ages from granites and U–Pb monazite ages from migmatitic gneisses, two episodes of regional metamorphism are inferred to have affected the Fosdick complex, one related to arc magmatism in the Devonian–Carboniferous and a second higher-grade event related to crustal thickening in the Cretaceous (Siddoway *et al.*, 2004; Korhonen *et al.*, 2010a, b, 2012; Brown *et al*., 2014; Yakymchuk *et al*., 2014). However, petrographic evidence of the Devonian–Carboniferous metamorphism is cryptic due to the Cretaceous overprint; it is primarily preserved in deeper structural levels of the complex exposed in the western and central Fosdick Mountains, where it is unambiguously recorded in Carboniferous age cores in monazite grains. By contrast, although the Cretaceous event is pervasive throughout the Fosdick complex, it is dominant at shallower structural levels in the east, where evidence of the earlier event in monazite is rare.

Devonian–Carboniferous metamorphism is recorded by core domains of monazite in paragneiss that yield U–Pb dates of 376–302 Ma (Korhonen *et al*., 2012). These ages overlap, but also slightly post-date the emplacement of the Ford Granodiorite suite (Yakymchuk *et al.*, 2014). The *P–T* conditions of this metamorphism have proven difficult to constrain due to uncertainty about the age of garnet growth and whether garnet was part of the Devonian–Carboniferous mineral paragenesis. Monazite associated with relict garnet or occurring as inclusions in garnet yielded U–Pb ages of 331–314 Ma from core domains but Cretaceous ages from rims (Korhonen *et al*., 2012). Garnet from migmatitic paragneisses and one migmatitic orthogneiss yielded Sm–Nd model ages of 102–99 Ma, which Korhonen *et al.* (2012) interpreted to record diffusional resetting of

Devonian–Carboniferous garnet during the Cretaceous. Based on this interpretation, the Devonian–Carboniferous *P–T* conditions were estimated to have been 820–870°C at 0.75–1.15 GPa (Korhonen *et al.*, 2010a, 2012). However, if garnet was not part of the Devonian–Carboniferous mineral paragenesis, then metamorphic temperatures are expected to have been significantly lower.

Cretaceous metamorphism is pervasive throughout the Fosdick complex. Using phase equilibria modelling of paragneiss and orthogneiss bulk compositions and assuming that Devonian–Carboniferous garnet was fully re-equilibrated during the Cretaceous, Korhonen *et al.* (2010a, 2012) constrained Cretaceous metamorphic conditions to 830–870°C at 0.60–0.75 GPa. U–Pb ages retrieved from monazite rims in migmatitic paragneisses range from 111 to 96 Ma (Korhonen *et al.*, 2012) and associated anatectic granites yielded U–Pb zircon ages of 115–100 Ma, with most between 107 and 100 Ma (Brown *et al.*, 2014). Two microgranites that crosscut the migmatitic fabrics yielded U–Pb zircon ages of *c.* 96 and 97 Ma (McFadden *et al.*, 2010a; Yakymchuk *et al.*, 2013a). This suggests that migmatites were below their solidi at this time, which is further supported by $^{40}Ar/^{39}Ar$ ages of hornblende, biotite, muscovite and K-feldspar from the Fosdick complex that yield ages ranging from 102 to 95 Ma (Richard *et al.*, 1994).

2.4 Petrography

2.4.1 Migmatitic paragneiss

Migmatitic paragneisses have a similar appearance in outcrop throughout the Fosdick complex. They are characterized by sub-horizontal stromatic layering, which is

generally parallel to alternating thicker metapelite layers, up to several tens of centimeters thick, and thinner metapsammite layers inferred to represent primary compositional layering inherited from the protolith (Fig. 2.3a). Leucosomes, which are concentrated in the metapelite layers, are between 0.1 and 30 cm thick and comprise 43–72 vol. % of the outcrop (Yakymchuk *et al.,* 2013b).

Paragneisses contain similar mineral assemblages and microstructures throughout the complex. Melanosomes are finer grained than leucosomes and typically contain biotite, quartz, cordierite, garnet, sillimanite, plagioclase, K-feldspar, ilmenite with or without magnetite. A strong grain-shape fabric is defined by aligned biotite and elongate cordierite. Leucosomes contain variable proportions of quartz, plagioclase and K-feldspar with or without biotite, garnet and cordierite (Fig. 2.3b). Trace amounts of late muscovite and chlorite are found in or adjacent to the leucosome component of the migmatites. Monazite, zircon and apatite occur in both leucosomes and melanosomes, where they are found as inclusions in rock-forming minerals or along grain boundaries.

Garnet is present in both leucosomes and melanosomes (Fig. 2.3a). In the leucosomes, garnet contains vermicular inclusions of quartz and rounded biotite grains, consistent with peritectic growth (Waters, 2001). In some cases, skeletal biotite–quartz intergrowths occur at the margin of these garnets (Fig. 2.3c), which suggests reaction of garnet with residual melt trapped along grain boundaries during cooling to the solidus (Waters, 2001). In the melanosome, coarse-grained garnet may contain aligned inclusions of fine-grained sillimanite (Fig. 2.3d), whereas fine-grained garnet is typically inclusion-free. Garnet in contact with cordierite is embayed (Fig. 2.3b, d) and partially resorbed garnet may be surrounded by coronae of cordierite.

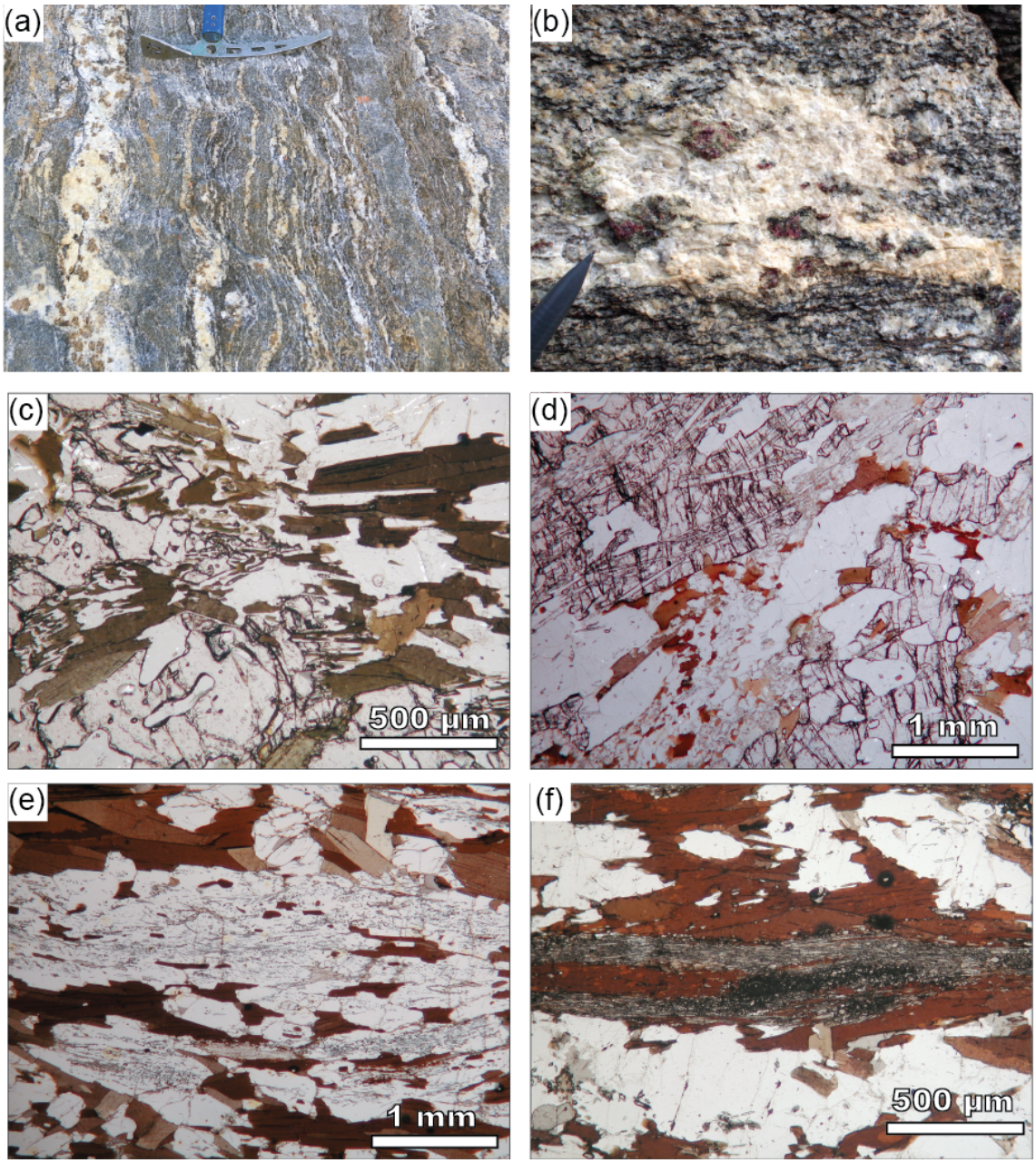

Fig. 2.3. (a) Paragneiss with stromatic layering and garnet spatially associated with leucosome. (b) Garnet in leucosome with evidence of patchy replacement by cordierite (green) and biotite. (c) Skeletal biotite–quartz intergrowth associated with the margin of garnet in paragneiss (sample 10CY-010). (d) Cordierite with relict garnet and aligned inclusions of sillimanite (10CY-023). (e) Sillimanite inclusions in cordierite with resorbed biotite (sample Y1-BB0013). (f) Sillimanite–biotite aggregate in a paragneiss (sample 10CY-021).

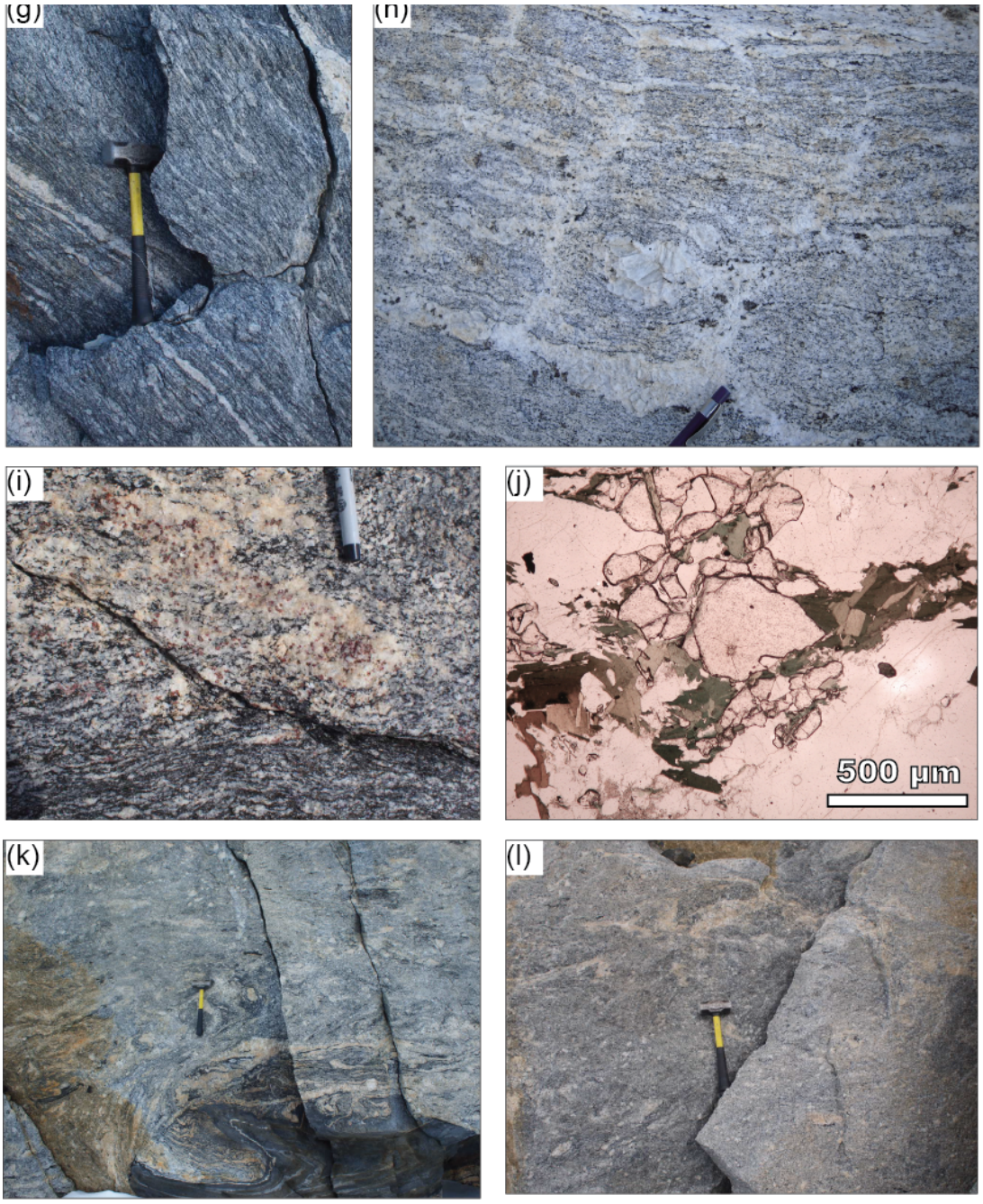

Fig. 2.3 continued. (g) Well-foliated garnet-bearing stromatic orthogneiss (sample Y1-LH066). (h) Light grey orthogneiss with discordant leucosome (sample 10CY-029). (i) Peritectic garnet in leucosome in an orthogneiss (sample Y1-IG053). (j) Well-armoured inclusion of monazite in garnet (sample Y1-LH066, monazite grain B.8). The margins of garnet are embayed when in contact with biotite. (k) Inhomogeneous diatexite with biotite-rich schlieren and a swirling foliation (sample Y1-IG071). (l) Homogeneous diatexite (sample Y1-IG073).

Cordierite occurs as elongate porphyroblasts (1–10 mm in length) in the melanosome, sometimes with aligned inclusions of sillimanite (Fig. 2.3e). It is less commonly found in the leucosome as coarse-grained irregular grains that are strongly pinnitized.

Sillimanite is found in all samples of migmatitic paragneiss, but most commonly it occurs as inclusions in cordierite (Fig. 2.3e) and garnet (Fig. 2.3d), and as fine-grained needles in quartz and feldspar. In samples from the sheeted leucogranite complex in the east, sillimanite is only present as inclusions in garnet and cordierite. In these rocks, sillimanite growth may have been concomitant with garnet growth (Vernon *et al.*, 2008), and is inferred to be relict in cordierite. This suggests that sillimanite is not part of the final solidus assemblage, which comprises cordierite, biotite, garnet, quartz, plagioclase, K-feldspar and ilmenite (with or without magnetite) with melt. Biotite–sillimanite aggregates are present in the melanosome of some samples (Fig. 2.3f) from the residual paragneiss unit and layered plutonic complex in the central and western sectors of the Fosdick complex, suggesting that sillimanite was an additional mineral in the solidus phase assemblage deeper in the complex.

2.4.2 Migmatitic orthogneiss

Stromatic migmatitic orthogneisses are divided into two groups based on appearance in outcrop. One group comprises dark grey orthogneisses with proportionally more biotite that defines a strong foliation (Fig. 2.3g; Y1-IG053, Y1-LH066, Y1-BB003, Y1-BG040), whereas a second group comprises light grey orthogneisses with proportionally less biotite and a larger volume of leucosome (Fig. 2.3h; 10CY-036,

10CY-029). In both groups, individual leucosomes, which are continuous over >20 cm, range from a few millimetres up to two metres in thickness. Although most leucosomes are parallel to the foliation, discordant leucosomes do occur, particularly in the light grey orthogneisses (Yakymchuk *et al.*, 2013b).

The migmatitic orthogneisses all have a similar mineral assemblage and microstructure. Garnets up to 4 cm across occur in both leucosome and melanosome; they may contain vermicular quartz inclusions or be inclusion free, and may show embayed margins when in contact with biotite (Fig. 2.3j). Commonly garnet is spatially associated with leucosome pods, consistent with a peritectic origin (Fig. 2.3i). Cordierite occurs in leucosomes less commonly than in melanosomes but is more commonly associated with discordant rather then stromatic leucosomes. Biotite occurs as isolated grains distributed throughout the matrix and as schliere parallel to the stromatic layering. Less commonly, schliere comprise fine-grained biotite with a shredded appearance and minor sillimanite. Monazite, zircon, and apatite are present in both leucosome and melanosome, where they are found as inclusions in rock-forming minerals or along grain boundaries. The solidus phase assemblage is interpreted include to garnet, biotite, quartz, plagioclase, K-feldspar and ilmenite with melt.

2.4.3 Diatexites

Diatexite migmatites are found in the structurally deepest portions of the Fosdick complex at Mt Iphigene (Siddoway *et al.*, 2004). In central Mt Iphigene, a representative diatexite body in migmatitic paragneiss grades from inhomogeneous diatexite near the margin to homogeneous diatexite towards the centre. Inhomogeneous diatexite contains

discontinuous rafts of paragneiss, megacrysts of feldspar, biotite-rich schlieren, and an irregular foliation (Fig. 2.3k). Homogeneous diatexite contains discrete biotite crystals and lacks rafts of paragneiss and schlieren (Fig. 2.3k). Both types of diatexite contain a solidus phase assemblage comprising quartz, plagioclase, K-feldspar and biotite with melt (with accessory ilmenite, zircon, monazite and apatite). In some cases, biotite is observed as rounded inclusions in plagioclase and quartz is found along grain boundaries as 'string of beads' microstructures. Both of these microstructures support an anatectic origin for the diatexites (e.g. Sawyer, 2010).

2.5 Geochemistry

2.5.1 Methods

Bulk chemical compositions of 12 paragneisses and 6 orthogneisses were determined by X-ray fluorescence analysis using a Panalytical 2404 XRF unit at Franklin and Marshall college following their standard procedures (Boyd and Mertzmann, 1987). An initial estimate of the H_2O wt% in each sample was obtained by loss on ignition. FeO contents were determined by Fe^{2+} titration and Fe_2O_3 contents were calculated by difference. The results are presented in Table 2.1 and plotted on a molar (Na+Ca)–(Fe*+Mg+Ti)–K diagram in Fig. 2.4 (Solar and Brown, 2001). Also plotted on Fig. 2.4 are the starting materials and glass compositions for melting experiments on materials similar to Ford Granodiorite suite and the Swanson Formation (Skjerlie *et al*., 1993; Patiño Douce and Harris, 1998; Koester *et al*., 2002). The experimental glasses from Skjerlie *et al.* (1993) represent analogues for melts derived from the Ford Granodiorite

Table 2.1 Compositions used for phase equilibria modeling

	Weight % (from XRF whole rock analyses)												
Sample	SiO_2	TiO_2	Al_2O_3	Fe_2O_3	FeO	MnO	MgO	CaO	Na_2O	K_2O	P_2O_5	LOI	Total
Paragneiss													
10CY-10	61.55	0.94	17.54	1.32	6.05	0.09	3.71	0.91	1.91	3.98	0.13	2.21	100.34
10CY-15	68.82	0.81	14.67	1.24	4.55	0.05	2.76	0.82	1.64	3.05	0.06	1.77	100.24
10CY-21	67.40	0.94	14.56	0.76	5.50	0.07	3.26	1.31	1.81	3.31	0.14	1.50	100.56
10CY-23	66.51	1.05	14.76	1.06	5.87	0.08	3.59	0.71	0.99	3.52	0.08	1.90	100.12
10CY-33	67.85	0.76	14.39	1.36	4.21	0.08	2.74	1.37	2.03	3.6	0.13	1.85	100.37
10CY-41	67.32	0.77	14.26	1.08	4.61	0.05	2.89	1.75	2.55	3.69	0.14	1.18	100.29
Y1-IG057	42.01	1.57	23.10	3.89	12.78	0.44	7.74	0.43	0.37	5.54	0.15	3.49	99.90
Y1-IG061	71.00	0.68	14.34	0.94	4.34	0.09	2.45	1.17	1.43	3.42	0.19	2.22	99.11
Y1-LH077	69.59	0.76	13.58	1.06	4.17	0.04	2.90	2.22	2.21	2.89	0.18	1.42	99.94
Y1-CB080	70.39	0.76	13.15	0.67	5.04	0.08	3.00	1.75	1.85	2.61	0.19	1.69	99.81
Orthogneiss													
10CY-036	73.02	0.26	14.22	0.42	1.47	0.04	0.75	1.80	3.18	4.19	0.07	0.49	99.91
10CY-029	71.95	0.20	14.80	0.54	1.47	0.05	0.73	1.43	2.79	5.22	0.10	0.58	99.86
Y1-IG053	65.51	0.89	16.60	1.03	3.86	0.07	2.02	3.95	3.40	2.20	0.30	1.01	100.84
Y1-LH066	68.77	0.70	14.52	0.52	3.60	0.07	1.60	1.78	3.09	4.08	0.24	0.80	99.77
Y1-BG040	71.23	0.29	15.49	0.39	1.48	0.05	0.87	1.78	4.12	3.27	0.10	0.82	99.89
Y1-BB003	70.88	0.51	14.77	0.69	2.47	0.05	1.11	1.59	2.80	4.65	0.21	0.69	100.42
Diatexite													
Y1-IG071	72.88	0.46	13.91	0.49	2.51	0.04	1.36	1.63	2.72	4.16	0.08	1.06	101.30

		Normalized molar proportions (mol.%)										
Sample	Figure	H_2O	SiO_2	Al_2O_3	CaO	MgO	FeO	K_2O	Na_2O	TiO_2	O	Total
Paragneiss												
10CY-10	2.16b	1.15	67.58	11.35	1.07	6.07	6.64	2.79	2.03	0.78	0.55	100
10CY-15	2.16b	0.92	74.27	9.34	0.95	4.44	5.11	2.10	1.72	0.65	0.51	100
10CY-21	2.14d, 2.16b	1.04	72.29	9.20	1.51	5.21	5.54	2.26	1.88	0.76	0.31	100
10CY-23	2.14a, 2.16b, 2.17a	1.82	71.43	9.34	0.82	5.75	6.13	2.41	1.03	0.85	0.43	100
10CY-33	2.14f, 2.16b	1.14	73.23	9.15	1.58	4.41	4.90	2.48	2.12	0.61	0.37	100
10CY-41	2.16b	1.64	71.68	8.94	2.00	4.58	4.96	2.50	2.64	0.62	0.43	100
Y1-IG057	2.14b, 2.16b	4.34	45.79	14.83	0.50	12.58	14.83	3.85	0.39	1.29	1.59	100
Y1-IG061	2.14c, 2.16b	0.75	75.68	9.01	1.34	3.89	4.62	2.33	1.48	0.55	0.38	100
Y1-LH077	2.14e, 2.16b	1.69	73.15	8.41	2.50	4.54	4.50	1.94	2.25	0.60	0.42	100
Y1-CB080	2.16b	1.15	74.43	8.19	1.98	4.73	4.99	1.76	1.90	0.61	0.27	100
Orthogneiss												
10CY-036	2.15c, 2.16c	0.70	78.73	9.04	2.08	1.21	1.66	2.88	3.32	0.21	0.17	100
10CY-029	2.15b, 2.16c	0.34	78.53	9.52	1.67	1.19	1.78	3.63	2.95	0.16	0.22	100
Y1-IG053	2.15a, 2.16c, 2.17c	1.59	69.84	10.43	4.51	3.21	4.26	1.50	3.52	0.71	0.42	100
Y1-LH066	2.15d, 2.16c	1.68	74.02	9.21	2.05	2.57	3.66	2.80	3.23	0.57	0.21	100
Y1-BG040	2.16c	0.73	77.25	9.90	2.07	1.41	1.66	2.26	4.34	0.24	0.15	100
Y1-BB003	2.16c	0.98	76.41	9.38	1.84	1.79	2.79	3.20	2.92	0.42	0.28	100
Diatexite												
Y1-IG071	2.16a	1.56	77.03	8.66	1.85	2.14	2.61	2.81	2.79	0.37	0.20	100
Melt reintegrated compositions												
10CY-23	2.17b	5.27	70.49	9.08	0.75	4.46	4.82	2.64	1.51	0.65	0.33	100
Y1-IG053	2.17d	2.29	69.71	10.30	4.33	3.08	4.13	1.59	3.49	0.68	0.40	100

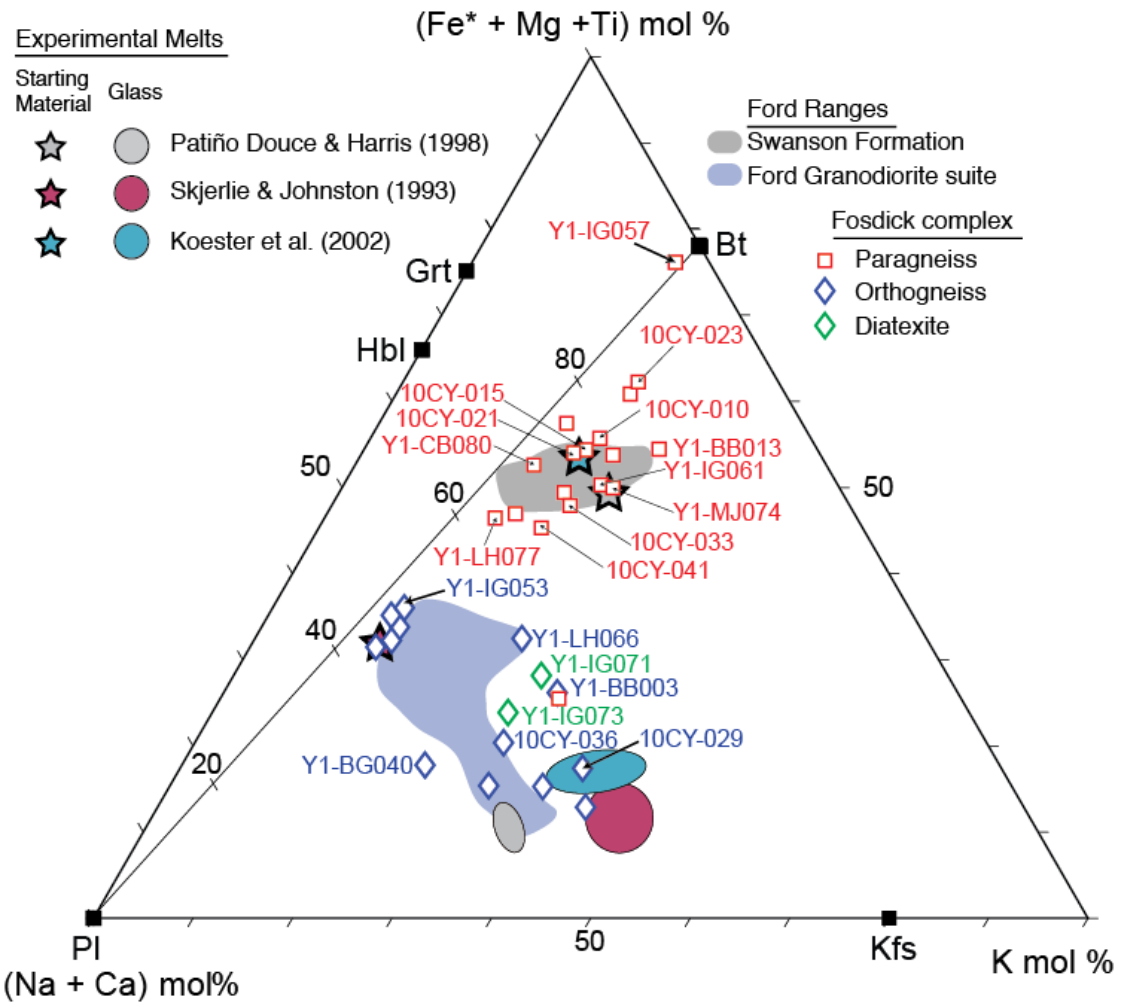

Fig. 2.4. (Fe* + Mg + Ti)–K–(Na + Ca) ternary diagram (after Solar and Brown, 2001) illustrating the compositional variability of paragneisses, orthogneisses, diatexites, the Ford Granodiorite suite and the Swanson Formation. Data from Korhonen *et al.* (2010a, b), Brown *et al.* (2014) and this study.

suite while the experimental glasses from Patiño Douce and Harris (1998) and Koester *et al.* (2002) represent analogues for melts derived from the Swanson Formation.

2.5.2 Migmatitic paragneisses

Whole rock chemical data for twelve samples of migmatitic paragneiss from across the Fosdick complex (Fig. 2.2) are combined with published data for an additional six samples (from Korhonen *et al.*, 2010a, b) to investigate the compositional variability of the paragneisses. In Fig. 2.4, migmatitic paragneiss compositions cluster around the compositional range for the Swanson Formation. Four paragneiss samples have lower Fe*+Mg+Ti and five samples have higher Fe*+Mg+Ti values than the Swanson Formation. The chemistry of the five samples that plot towards the Fe*+Mg+Ti apex in Fig. 2.4 are consistent with the loss of anatectic melt with a composition similar to the experimental glasses of Patiño Douce and Harris (1998) and Koester *et al.* (2002). Four samples that plot at lower Fe*+Mg+Ti values than the Swanson Formation have chemical compositions compatible with the early crystallization and accumulation of plagioclase from anatectic melt with a similar composition to the same glasses (Fig. 2.4).

2.5.3 Migmatitic orthogneisses

Whole rock chemical data for six samples of migmatitic orthogneiss from across the complex (Fig. 2.2) are combined with published data for an additional seven orthogneiss samples (three from Korhonen *et al.*, 2010a, b and four from Brown *et al.*, 2014) to investigate the compositional variability of the orthogneisses. In Fig. 2.4, the orthogneisses plot as two groups, One tightly-clustered group plots between the biotite–

plagioclase tie line and the most juvenile Ford Granodiorite suite compositions, close to the starting composition used by Skjerlie and Johnston (1993) in their experiments, whereas a second more variable group plots with the more evolved Ford Granodiorite suite compositions towards the experimental glass compositions. The five samples that comprise the first group plot just outside or at the edge of the compositional field for the Ford Granodiorite suite and away from the experimental glass compositions, consistent with the loss of anatectic melt with a composition similar to the glass compositions from the experiments of Skjerlie and Johnston (1993). Seven samples from the second group plot between the compositional range of the Ford Granodiorite suite and the experimental glass compositions in general (Fig. 2.4), consistent with the accumulation and/or retention of anatectic melt. The composition of sample Y1-BG040 plots outside the Ford Granodiorite suite field towards the plagioclase apex (Fig. 2.4), which suggests the early crystallization and accumulation of plagioclase from anatectic melt, and the last sample plots close to the feldspar edge of the phase diagram on the K-feldspar side (Fig. 2.4).

2.5.4 Diatexite

The two samples of diatexite migmatite from central Mt Iphigene (Fig. 2.2) have compositions that plot between the Ford Granodiorite suite field and the experimental melt compositions (Fig. 2.4), suggesting some addition of anatectic melt to Ford Granodiorite suite protoliths.

2.6 Garnet REE chemistry and Lu–Hf geochronology

2.6.1 Analytical Methods

Eight samples from across the Fosdick complex were chosen for REE analysis of garnets by LA-ICP-MS and Lu–Hf garnet geochronology (Fig. 2.5). They include 5 migmatitic paragneisses (K6-B51, K6-A24, Y1-IG061, Y1-IG057, 10CY-021), 2 migmatitic orthogneisses (K6-B51 and Y1-IG053) and one garnet-bearing granite (Y1-IG062). Garnet in thin section was analysed for the REE using an Agilent 7700s ICP–MS equipped with a Resonetic RESOlution M-50 193 nm ArF laser at the Geohistory Laboratory, Curtin University. Beam diameter was set at 50 μm. Count rates were normalized using ^{29}Si as the internal standard and two external standards were used (NIST-610 and -612). Data were reduced using the Iolite software package (v. 2.0, Paton *et al.*, 2011). Data are presented in Table A.1 of Appendix A.

For Lu–Hf garnet geochronology, garnet was separated from whole-rock samples using standard crushing and magnetic separation techniques at the mineral separation facility at the University of Maryland. Garnet fractions were then hand picked under a binocular microscope to obtain optically clear mineral separates free of visible inclusions.

Lu and Hf isotope analysis was conducted at Washington State University. Purified mineral fractions for geochronology were digested using tabletop dissolution in Savillex beakers to avoid incorporation of Hf from refractory mineral inclusions such as zircon (Scherer *et al.*, 2000). For each sample, one whole-rock fraction was dissolved using tabletop dissolution and a second whole-rock fraction was dissolved in Par-Bombs in an oven at 180°C for 72 hours. For each garnet separate, ~250 mg of garnet was weighed into Savillex Teflon beakers and put on a hot plate at 150°C for 24 hours. The

liquid was pipetted into Par-Bombs leaving residual material behind and was placed in an oven for 24 hours at 180°C. The chromatographic procedure for Lu and Hf separation is described in detail by Cheng *et al.* (2008) and Zirakparvar *et al.* (2010a).

All isotopic data were analysed using the ThermoFinnigan Neptune MC-ICP-MS at Washington State University. Procedures for analysis and data reduction of Lu and Hf isotopes are described in detail elsewhere (Vervoort *et al.*, 2004). Hf data were measured relative to the Hf external standard JMC 475. Final Hf solutions of unknowns were concentration matched to JMC 475 Hf standard solutions prior to determination of isotope ratios. Isotope ratios of unknowns were normalized to $^{179}Hf/^{177}Hf$ of 0.7325 using an exponential fitting curve. Individual analytical sessions were further normalized to the accepted $^{176}Hf/^{177}Hf$ ratio of JMC 475 (0.282160). The overall external uncertainties applied to measured data were 1% for $^{176}Lu/^{177}Hf$ and 0.01% for $^{176}Hf/^{177}Hf$, as encountered during the long-term reproducibility of external rock standards. Lu–Hf ages were calculated using the ^{176}Lu decay constant value of 1.867×10^{-11} yr^{-1} (Scherer et al., 2001; Söderlund et al., 2004). Lu–Hf isochron diagrams were produced with the program Isoplot/Ex (Ludwig, 2003) with errors at the 95% confidence level. Data are presented in Table 2.2.

2.6.2 Results

2.6.2.1 Garnet REE zoning

Representative Lu and Sm transects along with chondrite-normalized REE plots of garnet from paragneiss, orthogneiss and the granite are shown in Fig. 2.5. Lutetium concentrations and zoning in garnet within and between samples are highly variable whereas Sm zoning is nearly flat and concentrations are <1 ppm for all samples with the

Table 2.2 Lu and Hf isotope results

Sample	Lu (ppm)	Hf (ppm)	$^{176}Lu/^{177}Hf$	$^{176}Hf/^{177}Hf$	±
K6-A24; migmatitic paragneiss; Mt Avers					
K6-A24-WR-B1	0.405	7.035	0.008	0.282361	5
K6-A24-WR-S1	0.336	0.560	0.085	0.282549	7
K6-A24-G2	9.580	0.283	4.818	0.292388	5
K6-A24-G3	9.277	0.302	4.360	0.291727	12
K6-A24-G4	10.886	0.288	5.368	0.293798	6
Y1-IG057; migmatitic paragneiss; Mt Iphigene					
Y1-IG057-WR-B1	1.693	4.851	0.050	0.282552	4
Y1-IG057-WR-S1	1.322	0.752	0.249	0.282978	5
Y1-IG057-G1	5.900	0.642	1.304	0.285136	5
Y1-IG057-G2	5.335	0.612	1.236	0.285106	6
Y1-IG057-G3	5.408	0.643	1.193	0.284982	5
Y1-IG057-G4	4.396	0.613	1.018	0.284667	5
K6-B26; migmatitic paragneiss; Mt Bitgood					
K6-B26-WR-B1	0.202	5.872	0.005	0.282522	6
K6-B26-WR-S1	0.167	0.816	0.029	0.282595	5
K6-B26-G1	5.168	0.576	1.273	0.285108	5
K6-B26-G2	5.354	0.663	1.147	0.284920	6
K6-B26-G3	6.480	0.528	1.742	0.286429	6
K6-B26-G4	7.243	0.592	1.736	0.286136	5
Y1-IG062; garnet granite; Mt Iphigene					
Y1-IG062-WR-B1	0.597	2.023	0.042	0.282662	6
Y1-IG062-WR-S1	0.627	0.908	0.098	0.282788	7
Y1-IG062-G1	21.970	2.621	1.190	0.286586	6
Y1-IG062-G2	24.074	2.157	1.585	0.287505	6
Y1-IG062-G3	23.359	2.112	1.571	0.287489	7
Y1-IG062-G4	23.907	2.063	1.645	0.287646	5
K6-B51; migmatitic orthogneiss; Mt Bitgood					
K6-B51-WR-B1	1.593	5.924	0.038	0.282409	4
K6-B51-WR-S1	0.163	0.742	0.031	0.282611	6
K6-B51-G1	10.325	0.608	2.410	0.287377	6
K6-B51-G2	10.005	0.609	2.334	0.287211	5
K6-B51-G3	10.134	0.585	2.460	0.287557	7
K6-B51-G4	9.893	0.637	2.205	0.286868	5
Y1-IG061; migmatitic paragneiss; Mt Iphigene					
Y1-IG061-WR-B1	0.563	5.412	0.015	0.282383	5
Y1-IG061-WR-S1	0.526	0.404	0.185	0.282785	5
Y1-IG061-G1	7.845	0.346	3.216	0.289100	5
Y1-IG061-G2	8.483	0.366	3.291	0.289040	6
Y1-IG061-G3	7.886	0.339	3.305	0.289309	5
Y1-IG061-G4	7.268	0.347	2.975	0.288798	6
10CY-21; migmatitic paragneiss; Maigetter Peak					
10CY-21-WR-B1	0.468	7.735	0.009	0.282364	6
10CY-21-WR-S1	0.371	0.750	0.070	0.282573	7
10CY-21-G1	10.667	0.440	3.444	0.289884	7
10CY-21-G2	11.103	0.455	3.467	0.289877	7
10CY-21-G3	10.821	0.443	3.468	0.289761	6
10CY-21-G4	10.651	0.458	3.305	0.289585	6
Y1-IG053; migmatitic orthogneiss; Mt Iphigene					
Y1-IG053-WR-B1	0.241	5.498	0.006	0.282511	4
Y1-IG053-WR-S1	0.208	0.667	0.044	0.282611	6
Y1-IG053-G1	4.191	0.537	1.108	0.284889	6
Y1-IG053-G2	4.421	0.529	1.187	0.285060	6
Y1-IG053-G3	4.002	0.496	1.145	0.285032	6
Y1-IG053-G4	4.043	0.500	1.148	0.284914	7

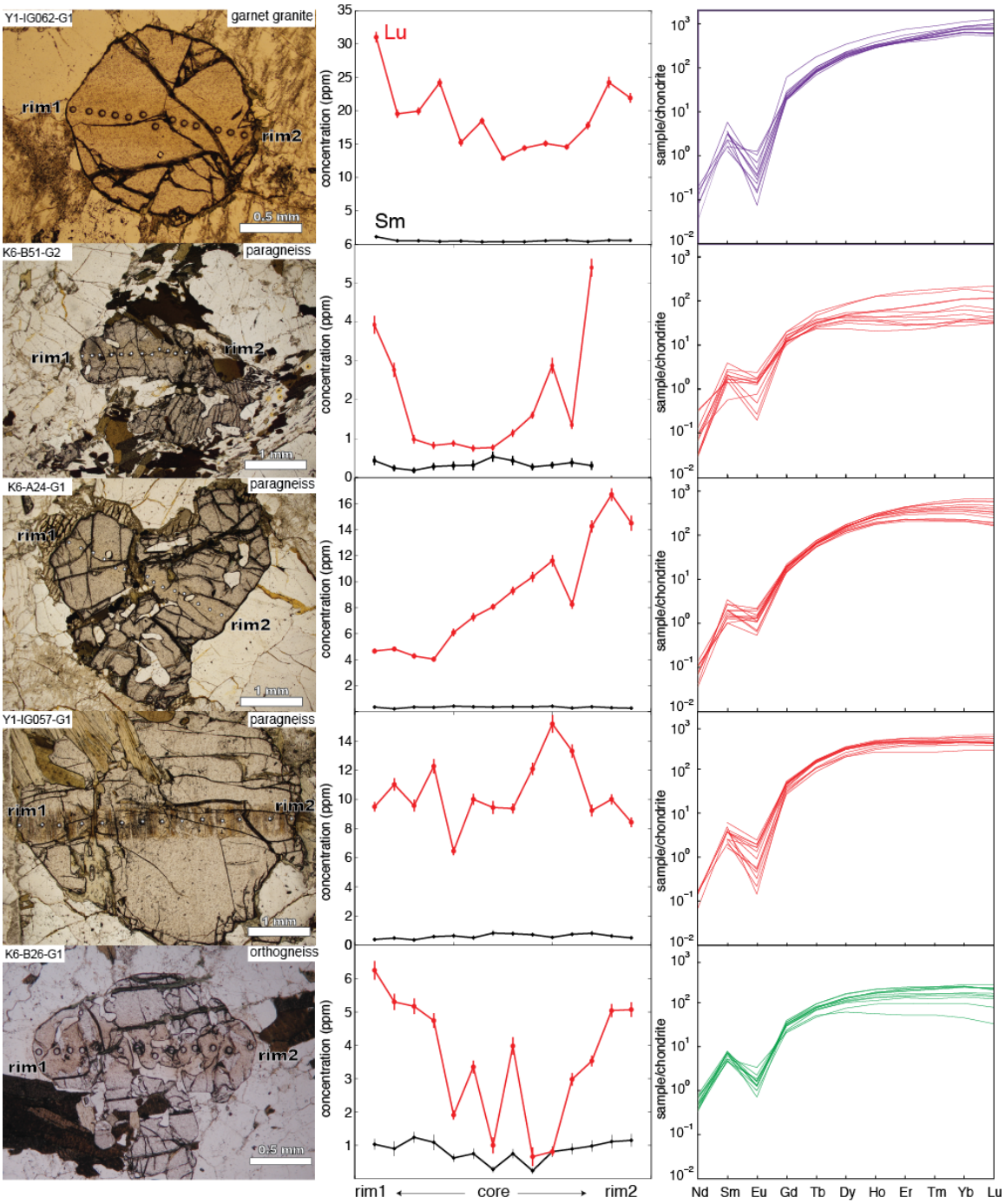

Fig. 2.5. Representative garnet REE traverses and chondrite normalized patterns (McDonough and Sun, 1995).

exception of the granite (Fig. 2.5). The most common zoning pattern for Lu shows rims that are enriched in Lu relative to cores. This zoning pattern is observed in both euhedral garnet grains (e.g. Y1-IG062 and K6-B26 in Fig. 2.5) as well as garnet grains that show embayed margins consistent with resorption (e.g. K6-B51 in Fig. 2.5). None of the analysed garnet grains show cores that are strongly Lu enriched relative to their rims. All analysed garnet grains show chondrite-normalized REE patterns with negative Eu anomalies and elevated HREE (Fig. 2.5).

2.6.2.2 Lu–Hf geochronology

The analytical data is presented in Table 2.2 and the Lu and Hf isotope values are plotted in Fig. 2.6. Two ages are calculated for each sample: (1) the age from regression of the isotope data on the Lu–Hf isochron diagram, and (2) a weighted mean of 'model' ages. Model ages are based on linear regression between Lu–Hf isotope data for each garnet fraction and an initial $^{176}Hf/^{177}Hf$ ratio calculated from linear regression of the whole-rock and garnet fraction isotope values for each sample. The model ages show the variation between garnet fractions from each sample used to calculate the isochron ages. Both of these ages are indistinguishable in this dataset.

For the paragneisses, sample 10CY-021 yields a Lu–Hf age of 115.6 ± 2.9 (MSWD = 13) with an initial $^{176}Hf/^{177}Hf$ of 0.28238 ± 15 ($\varepsilon_{Hf(115\ Ma)}$ = -12 ± 6) derived from four garnet fractions and two whole-rock fractions. Sample Y1-IG057 yields a Lu–

Fig. 2.6. Garnet Lu–Hf isochron diagrams.

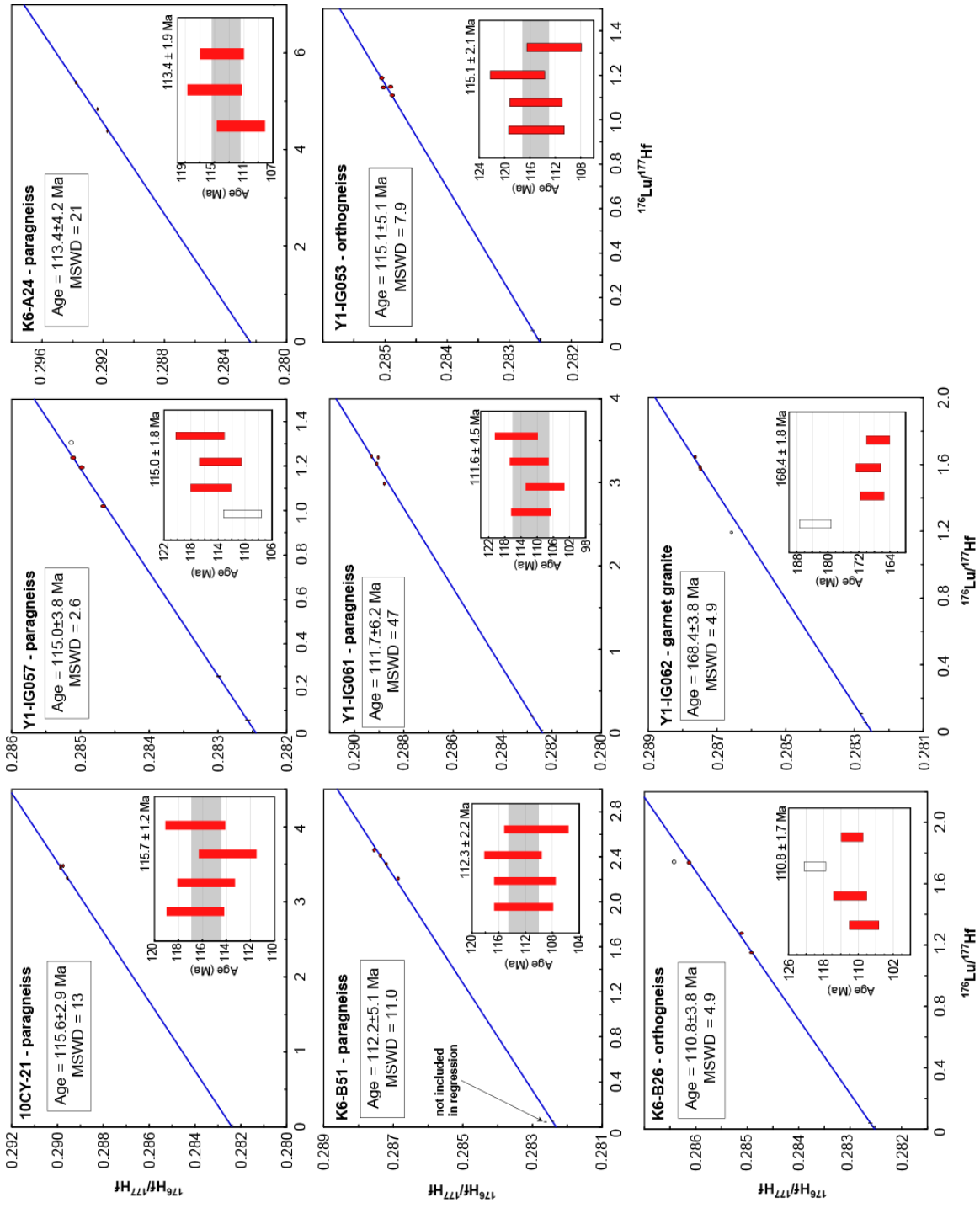
K6-A24 - paragneiss
Age = 113.4±4.2 Ma
MSWD = 21
113.4 ± 1.9 Ma
Y1-IG053 - orthogneiss
Age = 115.1±5.1 Ma
MSWD = 7.9
115.1 ± 2.1 Ma
Y1-IG057 - paragneiss
Age = 115.0±3.8 Ma
MSWD = 2.6
115.0 ± 1.8 Ma
Y1-IG061 - paragneiss
Age = 111.7±6.2 Ma
MSWD = 47
111.6 ± 4.5 Ma
Y1-IG062 - garnet granite
Age = 168.4±3.8 Ma
MSWD = 4.9
168.4 ± 1.8 Ma
10CY-21 - paragneiss
Age = 115.6±2.9 Ma
MSWD = 13
115.7 ± 1.2 Ma
K6-B51 - paragneiss
Age = 112.2±5.1 Ma
MSWD = 11.0
not included
in regression
112.3 ± 2.2 Ma
K6-B26 - orthogneiss
Age = 110.8±3.8 Ma
MSWD = 4.9
110.8 ± 1.7 Ma
Age (Ma)
176Hf/177Hf
176Lu/177Hf

Hf age of 115.0 ± 3.8 (MSWD = 2.6) with an initial $^{176}Hf/^{177}Hf$ of 0.282446 ± 63 ($\varepsilon_{Hf(115\ Ma)}$ = -9 ± 2) derived from three of four garnet fractions and two whole-rock fractions. Sample K6-A24 yields a Lu–Hf age of 113.4 ± 4.2 (MSWD = 21) with an initial $^{176}Hf/^{177}Hf$ of 0.28236 ± 30 ($\varepsilon_{Hf(115\ Ma)}$ = -12 ± 10) derived from three garnet fractions and two whole-rock fractions. Sample K6-B51 yields a Lu–Hf age of 112.2 ± 5.1 (MSWD = 11.0) with an initial $^{176}Hf/^{177}Hf$ of 0.28232 ± 20 ($\varepsilon_{Hf(115\ Ma)}$ = -14 ± 3) derived from four garnet fractions and one whole-rock fraction obtained by bomb dissolution. Sample Y1-IG061 yields a Lu–Hf age of 111.7 ± 6.2 (MSWD = 47) with an initial $^{176}Hf/^{177}Hf$ of 0.28239 ± 20 ($\varepsilon_{Hf(115\ Ma)}$ = -11 ± 10) derived from four garnet fractions and two whole-rock fractions.

For the orthogneisses, sample Y1-IG053 yields a Lu–Hf age of 115.1 ± 5.1 (MSWD = 7.9) with an initial $^{176}Hf/^{177}Hf$ of 0.282507 ± 88 ($\varepsilon_{Hf(115\ Ma)}$ = -7 ± 3) derived from four garnet fractions and two whole-rock fractions. Sample K6-B26 yields a Lu–Hf age of 110.8 ± 3.8 (MSWD = 4.9) with an initial $^{176}Hf/^{177}Hf$ of 0.282521 ± 77 ($\varepsilon_{Hf(115\ Ma)}$ = -7 ± 3) derived from three garnet fractions and the two whole-rock fractions.

Garnet granite sample Y1-IG062 yields a Lu–Hf age of 168.4 ± 1.8 (MSWD = 4.9) with an initial $^{176}Hf/^{177}Hf$ of 0.282506 ± 87 ($\varepsilon_{Hf(115\ Ma)}$ = -7 ± 3) from three of four garnet fractions and two whole-rock fractions. Brown et al. (2014) report zircon U–Pb dates for this sample that define Devonian–Carboniferous (393–324 Ma) and Cretaceous (114–98 Ma) populations. Therefore, the geological significance of the Lu–Hf garnet age, if any, is uncertain, and this sample is not considered further.

To summarize, paragneiss samples yield garnet Lu–Hf ages that range from *c.* 116 to 111 Ma and two orthogneiss samples yield ages of *c.* 115 and 111 Ma. For migmatitic

paragneisses and orthogneisses, these ages indicate that garnet growth occurred during Cretaceous metamorphism and that garnet is unlikely to have been part of the Devonian–Carboniferous metamorphic mineral paragenesis. Because cordierite partially replaces garnet in the migmatitic paragneisses (Fig. 2.3b, d), it is inferred to be part of the final Cretaceous metamorphic mineral paragenesis.

2.7 Monazite chemistry and geochronology

Monazite grains were identified in thin section using a backscatter electron detector. Wavelength dispersive X-ray element composition maps were collected using a JEOL JXA-8900R electron probe microanalyzer at the Center for Nanoscale Imaging, Spectroscopy and Properties Laboratory at the University of Maryland to identify homogenous compositional domains within each monazite grain. X-ray maps of U, Th, Pb, and Y were collected using an accelerating voltage of 15 kV, a 250 nA beam current and a beam diameter of 1–5 μm. Preliminary chemical dating and quantitative chemical analysis of monazite was conducted to target zones for SHRIMP analysis and to obtain quantitative chemical concentrations. For quantitative chemical analysis, the same operating conditions were used as those given above except that a constant beam diameter of 3 μm was used. The following analytical standards were used: synthetic REE and Y phosphate glasses, garnet 12442 for SiO_2, hornblende Kak for CaO, UO_2 for uranium, $PbCO_3$ for lead and $ThSiO_4$ for thorium. Multiple analyses of monazite standard GSC-8153 (506 ± 8 Ma; Reno *et al.*, 2012) were analysed between every ten to thirty unknown analyses. The complete analytical protocol for U–Th–Pb chemical dating is described in detail by Reno *et al.* (2012).

For SHRIMP U–Pb monazite geochronology of select samples, thin section fragments containing monazite were bored out, cast in 25 mm epoxy disks and coated with a thin membrane of gold. The India monazite standard Ind-1 (509 Ma, $^{206}Pb/^{238}U$=0.082133) was either included in the mounts or analysed on a separate mount. U–Pb isotope measurements were carried out using a SHRIMP-II at the John de Laeter Centre for Mass Spectrometry, Western Australia, and analysed with ~0.5 nA O_2 primary beam focused on to ~10 μm spots, a 5-scan duty cycle, and a mass resolution of ~5000. The complete analytical protocol is described in detail by Foster *et al.* (2000). Raw data were reduced using ISOPLOT 3 (Ludwig, 2003) and the SQUID 2 macro (Ludwig, 2001). The results of quantitative chemical analysis and U–Pb geochronology of monazite are presented in Table A.2 of Appendix A.

2.7.1 Migmatitic paragneisses

2.7.1.1 Monazite zoning

The grain sizes, Y zoning patterns and microstructural associations of monazite in the paragneisses are variable within and between samples. Monazite grains in thin section are typically <100 μm in length. The smallest grains are found as inclusions in the major rock-forming minerals, whereas the larger grains are commonly found along grain boundaries. Most monazites are spatially associated with biotite in the melanosome of the migmatitic paragneisses, either as inclusions or along grain boundaries between biotite and quartz, feldspar or cordierite. Chemical maps of Y zoning in monazite from a variety of microstructural settings are shown in Fig. 2.7a and b.

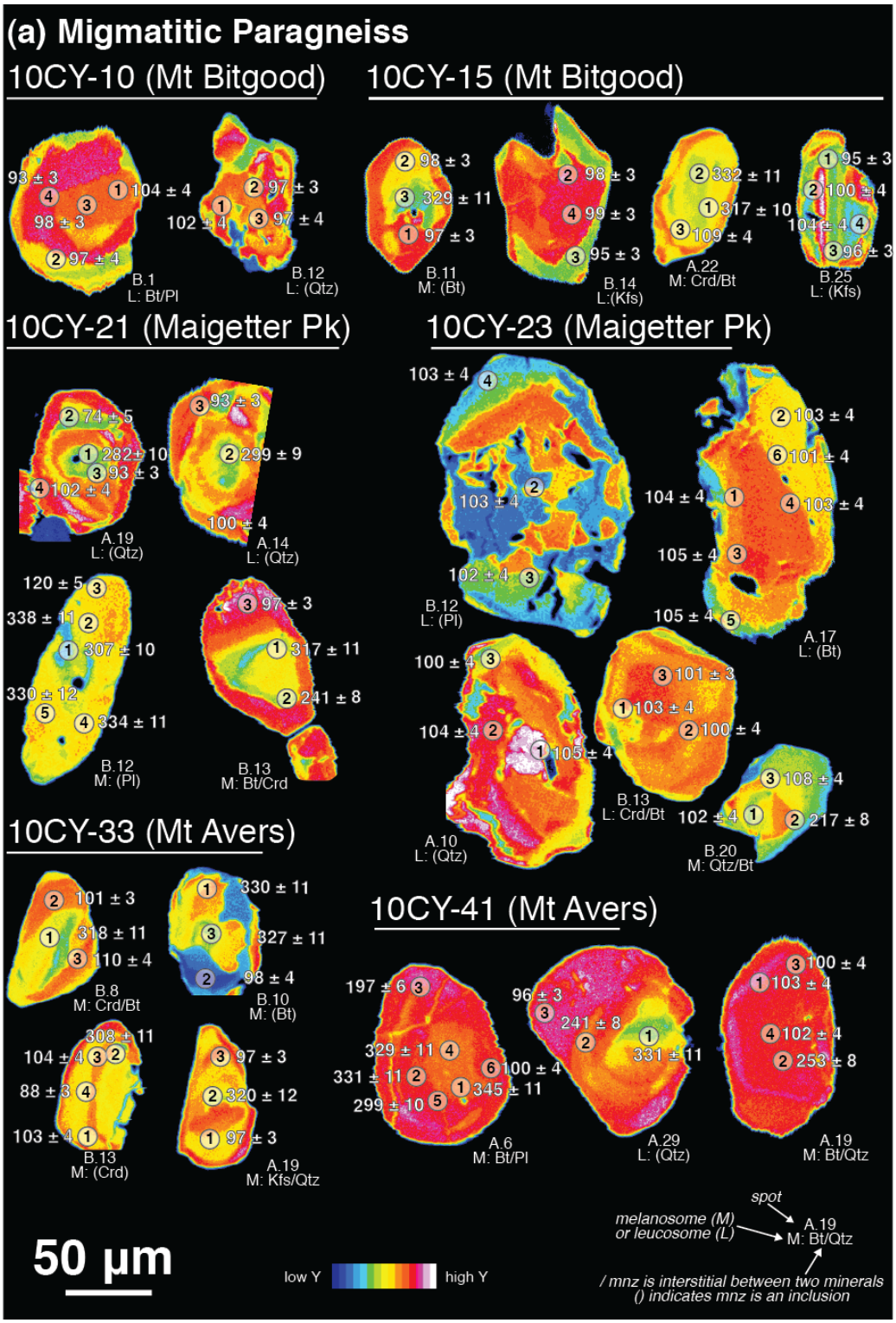

Fig. 2.7. Yttrium false colour X-ray compositional maps of monazite from paragneisses (a, b) and orthogneisses (c). SHRIMP analytical spots are indicated by ellipses and labelled with the $^{206}Pb/^{238}U$ dates and 1σ uncertainties.

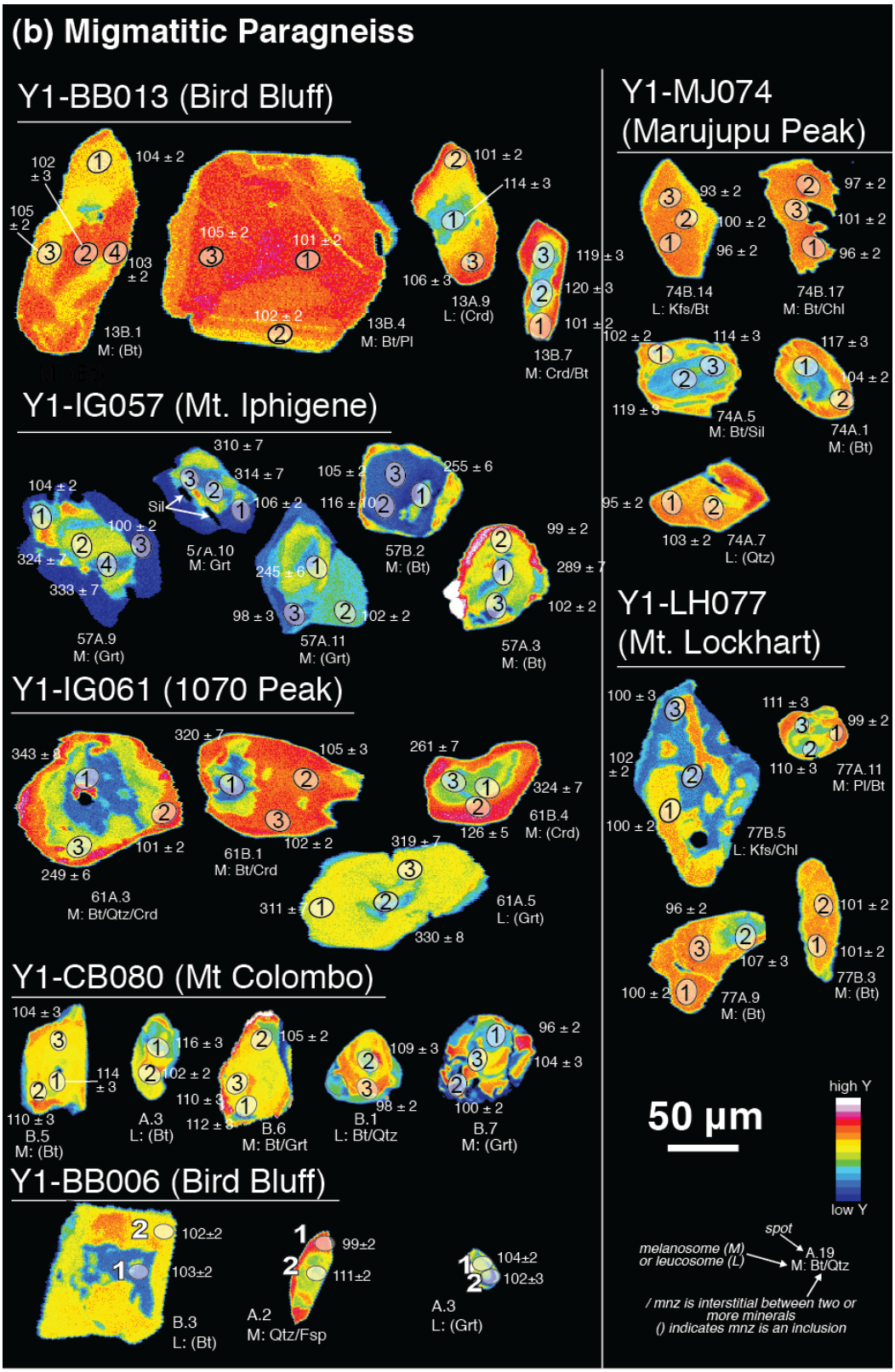

Fig. 2.7. continued

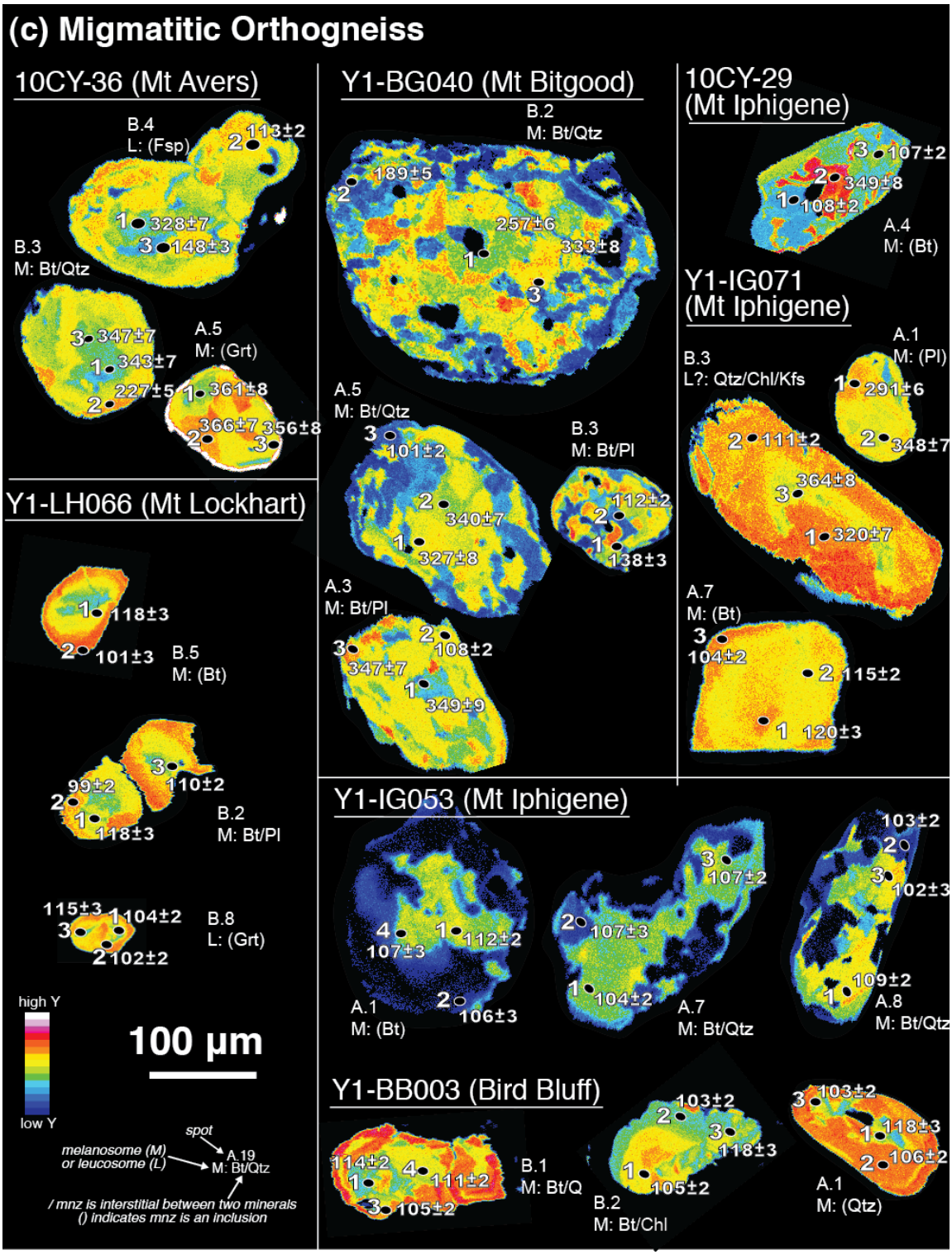

Fig. 2.7. continued

Monazite zoning patterns are highly variable (Fig. 2.7a, b). The most common zoning pattern observed shows Y-depleted cores mantled by relatively Y-enriched rims (Fig. 2.7a, b). Grains with this zoning pattern are found as inclusions in biotite, cordierite, feldspar and quartz and along grain boundaries. Nine out of ten monazite grains associated with cordierite, either as inclusions or along grain boundaries, that were dated in this study show this zoning pattern. The single exception is grain B.13 from sample 10CY-023, which shows flat Y zoning (Fig. 2.7a). Other zoning patterns include, from most to least common: flat zoning, patchy zoning, Y-enriched cores mantled by relatively Y-depleted rims, and oscillatory zoning. In general, monazite grains with patchy zoning are found along grain boundaries in leucosome.

Inclusions in monazite are rare and mostly consist of quartz and feldspar. One exception is a monazite inclusion in garnet (grain A.10 from sample Y1-IG057) that contains aligned inclusions of sillimanite (Fig. 2.7b).

Y_2O_3 contents of monazite range from 0.7 to 4.6 wt% and ThO_2 contents range from 1 to 18 wt%, with most ThO_2 between 3 and 6 wt% (Fig. 2.8). In general, the difference in Y_2O_3 concentrations between the Y-enriched and Y-depleted domains in individual monazite grains is ~1 wt%. For monazite grains with flat zoning, the difference in Y_2O_3 across individual grains is <0.5 wt%.

2.7.1.2 Monazite U–Pb geochronology

Fifty-six monazite grains were analysed for U–Pb geochronology from 13 paragneiss samples. Data are plotted for each sample as individual Tera–Waserberg

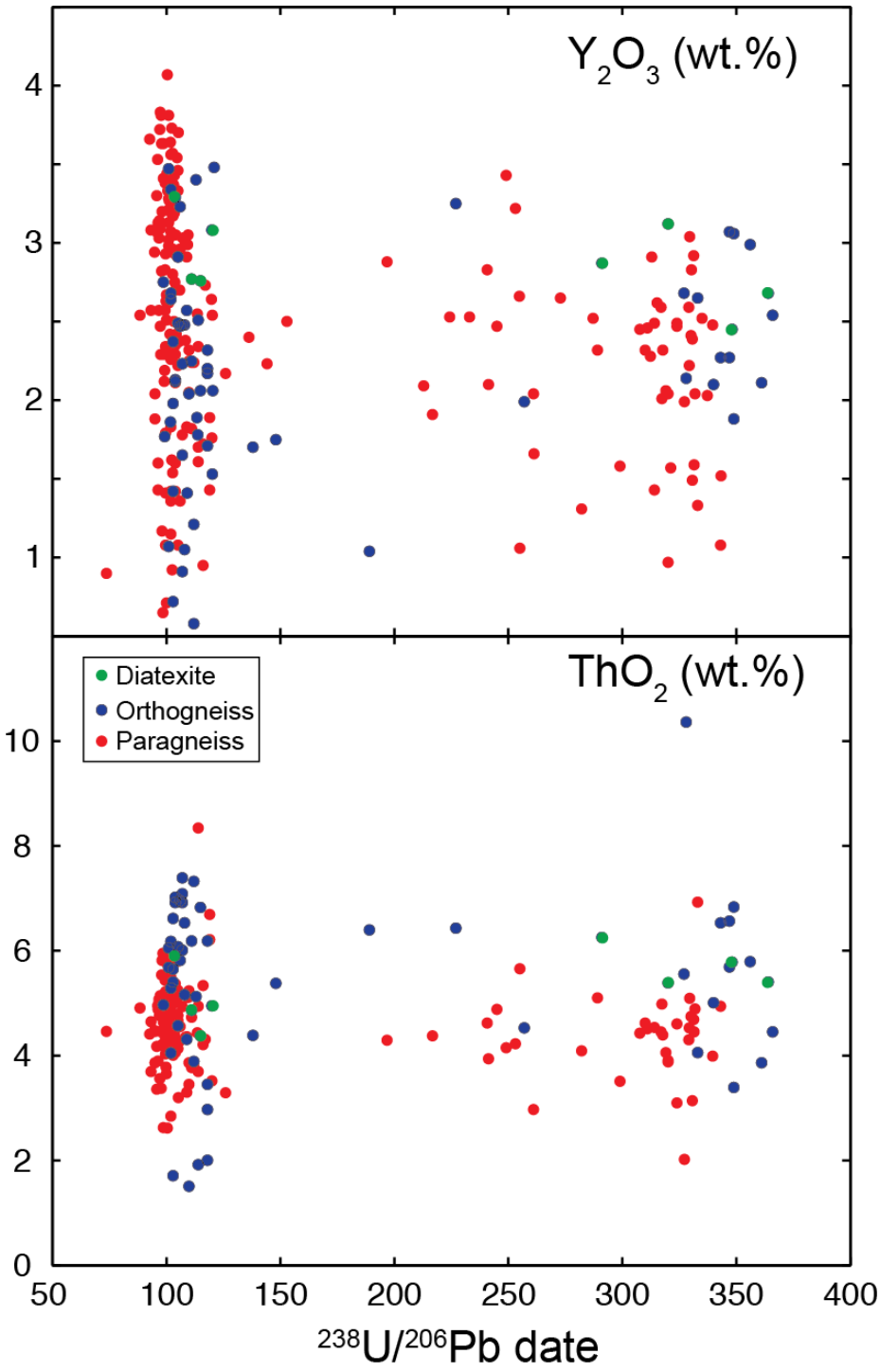

Fig. 2.8. Monazite $^{206}Pb/^{238}U$ dates plotted against Y_2O_3 and ThO_2.

(1972) concordia plots in Fig. 2.9. Geochronology results are described below by microstructural setting and are also summarized in Fig. 2.11a, c, e.

2.7.1.2.1 Monazite inclusions in garnet

Six monazite inclusions in garnet were dated from four samples. Three monazite inclusions in garnet from sample Y1-IG057 contain resorbed cores with patchy Y zoning surrounded by unzoned Y-depleted rims. The cores of these grains yield dates of 333–245 Ma (n = 5) and unzoned rims yield dates of 106–98 Ma (n = 3). One grain (A.10) from this sample also contains aligned sillimanite inclusions that truncate the boundary between the two chemical domains. One grain from sample Y1-IG061 has flat zoning with a Y-depleted core and yields dates of 330–311 Ma (n = 3). The two remaining grains from samples Y1-CB080 and Y1-BB006 yield dates of 104–96 Ma (n = 5).

When combined with the U–Pb monazite data from Korhonen *et al.* (2012), monazite inclusions in garnet yield dates that range from 333 to 96 Ma (n = 36). Cretaceous dates range from 110 to 96 Ma (with one value of *c*. 144 Ma; n = 18) with a median value of 102 Ma and an interquartile range of 105 to 102 Ma.

2.7.1.2.2 Monazite inclusions in cordierite

Three monazite inclusions in cordierite were dated from three samples. Monazite grain B.4 from sample Y1-IG061 has a Y-depleted and resorbed core that yields a date of *c*. 324 Ma and a Y-enriched rim that yields a date of *c.* 126 Ma. A third analysis yields a date of *c*. 261 Ma that is interpreted to have sampled the two domains of different ages and, therefore, is geologically meaningless. A monazite inclusion in cordierite from

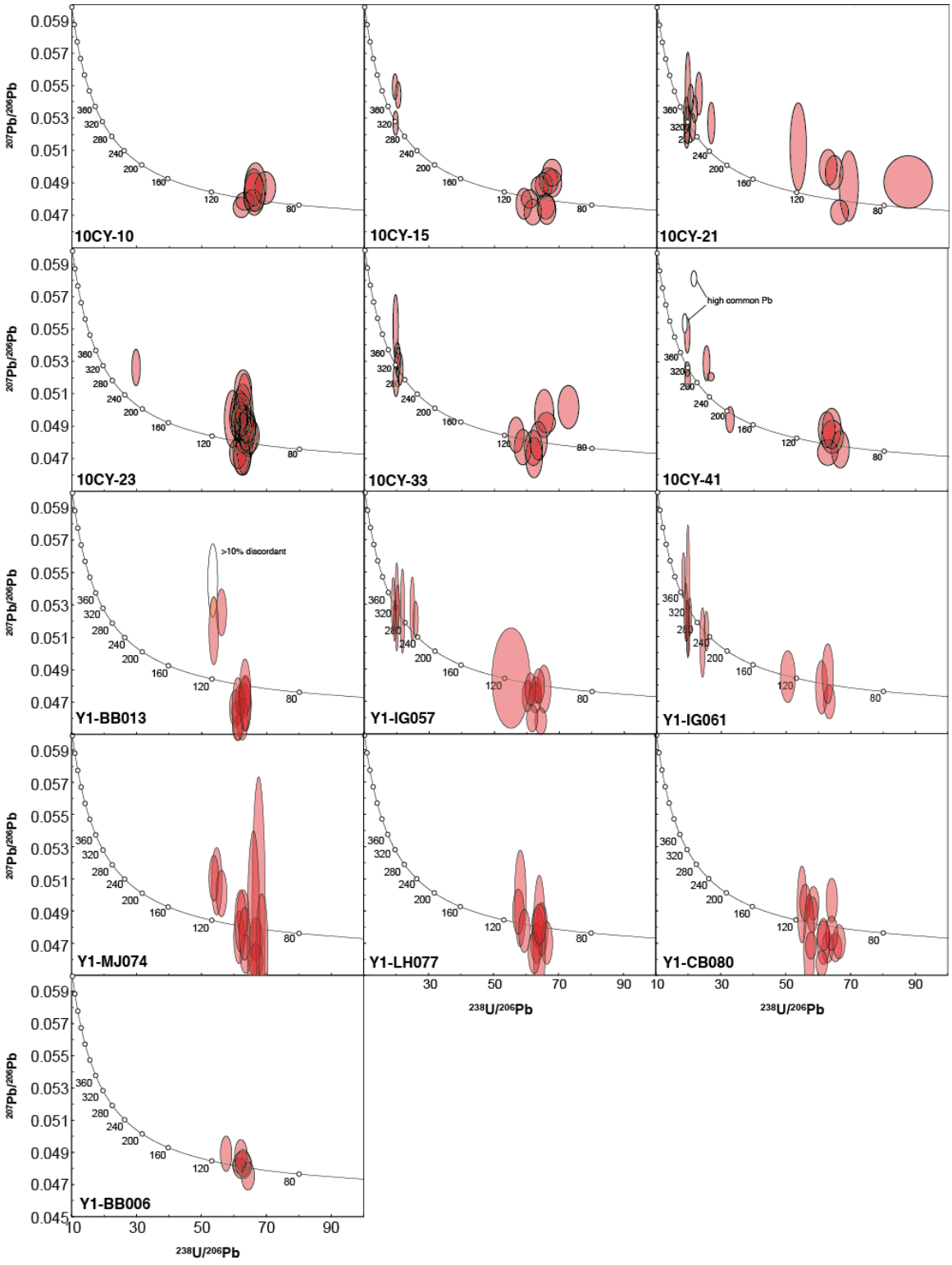

Fig. 2.9. U–Pb concordia diagrams for monazite from paragneiss.

sample Y1-BB0013 has a Y-depleted and resorbed core that yields a date of *c*. 114 Ma and a Y-enriched rim that yields two dates of *c*. 106 and *c*. 101 Ma. The third sample (10CY-033) contains a monazite inclusion in cordierite with a Y-depleted core that yields a date of 308 Ma, which is surrounded by concentric Y-enriched and Y-depleted rims that yield dates of *c*. 104, *c*. 103 and *c*. 88 Ma.

When combined with the U–Pb monazite data from Korhonen *et al.* (2012), monazite inclusions in cordierite yield dates ranging from 346 to 88 Ma (n = 28). Cretaceous dates range from *c*. 127 to *c*. 88 Ma (n = 20) with a median value of 103 Ma and an interquartile range of 106 to 97 Ma.

2.7.1.2.3 Monazite inclusions in biotite

Fifteen monazite inclusions in biotite were dated from twelve samples. Monazite grains show a wide variety of zoning patterns including, from most to least common: Y-depleted cores with relatively Y-enriched rims, patchy zoning, flat zoning, and Y-enriched cores with relatively Y-depleted rims (Fig. 2.7a, b). U–Pb dates range from to *c*. 330 to *c*. 96 Ma (n = 36).

When combined with the U–Pb monazite data from Korhonen *et al.* (2012), monazite inclusions in biotite yield dates ranging from *c*. 334 to *c*. 96 Ma (n = 47). Cretaceous dates range from *c*. 117 to *c*. 96 Ma (n = 34) with a median value of 103 Ma and interquartile range of 105 to 101 Ma.

2.7.1.2.4 Monazite inclusions in quartz and feldspars

Eleven monazite inclusions in quartz, plagioclase and K-feldspar were dated from six samples. Monazite shows a wide range of zoning patterns, including patchy zoning, Y-enriched cores surrounded by Y-depleted rims, concentric zoning, and flat zoning, but notably does not show Y-depleted cores surrounded by Y-enriched rims. U–Pb dates range from *c*. 340 to *c*. 74 Ma.

When combined with U–Pb monazite data from Korhonen *et al.* (2012), monazite inclusions in biotite yield dates ranging from *c*. 352 to *c*. 74 Ma (n = 52). Cretaceous dates range from *c*. 110 to *c*. 93 Ma (with one value of *c*. 121 Ma; n = 39) with a median value of 102 Ma and an interquartile range of 105 to 98 Ma.

2.7.1.2.5 Interstitial monazite

Nineteen grains of monazite that are interstitial between two or more major rock forming minerals were dated from twelve samples. These monazite grains show a variety of Y zoning patterns, but most have Y-depleted cores and Y-enriched rims. Grains with flat or patchy zoning generally yield dates of *c.* 100 Ma. Monazite with Y-depleted cores and Y-enriched rims yield either Devonian–Carboniferous or *c.* 110 Ma dates from cores and *c.* 100 Ma dates from rims.

When combined with the U–Pb monazite data from Korhonen *et al.* (2012), interstitial monazite yields dates ranging from *c*. 376 to *c*. 102 Ma (n = 87). Cretaceous dates range from *c*. 136 to *c*. 102 Ma (n = 58) with a median value of 102 Ma and an interquartile range of 109 to 100 Ma.

Seven monazite grains that are interstitial between cordierite and biotite, quartz or feldspar, were dated from six samples. Six of these grains contain low-Y cores that yield Carboniferous dates of *c*. 343–317 Ma (n = 4) or Cretaceous dates of *c*. 120 or *c*.109 Ma, whereas the high-Y rims of all of these grains range in age from *c*. 105 to *c*. 97 Ma. One grain contains flat zoning (B.13 from sample 10CY-023) and yields dates of *c*. 103–101 Ma.

2.7.2 Migmatitic orthogneisses

2.7.2.1 Monazite chemistry

Monazite grains in the orthogneisses are generally larger (100–400 μm in length) than monazite in the paragneisses (Fig. 2.7). Zoning patterns of monazite within and between samples is variable. Most grains contain patchy zoning with Y-enriched cores embayed by Y-depleted zones (Fig. 2.7c). Other zoning patterns include Y-depleted cores and Y-enriched rims. Monazite grains are found in both the melanosomes and leucosomes of the migmatitic orthogneisses, and most are located interstitially between biotite and quartz or feldspar. Some monazite grains occur as inclusions in biotite, feldspar and, rarely, garnet. Y_2O_3 contents range from 0.6 to 3.5 wt.% and ThO_2 contents range from 1.5 to 10.4 wt.% (Fig. 2.8). In general, the difference in concentration between Y-enriched and Y-depleted zones in individual grains is 0.5–1.5%.

2.7.2.2 Monazite U–Pb geochronology

Seventeen monazite grains were analysed for U–Pb isotopes from six orthogneiss samples. Data are plotted for each sample as individual Tera–Waserberg (1972)

concordia plots in Fig. 2.10. Geochronology results are presented below by microstructural setting and are summarized in Fig. 2.11a, c, f.

2.7.2.2.1 Monazite inclusions in garnet

Monazite inclusions in garnet are rare, but U–Pb dates were obtained from two grains, one from Y1-LH066 (grain B.8) and the other from 10CY-036 (grain A.5). The garnet that hosts grain A.5 from sample 10CY-036 is almost completely replaced by chlorite. This monazite grain has patchy Y zoning, yields dates of *c*. 366–356 Ma (n = 4) and has a very narrow Y-enriched rim that was too thin to date. Grain B.8 from sample Y1-LH066 is hosted in an inclusion-free garnet, which has radial cracks emanating from the inclusion (Fig. 2.3j), and yields dates of *c*. 115, *c*. 104 and *c*. 102 Ma.

When combined with the U–Pb monazite data from Korhonen *et al.* (2012), monazite inclusions in garnet yield dates ranging from *c*. 366 to *c*. 102 Ma (n = 9). Cretaceous dates range from *c*. 120 to *c*. 102 Ma (n = 6) and yield a median value of 111 Ma with an interquartile range of 115 to 104 Ma.

2.7.2.2.2 Monazite inclusions in biotite

Three monazite inclusions in biotite were dated from three samples. Two grains show resorbed and Y-enriched cores and Y-depleted rims (grain A.4 from sample 10CY-029 and grain A.1 from sample Y1-IG053) and one contains a Y-depleted core mantled

---

Fig. 2.10. U–Pb concordia diagrams for monazite from orthogneiss and the diatexite.

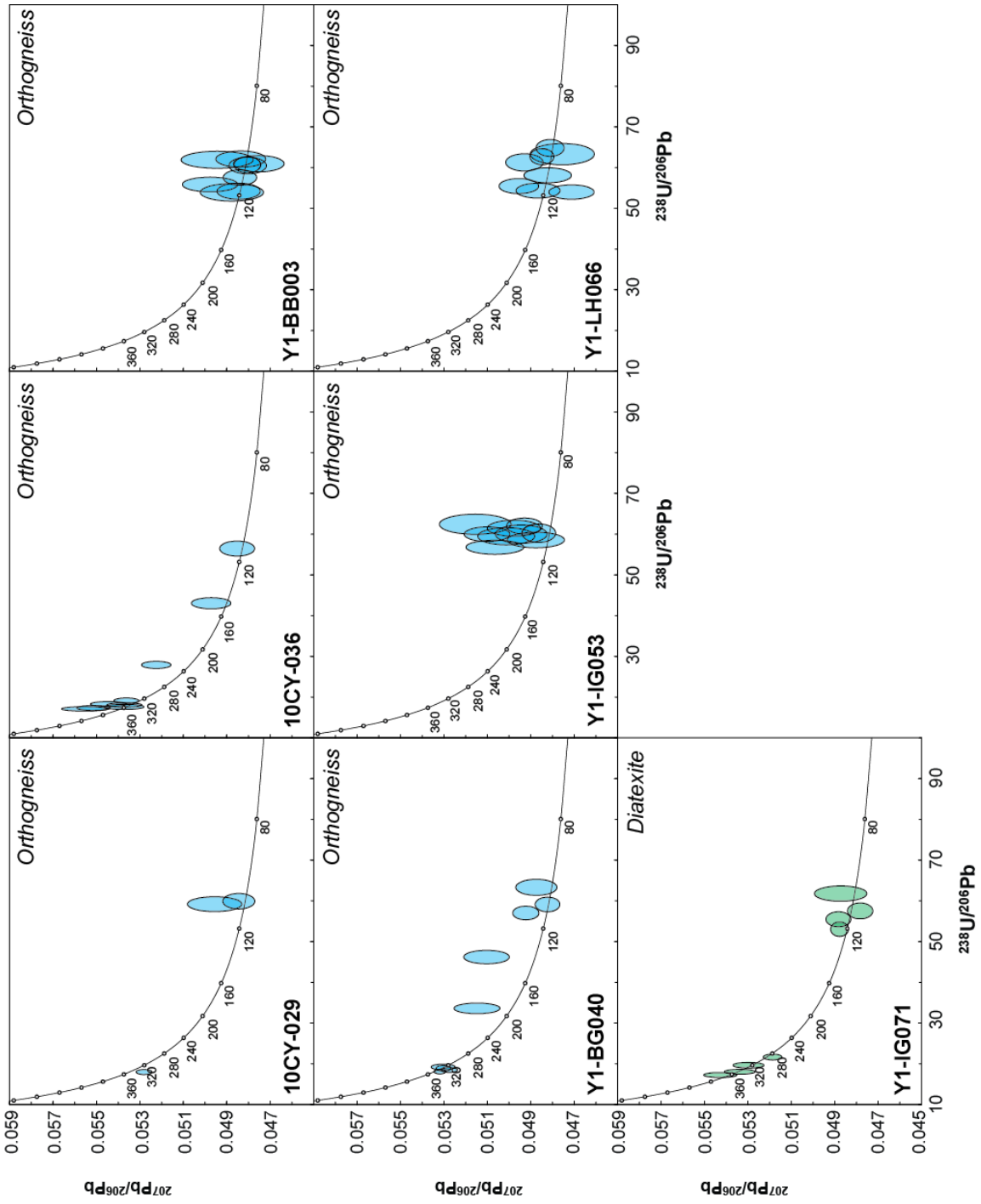
Orthogneiss
Y1-BB003
Orthogneiss
10CY-036
Orthogneiss
Y1-LH066
Orthogneiss
10CY-029
Orthogneiss
Y1-IG053
Orthogneiss
Y1-BG040
Diatexite
Y1-IG071
207Pb/206Pb
238U/206Pb

by a Y-enriched rim (grain B.5 from sample Y1-LH066). Y-enriched cores yield dates of *c*. 349 and *c*. 112 Ma and the Y-depleted rims yield dates of *c*. 108–106 Ma. For grain B.5 from sample Y1-LH066, the Y-depleted core yields a date of *c*. 118 Ma and the Y-enriched rim a date of *c*. 101 Ma.

When combined with the U–Pb monazite data from Korhonen *et al.* (2012), monazite inclusions in biotite yield dates ranging from *c*. 349 to *c*. 99 Ma (n = 13). Cretaceous dates range from *c*. 121 to *c*. 99 Ma (n = 14) and yield a median value of 107 Ma with an interquartile range of 116 to 102 Ma.

2.7.2.2.3 Monazite inclusions in quartz and feldspar

One monazite inclusion in quartz (grain A.1 in sample Y1-BB003) and one in plagioclase (grain B.4 in sample 10CY-036) were dated in this study. The monazite inclusion in quartz has a Y-depleted core that yields a date of *c*. 118 Ma and a Y-enriched rim that yields dates of *c*. 106 and *c*. 103 Ma. The monazite inclusion in plagioclase has patchy Y zoning with a Y-depleted core that yields two dates of *c*. 328 and *c*. 148 Ma and a Y-enriched rim that yields a date of *c*. 113 Ma.

When combined with the U–Pb monazite data from Korhonen *et al.* (2012), monazite inclusions in quartz and feldspar yield dates ranging from *c*. 328 to *c*. 98 Ma (n = 8). Cretaceous dates range from *c*. 118 to *c*. 98 Ma (n = 6) and yield a median value of 106 Ma with an interquartile range of 118 to 103 Ma.

2.7.2.2.4 Interstitial monazite

Ten grains interstitial between two or more minerals from five samples were dated in this study. Two samples (10CY-036, Y1-BG040) contain patchy zoned monazite that yields both Cretaceous (*c*. 118–99 Ma) and older dates (*c*. 349–189 Ma). Monazite from the three other samples (Y1-IG053, Y1-BB003, and Y1-LH066) yields only Cretaceous dates ranging from *c*. 118 to *c*. 102 Ma.

When combined with the U–Pb monazite data from Korhonen *et al.* (2012), monazite inclusions in quartz and feldspar yield dates ranging from *c*. 349 to *c*. 99 Ma (n = 29). Cretaceous dates range from *c*. 118 to *c*. 99 Ma (n = 18) and yield a median value of 107 Ma with an interquartile range of 111 to 103 Ma.

2.7.3 Diatexite migmatite

2.7.3.1 Monazite chemistry

Monazite grains from the diatexite analysed in this study range from 100 to 300 μm in size (Fig 7c). Zoning is generally patchy with subtle core and rim zoning. Y_2O_3 contents range from 2.4 to 3.3 wt% and ThO_2 contents range from 4.4 to 6.2 wt% (Fig. 2.8).

2.7.3.2 Monazite U–Pb geochronology

Three monazite grains from the diatexite sample (Y1-IG071) were dated as part of this study. One grain (A.1) occurs as an inclusion in plagioclase, has patchy Y zoning, and yields dates of *c*. 348 and *c*. 291 Ma. A second grain (A.7) occurs as an inclusion in biotite and has subtle Y zoning with a Y-enriched core, an intermediate zone that is relatively Y-depleted, and a Y-enriched rim. One analysis from each of these three zones

yields dates of *c*. 120, *c*. 115 and *c*. 104 Ma, respectively. A third grain (B.3) is interstitial between quartz, chlorite and K-feldspar and contains a Y-depleted core and a Y-enriched zone that truncates the core and is continuous with the Y-enriched rim. The Y-depleted core yields a date of *c*. 364 Ma, the Y-enriched zone a date of *c*. 320 Ma and the Y-enriched rim a date of *c*. 111 Ma.

2.7.4 Summary

For monazite in both migmatitic paragneisses and orthogneisses, data from this study combined with data from Korhonen *et al.* (2012) yield $^{206}Pb/^{238}U$ dates that range from *c*. 366 to *c*. 74 Ma, defining two main populations at *c*. 360–300 Ma and *c*. 120–95 Ma (Fig. 2.11). Ages intermediate between these age groups commonly represent analyses near the boundary between chemical domains or overlap multiple domains in monazite and are interpreted to represent mixed ages with no geological significance. No correlation is observed between microstructural setting and age for monazite in either the paragneisses or the orthogneisses (Fig. 2.11c–e). However, when grouped by microstructural setting, Cretaceous monazite from the orthogneisses has higher median $^{206}Pb/^{238}U$ dates compared with monazite from the same microstructural setting in the paragneisses, but the interquartile ranges overlap (Fig. 2.11a). The diatexite sample yields $^{206}Pb/^{238}U$ dates of *c*. 364–104 Ma from three monazite grains.

2.8 Phase equilibria modeling

The *P–T* conditions of both Devonian–Carboniferous and Cretaceous metamorphism are constrained using phase equilibria modelling. First, the methodology

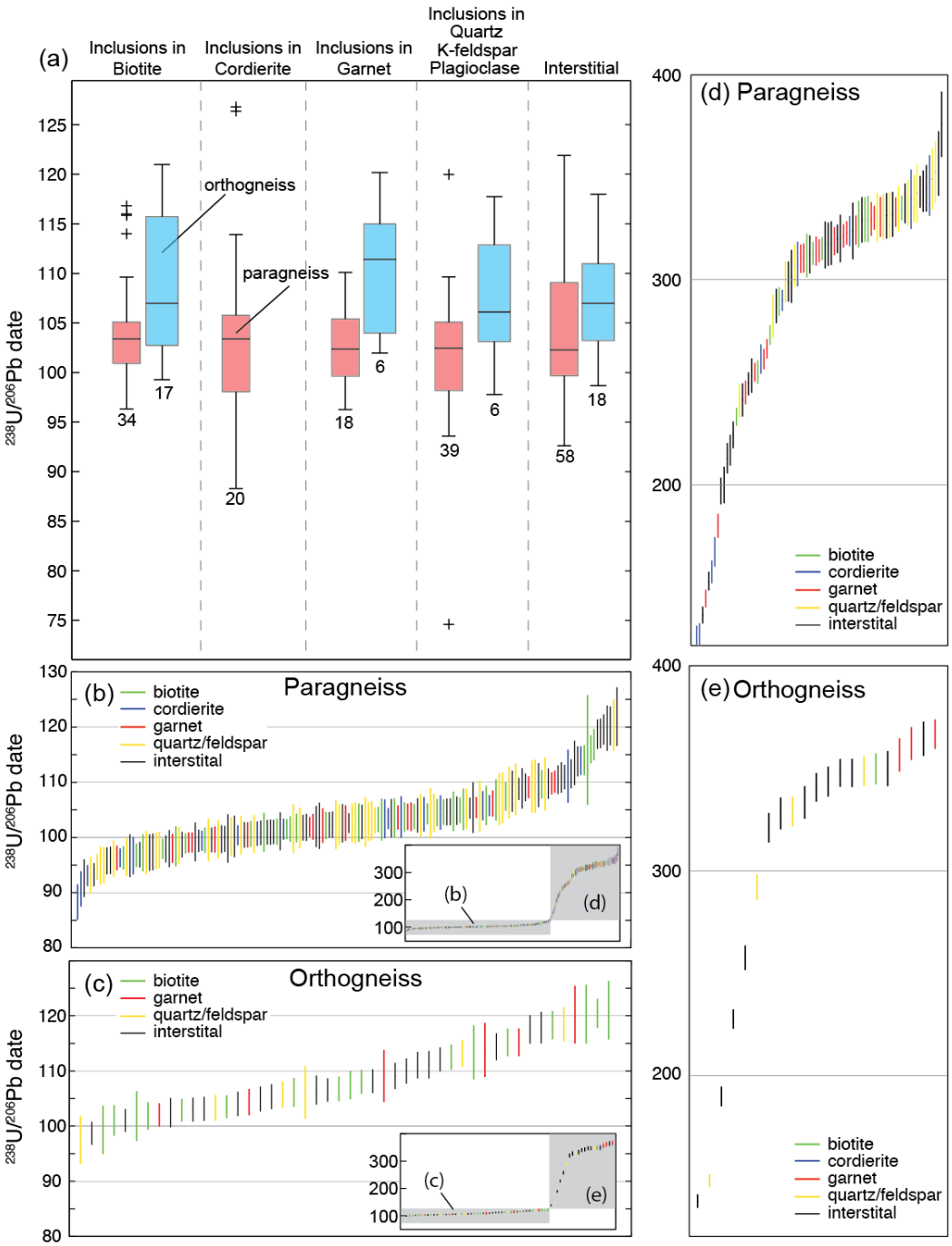

Fig. 2.11. (a) Box and whisker plots of monazite dates grouped by rock type and microstructural setting. (b) Cretaceous monazite $^{206}Pb/^{238}U$ dates (< 130 Ma) from paragneiss plotted with increasing age and colour coded by microstructural setting. (c) Cretaceous monazite $^{206}Pb/^{238}U$ dates (< 130 Ma) from orthogneiss plotted with increasing age and colour coded by microstructural setting. (d) Monazite $^{206}Pb/^{238}U$ dates > 130 Ma from the paragneisses plotted with increasing age and colour coded by microstructural setting. (e) Monazite $^{206}Pb/^{238}U$ dates > 130 Ma from the orthogneisses plotted with increasing age and colour coded by microstructural setting.

for calculation of the *P–T* pseudosections is described using a representative example of paragneiss (10CY-023). Second, the range of *P–T* conditions for the Devonian–Carboniferous metamorphism are determined by forward phase equilibria modelling of Swanson Formation compositions and a diatexite composition. Third, the Cretaceous *P–T* conditions of the solidus phase assemblage and the trajectory of the late portion of the decompression *P–T* path into this phase assemblage field are constrained by forward phase equilibria modelling of paragneiss and orthogneiss compositions. Fourth, inverse phase equilibria modelling is used to estimate the *P–T* conditions immediately prior to the metamorphic peak, and to determine the position of the garnet-in phase boundary.

2.8.1 Forward phase equilibria modelling

2.8.1.1 Methods

Calculations were performed using THERMOCALC v.3.34 (Powell and Holland, 1988) and the internally consistent dataset of Holland and Powell (Holland and Powell, 1998). Modelling was undertaken in the Na_2O–CaO–K_2O–FeO–MgO–Al_2O_3–SiO_2–H_2O–TiO_2–Fe_2O_3 (NCKFMASHTO) chemical system, which is currently the most realistic system to investigate melting for sedimentary and granitic protoliths (White *et al.*, 2007). Representative paragneiss and orthogneiss compositions (Fig. 2.4) and one diatexite composition (Y1-IG071) were modelled. The amount of O (or Fe^{3+}) measured by titration is used in the modelling.

The phases considered were: Crd – cordierite; Di – diopside; Ep – epidote; Grt – garnet; H_2O – aqueous fluid; Ilm – ilmenite; Kfs – K-feldspar; Ky – kyanite; Liq – silicate liquid/melt; Mag – magnetite; Ms – muscovite; Opx – orthopyroxene; Pl –

plagioclase; Pg – paragonite; Qtz – quartz; Rt – rutile; Sil – sillimanite; Spl – spinel; Ttn – titanite. The activity–composition (*a–x*) models for the phases considered are: biotite, garnet, and melt (White *et al.*, 2007); orthopyroxene and spinel–magnetite (White and Powell, 2002); cordierite and epidote (Holland and Powell, 1998); K-feldspar and plagioclase (Holland and Powell, 2003); white mica (Coggon and Holland, 2002); and ilmenite–hematite (White *et al.*, 2000). Phases modelled as pure end-members include: quartz, rutile, titanite, aqueous fluid (H_2O), kyanite and sillimanite.

The amount of H_2O in the bulk compositions was adjusted from the measured loss on ignition value so that the observed phase assemblage is stable just above the solidus to reflect the conditions where this assemblage is in equilibrium with the last remnants of melt (White *et al.*, 2004; Diener *et al.*, 2008; Korhonen *et al.*, 2010a). This was determined for each sample using $T–M_{H2O}$ pseudosections calculated at 0.7 GPa. An example of a $T–M_{H2O}$ pseudosection for paragneiss sample 10CY-023 is shown in Fig. 2.12a. The range of H_2O contents used to construct the $T–M_{H2O}$ pseudosections is from anhydrous ($M_{H2O} = 0$) to the total loss on ignition value for each sample assuming this corresponds entirely to H_2O ($M_{H2O} = 1$). Using these diagrams, a range of H_2O contents was determined where the observed phase assemblage is just stable at the solidus (Fig. 2.12a). For this range of H_2O contents, the modes of minerals and melt were calculated along the solidus (Fig. 2.12b). Using the mineral modes from the model, a value of H_2O was chosen based on the approximate mineral modes of the major ferromagnesian minerals observed in thin section for each sample.

Fig. 2.12. (a) $T–M_{H2O}$ diagram calculated at 0.7 GPa. (b) Mode diagram showing the proportion of different minerals along the solidus as a function of bulk H_2O content.

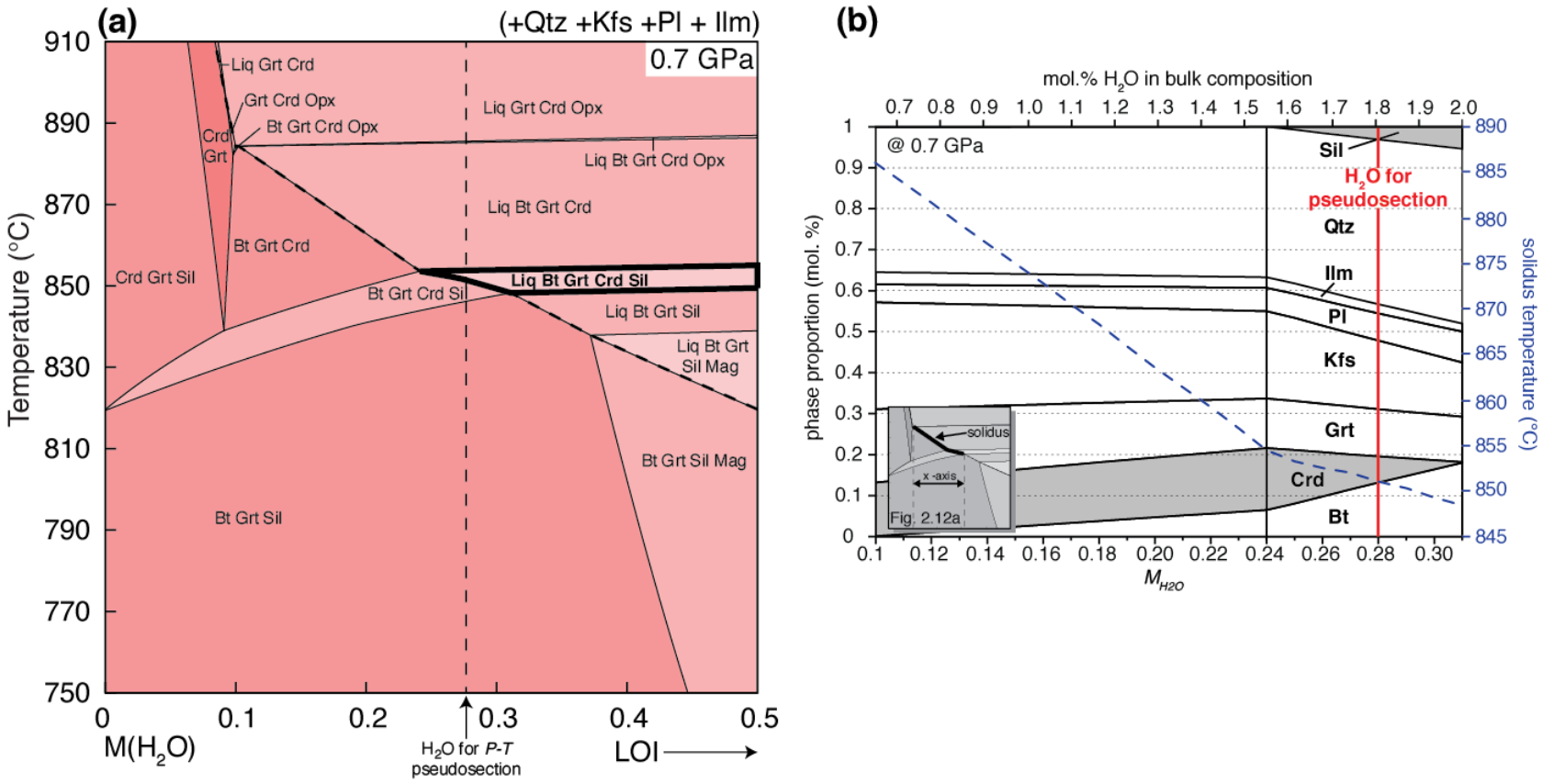
(a)
(+Qtz +Kfs +Pl + Ilm)
0.7 GPa
Liq Grt Crd
Grt Crd Opx
Bt Grt Crd Opx
Crd
Grt
Liq Grt Crd Opx
Liq Bt Grt Crd Opx
Liq Bt Grt Crd
Bt Grt Crd
Crd Grt Sil
Bt Grt Crd Sil
Liq Bt Grt Crd Sil
Liq Bt Grt Sil
Liq Bt Grt Sil Mag
Bt Grt Sil Mag
Bt Grt Sil
Temperature (°C)
910
890
870
850
830
810
790
770
750
0
0.1
0.2
0.3
0.4
0.5
M(H2O)
H2O for P-T pseudosection
LOI
(b)
mol.% H2O in bulk composition
0.7 0.8 0.9 1.0 1.1 1.2 1.3 1.4 1.5 1.6 1.7 1.8 1.9 2.0
@ 0.7 GPa
Sil
H2O for pseudosection
Qtz
Ilm
Pl
Kfs
Grt
Crd
Bt
phase proportion (mol. %)
solidus temperature (°C)
890
885
880
875
870
865
860
855
850
845
1
0.9
0.8
0.7
0.6
0.5
0.4
0.3
0.2
0.1
0
0.1 0.12 0.14 0.16 0.18 0.20 0.22 0.24 0.26 0.28 0.30
MH2O
solidus
x -axis
Fig. 2.12a

2.8.1.2 Devonian–Carboniferous metamorphism

Based on the Lu–Hf garnet geochronology presented above, it is clear that garnet is not part of the Devonian–Carboniferous metamorphic assemblage in both the paragneiss and the orthogneiss. Two approaches are used to constrain the *P–T* conditions of Devonian–Carboniferous metamorphism. First, a *P–T* pseudosection is constructed for one diatexite composition (Y1-IG071) and is shown in Fig. 2.13a. Diatexites are found in the deepest structural levels in the Fosdick complex (Siddoway *et al.*, 2004), yield Devonian–Carboniferous and Cretaceous U–Pb zircon ages, and have Hf and O isotope values consistent with mixing Ford Granodiorite suite magma or melt derived from anatexis of the Ford Granodiorite suite with Swanson Formation en masse or melt derived from anatexis of the Swanson Formation (Yakymchuk *et al.*, 2014). On balance, the diatexites are interpreted to have formed during the Devonian–Carboniferous metamorphic event.

The interpreted solidus phase assemblage for the diatexites includes liquid, biotite, K-feldspar, quartz, plagioclase and ilmenite. In Fig. 2.13a, the stability field of this assemblage plots at temperatures of 700–800°C at pressures of 0.45–1.10 GPa. Although the phase equilibria modelling predicts the presence of <1% sillimanite at these *P–T* conditions, such a small quantity is within the uncertainty of the modelling and the absence of sillimanite in the diatexite samples is acceptable. The absence of peritectic minerals indicative of biotite-breakdown melting (e.g. garnet and cordierite) suggests that the diatexites may have formed by muscovite-breakdown melting and/or fluid-fluxed melting at temperatures below the stability field of garnet and cordierite.

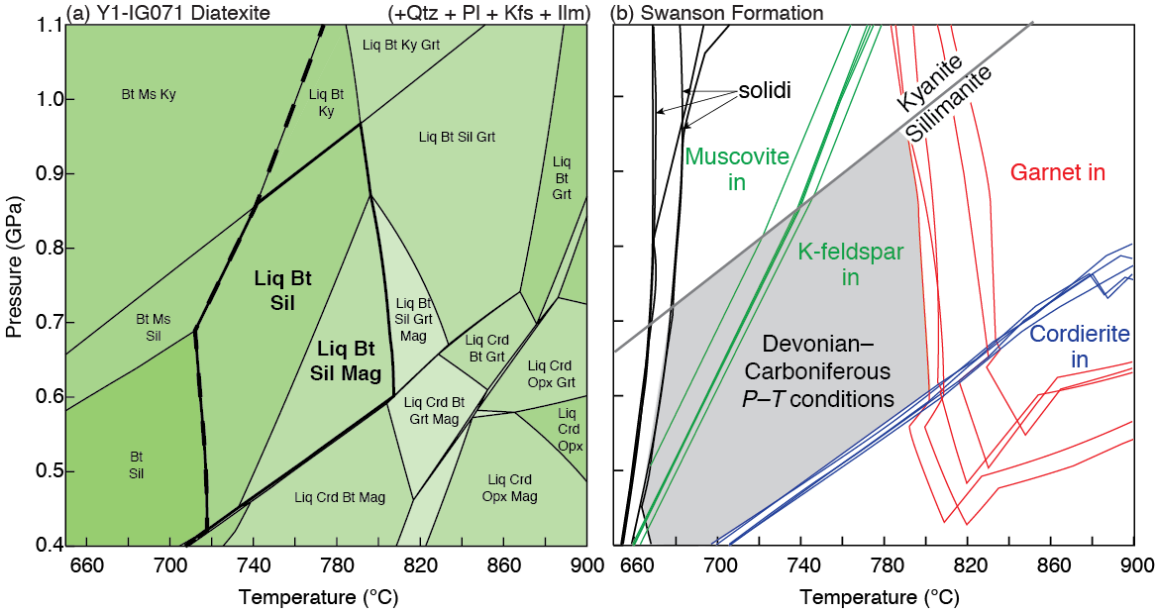

Fig. 2.13. (a) *P–T* pseudosection for a sample of inhomogeneous diatexite (Y1-IG071). The bold dashed line is the solidus. The field that contains the observed assemblage is bounded by a bold solid black line. (b) *P–T* diagram of select field boundaries from five Swanson Formation compositions from Korhonen et al. (2010a) and Yakymchuk et al. (2013b). The grey box contains the interpreted Devonian–Carboniferous phase assemblage.

A second approach to constrain the *P–T* conditions for the Devonian–Carboniferous metamorphism is to forward model representative compositions of the Swanson Formation (e.g. Korhonen *et al.*, 2010a). The field boundaries of garnet, cordierite, muscovite and melt are compiled from *P–T* pseudosections for five Swanson Formation compositions from Korhonen *et al.* (2010a) and Yakymchuk *et al.* (2013b) in Fig. 2.13b. Because both garnet and cordierite are part of the Cretaceous metamorphic mineral paragenesis, the *P–T* conditions of Devonian–Carboniferous metamorphism are restricted to temperatures lower than the stability field of these minerals. In addition, the absence of kyanite from rocks in the Fosdick complex restricts pressures to <0.70–0.95 GPa with increasing temperature (Fig. 2.13b). It is unclear if K-feldspar in the paragneisses is part of the metamorphic mineral paragenesis for both the Devonian–Carboniferous and Cretaceous metamorphic events or only the Cretaceous event. Using forward modelling of Swanson Formation compositions, the estimated *P–T* conditions for the Devonian–Carboniferous metamorphism are 660–800°C at 0.45–1.0 GPa (Fig. 2.13a).

2.8.1.3 Cretaceous metamorphism

P–T pseudosections calculated for four representative compositions (Fig. 2.4) of the migmatitic paragneiss are shown in Fig. 2.14. The phase assemblage fields on the *P–T* pseudosections for these samples have similar topologies, with the exception of Y1-IG057. The pseudosection for this last sample has a more complex topology due to the presence of spinel at higher temperatures.

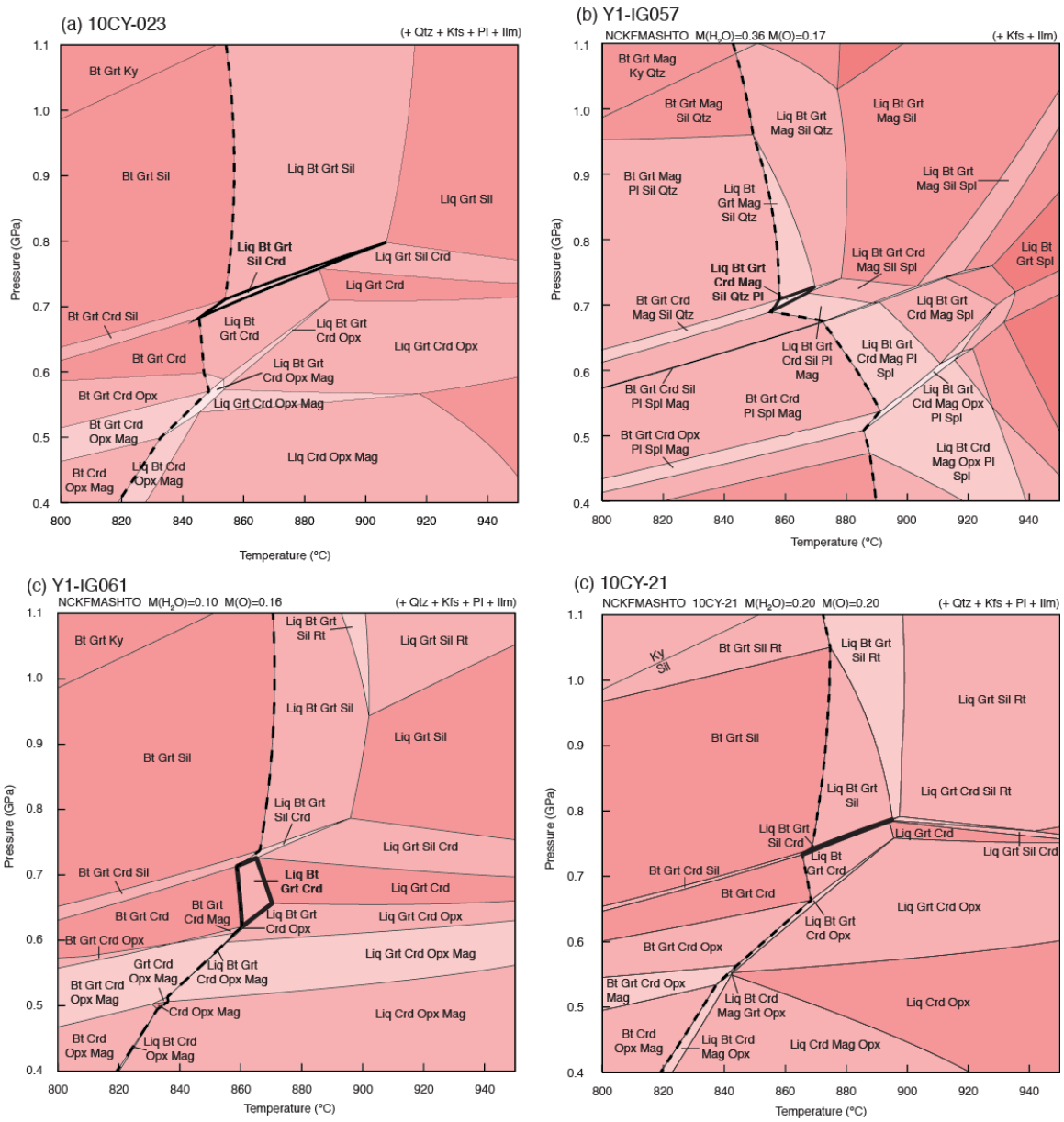

Fig. 2.14. *P–T* pseudosections for four representative migmatitic paragneiss compositions. The bold dashed line is the solidus. The field that contains the inferred solidus phase assemblage after decompression for each sample is bounded by a bold solid black line.

Sample Y1-IG061 contains a solidus phase assemblage that includes cordierite, garnet, biotite and liquid (with quartz, plagioclase, K-feldspar and ilmenite). The solidus phase assemblage for other three samples also contains sillimanite (10CY-021, 10CY-023 and Y1-IG057). The solidi that bound the low temperature portion of the stability fields for the inferred solidus phase assemblages for these four samples range from 845 to 865°C at pressures of 0.60 to 0.75 GPa. The maximum temperature for these assemblages is restricted by the biotite-out field boundaries, which range from 870 to 890°C (Fig. 2.14), and the absence of orthopyroxene suggests that pressures were > 0.6 GPa at these temperatures.

Prior to the growth of cordierite, the phase assemblage included garnet, biotite, sillimanite, and liquid (with quartz, plagioclase, K-feldspar, and ilmenite with or without magnetite) in all four samples. The stability field for this assemblage plots at higher pressures and at similar or slightly higher temperatures compared with the solidus phase assemblage. The upper temperature limit of this earlier assemblage is constrained by the biotite-out field boundary at 900–910°C for samples 10CY-021, 10CY-023 and Y1-IG061 and by the quartz-out field boundary at 880°C for sample Y1-IG057 (Fig. 2.14). The maximum pressure for this assemblage is limited to <1.2 GPa at these temperatures by the absence of kyanite. The field boundaries that separate the earlier cordierite-absent assemblage from the cordierite-present assemblage have relatively shallow slopes in *P–T* space (Fig. 2.14). Therefore, a *P–T* path with a strong component of decompression with or without slight cooling is required to explain the observed phase assemblages in paragneisses from the Fosdick complex.

P–T pseudosections calculated for four representative samples of migmatitic orthogneiss are shown in Fig. 2.15. For the two samples that plot towards the plagioclase–K-feldspar join in Fig. 2.4 (10CY-029 and 10CY-036), the topology of the *P–T* pseudosections resemble those for the paragneisses (Fig. 2.15b, c). For the other two samples (Y1-IG053 and Y1-LH066), orthopyroxene is stable at $T > 840–900$°C for pressures of 0.5–1.1 GPa (Fig. 2.15a, d). All of these samples contain a solidus phase assemblage that includes garnet, biotite and liquid in addition to quartz, plagioclase, K-feldspar and ilmenite with or without magnetite. The solidi that bound the low temperature portion of the stability fields for these phase assemblages range from 800 to 850°C at pressures of >0.60 GPa, whereas the maximum temperatures are limited by the biotite-out or orthopyroxene-in field boundaries at higher temperatures, which range from 860 to 870°C at 0.7 GPa (Fig. 2.15).

2.8.1.4 Summary

To constrain the *P–T* conditions of both metamorphic events, the stability fields of the solidus phase assemblages for the diatexite, paragneisses and orthogneisses as well as *P–T* constraints from forward modelling of Swanson Formation compositions are summarized in Fig. 2.16. For Devonian–Carboniferous metamorphism, the overlapping region of the *P–T* estimates from the diatexite and forward modelling of Swanson Formation compositions restricts *P–T* conditions to 720–800°C at pressures of 0.45 to 0.95 GPa (Fig. 2.16a). Significantly higher temperatures were attained during Cretaceous metamorphism. For the orthogneisses, Cretaceous *P–T* conditions of 800–850°C at pressures of >0.60–0.70 GPa are recorded by the solidus assemblage (Fig. 2.16c). For the

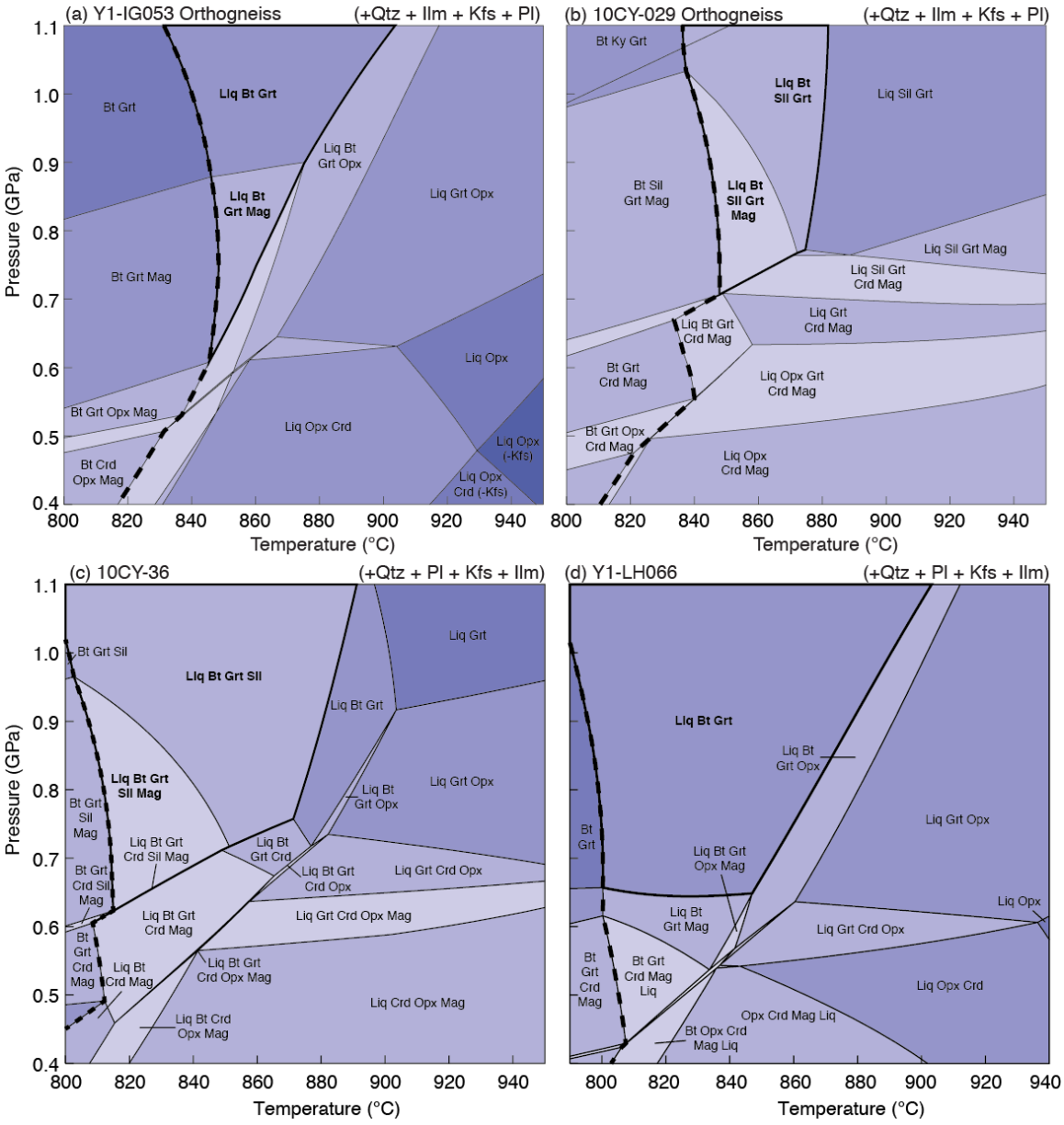

Fig. 2.15. *P–T* pseudosections for four representative migmatitic orthogneiss compositions. The bold dashed line is the solidus. The field that contains the inferred solidus phase assemblage after decompression for each sample is bounded by a bold solid black line.

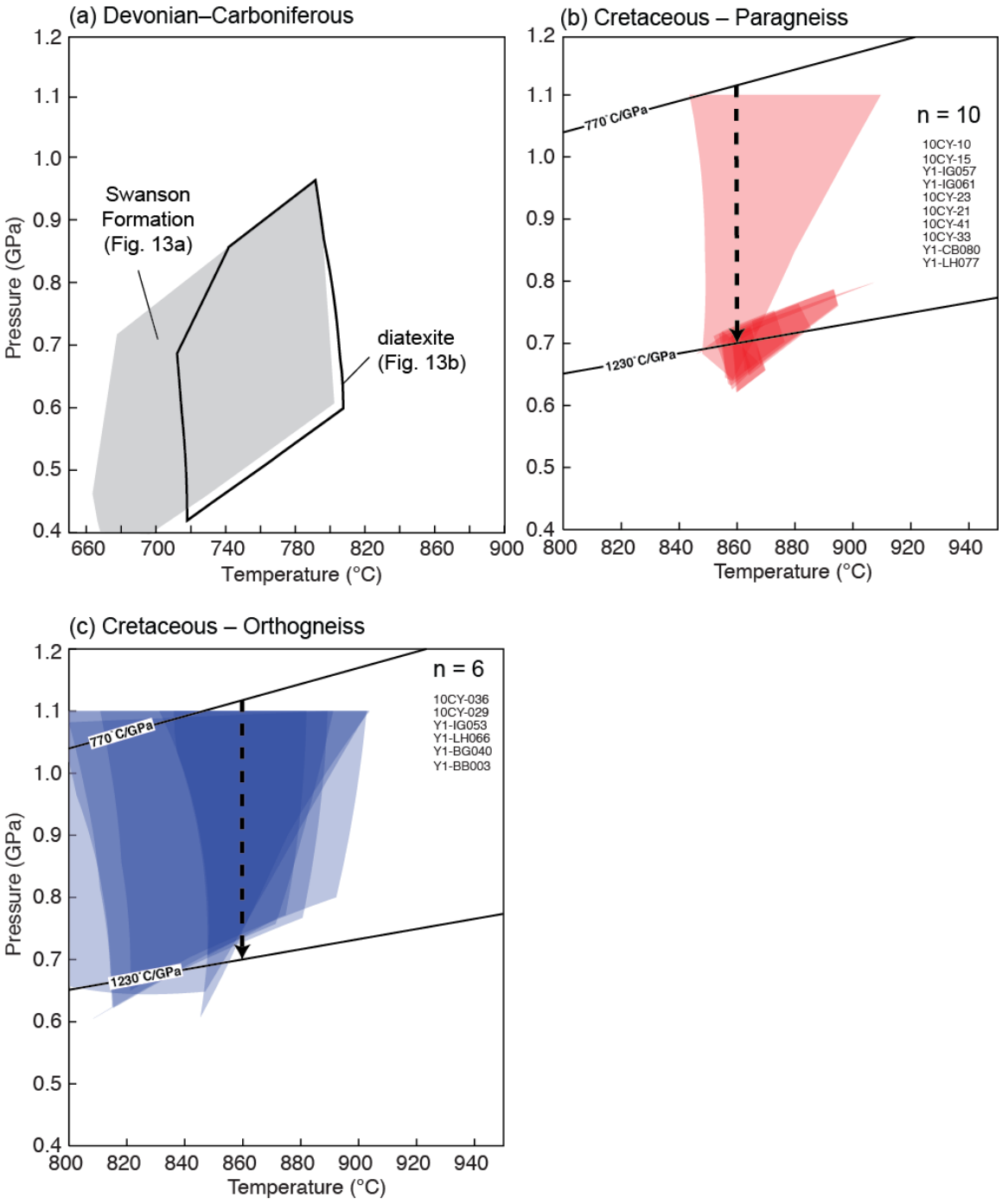

Fig. 2.16. Summary diagram of *P–T* estimates. (a) Devonian–Carboniferous solidus phase assemblage of diatexite and stability field of the inferred phase assemblage of the Swanson Formation. (b) Overlapping fields for the inferred Cretaceous solidus phase assemblage of paragneisses. (c) Overlapping fields for the inferred Cretaceous solidus phase assemblage of orthogneisses. The two apparent thermal gradients in (b) and (c) are from Yakymchuk *et al.* (2013b).

paragneisses, Cretaceous *P–T* conditions of 850–880°C at pressures of 0.65 to 0.80 GPa are recorded by the solidus assemblage after decompression from higher pressures either isothermally or with slight cooling (Fig. 2.16b). The amount of decompression can be approximated by using two apparent thermal gradients from Yakymchuk *et al.* (2013b): one is for a thickened crust in the Ford Ranges prior to regional extension (770°C/GPa) and the other is for thinned crust that intersects the overlapping stability fields for the solidus phase assemblage fields for the migmatitic paragneisses in the Fosdick complex (1230°C/GPa). Using this approach, the tectonic transition from thickened to thinned crust resulted in 0.4 GPa of decompression.

2.8.2 Inverse phase equilibria modelling

2.8.2.1 Methods

Although the *P–T* conditions for the solidus phase assemblages in the Cretaceous are well constrained by forward phase equilibria modelling of the residual paragneiss and orthogneiss compositions (Figs 2.14–2.16), the *P–T* conditions and trajectory of the prograde path and the amount of melt that could have been produced from their protoliths cannot be determined from these *P–T* pseudosections. Of particular interest are the *P–T* conditions for the garnet-in field boundary, which may be used to link the Lu–Hf ages to the *P–T* conditions of garnet. Because the migmatitic paragneisses and orthogneisses are residual compositions that have likely lost melt episodically up to peak *P–T* (e.g. Yakymchuk and Brown, 2014a), the pseudosections constructed for these bulk compositions are only appropriate for investigating the peak *P–T* conditions and the immediately post-peak retrograde *P–T* path.

To place constraints on the prograde path, inverse phase equilibria modelling is used in which a model melt composition is reintegrated down temperature in a stepwise manner into a representative paragneiss composition (10CY-023) and a representative orthogneiss composition (Y1-IG053)(e.g. White *et al.*, 2005; Indares *et al.*, 2008; Guilmette *et al.*, 2011; Korhonen et al., 2013b). Starting from the middle of the low temperature boundary that constrains the solidus phase assemblage field (Fig. 2.17a, c), melt is reintegrated down temperature from the solidus into the composition along a simple isobaric prograde *P–T* path at 0.7 GPa. The composition of the melt does not change significantly within the *P–T* range of a given phase assemblage field, but does change significantly across field boundaries where different mineral assemblages are stable. Therefore, melt is re-integrated at phase assemblage field boundaries in a quantity to just stabilize this new assemblage at the solidus. This process was repeated until the H_2O-saturated (wet-) solidus was encountered at ~660°C. The resultant composition represents that of a model protolith and the total quantity of melt reintegrated into each composition is an approximation of the amount of melt lost during prograde metamorphism.

The melt compositions and the stepwise changes in the melt-reintegrated compositions are shown on the ternary diagram in Fig. 2.18. The final model composition is relatively insensitive to the trajectory of the *P–T* path, assuming geologically reasonable conditions. However, the amount of water in the final composition is sensitive to the pressure at which the *P–T* path crosses the wet solidus, which has consequences for the total amount of melt re-integrated into the composition. If the *P–T* path crosses the wet solidus at higher or lower pressures, the amount of melt reintegrated back into the

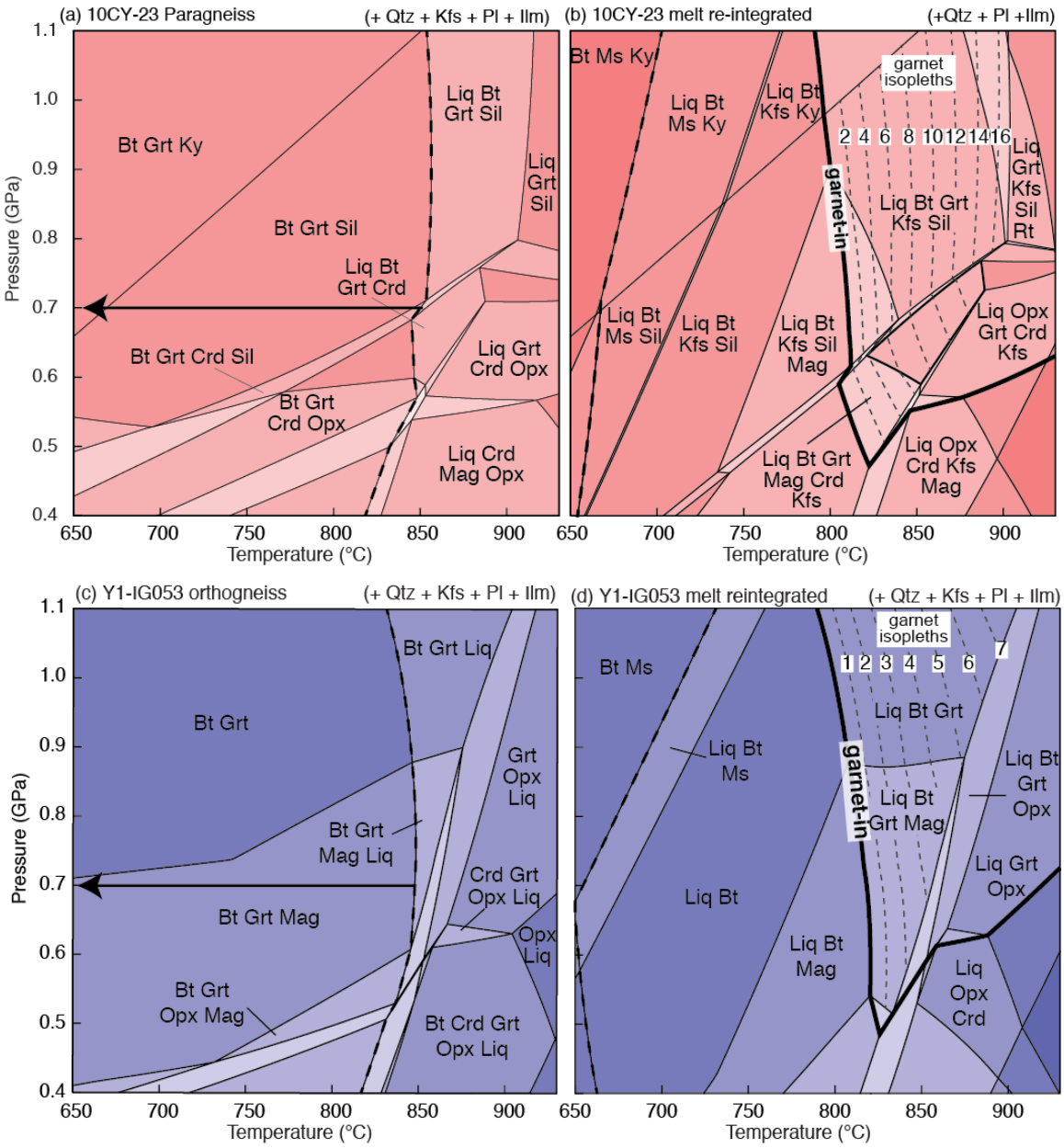

Fig. 2.17. *P–T* pseudosections for (a) paragneiss, (b) melt-reintegrated paragneiss, (c) orthogneiss, and (d) melt re-integrated orthogneiss.

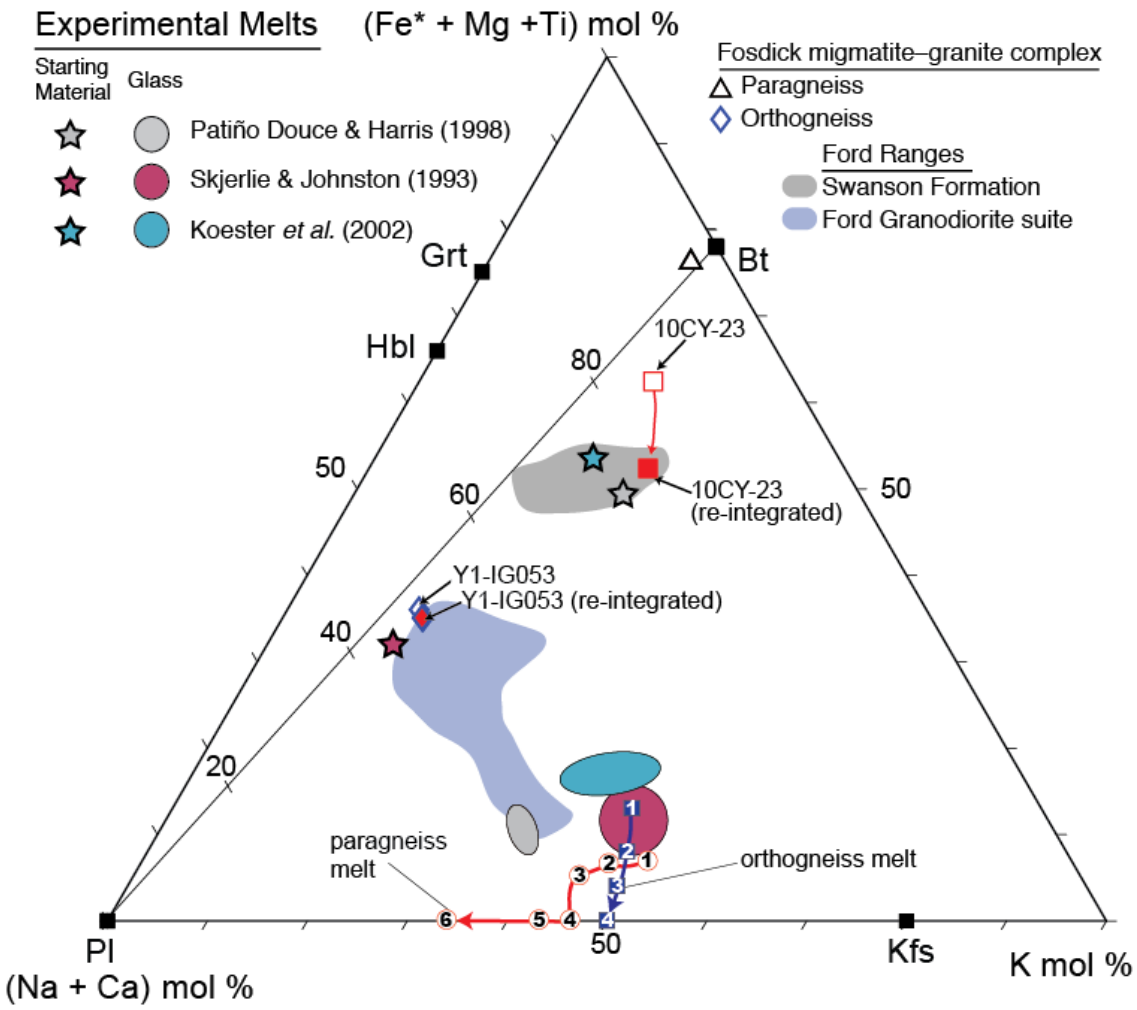

Fig. 2.18. (Fe* + Mg + Ti)–K–(Na + Ca) ternary diagram (after Solar and Brown, 2001) illustrating the melt compositions used in melt reintegration and the trajectories of evolving melt and melt-reintegrated source compositions. The arrows track these compositions down temperature to the solidus.

composition in these examples at 0.7 GPa will be slightly underestimated or overestimated.

2.8.2.2 Results

A total of 24 mol.% melt was reintegrated into the composition of 10CY-023 and the resulting *P–T* pseudosection is shown in Fig. 2.17b. It should be noted that the chemical composition of 10CY-023 plots at higher Fe* + Mg + Ti values than the compositional field of the Swanson Formation in Fig. 2.18. As melt is reintegrated into the composition of 10CY-023, it tracks towards and into the compositional field of the Swanson Formation in Fig. 2.18. In this case, an acceptable model protolith composition is achieved.

For the melt reintegrated composition, the solidus is at lower temperatures of ~660°C, as would be expected for a fertile metasedimentary rock that has not lost any melt. The garnet-in field boundary is located at 790–810°C, which is consistent with the garnet-in field boundaries calculated for the Swanson Formation compositions shown in Fig. 2.13b. This model protolith composition could have generated ~24 mol.% melt, although a small portion of this melt could have been generated and possibly drained during earlier Devonian–Carboniferous metamorphism.

A total of ~5% melt was reintegrated into the composition of orthogneiss migmatite sample Y1-IG053 resulting in the pseudosection shown in Fig. 2.17d. Although the total amount of melt reintegrated is small, the model protolith composition does plot just inside the compositional field of the Ford Granodiorite suite in Fig. 2.18. The solidus in the melt reintegrated composition is <660°C and the garnet-in field

boundary ranges from 780–810°C, both of which are similar to those for the model protolith for paragneiss 10CY-023.

There are a range of possible prograde paths that are compatible with the stability field of the interpreted phase assemblages prior to decompression for the model protolith compositions. The prograde path is restricted to pressures below the kyanite stability field for the paragneiss protoliths and above the cordierite stability field for both the paragneiss and orthogneiss protoliths. At the garnet-in field boundary at 790–810°C for the paragneiss protoliths, this restricts pressure to between 0.60 and 0.95 GPa, which corresponds to apparent thermal gradients that range between 830°C/GPa and 1350°C/GPa.

2.9 Discussion

2.9.1 Lu–Hf garnet ages

Linking Lu–Hf and Sm–Nd garnet ages to the history of garnet growth and/or consumption requires knowledge about where the parent nuclides (Sm or Lu) are concentrated in garnet (e.g. Baxter *et al.*, 2013; Smit *et al.*, 2013). For example, if Lu is concentrated in the core of garnet, which is expected for subsolidus garnet growth (e.g. Zirakparvar *et al.*, 2010), then the Lu–Hf age will be biased towards this Lu-enriched zone, which represents the first increments of garnet growth (e.g. Skora *et al.*, 2006). Alternatively, if Lu is concentrated in the rim of garnet, then the Lu–Hf age may be biased towards the last increments of garnet growth or, in the case of resorption, the timing of garnet breakdown and Lu enrichment in the rim. A complication in the case of

resorption is that redistribution of Lu and Hf at high temperatures may result in Lu–Hf ages that are younger than the true age of resorption (Kelly *et al.*, 2011).

In the Fosdick complex, both euhedral garnet (Fig. 2.5, K6-B26-G1) and garnet that shows microstructural evidence for resorption (Fig. 2.5, K6-B51-G2) in migmatitic paragneisses and orthogneisses have Lu-enriched rims. Therefore, an additional mechanism is required to produce Lu-rich rims in garnet that does not show microstructural evidence for resorption. One possibility is the breakdown of a Lu-rich mineral during the final stages of garnet growth. Lutetium-rich minerals that may be present during garnet growth in the gneisses include monazite, apatite and zircon. Bea *et al.* (1994) report Lu concentrations of monazite (64 and 80 ppm), apatite (19 and 40 ppm) and zircon (9 ppm) from peraluminous migmatites that are generally much greater than the Lu concentrations measured in garnet in this study (generally <15 ppm, Table A.1 in Appendix A).

During prograde metamorphism above the solidus, the proportions of monazite and zircon are expected to decrease in order to saturate the anatectic melt in LREE and Zr (e.g. Kelsey *et al.*, 2008; Yakymchuk and Brown, 2014b). For most LREE and Zr bulk rock compositions of pelites and greywackes during prograde metamorphism, monazite is expected to be mostly consumed at $T > 800$°C whereas some zircon is expected to survive (Yakymchuk and Brown, 2014b). The only rock-forming Lu-rich mineral present in the paragneisses and orthogneisses from the Fosdick complex is garnet, which has Lu concentrations that range from 1 to 16 ppm (Fig. 2.5). The other minerals stable in the suprasolidus phase assemblage (biotite, cordierite, quartz, plagioclase, K-feldspar and

ilmenite) are not expected to have appreciable concentrations of Lu (e.g. Bea et al., 1994).

The dissolution of monazite and zircon is non-linear and increases at higher temperatures (Kelsey *et al.*, 2008; Yakymchuk and Brown, 2014b). Therefore, the rate of monazite and zircon dissolution is expected to be highest at peak *P–T*. This coincides with the final stages of garnet growth in the case of migmatitic paragneiss and orthogneiss from the Fosdick complex and may result in Lu-enriched rims. During decompression above the solidus, cordierite growth at the expense of biotite, sillimanite and garnet is expected based on the phase equilibria modelling presented above for the paragneisses (Fig. 2.14), which will result in the resorption of garnet. The amount of garnet resorption expected in paragneisses during the *P–T* evolution discussed above can be approximated using the garnet mol.% isopleths shown in Fig. 2.19a. In Fig. 2.19a, a *P–T* path that is consistent with the observed phase assemblages in the migmatitic paragneisses is composed of two segments: first, isothermal decompression at 870°C from the cordierite-absent field through the garnet–cordierite–sillimanite trivariant field and into the sillimanite-absent field, and second, isobaric cooling from 870°C to the solidus at ~845°C. During the first segment, roughly 7% of the garnet present prior to decompression is expected to have been consumed and during the second segment, about 29% of the remaining garnet is expected to have been consumed. Therefore, for sample 10CY-023, approximately one-third of the amount of garnet present prior to decompression is expected to have been consumed upon cooling to the solidus. If Lu concentrates in a narrow zone around the edge of the garnet, this amount of resorption may result in significant Lu enrichment of the rim.

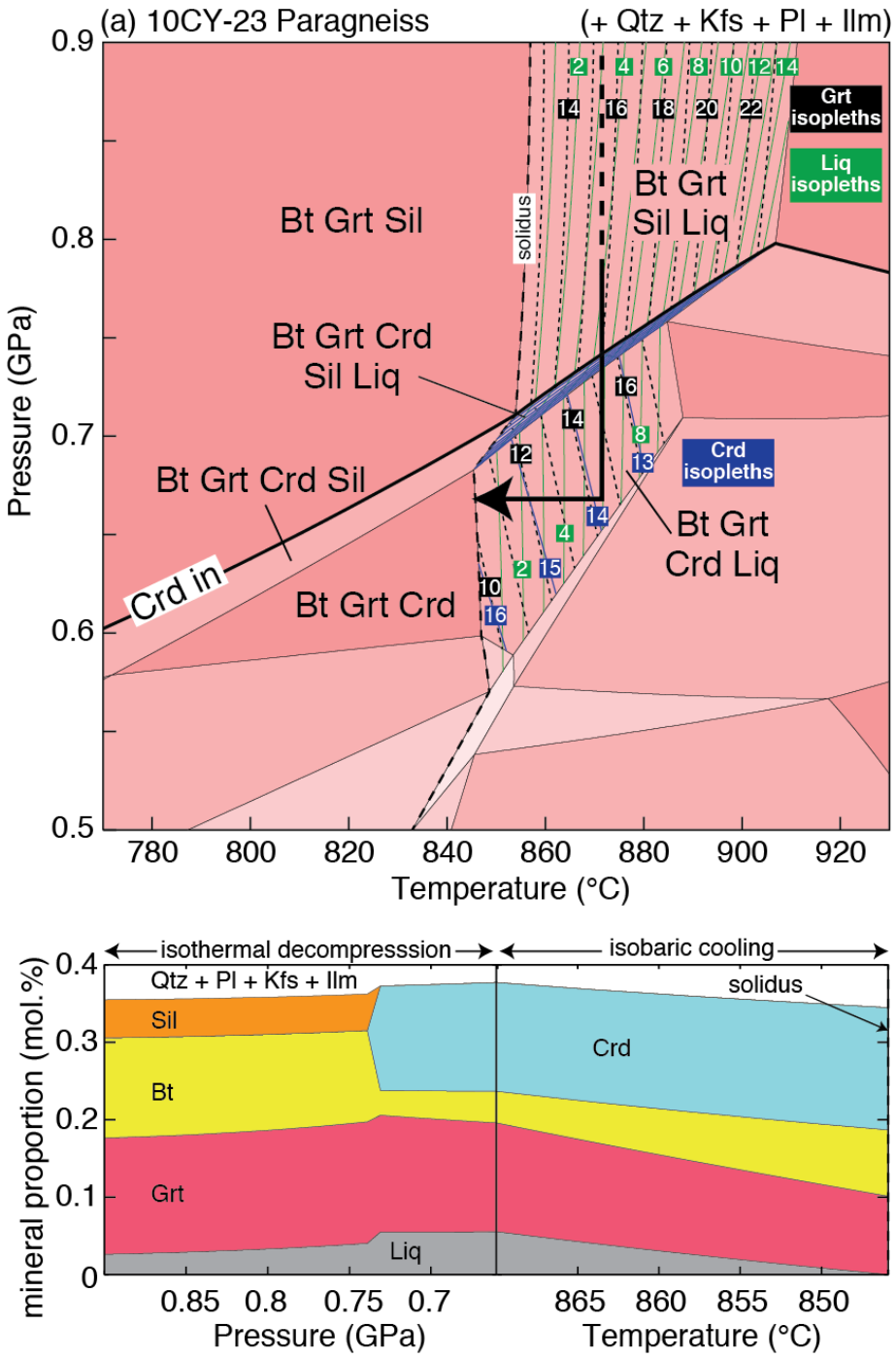

Fig. 2.19. (a) *P–T* pseudosection for sample 10CY-023 showing a simple *P–T* evolution that is consistent with the observed mineral assemblages in migmatitic paragneiss. Isopleths of garnet, cordierite and liquid proportions are in mol.% (approximately equivalent to vol.% in nature). (b) *P–T*–mode diagram illustrating the changes in the relative proportion of minerals along the *P–T* path shown in (a).

It therefore seems permissible that the Lu-rich rims of garnet grains may represent the product of Lu-rich accessory mineral breakdown close to peak *P–T* and/or garnet resorption during decompression and the initial stages of cooling. In the first scenario, the Lu–Hf age will be biased towards the final stages of garnet growth immediately prior to peak *P–T*. In the second scenario, the age will be weighted towards the timing of garnet resorption during the initial stages of decompression and cooling immediately after peak *P–T*. Therefore, the garnet Lu–Hf ages of *c.* 116–111 Ma are interpreted to record the approximate timing of peak metamorphism.

The Lu–Hf and Sm–Nd ages of garnet and $^{206}Pb/^{238}U$ dates of monazite of paragneiss and orthogneiss from the Fosdick complex are summarized in Fig. 2.20. For two paragneiss samples and one orthogneiss sample, the Sm–Nd garnet ages are ~10 Myr younger than the Lu–Hf garnet ages. Lu–Hf ages that are older than Sm–Nd ages from the same garnet separates have been documented in other studies (e.g. Scherer *et al.*, 2000; Kylander-Clark *et al.*, 2007; Smit *et al.*, 2010; Cheng *et al.*, 2010). In many cases the difference in age has been attributed to a higher closure temperature for Lu–Hf compared with Sm–Nd in garnet (e.g. Scherer *et al.*, 2000; Smit *et al.,* 2013). An alternative explanation is that the two isotope systems record different portions of the garnet growth history (e.g. Lapen *et al.*, 2003; Skora *et al.*, 2009). For example, if Lu was concentrated in the core and Sm was even distributed throughout garnet, the Lu–Hf age would be biased towards the early stages of garnet growth whereas the Sm–Nd age would represent an integrated age for the garnet. The lack of Lu-rich cores in garnet from the Fosdick complex makes this second scenario less likely. Therefore, the first interpretation in which the temperature of peak metamorphism was above the closure temperature for

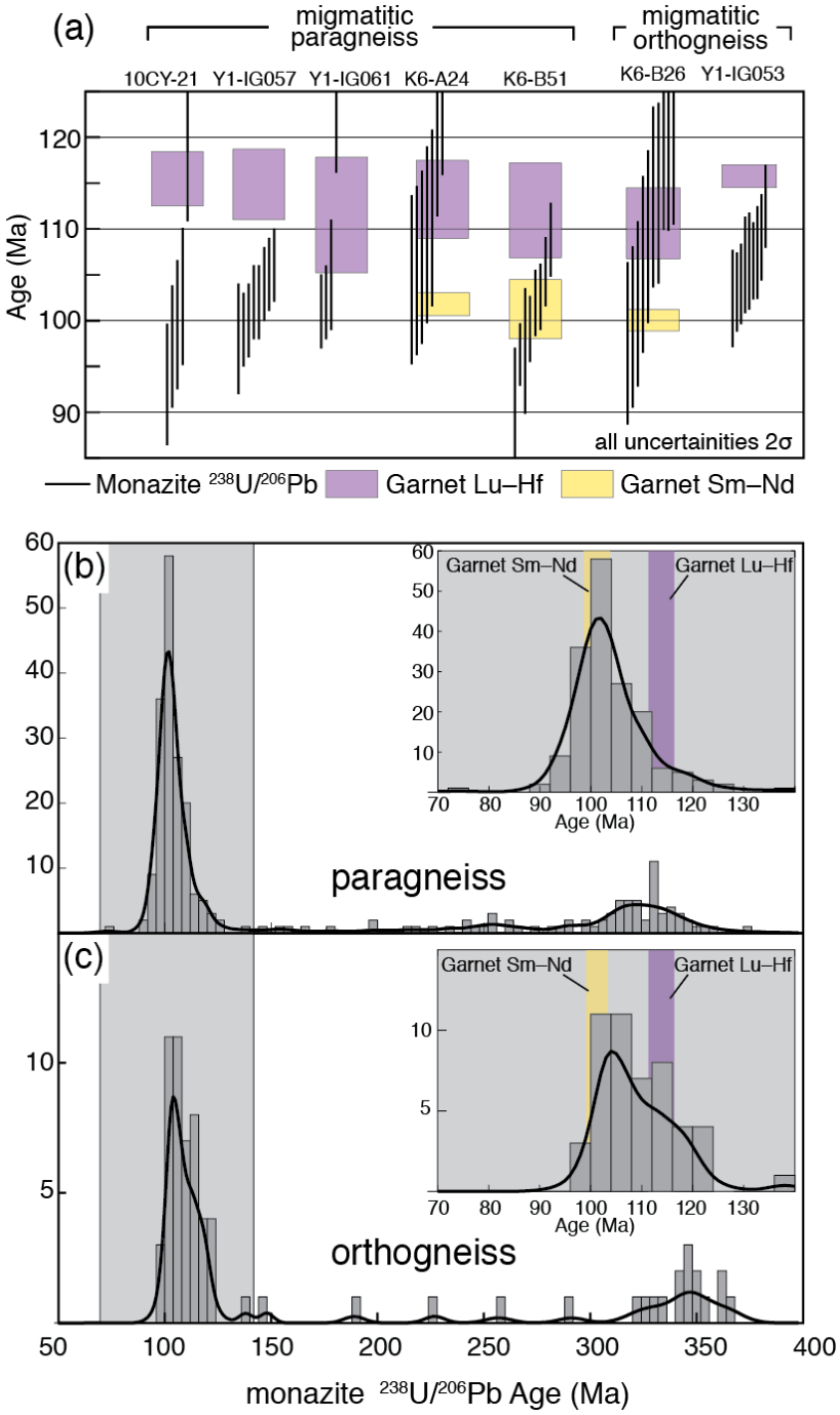

Fig. 2.20. Compilations of U–Pb monazite ages and Lu–Hf and Sm–Nd garnet ages. (a) Summary of monazite and garnet age data from individual samples. (b) Histogram and probability distribution plots for $^{206}Pb/^{238}U$ monazite dates from paragneiss. (c) Histogram and probability distribution plots for $^{206}Pb/^{238}U$ monazite dates from orthogneiss.

the Sm–Nd system in garnet is preferred, and the Sm–Nd ages are interpreted to record exhumation and cooling of the Fosdick complex.

Numerical modelling of Nd diffusion in garnet by Smit *et al.* (2013) suggests that the closure temperature of Nd in garnet with sub-millimeter radii that underwent cooling rates <50°C/Myr is <800°C (using the Nd diffusion data of van Orman et al., 2002), which is below the temperatures recorded by migmatites in the Fosdick complex. The Sm–Nd ages of garnet overlap the peak in the distribution of Cretaceous monazite U–Pb ages from both paragneiss and orthogneiss (Fig. 2.20b, c), which is interpreted to record fast cooling to the solidus. The narrow range of $^{40}Ar/^{39}Ar$ ages for amphibole, biotite, muscovite and K-feldspar of 102 to 95 Ma (Richard *et al.*, 1994) provides supporting evidence for fast cooling in the Fosdick complex. Therefore, the Sm–Nd ages are interpreted as cooling ages related to exhumation.

2.9.2 Linking monazite ages to P–T paths in polyphase migmatites

Monazite with multiple chemical domains that yield different dates can potentially be used to date different points or segments along *P–T* paths (e.g. Gibson *et al.*, 2004; Martins *et al.*, 2009; Reno *et al.*, 2011; Korhonen *et al.*, 2012, 2013). Above the solidus, the growth and dissolution of monazite is strongly dependent on the quantity and chemistry of melt as well as the *P–T* conditions (e.g. Rapp and Watson, 1986; Watson *et al.*, 1989; Stepanov *et al.*, 2012). Monazite is expected to be mostly to completely consumed along prograde *P–T* paths above the solidus during closed system melting (Kelsey *et al.*, 2008) and in rocks that have experienced multiple melt drainage events (Yakymchuk and Brown, 2014b). Monazite is not expected to grow during heating

above the solidus with the possible exception that limited prograde growth may occur due to melt-enhanced Ostwald ripening (Nemchin *et al.*, 2001).

The preservation of anhydrous high-grade mineral assemblages in migmatites and residual granulites requires significant melt drainage during heating (White and Powell, 2002; Diener *et al.*, 2008; Korhonen *et al.*, 2010a, Yakymchuk and Brown, 2014a). In some residual granulites and migmatites, these anhydrous minerals have thin quartz or feldspar films that are interpreted to represent pseudomorphs after grain-boundary melt (Holness and Sawyer, 2008). During cooling to the solidus, this residual melt along grain boundaries may promote the growth of retrograde mineral assemblages and the growth or recrystallization of accessory monazite (Korhonen *et al.*, 2013). Below the solidus fluid infiltration may promote dissolution and re-precipitation of monazite (e.g. Harlov and Hetherington, 2010; Harlov *et al.*, 2011; Williams *et al.*, 2011; Kelly *et al.*, 2012; Lasalle *et al.*, 2014). With this framework for monazite growth and dissolution in mind, the age and chemistry of monazite grains is explored to determine how they may relate to different segments of the polyphase metamorphic history in migmatites from the Fosdick complex.

2.9.2.1 Devonian–Carboniferous monazite domains

Monazite with Devonian–Carboniferous ages occurs mostly as cores surrounded by Cretaceous rims in a variety of microstructural settings in both the paragneisses and orthogneisses (Fig. 2.11d, e). Two monazite grains, one from a resorbed garnet that has been replaced by biotite in paragneiss sample 10CY-036 and another included in garnet from paragneiss sample Y1-IG061 yield only Devonian–Carboniferous dates, but have

narrow, sometimes discontinuous Y-enriched rims inferred to have been generated by garnet breakdown to biotite in the presence of melt during cooling to the solidus in the Cretaceous. One monazite grain in orthogneiss sample Y1-BG040 yields two discordant dates of *c.* 257 and *c*. 189 Ma (Fig. 2.10) from patchy zones (Fig. 2.7c) that are interpreted to represent analyses that overlap Devonian–Carboniferous and Cretaceous age domains.

Linking the age and chemistry of the Devonian–Carboniferous cores of some monazite grains to the *P–T* evolution is difficult because of extensive resorption, new monazite growth during Cretaceous metamorphism and the uncertainties in the *P–T* path during Devonian–Carboniferous metamorphism. Devonian–Carboniferous monazites dates from paragneisses and orthogneisses reported in Korhonen *et al.* (2012) and this study (376–299 Ma) are mostly younger than Devonian–Carboniferous plutonic rocks that crop out within (370–355 Ma) and outside (375–345 Ma) the Fosdick complex. For orthogneisses, the peak in the distribution of monazite dates (*c.* 347; Fig. 2.20c) coincides with the emplacement of the youngest members of the Ford Granodiorite suite (Yakymchuk et al., 2014), whereas in paragneisses, the peak in the distribution is at *c.* 326 (Fig. 2.20b), which is younger than the crystallization age of the youngest Carboniferous granites both inside and outside the Fosdick Complex.

The diatexites represents possible relicts of Devonian–Carboniferous metamorphism and partial melting (Yakymchuk *et al.*, 2014). Inhomogeneous diatexite sample Y1-IG071 contains zircon with resorbed oscillatory zoned cores that yield SHRIMP U–Pb dates of *c.* 376–357 Ma (or Precambrian dates that are interpreted to be inherited) and rims that yield dates of *c.* 318–305 Ma or 109–104 Ma (Yakymchuk et al.,

2014). The rims are interpreted to record the timing of anatectic melt crystallization in the rock during both the Devonian–Carboniferous metamorphism and the Cretaceous reworking (Yakymchuk et al., 2014). Devonian–Carboniferous U–Pb monazite dates in this sample range from 364 to 291 Ma, which overlap with Carboniferous dates from rims in zircon and are interpreted to record the protracted crystallization of anatectic melt. The range of Devonian–Carboniferous dates from monazite is interpreted to represent protracted crystallization from residual melt along grain boundaries during cooling after the cessation of arc-related magmatism at *c.* 345 Ma.

2.9.2.2 Monazite inclusions in garnet

Monazite inclusions in garnet in the paragneisses and orthogneisses commonly have Devonian–Carboniferous cores and Cretaceous rims. The cores are interpreted to be monazite relicts from the earlier metamorphic event that were included in garnet that grew during Cretaceous reworking. However, the dates obtained from rims and from monazite inclusions without cores are mostly <110 Ma (Fig. 2.11a, b, c), which is younger than the Lu–Hf garnet ages of 116–111 Ma. Mineral inclusions that yield dates that are younger than the age of their host minerals are not uncommon. For example, Reno *et al.* (2011) interpreted Y-enriched zones in monazite inclusions in garnet to represent high-temperature retrograde growth of monazite during melt crystallization.

In this study, monazite inclusions in garnet from the Fosdick complex are always associated with fractures in garnet and the fractures usually extend to the edge of the grain (e.g. Fig. 2.3j). The fractures commonly contain biotite, which is part of the solidus phase assemblage and suggests that the cracks predate or are coeval with the final

crystallization of melt. Therefore, the fractures represent potential fast diffusion pathways at temperatures above or close to the solidus. The concentrations of P and Y in garnet (Villaseca *et al.*, 2003; Kohn and Malloy, 2004), and possibly the rare earth elements (McFarlane et al., 2005), are generally sufficient that in the presence of an additional LREE source, such as a pre-existing grain of monazite or melt, the growth of monazite during garnet breakdown is plausible (Reno *et al.*, 2011; Korhonen *et al.*, 2012). Therefore, a plausible explanation for the <110 Ma dates obtained from monazite inclusions in garnet is that they represent growth and/or recrystallization during garnet breakdown in the presence of melt during cooling from peak *P–T*.

2.9.2.3 Linking Cretaceous monazite to garnet breakdown during decompression

Monazite in paragneisses from across the Fosdick complex yield dominantly Cretaceous dates that are mostly in the range *c*. 110–95 Ma (Fig. 2.20b). Although monazite chemical zoning is variable, the most common zoning pattern is Y-depleted cores that yield dates that are either Carboniferous or *c.* 118–107 Ma and relatively Y-enriched rims that yield dates of 106–95 Ma, which is typical of monazite included in cordierite for example. Yttrium zoning in monazite has been linked to the breakdown or growth of relatively Y-rich phases, such as xenotime and garnet, in metamorphic rocks (Gibson *et al.*, 2004; Martins *et al.*, 2009; Högdahl *et al.*, 2012; Korhonen *et al.*, 2012). No xenotime was found in the migmatitic paragneisses and it is not expected to be stable at the estimated *P–T* conditions of metamorphism, which were well above the expected stability field of xenotime in pelitic rocks (< 0.5 GPa and below the wet solidus; Spear and Pyle, 2010).

Most monazite growth in residual metamorphic rocks is expected to occur within 50°C of the solidus during cooling from peak metamorphic conditions accompanying the crystallization of residual anatectic melt along grain boundaries (Kelsey *et al.*, 2008; Yakymchuk and Brown, 2014b). Garnet exerts a strong control on the Y budget in migmatites because of its high Y concentrations compared with other rock forming minerals (e.g. Bea et al., 1994). In the migmatitic paragneisses and orthogneisses from the Fosdick complex the measured Y concentrations in garnet are 50 to 560 ppm (Table A.1 in Appendix A). Because monazite strongly partitions Y in pelitic rocks, the breakdown of garnet to cordierite and biotite, and the concurrent growth of monazite during cooling to the solidus generated the Y-enriched rims (e.g. Foster et al., 2000; Rubatto et al., 2001; Gibson et al., 2004; Rubatto et al., 2013). Thus, the *c.* 106–100 Ma monazite dates record the timing of exhumation and cooling of the Fosdick complex. Rapid cooling consistent with extension and dome formation is demonstrated by: (1) 107–100 Ma crystallization ages of granites associated with the migmatites (Brown *et al.*, 2014); (2) Sm–Nd ages of garnet which suggest cooling below ~800°C (e.g. Smit *et al.*, 2013) at 102–99 Ma, (3) U–Pb crystallization ages of 97 and 96 Ma from two microgranite dykes that crosscut the migmatitic fabrics (McFadden *et al.*, 2010a; Brown *et al.*, 2014), and (4) $^{40}Ar/^{39}Ar$ ages of 102–95 Ma retrieved from amphibole, biotite, muscovite and K-feldspar (Richard *et al.*, 1994). Furthermore, evidence of regional extension is supported by mafic dykes associated with tensile structures throughout the Ford Ranges that yielded $^{40}Ar/^{39}Ar$ ages of 104–96 Ma (Siddoway *et al.*, 2005).

The geological significance of the Y-depleted monazite cores that yield dates of 118–107 Ma is less certain. Growth of monazite during prograde melting is not generally

expected (e.g. Kelsey *et al.*, 2008; Yakymchuk and Brown, 2014b), but prograde melt-enhanced Ostwald Ripening is a plausible mechanism that might explain these dates (Nemchin *et al.*, 2001).

Finally, the geological significance of monazite dates younger than the timing of crossing the solidus (*c.* 100–97 Ma), i.e. those in the range *c.* 97–93 Ma (n = 18, with three younger dates of 91, 88 and 74 Ma) is addressed. Melt crystallization in the Fosdick complex would have liberated fluid at the solidus both at the level of exposure and at depth that are postulated to have recrystallized monazite by dissolution–reprecipitation (e.g. Reno et al., 2011).

2.9.2.4 Spatial variation in monazite U–Pb dates across the Fosdick complex

In Fig. 2.21, the U–Pb dates reported in this study are combined with the SHRIMP U–Pb monazite dates of Korhonen *et al.* (2012) to evaluate the similarities and differences in the timing of monazite growth across the Fosdick complex. In the western portion of the Fosdick complex stretching from Mt Avers to Maigetter Peak in the west, with three exceptions samples contain both Carboniferous and Cretaceous monazite. The three exceptions (migmatitic paragneisses 10CY-023 and Y1-MJ074, and migmatitic orthogneiss Y1-IG053) are interpreted to have been more strongly overprinted by the Cretaceous metamorphism compared with the other samples.

Fig. 2.21. Monazite $^{206}Pb/^{238}U$ dates and 2σ uncertainties from migmatitic paragneiss (black lines) and orthogneiss (blue lines) from Korhonen *et al.* (2012) and this study plotted from west to east across the Fosdick migmatite–granite complex.

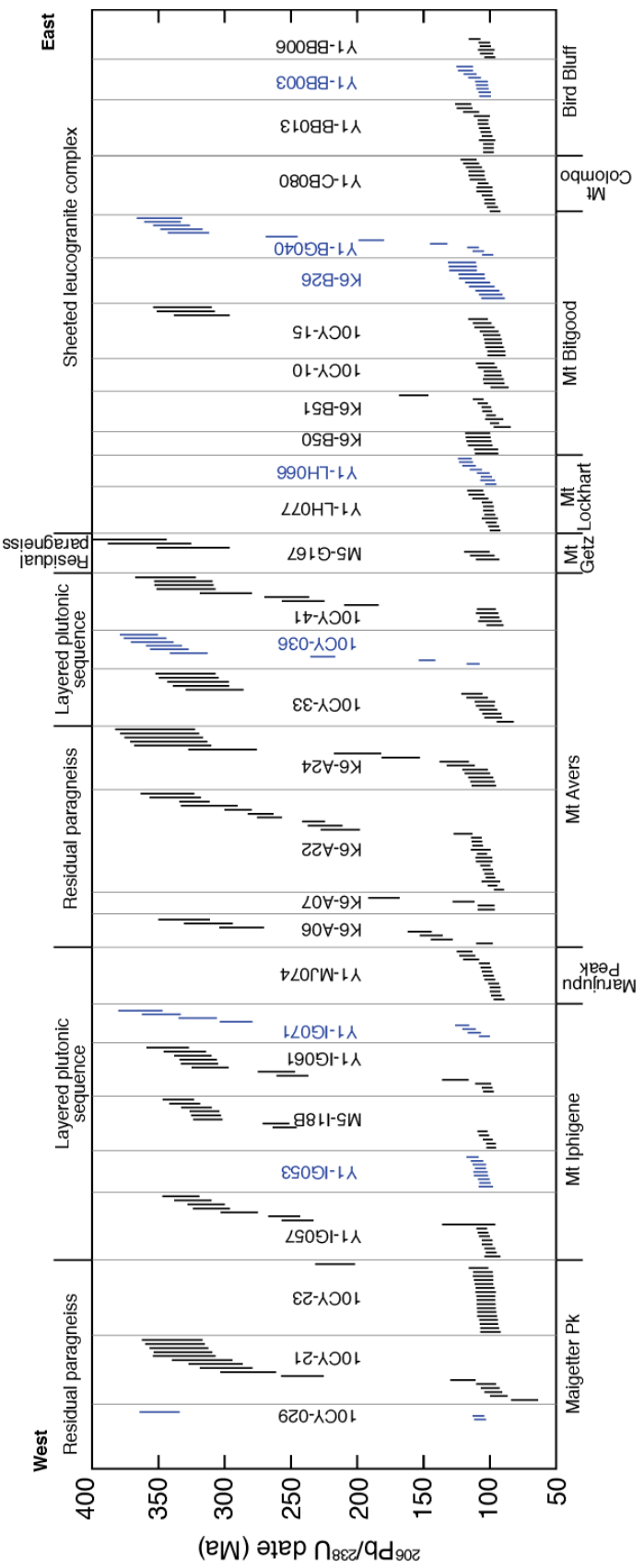
West
East
Residual paragneiss
Residual paragneiss
Layered plutonic sequence
Residual paragneiss
Layered plutonic sequence
Sheeted leucogranite complex
Residual paragneiss
Sheeted leucogranite complex
Maigetter Pk
Mt Iphigene
Marujupu Peak
Mt Avers
Mt Getz
Mt Lockhart
Mt Bitgood
Mt Colombo
Bird Bluff
10CY-029
10CY-21
10CY-23
Y1-IG057
Y1-IG053
M5-118B
Y1-IG061
Y1-IG071
Y1-MJ074
K6-A06
K6-A07
K6-A22
K6-A24
10CY-33
10CY-036
10CY-41
M5-G167
Y1-LH077
Y1-LH066
K6-B50
K6-B51
10CY-10
10CY-15
K6-B26
Y1-BG040
Y1-CB080
Y1-BB013
Y1-BB003
Y1-BB006
400
350
300
250
200
150
100
50
206Pb/238U date (Ma)

In the eastern portion of the Fosdick complex stretching from Bird Bluff to Mt Lockhart, with two exceptions monazite grains yield Cretaceous dates in both paragneiss and orthogneiss. First, an orthogneiss from Mt Bitgood (Y1-BG040) yields five dates ranging from 349 to 327 Ma from strongly resorbed cores in monazite grains that also yield dates of *c.* 100 Ma from rim domains. Second, two grains from a paragneiss (10CY-015) from Mt Bitgood yield three dates of *c*. 322–317 Ma from Y-depleted cores that are surrounded by Y-enriched rims yielding dates of *c.* 100 Ma. These samples provide evidence of Devonian–Carboniferous monazite growth in the eastern portion of the Fosdick complex, which was previously unrecognised (Korhonen *et al.*, 2012).

The eastern portion of the Fosdick complex represents an accumulation zone for granite magma produced during Cretaceous anatexis (Korhonen *et al.*, 2010b; Brown et al., 2014). A possible explanation for the paucity of Devonian–Carboniferous monazite in migmatites from the eastern portion of the complex is pervasive infiltration and reworking of paragneisses and orthogneisses as magma accumulated in sub-horizontal and layer-parallel sills in this region. In the western portion of the complex, Cretaceous granites occur mainly as discordant dykes in petrographic continuity with stromatic leucosomes in host migmatites that were contributing melt to the dykes (Brown *et al.*, 2014), which limited dissolution of monazite in the host migmatites. Alternatively, Korhonen *et al.* (2010a, b, 2012) suggested that the eastern portion of the complex may have remained subsolidus during the Devonian–Carboniferous event owing to a shallower structural position. The absence of Devonian–Carboniferous diatexites in the eastern portion of the complex supports this possibility, but does not exclude the reworking during the accumulation of Cretaceous granites.

2.9.3 Regional implications

2.9.3.1 Devonian–Carboniferous

West Antarctica occupied a segment of the East Gondwana margin that was contiguous with the western Province of New Zealand and the Tasmanides of eastern Australia in Phanerozoic reconstructions (Fig. 2.1; Veevers, 2012). In eastern Australia, the Tasmanides orogen is attributed to alternating extensional and contractional tectonics associated with a west-dipping subduction zone that migrated oceanward from the Cambrian to the Permian (see Glen, 2013 for an overview). The Tasmanides represent the type example of a circum-pacific accretionary orogen (Collins, 2002) and models of its tectonic evolution are commonly extrapolated along external orogenic systems around the Pacific rim (e.g. Collins et al., 2011). Comparing the *P–T* evolutions of metamorphic rocks from different locations along and across strike of the East Gondwana active margin provides insight into the similarities and differences in the processes operating along and across an active continental margin system.

High-grade metamorphic rocks in the Tasmanides are limited to the products of regional aureole high-temperature and low-pressure (HT–LP) metamorphism. In the Lachlan Fold Belt, the Cooma Complex migmatites record HT–LP metamorphism ($T >$ 650°C at $P < 0.40$ GPa; Johnson and Vernon, 1995) at *c.* 433 Ma (Williams, 2001). These rocks are interpreted to record counterclockwise *P–T* paths and isobaric cooling (Johnson and Vernon, 1995), and Morand (1990) reported similar HT–LP metamorphism (T of 700°C at P of 0.35 GPa) from migmatites in the Omeo Metamorphic Complex. In the Wongwibinda Metamorphic Complex of the southern New England Orogen, HT–LP metamorphic rocks record *P–T* conditions of up to 660°C at $P < 0.35$ GPa and are

associated with Late Carboniferous–Early Permian S-type granites (Craven *et al.*, 2012). Monazite and zircon from these the high-grade rocks yield U–Pb ages *c.* 297 and 291 Ma, respectively, which are interpreted to date high-temperature metamorphism (Craven *et al.*, 2012). The close association of HT–LP metamorphism and S-type granite production is interpreted to be the product of an extensional geodynamic setting (Craven *et al.*, 2012).

In the Western Province of New Zealand, Devonian–Carboniferous anatexis is reported in the Bonar Range (Scott *et al.*, 2011). *P–T* conditions of 670°C at 0.51 GPa are estimated from thermobarometry and U–Pb monazite ages of 378–352 Ma from paragneisses are interpreted to record the approximate timing of exhumation and melting (Scott *et al*., 2011). Granites from the temporally associated Karamea suite (371–351 Ma; Tulloch *et al*., 2009; Sagar and Palin, 2013) have εNd values of -3 to -9 and estimated magma $\delta^{18}O$ values of 10.8 to 12.5‰ (Tulloch *et al.,* 2009), which indicates that these granites were derived primarily from a metasedimentary source. The high apparent thermal gradient of the estimated *P–T* conditions of the high-grade metamorphic rocks (~1300°C/GPa), their association with the S-type Karamea granite suite, and presence of contemporaneous mafic rocks (Turnbull *et al.*, 2013), led Scott *et al.* (2011) to suggest that elevated heat flow associated with regional extension, possibly resulting from roll back of the subducting slab, was the primary cause of crustal melting at this time in the Western Province.

Although a wide range of *P–T* conditions are possible for Devonian–Carboniferous metamorphism in the Fosdick complex, the preserved mineral assemblages are inconsistent with HT–LP metamorphism and counterclockwise *P–T* paths

documented in the Tasmanides. In contrast to the emplacement of voluminous S-type granites in the Tasmanides and the Western Province, magmatism in the Ford Ranges is dominated by calc-alkaline magmatism with only minor S-type magmatism (e.g. Pankhurst *et al.*, 1998; Tulloch *et al.*, 2009; Yakymchuk *et al.*, 2014). The apparent thermal gradient of Devonian–Carboniferous metamorphism in the Fosdick complex is consistent with the range of apparent thermal gradients documented from continental magmatic arcs (e.g. Rothstein and Manning, 2003). Thus, that Devonian–Carboniferous metamorphism in the Fosdick complex is interpreted to have been the product of regional heating associated with the development of an active continental magmatic arc.

2.9.3.2 Cretaceous

U–Pb ages of Y-enriched zones from monazite in migmatitic paragneisses from the Fosdick complex suggest that exhumation and cooling had started by *c.* 106 Ma, preceding the breakup of Zealandia from West Antarctica at *c.* 83 Ma (Eagles *et al.*, 2004; Siddoway, 2008). In the western Province of New Zealand, high-grade metamorphic rocks of Cretaceous age crop out in Fiordland and the Paparoa metamorphic complex. In Fiordland, Scott and Cooper (2006) report U–Pb zircon and titanite ages from the Mount Irene Shear Zone that suggest a transition from a convergent to an extensional tectonic regime between 111 and 108 Ma. Stowell *et al.* (2014) used results from Sm–Nd garnet and U–Pb zircon geochronology of metadioritic granulites in Fiordland to argue for a change in tectonics from convergence to extension within 5 Myr and extensional collapse initiating at c. 111 Ma.

In the Paparoa Range, rapid cooling occurred from *c*. 110 to 90 Ma as determined by $^{40}Ar/^{39}Ar$ geochronology of high-grade metamorphic rocks (Spell et al., 2000). More recently, Schulte *et al.* (2014) reported a Rb–Sr age of *c.* 116 Ma from amphibolite facies mylonites that were associated with the detachment responsible for exhuming the Paparoa metamorphic complex, which suggests that extension had begun by this time.

Garnet Lu–Hf ages reported in this study suggest that peak metamorphic conditions were reached at *c.* 116–111 Ma and U–Pb monazite ages from Y-enriched rims document exhumation at suprasolidus conditions by *c.* 106 Ma, with cooling to the solidus being essentially complete by *c.* 100 Ma. This suggests orogenic collapse and exhumation of the Fosdick migmatite–granite complex as a gneiss dome had begun by *c*. 106 Ma, which supports geophysical studies in West Antarctica that indicated breakup of the margin had begun by *c*. 110–100 Ma (Siddoway *et al.*, 2005). Together with the extension documented from the Western Province of New Zealand, this suggests an episode of regional lithospheric extension preceding the final separation of Zealandia from West Antarctica at *c.* 83 Ma (Eagles *et al.*, 2004; Siddoway, 2008).

2.10 Conclusions

Garnet and monazite geochronology coupled with phase equilibria modelling provides a powerful tool to decode the *P–T–t* paths of polyphase high-grade metamorphic rocks. In the Fosdick migmatite–granite complex, Devonian–Carboniferous metamorphism is recorded by U–Pb ages of monazite cores and quantified using phase equilibria modelling of diatexite and protolith compositions. This episode of metamorphism is interpreted to be associated with waning calc-alkaline arc-related magmatism in the Ford Ranges, whereas metamorphic rocks in New Zealand and the

Tasmanides record lithospheric extension, as evidenced by contrasting the *P–T* evolution of high-grade rocks in between West Antarctica and these locations. Lu–Hf garnet geochronology yields ages of 116–111 Ma that are interpreted to record the timing of peak metamorphism in the Cretaceous whereas U–Pb ages of monazite record crystallization of residual melt along grain boundaries during cooling to an elevated solidus. Ages obtained from Y-enriched rims in monazite grains associated with cordierite are interpreted to represent growth during the breakdown of garnet in the presence of melt during decompression and cooling at 106–100 Ma. This suggests that exhumation of the Fosdick complex was underway at this time, which broadly corresponds to the timing of exhumation in high-grade metamorphic rocks in the Western Province of New Zealand. The final breakup of the East Gondwana margin and the separation of Zealandia from West Antarctica followed *c.* 25 Myr later.

Chapter 3: Are cumulate granites typical of migmatitic gneiss domes? An example from the Fosdick Mountains of Marie Byrd Land, West Antarctica

3.1 Abstract

In the Cretaceous Fosdick migmatite–granite complex, *P–T* phase equilibria modelling of migmatitic paragneisses and orthogneisses, and the occurrence of leucosome-bearing normal-sense shear zones are consistent with suprasolidus conditions in the complex extending into the early stages of doming and exhumation. Sub-horizontal sheeted granites at shallower structural levels and variably oriented granites in networks at deeper structural levels within the complex commonly have coarse blocky plagioclase and/or K-feldspar grains within interstitial quartz, consistent with early crystallization of feldspar. The granites yield U–Pb zircon crystallization ages from 115 to 100 Ma, with a dominant grouping at 107–100 Ma, which corresponds to the timing of dome formation during the regional oblique extension that facilitated exhumation of the complex. They have whole rock Sr and Nd and zircon Hf and O isotope compositions consistent with derivation from high-grade orthogneiss equivalents of the Ford Granodiorite suite (dominant component), a series of Devonian–Carboniferous calc-alkaline igneous rocks, and paragneisses equivalents to the host Swanson Formation (subordinate component), a Cambrian–Ordovician metaturbidite sequence, both of which are exposed within the Ford Ranges outside the Fosdick complex. However, the major and trace element chemistry of these granites is highly variable and they typically have large positive Eu anomalies,

features inconsistent with the composition of primary crustal melts predicted from such source materials, but consistent with the early accumulation of feldspar and quartz and subsequent drainage of fractionated melt. The granites in networks are interpreted to represent clogging of magma transport channels through the middle crust as melt drainage slowed during doming and exhumation, whereas the sheeted granites record collapse of sub-horizontal partially-crystallized layers of magma by filter pressing and melt loss during vertical shortening associated with doming and exhumation. These processes separated cumulate-rich residues from evolved melt. Outside the Fosdick complex at shallower structural levels, four widely spaced granites have U–Pb zircon crystallization ages of 105–102 Ma. Three of these granites from the Ross Province have geochemical characteristics, including higher total rare earth element concentrations and moderate negative Eu anomalies, similar to a late microgranite from inside the Fosdick complex. Zircon Hf and O isotope compositions for these granites are consistent with sources similar to those for the granites inside the Fosdick complex. The fourth granite, from the Amundsen Province, has zircon Hf and O isotope compositions that require a juvenile source, suggesting that it is unrelated to granites from the Ross Province.

The results of this study are likely to be widely applicable to granites in other migmatitic gneiss domes. Thus, caution is urged when estimating melt proportions from the volume of granite in these domes, since the granites may not represent primary crustal melt compositions. Furthermore, this study demonstrates that crystallization began during migration and emplacement of granite magma, allowing more evolved melts to ascend to mid-crustal levels. Thus, it is likely that as minerals accumulate and/or the rate of magma flow declines, the transport conduits may become clogged, restricting the flow and

allowing separation of evolved melt from cumulate. This is likely to be a rate-limiting step on timescales of late-stage melt extraction from suprasolidus crust. Finally, evolved melt drained from cumulate granites is likely to have higher concentrations of the heat producing elements. This will have implications for the tectonic history of large hot mountain belts, cooling of ultrahigh-temperature metamorphic terrains, priming the crust for future ultrahigh-temperature metamorphic events, Proterozoic 'hot' orogenesis, and the long-term stability of the continental crust.

3.2 Introduction

The generation and segregation of granite melt in the deep continental crust followed by extraction, ascent and emplacement of magma into the upper crust is an important process by which the continental crust has become differentiated into a depleted lower portion and a complementary enriched upper portion (Sawyer et al., 2011; Brown, 2013). Reworking of the crust by this process plays a major role in the redistribution of mass and energy within the continents as well as the heat producing elements. This has important implications for the tectonic history of large hot mountain belts (Jamieson et al., 2011), cooling ultrahigh-temperature (UHT) metamorphic terrains (Korhonen et al., 2013), priming the crust for future UHT metamorphic events (Clark et al., 2011), the particular style of some Proterozoic 'hot' orogens (McLaren and Powell, 2014), and the long-term stability of the continental crust (Sandiford and McLaren, 2002).

The composition of melt produced by fluid-absent hydrate-breakdown reactions in deep crustal settings has been determined from experimental melting studies (Skjerlie

et al., 1993; Patiño Douce and Harris, 1998; Koester et al., 2002), the analysis of former melt inclusions in peritectic minerals (Cesare et al., 2007; Acosta-Vigil et al., 2007; Ferrero et al., 2011, 2012, 2014; Bartoli et al., 2013) and thermodynamic modelling (White et al., 2011). However, the liquid compositions obtained in these studies may not be representative of the melt extracted from the deep crust during anatexis due to the processes associated with melt–residuum separation during extraction and ascent, including peritectic mineral entrainment and dissolution (Brown et al., 1999; Villaros et al., 2009; Taylor and Stevens, 2010; Clemens and Stevens, 2012). Also, during lower temperature crustal melting, the type and rate of accessory mineral dissolution versus the rate of melt extraction may lead to isotopic disequilibrium between melt and residue (Sawyer, 1991; Watt and Harley, 1993; Zeng et al., 2005*a*, *b*, *c*). Finally, fractional crystallization during transport may modify melt compositions to generate contrasting cumulate-dominated and fractionated granites (e.g. Sawyer, 1987; Milord et al., 2001; Solar and Brown, 2001; Morfin et al., 2014). Using the benchmarks from experiments, melt inclusions and thermodynamic modelling in conjunction with geochemical data obtained from source materials, anatectic residua and granites enables these processes to be discriminated in nature.

In the Ford Ranges of Marie Byrd Land, West Antarctica, in the core of a dome structure exposed in the Fosdick Mountains, granites emplaced into migmatites at shallower structural levels may be linked to granite in transport channels cutting migmatites exposed at deeper structural levels. Although much of the granite within the Fosdick migmatite–granite complex (hereafter the Fosdick complex) was likely trapped during migration from deeper in the crust, the associated migmatitic gneisses represent

useful analogues of the deeper source materials. Here, we report whole rock and zircon geochemical data for migmatitic gneisses and granites from different structural levels within the Fosdick complex as well as for the putative lower-grade protoliths of the gneisses exposed outside the complex. In addition, we report data for four widely spaced granites from outside the Fosdick complex that were emplaced contemporaneously with the dominant period of granite crystallization inside the complex. This comprehensive dataset allows us to discuss the processes that control the composition of crustal granites from source to sink.

Cretaceous granites within the Fosdick complex were derived from two distinct sources, a metasedimentary protolith, represented outside the complex by the Swanson Formation, and a calc-alkaline plutonic protolith, represented outside the complex by the Ford Granodiorite suite, during a high-temperature metamorphic event that culminated in dome formation and exhumation of the deep crust. The chemistry of the Cretaceous granites is highly variable. This variability is attributed to fractional crystallization, which allowed the accumulation of early-crystallized minerals, and drainage of evolved melt during doming. Such cumulate granites may be typical of migmatitic gneiss domes due to syntectonic crystallization and filter pressing. Fractionated melt complementary to the cumulate granites inside the Fosdick complex may be represented by the Cretaceous Byrd Coast granite suite, which was emplaced into the upper crust outside the complex (Korhonen et al., 2010*b*).

3.3 Regional Geology

3.3.1 West Antarctica

In the Phanerozoic, the continental margin of East Gondwana was an active convergent plate margin that stretched from eastern Australia through Antarctica to South America (Veevers, 2012; Fig. 3.1a). The Western Province of New Zealand and the Tasmanides of East Australia were once contiguous with Marie Byrd Land and north Victoria Land in Antarctica prior to the breakup of the continental margin of East Gondwana (Fig. 3.1a; Veevers, 2012). Based on Nd model ages of granites, Pankhurst et al. (1998) separated Marie Byrd Land into the Ross Province in the west and the Amundsen Province in the east. Paleomagnetic data suggest that these two provinces were amalgamated in the Lower Cretaceous (DiVenere et al., 1995; Luyendyk et al., 1996), but the boundary between the two provinces is unexposed and is believed to be oblique to the present coastline (Fig. 3.1c; DiVenere et al., 1995; Pankhurst et al., 1998). A diachronous shift from oblique convergence to oblique divergence along the plate margin during the Albian predated the development of the West Antarctic rift system that eventually separated Zealandia, a continental terrane that included the Western Province of New Zealand, from West Antarctica (Weaver et al., 1994; Mukasa and Dalziel, 2000; Tulloch et al., 2009*b*; McFadden et al., 2010*a*,*b*). The geodynamic cause of the change to regional extension has been discussed widely, but is beyond the scope of this paper.

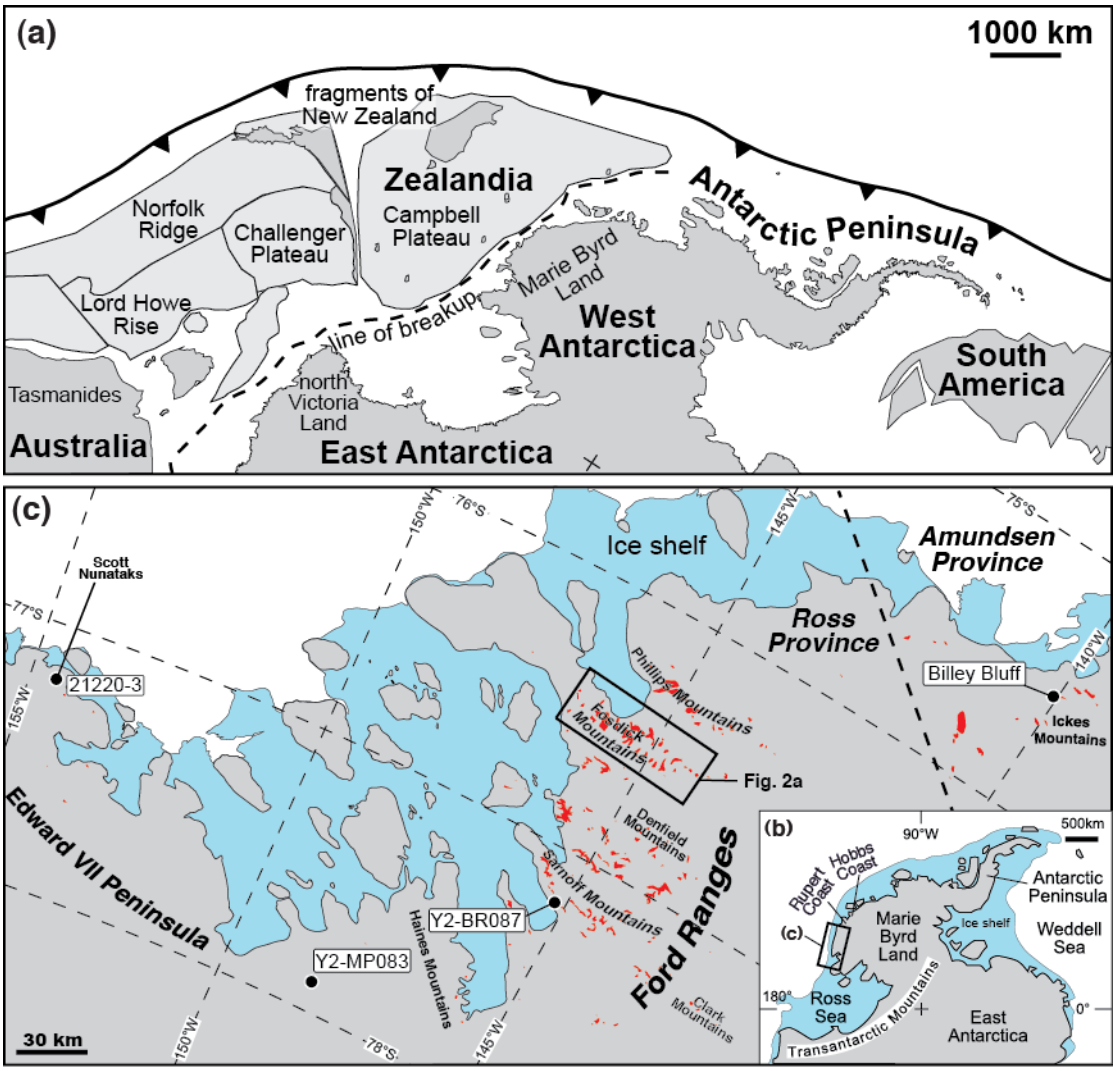

Fig. 3.1. (a) Geometrical reconstruction of the East Gondwana active convergent margin (modified from Veevers, 2012, fig. 4). (b) Location of the study area in Antarctica. (c) Geographic map of the Ford Ranges with the locations for granite samples outside the Fosdick complex. The inferred location of the boundary between the Ross and Amundsen provinces is from Mukasa and Dalziel (2000).

3.3.2 Ford Ranges

3.3.2.1 Outside the Fosdick Mountains

The Ford Ranges are located in Marie Byrd Land, which lies along the eastern side of the Ross Sea in West Antarctica (Fig. 3.1b, c). The oldest exposed unit in the Ford Ranges and elsewhere in the Ross Province is the Cambrian–Ordovician Swanson Formation, a metaturbidite sequence with detrital zircon ages indicating derivation from granite protoliths in the Ross–Delamerian orogen and largely unexposed Proterozoic basement (Pankhurst et al., 1998; Yakymchuk et al., 2014). The Swanson Formation comprises folded and cleaved metagreywackes and slates of sub-greenschist to greenschist facies due to deformation and regional metamorphism dated at *c*. 450 Ma (Adams, 1986).

In the Ross Province, Devonian–Carboniferous calc-alkaline plutonism is represented by the Ford Granodiorite suite, which was intruded into the Swanson Formation. In the Ford Ranges, these granodiorites have yielded whole rock Rb–Sr isochron and SHRIMP U–Pb zircon ages in the range 375–339 Ma (Adams, 1987; Pankhurst et al., 1998; Siddoway and Fanning, 2009; Tulloch et al., 2009*a*; Yakymchuk et al., 2014). This episode of magmatism, which is recognized across and along the East Gondwana margin (Muir et al., 1996; Mukasa and Dalziel, 2000; Siddoway and Fanning, 2009), has been attributed to subduction (Borg et al., 1987; Weaver et al., 1991) or back-arc extension (Muir et al., 1996; Siddoway and Fanning, 2009; Tulloch et al., 2009*a*).

Cretaceous activity is widespread in Marie Byrd Land. In the Amundsen Province, the Demas Range migmatite complex on the Rupert and Hobbs Coasts (Fig. 3.1b) has yielded conventional U–Pb zircon lower intercept ages of ca. 128–113 Ma

(Mukasa and Dalziel, 2000), while I-type granites here and further east have yielded conventional U–Pb zircon lower intercept ages of ca. 124–98 Ma (Mukasa and Dalziel, 2000). In both the Ross and Amundsen Provinces, Cretaceous A-type granites (Weaver et al., 1991), including the Byrd Coast Granite suite in the Ford Ranges (Adams, 1987), were emplaced during a period of crustal extension (Weaver et al., 1994; Mukasa and Dalziel, 2000). These granites have yielded whole rock Rb–Sr isochron ages of ca. 142, 131 and 110 Ma in the Ford Ranges (Adams, 1987) and ca. 101–95 Ma in the Edward VII Peninsula (Fig. 3.1c; Weaver et al., 1992), and conventional U–Pb zircon lower intercept ages of ca. 102–98 Ma along the Rupert and Hobbs Coasts and further east (Mukasa and Dalziel, 2000). Korhonen et al. (2010*a*) argued that the Byrd Coast Granite suite in the Ford Ranges is related to the contemporaneous granites in the Fosdick complex by fractional crystallization, with the initial melt being derived from a Ford Granodiorite suite source. This is consistent with the petrogenesis of A-type granites in the Edward VII Peninsula, where the chemical composition of the least fractionated rocks indicates an I-type source and the isotope composition permits derivation from the regionally exposed Devonian–Carboniferous granodiorites (Weaver et al., 1992).

3.3.2.2. The Fosdick migmatite–granite complex

In the Fosdick Mountains, Cretaceous extensional deformation has exposed a migmatite–granite complex as an 80 km by 15 km elongate dome of deeper crustal rocks. The Fosdick complex is bounded to the north by the inferred Balchen Glacier fault, a steep dextral strike-slip fault (Siddoway et al., 2004, 2005), and to the south by the South

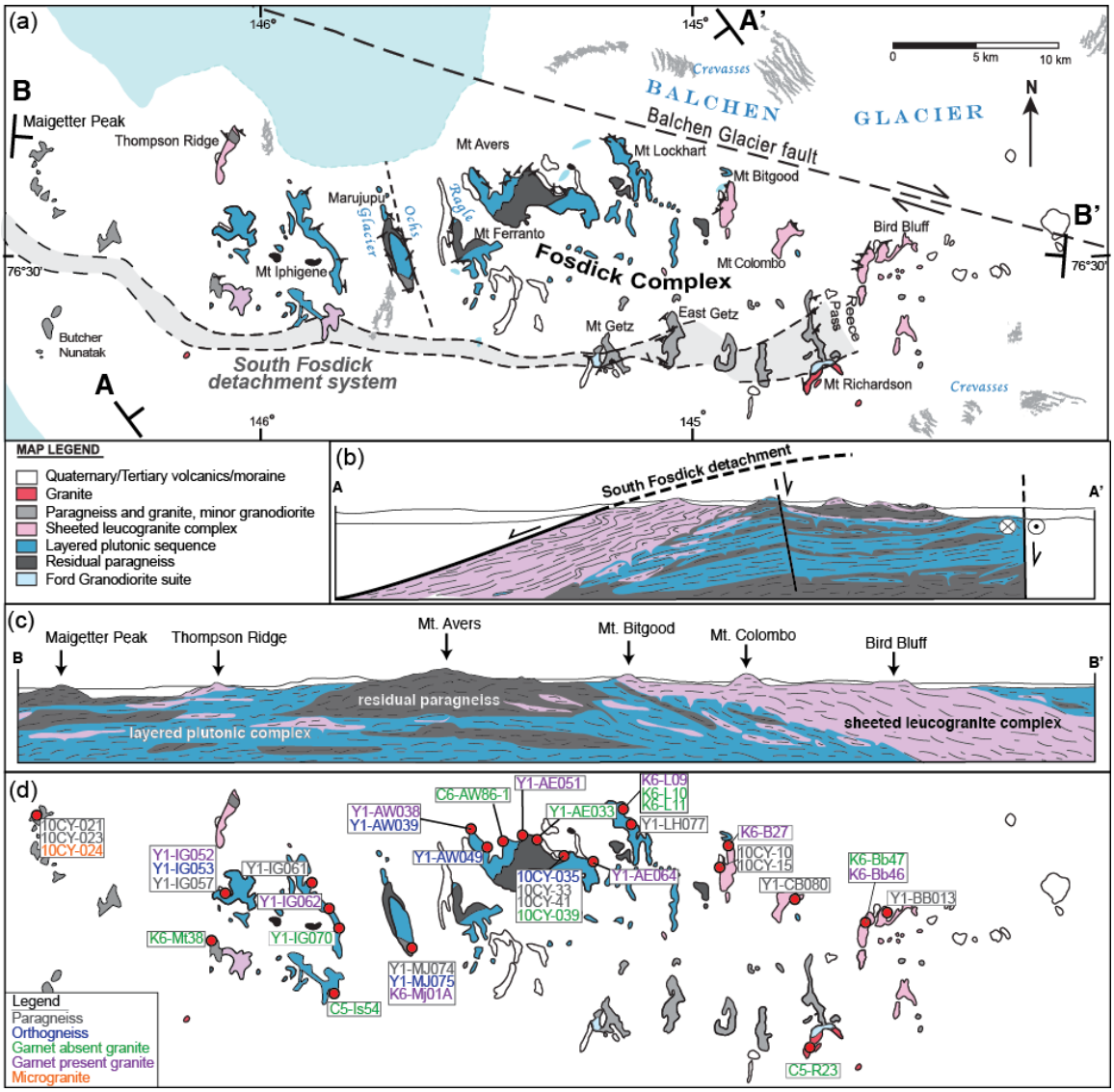

Fig. 3.2. (a) Geological map and (b, c) schematic cross-sections (no vertical exaggeration) of the Fosdick migmatite–granite complex (modified from Siddoway et al., 2004a; McFadden et al., 2010b; Yakymchuk et al., 2013a). (d) Sample location map of the Fosdick complex.

Fosdick detachment, a south-dipping, dextral oblique detachment zone (McFadden et al., 2010*a*). The complex comprises layered sequences of migmatitic paragneisses and orthogneisses, and associated granites that are all crosscut by mafic dykes (Fig. 3.2; Richard et al., 1994). Based on whole-rock geochemistry and, for the paragneisses a similar distribution of detrital zircon age populations, the migmatitic gneisses are inferred to be the high-grade metamorphic equivalents of the Swanson Formation and the Ford Granodiorite suite, respectively (Siddoway et al., 2004; Korhonen et al., 2010*b*; Yakymchuk et al*.,* 2013*a*). Two periods of granite magmatism have been documented in the Fosdick complex: one in the Devonian–Carboniferous and one in the Cretaceous (Siddoway et al., 2004; Korhonen et al., 2010*b*; Yakymchuk et al., 2014). Granites associated with Cretaceous metamorphism and extensional doming are the principal focus of this study.

The Fosdick complex comprises several lithological units that consist of similar rock types but in different proportions. In the western and central Fosdick Mountains, at deeper structural levels in the complex, a layered plutonic sequence dominates much of the outcrop from Mt Iphigene to Mt Lockhart (Fig. 3.2). This unit is composed of 10 m- to 100 m-thick sheets of migmatitic orthogneiss, m- to dam-thick sheets of granite, granodiorite and diorite, and minor m- to 10 m-thick layers of migmatitic paragneiss. At Maigetter Peak in the extreme west of the study area and around Mt Avers in the centre (Fig. 3.2), a thick unit of residual paragneiss dominates the outcrops and orthogneisses are rare. The residual paragneiss unit is mostly a stromatic metatexite migmatite with cm- to dm-scale compositional layering that comprises alternating concordant garnet- and/or cordierite-bearing leucosomes and biotite–sillimanite-bearing melanosomes (Korhonen et

al., 2010*a*; McFadden et al., 2010*a*; Yakymchuk et al., 2013*b*). These leucosomes commonly link with granites cutting across the stromatic layering. In the eastern Fosdick Mountains, at shallower structural levels, a sheeted leucogranite complex dominates the outcrop from Mt Bitgood to Bird Bluff (Fig. 3.2). This unit is composed of up to 100 m-thick subhorizontal leucogranites interlayered with 1–10 m-thick migmatitic paragneiss and orthogneiss horizons. A prominent subhorizontal foliation is defined by biotite and sillimanite and is parallel to alternating leucogranite sheets and layers of gneiss. Cretaceous mafic dykes in this unit are generally folded and boudinaged (Siddoway et al., 2005; McFadden et al., 2010*a*; Saito et al., 2013).

Based on U–Pb zircon and monazite ages, two episodes of regional metamorphism affected the Fosdick complex, one related to arc magmatism in the Devonian–Carboniferous and a second higher-grade event due to crustal thickening in the Lower Cretaceous (Siddoway et al., 2004; Korhonen et al., 2010*a*, *b*, 2012). The Devonian–Carboniferous metamorphism is cryptic due to the Cretaceous overprint; it is primarily preserved in deeper structural levels of the complex exposed in the western and central Fosdick Mountains, where it is unambiguously recorded in Carboniferous-age cores in monazite grains. By contrast, although the Cretaceous event is pervasive throughout the Fosdick complex, it is dominant at shallower structural levels in the east, where evidence of the earlier event is absent or was obliterated even in monazite.

The core domains in monazite from paragneisses have U–Pb ages of 376–302 Ma (Korhonen et al., 2012), which overlap, but also slightly post-date the emplacement of the Ford Granodiorite suite (Yakymchuk et al., 2014). The pressure (*P*) and temperature (*T*) conditions of this metamorphism have proven difficult to constrain due to uncertainty

about the age of peritectic garnet (Korhonen et al., 2012). However, recent Lu–Hf garnet geochronology indicates that garnet is part of the Cretaceous metamorphic phase assemblage (Yakymchuk et al., 2013*c*). Without garnet in the phase assemblage, peak conditions of the older metamorphic event are estimated to have been 680–800°C at 0.60–0.95 GPa (C. Yakymchuk, unpublished data). Most of the granites without significant gneissosity associated with this event could have been derived by one or more of several related processes: mixing between Ford Granodiorite suite magmas and anatectic melt derived from Swanson Formation; assimilation of Swanson Formation en masse in Ford Granodiorite suite magmas; mixing between anatectic melt derived from the Ford Granodiorite suite and anatectic melt derived from Swanson Formation; and, assimilation of Swanson Formation en masse into anatectic melt derived from the Ford Granodiorite suite (Yakymchuk et al., 2014). One granite has chemical and isotopic characteristics consistent with derivation by anatexis of Swanson Formation without any contribution from the Ford Granodiorite suite (Korhonen et al., 2010*b*).

For the Cretaceous metamorphism, Korhonen et al. (2010*a*) calculated peak metamorphic conditions of 830–870°C at 0.60–0.75 GPa. The significantly higher temperatures for the younger metamorphism combined with the monazite and garnet geochronology indicate that the dominant anatectic event in the formation of the migmatitic gneisses occurred during the Cretaceous. This is consistent with the occurrence of Cretaceous-age zircon in some of the migmatitic gneisses dated in this study, as discussed below. Korhonen et al. (2010*b*) divided the Cretaceous granites into two distinct groups. An older group of granites (*c*. 115–110 Ma) was interpreted to have been derived largely from a Ford Granodiorite suite source, whereas a younger group of

granites (*c*. 109–102 Ma) was largely explained by anatexis of Swanson Formation source materials with variable fertility as a result of modification by melt loss during the Carboniferous metamorphism.

Mafic magma was emplaced into the Fosdick complex during and after final crystallization of residual melt within the migmatitic gneisses. These rocks have yielded U–Pb zircon ages of ca. 113–111 Ma and U–Pb zircon and titanite ages of 100–97 Ma, respectively (McFadden et al., 2010*a*, Saito et al., 2013). Whole rock geochemistry and Nd–Sr isotope systematics were used to argue that melting started in mantle with higher LILE/HFSE ratios, such as mantle metasomatized by LILE-enriched slab-derived fluids, then shifted to a source with lower LILE/HFSE ratios. This change was interpreted to record the transition to extension that ultimately led to the formation of the West Antarctic Rift system (Siddoway, 2008; McFadden et al., 2010*a*, Saito et al., 2013).

3.4 Field relations and petrography

3.4.1 Swanson Formation

Outside the Fosdick Mountains, the Swanson Formation is dominated by poorly sorted metagreywacke with subordinate amounts of slate and phyllite and rare ovoid calcareous nodules. Finer-grained layers have proportionally more biotite and less quartz; the schistosity is defined by the parallel alignment of biotite. In aureoles around granites, the finer-grained layers contain poikilitic cordierite giving these rocks a spotted texture.

3.4.2 Ford Granodiorite suite

The Ford Granodiorite suite is well exposed outside the Fosdick Mountains, where it forms kilometer-scale plutons that crop out as isolated peaks in the Ford Ranges. The Ford Granodiorite suite ranges in composition from granodiorite to monzogranite, with the former being the most common (Weaver et al., 1991; Yakymchuk et al., 2014). These rocks are generally equigranular, although some outcrops are porphyritic with plagioclase phenocrysts, and typically unfoliated. Brown biotite dominates over green hornblende as the dominant ferromagnesian mineral. Accessory minerals include zircon, apatite, monazite, titanite and oxides.

3.4.3 The Fosdick complex

3.4.3.1. Migmatitic gneisses

3.4.3.1.1 Paragneiss

Migmatitic paragneiss is composed of alternating thicker metapelite layers, up to several tens of centimeters thick, and thinner metapsammite layers (Fig. 3.3a). Leucosome is concentrated in the metapelite layers, defining a stromatic layering that is generally parallel to primary compositional layering and sub-horizontal to shallow-dipping throughout the Fosdick complex. Leucosomes are between 0.1 and 30 cm thick and comprise 43–72 vol. % of the outcrop (Yakymchuk et al., 2013*b*). They include quartz, plagioclase and K-feldspar with or without biotite, garnet and cordierite (Fig. 3.3c). Melanosomes are finer grained than leucosomes and typically contain biotite, quartz, cordierite, garnet, sillimanite, plagioclase, K-feldspar, and rare oxides. Accessory

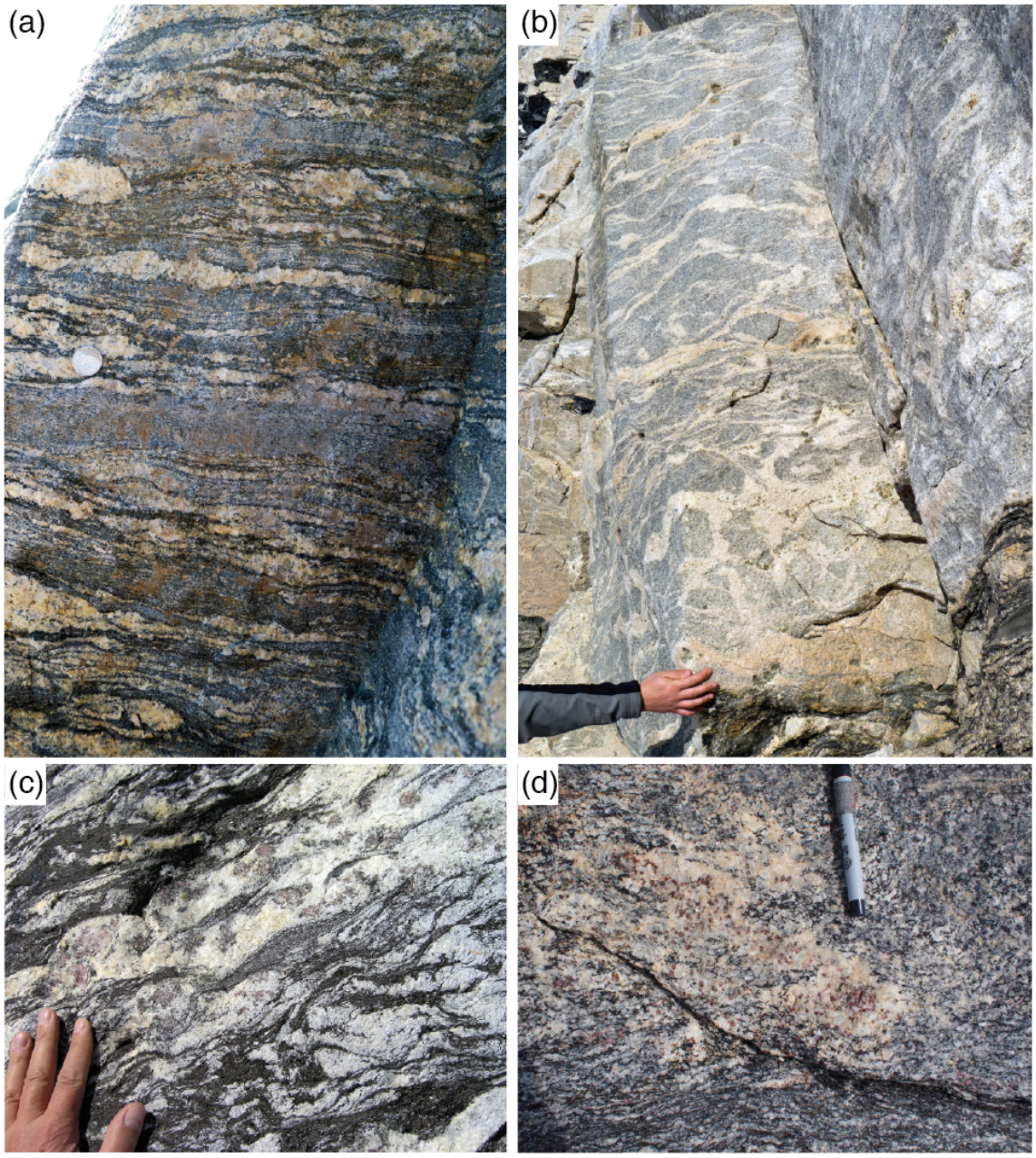

Fig. 3.3. (a) Stromatic leucosome in migmatitic paragneiss. (b) Anastomosing network of leucosome in migmatitic orthogneiss. (c) Peritectic garnet and cordierite in leucosome in migmatitic paragneiss (sample 10CY-21). (d) Peritectic garnet surrounded by leucosome in migmatitic orthogneiss (sample Y1-IG053).

monazite, zircon and apatite are found as inclusions in the rock-forming minerals or along grain boundaries.

Garnet (up to 5 cm in size) occurs in both the leucosomes and melanosomes of the migmatitic paragneiss. Garnets in the leucosome contain vermicular inclusions of quartz and rounded biotite grains, whereas larger garnets in the melanosome contain aligned inclusions of fine-grained sillimanite but smaller garnets are typically inclusion-free. Garnets, which may be surrounded by coronae of cordierite, show little variation in composition (Korhonen et al., 2012). Variably pinnitized cordierite is present as elongate porphyroblasts (1–10 mm in length, with aligned inclusions of sillimanite) in the melanosomes, but is less common in the leucosomes. Sillimanite occurs intergrown with biotite in some samples from the residual paragneiss unit.

3.4.3.1.2 Orthogneiss

Migmatitic orthogneiss is more homogeneous than the paragneiss (Fig. 3.3b). There is a shallow to moderately dipping foliation defined by the parallel alignment of individual biotite grains. Stromatic leucosomes are present, but they form an anastomosing network rather than the strongly defined layering of the migmatitic paragneiss (Fig. 3.3b). The melanosomes are medium to coarse grained with a mineral assemblage of quartz, plagioclase, K-feldspar and biotite, with or without peritectic garnet. Individual leucosomes, which are continuous over >20 cm, range from a few millimeters to up to two meters in thickness. Contiguous with these are leucosomes in normal-sense shear zones. Leucosome contains the same mineralogy as the melanosome, but commonly with coarse tabular feldspar phenocrysts and lesser amounts of biotite.

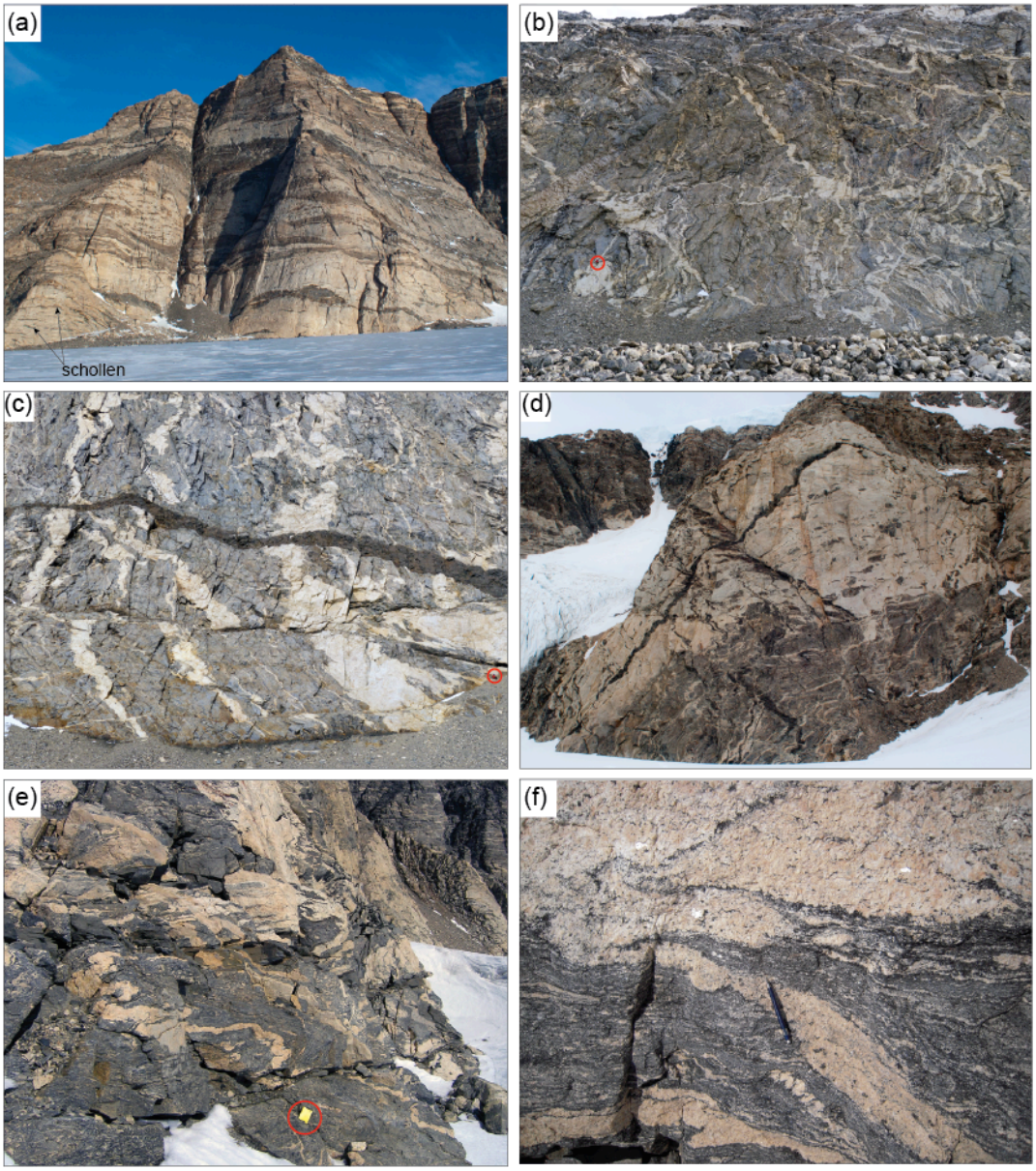

Fig. 3.4. (a) Sheeted leucogranite complex in the Eastern Fosdick Mountains. Sub-horizontal meter- to decameter-scale leucogranite sheets contain schollen of paragneiss, orthogneiss and mafic rocks. Cliff height is approximately 600 m. (b) Residual paragneiss unit with multiple discordant leucogranite bodies that intersect to form a pipe in the center of the photograph. Red circle indicates a person for scale. (c) Concordant and discordant granite bodies in migmatite paragneiss. The red circle contains a person for scale and the sampling location of Y1-AE051. (d) Heterogeneous garnet-bearing granite that contains schollen of paragneiss and mafic rocks (sample Y1-IG062). The cliff height is approximately 100m. (e) Discordant granites intruding migmatite paragneiss (sample 10CY-41). Field notebook for scale. (f) K-feldspar rich granite (sample 10CY-039).

Peritectic garnet (up to 4 cm across) may occur in both leucosomes and melanosomes (Fig. 3.4d), but cordierite is less common and typically occurs in discordant leucosomes as inclusion free euhedral grains. Accessory zircon, monazite and apatite occur as inclusions in the rock-forming minerals or along grain boundaries.

3.4.3.2. Cretaceous granites

Cretaceous granites throughout the Fosdick complex exhibit a range of field relationships with the host rock, have variable mineralogy and microstructures, and may be heterogeneous at the dm- to m-scale. Individual granite bodies vary from dykes to tabular sills (Fig. 3.4a-d) and range from dm to dam thick. In the east, at shallower structural levels, most granites are concordant with the dominant sub-horizontal foliation throughout the Fosdick complex (Fig. 3.4a), whereas to the west at deeper structural levels, the granites tend to be discordant (Fig. 3.4b-e), in some cases intersecting to form cylindrical structures (Fig. 3.4b) that may represent conduits for faster melt transport (Brown, 2013). These discordant granites generally show petrographic continuity with concordant leucosome and granite in the host rock, and have similar mineralogy, mode and grain size (Fig. 3.4f), which is inferred to record simultaneous final crystallization. Thus, the leucosomes and granites are interpreted to have formed part of the same melt extraction network (e.g. Yakymchuk et al., 2013*b*). Schollen of paragneiss, orthogneiss and mafic rock are commonly present aligned parallel to the layering in the wall rocks (Fig. 3.4a), and schlieren of biotite ± garnet ± cordierite occur locally in the smaller granites and towards the margins of larger granites.

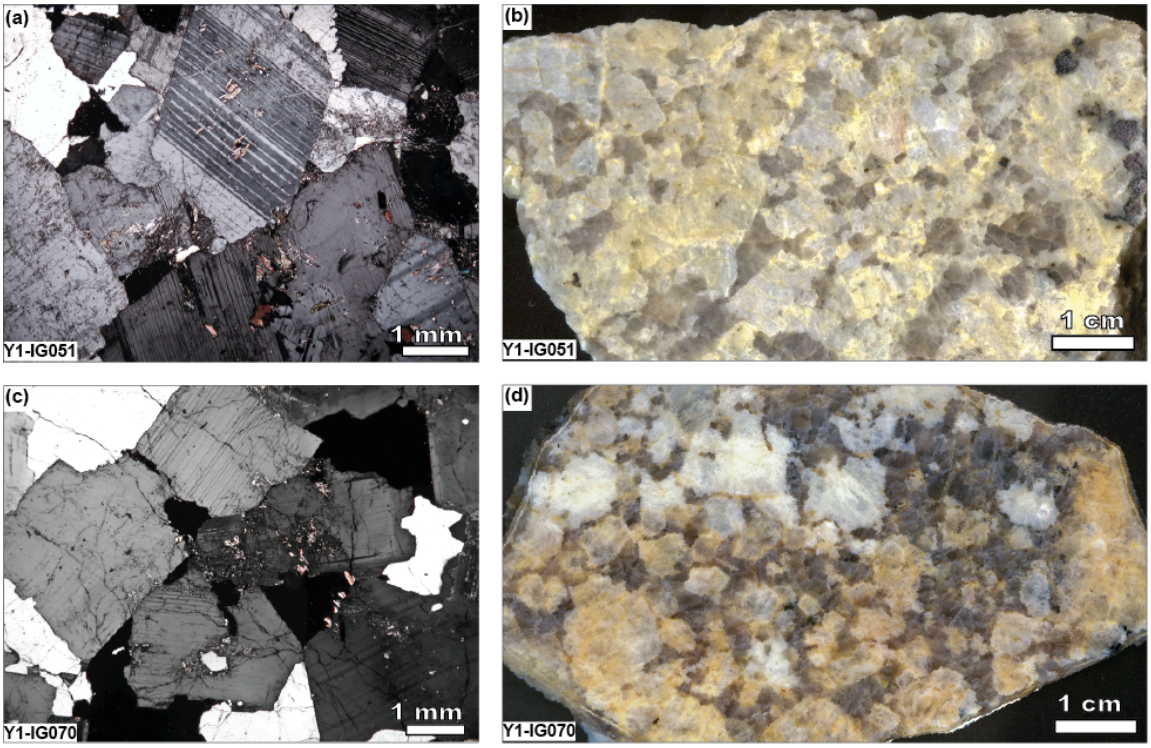

Fig. 3.5. Cumulate microstructures in Cretaceous granites from the Fosdick migmatite–granite complex. (a, b) Coarse plagioclase grains with interstitial quartz and K-feldspar. (c, d) Euhedral plagioclase grains in contact with interstitial quartz. (e, f) Interlocking plagioclase and K-feldspar crystals with interstitial quartz. (g, h) Heterogeneous K-feldspar granite with coarse-grained phenocrysts of K-feldspar. (i, j) Granite comprising K-feldspar and plagioclase grains with interstitial quartz.

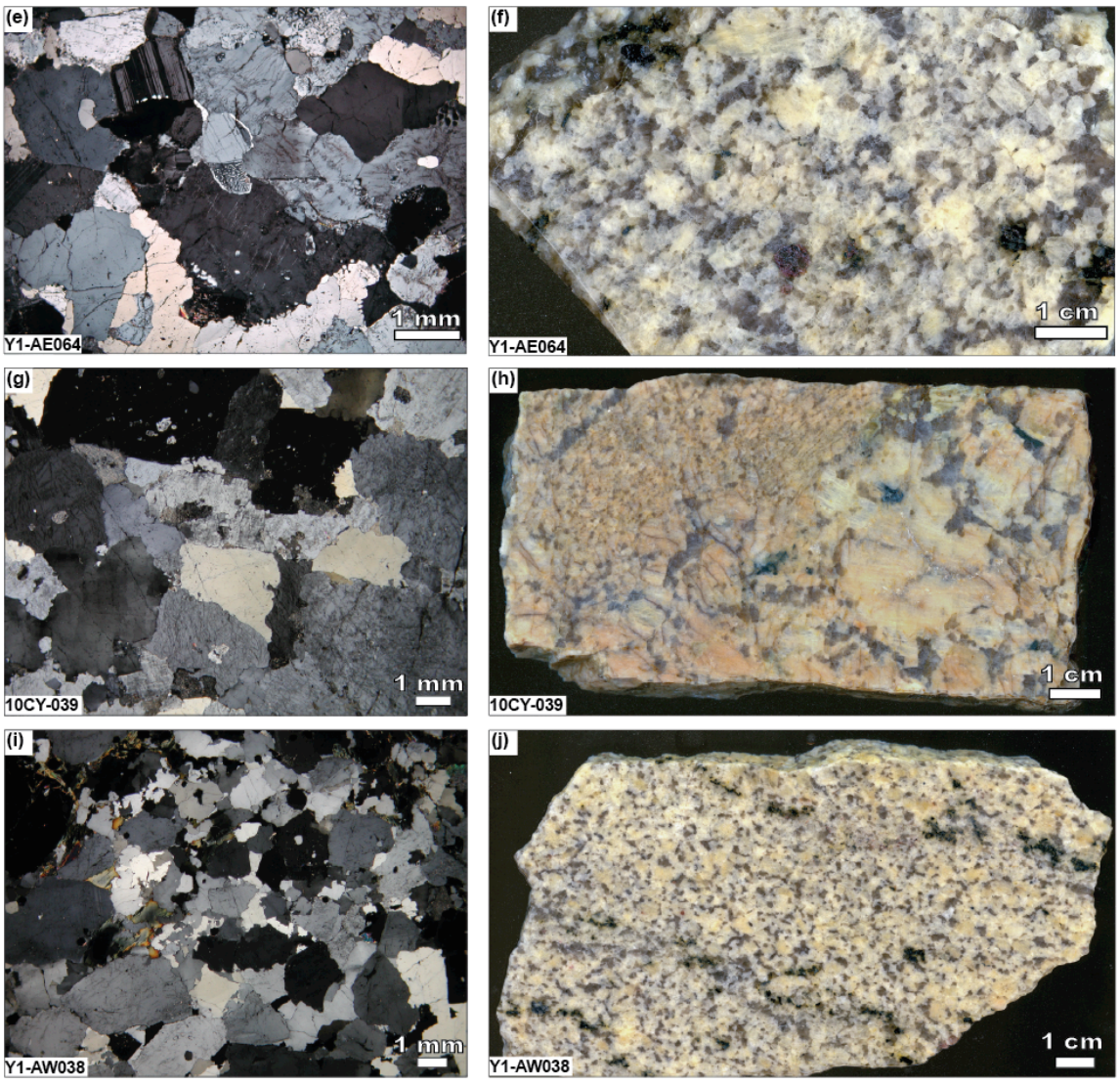

Fig. 3.5. c*ontinued*.

Granites range from medium- to coarse-grained and some individual bodies comprise discontinuous layers with different mean grain sizes. Discordant granites are commonly coarser-grained in the centre and finer-grained towards the margins; they may include peritectic garnet or cordierite. They are leucocratic with variable proportions of biotite and many contain garnet and/or cordierite. Many granites contain blocky euhedral plagioclase or K-feldspar with interstitial quartz (Fig. 3.5).

Nine Cretaceous granites from inside the Fosdick complex were investigated as part of this study. Samples 10CY-039, Y1-AE064 and Y1-AW038 are biotite ± garnet granites collected from Mt Avers in the Central Fosdick Mountains; they are characterized by coarse-grained K-feldspars. The remaining six samples are from Mt Avers (Y1-AE033, Y1-AE051; C6-AW86-1) and Mt Iphigene (Y1-IG052, Y1-IG062, and Y1-IG070); they are medium-to coarse-grained biotite + K-feldspar ± garnet ± cordierite granites with euhedral tabular plagioclase. In addition, ten Cretaceous granites for which analytical data were reported in Korhonen et al. (2010*b*) are included in the discussion of granite petrogenesis.

Microgranites are common throughout the Fosdick complex crosscutting both the stromatic layering in the migmatites and the granites. One sample of a representative microgranite from Maigetter Peak in the west (Fig. 3.2a; 10CY-024) is included in the study. It comprises quartz, K-feldspar, plagioclase, biotite and muscovite, with accessory zircon, apatite and monazite.

3.4.4. Cretaceous granites outside the Fosdick complex

Four spatially distributed granites from across Marie Byrd Land, three from the Ross Province and one from the Amundsen Province, were selected to assess the similarities and differences in the ages and putative sources for granites within and outside the Fosdick complex and between the two provinces. Sample Y2-BR087 (Bailey Ridge) is a biotite granite with perthitic K-feldspar from the southern Ford Ranges. Sample Y2-MP098 (McKinley Peak) was sampled from an isolated nunatak ~110 km to the southwest of Bailey Ridge (Fig. 3.1c) and is a coarse-grained biotite granite with perthitic K-feldspar. Sample 21220-3 is a biotite leucogranite that is associated with migmatitic garnet–cordierite gneisses from the Scott Nunataks on the Edward VII Peninsula (Smith, 1996). The final sample, from Billey Bluff (Ickes Mountains, Amundsen Province), is a coarse grained biotite-granite with perthitic K-feldspar. This granite is distinguished from those in the Ross Province by the presence of rounded mafic enclaves up to 20 cm in diameter.

3.5. Analytical procedures

Analytical procedures followed current practice in each of the laboratories where data was collected; no new procedures were developed during the course of this study. The methods are described in detail in Appendix B.

3.6. Zircon U–Pb geochronology

Zircon was analysed using laser ablation–inductively-coupled plasma–mass spectrometry (LA-ICP-MS) at the University of Arizona LaserChron center and by

sensitive high-resolution ion microprobe (SHRIMP) at the Australian National University Research School of Earth Sciences. CL images of representative zircons from each sample are shown in Fig. 3.6. U–Pb data are presented in Tables B.4 (LA-ICP-MS) B.5 (SHRIMP) in Appendix B. Concordia plots for each sample are shown in Fig. 3.7 for the LA-ICP-MS data and Fig. 3.8 for the SHRIMP data.

3.6.1 The Fosdick complex

3.6.1.1 Orthogneisses

Zircons from sample Y1-AW039 show oscillatory zoning; they are a mix of elongate and stubby, euhedral to anhedral grains and some have xenocrystic cores (Fig. 3.6). LA-ICP-MS data from this sample yielded a generally uniform age of 368.5 ± 5.3 (Fig. 3.7; n = 15; MSWD = 1.1), which is interpreted as the crystallization age of the Ford Granodiorite suite protolith.

Magmatic zircons from sample Y1-IG053 are stubby to elongate, prismatic and oscillatory zoned; a few grains have bright, resorbed cores (Fig. 3.6). LA-ICP-MS data from this sample yielded a Devonian age of 366.8 ± 6.2 Ma (Fig. 3.7; n = 23 of 24; MSWD = 2.9). By contrast, SHRIMP data yielded a range of dates from 390 to 345 Ma (with three dates of 533, 300 and 287 Ma), with a dominant group of 14 dates that yielded an age of 366.6 ± 2.2 (MSWD = 0.56), essentially the same as the LA-ICP-MS age (Figs 3.7, 3.8). The two younger SHRIMP dates of 300 and 287 Ma are from narrow dark rims that mantle bright oscillatory zoned cores with ages of 382 and 365 Ma, respectively. These younger dates are interpreted to result from modification by the

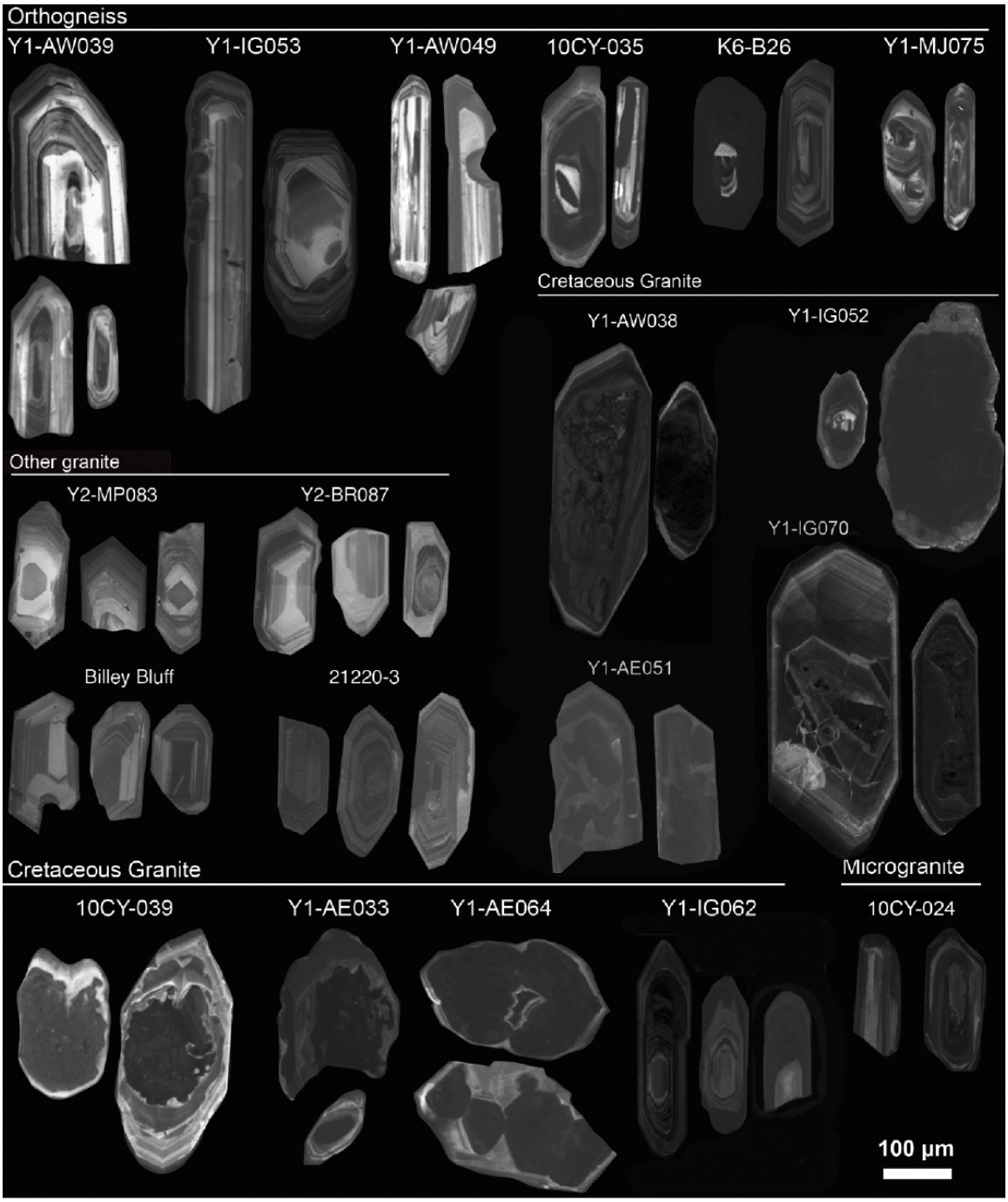

Figure 6

Fig. 3.6. Cathodoluminescence images of representative zircon grains from orthogneisses, Cretaceous granites, granites from outside the Fosdick complex, and a microgranite. Cathodoluminescence images were collected on different dates and so exhibit some variation in quality/sharpness. The contrast of images of individual zircons was adjusted to best display internal zoning.

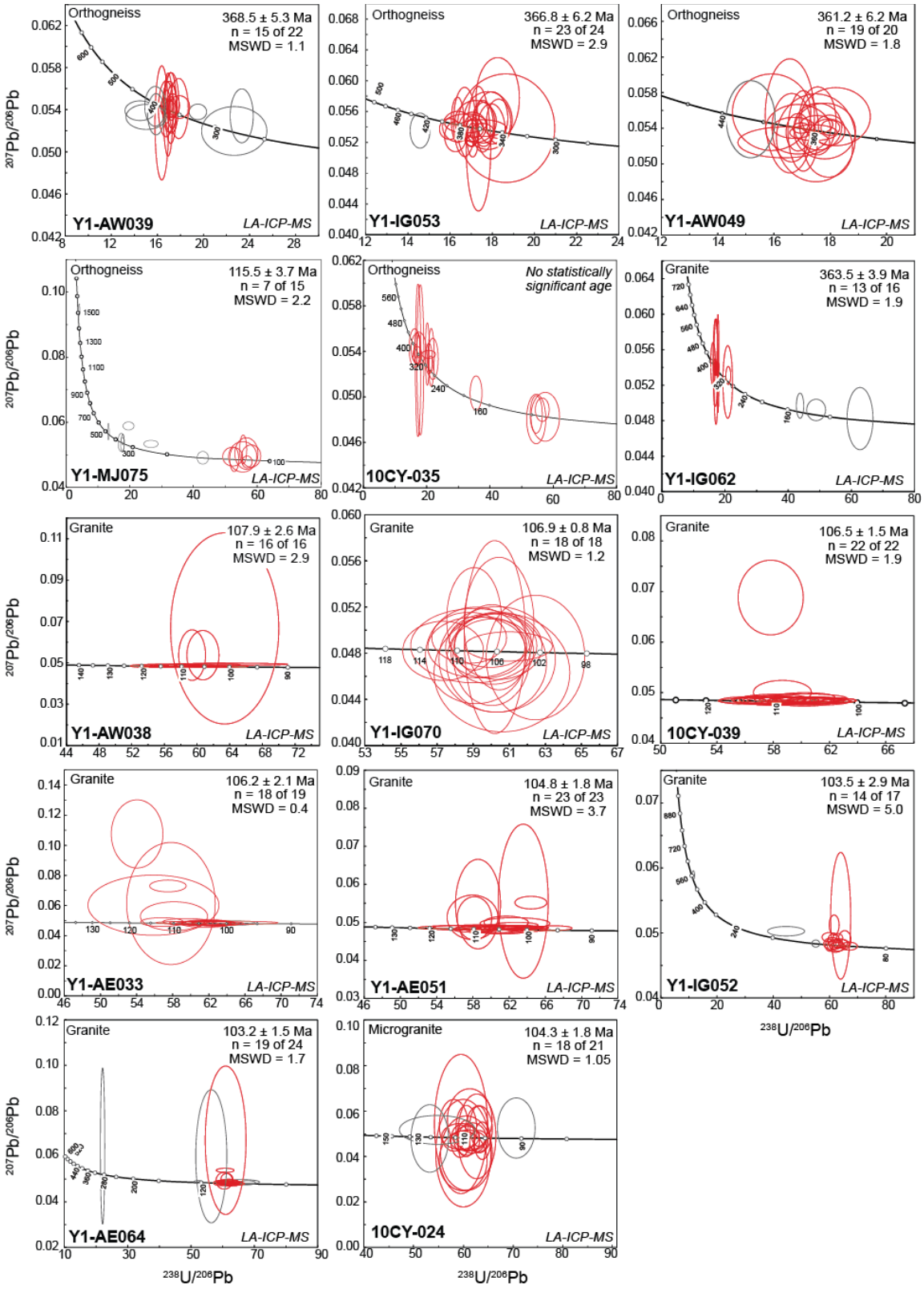

Fig. 3.7. U–Pb Tera–Wasserberg (1972) concordia plots of LA-ICP-MS zircon data for orthogneisses and granites. Data-point error ellipses and age uncertainties are reported at 2σ confidence.

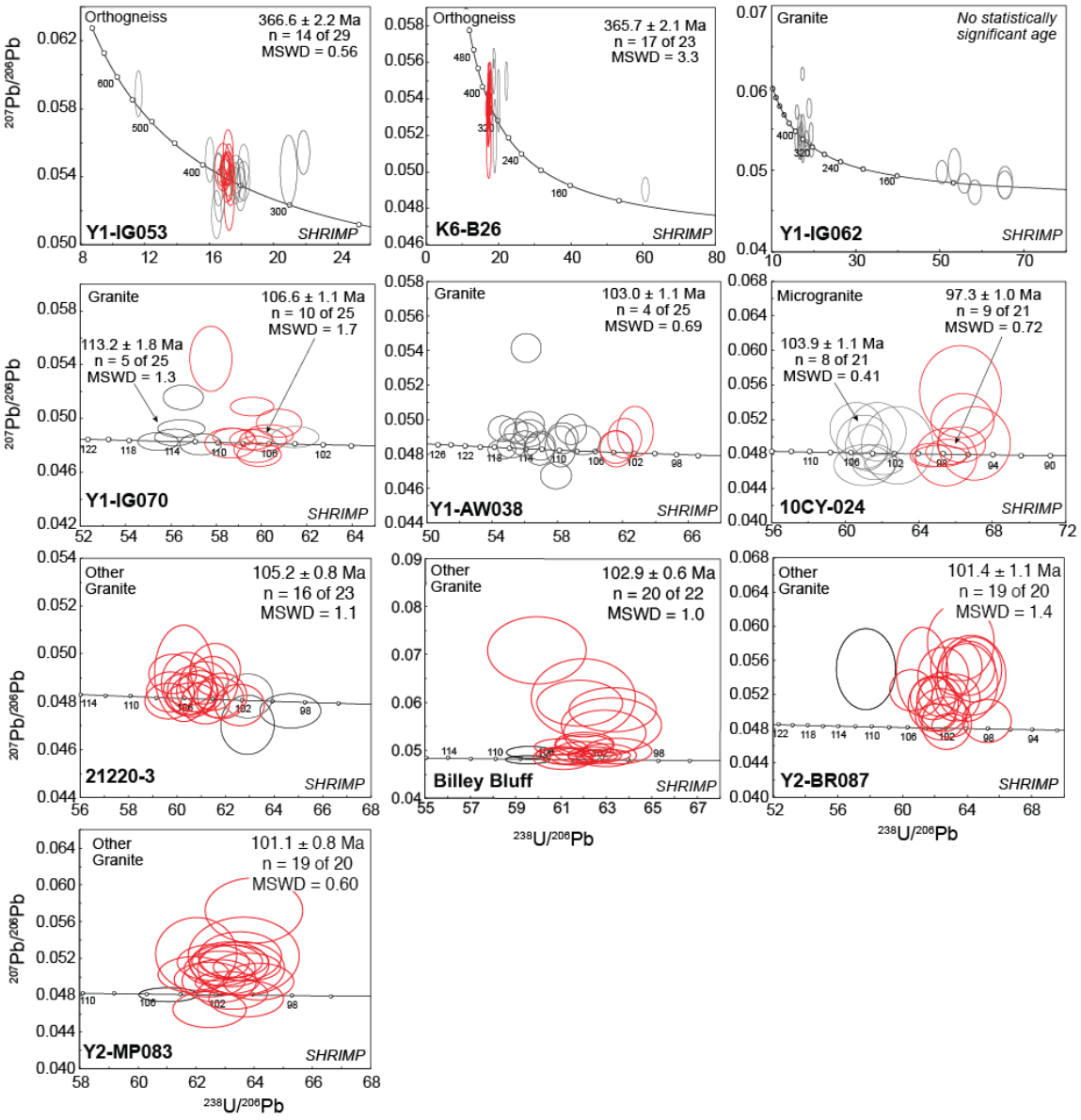

Fig. 3.8. U–Pb Tera–Wasserberg (1972) concordia plots of SHRIMP zircon data for orthogneisses and granites from inside and outside the Fosdick complex. Data-point error ellipses and age uncertainties are reported at 2σ confidence.

Cretaceous metamorphic overprint. Therefore, the *c*. 366 Ma age is interpreted to be the crystallization age of the Ford Granodiorite suite protolith.

Zircons from sample K6-B26 are elongate and prismatic with oscillatory zoning (Fig. 3.6). A minor population of zircon has resorbed bright oscillatory-zoned cores mantled by dark rims (Fig. 3.6). SHRIMP data from zircons with simple oscillatory zoning in this sample yielded a range of dates from *c*. 376 to *c*. 335 Ma, with three younger dates of 317, 285 and 105 Ma. A group of 17 of the oldest dates yielded an age of 365.7 ± 2.1 (Fig. 3.8; MSWD = 3.3). The younger dates are interpreted to result from modification by the Cretaceous metamorphic overprint. A single date of *c.* 105 Ma, which is from a dark rim surrounding a resorbed and bright oscillatory-zoned core, is interpreted to represent new zircon growth from anatectic melt. The Devonian age is interpreted to be the crystallization age of the Ford Granodiorite suite protolith.

Oscillatory zoned magmatic zircons from sample Y1-AW049 are stubby to elongate and prismatic; a few grains have embayed cores (Fig. 3.6). LA-ICP-MS data from this sample yielded a Devonian age of 361.2 ± 6.2 (Fig. 3.7; n = 19 of 20; MSWD = 1.8), which is interpreted to be the crystallization age of the Ford Granodiorite suite protolith.

Zircons from Y1-MJ075 are stubby to elongate and show evidence of recrystallization (Fig. 3.6). The LA-ICP-MS data yielded dates that range from *c*. 1520 to *c*. 100 Ma for this sample, with a dominant population that gave an age of 115.5 ± 3.7 (Fig. 3.7; n = 7; MSWD = 2.2), which is interpreted to date the Cretaceous high-grade metamorphic event.

Zircons from sample 10CY-035 are elongate and prismatic, but have cores that show evidence of recrystallization with darker zoned mantles surrounded by very thin bright rims (Fig. 3.6). LA-ICP-MS data from this sample yielded a range of dates from *c*. 380 to *c*. 100 Ma, with three dominant populations at 360 Ma and 320 Ma, from the darker zoned mantles, and 100 Ma, from the bright rims (Fig. 3.7). The Cretaceous age group at *c*. 100 Ma is interpreted to record the Cretaceous metamorphic overprint, whereas the older age groups likely represent the Ford Granodiorite suite protolith age and the effects of Carboniferous recrystallization, respectively.

3.6.1.2 Cretaceous granites

Granites from Mt Iphigene (Y1-IG070, Y1-IG052) and from Mt Avers (Y1-AW038, Y1-AE033, 10CY-039, Y1-AE051, Y1-AE064) have zircons that are euhedral to anhedral with dark and generally unzoned cores mantled by bright oscillatory-zoned rims (Fig. 3.6). The U–Pb ages of the dark cores could not be measured due to high concentrations of ^{204}Pb. LA-ICP-MS data from the bright rims for these samples yielded weighted mean ages that range from *c*. 108 to *c*. 103 Ma (Fig. 3.7). Zircons from the microgranite sample, 10CY-024, yielded an age of 104.3 ± 1.8 Ma (Fig. 3.7; n = 18; MSWD = 1.05).

Zircons from three of these granites were also analysed using the SHRIMP. For sample Y1-IG070, ^{206}Pb/^{238}U dates range from *c*. 115 to *c*. 104 Ma (with one date of *c*. 126 Ma); an older group defined an age of 113.2 ± 1.8 Ma (Fig. 3.8; n = 5; MSWD = 1.3), whereas a younger group yielded an age of 106.6 ± 1.1 Ma (Fig. 3.8; n = 10; MSWD = 1.7). The younger age is interpreted as the timing of crystallization, whereas

the older age may represent grains scavenged during reworking of a slightly older Cretaceous component. For sample Y1-AW038, $^{206}Pb/^{238}U$ dates range from *c*. 117 to *c*. 102 (excluding two dates of *c*. 326 and *c*. 143 Ma); a group of younger dates yielded an age of 103.0 ± 1.1 Ma (Fig. 3.8; n = 4; MSWD = 0.69), interpreted as the crystallization age of the granite. This age is younger than the LA-ICP-MS age (Fig. 3.7), which may have been affected by the zircons from a slightly older Cretaceous component. For sample 10CY-024, $^{206}Pb/^{238}U$ dates range from *c*. 105 to *c*. 95 Ma; an older group defined an age of 103.9 ± 1.1 Ma (Fig. 3.8; n = 8; MSWD = 0.41), whereas a younger group yielded an age of 97.3 ± 1.0 Ma (Fig. 3.8; n = 9; MSWD = 0.72). The younger age is interpreted as the timing of crystallization of the granite, whereas the older group may represent grains scavenged during reworking of a slightly older Cretaceous component.

An additional granite from Mt Iphigene (Y1-IG062) yielded zircons that are zoned, and predominantly prismatic and euhedral, although a few grains have bright zoned cores that show evidence of recrystallization (Fig. 3.6). This sample contains both Devonian–Carboniferous and Cretaceous zircon age populations, with three Permian dates (Fig. 3.7, 3.8). The older population includes concordant dates from *c*. 393 to *c*. 324 Ma (LA-ICP-MS and SHRIMP); for the LA-ICP-MS data, 13 analyses define an age of 363.5 ± 3.9 Ma (Fig. 3.7; MSWD = 1.9), which likely reflects a population of zircon grains inherited from the Ford Granodiorite suite. The younger population includes dates from *c*. 114 to *c*. 98 Ma (LA-ICP-MS and SHRIMP); no statistically significant age can be calculated from this data. Based on field relations as well as the Cretaceous zircon dates, this granite in interpreted to be of Cretaceous age.

3.6.2. Cretaceous granites from outside the Fosdick complex

3.6.2.1 Ross Province

Sample 21220-3 contains a dominant population of slender prismatic zircon grains with oscillatory zoning that are dark under CL (Fig. 3.6). Although some grains have dark CL cores, two cores that are bright under CL yielded dates of *c*. 1973 and *c*. 1098 Ma, and one rim analysis gave a date of *c*. 373 Ma. These are interpreted to be inherited elements. A weighted $^{206}Pb/^{238}U$ age of 105.2 ± 0.8 Ma (Fig. 3.8; MSWD=1.1), calculated from a group of 16 analyses, is interpreted as the crystallization age of the granite. Sample Y2-BR087 contains a dominant population of euhedral zircon grains with simple oscillatory zoning in CL (Fig. 3.6). Some grains have dark zoned CL cores and brighter oscillatory-zoned rims (Fig. 3.6). A dominant group of 19 out of 20 analyses yielded a weighted $^{206}Pb/^{238}U$ age of 101.4 ± 1.1 Ma (Fig. 3.8; MSWD=1.4), which is interpreted as the crystallization age of the granite. Sample Y2-MP083 contains a dominant population of euhedral grains with typical oscillatory igneous zoning (Fig. 3.6). A dominant group of 19 out of 20 analyses yielded a weighted $^{206}Pb/^{238}U$ age of 101.1 ± 0.8 Ma (Fig. 3.8; MSWD=0.60), which is interpreted as the crystallization age of the granite.

3.6.2.2 Amundsen province

The sample from Billey Bluff contains a dominant population of euhedral, elongate to subequant zircon grains with simple igneous oscillatory zoning (Fig. 3.6). A group of 20 out of 22 analyses yielded a weighted $^{206}Pb/^{238}U$ age of 102.9 ± 0.6 Ma (Fig. 3.8; MSWD=1.1), which is interpreted as the crystallization age of the granite.

3.7 Geochemistry

3.7.1 Major oxide, trace element and rare earth element chemistry

Major oxide, trace element and rare earth element (REE) analyses are presented in Table B.2 in Appendix B. These data are combined with published data and shown as variation diagrams for major oxides and trace elements in Figs 3.9 and 3.10, and as chondrite-normalized REE patterns in Figs 3.11 and 3.12.

3.7.1.1 Swanson Formation

Samples of the Swanson Formation have SiO_2 contents ranging from 61 to 74 wt %; they are peraluminous with aluminum saturation indices (ASI= Molar $[Al_2O_3/(CaO+Na_2O+K_2O)]$) of 1.28–2.00 (Fig. 3.9). With increasing SiO_2, CaO, Na_2O and P_2O_5 remain relatively constant, whereas Al_2O_3, FeO*+MgO+TiO_2 and K_2O decrease (Fig. 3.9). With the exception of U, Zr and La, which are positively correlated with increasing SiO_2 (Fig. 3.10), and Rb and Rb/Sr, which are slightly negatively correlated with increasing SiO_2 (Fig. 3.10), trace element concentrations remain relatively constant (Fig. 3.10). The Swanson Formation exhibits a narrow range of REE abundances and smooth normalized REE patterns (Fig. 3.11) that are concave down for the LREE (La–Sm), with La_N/Lu_N of 8.64–10.2 and moderate negative Eu anomalies (Eu_N/Eu_N^* = 0.62–0.70).

3.7.1.2 Ford Granodiorite suite

Samples of the Ford Granodiorite suite have SiO_2 contents ranging from 64 to 76 wt % (Fig. 3.7); they are metaluminous to peraluminous, with ASI = 0.90–1.12 (Fig. 3.9).

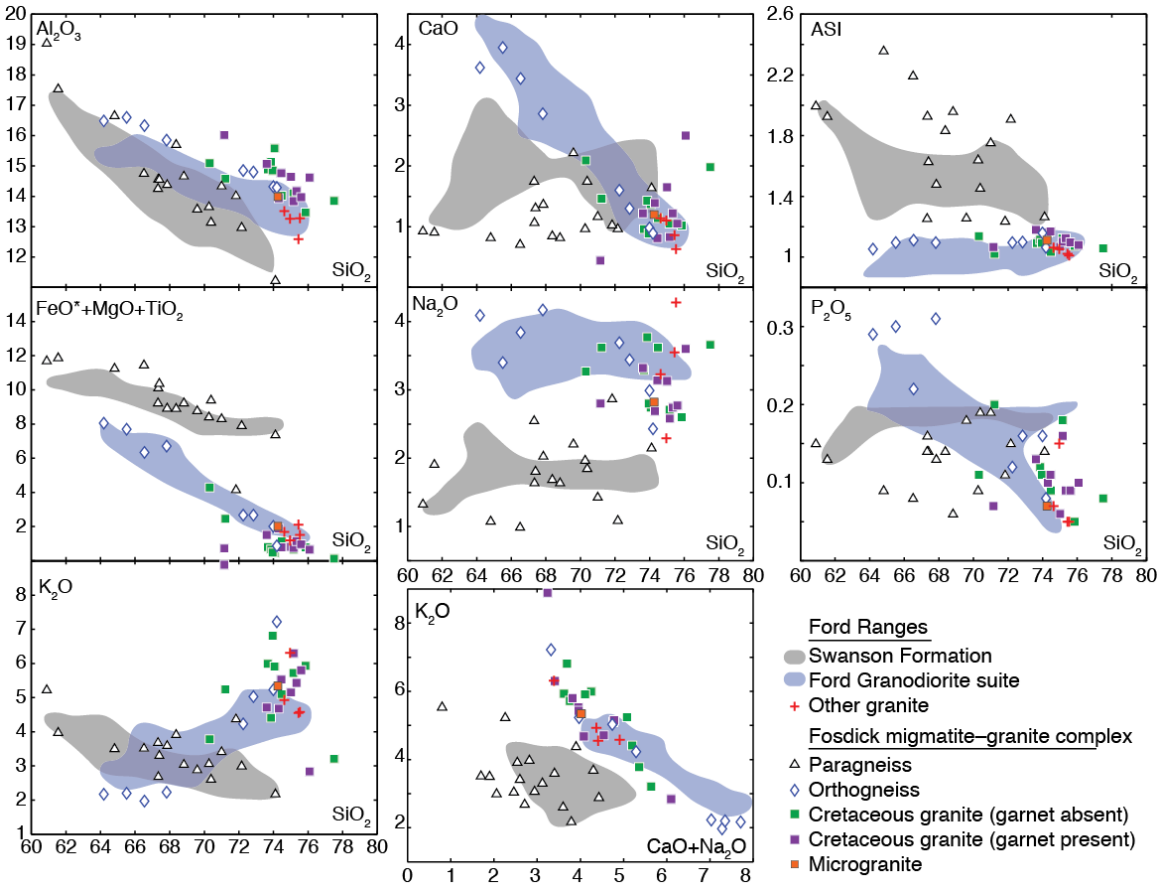

Fig. 3.9. Select major oxide data for Swanson Formation, paragneisses, Ford Granodiorite suite, orthogneisses, Cretaceous granites, granites from outside the Fosdick complex, and a microgranite. Ford Granodiorite suite samples include data from Korhonen et al. (2010b), Weaver et al. (1991, 1992), Pankhurst et al. (1998), Tulloch et al. (2009). FeO* represents total ferrous iron. Aluminum saturation index (ASI) = molar [Al_2O_3 / ($CaO + Na_2O + K_2O$)]. Oxides are plotted as weight percent.

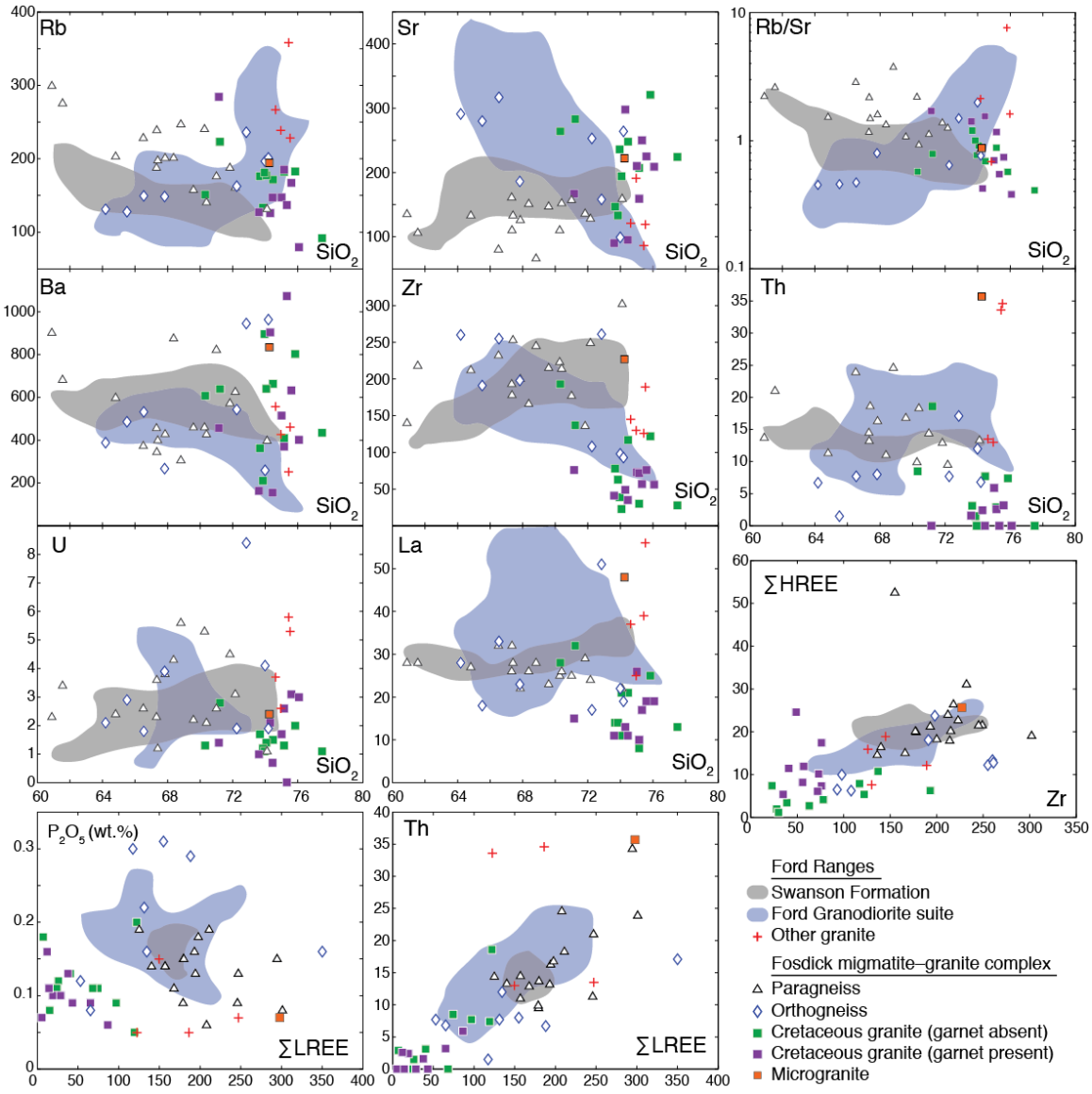

Fig. 3.10. Select trace element data for Swanson Formation, paragneisses, Ford Granodiorite suite, orthogneisses, Cretaceous granites, granites from outside the Fosdick complex, and a microgranite. Ford Granodiorite samples include data from Korhonen et al. (2010b), Weaver et al. (1991, 1992), Pankhurst et al. (1998) and Tulloch et al. (2009). Trace elements are plotted as parts per million (ppm).

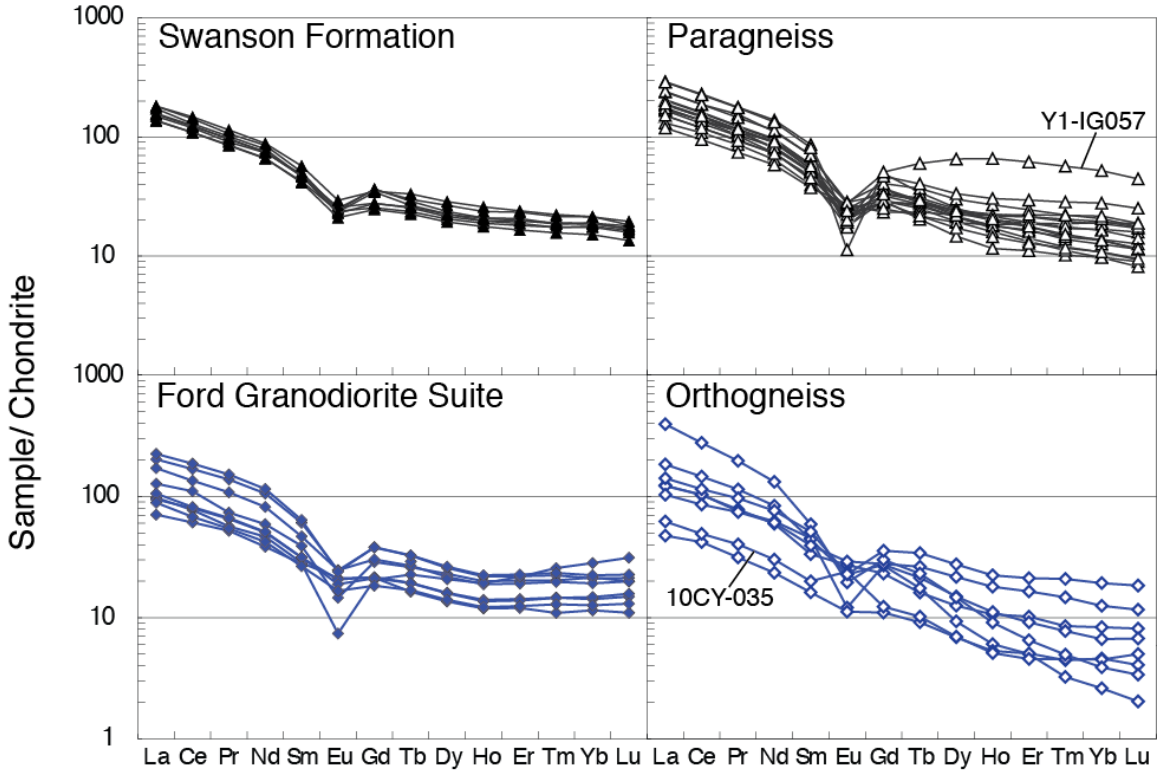

Fig. 3.11. Rare earth element (REE) chondrite-normalized (McDonough and Sun, 1995) patterns for paragneiss, orthogneiss and their putative protoliths. Data from Korhonen et al. (2010b) and this study.

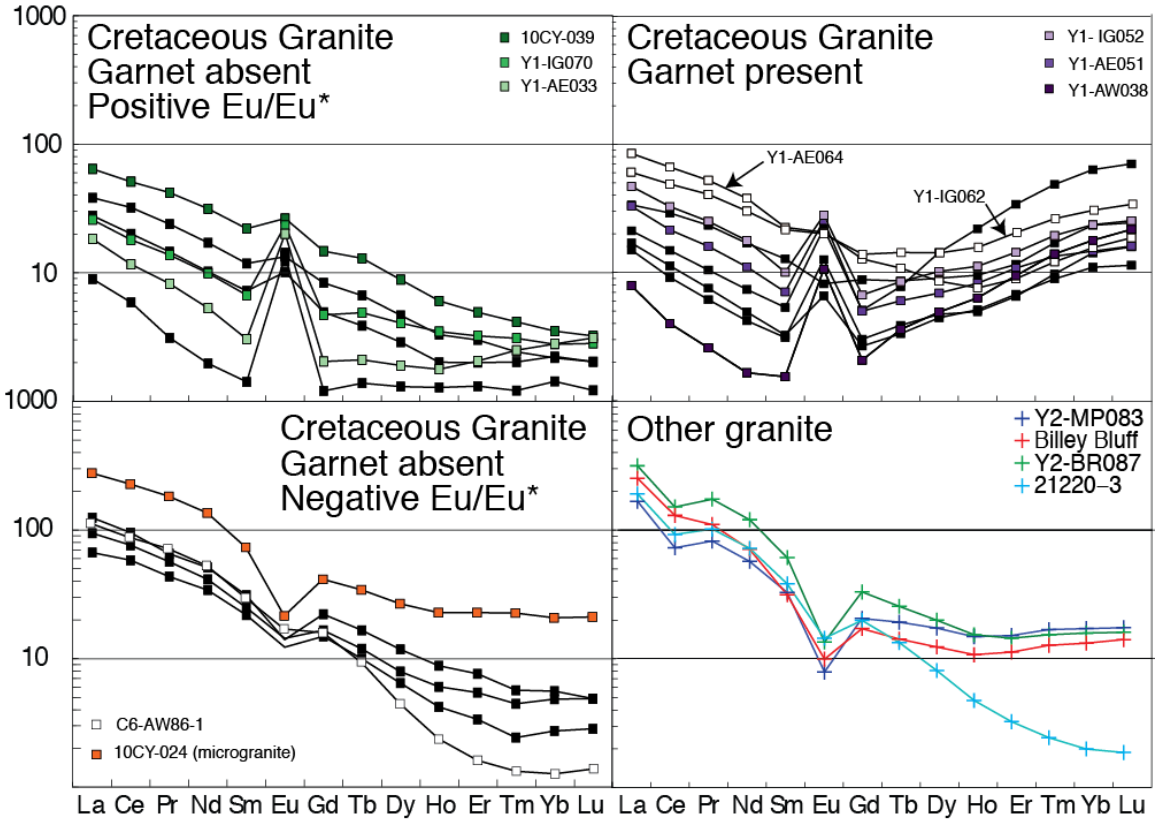

Fig. 3.12. Rare earth element (REE) chondrite-normalized (McDonough and Sun, 1995) patterns for Cretaceous granites from the Fosdick complex (data from Korhonen et al. (2010b) and this study) and granites from outside the Fosdick complex.

With increasing SiO_2, Al_2O_3, FeO*+MgO+TiO_2, CaO, P_2O_5, Ba, U, Sr and Zr generally decrease, Na_2O, La and Th remain relatively constant, and K_2O, Rb and Rb/Sr tend to increase (Figs 3.9, 3.10). These rocks have a wide range of REE abundances, smooth to concave down LREE patterns and smooth to concave up HREE (Gd–Lu) patterns (Fig. 3.11), La_N/Lu_N of 2.3–9.92 and variable negative Eu anomalies (Eu_N/Eu_N*=0.31–0.85).

3.7.1.3. The Fosdick complex

3.7.1.3.1 Paragneisses and orthogneisses

Paragneisses have major oxide and trace element abundances, and geochemical trends that are similar to those for the Swanson Formation, although sometimes with more variability (Figs 3.9, 3.10). The aluminum saturation indices and Rb/Sr ratios tend to be higher than the Swanson Formation, whereas CaO, P_2O_5 and Sr tend to be lower. One biotite-rich paragneiss sample, Y1-IG057, has 42 wt % SiO_2, an ASI value of 3.13 and higher FeO*+MgO+TiO_2, Al_2O_3, Rb, Rb/Sr, and Th, and lower CaO, Na_2O, and Sr than the other samples. The paragneisses have a wider range of REE concentrations than the Swanson Formation, but otherwise show similar chondrite-normalized REE patterns (Fig. 3.11), with La_N/Lu_N of 6.3–22.2 and variable negative Eu anomalies (Eu_N/Eu_N* = 0.17–0.90). Sample Y1-IG057 has elevated HREE compared with the other samples.

Orthogneisses have major oxide and trace element abundances and trends that are consistent with a Ford Granodiorite suite parentage (Figs 3.9, 3.10). Al_2O_3 and ASI are slightly higher, whereas Th is lower (Figs 3.9, 3.10); K_2O is lower and P_2O_5 higher at low SiO_2 (Figs 3.9). The orthogneisses have a wider range of REE concentrations than the Ford Granodiorite suite, with La_N/Lu_N of 7.7–116.8, more variability in the HREE

patterns (Fig. 3.11), and, with one exception (10CY-035, Eu_N/Eu_N^* = 1.48), negative Eu anomalies (Eu_N/Eu_N^* = 0.33–0.96).

3.7.1.3.2 Cretaceous granites

The granites have a limited range of silica contents (70–76 wt %), with ASI values similar to the orthogneisses. Al_2O_3, FeO*+MgO+TiO_2, Rb, Rb/Sr, Zr, La and Th are generally negatively correlated with increasing SiO_2, whereas K_2O increases with increasing SiO_2 except for two high silica granites (Figs 3.9, 3.10). CaO, Na_2O, P_2O_5, Ba, U and Sr show no clear trend, although Ba and Sr are highly variable (Figs 3.9, 3.10). There is no discernable difference between the garnet present and the garnet absent variants. The microgranite (10CY-024) has oxide and trace element abundances similar to the other granites, except for elevated Ba, Zr, La and Th (Figs 3.9, 3.10). The granites exhibit strong covariation between K_2O and CaO+Na_2O (Fig. 3.9). Although quite variable, P_2O_5 is negatively correlated with ΣLREE, whereas Th is positively correlated ΣLREE and Zr is positively correlated ΣHREE (Fig. 3.10).

The granites have lower ΣREE relative to the potential sources in the Ford Ranges and low to moderate negative slopes (La_N/Lu_N of 0.30–25.6; Fig. 3.12). Some garnet absent granites have small negative Eu anomalies, but a majority of them, and all but one of the garnet present granites, have variable, typically large positive Eu anomalies (Eu/Eu* = 0.37–10.3); this variation is unrelated to SiO_2 content. Given the low Rb/Sr ratios of these granites, the REE patterns are interpreted to be due to accumulation of feldspar. The garnet present granites have rising, concave downward HREE patterns, as expected from the presence of garnet (Fig. 3.12). One garnet absent granite (C6-AW86-1)

has a steep normalized REE pattern (La_N/Lu_N = 82.6) showing strong depletion in the HREE but with a concave up slope (Fig. 3.12). The microgranite has a REE pattern similar to the Ford Granodiorite suite, with La_N/Lu_N of 13.1 and a concave downward chondrite-normalized LREE slope but a concave upward chondrite-normalized HREE slope, and a negative Eu anomaly (Eu/Eu* = 0.37).

3.7.1.4 Cretaceous granites from outside the Fosdick complex

Although widely distributed, the four granites from outside the Fosdick complex plot with the more evolved granites from inside the Fosdick complex, including the microgranite, in terms of major oxides, and have similar ASI values (Fig. 3.9). However, there are differences in trace element concentrations. Although variable, the granites from outside the Fosdick complex have higher Rb, U and Rb/Sr and lower Ba, Sr and Zr than the microgranite (Fig. 3.10). Three of the granites have similar chondrite normalized REE patterns to the microgranite, but lower ΣREE concentrations (Fig. 3.12); the patterns are also similar to the chondrite normalized REE patterns for the Ford Granodiorite suite samples (Fig. 3.11). The granite from Scott Nunataks (21220-3) has a similar chondrite normalized REE pattern to sample C6-AW86-1 from inside the Fosdick complex, but lower ΣREE concentrations (Fig. 3.12).

3.7.2 Sr and Nd isotope compositions

Nd and Sr isotope results for 21 samples are presented in Table B.3 in Appendix B and are summarized, together with additional data from the literature, in Fig. 13. Although the Cretaceous metamorphism is the dominant anatectic event in the Fosdick

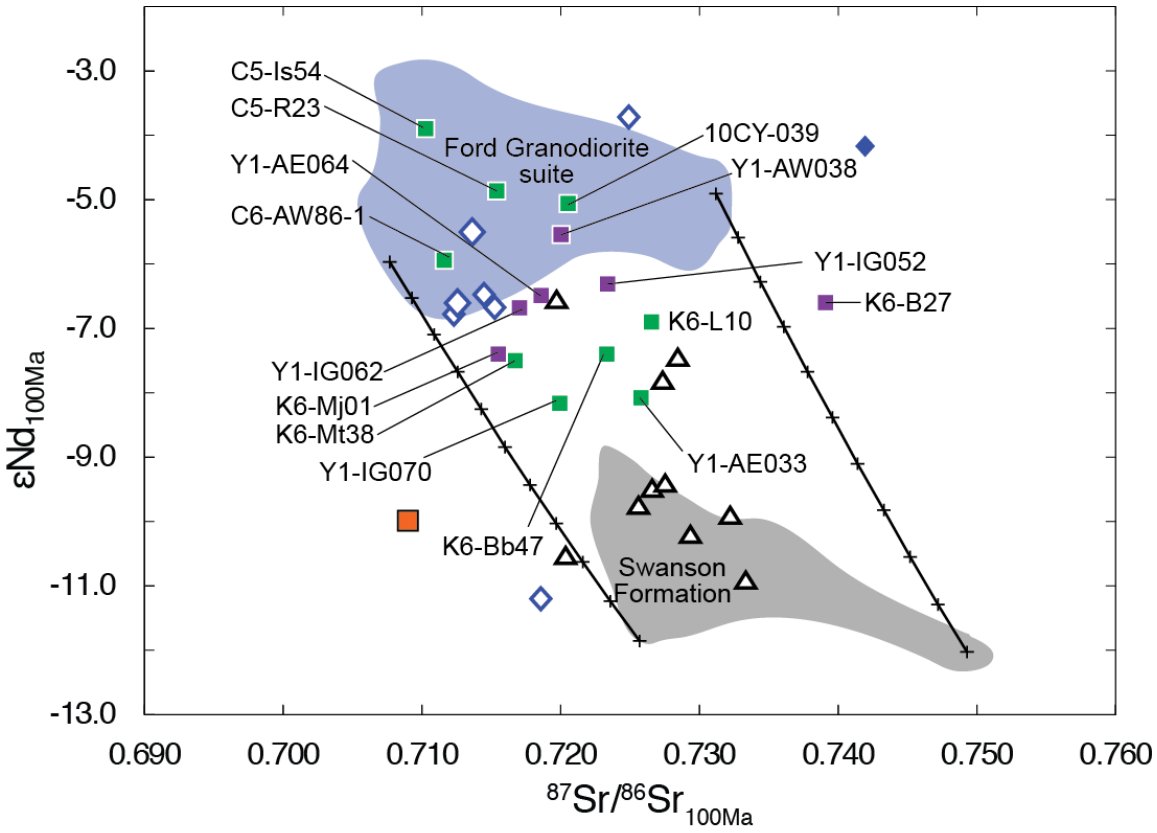

Fig. 3.13. Sr–Nd isotopic compositions at 100 Ma for source rocks and granites from the Ford Ranges, which includes data from Korhonen et al. (2010b), Weaver et al. (1992) and Weaver et al. (1991). Tick marks along mixing curve are at 10% increments. Legend is the same as in Fig. 3.7.

complex, for completeness the Sr and Nd isotope compositions for the migmatitic gneisses are given for 360 and 100 Ma in Table B.4 in Appendix B, but are only plotted for 100 Ma in Fig. 3.13.

3.7.2.1 The Fosdick complex

3.7.2.1.1 Migmatitic gneisses

Paragneisses have $^{87}Sr/^{86}Sr_{360Ma}$ values that range from 0.695066 to 0.720852 and εNd_{360Ma} values that range from -8.3 to -4.0. However, three of these samples have unrealistic $^{87}Sr/^{86}Sr$ ratios that are lower than the initial solar system $^{87}Sr/^{86}Sr$ ratio. One strongly residual paragneiss (sample Y1-IG057) yields a calculated $^{87}Sr/^{86}Sr_{360Ma}$ ratio of 0.313076. Orthogneiss samples have $^{87}Sr/^{86}Sr_{360Ma}$ values of 0.707423–0.710921 and εNd_{360Ma} values ranging from -4.5 to -0.2, with one value of -9.1.

For the Cretaceous, paragneiss samples have $^{87}Sr/^{86}Sr_{100Ma}$ values that vary from 0.719704 to 0.733346 and εNd_{100Ma} values that range from -10.9 to -6.6 (Fig. 3.13), generally consistent with a Swanson Formation parentage. When the data are corrected to 100 Ma, all samples have realistic $^{87}Sr/^{86}Sr$ ratios, confirming that that the dominant anatectic event occurred in the Cretaceous. Orthogneiss samples have $^{87}Sr/^{86}Sr_{100Ma}$ values that vary from 0.712295 to 0.724913 and εNd_{100Ma} values that range from -6.8 to -3.7 (with one value of -11.2) generally consistent with a Ford Granodiorite suite parentage.

3.7.2.1.2 Cretaceous granites

Granites within the Fosdick complex have $^{87}Sr/^{86}Sr_{100Ma}$ ratios that vary from 0.711604 to 0.725792 and εNd_{100Ma} values that range from -8.2 to -5.1 (Fig. 3.13). The microgranite (10CY-024) has an $^{87}Sr/^{86}Sr_{100Ma}$ ratio of 0.708989 and a εNd_{100Ma} value of -10.0 (Fig. 3.13).

3.7.3 Hf and O isotope compositions in zircon

Ten samples were selected for Hf and O isotope analysis of zircon; the data are given in Table B.6 in Appendix B and summarized, together with an additional sample (C6-AW86-1, data from Yakymchuk et al., 2013*b*), in Figs 3.14–3.16.

3.7.3.1 Fosdick complex

3.7.3.1.1 Orthogneiss

Sample Y1-IG053 contains zircon with εHf_{360} values of -4.3 to -0.2, $\delta^{18}O$ values of 8.3 to 9.3 (Fig. 3.14), and weighted means of -2.8 ± 0.4 and 8.8 ± 0.1, respectively (2σ; 19 of 20). Sample K6-B26 contains zircon with εHf values of -4.2 to -0.6, $\delta^{18}O$ values of 8.0 to 9.7 (Fig. 3.14), and weighted means of -2.1 ± 0.4 and 8.6 ± 0.2, respectively (2σ; 18 of 19). A single Cretaceous spot yields εHf_{100} and $\delta^{18}O$ values of -6.1 and 9.8.

3.7.3.1.2 Cretaceous granites

Sample Y1-AW038 contains zircon with εHf_{100} values of -6.6 to -3.3, $\delta^{18}O$ values of 8.8 to 9.9 (Fig. 3.15), and weighted means of -5.0 ± 0.3 and 9.3 ± 0.2, respectively (2σ; n = 18). Sample Y1-IG070 contains zircon with εHf_{100} values of -7.1 to -4.0, $\delta^{18}O$ values

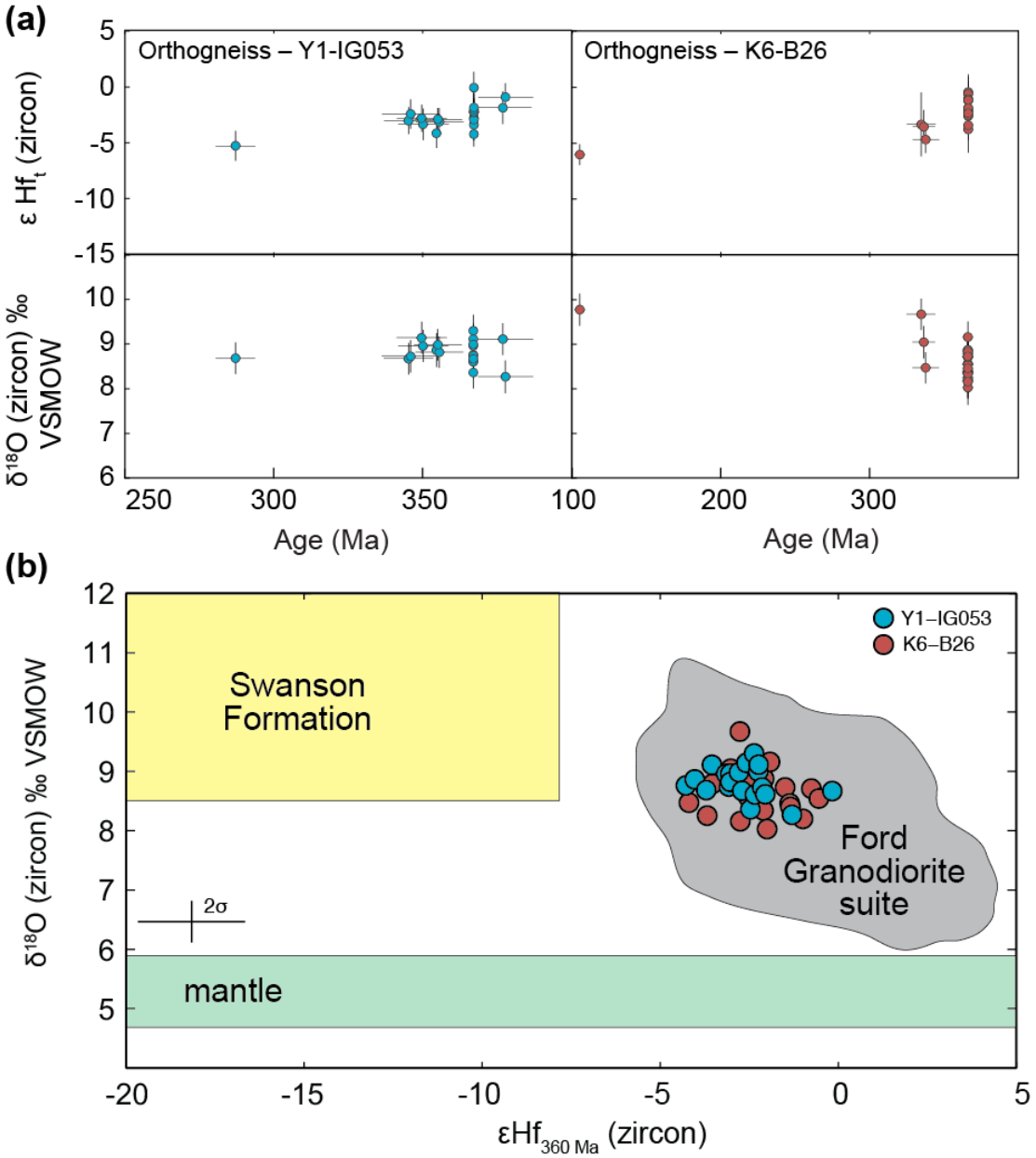

Fig. 3.14. (a) Plots of $\delta^{18}O$ and εHf_t versus $^{206}Pb/^{238}U$ age for migmatitic orthogneisses. (b) $\delta^{18}O$ plotted against εHf_{100} for migmatitic orthogneiss. The range of εHf values for the Swanson Formation represents the interquartile range of zircon values recalculated to 360 Ma and the $\delta^{18}O$ value range is from oxygen isotope analysis of six whole-rock samples (Yakymchuk et al., 2014). The εHf and $\delta^{18}O$ values of the Ford Granodiorite are from Yakymchuk et al. (2013a, 2014). The $\delta^{18}O$ values of mantle-derived rocks is 5.3 ± 0.6‰ (Valley et al., 1998). The cross in the bottom left shows the approximate ±2σ uncertainties for individual Hf and O isotope values.

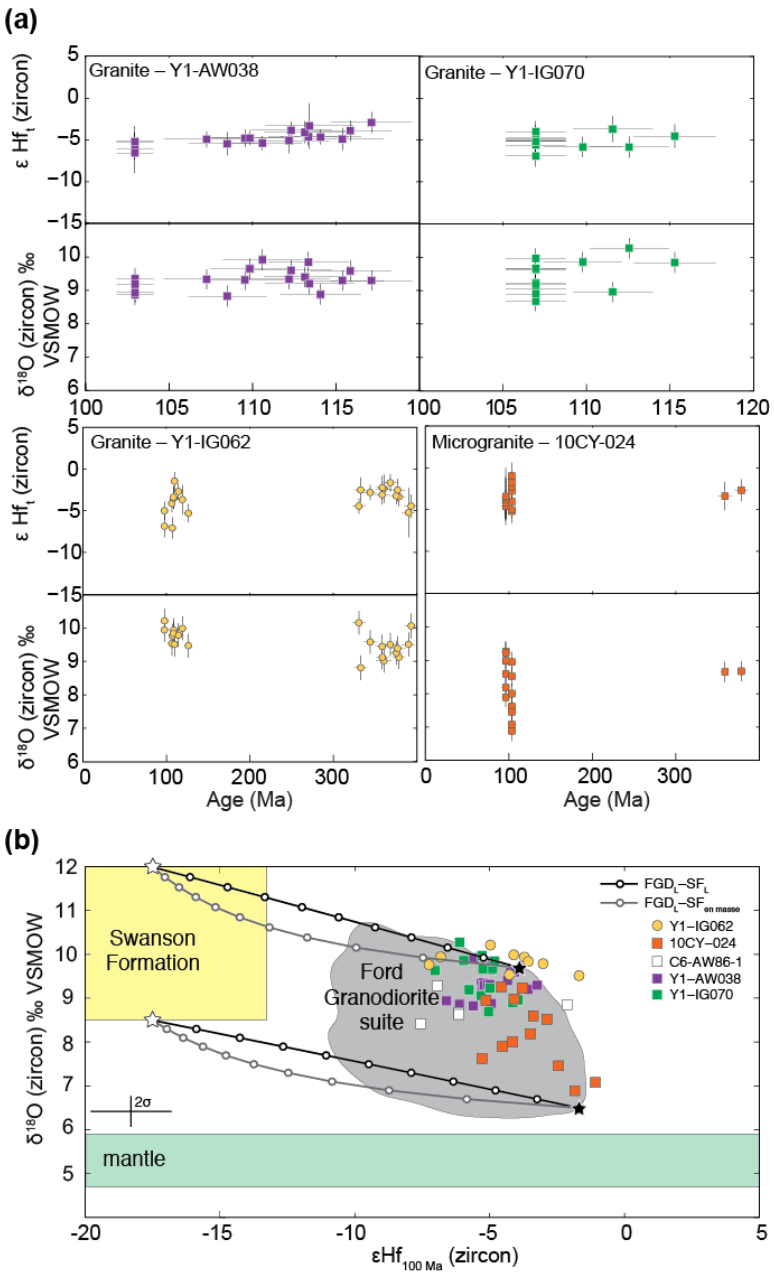

Fig. 3.15. (a) Plots of $\delta^{18}O$ and εHf_t versus $^{206}Pb/^{238}U$ age for Cretaceous granites from the Fosdick complex. (b) $\delta^{18}O$ plotted against εHf_{100} for granites in the Fosdick complex. The range of εHf values for the Swanson Formation represents the interquartile range of zircon values recalculated 100 Ma and the $\delta^{18}O$ value range is from oxygen isotope analysis of six whole-rock samples (Yakymchuk et al., 2014). The εHf and $\delta^{18}O$ values of the Ford Granodiorite are from Yakymchuk et al. (2013a, 2014). The $\delta^{18}O$ values of mantle-derived rocks is 5.3 ± 0.6‰ (Valley et al., 1998). Two binary mixing models were calculated for mixing between anatectic melt from the Ford Granodiorite suite (FGD) with anatectic melt from the Swanson Formation or the assimilation of the Swanson Formation en masse using representative end members of each source as discussed in the text. The cross in the bottom left shows the approximate ±2σ uncertainties for individual Hf and O isotope values.

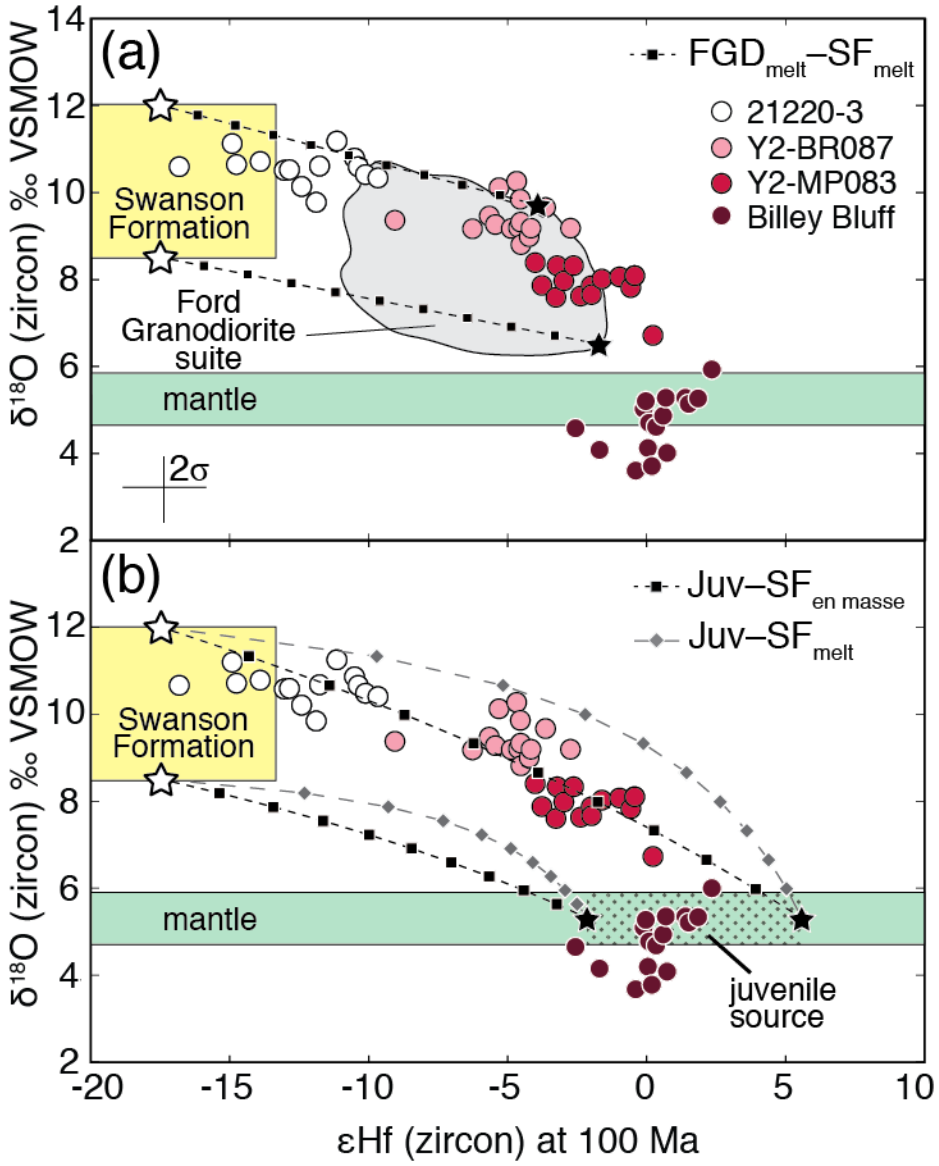

Fig. 3.16. Plots of $\delta^{18}O$ and εHf_{100} values from individual zircon grains from samples of granites from outside the Fosdick complex as well as the potential source rocks. The range of εHf values for the Swanson Formation represents the interquartile range of zircon values recalculated 100 Ma and the $\delta^{18}O$ value range is from oxygen isotope analysis of six whole-rock samples (Yakymchuk et al., 2014). The εHf and $\delta^{18}O$ values of the Ford Granodiorite are from Yakymchuk et al. (2013*a*, 2014). The $\delta^{18}O$ values of mantle-derived rocks is 5.3 ± 0.6‰ (Valley et al., 1998). (a) Binary mixing model between melt derived from anatexis of the Ford Granodiorite suite (FGD) and the Swanson Formation (SF) as discussed in the text. The cross in the bottom left shows the approximate ±2σ uncertainties for individual Hf and O isotope values. (b) Binary mixing model between a juvenile magma (Juv) and en masse assimilation of Swanson Formation (SF) or melt derived by anatexis of the Swanson Formation as discussed in the text.

of 8.7 to 10.3 (Fig. 3.15), and weighted means of -5.3 ± 0.5 and 9.4 ± 0.3, respectively (2σ; n = 13). Sample 10CY-024 contains zircon with εHf_{100} values of -5.3 to -1.1, $\delta^{18}O$ values of 6.7 to 9.3 (Fig. 3.15), and weighted means of -3.8 ± 0.8 and 8.1 ± 0.5, respectively (2σ; n = 13).

Sample Y1-IG062 contains both Devonian–Carboniferous and Cretaceous zircon (Fig. 3.15a). Devonian–Carboniferous zircon spots have εHf_{360} values of -5.9 to -1.9, $\delta^{18}O$ values of 8.8 to 10.2, and weighted means of -3.1 ± 0.6 and 9.4 ± 0.2, respectively (2σ; 12 of 13). Cretaceous zircon spots have εHf_{100} values of -7.3 to -1.7, $\delta^{18}O$ values of 9.5 to 10.2, and weighted means of -4.2 ± 1.4 and 9.8 ± 0.2, respectively (2σ; n = 9).Devonian–Carboniferous zircon εHf values recalculated to 100 Ma are -11.6 to -7.5, which is less radiogenic than most Cretaceous zircon. Cretaceous zircon εHf values recalculated to 360 Ma are -1.6 to +4.0, which are more radiogenic than the Devonian–Carboniferous zircon. This does not support closed-system dissolution–reprecipitation of zircon. Furthermore, Cretaceous zircon generally has higher $\delta^{18}O$ values than Devonian–Carboniferous zircon (Fig. 3.15a).

3.7.3.2 Cretaceous granites from outside the Fosdick complex

Zircon Hf and O isotope results for the four granites from outside the Fosdick complex are summarized in Fig. 3.16. Sample 21220-3 contains zircons with εHf values that range from -16.8 to -9.7, $\delta^{18}O$ values that vary from 9.8 to 11.2, and weighted means of -11.8 ± 1.0 and 10.7 ± 0.2, respectively (2σ: 14 of 15). Sample Y2-BR087 contains zircons with εHf values that range from -6.3 to -2.7 (with one value of -9.0), $\delta^{18}O$ values that vary from 9.0 to 10.3, and weighted means of -4.5 ± 0.5 and 9.4 ± 0.2, respectively

(2σ; 15 of 17). Sample Y2-MP083 contains zircons with εHf values that range from -4.0 to -0.4 (one value of +0.2), $\delta^{18}O$ values that vary from 7.6 to 8.4 (one value of 6.7), and weighted means of -1.9 ± 0.8 and 8.0 ± 0.2, respectively (2σ; 14 of 15). The granite from Billey Bluff in the Amundsen Province contains zircon with εHf values that range from -2.6 to +2.3, $\delta^{18}O$ values that vary from +3.6 to +5.9, and weighted means of 0.6 ± 0.5 and +4.7 ± 0.4, respectively (2σ: 15 of 16).

3.8 Discussion

As noted in the introduction, the major oxide and trace element concentrations and the isotope composition of anatectic melts may be modified by processes such as melt–residuum separation and the type and rate of accessory mineral dissolution versus the rate of melt extraction that operate in the source. Peritectic mineral entrainment and dissolution or fractional crystallization during transport and after emplacement are expected to affect the major oxide and trace element distributions of the evolving granites, but are less likely to affect the isotope compositions. In addition, during the Cretaceous high-grade metamorphism the temperature exceeded 870 ºC at the end of the prograde evolution and remained above 870 ºC during decompression related to exhumation and dome formation. At these temperatures, the rate of dissolution of accessory minerals in relation to the rate of melt extraction is expected to be high enough that significant isotope disequilibrium between melt and source is not anticipated. Therefore, in this study the whole-rock Sr and Nd, and zircon Hf and O isotope values are used to constrain potential sources and their proportional contribution to the granites. By contrast, the major oxide and trace element chemistry is used to constrain processes that

modify magma chemistry during magma extraction, ascent and emplacement. With these issues in mind, we turn to the origin and evolution of the granites.

3.8.1 The Fosdick complex

3.8.1.1 Protoliths of the migmatitic gneisses

The paragneisses have major oxide and trace element compositions that are sufficiently similar to the Swanson Formation to conclude that they are likely to be the high-grade equivalents of these metasedimentary protoliths (Figs 3.9, 3.10, 3.11). Exceptions such as higher FeO*+MgO+TiO_2 and ASI at low SiO_2, and higher Th and U are consistent with modification of the composition by variable loss of granite melt and variable retention of accessory minerals in the residue. When age corrected to 100 Ma, which is the preferred age for the dominant anatectic event, two-thirds of the paragneiss samples have Sr and Nd isotope compositions similar to those of the Swanson Formation (Fig. 3.13), supporting this interpretation (cf. Korhonen et al., 2010*b*). For the exceptions, two of the three paragneisses have lower P_2O_5 than the Swanson Formation but all three have higher ΣLREE and Th contents, suggesting that monazite was retained in the source during melting. However, these samples also have more radiogenic εNd isotope compositions, indicating that monazite retention in the source is not a viable explanation for the mismatch between these data and the field defined by the Swanson Formation samples. We suggest that a more likely explanation for the mismatch is variable diffusive exchange with migrating anatectic melt derived from the Ford Granodiorite suite source (cf. Elburg, 1996; Lesher, 1996).

The orthogneisses have major oxide and trace element compositions that are close to those for the Ford Granodiorite suite, consistent with the hypothesis that they are the high-grade equivalents of these igneous protoliths (Figs 3.9, 3.10, 3.11; cf. Korhonen et al., 2010b). Exceptions such as lower K_2O and ΣREE, and higher Al_2O_3 at low SiO_2, are consistent with modification of the composition by variable loss of granite melt and variable dissolution of accessory minerals in the source. With one outlier, the orthogneisses have Nd and Sr isotope compositions similar to those of the Ford Granodiorite suite at both 360 Ma (not shown) and 100 Ma (Fig. 3.13). Sample Y1-AW039 is an enclave of orthogneiss within Cretaceous granite that was emplaced into the thick unit of residual paragneiss at Mt Avers. Although this sample has high P_2O_5 and low Th, suggesting that apatite was retained in the source during melting, we suggest the less radiogenic εNd is more likely to be the result of variable diffusive exchange with paragneiss during melting prior to incorporation of the enclave into the Cretaceous granite (cf. Elburg, 1996; Lesher, 1996). Because the zircons in the orthogneisses yield mostly Devonian–Carboniferous ages, their Hf and O isotope compositions were age corrected to 360 Ma. These zircons have Hf and O isotope compositions that lie within the range for zircons from the Ford Granodiorite suite samples (Fig.3.14), supporting the interpretation that the orthogneisses were derived from this protolith.

3.8.1.2. Petrogenesis of Cretaceous granites

3.8.1.2.1 Constraints from whole rock geochemistry

To determine whether the Cretaceous granites could represent primary crustal melt compositions derived from a Ford Granodiorite suite/orthogneiss source or a

Swanson Formation/paragneiss source or some combination of these, the granites are evaluated in the normative Qtz–Ab–Or diagram in Fig. 3.17 (Ebadi and Johannes, 1991) and the molar (Na+Ca)–(Fe*+Mg+Ti)–K diagram in Fig. 3.18 (Solar and Brown, 2001). In the absence of melting experiments on the putative source rocks, experimental melt compositions from Skjerlie et al. (1993), Patiño Douce and Harris (1998) and Koester et al. (2002) are used as analogs based on similarity in chemical composition of the starting materials to the source compositions. The experimental melts from Skjerlie et al. (1993) represent proxies for melts derived from the Ford Granodiorite suite while the experimental results of Patiño Douce and Harris (1998) and Koester et al. (2002) represent proxies for melts derived from the Swanson Formation. Average glass compositions from these three sets of melting experiments are shown in Fig. 3.17, and both the starting compositions and fields of glass compositions are plotted in Fig. 3.18. In Fig. 3.17, many of the granites plot within the field of melt inclusions and between the average compositions of the experimental glasses; they are characterized by sub equal proportions of normative quartz, plagioclase and K-feldspar. The most plagioclase rich granites (Fig. 3.5, Y1-AE051 and Y1-IG070) plot towards the Qtz–Ab edge of the diagram, whereas the most K-feldspar rich granite (Fig. 3.5, Y1-AW038) plots towards the Or apex.

In Fig. 3.18, except for the microgranite, none of the granites plot within the fields defined by experimental glass compositions. Several granites, both garnet absent and garnet bearing, plot between the fields defined by experimental glasses and may represent compositions close to primary crustal melts. These granites also plot in the centre of the array of granite compositions in the plot of K_2O vs $CaO+Na_2O$ (Fig. 3.9), and two garnet

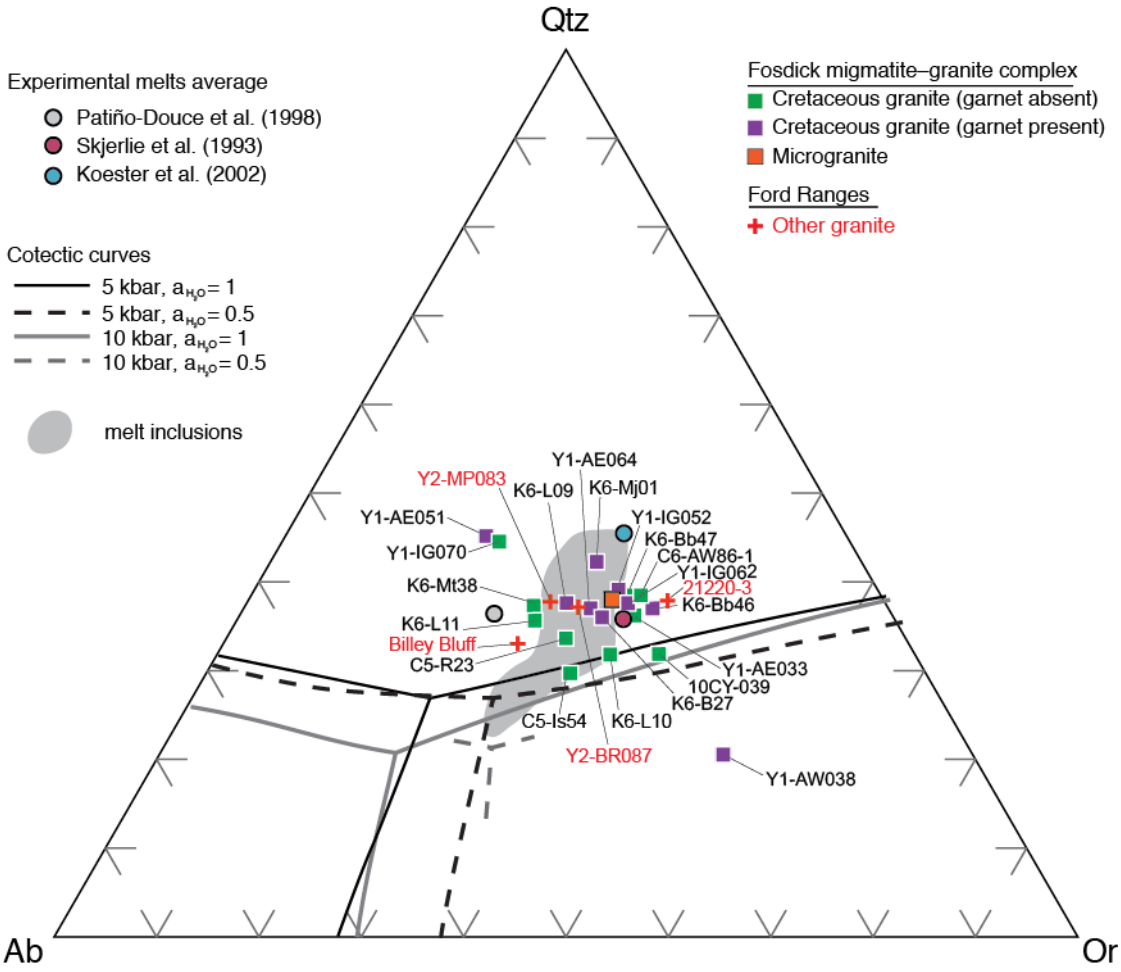

Fig. 3.17. CIPW Q–Ab–Or diagram (wt %) comparing the composition of granites in this study with the average experimental melt compositions, the composition of melt inclusions in the grey field (Cesare et al., 2007; Acosta-Vigil et al., 2007; Ferrero et al., 2011, 2012, 2014; Bartoli et al., 2013) and cotectic curves for haplogranitic compositions (Ebadi and Johannes, 1991).

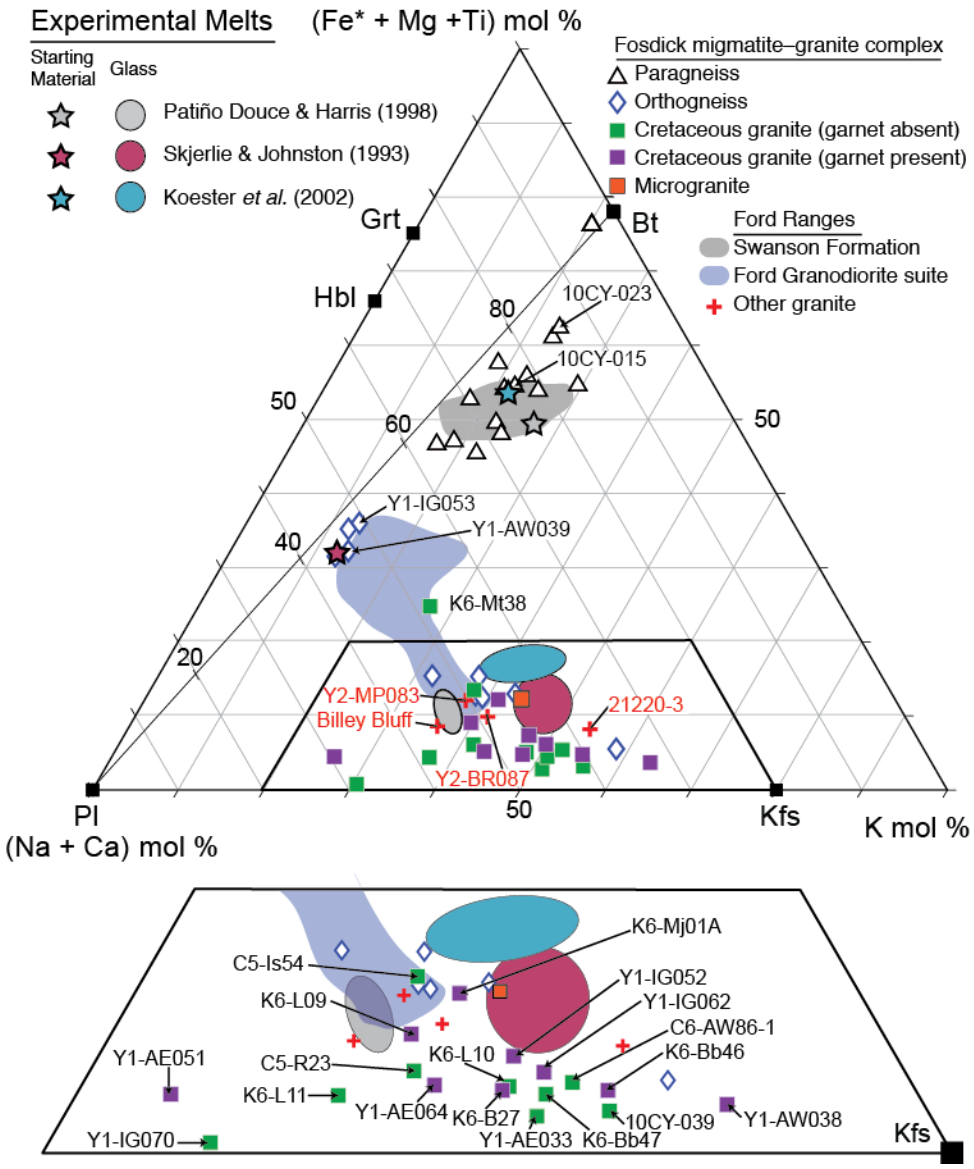

Fig. 3.18. Ternary (Na+Ca)–(Fe*+Mg+Ti)–K plot (after Solar and Brown, 2001).

absent granites from this group (C5-R23 and C5-Is54) have the highest ΣREE concentrations and only small negative Eu anomalies (Fig. 3.12). The most plagioclase rich granite (Y1-AE051) plots at the low K_2O end of the granite array in the plot of K_2O vs $CaO+Na_2O$, whereas the most K-feldspar rich granite (Y1-AW038) plots at the high K_2O end of the array (Fig. 3.9). Since the granites exhibit early-crystallized feldspar (Fig. 3.5), they cannot be related by simple fractional crystallization and separation of cumulate minerals from evolved melt, and each granite must represent the cumulate products derived from a suite of variably fractionated melts. Thus, each batch of melt that migrated through the Fosdick complex followed its own fractional crystallization trend, as might be expected from episodic drainage of melt from the suprasolidus crust and the growing body of data supporting the incremental construction of injection complexes and granite plutons (Brown 2013; Yakymchuk et al. 2013*b*, *c*; Morfin et al. 2013, 2014).

The covariation between K_2O and $CaO+Na_2O$ indicates that quartz, sodic plagioclase and K-feldspar were present on the liquidus (Morfin et al., 2014). Bearing in mind that the compositions of most of the granites are displaced towards the K-feldspar–plagioclase join relative to the experimental glass compositions in Fig. 3.18, these observations are consistent with the early accumulation of plagioclase in the less evolved magmas and K-feldspar in the more evolved magmas (Morfin et al., 2014). The feldspar microstructures (Fig. 3.5), the low ΣREE contents and the moderate to large positive Eu anomalies of the granites are consistent with a cumulate origin for many of them.

By projecting from a likely melt composition through each sample onto the K-feldspar–plagioclase edge in the molar (Na+Ca)–(Fe*+Mg+Ti)–K diagram (Fig. 3.18), an estimate may be made of the amount and mode of cumulate material present in each

granite (Solar and Brown, 2001; Korhonen et al., 2010b). The cumulate proportions were evaluated relative to the glass composition from the experiments of Skjerlie et al. (1993). Using this method, the Cretaceous granites comprise 30% to 90% cumulate material composed of variable proportions of K-feldspar (dominant) and plagioclase (subordinate). As pointed out by Morfin et al. (2014), the dominance of K-feldspar indicates that the melts were sufficiently evolved due to early plagioclase fractionation in the source that they were able to crystallize K-feldspar at the level of emplacement. Thus, the melts are inferred to have been derived from deeper in the crust, as discussed below. The cumulate model may be evaluated further using the large-ion lithophile elements, as shown on Fig. 3.19. In Fig. 3.19, the effects of fractional crystallization of plagioclase, K-feldspar and biotite are shown for two representative starting melt compositions with Rb, Sr and Ba concentrations of 120 or 400 ppm, 75 or 400 ppm and 100 or 800 ppm, and Rb/Sr ratios of 1 or 2, respectively. Fractional crystallization is modeled using the average of the partition coefficients reported by Nash and Crecraft (1985). For the Cretaceous granites from inside the Fosdick complex, biotite does not play any role, and the trends in the data are reproduced satisfactorily by accumulation of dominantly K-feldspar with only a subordinate role for plagioclase (Fig. 3.19).

In the Fosdick complex, with the exception of a small amount of zircon, there is no geochemical evidence to support a major role for peritectic and/or residual mineral entrainment from the source. Garnet and biotite schlieren are observed locally in the smaller granites and at the edges of the larger granites comprising the network of transport conduits cutting through the migmatitic gneisses, which suggests that entrainment of peritectic garnet and/or residual zircon could have contributed to the

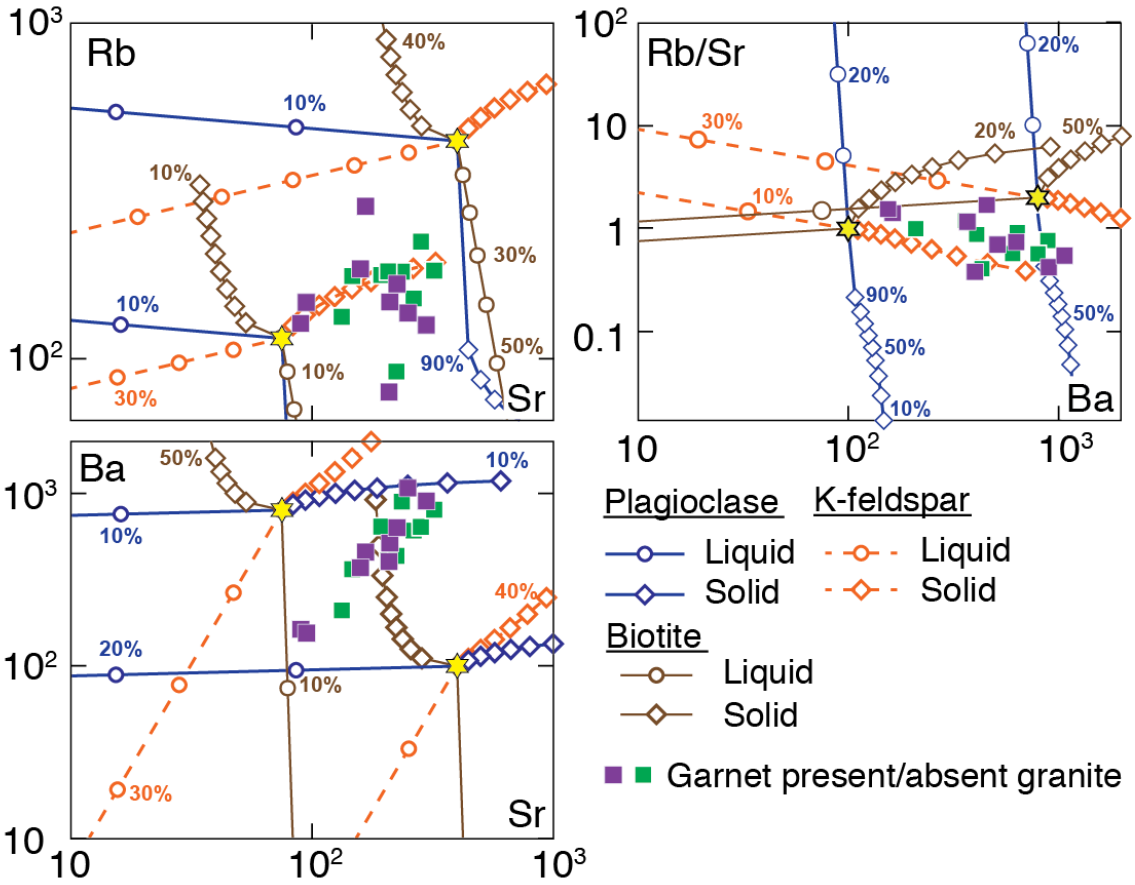

Fig. 3.19. Log–log trace element plots of Rb, Sr, Ba and Rb/Sr showing fractionation trends for K-feldspar, plagioclase and biotite compared with the Cretaceous granites from the Fosdick migmatite–granite complex. The amount of fractional crystallization is shown by 10% increments. Distribution coefficients for Rb, Sr, and Ba in K-feldspar and plagioclase are the average of values reported for each mineral in Nash and Crecraft (1985).

elevated HREE patterns in some of the Cretaceous garnet bearing granites. However, there is no trend among the granites projecting back to either the Ford Granodiorite suite or Swanson Formation source compositions or towards garnet and/or biotite in Fig. 3.18. We conclude that peritectic and/or residual mineral entrainment was a subordinate process that locally may have affected the chemistry of these granites, but it was not the dominant process controlling the chemistry of granites within the Fosdick complex.

3.8.1.2.2 Constraints from whole rock Sr and Nd isotopes

The Cretaceous granites have whole-rock Sr and Nd isotope compositions that vary from overlapping the range for the Ford Granodiorite suite and the orthogneisses to values that lie between this range and the range for the Swanson Formation and the paragneisses (Fig. 3.13). One of the garnet absent granites (C6-AW86-1) was originally argued to be part of the Devonian–Carboniferous suite (Siddoway and Fanning, 2009), but the presence of Cretaceous zircon and its geochemical characteristics indicate that it is likely to be Cretaceous in age.

For Sr and Nd isotope compositions recalculated to 100 Ma, binary mixing lines were calculated using the Sr and Nd concentrations and isotope values of more and less radiogenic end members of the Swanson Formation and the Ford Granodiorite suite (Fig. 3.13). These binary mixing lines also enclose the Sr and Nd isotope values for most of the orthogneisses and paragneisses (Fig. 3.13). For four of the Cretaceous granites, the Sr and Nd isotope compositions are consistent with being derived solely from a source similar to the Ford Granodiorite suite, whereas the Sr and Nd isotope compositions of the remainder allow a contribution of up to 40% from a source similar to the Swanson Formation.

3.8.1.2.3 Constraints from Hf and O isotopes in zircon

The εHf values of detrital zircons in the Swanson Formation, recalculated to 100 Ma, varies from -3 to -73, with a median value of -17.5 and an interquartile range of -13.9 to -30.3, and the $\delta^{18}O$ value of zircons that crystallized from melt produced from the Swanson Formation are expected be ~8.5–12‰, with a mean value of 10.5‰ (Yakymchuk et al., 2014). These values for Swanson Formation are shown on Fig. 3.15, together with a field for zircons from the Ford Granodiorite suite at 100 Ma.

Hafnium and O isotope data for zircons from samples Y1-IG070, Y1-AW038 and C6-AW86-1 plot within the field defined by the Ford Granodiorite suite, but in the sector with more radiogenic εHf_{100} values and higher $\delta^{18}O$ values (Fig. 3.15b). Samples Y1-IG070 and Y1-AW038 have a similar range and mean εHf_{100} and $\delta^{18}O$ values. In addition, both samples have nearly identical $^{87}Sr/^{86}Sr$ ratios, but sample Y1-IG070 has a εNd_{100} value of -8.2 whereas sample Y1-AW038 has a more radiogenic value of -5.5 (Fig. 3.13). This suggests decoupling of the Nd isotope systematics from the other isotope systems for sample Y1-IG070. Since both granites have similar very low P_2O_5 and ΣREE, and Th is below detection, decoupling is unlikely to be due to accessory mineral behavior in the source. We speculate that this difference might be due to variable diffusive exchange during melt extraction from the source. By contrast, although zircons from sample Y1-IG062 have a similar range of εHf_{100} values to the other granites, many plot at slightly higher values of $\delta^{18}O$ than the Ford Granodiorite suite and lie above the Ford Granodiorite suite field in Fig. 3.15b.

Zircons from the microgranite (sample 10CY-024) plot within the field defined by the Ford Granodiorite suite, but in the sector with more radiogenic εHf_{100} values and over

a wider range of $\delta^{18}O$ values that tend to be lower than the granites (Fig. 3.15b). This could suggest derivation from the more primitive members of the Ford Granodiorite suite and/or input from a more juvenile source. This sample also has non-radiogenic εNd and $^{87}Sr/^{86}Sr$ values (Fig. 3.13), low P_2O_5 and elevated ΣREE and Th contents, consistent with significant monazite dissolution during melting of a Ford Granodiorite suite source.

Using the εHf_{100} and $\delta^{18}O$ data discussed above, limits may be placed on the amount of Swanson Formation (or paragneiss) that might have been involved in the petrogenesis of these granites. Binary mixing lines were calculated that connect representative end-member compositions of the Swanson Formation and the Ford Granodiorite suite (Fig. 3.15b). Two scenarios are modeled, one in which anatectic melt derived from the Ford Granodiorite suite is mixed with anatectic melt derived from the Swanson Formation and one where it is mixed with Swanson Formation en masse by assimilation. The curvature of the mixing lines is most sensitive to the relative concentrations of Hf in each of the end-members. For the Swanson Formation, an average whole-rock concentration of 3.2 ppm was assigned based on bulk chemical analyses (Korhonen et al., 2010*a*). For anatectic melt derived from the Swanson Formation or the Ford Granodiorite suite, a concentration of 1.0 ppm is used (e.g. Yakymchuk et al., 2013*a*). If anatectic melt derived from the Ford Granodiorite suite mixed with anatectic melt derived from the Swanson Formation, then the maximum contribution from the latter is 30% (Fig. 3.15). By contrast, for en masse assimilation of the Swanson Formation, the limit is 10% (Fig. 3.15).

Based on the Hf and O isotope geochemistry, the Cretaceous granites could have been derived from a source similar to the Ford Granodiorite suite with a variable input of

up to 30–40% from a source similar to the Swanson Formation. In this model, no juvenile input is required. A juvenile input cannot be ruled out by the isotope data alone, since mixing between magma from an appropriate mantle source and an upper crustal source similar to the Swanson Formation will also enclose the data shown in Fig. 3.15, as discussed for Devonian–Carboniferous granites in the Fosdick complex by Yakymchuk et al. (2014) and below for the Cretaceous granites from outside the Fosdick complex. However, since there is no evidence of any juvenile input, the parsimonious interpretation favours derivation of the granites from the putative crustal sources.

3.8.1.3. Fertility of the source rocks during the Cretaceous

For the crustal level exposed in the Fosdick complex, previous forward modelling of phase equilibria for Swanson Formation and Ford Granodiorite suite compositions suggested that the former could have produced up to 30 vol. % melt but the latter less than 5 vol. % melt at the peak of Cretaceous metamorphism (Korhonen et al., 2010*a*). However, it is likely that some melt was generated and lost during the Devonian–Carboniferous arc-related metamorphism, at least from the Swanson Formation protoliths, in which case these estimates will be maxima. The effect of the Devonian–Carboniferous metamorphism and melting on the fertility of these sources is evaluated below using phase equilibria forward modelling.

Calculations were performed using THERMOCALC v.3.35 (Powell and Holland, 1988) and the internally consistent dataset of Holland and Powell (1998). Modelling was undertaken in the Na_2O–CaO–K_2O–FeO–MgO–Al_2O_3–SiO_2–H_2O–TiO_2–Fe_2O_3 (NCKFMASHTO) chemical system using the activity–composition models and

procedure described in Yakymchuk et al. (2013*a*). *P–T* pseudosections calculated for representative samples of the Swanson Formation (sample 10CY-002) and the Ford Granodiorite suite (sample R7218 from Weaver et al., 1991) from outside the Fosdick complex, and for a representative migmatitic paragneiss (sample 10CY-015) and orthogneiss (sample Y1-IG053) from inside the Fosdick complex are shown in Fig. 3.20.

These phase diagrams show the stable phase assemblage and the amount of melt (as mol. % (~vol. %) isopleths) generated in a closed (undrained) system at *P–T*, for each composition. Peak conditions for the Devonian–Carboniferous metamorphic event are estimated to have been 680–800°C at 0.60–0.95 GPa (C. Yakymchuk, unpublished data). At these *P–T* conditions, the Swanson Formation composition could have produced up to 10 mol. % melt, but the Ford Granodiorite suite composition would only have produced <1 mol. % melt (Fig. 3.20a, b). Melt drainage from the suprasolidus crust is expected when the proportion of melt reaches ~7 vol. % (e.g. Rosenberg and Handy, 2005; Brown, 2010). Therefore, the Swanson Formation composition modeled was likely to have lost melt at least once during the Devonian–Carboniferous metamorphism, resulting in a less fertile composition for melting during the Cretaceous metamorphism. Although there is variation in the fertility of the Swanson Formation, this confirms that melt volumes predicted by Korhonen et al. (2010*a*) for the Cretaceous metamorphism must represent maxima. By contrast, the Ford Granodiorite suite is likely to have retained its original fertility through the Devonian–Carboniferous metamorphism and into the Cretaceous event.

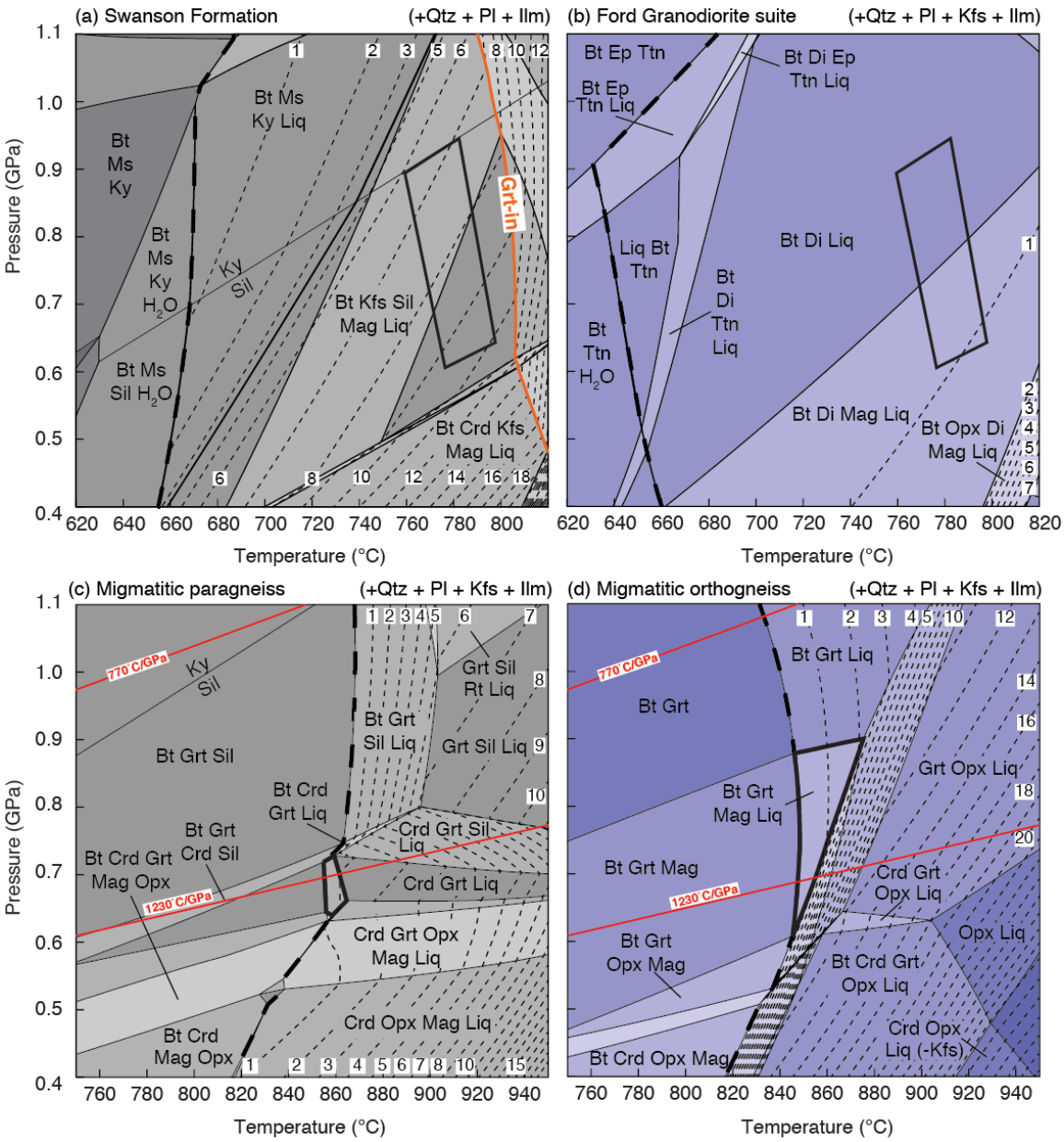

Fig. 3.20. Calculated *P–T* pseudosections for a representative composition of: (a) Swanson Formation, (b) Ford Granodiorite suite, (c) migmatitic paragneiss, and (d) migmatitic orthogneiss. The thick dashed line represents the solidus and the thin dashed lines represent melt isopleths in mol.% (~vol.%). The fields outlined by the thick black lines represents the peak *P–T* conditions in the Devonian–Carboniferous (C. Yakymchuk, unpublished) in (a) and (b), and the Cretaceous from Korhonen et al. (2010*a*) in (c) and (d). The red lines in (c) and (d) represent a thermal gradient for a thickened crust in Marie Byrd Land prior to crustal thinning associated with the exhumation of the Fosdick complex (770°C/GPa) and an average thermal gradient for the Cretaceous *P–T* conditions for the Fosdick complex (1230°C/GPa) from Yakymchuk et al. (2013a).

Phase equilibria modelling of the residual gneisses (Fig. 3.20c, d) provides information about the amount of melt left in the source after loss along the prograde evolution and throughout decompression to the final solidus assemblage at *P* of 0.75–0.6 GPa and *T* of 870–830°C. The representative residual paragneiss is expected to have retained <2 vol. % melt at these *P–T* conditions, whereas the orthogneiss could have retained up to 6 vol. % melt. However, it is clear from these *P–T* pseudosections that melt was potentially still available at higher *P–T* conditions in the source beneath the Fosdick complex during the doming event, particularly in the orthogneiss composition.

Even if the maximum of 30 vol. % melt was generated from the Swanson Formation during Cretaceous metamorphism at the depth of exposure, this is much less than the amount of leucosome and granite measured at outcrop in the migmatitic gneisses, which generally ranges from 40 vol. % to 70 vol. % (Yakymchuk et al., 2013*b*). Therefore, it is likely that a significant proportion of the leucosome and granite in the Fosdick complex was sourced from deeper in the crust where ambient temperatures were higher. This is consistent with geophysical surveys across the Ford ranges, which show that the crust beneath the Fosdick complex is composed of rocks similar to the Swanson Formation and Ford Granodiorite suite (Ferraccioli et al., 2000; Luyendyk et al., 2003).

Crustal thinning due to doming and exhumation increases the apparent thermal gradient. Yakymchuk et al. (2013*b*) suggested that the apparent thermal gradient in the Fosdick complex prior to doming was on the order of 770°C/GPa, whereas the apparent thermal gradient that passes through *P–T* conditions for the end of doming is on the order of 1230°C/GPa (Fig. 3.20c, d). Extrapolating from these *P–T* conditions, it is clear that the gneisses not far beneath the Fosdick complex would have undergone a much greater

degree of partial melting that could have sourced the excess leucosome and granite within the complex. At 950°C, which equates to roughly 3 km below the Fosdick complex along the 1230°C/GPa apparent thermal gradient, the paragneiss modeled would have had ~11 vol. % melt still available for extraction and the orthogneiss ~20 vol. % melt (Fig. 3.20c, d).

The forward modelling shows that the dominant source for granite magma at depth beneath the Fosdick complex during the Cretaceous metamorphism was likely to have been the high-grade equivalents of the Ford Granodiorite suite. By contrast, magma derived from paragneisses equivalent to the Swanson Formation would have been subordinate due to the reduced fertility after Devonian–Carboniferous metamorphism and consequent upon melt drainage during prograde heating to peak temperatures for the Cretaceous metamorphism (cf. Yakymchuk and Brown, 2014a). The predictions about magma sources based on the modelling are consistent with the Sr, Nd, Hf and O isotope data from the Cretaceous granites, which require a larger component derived from a source similar to the Ford Granodiorite suite and a smaller component derived from a source similar to the Swanson Formation (Figs 3.13, 3.15).

3.8.2 Petrogenesis of the Cretaceous granites from outside the Fosdick complex

3.8.2.1 Constraints from whole rock geochemistry

The whole rock compositions for the granites from outside the Fosdick complex are plotted in the normative Qtz–Ab–Or diagram in Fig. 3.17 (Ebadi and Johannes, 1991) and the molar (Na+Ca)–(Fe*+Mg+Ti)–K diagram in Fig. 3.18 (Solar and Brown, 2001). In Fig. 3.17, three of the granites plot within the main cluster of granites from inside the

Fosdick complex, within the fields for melt inclusions and the average compositions of the experimental glasses. Sub equal proportions of normative quartz, plagioclase and K-feldspar characterize these three granites. The granite from Billey Bluff plots outside this cluster towards the Ab–Qtz join. This sample is dominated by coarse-grained perthitic K-feldspar with quartz and minor plagioclase. Although variable, the granites from outside the Fosdick complex plot with the main cluster of granites from inside the complex (Fig. 3.18). Three of the four granites also plot close to the centre of the array of cumulate granite compositions in the plot of K_2O vs $CaO+Na_2O$ (Fig. 3.9). By contrast, the granite from the Scott Nunataks plots at higher K_2O and lower $CaO+Na_2O$ (Fig. 3.9). All four granites could represent primary crustal melts, albeit not necessarily from a single source.

3.8.2.2 Constraints from Hf and O isotopes

3.8.2.2.1 Southern Ford Ranges

The zircon Hf and O values for the two granites from the southern limit of the Ford Ranges (Y2-MP083 and Y2-BR087) have a similar range of Hf and O values to those for much of the Ford Granodiorite suite (Fig. 3.16a). Thus, although some εHf values from these samples are slightly more radiogenic than the Ford Granodiorite suite field, it nonetheless represents a plausible source for these granites. However, a small component from the Swanson Formation might be involved nonetheless. Binary mixing lines for anatectic melt derived from the Ford Granodiorite suite mixed with anatectic melt derived from the Swanson Formation were calculated (Fig. 3.16a), as discussed above for the granites inside the Fosdick complex. If melt derived from the Ford

Granodiorite suite was contaminated by melt derived from the Swanson Formation, then the maximum contribution from the latter is 10–20% (Fig. 3.16a).

Notwithstanding that the Ford Granodiorite suite represents the most likely source, the Hf and O data alone cannot rule out the possibility of mixing between a juvenile magma and the Swanson Formation to generate these granites. To evaluate a possible juvenile input two scenarios are considered: one where the juvenile magma assimilates Swanson Formation en masse and another where a juvenile magma mixes with anatectic melt derived from the Swanson Formation. For a juvenile source, the range of εHf values is derived from the εNd signature of Cretaceous mafic dykes emplaced in the Ford Ranges (Saito et al., 2013), using the correlation for juvenile mantle-derived rocks of Vervoort and Blichert-Toft (1999), the $\delta^{18}O$ value is take as the average $\delta^{18}O$ value of zircons crystallized from mantle-derived magmas (Valley et al., 1998), and the Hf concentration is taken as 4.6 ppm, which is the average Hf concentration of Cretaceous mafic rocks in Marie Byrd Land (Storey et al., 1999). For the Swanson Formation, the εHf value assigned is the median detrital zircon εHf value recalculated to 100 Ma while the $\delta^{18}O$ values represent the range of six whole-rock analyses, both from Yakymchuk et al. (2014). The Hf concentration of the Swanson Formation and anatectic melt are the same as those used above in modelling the Cretaceous granites.

The mixing field between magma from the juvenile source and assimilation of Swanson Formation en masse does not reproduce the measured values for the two granites (Fig. 3.16b). However, the mixing field between the juvenile magma and anatectic melt derived from the Swanson Formation encompasses all of the data for Y2-BR087 and Y2-MP083. For Y2-BR087, 60–80% anatectic melt from the Swanson

Formation is required to produce the measured Hf and O values, whereas for sample Y2-MP083, 20–60% anatectic melt is sufficient (Fig. 3.16b). However, since there is no evidence of any juvenile input, the parsimonious interpretation favours derivation of the granites from a dominantly Ford Granodiorite suite source.

3.8.2.2.2 Scott Nunataks, Edward VII Peninsula

Zircon Hf and O compositions from sample 21220-3 from the Scott Nunataks to the west of the Ford Ranges overlap values for the Swanson Formation, which suggests that this granite may have involved a significant component from this source (Fig. 3.16b). Using the same binary mixing lines for mixing of anatectic melts derived from the Ford Granodiorite suite and the Swanson Formation, as discussed above, this granite could represent a magma comprising 10–60% melt derived from the Ford Granodiorite suite mixed with 40–90% melt derived from the Swanson Formation (Fig. 3.16a). As discussed above, the Hf and O data alone cannot rule out the possibility of mixing between a juvenile magma and the Swanson Formation to generate this granite, but the proportion of melt derived from Swanson Formation or for en masse assimilation of Swanson Formation are large, >85% and >75%, respectively (Fig. 3.16b), making this model less likely.

3.8.2.2.3 Billey Bluff, Amundsen Province

The granite from Billey Bluff (Fig. 3.1c) contains zircon with $\delta^{18}O$ values that are mantle-like (5.3 ± 0.6‰ at 2σ; Valley et al., 1998) or below mantle values (Fig. 3.20). These zircons also have relatively unradiogenic εHf values ranging from -2.5 to +2.3,

consistent with a juvenile source, perhaps related to the source of the Cretaceous mafic dykes emplaced throughout Marie Byrd Land (Storey et al., 1999). As can be seen from Fig. 3.20, the εHf values of zircons from the Billey Bluff sample are consistent with derivation from such a source, which is also consistent with the presence of rounded mafic enclaves in the granite at outcrop. However, this juvenile source is unlikely to be the depleted mantle, because the zircon εHf values are well below those expected for new crust derived from it at this time (~+13; Dhuime et al., 2011). A more plausible source is a Proterozoic mafic underplate that melted during the transition from oblique convergence to oblique extension during the Cretaceous. The different source required for this granite may relate to its location within the Amundsen Province.

Roughly one-third of the analysed zircons have $\delta^{18}O$ values below that of the mantle, which leads to the possibility that the magma composition was influenced by infiltration of meteoric fluids. This may result from intrusion of meteoric water directly into the magma chamber—although this is generally considered to be unlikely (e.g. Norton and Taylor, 1979)—or through assimilation of hydrothermally altered wall rock (e.g. Taylor and Sheppard, 1986). Such hydrothermal alteration is documented in the Ross Province by negative whole-rock $\delta^{18}O$ values for two samples of the Swanson Formation collected from the contact aureole of a Cretaceous granite (Yakymchuk et al., 2014). However, assimilation of low $\delta^{18}O$ Swanson Formation may be ruled out because the low $\delta^{18}O$ values of the Billey Bluff granite are not coupled with the more radiogenic εHf values expected from such a process.

3.8.3 Cumulate granites in migmatitic gneiss domes

The variable major oxide and trace element chemistry, dominance of pronounced positive Eu anomalies and location close to the K-feldspar–plagioclase edge of the molar (Na+Ca)–(Fe*+Mg+Ti)–K diagram in Fig. 3.18 for many of the Cretaceous granites inside the Fosdick complex are features consistent with fractional crystallization and accumulation of feldspar. Granites forming sub-horizontal sheets and discordant networks inside the Fosdick complex commonly contain coarse euhedral feldspars, consistent with a cumulate origin. However, the covariation between K_2O and $CaO+Na_2O$ for these cumulate granites indicates fractionation of feldspar during transport from the source prior to entrapment at their present structural level within the complex. This process may involve continuous separation of feldspar from the evolving liquid in the manner proposed by Morfin et al. (2014), and might be the mechanism that operated in the granite networks within the deeper crust of the Fosdick complex. However, after entrapment, melt drainage from the crystallizing granites within the Fosdick complex appears to have been related to dome formation, particularly in the sheeted leucogranite complex immediately below the South Fosdick detachment system. These granites are interpreted to record the collapse of sub-horizontal partially crystallized layers of magma by filter pressing (e.g. Brown et al., 1995) during vertical shortening associated with dome exhumation, leaving behind cumulate-rich residues. The evolved melt likely drained to shallow crustal levels and the resulting granites may have been lost to erosion. Some of this evolved melt may be preserved in the Byrd Coast granite suite, as discussed by Korhonen et al. (2010*b*).

The Cretaceous granites inside the Fosdick complex crystallized between 115 and 100 Ma, with a dominant grouping at 107–100 Ma (Fig. 3.21). This time frame corresponds to a period of transition in regional tectonics from oblique convergence to oblique extension that facilitated dome formation and exhumation of the Fosdick complex (Siddoway, 2005, 2008; McFadden et al., 2010*a*, *b*). Exhumation was likely a fast process. The full set of geochronological data now available for the Fosdick complex is compiled in Fig. 3.21, from which it is clear that the main period of granite crystallization both inside and outside the complex, 107–100 Ma and 105-102 Ma, respectively, overlaps the younger period of emplacement of mafic dykes during lithosphere extension (Saito et al., 2013). In addition, these granite ages overlap the younger part of the range of U–Pb metamorphic ages retrieved from monazite, the post-peak Sm-Nd ages retrieved from garnet, and the $^{40}Ar/^{39}Ar$ ages retrieved from hornblende (Fig. 3.21). Rapid cooling due to dome formation and exhumation of the middle crust is confirmed by the overlapping crystallization ages of the microgranites and younger mafic dykes with the $^{40}Ar/^{39}Ar$ ages retrieved from biotite, muscovite and K-feldspar (Fig. 3.21).

The results of this study contribute to a growing body of work that suggests leucosomes in migmatites and associated granites represent accumulations of feldspar and quartz and do not reflect primary crustal melt compositions (e.g. Cuney and Barbey, 1982; Milord et al., 2001; Solar and Brown, 2001; Johannes et al., 2003; Korhonen et al., 2010*b*; Morfin et al., 2014). There are two important implications if granites in migmatitic gneiss domes are typically cumulate. First, it is possible that the accumulation

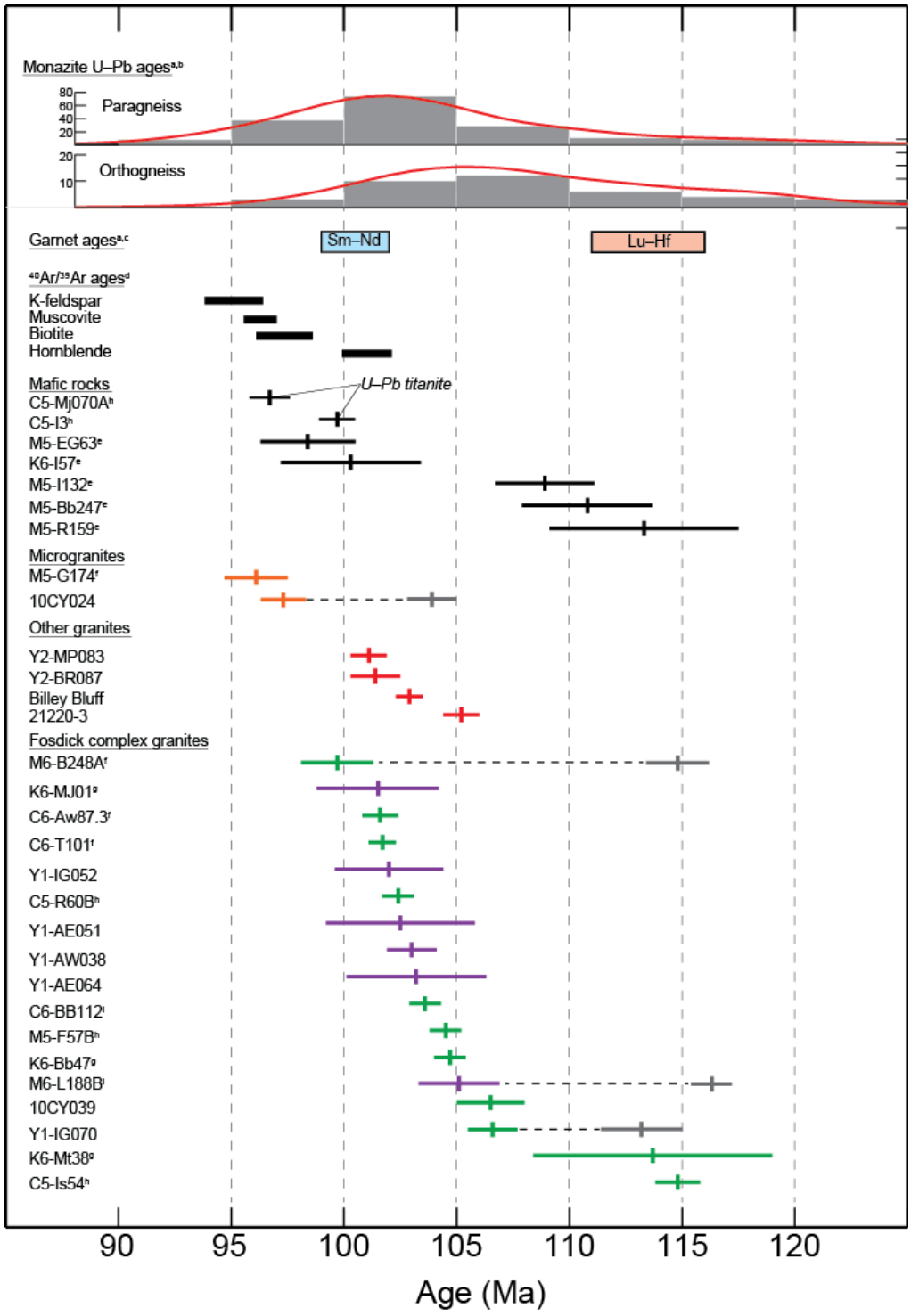

Fig. 3.21. Compilation of geochronological data from rocks inside and outside the Fosdick migmatite–granite complex. Data sources as follows: [a]Korhonen et al. (2012), [b]Yakymchuk et al. (unpublished), [c]Yakymchuk et al. (2013*c*), [d]Richard et al. (1994), [e]Saito et al. (2013), [f]Yakymchuk et al. (2013*b*), [g]Korhonen et al. (2010*b*), [h]McFadden et al. (2010*a*), [i]McFadden et al. (2010*b*).

of early-crystallized minerals in magma transport conduits may restrict the flow of melt and even locally clog the plumbing system. This possibility may need to be considered as a rate-limiting step in estimating the timescales of melt extraction from the deep crust. Second, the drained melt is likely to have more evolved compositions than are represented by melt inclusions in migmatites and, in particular, it is likely to have higher concentrations of the heat producing elements. This will have important implications for the tectonic history of large hot mountain belts (Jamieson et al., 2011), cooling ultrahigh-temperature (UHT) metamorphic terrains (Korhonen et al., 2013), priming the crust for future UHT metamorphic events (Clark et al., 2011), the particular style of some Proterozoic 'hot' orogens (McLaren and Powell, 2014), and the long-term stability of the continental crust (Sandiford and McLaren, 2002).

3.9 Conclusions

In the Fosdick migmatite–granite complex of Marie Byrd Land in West Antarctica, Cretaceous granites have Sr, Nd, Hf and O isotope values consistent with derivation from Ford Granodiorite suite and Swanson Formation sources. However, the major oxide and trace element concentrations of the granites are more variable; they reflect fractional crystallization and the accumulation of early-crystallized feldspar and quartz during magma ascent and emplacement. This conclusion is supported by the cumulate microstructures, low ΣREE contents and common positive Eu anomalies that characterize the Cretaceous granites in the Fosdick complex. In a wider context, we suggest that granites in migmatite complexes typically may not represent melt compositions and are more likely to be cumulates left after melt drainage. Thus, the

amount of granite hosted within migmatitic crust cannot be used as an estimate of melt volume. Conversely, granites that have crystallized at shallower levels in the crust from the complementary fractionated melts are likely to be more evolved than primary melt compositions.

Chapter 4: Paleozoic evolution of western Marie Byrd Land, Antarctica

4.1 Abstract

The history of crustal evolution and reworking during Paleozoic subduction along the former East Gondwanan plate margin is investigated using age and isotope characteristics of zircons from Cambrian–Ordovician sedimentary rocks, and whole-rock and zircon geochemistry from the Devonian–Carboniferous Ford Granodiorite suite and associated granites from the Ford Ranges in western Marie Byrd Land. Detrital zircons from the Swanson Formation, a widespread metaturbidite sequence, define late Paleoproterozoic, late Mesoproterozoic and Neoproterozoic–Cambrian populations. The late Paleoproterozoic group records magmatism derived from a mixed juvenile and crustal source. By contrast, the late Mesoproterozoic group yields Hf isotope values consistent with derivation from a juvenile Mesoproterozoic source inferred to represent an unexposed Grenville-age orogenic belt beneath the East Antarctic Ice sheet. Finally, reworking of this older material during Ross–Delamerian orogenesis is documented by the Hf isotope values of the Neoproterozoic–Cambrian population. New U–Pb ages from the Devonian–Carboniferous Ford Granodiorite suite across western Marie Byrd Land extend the period of arc magmatism from 375 to 345 Ma. For four younger samples of Ford Granodiorite, Hf and O isotope values in zircon suggest involvement of a larger (meta-)sedimentary component in the petrogenesis than for two older samples. This contrasts with the secular trend towards more juvenile values documented in Silurian to

Permian granite suites from the Tasmanides of eastern Australia and more juvenile values from Famennian–Tournasian granite suites in New Zealand, pieces of continental crust that were once contiguous with western Marie Byrd Land along the East Gondwana margin. The differences may relate to an along-arc change from the typical extensional accretionary mode in eastern Australia to a neutral or an advancing mode in West Antarctica, and to an across-arc difference in distance from the trench between the New Zealand fragments of Zealandia and western Marie Byrd Land. The associated granites most likely record reworking of early Ford Granodiorite suite members during arc magmatism.

4.2 Introduction

The former active margin of East Gondwana represents one of the most long-lived and extensive active margins in the Phanerozoic (e.g. Cawood, 2005; Collins et al., 2011; Harley et al., 2013). Information about the evolution and reworking of this margin is recorded in the geology and geochemistry of the sedimentary, igneous and metamorphic rocks that crop out in different regions that were once contiguous, including: the Tasmanides of Eastern Australia; the Western Province of New Zealand; north Victoria Land; Marie Byrd Land; the Antarctic Peninsula; and the western margin of South America. The New Zealand–Antarctica segment of the former active margin links the geology of eastern Australia to the east (present co-ordinates) to that of the Antarctic Peninsula and South America to the west (present co-ordinates). The relatively well-understood Tasmanides in eastern Australia represent the type example of an extensional accretionary orogen (Collins, 2002). However, it is of interest to know how the tectonic

evolution of this margin might have changed along strike to the west. In Antarctica, the relatively simple tectonic history of western Marie Byrd Land compared to north Victoria Land (e.g. Borg et al., 1986) makes it an ideal location to study the Paleozoic history of this portion of the East Gondwana margin. Thus, the results of the study we report herein enable a comparison with the well-characterized evolutionary history of eastern Australia and with recently published data from the formerly contiguous parts of New Zealand.

The scarcity of outcrop and difficulty of access in West Antarctica due to the extensive ice cover has limited our understanding of the geology of Marie Byrd Land. Based on a few pioneering studies (Pankhurst et al., 1998; Mukasa and Dalziel, 2000), the tectonic history of this region has been inferred from the geochemistry and geochronology of sedimentary and igneous rocks exposed as isolated peaks. Outstanding issues to be addressed in western Marie Byrd Land include: 1) the provenance of Cambrian–Ordovician sedimentary rocks; 2) the duration of Devonian–Carboniferous magmatism, which, at present, is constrained mostly by whole-rock Rb–Sr isochron ages; and, 3) the petrogenesis of the Devonian–Carboniferous Ford Granodiorite suite and associated granites.

In this study we report geochemical data from detrital zircons from the Cambrian–Ordovician Swanson Formation and related paragneisses, and for whole rocks and igneous zircons from the Devonian–Carboniferous Ford Granodiorite suite and associated granites and diatexites to investigate crustal evolution and reworking in western Marie Byrd Land. Detrital zircon age distributions and Hf isotope measurements from the (meta-) sedimentary rocks document a major crust-forming event in the Mesoproterozoic during the transition from Nuna to Rodinia and extensive crustal reworking during Ross–

Delamerian orogenesis. For the Ford Granodiorite suite, Sr–Nd isotope geochemistry combined with Hf and O data from zircons suggest that they were the products of mixing between juvenile magma and the host (meta-) sedimentary rocks in an active arc environment. The more variable geochemistry of the granites and diatexites suggest they were likely derived from a Ford Granodiorite suite source with a variable Swanson Formation component, although a juvenile component cannot be ruled out. This information coupled with data from the literature allows us to address the similarities and differences in the proportion of crustal growth to crustal reworking along a Phanerozoic convergent plate margin system (cf. Yakymchuk et al., 2013a).

4.3 Regional Geology

Marie Byrd Land of West Antarctica (Fig. 4.1a) was once contiguous with the Western Province of New Zealand, north Victoria Land, and the Lachlan Fold Belt of eastern Australia prior to the breakup of the active continental plate margin of Gondwana during the Upper Cretaceous (Fig. 4.1b). Based on Nd model ages of granites, Pankhurst et al. (1998) divided Marie Byrd Land into the Ross Province in the west and the Amundsen Province in the east. The boundary between the two provinces is unexposed and is believed to be oblique to the present coastline (Fig. 4.2; DiVenere et al., 1995; Pankhurst et al., 1998). Paleomagnetic data suggest that these two provinces were amalgamated in the Cretaceous (DiVenere et al., 1995; Luyendyk et al., 1996) prior to the separation of Zealandia from West Antarctica (Fig. 4.1b).

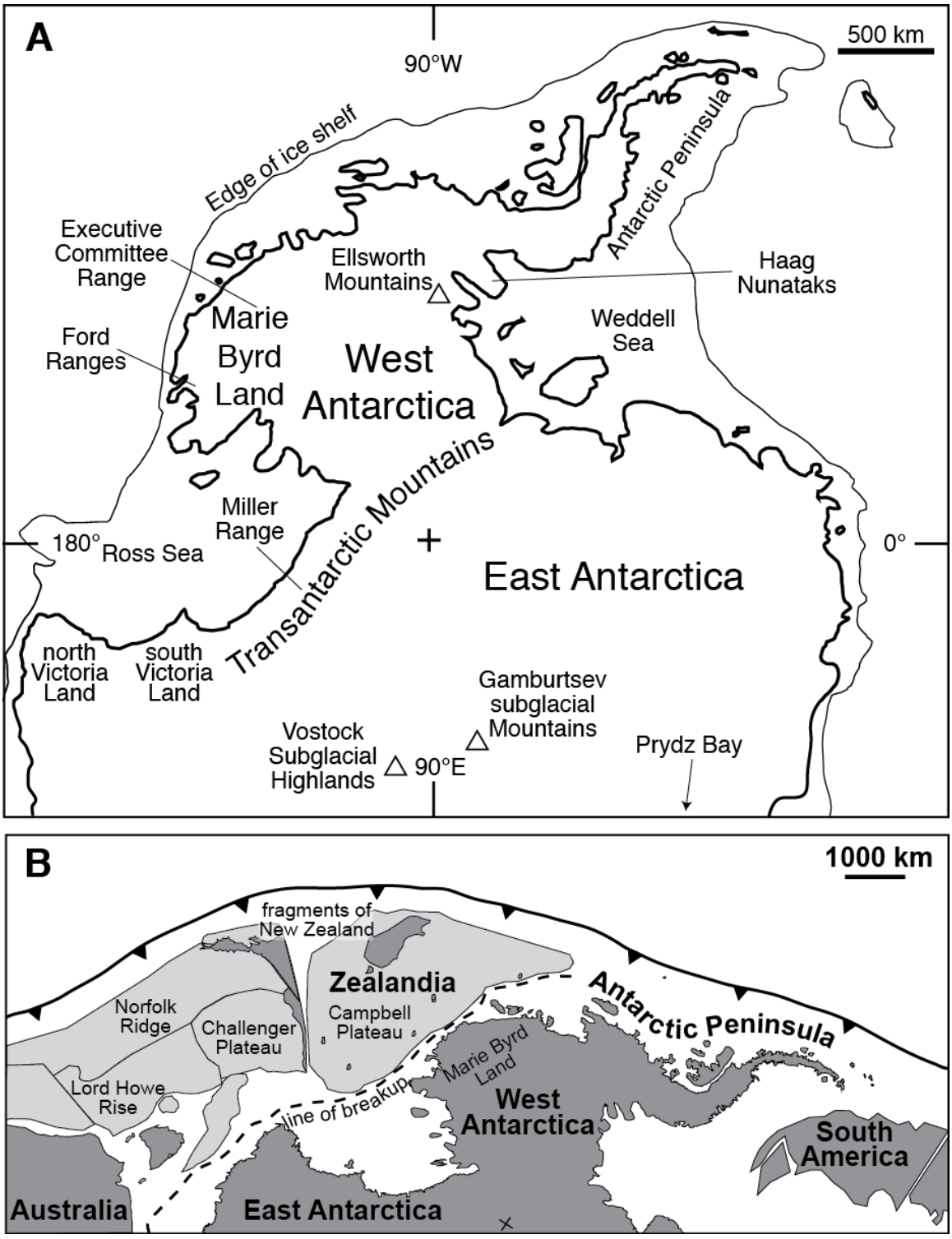

Fig. 4.1. (A) Map of part of Antarctica to show locations referred to in the text. (B) Geometrical reconstruction of the East Gondwana active convergent margin (modified from Veevers, 2012, fig. 4).

In the Ross Province, the Neoproterozoic–Cambrian Swanson Formation is the oldest exposed unit (Bradshaw et al., 1983; Pankhurst et al., 1998; Adams, 1986, 2004). It is a folded and cleaved turbidite sequence that accumulated outboard of the Cambrian Ross–Delamerian Orogen. In a regional context, based on the similarity of U–Pb ages of detrital zircons, the Swanson Formation has been correlated with the Robertson Bay Group in north Victoria Land and the Greenland Group in the Western Province of New Zealand (Ireland et al., 1998; Adams et al., 2013). Paleocurrent data from the Swanson Formation has been interpreted to suggest flow predominately towards the North (Bradshaw et al., 1983), indicating a source terrain to the south.

The Swanson Formation is intruded by the Devonian–Carboniferous Ford Granodiorite suite, which was associated with a major pulse of Paleozoic calc-alkaline magmatism along the length of the East Gondwanan continental margin (Weaver et al., 1991; Weaver et al., 1992; Muir et al., 1994; Storey et al., 1999; Mukasa and Dalziel, 2000) that has been variously attributed to subduction (Weaver et al., 1991) or back-arc extension (Muir et al., 1996; Tulloch et al., 2009). Rb–Sr whole-rock geochronology from the Ford Granodiorite suite yielded ages of 380–353 Ma (Adams, 1987). U–Pb ages of ca. 375 and 373 Ma from two Ford Granodiorite suite samples have been used to argue that this magmatism represented only a short-lived pulse of activity (Pankhurst et al., 1998; Yakymchuk et al., 2013a). A broader span for magmatic activity is suggested by

---

Fig. 4.2. The inset at the top, left shows the location of the study area in western Marie Byrd Land in West Antarctica. The main map shows sample localities in the study area. The thick dashed line separating the Ross Province from the Amundsen Province is taken from Pankhurst et al. (1998). The inset at the bottom, right shows sample localities in the Fosdick migmatite–granite complex.

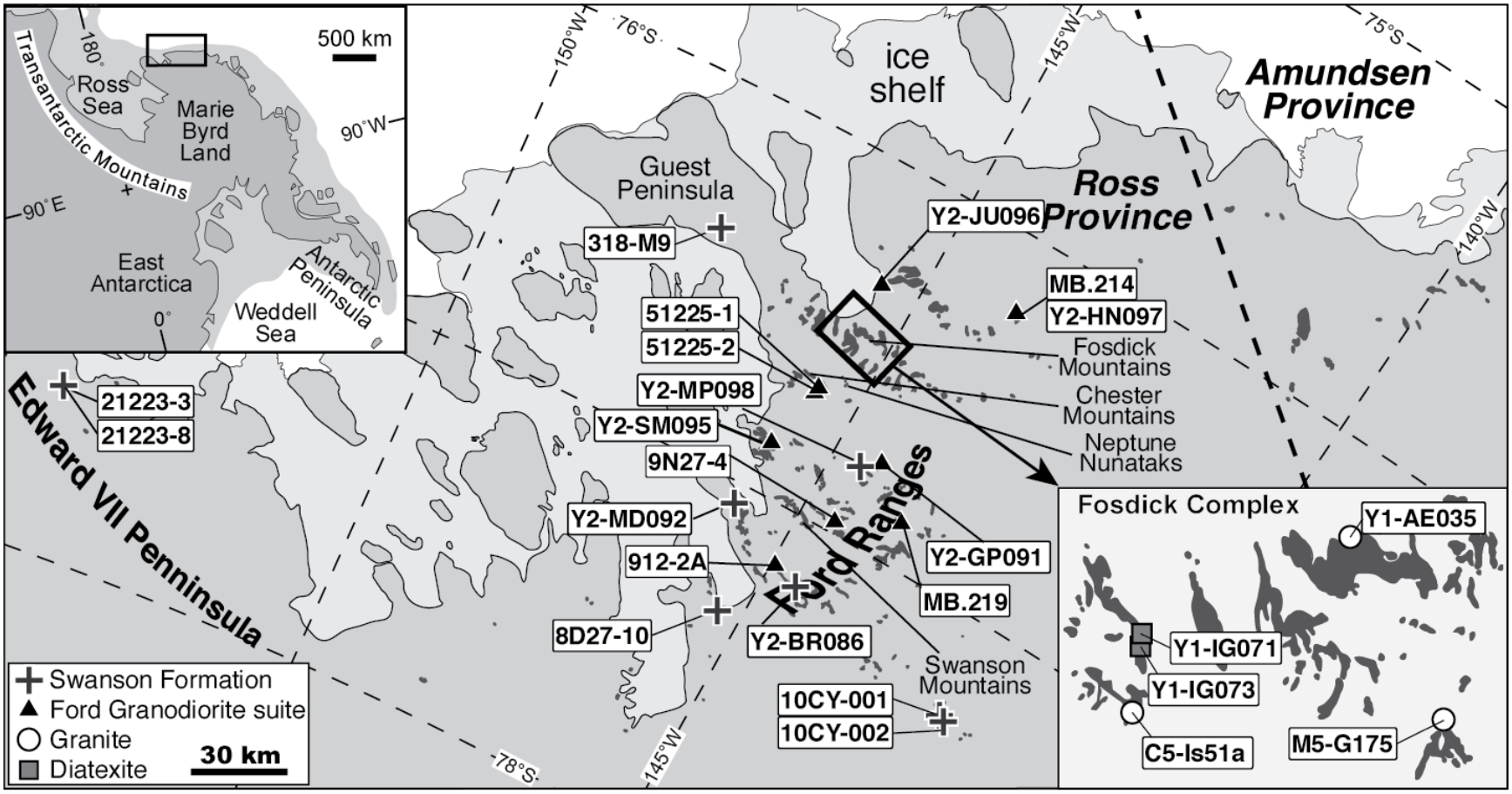
500 km
Transantarctic Mountains
180°
Ross Sea
Marie Byrd Land
90°W
90°E
East Antarctica
Antarctic Peninsula
0°
Weddell Sea
150°W
76°S
ice shelf
145°W
75°S
Amundsen Province
Ross Province
140°W
Guest Peninsula
318-M9
Y2-JU096
MB.214
Y2-HN097
51225-1
51225-2
Fosdick Mountains
Chester Mountains
Neptune Nunataks
Y2-MP098
Y2-SM095
9N27-4
21223-3
21223-8
Edward VII Penninsula
Y2-MD092
912-2A
Y2-GP091
MB.219
Ford Ranges
8D27-10
Y2-BR086
Swanson Mountains
10CY-001
10CY-002
Fosdick Complex
Y1-AE035
Y1-IG071
Y1-IG073
C5-ls51a
M5-G175
Swanson Formation
Ford Granodiorite suite
Granite
Diatexite
30 km
78°S
145°W

U–Pb SHRIMP zircon ages of 369–353 Ma for granites within the Fosdick migmatite–granite complex (Fig. 4.2, inset; Siddoway and Fanning, 2009) and U–Pb monazite ages of ca. 359 and 351 Ma for two-mica granites (Tulloch et al., 2009). A syenogranite sample from Bruner Hill on the Hobbs coast sampled close to the inferred boundary between the Ross and Amundsen Provinces yielded a U–Pb age of 339 ± 6 Ma (Pankhurst et al., 1998). However, it has remained unclear if these data sampled short-lived magmatic pulses or a protracted magmatic history during the Devonian–Carboniferous. Contemporaneous magmatism is recorded in the Admiralty Intrusives of north Victoria Land (Borg et al., 1986; Fioretti et al., 1997), the Karamea suite in the Western Province of New Zealand (Tulloch et al., 2009), and in the Melbourne terrane in the Tasmanides of Eastern Australia (Chappell et al., 1988).

In the Amundsen Province of eastern Marie Byrd Land, metasedimentary rocks appear to be absent and magmatism occurred in the Ordovician–Silurian (450–420 Ma) and in the Permian (ca. 276 Ma; Pankhurst et al., 1998). Coeval magmatism is reported in the Antarctic Peninsula (including Thurston Island; Pankhurst et al., 1993) and in the Median Tectonic Zone in New Zealand (Muir et al., 1998). Granites in the Amundsen Province yield younger Nd model ages (1.3–1.0 Ga) than granites from the Ross Province (1.5–1.3 Ga; Pankhurst et al., 1998), which, together with the paleomagnetic evidence (DiVenere et al., 1995; Luyendyk et al., 1996), provided the basis for the subdivision of Marie Byrd Land.

High-grade metamorphosed equivalents of the Swanson Formation and the Ford Granodiorite suite are exposed in a migmatite–granite complex in the Fosdick Mountains of western Marie Byrd Land (Fig. 4.2, hereafter the Fosdick complex; Richard et al.,

1994; Siddoway and Fanning, 2009; Korhonen et al., 2010a, b; Yakymchuk et al., 2013b). Based on phase equilibria modeling and U–Pb ages of monazite, two metamorphic events have been documented in the Fosdick complex, one in the Devonian–Carboniferous and a higher-grade overprint in the Cretaceous (Korhonen et al., 2010b, 2012). Hf and O isotope compositions of zircons from Devonian–Carboniferous granites in the Fosdick complex indicate that they represent a binary mixture sourced from Ford Granodiorite suite and Swanson Formation components (Yakymchuk et al., 2013a). In contrast, Hf and O isotope compositions of zircons from Cretaceous granites indicate input from an unexposed juvenile source in addition to the crustal sources. In general, both the Devonian–Carboniferous and Cretaceous granites in the Ross Province have more evolved Hf isotope values than granites from correlative localities across the East Gondwanan margin, including the Western Province of New Zealand and the Tasmanides in eastern Australia. Yakymchuk et al. (2013a) interpreted this difference to record a larger proportion of crustal reworking in the Ross Province compared with a higher proportion of crustal growth in the Western Province and the Lachlan Fold Belt.

In the Ross Province, Cretaceous magmatism is also represented by the Byrd Coast Granite suite, which intrudes both the Swanson Formation and the Ford Granodiorite suite (Adams, 1987; Siddoway et al., 2004a; Korhonen et al., 2010a). Whole rock Rb–Sr isochron ages were interpreted to record two magmatic pulses, one at ca. 140 and the other at ca. 110 Ma (Adams, 1987; Weaver et al., 1991). The emplacement of the Byrd Coast Granite suite was contemporaneous with that of the Separation Point batholith in the Western Province of New Zealand (Bolhar et al., 2008). Together, these Cretaceous granite suites represent magmatism during continental margin extension that

preceded the breakup of Marie Byrd Land (Siddoway et al., 2004a, b; McFadden et al., 2010) and separation of Zealandia from West Antarctica (Mortimer et al., 2006) during the Upper Cretaceous (Fig. 4.1b).

4.4 Analytical Methods

A detailed description of analytical methods together with Tables C1–C9 listing sample locations and the complete analytical data set are in Appendix C. Zircon mineral separates were obtained from bulk rock samples using standard crushing, magnetic, and heavy liquid separation methods in the mineral separation facility at the University of Maryland; zircons were mounted in epoxy disks. The zircons were imaged in transmitted light and studied using a cathodoluminescence detector to characterize the internal zoning of each zircon and to avoid analysis of inclusions.

Four Ford Granodiorite suite samples from outside the Fosdick complex in western Marie Byrd Land and two diatexites from inside the Fosdick complex (Table 4.1, Fig. 4.2) were selected for zircon U–Pb, O, and Lu–Hf isotope analysis at the Research School of Earth Sciences (RSES), Australian National University following the protocol given in Yakymchuk et al. (2013a). U–Pb isotope ratios were collected with a SHRIMP–II, oxygen isotope ratios were measured with a SHRIMP–II or SHRIMP-SI, and Lu–Hf measurements were conducted by laser ablation multi-collector inductively coupled plasma mass spectroscopy (LA–MC–ICPMS) using the RSES Neptune MC–ICP–MS coupled with a HelEx 193 nm ArF Excimer laser.

Detrital zircons from two Swanson Formation samples and igneous zircons from two Ford Granodiorite suite samples from outside the Fosdick complex in western Marie

Table 4.1. Analytical information by sample

	ANU		U. Arizona		U. Maryland	
Sample	U–Pb	Hf, O	U–Pb	Hf	Sr, Nd	REE
Swanson Formation						
10CY-001					x	x
10CY-002					x	x
Y2-BR086					x	x
Y2-MD092			x	x	x	x
Y2-MP098			x	x	x	x
Metsedimentary gneisses						
318-M9			x			
21223-3			x			
21223-8			x			
8D27-10	x[1]	x[1]	x			
Ford Granodiorite Suite						
MB.214	x[2]	x[1]				
MB.219	x[2]	x[1]				
912-2A	x	x			x	x
9N27-4	x	x			x	x
51225-1			x		x	x
51225-2	x	x	x		x	x
Y2-GP091			x		x	x
Y2-HN097						x
Y2-JU096	x	x	x		x	x
Y2-SM095					x	x
Devonian–Carboniferous Granite						
Y1-AE035			x		x	x
C5-Is51a	x[1]	x[1]			x[3]	x[3]
M5-G175	x[1]	x[1]			x	x
Diatexite						
Y1-IG071	x	x	x		x	x
Y1-IG073	x	x	x		x	x

[1]Yakymchuk et al. (2013a); [2]Pankhurst et al. (1998); [3]Korhonen et al. (2010a)

Byrd Land, as well as zircons from three paragneisses from outside the Fosdick complex, and two diatexites and one granite from inside the complex (Table 4.1, Fig. 4.2) were analyzed for U–Pb geochronology at the University of Arizona Laserchron facility following the protocol outlined in Gehrels et al. (2008). For the two Swanson Formation samples, Lu and Hf isotopes were also measured in zircon at the University of Arizona Laserchron facility following the procedure described in Cecil et al. (2011). The analyses involve ablation of zircon with a New Wave DUV193 Excimer laser while isotope ratios were measured with a Nu HR–ICP–MS.

Strontium, Rb, Nd and Sm isotope compositions for five whole-rock samples of the Swanson Formation, six whole-rock samples of the Ford Granodiorite suite, and three Devonian–Carboniferous granites (Table C.3 in Appendix C, Fig. 4.2) were acquired at the University of Maryland following the procedure outlined in Korhonen et al. (2010a). Eight Swanson Formation samples were selected for whole-rock oxygen-isotope analysis at the University of Wisconsin using laser fluorination (Valley et al., 1995).

4.5 Sample descriptions and U–Pb results

4.5.1 Detrital zircons from the Swanson Formation samples and the paragneisses

U–Pb results for detrital zircon from the Swanson Formation samples and the paragneisses from the Ford Ranges and Scott Nunataks, including data for one sample reported previously in Yakymchuk et al. (2013a), together with a sample from the Swanson Mountains (Fig. 4.2) from Adams et al. (2013), are plotted as histograms and normalized probability distributions in Figure 4.3. Data are presented in Table C.6 of Appendix C.

Sample Y2-MD092, from Mount Dolber in the Sarnoff Mountains (Fig. 4.2; 77°04'S, 145°45'W), is a thinly bedded metagreywacke with a foliation defined by the parallel alignment of biotite. Zircon U–Pb dates range from 435 to 3034 Ma with distribution peaks at ca. 554, 1048 and 1763 Ma (Fig. 4.3b). The youngest group of four dates that overlap at 2σ yields a weighted mean age of 489 ± 14 Ma.

Sample Y2-MP098, from Mount Passel in the central Ford Ranges (Fig. 4.2; 76°54'S, 144°52'W), is a poorly sorted metagreywacke containing angular clasts of quartz, feldspar and lithic fragments in a fine-grained matrix. Zircon U–Pb dates range from 508 to 2797 Ma with distribution peaks at ca. 577, 1037 and 1725 Ma (Fig. 4.3c). The youngest group of four dates that overlap at 2σ yields a weighted mean age of 514.0 ± 4.8 Ma.

Sample 8D27-10 is a calc-silicate gneiss from Mt Woodward in the Ford Ranges (145°47'W, 77°18'S; Yakymchuk et al., 2013a). Zircon U–Pb dates range from 500 to 3490 Ma with peaks at ca. 570, 1096, and 1736 Ma (Fig. 4.3d). The youngest group of four dates that overlap at 2σ yields a weighted mean age of 532.5 ± 5.3 Ma.

Sample 318-M9 is a folded biotite-paragneiss from Mitchell Peak on the Guest Peninsula (Fig. 4.2). Zircon U–Pb dates range from 328 to 2457 Ma with distribution peaks at ca. 548, 1084 and 1704 Ma (Fig. 4.3e). The youngest group of four dates that overlap at 2σ yields a weighted mean age of 509 ± 17 Ma.

Samples 21220-3 and 21220-8 are paragneisses from Scott Nunataks (Smith, 1996). Both samples were collected from the same outcrop, so the age data sets are

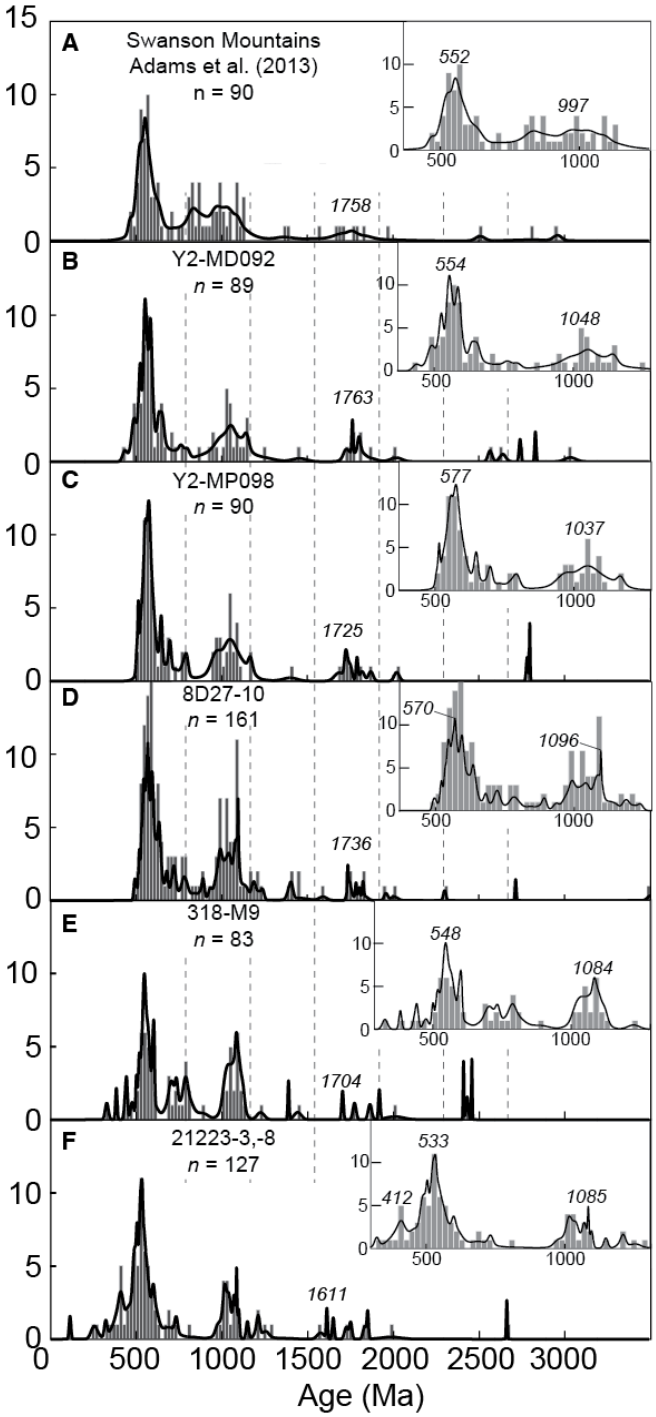

Fig. 4.3. Histograms and normalized probability distribution curves of U–Pb ages retrieved from detrital zircon in the Swanson Formation (A–C) and metasedimentary rocks (D–G) outcropping in western Marie Byrd Land.

pooled. Dates range from 114 to 2661 Ma with distribution peaks at ca. 533, 1085, and 1611 Ma as well as a small peak at ca. 412 Ma (Fig. 4.3f). The youngest group of four dates that overlap at 2σ yields a weighted mean age of 387 ± 22 Ma.

In summary, individual U–Pb dates for detrital zircons from the Swanson Formation range from ca. 435 to ca. 3034 Ma (Fig. 4.3a–c); zircons from the paragneisses have similar age distributions, but with a small number of younger dates (Fig. 4.3d–f). Although Archean grains are present, they make up only a minor portion of the population. The dominant zircon population in all samples is Neoproterozoic–Cambrian, with dates ranging from ca. 500 to ca. 750 Ma and age peaks at ca. 533 to ca. 576 Ma (Fig. 4.3). The second significant population in each sample comprises mostly Mesoproterozoic dates that range from ca. 930 to ca. 1180 Ma with age peaks at ca. 997 to ca. 1096 Ma (Fig. 4.3). The third and most poorly defined population in all samples comprises mostly Paleoproterozoic dates that extend from ca. 1560 to ca. 1930 Ma with age peaks at ca. 1611 to ca. 1763 Ma (Fig. 4.3).

4.5.2 Ford Granodiorite suite, granites and diatexites

Representative cathodoluminescence (CL) images of zircons from six Ford Granodiorite suite samples, two diatexite samples and one Devonian–Carboniferous granite dated in this study are shown in Figure 4.4. U–Pb results are summarized below and plotted on U–Pb Tera–Wasserberg concordia diagrams and as probability distributions (with stacked histograms) in Figure 4.5. Data are presented in Tables C.4 (SHRIMP) and C.5 (LA-ICP-MS) of Appendix C.

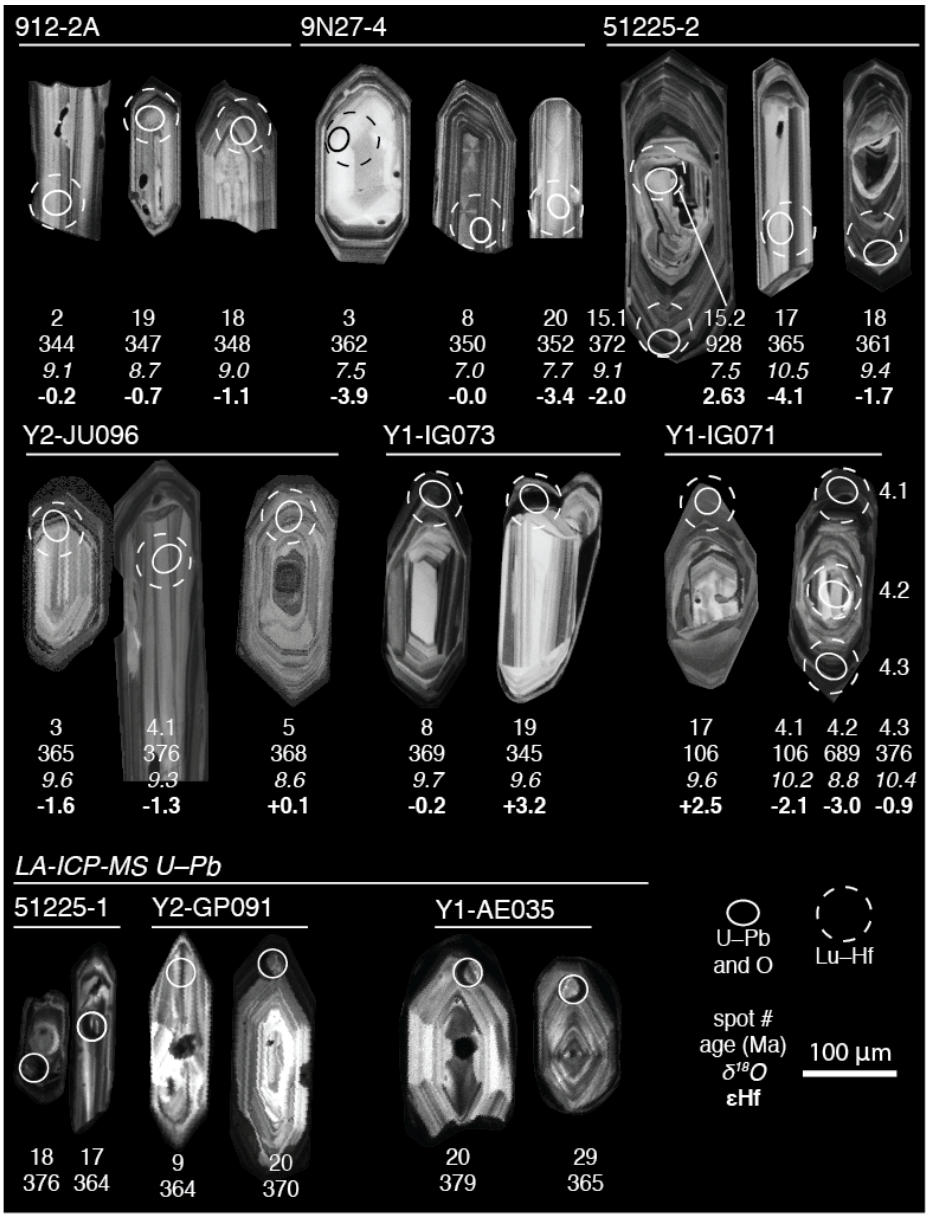

Fig. 4.4. Cathodoluminescence images of representative zircon grains from the Ford Granodiorite suite and Devonian–Carboniferous diatexites and granites from the Fosdick migmatite–granite complex. Ellipses mark the location of U–Pb, O and Hf isotope spot analyses. Cathodoluminescence images were collected on different dates and so exhibit some variation in quality/sharpness. The contrast of images of individual zircons was adjusted to best display internal zoning.

Fig. 4.5. U–Pb Tera–Wasserberg (1972) concordia and probability density plots of zircon data from the Ford Granodiorite suite and Devonian–Carboniferous diatexites and granites from the Fosdick migmatite–granite complex. Data-point error ellipses are at 95% confidence. Age uncertainties are reported at 2σ confidence.

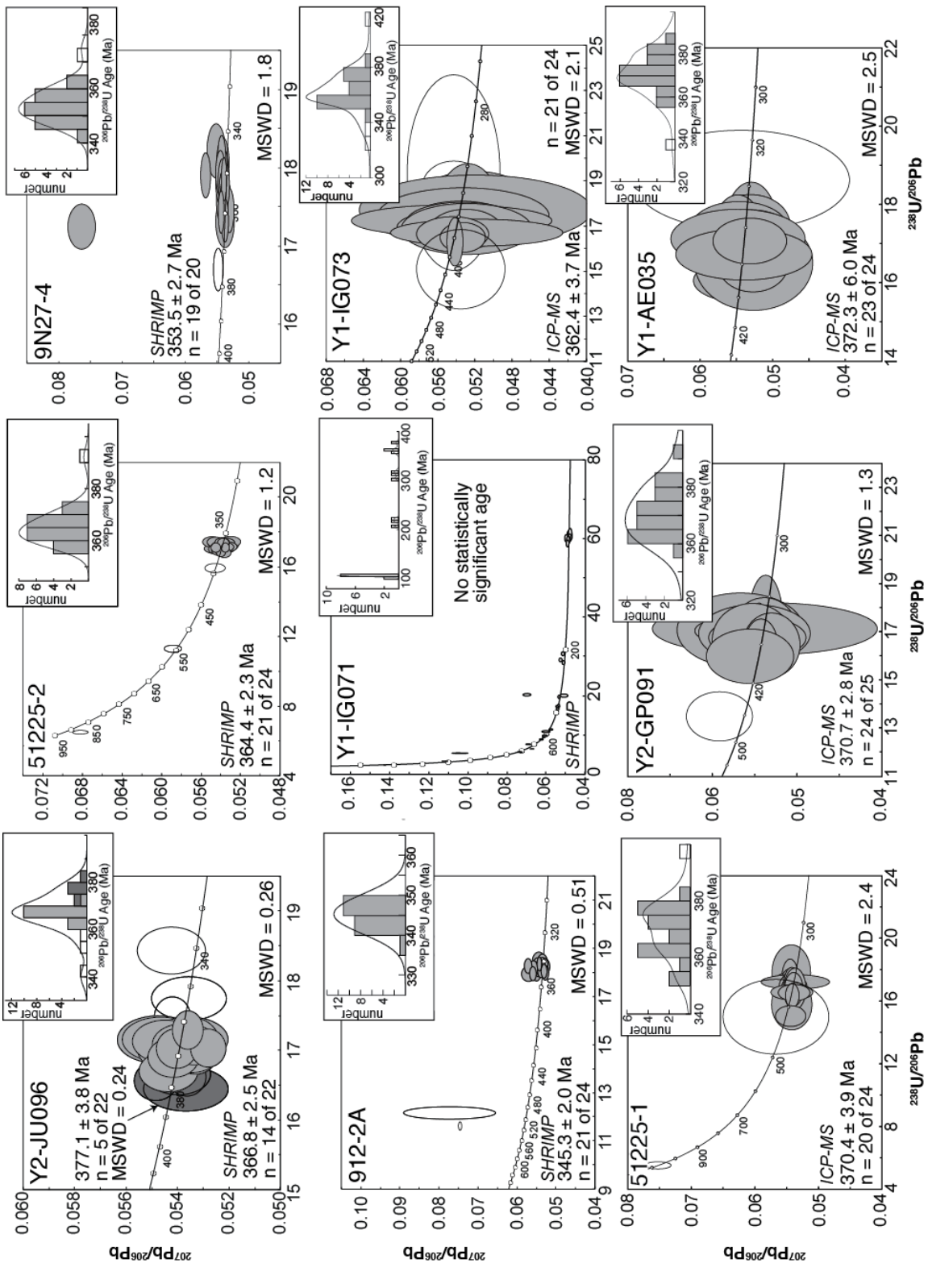
Y2-JU096
377.1 ± 3.8 Ma
n = 5 of 22
MSWD = 0.24
SHRIMP
366.8 ± 2.5 Ma
n = 14 of 22
MSWD = 0.26
912-2A
SHRIMP
345.3 ± 2.0 Ma
n = 21 of 24
MSWD = 0.51
51225-1
ICP-MS
370.4 ± 3.9 Ma
n = 20 of 24
MSWD = 2.4
51225-2
SHRIMP
364.4 ± 2.3 Ma
n = 21 of 24
MSWD = 1.2
Y1-IG071
No statistically significant age
SHRIMP
Y2-GP091
ICP-MS
370.7 ± 2.8 Ma
n = 24 of 25
MSWD = 1.3
9N27-4
SHRIMP
353.5 ± 2.7 Ma
n = 19 of 20
MSWD = 1.8
Y1-IG073
ICP-MS
362.4 ± 3.7 Ma
n = 21 of 24
MSWD = 2.1
Y1-AE035
ICP-MS
372.3 ± 6.0 Ma
n = 23 of 24
MSWD = 2.5
number
206Pb/238U Age (Ma)
207Pb/206Pb
238U/206Pb

4.5.2.1 Ford Granodiorite suite

Sample Y2-JU096, from Mount June in the Phillips Mountains (Fig. 4.2; 76°15', 145°16'W), is a biotite granodiorite. Euhedral prismatic grains with simple igneous zoning dominate the zircon population in this sample (Fig. 4.4). A weighted $^{206}Pb/^{238}U$ age of 366.8 ± 2.5 Ma (MSWD=0.26) was calculated from a dominant group of 14 analyses. An older group of 5 analyses yields an age of 377.1 ± 3.8 Ma (MSWD=0.24). The younger age group is interpreted as the crystallization age of this granodiorite (Fig. 4.5), whereas the older age group may represent grains scavenged during reworking of an older component.

Sample 51225-2, from the Chester Mountains (Fig. 4.2; 76°40'S, 145°35'W), is a biotite granodiorite. Euhedral prismatic grains with simple igneous zoning dominate the zircon population in this sample, although some grains contain inherited cores with truncated oscillatory igneous zoning (Fig. 4.4). Two older dates of 547 and 928 Ma are interpreted to be from inherited cores. A weighted $^{206}Pb/^{238}U$ age of 364.4 ± 2.3 Ma (MSWD=1.2) was calculated from a dominant group of 21 of the 24 analyses. This is interpreted as the crystallization age of the granodiorite (Fig. 4.5).

Sample 9N27-4, from Mount Ralph in the central Ford Ranges (Fig. 4.2; 76°58'S, 144°32'W), is a hornblende–biotite granodiorite that represents the least fractionated Ford Granodiorite suite sample reported in Korhonen et al. (2010a). Euhedral prismatic grains with simple igneous zoning dominate the zircon population in this sample, some of which contain inherited cores with truncated oscillatory igneous zoning (Fig. 4.4). A weighted $^{206}Pb/^{238}U$ age of 353.5 ± 2.7 Ma (MSWD=1.8) was calculated from a dominant

group of 19 of the 20 analyses. This is interpreted as the crystallization age of the granodiorite (Fig. 4.5).

Sample 912-2A, from the Asman Ridge in the Sarnoff Mountains (Fig. 4.2; 77°10'S, 144°48'W), is a K-feldspar phyric biotite granite that represents a relatively fractionated member of the Ford Granodiorite suite (Korhonen et al., 2010a). Euhedral prismatic grains with simple igneous zoning dominate the zircon population in this sample (Fig. 4.4). Two older dates of 523 and 498 Ma are interpreted to be from inherited cores. A weighted $^{206}Pb/^{238}U$ age of 345.3 ± 2.0 Ma (MSWD=0.51) was calculated from a dominant group of 21 of the 24 analyses. This is interpreted as the crystallization age of the granite (Fig. 4.5).

Sample 51225-1 is a biotite granodiorite from the Chester Mountains (Fig. 4.2; 76°40'S, 145°35'W). Euhedral prismatic grains with oscillatory zoning dominate the zircon population in this sample. A weighted $^{206}Pb/^{238}U$ age of 370.4 ± 3.9 Ma (MSWD=2.4) was calculated from a dominant group of 20 of the 24 analyses. This is interpreted as the crystallization age of the granodiorite (Fig. 4.5).

Sample Y2-GP091 is a biotite granodiorite from Greer Peak (Fig. 4.2; 76°47'S, 144°26'W). Zircons are generally euhedral and oscillatory zoned. A weighted $^{206}Pb/^{238}U$ age of 370.7± 2.8 Ma (MSWD=1.3) was calculated from 24 of the 25 analyses. This is interpreted as the crystallization age of the granodiorite (Fig. 4.5).

4.5.2.2 Devonian–Carboniferous granites and diatexites

Three granites and two diatexites (sensu Brown, 1973; essentially anatectic granites), interpreted to be associated with the Devonian–Carboniferous metamorphism

in the Fosdick complex, are included in this study. Granite sample M5-G175 is from Mt Getz (Fig. 4.2) and sample C5-Is51a is from Mt Iphigene; both were described and dated in Siddoway and Fanning (2009), and yielded crystallization ages of 369.2 ± 2.5 Ma and 353.4 ± 3.2 Ma, respectively. Sample Y1-AE035, also from Mt Avers, is a dark grey equigranular unfoliated granodiorite similar in appearance to the Ford Granodiorite suite rocks outside the Fosdick complex. Zircons from sample Y1-AE035 are zoned and comprise prismatic elongate grains and euhedral stubby grains; 23 of the 24 analyses define an age of 372.3 ± 6.0 Ma (MSWD = 2.5).

The diatexite samples were collected from Mt Iphigene in the western sector of the Fosdick complex (Fig. 4.2), where a gradation occurs from inhomogeneous diatexite with schlieren (sample Y1-IG071) near the contact with the host migmatitic paragneiss into a homogeneous diatexite or anatectic granite (sample Y1-IG073). Both samples contain quartz, plagioclase, K-feldspar and biotite, but sample Y1-IG071 also contains muscovite.

Zircons from the inhomogeneous diatexite (Y1-IG071) are euhedral to anhedral and elongate to stubby with zoned cores that show evidence of recrystallization. The cores are surrounded by a darker zoned inner rim and then by a thin, bright outer rim. The darker zoned rim is interpreted to record protolith crystallization, while the bright rim is interpreted to reflect the timing of melt crystallization in this anatectic rock. Zircons record a range of dates from 2277 to 104 Ma, with two dominant age populations of 376–305 Ma and 109–104 Ma. Although no statistically significant age can be calculated from these data, the older group of dates is inferred to be related to the formation of the inhomogeneous diatexite and the younger group to the effects of the Cretaceous

overprint. For the purpose of subsequent modeling, a notational age of 360 Ma is assigned to this sample.

Zircons from the homogeneous diatexite (Y1-IG073) are euhedral to subhedral, elongate prismatic grains with zoned cores that show evidence of recrystallization. They yield a range of dates from 379 to 326 Ma (LA-ICP-MS and SHRIMP). For the LA-ICP-MS data, 21 of the 24 analyses define an age of 362.4 ± 3.7 Ma (MSWD = 2.1), which is interpreted as the age of formation of the homogeneous diatexite.

4.6 Major oxide and trace element geochemistry

The geochemistry of the samples from this study (Table C.2 in Appendix C), combined with geochemical data from Korhonen et al. (2010a) and Weaver et al. (1991, 1992), Pankhurst et al. (1998) and Tulloch et al. (2009) for 15 Ford Granodiorite suite samples, is plotted as a series of Harker diagrams in Figure 4.6. Normalized rare earth element (REE) patterns are given in Figure 4.7.

4.6.1 Swanson Formation

The Swanson Formation has SiO2 contents ranging from 61 to 74 wt % (Fig. 4.6); although variable, individual samples are peraluminous with aluminum saturation indices (ASI= Molar [Al_2O_3/(CaO+Na_2O+K_2O)]) of 1.24–2.00, decreasing with increasing SiO_2. With increasing SiO_2, TiO_2, CaO, Na_2O, U, Th, Sr, Ba and La remain relatively constant, whereas Al_2O_3, K_2O, FeO*+MgO, Rb and Rb/Sr decrease, and Zr increases (Fig. 4.6). The Swanson Formation has limited variation in REE abundances; individual

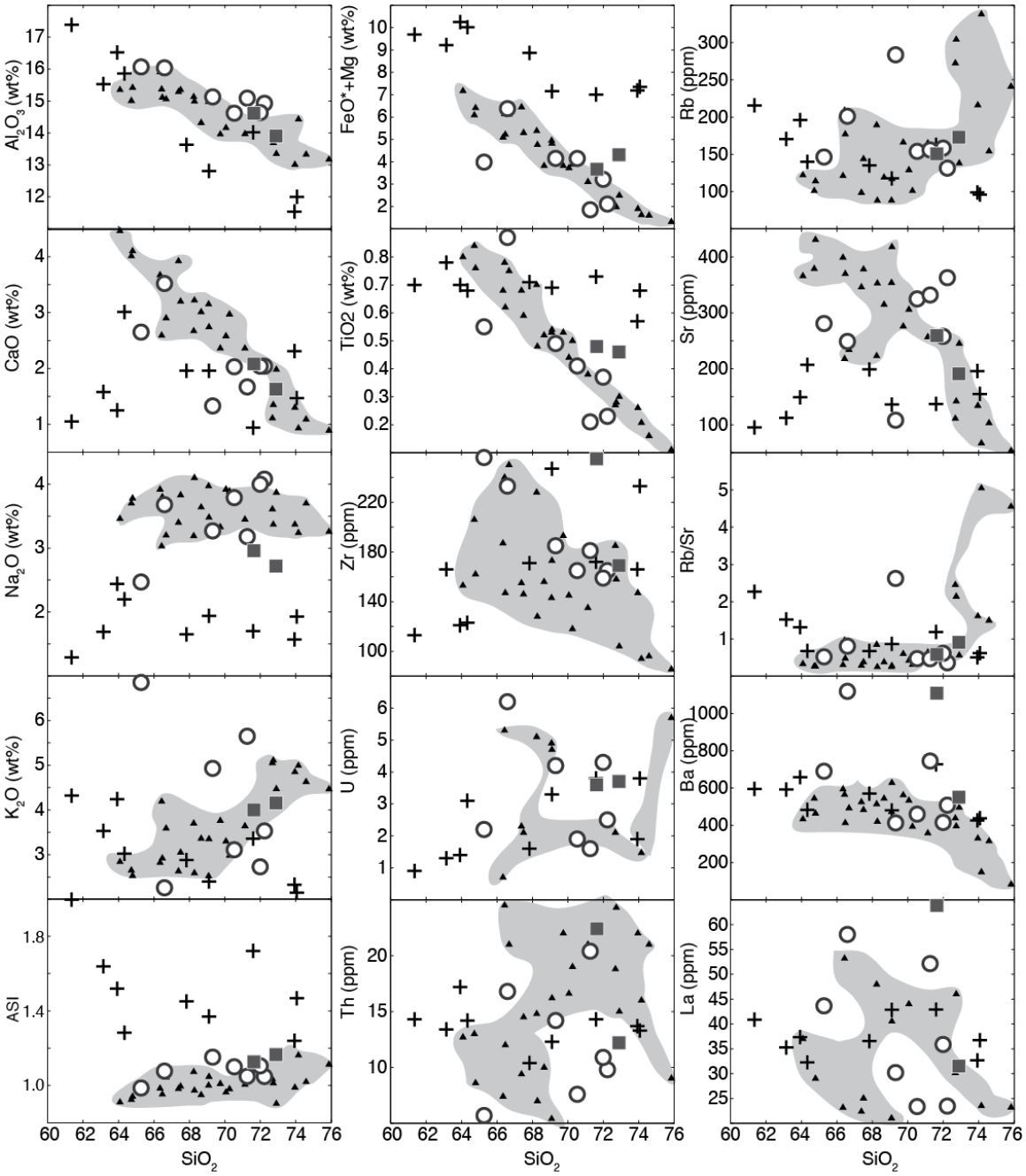

Fig. 4.6. Major and trace element data for samples as determined by XRF. Ford Granodiorite suite samples include data from Korhonen et al. (2010a), Weaver et al. (1992), Pankhurst et al. (1998) and Tulloch et al. (2009) as well as the new data from this study. FeO* represents total iron as ferrous. Trace elements are plotted as parts per million (ppm).

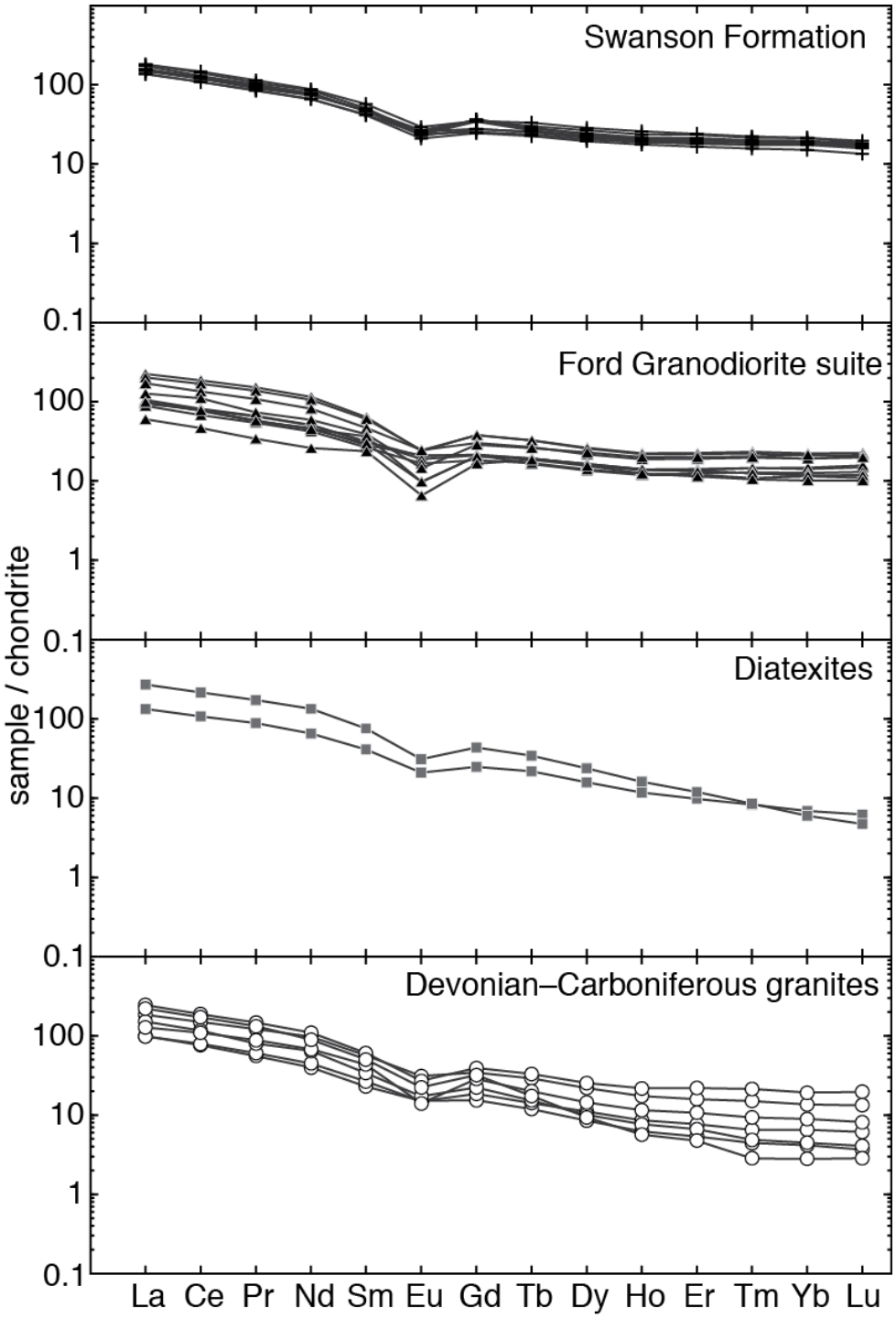

Fig. 4.7. Chondrite-normalized (McDonough and Sun, 1995) rare earth element patterns of newly-analyzed samples from this study as well as additional data from Korhonen et al. (2010a) and Tulloch et al. (2009).

samples are characterized by smooth normalized patterns (Fig. 4.7) that are concave down for the LREE (La–Sm) and flat for the HREE, with consistent LaN/LuN of 7.6–10.6 and moderate negative Eu anomalies (EuN/EuN* = 0.55–0.70).

4.6.2 Ford Granodiorite suite

The Ford Granodiorite suite has SiO_2 contents ranging from 64 to 76 wt % (Fig. 4.6); individual samples vary from metaluminous to peraluminous with increasing SiO_2 (ASI = 0.91–1.16). With increasing SiO_2, K_2O and Th increase, and although Rb, Sr and Rb/Sr are variable at SiO_2 <71 wt %, at SiO_2 >71 wt % Rb increases, Sr decreases and Rb/Sr increases (Fig. 4.6). By contrast, Al_2O_3, CaO, FeO*+MgO, TiO_2, Zr, and Ba decrease, whereas Na_2O and La remain relatively constant and U is highly variable (Fig. 4.6). The Ford Granodiorite suite has a wider range of REE abundances than the Swanson Formation; individual samples have smooth to concave down LREE patterns and smooth to concave up HREE (Gd–Lu) patterns (Fig. 4.7), with LaN/LuN of 5.9–15.2 and variable negative Eu anomalies (EuN/EuN* = 0.33–0.85).

4.6.3 Devonian–Carboniferous granites and diatexites

Devonian–Carboniferous granites have SiO_2 contents ranging from 65 to 72 wt % (Fig. 4.6); they are metaluminous to peraluminous (ASI = 0.99–1.20). Although the geochemistry is variable with increasing SiO_2, the granites show decreasing Al_2O_3, CaO, FeO*+MgO, TiO_2, Zr and Ba, whereas K_2O, U, Th, Rb Sr, Rb/Sr and La show no trend and Na_2O increases (Fig. 4.6). The granites have elevated LREE and depressed HREE relative to the Ford Granodiorite suite; individual samples have concave down LREE

patterns and smooth to concave up HREE patterns (Fig. 4.7), with LaN/LuN of 12.5–77.3 and variable negative Eu anomalies (EuN/EuN* = 0.39–0.79).

The two diatexites have SiO_2 of 72 and 73 wt%; they are both peraluminous (ASI = 1.13 and 1.16) with Rb/Sr ratios <1. Sample Y1-IG073 has higher Zr, Th, Ba and La, but otherwise the major oxides and other trace element abundances are comparable to each other (Fig. 4.6). The diatexites have steep chondrite-normalized REE patterns (LaN/LuN = 55.2 and 21.8) with elevated LREE and depressed HREE relative to the Ford Granodiorite suite and negative Eu anomalies (EuN/EuN* = 0.52 and 0.64) similar to those of the granites (Fig. 4.7).

4.7 Sm–Nd results

Newly analyzed samples of the Swanson Formation $^{87}Sr/^{86}Sr_{360Ma}$ values of 0.711890–0.720484 and εNd_{360Ma} values that range from -9.3 to -6.3 (Fig. 4.8), whereas newly analyzed samples of the Ford Granodiorite suite have $^{87}Sr/^{86}Sr_{360Ma}$ values of 0.705231–0.709237 and εNd_{360Ma} values that range from -3.1 to -0.2 (Fig. 4.8). Two newly analyzed Devonian–Carboniferous granites (Y1-AE035 and M5-G175) have $^{87}Sr/^{86}Sr_{360Ma}$ values of 0.707518 and 0.709056, and εNd_{360Ma} values of -4.3 and -3.8, respectively (Fig. 4.8). The homogenous diatexite (Y1-IG073) has $^{87}Sr/^{86}Sr_{360Ma}$ of 0.709360 and a εNd_{360Ma} value of -4.3 (Fig. 4.8), whereas the inhomogeneous diatexite (Y1-IG071) has $^{87}Sr/^{86}Sr_{360Ma}$ of 0.704513 and a εNd_{360Ma} value of -5.7 (Fig. 4.8).

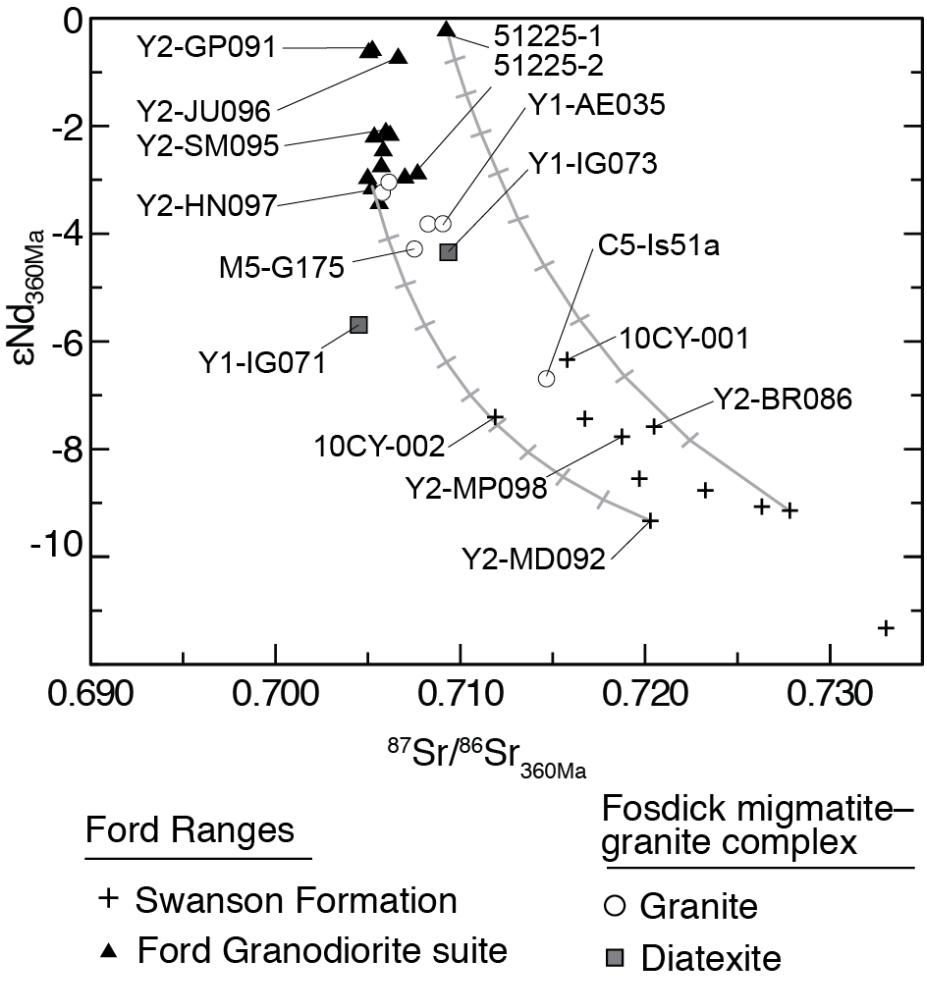

Fig. 4.8. Sr–Nd isotopic compositions at 360 Ma of samples from this study and additional data from Korhonen et al. (2010a), Weaver et al. (1992), and Pankhurst et al. (1998). Tick marks along mixing curve are at 10% increments.

4.8 Hf and O results

4.8.1 Swanson Formation and calc-silicate gneiss

U–Pb, Hf and O data from detrital zircons are plotted in Figure 4.9 and summarized in Table C.8 in Appendix C. Detrital zircons from sample Y2-MP098 yielded εHf_t values that range from -24.5 to 9.7 (Fig. 4.9a), but most are negative (26 of 45). Sample Y2-MD092 contains detrital zircons with εHf_t values that range from -13.4 to 8.2 (Fig. 4.9a), but again most are negative (25 of 49).

Detrital zircons from sample 8D27-10 (calc-silicate gneiss) define the same U–Pb age populations as samples of the Swanson Formation. Therefore, published data for this sample (Yakymchuk et al., 2013a) have been included in the final data set for the Swanson Formation discussed below. This sample has εHf_t values that range from -3.7 to +6.0, with two values of -11.4 and +8.9 (Fig. 4.9a; Yakymchuk et al., 2013a). The range of $\delta^{18}O$ values for detrital zircons from the calc-silicate gneiss (8D27-10) is from 6.4 to 10.8 ‰, with one value of 16.6 ‰ (Fig. 4.9b; Yakymchuk et al., 2013a). Zircons from the Neoproterozoic–Cambrian and Mesoproterozoic populations both have a similar range of $\delta^{18}O$ values that are between those expected for zircon crystallized from juvenile magmas and those derived solely from a supracrustal source (Fig. 4.9b).

Combining data from the three samples yields a range of εHf values for each of the three age populations, as follows. For the Neoproterozoic–Cambrian population, εHf values mostly lie between -10 and +3, whereas for the Mesoproterozoic population, most εHf values range from +1 to +10. For the Paleoproterozoic population, εHf values vary from -7 to +7, but most are negative with one value of -17, and, Archean grains have only negative εHf values that range from -6.1 to -0.4.

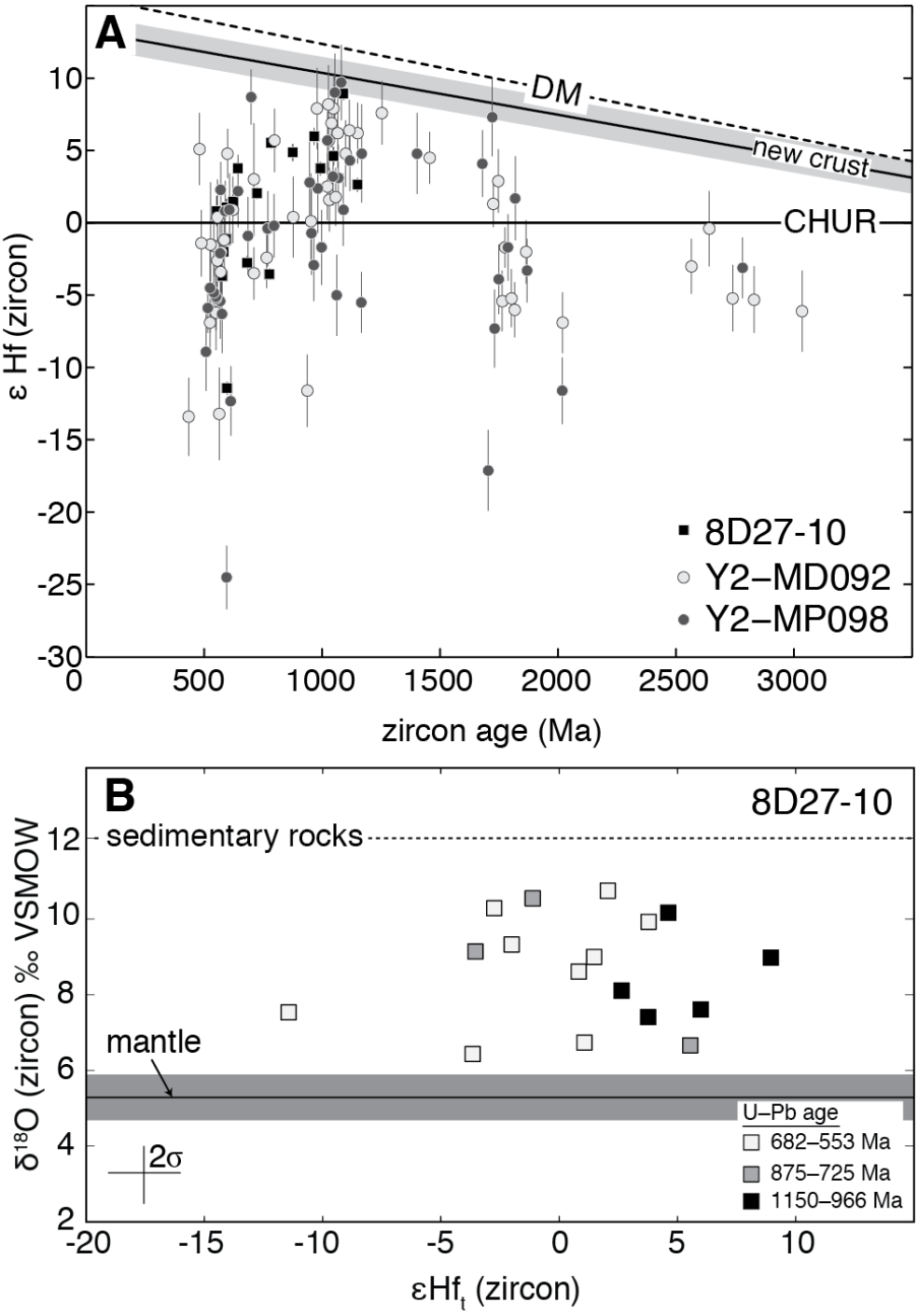

Fig. 4.9. (A) Hf evolution diagram for detrital zircons from the Swanson Formation. Reference evolution line for depleted mantle (DM) is from Vervoort and Blichert-Toft (1999) and for new crust is from Dhuime et al. (2011). (B) Hf and O isotope values of detrital zircon from a sample of calc-silicate gneiss (8D27-10). The $\delta^{18}O$ values of the mantle (5.3 ± 0.6‰) and sedimentary rocks (~12‰) are from Valley et al. (1998) and O'Neil and Chappell (1977), respectively.

Six of the eight samples yielded whole-rock $\delta^{18}O$ oxygen values that range from +10.00 to +13.48 (Table C.7 in Appendix C), which give an average value of +11.94. Two samples (10CY-001 and 10CY-002) are metasedimentary hornfels collected from the contact aureole of a Byrd Coast granite suite pluton in the Clark Mountains; these samples yielded whole-rock $\delta^{18}O$ values of -6.89 and -9.16, respectively.

4.8.2 Ford Granodiorite suite and diatexites

The individual Hf and O results vs. crystallization age for zircons from the Ford Granodiorite suite and diatexite samples from this study are plotted in Figure 4.10 and summarized in Table C.9 in Appendix C. Zircons from sample Y2-JU096 have εHf_t values that range from -4.4 to +1.7, and $\delta^{18}O$ values that vary from 7.4 to 9.6, with weighted means of -1.6 ± 1.1 and 8.8 ± 0.3, respectively (2σ; 13 of 18). An older population of zircon from this sample yielded εHf_t values that range from -3.8 to -0.7, and $\delta^{18}O$ values that vary from 8.0 to 9.9 (5 of 18). Zircons from sample 51225-2 have εHf_t values that range from -4.5 to +0.4 (with two values of -8.6 and -9.5), and $\delta^{18}O$ values that vary from 8.4 to 10.5 (with two values of 4.6 and 7.5), with weighted means of -2.1 ± 1.0 and 9.5 ± 0.3, respectively (2σ; 15 of 17). Zircons from sample 9N27-4 have εHf_t values that range from -5.3 to +0.2, and $\delta^{18}O$ values that vary from 7.0 to 9.7, with weighted means of -3.3 ± 1.0 and 7.6 ± 0.3, respectively (2σ; 13 of 15). Zircons from sample 912-2A have εHf_t values that range from -4.8 to +1.9 (with one value of -13.8), and $\delta^{18}O$ values that vary from 8.0 to 9.3 (with one value of 7.4), with weighted means of -1.9 ± 0.8 and 8.7 ± 0.2, respectively (2σ; 14 of 15).

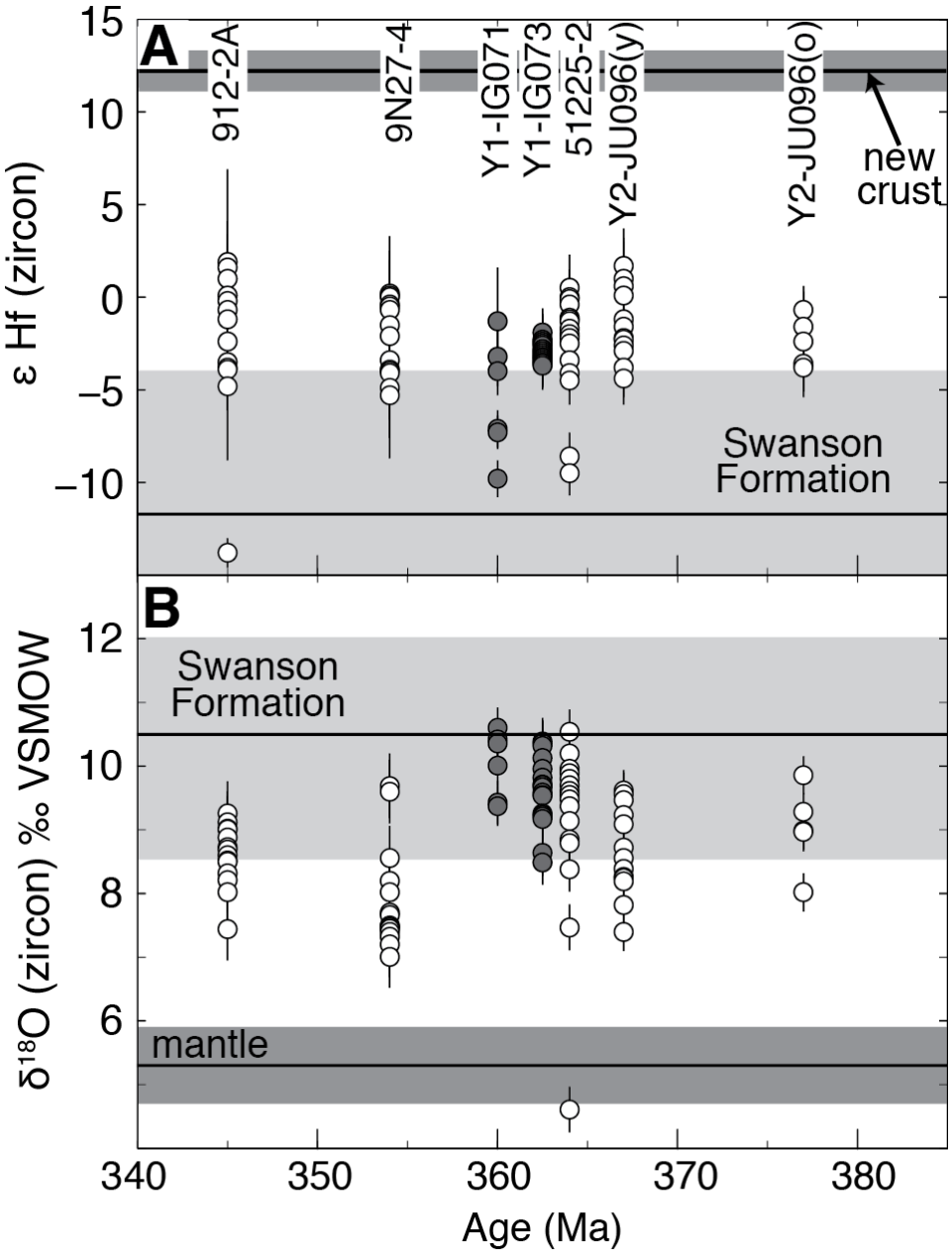

Fig. 4.10. Plots of $\delta^{18}O$ and εHf_t versus $^{206}Pb/^{238}U$ crystallization age for zircons from four Ford Granodiorite suite samples and two diatexites. Note that the two age populations for sample Y2-JU096. Uncertainties are ±2σ for $\delta^{18}O$ and εHf_t. The εHf_t for new crust is taken from Dhuime et al. (2011; +12.2 ± 1.1) and $\delta^{18}O$ for the mantle is from Valley et al. (1998; 5.3 ± 0.6‰). The εHf_t (median value of -11.7 and an interquartile range of -3.5 to -19.9) and $\delta^{18}O$ (8.5–12‰, with a mean value of 10.5‰) values chosen for the Swanson Formation are discussed in the text.

The inhomogeneous diatexite (Y1-IG071) yields a wide range of U–Pb ages with two dominant populations: Devonian–Carboniferous and Cretaceous (Fig. 4.5). Zircons from the older population have εHf_{360} values of -9.8 to -1.3, and $\delta^{18}O$ values of 9.4 to 10.6, with weighted means of -6.9 ± 2.7 and 10.0 ± 0.6, respectively (2σ; n = 6). Zircons from the younger population have εHf100 values of -10.0 to -4.7 (one value of -13.5), and $\delta^{18}O$ values of 9.5 to 10.2 (one value of 4.7), with weighted means of -7.2 ± 1.2 and 9.8 ± 0.2, respectively (2σ; 9 of 10). The homogenous diatexite (Y1-IG073) contains only Devonian–Carboniferous zircons that have εHf_t values of -3.9 to -2.1, and $\delta^{18}O$ values of 8.5 to 10.4, with weighted means of -3.1 ± 0.3 and 9.6 ± 0.2, respectively (2σ; 18 of 19).

4.9 Discussion

4.9.1 Possible sources for the Swanson Formation detrital zircons

The U–Pb ages and εHf values from detrital zircons may be used to assess potential sources for each zircon population identified in the Swanson Formation samples, as discussed below. The plausibility of these potential source materials based on U–Pb ages and εHf_t values is evaluated using a εHf evolution plot in Figure 4.11.

Paleoproterozoic (ca. 1.7 Ga) zircons from the Swanson Formation have εHf values that range from -7 to +7, with one value of -17 (Fig. 4.11). The Nimrod Group, which crops out in the Miller Range of central Transantarctic Mountains, includes rocks with zircon of the same age range (Goodge and Fanning, 2002). Igneous zircons from Archean layered gneisses in the Nimrod Group have metamorphic overgrowths dated at 1730–1720 Ma. In addition, a single deformed granodiorite yielded a crystallization age of ca. 1730 Ma (Goodge et al., 2001). This exposure of Precambrian basement in the

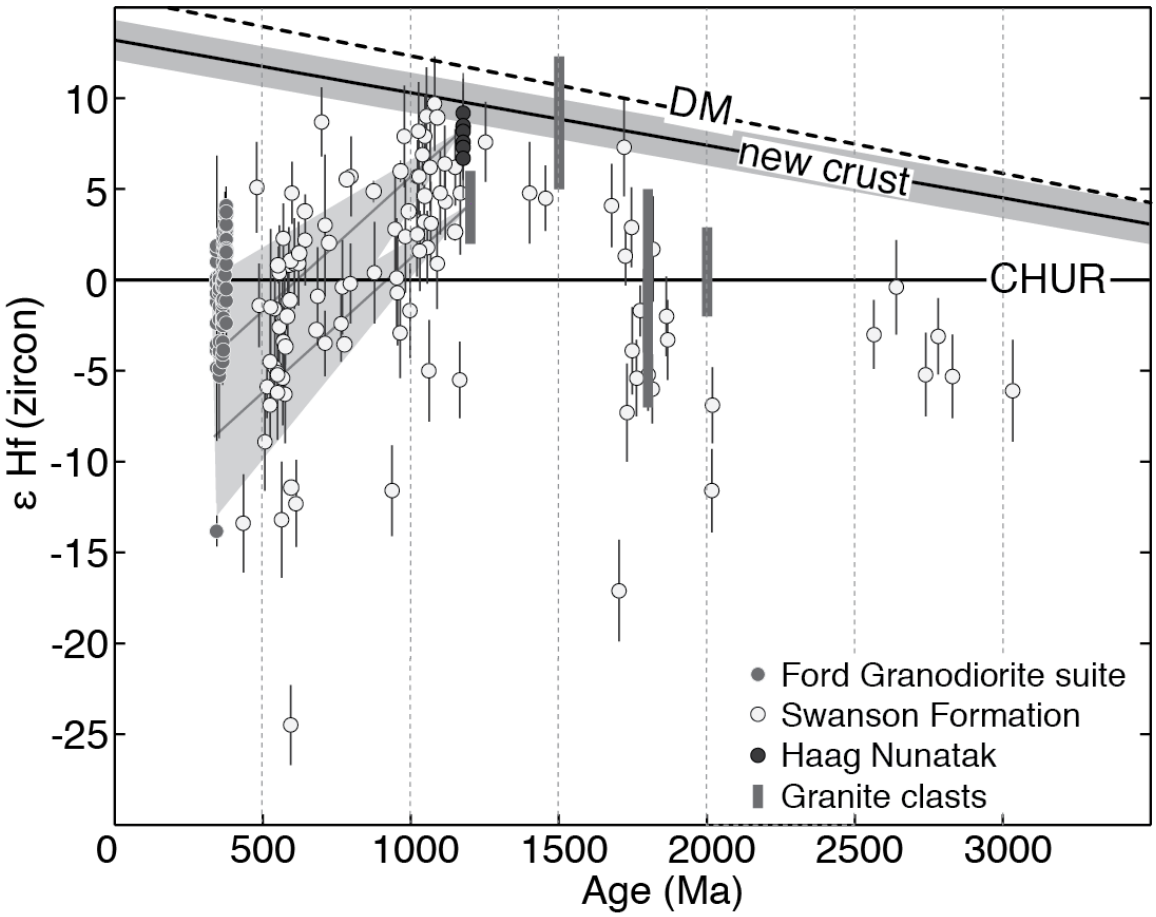

Fig. 4.11. Hf evolution diagram to show data for detrital zircons from the Swanson Formation, igneous zircon from the Ford Granodiorite suite, zircon from the gneiss at Haag Nunataks (from Flowerdew et al., 2007), and zircon from granite clasts (from Goodge et al., 2013). Reference evolution lines for the depleted mantle (DM) are from Vervoort and Blichert-Toft (1999) and for new crust are from Dhuime et al. (2011). The dark grey εHf evolution lines from the gneiss at Haag Nunatak and Mesoproterozoic granite clasts were constructed using the average $^{176}Lu/^{177}Hf$ value of crustal rocks (0.0115) and the light grey fields extend to ±1σ of this average (Vervoort and Patchett, 1996; Vervoort et al., 1999).

central Transantarctic Mountains, which is inferred to continue under the ice (Goodge and Finn, 2010), represents a possible source for the Paleoproterozoic and older zircons in the Swanson Formation samples.

Mesoproterozoic zircons in the Swanson Formation have positive εHf values, suggesting a relatively juvenile source. The gneiss at Haag Nunataks, located to the northeast of the Ellsworth Mountains (Flowerdew et al., 2007), is the only exposure of probable Mesoproterozoic basement in West Antarctica. An Rb–Sr whole-rock isochron age of 1176 ± 76 Ma was interpreted to date crystallization of the protolith of this gneiss (Millar and Pankhurst, 1987). In addition, εHf_t values from zircon range from +6.7 to +9.2 (Flowerdew et al., 2007) and whole-rock Nd isotope analysis yielded a depleted mantle model age of ca. 1250 Ma (Storey et al., 1994). Taken together, these data suggest that the gneiss at Haag Nunataks represents a relatively juvenile addition to the crust during the Mesoproterozoic, qualifying it as a potential source for this population of detrital zircons.

Other possible sources for Mesoproterozoic detrital zircons in the Swanson Formation lie beneath the Antarctic ice sheet. For example, Tochilin et al. (2012) report detrital zircon U–Pb age populations of 512–540 Ma and 800–1100 Ma from Oligocene–Quaternary sedimentary rocks in drill core from the Prydz Bay region, which is estimated to drain roughly 16% of the East Antarctica Ice Sheet. In addition, direct samples of the bedrock beneath the Antarctic ice sheet are provided by clasts from glacial moraines (e.g. Goodge et al., 2010, 2012). Zircons from granite clasts in quaternary glacial tills in the Central Transantarctic Mountains yielded εHf_t values of +2 to +6 at ca. 1.2 Ga (Goodge et al., 2013). These clasts suggest the presence of a Mesoproterozoic orogenic belt under

the ice inland from the Transantarctic Mountains that has been speculatively linked to the Gamburtsev Subglacial Mountains and the Vostok Subglacial Highlands of East Antarctica (e.g. Elliot et al., 2014).

The Mesoproterozoic population of detrital zircons from the Swanson Formation is younger than both the gneiss at Haag Nunataks and the granite clasts from the Central Transantarctic Mountains (Fig. 4.11). However, for an average crustal $^{176}Lu/^{177}Hf$ ratio (Vervoort and Patchett, 1996; Vervoort et al., 1999), within $\pm 1\sigma$ uncertainty, the εHf evolution lines from these potential sources enclose most of the Mesoproterozoic detrital zircon data from the Swanson Formation samples. This permits the Mesoproterozoic zircons to have been derived from source materials similar to these examples.

Mesoproterozoic zircons from sample 8D27-10 yielded $\delta^{18}O$ values above those expected for juvenile material derived directly from the mantle (Fig. 4.9b), which indicates the involvement of a supracrustal component. This is consistent with crustal reworking during a Mesoproterozoic orogenic event. If these zircon grains were derived from rocks inland of the Transantarctic mountains, which seems likely, the $\delta^{18}O$ values of the zircons lends support to the existence of Grenville-age orogenic belt exposed beneath the East Antarctic Ice sheet (e.g. Goodge et al., 2010; Elliot et al., 2014).

The Neoproterozoic–Cambrian population of zircons from the Swanson Formation contains more evolved εHf values than the Mesoproterozoic population, which is consistent with derivation from igneous and metamorphic rocks associated with crustal reworking in the Ross–Delamerian orogen (Ireland et al., 1998; Adams et al., 2013). In the central Transantarctic Mountains, the oldest intrusive rocks are dated at ca. 550 Ma (Rowell et al., 1993) and widespread magmatism associated with the Ross Orogen is

dated at 520–480 Ma (Goodge et al., 2012; Paulsen et al., 2013). In the Wilson Terrane of north Victoria Land, the Granite Harbour Intrusives have been dated at 520–490 Ma (Borg et al., 1986; Vetter et al., 1987; Dallai et al., 2003; Goodge et al., 2012). Although there are no reported εHf values for these rocks, some diorites, granites and granodiorites have $\delta^{18}O$ values consistent with a significant crustal component (Dallai et al., 2003). In the Dry Valleys of south Victoria Land, a minor episode of magmatism at 530–505 Ma was followed by the emplacement of a large volume of calc-alkaline granite at 505–500 Ma (Allibone and Wysoczanski, 2002). However, most zircons from the Neoproterozoic–Cambrian population from the Swanson Formation are older than most igneous and metamorphic rocks reported from the Ross Orogen as described above. Evidence of an older potential source comes from the Central Transantarctic Mountains where glacial clasts in moraines are inferred to be samples of the subglacial bedrock. These rocks have U–Pb zircon ages of 590–490 Ma (Goodge et al., 2012).

Most ages from the Neoproterozoic–Cambrian population of zircons from the Swanson Formation are older than most of igneous rocks from north Victoria Land and the Transantarctic Mountains, with the exception of a ca. 590 Ma glacial clast reported in Goodge et al. (2012). However, most of these zircons plot along the same εHf evolution lines as the Mesoproterozoic population of detrital zircons discussed above (Fig. 4.11). This suggests that most of the detrital zircons in the Swanson Formation could have been derived from crust, or sedimentary derivatives of crust, that is similar to the gneiss at Haag Nunataks and the Mesoproterozoic granite clasts that originated from beneath the East Antarctic ice sheet.

4.9.2 Detrital zircon provenance across the former margin of East Gondwana

The three age populations of detrital zircons from the Swanson Formation are broadly consistent with the provenance of Early Paleozoic sediments along the East Gondwana margin, which extended from Australia through West Antarctica and the Antarctic Peninsula into South America (Ireland et al., 1998; Adams, 2010; Adams et al., 2013). In particular, the detrital zircon patterns of the Swanson Formation are similar to those from the Lachlan Group in eastern Australia (Ireland et al., 1998), the Robertson Bay Group in North Victoria Land, and the Greenland Group in the Western Province of New Zealand (Ireland et al., 1998; Adams et al., 2013). The maximum depositional ages and the youngest zircon ages are similar for these three groups and the Swanson Formation. In addition, the U–Pb age distributions of detrital zircons from the Swanson Formation are similar to those from metasedimentary rocks from the Trinity Peninsula Group and Fitzgerald Quartzite on the Antarctic Peninsula (Flowerdew et al., 2006; Bradshaw et al., 2012) and sedimentary rocks from the Ellsworth–Whitmore Mountains (Flowerdew et al., 2007).

In general, the εHf_t values of Neoproterozoic–Cambrian and Mesoproterozoic populations of zircons from sedimentary rocks deposited along the East Gondwana margin are similar to those from the Swanson Formation. For example, the Trinity Peninsula Group on the Antarctic Peninsula has detrital zircon age populations of 1100–1000 Ma and 620–500 Ma for which the majority of εHf values from each group range from +2 to +12 and -8 to +2, respectively (Bradshaw et al., 2011). Flowerdew et al. (2006) report juvenile Hf isotope values from older zircon populations and less radiogenic Hf isotope values from the dominant (ca. 540 Ma) zircon population in the

Fitzgerald Quartzite. Neoproterozoic–Cambrian zircons from the Greenland Group in New Zealand yield εHf values of -20 to +8 (Nebel-Jacobsen et al., 2011). Ordovician volcaniclastic rocks deposited on the margin of the Macquarie Arc in the Tasmanides also show negative εHf values for Neoproterozoic–Cambrian zircons and slightly negative to positive values for 1250–970 Ma detrital zircons (Glen et al., 2011).

The similarity of U–Pb ages and εHf values of detrital zircons from Cambrian–Ordovician sedimentary rocks deposited across the East Gondwana margin suggest a laterally extensive source region. Neoproterozoic–Cambrian zircons reflect predominately crustal reworking and likely originated from the Ross–Delamerian orogen and its putative inland extension beneath the Antarctic ice sheet. The location of an extensive source of relatively juvenile Mesoproterozoic material is more problematic, but the Grenville-age orogenic belt hypothesized to occur beneath the East Antarctic ice sheet is a possible solution.

4.9.3 $\delta^{18}O$ values of the Swanson Formation

Sedimentary rocks and granites derived from them can be distinguished from granites with juvenile sources using oxygen isotopes (e.g. O'Neil and Chappell, 1977). To evaluate the proportional contribution of the Swanson Formation to the petrogenesis of granites in western Marie Byrd Land it is necessary to know the εHf values of the detrital zircon and the $\delta^{18}O$ values of whole-rock samples. For six of the eight samples of Swanson Formation, whole-rock values range from 10.00 to 13.48‰, which are similar to values expected for most sedimentary rocks (12‰; O'Neil and Chappell 1977). However, these values are lower than whole-rock values reported for the correlative

Greenland Group of 13.7–16.2‰ (Tulloch et al., 2009) used by Yakymchuk et al. (2013a) to model mixing of material between the Ford Granodiorite suite and the Swanson Formation. During partial melting, oxygen isotope fractionation between zircon and granitic magma will result in igneous zircons that have $\delta^{18}O$ values less than the source rock by 1–2‰ (Valley et al., 1994; Valley, 2003). Therefore, using a $\Delta^{18}O_{Zrc\text{-}WR}$ correction of -1.5‰ for isotope fractionation, newly crystallized zircons in granites derived from partial melting of the Swanson Formation are expected to have a $\delta^{18}O$ values of ~8.5–12‰.

Two Swanson Formation samples from the contact aureole around a Byrd Coast Granite suite pluton show negative whole-rock $\delta^{18}O$ values of -6.89 and -9.16‰ (Table C.7 in Appendix C). Negative values are consistent with hydrothermal alteration associated with an active magma chamber at a shallow enough depth to allow the penetration of negative $\delta^{18}O$ meteoric water. A strong isotope exchange between the rocks and meteoric water is needed to produce the negative isotope values observed in these two samples. Furthermore, the strongly negative $\delta^{18}O$ values of the meteoric water necessary for hydrothermal alteration of these two Swanson Formation samples require high latitudes, consistent with the position of western Marie Byrd Land during the Cretaceous (e.g. DiVenere et al., 1994).

4.9.4 Petrogenesis of the Ford Granodiorite suite, the granites and the diatexites

4.9.4.1 Temporal changes in Hf and O isotopes in zircon

For a fuller assessment of the relationships among the Ford Granodiorite suite, the granites and the diatexites, and due consideration of their petrogenesis, the six new Hf

and O isotope datasets reported in this study have been combined with published information for four additional samples (from Yakymchuk et al., 2013a; Ford Granodiorite suite samples MB.214.W and MB.219.W, and granite samples M5-G175 and C5-Is51A). The combined dataset is shown as ten box-and-whisker plots for εHf_t and $\delta^{18}O$ vs. age in Figure 4.12. Box-and-whisker plots are used because the data are not normally distributed. These plots provide a graphical summary of dataset characteristics based on percentile rank analysis and plotting the maximum and minimum dataset values. Importantly, the underlying statistics are more resistant toward individual outliers than other methods of analysis (Tukey, 1977). Also, the compact nature of the plots allows side-by-side comparison of individual sample datasets. Nonparametric statistics may be used to evaluate if the distributions of zircon εHf_t and $\delta^{18}O$ values are significantly different between samples of the Ford Granodiorite suite, and between these and the granites and diatexites. We use the nonparametric Kruskal–Wallis test (Kruskal and Wallis, 1952) that is analogous to a parametric analysis of variances (ANOVA) test, except that it does not require data that are normally distributed.

As can be seen from Figure 4.12, the ages of the two granites and the two diatexites from inside the Fosdick complex fall within the range for the six Ford Granodiorite suite samples from outside the Fosdick complex. The Ford Granodiorite suite samples divide into two groups. The two oldest members of the suite (MB.214 and MB.219) have zircon with the most radiogenic εHf_t and the lowest $\delta^{18}O$ values, whereas the four younger samples have zircons with more evolved εHf_t and higher $\delta^{18}O$ values (Fig. 4.12). Based on results from the Kruskal–Wallis test, samples within each group are

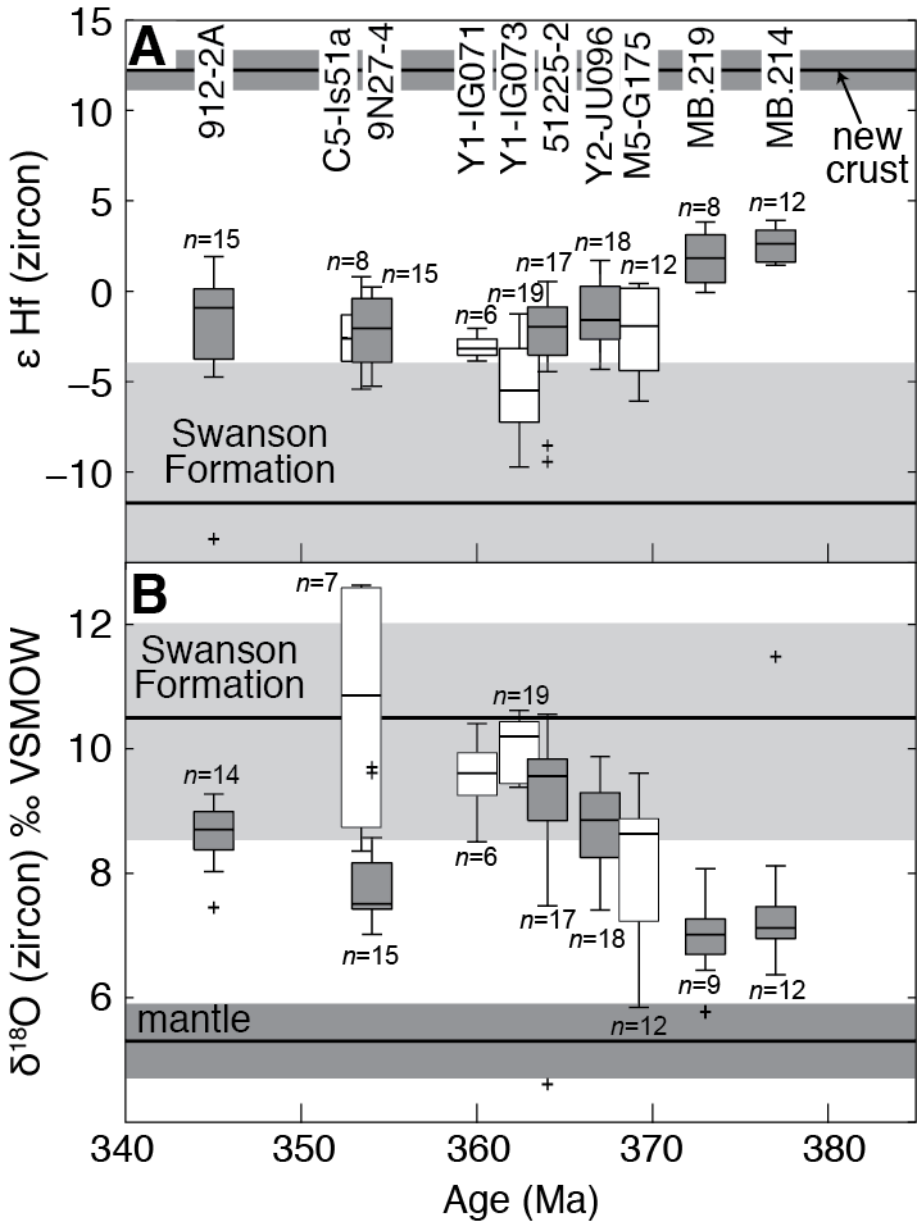

Fig. 4.12. Box-and-whisker plots for εHf_t and $\delta^{18}O$ versus $^{206}Pb/^{238}U$ zircon crystallization age for members of the Ford Granodiorite suite, and samples of the associated granites and diatexites. Data for samples MB.214, MB.219, M5-G175 and C5-Is51a are from Yakymchuk et al. (2013a). The crystallization age for sample Y1-IG071 is taken to be 360 Ma, as discussed in the text. The εHf_t for new crust is taken from Dhuime et al. (2011; +12.2 ± 1.1) and $\delta^{18}O$ for the mantle is from Valley et al. (1998; 5.3 ± 0.6‰). The εHf_t (median value of -11.7 and an interquartile range of -3.5 to -19.9) and $\delta^{18}O$ (8.5–12‰, with a mean value of 10.5‰) values chosen for the Swanson Formation are discussed in the text.

Table 4.2. *p* values for Kruskal-Wallis test of zircon εHf$_t$ and δ18O distributions for pairs of Ford Granodiorite suite samples

εHf (zircon)	MB.219	MB.214	M5-G175	Y1-IG071	Y2-JU096	51225-2	Y1-IG073	9N27-4	C5-Is51a	912-2A
MB.219	–	0.14	**0.00**	**0.00**	**0.00**	**0.00**	**0.00**	**0.00**	**0.00**	**0.00**
MB.214	0.14	–	**0.00**	**0.00**	**0.00**	**0.00**	**0.00**	**0.00**	**0.00**	**0.00**
M5-G175	**0.00**	**0.00**	–	**0.05**	0.43	0.76	0.31	0.81	0.76	0.68
Y1-IG071	**0.00**	**0.00**	**0.05**	–	**0.01**	0.06	0.07	**0.04**	0.09	**0.03**
Y2-JU096	**0.00**	**0.00**	0.43	**0.01**	–	0.29	**0.00**	0.28	0.19	0.77
51225-2	**0.00**	**0.00**	0.76	0.06	0.29	–	**0.02**	0.81	0.52	0.40
Y1-IG073	**0.00**	**0.00**	0.31	0.07	**0.00**	**0.02**	–	0.23	0.34	0.11
9N27-4	**0.00**	**0.00**	0.81	**0.04**	0.28	0.81	0.23	–	0.65	0.41
C5-Is51a	**0.00**	**0.00**	0.76	0.09	0.19	0.52	0.34	0.65	–	0.37
912-2A	**0.00**	**0.00**	0.68	**0.03**	0.77	0.40	0.11	0.41	0.37	–

$\delta^{18}O$ (zircon)	MB.219	MB.214	M5-G175	Y1-IG071	Y2-JU096	51225-2	Y1-IG073	9N27-4	C5-Is51a	912-2A
MB.219	–	0.13	**0.01**	**0.00**	**0.00**	**0.00**	**0.00**	**0.00**	**0.00**	**0.00**
MB.214	0.13	–	0.12	**0.00**	**0.00**	**0.00**	**0.00**	**0.02**	**0.00**	**0.00**
M5-G175	**0.01**	0.12	–	**0.00**	0.16	**0.01**	**0.00**	0.38	**0.02**	0.53
Y1-IG071	**0.00**	**0.00**	**0.00**	–	**0.00**	0.06	0.10	**0.00**	0.48	**0.00**
Y2-JU096	**0.00**	**0.00**	0.16	**0.00**	–	**0.03**	**0.00**	**0.00**	**0.02**	0.53
51225-2	**0.00**	**0.00**	**0.01**	0.06	**0.03**	–	0.35	**0.00**	0.14	**0.00**
Y1-IG073	**0.00**	**0.00**	**0.00**	0.10	**0.00**	0.35	–	**0.00**	0.28	**0.00**
9N27-4	**0.00**	**0.02**	0.38	**0.00**	**0.00**	**0.00**	**0.00**	–	**0.00**	**0.01**
C5-Is51a	**0.00**	**0.00**	**0.02**	0.48	**0.02**	0.14	0.28	**0.00**	–	**0.03**
912-2A	**0.00**	**0.00**	0.53	**0.00**	0.53	**0.00**	**0.00**	**0.01**	**0.03**	–

For *p* values <0.05, the null hypothesis that the two groups sample the same population is rejected.

likely to have sampled the same population, whereas the two groups of samples are likely to have sampled different populations (Table 4.2). The εHf_t and $\delta^{18}O$ values for the granites and diatexites are similar to the younger group of Ford Granodiorite suite samples (Fig. 4.12, Table 4.2). These data suggest a change at ca. 370 Ma towards a larger contribution from the Swanson Formation in the petrogenesis of the younger rocks. This change is consistent with the study of Tulloch et al. (2009), who reported monazite $^{207}Pb/^{235}U$ ages of ca. 359 Ma and ca. 351 Ma from muscovite–biotite granites from the Chester Mountains and Neptune Nunataks (locations in Fig. 4.2), respectively, consistent with the postulated increasing contribution from a sedimentary source after ca. 370 Ma.

4.9.4.2 Potential source rocks

Zircons from the Ford Granodiorite suite, the granites and the diatexites exhibit a range of $\delta^{18}O$ and εHf values. Many arc-related granitoids are thought to represent a mixture of two or more source components (e.g. Kemp et al., 2009; Miles et al., 2014). The Hf and O isotope composition of zircon provides a potentially powerful tool to evaluate the nature and proportional contribution of these source components to granitoid petrogenesis (e.g. Kemp et al., 2007). These proportions may be evaluated if the isotope composition of the source components is known and if they are sufficiently distinct from one another. Hf isotopes may be used to distinguish between juvenile and ancient source components, whereas O isotopes may be used to determine if source components have been subjected to surface processes, such as weathering and sedimentation, as indicated by high $\delta^{18}O$ values (e.g. Hawkesworth and Kemp, 2006).

The majority of Hf in most crustal rocks is found in zircon. Therefore, the Hf isotope composition of zircon in igneous rocks is expected to be similar to the Hf isotope composition of the magmas from which they crystallized. By contrast, the Hf isotope composition of metasedimentary rocks and anatectic melts derived from is expected to be similar to the range of values for the detrital zircons. For oxygen, isotope fractionation between zircon and granite magma will result in igneous zircons that have slightly lower $\delta^{18}O$ values (Valley et al., 1994; Valley 2003). By contrast, the $\delta^{18}O$ composition measured in detrital zircon may not be representative of the whole-rock value because oxygen is a major component in all of the major rock forming minerals, including those that have formed at or near the surface. Therefore, granites derived by anatexis from sedimentary protoliths may not have similar oxygen isotope compositions to detrital zircons in the source, but they are expected have a composition similar to the whole-rocks.

For the Ford Granodiorite suite, one potential source component is the regionally distributed Swanson Formation. The εHf values of detrital zircons in the Swanson Formation, recalculated to 360 Ma, varies from +2 to -67, with a median value of -11.7 and an interquartile range of -3.5 to -19.9 (Figs 4.10, 4.12 and 4.13). As discussed above, the $\delta^{18}O$ value of zircons that crystallized from melt produced from the Swanson Formation are expected to have values of ~8.5–12‰, with a mean value of 10.5‰ (Figs 4.10, 4.12 and 4.13). The Hf isotope composition of zircons from the Ford Granodiorite suite reported in this study is more radiogenic than most detrital zircons from the Swanson Formation (Fig. 4.10a). This suggests the involvement of a source more juvenile than the Swanson Formation.

The calc-alkaline chemistry of the Ford Granodiorite suite and its emplacement during a period of widespread arc magmatism along the East Gondwanan plate margin suggests the possible involvement of juvenile magma sourced from the arc mantle or a mafic underplate derived from it. Such a source is inferred to have a $\delta^{18}O$ value of 5.3 ± 0.6‰ (Valley et al., 1998). The εHf of this source may range from that expected for new crust (+12.2 at 360 Ma; Dhuime et al., 2011) to less radiogenic values associated with an enriched mantle above a subducting slab. The εHf values for modified sub-continental lithospheric mantle may range from 0 (CHUR) to +10 (Griffin et al., 2000). Therefore, for the purpose of petrogenetic modeling, two end-member εHf values of 0 (CHUR) and +12.2 (new crust) have been chosen to represent the juvenile source.

Excluding outliers (Fig. 4.12), data from the Ford Granodiorite suite reported in this study have εHf_t values that plot between those for the Swanson Formation and those for the juvenile source (Fig. 4.10a). This suggests that a petrogenetic scenario similar to the model developed for granites in the Lachlan Fold Belt may be applicable to the Ford Granodiorite suite. The Lachlan granites were interpreted to be the mixed products of sedimentary material reworked by juvenile magma in the deep crust (Kemp et al., 2007). Accordingly, binary mixing curves between Swanson Formation and mantle have been calculated to evaluate this model for the petrogenesis of the Ford Granodiorite suite. Four scenarios are modeled: two where different juvenile magma compositions, discussed above, are mixed with Swanson Formation en masse and two where these same juvenile magma compositions are mixed with anatectic melt derived from the Swanson Formation.

The curvature of the mixing lines is most sensitive to the relative concentrations of Hf in each of the end-members. There are no data available for mafic rocks of an appropriate age in Marie Byrd Land. Therefore, for the juvenile source, an Hf concentration of 2.3 ppm is used, which is a representative composition for mafic rocks temporally associated with Devonian granites in the Lachlan Fold Belt (e.g. Kemp et al., 2007). For the Swanson Formation, an average whole-rock concentration of 3.2 ppm was assigned based on bulk chemical analyses (Korhonen et al., 2010a). For melt derived from the Swanson Formation, a concentration of 1.0 ppm is used, which represents the average Hf concentration of deep crustal granites that were interpreted to be derived predominately from a Swanson Formation source inside the Fosdick complex (1.0 ppm; Korhonen et al., 2010a).

Fig. 4.13. (A) Plots of $\delta^{18}O$ versus εHf_t for individual zircons from the four newly-analyzed members of the Ford Granodiorite suite. Binary mixing lines connect representative end-members of each of the sources modeled—the mantle (Juv) and the Swanson Formation (SF). Small filled circles on each line display 10% increments. (B) Field to show the range of $\delta^{18}O$ and εHf_t values for the data shown in (A). Binary mixing lines between anatectic melt derived from the Ford Granodiorite suite (FGD) and Swanson Formation either assimilated en masse or as anatectic melt separated from the Swanson Formation. Two representative end-member εHf_t and $\delta^{18}O$ values are used to evaluate the contribution from the oldest and most juvenile end-members of the Ford Granodiorite suite, as discussed in the text. (C) Plots of $\delta^{18}O$ and εHf_t values from individual zircons from granites and diatexites in the Fosdick migmatite–granite complex. The field for the full range of $\delta^{18}O$ and εHf_t values retrieved from the Ford Granodiorite suite represents one of the end-member source compositions used in the modeling. Multiple binary mixing scenarios for the petrogenesis of the granites and diatexites are evaluated, as discussed in the text. Also shown in all three figures are end-member εHf values for the mantle, corresponding to CHUR and a value expected for new crust, respectively, as discussed in the text. The $\delta^{18}O$ value of the mantle is 5.3 ± 0.6‰ (Valley et al., 1998). The εHf_t (median value of -11.7 and an interquartile range of -3.5 to -19.9) and $\delta^{18}O$ (8.5–12‰, with a mean value of 10.5‰) values chosen for the Swanson Formation are discussed in the text.

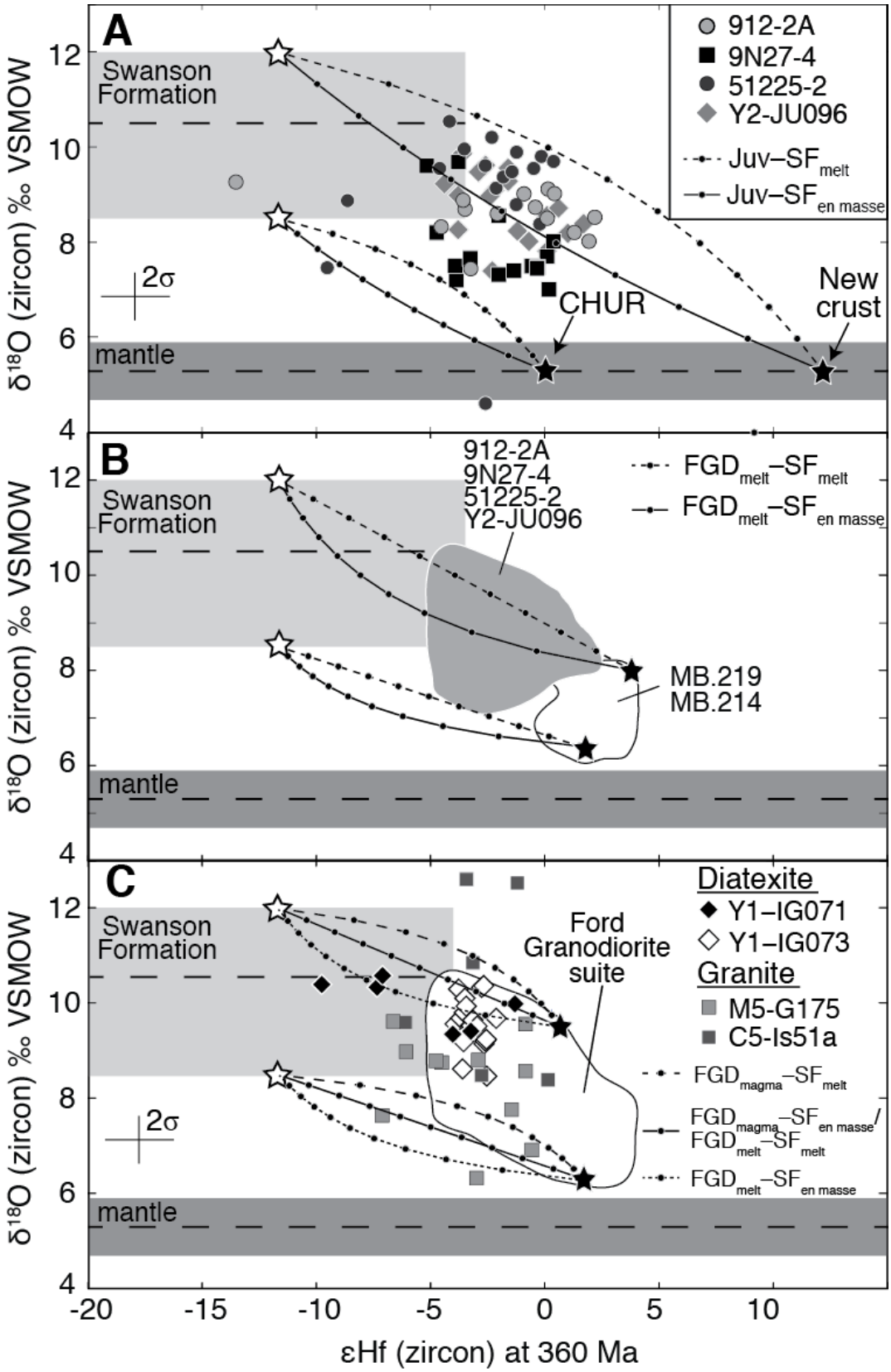
A
912-2A
9N27-4
51225-2
Y2-JU096
Juv–SF melt
Juv–SF en masse
Swanson Formation
2σ
CHUR
New crust
mantle
B
912-2A
9N27-4
51225-2
Y2-JU096
FGD melt–SF melt
FGD melt–SF en masse
Swanson Formation
MB.219
MB.214
mantle
C
Diatexite
Y1–IG071
Y1–IG073
Granite
M5-G175
C5-Is51a
Ford Granodiorite suite
Swanson Formation
FGD magma–SF melt
FGD magma–SF en masse/
FGD melt–SF melt
FGD melt–SF en masse
2σ
mantle
δ18O (zircon) ‰ VSMOW
12
10
8
6
4
-20
-15
-10
-5
0
5
10
εHf (zircon) at 360 Ma

For the four younger Ford Granodiorite suite samples analyzed in this study, a large proportion of the Hf and O isotope compositions of the zircons may be explained by this model, particularly for mixing magma from the juvenile source with anatectic melt from the Swanson Formation (Fig. 4.13a). This is consistent with rare zircon cores within some samples that correspond to the two main age populations found in the Swanson Formation and paragneiss detrital zircons. Mixing between juvenile magma and 40–80% anatectic melt derived from the Swanson Formation is required to explain the range of measured values for the Ford Granodiorite suite samples (Fig. 4.13a).

An alternative scenario that cannot be ruled out by the data is one in which the earliest members of the Ford Granodiorite suite are reworked in the deep crust, generating melts that mix with those derived from the Swanson Formation or assimilate Swanson Formation en masse to produce the younger members of the Ford Granodiorite suite. To explore this scenario the data from this study are combined with data from Yakymchuk et al. (2013a). These data are plotted as two fields in Figure 4.13b, one for two older members of the Ford Granodiorite suite (samples MB.214 and MB.219) and a second for the four younger members of the Ford Granodiorite suite shown in Figure 4.13a. Most of the Hf and O isotope compositions of zircons from the younger members of the Ford Granodiorite suite may be explained by mixing of anatectic melt from older members of the suite with anatectic melt from the Swanson Formation (Fig. 4.13b). This is consistent with the small population of slightly older zircon dates from sample Y2-JU096 that yielded an age of ca. 377 Ma (Fig. 4.5). However, the Hf and O isotope composition of zircons from samples MB.214 and MB.219 also lie inside the curves for juvenile magma mixing with melts derived from the Swanson Formation or for

assimilation of Swanson Formation en masse (compare the fields in Fig. 4.13b with the model mixing curves in Fig. 4.13a). Thus, any contribution to the petrogenesis of the younger members of the Ford Granodiorite suite derived by reworking of these older compositions would have been masked by any ongoing input from the juvenile mantle source, and the two alternative scenarios cannot be distinguished.

4.9.5. The granites and diatexites

The granites and diatexites generally have whole-rock Sr and Nd, and zircon Hf and O isotope compositions that lie between those of the most primitive Ford Granodiorite suite members and the least evolved Swanson Formation (Figs. 4.6 and 4.13). This observation permits a variety of plausible scenarios for the petrogenesis of the granites and diatexites.

The first possibility is that juvenile magma could have assimilated Swanson Formation en masse or mixed with anatectic melt derived from the Swanson Formation in a fashion similar to the model proposed for the petrogenesis of the Ford Granodiorite suite (compare the data in Fig. 4.13c with the model mixing curves in Fig. 4.13a). However, this option considered the least likely based on the variable oxide and trace element distributions of the granites and diatexites compared with the more regular distributions shown by the Ford Granodiorite suite samples (Fig. 4.6) and the differences in REE patterns (Fig. 4.7).

Four alternative possibilities are: (1) Ford Granodiorite suite magmas could have mixed with anatectic melt derived from the Swanson Formation, (2) Ford Granodiorite suite magmas could have assimilated Swanson Formation en masse, (3) melt derived

from early-crystallized members of the Ford Granodiorite suite by anatexis could have mixed with anatectic melt derived from the Swanson Formation, and (4) melt derived from early-crystallized members of the Ford Granodiorite suite by anatexis could have assimilated Swanson Formation en masse, as proposed by Korhonen et al. (2010a).

First, we evaluate these four options using the Sr and Nd isotope compositions recalculated to 360 Ma. Figure 4.8 shows binary mixing lines that connect representative compositions of the Swanson Formation and the Ford Granodiorite suite calculated using the Sr and Nd concentrations and isotope values of more and less radiogenic end-member samples (Fig. 4.8). With the exception of granite sample C5-Is51a (reported by Korhonen et al., 2010a) and the inhomogeneous diatexite (Y1-IG071), the granites plot between the two sources but closer to the Ford Granodiorite suite. The Sr and Nd isotope values of the granites and the homogeneous diatexite allow a contribution of up to 30 vol.% Swanson Formation (Fig. 4.8). The inhomogeneous diatexite (Y1-IG071) plots at less radiogenic εNd values than the Ford Granodiorite suite but also at lower $^{87}Sr/^{86}Sr_{360}$ values than the Swanson Formation (Fig. 4.8). This sample contains a significant population of 100 Ma zircons. If the Sr and Nd isotope ratios are recalculated to 100 Ma, the inhomogeneous diatexite falls between the εNd and $^{87}Sr/^{86}Sr_{100}$ values of two putative sources, which is interpreted to indicate that this sample records the effects of the Cretaceous overprint.

Second, we use the zircon Hf and O isotope compositions. Figure 4.13C shows binary mixing lines that connect representative compositions of the Swanson Formation and the Ford Granodiorite suite. These were calculated using Hf concentrations of 3.3 ppm for the Ford Granodiorite suite magmas and 1.0 ppm for anatectic melts derived from early members of the Ford Granodiorite suite combined with the Hf concentrations

discussed above for the Swanson Formation. Note that assimilation of Swanson Formation en masse by Ford Granodiorite suite magma and mixing of anatectic melts derived from early members of the Ford Granodiorite suite with those derived from the Swanson Formation yield similar binary mixing curves that cannot be distinguished in Figure 4.13C. The modeling permits by all four petrogenetic scenarios discussed above; in almost all cases the proportion of Ford Granodiorite suite component required by the data is greater than the Swanson Formation component.

To further test these two alternatives, the major-element compositional variability of Devonian–Carboniferous granites and diatexites is investigated using the ternary system (Na+Ca)–(Fe*+Mg+Ti)–K (Solar and Brown, 2001). Because there have been no melting experiments done on either the Ford Granodiorite suite or the Swanson Formation, experimental melt compositions from Skjerlie et al. (1993) and Patiño Douce and Harris (1998) were used based on similarity in chemical composition of the experimental starting materials to the putative sources of the granites. The experimental melts from Skjerlie et al. (1993) were used as proxies for melts derived from the Ford Granodiorite suite while the experimental results of Patiño Douce and Harris (1998) were used to infer melt compositions derived from the Swanson Formation. The compositions of the starting materials and melts are plotted along with samples from the Swanson Formation, Ford Granodiorite suite, and the granites and diatexites in Figure 4.14. There is a wide range of possible granite and diatexite compositions that may be achieved by assimilation or mixing between Ford Granodiorite suite compositions, Swanson Formation compositions and melts derived from each, as shown by the shaded areas in

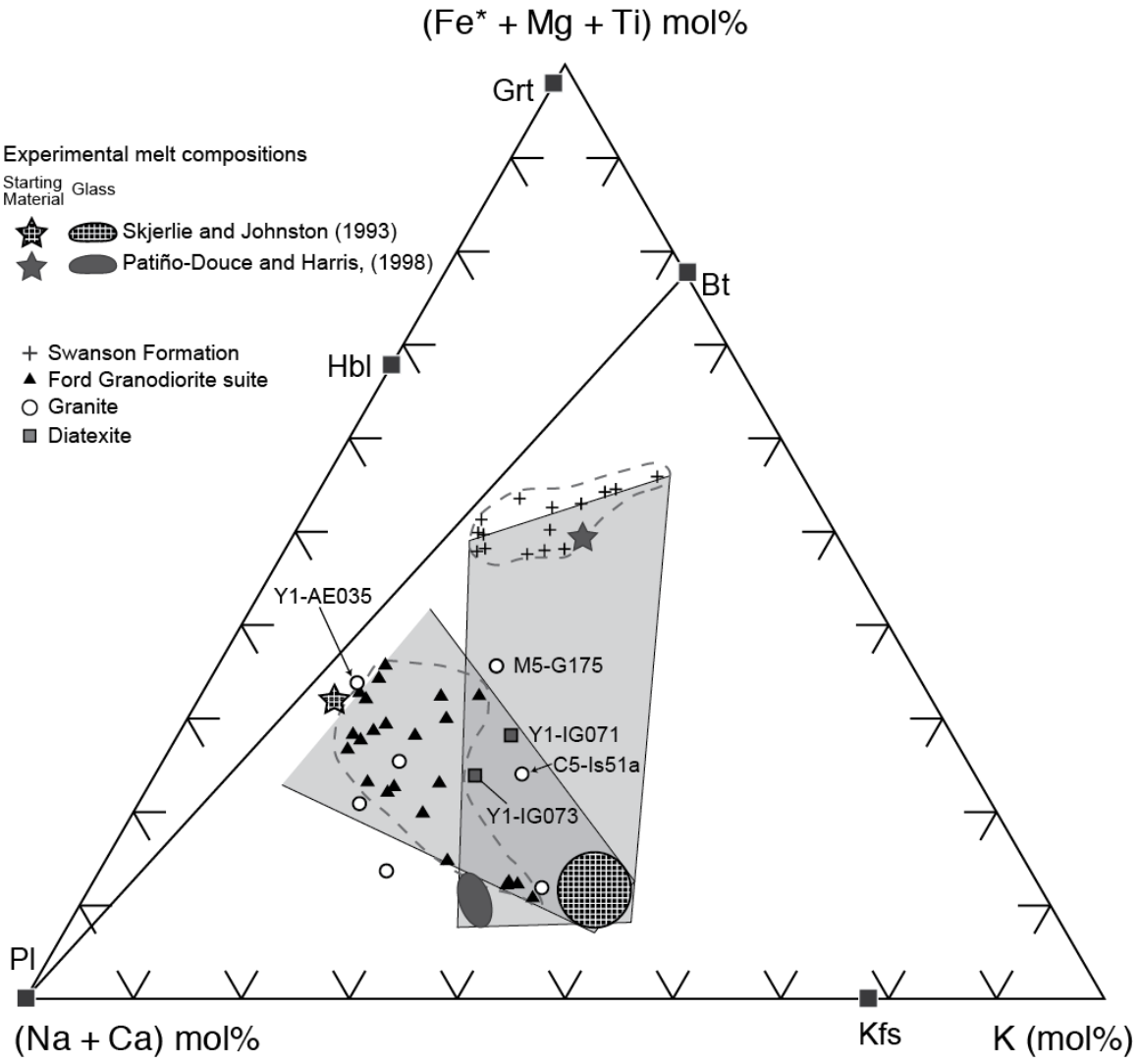

Fig. 4.14. To show the full dataset discussed in the text plotted on the ternary (Na+Ca)–(Fe*+Mg+Ti)–K plot of Solar and Brown (2001) to assess petrogenetic models for the granites and diatexites. Starting materials and experimental melt compositions are taken from Skjerlie et al. (1993) and Patiño Douce and Harris (1998), as discussed in the text. The shaded areas represent the range of possible granite and diatexite compositions that may be achieved by assimilation or mixing between Ford Granodiorite suite compositions and Swanson Formation en masse or as anatectic melt separated from residue.

Figure 4.14, particularly given the propensity of crustal melts to entrain peritectic residue (Clemens et al., 2011; Clemens and Stevens, 2012). As a result, the four alternative petrogenetic scenarios considered—that Ford Granodiorite suite magmas or melts derived from early-crystallized members of the suite could have assimilated Swanson Formation en masse or mixed with anatectic melt derived from the Swanson Formation—cannot be discriminated.

4.9.6 Wider Considerations

4.9.6.1 Implications for a Proterozoic basement

An outstanding question in western Marie Byrd Land is the nature and age of the basement to the Swanson Formation. Evidence supporting a Proterozoic basement includes: (1) inherited zircons in granites that yield Proterozoic ages or Proterozoic concordia upper intercept ages (Pankhurst et al., 1998; Mukasa and Dalziel, 2000); (2) Proterozoic Nd model ages for the Ford Granodiorite suite (Pankhurst et al., 1998); and (3) Proterozoic Os isotope model ages for peridotite xenoliths from the upper mantle beneath Eastern Marie Byrd Land, which assumes that the crust and underlying mantle are temporally coupled (Handler et al., 2003). However, aeromagnetic anomalies north Victoria Land led Finn et al. (1999) to suggest that sedimentary rocks that make up the Robertson Bay Terrane—proposed to be correlative with the Swanson Formation in Marie Byrd Land—were deposited on forearc oceanic crust. The geological and geochemical evidence for the age of the basement to the Swanson Formation is evaluated below.

Granites from Marie Byrd Land commonly contain zircons with xenocrystic cores that may reflect inheritance from a Precambrian source (e.g. Mukasa and Dalziel, 2000), or alternatively, these grains may represent detrital zircons scavenged from sedimentary rocks during formation and/or emplacement. In the Ford Granodiorite suite, eleven inherited zircon grains have been identified in analyzed samples (Pankhurst et al., 1998; this study). These zircons yield dates of 762–499 Ma (7 grains) and 1074–762 Ma (4 grains). The similarity of these age populations to the Neoproterozoic–Cambrian and Mesoproterozoic zircon age populations in the Swanson Formation suggests the possibility of scavenged detrital zircon grains, which is supported by the requirement for a Swanson Formation component in the petrogenesis of the Ford Granodiorite suite. Therefore, these inherited grains do not provide direct evidence of a Precambrian basement beneath western Marie Byrd Land.

The Ford Granodiorite suite yields Proterozoic Nd model ages that have been interpreted to reflect a Proterozoic basement in western Marie Byrd Land (Pankhurst et al., 1998). However, the Ford Granodiorite suite represents a mixture of juvenile (mantle-derived) and metasedimentary components, as demonstrated by the elevated $\delta^{18}O$ values of the zircons (Fig. 4.10). Therefore, the Nd model ages likely represent hybrids resulting from a mixture of two components and they may not reflect the true age of the basement.

Handler et al. (2003) document Mesoproterozoic Os model ages from mantle xenoliths in Cenozoic volcanic rocks from the Executive Committee Range in Marie Byrd Land, which is ~500 km away from the Ford Ranges. The partial melting and subsequent stabilization of mantle lithosphere at this time likely resulted in additions of juvenile magma to the crust, which potentially could represent a nearby source for

Mesoproterozoic detrital zircons with juvenile εHf values similar to those in the Swanson Formation. However, given the distance between the Ford Ranges and the Executive Committee Range, it is not required that the Swanson Formation was deposited on this Proterozoic basement.

An alternative model is that the Swanson Formation was deposited on a Paleozoic oceanic basement, as has been proposed for the Robertson Bay Terrane in north Victoria Land (Finn et al., 1999) and for the Lachlan Orogen (Foster et al., 2009). A positive test of this hypothesis would be the retrieval of Paleozoic Os model ages from mantle xenoliths that occur in Cenozoic volcanic rocks in the Ford Ranges.

4.9.6.2 Correlation along the East Gondwana margin

The former active margin of East Gondwana represents one of the most extensive and long-lived active margins in the Phanerozoic and is the type example of an external (circum-Pacific) orogenic system (Collins et al., 2011). Parts of the landmasses of Australia and New Zealand (Zealandia) were situated along the active margin of East Gondwana together with north Victoria Land and Marie Byrd Land from the Paleozoic through the final breakup of East Gondwana in the Cretaceous (Fig. 4.1b). The ages and isotope values of granites from different segments along the East Gondwana margin can provide insight into the similarities and differences in the processes operating along an active continental margin (e.g. Yakymchuk et al., 2013a). However, such a comparison is limited by the paucity of zircon Hf isotope data from granites in New Zealand and north Victoria Land. Therefore, in this section we use both whole-rock Nd and zircon Hf isotope data from granites in each of these locations, as shown in Figure 4.15.

In eastern Australia, the Tasmanides orogen is attributed to alternating extensional and contractional tectonics associated with a west-dipping subduction zone that migrated oceanward from the Cambrian to the Permian (e.g. Collins, 2002; Glen, 2005; Cawood, 2005). A protracted period of Silurian to Devonian silicic magmatism is recorded in the Tasmanides with minor Carboniferous magmatism. These granites record a progression towards more radiogenic whole-rock εNd and zircon εHf values with time (Fig. 4.15a, b), which has been tied to crustal growth accompanying slab rollback and back-arc rifting after crustal thickening (Kemp et al., 2009). Granites from the Western Province of New Zealand show a similar trend, although at a later time than the granites from the Tasmanides (Fig. 4.15a). In contrast, the Ford Granodiorite suite and its correlatives in north Victoria Land were emplaced over relatively short periods in the Devonian–Carboniferous and do not show the same temporal trends (Fig. 4.15a, b).

In north Victoria Land, correlative Devonian–Carboniferous igneous rocks include the Admiralty Intrusives (371–351 Ma; Borg et al., 1987; Fioretti et al. 1997; Henjes-Kunst and Kreuzer, 2003), the Salamander Granite complex (ca. 347 Ma; Henjes-Kunst and Kreuzer, 2003), and associated volcanic rocks (369–357 Ma; Henjes-Kunst and Kreuzer 2003). Although there is only limited Nd isotope data from the Admiralty Intrusives in north Victoria Land (Borg et al., 1986), they have a similar range of εNd values to those from the Ford Granodiorite suite (Fig. 4.15a). The ages of these rocks were constrained by Rb–Sr isochrons to the range 393–364 Ma. Thus, these granites are generally older than the Ford Granodiorite suite. However, Henjes-Kunst and Kreuzer (2003) report Ar–Ar biotite ages and one U–Pb zircon age from other Admiralty Intrusive rocks in the range 371–354 Ma, which casts some doubt about the veracity of the Rb–Sr

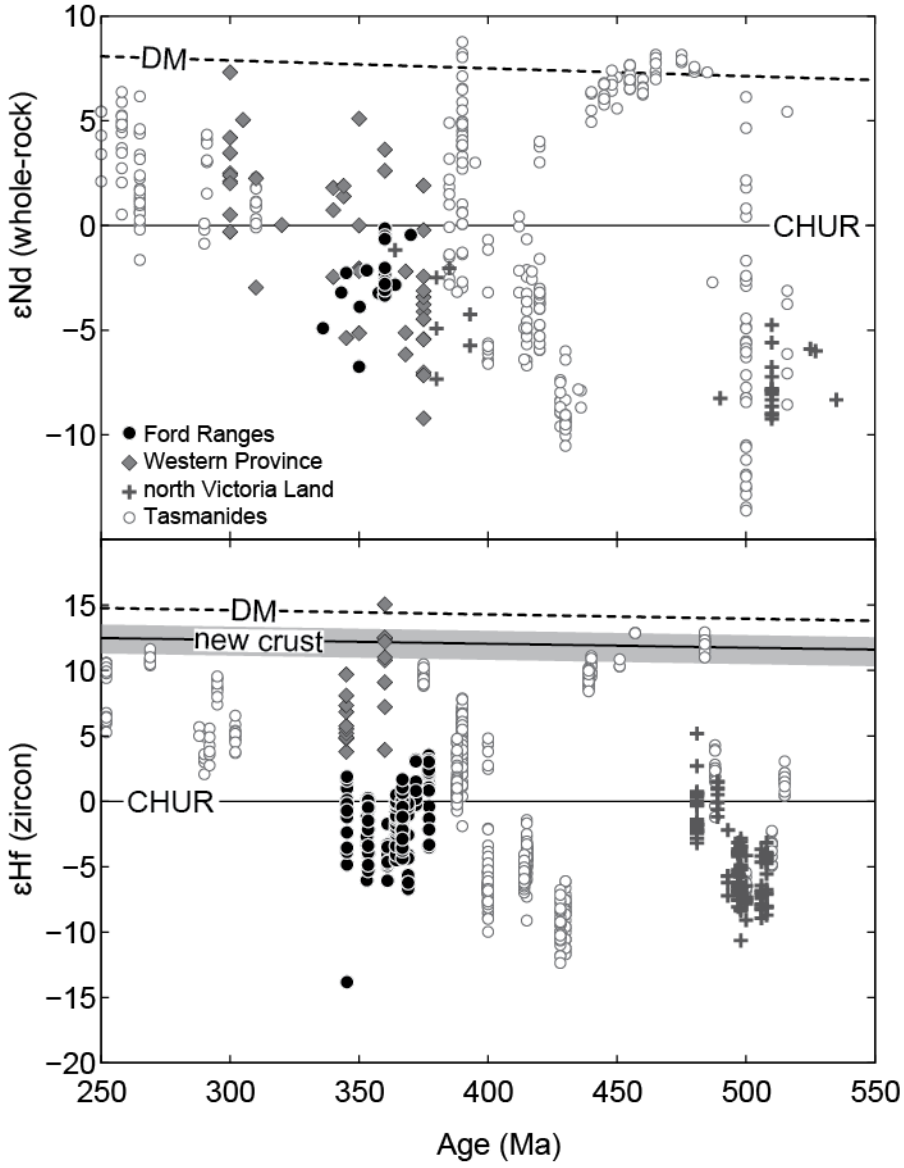

Fig. 4.15. Compilation of whole rock Nd (A) and zircon Hf (B) isotope data for igneous rocks from the eastern Gondwana margin. Data sources include: western Marie Byrd Land (Pankhurst et al., 1998; Korhonen et al., 2010; Yakymchuk et al., 2013a; this study), the Western Province of New Zealand (Muir et al., 1996; Scott et al., 2009; Tulloch et al., 2009), north Victoria Land (Borg et al., 1986; Armienti et al., 1990; Borg and DePaolo, 1991; Bomparola et al., 2007), and the Tasmanides (Kemp et al., 2007; Kemp et al., 2009 and references therein). Reference evolution lines for the depleted mantle (DM) are from Vervoort and Blichert-Toft (1999) and for new crust are from Dhuime et al. (2011) for Hf and from DePaolo (1981) for Nd.

ages. Assuming contemporaneity between the Ford Granodiorite suite and the Admiralty Intrusives, the Nd isotope data suggest both were derived from an isotopically similar source.

In the Western Province of New Zealand, Devonian–Carboniferous igneous rocks coeval with the Ford Granodiorite suite include the Karamea–Paringa suite (371–351 Ma; Tulloch et al, 2009; Sagar and Palin, 2013) and the Ridge–Tobin suite (355–342 Ma; Tulloch et al, 2009). Granites from the volumetrically dominant Karamea suite have εNd values of -3 to -9 and estimated magma $\delta^{18}O$ values of 10.8 to 12.5‰ (Tulloch et al., 2009), which indicates that these granites were derived primarily from a metasedimentary source. Younger granite suites from the Western Province generally have more radiogenic εNd and εHf zircon values (Fig. 4.15a, b) and more mantle-like $\delta^{18}O$ values than the Ford Granodiorite suite. In the Western Province, the high $\delta^{18}O$ values of the Karamea suite granites, their rapid emplacement (370–368 Ma; Tulloch et al., 2009), occurrence of contemporaneous mafic rocks (Turnbull et al., 2013), and partial melting at low pressures (~670°C at 0.3–0.5 GPa; Scott et al., 2011) may indicate a period of lithospheric extension and asthenospheric upwelling. Scott et al. (2011) suggest that crustal thinning may have been related to slab rollback or subduction cessation along this portion of the East Gondwana margin. The lack of similar trends towards more radiogenic εNd values over time in Devonian–Carboniferous granites in western Marie Byrd Land and north Victoria Land (Fig. 4.15a) and the paucity of associated mafic rocks does not support a period of back-arc extension in these regions at this time. Therefore, the effects of slab rollback and lithospheric extension may be confined to the Western

Province of New Zealand, which may have occupied a position closer to the subduction trench in the Devonian–Carboniferous (Veevers, 2012).

Overall, the changes in isotope composition and source characteristics recorded by arc-related granitoids from eastern Australia to north Victoria Land to the Western Province of New Zealand and Marie Byrd Land may relate to an along-arc change from the typical extensional accretionary mode in eastern Australia to a neutral or an advancing mode in West Antarctica, and to an across-arc difference in distance from the trench between the New Zealand fragments of Zealandia and western Marie Byrd Land.

4.10. Conclusions

The new U–Pb ages and Hf-isotope compositions of detrital zircons from the Swanson Formation and equivalent metasedimentary rocks combined with published data reveals three principal age populations. The largest population comprises Neoproterozoic–Cambrian zircons with evolved Hf isotope values consistent with derivation from reworked Mesoproterozoic crust. These zircons were likely sourced from a region of igneous and metamorphic rocks associated with the Ross–Delamerian Orogen that now lies beneath the East Antarctic ice sheet. A second population of Mesoproterozoic detrital zircons with juvenile Hf isotope values is consistent with derivation from crust, or sedimentary derivatives of crust, similar to the gneiss that outcrops at Haag Nunataks and granite clasts that originated from a Mesoproterozoic orogenic belt located beneath the Antarctic ice sheet. A third population of Paleoproterozoic zircons could have been sourced from Precambrian basement exposed in the central Transantarctic Mountains.

A combination of whole-rock geochemistry, including Nd and Sr isotope data, and zircon U–Pb, Hf and O isotope data from the Ford Granodiorite suite and associated granites and diatexites, combined with whole-rock oxygen isotope data from the Swanson Formation, provides important constraints on the evolution of the Paleozoic crust in western Marie Byrd Land. Zircons from the Ford Granodiorite suite, and from Devonian–Carboniferous granites and diatexites define a short-lived period of magmatism in the Devonian–Carboniferous (375–345 Ma). The Hf and O isotope compositions of zircons from the oldest Ford Granodiorite suite samples are consistent with mixing of a juvenile magma with Swanson Formation in an active arc setting. Isotope values of zircons from the younger members of the Ford Granodiorite suite are also compatible with this petrogenetic scenario but require a larger proportion of Swanson Formation. Alternatively, these younger members may have been derived by anatectic reworking of older members of the Ford Granodiorite suite and mixing with Swanson Formation either en masse or as melts in the deep crust. The Devonian–Carboniferous granites and diatexites from the Fosdick complex represent Ford Granodiorite suite magmas or anatectic melt derived from early-crystallized members of the suite that assimilated Swanson Formation en masse or mixed with anatectic melt derived from the Swanson Formation. The Ford Granodiorite suite and the granites and diatexites do not show the same temporal trends in source compositions recorded by similar-age circum-Pacific granite suites in Eastern Australia, north Victoria Land and the Western Province of New Zealand.

Chapter 5: Behaviour of zircon and monazite during crustal melting

5.1 Abstract

Ages retrieved from accessory minerals in high-grade metamorphic rocks place important constraints on the timing of events and the rates of tectono-metamorphic processes operating in the deep crust. In suprasolidus rocks, the dissolution and growth of zircon and monazite are strongly dependent on the *P–T* conditions of metamorphism and the chemistry and quantity of anatectic melt present. Along a clockwise *P–T* path, prograde heating above the solidus leads to episodic melt loss and changes in melt chemistry that have important implications for the dissolution and growth of zircon and monazite. In this study, phase equilibria modelling of open-system melting is coupled with experimental data on zircon and monazite solubility to evaluate the stability of these minerals at suprasolidus conditions along several schematic clockwise *P–T* paths. In migmatite melanosomes and residual granulites, some zircon is expected to survive heating to peak temperature and subsequent isothermal decompression, whereas monazite may be completely consumed, consistent with the observation that inherited cores are less common in monazite than in zircon. After decompression, during cooling to the solidus, new zircon and monazite growth from melt trapped along grain boundaries in melanosomes and residual granulites is expected to be limited. By contrast, leucosomes in migmatites and anatectic granites are predicted to contain mostly newly-formed zircon and monazite with minimal inherited components, unless significant entrainment of these minerals from the source occurs. The preservation of cores inside newly-formed zircon,

as observed in many anatectic granites, demonstrates that segregation, ascent and emplacement is commonly fast enough to limit dissolution of these inherited grains.

5.2 Introduction

Accessory minerals such as zircon and monazite are important in studies of high-grade migmatites and residual granulites, and related anatectic granites because they may be dated using isotopic or chemical methods. Thus, these minerals have the potential to place temporal constraints on metamorphic *P–T* paths retrieved from migmatites and residual granulites, especially if accessory mineral growth can be tied to a particular part of the *P–T* path (Rubatto 2002; Harley et al. 2007; Williams et al. 2007; Kelsey et al. 2008; Reno et al. 2012; Korhonen et al. 2013a), and to provide crystallization ages for anatectic granites. For example, sometimes it is possible to link ages obtained from accessory minerals to specific metamorphic reactions or to particular co-existing minerals (Degeling et al. 2001; Hermann and Rubatto 2003; Whitehouse and Platt 2003; Rubatto et al. 2006; Harley and Kelly 2007; Harley et al. 2007; Baldwin and Brown 2008; Rubatto et al. 2013), which may enable constraints to be placed on rates of orogenic processes as well as the timing of events. However, our knowledge of the dissolution and growth of zircon and monazite in suprasolidus crust in relation to the *P–T* evolution and the changing bulk chemistry during melting is limited to a few pioneering studies (Kelsey et al. 2008; Spear and Pyle 2010; Kelsey and Powell 2011; Skrzypek et al. 2012). In particular, the role of open-system melting and melt loss on the stability of accessory minerals in suprasolidus rocks has received insufficient attention given that the ages

obtained from these minerals are integral to documenting the nature and timescales of tectono-metamorphic processes in the residual deep crust.

Partial melting of the deep crust and drainage of melt to the shallow crust is the principal mechanism by which the continental crust is chemically differentiated into a refractory lower portion and a complementary enriched upper portion. At the local scale, suprasolidus crust may behave as a closed (melt is retained) or open (melt is drained) or conditionally open (cyclic closed and open) system (Handy et al. 2001; Brown 2013). Melt extraction in conditionally open systems is expected to occur when the melt connectivity transition is reached at *c.* 7 vol.% melt (Rosenberg and Handy 2005). Relatively fertile clastic metasedimentary rocks may produce up to 50–60 vol.% melt at 900 °C in granulite and ultrahigh temperature (UHT) metamorphic terrains (Clemens 2006). Therefore, such rocks are expected to experience multiple melt loss events during a single orogenic cycle (Brown 2013). As melt is drained from the source, the bulk composition becomes progressively more residual and the chemistry of the melt in equilibrium with the residue evolves accordingly.

The behaviour of zircon and monazite under suprasolidus conditions is complex, being controlled by both physical and chemical factors (Brown 2013). These factors include: the microstructural location of the accessory minerals, whether they occur along grain boundaries or sequestered as inclusions, and the stability of the major rock-forming minerals if they occur as inclusions (Watson et al. 1989; Bea et al. 2006); the kinetics of dissolution (Bea 1996; Watson 1996); the extent of anatexis (Rubatto et al. 2001); the chemistry of the melt (Watson and Harrison 1983; Rapp et al. 1987; Stepanov et al. 2012); the *P–T* path (Roberts and Finger 1997); and, the rate of melt extraction (Watt et

al. 1996). A further complication is the crystal–size distribution and the role that Ostwald ripening might play during the prograde evolution (Nemchin and Bodorkos 2000; Nemchin et al. 2001). In this study, phase equilibria modelling of pelite and greywacke along four schematic *P–T* paths is coupled with experimental data for zircon and monazite solubility to evaluate the consequences of melt loss on the dissolution and growth of zircon and monazite in residual source rocks, extending the discussion begun by Kelsey et al. (2008).

5.3 Methods

5.3.1 Phase equilibria modelling

The *P–T* conditions at which fluid-absent melting occurs and the quantity and the chemistry of melt produced from clastic metasedimentary rocks during closed system melting may be determined by forward modelling using *P–T* pseudosections constructed for the initial bulk chemical compositions (e.g. White et al. 2007; Johnson et al. 2008; Brown and Korhonen 2009). In addition, by using a series of *P–T* pseudosections calculated for bulk chemical compositions modified by a succession of melt loss events, the effects of melt loss on future melt production, total melt production, and melt chemistry on the preservation of peritectic mineral assemblages may be evaluated for open system behaviour (White and Powell 2002; Brown and Korhonen 2009; Korhonen et al. 2010a; Yakymchuk and Brown 2014a).

In this study, calculations were performed using THERMOCALC v.3.35 (Powell and Holland 1988) and the internally consistent dataset of Holland and Powell (1998) together with the most recent activity–composition (a–x) models for the phases of

interest, which are listed in Yakymchuk and Brown (2014a). Modelling was undertaken in the Na_2O–CaO–K_2O–FeO–MgO–Al_2O_3–SiO_2–H_2O–TiO_2–Fe_2O_3 chemical system, which is currently the most realistic system to investigate melting for clastic metasedimentary rocks (White et al. 2007). Two rock types were considered: an average amphibolite facies pelite (Ague 1991) and an average passive margin greywacke (Yakymchuk and Brown 2014a). The amount of water in the modelled compositions for the pelite and the greywacke was adjusted so that there is minimal (<0.1 mol%) free H2O at the solidus at 1.2 GPa, which is consistent with fluid-absent conditions above the solidus (White and Powell 2002; White 2003; White et al. 2005). If the modelled prograde path crossed the solidus at lower or higher pressures, the quantity of melt produced will be slightly overestimated and underestimated, respectively. The chemistry and quantity of melt expected at *P–T* was determined using the 'read rbi' script in THERMOCALC.

In this study, the range of pressures and temperatures modelled is typical of those retrieved from migmatites and high-pressure granulites in orogenic belts (e.g. Harley 1998; Teyssier and Whitney 2002; O'Brien and Rötzler 2003). After prograde heating to the metamorphic peak, near-isothermal decompression is commonly documented in migmatite–gneiss domes (Whitney et al. 2013) and in granulites (Harley 1998), consistent with clockwise *P–T* paths. Furthermore, many granulites and ultrahigh-temperature metamorphic rocks record close-to-isobaric cooling after decompression (Harley 1998).

Crustal melting is modelled for each of the two rock types along four schematic clockwise *P–T* paths as shown in Fig. 5.1, which is a closed system *P–T* phase diagram

simplified from the *P–T* pseudosections in Yakymchuk and Brown (2014a). However, during orogenesis melt drainage from the anatectic zone to shallow crustal levels is to be expected (Brown 2013). Thus, this study concentrates on open system crustal melting. Open system melting for the same four *P–T* paths is modelled as follows. At each point along the *P–T* path where the melt fraction reaches the melt connectivity transition of 7 mol.% (*c*. 7 vol% in nature), six-sevenths of the melt produced is removed from the bulk chemical composition, leaving one-seventh (*c*. 1 vol.% in nature) that is assumed to have been retained on grain boundaries (Yakymchuk and Brown 2014a). After a melt loss event, the residual bulk chemical composition is used to calculate a new *P–T* pseudosection that remains valid until the next melt loss event is reached. Figures 5.2 and 5.3 are *P–T* phase diagrams for open-system melting simplified from the pseudosections in Yakymchuk and Brown (2014a), this study also includes a discussion of the general effects of melt loss on melt production and tectonics.

Three of the four *P–T* paths modelled for open system behaviour comprise three segments: an isobaric heating segment at 1.2 GPa beginning at the solidus and extending to the peak temperature, an isothermal decompression segment from 1.2 to 0.7 or 0.4 GPa at three different peak temperatures (750 °C, 820 °C, 890 °C), and an isobaric cooling segment starting at 0.7 or 0.4 GPa and extending to the solidus (Fig. 5.2). These peak temperatures were chosen so that the *P–T* paths cross the main hydrate-breakdown melting reactions typically encountered by pelites and greywackes during exhumation after collisional orogenesis (cf. Yakymchuk and Brown 2014a). The fourth *P–T* path modelled is a clockwise *P–T* path that reaches peak high-pressure granulite facies conditions of 1.8 GPa at 860 °C after prograde heating from the solidus at 1.2 GPa and

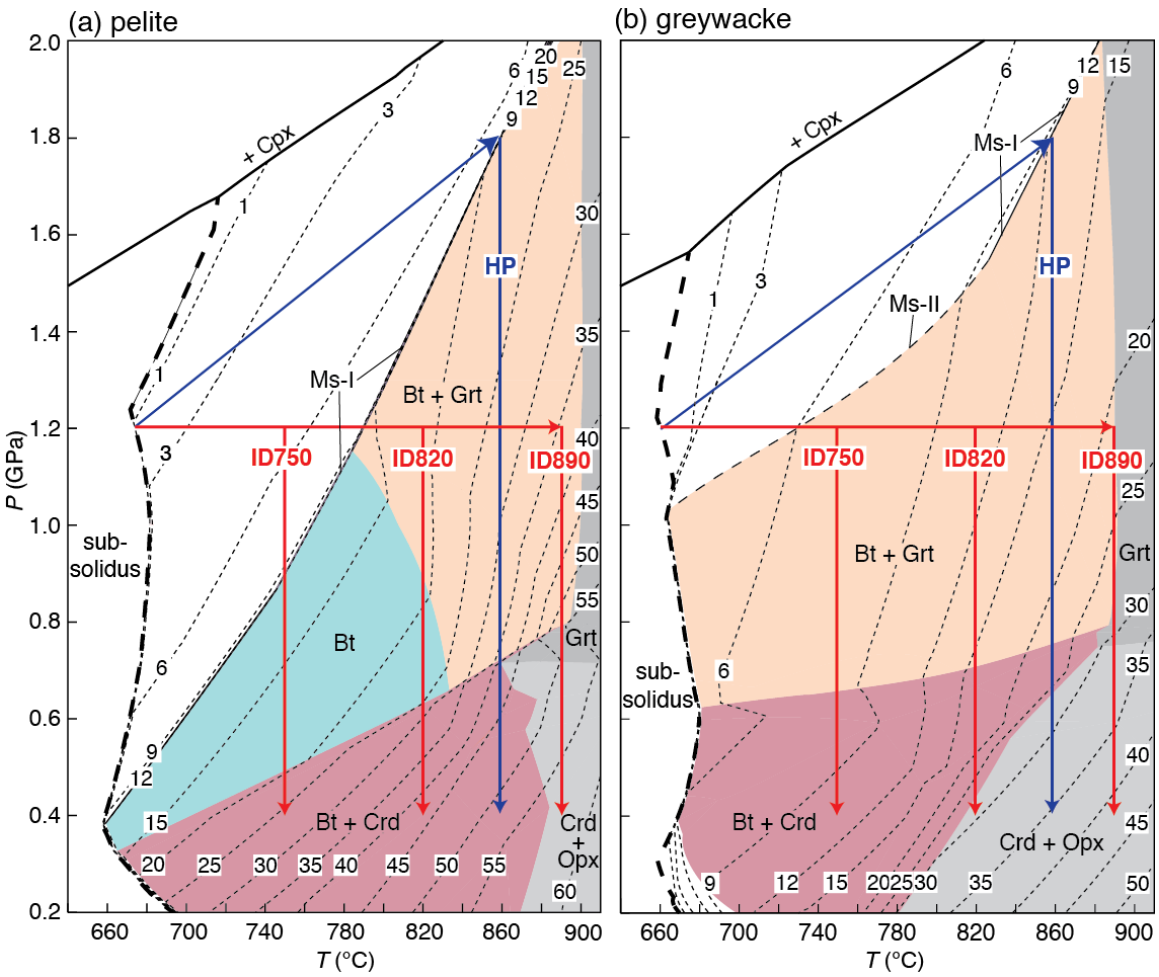

Fig. 5.1. Simplified pressure (P)–temperature (T) phase diagrams calculated for closed system melting for: (a) an average amphibolite-facies pelite, and (b) an average passive margin greywacke (modified from Yakymchuk and Brown 2014a). Mineral abbreviations are: Bt–biotite, Cpx–clinopyroxene, Crd–cordierite, Grt–garnet, Ms–muscovite, and Opx–orthopyroxene. Shaded fields are the principal stability fields of the major rock-forming ferromagnesian minerals. Lines 'Ms–I' and 'Ms–II' represent the boundaries for the muscovite to K-feldspar reaction and the K-feldspar-absent muscovite-out reaction, respectively. The thick dashed line is the fluid-present solidus and the short dashed lines represent isopleths of mol.% melt (approximately equivalent to vol.% melt in nature). Four schematic *P–T* paths are shown and are discussed in the text. These diagrams are derived from the fully labelled pseudosections presented in Yakymchuk and Brown (2014a). Most melt mol.% isopleths have positive slopes, which indicates that melt is produced during heating and decompression.

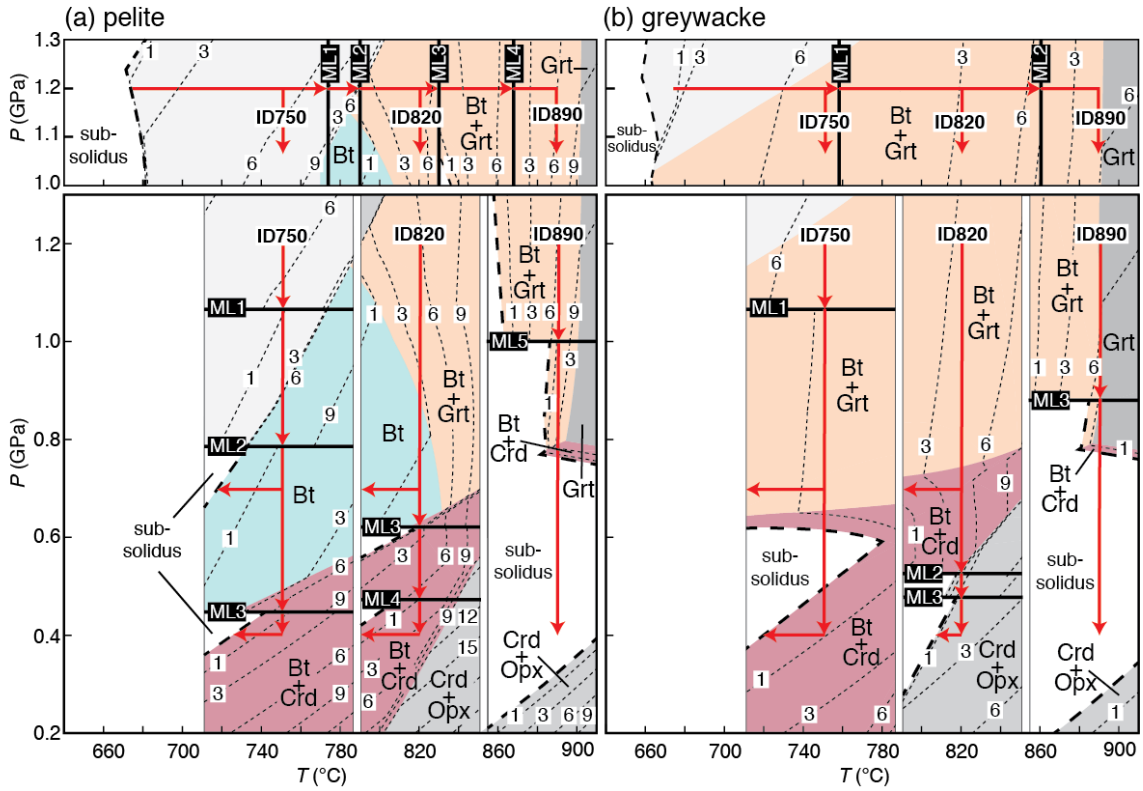

Fig. 5.2. Composite *P–T* diagrams for conditionally open-system melting for each of the different isobaric heating–isothermal decompression *P–T* paths (paths ID750, ID820, and ID890 in Fig. 5.1) modelled for (a) pelite and (b) greywacke. Also labelled are isobaric cooling paths at 0.7 and 0.4 GPa from the decompression segment of the *P–T* path to the solidus for paths ID750 and ID820. Each diagram comprises a series of panels that are arranged from low to high temperature and stacked from high to low pressure calculated for incrementally melt-depleted bulk compositions along each *P–T* path. The heavy dashed line is the fluid-absent solidus and the short dashed lines represent isopleths of mol.% melt (approximately equivalent to vol.% melt in nature). Each panel shows melt mol.% isopleths and the stability field of major ferromagnesian minerals. Melt loss (ML) events are located on the seams between the panels. After a melt loss event, the solidus is displaced to higher temperatures and melt isopleths generally become steeper at pressures above the stability field of cordierite. Therefore, the amount of melt produced during decompression in a conditionally open system is less than that for a closed system (Fig. 5.1).

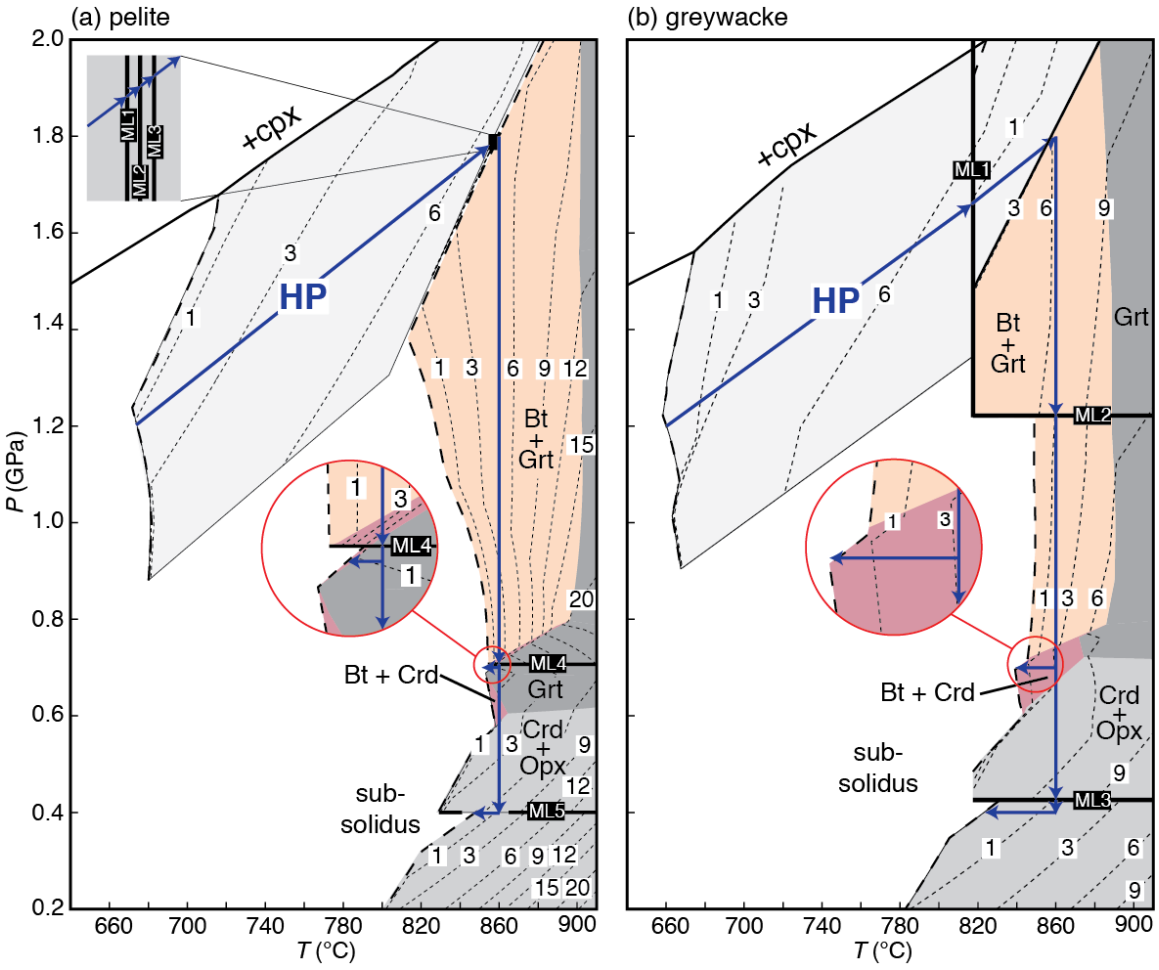

Fig. 5.3. Composite *P–T* diagrams for conditionally open-system melting for the high pressure *P–T* path (path HP in Fig. 5.1) calculated for (a) pelite and (b) greywacke. Also labelled are isobaric cooling paths at 0.7 and 0.4 GPa from the decompression segment of the *P–T* path to the solidus. Each diagram comprises a series of panels arranged low to high temperature and stacked from high to low pressure calculated for incrementally melt-depleted bulk compositions. The heavy dashed line is the fluid-absent solidus and the short dashed lines represent isopleths of mol.% melt (approximately equivalent to vol.% melt in nature). Each panel shows melt mol.% isopleths and the stability field of major ferromagnesian minerals. Melt loss (ML) events are located on the seams between the panels. Note that the trajectory of the decompression path is nearly parallel to the melt isopleths for both rock types, which indicates relatively little melt is produced during decompression. Most melt is generated during heating, although melt is also produced along the low-pressure segment of the decompression path within the stability field of cordierite at $P < 0.7$ GPa.

before isothermal decompression and isobaric cooling to the solidus at 0.7 or 0.4 GPa (Fig. 5.3).

5.3.2 Zr and LREE concentrations of the source and melt

The amount of zircon and monazite dissolution during crustal melting is dependent on the bulk rock concentrations of zirconium (Zr) and light rare-earth elements (LREE) in the source, and the concentration of these elements required to saturate the anatectic melt assuming that the melt does not drain from the system prior to saturation. The solubility of zircon and monazite varies with *P–T* and the major element chemistry of the melt. In this study, the major element chemistry of the melt along each *P–T* path is retrieved from THERMOCALC and combined with solubility equations for zircon and monazite.

For zircon, we use the solubility equation of Boehnke et al. (2013). Using the zircon solubility equation of Kelsey et al. (2008), which is based on the experimental data of Harrison and Watson (1983), produces an indistinguishable difference in the zircon dissolution plots discussed below. For monazite there are two alternate solubility equations that yield different rates of dissolution. Kelsey et al. (2008) presented a solubility equation for monazite based on the experimental data of Rapp et al. (1987). More recently, Stepanov et al. (2012) developed a solubility equation for monazite that is more strongly dependent on temperature and the amount of water in the anatectic melt than the equation of Kelsey et al. (2008). Based on their new solubility equation, Stepanov et al. (2012) argued that unrealistically high LREE concentrations in melt were predicted by the equation of Kelsey et al. (2008) and they suggested that the conclusions

of Kelsey et al. (2008) with respect to differences in the solubility of zircon and monazite require re-evaluation. Therefore, in this study we have used the monazite solubility equations of both Kelsey et al. (2008) and Stepanov et al. (2012) to calculate the amount of monazite dissolution along the *P–T* paths. This allows for a comparison of both sets of results in relation to evidence from residual migmatites and granulites.

The concentrations of Zr and LREE in pelites and greywackes are broadly similar, with Zr of *c*. 200 ppm and LREE of 150–200 ppm for pelites and Zr of 100–200 ppm and LREE of 50–150 ppm for greywackes (Taylor and McLennan 1985). Metasedimentary migmatites generally have Zr concentrations of 80–270 ppm and LREE concentrations of 30–300 ppm (e.g. Sawyer 1986; Solar and Brown 2001; Guernina and Sawyer 2003; Korhonen et al. 2010b), although Zr concentrations are >300 ppm in some kinzigites and stronalites of the Ivrea zone (Bea and Montero 1999). Based on these data, we use initial values of 50, 150 and 300 ppm for both Zr and LREE, which encompass the range of concentrations of most pelites, greywackes and metasedimentary migmatites. In this study, the bulk chemical composition of the system prior to any melt loss is referred to as the protolith composition. After one or more melt loss events the resultant melt-depleted bulk chemical composition is referred to as the source composition.

5.3.3 Zircon and monazite dissolution

The amount of accessory mineral dissolution is calculated following the method of Kelsey et al. (2008). First, the saturation concentrations of the melt in ppm are calculated as follows. The major element concentration of the anatectic melt at *P–T* is retrieved from THERMOCALC. This information is combined with: (1) the solubility

equations of Boehnke et al. (2013), Kelsey et al. (2008) and Stepanov et al. (2012), and (2) stoichiometric concentrations of Zr in zircon (497 664 ppm Zr) and LREE in monazite (566 794 ppm LREE) to determine the saturation concentrations of Zr and LREE in ppm (Kelsey et al. 2008). These 'initial saturation concentrations' do not account for the proportion of anatectic melt nor the bulk rock concentrations of Zr and LREE.

Second, the initial saturation concentrations of Zr or LREE (ppm) are multiplied by the proportion of anatectic melt (retrieved from THERMOCALC) to arrive at concentrations in ppm that are required to saturate the melt in the equilibration volume of the rock. Finally, these values are divided by the bulk rock chemical concentrations of Zr and LREE (50, 150 and 300 ppm). The result is the proportion of zircon or monazite dissolution required to saturate the anatectic melt in Zr and LREE in the equilibration volume of the rock. This value is subtracted from 100% and the results are reported as percent remaining relative to the amount of zircon and monazite existing at the fluid-present solidus for each *P–T* path.

At each melt loss event, the percentage of subsequent zircon and monazite dissolution is normalized to the percentage of zircon and monazite present immediately prior to the melt loss event. Therefore, calculations yield the proportion of zircon or monazite remaining along the *P–T* path relative to the amount of zircon or monazite originally existing at the fluid-present solidus.

5.4 Results

5.4.1 Melt production in an undrained (closed) system

Figure 5.1a and 5.1b show the stability field of major ferromagnesian minerals and the amount of melt produced across the range of *P–T* modelled. For the pelite, the fluid-present solidus is located at 660–680 °C from 0.4 to 1.2 GPa but at higher temperatures at $P < 0.4$ GPa and $P > 1.2$ GPa. For the greywacke, the fluid-present solidus is located at c. 670 °C up to 1.5 GPa. For both the pelite and the greywacke, garnet is stable at high pressures and at high temperatures at $P > 0.6$ GPa. Cordierite is stable at $P < 0.3$–0.8 GPa with increasing temperature for the pelite (Fig. 5.1a) and at $P < 0.6$–0.7 GPa with increasing temperature for the greywacke (Fig. 5.1b). Orthopyroxene is stable at $P < 0.7$ GPa at $T > 840$ °C for the pelite and at $P < 0.7$ GPa at temperatures >760 °C for the greywacke. For both rock types, biotite is unstable above 890–900 °C at $P > 0.7$ GPa and stable to lower T at $P < 0.7$ GPa. The *P–T* field of interest is bounded by the stability of clinopyroxene at high P for both rock types.

The amount of melt present at *P–T* is shown in Fig. 5.1 by melt mol.% isopleths. Melt mol.% isopleths are generally steep in the stability field of garnet and have shallower slopes in the stability field of cordierite. The melt isopleths for the pelite (Fig. 5.1a) are more closely spaced than those for the greywacke (Fig. 5.1b).

For the pelite, the total amount of melt produced along the *P–T* paths ID750, ID820, ID890 and HP is 26, 43, 58 and 52 mol.%, respectively (Fig. 1a). For the greywacke, the total amount of melt produced along the *P–T* paths ID750, ID820, ID890 and HP is 11, 29, 42 and 35 mol.%, respectively (Fig. 5.1b). However, as discussed

above, this is unrealistic and melt is expected to drain from the system at the melt connectivity transition in nature.

5.4.2 Zircon and monazite behaviour in an undrained (closed) system

For closed system behaviour, the amount of zircon and monazite dissolution along *P–T* paths ID750, ID820 and ID890 is shown in Fig. 5.4 (redrawn from data in Kelsey et al. 2008 for the metapelite and psammite compositions used in their work). In an undrained system, assuming bulk rock concentrations of 200 ppm Zr and 500 ppm LREE, for the pressure range of interest here (1.2 to 0.4 GPa), the dissolution contours for zircon and monazite plot with moderate to steep positive slopes in a *P–T* diagram for both the metapelite and psammite.

For an isobaric prograde evolution at 1.2 GPa, zircon persists to ultrahigh temperatures in both the metapelite and the psammite (Fig. 5.4a, c). Only during decompression along the ID890 path is zircon completely consumed at 0.6 GPa for the metapelite and 0.8 GPa for the psammite. In contrast, during isobaric heating, complete dissolution of monazite is predicted to occur within 120 °C of the fluid-present solidus for the metapelite (Fig. 5.4b) and within 180 °C for the psammite (Fig. 5.4d). During decompression, for the metapelite, all remaining monazite is consumed along path ID750 (Fig. 5.4c). For the psammite, c. 10% monazite survives after decompression along path ID750 (Fig. 5.4d). The dissolution contours for both zircon and monazite are more closely spaced at high temperature, which suggests that dissolution of these minerals is non-linear and increases with temperature. Since the system is undrained, after

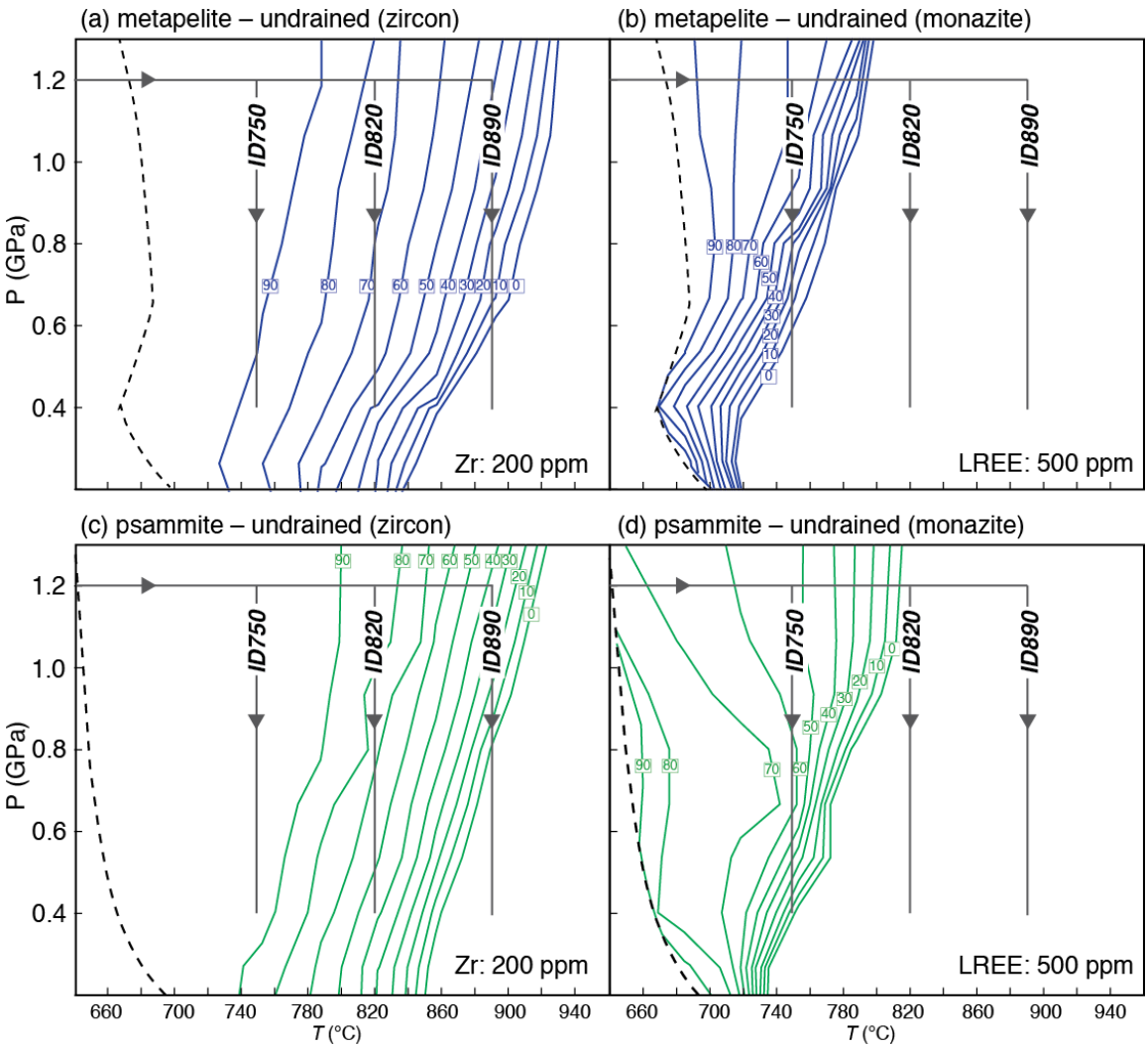

Fig. 5.4. *P–T* diagrams to show the stability of zircon and monazite during closed system partial melting (modified from Kelsey et al. 2008). Contours represent the proportion of zircon or monazite remaining. The heavy dashed line is the fluid-present solidus. In an undrained system, monazite is expected to be mostly or completely consumed during the *P–T* evolution. With the exception of the highest-temperature *P–T* path (ID890), most zircon is expected to survive.

decompression both zircon and monazite will crystallize during cooling to the fluid-present solidus, as discussed by Kelsey et al. (2008).

5.4.3 Melt production in a drained (conditionally open) system

The *P–T* phase diagrams in Fig. 5.1 are only appropriate for evaluating the amount of melt produced up to the melt connectivity transition at 7 mol.%. *P–T* phase diagrams for progressively melt-depleted compositions are presented in Figs 5.2a and 5.3a for the pelite and Figs 5.2b and 5.3b for the greywacke. Each diagram comprises a series of panels that are calculated for incrementally melt-depleted bulk compositions along each *P–T* path. Each panel shows melt mol.% isopleths and the stability field of major ferromagnesian minerals. Melt loss events are located as the seams between the panels. For the isobaric heating segment of the moderate pressure *P–T* paths, phase diagram panels are stacked from low to high temperature, representing the initial protolith compositions and progressively more residual source compositions following melt loss events (Figs 5.2a, b). For the decompression segment of the moderate pressure *P–T* paths phase diagram panels are stacked from high to low pressure, representing progressively more residual source compositions following melt loss events (Figs 5.2a, b). For the high-pressure *P–T* path for both rock types, the heating segment is shown by the panel in the low T–high *P* portion of the diagrams (Figs 5.3a, b) and the isothermal decompression segment consists of a series of panels stacked from high to low pressure on the high *T* portion of the diagrams (Figs 5.3a, b).

Melt mol.% isopleths are steeper for residual compositions compared with the original undrained bulk compositions (compare Fig. 5.1 with Figs 5.2 and 5.3). In some

cases melt isopleths are negatively sloping for residual compositions (e.g. the pelite ID820 path in Fig. 5.2a), which indicates that decompression across these isopleths crystallizes melt. For the pelite and greywacke, the ID890 path crosses the solidus at c. 0.8 GPa. For the greywacke, the ID750 crosses the solidus at 0.6 GPa and re-crosses it at 0.5 GPa due to the up temperature kink in the solidus (Fig. 5.2b).

The amount of melt generated along each *P–T* path for the drained situation is significantly less than the melt produced for the undrained situation. For the pelite in a drained system, the total amount of melt produced along the *P–T* paths ID750, ID820, ID890 and HP is 20, 28, 30 and 31 mol.%, respectively, which is 6–28 mol.% less than the undrained situation (Yakymchuk and Brown 2014a). For the greywacke in a drained system, the total amount of melt produced along the *P–T* paths ID750, ID820, ID890 and HP is 8, 20, 18 and 19 mol.%, respectively, which is 3–24 mol.% less than the undrained situation (Yakymchuk and Brown 2014a).

5.4.4 Zircon and monazite behaviour in a drained (conditionally open) system

The amounts of zircon and monazite dissolution are plotted along the corresponding *P–T* path segments, as summarized in Figs 5.5a and 5.6a for the pelite and Figs 5.7a and 5.8a for the greywacke. These amounts are shown as plots of % remaining in Figs 5.5b–d, 5.6b–d for the pelite and Figs 5.7b–d, 5.8b–d for the greywacke for the range of starting concentrations of Zr and LREE (50, 150 and 300 ppm). In addition, the proportions of new zircon and monazite growth during isobaric cooling to the solidus at 0.7 and 0.4 GPa, normalized to the amount of zircon and monazite present at peak T, are shown in Fig. 5.9 for the pelite and Fig. 5.10 for the greywacke.

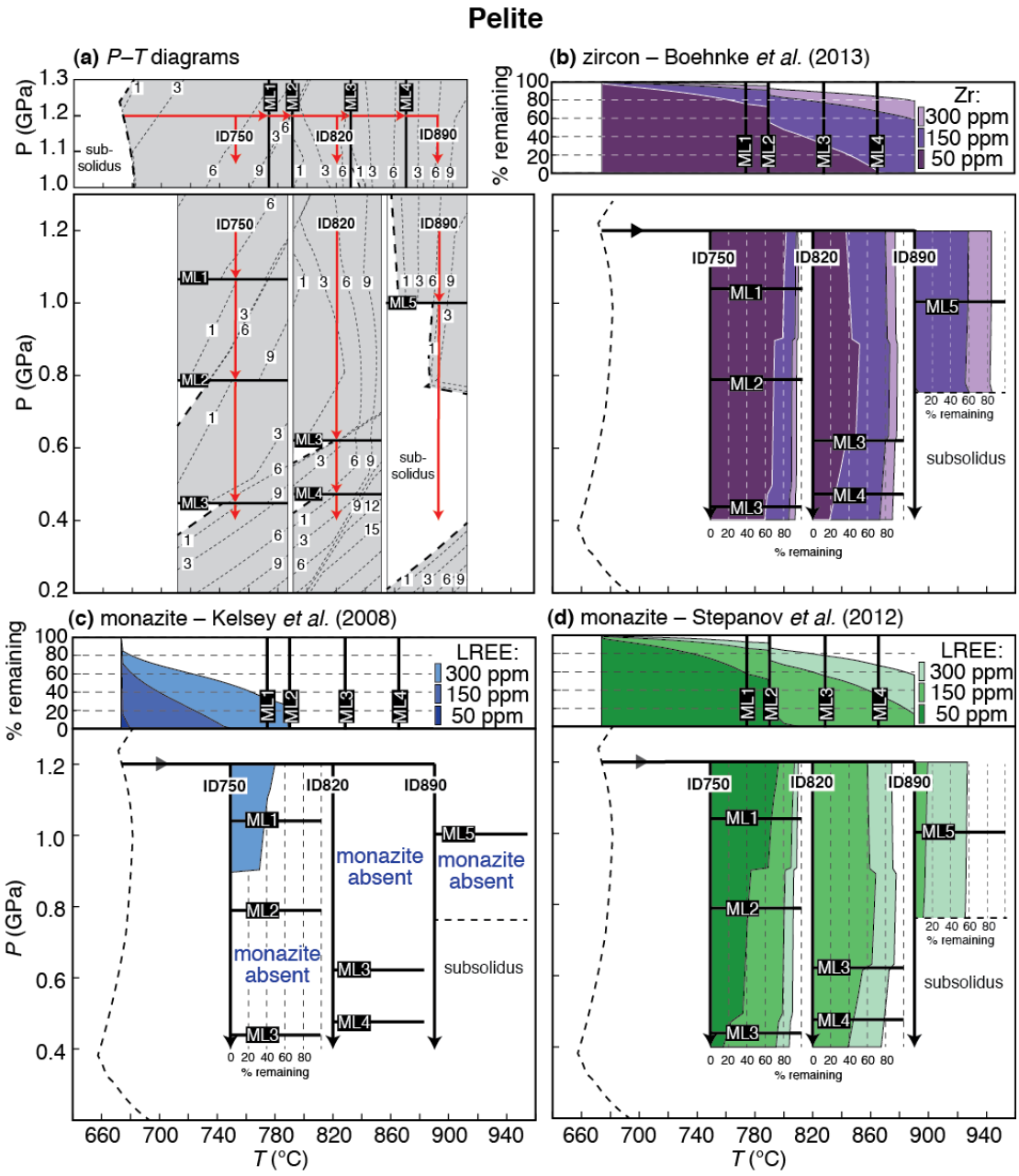

Fig. 5.5. (a) Composite *P–T* diagrams for conditionally open-system melting of a pelite along the moderate pressure *P–T* paths (paths ID750, ID820, and ID890 in Fig. 5.1) simplified from Fig. 5.2a. (b–d) *P–T* diagrams of the calculated proportion of zircon (b) and monazite (c, d) remaining during open-system melting of a pelite along the moderate pressure *P–T* paths. Results are presented from the monazite solubility equations of Kelsey et al. (2008) in (c) and Stepanov et al. (2012) in (d). Three initial concentrations (50, 150, and 300 ppm) were modelled. Note that the "% remaining" fields for the lower Zr and LREE concentrations cover portions of the fields for the higher concentrations. The dashed line is the fluid-present solidus. Most zircon is expected to survive the *P–T* evolution, except for protoliths with very low (50 ppm) initial Zr concentrations. Depending on the solubility equation used, monazite is expected to be completely (c) or mostly consumed (d) during the *P–T* evolution.

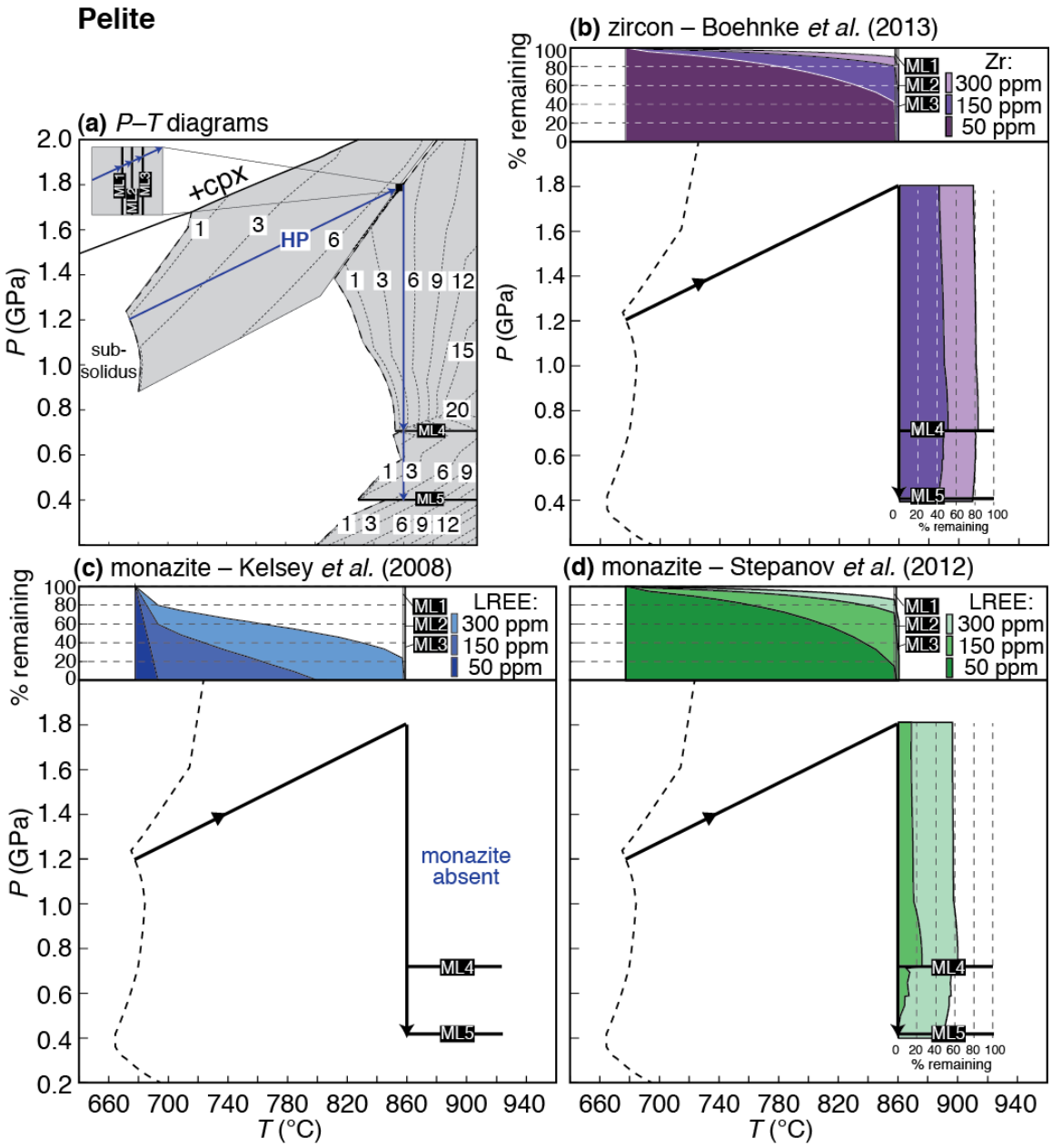

Fig. 5.6. (a) Composite *P–T* diagram for conditionally open-system melting of a pelite along the high pressure *P–T* path (path HP in Fig. 5.1) simplified from Fig. 5.3a. (b–d) *P–T* diagrams of the calculated proportion of zircon (b) and monazite (c, d) remaining during open-system melting of a pelite along the high pressure *P–T* path. Results are presented from the monazite solubility equations of Kelsey et al. (2008) in (c) and Stepanov et al. (2012) in (d). Three initial concentrations (50, 150, and 300 ppm) were modelled. Note that the "% remaining" fields for the lower Zr and LREE concentrations cover portions of the fields for the higher concentrations. The dashed line is the fluid-present solidus. Some zircon is expected to survive decompression, except for protoliths with low initial Zr concentrations, whereas monazite is expected to be mostly or completely consumed.

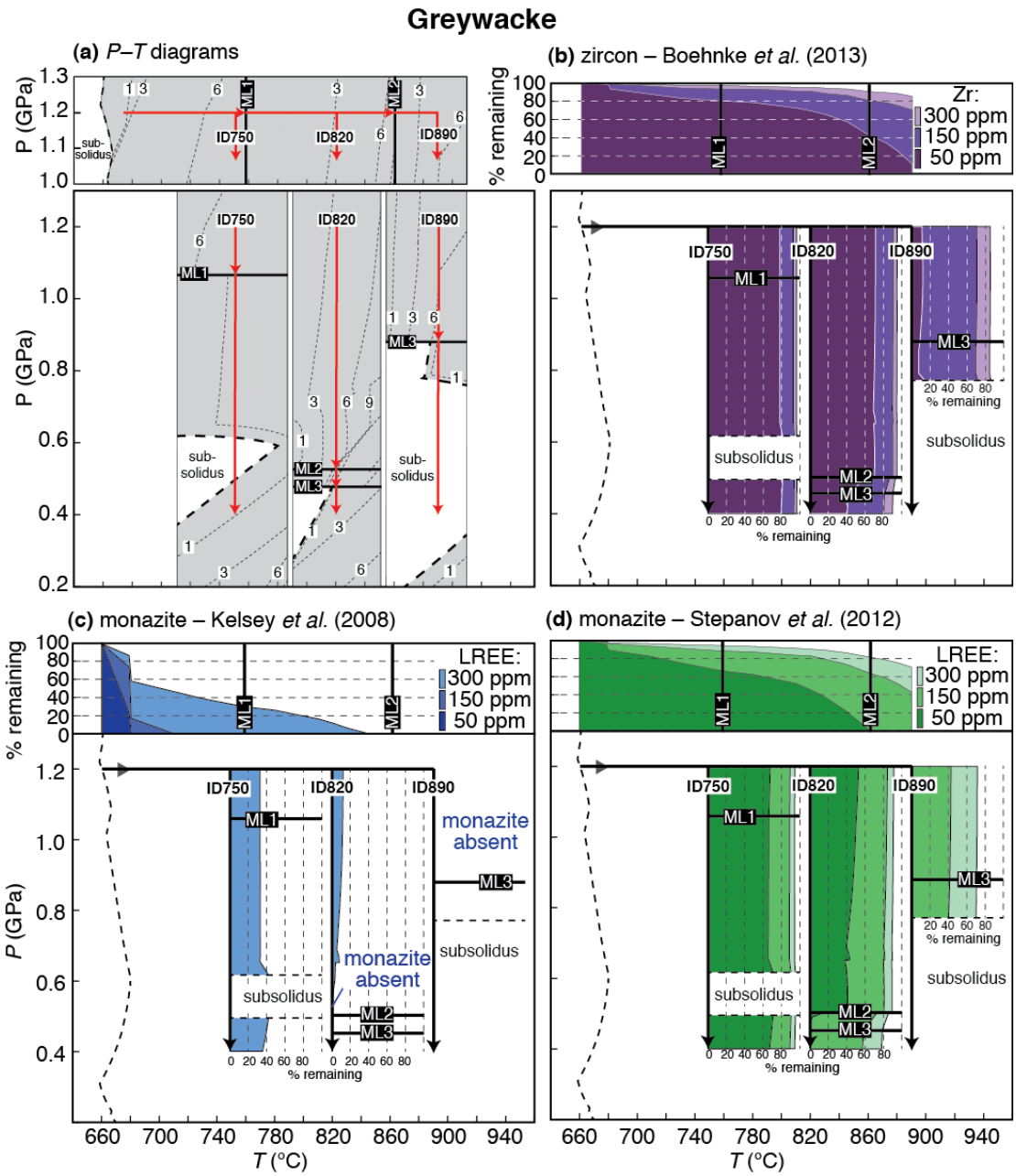

Fig. 5.7. (a) Composite *P–T* diagrams for conditionally open-system melting of a greywacke along the moderate pressure *P–T* paths (paths ID750, ID820, and ID890 in Fig. 5.1) simplified from Fig. 5.2b. (b–d) *P–T* diagrams of the calculated proportion of zircon (b) and monazite (c, d) remaining during open-system melting of a greywacke along the moderate pressure *P–T* paths. Results are presented from the monazite solubility equations of Kelsey et al. (2008) in (c) and Stepanov et al. (2012) in (d). Three initial concentrations (50, 150, and 300 ppm) were modelled. Note that the "% remaining" fields for the lower Zr and LREE concentrations cover portions of the fields for the higher concentrations. The dashed line is the fluid-present solidus. Except for protoliths with low initial Zr concentrations (50 ppm), most zircon is expected to survive the *P–T* evolution, whereas proportionally more monazite dissolution is predicted for higher-temperature *P–T* paths.

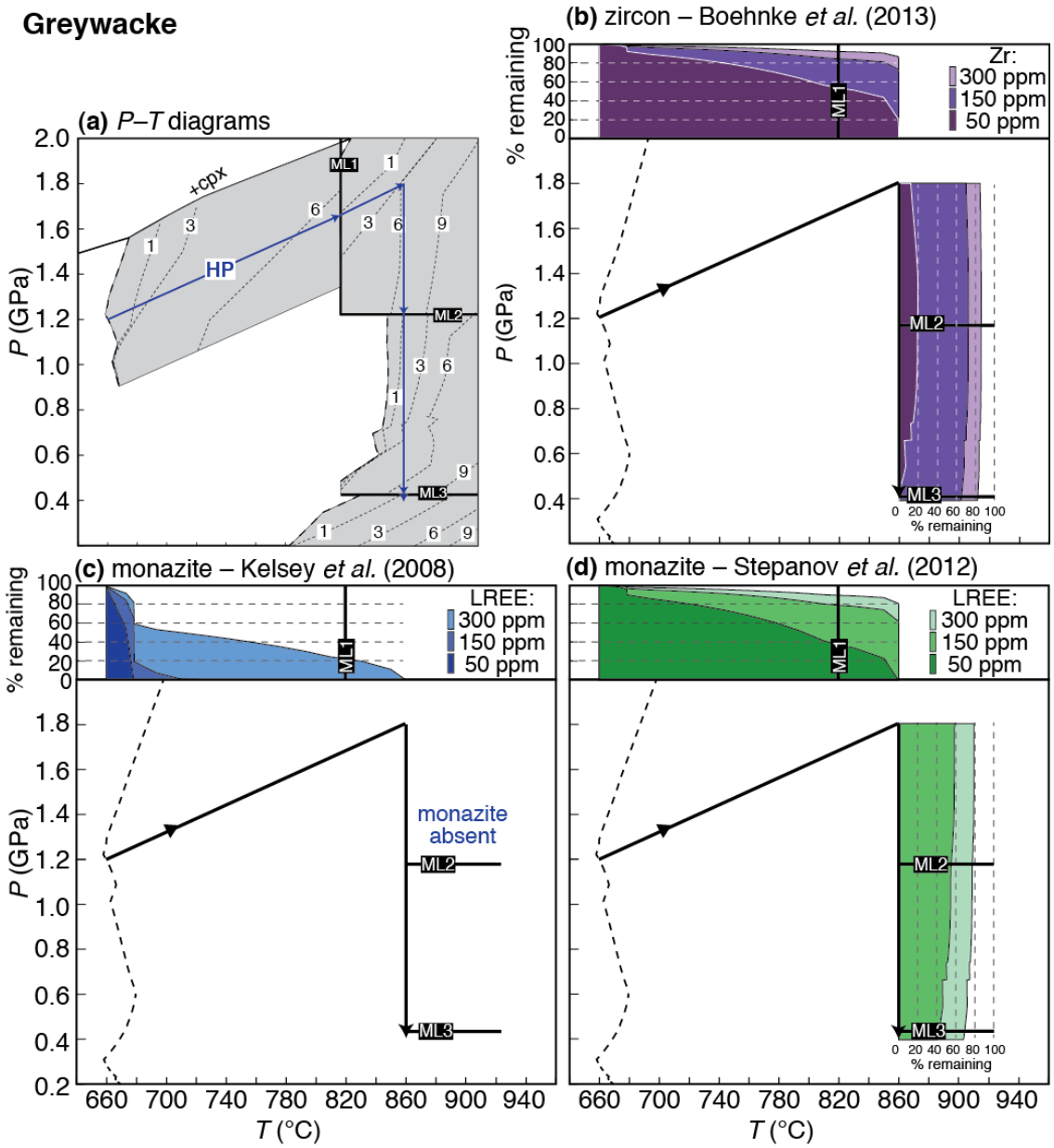

Fig. 5.8. (a) Composite *P–T* diagram for conditionally open-system melting of a greywacke along the high pressure *P–T* path (path HP in Fig. 5.1) simplified from Fig. 5.3b. (b–d) *P–T* diagrams of the calculated proportion of zircon (b) and monazite (c, d) remaining during open-system melting of a greywacke along the high pressure *P–T* path. Results are presented from the monazite solubility equations of Kelsey et al. (2008) in (c) and Stepanov et al. (2012) in (d). Three initial concentrations (50, 150, and 300 ppm) were modelled. Note that the "% remaining" fields for the lower Zr and LREE concentrations cover portions of the fields for the higher concentrations. The dashed line is the fluid-present solidus. Most zircon is expected to survive heating and decompression, except for protoliths with low initial Zr concentrations, whereas monazite is predicted to be mostly consumed, except for protoliths with high initial LREE concentrations.

Some zircon is expected to survive heating and decompression for initial Zr concentrations of 150 and 300 ppm for both the pelite (Figs 5.5b, 5.6b) and greywacke (Figs 5.7b, 5.8b). For pelite with an initial Zr concentration of 150 ppm, along paths ID750, ID820, ID890 and HP the amount of zircon remaining at the end of each path is 87, 73, 59, and 40%, respectively. For a greywacke with an initial Zr concentration of 150 ppm, along paths ID750, ID820, ID890 and HP the amount of zircon remaining at the end of each path is 93, 80, 71, and 65%, respectively. For lower initial concentrations of Zr (50 ppm), the amount of zircon remaining is much less and is completely consumed along paths ID890 and HP for the pelite and path HP for the greywacke (Figs 5.5b, 5.6b, 5.8b).

Using the monazite solubility equation of Kelsey et al. (2008) monazite is predicted to be completely consumed along the low temperature part of the prograde segment of most *P–T* paths modelled. For an initial LREE concentration of 150 ppm, during isobaric heating monazite is completely consumed at 750 °C for the pelite (Fig. 5.5c) and at 710 °C for the greywacke (Fig. 5.7c). For the lowest LREE concentration modelled (50 ppm), monazite is completely consumed within a few tens of degrees above the fluid-present solidus (Figs 5.5c, 5.7c). For the highest LREE concentration modelled (300 ppm), only the ID750 path for the greywacke has monazite (35%) that survives decompression (Fig. 5.7c).

The amount of monazite dissolution is significantly less using the solubility equation of Stepanov et al. (2012). In this case, monazite survives heating and high *T* decompression in both the pelite and the greywacke, except for the lowest LREE concentration of 50 ppm. For isobaric heating to 890 °C and an initial LREE

concentration of 150 ppm, 13% monazite remains for the pelite and 43% remains for the greywacke (Figs 5.5d, 5.7d). For pelite with an initial LREE concentration of 150 ppm along paths ID750, ID820, and ID890 the amount of monazite remaining is 71, 39 and 14%, respectively (Fig. 5.5d), whereas monazite is completely consumed during decompression along the HP path (Fig. 5.6d). For the greywacke, the amount of monazite remaining at the end of paths ID750, ID820, ID890 and HP is 89, 57, 41, and 40%, respectively (Figs 5.7d, 5.8d).

During isobaric cooling to the solidus, the amount of new zircon growth in the source varies from <1% to ~32% relative to the residual amount of zircon present in the pelite after isothermal decompression and from <1% to ~52% relative to the residual amount of zircon present in the greywacke (Figs 5.9 and 5.10). Similarly, using the Stepanov et al. (2012) dissolution equation, the amount of new monazite growth ranges

---

Fig. 5.9. Temperature–proportion diagrams for zircon, monazite and melt in pelite during cooling from the decompression segment of the *P–T* path to the solidus. The proportion of new zircon and monazite growth calculated relative to the amount of zircon and monazite present at the beginning of cooling is shown as coloured fields for three protoliths with initial Zr and LREE concentrations of 50, 150, and 300 ppm, respectively. The coloured numbers in the top-right corner of each plot represent the percentage of zircon and monazite at the solidus relative to starting amounts at the fluid-present solidus at the beginning of the *P–T* paths modelled (Figs 5.5 and 5.6). Note that the fields for the higher Zr and LREE concentrations cover portions of the fields for the lower concentrations. The proportion of monazite was calculated using the Stepanov *et al.* (2012) solubility equation. The heavy dashed line represents the amount of melt remaining (scale on the right hand side of each plot). In general, the amount of new zircon and monazite crystallization is small. For protoliths with low initial Zr and LREE concentrations, the proportions of new zircon and monazite relative to the remaining zircon and monazite is greater than in protoliths with higher initial concentrations, but this simply reflects the fact that the proportion of residual zircon and monazite at the end of any *P–T* path is much less for these protoliths.

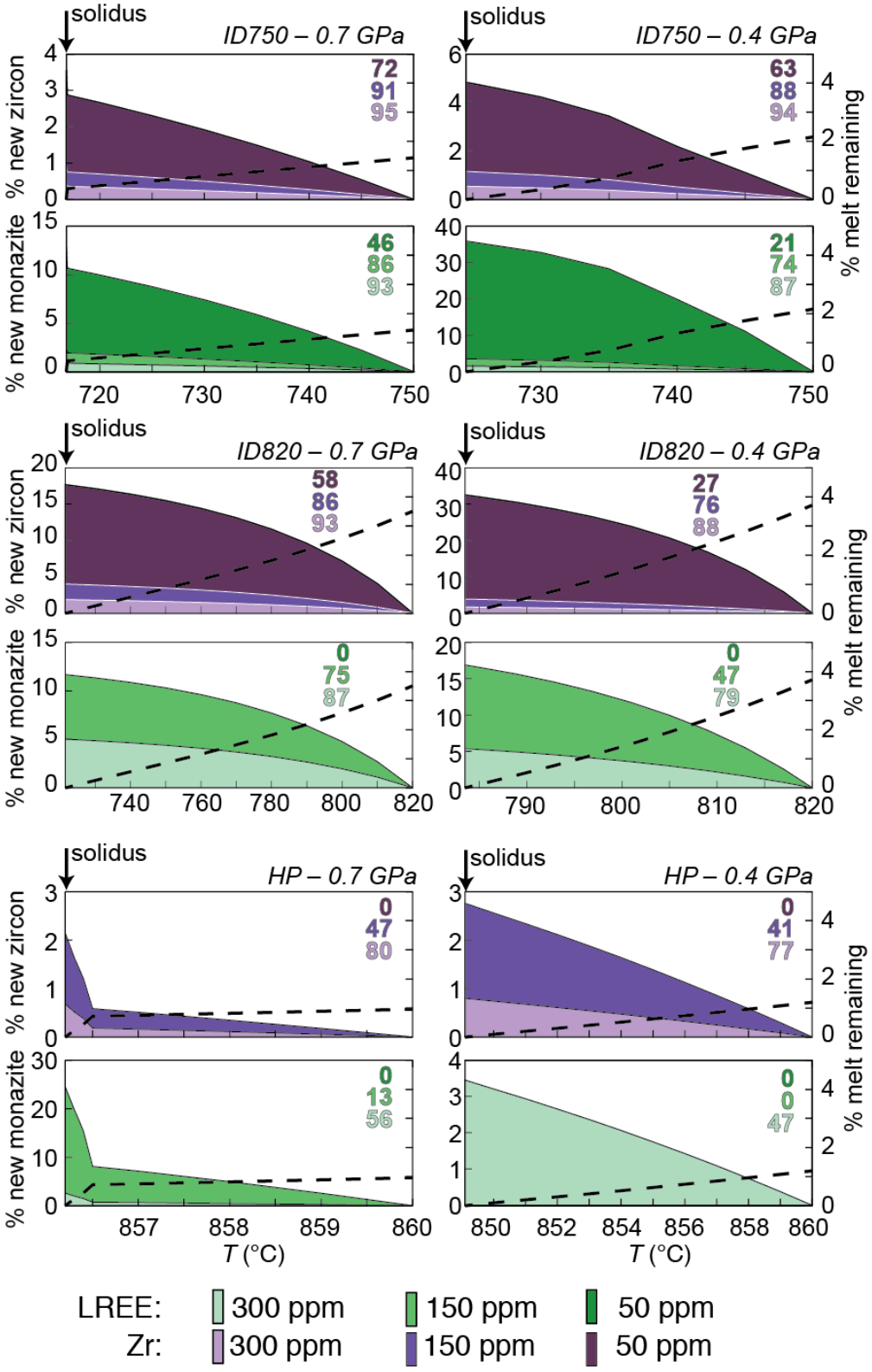
Pelite
solidus
ID750 – 0.7 GPa
72
91
95
46
86
93
ID750 – 0.4 GPa
63
88
94
21
74
87
ID820 – 0.7 GPa
58
86
93
0
75
87
ID820 – 0.4 GPa
27
76
88
0
47
79
HP – 0.7 GPa
0
47
80
0
13
56
HP – 0.4 GPa
0
41
77
0
0
47
% new zircon
% new monazite
% melt remaining
T (°C)
LREE: 300 ppm 150 ppm 50 ppm
Zr: 300 ppm 150 ppm 50 ppm

from <1% to ~35% for the pelite and from <1% to ~50% for the greywacke relative to the residual amount of monazite present after isothermal decompression (Figs 5.9 and 5.10).

For protolith compositions with the lowest initial Zr and LREE concentrations there is a high proportion of new zircon and monazite relative to the inherited amount. However, the total amounts of zircon and monazite present at the elevated solidus after isobaric cooling are quite small relative to the initial quantity at the fluid-present solidus (compare Figs 5.5–5.8 and 5.9–5.10). The new zircon and monazite may occur as new grains, but is more likely to be present as significant overgrowths on residual cores. For higher initial Zr and REE concentrations, new growth during cooling to the solidus is predicted to be low in relation to the residual amount, and zircon and monazite grains are expected to contain large inherited cores with narrow rim overgrowths. In some cases, no new growth of zircon and monazite is expected during cooling because melt drainage has

---

Fig. 5.10. Temperature–proportion diagrams for zircon, monazite and melt in greywacke during cooling from the decompression segment of the *P–T* path to the solidus. The proportion of new zircon and monazite growth calculated relative to the amount of zircon and monazite present at the beginning of cooling is shown as coloured fields for three protoliths with initial Zr and LREE concentrations of 50, 150, and 300 ppm, respectively. The coloured numbers in the top-right corner of each plot represent the percentage of zircon and monazite at the solidus relative to starting amounts at the fluid-present solidus at the beginning of the *P–T* paths modelled (Figs 5.7 and 5.8). Note that the fields for the higher Zr and LREE concentrations cover portions of the fields for the lower concentrations. The proportion of monazite was calculated using the Stepanov et al. (2012) solubility equation. The heavy dashed line represents the amount of melt remaining (scale on the right hand side of each plot). In general, the amount of new zircon and monazite growth is small. For protoliths with low initial Zr and LREE concentrations, the proportions of new zircon and monazite growth relative to the remaining zircon and monazite is greater than in protoliths with higher initial concentrations, but this simply reflects the fact that the proportion of residual zircon and monazite at the end of any *P–T* path is much less for these protoliths.

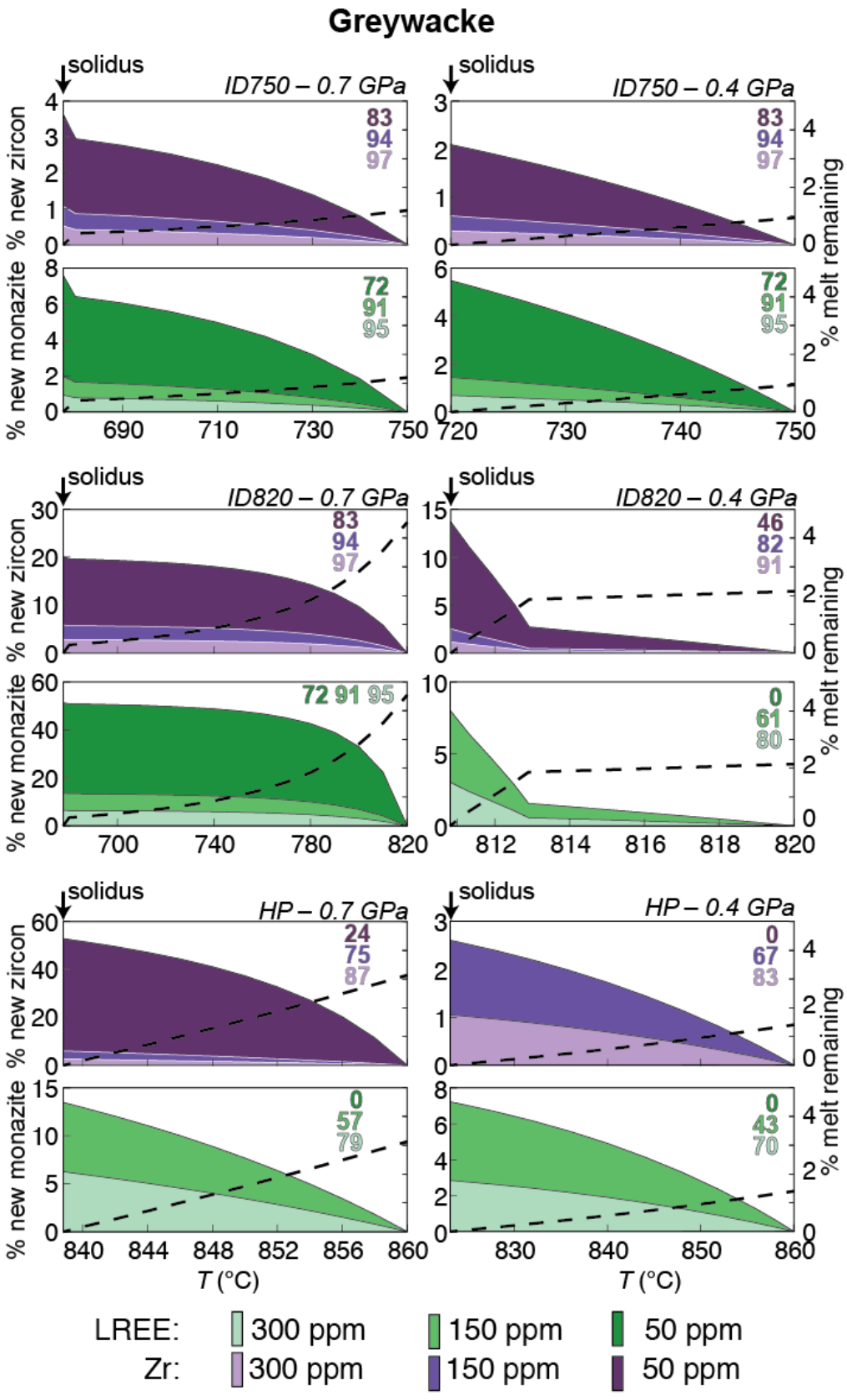
Greywacke
solidus
ID750 – 0.7 GPa
ID750 – 0.4 GPa
ID820 – 0.7 GPa
ID820 – 0.4 GPa
HP – 0.7 GPa
HP – 0.4 GPa
% new zircon
% new monazite
% melt remaining
T (°C)
83 94 97
72 91 95
46 82 91
0 61 80
24 75 87
0 67 83
0 57 79
0 43 70
LREE: 300 ppm 150 ppm 50 ppm
Zr: 300 ppm 150 ppm 50 ppm

completely depleted the source in Zr and LREE. This is the case for monazite dissolution for most of the scenarios modelled using the Kelsey et al. (2008) dissolution equation.

In summary, except for very low (50 ppm) initial Zr concentrations, most zircon is likely to survive during prograde heating through the granulite facies. The amount of dissolution expected for monazite is very different according to which of the two solubility equations is used. Using the equation of Kelsey et al. (2008), monazite is completely consumed along the low temperature part of all *P–T* paths for the pelite and along most *P–T* paths for the greywacke. In contrast, using the equation proposed by Stepanov et al. (2012), for lower LREE concentrations monazite may be consumed in both the pelite and the greywacke along all *P–T* paths, but for higher LREE concentrations some monazite is expected to survive. During cooling to the solidus from peak T, the amount of new zircon and monazite growth is expected to be limited in the melanosome.

5.5 Discussion

5.5.1 Limitations and assumptions

The limitations and assumptions of the methodology applied here to zircon and monazite dissolution are discussed in detail in Kelsey et al. (2008), but are briefly described next for completeness. In addition to the inherent uncertainties in the zircon and monazite solubility equations of Boehnke et al. (2013), Kelsey et al. (2008) and Stepanov et al. (2012), the following assumptions apply to the modelling presented here: (1) all of the Zr and LREE required for saturation is contributed by dissolving zircon and monazite; (2) no zircon or monazite is sequestered away from the reaction volume, such

as grains forming inclusions in major rock forming minerals; (3) no Zr or LREE is partitioned into other minerals (e.g. Zr in rutile and/or garnet); (4) no zircon or monazite is produced due to the breakdown of Zr- and LREE-bearing minerals during the *P–T* evolution; and (5) both zircon and monazite are stoichiometric. In addition, for open system behaviour, we assume that no zircon or monazite is entrained in the extracted melt.

The effects of some of these assumptions on the application of the results to natural examples are difficult to address except on a case-by-case basis. However, sequestration of zircon and monazite away from the reaction volume and partitioning of Zr or LREE into other minerals are problems in common to any application to migmatites and residual granulites. Sequestration of zircon or monazite away from the reaction volume or partitioning of Zr and LREE into major rock forming minerals will decrease the 'effective' concentration of the source. For example, consider a rock with a bulk Zr concentration of 200 ppm. If one-quarter of the zircon by mass in the rock is sequestered away from the reaction volume as inclusions in major rock forming minerals that do not participate in the partial melting reactions, a proportion consistent with the experimental and natural data reported by Watson et al. (1989), then the effective concentration of the source is 150 ppm Zr. In this case, the calculations presented in this study for 150 ppm Zr are appropriate for evaluating the proportion of zircon dissolution in this rock. Similarly, if 30 ppm Zr is partitioned into garnet (Kelsey and Powell 2011), and assuming no inclusion of zircon in rock-forming minerals, then the effective concentration of the source is 170 ppm Zr.

In nature, decompression would be isentropic rather than isothermal, unless heat is advected through the crust faster than the cooling rate during decompression, for example due to ascending superheated melt, or unless the *P–T* path involves additional heating or cooling. Synchronous cooling and decompression would promote melt crystallization and zircon/monazite growth. By contrast, heating during decompression promotes increased dissolution of zircon/monazite. Therefore, the amounts of melt production and zircon/monazite dissolution are representative of the schematic decompression paths modelled and must be modified for application to natural decompression paths.

5.5.2 Source Zr and LREE depletion and enrichment during open-system melting

The extraction of Zr and LREE saturated melt has implications for the concentration of these elements in the source along the remainder of the *P–T* path. Extraction of melt with lower concentrations of Zr and LREE than the source will lead to relative enrichment of the source whereas loss of melt with higher concentrations will lead to relative depletion of the source (Rapp et al. 1987). The saturation values for Zr and LREE calculated along the prograde path at 1.2 GPa for the pelite and greywacke are compared with the source compositions in Fig. 5.11.

The changes in the Zr concentrations of pelite and greywacke after incremental melt loss are shown in Fig. 5.11a, b. Depending on the initial bulk rock Zr concentration and the saturation concentration of the melt, the source may become enriched or depleted in Zr. For example, consider a starting composition of 150 ppm for the pelite (Fig. 5.11a). At each melt loss event, the extracted melt has a greater concentration of Zr (176, 180,

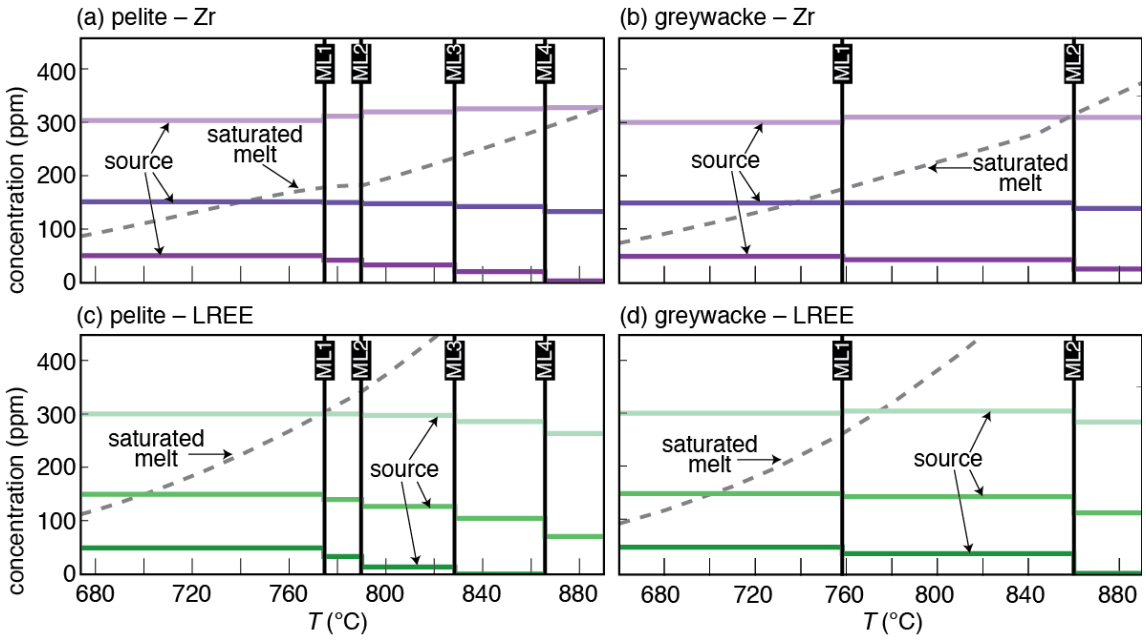

Fig. 5.11. Concentrations of the Zr and LREE in the source and melt for conditionally open system behaviour along an isobaric heating path at 1.2 GPa for pelite (a, c) and greywacke (b, d). The concentrations of these elements in the source changes in a stepwise fashion after each melt loss event. The saturation concentration of the melt is shown by the dashed curve. Extraction of saturated melt with higher Zr or LREE concentrations than the source will deplete the source in these elements. In these cases, proportionally more zircon and monazite dissolution is required to saturate the melt for the remainder of the heating path.

221, 286 ppm) than the source (Fig. 5.11a). This results in the progressive depletion of the source in Zr. In contrast, for a pelite with an initial composition of 300 ppm Zr, at each melt loss event the extracted melt has a lower concentration of Zr than the source. This leads to incremental source enrichment (Fig. 5.11a).

Source depletion is most pronounced for pelite and greywacke with starting concentrations of 50 ppm Zr. At each melt loss event along the isobaric heating path, the melt is always relatively enriched in Zr compared with the source (Fig. 5.11a, b), which leads to its incremental depletion. At the end of the isobaric heating path at 890 °C, the concentration of Zr is expected to be c. 5 ppm for the pelite (Fig. 5.11a) and c. 30 ppm for the greywacke (Fig. 5.11b).

The concentration of LREE in the saturated melt is higher than the range of initial protolith concentrations modelled at each melt loss event (Fig. 5.11c, d), with the exception of LREE concentrations >260 ppm for the greywacke prior to ML1 (Fig. 5.11d). This results in the progressive depletion of the source in LREE for most natural LREE concentrations, and during open-system melting the concentration of LREE in the source almost always decreases after each melt loss event. A consequence of the lower effective LREE concentration is that more monazite is required to dissolve to saturate the melt during open-system melting than during closed system behaviour, where the effective bulk concentration remains constant (Kelsey et al. 2008). In nature the melt may be undersaturated in Zr and LREE if there is insufficient time for melt–residue equilibration prior to melt drainage (Watt et al. 1996). Thus, care is required in applying our results directly to natural examples. This is discussed further below.

5.5.3 Zr and LREE undersaturation in granites and leucosomes

In this study, melt is assumed to be saturated in Zr and LREE along the *P–T* path, as expected based on experimental data (Rapp and Watson 1986; Watson and Harrison 1983; Stepanov et al. 2012; Boehnke et al. 2013). However, leucosomes in migmatites and anatectic granites are commonly undersaturated in Zr and LREE when compared with protolith compositions (Bea et al. 1994; Ayres and Harris 1997; Zeng et al. 2005a,b,c). Furthermore, melanosomes in migmatites and residual granulites that have experienced melt loss do not show the drastic depletion of Zr and LREE that may be expected from the drainage of saturated melt (Sawyer 1986; Sawyer and Barnes 1988; Bea and Montero 1999; Solar and Brown 2001; Guernina and Sawyer 2003; Villaseca et al. 2003, 2007; Korhonen et al. 2010b).

Undersaturation of melt in Zr and LREE is unlikely to be due to inhibited accessory mineral dissolution during partial melting in the source based on the experimental data (Harrison and Watson 1983; Rapp and Watson 1986). If accessory mineral dissolution is not inhibited, then melting and melt extraction must have occurred faster than mineral–melt equilibration to generate undersaturated melt compositions, which is considered to be possible in migmatite terrains that have undergone strong syn-anatectic deformation where melt escape is expected to be more rapid (Sawyer 1991; Watt and Harley 1993; Watt et al. 1996).

Another factor may be the proportion of accessory minerals sequestered in the major rock forming minerals (Watson et al. 1989; Bea 1996). Until the stability of the host minerals is exceeded, the Zr and LREE budget of the source rocks will be dominated by accessory mineral grains in the rock matrix (Watson et al. 1989). The stability of these

host minerals is controlled by the bulk composition of the rock and the *P–T* conditions of metamorphism. Fortunately, the stability of the common rock-forming minerals is well constrained for most clastic metasedimentary rocks up to UHT conditions (Johnson et al. 2008; Brown and Korhonen 2009).

A likely host for zircon and monazite in high-grade metamorphic rocks is biotite. Biotite is used in the following example because its proportion decreases with increasing temperature above the stability field of muscovite in most pelites and greywackes. However, we acknowledge that biotite is not the only potential host for zircon and monazite during prograde metamorphism. As biotite is consumed during fluid-absent melting accessory minerals may be liberated to enable interaction with the melt, which should yield leucosomes and anatectic granites with concentrations of these elements closer to saturation values, or if significant accessory minerals are entrained in the melt, even supersaturated concentrations (Brown 2013). A possible example of supersaturation occurs in migmatite from the southern Appalachian orogen where very high Zr concentrations were measured in leucosome; this was attributed to the physical concentration of newly crystallized zircon by inclusion in peritectic plagioclase and garnet during biotite breakdown (Moecher et al. 2004).

In clastic metasedimentary rocks biotite is consumed during melting to produce peritectic garnet at high P, cordierite at low P, or orthopyroxene at low *P* and high *T* (Fig. 5.1; also see Yakymchuk and Brown 2014a). For the *P–T* paths modelled at 1.2 GPa in this study, the effects of accessory mineral sequestration are expected to be most important for $T < 790$ °C for the pelite (Fig. 5.12a) and < 780 °C for the greywacke (Fig. 5.12b) where the proportion of biotite does not change significantly. For the higher

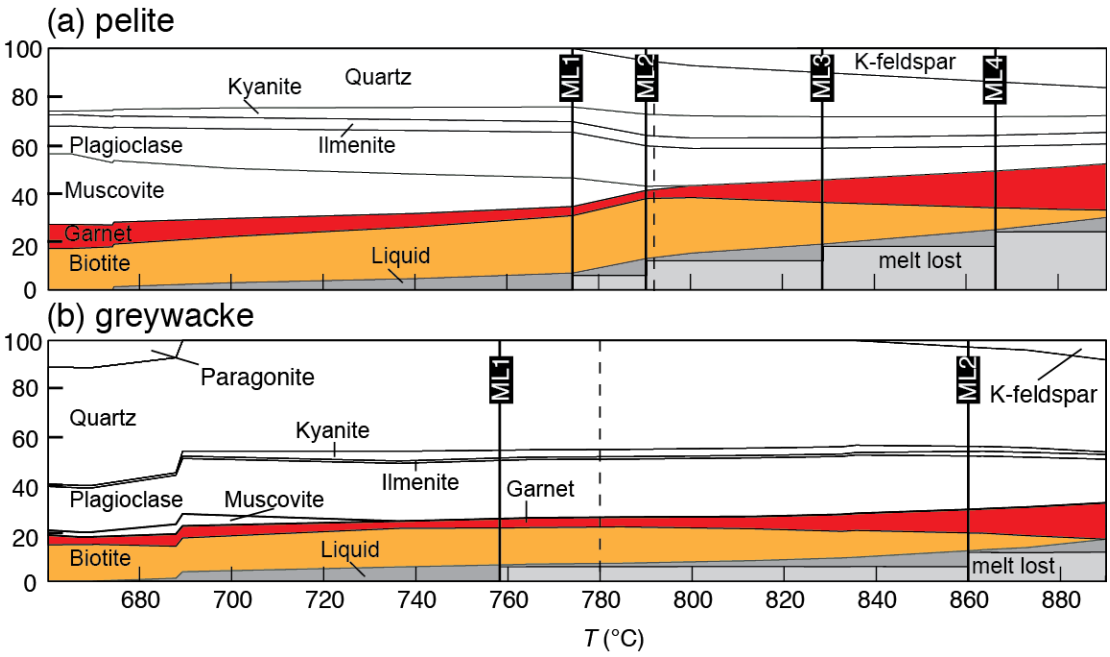

Fig. 5.12. Molar proportions of phases plotted against temperature for conditionally open system behaviour along an isobaric heating path at 1.2 GPa for pelite (a) and greywacke (b). The vertical dashed lines represent the temperatures at which the proportion of biotite decreases significantly during heating due to fluid-absent hydrate-breakdown melting. Because biotite is a common host for zircon and monazite, the breakdown of biotite during heating above these temperatures will liberate these minerals and make them available for reaction with melt.

temperature paths, as biotite is consumed—at $T > 790$ °C for the pelite and at $T > 780$ °C for the greywacke—any zircon and monazite sequestered in biotite will become progressively available for reaction. However, the peritectic products of the incongruent melting reaction (e.g. garnet in Fig. 5.12) may sequester accessory minerals and may also partition trace elements versus melt. Thus, with increasing temperature garnet may concentrate an increasing amount of Zr, and K-feldspar and plagioclase may concentrate an increasing amount of LREE than at lower metamorphic grades (Fraser et al. 1997; Villaseca et al. 2003, 2007). As a result Zr and LREE liberated from the breakdown of accessory minerals may not all enter the melt but some may partition into peritectic minerals. Zirconium may also be partitioned into rutile in high-pressure granulites (Zack et al. 2004; Tomkins et al. 2007; Ewing et al. 2013). There has been some progress in modelling the partitioning of Zr between zircon, melt, garnet, and rutile during anatexis of crustal rocks (Kelsey and Powell 2011; Skrzypek et al. 2012), but our understanding of the suprasolidus behaviour of the LREE is still limited.

A potentially important factor that may control the amount of zircon and monazite dissolution within a given time frame may be the crystal size distribution inherited from the subsolidus protolith (Nemchin and Bodorkos 2000). Nemchin et al. (2001) coupled a numerical model for Ostwald ripening with zircon morphology and zoning data from the Tickalara metamorphic rocks in Australia to suggest that, in the presence of melt, smaller zircon was preferentially dissolved and then new zircon was precipitated on the crystal faces of larger grains. When present smaller grains will preferentially contribute Zr to the melt, which increases the preservation potential of the larger grains. In the absence of smaller grains, dissolution of the larger grains is needed to saturate the melt in Zr. The

time required for complete dissolution of larger grains of zircon (and monazite) is significantly longer than for smaller grains. For example, for zircon grains with a diameter of 200 μm the time required for complete dissolution is >1 order of magnitude larger than for grains with a diameter of 50 μm (Harrison and Watson, 1983), whereas for monazite grains with a diameter of 50 μm, the time required for complete dissolution is >2.5 orders of magnitude longer than for grains with a diameter of 5 μm (Rapp and Watson 1986). Therefore, the pre-anatectic crystal size distribution may have important consequences for the preservation of inherited zircon (and monazite).

5.5.4 Consequences of monazite dissolution for Sm–Nd isotopes in granites

The Sm–Nd isotope system is commonly used to link granites emplaced in the upper crust to their sources in the deep crust. The amount of dissolution or entrainment of apatite and monazite in melt may modify the Nd-isotope ratio so that the leucosome is either more or less radiogenic than the source. This has been documented in Himalayan leucogranites (Ayres and Harris 1997), the Goat Ranch migmatite complex associated with the Sierra Nevada batholith (Zeng et al. 2005a,b,c) and the Fosdick migmatite–granite complex in West Antarctica (Korhonen et al. 2010b). Leucosome with less radiogenic Nd-isotope values is consistent with monazite dissolution and inhibited apatite dissolution, possibly in relatively low temperature melts where water content is relatively high. Melt with relatively high water content favours monazite dissolution whereas apatite dissolution is independent of water content (Harrison and Watson 1983). Leucosomes with more radiogenic values than the source are attributed to a larger contribution of apatite dissolution and a lesser contribution from monazite.

In this study, monazite is predicted to dissolve along the prograde path (Figs 5.5–5.8) and is either completely or mostly consumed by 890 °C according to the particular solubility equation used. The decreased proportion of monazite available at high temperature may enhance the dissolution of apatite to provide the LREE needed for saturation. Furthermore, relatively little melt production or accessory mineral dissolution is predicted during decompression compared with heating, which indicates that disequilibrium of Nd isotopes between the source and the melt is most likely to record prograde metamorphism rather than decompression.

5.5.5 Distribution of heat producing elements in the crust

The decay of radioactive elements in the thickened continental crust is one of the principal sources of heat for regional metamorphism, particularly for granulite and UHT metamorphism (Clark et al. 2011). In the continental crust, accessory minerals such as zircon and monazite are important hosts for the radioactive elements thorium and uranium. Contributions to the radiogenic heat flux of the Earth from the decay of potassium were important in the Archean but have become less so over time (Arevalo et al. 2009). Therefore, the distribution of zircon and monazite in the crust has important implications for the partitioning of heat-producing elements throughout the crust.

Whole-rock chemical data from low and high-grade rocks in the Ivrea Zone (kinzigites versus stronalites) has been used to suggest that geochemical changes accompanying partial melting and melt extraction have only a minor influence on the distribution of heat-producing elements in the deep crust (Bea and Montero 1999). This contrasts with the view that there is a secular change in the distribution of heat-producing

elements in different levels of the crust (Sandiford and McLaren 2002; Sandiford et al. 2002) and that there is a significant depletion of these elements in the deep crust compared to the upper crust (Rudnick and Gao 2003). The latter view is supported by the results of this study, which suggest that zircon and monazite are expected to be partially to completely dissolved during high *T* metamorphism and the extraction of this melt will deplete the residue in these elements.

One possible explanation for this discrepancy in the Ivrea zone might be that melt extraction was sufficiently fast that the melt was severely undersaturated in Zr and LREE. However, based on the calculations of Harrison and Watson (1983) and Rapp and Watson (1986) for water-undersaturated melts, timescales for melt extraction have to be significantly less than 1,000 years. Alternatively, the stronalites could represent a mix of residue, crystallised in situ melt and early crystallized cumulates formed from melt transferring from the deeper crust (e.g. Brown 2010; Morfin et al. 2013; Yakymchuk et al. 2013; Korhonen et al. 2013b). In support of the second explanation, we note that metasedimentary diatexites from the Ivrea zone contain more quartz and feldspar than expected from phase equilibria modelling, which suggests that these rocks represent melt accumulation zones or that melt escape was inefficient (Redler et al. 2013).

5.5.6 Interpreting accessory mineral ages

As discussed above, the factors that control zircon and monazite dissolution and growth in suprasolidus rocks are complex and the significance of U–Pb ages retrieved from them should be assessed on a case-by-case basis. However, some general conclusions may be drawn from the modelling presented in this study.

Except for very low whole-rock concentrations of Zr, some zircon is expected to survive high *T* metamorphism and partial melting. In contrast, except for highest LREE concentrations modelled, pre-existing subsolidus monazite is expected to be less abundant in the source than zircon, but monazite is expected to be more abundant in leucosomes and granites. Furthermore, for rocks with average concentrations of Zr and LREE only limited new growth of zircon and monazite is expected to have occurred in melanosomes in migmatites or in residual granulites during cooling to the solidus. These results are consistent with the study of Williams (2001), who documented the morphology and determined the age of zircon and monazite growth in migmatites from the Cooma complex of southeastern Australia. Williams (2001) noted that in melanosomes most zircon survived the prograde evolution and became surrounded by thin overgrowths during cooling to the solidus, whereas in leucosomes more prismatic zircon mostly represents new growth. By contrast, subsolidus monazite mostly vanished from the rock during the prograde evolution and inherited cores are scarce (Williams 2001); new monazite is more abundant in leucosomes than melanosomes, as would be expected from this study.

Zircon and monazite have similar closure temperatures for Pb for similar grain sizes and cooling rates (Cherniak et al. 2004). However, a common observation in high-grade metamorphic rocks is that zircon yields older ages than monazite, although there are exceptions (Korhonen et al. 2013a). A possible explanation is that zircon and monazite growth during cooling is non-linear and growth rates are expected to be higher at initial supersaturation, which may occur at higher temperatures for zircon (Kelsey et al. 2008; Fig. 5.4). The results of this study support non-linear rates of zircon and monazite

growth during cooling (Fig. 5.9, 5.10), but we emphasize that this rate is proportional to the change in the amount of melt. In addition, the effective Zr and LREE bulk-rock concentrations have a strong control on the amount of new zircon and monazite growth (Figs 5.9 and 5.10).

The timing of events and the rates of tectono-metamorphic processes operating in the deep crust rely on the correct interpretation of ages retrieved from accessory minerals. In migmatites and residual granulites, intrasample ranges of concordant U–Pb zircon ages and intersample variation in weighted mean ages within a single metamorphic event complicate the interpretation of age data (Reno et al. 2012; Korhonen et al. 2013a). Consider, for example, whether ranges of concordant ages in depleted source rocks record the duration of a process such as crustal melting or simply register the time taken for melt trapped by the percolation threshold to crystallize during exhumation and cooling. To distinguish between these different interpretations it may be necessary to evaluate the oxygen isotope composition of zircon in addition to U–Pb age data. For example, Jeon et al. (2012) used the difference in oxygen isotope compositions and U–Pb ages of zircon cores and rims from granites in eastern Australia to constrain the timing of crustal recycling to less than 15 My.

In migmatites and granulites, we might ask whether weighted mean ages record the timing of final crystallization of trapped melt at the solidus and, if so, whether differences in weighted mean ages between samples represent variations in the solidus temperature according to the degree of melt depletion? In variably depleted source rocks that record a range of suprasolidus *P–T* conditions, a range of concordant U–Pb ages from matrix zircon grains is likely to register the time taken for melt trapped on grain

boundaries to crystallize during cooling to the solidus. However, given the non-linear rate of zircon growth during cooling (Watson 1996; Harrison et al. 2007; Kelsey et al. 2008; this study), weighted mean ages may not represent the timing of final crystallization of trapped melt close to the solidus unless the solidus is very elevated. Williams (2001) also noted that monazite in both melanosomes and leucosomes grew in two stages: rapidly at first, trapping inclusions of melt and aluminosilicate, and then more slowly. Based on the modelling reported here, the proposal by Korhonen et al. (2013a) that differences in weighted mean ages among samples from ultrahigh temperature granulites from the Eastern Ghats Province most likely represent variations in the solidus temperature according to the degree of melt depletion seems reasonable.

For matrix monazite grains, U–Pb monazite ages retrieved from source rocks are predicted to record new growth during cooling to the solidus. However, given the different saturation curves for Zr and LREE (Fig. 5.11), this monazite is likely to have grown closer to the solidus than zircon and, as a result, weighted mean ages are more likely to register the timing of final crystallization of trapped melt close to the solidus. Furthermore, differences in weighted mean ages among samples are very likely to represent variations in the solidus temperature according to the degree of melt depletion (Reno et al. 2012; Korhonen et al. 2013a).

One last issue to consider is that of suprasolidus prograde growth as argued in several studies, some of which are discussed below. Based on the results of this study, it is hard to understand how zircon may grow during the suprasolidus prograde evolution except as a result of Ostwald ripening (Nemchin et al. 2001). It is intrinsically difficult to distinguish prograde from retrograde zircon growth in the presence of anatectic melt,

even where REE partitioning data and Ti-in-zircon thermometry are used in combination with geochronology (Baldwin and Brown 2008).

In the case of the Val Malenco granulites, which are located in northern Italy, the first stage of new zircon growth was linked to the beginning of fluid-absent muscovite-breakdown partial melting by Hermann and Rubatto (2003). Although these authors did not explicitly discuss the mechanism of growth of new zircon, we suggest that melt-enhanced Ostwald ripening may have been responsible for the first-stage overgrowth that trapped prograde muscovite and K-feldspar, and also biotite, as inclusions against inherited cores of zircon.

In the Ivrea–Verbano Zone of northern Italy, Ewing et al. (2013) have recently shown that the age of the regional granulite facies metamorphism was c. 316 Ma, older than determined by Vavra et al. (1996) at c. 296 Ma, which calls into question the interpretation of prograde growth of zircon as proposed by Vavra et al. (1996). Since these authors related the different types of zoning in sequential overgrowths on inherited cores in zircon to growth in the presence of anatectic melt, we infer that this zircon more likely represents growth during cooling to the solidus. As recognized in both studies, the zircon morphologies are complex and partly reflect younger recrystallization of pre-existing zircon in the presence of fluid.

At Mount Stafford in central Australia, many of the features ascribed to prograde growth of zircon and monazite (Rubatto et al. 2006) are also compatible with growth during cooling from the metamorphic peak to the solidus. Examples include core–rim structure in monazite marked by subtle age differences, which could reflect variation in monazite saturation, and an increasing Eu anomaly in monazite co-precipitating with K-

feldspar, which could occur during melt crystallization. The microstructure of these migmatites is extremely complex, with patchy distribution of minerals and multiple assemblages within any one thin section (White et al. 2003), making interpretations ambiguous. In particular, the occurrence of idioblastic K-feldspar and garnet is equally consistent with peritectic production or crystallization from melt, and it is unclear whether these minerals are late prograde or early retrograde, or, if both occur, how much of each type is present (White et al. 2003). Although these issues suggest caution in accepting an interpretation of prograde growth, given the short time scale for the regional-scale metamorphism in this area, the age of c. 1.8 Ga surely records the metamorphic peak within uncertainty.

5.6 Conclusions

Results of phase equilibria modelling of open-system melting of pelite and greywacke suggest that zircon is expected to survive the prograde evolution to peak temperature and subsequent isothermal decompression in both protoliths, whereas monazite may be mostly consumed. Melt loss from the residue is expected to progressively deplete the source of Zr and LREE, which may enhance the dissolution of zircon and monazite during heating to the metamorphic peak. Newly formed zircon and monazite are expected to be scarce in residues but more abundant in leucosomes in migmatites and in anatectic granites. Although there are many complicating factors, including mineral sequestration and partitioning of Zr and LREE between peritectic minerals and melt, the phase equilibria modelling of zircon and monazite behaviour during open-system melting presented here improves upon previous studies that were

largely restricted to closed system melting. Thus, this study provides a better framework within which to relate the U–Pb ages of accessory minerals to *P–T* paths, with the ultimate goal of better constraining the timing of events and the rates of tectono-metamorphic processes during orogenesis.

Chapter 6: Consequences of open system melting in tectonics

6.1 Abstract

Partial melting and melt drainage from deep suprasolidus crust in orogens has important consequences for tectonics. Melt extraction along prograde segments of clockwise *P–T* paths reduces fertility and increases the density and strength of residual crust, which has implications for further melt production during decompression. Using calculated *P–T* phase diagrams, implications of stepwise melt loss along clockwise *P–T* paths for pelite and greywacke are assessed, and density of the progressively more residual source and the potential role of buoyancy in the exhumation of deep crustal rocks are evaluated. Two model *P–T* paths are considered: isobaric heating at 1.2 GPa followed by decompression to 0.4 GPa at 750°C, 820°C and 890°C, and prograde heating from the fluid-present solidus at 1.2 GPa to 860°C at 1.8 GPa followed by isothermal decompression to 0.4 GPa. Both closed system (undrained) and conditionally open system (drained by intermittent melt loss) conditions are assessed. If melt is drained along clockwise *P–T* paths in suprasolidus crust then lower quantities of melt will be generated during decompression than sometimes inferred in tectonic models. Instead, the role of melt transfer through suprasolidus crust and melt accumulation at shallow levels in the anatectic zone should be considered rather than simply invoking the generation of large volumes of melt in decompressing crust.

6.2 Introduction

The presence of melt in the continental crust influences the tectonic evolution of orogens (Brown 1994; Brown and Solar 1998; Schilling and Partzsch 2001; Rey et al.

2009). Based on inferences from petrogenetic grids and *P–T* pseudosections, decompression melting across hydrate-breakdown reactions has been proposed as an important factor enhancing exhumation of high-grade metamorphic terrains and the formation of migmatitic gneiss domes and metamorphic core complexes (Zeitler and Chamberlain 1991; Zeitler et al. 1993; Harris and Massey 1994; Brown and Dallmeyer 1996; Burg et al. 1998; Norlander et al. 2002; Teyssier and Whitney 2002; Whittington and Treloar 2002; Booth et al. 2004, 2009; Harris et al. 2004; Whitney et al. 2004; Brown 2005; Rey et al. 2009, 2011; King et al. 2011; Žák et al. 2011; Whitney et al. 2013), and in the exhumation of ultrahigh-pressure metamorphic rocks (Auzanneau et al. 2006; Whitney et al. 2009; Hacker et al. 2010; Jamieson et al. 2011; Labrousse et al. 2011; Gordon et al. 2012; Sizova et al. 2012; Butler et al. 2013; Chen et al. 2013; Xu et al. 2013). However, melt productivity is strongly dependent on the fertility of the crust at the temperature of interest. Consequently, the amount of melt generated during exhumation may be quite small if, as expected, the system is open along the prograde segment of clockwise *P–T* paths and melt drains from the deeply buried crust reducing its fertility prior to decompression. If this is the general case, then some models for the structural and thermal development of migmatitic gneiss domes and metamorphic core complexes may require reevaluation.

6.3 Fluid-fluxed versus fluid-absent melting

6.3.1 Fluid-fluxed melting

Crystalline rocks have extremely low porosity and contain very little pore fluid at near-solidus conditions in the deep crust (Yardley 2009). As a result the amount of melt

produced in the crust at the fluid-present solidus is minimal. However, in some circumstances infiltration of H_2O-rich fluid into high-grade metamorphic rocks promotes additional melting at temperatures only modestly above the solidus (Brown 2010b). Examples of such fluid-fluxed melting occur in contact aureoles around plutons (Pattison and Harte 1988; Johnson et al. 2003; Droop and Brodie 2012), in shear zones (Johnson et al. 2001; Slagstad et al. 2005; Berger et al. 2008; Genier et al. 2008; Sawyer 2010; Reichardt and Weinberg 2012), in extensional fracture systems (Ward et al. 2008), and in rocks adjacent to those with higher temperature solidi that may still be undergoing subsolidus dehydration (White et al. 2005).

There is a net volume reduction during fluid-fluxed melting, which, in the absence of strong syn-anatectic deformation, may tend to inhibit melt escape (Clemens and Droop 1998; Brown 2010a), and at typical crustal pressures fluid-present melting reactions have negative slopes in pressure–temperature (*P*–*T*) space, which limits the amount of decompression that may occur before the melt crystallizes at the fluid-present solidus. Therefore, although fluid-fluxed melting may locally produce a large volume of melt (Sawyer et al. 2011), some of which may migrate within the anatectic zone, that melt is likely to be trapped rather than expelled (Milord et al. 2001). Thus, fluid-fluxed melting is not thought to be significant at the crustal scale (Clemens 2006) and is not considered further in this study.

6.3.2 Fluid-absent melting

With increasing temperature after crossing the fluid-present solidus, in the absence of infiltration of H_2O-rich fluid, melting of crustal rocks progresses under fluid-

absent conditions. Thus, at pressures above c. 0.4 GPa along clockwise *P–T* paths melting continues by consumption of feldspar(s) and quartz or via breakdown of muscovite, biotite or hornblende according to protolith composition (White et al. 2001; Clemens 2006; Brown and Korhonen 2009; Brown 2013).

In contrast to fluid-fluxed melting, there is a net volume increase during fluid-absent melting, which promotes melt escape regardless of syn-anatectic deformation (Clemens and Droop 1998; Powell et al. 2005; Brown 2010a). Fluid absent, hydrate-breakdown reactions generally have positive slopes in *P–T* space and may be crossed by clockwise *P–T* paths with various types of heating and/or decompression segments. These reactions are commonly represented simply as univariant curves on petrogenetic grids (e.g. Clemens and Droop 1998; Spear et al. 1999), which may give a misleading impression of the efficacy of decompression melting along these *P–T* paths since neither the fertility of a particular protolith nor the effects of melt loss are considered.

Assuming no heat flow limit, the amount of anatectic melt that can be produced by fluid-absent melting reactions in crustal rocks is controlled by the *P–T* path, and is strongly dependent on the bulk chemical composition of the protolith, the proportion of hydrous (micas and amphiboles) and anhydrous (feldspar and quartz) reactants, and the length of time above the solidus (White et al. 2001; Brown and Korhonen 2009). The protolith may be chemically fertile and yield a relatively large quantity of melt during evolution to a given peak *P–T* condition, as is the case for most pelitic rocks because they contain a large proportion of hydrous minerals (assuming sufficient quartz and feldspar), or it may have a lower fertility and produce less melt during evolution to a given peak *P–*

T condition, as is the case for most greywacke, igneous and melt-depleted (residual) rocks.

The principal mechanism that reduces the fertility of suprasolidus deep crustal rocks is drainage of melt to shallow crustal levels. Evidence for melt loss in nature is found in exposures of deep crustal migmatite complexes and granulite terranes that preserve high-grade metamorphic assemblages (White and Powell 2002; Guernina and Sawyer 2003; Reno et al. 2012; Korhonen et al. 2013), have bulk chemical compositions that are consistent with the extraction of anatectic melt (Sawyer 1991; Solar and Brown 2001; Korhonen et al. 2010a, b, 2012), and exhibit structures consistent with volume reduction by drainage of melt (Bons et al. 2008).

For melt extraction, the melt must form an interconnected network of grain edge channels and the matrix must compact. The permeability threshold for crustal melts is likely to be low (Laporte et al. 1997). In melt infiltration experiments in quartzite an interconnected network of grain edge melt channels was developed at a permeability threshold of c. 4 vol.%, although the high viscosity of the melt may limit migration in nature (Laporte et al. 1997). This is similar to the threshold of c. 5 vol.% derived from a numerical modelling study of melt extraction from crustal rocks (Rabinowicz and Vigneresse 2004). A maximum value for this critical threshold is suggested to be c. 7 vol.%, based on an analysis of deformation experiments on melt-bearing aggregates, which corresponds to the point where >80% of grain boundaries become melt bearing (referred to as the melt connectivity transition (MCT); Rosenberg and Handy 2005).

At the local scale, suprasolidus crust may behave as a closed (melt is retained) or open (melt drains) or conditionally open (cyclic closed and open) system, although

overall the suprasolidus crust must be an unconditionally open system since it represents the source for upper crustal granites (Handy et al. 2001; Brown 2013). As melt volume increases it reaches the critical threshold for extraction at which point the melt nucleates rheological instabilities that may lengthen and connect to allow melt drainage (Handy et al. 2001; Brown 2004, 2010a, 2013). However, the melt is unlikely to drain continuously owing to the effects of dilatancy and/or strain hardening (Rutter and Mecklenburgh 2006). The amount of melt buildup required to trigger a local drainage event and the frequency of these events will be a function of strain rate and temperature. At higher temperatures and lower strain rates the suprasolidus crust may deform by granular flow (Rutter and Mecklenburgh 2006). In these circumstances, it is plausible that if the melt production rate locally exceeds the melt segregation rate, melt could be squeezed out of the suprasolidus crust fast enough to pre-empt the formation of rheological instabilities so that locally the suprasolidus crust could become unconditionally open (Handy et al. 2001). The variability in the amount and style of leucosome preserved in migmatites and migmatitic granulites compared with some ultrahigh temperature granulites suggests that this may be the case at the highest crustal temperatures.

In general, the process of melt extraction is considered to be cyclic with pulses of melt build up and melt drainage as the amount of melt in the system reaches the critical threshold for extraction (Handy et al. 2001; Brown and Korhonen 2009; Brown 2010a; Hobbs and Ord 2010; Brown 2013; Yakymchuk et al. 2013a). Accordingly, in this study the suprasolidus crust is treated as a conditionally open system, whereby it is closed during melt accumulation up to the critical threshold for extraction then open during melt drainage. However, in the presence of syn-anatectic deformation, the critical threshold for

melt extraction is likely to be less than the MCT and drainage events may be closely spaced in time (Brown 2010b).

After each melt drainage event, the progressively more residual source will produce proportionally less melt than its relatively fertile precursor. Therefore, if the suprasolidus crust undergoes significant melt loss prior to decompression, the amount of melt that can be produced during decompression will be significantly reduced. In this study, phase equilibria modelling is used to investigate melt production and episodic melt loss along clockwise *P–T* paths involving a prograde heating segment followed by an isothermal decompression segment to quantify this effect.

6.3.3 Potential implications for tectonics

Partial melting has several implications for crustal-scale rheology and tectonics (Brown 2001a,b,c). The limited importance of intra-crystalline plasticity, deduced from the microstructure of migmatites and modelling based on extrapolation of laboratory-determined constitutive flow laws, indicates that melt-bearing crust will be extremely weak and able to flow at fast geological strain rates at differential stresses from 100 MPa down to 1 MPa or less (Albertz et al. 2005; Rutter and Mecklenburgh 2006; Hobbs and Ord 2010). Therefore, vertical intervals in the crust that are partially molten or that contain more melt at a given *P–T* condition than adjacent intervals should be effective tectonic detachment horizons (Rutter and Mecklenburgh 2006).

It has been proposed that decompression of relatively fertile crust at upper amphibolite facies conditions could produce sufficient melt to localize major shear zones and facilitate exhumation, and in addition that exhumation would promote more melting

in a feedback relation (e.g. Davidson et al. 1994; Brown and Solar 1998; Beaumont et al. 2001; Vanderhaeghe and Teyssier 2001; Jamieson et al. 2011; Montési 2013). Moreover, it has also been posited that decompression of residual crust at granulite facies conditions could produce sufficient melt to affect exhumation by localizing an extensional detachment (e.g. Brown and Dallmeyer 1996).

To assess these two postulates it is critical to examine the production and drainage of melt along the prograde *P–T* path prior to any decompression because melt loss reduces source fertility (Brown and Korhonen 2009), which will affect melt production during exhumation. The modelling reported here places constraints on the quantity of melt that can be produced from progressively more residual rocks during decompression. For peak temperatures above c. 750°C, the results of the modelling show that most of the melt generated is drained from the system along the prograde segment of the *P–T* path before any decompression occurs (cf. Guilmette et al. 2011). As a result, only a relatively small amount of anatectic melt may be produced during decompression, unless decompression extends to low pressures where melting reactions produce cordierite, and in some cases melting may terminate partway along the decompression segment. These results have clear implications for the contribution of melt-enhanced exhumation to the tectonic evolution of orogens.

In addition, it has been suggested that the decrease in density associated with closed-system partial melting would produce density inversions within the crust that could promote buoyancy-driven exhumation under certain circumstances (Rey et al. 2009). However, in conditionally open systems, cyclic melt drainage increases the

density of the residue, which may hinder buoyancy-driven exhumation if melt is lost along the prograde *P–T* path.

6.4 Phase equilibria modelling

The *P–T* conditions at which fluid-absent melting occurs and the quantity of melt that could be produced from clastic sedimentary rocks during closed system melting may be determined by forward modelling using *P–T* pseudosections constructed for the initial bulk chemical compositions (e.g. White et al. 2007; Johnson et al. 2008; Brown and Korhonen 2009). In addition, by using a series of *P–T* pseudosections for bulk chemical compositions modified by a succession of melt loss events, the effects of melt drainage on future melt production and total melt production, and on the preservation of peritectic mineral assemblages may be evaluated for open system behaviour (White and Powell 2002; Brown and Korhonen 2009; Korhonen et al. 2010a).

Two bulk chemical compositions are modelled, an average amphibolite-facies pelite composition (from Ague 1991; Table 6.1) and an average passive margin greywacke composition (see below), as they are considered to be representative of the dominant components of turbidite sequences that are likely to be involved in orogenesis at convergent plate boundaries. In the case of greywackes, the major element compositions vary significantly within and across different tectonics regimes (Barnes 1990; Floyd et al. 1990; Korsch et al. 1993; Banerjee and Bhattacharya 1994; Gill et al. 1994; Gu 1994; McDaniel et al. 1994; Duller and Floyd 1995; Roser et al. 1996; Hayashi et al. 1997; Holail and Moghazi 1998; Kalsbeek et al. 1998; Hegner et al. 2005; Wanas and Abdel-Maguid 2006; Kiminami and Fujii 2007; Dostal and Keppie 2009). Collisional

Table 6.1. *Bulk compositions (wt%) of metapelite and greywacke used in the construction of pseudosections*

	H_2O	SiO_2	Al_2O_3	CaO	MgO	Fe_2O_3T	K_2O	Na_2O	TiO_2	$Fe^{3+}/(Fe^{2+} + Fe^{3+})$
Metapelite[a]	3.02	56.25	20.18	1.54	3.23	9.31	4.02	1.80	1.05	0.33
Greywacke[b]	2.94	70.94	12.72	0.98	2.35	5.10	1.81	2.68	0.63	0.15

[a]Average amphibolite-facies metapelite (Ague 1991)

[b]Average of 33 passive margin greywacke samples that contain 69–76 wt.% SiO_2 and $Na_2O > 1.5$ wt.% (McDaniel *et al.* 1994; Roser *et al.* 1996; Kalsbeek *et al.* 1998; Hegner *et al.* 2005; Dostal & Keppie 2009)

orogenesis typically involves passive margin turbidites and subordinate amounts of arc-derived greywackes. Thus, for the modelling in this study an average chemical composition of 33 passive margin greywackes that have SiO2 of 69–76 wt% and Na2O >1.5 wt% was chosen (McDaniel et al. 1994; Roser et al. 1996; Kalsbeek et al. 1998; Hegner et al. 2005; Dostal and Keppie 2009; Table 6.1) and 15% of the iron was assumed to be ferric.

Calculations were performed using THERMOCALC v.3.35 (Powell and Holland 1988) and the internally consistent dataset of Holland and Powell (1998). Modelling was undertaken in the Na_2O–CaO–K_2O–FeO–MgO–Al_2O_3–SiO2–H_2O–TiO_2–Fe_2O_3 chemical system, which is currently the most realistic system to investigate melting of pelites and greywackes (White et al. 2007). The phases considered were: Crd – cordierite; Cpx – clinopyroxene; Grt – garnet; H_2O – aqueous fluid; Ilm – ilmenite; Kfs – K-feldspar; Ky – kyanite; Liq – silicate liquid/melt; Mag – magnetite; Ms – muscovite; Opx – orthopyroxene; Pl – plagioclase; Pg – paragonite; Qtz – quartz; Rt – rutile; Sil – sillimanite; Spl – spinel. The activity–composition (a–x) models for the phases considered are: biotite, garnet, and melt (White et al. 2007); clinopyroxene (Green et al. 2007); orthopyroxene and spinel–magnetite (White and Powell 2002); cordierite and epidote, K-feldspar and plagioclase (Holland and Powell 2003); white mica (Coggon and Holland 2002); ilmenite–hematite (White et al. 2000); and hornblende (Diener et al. 2007). Phases modelled as pure end-members include: quartz, rutile, aqueous fluid (H_2O), kyanite and sillimanite.

The results of the phase equilibria modelling are displayed as *P–T* pseudosections. The amount of water in the modelled compositions for the pelite and the greywacke were

adjusted so that there is minimal (<0.1 mol%) free H_2O at the solidus at 1.2 GPa, which is consistent with fluid-absent conditions above the solidus (White and Powell 2002; White 2003; White et al. 2005). If the modelled prograde path crossed the solidus at lower or higher pressures, the quantity of melt produced will be slightly overestimated and underestimated, respectively.

6.4.1 P–T paths

First three model clockwise *P–T* paths for moderate crustal pressures, each with two segments, are investigated. These model paths comprise an isobaric heating segment at 1.2 GPa beginning at the solidus, and an isothermal decompression segment from 1.2 to 0.4 GPa at three different temperatures.

The pressure range chosen was based on two criteria. First, 1.2 GPa represents a typical pressure for decompression to begin in many orogenic belts, based on *P–T* paths retrieved from migmatites at lower temperatures (Teyssier and Whitney 2002) and granulites characterized by close-to-isothermal decompression at higher temperatures (Harley 1998). Also, this pressure is similar to the upper part of the range in the petrogenetic grid for partial melting of pelites from the study by Spear et al. (1999). Finally, 1.2 GPa corresponds approximately to the depth of the solidus in the thermo-mechanical models for the development of metamorphic core complexes from Rey et al. (2009). Second, 0.4 GPa represents a pressure below the melt-producing garnet-to-cordierite reaction for closed system melting of pelite and greywacke compositions across a range of suprasolidus temperatures (Spear et al. 1999; Brown and Korhonen 2009).

Temperatures were selected so that the decompression segment of the *P–T* paths was likely to cross the main hydrate-breakdown melting reactions typically encountered by pelites and greywackes during exhumation after collisional orogenesis. Muscovite breakdown is predicted to occur during decompression at upper amphibolite facies conditions whereas biotite breakdown takes place over a wide range of temperatures in the granulite facies (e.g. Brown 2013). Thus, decompression was modelled at temperatures of 750°C, 820°C and 890°C.

Second, one additional *P–T* path is investigated that replicates the typical evolution of high-pressure granulites (O'Brien and Rötzler 2003) and also post-peak-pressure segments of the exhumation paths of some ultrahigh pressure metamorphic rocks (Hacker et al. 2010; Chen et al. 2013; Xu et al. 2013). For this case, *P–T* pseudosections are constructed to show the evolution of melt production along a clockwise *P–T* path up to a peak pressure of 1.8 GPa followed by decompression. The model *P–T* path comprises two segments, a prograde heating segment from the solidus at 1.2 GPa up to peak *P–T* of 860°C at 1.8 GPa followed by an isothermal decompression segment to 0.4 GPa.

6.4.2 Modelling melt drainage

Melt drainage is modelled based on observations from residual rocks and rock deformation experiments. Peritectic and residual mineral grains in some granulites have thin quartz or feldspar films that are interpreted to represent pseudomorphs after grain-boundary melt, but in other granulites these films are absent. These features suggest that some melt may have been retained on grain boundaries in residual rocks after melt

extraction, which we approximate as 1 vol.%, although if melt also crystallized as overgrowths on preexisting grains this value could be an underestimate (Sawyer 2001; Marchildon and Brown 2002; Holness and Sawyer 2008). One volume percent melt approximates 1 mol% melt on a one-oxide basis in the phase equilibria modelling (White and Powell 2002; Brown and Korhonen 2009) and this value was taken as the proportion of melt retained after a modelled melt drainage event. Thus, by taking the MCT of Rosenberg and Handy (2005) as a likely maximum threshold for melt drainage (7 vol.% melt or approximately 7 mol% melt in the phase equilibria modelling), the amount of melt to be extracted was set at 6 mol%, leaving 1 mol% in the residue.

This procedure was executed by removing six sevenths of the melt present where the *P–T* path intersects the 7 mol% melt isopleth using the 'read-bulk-info' script in THERMOCALC. After melt extraction, the residual bulk chemical composition was used to calculate a new pseudosection for the next increment along the *P–T* path. This procedure was repeated at every *P–T* point where the melt content reached 7 mol% along the *P–T* path, resulting in up to five melt drainage events along the highest-temperature *P–T* path modelled (Tables 6.2–6.3). In between melt drainage events the bulk chemical composition represents a mix of both melt and residue, which are assumed to be in chemical equilibrium, and the fertility of the source as modelled changes in a stepwise fashion at each melt loss event.

For a conditionally open system, the density evolution along the decompression segment of the *P–T* paths for suprasolidus pelite and greywacke is modelled as follows. Using the 'read sv' script in THERMOCALC, molar volume was calculated so that molar proportions could be converted to weight proportions. After each melt loss event, the

Table 6.2. *Bulk compositions (mol%) of the metapelite used in the construction of pseudosections*

Figure	*P–T* segment	ML	*P*	*T*	H_2O	SiO_2	Al_2O_3	CaO	MgO	FeO	K_2O	Na_2O	TiO_2	O
6.1a, 6.6a	undrained	–	–	–	6.85	59.62	12.61	1.75	5.11	7.44	2.73	1.85	0.83	1.23
6.1c	IBH	ML1	1.20	774	5.36	59.89	12.95	1.81	5.43	7.89	2.75	1.73	0.88	1.31
6.1c	–	ML2	1.20	790	3.95	60.05	13.30	1.86	5.77	8.38	2.72	1.64	0.94	1.40
6.1c	–	ML3	1.20	828	2.68	60.04	13.64	1.91	6.12	8.89	2.68	1.56	1.00	1.49
6.1c	–	ML4	1.20	866	1.54	59.87	13.97	1.95	6.50	9.43	2.62	1.49	1.06	1.58
6.2a	ID750	ML1	1.04	750	5.34	59.87	12.97	1.82	5.43	7.90	2.75	1.73	0.88	1.31
6.2b	–	ML2	0.77	750	4.11	59.77	13.33	1.90	5.77	8.39	2.72	1.66	0.94	1.40
6.2c	–	ML3	0.44	750	3.20	59.27	13.71	2.00	6.14	8.92	2.67	1.61	1.00	1.49
–	ID820	ML1	1.20	774	5.36	59.89	12.95	1.81	5.43	7.89	2.75	1.73	0.88	1.31
6.3a	–	ML2	1.20	790	3.95	60.05	13.30	1.86	5.77	8.38	2.72	1.64	0.94	1.40
6.3b	–	ML3	0.62	820	3.21	59.51	13.62	1.94	6.12	8.87	2.66	1.59	1.00	1.49
6.3c	–	ML4	0.47	820	2.59	58.78	13.98	2.03	6.49	9.38	2.58	1.54	1.06	1.58
–	ID890	ML1	1.20	774	5.36	59.89	12.95	1.81	5.43	7.89	2.75	1.73	0.88	1.31
–	–	ML2	1.20	790	3.95	60.05	13.30	1.86	5.77	8.38	2.72	1.64	0.94	1.40
–	–	ML3	1.20	828	2.68	60.04	13.64	1.91	6.12	8.89	2.68	1.56	1.00	1.49
6.4a	–	ML4	1.20	866	1.54	59.87	13.97	1.95	6.50	9.43	2.62	1.49	1.06	1.58
6.4b	–	ML5	1.00	890	0.64	59.41	14.30	1.99	6.89	10.00	2.53	1.43	1.13	1.68
–	HP	ML1	1.80	858	5.47	59.91	12.90	1.79	5.42	7.89	2.77	1.66	0.88	1.31
–	–	ML2	1.80	859	4.01	60.22	13.20	1.83	5.76	8.38	2.81	1.47	0.94	1.40
6.6b	–	ML3	1.80	859	2.45	60.54	13.53	1.87	6.11	8.89	2.85	1.27	1.00	1.49
6.6b	–	ML4	0.71	860	1.74	59.97	13.83	1.93	6.48	9.42	2.76	1.23	1.06	1.58
6.6b	–	ML5	0.40	860	1.27	59.06	14.21	2.01	6.86	9.93	2.66	1.19	1.13	1.68

HP: high pressure; IBH: Isobaric heating; ID: isothermal decompression; ML: melt loss event; *P*: pressure (GPa); *T*: temperature (°C)

Table 6.3. *Bulk compositions (mol%) of the greywacke used in the construction of pseudosections*

Figure	*P–T* segment	ML	*P*	*T*	H_2O	SiO_2	Al_2O_3	CaO	MgO	FeO	K_2O	Na_2O	TiO_2	O
6.7a, 6.12a	undrained	–	–	–	4.04	74.73	7.89	1.11	3.43	4.04	1.22	2.74	0.50	0.31
6.7c	IBH	ML1	1.20	759	2.25	76.07	7.95	1.15	3.64	4.28	1.21	2.60	0.53	0.33
6.7c	IBH	ML2	1.20	862	1.04	76.96	7.93	1.18	3.86	4.52	1.12	2.49	0.57	0.35
6.8	ID750	ML1	1.06	750	2.30	76.00	7.95	1.15	3.64	4.28	1.22	2.59	0.53	0.33
6.9a	ID820	ML1	1.20	759	2.25	76.06	7.95	1.15	3.64	4.28	1.21	2.60	0.53	0.33
6.9b	–	ML2	0.50	820	1.52	76.47	7.95	1.20	3.85	4.47	1.09	2.54	0.57	0.35
6.9c	–	ML3	0.46	820	0.79	76.85	7.95	1.26	4.07	4.68	0.95	2.49	0.60	0.37
–	ID890	ML1	1.20	759	2.25	76.06	7.95	1.15	3.64	4.28	1.21	2.60	0.53	0.33
6.10a	–	ML2	1.20	862	1.04	76.95	7.93	1.18	3.86	4.52	1.12	2.49	0.57	0.35
6.10b	–	ML3	0.88	890	0.18	77.52	7.86	1.21	4.08	4.76	1.00	2.41	0.60	0.37
6.12b	HP	ML1	1.68	820	2.32	76.09	7.91	1.13	3.64	4.28	1.22	2.56	0.53	0.33
6.12b	–	ML2	1.22	860	1.08	77.00	7.89	1.16	3.86	4.51	1.13	2.46	0.57	0.35
6.12b	–	ML3	0.42	860	0.53	77.26	7.87	1.21	4.07	4.71	0.98	2.40	0.60	0.37

HP: high pressure; IBH: Isobaric heating; ID: isothermal decompression; ML: melt loss event; *P*: pressure (GPa); *T*: temperature (°C)

more residual bulk chemical composition is used to calculate the weight proportions up to the next melt loss event. The density of the melt was calculated using the silicate melt end-member properties in the Holland and Powell (1998) dataset coupled with the composition of the melt at each *P–T* of interest retrieved from THERMOCALC.

6.4 Isobaric heating and isothermal decompression for a pelite at moderate crustal pressures

6.4.1 The initial P–T pseudosection

A pseudosection for the pelite for the *P–T* range 0.2–1.3 GPa and 640–910°C is shown in Fig. 6.1a. This pseudosection is similar to that presented in Brown and Korhonen (2009), except that it is saturated with H_2O at a higher pressure (1.2 GPa v. 0.9 GPa), which increases the proportion of melt generated at a given *P–T* condition and shifts the K-feldspar and quartz stability fields at low pressures (<0.5 GPa) to lower temperatures (c. 50°C). Garnet is stable at high pressures and at high temperatures at $P >$ 0.6 GPa. Kyanite or sillimanite is stable at $P >$ 0.7–0.8 GPa, whereas sillimanite is stable at lower pressures over the full temperature range. Cordierite is stable at $P <$ 0.3–0.8 GPa with increasing temperature and orthopyroxene is stable at $P <$ 0.7 GPa at $T >$ 840°C. Ilmenite and plagioclase are stable across the full *P–T* range shown. The amount of melt expected at a specific *P–T* condition is shown by isopleths of mol% melt. These isopleths have steeper slopes in the garnet stability field but shallower slopes in the cordierite stability field.

6.4.1 Isobaric heating at 1.2 GPa followed by decompression in an undrained (closed) system

In an undrained (closed) system, the amount of melt produced from the pelite along the isobaric heating segment at 1.2 GPa at the temperature of the highest-temperature decompression segment modelled (890°C) is 36 mol% (Fig. 6.1a). This result is consistent with that obtained in the study by Spear et al. (1999) for a pressure of 1.0 GPa. The modes along this isobaric heating segment are shown on a temperature–phase proportion diagram in Fig. 6.1b. The isopleths of mol% melt have positive slopes (Fig. 6.1a), so isothermal decompression at any temperature along this prograde segment results in an increase in the amount of melt. However, as discussed above, this is

---

Fig. 6.1. (a) *P–T* pseudosection calculated for an average amphibolite facies pelite assuming undrained (closed system) conditions. The heavy dashed line is the solidus and the coloured dashed lines are contours of mol% melt. (b) Molar proportion of phases plotted against temperature for isobaric heating for a closed system. (c) A composite *P–T* diagram comprising five pseudosection panels arranged from low to high temperature for drained (conditionally open system) conditions. The lowest temperature panel is appropriate for isobaric heating up to the first melt loss (ML) event, which leads to the second panel at higher temperature calculated for the drained composition. This panel is appropriate for investigating phase relations until the second melt loss event and so on. The heavy dashed line is the solidus and the coloured dashed lines represent contours of mol% melt. (d) Molar proportion of phases plotted against temperature for isobaric heating for a conditionally open system. Phase assemblages are as follows in addition to Pl and Ilm: A. Grt Bt Ky Ms Liq H_2O Qtz; B. Grt Bt Ky Ms Mag H_2O Qtz; C. Grt Bt Ky Ms Mag Liq H_2O Qtz; D. Bt Ky Ms Mag Liq H_2O Qtz; E. Grt Bt Ky Ms Mag Liq Qtz; F. Grt Bt Ky Ms Mag Kfs Liq Qtz; G. Grt Bt Ky Ms Kfs Liq Qtz; H. Bt Ky Ms Mag Kfs Liq Qtz; I. Grt Sil Kfs Liq Qtz; J. Grt Bt Sil Crd Kfs Liq Qtz; K. Grt Sil Crd Kfs Liq Qtz; L. Grt Sil Kfs Liq; M. Grt Sil Crd Kfs Liq; N. Grt Sil Crd Mag Kfs Liq Qtz; O. Grt Sil Crd Mag Kfs Liq; P. Grt Crd Mag Kfs Liq Qtz; Q. Grt Crd Mag Kfs Liq; R. Grt Bt Crd Mag Kfs Liq; S. Grt Bt Opx Crd Mag Kfs Liq; T. Grt Opx Crd Mag Kfs Liq; U. Bt Opx Crd Mag Kfs Liq Qtz; V. Grt Bt Opx Crd Mag Kfs Liq Qtz; W. Bt Sil Ms Mag Kfs H_2O Qtz; X. Bt Sil Mag Kfs Liq H_2O Qtz; Y. Bt Sil Crd Mag Kfs Liq H_2O Qtz; Z. Bt Sil Crd Mag Kfs H_2O Qtz; AA. Bt Crd Mag Kfs H_2O Qtz; AB. Bt Opx Crd Mag Liq; AC. Bt Crd Mag Liq; AD. Crd Mag Liq; AE. Grt Bt Ky Mag Kfs Liq Qtz; AF. Bt Ky Mag Kfs Liq Qtz.

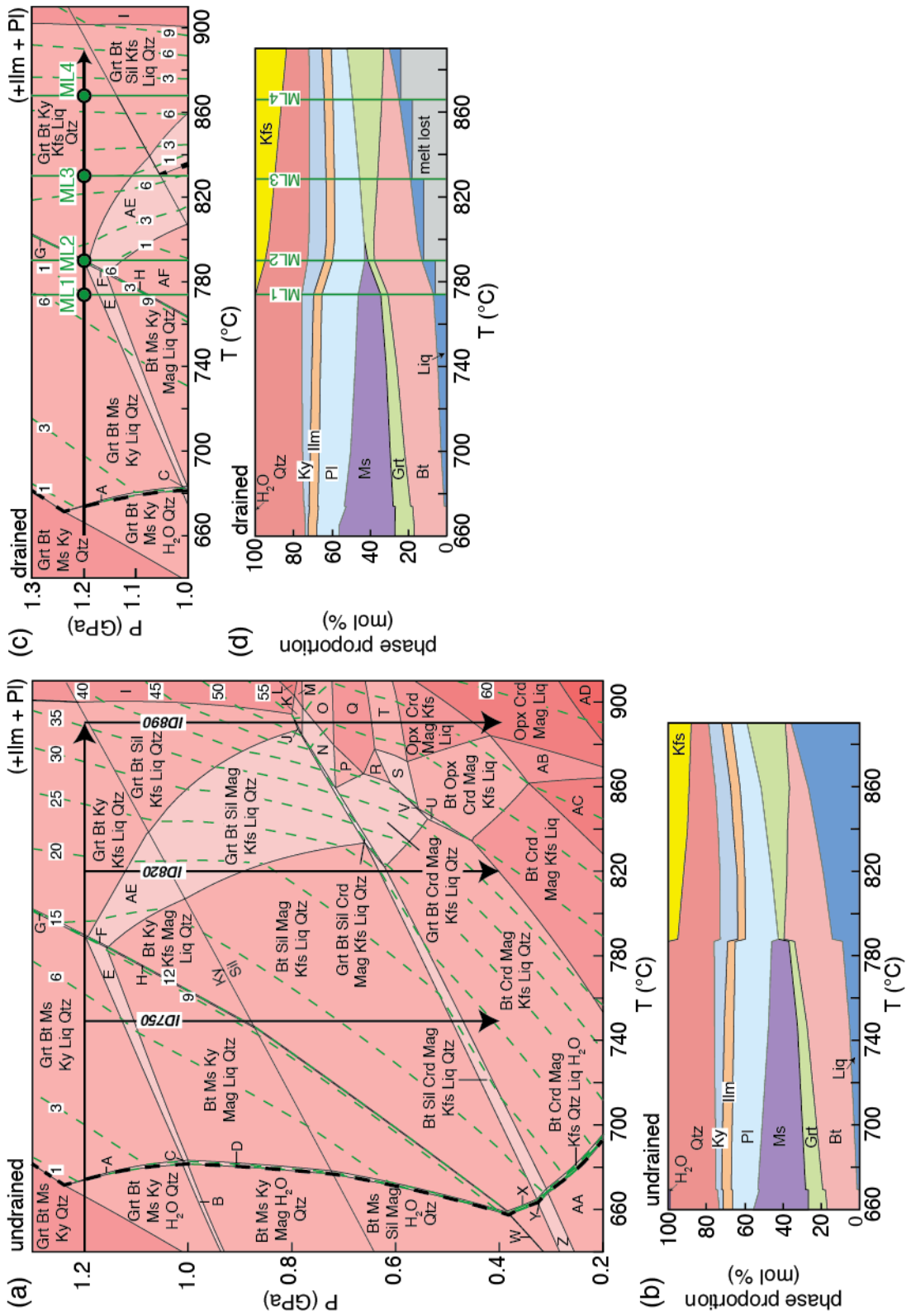
(a)
undrained
(+Ilm + Pl)
P (GPa)
T (°C)
(b)
phase proportion (mol %)
(c)
drained
(d)
ML1
ML2
ML3
ML4
melt lost
Liq
Kfs
Qtz
Ky
Ilm
Pl
Ms
Grt
Bt

unrealistic in the general case and melt will drain from the system at or before the MCT in nature.

6.4.2 Isobaric heating at 1.2 GPa in a drained (conditionally open) system

If the system is considered drained (conditionally open) with melt extraction occurring at the MCT, then four melt loss events will occur along the same isobaric heating path discussed in the previous section. For the drained situation, a composite of five pseudosection panels arranged from low to high temperature, representing the initial protolith composition and a sequence of progressively more residual bulk chemical compositions following melt loss events, is shown in Fig. 6.1c. The lowest temperature panel is part of the pseudosection for the undrained situation shown in Fig. 6.1a and is appropriate for the isobaric heating segment up to the first melt loss event, after which the next panel up-temperature represents the pseudosection calculated for the residual bulk chemical composition after the first drainage event. This panel is appropriate for continued isobaric heating until the second melt loss event and so on (Fig. 6.1c). Thus, the drainage events are located on the seams between the panels. The changes in modes for a drained system are shown in Fig. 6.1d. Isobaric heating from the solidus to 890°C yields a cumulative total of 30 mol% melt, which is less than the cumulative total of 36 mol% melt produced along this path for the undrained case. More importantly, the bulk chemical compositions at temperatures above the first melt loss event become increasingly residual at each melt extraction step (Table 6.2), which will affect the amount of melt produced during decompression in comparison with the undrained case, as discussed next.

6.4.3 Isothermal decompression in a drained (conditionally open) system

Changes to the topology of the pseudosections and the slope of melt mol% isopleths due to stepwise melt extraction along each of the three isobaric heating–isothermal decompression *P–T* paths modelled, ID750, ID820 and ID890 in Fig. 6.1a, are shown in Figs 6.2–6.4, and the results are summarized in Table 6.4. The history of melting and melt loss along each of these three *P–T* paths is described below.

For the lowest temperature *P–T* path (path ID750 in Fig. 6.1a), isobaric heating from the solidus to 750°C produces 5 mol% melt (Fig. 6.1a). Isothermal decompression from 1.20 to 1.04 GPa produces an additional 2 mol% melt (Fig. 6.1a), which is enough to reach the MCT and trigger melt extraction. After this melt loss event (ML1), the residual bulk chemical composition, including the 1 mol% melt retained, based on observations from residual rocks in nature, was used to calculate a new pseudosection, which is shown in Fig. 6.2a. Two additional melt loss events are encountered along the isothermal decompression path. ML2 occurs at 0.79 GPa, at a pressure just below the narrow muscovite–K-feldspar trivariant field, as shown in Fig. 6.2a. The pseudosection calculated for the residual bulk chemical composition after the second melt loss event is shown in Fig. 6.2b. ML3 occurs at 0.44 GPa within the stability field of cordierite, as shown in Fig. 6.2b, resulting in the pseudosection shown in Fig 6.2c. The pseudosections for the melt-depleted compositions in Fig. 6.2 show elevated solidi and an increased stability field for K-feldspar compared to the pseudosection for the undrained composition (Fig. 6.1a).

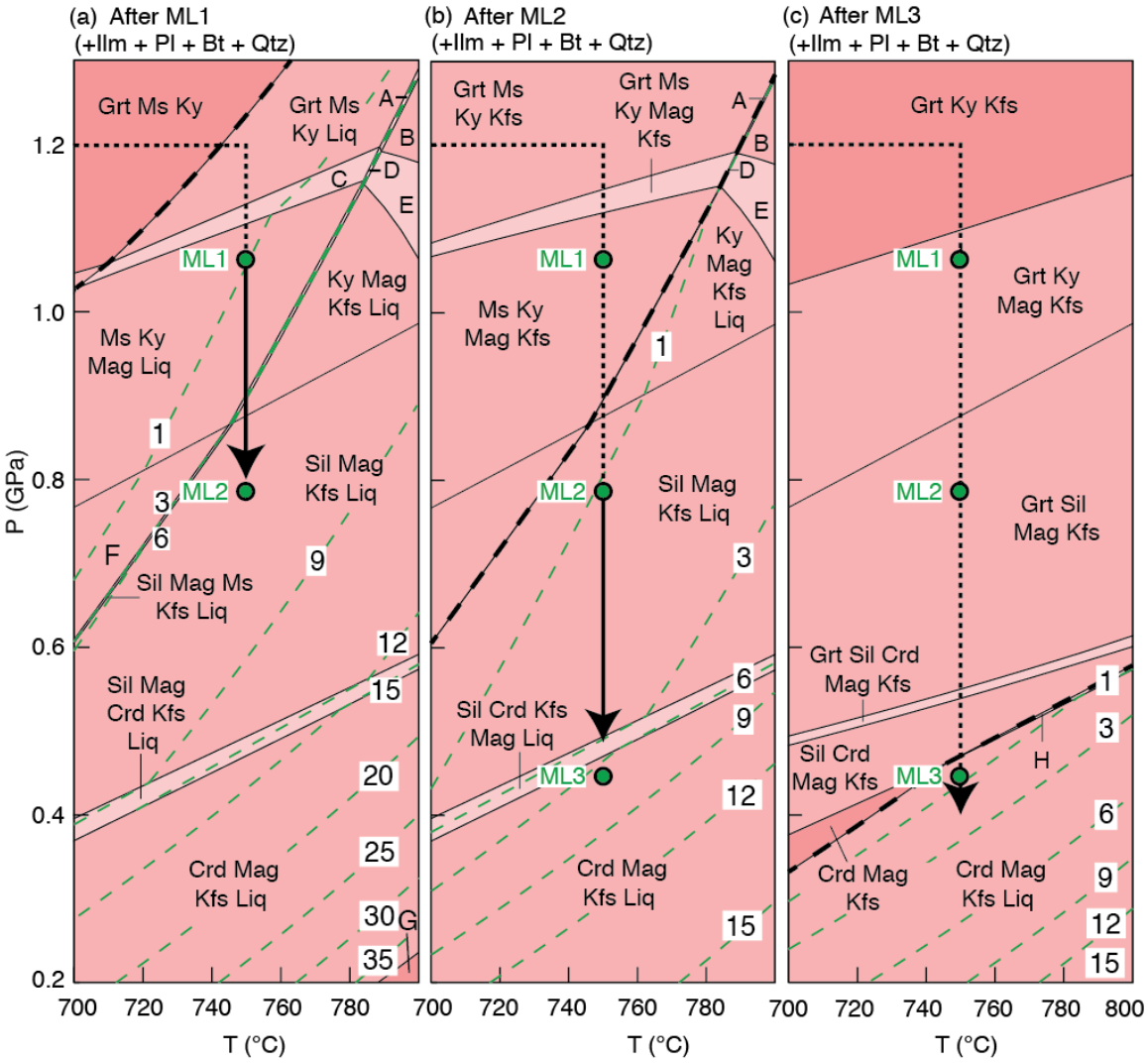

Fig. 6.2. *P–T* pseudosections for the pelite calculated after successive melt loss (ML) events along a *P–T* path comprising a prograde isobaric heating segment at 1.2 GPa followed by isothermal decompression at 750°C. The heavy dashed line is the solidus and the coloured dashed lines are contours of mol% melt. Phase assemblages are as follows in addition to Ilm, Pl, Bt and Qtz: A. Grt Ky Ms Kfs Liq; B. Grt Ky Kfs Liq; C. Grt Ky Ms Mag Liq; D. Grt Ky Ms Mag Kfs Liq; E. Grt Ky Mag Kfs Liq; F. Ms Sil Mag Liq; G. Crd Mag Kfs Liq (-Qtz); H. Sil Crd Mag Kfs Liq.

Table 6.4. *Summary of modelling results for open system melting*

P–T path	Figure	prograde segment		isothermal decompression segment				summary	
		melt loss events	melt produced (mol%)	melt loss events	melt produced (mol%)	melt consumed (mol%)	solidus crossed	total melt loss events	cumulative melt produced (mol%)
Metapelite									
ID750	6.2	0	5	3	15	0	–	3	20
ID820	6.3	2	18	2	14	4	–	4	28
ID890	6.4	4	30	1	3	3	0.76 GPa	5	30
HP	6.6	3	23	2	10	2	–	5	31
Greywacke									
ID750	6.9	0	7	1	2	1	0.61 GPa	1	8
ID820	6.10	1	9	2	11	0	–	3	20
ID890	6.12	1	17	1	2	1	0.77 GPa	2	18
HP	6.12	1	12	2	7	0	–	3	19

For the intermediate *P–T* path (path ID820 in Fig. 6.1a), isobaric heating from the solidus to 820°C results in two melt loss events prior to decompression; the first occurs at 774°C before the *P–T* path reaches the narrow muscovite–K-feldspar trivariant field, whereas the second occurs within this phase assemblage field at 790°C (Figs 6.1c, 6.3). In the pseudosection for the melt-depleted composition after ML2, isopleths of mol% melt have negative slopes at intermediate temperatures and moderate pressures so that isothermal decompression will initially consume melt, garnet and K-feldspar to produce biotite and plagioclase until the *P–T* path reaches 0.89 GPa, where the isopleths of mol% melt return to positive slopes (Fig. 6.3a). Melting continues to the cordierite-bearing field as shown in Fig. 6.3a, where a third melt loss event occurs at 0.63 GPa (ML3 in Fig. 6.3a). A fourth melt loss event occurs at 0.47 GPa (ML4 in Fig. 6.3b). After four drainage events, the pseudosection in Fig. 6.3c shows an elevated solidus reflecting the residual bulk chemical composition.

For the highest temperature *P–T* path (path ID890 in Fig. 6.1a), isobaric heating from the solidus to 890°C results in four melt loss events prior to decompression (Figs 6.1c, 6.4). The pseudosection for the melt-depleted bulk chemical composition after four drainage events (Fig. 6.4a) shows an elevated solidus at c. 860°C at moderate pressure conditions and steep isopleths of mol% melt at $P > 0.8$ GPa. Along the isothermal decompression segment at 890°C a fifth and final melt loss event occurs at 1.0 GPa (ML5 in Fig. 6.4a). After five drainage events, the pseudosection in Fig. 6.4b shows a reduced stability field for biotite, which is only stable at $P > 0.7$ GPa. During continued decompression from ML5 the *P–T* path crosses the biotite-out field boundary at 0.79 GPa and the solidus at 0.76 GPa, producing a subsolidus assemblage that includes garnet,

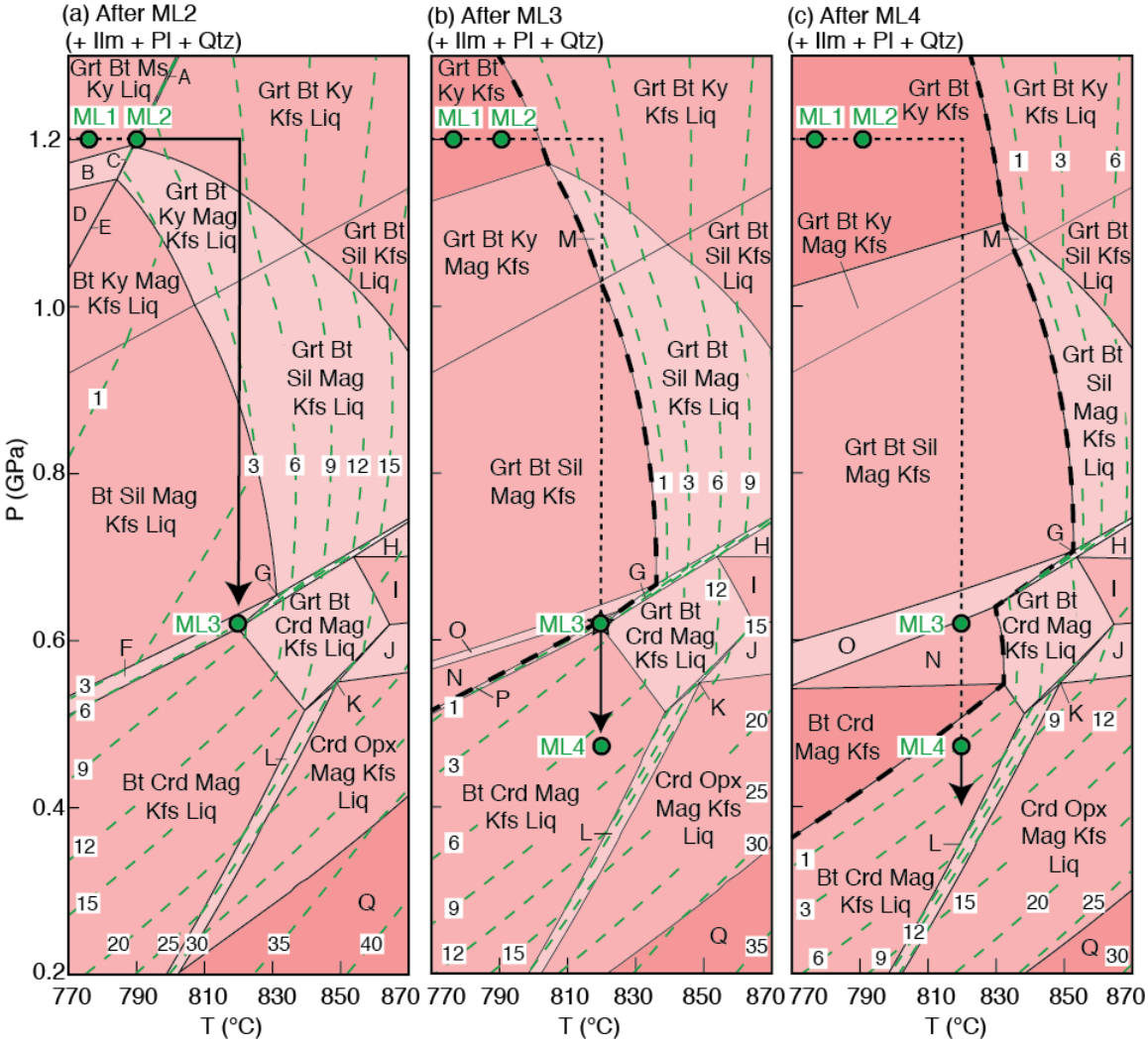

Fig. 6.3. *P–T* pseudosections for the pelite calculated after successive melt loss (ML) events along a *P–T* path comprising a prograde isobaric heating segment at 1.2 GPa followed by isothermal decompression at 820°C. The heavy dashed line is the solidus and the coloured dashed lines represent contours of mol% melt. Phase assemblages are as follows in addition to Ilm, Qtz and Pl: A. Grt Bt Ky Ms Kfs Liq; B. Grt Bt Ky Ms Mag Liq; C. Grt Bt Ky Ms Mag Kfs Liq; D. Bt Ky Ms Mag Liq; E. Bt Ky Ms Mag Kfs Liq; F. Bt Sil Crd Mag Kfs Liq; G. Grt Bt Sil Crd Mag Kfs Liq; H. Grt Sil Crd Mag Kfs Liq; I. Grt Crd Mag Kfs Liq; J. Grt Opx Crd Mag Kfs Liq; K. Grt Bt Opx Crd Mag Kfs Liq; L. Bt Opx Crd Mag Kfs Liq; M. Grt Bt Ky Mag Liq; N. Grt Bt Crd Mag Kfs; O. Grt Bt Sil Crd Mag Kfs; P. Grt Bt Crd Mag Kfs Liq; Q. Opx Crd Mag Kfs Liq (-Qtz).

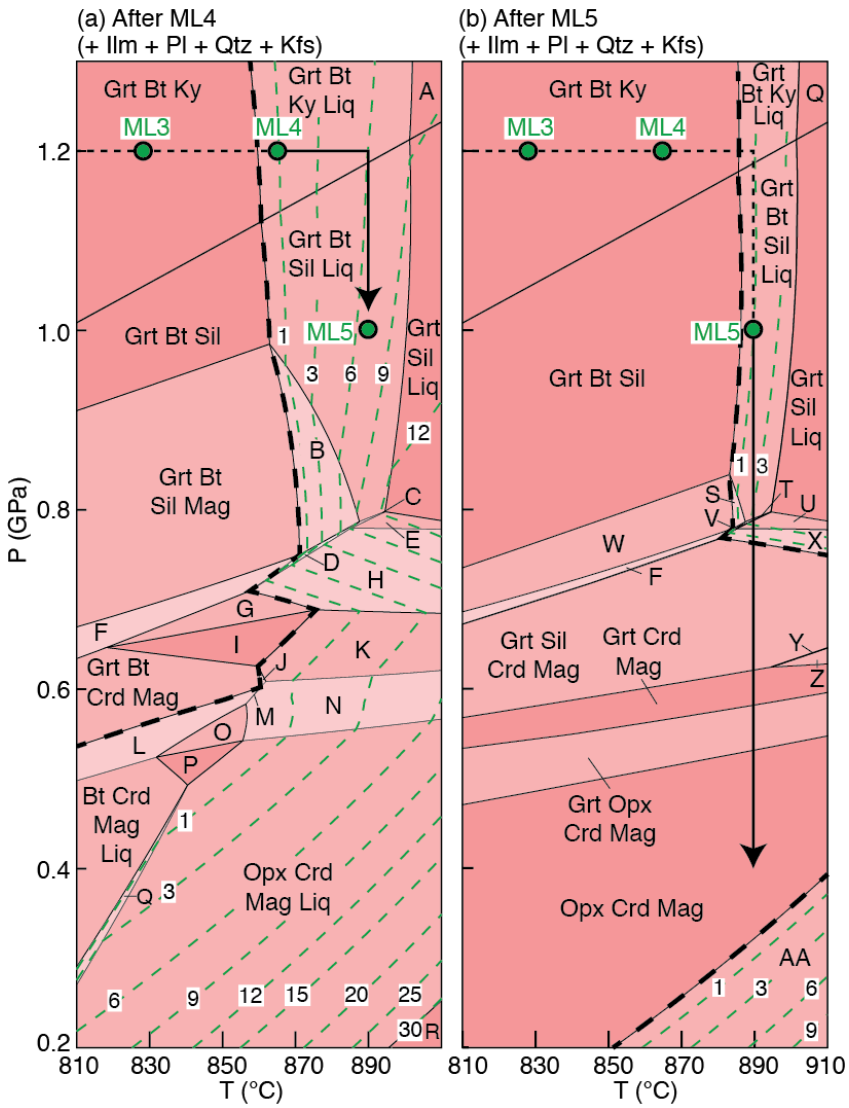

Fig. 6.4. *P–T* pseudosections for the pelite calculated after successive melt loss (ML) events along a *P–T* path comprising a prograde isobaric heating segment at 1.2 GPa followed by isothermal decompression at 890°C. The heavy dashed line is the solidus and the coloured dashed lines represent contours of mol% melt. Phase assemblages are as follows in addition to Ilm, Pl, Kfs and Qtz: A. Grt Ky Liq; B. Grt Bt Sil Mag Liq; C. Grt Bt Sil Crd Liq; D. Grt Bt Sil Crd Mag Liq; E. Grt Sil Crd Liq; F. Grt Bt Sil Crd Mag; G. Grt Bt Crd Mag; H. Grt Bt Crd Mag Liq; I. Grt Crd Mag; J. Grt Bt Opx Crd Mag; K. Grt Crd Mag Liq; L. Grt Bt Crd Mag Liq; M. Grt Bt Opx Crd Mag Liq; N. Grt Opx Crd Mag Liq; O. Grt Crd Mag Liq; P. Crd Mag Liq; Q. Bt Opx Crd Mag Liq; R. Opx Crd Mag Liq (-Qtz); S. Grt Bt Sil Mag Liq; T. Grt Bt Sil Crd Liq; U. Grt Bt Sil Mag Liq; V. Grt Bt Sil Crd Liq; W. Grt Bt Sil Mag; X. Grt Bt Sil Crd Mag Liq; Y. Grt Sil Crd Mag Spl; Z. Grt Crd Mag Spl; AA. Opx Crd Mag Liq.

sillimanite, cordierite and magnetite (in addition to quartz, plagioclase, ilmenite, and K-feldspar; Fig. 6.4b).

6.4.4 Summary

Composite *P–T* diagrams for each of the three isobaric heating–isothermal decompression paths are shown in Fig. 6.5a, b and c. Each diagram comprises pseudosection panels for a range of pressure, taken from Figs 6.2, 6.3 and 6.4 and stacked from high to low pressure, representing the evolution between melt loss events. Thus, the drainage events are located on the seams between the panels. The changes in modes along each isothermal decompression segment are shown on pressure–phase proportion diagrams in Fig. 6.5d, e and f.

Of particular interest is the quantity of melt present and the amount of melt that has been extracted at any pressure, and the cumulative amount of melt that was generated along each path. Along paths ID750, ID820 and ID890, melting yielded cumulative totals of 20, 28 and 30 mol% melt, respectively (Table 6.4). Although most melt is produced along the highest temperature *P–T* path, most of this melt is drained from the system prior to decompression; along the decompression segment the system becomes melt absent below 0.76 GPa. A large increase in melt over a small *P–T* range occurs when a

---

Fig. 6.5. (a, b, c) Composite *P–T* diagrams comprising multiple pseudosection panels taken from Figs 6.2, 6.3 and 6.4 and stacked from high to low pressure for each of the different isobaric heating–isothermal decompression *P–T* paths modelled for the pelite. Each pseudosection panel shows the evolution between melt drainage events and the melt drainage events are located on the seams between the panels. The heavy dashed line is the solidus and the coloured dashed lines represent contours of mol% melt. (d, e, f) Molar proportion of phases plotted against pressure for each of the three decompression paths.

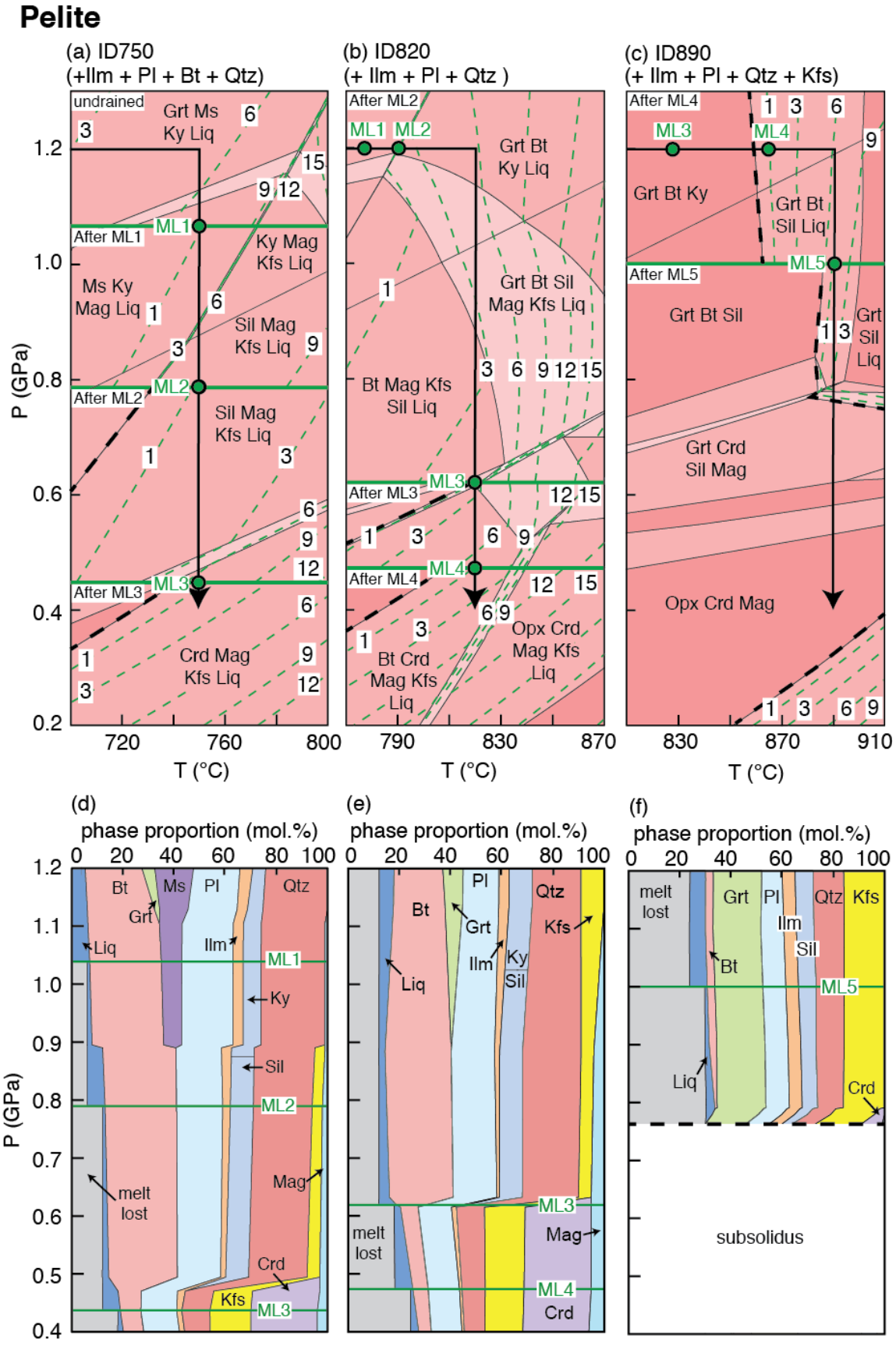
Pelite
(a) ID750
(+Ilm + Pl + Bt + Qtz)
(b) ID820
(+ Ilm + Pl + Qtz)
(c) ID890
(+ Ilm + Pl + Qtz + Kfs)
P (GPa)
T (°C)
undrained
Grt Ms
Ky Liq
After ML1
ML1
Ky Mag
Kfs Liq
Ms Ky
Mag Liq
Sil Mag
Kfs Liq
After ML2
ML2
Sil Mag
Kfs Liq
After ML3
ML3
Crd Mag
Kfs Liq
After ML2
ML1
ML2
Grt Bt
Ky Liq
Grt Bt Sil
Mag Kfs Liq
Bt Mag Kfs
Sil Liq
After ML3
ML3
After ML4
ML4
Opx Crd
Mag Kfs
Liq
Bt Crd
Mag Kfs
Liq
After ML4
ML3
ML4
Grt Bt Ky
Grt Bt
Sil Liq
After ML5
ML5
Grt Bt Sil
Grt
Sil
Liq
Grt Crd
Sil Mag
Opx Crd Mag
(d)
(e)
(f)
phase proportion (mol.%)
Bt
Ms
Pl
Qtz
Grt
Liq
Ilm
ML1
Ky
Sil
ML2
Mag
melt
lost
Crd
Kfs
ML3
ML4
subsolidus

path crosses the muscovite–K-feldspar trivariant field either through decompression (path ID750) or heating (paths ID820 and ID890). For the two higher temperature *P–T* paths initial decompression produces little additional melt. For path ID820, it is only after decompression passes below 0.6 GPa that extensive melting occurs through the breakdown of biotite and sillimanite to produce cordierite and melt.

6.5 High *P–T* isothermal decompression for a pelite

6.5.1 Undrained (closed) system

A pseudosection for the pelite for the *P–T* range 0.2–2.0 GPa and 640–910°C is shown in Fig. 6.6a. Between 0.2 and 1.3 GPa this pseudosection is the same as Fig. 6.1a, but at higher pressures rutile and clinopyroxene are stable. Isopleths of mol% melt have steep slopes at high pressures. In an undrained (closed) system, the amount of melt produced from the pelite along the prograde segment from the solidus at 1.2 GPa to 860°C at 1.8 GPa is 20 mol% (Fig. 6.6a). Isothermal decompression from 1.8 to 0.4 GPa at 860°C generates an additional 32 mol% melt, yielding a cumulative total of 52 mol% for this *P–T* evolution (Fig. 6.6a). However, as discussed above, this is unrealistic in the general case and melt will drain from the system at or before the MCT in nature.

6.5.2 Drained (conditionally open) system

If the system is considered drained (conditionally open) then three melt loss events will occur along the same prograde path discussed in the previous section. The pseudosection for the undrained situation, shown in Fig. 6.6a, is only appropriate until the first melt loss event. Three melt loss events occur along the prograde segment of the *P–T*

path within the narrow muscovite–K-feldspar trivariant field at 1.79 GPa and 859°C (ML1, ML2 and ML3 in the insert in Fig. 6.6b). For the drained situation, a composite of three pseudosection panels stacked from high to low pressure is shown in Fig. 6.6b, representing the evolution after ML3 at high pressure and for the last two melt drainage events with decreasing pressure.

The top panel of Fig. 6.6b shows steep to negatively sloping isopleths of mol% melt at $P > 0.8$ GPa, so that isothermal decompression from 1.80 to 0.72 GPa consumes 2 mol% melt. A fourth melt drainage event is encountered at 0.71 GPa in the cordierite–garnet–sillimanite trivariant field (ML4 in Fig. 6.6b), resulting in the pseudosection

---

Fig. 6.6. (a) *P–T* pseudosection calculated to higher pressures for an average amphibolite-facies pelite composition assuming undrained (closed system) conditions. (b) A composite *P–T* diagram comprising three pseudosection panels, stacked from high to low pressure, for drained (conditionally open system) conditions. Each panel is appropriate for decompression from one melt loss event to the next. The heavy dashed line is the solidus and the coloured dashed lines represent contours of mol% melt. (c,d) Molar proportion of phases for the prograde (c) and decompression (d) segments of the modelled *P–T* path during conditionally open system melting. Phase assemblages are as follows in addition to Ilm and Pl: A. Grt Bt Ky Ms Liq H_2O Qtz; B. Grt Bt Ky Ms Mag H_2O Qtz; C. Grt Bt Ky Ms Mag Liq H_2O Qtz; D. Bt Ky Ms Mag Liq H_2O Qtz; E. Grt Bt Ky Ms Mag Liq Qtz; F. Grt Bt Ky Ms Mag Kfs Liq Qtz; G. Grt Bt Ky Ms Kfs Liq Qtz; H. Bt Ky Ms Mag Kfs Liq Qtz; I. Grt Sil Kfs Liq Qtz; J. Grt Bt Sil Crd Kfs Liq Qtz; K. Grt Sil Crd Kfs Liq Qtz; L. Grt Sil Kfs Liq; M. Grt Crd Kfs Liq; N. Grt Crd Mag Kfs Liq Qtz; O. Grt Crd Mag Kfs Liq; P. Grt Crd Mag Kfs Liq Qtz; Q. Grt Crd Mag Kfs Liq; R. Grt Bt Crd Mag Kfs Liq; S. Grt Bt Opx Crd Mag Kfs Liq; T. Grt Opx Crd Mag Kfs Liq; U. Bt Opx Crd Mag Kfs Liq Qtz; V. Grt Bt Opx Crd Mag Kfs Liq Qtz; W. Bt Sil Ms Mag Kfs H_2O Qtz; X. Bt Sil Mag Kfs Liq H_2O Qtz; Y. Bt Sil Crd Mag Kfs Liq H_2O Qtz; Z. Bt Sil Crd Mag Kfs H_2O Qtz; AA. Bt Crd Mag Kfs Qtz H_2O; AB. Bt Opx Crd Mag Liq; AC. Bt Crd Mag Liq; AD. Crd Mag Liq; AE. Grt Bt Ms Rt Liq Qtz; AF. Grt Ky Ms Rt Liq Qtz; AG. Grt Bt Ky Ms Rt Kfs Liq Qtz; AH. Grt Bt Ky Ms Rt Kfs Liq Qtz (-Pl); AI. Grt Bt Ky Ms Kfs Liq Qtz (-Pl); AJ. Grt Bt Ky Ms Kfs Liq Qtz (-Pl); AK. Grt Bt Ky Rt Kfs Liq Qtz (-Pl); AL. Grt Ky Rt Kfs Liq Qtz (-Pl); AM. Grt Ky Kfs Liq Qtz (-Pl); AN. Grt Ky Kfs Liq Qtz (-Pl); AO. Grt Bt Ky Kfs Liq Qtz (-Pl); AP. Grt Bt Sil Mag Kfs Liq Qtz; AQ. Grt Bt Sil Crd Mag Kfs Liq Qtz; AR. Grt Bt Crd Mag Kfs Liq Qtz; AS. Grt Opx Crd Mag Kfs Liq Qtz; AT. Grt Bt Sil Crd Mag Kfs Qtz; AU. Grt Bt Crd Mag Kfs Qtz; AV. Grt Bt Opx Crd Mag Kfs Qtz; AW. Opx Crd Mag Kfs Qtz; AY. Bt Opx Crd Mag Kfs Liq Qtz.

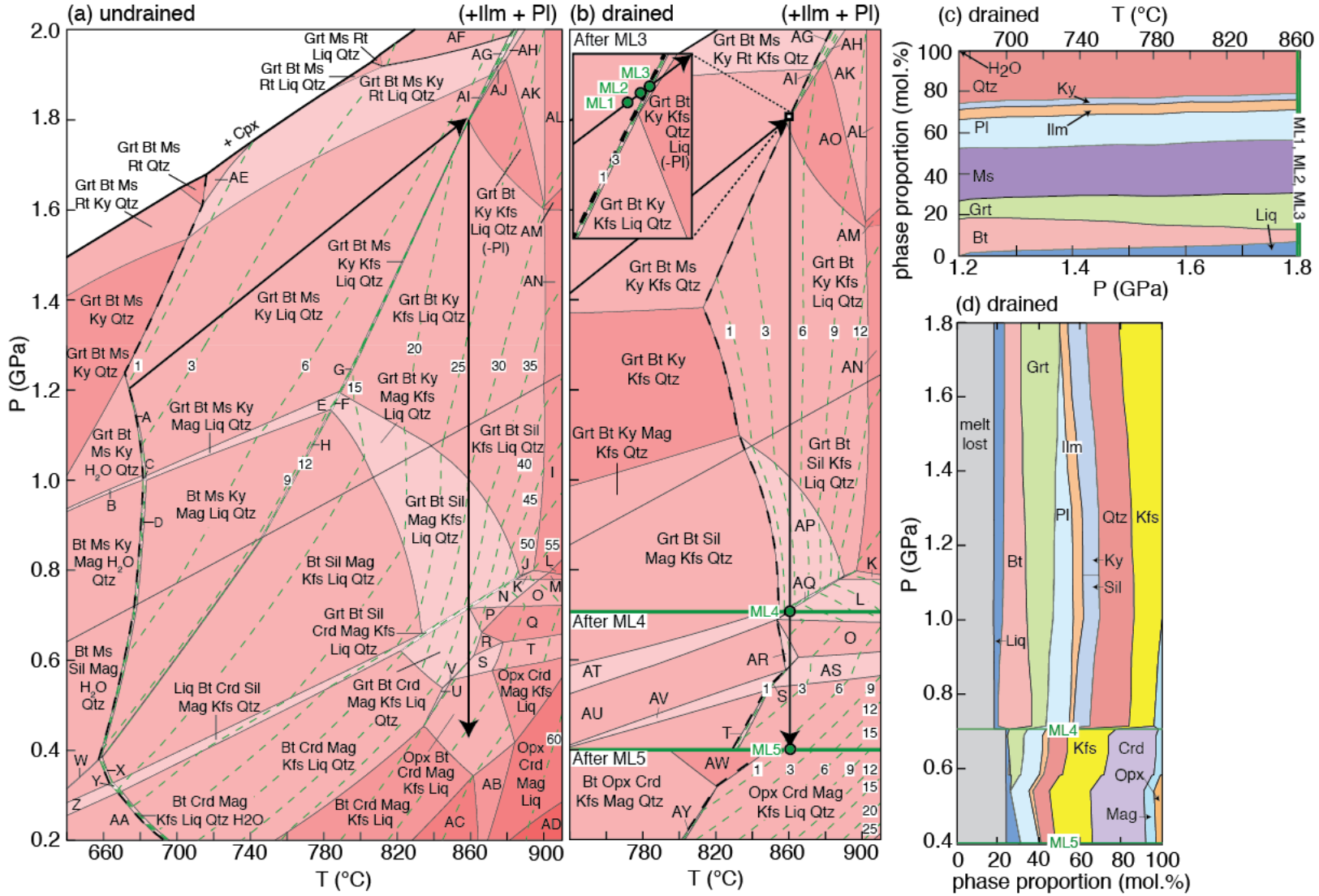
(a) undrained
(+Ilm + Pl)
(b) drained
(+Ilm + Pl)
(c) drained
(d) drained
P (GPa)
T (°C)
phase proportion (mol.%)
After ML3
After ML4
After ML5
ML1
ML2
ML3
ML4
ML5
Grt Ms Rt Liq Qtz
Grt Bt Ms Rt Liq Qtz
Grt Bt Ms Ky Rt Liq Qtz
+ Cpx
Grt Bt Ms Rt Qtz
Grt Bt Ms Rt Ky Qtz
Grt Bt Ms Ky Qtz
Grt Bt Ms Ky Liq Qtz
Grt Bt Ms Ky Kfs Liq Qtz
Grt Bt Ky Kfs Liq Qtz (-Pl)
Grt Bt Ky Mag Kfs Liq Qtz
Grt Bt Sil Kfs Liq Qtz
Grt Bt Ms Ky Mag Liq Qtz
Grt Bt Ms Ky H2O Qtz
Bt Ms Ky Mag Liq Qtz
Grt Bt Sil Mag Kfs Liq Qtz
Bt Ms Ky Mag H2O Qtz
Bt Sil Mag Kfs Liq Qtz
Grt Bt Sil Crd Mag Kfs Liq Qtz
Bt Ms Sil Mag H2O Qtz
Liq Bt Crd Sil Mag Kfs Qtz
Grt Bt Crd Mag Kfs Liq Qtz
Opx Crd Mag Kfs Liq
Bt Crd Mag Kfs Liq Qtz
Opx Bt Crd Mag Kfs Liq
Bt Crd Mag Kfs Liq
Opx Crd Mag Liq
Bt Crd Mag Kfs Liq Qtz H2O
Grt Bt Ms Ky Rt Kfs Qtz
Grt Bt Ky Kfs Qtz
Grt Bt Ky Mag Kfs Qtz
Grt Bt Sil Mag Kfs Qtz
Grt Bt Sil Kfs Liq Qtz
Bt Opx Crd Kfs Mag Qtz
Opx Crd Mag Kfs Liq Qtz
H2O
Qtz
Ky
Pl
Ilm
Ms
Grt
Bt
Liq
Sil
Kfs
Crd
Opx
Mag
melt lost

forming the middle panel of Fig. 6.6b. A final melt drainage event occurs at 0.40 GPa (ML5 in Fig. 6.6b), resulting in the pseudosection forming the lower panel of Fig. 6.6b.

The changes in modes along the prograde segment of the *P–T* path from the solidus at 1.2 GPa to peak *P–T* at 1.8 GPa and 860°C, and for the decompression segment to 0.4 GPa are shown on the two pressure–phase proportion diagrams in Fig. 6.6c, d. The full *P–T* evolution yields a cumulative total of 31 mol% melt, which is less than the 52 mol% produced along this path for the undrained case.

6.6 Isobaric heating and isothermal decompression for a greywacke at moderate crustal pressures

6.6.1 The initial P–T pseudosection

A pseudosection for the passive margin greywacke for a *P–T* range of 0.2–1.3 GPa and 640–910°C is shown in Fig. 6.7a. This composition is less fertile than the pelite and contains different mineral assemblages over the modelled *P–T* range. Garnet is stable at high pressures across the diagram. Kyanite or sillimanite is stable at $P > 0.4$–0.8 GPa. Muscovite and paragonite are restricted to $P > 1.0$ GPa. Cordierite is stable at *P* of 0.6–0.8 GPa with increasing temperature and orthopyroxene is stable at $P < 0.7$ GPa at temperatures >760°C. K-feldspar is stable at $P > 0.8$ GPa at high temperatures. Rutile is stable at high pressures at $T > 850$°C. Quartz, plagioclase and ilmenite are stable across the full *P–T* range shown.

Melt mol% isopleths have steeper slopes in the garnet stability field, shallower slopes in the cordierite stability field and negative to positive slopes in the narrow garnet–sillimanite–cordierite trivariant field (Fig. 6.7a). In contrast to the pelite (Fig. 6.1a), the

melt isopleths in the pseudosection for the greywacke are more evenly spaced (Fig. 6.7a). This indicates that melt is produced more gradually across the modelled *P–T* range for the greywacke as opposed to the pelite, where melt may be produced in pulses across narrow low-variance fields (cf. Johnson et al. 2008).

6.6.2 Isobaric heating at 1.2 GPa followed by decompression in an undrained (closed) system

In an undrained (closed) system, the amount of melt produced from the greywacke along the isobaric heating segment at 1.2 GPa is 21 mol% (Fig. 6.7a). This is at the low end of the range of results for the model calculations of Johnson et al. (2008) for seven greywacke compositions at the lower pressure of 0.7 GPa, where melt volume

---

Fig. 6.7. (a) *P–T* pseudosection calculated for the greywacke assuming undrained (closed system) conditions. The heavy dashed line is the solidus and the coloured dashed lines represent contours of mol% melt. (b) Molar proportion of phases plotted against temperature for isobaric heating for a closed system. (c) A composite *P–T* diagram comprising three pseudosection panels arranged from low to high temperature for drained (conditionally open system) conditions. The lowest temperature panel is appropriate for isobaric heating up to the first melt loss (ML) event, which leads to the second panel at higher temperatures calculated for the drained composition. This panel is appropriate for investigating phase relations until the second melt loss event and so on. The heavy dashed line is the solidus and the coloured dashed lines represent contours of mol% melt. (d) Molar proportion of phases plotted against temperature for isobaric heating for a conditionally open system. Phase assemblages are as follows in addition to Ilm, Pl, and Qtz: A. Grt Bt Pg Ms; B. Grt Bt Pg Ms Liq H_2O; C. Grt Bt Pg Ms H_2O; D. Grt Bt Pg; E. Grt Bt Pg H_2O; F. Grt Bt Ky Pg H_2O; G. Grt Bt Sil Mag H_2O; H. Grt Bt Sil Crd Mag Liq H_2O; I. Grt Bt Sil Crd Mag H_2O; J. Bt Sil Crd Mag Liq H_2O; K. Bt Sil Crd Liq; L. Bt Sil Crd Liq H_2O; M. Bt Crd Liq; N. Bt Sil Crd H_2O; O. Bt Crd Liq H_2O; P. Bt Crd H_2O; Q. Bt Crd Mag H_2O; R. Grt Sil Rt Liq; S. Grt Sil Kfs Liq; T. Grt Sil Liq; U. Grt Sil Crd Liq; V. Grt Crd Liq; W. Grt Bt Crd Liq; X. Grt Bt Opx Crd Liq; Y. Grt Opx Crd Mag Liq; Z. Grt Bt Pg Ms Rt; AA. Grt Bt Pg Ms Liq; AB. Grt Bt Pg Ms Rt Liq; AC. Grt Bt Ky Pg Ms Rt Liq; AD. Grt Bt Ky Ms Rt Liq. AD, Grt Bt Ms Ky Rt Liq; AE, Grt Bt Ky Kfs Liq; AF, Grt Bt Ky Kfs Rt Liq; AG, Grt Ky Kfs Rt Liq; AH, Grt Bt Sil Kfs Rt Liq.

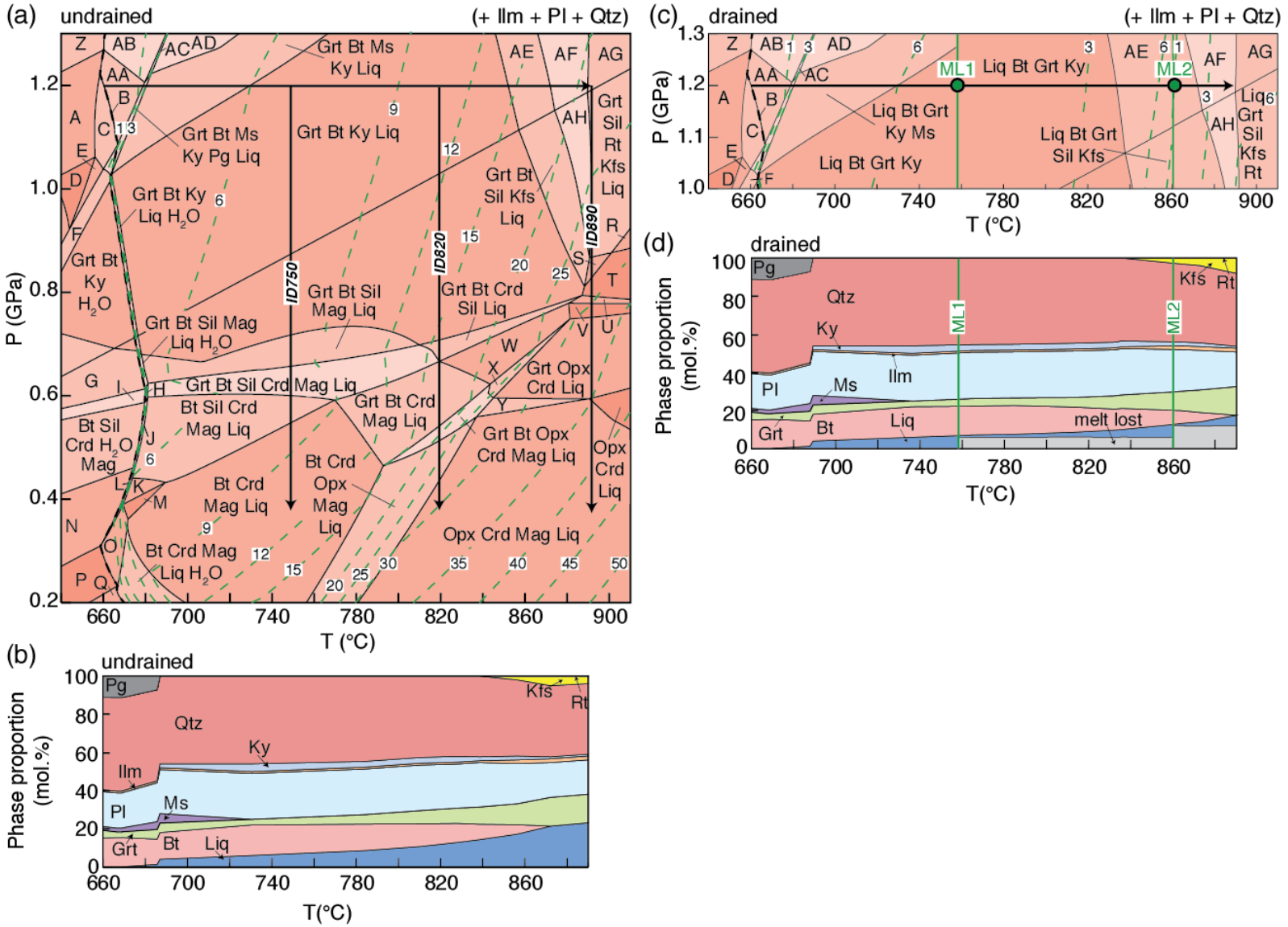
(a)
undrained
(+ Ilm + Pl + Qtz)
P (GPa)
T (°C)
Grt Bt Ms Ky Liq
Grt Bt Ms Ky Pg Liq
Grt Bt Ky Liq
Grt Bt Ky Liq H2O
Grt Bt Ky H2O
Grt Bt Sil Mag Liq H2O
Grt Bt Sil Mag Liq
Grt Bt Sil Crd Mag Liq
Bt Sil Crd Mag Liq
Bt Sil Crd H2O Mag
Grt Bt Crd Mag Liq
Grt Bt Crd Sil Liq
Grt Bt Sil Kfs Liq
Grt Opx Crd Liq
Grt Bt Opx Crd Mag Liq
Bt Crd Mag Liq
Bt Crd Opx Mag Liq
Opx Crd Mag Liq
Bt Crd Mag Liq H2O
Grt Sil Rt Kfs Liq
Opx Crd Liq
ID750
ID820
ID890
(b)
undrained
Phase proportion (mol.%)
T(°C)
Pg
Qtz
Ky
Kfs
Rt
Ilm
Pl
Ms
Grt
Bt
Liq
(c)
drained
(+ Ilm + Pl + Qtz)
P (GPa)
T (°C)
ML1
ML2
Liq Bt Grt Ky
Liq Bt Grt Ky Ms
Liq Bt Grt Sil Kfs
Liq Grt Sil Kfs Rt
(d)
drained
Phase proportion (mol.%)
T(°C)
melt lost

would be expected to be higher. The changes in modes along this isobaric heating segment are shown on a temperature–phase proportion diagram in Fig. 6.7b. At $T >$ 790°C, the isopleths of mol% melt have positive slopes from 1.2 GPa to 0.2 GPa, so isothermal decompression at any temperature >790°C along this prograde segment results in an increase in the amount of melt. However, as discussed above, this is unrealistic in the general case and melt will drain from the system at or before the MCT in nature. At temperatures <790°C, the isopleths of mol% melt have negative slopes from 680°C to 790°C at c. 0.6 GPa in the garnet–sillimanite–cordierite trivariant field, so that isothermal decompression at a temperature <790°C will first produce melt and then consume melt, before producing melt again at low pressure.

6.6.3 Isobaric heating at 1.2 GPa in a drained (conditionally open) system

If the system is considered drained (conditionally open) then two melt loss events will occur along the isobaric heating path. For the drained situation, a composite of three pseudosection panels arranged from low to high temperature, representing the initial protolith composition and two residual bulk chemical compositions following drainage events (Table 6.3), is shown in Fig. 6.7c. The changes in modes for a drained system are shown in Fig. 6.7d. Isobaric heating from the solidus to 890°C yields a cumulative total of 17 mol% melt, which is c. 80% of that produced in the undrained situation and roughly half the amount of melt that would be generated from an average pelite at the same *P–T* conditions.

6.6.4 Isothermal decompression in a drained (conditionally open) system

Changes to the topology of the pseudosections and the slope of melt mol% isopleths due to stepwise melt extraction along each of the three isobaric heating–isothermal decompression *P–T* paths modelled, ID750, ID820 and ID890 in Fig. 6.7a, are shown in Figs 6.8–6.10, and the results are summarized in Table 6.4. The history of melting and melt loss for isobaric heating and decompression along each of these three *P–T* paths is described below.

For the lowest temperature *P–T* path (path ID750 in Fig. 6.7a), isobaric heating from the solidus to 750°C produces 6.7 mol% melt (Fig. 6.7a). Isothermal decompression from 1.20 to 1.06 GPa produces an additional 0.3 mol% melt, which is enough to reach the MCT and trigger melt extraction. After this first melt loss event, the pseudosection calculated for the residual composition shows isopleths of mol% melt that are steeply positive above the stability field of cordierite, whereas isopleths of mol% melt have negative slopes in the garnet–cordierite–sillimanite trivariant field, a feature that reflects an up-temperature kink in the solidus (Fig. 6.8). Decompression at 750°C through this field consumes melt before crossing the solidus at 0.61 GPa. With continued decompression, the solidus is re-crossed at 0.50 GPa.

For the intermediate *P–T* path (path ID820 in Fig. 6.7a), isobaric heating from the solidus to 820°C results in one melt loss event at 758°C. The pseudosection for the melt-depleted composition after ML1 is shown in Fig. 6.9a. Two additional melt loss events are encountered along the isothermal decompression path. The first occurs at 0.50 GPa (ML2), within the biotite–orthopyroxene trivariant field, as shown in Fig. 6.9a. The second occurs at 0.46 GPa (ML3) within same stability field, as shown in Fig. 6.9b. The

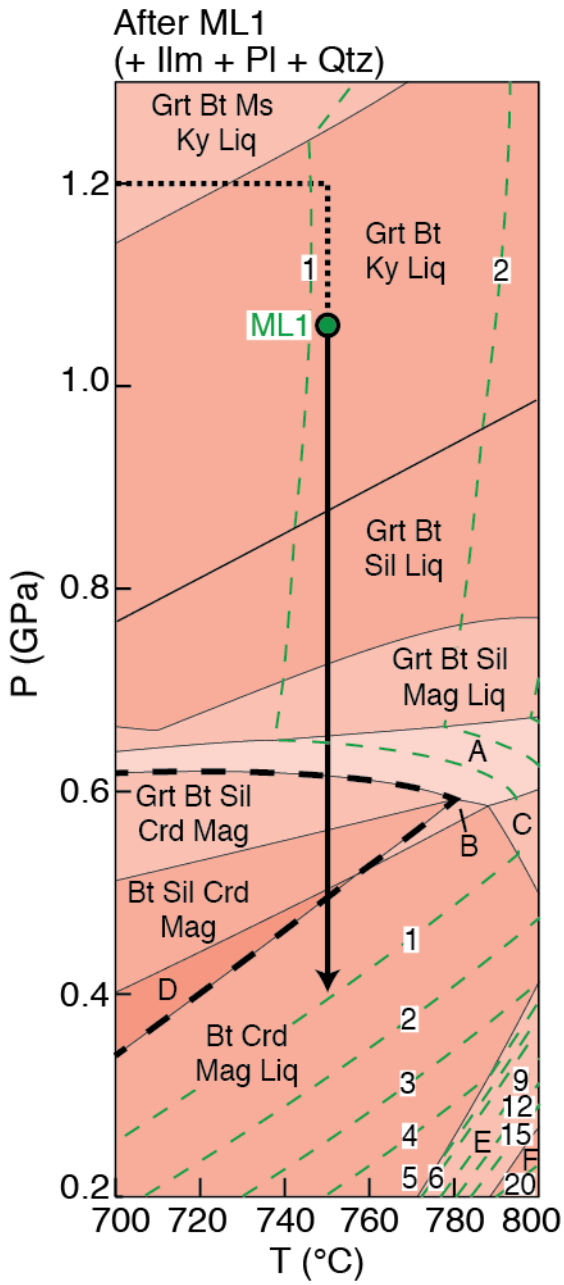

Fig. 6.8. *P–T* pseudosection for the greywacke calculated after a single melt loss (ML) event along a *P–T* path comprising a prograde isobaric heating segment at 1.2 GPa followed by isothermal decompression at 750°C. The heavy dashed line is the solidus and the coloured dashed lines represent contours of mol% melt. Phase assemblages are as follows in addition to Ilm, Pl, and Qtz: A. Grt Bt Sil Crd Mag Liq; B. Bt Sil Crd Mag Liq; C. Grt Bt Crd Mag Liq; D. Bt Crd Mag; E. Bt Opx Crd Mag Liq; F. Opx Crd Mag Liq.

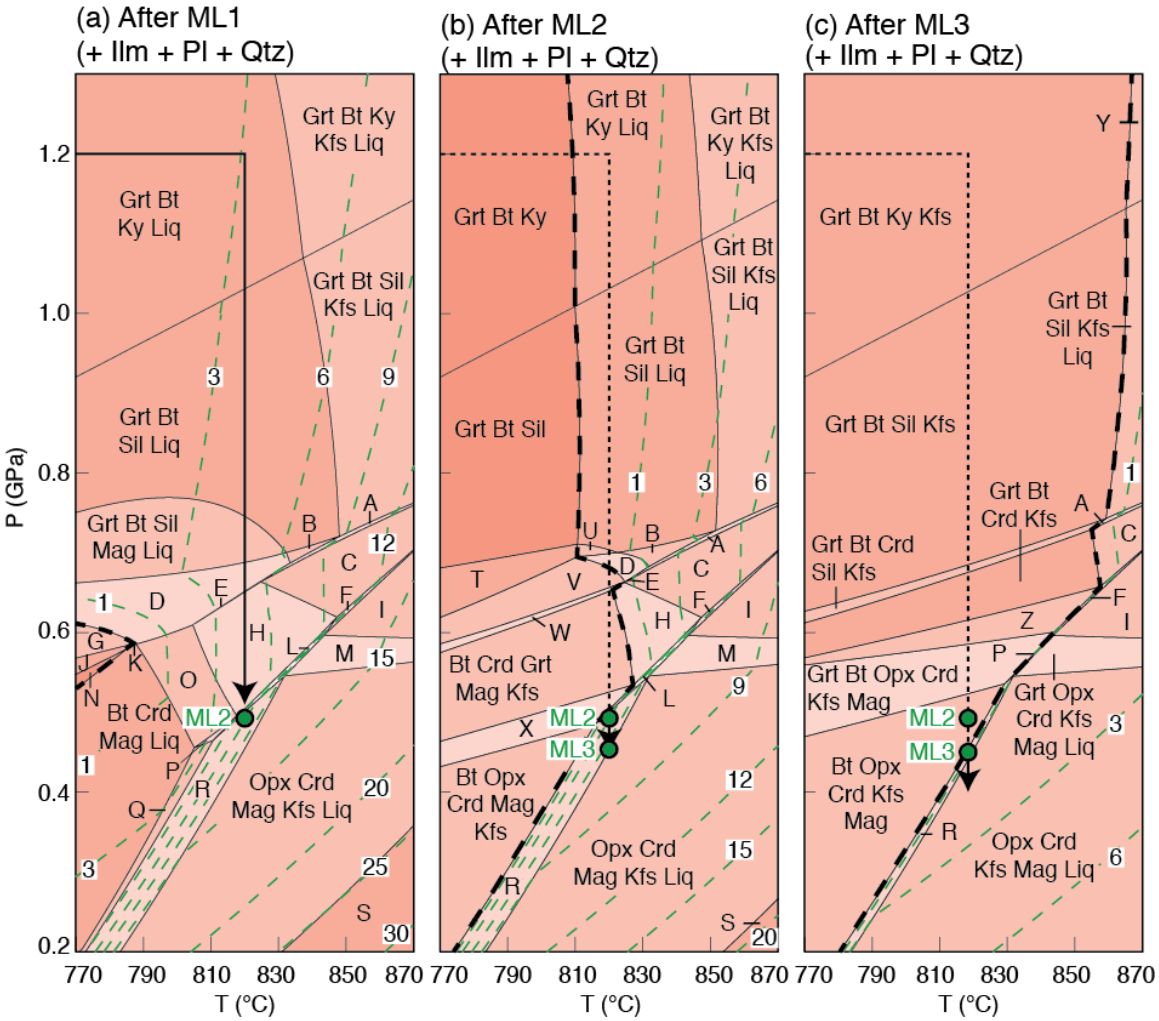

Fig. 6.9. *P–T* pseudosections for the greywacke calculated after successive melt loss (ML) events along a *P–T* path comprising a prograde isobaric heating segment at 1.2 GPa followed by isothermal decompression at 820°C. The heavy dashed line is the solidus and the coloured dashed lines represent contours of mol% melt. Phase assemblages are as follows in addition to Ilm, Pl, and Qtz: A. Grt Bt Sil Crd Kfs Liq; B. Grt Bt Sil Crd Liq; C. Grt Bt Crd Kfs Liq; D. Grt Bt Sil Crd Mag Liq; E. Grt Bt Sil Crd Mag Kfs Liq; F. Grt Bt Opx Crd Kfs Liq; G. Grt Bt Sil Crd Mag; H. Grt Bt Crd Mag Kfs Liq; I. Grt Opx Crd Kfs Liq; J. Bt Sil Crd Mag; K. Bt Sil Crd Mag Liq; L. Grt Bt Opx Crd Mag Kfs Liq; M. Grt Opx Crd Mag Kfs Liq; N. Bt Crd Mag; O. Grt Bt Crd Mag Liq; P. Grt Bt Opx Crd Mag Liq; Q. Opx Crd Mag Liq; R. Opx Crd Mag Kfs Liq; S. Opx Crd Mag Liq; T. Grt Bt Sil Mag; U. Grt Bt Sil Mag Liq; V. Grt Bt Sil Crd Mag; W. Grt Bt Sil Crd Mag Kfs; X. Grt Bt Opx Crd Mag Kfs; Y. Grt Bt Ky Kfs Liq; Z. Grt Bt Opx Crd Kfs.

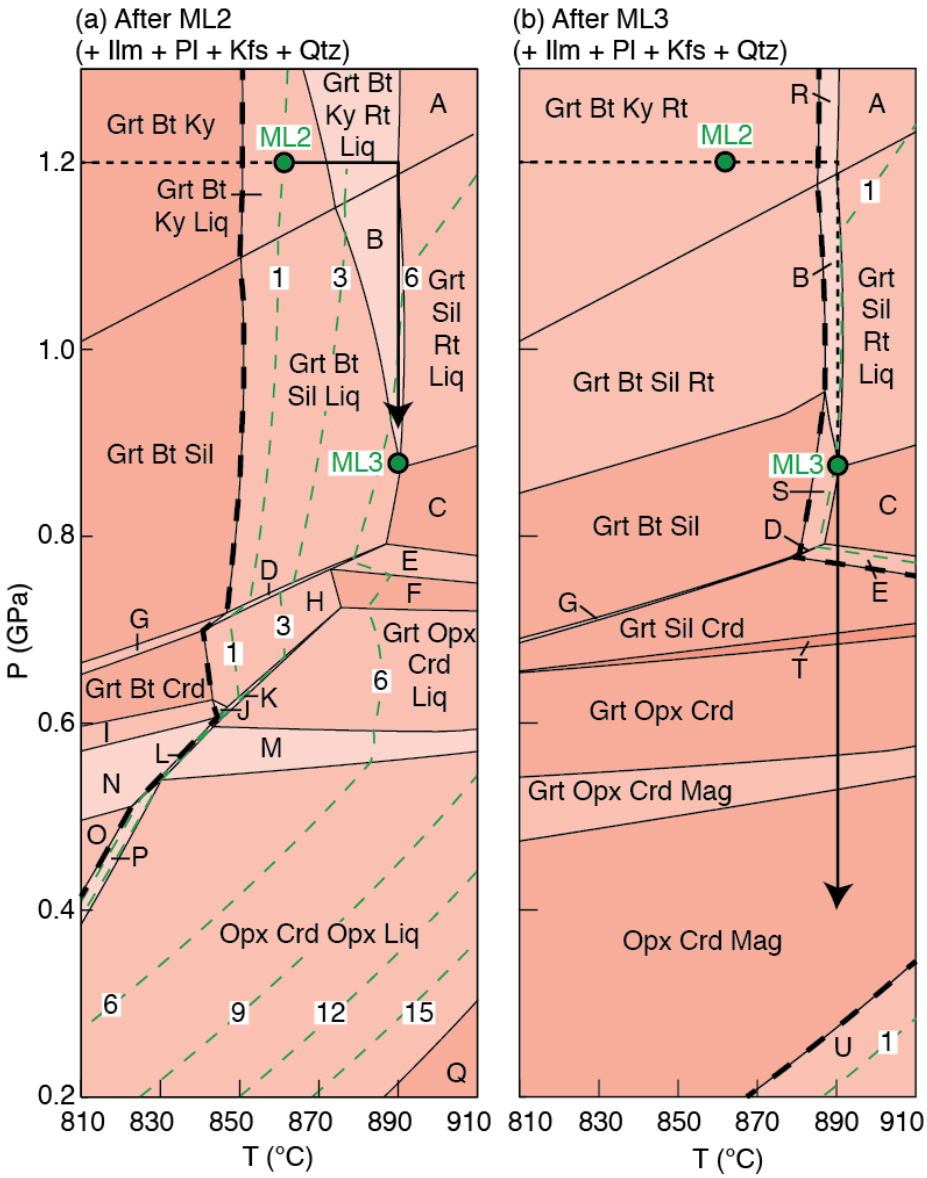

Fig. 6.10. *P–T* pseudosections calculated for the greywacke after successive melt loss (ML) events along a *P–T* path comprising a prograde isobaric heating segment at 1.2 GPa followed by isothermal decompression at 890°C. The heavy dashed line is the solidus and the coloured dashed lines represent contours of mol% melt. Phase assemblages are as follows in addition to Ilm, Pl, Kfs and Qtz: A. Grt Ky Rt Liq; B. Grt Bt Sil Rt Liq; C. Grt Sil Liq; D. Grt Bt Sil Crd Liq; E. Grt Sil Crd Liq; F. Grt Crd Liq; G. Grt Bt Sil Crd; H. Grt Bt Crd Liq; I. Grt Bt Crd Mag; J. Grt Bt Crd Mag Liq; K. Grt Bt Opx Crd Liq; L. Grt Bt Opx Crd Mag Liq; M. Grt Opx Crd Mag Liq; N. Grt Bt Opx Crd Mag; O. Bt Opx Crd Mag; P. Bt Opx Crd Mag Liq; Q. Opx Crd Mag Liq (-Kfs); R. Grt Bt Ky Rt Liq; S. Grt Bt Sil Liq; T. Grt Crd; U. Opx Crd Mag Liq.

pseudosections for the melt-depleted compositions in Fig. 6.9 show elevated solidi and an increased stability for orthopyroxene and K-feldspar compared to the undrained situation (Fig. 6.7a). Isopleths of mol% melt have positive slopes except in the garnet–cordierite–sillimanite trivariant field where the isopleths have negative slopes (Fig. 6.9).

For the highest temperature *P–T* path (path ID890 in Fig. 6.7a), isobaric heating from the solidus to 890°C results in two melt loss events. The pseudosection for the melt-depleted composition after two drainage events (Fig. 6.10a) shows an elevated solidus at c. 850°C at high- to moderate-pressure conditions and steep isopleths of mol% melt at $P > 0.8$ GPa. Along the isothermal decompression segment at 890°C, a third and final melt loss event occurs at 0.88 GPa (ML3; Fig. 6.10a). After three drainage events, the pseudosection in Fig. 6.10b shows a reduced stability field for biotite, which is only stable at $P > 0.7$ GPa. During continued decompression from ML3 the *P–T* path crosses the biotite-out field boundary at 0.86 GPa and the solidus at 0.77 GPa, producing a subsolidus assemblage that includes garnet, sillimanite and cordierite (in addition to quartz, plagioclase, ilmentite, and K-feldspar; Fig. 6.10b).

6.6.5 Summary

Composite *P–T* diagrams for each of the three isobaric heating–isothermal decompression paths are shown in Fig. 6.11a, b and c. Each diagram comprises pseudosection panels for a range of pressure, taken from Figs 6.8, 6.9, and 6.10 and stacked from high to low pressure, representing the evolution between melt loss events. Thus, the drainage events are located on the seams between the panels. The changes in

modes along each isothermal decompression segment are shown on pressure–phase proportion diagrams in Fig. 6.11d, e and f.

Of particular interest is the quantity of melt present and the amount of melt that has been lost at any pressure, and the cumulative amount of melt that was generated along each path for the greywacke. Along paths ID750, ID820 and ID890, melting yielded cumulative totals of 8, 20 and 18 mol% melt, respectively (Table 6.4). Decompression at 820°C produced the most melt during decompression but most of that was generated at $P < 0.5$ GPa. The highest temperature decompression segment (ID890) produced 2 mol% less melt in total than the decompression segment at lower temperature (ID820; Table 6.4). This feature is a result of the additional melt loss event during heating to 890°C, which depletes the residue sufficiently that the low-pressure melt-producing equilibria are displaced to ultrahigh temperatures and are not crossed by this path. In contrast to the pelite, the isobaric heating and initial decompression paths for the greywacke do not encounter a muscovite–K-feldspar trivariant field and, therefore, melt is generated in a more gradual fashion. For path ID820 it is only at $P < 0.5$ GPa that voluminous melting occurs through the breakdown of biotite and garnet to produce orthopyroxene and melt.

Fig. 6.11. (a, b, c) Composite *P–T* diagrams comprising multiple pseudosection panels taken from Figs 6.8, 6.9 and 6.10 and stacked from high to low pressure for each of the different isobaric heating–isothermal decompression *P–T* paths modelled for the greywacke. Each pseudosection panel shows the evolution between melt drainage events and the melt drainage events are located on the seams between the panels. The heavy dashed line is the solidus and the coloured dashed lines represent contours of mol% melt. (d, e, f) Molar proportion of phases plotted against pressure for the three decompression paths.

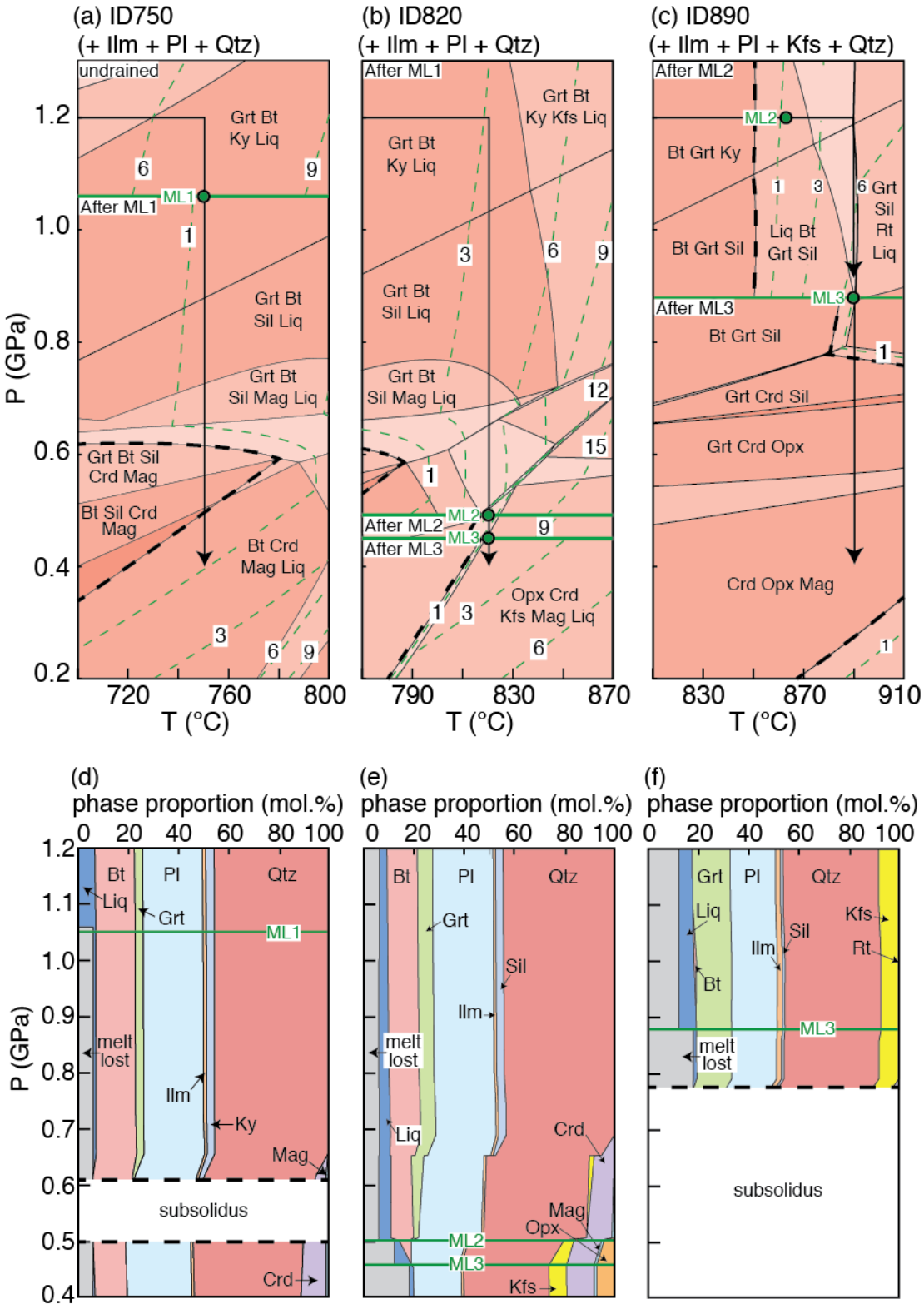
(a) ID750
(+ Ilm + Pl + Qtz)
undrained
Grt Bt
Ky Liq
6
9
After ML1
ML1
1
Grt Bt
Sil Liq
Grt Bt
Sil Mag Liq
Grt Bt Sil
Crd Mag
Bt Sil Crd
Mag
Bt Crd
Mag Liq
3
6
9
P (GPa)
1.2
1.0
0.8
0.6
0.4
0.2
720
760
800
T (°C)
(b) ID820
(+ Ilm + Pl + Qtz)
After ML1
Grt Bt
Ky Kfs Liq
Grt Bt
Ky Liq
3
6
9
Grt Bt
Sil Liq
Grt Bt
Sil Mag Liq
12
15
1
After ML2
ML2
After ML3
ML3
9
Opx Crd
Kfs Mag Liq
1
3
6
790
830
870
T (°C)
(c) ID890
(+ Ilm + Pl + Kfs + Qtz)
After ML2
ML2
Bt Grt Ky
1
3
6
Grt
Sil
Rt
Liq
Bt Grt Sil
Liq Bt
Grt Sil
After ML3
ML3
Bt Grt Sil
1
Grt Crd Sil
Grt Crd Opx
Crd Opx Mag
1
830
870
910
T (°C)
(d)
phase proportion (mol.%)
0
20
40
60
80
100
Bt
Liq
Pl
Grt
Qtz
ML1
melt
lost
Ilm
Ky
Mag
subsolidus
Crd
P (GPa)
1.2
1.1
1.0
0.9
0.8
0.7
0.6
0.5
0.4
(e)
phase proportion (mol.%)
Bt
Pl
Qtz
Grt
Sil
Ilm
melt
lost
Liq
Crd
Mag
Opx
ML2
ML3
Kfs
(f)
phase proportion (mol.%)
Grt
Pl
Qtz
Liq
Kfs
Sil
Ilm
Rt
Bt
ML3
melt
lost
subsolidus

6.7 High *P–T* isothermal decompression for a greywacke

6.7.1 Undrained (closed) system

A pseudosection for the greywacke for the *P–T* range of 0.2–2.0 GPa and 640–910°C is shown in Fig. 6.12a. This pseudosection is the same as Fig. 6.7a between 0.2 and 1.3 GPa but contains clinopyroxene at high pressures and a narrow muscovite–K-feldspar divariant field at $P > 1.5$ GPa. Isopleths of mol% melt have steep positive slopes at high pressures. In an undrained (closed) system, the amount of melt produced from the greywacke along the prograde segment from the solidus at 1.2 GPa to 860°C at 1.8 GPa is 12 mol% (Fig. 6.12a). Isothermal decompression from 1.8 to 0.4 GPa at 860°C generates an additional 24 mol% melt, yielding a cumulative total of 36 mol% for this *P–T* evolution (Fig. 6.12a). However, as discussed above, this is unrealistic in the general case and melt will drain from the system at or before the MCT in nature.

6.7.2 Drained (conditionally open) system

If the system is considered drained (conditionally open) then one melt loss event will occur along the prograde path. The pseudosection for the undrained situation, shown in Fig. 6.12a, is only appropriate until the bulk chemical composition changes at the first melt loss event, shown in Fig. 6.12b. After this, for the drained situation, three additional pseudosection panels stacked from high to low pressure along the decompression *P–T* path are shown in Fig. 6.12b.

One melt loss event occurs along the prograde segment at 1.68 GPa and 820°C. The pseudosection forming the high-*P*–high-*T* panel of Fig. 6.12b, which is the result after this first drainage event, shows steep isopleths of mol% melt at $P > 0.75$ GPa.

Isothermal decompression from 1.80 to 1.22 GPa produces 1 mol% melt, enough to trigger a second melt loss event (ML2). A third and final melt loss event occurs at 0.42 GPa (ML3).

The changes in modes along the prograde segment of the *P–T* path from the solidus at 1.2 GPa to peak *P–T* at 1.8 GPa and 860°C, and for the decompression segment to 0.4 GPa are shown on the two pressure–phase proportion diagrams in Fig. 6.12c, d. The full *P–T* evolution yields a cumulative total of 19 mol% melt, which is

---

Fig. 6.12. (a) *P–T* pseudosection calculated to higher pressures for the greywacke assuming undrained (closed system) conditions. (b) A composite *P–T* diagram comprising four pseudosection panels, with the three high-temperature panels stacked from high to low pressure, for drained (conditionally open system) conditions. Each of the high-temperature panels is appropriate for decompression from one melt loss event to the next. The heavy dashed line is the solidus and the coloured dashed lines represent contours of mol% melt. (c, d) Molar proportion of phases for the prograde (c) and decompression (d) segments of the modelled *P–T* path during conditionally open system melting. Phase assemblages are as follows in addition to Ilm, Pl and Qtz: A. Grt Bt Pg Ms Rt; B. Grt Bt Pg Ms Rt Liq; C. Grt Bt Ky Pg Ms Rt Liq; D. Grt Bt Ky Ms Liq; E. Grt Bt Pg Ms; F. Grt Bt Pg Ms Liq; G. Grt Bt Pg Ms Liq H_2O; H. Grt Bt Ky Pg Ms Liq; I. Grt Bt Pg Ms H_2O; J. Grt Bt Ky Pg Ms H_2O; K. Grt Bt Pg H_2O Liq; L. Grt Bt Pg; M. Grt Bt Ky Pg Ms Liq H_2O; N. Grt Bt Ky H_2O; O. Grt Bt Ky Pg H_2O; P. Grt Bt Ky Liq H_2O; Q. Grt Bt Ky Mag H_2O; R. Grt Bt Sil Mag H_2O; S. Grt Bt Sil Mag Liq H_2O; T. Grt Bt Sil Mag Liq; U. Grt Bt Sil Crd Mag H_2O; V. Grt Bt Sil Crd Mag Liq H_2O; W. Grt Bt Sil Crd Mag Liq; X. Bt Sil Crd Mag Liq H_2O; Y. Bt Crd Mag H_2O; Z. Bt Crd Mag Liq H_2O; AA. Bt Crd Mag Liq; AB. Grt Bt Crd Mag Liq; AC. Grt Bt Opx Crd Mag Liq; AD. Bt Opx Crd Mag Liq; AE. Grt Bt Ms Rt; AF. Grt Bt Ms Rt Liq; AG. Grt Ms Rt Liq; AH. Grt Bt Ky Ms Liq; AI. Grt Bt Ky Ms Rt Kfs Liq; AJ. Grt Bt Ky Ms Kfs Liq; AK. Grt Bt Ky Liq; AL. Grt Bt Ky Kfs Liq; AM. Opx Crd Mag Kfs; AN. Bt Sil Crd Mag H_2O; AO. Bt Crd H_2O; AP. Grt Bt Sil Rt Kfs Liq; AQ. Grt Bt Sil Crd Kfs; AR. Grt Bt Crd Kfs; AS. Grt Bt Crd Mag Kfs; AT. Grt Bt Opx Crd Mag Kfs; AU. Grt Sil Kfs Liq; AV. Grt Sil Crd Kfs Liq; AW. Grt Bt Sil Crd Kfs Liq; AX. Grt Crd Kfs Liq; AY. Grt Bt Crd Kfs Liq; AZ. Grt Bt Crd Mag Kfs Liq; BA. Grt Bt Opx Crd Kfs Liq; BB. Grt Bt Opx Crd Mag Kfs Liq; BC. Grt Opx Crd Mag Kfs Liq; BD. Bt Opx Crd Mag Kfs; BE. Bt Opx Crd Mag Kfs Liq; BF. Bt Crd Liq H_2O; BG. Bt Crd Mag Liq H_2O; BH. Grt Opx Crd Mag Liq; BI. Opx Crd Liq; BJ. Grt Sil Kfs Liq; BK. Grt Sil Rt Kfs Liq; BL. Grt Bt Sil Kfs Liq; BM. Bt Crd Liq.

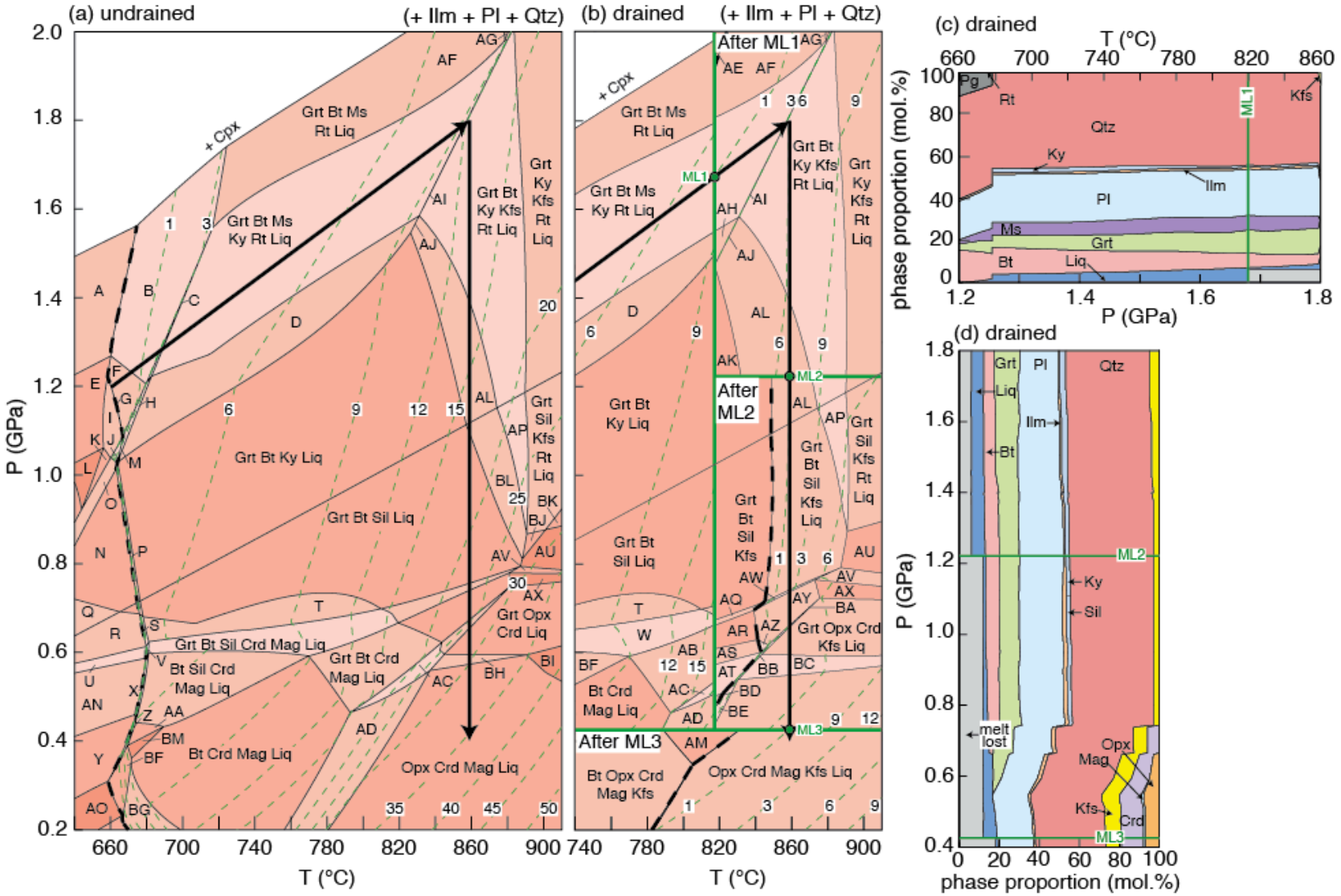
(a) undrained
(+ Ilm + Pl + Qtz)
(b) drained
(+ Ilm + Pl + Qtz)
(c) drained
(d) drained
P (GPa)
T (°C)
phase proportion (mol.%)
+ Cpx
Grt Bt Ms Rt Liq
Grt Bt Ms Ky Rt Liq
Grt Bt Ky Kfs Rt Liq
Grt Ky Kfs Rt Liq
Grt Bt Ky Liq
Grt Bt Sil Liq
Grt Sil Kfs Rt Liq
Grt Opx Crd Liq
Grt Bt Sil Crd Mag Liq
Bt Sil Crd Mag Liq
Grt Bt Crd Mag Liq
Bt Crd Mag Liq
Opx Crd Mag Liq
After ML1
After ML2
After ML3
Grt Bt Sil Kfs Liq
Grt Opx Crd Kfs Liq
Bt Opx Crd Mag Kfs
Opx Crd Mag Kfs Liq
ML1
ML2
ML3
Pg
Rt
Qtz
Ky
Ilm
Pl
Ms
Grt
Bt
Liq
Kfs
Sil
Crd
Opx
Mag
melt lost

approximately half the amount of melt that would be generated during closed system melting along the same *P–T* path.

6.8 Discussion

6.8.1 Limitations of the modelling

There are two principal limitations and two caveats on the phase equilibria modelling discussed above. The first limitation concerns the inherent uncertainties associated with the internally consistent thermodynamic data and the activity–composition models used in calculating the pseudosections (Powell and Holland 2008). Notwithstanding that these uncertainties are real, the overall form of the suprasolidus phase diagram for both pelite and greywacke is well constrained by information from natural mineral assemblages in rocks and data from melting experiments (White et al. 2011), and the overall topology of phase diagrams is thought to be correct even though the locations in *P–T* space may be more uncertain due to the second limitation.

The second limitation concerns the simplifications necessary to model phase equilibria in the complex chemical systems found in nature. The model chemical system used in this study does not take into account minor components such as manganese in garnet (Johnson et al. 2003; Johnson and Brown 2004; Zuluaga et al. 2005), fluorine in biotite (Peterson et al. 1991; Hensen and Osanai 1994), zinc in spinel (Nichols et al. 1992), and mixed volatile equilibria (Evans et al. 2010). Although these effects are unlikely to detract from the conclusions of this study, they are real and may modify the details of the location of reactions in *P–T* space (White et al. 2007). Additionally, the proportion of ferric to ferrous iron affects the stability of oxides such as ilmenite,

hematite, and magnetite, as well as the silicate minerals (Boger et al. 2012). However, the bulk compositions considered in this study are not strongly oxidized and small variations in the oxidation state are not expected to exert a major control on the quantity of the anatectic melt.

The first caveat concerns melt extraction. In this study, melt is allowed to drain from the system when the proportion reaches the MCT at c. 7 vol.%. However, strictly the MCT is a rheological transition and not a percolation threshold. It represents the significant structural change in suprasolidus crust with increasing proportion of melt due to the formation of a connected melt network (Rosenberg and Handy 2005). The threshold for melt extraction in systems undergoing syn-anatectic deformation is unknown, but is commonly considered to be lower than this value (Brown 2010b). Thus, a melt extraction threshold of 7 mol% melt (c. 7 vol.%) was chosen as a reasonable upper limit. A lower threshold should not result in significant changes to the phase assemblage field boundaries, although it would change the number of melt drainage events for any particular *P–T* path.

The second caveat concerns aspects of the *P–T* paths modelled. The rate of change of temperature will be important along the prograde segment in nature, but is not considered in this study. Also, the decompression segment of the *P–T* path is nature will not be isothermal. In adiabatic–isentropic systems melting during decompression must lead to cooling, because temperature is a dependent variable and melting consumes heat of fusion. Thus, a simple view of decompression melting as an isothermal process cannot be correct unless, perhaps, superheated melt is ascending through the crust advecting heat at a faster rate than the rate of decompression. Therefore, modelling the decompression

segment to be isothermal yields the maximum amount of melt that may be produced without additional heat.

6.8.2 Issues related to crustal melting

In the absence of fluid infiltration, melting immediately above the fluid-present solidus continues by consuming quartz and feldspar with the melt becoming drier as it increases in amount until a hydrate-breakdown melting reaction is crossed (White et al. 2001; Brown and Korhonen 2009; Brown 2013). For a given bulk chemical composition, the rate of melt production during prograde heating and isothermal decompression varies with the phase assemblage. This information is reflected in the spacing and orientation of isopleths of mol% melt in the various phase assemblage fields in the pseudosections discussed above.

For example, in the pelite, muscovite-breakdown melting occurs across the narrow low-variance phase assemblage field that extends from c. 660°C at 0.4 GPa to c. 890°C at 2.0 GPa (Figs 6.1a, 6.6a). In this field, isopleths of mol% melt are more closely spaced than in adjacent higher-variance fields, reflecting the pulse of melt that is produced by this reaction for a small rise in temperature. The dramatic volume increase associated with this reaction (Rushmer 2001; Powell et al. 2005) should guarantee melt escape.

In contrast, biotite-breakdown melting occurs over a wider range of *P–T* conditions and together with the smaller volume change associated with this reaction (Rushmer 2001) facilitates a more gradual buildup to several melt extraction events during the prograde evolution to the highest temperatures considered in this study. This

melt loss is reflected in the spacing and orientation of the isopleths of mol% melt in the *P–T* pseudosections for each of the more residual bulk chemical compositions considered (Figs 6.5, 6.6b, 6.11, 6.12b). For example, as the bulk chemical compositions become more residual, melt production during decompression in the stability field of garnet may become negligible, as reflected in the steep isopleths of mol% melt. However, where the isopleths are shallow, such as in the cordierite stability fields in the low *P–T* portion of the pseudosections, melting during isothermal decompression may be effective (Figs 6.1a, 6.7a).

6.8.3 Implications for buoyancy and rheology

Melt retention and/or decompression melting have been invoked as facilitating the exhumation of the deep crust during the formation of migmatitic gneiss domes and metamorphic core complexes (references earlier). Certainly, a weak and/or buoyant lower crust, and a weak mantle are considered important in allowing the lower crust to flow so that it may compensate for localized thinning of the upper crust during dome formation (Tirel et al. 2004, 2008). In undrained suprasolidus crust, the presence of a large volume of melt will significantly weaken the rheology and enhance the buoyancy, either or both of which could contribute to the exhumation mechanism, except that, as discussed above, undrained conditions are unlikely to occur in nature. Furthermore, it has been argued that a feedback relationship between decompression and increasing melt fraction could develop that might be important in the structural and thermal development of such domes and core complexes (e.g. Teyssier and Whitney 2002; Whitney et al. 2004). To evaluate this possible feedback relationship, Rey et al. (2009) used a series of 2D numerical

experiments to assess the impact of fluid-absent, hydrate-breakdown partial melting on the density and rheology of the crust for undrained conditions. In these experiments, the peak melt fraction of 35 vol.% is constrained to occur at the base of the crust at 1,000°C; thus, these experiments are for closed system melting.

Rey et al. (2009) assumed a linear reduction in density from the solidus to the liquidus of 13% (although it is unclear how this value was derived), so for a melt fraction of 35 vol.% the reduction in density is > 4%. Based on the phase equilibria modelling used in this study, for heating to 1.8 GPa in an undrained system, at 890°C the pelite has 25 mol% melt, which yields a c. 4% reduction in density, whereas the greywacke has 16 mol% melt, which yields a c. 3% reduction in density. However, if the assumption of undrained behaviour is invalid, the density change will be less than these values.

The density evolution of the suprasolidus pelite and greywacke relative to the immediately subsolidus fertile protolith at the same pressure during decompression from 1.2 GPa for a drained (conditionally open) system is shown in Fig. 6.13. The densities of the suprasolidus pelite and greywacke show stepped changes that relate either to drainage of melt at the MCT or a change in the associated residual mineral assemblage.

The change in density during decompression varies as follows: for the pelite at 750°C from -4 (less dense) to +1% (more dense), at 820°C from -4 to +1% and at 890°C from +3 to +5%; and, for the greywacke at 750°C from -1 to +1%, at 820°C from -1 to +1% and at 890°C from 0 to +4%. However, the high negative values for the pelite at 750°C and 820°C only occur at low pressure. For most of the decompression segment at 750°C the change in density varies from -2 to +1%, with the negative excursion starting at 0.49 GPa (Fig. 6.13), and for most of the decompression segment at 820°C the change in

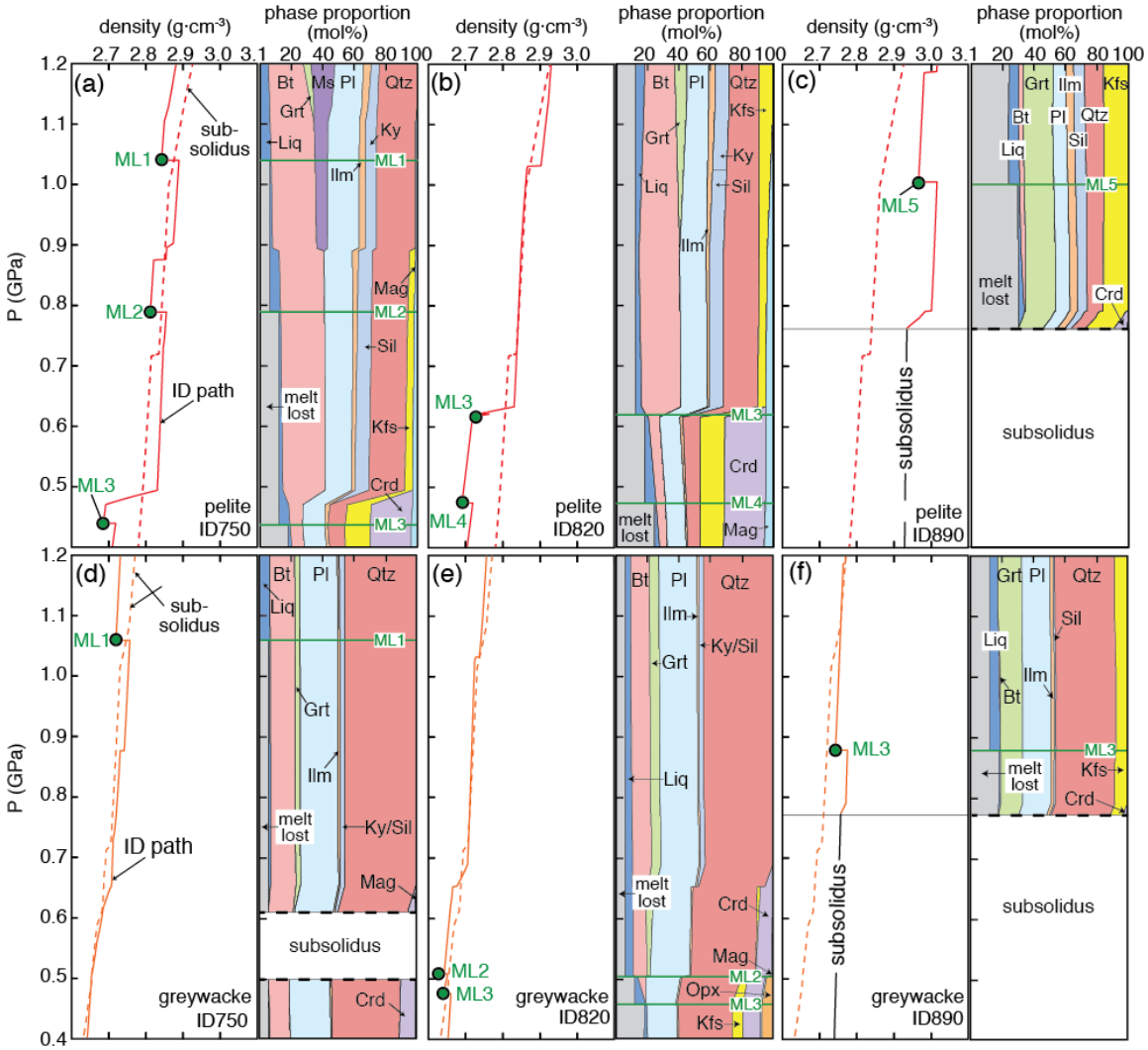

Fig. 6.13. Changes in density and phase proportions v. pressure for the pelite (a, b, c) and the greywacke (d, e, f) for conditionally open system melting along the three decompression paths modelled in this study. The dashed curve represents the change in density for the subsolidus protolith at temperatures immediately below the fluid-present solidus.

density varies from c. 0 to +1%, with the negative excursion starting at 0.63 GPa (Fig.6.13). Thus, for a drained system the decrease in density may not contribute significantly to the exhumation of melt-bearing crust during decompression at lower temperatures, and at higher temperatures a density increase is expected.

Whether a reduction in density is an important factor in exhumation depends on the tectonic mode (Rey et al. 2001). For boundary-driven extension, space for doming and formation of a metamorphic core complex is generated by far-field horizontal extension and the buoyancy of the melt bearing crust is not important, although it may play a significant role in the internal dynamics of the suprasolidus crust during decompression (Rey et al. 2009). In contrast, if lateral variation in gravitational potential energy drives extension, then space for doming and the formation of a metamorphic core complex must be generated by redistribution of mass, in which case the buoyancy of the melt-bearing crust will be integral to the process (Rey et al. 2001).

Notwithstanding the discussion above, migmatites in domes commonly have >20 vol.% leucosome and sometimes 40–60 vol.% leucosome and/or leucogranite at outcrop, but this does not typically represent in situ melting (Brown 1994; Nyman et al. 1995; Marchildon and Brown 2003; Morfin et al. 2013; Yakymchuk et al. 2013a). Although melt is present throughout the evolution for several of the *P–T* paths modelled in this study (for decompression from 1.2 GPa, the pelite paths ID750 and ID820, and the greywacke path ID820, and for decompression from 1.8 GPa for both the pelite and the greywacke), the amount of melt at any given point along these *P–T* paths is always low because melt is expected to escape at or before the MCT in nature. Furthermore, observations from some migmatitic gneiss domes and metamorphic core complexes

suggest that upward movement of melt and its accumulation below a developing detachment rather than just decompression of the suprasolidus crust may be important in controlling the dynamics of dome formation. For example in the Domaine Sud-Armoricain in Brittany, France a feedback relation has been postulated between dextral transtensive deformation, decompression melting and lower crustal doming, and between dome amplification, melt extraction and emplacement in developing extensional detachments, and core complex formation (Brown and Dallmeyer 1996; Brown 2005). Similarly, the Fosdick migmatite dome in Marie Byrd Land, West Antarctica formed during a transition from wrench to oblique extensional deformation that focused melt ascent and led to initiation of an overlying detachment that trapped melt to form a sheeted leucogranite complex (Korhonen et al. 2010a, b, 2012; McFadden et al. 2010a, b; Yakymchuk et al. 2013b).

Perhaps the large volume of leucosome and/or leucogranite observed at outcrop represents a combination of two features? First, the leucosomes may represent peritectic or cumulate material that mark extraction pathways for melt generated locally during the prograde evolution (Sawyer 1987; Solar and Brown 2001; White et al. 2004) whereas, second, the leucogranites may represent melt trapped during migration from deeper suprasolidus crust (Brown and Solar 1999; Brown 2010a,b; Morfin et al. 2013; Yakymchuk et al. 2013a). Indeed, it may be entrapment of melt that provides the buoyancy required in some circumstances for doming. Such a postulate is consistent with the dominance of leucodiatexite and leucogranite in the core of the Naxos migmatitic gneiss dome (Kruckenberg et al. 2010). Here, the preferred model involves a combination of buoyancy- and isostasy-driven processes to form the dome with gravitational

instabilities and/or overturning of high melt fraction diatexites leading to the growth of internal subdomes (Kruckenberg et al. 2011).

To evaluate the density change associated with melt accumulation, the density of anatectic melt has been calculated along a portion of the ID750 and ID820 decompression paths (from 0.7 to 0.4 GPa) for both the pelite and the greywacke residual compositions. The change in density with increasing accumulation of melt is shown in Fig. 6.14 for different volumetric proportions of melt and melt-bearing residual crust. The accumulation of melt decreases the density well below that of subsolidus crust at the same pressure in both rock types. For example, if a pelite or greywacke accumulates 50 vol.% melt, it is expected to be c. 10% less dense than the equivalent subsolidus crust (Fig. 6.14), which may be enough to provide the buoyancy required for doming where necessary. This result is consistent with the conclusion of Rey et al. (2011) that buoyancy forces only have a significant impact on the development of domes when melt buoyancy is large (and/or extensional strain rates in the upper crust are low).

In their numerical experiments, for melt-bearing crust with melt fractions up to 15 vol.% Rey et al. (2009) use the same viscosity as for subsolidus crust. Above 15 vol.% melt a drop of three orders of magnitude in viscosity is allowed as melt fraction increases to >30 vol.%. Results from their numerical experiments suggest that the reduced viscosity at higher melt fractions enhances the upward advection of material and heat during boundary-driven extension. However, the assertion that melt-bearing crust with <15 vol.% melt has the same viscosity as subsolidus crust contrasts with the view taken in this study that there is a fundamental drop in strength during progressive crustal melting that occurs within the first c. 7 vol.% of melt generated (Rosenberg and Handy

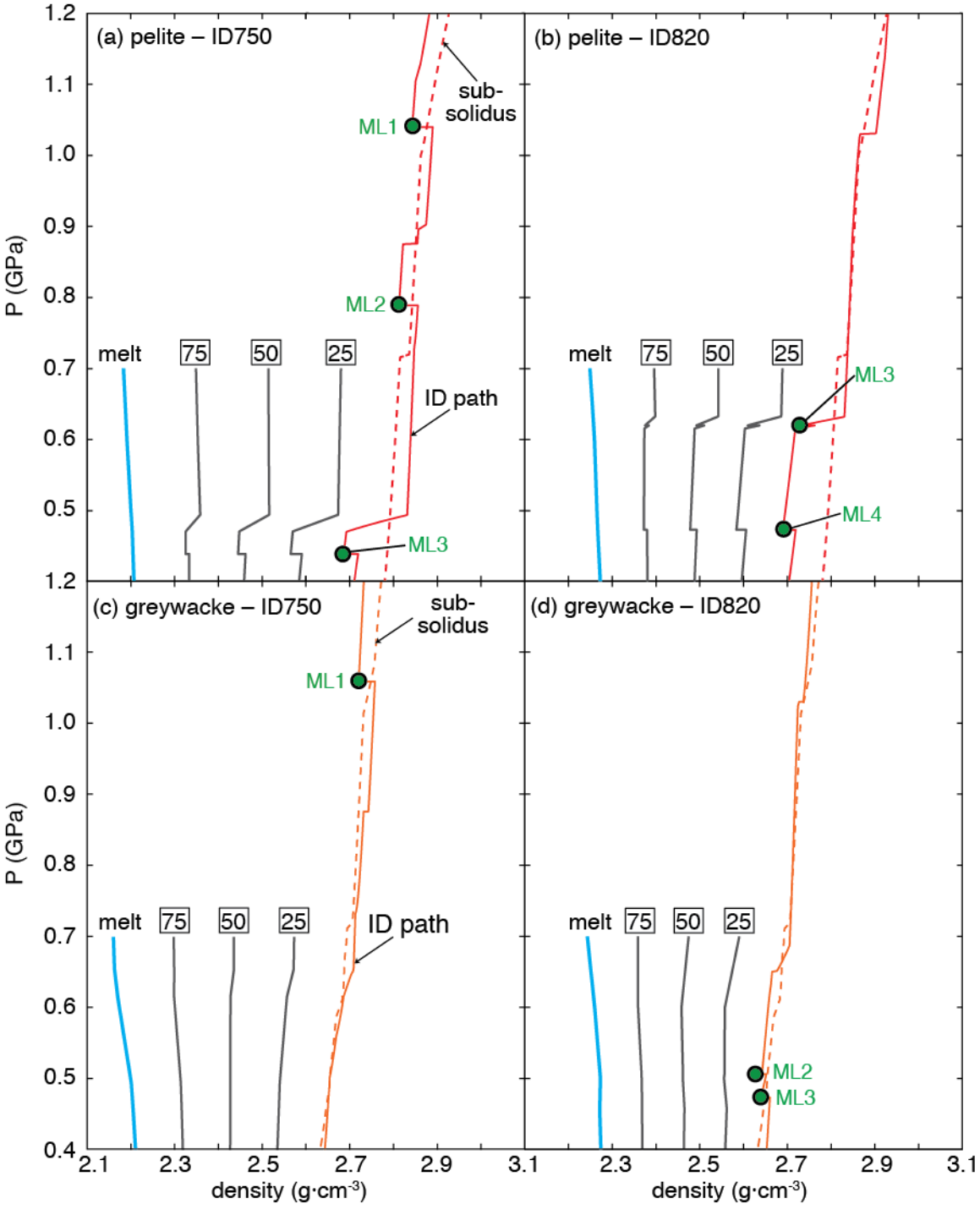

Fig. 6.14. The change in density (blue curves) v. pressure for anatectic melt for the interval 0.7–0.4 GPa along the ID750 and ID820 decompression segments for pelite (a, b) and greywacke (c, d). The three grey curves on each plot show the change in density for mixtures of melt (proportion of melt indicated on the diagram) and residual suprasolidus pelite and greywacke, respectively.

2005). This drop in strength relates to wetting c. 80% of grain boundaries (the MCT, discussed earlier), which facilitates melt drainage (Brown 2007, 2010b, 2013; cf. Clemens and Droop 1998; Rabinowicz and Vigneresse 2004), and melt drainage leads to hardening.

Although Rey et al. (2009) concede that melt fractions of <15 vol.% may have significant implications for outcrop-scale melt migration and rheology, they argue that this will have little impact on the regional-scale development of migmatitic gneiss domes and metamorphic core complexes. Notwithstanding this assertion, this view may be fundamentally flawed if melt migration at the MCT limits the maximum melt fraction generated in situ to no more than c. 7 vol.% between melt loss events because this limits the drop in viscosity to less than one order of magnitude (Rosenberg and Handy 2005). In this context, it is not important how the melt is extracted but that it happens each time the melt volume reaches the MCT. Whether the reduction in strength leading up to this threshold is sufficient remains to be determined, but if a larger weakening effect is required, it is likely to be related to migration and accumulation of melt, as discussed above.

6.8.4 Comparisons with natural systems

The isobaric heating–isothermal decompression *P–T* paths modelled in this study are comparable to those documented from natural systems. For example, near-isothermal decompression paths at high-T and at moderate pressures (Figs 6.1, 6.7) are reported from migmatitic gneiss domes and metamorphic core complexes, and from granulite

terrains; they commonly record > 0.4 to < 0.8 GPa of high-temperature decompression (Harley 1998; Teyssier and Whitney 2002).

As an illustration consider the study by Norlander et al. (2002) from the Thor–Odin dome in the Shuswap metamorphic core complex of the Canadian Cordillera. These authors used mineral assemblages and reaction microstructures in silica-undersaturated aluminous rocks that occur as boudins in migmatites to estimate decompression of > 0.4 GPa, from P > 0.8–1.0 GPa to P < 0.5 GPa, at temperatures of 750–800 °C, which they argued was coeval with partial melting. A more startling example is provided in the Namche Barwa in the eastern Himalayan syntaxis. Here there are surface exposures of gneisses that equilibrated at 1.0–1.4 GPa and 700–900 °C only c. 10 Myr ago associated with granites that are younger than 10 Ma in age (Booth et al. 2004, 2009). This is consistent with migration of melt through the crust and its accumulation at shallow levels, as proposed in this study.

The amount of high-temperature decompression modelled in the present study (0.8 GPa) is similar to upper estimates of the amount of decompression associated with the formation of migmatitic gneiss domes and metamorphic core complexes. Depending on temperature, if the amount of decompression from peak P is < 0.8 GPa then the amount of melt produced may be significantly less than modelled here. For example, for the ID820 decompression path in both the pelite and the greywacke most melt is produced in the cordierite stability field at low pressures. Therefore, if decompression terminates before reaching the cordierite stability field little melt will be produced and melt may even be consumed during decompression (Fig. 6.5b).

As an example take the study by Guilmette et al. (2011), from migmatites in the Namche Barwa in the eastern Himalayan syntaxis. These authors determined that melt was produced mostly along the prograde segment of the *P–T* path, which involved both increasing *P* and *T* to the peak of 1.4–1.5 GPa and 850°C. During decompression to 0.9 GPa and 800°C c. 1–2 vol.% melt may have been produced by close-to-isothermal decompression or decompression accompanied by heating. In these circumstances rather than the generation of large volumes of melt in decompressing crust it may be necessary to call on melt transfer through the suprasolidus crust and melt accumulation at shallow levels to explain the observed volumes of leucosome and/or granite in some migmatitic gneiss domes and metamorphic core complexes. On the other hand, if decompression extends down to c. 0.4 GPa, then melting via cordierite producing melting reactions, for example along the ID750 and ID820 paths for both pelite and greywacke, may generate leucogranite melts at shallow depths in the crust that may facilitate core complex formation as suggested for the Domaine Sud-Armoricain in Brittany, France (Brown and Dallmeyer 1996; Brown 2005).

The high-pressure *P–T* path (Figs 6.6, 6.12) modelled in this study is typical of those documented from high-pressure granulite terrains (O'Brien and Rötzler 2003) and similar to the post-peak-pressure segment of some exhumation paths for ultrahigh pressure metamorphic (UHPM) terranes that apparently melted during decompression at temperatures >800°C (Chen et al. 2013; Xu et al. 2013). This study considered 1.4 GPa of decompression from a peak at 1.8 GPa and 860°C (Figs 6.6, 6.12). In this case most of the decompression segment of the *P–T* path occurs parallel to melt mol% isopleths in the *P–T* pseudosections for drained conditions (Figs 6.6, 6.12); in nature, with slight cooling

during decompression, such a *P–T* path might lead to crystallization of melt rather than increased melting. Nearly all of the melt produced along the high *P–T* isothermal decompression segments in this study was generated in the stability field of cordierite at low pressures (Figs 6.6, 6.12). Halting decompression before reaching the cordierite stability field will limit or even prevent melting during decompression for both the pelite and the greywacke. Once again it may be necessary to call on melt transfer through the suprasolidus crust and melt accumulation at shallow levels to explain the observed volumes of leucosome and/or granite in these terrains.

6.8.5 Decompression melting and tectonics

The non-linear decrease in the strength of suprasolidus crustal rocks with increasing melting (Rosenberg and Handy 2005) means that melt-bearing horizons in the crust should be weak and could tend to localize strain. This may have significant implications for both small-scale strain partitioning (Handy et al. 2001) and large-scale tectonics of hot orogens (Jamieson et al. 2011). Furthermore, melt crystallization is strain-rate dependent, so that at high strain rates deformation will tend to be concentrated in melt-bearing layers, which could lead to crystallization (Misra et al. 2011). Crystallization would partition strain away from these early-formed migmatites to other melt-bearing layers. Thus, the high-strain rheology of the orogenic crust is predicted to be cyclic, with long-term creep interrupted by numerous weakening events associated with the propagation and interconnection of melt-filled veins and strengthening events associated with melt drainage or crystallization of leucosomes. Spatially intermittent

weakening followed by hardening within a suprasolidus crust may be important for the large-scale tectonics of hot orogens.

Over the past twenty years new insights have been gained from geophysical surveys and numerical experiments on the role of melting in the development of orogenic belts (e.g. Nelson et al. 1996; Babeyko et al. 2002). The geophysical data have enabled the amount of melt present under orogenic plateaux to be quantified (Schilling and Partzsch 2001; Unsworth et al. 2005), which is thought to be the weakening mechanism that enables the crust to flow in response to gravity or tectonic stress (Clark and Royden 2000), and the numerical experiments have led to the proposal that the inner core of the Himalaya acted as a melt-weakened orogenic channel that extruded towards a region of lower pressure at the topographic front of the mountain range (Beaumont et al. 2001). Other studies have proposed analogous mechanisms for exhumation of the orogenic core in the North American Cordillera (Brown and Gibson 2006) and the Appalachians (Hatcher and Merschat 2006).

A major question that arises from these studies is whether melting initiates during or prior to decompression? If melting begins before exhumation, weak melt-bearing crust may localize detachments (Hollister 1993). If melting is a response to exhumation, then detachments that formed prior to melting were not related to melt-weakening of the crust. The phase equilibria modelling presented in this study indicates that melting begins along the prograde segment of clockwise *P–T* paths prior to decompression, and that at granulite facies conditions multiple melt drainage events may occur prior to decompression. Thus major extensional shear zones that play a key role in exhuming high-grade migmatite terranes in orogens are likely to have been initiated in melt-

weakened crust prior to exhumation. The results of the phase equilibria modelling also show that melting may cease and any trapped melt may crystallize during decompression at higher temperatures, leading to an increase in strength under these conditions.

6.9 Conclusions

Phase equilibria modelling of average amphibolite facies pelite and passive margin greywacke highlights the importance of evaluating progressive melt generation and intermittent melt loss prior to and during suprasolidus decompression. Cyclic drainage of melt along a clockwise *P–T* path has implications for the amount of melt that may be generated during decompression, the change in density of suprasolidus crust, and variations in the strength of suprasolidus crust. Stepwise drainage of melt along the prograde segment of any clockwise *P–T* path reduces the fertility of the source rock prior to decompression. The results presented here demonstrate that the quantity of melt generated during decompression may be significantly less than invoked in some tectonic models.

The limited density decrease accompanying open system melting of both the pelite and the greywacke is not likely to contribute to buoyant exhumation of suprasolidus crust. Although cyclic melt drainage will limit the maximum amount of melt in a residual rock to <7 vol.%, maybe this does weaken the crust sufficiently to promote the formation of migmatitic gneiss domes and metamorphic core complexes? Alternatively, it may be the accumulation of melt in the upper levels of migmatite complexes that weakens the crust sufficiently to enable the formation of detachments and the formation of migmatitic gneiss domes and metamorphic core complexes. In addition,

migration and accumulation of melt will reduce the density of the upper parts of the suprasolidus crust, which may enable doming in circumstances where buoyancy is required for domes to form.

Chapter 7: Leucosome distribution in migmatitic paragneisses and orthogneisses: a record of self-organized melt migration and entrapment in a heterogeneous partially molten crust

7.1 Abstract

The thickness and spatial distribution of foliation-parallel leucosomes in metric to decametric scale interlayered units of migmatitic paragneiss and orthogneiss from the Fosdick migmatite–granite complex in West Antarctica are quantified along one-dimensional transects. This study demonstrates that leucosomes in stromatic metatexite migmatites have thickness and spacing distributions consistent with being sampled from a power-law (scale-invariant) distribution. However, leucosome distribution in the paragneisses and orthogneisses yields different scaling exponents and the largest leucosomes in orthogneiss are thicker than those in the paragneiss by approximately half an order of magnitude. The difference in the spatial distribution and maximum thickness of leucosomes between the two rock types is attributed to the decimetric scale of inherited compositional layering in migmatitic paragneiss that restricted the development of larger leucosomes compared with an absence of such heterogeneity in migmatitic orthogneiss that allowed thicker leucosomes to form. Phase equilibria modelling of the protoliths of the paragneisses and orthogneisses shows that at Cretaceous peak metamorphic conditions the spectrum of metasedimentary protolith compositions could have produced 8–48 vol.% melt and the range of igneous protolith compositions could have produced 3–17 vol.% melt at the crustal depth exposed, which is generally less than

the volume of leucosome at outcrop (43–72 and 39–67 vol.%, respectively, in the paragneiss and orthogneiss). This discrepancy indicates that the Fosdick complex acted as both a source of melt production and a zone of melt entrapment, whereby some of the melt derived from deeper in the crust has partially crystallized during migration to shallower levels in the crust. The observed power-law behaviour of leucosomes is consistent with the hypothesis that intracrustal differentiation by anatexis and granite magmatism is scale-invariant and represents a self-organized critical system. The interaction of this critical system with the compositional layering in the paragneisses and the interlayering between paragneiss and orthogneiss accounts for the three-dimensional distribution of leucosome in stromatic metatexite migmatites.

7.2 Introduction

The partial melting of crustal rocks and the redistribution of the melt are the principal processes that differentiate the continental crust to produce a refractory lower portion and a complementary enriched upper portion (e.g. Vielzeuf et al., 1990; Brown and Rushmer, 2006; Brown, 2010a, b; Sawyer et al., 2011). The variable extent of partial melting according to lithology and/or the intrusion of granite magma creates domains with different rheologies that play a key role in focusing strain during the build up and collapse of orogens (Hollister and Crawford, 1986; Davidson et al., 1994; Vanderhaeghe and Teyssier, 2001; Jamieson et al., 2011).

For the process of crustal differentiation to be effective, an interconnected melt-flow network must be activated in the deeper suprasolidus crust to enable the extraction and ascent of anatectic melt to shallower subsolidus crust where it may accumulate in

plutons (Wickham, 1987; Brown, 1994; Vanderhaeghe, 1999; Solar and Brown, 2001; Brown 2010a, Hobbs and Ord, 2010). Formerly suprasolidus crust is represented by migmatites and granulites exposed at the surface. In such rocks, leucosome provides evidence of former melt-flow networks that existed at multiple scales from grain boundary films to centrimetric- and metric-scale veins. Ultimately these networks link to metric- and decametric-scale tabular and cylindrical bodies of granite that represent former transport conduits for melt.

The fertility of crustal protoliths at *P–T* varies with the amount of H_2O-rich fluid present and the proportions of both hydrous and anhydrous minerals in the protoliths. In general, in the absence of any influx of H_2O-rich fluid, metasedimentary protoliths are more fertile than metaigneous protoliths (Clemens, 2006). Most studies of melt-flow networks have concentrated on measuring the spatial distribution of leucosome in metasedimentary rocks (Tanner, 1999; Marchildon and Brown, 2003; Bons et al., 2004; Soesoo et al., 2004; Soesoo and Urtson, 2009; Bonamici and Duebendorfer, 2010; Hall and Kisters, 2012), since these lithologies are fertile, producing up to 50–60 vol.% melt at 900°C (Clemens, 2006). However, partial melting of metaigneous rocks, such as tonalities and granodiorites, also may produce a significant quantity of melt if the temperatures are high enough or if melting is fluxed by the addition of an H_2O-rich fluid. For example, tonalites may produce up to 40 vol.% melt by hydrate-breakdown reactions (Clemens, 2006) and an estimated 10–48 vol.% melt (average 30 vol.%) was produced through H_2O-fluxed partial melting of metaigneous rocks in the Opatica subprovince of the Canadian shield (Sawyer, 1998). Additionally, the elemental compositions of granites worldwide are consistent with the input of melt derived from both metasedimentary and

metaigneous sources (Clemens and Stevens, 2012). The spatial distribution of melt-transfer networks produced in suprasolidus metaigneous rocks has received less attention even though anatexis of metaigneous lower crust must play a significant role in the differentiation of the continental crust.

Primary compositional layering in rocks may represent a mechanical anisotropy that affects the development of organized networks of veins in both subsolidus and suprasolidus rocks. Several studies have quantitatively demonstrated that inherited anisotropies control the spatial distribution of veins in subsolidus rocks (Gillespie et al., 1999; Fagereng, 2011). Inherited anisotropies have also been suggested to control the spatial distribution of leucosome in suprasolidus rocks (e.g. Brown and Solar, 1998; Marchildon and Brown, 2003), although this has not been tested quantitatively.

In this contribution, the spatial distribution of leucosome in metasedimentary and metaigneous rocks is measured to test the hypothesis that leucosome networks are scale-invariant and part of a self-organized critical system, and to evaluate the effect of pre-existing heterogeneities on leucosome network development. Measurements were conducted in the Fosdick migmatite–granite complex in West Antarctica, which contains both migmatitic paragneisses and orthogneisses derived from metasedimentary and metaigneous protoliths that preserve petrographic and geochemical evidence of partial melting (Siddoway et al., 2004a; Korhonen et al., 2010a, b, 2012). The protolith of these gneisses was a turbidite sequence and a granodiorite suite, providing a contrast between heterogeneous (anisotropic) and relatively homogeneous (isotropic) source layers. The interlayering of these contrasting source layers at metric to decametric scales permits investigation of whether the heterogeneity of the metasedimentary protolith affects the

thickness and spatial distribution of leucosome compared to leucosome in the homogeneous plutonic protolith.

7.3 Scale invariance

The scale invariance of geological structures is a ubiquitous phenomenon (Kruhl and Renftel, 1994; Barton and La Pointe, 1995; Turcotte, 1997; Kruhl, 2013). Self-similar folds, the spacing of fractures, and S–C fabrics are but a few of the examples in structural geology that are scale-invariant from the micro- to macroscale (Gillespie et al., 1993; Turcotte, 1997; Gillespie et al., 1999; Hippertt, 1999). The spatial distribution of formerly melt-bearing structures, such as the thickness and spacing of dunite layers in ophiolites (Kelemen et al., 2000; Braun and Kelemen, 2002), the thickness and spacing of leucosome layers in migmatites (Tanner, 1999; Marchildon and Brown, 2003; Bonamici and Duebendorfer, 2010; Pereira et al., 2013) and the thickness of associated granite dykes (Brown, 2005), has also been proposed to be scale-invariant, although sometimes the scale of observations is limited. If these features are scale-invariant, this will have important implications for the extrapolation of these structures from outcrop to map scale, which will enable the interpretation of spatially limited data (e.g. Gillespie et al., 1993; Kruhl, 2013). Scale invariance can be a physical (spatial or temporal) manifestation of self-organized critical behavior, a concept that has found wide applications across the physical sciences (Bak et al., 1988).

Melt extraction has been argued to represent a self-organized critical process (Brown, 2010b; Hobbs and Ord, 2010; Hall and Kisters, 2012). A spatial signal of self-organized criticality in the melt extraction process is the scale invariance of formerly

melt-bearing structures. Although several studies have proposed that the spatial distribution of leucosome in migmatites is scale invariant (Tanner, 1999; Marchildon and Brown, 2003; Bons et al., 2004; Bonamici and Duebendorfer, 2010; Bons et al., 2010; Hall and Kisters, 2012), Marchildon and Brown (2003) argued that the spatial distributions of leucosome networks in Southern Brittany, France exhibited only limited scale invariance. These authors (Marchildon and Brown, 2003) proposed that pre-existing anisotropies in the rock (e.g. compositional layering and foliation) and the syn-anatectic strain regime controlled the spatial distribution of leucosome.

The limitation of these previous studies is that nearly all of the leucosome network measurements were conducted on anisotropic gneisses derived from metasedimentary protoliths (Tanner, 1999; Marchildon and Brown, 2003; Bons et al., 2004; Bonamici and Duebendorfer, 2010; Bons et al., 2010; Hall and Kisters, 2012). The spatial distribution of melt-transfer networks produced in formerly suprasolidus metaigneous rocks has received less attention, but such protoliths can produce significant volumes of melt during high-temperature metamorphism (Clemens, 2006; Korhonen et al., 2010a). Additionally, metaigneous protoliths tend to be homogeneous and isotropic in comparison with metasedimentary rocks. These differences are commonly carried through to the suprasolidus realm and are readily apparent by visual comparison of the migmatitic paragneisses and orthogneisses of this study (Fig. 7.1). The Fosdick migmatite–granite complex in West Antarctica provides an opportunity to evaluate the effect of pre-existing heterogeneities on the spatial distribution of leucosome networks in migmatite terranes because the complex comprises interlayered metasedimentary and

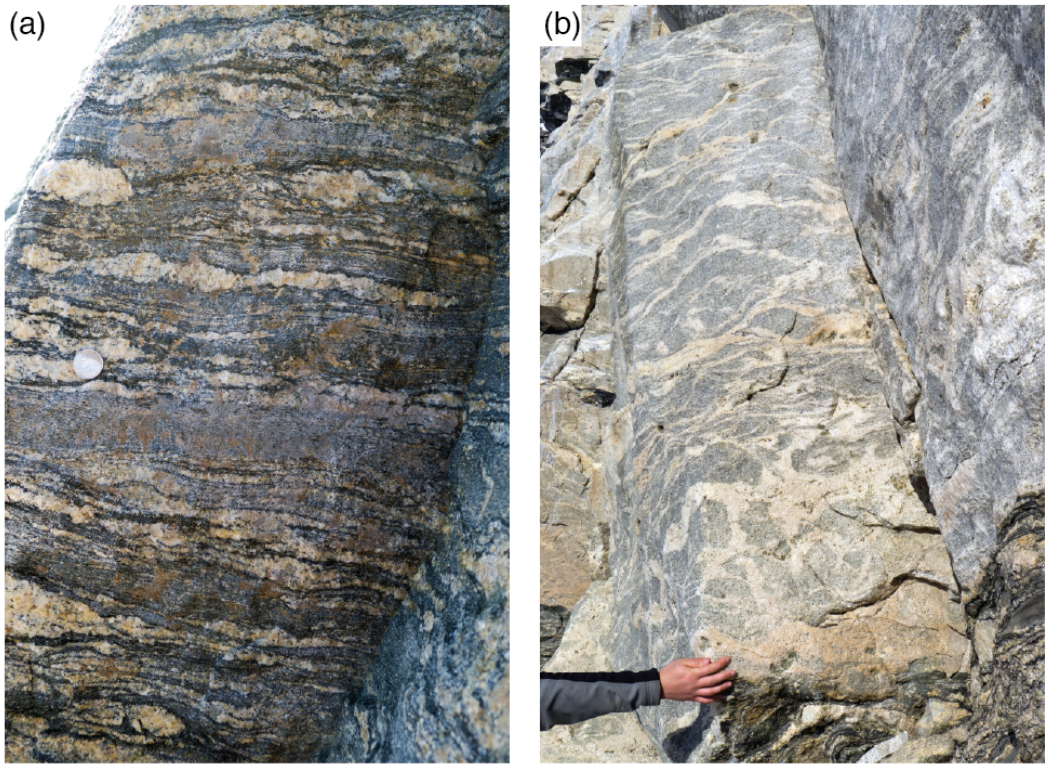

Fig. 7.1. (a) Migmatitic paragneiss with alternating layers of metapelitic and metapsammitic material derived from a heterogeneous protolith with a strongly anisotropic fabric (diameter of coin is 2.4 cm). Most leucosome is concentrated in the metapelite layers. (b) Migmatitic orthogneiss derived from a more homogenous protolith without any strong fabric anisotropy.

metaigneous protoliths that have experienced the same metamorphic history (Korhonen et al., 2010a, b, 2012).

7.4 Geology of the Fosdick migmatite–granite complex

7.4.1 Regional setting

Leucosome network measurements were conducted on migmatites located in the Fosdick migmatite–granite complex exposed in the Ford Ranges of Marie Byrd Land in West Antarctica (Fig. 7.2). In the Ford Ranges, the early Paleozoic Swanson formation is the oldest exposed unit (Bradshaw et al., 1983; Pankhurst et al., 1998; Adams, 2004). It is a folded and cleaved turbidite sequence (Fig. 7.3a) that accumulated outboard of the Cambrian Ross–Delamerian Orogen. The Devonian–Carboniferous Ford Granodiorite suite (Fig. 7.4a) intrudes the Swanson Formation. The emplacement of the Ford Granodiorite suite was associated with a major pulse of Paleozoic calc-alkaline magmatism along the East Gondwana continental margin (Weaver et al., 1991, 1992; Muir et al., 1994; Weaver et al., 1994; Pankhurst et al., 1998; Storey et al., 1999; Mukasa and Dalziel, 2000), which has been variously attributed to subduction (Weaver et al., 1991) or back-arc extension (Muir et al., 1996; Tulloch et al., 2009).

Cretaceous oblique extensional deformation that preceded the final breakup of East Gondwana and formation of the West Antarctic Rift System has exposed a high-grade migmatite–granite complex in the Fosdick Mountains of West Antarctica (Richard et al., 1994; Siddoway et al., 2004b, 2005; Siddoway, 2008). The complex forms an elongate (80 x 15 km) gneiss dome composed of migmatitic orthogneisses and paragneisses, multiple generations of granite, and subordinate intrusive mafic rocks

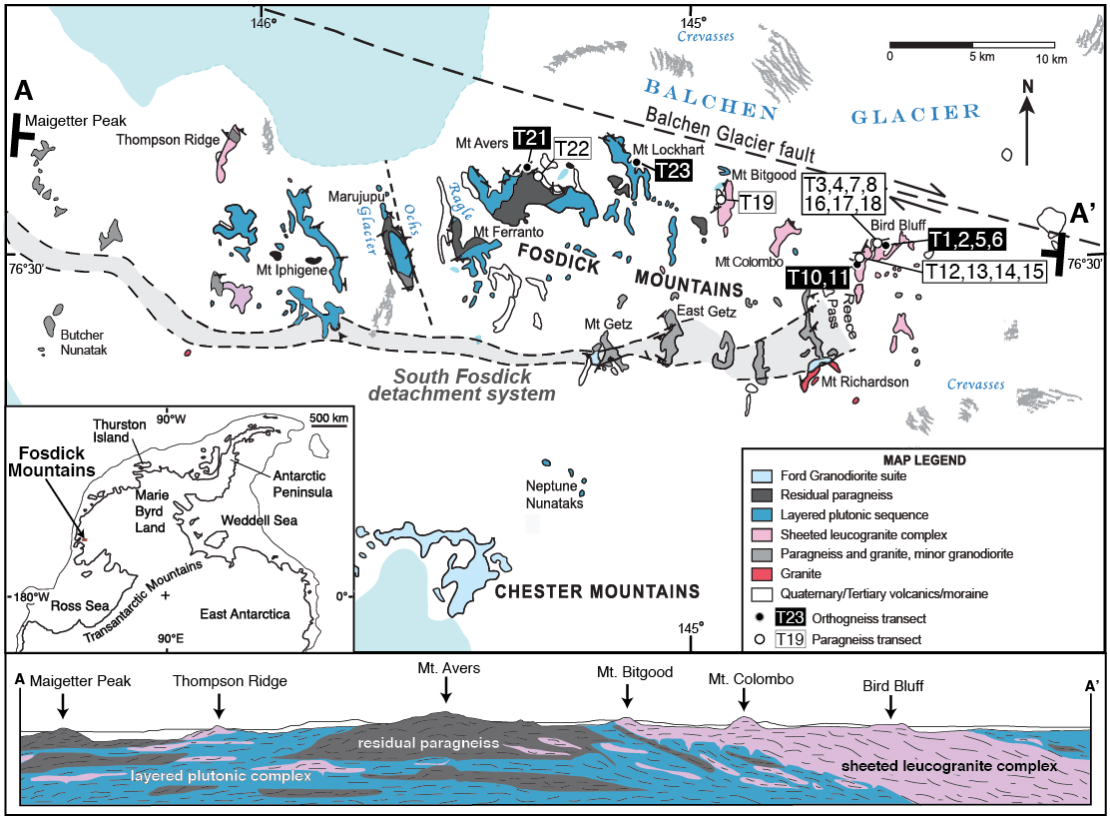

Fig. 7.2. Geological map and schematic cross-section (no vertical exaggeration) of the Fosdick migmatite–granite complex to show the location of one-dimensional transects through migmatitic paragneisses and orthogneisses within the residual paragneiss, the layered plutonic sequence and the sheeted leucogranite complex (map and section modified from Siddoway et al., 2004a; McFadden et al., 2010b).

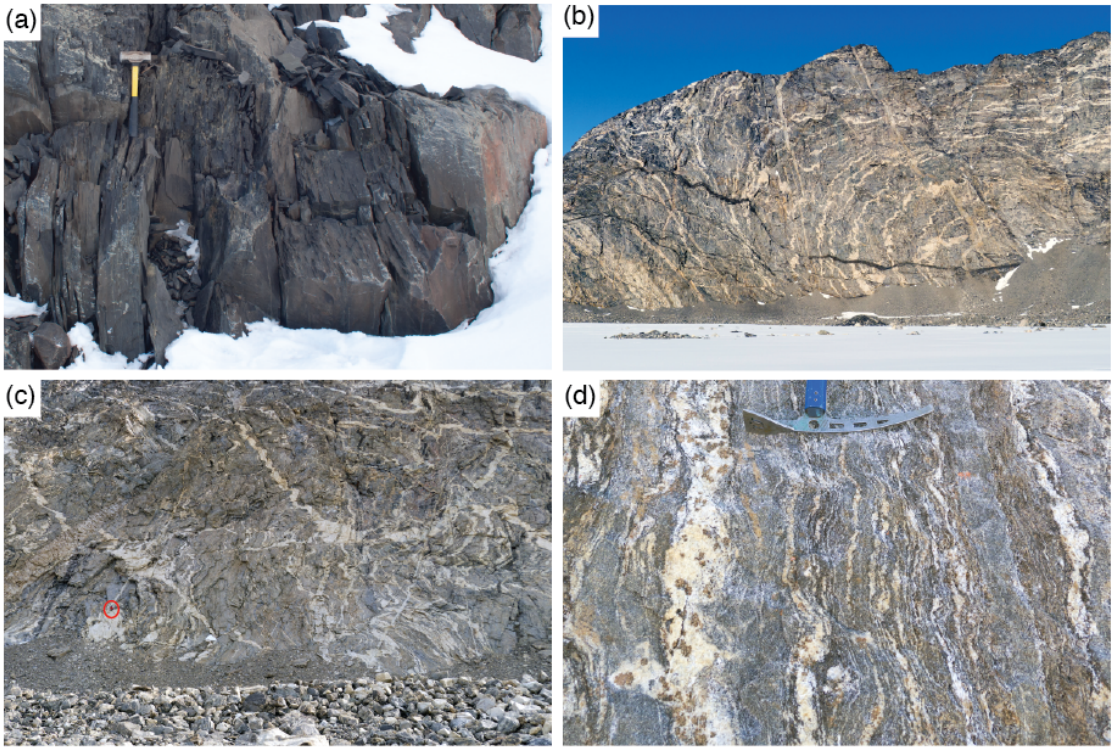

Fig. 7.3. (a) Outcrop of the putative protolith of the migmatitic paragneiss in the Fosdick complex—the Swanson Formation. (b) Large-scale fold of the residual paragneiss unit, including the associated discordant granites, at East Mt Avers looking south (cliff height 150 m). (c) Intersection of crosscutting dykes in the residual paragneiss unit at East Mt Avers. The near-vertical dyke in the lower right exhibits broad open folds with sub-horizontal axial surfaces. (d) Stromatic metatexite migmatite with alternating layers of metapelite and metapsammite and garnet-bearing leucosomes. The absence of significant retrogression of the garnet is consistent with melt loss from this outcrop.

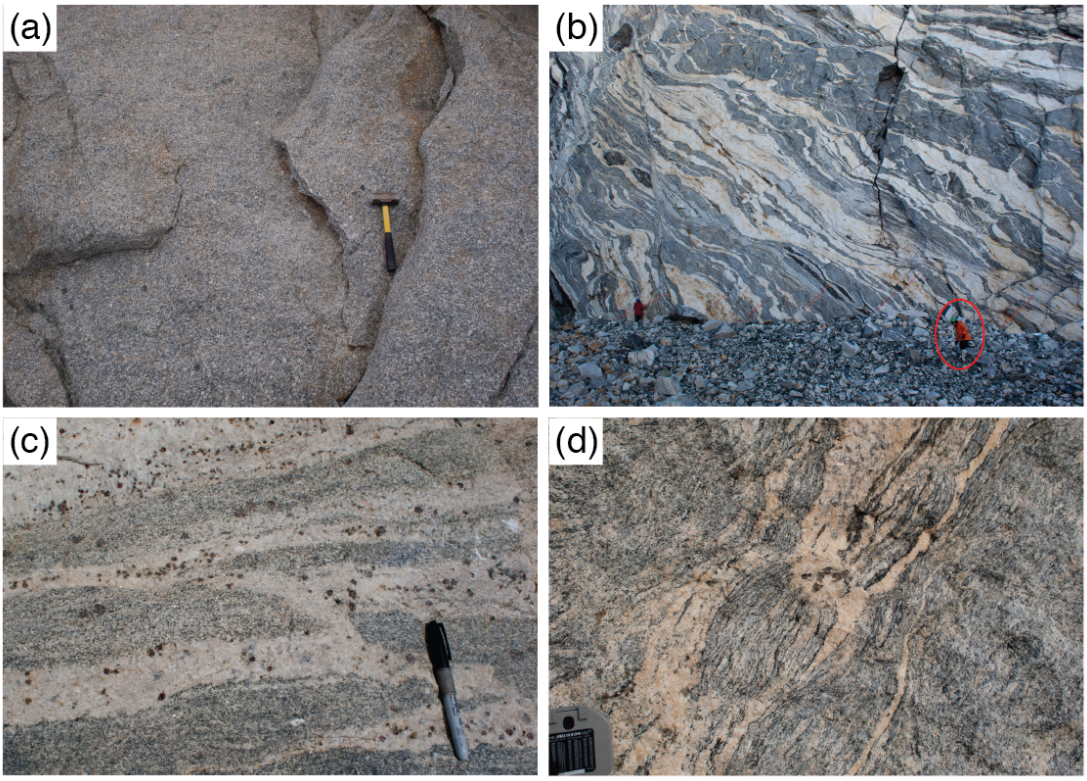

Fig. 7.4. (a) Outcrop of the putative protolith of the migmatitic orthogneiss in the Fosdick complex—the Ford Granodiorite suite. (b) Stromatic layering in the migmatitic orthogneiss truncated by steep normal-sense shear bands. (c) Garnet-bearing leucosome and melanosome in migmatitic orthogneiss from South Bird Bluff. The absence of significant retrogression of the garnet is consistent with melt loss from this outcrop. (d) Garnet-bearing leucosome in an interboudin partition in a migmatitic orthogneiss. The absence of significant retrogression of the garnet is consistent with melt loss from this outcrop.

(Richard et al., 1994; Siddoway et al., 2004a; Korhonen et al., 2010a, b, 2012; McFadden et al., 2010a, b; Saito et al., 2013; Yakymchuk et al., 2013). The geochemistry of the gneisses exposed in the Fosdick complex is consistent with the hypothesis that they represent the high-grade metamorphosed equivalents of the Swanson Formation and the Ford Granodiorite suite that crop out in the surrounding mountain ranges (Korhonen et al., 2010a, b). The similarity of zircon age spectra from the Swanson Formation and migmatitic paragneiss in the Fosdick complex and the cores of inherited zircons in granites support this interpretation (Siddoway et al., 2004a; Yakymchuk et al., 2013).

7.4.2 Geological units

The geology of the Fosdick complex comprises three principal units that consist of similar rock types, but in different proportions (after McFadden et al., 2010a). The layered plutonic sequence and the residual paragneiss units comprise the structurally deepest domain exposed in the western and central Fosdick Mountains stretching from Mt Avers to Mt Iphigene (Fig. 7.2). This domain is composed of migmatitic orthogneisses and paragneisses that are both intruded by multiple generations of granite. The interlayered gneisses with their synmigmatitic foliation and the granites are affected by decimeter-to-kilometer scale recumbent folds (Fig. 7.3b). These folds have sub-horizontal hinges that trend northeast–southwest, which is roughly parallel to a sparse and weakly developed mineral elongation lineation (Siddoway et al., 2004a). The third unit, the sheeted leucogranite complex, is part of a shallower domain in the eastern part of the Fosdick Mountains, stretching from Mt Bitgood to Bird Bluff (Fig. 7.2), which is

composed of sub-horizontal decameter-scale granite sheets with subordinate migmatitic orthogneisses and paragneisses.

The Fosdick complex is bounded to the north by the Balchen Glacier fault, an inferred sub-vertical dextral strike-slip fault (Siddoway et al., 2004b, 2005), and to the south by the shallowly south-dipping South Fosdick Detachment zone (Fig. 7.2; Richard et al., 1994; Siddoway et al., 2004a; McFadden et al., 2010a). Movement across the South Fosdick detachment zone occurred within the interval from c. 107 to c. 96 Ma, as determined by U–Pb ages of monazite and zircon from syn- to post-tectonic granites (Richard et al., 1994; McFadden et al., 2007; McFadden et al., 2010a). The South Fosdick Detachment zone facilitated the rapid exhumation and cooling of the Fosdick complex—indicated by overlapping ^{40}Ar–^{39}Ar cooling ages from biotite, muscovite, and K-feldspar (Richard et al., 1994)—during a transition from wrench deformation to oblique divergence in Marie Byrd Land (McFadden et al., 2010b).

7.4.3 Rock types

7.4.3.1 Migmatitic Paragneiss

Stromatic metatexite migmatite derived from paragneiss crops out across the Fosdick complex. Metapelitic layers are dominant over metapsammitic layers; metapsammitic layers contain proportionally less leucosome than metapelitic horizons (Figs 7.1a, 7.3d). In the metapelitic layers, leucosome is concordant with the sub-horizontal compositional layering and is linked by deformation bands to leucosome in the metapsammitic layers. Late-stage normal-sense shear bands are common and may

truncate migmatitic layering. Leucosome and melanosome components of the metasedimentary migmatites contain peritectic garnet and cordierite (Figs 7.3d, 7.4c, d).

In the paragneiss, the leucosomes form laterally continuous sub-horizontal layers in stromatic metatexite migmatite (Fig. 7.3d, 7.5a). These leucosomes are parallel to the compositional layering in the migmatites and range in thickness from millimetres to decimetres. Leucosome layers may have planar lower contacts and irregular upper contacts against melanosome (Fig. 7.6), similar to the cauliflower structures described by Burg and Vanderhaeghe (1993), suggesting that the thick leucosome in Fig. 7.6 is right-way up. Leucosomes may be boudinaged and are sometimes deformed into intrafolial recumbent isoclinal folds. Leucosome also occurs in dilatant structures associated with shear bands and in inter-boudin partitions. Leucosomes contain variable proportions of quartz, plagioclase, and K-feldspar with or without biotite, garnet, and cordierite. The grain size of quartz and feldspar in thicker leucosomes is proportionally coarser (2–3 mm) than the grain size in thinner leucosomes (1–2 mm). Penetrative axial planar fabrics are not observed at outcrop and there is no evidence of subsolidus recrystallization of quartz and feldspar in thin section, which suggests that much of the deformation was imposed while the migmatite was suprasolidus, albeit with only a low melt fraction present.

Discordant dyke-like bodies of granite that range from several centimetres to many metres wide crosscut the foliation and stromatic layering at variable angles, sometimes intersecting to form decametric cylindrical bodies of granite (Fig. 7.3c). These discordant granites exhibit petrographic continuity (similar mineralogy, mode and microstructure) with millimetre- to centimetre-scale foliation-parallel leucosomes. This

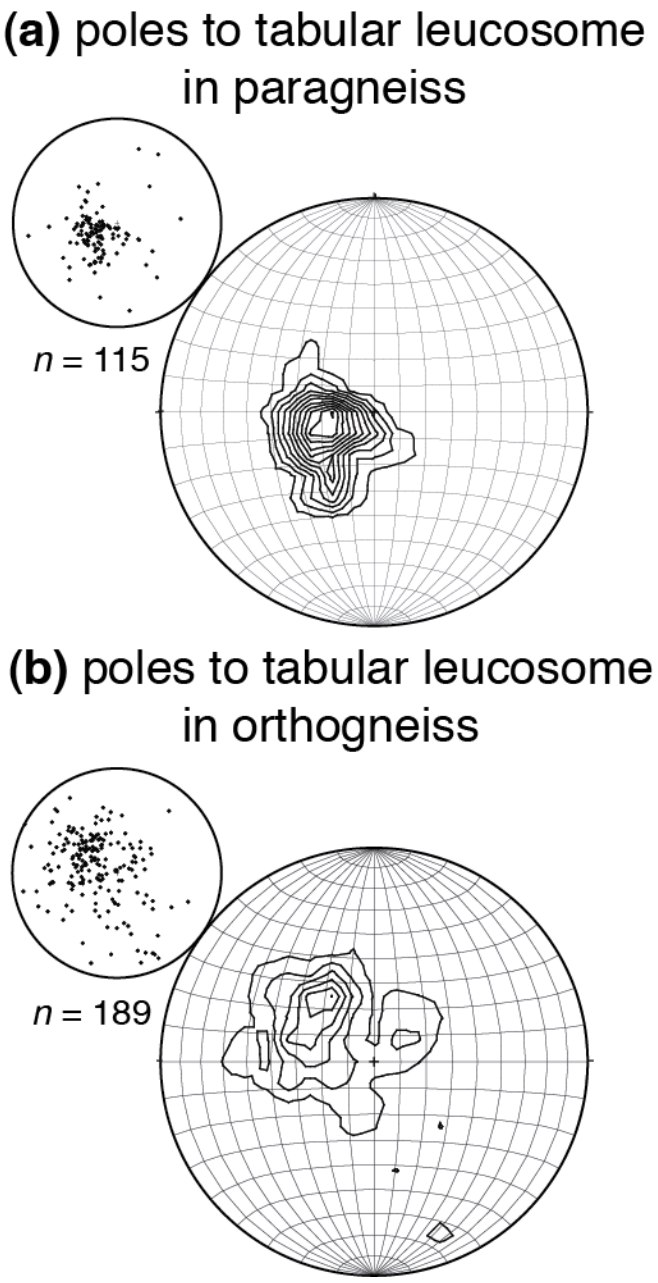

Fig. 7.5. Equal-area stereographic projection of orientation data of leucosomes in migmatitic paragneiss (a) and migmatitic orthogneiss (b). Contours are calculated 2% area intervals.

suggests that the material in the leucosomes and the discordant granites crystallised at the same time and formed part of the same melt extraction network (e.g. Marchildon and Brown, 2003). Some of the discordant granites define broad open folds with metre-scale wavelengths and sub-horizontal axial surfaces (Fig. 7.3c).

7.4.3.2 Migmatitic Orthogneiss

The migmatitic orthogneiss has a shallow to moderately dipping foliation (Fig. 7.5b) defined by the parallel alignment of individual biotite grains. Normal-sense shear zones are widespread and commonly contain leucosome that is contiguous with leucosomes that lie parallel to the foliation (Fig. 7.4b). Peritectic garnet up to 4 cm across occurs in both leucosome and melanosome components of the migmatitic orthogneiss (Fig. 7.4c). Peritectic cordierite occurs in leucosome less commonly. Individual leucosomes, which are continuous over >20 cm, range from a few millimetres to up to two metres in thickness and are most commonly parallel to the foliation, but also occupy dilational sites that may represent the ductile collapse of melt-filled extensional fractures (Fig. 7.4d; Druget and Carreras, 2006). The grain size of leucosomes in the migmatitic orthogneiss is generally coarser (2–6 mm) than that of equivalent sized leucosomes in the migmatitic paragneisses (1–3 mm). Some leucosomes contain well-defined mm-scale mafic schlieren dominated by biotite, but there is no systematic difference in mineralogy or orientation of these leucosomes compared to leucosomes without schlieren. Leucosomes are petrographically continuous with discordant granites that crosscut the dominant foliation.

7.4.4 Metamorphic history

Based on U–Pb monazite and zircon ages, two episodes of high-grade metamorphism affected the Fosdick complex, one in the Devonian–Carboniferous and another in the Cretaceous (Siddoway et al., 2004a; Korhonen et al., 2010a, b, 2012). Granites exposed in the Fosdick complex yield Devonian–Carboniferous and Cretaceous ages (Siddoway and Fanning, 2009; Korhonen et al., 2010b; McFadden et al., 2010a; Yakymchuk et al., 2013). Although phase equilibria modelling indicates that the metamorphic pressures and temperatures were sufficient during both episodes to partially melt the Swanson Formation and the Ford Granodiorite suite, the Cretaceous event was dominant and, except for some granites, evidence of the Carboniferous event is cryptic (Korhonen et al., 2010a, 2012).

The relatively well-constrained Cretaceous metamorphic event is characterized by cordierite- and garnet-bearing assemblages that yield pressures of 0.60–0.75 GPa at temperatures of 830–870°C (Korhonen et al., 2010a, 2012). Whether garnet was produced in the migmatitic paragneiss during the relatively poorly-constrained Carboniferous event is ambiguous because U–Pb geochronology of monazite inclusions in garnet preserve Carboniferous ages in core domains while garnet yields Cretaceous Sm–Nd model ages (Korhonen et al., 2012). If garnet was produced during the Carboniferous metamorphic event, Carboniferous peak metamorphic conditions are estimated to have been 0.75–1.15 GPa and 820–870°C (Korhonen et al., 2012). If garnet is not part of the Carboniferous metamorphic assemblage, as seems likely, then the Carboniferous peak metamorphic conditions are estimated to have been 0.60–0.95 GPa and 760–800°C. As a result, the degree of partial melting during the Carboniferous event

is unknown. However, Carboniferous diatexites in the layered plutonic complex do not contain garnet (Siddoway and Fanning, 2009), which may indicate partial melting outside the stability field of garnet at lower temperatures, possibly due to H_2O-rich fluid-fluxed melting.

Monazite from migmatitic paragneiss yields dominantly Cretaceous ages across the Fosdick complex (Korhonen et al., 2012; C. Yakymchuk, unpublished data). If fluid-absent partial melting did occur during the Carboniferous event, then melt loss would have been required to preserve peak Carboniferous metamorphic assemblages (Korhonen et al., 2010a). However, if, as seems likely, the Cretaceous metamorphic event achieved higher *P–T* conditions than the Carboniferous event, additional anatectic melt would have been produced from these depleted rocks during the Cretaceous regardless. This interpretation is supported by the trace element and isotope chemistry of leucosomes in both the migmatitic paragneisses and the migmatitic orthogneisses, which is consistent with the hypothesis that they were produced during the Cretaceous rather than the Carboniferous metamorphic event (Korhonen et al., 2010b). Therefore, the leucosome networks in the stromatic metatexite migmatites derived from both the paragneiss and orthogneiss protoliths are interpreted to have formed during the Cretaceous metamorphic event across the Fosdick complex.

7.5 Methods

The hypothesis that leucosome networks are scale-invariant is evaluated by measuring the spatial distribution of leucosome in migmatitic paragneisses (Fig. 7.6) and orthogneisses (Fig. 7.4b) on relatively flat outcrop surfaces in the Fosdick complex.

Stromatic leucosomes define approximately tabular geometries in three dimensions. Therefore, the three-dimensional spatial distribution may be evaluated using one-dimensional transects (Gillespie et al., 1999), along which the thickness and spacing of individual leucosome layers are measured and the position of each leucosome along the transect is noted (Gillespie et al., 1993; Marchildon and Brown, 2003; Bonamici and Duebendorfer, 2010; Bons et al., 2010). The fundamental assumptions of this method are that all of the leucosomes encountered along a particular transect are part of the same interconnected network, which is justified by the observed petrographic continuity of the leucosome networks, and that any penetrative subsolidus deformation was homogeneous, which should not be an issue in this study given the typical igneous microstructure of the leucosomes and the inferred limited nature of any subsolidus deformation.

Transects were conducted on foliation-perpendicular and near-vertical rock faces at eight locations across the Fosdick complex (Fig. 7.2). Transects ranged from 1 m to 22 m in length (Table 7.1). Transects were chosen at each locality based on the line that could provide the longest layer-perpendicular section. Also, the transects were chosen from sections without mafic rafts, macroscopic faults or shear zones, and without cross-cutting pegmatite and microgranite dykes that exhibit sharp discordant contacts with leucosomes, since these most likely represent magma intruded into subsolidus rock. Sections were measured following the method of Bonamici and Duebendorfer (2010) by attaching flagging tape to the rock face and marking the contacts of individual leucosome layers along the tape with a thin black marker with a tip size of less than a millimeter. The limit of resolution that was used was equivalent to that of the average grain size of

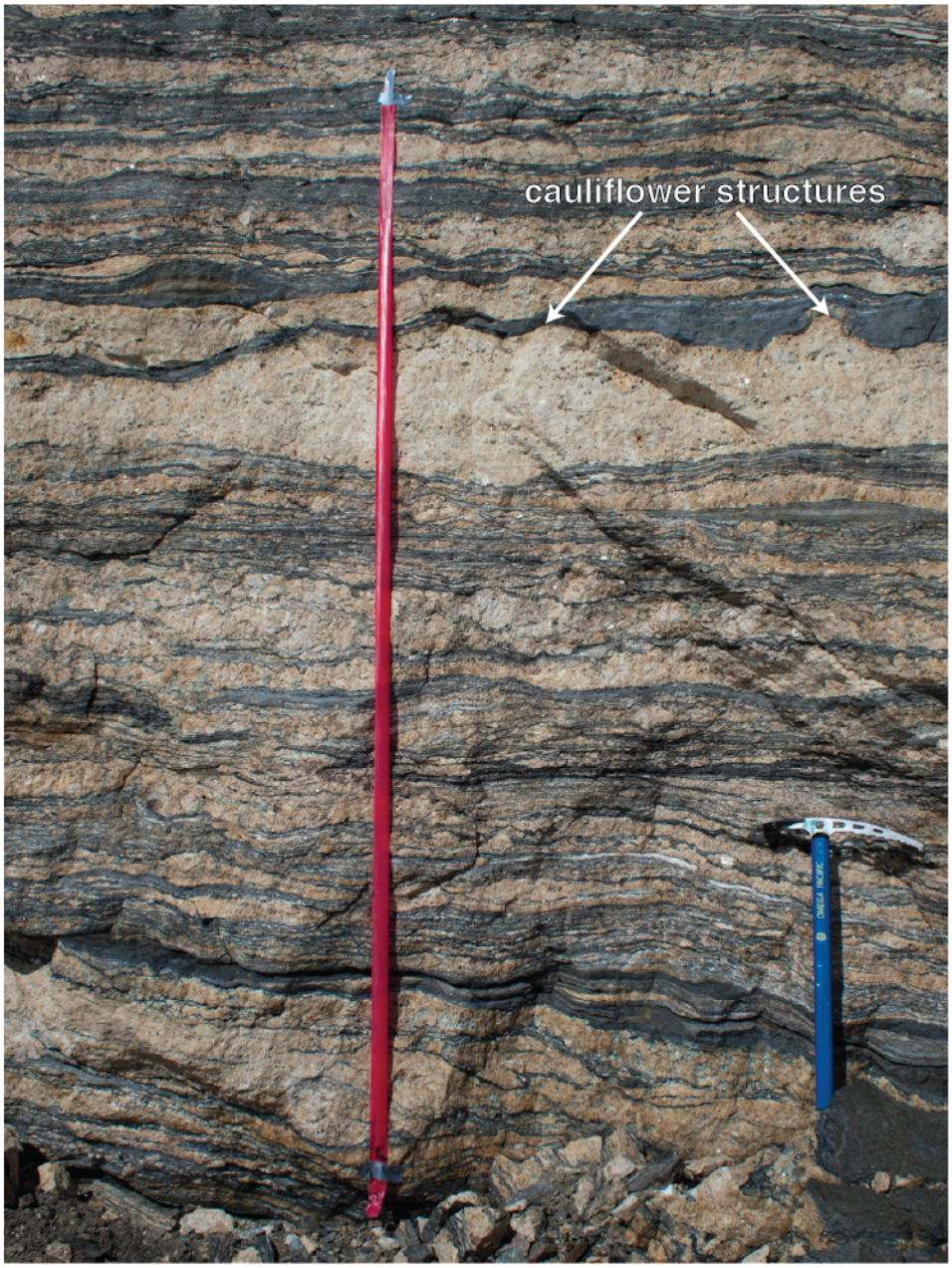

Fig. 7.6. Example of a portion of a line transect (T19) through migmatitic paragneiss at Mt Bitgood. The cauliflower structures suggest that this sequence is right-way up.

Table 7.1. Transect Information

Transect information						*Maximum likelihood estimation*					
Transect name	**Location**	**Transect length (mm)**	**Vol.% Leucosome**	**Number of leucosomes**	**Largest leucosome (mm)**	X_{min}	α	±	n_{tail}	p[a]	**Scaling exponent (*D*)**
Paragneiss transects											
T3	Bird Bluff North	4228	49.6	197	130	5	2.0	0.4	113	**0.00**	–
T4	Bird Bluff North	6004	47.4	300	99	8	2.2	0.2	98	0.32	1.2
T7	Bird Bluff North	3717	55.8	236	127	20	2.8	0.5	31	0.52	1.8
T8	Bird Bluff North	2800	47.1	150	241	6	2.1	0.3	28	0.79	1.1
T12	Bird Bluff South	1591	51.6	89	61	9	2.3	0.4	30	0.28	1.3
T13	Bird Bluff South	962	66.7	69	71	1	1.6	0.3	69	**0.02**	–
T14	Bird Bluff South	1043	50.6	84	30	2	1.8	0.6	63	**0.00**	–
T15	Bird Bluff South	1081	60.1	68	99	2	1.8	0.2	49	**0.05**	–
T16	Bird Bluff North	1310	43.1	81	50	6	2.3	0.4	29	0.49	1.3
T17	Bird Bluff North	1324	45.4	101	29	5	2.4	0.5	46	0.12	1.4
T18	Bird Bluff North	1397	45.7	112	29	2	1.9	0.5	84	**0.00**	–
T19	Mt Bitgood	3986	72.0	200	444	4	2.0	0.1	125	0.79	1.0
T22	East Mt Avers	8224	58.7	424	300	10	2.2	0.2	112	0.51	1.2
Orthogneiss transects											
T1	Bird Bluff North	4020	39.5	44	251	21	2.3	0.3	22	0.46	1.3
T2	Bird Bluff North	1552	38.9	49	80	8	2.4	0.3	25	0.16	1.4
T5	Bird Bluff North	1570	57.1	27	170	20	2.4	0.5	15	0.87	1.4
T6	Bird Bluff North	966	50.0	68	31	7	2.7	0.5	28	0.14	1.7
T10	Bird Bluff South	1542	52.8	32	84	8	2.0	0.5	30	**0.04**	–
T11	Bird Bluff South	1916	48.6	35	102	28	2.9	0.6	13	0.76	1.9
T21	East Mt Avers	21824	67.2	640	1097	25	2.2	0.2	114	0.70	1.2
T23	Mt Lockhart	21388	61.1	170	2298	7	1.7	0.1	132	0.45	0.7
Combined transects											
Paragneiss	–	–	–	2108	444	34	2.8	0.2	381	0.36	1.8
Orthogneiss	–	–	–	1060	2298	23	2.1	0.1	276	0.99	1.1

[a]Transects with $p<0.10$ contain a distribution of leucosomes that is inconsistent with the hypothesis that they were sampled from a power-law distributio

the rock, which was 2–3 mm for migmatitic orthogneiss and 1–2 mm for migmatitic paragneiss. From these data the thickness and centre point of leucosomes were calculated as well as the centre-to-centre spacing between adjacent leucosomes. Transect lines were not corrected for obliquity to the leucosome arrays, as it has no effect on the shape of the resultant cumulative frequency plots that are used to evaluate scale invariance (e.g. Gillespie et al., 1999).

7.6 Results

7.6.1 Results

Synthetic curves generated by Gillespie et al. (1999) for vein sets show the general trends expected for four types of spatial distributions (Fig. 7.7). For cumulative thickness plots, constant distributions show linear trends (Fig. 7.7a) and random distributions are characterized by nearly linear undulating curves (Fig. 7.7c), whereas Kolmogorov power-law distributions (e.g. Epstein, 1947) and fractal power-law distributions show well-developed stair-stepping features separated by gradually rising segments (Fig. 7.7e, g). The large vertical steps on the plots indicate relatively large increases in cumulative leucosome thickness—the result of the transect passing through relatively thick leucosomes. Gradually rising trends indicate small additions to the cumulative thickness and are characteristic of segments of transects composed of relatively thin leucosomes. Large horizontal steps on the plots indicate segments where transects crossed melanosome and, therefore, do not contribute to the cumulative leucosome thickness.

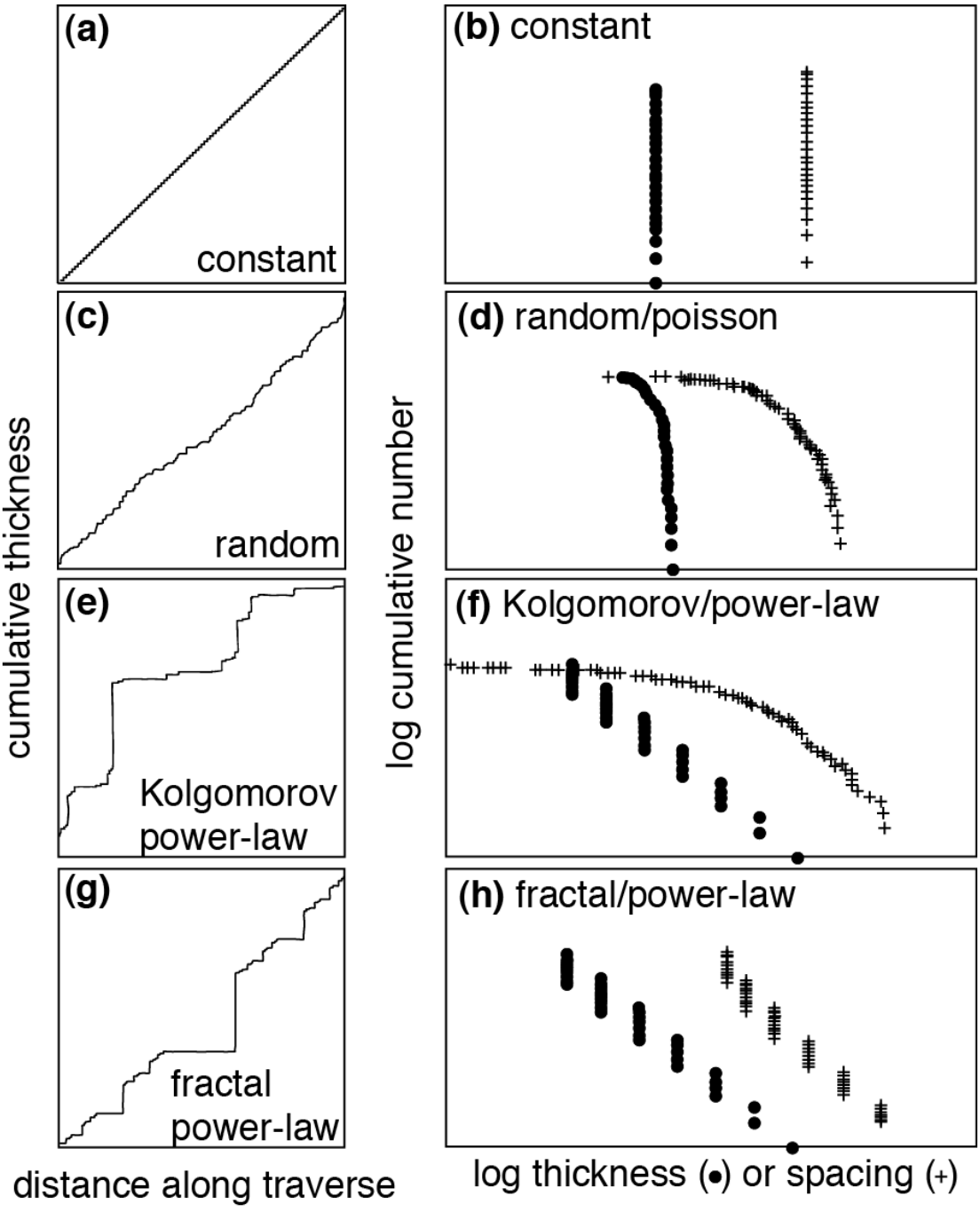

Fig. 7.7. Synthetic data from four representative vein set distributions plotted as cumulative thickness curves (a, c, e, g) and as log–log plots of cumulative number of vein spacing or vein frequency (b, d, f, h; modified after Gillespie et al., 1999).

The cumulative number of leucosomes plotted against leucosome thickness or leucosome spacing data on log–log diagrams are used to quantitatively evaluate power-law behaviour (Fig. 7.7). The cumulative number is the number of leucosomes with a thickness or spacing greater than or equal to a given value. A constant or periodic distribution of leucosomes is characterised by spacing and thickness data that plot as vertical lines (Fig. 7.7b). A random distribution defines downward concave curves for both spacing and thickness data (Fig. 7.7d). A Kolmogorov power-law distribution has thickness data that follow a linear trend and spacing data that follow a lognormal (concave down) trend (Fig. 7.7f). A fractal power-law distribution yields linear trends for arrays of both thickness and spacing data (Fig. 7.7h).

The results for each transect are summarized in Table 7.1 and the primary data from all transects are presented in Fig. D.1 in Appendix D. Here, the results from four transects through migmatitic paragneiss and four transects through migmatitic orthogneiss are discussed in detail. The four selected datasets are from the two longest transects and two representative datasets from the shorter transects from each rock type to investigate the sensitivity of the results to the length of the transect. Results are presented as cumulative plots of thickness (Figs 7.8, 7.9) to qualitatively evaluate scale-invariant trends and as log–log plots of cumulative number against thickness or spacing (Figs 7.10, 7.11) to quantitatively evaluate if the data are consistent with constant, random, Kolmogorov power law or fractal power law distributions. The spacing between leucosomes was determined by assigning a point to the centre of the leucosome and the distance between these centre-points is the calculated spacing between leucosomes.

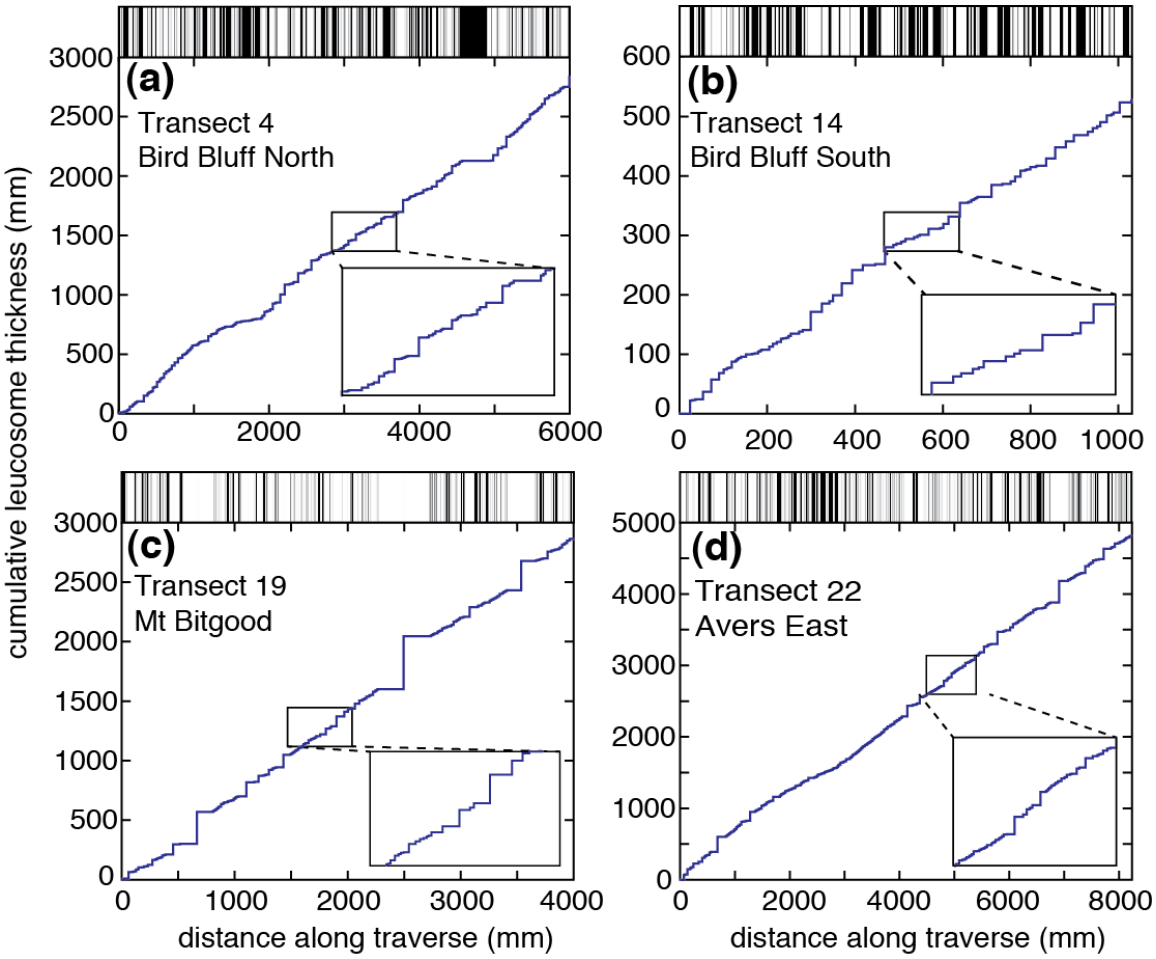

Fig. 7.8. Representative cumulative leucosome thickness plotted against transect length for transects through migmatitic paragneiss and composite one-dimensional rock-type profiles. Horizontal segments of the curves represent the distance between the centres of individual leucosomes and the vertical segments represent the thickness of an individual leucosome. White portions of the one-dimensional rock-type profiles indicate segments of leucosome and black portions indicate segments of melanosome. Cumulative leucosome thickness plots for all transects are presented in Fig. D.1 in Appendix D.

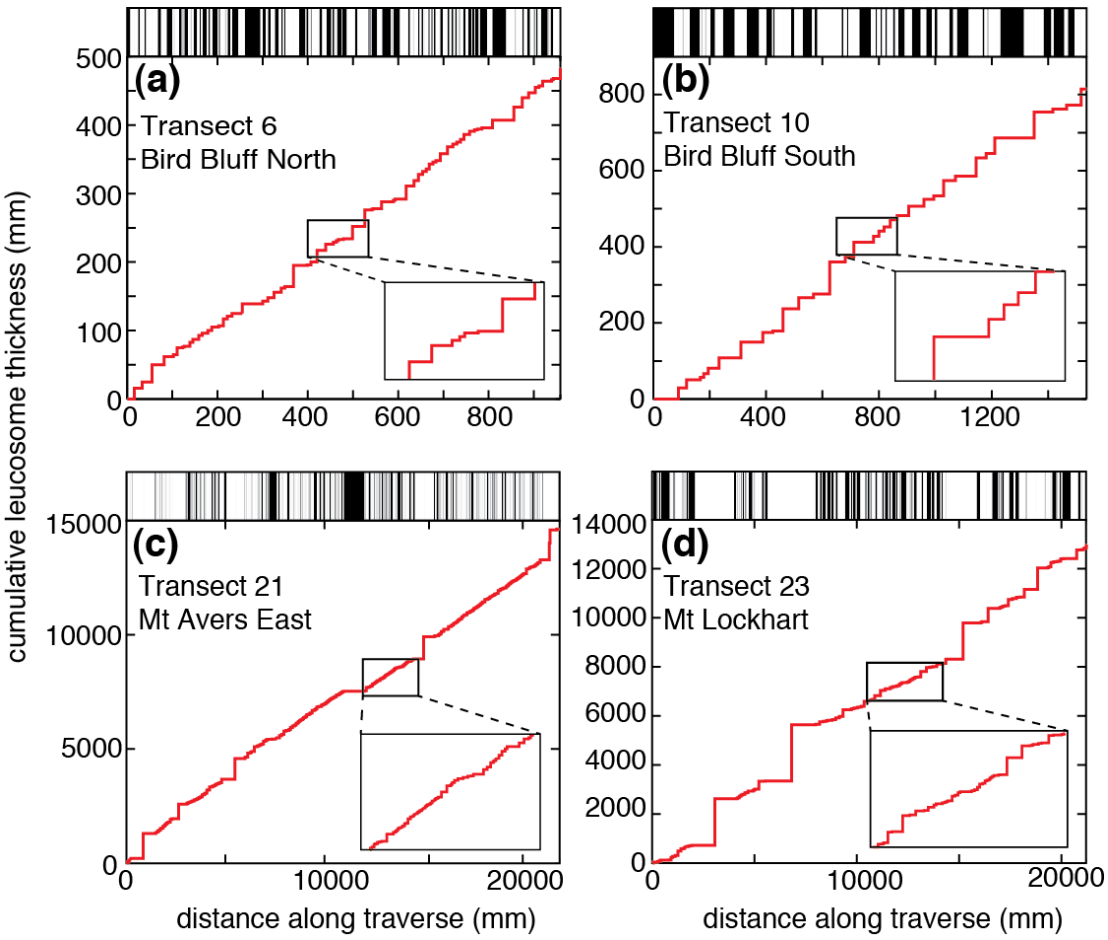

Fig. 7.9. Representative cumulative leucosome thickness plotted against transect length for transects through orthogneiss and composite one-dimensional rock-type profiles. Horizontal segments of the curves represent the distance between the centres of individual leucosomes and the vertical segments represent the thickness of an individual leucosome. White portions of the one-dimensional rock-type profiles indicate segments of leucosome and black portions indicate segments of melanosome. Cumulative leucosome thickness plots for all transects are Fig. D.1 in Appendix D.

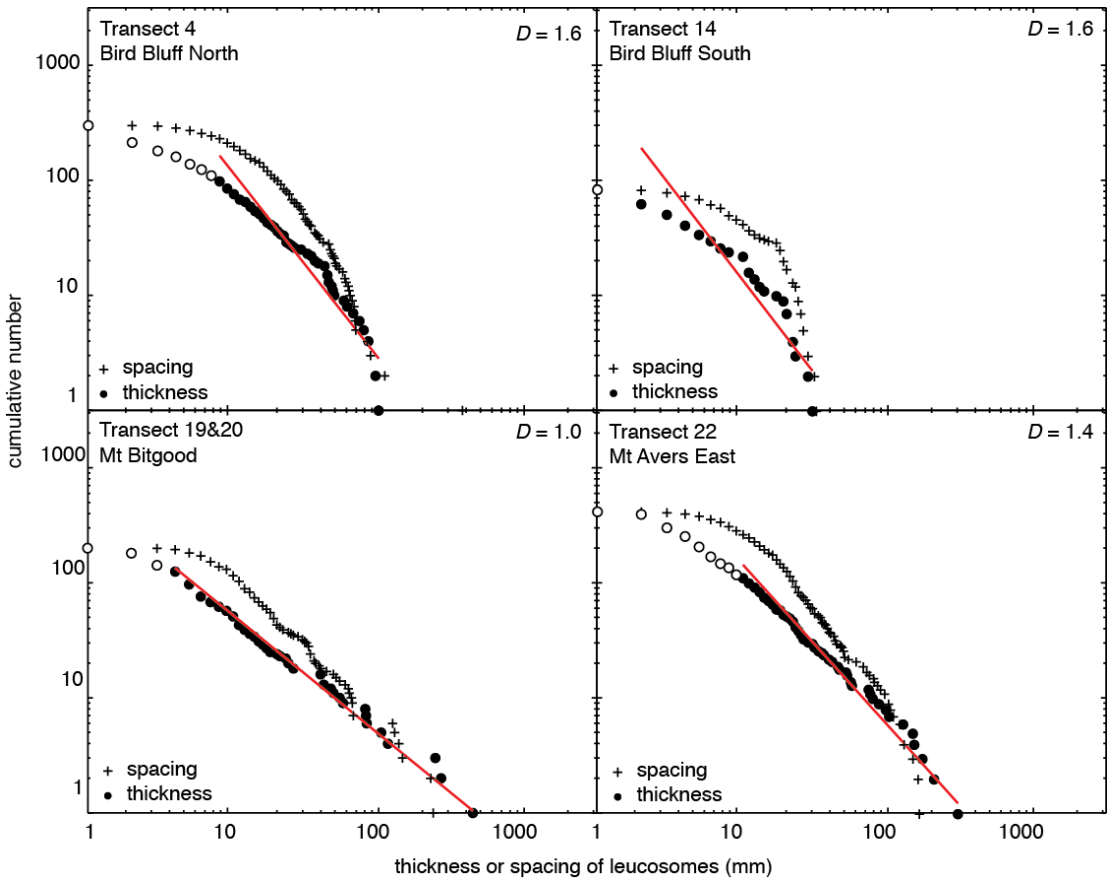

Fig. 7.10. Representative log–log plots of line transect results of spacing and thickness for migmatitic paragneiss. Thickness and spacing symbols on the ordinate represent the number of leucosomes with a spacing or thickness equal to or greater than the value on the abscissa. Open symbols indicate leucosome thickness values that are below x_{min} and are not included in the estimate for the scaling exponent (D). Red lines indicate the best fit for power-law behaviour using the maximum likelihood method. Spacing and thickness plots for all transects are presented Fig.D.1 in Appendix D.

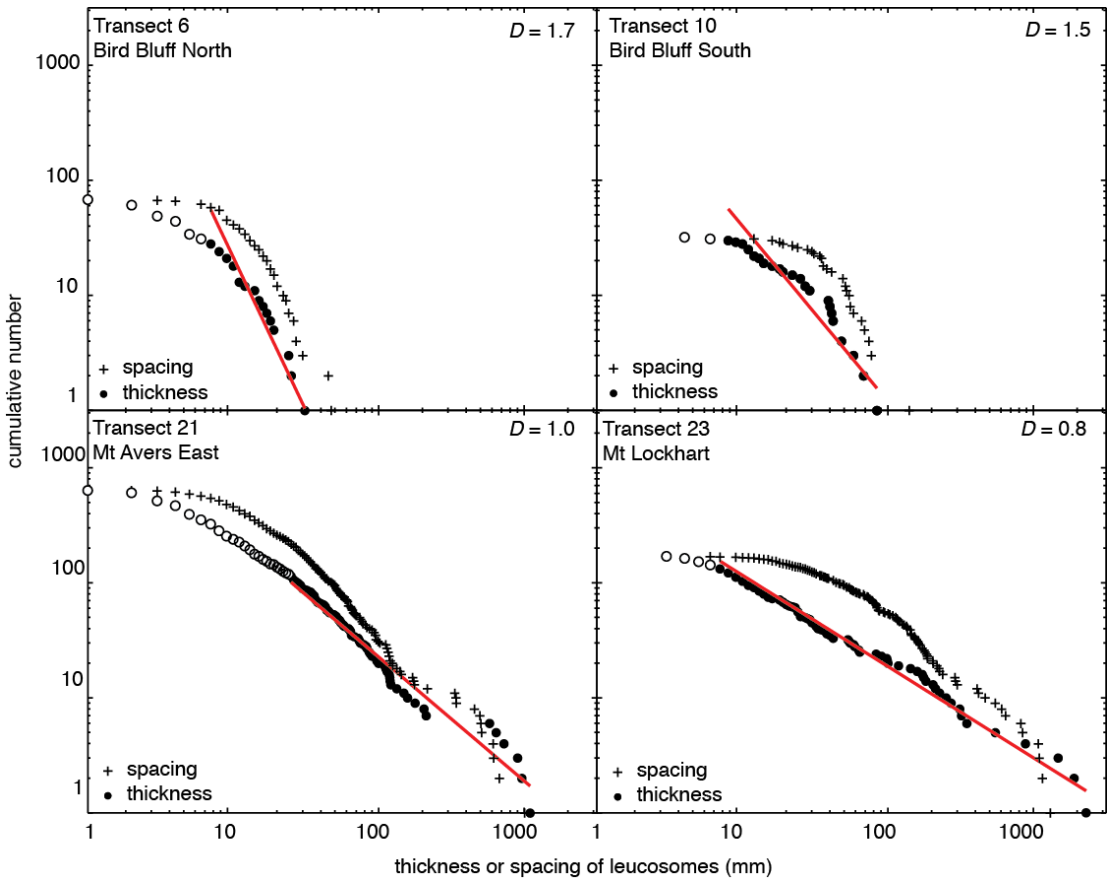

Fig. 7.11. Representative log–log plots of line transect results of spacing and thickness for migmatitic orthogneiss. Thickness and spacing symbols on the ordinate represent the number of leucosomes with a spacing or thickness equal to or greater than the value on the abscissa. Open symbols indicate leucosome thickness values that are below x_{min} and are not included in the estimate for the scaling exponent (D). Red lines indicate the best fit for power-law behaviour using the maximum likelihood method. Spacing and thickness plots for all transects are Fig. D.1 in Appendix D.

7.6.2 Estimate of scaling exponent

On a log–log plot, thickness data sampled from an underlying power-law distribution will plot along a linear trend. The slope of the line is the scaling exponent of the power-law function and has implications for characterizing the spatial clustering of leucosomes and the proportion of smaller to larger leucosomes (Gillespie et al. 1993, 1999). The significance of the fitted distribution to the thickness data is commonly evaluated using least-squares regression (Tanner, 1999; Soesoo et al., 2004; Bonamici and Duebendorfer, 2010). However, the data commonly define subtle concave down trends whereas least-square regression assumes a linear fit is an appropriate fit to the data, which is not always the case (Marchildon and Brown, 2003) and can produced biased results (e.g. Bonnet et al., 2001).

The central straight segment of the concave curves is commonly used to obtain an estimate of the scaling exponent, where the downward curvature at small thickness or spacing values is attributed to undersampling (Turcotte, 1997; Marchildon and Brown, 2003; Bonamici and Duebendorfer, 2010). It is common practice to visually estimate the central straight part of the segment and conduct linear regression from a minimum value (x_{min})—representing the estimated lower bound of power-law behavior—to the largest value. Marchildon and Brown (2003) plotted the change in slope between adjacent data points to determine if a central straight segment existed.

An alternative approach is to use the maximum likelihood estimation method of Clauset et al. (2009), whereby each possible value of x_{min} is tested so that the probability distribution of the data above it is as similar as possible to the best-fit power-law distribution

$$p(x) \approx x^{-\alpha}, \qquad (1)$$

where p(x) is the probability distribution, x is the property of interest (e.g. thickness or spacing of leucosomes), and α is the scaling exponent of the power law (Clauset et al., 2009). For each possible value of x_{min}, the scaling exponent is estimated using the maximum likelihood method and the Kolmogorov–Smirnov goodness-of-fit statistic is calculated. The value of x_{min} that yields the minimum value for the Kolmogorov–Smirnov statistic out of all possibilities and the corresponding value of α are retained (Clauset et al., 2009). The scaling exponent for the probability distribution (α) calculated using the method above is related to D, the scaling exponent, or fractal dimension (Turcotte, 1997; Tanner, 1999) of a cumulative distribution (Figs 7.10, 7.11) by the relationship (Bonnet et al., 2001)

$$D = \alpha - 1. \qquad (2)$$

The best estimates of the scaling exponents for the thickness data are summarized in Table 7.1. The thickness data with values smaller than x_{min} are plotted as open symbols and the data with values larger than and equal to x_{min} are shown as solid symbols in Figs 7.10 and 7.11. Fifteen transects (1, 2, 4, 5, 6, 7, 8, 11, 12, 16, 17, 19, 21, 22, 23) contain leucosome distributions that are consistent with the hypothesis that they were sampled from a power-law distribution (Table 7.1). The spatial distribution of leucosomes from the remaining six transects (3, 10, 13, 14, 15, 18) are inconsistent with being sampled from a power-law distribution.

7.6.3 Transects through migmatitic paragneiss

Transects through the migmatitic paragneiss ranged from 1 to 8 m in length. These transects contained between 69 and 424 individual leucosome layers with thicknesses from 1 to 444 mm, yielding between 43 and 72 vol.% leucosome along the traverse (Table 7.1). The cumulative thickness curves from three transects closely resemble those for a synthetic random distribution of veins (Figs 7.7c, 7.8a, b, d). The cumulative thickness curve for transect 19 contains three large steps that indicate that the line of measurement passed through relatively thick leucosomes at these locations; the pattern resembles a cumulative thickness curve for a power-law distribution, either Kolmogorov or fractal (Figs 7.7e, 7.8c).

Leucosome spacing data from migmatitic paragneiss transects show strong concave down trends, which are inconsistent with the linear trends expected for a fractal power-law distribution (Fig. 7.10). Leucosome thickness data define trends on the cumulative plots that are generally concave down (Fig. 7.10); however, the tails of the cumulative distribution from 8 of 13 transects are consistent with the hypothesis that they were sampled from a power-law distribution (Table 7.1). Estimates of the scaling exponents range from 1.0 to 1.8; the two longest transects yield values of 1.0 and 1.2. The estimated lower-limit of power-law behaviour varies between transects from 4 to 20 mm, which suggests that the smaller leucosomes do not follow power-law behaviour, which may be attributed to undersampling or that power-law behaviour breaks down below this threshold limit.

7.6.4 Transects through migmatitic orthogneiss

Transects through the migmatitic orthogneiss ranged from 1 to 22 m in length. These transects contained between 27 and 640 individual leucosomes with thicknesses from 1 to 2298 mm, yielding between 39 and 67 vol.% leucosome (Table 7.1). The thickest leucosomes measured in the migmatitic orthogneiss are nearly an order of magnitude larger than the thickest leucosomes measured in the paragneiss, which corroborates qualitative field observations that the migmatitic orthogneiss contains a larger range of leucosome sizes than the migmatitic paragneiss.

Two of the cumulative thickness plots show stair-steeping morphologies (Fig. 7.9b, d), which visually resemble the cumulative thickness plots for a power-law distribution, either Kolmogorov power-law or fractal power-law (Fig. 7.7e, g). The other two transects resemble the plots for a random distribution (Fig. 7.9a, c).

Spacing data of leucosomes from migmatitic orthogneiss yield well-defined concave down trends, which is inconsistent with a fractal distribution (Fig. 7.11). Thickness data from the migmatitic orthogneiss show subtler concave down trends (Fig. 7.11). The closest to linear trends are represented by transects 21 and 23 (Fig. 7.11). Estimated scaling exponents range between 0.7 and 1.9, with the two longest transects yielding values of 0.7 and 1.2 (Table 7.1). The lower-limit of power-law behaviour varies between 7 and 28 mm thickness, which suggests either that the smaller leucosomes were undersampled, or that power-law behaviour breaks down for smaller leucosome thicknesses. In general, these estimated lower limits of power-law behaviour from the migmatitic orthogneiss are greater than those determined from the migmatitic paragneiss.

7.7 Phase equilibria modelling

The quantity of melt produced from the migmatitic paragneisses and orthogneisses at any *P–T* condition may be evaluated using phase equilibria modelling (e.g. White et al., 2007; Johnson et al., 2008; Korhonen et al., 2010a). *P–T* pseudosections were calculated for three samples that are representative of the range of bulk chemical compositions for each of the Swanson Formation and the Ford Granodiorite suite (Fig. 7.12). These phase diagrams allow a comparison to be made between the amount of leucosome measured at outcrop in the migmatites and the amount of melt predicted to have been produced at peak *P–T* conditions, assuming no drainage of melt out of the system (i.e. closed system behaviour). Since melt loss is expected, based on the preservation of peritectic minerals in leucosomes (Figs 7.3d and 7.4c; Brown, 2002; White and Powell, 2002), if leucosomes were derived solely from in situ partial melting the volume of leucosome preserved should be less than the amount of melt predicted to have been produced. However, if the volume of leucosome preserved approaches or exceeds that predicted to have been produced, this implies crystallization of additional melt migrating through the complex to shallower crustal levels (e.g. Nyman et al., 1995; Hartel and Pattison, 1996; Marchildon and Brown, 2003; Guernina and Sawyer, 2003; Morfin et al., 2013).

Bulk rock compositions of samples 10CY-002, Y2-SM095, Y2-MS089, and Y2-MP098 were determined by X-ray fluorescence at Franklin and Marshall College following their standard procedures (Table 7.2; Boyd and Mertzmann, 1987). FeO contents of these samples were analysed by Fe2+ titration and Fe2O3 contents were

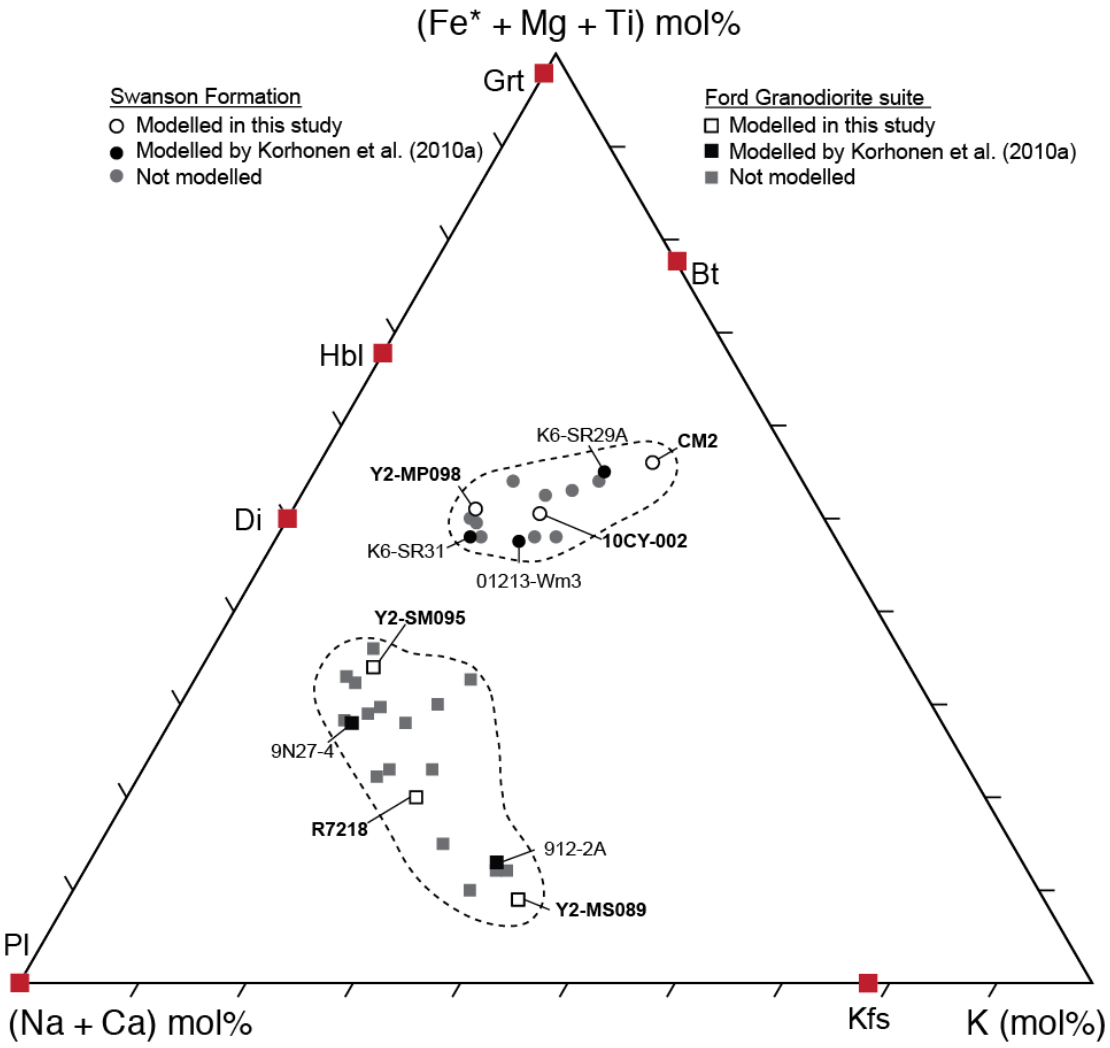

Fig. 7.12. (Fe* + Mg + Ti)–K–(Na + Ca) ternary diagram (after Solar and Brown, 2001) illustrating the compositional variability for Ford Granodiorite suite and Swanson Formation rocks.

Table 7.2. Bulk compositions used for phase equilibria modelling (mol.%)

	H_2O	SiO_2	Al_2O_3	CaO	MgO	FeO	K_2O	Na_2O	TiO_2	O	Total
Ford Granodiorite suite											
Y2-MS089	1.34	80.78	8.62	1.00	0.42	0.90	3.31	3.39	0.12	0.11	100
R7218	3.70	75.24	8.71	2.67	1.44	1.94	2.46	3.54	0.30	0.10[a]	100
Y2-SM095	2.06	70.65	9.45	4.41	3.68	3.59	1.76	3.46	0.53	0.42	100
Swanson Formation											
CM2	6.44	65.48	11.42	0.52	5.23	5.71	3.17	1.14	0.61	0.28[a]	100
10CY-002	5.56	65.69	10.00	1.38	5.76	5.58	2.78	2.43	0.54	0.28	100
Y2-MP098	2.63	76.19	7.28	1.62	4.26	3.94	1.41	1.93	0.53	0.22	100

[a]10% of iron assumed to be ferric. All other Fe^{2+}/Fe^{3+} values were determined by titration.

calculated by difference. Sample CM2 was analysed as part of a previous study (Siddoway, unpublished data) and sample R7218 is a Ford Granodiorite suite sample reported in Weaver et al. (1991). For these two samples, 10% of the total iron is assumed to be ferric (Table 7.2). The amount of melt produced across the modelled *P–T* range is relatively insensitive to the amount of ferric to ferrous iron. The amount of water in the average bulk compositions for all samples was adjusted so that there is minimal (~0.01 mol%) free H_2O at the solidus at 0.7 GPa, which is consistent with fluid-absent conditions above the solidus (White and Powell, 2002; White, 2003; White et al., 2005). If the actual prograde path crossed the solidus at lower or higher pressures, this approach would slightly overestimate and underestimate the quantity of melt produced, respectively.

Calculations were performed using THERMOCALC v.3.35 (Powell and Holland, 1988) and the internally consistent dataset of Holland and Powell (1998). Modelling was undertaken in the Na_2O–CaO–K_2O–FeO–MgO–Al_2O_3–SiO_2–H_2O–TiO_2–Fe_2O_3 (NCKFMASHTO) chemical system, which is currently the most realistic system to investigate melting for metasedimentary and metaigneous protoliths (White et al., 2007). The phases considered were Crd – cordierite; Di – diopside; Ep – epidote; Grt – garnet; H_2O – aqueous fluid; Ilm – ilmenite; Kfs – K-feldspar; Ky – kyanite; Liq – silicate liquid/melt; Mag – magnetite; Ms – muscovite; Opx – orthopyroxene; Pl – plagioclase; Pg – paragonite; Qtz – quartz; Rt – rutile; Sil – sillimanite; Spl – spinel; Ttn – titanite. The activity–composition (a–x) models for the phases considered are: biotite, garnet, and melt (White et al., 2007); orthopyroxene and spinel–magnetite (White and Powell, 2002); cordierite and epidote (Holland and Powell, 1998); K-feldspar and plagioclase (Holland

and Powell, 2003); white mica (Coggon and Holland, 2002); ilmenite–hematite (White et al., 2000); clinopyroxene (Green et al., 2007); and hornblende (Diener et al., 2007). Phases modelled as pure end-members include: quartz, rutile, titanite, aqueous fluid (H_2O), and the aluminosilicates.

P–T pseudosections calculated for three Swanson Formation (Fig. 7.13) and three Ford Granodiorite suite (Fig. 7.14) compositions show the stable phase assemblages and melt isopleths—curves that connect equal amounts of melt in mol.% (approximately vol.%)—across the modelled *P–T* conditions. Swanson Formation compositions yield 8–48 mol.% melt and Ford Granodiorite suite compositions produce 3–17 mol.% melt at estimated Cretaceous peak metamorphic conditions (855–890°C and 0.63–0.76 GPa; Korhonen et al., 2010a, 2012). Migmatitic paragneisses and orthogneisses in the Fosdick complex contain a greater proportion of leucosome (39–72 vol.%) than the quantities estimated through phase equilibria modeling. Additionally, some of the melt produced in situ must have been lost to preserve the peak mineral assemblages observed in the Fosdick complex (Korhonen et al., 2010a). The total amount of leucosome measured in the Fosdick complex, therefore, must represent the minimum integrated product of leucosome derived from in situ partial melting and melt that originated from deeper in the Fosdick complex.

Fig. 7.13 Calculated *P–T* pseudosections for three Swanson Formation compositions. The thick dashed line represents the solidus and the thin dashed lines represent melt isopleths in mol.% (~vol.%). Estimated Cretaceous peak *P–T* conditions are shown on each diagram as a field bounded by a heavy black line. The thick grey line shows an average thermal gradient for the Cretaceous *P–T* conditions for the Fosdick complex (1230°C/GPa). Fully labelled versions of these pseudosections are in Fig. D2 in Appendix D.

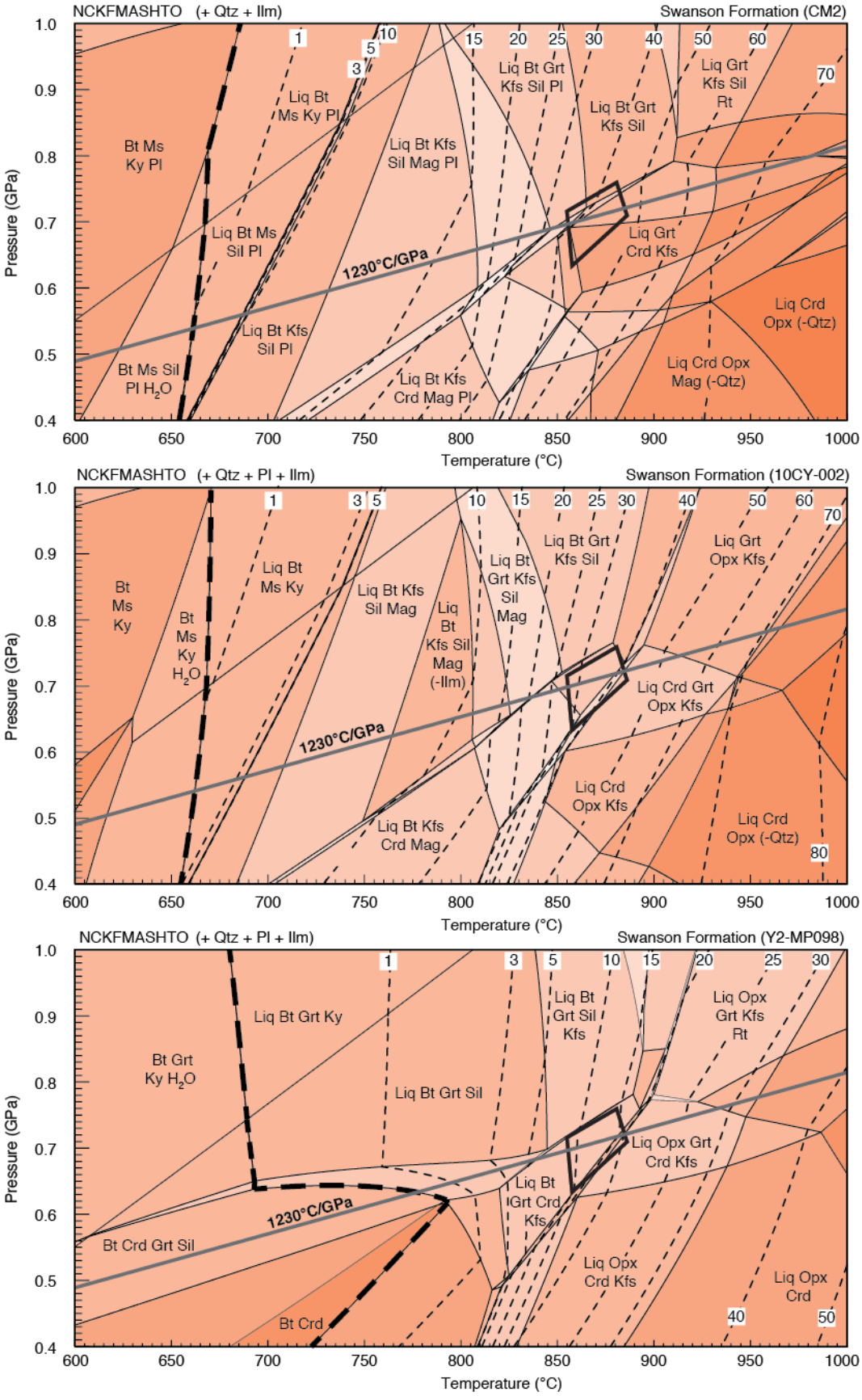
NCKFMASHTO (+ Qtz + Ilm)
Swanson Formation (CM2)
Pressure (GPa)
Temperature (°C)
Bt Ms Ky Pl
Liq Bt Ms Ky Pl
Liq Bt Kfs Sil Mag Pl
Liq Bt Grt Kfs Sil Pl
Liq Bt Grt Kfs Sil
Liq Grt Kfs Sil Rt
Liq Bt Ms Sil Pl
Liq Grt Crd Kfs
1230°C/GPa
Liq Bt Kfs Sil Pl
Liq Crd Opx (-Qtz)
Bt Ms Sil Pl H2O
Liq Bt Kfs Crd Mag Pl
Liq Crd Opx Mag (-Qtz)
NCKFMASHTO (+ Qtz + Pl + Ilm)
Swanson Formation (10CY-002)
Bt Ms Ky
Bt Ms Ky H2O
Liq Bt Ms Ky
Liq Bt Kfs Sil Mag
Liq Bt Kfs Sil Mag (-Ilm)
Liq Bt Grt Kfs Sil Mag
Liq Bt Grt Kfs Sil
Liq Grt Opx Kfs
Liq Crd Grt Opx Kfs
1230°C/GPa
Liq Crd Opx Kfs
Liq Bt Kfs Crd Mag
Liq Crd Opx (-Qtz)
NCKFMASHTO (+ Qtz + Pl + Ilm)
Swanson Formation (Y2-MP098)
Liq Bt Grt Ky
Bt Grt Ky H2O
Liq Bt Grt Sil
Liq Bt Grt Sil Kfs
Liq Opx Grt Kfs Rt
Liq Opx Grt Crd Kfs
1230°C/GPa
Liq Bt Grt Crd Kfs
Bt Crd Grt Sil
Liq Opx Crd Kfs
Liq Opx Crd
Bt Crd

7.8 Discussion

7.8.1 Scale invariance of crustal melting

The differentiation of the continental crust by anatexis and melt loss requires the continuous organization of melt from the initial sites of melt generation—along grain boundaries—via segregation in vein networks into ascent conduits that ultimately feed plutons at high crustal levels (e.g. Brown, 2010b). The spatial distribution of ascent conduits and intrusive complexes at higher structural levels suggests that these features are scale-invariant (McCaffrey and Petford, 1997; Tanner, 1999; Cruden and McCaffrey, 2001; Bons et al., 2004; Brown, 2005; Cruden, 2006; Koukouvelas et al., 2006). Whether stromatic leucosomes are scale-invariant has remained unclear. Marchildon and Brown (2003) suggest that the measured spatial distribution of leucosome in stromatic migmatites from Southern Brittany is inconsistent with power-law behaviour and they attribute this to the control of pre-existing heterogeneities (relict bedding features and tectonic foliation) on the spatial distribution of melt-bearing structures. Soesoo et al. (2004) and Bons et al. (2004) argue that the spatial distribution of leucosome in drill cores from the Estonian basement and from outcrops in southern Finland follow power-law distributions over two to three orders of magnitude. Bonamici and Duebendorfer

---

Fig. 7.14. Calculated *P–T* pseudosections for three Ford Granodiorite suite compositions. The thick dashed line represents the solidus and the thin dashed lines represent melt isopleths in mol.% (~vol.%). Estimated Cretaceous peak *P–T* conditions are shown on each diagram as a field bounded by a heavy black line. The thick grey line shows an average thermal gradient for the Cretaceous *P–T* conditions for the Fosdick complex (1230°C/GPa). Fully labelled versions of these pseudosections are Fig. D2 in Appendix D.

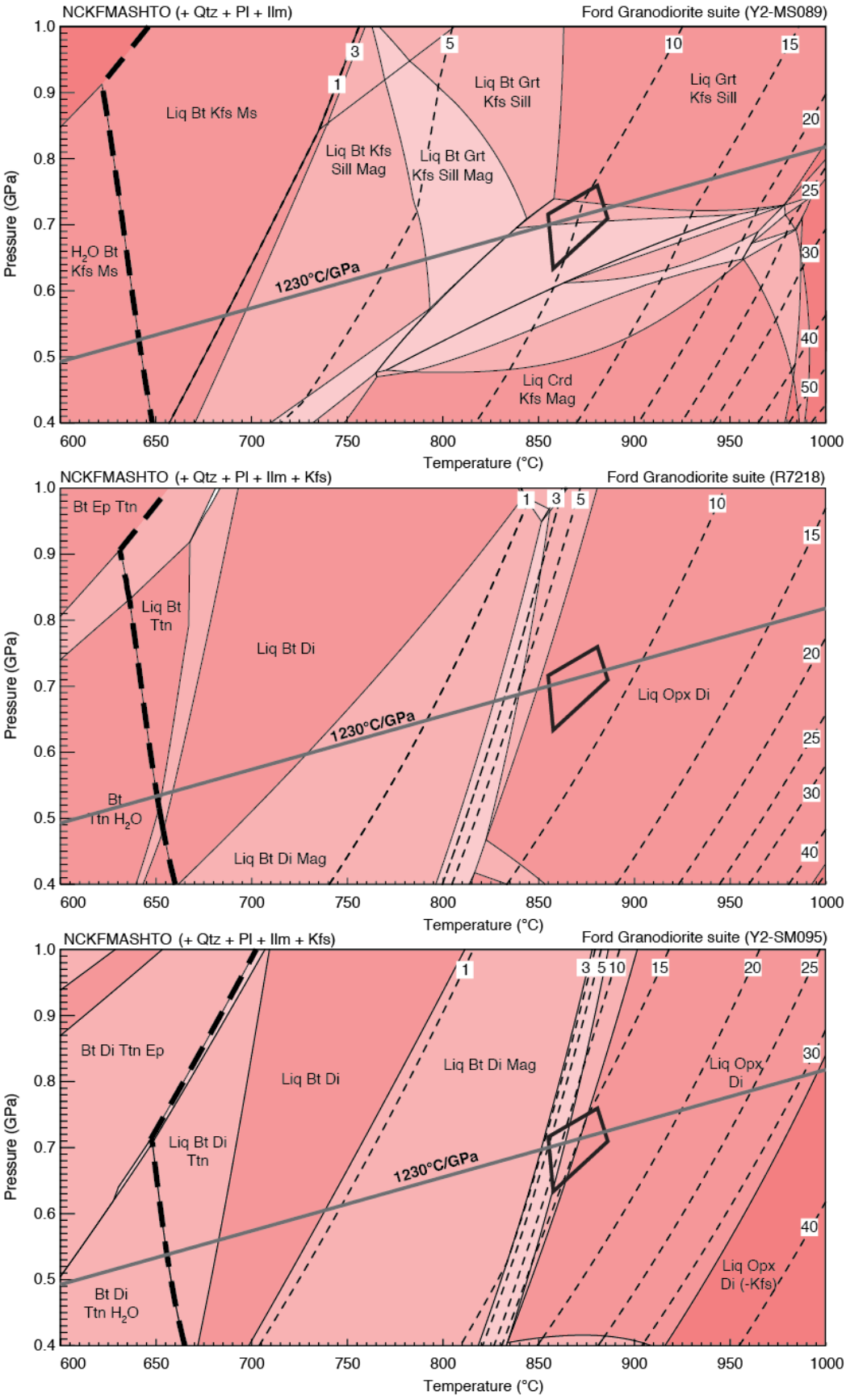
NCKFMASHTO (+ Qtz + Pl + Ilm)
Ford Granodiorite suite (Y2-MS089)
Liq Bt Kfs Ms
Liq Bt Kfs Sill Mag
Liq Bt Grt Kfs Sill
Liq Bt Grt Kfs Sill Mag
Liq Grt Kfs Sill
H2O Bt Kfs Ms
1230°C/GPa
Liq Crd Kfs Mag
NCKFMASHTO (+ Qtz + Pl + Ilm + Kfs)
Ford Granodiorite suite (R7218)
Bt Ep Ttn
Liq Bt Ttn
Liq Bt Di
Liq Opx Di
Bt Ttn H2O
Liq Bt Di Mag
NCKFMASHTO (+ Qtz + Pl + Ilm + Kfs)
Ford Granodiorite suite (Y2-SM095)
Bt Di Ttn Ep
Liq Bt Di
Liq Bt Di Mag
Liq Opx Di
Liq Bt Di Ttn
Bt Di Ttn H2O
Liq Opx Di (-Kfs)
Pressure (GPa)
Temperature (°C)

(2010) suggest that leucosomes from stromatic migmatites in the Hualapai Mountains in Arizona display limited scale invariance over one to two orders of magnitude.

The scaling exponents of leucosome power-law distributions estimated from previous studies and this study are summarized in Table 7.3. Of the previous studies, only Marchildon and Brown (2003) and Bonamici and Duebendorfer (2010) attempted to evaluate the statistical significance of the estimated scaling exponent. Marchildon and Brown (2003) evaluated the change in slope of the power-law distribution and concluded that the data show limited scale invariance over less than one order of magnitude. Bonamici and Duebendorfer (2010) used least-squared regression and argued that the high correlation coefficients were evidence that the power-law fits were statistically significant. However, least squares linear regression assumes linear behaviour and has been known to lead to biases in the estimate of the scaling exponent (Bonnet et al., 2001). Plotting the data as a cumulative distribution also limits the scatter around any curve. Therefore, high correlation coefficients do not necessarily suggest a significant fit (Walsh and Watterson, 1993). The maximum likelihood method employed in this study does not assume a linear fit (e.g. Clauset et al., 2009) and the scaling exponents are interpreted to be significant for 15 out of 21 transects (Table 7.1).

Results of this study suggest that the spatial distributions of stromatic leucosome in migmatitic paragneisses and orthogneisses are consistent with being sampled from power-law distributions. The transects that do not exhibit power-law relationships are typically shorter with fewer sampled leucosomes; these transects typically record only 1–2 orders of magnitude of leucosome thickness variation. The curvature of the thickness data from these transects qualitatively resembles a random or unclustered distribution

Table 7.3. Results of other 1-D transect studies in high-grade metamorphic rocks

Feature	Scaling exponent (*D*)	Location	Reference
Leucosome	1.3	Port Navalo	Bons *et al.* (2009)
Leucosome	1.06–1.84	Hualapai Mountains	Bonamici and Dubendorfer (2010)
Leucosome	Not power-law	Southern Brittany	Marchildon and Brown (2003)
Leucosome	1.15–1.9	Estonian basement	Soesoo *et al.* (2004)
Leucosome	0.7–1.9	West Antarctica	This study
Granite veins	1.09	Estonian basement	Soesoo *et al.* (2004)
Granite veins	1.11	Port Navalo	Brown (2005)

(Fig. 7.7d). The longer transects presented in this study consistently show power-law distributions with scaling exponents that are systematically smaller than scaling exponents estimated for the shorter transects. The higher values of scaling exponents for the shorter transects may be the result of the maximum likelihood method of Clauset et al. (2009), which fits the linear segment to the entire tail of the dataset, where the strong concave down shape at the tail may be an artificial product of an insufficiently large dataset.

Larger leucosomes that pass outside the transect may be incompletely sampled—termed the censoring effect (Bonnet et al., 2001)—and this would artificially increase the slope of the scaling exponents at higher values. The effect of censoring is minimized by conducting longer transects; therefore, shorter transects are more likely to suffer from censoring effects and the calculated scaling exponents may be significantly larger than the true value. The results of the shorter transects presented in this study closely resemble those presented by Marchildon and Brown (2003). Thus, if leucosome thickness values are approximated by power-law distributions, shorter transects may be insufficient to sample adequately the power-law distribution leading to the appearance of a random distribution of leucosome thicknesses and an artificially inflated scaling exponent. The

spatial distribution of leucosome from southern Brittany may be consistent with power-law behaviour, but longer transects would be needed to test this hypothesis.

7.8.2 Combined transects of migmatitic orthogneiss and migmatitic paragneiss

The measured leucosome networks in each of the migmatitic paragneisses and orthogneisses across the complex are geometrically similar and sample a structural distance of approximately 5 km from Mt Avers to Bird Bluff (Fig. 7.2). Both rock types are interpreted to have been at *P–T* conditions above their respective solidi concurrently (Korhonen et al., 2012). Therefore, the full catalogue of data from each of the migmatitic paragneiss and orthogneiss transects may be pooled into two combined datasets to evaluate the differences between the spatial distribution of leucosome networks in the different host rocks. This same approach was used by Simpson (2000), who combined the results from several small transects into one comprehensive transect in order to investigate the spacing between veins.

The data from transects through both migmatitic paragneiss and migmatitic orthogneiss are plotted on a probability distribution plot in Fig. 7.15, which normalizes the cumulative number of the datasets to a value of one so that the two datasets are directly comparable. Using the maximum likelihood estimate method described above, data from the migmatitic paragneiss define a scaling exponent (α) of 2.9 and data from the migmatitic orthogneiss yield a value of 2.1; these correspond to cumulative scaling exponents (D), or fractal dimensions, of 1.9 and 1.1, respectively. These scaling exponents suggest that for one order of magnitude increase in leucosome thickness there are 79 and 13 times fewer leucosomes in the migmatitic paragneiss and orthogneiss,

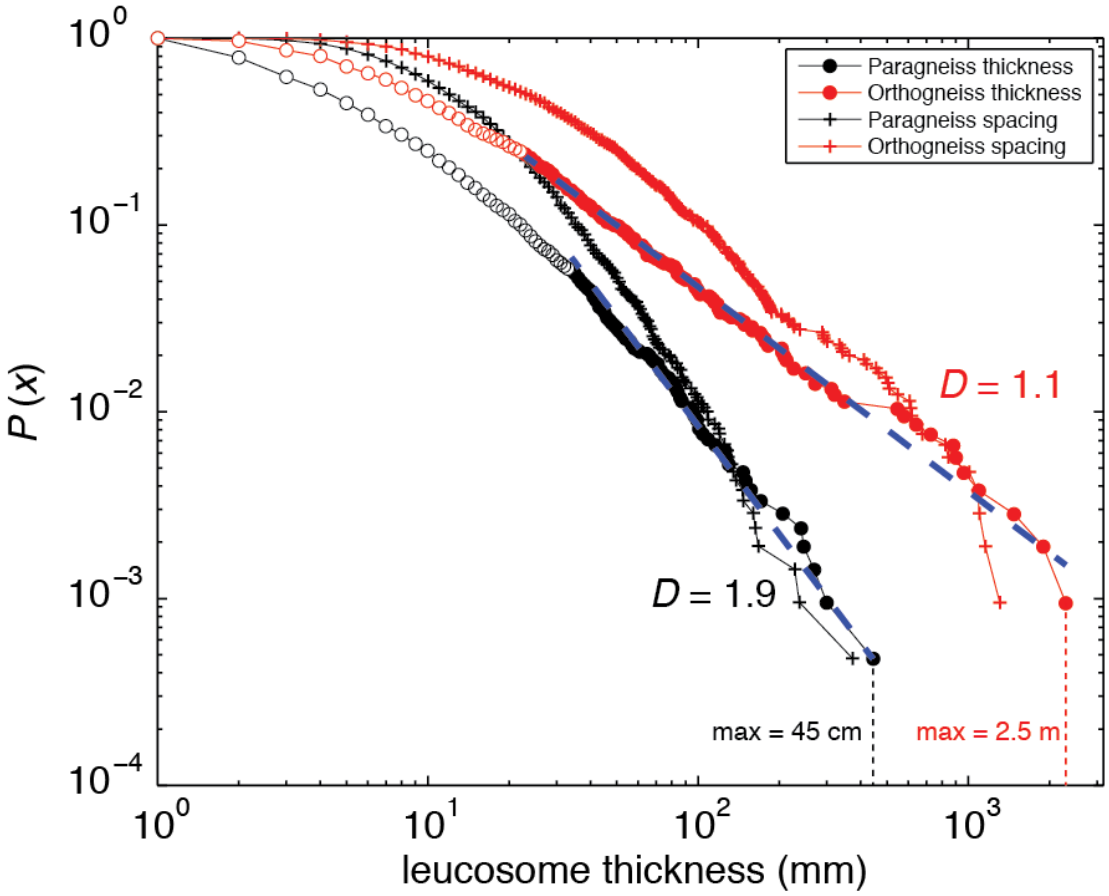

Fig. 7.15. Log–log probability distribution plot of pooled results from transects through migmatitic paragneiss (n = 13) and migmatitic orthogneiss (n = 8). Thickness and spacing symbols on the ordinate represent the number of leucosomes with a spacing or thickness equal to or greater than the value on the abscissa. Open symbols indicate leucosome thickness values that are below x_{min} and are not included in the estimate for the scaling exponent (D). Blue dashed lines indicate the best fit for power-law behaviour using the maximum likelihood method.

respectively. Both datasets are consistent with the hypothesis that they were sampled from a power-law distribution (Table 7.1). Leucosome thickness data from the migmatitic orthogneiss follow power-law behaviour over two orders of magnitude whereas the leucosomes thickness data from the migmatitic paragneiss follow power-law behaviour over just over one order of magnitude. The x_{min} values for the migmatitic paragneiss and migmatitic orthogneiss datasets are 34 and 23 mm, respectively, which suggest that power-law behaviour breaks down at leucosome thicknesses of a few centimetres.

The significantly different scaling exponents between the leucosome distributions in the migmatitic paragneiss and orthogneiss have important consequences for quantifying the spatial distribution of leucosomes in the different rock types. The higher scaling exponent from the plots of leucosome from the migmatitic paragneiss suggest that: (1) there are proportionally more smaller leucosomes in the migmatitic paragneiss when compared with the migmatitic orthogneiss; (2) there are fewer larger leucosomes in the migmatitic paragneiss when compared with the migmatitic orthogneiss; and, (3) the largest leucosomes in the migmatitic paragneiss are smaller than the largest leucosomes in the migmatitic orthogneiss by approximately one order of magnitude. These inferences are supported by qualitative outcrop observations that the migmatitic orthogneiss contains thicker leucosomes and that the migmatitic paragneiss contains a larger proportion of smaller leucosomes. The thickness of the largest leucosomes measured in the migmatitic paragneiss (decimetre-scale) is approximately the same as the distance between metapsammitic and metapelitic layers in the migmatitic paragneiss (Figs 7.1a, 7.3d, 7.15), which is inferred to reflect the compositional layering relict from the sedimentary protolith. This suggests that compositional layering in the migmatitic paragneiss may

have limited the maximum thickness of the largest leucosomes. In contrast, the maximum thickness of the largest leucosomes measured in the migmatitic orthogneiss (metre-scale) is inferred to have been limited by the length scale of gradients in melt pressure driving melt from grain boundaries to veins.

7.8.3 Inherited anisotropy

Melt segregation in migmatites is controlled predominately by the applied differential stress, volume-change driven convection and gravity-driven compaction (Brown et al., 1995). Melt migration driven by these processes may be limited by pre-existing heterogeneities in the host rock (e.g. van der Molen, 1985; Johannes, 1988; McLellan, 1988; Maaløe, 1992; Brown and Solar, 1998; Marchildon and Brown, 2003) and pre-existing heterogeneities may focus melt flow into layer-parallel conduits (Collins and Sawyer, 1996). Additionally, anisotropy, whether primary (compositional) or secondary (tectonic fabric), produces rheological contrasts between adjacent layers that respond differently to strain as a result, generating dilatant structures where melt may accumulate and drain (e.g. van de Molen, 1985; Brown, 1994; Sawyer, 1994; Druget and Carreras, 2006). The feedback relationship between partial melting, melt extraction, mineral growth and fabric development during high-grade metamorphism and partial melting within different layers will produce horizons with variable permeabilities to percolating anatectic melt.

More pelitic layers in metasedimentary sequences have a higher mode of mafic minerals, particularly micas that typically form a strongly defined foliation. The foliation may form a mechanical barrier to melt flow, as suggested by Burg and Vanderhaeghe

(1993). Alternatively, the crystalline anisotropy induced by the preferred orientation of the micas may result in low permeability normal to these layers (Laporte and Watson, 1995). Therefore, the primary compositional layering will exert a strong control on melt flow. Syn-anatectic tectonic fabrics may enhance primary compositional anisotropies, these composite layers also may hinder layer-perpendicular percolation, and melt may preferentially migrate parallel to these layers, limiting the thickness of leucosomes. In a rock that is homogeneous and closer to isotropic, as long as there is enough melt present along grain boundaries to remain interconnected (under static conditions < 5 vol.%; Lupulescu and Watson, 1999), the direction of melt migration will be controlled by gradients in melt pressure, which may allow for the development of thicker leucosomes. The dominant morphology of both the migmatitic paragneisses and orthogneisses is stromatic with tabular leucosomes, which suggests that the first order control on leucosome geometry was similar. However, the largest leucosome measured in a migmatitic paragneiss is 45 cm thick, whereas the largest leucosomes measured in the migmatitic orthogneiss is 2.5 m thick (Fig. 7.15), a difference of half an order of magnitude.

The protolith of the migmatitic paragneiss in the Fosdick complex—the Swanson Formation—is a turbidite sequence that contains intercalated layers of psammitic and pelitic material that would have produced different quantities of anatectic melt. The thickness of these compositional layers in the migmatitic paragneiss inherited from the protolith is on the order of tens of centimetres (Fig. 7.3d), roughly the same as the size of the largest leucosomes encountered in the migmatitic paragneiss. The protolith of the migmatitic orthogneiss in the Fosdick complex—the Ford Granodiorite suite—is

homogeneous and closer to isotropic (Fig. 7.4a). Initial fabrics in the migmatitic orthogneiss are defined by distributed biotite grains rather than by continuous melanosome layers (Fig. 7.4c and d), although biotite-rich schlieren develop in association with leucosomes (Fig. 7.4d). In the migmatitic orthogneiss the thicker leucosomes occur in the longer traverses, which were measured across thicker layers of orthogneiss (e.g. Fig. 7.4b). Melt migration perpendicular to the weak foliation in the orthogneiss may have occurred over length scales up to 2.5 m driven by gradients in melt pressure, although melt migration through the migmatites would have occurred via the larger melt channels. Notwithstanding, the local stress field is expected to have controlled the overall orientation of the leucosomes that form, leading to the foliation-parallel stromatic morphology. The thinner leucosomes measured in the migmatitic paragneiss, when compared with the relatively thicker leucosomes in the migmatitic orthogneiss, are consistent with the hypothesis that the layering inherited from the sedimentary protolith exerted some control on the maximum thickness of leucosomes in the migmatitic paragneiss.

7.8.4 Melt migration and entrapment

Stromatic metatexite migmatites in the Fosdick complex contain a larger volume of leucosome than predicted from phase equilibria modeling for in situ melt generation and retention, even in a closed system. Based on geophysical surveys across the Ford ranges, the crust beneath the Fosdick complex is inferred to represent Swanson Formation and Ford Granodiorite suite (Ferraccioli et al. 2000; Luyendyk et al. 2003). Therefore, the amount of melt that could have been produced at deeper crustal levels may

be assessed using the *P–T* pseudosections introduced above and considering the thermal evolution of an extending thick crustal segment. The thermal evolution of thickened and thinned orogenic crust has been most recently discussed by Clark et al. (2011), and the behavior of lower crust during exhumation and doming has been modelled by various groups (e.g. Tirel et al., 2008; Rey et al., 2009).

Crustal thinning increases the apparent thermal gradient in the manner shown in Fig. 7.16. An average thermal gradient for the Cretaceous *P–T* conditions for the Fosdick complex (1230°C/GPa) is shown in Figs 7.13 and 7.14. Extrapolating from these *P–T* conditions to deeper crustal levels beneath the Fosdick complex at temperatures of 860–1000°C shows that Swanson Formation compositions could have produced 10–80 mol.% melt and Ford Granodiorite suite compositions could have produced 10–32 mol.% melt (Figs 7.13, 7.14). Considering the area of the Fosdick complex, potentially a very large volume of melt was transferred through the complex to shallower levels in the crust. Melt drainage limits the amount of in situ melt present in the suprasolidus crust at a given time (Brown 2010a, 2013). The strength of melting crust decreases sharply with increasing melt fraction until a critical threshold, termed the melt connectivity transition, at ~7 vol.% melt where > 80% of grain boundaries become melt bearing (Rosenberg and Handy, 2005). At this threshold, in the absence of syn-anatectic deformation melt, melt migration is expected. However, applied differential stress during crustal anatexis generates gradients in melt pressure that are likely to promote melt segregation and extraction at melt fractions <7 vol.% (Brown 2007, 2010a, b, 2013), leaving approximately 1 vol.% melt retained on grain boundaries (Sawyer, 2001; Marchildon and Brown, 2002; Holness and Sawyer, 2008).

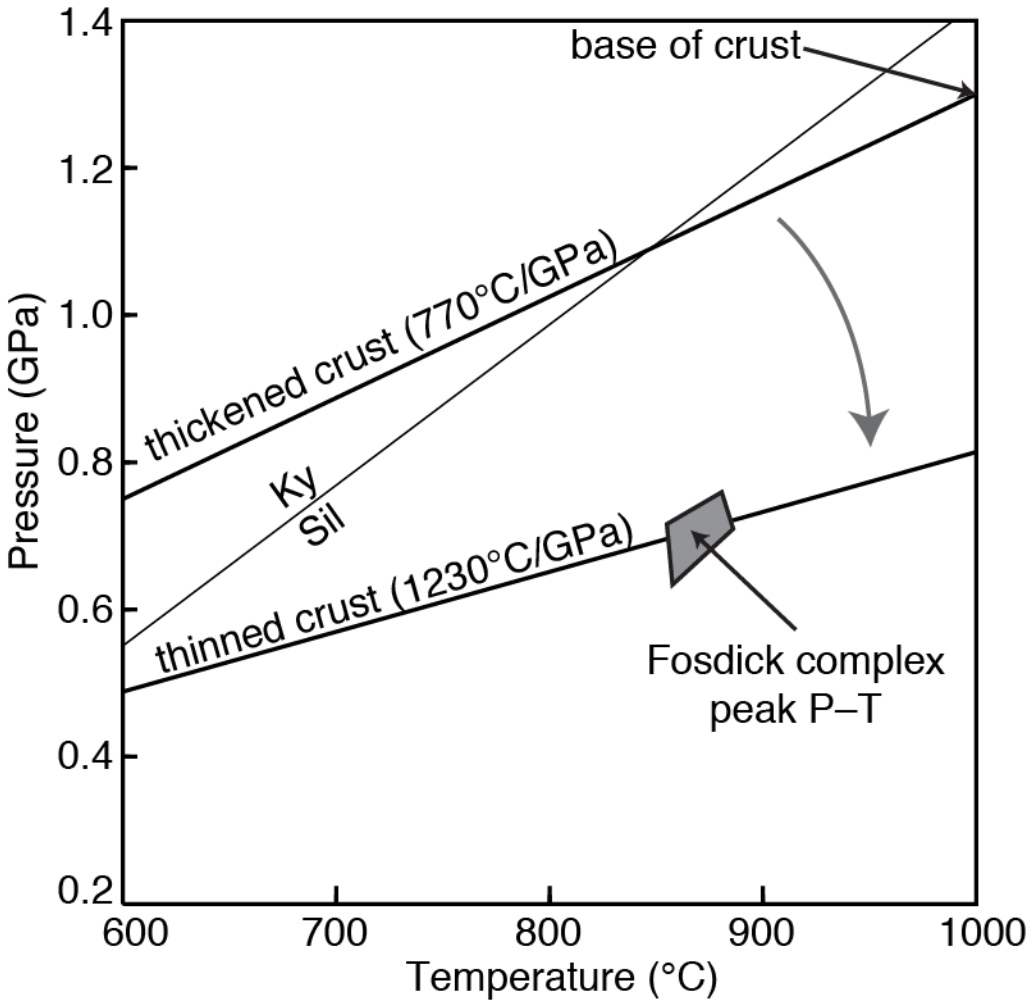

Fig. 7.16. The evolution of the apparent thermal gradient during the transition from thickened to thinned orogenic crust responsible for Cretaceous peak *P–T* conditions of the Fosdick complex.

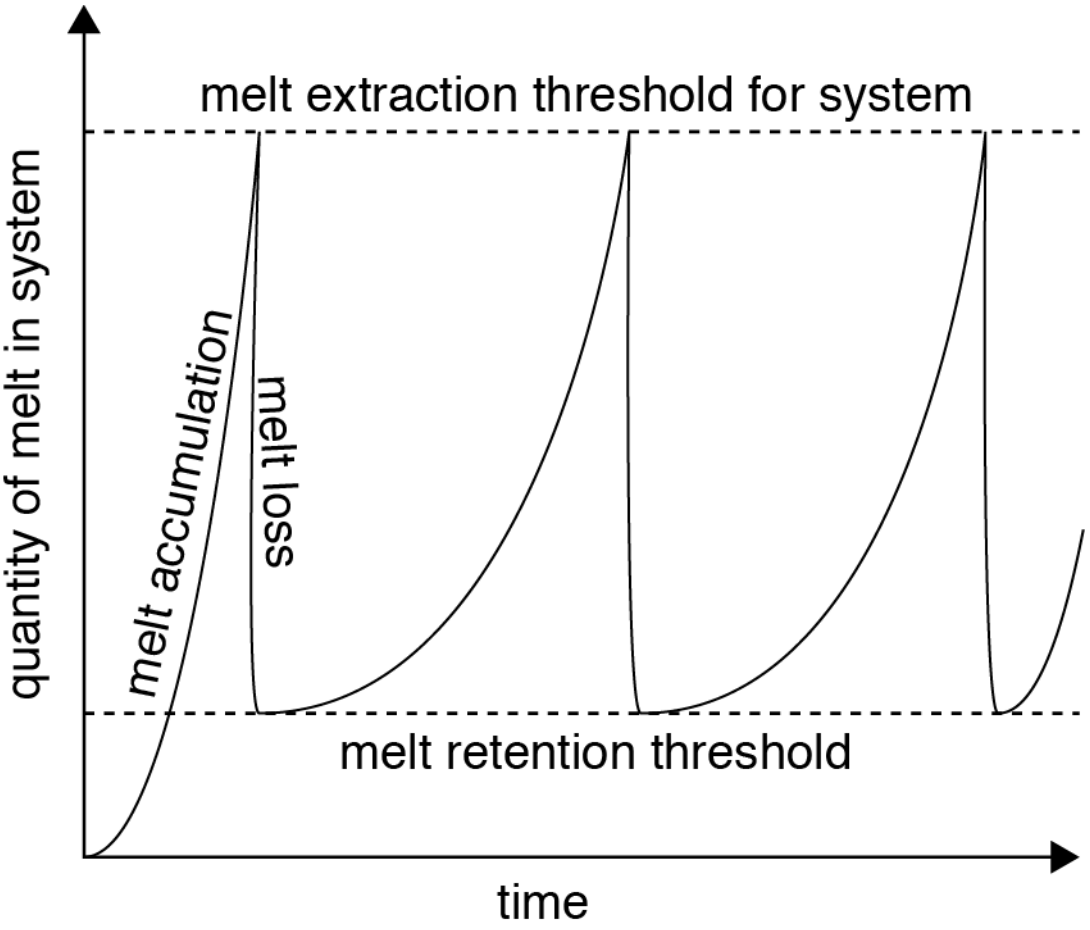

Fig. 7.17. Schematic graph illustrating the cyclical and pulsed nature of melt production and extraction. The amount of melt increases until it reaches some critical threshold where melt can escape. This threshold will vary with the amount and nature of strain imposed on the system. The system will evolve towards the critical state regardless of any perturbation imposed on it.

Given the quantity of melt calculated to have been produced in the crust of the Fosdick complex (10–80 mol.%), it is expected that melt extraction occurred via multiple drainage events during repeated cycles of melt buildup and melt loss (Fig. 7.17). This postulate is compatible with geochemical and geochronological evidence for the incremental growth of upper crustal plutons (e.g. Pressley and Brown, 1999; Mahan et al., 2003; Coleman et al., 2004; Miller, 2008; de Saint Blanquat et al., 2011; Schoene et al., 2012, Barboni et al., 2013).

It is likely that melt generated in the deeper crust beneath the Fosdick complex will have been transported through it, probably multiple times as a result of the episodic drainage of melt from the deeper crust. Furthermore, it is likely that some of this melt passing through will have been trapped in the complex en route. Thus, the Fosdick complex represents a level in the crust where melt was generated and lost, through which melt was transported and in which some fugitive melt was trapped. Therefore, the total amount of leucosome and granite observed in outcrop represents the integrated product of some of the melt generated in situ and melt that partially crystallized cumulate materials during transport through or was trapped to crystallize as granite. Thus, migmatite–granite complexes in the lower- to middle-crust are not only sites of melt production, but also represent zones of melt transfer and accumulation (Brown, 2008, 2010a, b; Morfin et al., 2013).

7.8.5 The Devil's plumbing system: self-organized criticality from bottom to top

Processes during orogenesis and melting are linked by nonlinear functional relations, so there are generally no simple links between cause and effect (Stüwe, 2007).

As a result, anatectic systems have the potential to change or reorganize in unpredictable ways, for example by switching from melt segregation and storage to melt extraction and drainage (Brown, 2010b). The size–frequency distributions of both granite-filled conduits inferred to have drained melt from migmatites (Soesoo et al., 2004; Brown, 2005) and granite plutons inferred to have captured the fugitive melt (Bons and Elburg, 2001; Cruden and McCaffrey, 2001; Cruden, 2006; Koukouvelas et al., 2006) follow power-law behaviour. Although not as definitive due to the limited range of sizes, the results of this study suggest that leucosome networks also exhibit power-law behaviour, similar to the results of other studies of migmatites (Tanner, 1999; Marchildon and Brown, 2003; Bons et al., 2004; Soesoo et al., 2004; Bonamici and Duebendorfer, 2010; Hall and Kisters, 2012; Pereira et al., 2013). Thus, the melt flow networks that enabled intracrustal differentiation by crustal anatexis likely exhibit power-law behaviour (cf. Brown, 2010b).

Nonlinear systems in which events of all sizes occur and where the size distribution of these events follows a power-law distribution exhibit self-organized criticality (e.g. Bak et al., 1988). Although events of all sizes occur in the critical state, large events are less likely than small events. Regardless of the initial configuration of the system or of any imposed perturbation on the system, such as a melt loss event, it will return to the critical state. A critical threshold where melt escape may occur is an example of such a critical state (Fig. 7.17), but in nature it must also be coupled with a spatial length scale. Melt drainage at the critical threshold will move the system away from its critical state, but in response the system self-organizes to re-attain the critical state.

The feedback relations between processes involved in orogenesis and those associated with crustal melting produce a complex system of nonlinear interactions (e.g. Stüwe, 2007; Brown, 2010b) during which the permeability of the system to migrating melt will dynamically adjust to achieve a state of maximum entropy production rate (Hobbs and Ord, 2010). Therefore, the system will tend to develop an interconnected melt flow network from bottom to top, regardless of perturbations imposed on it. The scale-invariant signal measured in leucosome networks coupled with similar signals measured from feeder conduits and plutons supports the hypothesis that melt extraction from the anatectic zone is a self-organized critical process.

7.9 Conclusions

The spatial patterning of stromatic leucosome measured in both migmatitic paragneisses and orthogneisses in the Fosdick migmatite–granite complex is consistent with power-law distributions. The scaling exponent of the power-law relationship that describes the distribution of leucosomes in migmatitic paragneiss is larger than that for migmatitic orthogneiss, which suggests that a greater proportion of smaller leucosomes contribute to the total leucosome volume in migmatitic paragneiss and a proportionally larger number of thicker leucosomes contributes to the total volume of leucosome in migmatitic orthogneiss.

The thickness of the largest leucosomes measured in the migmatitic paragneiss is similar to the spacing between metasedimentary layers in the migmatitic paragneiss, which suggests that the thickness of leucosomes in migmatitic paragneiss may have been spatially restricted by the inherited compositional layering. In contrast, migmatitic

orthogneiss may have been able to develop thicker leucosomes due to the absence of compositional heterogeneity and strong fabrics. Notwithstanding these differences, the common stromatic structure of the metatexite migmatites derived from both protoliths suggests that the regional stress field associated with the Cretaceous oblique extensional deformation exerted a primary control on leucosome morphology.

The amount of leucosome measured at outcrop is greater than the amount of melt predicted to have been generated in situ from phase equilibria modelling of both protolith compositions, which suggests that the volume of leucosome represents an integrated product of melting in situ and infiltration of melt derived from deeper crustal levels, some of which crystallized while in transit through the Fosdick complex. Hence, the regional stress field combined with the presence or absence of compositional heterogeneity and anisotropy rather than fertility of the host rocks are the major factors governing the three dimensional spatial distribution of leucosomes. The spatial distribution of leucosomes follows power-law behaviour over 1–2 orders of magnitude, and, when coupled with power-law signals detected from ascent conduits and upper-crustal plutons, supports the hypothesis that intracrustal differentiation by melt extraction from the lower-crust is a self-organized critical process.

Chapter 8: Anatectic reworking and differentiation of continental crust along the active margin of Gondwana: a zircon Hf–O perspective from West Antarctica

8.1 Abstract

The Fosdick migmatite–granite complex of West Antarctica preserves evidence of two crustal differentiation events along a segment of the former active margin of Gondwana, one in the Devonian–Carboniferous and another in the Cretaceous. The Hf–O isotope composition of zircons from Devonian–Carboniferous granites is explained by mixing of material from two crustal sources represented by the high-grade metamorphosed equivalents of a Lower Paleozoic turbidite sequence and a Devonian calc-alkaline plutonic suite, consistent with an interpretation that the Devonian–Carboniferous granites record crustal reworking without input from a more juvenile source. The Hf–O isotope composition of zircons from Cretaceous granites reflects those same two sources, together with a contribution from a more juvenile source that is most evident in the detachment-hosted, youngest granites. The relatively nonradiogenic εHf isotope characteristics of zircons from the Fosdick complex granites are similar those from the Permo-Triassic granites from the Antarctic Peninsula. However, the Fosdick complex granites contrast with coeval granites in other localities along and across the former active margin of Gondwana, including the Tasmanides of Australia and the Western Province of New Zealand, where the wider range of more radiogenic εHf values of zircon suggests that crustal growth through the addition of juvenile material plays a

larger role in granite genesis. These new results highlight prominent arc-parallel and arc-normal variations in the mechanisms and timing of crustal reworking versus crustal growth along the former active margin of Gondwana.

8.2 Introduction

Convergent margins are the primary location for the growth and differentiation of the continental crust (e.g. Taylor 1967; Rudnick 1995; Davidson and Arculus 2006; Bahlburg et al. 2009; Cawood et al. 2009; Kemp et al. 2009; Mišković and Schaltegger 2009). The relative proportions of crustal growth versus crustal reworking that operate in magmatic arcs can be deciphered using the geochemistry and isotope characteristics of granites (sensu lato) that were emplaced at significantly higher crustal levels than where they were generated. Granites are commonly mixtures of more than one source component. The relative contribution of the source components can be evaluated by modelling the proportions of each required to achieve the isotope composition of the granites, where the source components are usually a well-constrained supracrustal end-member and a less well-constrained (commonly inferred) infracrustal or more juvenile end-member (Kemp et al. 2006a, 2007; Appleby et al. 2009; Tulloch et al. 2009). In the case of predominantly crustal reworking this approach may be extended to exposed crustal sections that record evidence of in situ partial melting of the putative sources as well as granites that represent melts trapped during migration to higher crustal levels, to obtain a quantitative evaluation of the proportion of crustal reworking versus crustal growth in a convergent margin system.

In this study, we report the results of Hf–O isotope analyses of zircons from two generations of granite in the Fosdick migmatite–granite complex (hereafter Fosdick complex) of West Antarctica, which is located along the former active margin of Gondwana (e.g. Siddoway and Fanning 2009). The granites are hosted in the high-grade equivalents of a supracrustal sequence and an infracrustal calc-alkaline intrusive suite (Korhonen et al. 2010a,b) in the Ford Ranges of western Marie Byrd Land (Adams 1987; Weaver et al. 1991). The supracrustal sequence has been correlated with similar units in western New Zealand and the Lachlan Belt of eastern Australia (Gibson and Ireland 1996; Ireland et al. 1998; Pankhurst et al. 1998; Nebel-Jacobsen et al. 2011; Scott et al. 2009). The Hf–O isotope signatures of zircons from Devonian–Carboniferous granites in the Fosdick complex suggest that crustal reworking was the dominant process for production of granites in this segment of the former active margin of Gondwana at that time. However, an isotopically more juvenile source is required to explain the wider range of εHf values in zircons from the Cretaceous granites, and this source was particularly important as a component in the youngest granites emplaced in the detachment zone that was responsible for unroofing the Fosdick complex at c. 100 Ma.

Temporal variations in isotope characteristics may be attributable to different plate margin characteristics in the Devonian–Carboniferous compared with the Cretaceous and also to different stages in the strain evolution within the Cretaceous event. Although the Hf–O and Nd isotope characteristics of Fosdick complex granites are similar to the Permo-Triassic granites from the Antarctic Peninsula, they contrast with Hf–O and Nd isotope results from other localities along and across the former active margin of Gondwana, such as the Tasmanides of Australia (e.g. Kemp et al. 2009) and

the Western Province of New Zealand (Bolhar et al. 2008), suggesting significant margin-parallel and margin-perpendicular variations in both the amount and nature of crustal reworking versus crustal growth with time.

8.3 Geological Setting

Marie Byrd Land, West Antarctica, is situated along the former active margin of Gondwana (Fig. 8.1a, b; Ireland et al. 1998; Adams 2004; Tulloch et al. 2009). Pankhurst et al. (1998) divide Marie Byrd Land into an inboard Ross province and outboard Amundsen province that became amalgamated in the Lower Cretaceous (DiVenere et al. 1995). The Amundsen province records two episodes of calc-alkaline magmatism, from 450 to 420 Ma and at c. 275 Ma, respectively, that yield Nd model ages of 1000–1300 Ma (Pankhurst et al. 1998). The geology of the Ross province is dominated by the Lower Paleozoic Swanson Formation, an unmetamorphosed to low-metamorphic grade turbidite sequence that accumulated outboard of the Ross–Delamerian Orogen (Bradshaw et al. 1983; Adams 1986; Ireland et al. 1998; Adams 2004), and Devonian–Carboniferous intrusive calc-alkaline magmatic rocks (c. 375–355 Ma) designated as the Ford Granodiorite suite (Fig. 8.1c; Weaver et al. 1991; Pankhurst et al. 1998; Mukasa and Dalziel 2000). The high-grade metamorphosed equivalents of these rock units crop out in the Fosdick complex (Fig 1c, d; Siddoway et al., 2004). Additionally, there is evidence of a Proterozoic basement underlying the Ross province (Flowerdew et al. 2007; Adams and Griffin 2012).

The Swanson Formation has been correlated with the Greenland Group in New Zealand, the Lachlan Supergroup in Eastern Australia, and the Robertson Bay

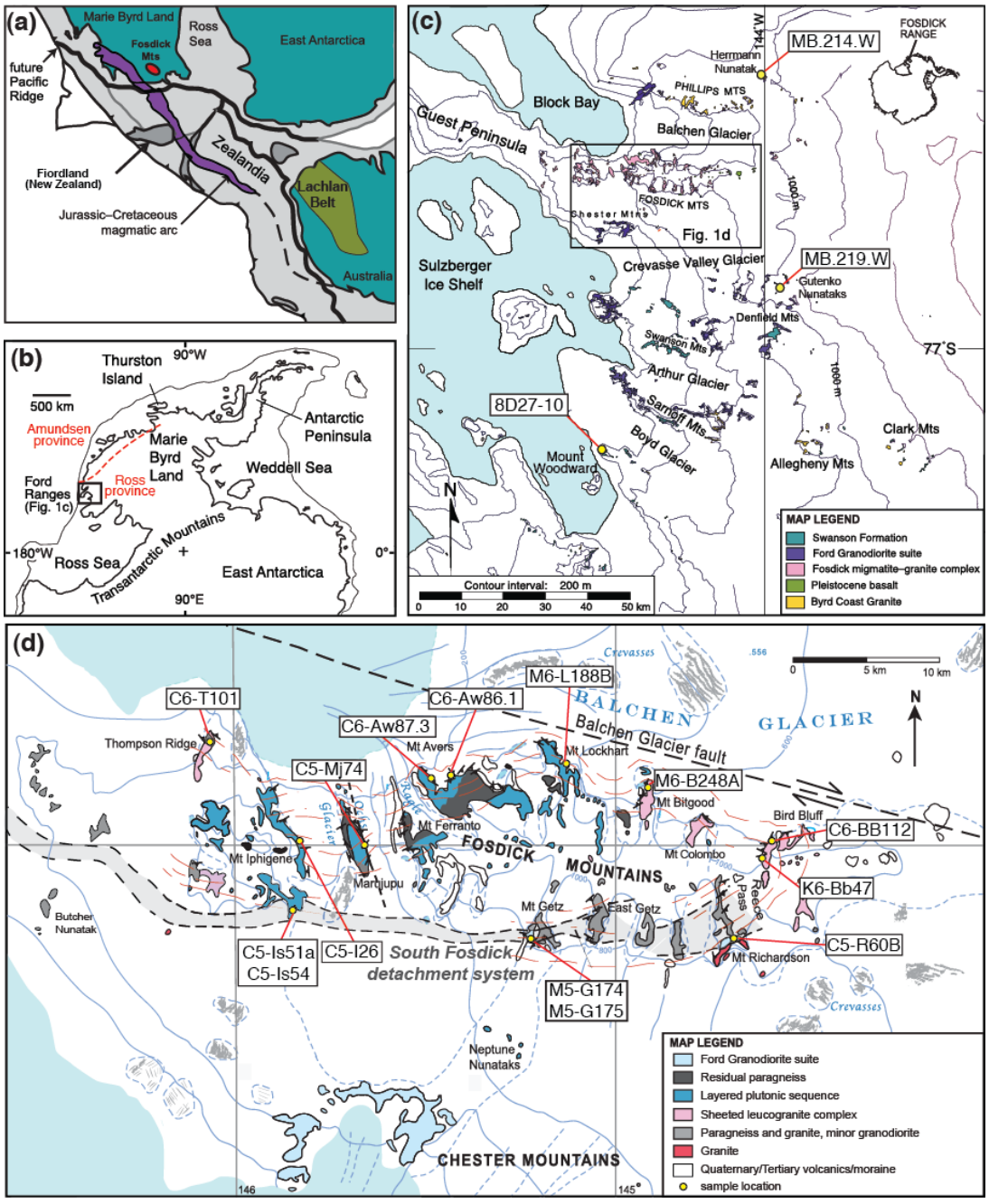

Fig. 8.1. To show the geological setting of the Fosdick migmatite–granite complex and a tectonic reconstruction of the eastern Gondwana margin. (a) Tectonic reconstruction of the East Gondwana margin at 95 Ma (modified from Tulloch et al. 2006). (b) West Antarctica and the location of the Ford Ranges. The inferred location of the boundary between the Ross and Amundsen provinces is from Mukasa and Dalziel (2000). (c) Geological map of the Ford Ranges (Siddoway 2008) with the locations for sample sites outside the Fosdick migmatite–granite complex. (d) Geological map of the Fosdick migmatite–granite complex (McFadden et al. 2010b). Samples used in this study are indicated in (c) and (d). Figures modified from Korhonen et al. (2010b).

Group in northern Victoria Land (Adams 1986, 2004; Ireland et al. 1998). The Ford Granodiorite suite is the manifestation, in Marie Byrd Land, of Devonian–Carboniferous calc-alkaline magmatism along the former active margin of Gondwana. Coeval suites along the margin include the Karamea Batholith in New Zealand (Muir et al. 1996; Tulloch et al. 2009), the Admiralty Intrusives in northern Victoria Land (Muir et al. 1996), and granites in the Melbourne terrane of the Lachlan Belt in Australia (Chappell et al. 1988; Tulloch et al. 2009). In Marie Byrd Land, both the Swanson Formation and the Ford Granodiorite suite are intruded by the Lower Cretaceous Byrd Coast Granite suite (Fig. 8.1c; Adams 1987; Siddoway 2008), which is the main plutonic phase emplaced during intracontinental extension that preceded breakup between Marie Byrd Land (Siddoway et al. 2004b, 2005; McFadden et al. 2010a) and Zealandia (Mortimer 2004).

Cretaceous oblique divergence and extreme lithospheric thinning preceding breakup of Gondwana in the Pacific sector has exposed a high-grade migmatite–granite complex in the Fosdick Mountains (McFadden et al. 2010a, b). Nd–Sr isotope geochemistry (Fig. 8.2) and U–Pb ages of paragneisses and orthogneisses exposed in the Fosdick complex suggest that these are the products of partial melting due to high-grade metamorphism of Swanson Formation and Ford Granodiorite suite protoliths, respectively (Siddoway et al. 2004a; Korhonen et al. 2010b, 2012; McFadden et al. 2010b). A comparison of zircon age spectra from the Swanson Formation, paragneisses in the Fosdick complex and the cores of inherited zircons in granites support this interpretation (Fig. 8.3).

Two episodes of high-grade metamorphism and partial melting in the Fosdick complex have been identified as follows: a Devonian–Carboniferous event at pressures of

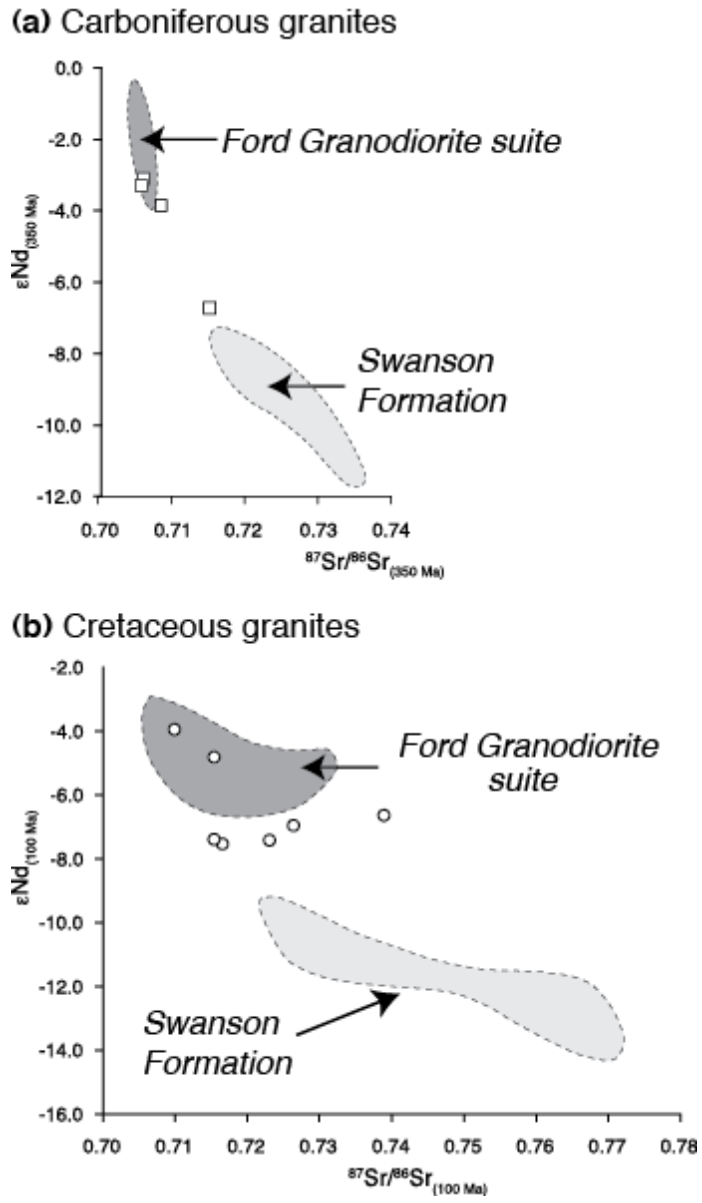

Fig. 8.2. Sr–Nd isotope results for granites from the Fosdick complex. Modified from Korhonen et al. (2010b). Devonian–Carboniferous (a) and Cretaceous (b) granites plot between fields defined by Swanson Formation and Ford Granodiorite suite samples.

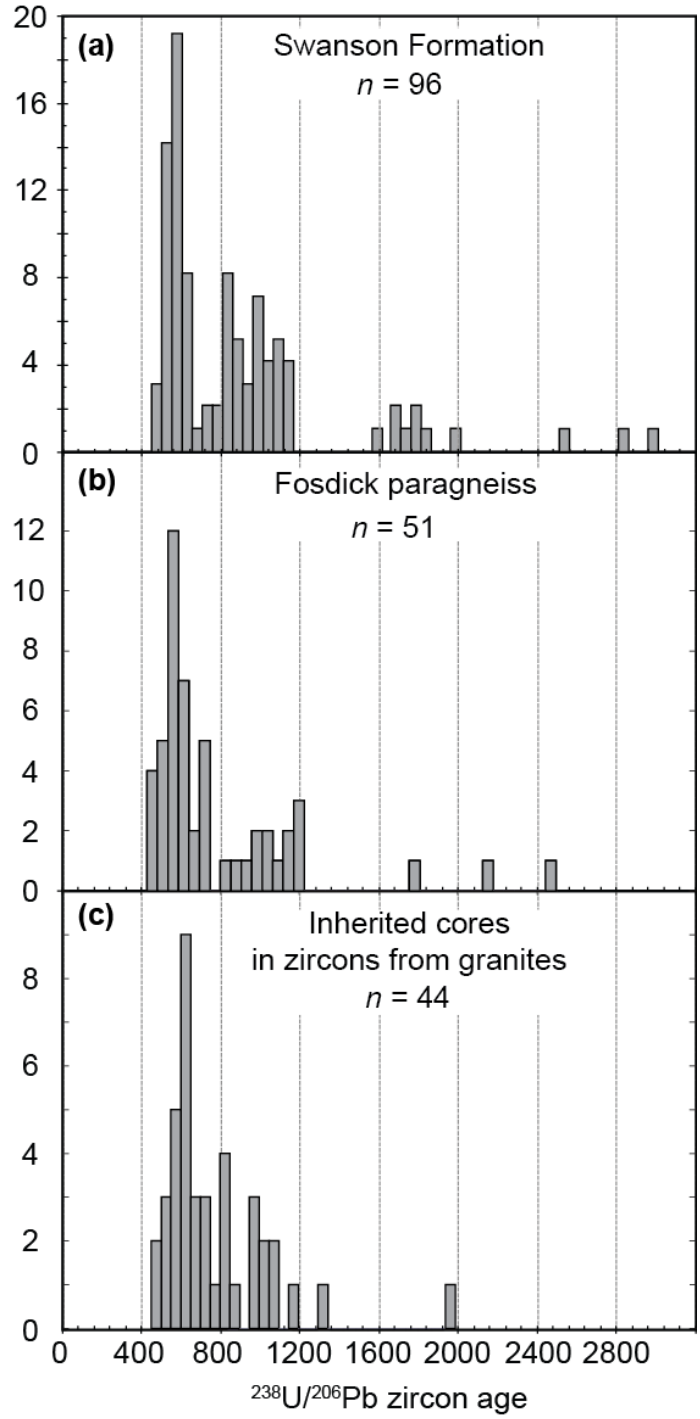

Fig. 8.3. Histograms of $^{206}Pb/^{238}U$ ages from: (a) detrital zircons from the Swanson Formation (Pankhurst et al. 1998); (b) zircon ages >400 Ma from paragneiss in the Fosdick migmatite–granite complex with (Siddoway et al. 2004a); (c) inherited cores of zircons ages >400 Ma from granites within the Fosdick migmatite–granite complex (Korhonen et al. 2010b; McFadden et al. 2010a, b; this study).

0.75–1.15 GPa and temperatures of ~870°C, and a Cretaceous event at pressures of 0.60–0.75 GPa and temperatures of 830–870°C (Korhonen et al. 2010a, 2012). Elevated temperatures and crustal melting in the Paleozoic are attributed to thickening of the continental margin during calc-alkaline arc magmatism represented by the Ford Granodiorite suite (Pankhurst et al. 1998; Siddoway and Fanning 2009), and in the Mesozoic are attributed to moderate thickening followed by lithosphere thinning during intracontinental extension across the West Antarctic rift system (Siddoway 2008). Coeval with Cretaceous rifting, mafic dykes of c. 113 Ma to c. 98 Ma age were intruded throughout the Fosdick complex (Saito et al. 2013).

Phase equilibria modelling of the protolith compositions indicates that the metamorphic pressures and temperatures were sufficient during both episodes to partially melt both the Ford Granodiorite suite and the Swanson Formation (Korhonen et al. 2010a). Devonian–Carboniferous granites within the Fosdick complex are found as m- to dm-scale layers within residual paragneiss exposed at Mt Avers and in the western Fosdick range, and m- to dm-scale laterally continuous sheets in the 'layered plutonic complex' (McFadden et al., 2010a) in the central to western Fosdick Mountains (Fig. 8.1d). Cretaceous granites occupy three distinct structural settings: (1) sub-vertical sheets concordant with foliation in host gneisses on the north side of the complex, emplaced during a Cretaceous wrench deformation phase along the Balchen Glacier fault (Fig. 8.1d); (2) sub-horizontal sheets concordant with layering in the host gneisses in the eastern and southern Fosdick Mountains that form a sheeted leucogranite complex (Fig. 8.1d) associated with the South Fosdick detachment zone; and, (3) discordant granites

emplaced late in the structural development of the South Fosdick detachment zone (Fig. 8.1d; McFadden et al. 2010a,b).

8.4 Sample descriptions

Fifteen samples comprising thirteen granites, one mafic gneiss, and one calcareous argillite (Table 8.1), for which U–Pb zircon ages were determined in this study or for which previously dated zircons were available, were selected for Lu–Hf and O isotope analysis at the Research School of Earth Sciences, Australian National University. In addition, zircon separates from two samples of the Ford Granodiorite suite from outside the Fosdick Mountains (MB.214.W and MB.219.W), collected by Pankhurst et al. (1998) and made available for this study, were analysed for Lu–Hf and O isotope compositions to provide an important baseline for the study of crustal differentiation in the Fosdick complex. The thirteen granites from the Fosdick complex selected for this study have been interpreted as the products of crustal melting either in the Devonian–Carboniferous or the Cretaceous (Siddoway and Fanning 2009; Korhonen et al. 2010b). Descriptions of the samples selected for Hf and O isotope analysis follow, with sample localities shown in Figure 8.1.

Exposures of Swanson Formation at Mount Woodward (for location: Fig. 8.1c) consist of greenschist grade red-brown argillite containing cm- to dm-scale layers and nodules of pale green calc-silicate rock. The calcareous argillite was sampled (8D27-10) to assess the detrital zircon population of the lower grade metasedimentary rocks.

The Devonian–Carboniferous calc-alkaline Ford Granodiorite suite comprises granodiorite to monzogranite that is metaluminous to weakly peraluminous in

Table 8.1. *Summary of rock types and U–Pb zircon ages for study samples.*

Sample	Location	$^{206}Pb/^{238}U$ age (Ma, 2σ)	Rock name	U–Pb age reported	Latitude	Longitude
MB.214.1W	Gutenko Nunataks	376.9 ± 5.7	Ford Granodiorite	Pankhurst *et al.* (1998)	*76.817°S*	*143.700°W*
MB.219.1W	Hermann Nunatak	372.5 ± 6.5	Ford Granodiorite	Pankhurst *et al.* (1998)	*76.233°S*	*143.900°W*
M5-G175	Mt Getz	369.2 ± 2.5	Biotite-granodiorite	Siddoway & Fanning (2009)	*76.553°S*	*145.220°W*
C5-I26	Mt Iphigene	364.4 ± 2.5	Cordierite-leucogranite	Siddoway & Fanning (2009)	*76.497°S*	*145.824°W*
C6-Aw86.1	Mt Avers, W	360.6 ± 3.6	Leucogranite	Siddoway & Fanning (2009)	*76.460°S*	*145.424°W*
C5-Is51a	Mt Iphigene, SE	353.4 ± 3.2	Monzogranite orthogneiss	Siddoway & Fanning (2009)	*76.527°S*	*145.810°W*
C5-Mj74	Marujupu Peak	*c.* 146–114	Mafic gneiss	this study	*76.518°S*	*145.646°W*
M6-L188B	Mt Lockhart, E	116.3 ± 1.0	garnet–cordierite granite	McFadden *et al.* (2010b)	*76.441°S*	*145.189°W*
M6-B248A	Mt Bitgood	114.8 ± 1.4	Two-mica granite	this study	*76.464°S*	*145.913°W*
C5-Is54	Mt Iphigene, SE	114.8 ± 1.0	Biotite-monzogranite	McFadden *et al.* (2010a)	*76.528°S*	*145.805°W*
K6-Bb47	Bird Bluff	104.7 ± 0.7	Cordierite-granite	Korhonen *et al.* (2010b)	*76.501°S*	*144.598°W*
C6-BB112	Bird Bluff	103.6 ± 0.7	Biotite-granite	McFadden *et al.* (2010b)	*76.500°S*	*144.580°W*
C5-R60B	Mt Richardson	102.4 ± 0.7	Leucogranite	McFadden *et al.* (2010a)	*76.548°S*	*144.687°W*
C6-T101	Thompson Ridge	101.7 ± 0.6	Cordierite-leucogranite	this study	*76.435°S*	*145.047°W*
C6-Aw87.3	Mt Avers W	101.6 ± 0.8	Biotite-granite	this study	*76.466°S*	*145.464°W*
M5-G174	Mt Getz	96.1 ± 1.4	Two-mica granite	McFadden *et al.* (2010a)	*76.553°S*	*145.220°W*
8D27-10	Ford Ranges	*c.* 1500–500	Calcareous argillite	this study	*77.291°S*	*145.473°W*

composition (Weaver et al. 1991). Sample MB.214.W is a hornblende–biotite–titanite granodiorite from Gutenko Nunataks (Fig. 8.1c) to the south of the Fosdick Mountains. Sample MB.219.W from Hermann Nunataks in the eastern Phillips Mountains (Fig. 8.1c) is a massive equigranular granodiorite that hosts mafic enclaves. For these two samples, Hf and O isotope analyses were obtained for the same zircon grains used for SHRIMP U–Pb age determinations reported in Pankhurst et al. (1998).

Four Devonian–Carboniferous granites from the Fosdick complex (Fig. 8.1d) were sampled as follows. Sample M5-G175 is a representative dark, medium-grained, equigranular biotite granodiorite, affected by only limited anatexis and subsequent solid-state deformation, that forms plutons at Mt Getz and Mt Richardson within host migmatitic orthogneisses and paragneisses (Siddoway and Fanning 2009). Sample C5-Is51A from Mt Iphigene is a migmatitic monzogranite orthogneiss with large Carlsbad-twinned feldspars that is a common metaplutonic rock type in the Fosdick complex. The gneissic foliation forms dm-scale folds. A second sample from Mt Iphigene, C5-I26, is a porphyritic cordierite leucogranite from an irregular narrow dyke that cuts across foliation and folds. A leucogranite, C6-Aw86-1, was collected from Mt Avers, a large massif in the central Fosdick complex that is made up of residual paragneiss and intermediate metaplutonic rocks. The sample is from a 2 m-thick concordant sill of white K-feldspar granite within residual paragneiss. The granite exhibits a weak foliation defined by sparse biotite.

For the Cretaceous, samples were selected to be representative of granites emplaced within three structural settings that developed successively during wrench to transtensive deformation (McFadden et al. 2010b) that led to detachment-controlled

exhumation of the Fosdick complex (McFadden et al. 2010a). The distribution of samples allows an evaluation of whether there were short-term tectonic controls on the source evolution of the Cretaceous granites.

Based on relative age relationships (McFadden et al. 2010b), three older granites from the wrench phase are: C5-Is54, a medium-grained K-feldspar–biotite monzogranite, forming a ~ 4 m-thick sill within migmatitic orthogneiss and paragneiss at SE Mt Iphigene; M6-L188B, a representative medium-grained garnet–cordierite–K-feldspar granite that forms sills and dykes within medium-grained biotite granodiorite at Mt Lockhart; and M6-B248A, a discordant two-mica granite emplaced as a steeply oriented dyke cutting paragneisses at Mt Bitgood (Fig. 8.1d).

Two samples, K6-Bb47 and C6-BB112 from Bird Bluff, which were emplaced during oblique motion on the South Fosdick detachment zone (Fig. 8.1d; McFadden et al. 2010a), are representative of granites forming the sheeted leucogranite complex. K6-Bb47 is a massive concordant to discordant, coarse-grained K-feldspar granite that contains cordierite (Korhonen et al. 2010b). C6-BB112 was sampled from a 20 m-thick dyke of unfoliated K-feldspar porphyritic granite containing biotite and smokey quartz.

Finally, four samples are representative of granites emplaced late in the structural development of the South Fosdick detachment zone. The granites cut host rock foliation but lack well-developed internal foliation. C6-T101 is a sample of grey quartz-rich leucogranite that contains nodular to dendritic cordierite, intruded into biotite–quartz–feldspar migmatitic gneisses at Thompson Ridge in the northwestern Fosdick Mountains. C6-Aw87.3 is K-feldspar–biotite granite collected from the margin of a sigmoidal-shaped granite body that intruded orthogneisses within the layered plutonic complex of Mt

Avers. Sample C5-R60B is a light grey, medium grained hypidiomorphic-granular K-feldspar leucogranite, collected within the South Fosdick detachment zone at Mt Richardson. The contacts of the leucogranite are both concordant and discordant to solid-state foliation in host gneisses, and the leucogranite lacks a foliation. The youngest sample, M5-G174 from Mt Getz, is one in an array of equigranular, medium-grained, two-mica granite dykes that crosscut the gneissic foliation (Fig. 8.1d). Discordant dikes of this generation exist throughout the central Fosdick complex from Ochs Glacier to Mts Getz and Bitgood (Fig. 8.1d).

A single mafic gneiss sample, C5-Mj74, is an apatite-rich garnet–biotite gneiss collected from Marujupu Peak within the layered plutonic complex of the central Fosdick Mountains (Fig. 8.1d). Garnets are spatially associated with coronae of leucocratic material that suggests a peritectic origin.

8.5 Methods

U–Pb zircon age determinations were made using SHRIMP II at the Research School of Earth Sciences, Australian National University (RSES-ANU) and SHRIMP IIe at Geoscience Australia, following the procedures described in Williams (1998 and references therein). Data were reduced using the SQUID Excel Macro of Ludwig (2001). The zircon U/Pb ratios have been normalized relative to a value of 0.0668 for the Temora reference zircon, equivalent to an age of 417 Ma (Black et al. 2003); analytical uncertainties for the respective analytical sessions are given in the footnotes to Table 8.2. Uncertainties reported in Table 8.2 for individual analyses (ratios and ages) are given at the 1σ level. Tera–Wasserburg concordia plots (Tera and Wasserburg 1972), probability

Table 8.2. Tabulation of SHRIMP U-Pb-Th zircon results.

C6-T101

Grain spot	U (ppm)	Th (ppm)	Th/U	$^{206}Pb^*$ (ppm)	$^{204}Pb/^{206}Pb$	f_{206} %	Total $^{238}U/^{206}Pb$	±	$^{207}Pb/^{206}Pb$	±	Radiogenic $^{206}Pb/^{238}U$	±	Age (Ma) $^{206}Pb/^{238}U$	±
1.1 c	176	83	0.470	2.4	-	0.70	62.32	0.87	0.0536	0.0019	0.0159	0.0002	101.9	1.4
2.1 c	642	161	0.251	84.0	0.000006	0.29	6.567	0.069	0.0718	0.0003	0.1518	0.0016	911	9
2.2 r	1868	17	0.009	61.3	0.000053	0.24	26.19	0.27	0.0529	0.0004	0.0381	0.0004	241.0	2.5
3.1 c	113	108	0.956	1.5	0.001969	0.79	64.10	1.01	0.0543	0.0019	0.0155	0.0002	99.0	1.6
4.1 c	257	265	1.033	3.5	0.000381	0.02	62.36	0.80	0.0482	0.0012	0.0160	0.0002	102.5	1.3
5.1 c	614	564	0.919	8.4	0.000377	0.22	62.89	0.71	0.0498	0.0008	0.0159	0.0002	101.5	1.1
6.1 c	232	122	0.527	3.2	0.000034	0.26	61.54	0.81	0.0501	0.0013	0.0162	0.0002	103.6	1.4
7.1 c	368	236	0.643	5.1	0.000051	0.03	61.46	0.75	0.0484	0.0010	0.0163	0.0002	104.0	1.3
7.2 r	740	35	0.047	10.2	0.000004	<0.01	62.58	0.70	0.0477	0.0007	0.0160	0.0002	102.2	1.1
8.1 c	113	104	0.919	1.5	0.000287	0.79	63.73	1.00	0.0543	0.0019	0.0156	0.0002	99.6	1.6
9.1 c	219	87	0.397	3.0	0.000278	0.20	62.82	0.84	0.0497	0.0013	0.0159	0.0002	101.6	1.4
10.1 c	137	67	0.487	1.8	0.000634	0.63	63.88	0.95	0.0530	0.0017	0.0156	0.0002	99.5	1.5
11.1 c	109	71	0.649	1.5	0.000519	0.76	62.71	1.00	0.0541	0.0020	0.0158	0.0003	101.2	1.6
11.2 r	924	4	0.004	12.4	-	<0.01	63.98	0.70	0.0477	0.0006	0.0156	0.0002	100.0	1.1
12.1 c	180	141	0.782	2.5	-	0.46	62.66	0.87	0.0517	0.0015	0.0159	0.0002	101.6	1.4
13.1 r	465	240	0.515	6.3	0.000131	0.07	63.04	0.74	0.0486	0.0013	0.0159	0.0002	101.4	1.2
14.1 c	233	111	0.476	11.9	0.000001	<0.01	16.79	0.19	0.0533	0.0007	0.0596	0.0007	373.4	4.2
14.2 r	1718	58	0.034	23.7	-	0.03	62.17	0.65	0.0483	0.0005	0.0161	0.0002	102.8	1.1
15.1 c	176	141	0.802	2.4	-	0.51	62.21	0.87	0.0521	0.0015	0.0160	0.0002	102.3	1.4
15.2 r	2365	5	0.002	32.3	0.000023	0.08	62.86	0.65	0.0487	0.0004	0.0159	0.0002	101.7	1.1
16.1 r	2361	5	0.002	32.3	0.000044	0.07	62.85	0.65	0.0486	0.0004	0.0159	0.0002	101.7	1.0
17.1 r	2458	5	0.002	33.5	0.000001	0.04	63.12	0.66	0.0484	0.0004	0.0158	0.0002	101.3	1.1
18.1 r	2171	6	0.003	29.8	-	<0.01	62.56	0.65	0.0479	0.0004	0.0160	0.0002	102.2	1.1
19.1 r	368	119	0.324	5.0	0.000394	0.16	62.89	0.76	0.0493	0.0010	0.0159	0.0002	101.5	1.2

Note: Error in Temora reference zircon calibration was 0.34% for the analytical session.

M6-B248A

Grain spot	U (ppm)	Th (ppm)	Th/U	$^{206}Pb^*$ (ppm)	$^{204}Pb/^{206}Pb$	f_{206} %	Total $^{238}U/^{206}Pb$	±	$^{207}Pb/^{206}Pb$	±	Radiogenic $^{206}Pb/^{238}U$	±	Age (Ma) $^{206}Pb/^{238}U$	±
1.1 r	1108	4	0.003	17.1	0.000183	0.14	55.76	0.62	0.0494	0.0007	0.0179	0.0002	114.4	1.3
1.2 c	276	54	0.197	80.4	0.000060	0.09	2.952	0.033	0.1167	0.0009	0.3384	0.0038	1879	18
2.1 c	369	147	0.399	18.5	0.000083	0.00	17.16	0.20	0.0539	0.0007	0.0583	0.0007	365.2	4.1
3.1 r	1620	8	0.005	28.2	0.000076	0.20	49.36	0.59	0.0502	0.0005	0.0202	0.0002	129.0	1.5
3.2 c	318	97	0.304	45.0	0.000009	0.02	6.062	0.067	0.0730	0.0005	0.1649	0.0018	984	10
4.1 r	3223	167	0.052	45.2	0.000018	0.07	61.32	0.64	0.0487	0.0009	0.0163	0.0002	104.2	1.1
4.2 c	689	180	0.262	34.1	0.000054	0.29	17.34	0.19	0.0561	0.0007	0.0575	0.0006	360.4	3.8
5.1 r	2711	4	0.002	41.0	0.000030	0.10	56.86	0.59	0.0491	0.0004	0.0176	0.0002	112.3	1.2
6.1 c	460	323	0.701	46.4	0.000006	0.01	8.526	0.093	0.0632	0.0005	0.1173	0.0013	715	7
7.1 r	2234	8	0.004	34.1	0.000032	0.00	56.33	0.59	0.0483	0.0005	0.0178	0.0002	113.4	1.2
8.1 r	543	74	0.136	7.3	0.000533	0.45	63.88	0.79	0.0516	0.0012	0.0156	0.0002	99.7	1.2
9.1 r	1565	5	0.003	24.3	0.000046	0.10	55.37	0.60	0.0491	0.0006	0.0180	0.0002	115.3	1.2
10.1 r	2083	6	0.003	29.3	0.000121	0.10	61.03	0.65	0.0489	0.0005	0.0164	0.0002	104.7	1.1
10.2 c	217	127	0.584	25.9	0.000012	0.02	7.211	0.087	0.0678	0.0007	0.1386	0.0017	837	9
11.1 r	1837	84	0.046	28.6	0.000120	0.09	55.09	0.59	0.0491	0.0006	0.0181	0.0002	115.8	1.2
12.1 c	116	85	0.732	1.6	-	0.96	63.60	1.19	0.0556	0.0043	0.0156	0.0003	99.6	1.9
13.1 r	373	53	0.142	5.0	0.000535	0.16	64.04	0.84	0.0493	0.0013	0.0156	0.0002	99.7	1.3
13.2 c	199	116	0.583	9.8	0.000092	0.16	17.40	0.22	0.0550	0.0010	0.0574	0.0007	359.6	4.4
14.1 c	139	156	1.125	2.2	0.001808	1.14	54.28	0.90	0.0574	0.0021	0.0182	0.0003	116.4	1.9
15.1 r	1653	25	0.015	26.4	0.000676	1.17	53.88	0.62	0.0577	0.0006	0.0183	0.0002	117.2	1.3
15.2 c	231	107	0.461	11.8	0.000011	0.03	16.84	0.20	0.0542	0.0011	0.0594	0.0007	371.8	4.5
16.1 r	2723	56	0.021	43.9	0.002316	4.38	53.30	0.56	0.0831	0.0013	0.0179	0.0002	114.6	1.2
17.1 c	576	131	0.228	9.0	-	0.18	55.08	0.66	0.0498	0.0010	0.0181	0.0002	115.8	1.4
18.1 r	667	199	0.298	33.2	0.000140	0.10	17.25	0.19	0.0546	0.0008	0.0579	0.0006	363.0	3.9
19.1 c	129	48	0.374	7.4	0.000226	0.40	14.93	0.20	0.0584	0.0012	0.0667	0.0009	416.4	5.5
20.1 c	1759	37	0.021	56.2	0.000092	2.94	26.88	0.28	0.0743	0.0005	0.0361	0.0004	228.6	2.4
21.1 r	1073	77	0.071	67.8	0.000486	1.03	13.60	0.18	0.0644	0.0005	0.0728	0.0010	452.8	5.9

Note: Error in Temora reference zircon calibration was 0.28% & 0.50% for the analytical sessions.

Table 8.2 continued. Tabulation of SHRIMP U-Pb-Th zircon results.

C6-Aw87.3

Grain spot	U (ppm)	Th (ppm)	Th/U	$^{206}Pb^*$ (ppm)	$^{204}Pb/^{206}Pb$	f_{206} %	Total $^{238}U/^{206}Pb$	±	$^{207}Pb/^{206}Pb$	±	Radiogenic $^{206}Pb/^{238}U$	±	Age (Ma) $^{206}Pb/^{238}U$	±
1.1 r	672	62	0.093	9.1	0.000146	0.10	63.60	0.71	0.0488	0.0007	0.0157	0.0002	100.5	1.1
2.1 c	497	210	0.424	23.8	0.000013	0.11	17.89	0.19	0.0544	0.0007	0.0558	0.0006	350.3	3.7
2.2 r	771	66	0.086	10.7	0.000047	<0.01	61.97	0.68	0.0479	0.0007	0.0161	0.0002	103.2	1.1
3.1 c	359	103	0.287	15.3	-	0.06	20.18	0.29	0.0531	0.0006	0.0495	0.0007	311.6	4.4
3.2 r	1769	17	0.010	30.2	0.000053	0.09	50.23	0.57	0.0493	0.0004	0.0199	0.0002	127.0	1.4
4.1 r	607	46	0.076	8.4	0.000031	0.14	62.35	0.71	0.0492	0.0008	0.0160	0.0002	102.4	1.2
5.1 c	553	46	0.082	7.5	0.000100	0.20	63.40	0.72	0.0496	0.0008	0.0157	0.0002	100.7	1.1
6.1 r	718	66	0.091	9.7	-	0.18	63.68	0.71	0.0494	0.0007	0.0157	0.0002	100.3	1.1
7.1 r	651	48	0.074	8.8	0.000044	0.06	63.66	0.71	0.0485	0.0007	0.0157	0.0002	100.4	1.1
8.1 r	762	71	0.093	10.5	-	<0.01	62.03	0.69	0.0472	0.0007	0.0161	0.0002	103.2	1.1
9.1 r	2774	6	0.002	110.4	0.000017	0.03	21.59	0.23	0.0524	0.0002	0.0463	0.0005	291.8	3.0
10.1 c	683	61	0.089	9.2	0.000029	0.15	63.58	0.71	0.0492	0.0007	0.0157	0.0002	100.5	1.1
11.1 r	611	48	0.078	8.2	0.000165	0.21	63.98	0.72	0.0497	0.0008	0.0156	0.0002	99.8	1.1
12.1 r	675	62	0.092	9.1	0.000087	<0.01	63.71	0.71	0.0479	0.0009	0.0157	0.0002	100.4	1.1
13.1 c	917	69	0.075	12.6	-	0.05	62.32	0.68	0.0485	0.0006	0.0160	0.0002	102.6	1.1
14.1 r	2971	5	0.002	143.0	0.000008	<0.01	17.85	0.18	0.0534	0.0003	0.0560	0.0006	351.5	3.6
15.1 r	810	77	0.094	11.1	0.000150	0.12	62.90	0.69	0.0490	0.0007	0.0159	0.0002	101.6	1.1
16.1 r	2434	7	0.003	112.0	0.000015	0.02	18.66	0.21	0.0533	0.0002	0.0536	0.0006	336.4	3.6
17.1 r	1280	11	0.009	20.4	0.000113	0.12	53.76	0.57	0.0494	0.0005	0.0186	0.0002	118.7	1.2
18.1 c	903	69	0.076	12.4	0.000083	<0.01	62.75	0.68	0.0479	0.0006	0.0159	0.0002	101.9	1.1
19.1 c	309	179	0.579	4.1	0.000188	0.12	64.78	0.80	0.0489	0.0011	0.0154	0.0002	98.6	1.2
20.1 r	2898	348	0.120	148.8	0.000004	<0.01	16.73	0.17	0.0541	0.0002	0.0598	0.0006	374.3	3.7
21.1 c	314	123	0.392	13.7	0.000031	<0.01	19.63	0.22	0.0525	0.0006	0.0509	0.0006	320.3	3.6

Note: Error in Temora reference zircon calibration was 0.34% for the analytical session.

K6-Bb47

Grain spot	U (ppm)	Th (ppm)	Th/U	$^{206}Pb^*$ (ppm)	$^{204}Pb/^{206}Pb$	f_{206} %	Total $^{238}U/^{206}Pb$	±	$^{207}Pb/^{206}Pb$	±	Radiogenic $^{206}Pb/^{238}U$	±	Age (Ma) $^{206}Pb/^{238}U$	±
1.1 r	1430	12	0.008	23.6	0.003051	5.59	52.00	0.56	0.0928	0.0010	0.0182	0.0002	116.0	1.3
2.1 r	3790	11	0.003	53.3	0.000041	0.08	61.05	0.63	0.0488	0.0004	0.0164	0.0002	104.6	1.1
3.1 r	2104	10	0.005	29.4	-	0.13	61.54	0.65	0.0491	0.0005	0.0162	0.0002	103.8	1.1
3.2 c	1557	354	0.227	124.7	0.000117	0.26	10.73	0.11	0.0612	0.0003	0.0930	0.0010	573.2	5.8
4.1 r	1483	17	0.011	21.0	0.000160	0.11	60.64	0.66	0.0490	0.0006	0.0165	0.0002	105.3	1.1
5.1 c	815	542	0.665	58.5	0.000009	0.01	11.97	0.13	0.0578	0.0004	0.0835	0.0009	517.1	5.3
6.1 r	3042	6	0.002	43.0	0.000089	0.20	60.74	0.64	0.0497	0.0004	0.0164	0.0002	105.1	1.1
7.1 r	1805	10	0.005	24.4	0.000044	0.20	63.49	0.68	0.0496	0.0006	0.0157	0.0002	100.5	1.1
8.1 r	1793	9	0.005	24.4	0.000049	0.10	63.22	0.74	0.0488	0.0006	0.0158	0.0002	101.1	1.2
9.1 r	1511	11	0.008	20.8	-	0.25	62.33	0.67	0.0500	0.0006	0.0160	0.0002	102.4	1.1
9.2 c	1227	15	0.012	16.9	0.000269	0.14	62.33	0.69	0.0492	0.0007	0.0160	0.0002	102.4	1.1
10.1 r	1240	12	0.010	17.7	0.000318	0.01	60.21	0.66	0.0482	0.0006	0.0166	0.0002	106.2	1.2
11.1 r	928	11	0.012	12.9	-	0.09	61.70	0.70	0.0488	0.0008	0.0162	0.0002	103.5	1.2
12.1 r	1014	5	0.005	13.9	0.000215	0.14	62.87	0.71	0.0491	0.0008	0.0159	0.0002	101.6	1.1
13.1 r	2340	9	0.004	32.1	-	0.08	62.69	0.66	0.0487	0.0005	0.0159	0.0002	101.9	1.1
14.1 r	1383	16	0.012	19.4	0.000064	0.05	61.26	0.74	0.0485	0.0006	0.0163	0.0002	104.3	1.3
15.1 r	1420	10	0.007	20.0	0.000145	0.14	61.14	0.68	0.0492	0.0006	0.0163	0.0002	104.4	1.2
16.1 r	1597	9	0.006	22.8	-	0.13	60.11	0.66	0.0492	0.0006	0.0166	0.0002	106.2	1.2
17.1 r	1264	13	0.010	17.7	0.000095	<0.01	61.31	0.67	0.0479	0.0007	0.0163	0.0002	104.3	1.1
18.1 r	1594	9	0.005	22.3	0.000165	0.05	61.40	0.66	0.0485	0.0006	0.0163	0.0002	104.1	1.1
19.1 r	1660	5	0.003	22.0	0.000191	0.18	64.90	0.70	0.0494	0.0006	0.0154	0.0002	98.4	1.1
19.2 c	620	36	0.058	40.1	0.000087	0.52	13.28	0.14	0.0605	0.0006	0.0749	0.0008	465.5	5.0
20.1 r	1379	9	0.007	18.8	-	0.05	63.11	0.69	0.0484	0.0006	0.0158	0.0002	101.3	1.1

Note: Error in Temora reference zircon calibration was 0.28% for the analytical session.

Table 8.2 continued. Tabulation of SHRIMP U-Pb-Th zircon results.

C6-Mj74

Grain spot	U (ppm)	Th (ppm)	Th/U	$^{206}Pb^*$ (ppm)	$^{204}Pb/^{206}Pb$	f_{206} %	$^{238}U/^{206}Pb$	Total $^{207}Pb/^{206}Pb$	±	Radiogenic $^{206}Pb/^{238}U$	±	Age (Ma) $^{206}Pb/^{238}U$	±
1.1 c	1405	86	0.06	23.1	0.000049	0.20	52.352	0.582	0.0500	0.0004	0.0191	0.0002	121.7	1.3
2.1 r	2467	1948	0.79	47.4	0.000016	0.08	44.721	0.467	0.0496	0.0003	0.0223	0.0002	142.4	1.5
3.1 c	1237	66	0.05	19.1	0.000029	0.09	55.762	0.591	0.0491	0.0004	0.0179	0.0002	114.5	1.2
4.1 c	1763	368	0.21	31.0	0.000021	0.02	48.839	0.516	0.0488	0.0004	0.0205	0.0002	130.6	1.4
5.1 c	462	55	0.12	8.6	-	0.14	45.945	0.511	0.0500	0.0007	0.0217	0.0002	138.6	1.5
6.1 r	1430	982	0.69	22.3	0.000311	0.85	55.014	0.584	0.0550	0.0004	0.0180	0.0002	115.2	1.2
7.1 c	1039	2921	2.81	17.2	0.000353	0.97	51.845	0.594	0.0561	0.0009	0.0191	0.0002	122.0	1.4
8.1 r	1753	671	0.38	28.4	0.000079	0.22	53.079	0.556	0.0502	0.0004	0.0188	0.0002	120.1	1.3
8.2 c	2052	6752	3.29	33.3	0.000847	1.73	52.974	0.552	0.0621	0.0004	0.0186	0.0002	118.5	1.2
9.1 c	1603	1171	0.73	30.1	0.000014	0.19	45.780	0.483	0.0503	0.0004	0.0218	0.0002	139.0	1.5
10.1 r	816	758	0.93	15.1	0.000062	0.31	46.412	0.496	0.0513	0.0005	0.0215	0.0002	137.0	1.5
11.1 r	766	9	0.01	67.8	-	0.11	9.710	0.126	0.0617	0.0004	0.1029	0.0014	631.2	8.0
12.1 r	667	114	0.17	13.1	0.000279	0.37	43.623	0.471	0.0519	0.0006	0.0228	0.0002	145.6	1.6
13.1 r	1127	1679	1.49	22.2	0.000065	0.11	43.605	0.496	0.0498	0.0004	0.0229	0.0003	146.0	1.7
14.1 c	572	200	0.35	10.3	0.000226	0.30	47.680	0.543	0.0511	0.0006	0.0209	0.0002	133.4	1.5
15.1 r	623	444	0.71	12.0	0.000107	0.21	44.575	0.484	0.0506	0.0006	0.0224	0.0002	142.7	1.5
16.1 c	233	148	0.63	4.3	0.000366	0.25	46.223	0.569	0.0508	0.0014	0.0216	0.0003	137.6	1.7
17.1 c	229	184	0.81	22.0	0.000072	<0.01	8.926	0.128	0.0621	0.0020	0.1121	0.0017	684.7	9.7
17.2 r	1527	341	0.22	103.6	-	0.16	12.672	0.131	0.0582	0.0003	0.0788	0.0008	488.9	4.9
18.1 c	744	355	0.48	14.5	0.000040	0.01	44.021	0.487	0.0490	0.0006	0.0227	0.0003	144.8	1.6
19.1 r	985	48	0.05	44.0	0.000062	0.13	19.231	0.206	0.0540	0.0006	0.0519	0.0006	326.4	3.4
19.2 c	530	5	0.01	65.6	0.000030	0.49	6.939	0.075	0.0719	0.0006	0.1434	0.0016	863.8	9.1
20.1 c	139	65	0.47	2.7	0.000101	0.17	44.632	0.626	0.0503	0.0015	0.0224	0.0003	142.6	2.0
21.1 r	447	6	0.01	8.3	0.000267	0.13	46.261	0.537	0.0498	0.0008	0.0216	0.0003	137.7	1.6
22.1 r	378	207	0.55	7.2	0.000191	0.33	45.311	0.536	0.0514	0.0009	0.0220	0.0003	140.3	1.7
23.1 /	501	85	0.17	8.9	0.000047	0.46	48.459	0.571	0.0523	0.0008	0.0205	0.0002	131.1	1.5
24.1 /	657	26	0.04	12.5	0.000359	1.13	45.184	0.643	0.0578	0.0007	0.0219	0.0003	139.5	2.0

Note: Error in Temora reference zircon calibration was 0.29% for the analytical session.

Notes pertaining to all analyses:

1. Uncertainties given at the one σ level.
2. Error in Temora reference zircon calibration not included in above errors but required when comparing data from different mounts.
3. f_{206} % denotes the percentage of ^{206}Pb that is common Pb.
4. Correction for common Pb for the U/Pb data has been made using the measured $^{238}U/^{206}Pb$ and $^{207}Pb/^{206}Pb$ ratios following Tera and Wasserburg (1972) as outlined in Williams (1998).

8D27-10

Grain. spot	U (ppm)	Th (ppm)	Th/U	$^{206}Pb^*$ (ppm)	$^{204}Pb/^{206}Pb$	f_{206} %	$^{238}U/^{206}Pb$	Total $^{207}Pb/^{206}Pb$	±	Radiogenic $^{206}Pb/^{238}U$	±	Age (Ma) $^{206}Pb/^{238}U$	±
1.1	330	143	0.43	27	0.000065	0.01	10.674	0.117	0.0593	0.0005	0.0937	0.0011	577	6
2.1	304	134	0.44	95	0.000028	0.04	2.740	0.030	0.1228	0.0007	0.3652	0.0042	2007	20
3.1	40	26	0.64	4	0.000675	0.22	8.944	0.145	0.0640	0.0016	0.1116	0.0019	682	11
4.1	98	63	0.64	8	0.000139	0.26	10.309	0.136	0.0619	0.0010	0.0968	0.0013	595	8
5.1	112	65	0.58	9	0.000190	0.14	10.546	0.135	0.0606	0.0009	0.0947	0.0012	583	7
6.1	75	17	0.23	9	-	<0.01	6.877	0.092	0.0726	0.0010	0.1455	0.0019	875	11
7.1	158	146	0.93	45	0.000003	0.01	3.037	0.034	0.1152	0.0006	0.3293	0.0037	1835	18
8.1	116	30	0.26	10	-	<0.01	9.521	0.119	0.0608	0.0009	0.1051	0.0013	644	8
9.1	232	207	0.89	35	0.000058	0.10	5.657	0.063	0.0735	0.0005	0.1766	0.0020	1048	11
10.1	516	296	0.57	82	0.000015	0.03	5.422	0.057	0.0758	0.0004	0.1844	0.0019	1091	11
11.1	285	73	0.26	32	0.000076	0.63	7.680	0.155	0.0705	0.0019	0.1294	0.0027	784	15
12.1	180	75	0.42	30	0.000035	0.06	5.120	0.061	0.0824	0.0022	0.1952	0.0023	1150	13
13.1	531	178	0.34	75	0.000009	0.01	6.107	0.065	0.0732	0.0003	0.1637	0.0017	977	10
14.1	583	354	0.61	40	-	0.07	12.602	0.133	0.0575	0.0004	0.0793	0.0009	492	5
15.1	278	69	0.25	39	0.000123	0.21	6.175	0.068	0.0722	0.0006	0.1616	0.0018	966	10
16.1	624	68	0.11	68	-	<0.01	7.833	0.116	0.0623	0.0021	0.1281	0.0020	777	11
17.1	386	106	0.27	55	0.000019	0.03	6.003	0.064	0.0738	0.0004	0.1665	0.0018	993	10
18.1	327	87	0.26	51	0.000033	0.06	5.494	0.059	0.0751	0.0004	0.1819	0.0020	1078	11
19.1	97	38	0.39	8	0.000094	0.18	9.830	0.134	0.0620	0.0010	0.1015	0.0014	623	8
20.1	633	3	0.00	48	0.000023	0.09	11.334	0.119	0.0591	0.0005	0.0881	0.0009	545	6
21.1	119	77	0.64	10	0.000288	0.18	10.275	0.128	0.0613	0.0009	0.0972	0.0012	598	7
22.1	77	16	0.21	6	-	0.14	10.364	0.141	0.0608	0.0011	0.0964	0.0013	593	8
23.1	113	60	0.53	12	0.000026	0.49	8.358	0.109	0.0676	0.0008	0.1191	0.0016	725	9
24.1	208	76	0.36	16	0.000146	0.07	11.164	0.128	0.0591	0.0007	0.0895	0.0010	553	6
25.1	391	55	0.14	31	-	0.04	10.941	0.118	0.0592	0.0005	0.0914	0.0010	564	6

Note: Error in Temora reference zircon calibration was 0.34%for the analytical session.

1. Uncertainties given at the one σ level.
2. Error in Temora reference zircon calibration not included in above errors but required when comparing data from different mounts.
3. f_{206} % denotes the percentage of ^{206}Pb that is common Pb.
4. For areas older than ~800 Ma correction for common Pb made using the measured $^{204}Pb/^{206}Pb$ ratio.
5. For areas younger than ~800 Ma correction for common Pb made using the measured $^{238}U/^{206}Pb$ and $^{207}Pb/^{206}Pb$ ratios following Tera and Wasserburg (1972) as outlined in Williams (1998).

density plots with stacked histograms, and weighted mean $^{206}Pb/^{238}U$ ages were calculated using ISOPLOT/EX (Ludwig 2003). Where appropriate the "Mixture Modelling" algorithm of Sambridge and Compston (1994) via ISOPLOT/EX has been used to un-mix statistical age populations or groups. From such groupings weighted mean $^{206}Pb/^{238}U$ ages have been calculated and the uncertainties reported as 95% confidence limits, including incorporation, in quadrature, of the uncertainty in the reference zircon calibration.

Following the U–Pb analyses, the SHRIMP 1–2 μm deep and approximately 20 μm in diameter U–Pb pits were lightly polished away and oxygen isotope analyses made in exactly the same location using SHRIMP II fitted with a Cs ion source and electron gun for charge compensation as described by Ickert et al. (2008). Oxygen isotope ratios were determined in multiple collector mode using an axial continuous electron multiplier (CEM) triplet collector, and two floating heads with interchangeable CEM–Faraday Cups. The Temora 2, Temora 3 (unpublished RSES-ANU internal reference standard) and FC1 reference zircons were analysed to monitor and correct for isotope fractionation. The measured $^{18}O/^{16}O$ ratios and calculated $\delta^{18}O$ values have been normalised relative to an FC1 weighted mean $\delta^{18}O$ value of +5.4 ‰ (Ickert et al. 2008). Reproducibility in the Duluth Gabbro FC1 reference zircon $\delta^{18}O$ value varied between analytical sessions, with most of the reference zircon analytical uncertainties in the range 0.32–0.41‰ (±2σ). As a secondary reference, the Temora 2 or Temora 3 zircons were analysed in the same sessions, which gave $\delta^{18}O$ values of +8.2‰ and +7.59‰, respectively, in agreement with data reported by Ickert et al. (2008) for Temora 2 and unpublished data for Temora 3.

Lu–Hf isotope measurements were conducted by laser ablation multicollector inductively coupled plasma mass spectroscopy (LA–MC–ICPMS) using the RSES Neptune MC–ICPMS coupled with a HelEx 193 nm ArF Excimer laser, following procedures similar to those described in Munizaga et al. (2008). For all analyses of unknowns or secondary standards, the laser spot size was ~47 μm in diameter. Laser ablation analyses targeted the same locations within single zircon grains used for both the U–Pb and oxygen isotope analyses described above. The mass spectrometer was first tuned to optimal sensitivity using a large grain of zircon from the Mud Tank carbonatite. Isotopic masses were measured simultaneously in static-collection mode. A gas blank was acquired at regular intervals throughout the analytical session (every 12 analyses). Typically the laser was fired with a 5–8 Hz repetition rate and 50–60 mJ energy. Data were acquired for 100 seconds, but in many cases only a selected interval from the total acquisition was used in data reduction.

Throughout the analytical session several widely used reference zircons (91500, FC-1, Mud Tank and Temora 2 or 3) were analysed to monitor data quality and reproducibility. Signal intensity for unknowns was typically ~5–6 V for total Hf at the beginning of ablation, and decreased over the acquisition time to 2 V or less. Isobaric interferences of ^{176}Lu and ^{176}Yb on the ^{176}Hf signal were corrected by monitoring signal intensities of ^{175}Lu and ^{173}Yb, ^{172}Yb and ^{171}Yb. The calculation of signal intensity for ^{176}Hf also involved independent mass bias corrections for Lu and Yb (see Munizaga et al. 2008 for further details). During the course of this data collection the reference zircons gave the following weighted mean ^{176}Hf/^{177}Hf ratios: 91500 = 0.282306 ± 6 (±2σ) for 23 of 25 analyses, Mud Tank = 0.282512 ± 4 for 27 of 28 analyses, FC-1 = 0.282185 ± 5 for

39 of 41 analyses, and Temora 2 = 0.282680 ± 7, for 16 Temora 2 grains analysed. These are within analytical uncertainty of the values reported by Woodhead and Hergt (2005).

8.6 Results of SHRIMP U–Pb analyses

New SHRIMP zircon U–Pb data for four granite samples (C6-T101, C6-Aw87.3, M6-B248A, and K6-Bb47), one mafic gneiss sample (C5-Mj74), and the calcareous argillite (8D27-10) were determined as part of this study. The results are plotted on Tera–Wasserberg concordia diagrams and as probability density plots (with stacked histograms) in Figure 8.5; the U–Pb isotope data are provided in Table 8.2. Populations of zircon were defined on the basis of morphological and cathodoluminescence (CL) characteristics (Fig. 8.4), the details of which are discussed for each new sample below.

SHRIMP U–Pb zircon data were previously published for eight of the granites included in this study (Table 8.1). Table 8.1 summarizes the U–Pb zircon ages, sample locations and rock types for all samples. Examination of the Hf and O isotope characteristics of the full suite of granite samples (Table 8.3; Figs G.1 and G.2 in Appendix G) will allow an assessment of the degree of crustal reworking versus crustal growth for the two episodes of granitic magmatism as well as any trends that may be linked to stages in the tectonic evolution.

8.6.1 M6-B248A (two-mica granite)

The heterogeneous zircon population from this sample can be subdivided into two morphological types: a) relatively coarse prismatic moderately zoned grains of moderate

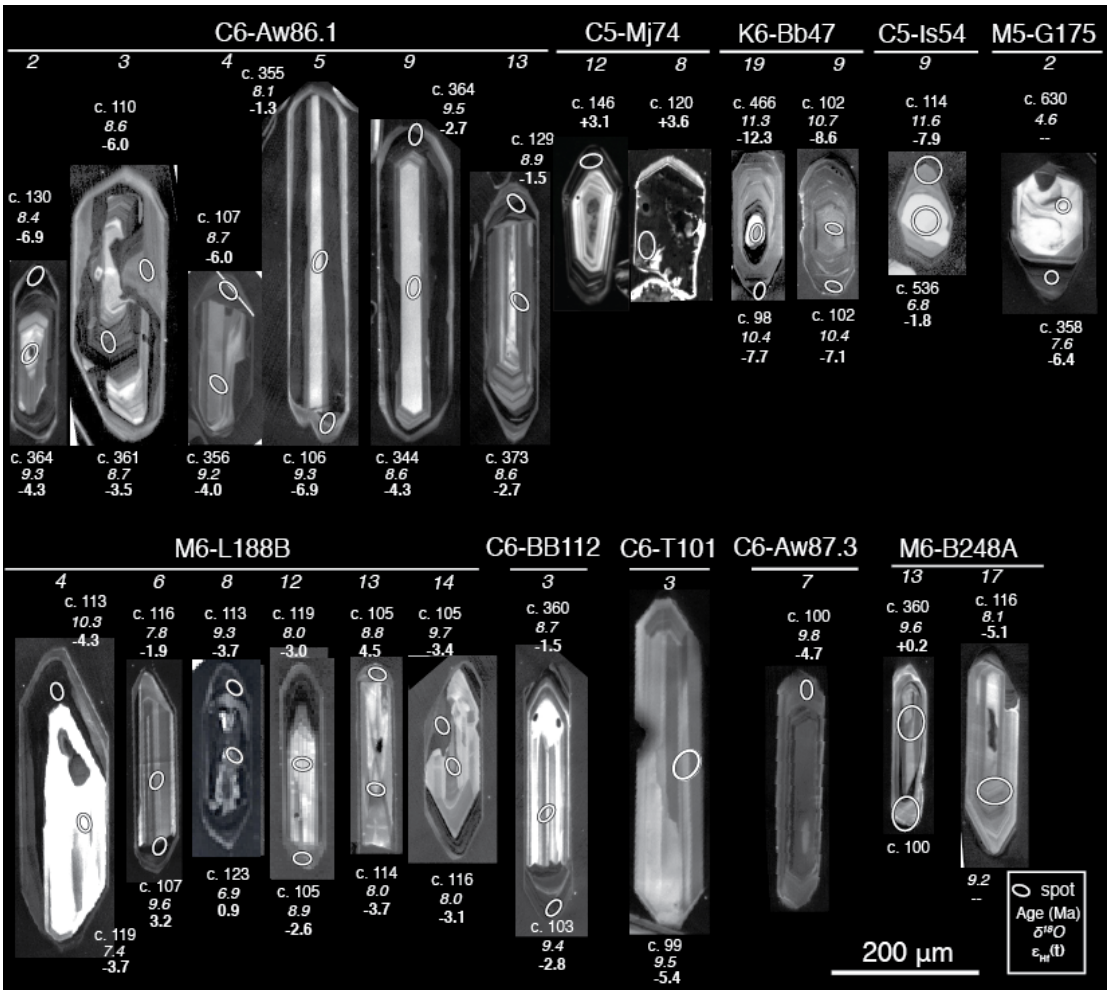

Fig. 8.4. Cathodoluminescence images of representative zircon grains from granites in the Fosdick complex dated in this study. Ellipses mark the location of U–Pb, O and Hf spot analyses. CL images were collected on different dates and so exhibit some variation in quality/sharpness. The contrast of images of individual zircons was adjusted to best display internal zoning. Most zircons display core–rim variability in Hf and O isotopes (Figs E.1 and E.2 in Appendix E). External reproducibility for Hf isotope measurements is ± 2 ε units.

Fig. 8.5. U–Pb concordia and probability density plots of zircon data from samples C5-Mj74 (a, b), M6-B248A (c, d), C6-Aw87.3 (e, f), K6-Bb47 (g, h), C6-T101 (i, j), and 8D27-10 (k, l). Data-point error ellipses are at 68.3% confidence.

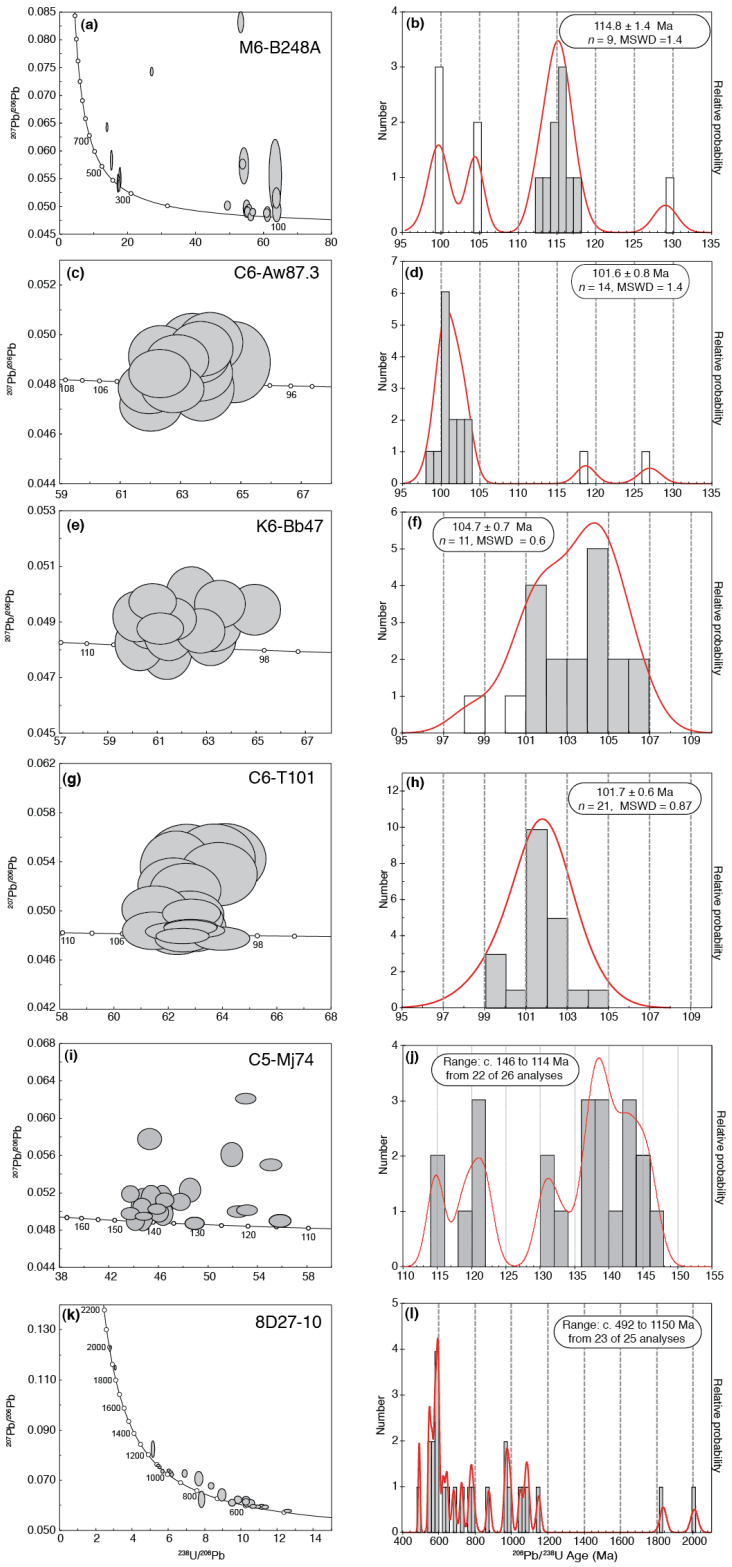
(a)
M6-B248A
(b)
114.8 ± 1.4 Ma
n = 9, MSWD =1.4
(c)
C6-Aw87.3
(d)
101.6 ± 0.8 Ma
n = 14, MSWD = 1.4
(e)
K6-Bb47
(f)
104.7 ± 0.7 Ma
n = 11, MSWD = 0.6
(g)
C6-T101
(h)
101.7 ± 0.6 Ma
n = 21, MSWD = 0.87
(i)
C5-Mj74
(j)
Range: c. 146 to 114 Ma
from 22 of 26 analyses
(k)
8D27-10
(l)
Range: c. 492 to 1150 Ma
from 23 of 25 analyses
Number
Relative probability
$^{238}U/^{206}Pb$
$^{207}Pb/^{206}Pb$
$^{206}Pb/^{238}U$ Age (Ma)

brightness in CL, and b) sub-equant small grains with nonsymmetrical oscillatory growth zones upon rounded inherited cores (Fig. 8.4). Truncation of sector and oscillatory zoning in the central areas against overgrowths indicates that these areas are inherited zircon components, consistent with $^{206}Pb/^{238}U$ ages of ≥ 360 Ma for such areas. The majority of the rim areas analysed are notable in that the Th/U ratios are ≤ 0.10, typical for metamorphic zircon, or zircon formed due to anatexis (i.e. enriched in U, so the apparent low Th/U is due to U enrichment rather than Th depletion as is common in high grade metamorphic zircon; Hoskin and Schaltegger 2003). A weighted mean $^{206}Pb/^{238}U$ age calculated from 9 low Th/U rim analyses is 114.8 ± 1.4 Ma (MSWD = 1.4; Fig. 8.5a, b) and is interpreted as the crystallization age of the granite.

8.6.2 C6-Aw87.3 (biotite-granite)

Zircons from this sample are large prismatic, moderately zoned grains with round terminations (Fig. 8.4). The grains are dark under CL, with indications that the central dark CL areas have zonation truncated. Six of the areas analysed yield Devonian to Carboniferous ages (Table 8.2). A weighted mean $^{206}Pb/^{238}U$ age calculated from 14 of 16 analyses of Cretaceous age, both rims and core areas, gives 101.6 ± 0.8 Ma (MSWD = 1.4; Fig. 8.5c, d) and is interpreted as the crystallization age of the granite. It is noteworthy that the majority of Cretaceous areas analysed have Th/U ratios <0.10, arising more from an enrichment in U (~600–900 ppm) rather than a depletion in Th (~50–60 ppm).

8.6.3 K6-Bb47 (cordierite-granite)

The dominant zircon population consists of prismatic blocky grains that are moderately dark under CL imaging, with few, wide oscillatory zones, with or without inherited cores (Fig. 8.4). Inherited central areas, if present, are unzoned and three analysed yield ages ranging from c. 465 to c. 575 Ma (Table 8.2; not shown on Fig. 8.5). Zircon areas that yield Cretaceous ages form two distinct $^{206}Pb/^{238}U$ age groupings, one at 104.7 ± 0.7 Ma (n = 11, MSWD = 0.6), which is interpreted as the crystallization age of the granite, and 101.6 ± 0.9 (n = 7, MSWD = 0.4; Fig. 8.5e, f). All these Cretaceous zircon analyses have Th/U ratios ≤ 0.12, corresponding to the highest U and lowest Th values of the four granite samples.

8.6.4 C6-T101 (cordierite-leucogranite)

Acicular prismatic zircon grains with oscillatory zoning are the dominant morphology in this sample (Fig. 8.4). A weighted mean $^{206}Pb/^{238}U$ age of 101.7 ± 0.6 Ma (n = 21, MSWD = 0.87) for analyses of grain central areas is considered to date the time of magmatic zircon crystallisation (Fig. 8.5g, h). The zircons have relatively high U and Th concentrations, and a majority of analyses yield elevated Th/U that are in the normal range for igneous zircon (Table 8.2). Older zircon components yield $^{206}Pb/^{238}U$ ages that range to c. 910 Ma.

8.6.5 C5-Mj74 (mafic gneiss)

Zircon grains from this sample are dominantly stubby, anhedral to subhedral grains that are complexly zoned, resorbed, and irregular, with a subordinate population of

blocky, prismatic, oscillatory-zoned grains (Fig. 8.4). This is a heterogeneous population of zircon grains as is evident for the resultant U–Pb ages which range from c. 865 Ma to Cretaceous. Twenty two of 26 analyses of cores and rims yield Cretaceous ages that range from c. 146 to c. 114 Ma (Fig. 8.5i, j), with 73% of these between c. 146 and c. 130 Ma in age. However, no significant age grouping or geological age can be made from this data set.

8.6.6 8D27-10 (calcareous argillite)

This sample yielded a heterogeneous zircon population that includes: small rounded cores (<180 μm) with uniform CL properties (range of luminescence in cores, from dark to bright) and narrow rim overgrowths; large prismatic grains (>225 μm) or grain fragments with oscillatory growth zones, rimmed by a narrow overgrowth that is medium to bright in CL; subangular uniform-coloured cores with a narrow rim overgrowth is dark in CL. There is truncation of faint sector and oscillatory zoning within the rounded cores against overgrowths, consistent with the derivation of the cores as inherited detrital grains. SHRIMP U–Pb analysis did not yield a coherent age group. Of 25 randomly selected grains, 8 fall in the range c. 552 to c. 675 Ma, with just one analysis that is <500 Ma (492 Ma). The majority of analysis spots yield older ages that scatter between c. 650 and c. 1150 Ma, with outliers at c. 1.8 and 2.0 Ga (Fig. 8.5k, l; Table 8.2).

8.7 Results of Hf–O analyses

The Hf and O isotope compositions of zircons from the Ford Granodiorite suite and zircons from granites from the Fosdick complex are summarized in Figures 8.6, 8.7,

and Table 8.3. To characterise both intra- and inter-sample variations of Hf and O isotope ratios in zircon, the results are presented by granite type (Ford Granodiorite suite; and Devonian–Carboniferous granites and Cretaceous granites within the Fosdick complex). An examination of core–rim relationships in zircons and zircon populations from individual samples is provided in Appendix G (Figs G.1, G.2).

Magmatic zircons from Ford Granodiorite samples MB.214.W and MB.219.W display a limited range of εHf_t values from -1 to +4 with $\delta^{18}O$ values ranging from 5.7‰ to 11.5‰ with most between 6.4 and 7.1‰ (Figs 8.6, 8.7). The samples are characterized by relatively radiogenic εHf_t values, low $\delta^{18}O$ signatures, and Proterozoic Lu–Hf depleted mantle model ages (Table 8.3).

Devonian–Carboniferous granites from the Fosdick complex show a wide range in εHf_t and $\delta^{18}O$ values from -7 to +1 and 5.8‰ to 12.6‰, respectively, that are more crust-like than the Ford Granodiorite suite (Figs 8.6, 8.7). Although some individual spot ages, and εHf_t and $\delta^{18}O$ values for M5-G175 overlap the ranges for the two Ford Granodiorite suite samples, suggesting that this granite may contain the highest proportion of melt component derived from the Ford Granodiorite suite among the Devonian-Carboniferous granites, the heterogeneous and relatively high $\delta^{18}O$ values nonetheless suggest a variable but significant contribution from a supracrustal source. The Devonian–Carboniferous granites (C5-Is51a, C5-I26, and C6-Aw86.1) from the Fosdick complex all have more elevated $\delta^{18}O$ values and less radiogenic εHf_t values than the Ford Granodiorite suite (Figs 8.6, 8.7b).

Cretaceous granites show a comparatively large spread in εHf_t, with values ranging from -16 to +5, and a wide range of $\delta^{18}O$ values that lie between 6.5‰ and

Table 8.3. Oxygen and Hafnium isotope data from zircon spot analyses.

Analysis spot ID	spot	Age (Ma)	$^{18}O/^{16}O$	± (10^{-7})	$\delta^{18}O$ ‰	± 2 se	$^{176}Hf/^{177}Hf$	± (10^{-6})	$^{176}Lu/^{177}Hf$	e Hf (i)	eHf (p)	± 2σ	t_{DM} (Ga)*
Gutenko Nunataks	***MB.214.1W***	Ford Granodiorite			*W143°42', S76°49'*								
1	/	369	0.0020390	2	7.10	0.48	0.282626	22	0.00077	-5.6	2.4	0.8	1.13
2	/	381	0.0020411	5	8.11	0.52	0.282634	28	0.00127	-5.3	2.8	1.0	1.12
3	/	376	0.0020375	5	6.36	0.53	0.282597	23	0.00094	-6.6	1.5	0.8	1.20
5	/	382	0.0020388	4	7.00	0.51	0.282638	24	0.00094	-5.2	3.1	0.8	1.10
6	/	378	0.0020391	5	7.13	0.53	0.282597	29	0.00139	-6.7	1.4	1.0	1.20
7	/	362	0.0020389	6	7.05	0.54	0.282619	27	0.00124	-5.9	1.9	1.0	1.16
8	/	354	0.0020400	6	7.56	0.55	0.282678	30	0.00207	-3.8	3.6	1.1	1.05
9	/	394	0.0020479	6	11.46	0.54	0.282656	24	0.00100	-4.6	3.9	0.9	1.06
10	/	371	0.0020384	4	6.80	0.51	0.282642	31	0.00118	-5.1	2.9	1.1	1.10
12	/	370	0.0020395	5	7.34	0.53	0.282602	46	0.00085	-6.5	1.6	1.6	1.19
13	/	380	0.0020386	4	6.89	0.51	0.282659	31	0.00079	-4.5	3.8	1.1	1.05
14	/	378	0.0020395	4	7.32	0.50	0.282603	47	0.00135	-6.4	1.6	1.7	1.19
Hermann Nunatak	***MB.219.1W***	Ford Granodiorite			*143°54'W, 76°14'S*								
1	/	398	0.0020397	3	7.44	0.49	0.282601	28	0.00165	-6.5	1.9	1.0	1.19
2	/	379	0.0020377	3	6.44	0.50	0.282660	27	0.00106	-4.4	3.8	1.0	1.06
3	/	396	0.0020392	5	7.20	0.52	0.282622	31	0.00188	-5.8	2.6	1.1	1.14
4	/	363	0.0020410	4	8.07	0.51	0.282571	22	0.00171	-7.6	0.1	0.8	1.27
5	/	375	0.0020388	4	7.01	0.50	0.282585	25	0.00188	-7.1	0.8	0.9	1.24
6	/	371	0.0020384	2	6.78	0.49	0.282611	26	0.00152	-6.1	1.7	0.9	1.18
7	/	811	0.0020346	2	4.93	0.48	0.282179	26	0.00121	-21.4	-4.0	0.9	1.89
9	/	364	0.0020391	2	7.14	0.48	0.282668	31	0.00162	-4.1	3.6	1.1	1.05
10	/	354	0.0020386	3	6.89	0.49	0.282571	28	0.00186	-7.6	-0.1	1.0	1.28
11.1	/	599	0.0020369	4	6.07	0.50	0.282170	23	0.00062	-21.7	-8.6	0.8	2.01
11.2	/	375	0.0020363	3	5.77	0.50							
Mt Getz	***M5-G175***	Biotite monzogranite			*145.22°S, 76.553°W*								
1	c	328	0.0020483	4	8.53	0.45	0.282565	27	0.00130	-7.8	-0.8	0.9	1.30
2.1	r	359	0.0020464	5	7.59	0.47	0.282386	22	0.00093	-14.1	-6.4	0.8	1.68
2.2	c	630	0.0020403	5	4.63	0.48							
3	r	376	0.0020458	4	8.75	0.28	0.282457	28	0.00160	-11.6	-3.6	1.0	1.52
4	/	367	0.0020458	4	8.71	0.29	0.282463	50	0.00146	-11.4	-3.6	1.8	1.51
5	r	368	0.0020437	4	6.26	0.46	0.282504	30	0.00115	-9.9	-2.0	1.1	1.41
6	r	363	0.0020474	4	9.53	0.28	0.282570	78	0.00206	-7.6	0.0	2.7	1.28
7	r	362	0.0020428	7	5.84	0.52	0.282569	30	0.00185	-7.6	0.0	1.1	1.28
9	r	360	0.0020437	5	7.72	0.32	0.282544	21	0.00077	-8.5	-0.7	0.7	1.32
10	/	371	0.0020462	3	8.95	0.24	0.282416	21	0.00104	-13.0	-5.0	0.7	1.61
11	r	379	0.0020476	4	9.59	0.26	0.282403	40	0.00140	-13.5	-5.4	1.4	1.64
15	c	370	0.0020420	3	6.85	0.25	0.282571	23	0.00102	-7.6	0.4	0.8	1.26
16	c	352	0.0020459	3	*8.77*	0.25	0.282506	27	0.00110	-9.9	-2.3	0.9	1.42
Mt Iphigene	***C5-I26***	Cordierite leucogranite			*145.824°S, 76.497°W*								
1.1	r	367	0.0020415	5	9.17	0.52	0.282512	23	0.00081	-9.7	-1.7	0.8	1.39
2.1	c	359	0.0020425	4	9.67	0.48	0.282552	31	0.00136	-8.2	-0.6	1.1	1.31
3.1	r	361	0.0020427	4	9.73	0.49	0.282471	26	0.00095	-11.1	-3.3	0.9	1.49
4.1	r	277		0			0.282550	24	0.00113	-8.3	-2.4	0.8	1.36
5.1	r	366	0.0020406	6	8.75	0.53	0.282495	17	0.00079	-10.2	-2.3	0.6	1.43
5.2	/	363	0.0020407	5	8.78	0.52	0.282476	21	0.00093	-10.9	-3.0	0.7	1.47
5.3	/	360	0.0020415	7	9.19	0.56	0.282510	28	0.00091	-9.7	-1.9	1.0	1.40
7.1	/	373	0.0020441	5	10.46	0.51	0.282494	28	0.00151	-10.3	-2.4	1.0	1.44
8.1	/	368	0.0020431	5	9.93	0.52	0.282457	23	0.00080	-11.59	-3.6	0.8	1.51
9.1	/	366	0.0020416	4	9.22	0.49	0.282474	25	0.00131	-11.0	-3.2	0.9	1.48
10.1	/	372	0.0020423	4	9.58	*0.48*	0.282452	23	0.00045	-11.8	-3.6	0.8	1.52
12.1	/	364	0.0020410	3	8.92	0.47	0.282544	20	0.00149	-8.5	-0.8	0.7	1.33
Mt Iphigene	***C5 Is 51a***	Leucogranite			*145.81°S, 76.527°W*								
1.1	c	351	0.0020490	6	9.57	0.36	0.282415	21	0.00103	-13.1	-5.5	0.7	1.60
3.1	c	353	0.0020465	19	8.34	0.97	0.282591	26	0.00093	-6.9	0.8	0.9	1.23
4.1	c	352	0.0020467	5	8.44	0.34	0.282509	30	0.00096	-9.8	-2.2	1.1	1.41
7.1	c	1055	0.0020436	6	6.92	0.35	0.282221	41	0.00191	-19.9	2.4	1.4	1.68
8.1	c	348	0.0020516	5	10.84	0.32	0.282498	34	0.00098	-10.1	-2.6	1.2	1.44
9.1	c						0.282441	23	0.00106	-12.2	-0.8	0.8	1.46
10.1	c	352	0.0020567	11	12.61	0.67	0.282492	30	0.00125	-10.4	-2.8	1.1	1.45
12.1		355	0.0020566	16	12.58	0.88							
13.1	c	374	0.0020565	5	*12.53*	0.47	0.282550	36	0.00048	-8.3	-0.1	1.3	1.30
14.1	c	360					0.282479	27	0.00129	-10.8	-3.1	1.0	1.48

Table 8.3 continued. Oxygen and Hafnium isotope data from zircon spot analyses.

Analysis spot ID	spot	Age (Ma)	$^{18}O/^{16}O$	± (10^{-7})	$\delta^{18}O$ ‰	± 2 se	$^{176}Hf/^{177}Hf$	± (10^{-6})	$^{176}Lu/^{177}Hf$	e Hf (i)	eHf (p)	± 2σ	t_{DM} (Ga)*
Marujupu Peak	***C5-Mj74***		Garnet-biotite gneiss		*145.659°S,*	*76.499°W*							
8.1	c	120	0.0020440	5	6.61	0.43	0.282804	42	0.00280	0.7	3.1	1.5	0.89
9.1	c	139	0.0020422	5	5.73	0.44	0.282919	44	0.00220	4.7	7.6	1.6	0.62
10.1	r	137	0.0020476	5	8.39	0.43	0.282384	20	0.00038	-14.2	-11.2	0.7	1.80
12.1	r	146	0.0020461	6	7.67	0.45	0.282799	28	0.00080	0.5	3.6	1.0	0.88
13.1	c	146	0.0020432	4	6.25	0.41	0.282913	32	0.00074	4.5	7.7	1.1	0.62
14.1	c	133	0.0020430	5	6.14	0.43	0.282876	24	0.00034	3.2	6.2	0.9	0.71
15.1	r	143	0.0020423	5	5.78	0.42	0.282807	28	0.00120	0.8	3.9	1.0	0.86
16.1	c	138	0.0020411	6	5.20	0.45	0.282611	61	0.00144	-6.1	-3.2	2.1	1.31
17.1	c	685					0.282798	43	0.00137	0.5	15.1	1.5	0.57
19.1	c	864	0.0020500	5	9.57	0.42	0.282429	29	0.00105	-12.6	-5.6	1.0	1.60
19.2	r	326					0.282144	24	0.00056	-22.7	-3.7	0.9	1.91
20.1	c	143	0.0020415	5	5.42	0.43	0.282872	45	0.00050	3.1	6.2	1.6	0.71
21.1	r	138	0.0020420	5	5.64	0.42	0.282895	24	0.00050	3.9	6.9	0.8	0.66
23.1	/	131					0.282813	36	0.00102	1.0	3.8	1.3	0.86
24.1	/	140	0.0020433	4	6.28	0.41	0.282975	41	0.00253	6.7	9.6	1.5	0.49
Mt Avers	***C6-Aw86.1***		Leucogranite		*145.424°S,*	*76.46°W*							
1.2	r	369	0.0020416	4	9.20	0.48	0.282465	38	0.00093	-11.3	-3.3	1.4	1.50
2.1	c	364	0.0020418	5	9.33	0.51	0.282441	26	0.00106	-12.2	-4.3	0.9	1.55
2.2	r	130	0.0020400	2	8.43	0.46	0.282509	21	0.00076	-9.8	-6.9	0.7	1.53
3.1	r	109	0.0020404	5	8.65	0.50	0.282549	24	0.00064	-8.3	-6.0	0.9	1.46
3.2	c	361	0.0020405	3	8.67	0.47	0.282469	20	0.00143	-11.2	-3.5	0.7	1.50
4.1	r	107	0.0020406	3	8.73	0.47	0.282548	46	0.00066	-8.4	-6.0	1.6	1.46
4.2	c	357	0.0020416	4	9.19	0.49	0.282453	31	0.00075	-11.7	-4.0	1.1	1.53
5.1	r	106	0.0020417	3	9.28	0.47	0.282525	19	0.00058	-9.2	-6.9	0.7	1.51
5.2	c	355	0.0020393	5	8.11	0.50	0.282532	28	0.00102	-9.0	-1.3	1.0	1.36
6.1	r	325					0.282442	28	0.00065	-12.1	-5.0	1.0	1.57
7.1	c	346	0.0020397	6	8.27	0.53	0.282471	25	0.00132	-11.1	-3.7	0.9	1.50
8.1	c	341	0.0020418	4	9.30	0.49	0.282407	23	0.00074	-13.4	-6.0	0.8	1.64
9.1	r	364	0.0020422	5	9.52	0.50	0.282483	18	0.00046	-10.7	-2.7	0.6	1.45
9.2	c	344	0.0020403	4	8.59	0.48	0.282457	22	0.00146	-11.6	-4.3	0.8	1.54
10.1	r	367	0.0020419	4	9.34	0.49	0.282446	22	0.00088	-12.0	-4.0	0.8	1.54
11.1	c	376	0.0020407	3	8.80	0.47	0.282450	30	0.00106	-11.9	*-3.8*	*1.1*	1.53
12.1	r	357	0.0020405	5	*8.66*	0.52	0.282439	27	0.00065	-12.3	-4.5	0.9	1.56
13.1	r	129	0.0020409	4	8.87	0.48	0.282663	19	0.00067	-4.3	-1.5	0.7	1.19
13.2	c	373	0.0020404	4	8.64	*0.48*	0.282484	31	0.00138	-10.6	-2.7	1.1	1.46
Mt Iphigene	***C5-Is54***		Leucogranite		*145.805°S,*	*76.528°W*							
1.1	r	114	0.0020400	2	7.54	0.38	0.282632	18	0.00181	-5.4	-3.0	0.7	1.27
3.1	r	109	0.0020412	4	8.09	0.41	0.282811	56	0.00215	0.9	3.2	2.0	0.88
4.1	r	564	0.0020428	3	8.91	0.40	0.281963	34	0.00158	-29.1	-17.1	1.2	2.51
5.1		115.3	0.0020420	3	8.48	0.39							
6.1	c	113	0.0020406	3	7.83	0.40	0.282686	20	0.00167	-3.5	-1.1	0.7	1.15
7.1	c	116	0.0020406	3	7.81	0.39	0.282703	44	0.00209	-2.9	-0.5	1.6	1.12
9.1	c	114	0.0020484	2	11.64	0.38	0.282492	18	0.00078	-10.4	-7.9	0.7	1.58
9.2	r	536	0.0020386	4	6.82	0.42	0.282399	12	0.00025	-13.7	-1.8	0.4	1.53
10.1	r	353	0.0020397	3	7.39	0.40	0.282614	16	0.00187	-6.1	1.4	0.6	1.19
11.1	r	115	0.0020414	3	8.23	0.40	0.282704	36	0.00150	-2.9	-0.4	1.3	1.11
12.1	r	117.4	0.0020471	3	*11.00*	0.39							
13.1		120.3	0.0020398	2	7.42	*0.39*							
14.1	r	110	0.0020420	3	8.50	0.39	0.282699	28	0.00143	-3.0	-0.7	1.0	1.12
14.2	c	601	0.0020379	2	6.50	0.38	0.282446	24	0.00058	-12.0	1.2	0.9	1.39
17.1	/	113	0.0020413	2	8.18	0.39	0.282635	33	0.00134	-5.3	-2.9	1.2	1.27
Mt Lockhart	***M6-L188B***		Biotite granite		*W145.189°,*	*S76.441°*							
1.1	r	103	0.0020426	2	9.20	0.34	0.282606	13	0.00043	-6.3	-4.1	0.5	1.33
2.1	c	114	0.0020393	2	7.59	0.34	0.282609	12	0.00029	-6.2	-3.7	0.4	1.32
3.1	r	118	0.0020440	3	9.87	0.35	0.282586	21	0.00036	-7.0	-4.4	0.7	1.37
4.1	c	119	0.0020389	2	7.40	0.34	0.282589	12	0.00029	-6.9	-4.3	0.4	1.36
4.2	r	113	0.0020449	2	10.31	0.33	0.282610	10	0.00058	-6.2	-3.7	0.4	1.32
5.1	c	116	0.0020404	3	8.12	0.36	0.282637	18	0.00061	-5.2	-2.7	0.6	1.26
6.1	r	107	0.0020434	3	9.61	0.35	0.282810	53	0.00093	0.9	3.2	1.9	0.88
6.2	c	116	0.0020398	2	7.84	0.34	0.282660	48	0.00072	-4.4	-1.9	1.7	1.21
7.1	c	120	0.0020389	2	7.40	0.34	0.282753	31	0.00092	-1.1	1.5	1.1	0.99
8.1	r	113	0.0020428	3	9.29	0.36	0.282610	26	0.00051	-6.2	-3.7	0.9	1.32
8.2	c	123	0.0020379	3	6.92	0.36	0.282737	26	0.00144	-1.7	0.9	0.9	1.03
11.1	c	115	0.0020395	3	7.71	0.35	0.282604	17	0.00040	-6.4	-3.9	0.6	1.33
12.1	r	105	0.0020419	2	8.86	0.34	0.282637	30	0.00078	-5.2	-3.0	1.1	1.26
12.2	c	119	0.0020402	2	8.02	0.34	0.282638	19	0.00061	-5.2	-2.6	0.7	1.25
13.1	r	105	0.0020417	2	*8.77*	0.34	0.282849	93	0.00118	2.3	4.5	3.3	0.79
13.2	c	114	0.0020399	3	7.89	*0.34*	0.282612	17	0.00112	-6.1	-3.7	0.6	1.32
14.1	r	105	0.0020437	3	9.74	0.35	0.282625	14	0.00045	-5.7	-3.4	0.5	1.29
14.2	c	116	0.0020401	4	7.99	0.37	0.282625	16	0.00049	-5.7	-3.1	0.6	1.28
15.1		375	0.0020431	2	9.46	0.34							
15.2		370	0.0020442	2	10.01	0.34							
16.1	c	116	0.0020426	2	9.19	0.33	0.282616	14	0.00039	-6.0	-3.4	0.5	1.30

Table 8.3 continued. Oxygen and Hafnium isotope data from zircon spot analyses.

Analysis spot ID	spot	Age (Ma)	$^{18}O/^{16}O$	± (10^{-7})	$\delta^{18}O$ ‰	± 2 se	$^{176}Hf/^{177}Hf$	± (10^{-6})	$^{176}Lu/^{177}Hf$	e Hf (i)	eHf (p)	± 2σ	t_{DM} (Ga)*
Mt Bitgood	***M6-B248A***	Granite			*145.913°S, 76.464°W*								
1.1	r	114	0.0020424	3	9.11	0.34	0.282349	17	0.00090	-15.4	-13.0	0.6	1.90
2.1	c	365	0.0020419	4	8.87	0.36	0.282542	34	0.00141	-8.6	-0.8	1.2	1.33
3.1	r	129	0.0020436	2	9.72	0.34	0.282543	34	0.00109	-8.6	-5.8	1.2	1.46
3.2	c	1011	0.0020412	2	8.50	0.34	0.282461	16	0.00082	-11.4	10.7	0.6	1.11
4.1	r	104	0.0020420	3	8.89	0.35							
4.2	c	360	0.0020413	3	8.59	0.35							
5.1	r	112	0.0020446	3	10.19	0.35	0.282554	35	0.00113	-8.2	-5.8	1.2	1.45
6.1	c	715	0.0020365	3	6.20	0.36	0.282378	37	0.00250	-14.4	0.4	1.3	1.54
7.1	r	113	0.0020450	2	10.41	0.34							
8.1	r	100	0.0020429	3	9.36	0.35	0.282575	26	0.00210	-7.4	-5.4	0.9	1.41
9.1	r	115	0.0020419	2	8.86	0.33	0.282718	39	0.001634	-2.4	0.1	1.4	1.08
10.1	r	105	0.0020456	3	10.67	0.34	0.282504	12	0.00044	-9.9	-7.6	0.4	1.56
10.2	c	837	0.0020443	3	10.03	0.34	0.282339	14	0.00046	-15.8	2.7	0.5	1.49
12.1	c	100	0.0020415	2	8.67	0.34	0.282611	25	0.00113	-6.2	-4.0	0.9	1.33
13.1	r	100	0.0020426	4	9.23	0.37							
13.2	c	360	0.0020435	2	9.65	0.34	0.282574	17	0.00130	-7.5	0.2	0.6	1.26
14.1	c	116	0.0020390	3	*7.42*	0.35	0.282613	17	0.00031	-6.1	-3.5	0.6	1.31
16.1	r	115	0.0020434	2	9.58	*0.33*	0.282598	18	0.00152	-6.6	-4.2	0.6	1.35
17.1	c	116	0.0020404	4	8.14	0.36	0.282641	12	0.00049	-5.1	-2.6	0.4	1.25
18.1	r	363	0.0020421	3	8.96	0.34	0.282522	27	0.00128	-9.3	-1.5	1.0	1.38
Bird Bluff	***C6-BB112***	Granite			*144.58°S, 76.501°W*								
1.1	/	103	0.0020449	5	9.42	0.47	0.282562	12	0.00221	-7.9	-5.7	0.4	1.44
3.1	r	106	0.0020433	4	*8.66*	*0.45*	0.282643	12	0.00212	-5.0	-2.8	0.4	1.26
3.2	c	360	0.0020434	4	8.72	0.44	0.282528	13	0.00168	-9.1	-1.5	0.5	1.37
9.1	r	101	0.0020437	5	8.84	0.46	0.282650	17	0.00248	-4.8	-2.7	0.6	1.24
10.1	/	361	0.0020447	4	9.32	0.45	0.282524	18	0.00256	-9.2	-1.8	0.6	1.39
12.1	r	104	0.0020439	4	8.95	0.45	0.282607	13	0.00229	-6.3	-4.1	0.5	1.34
13.1	r	103	0.0020465	5	10.22	0.46	0.282636	15	0.00247	-5.3	-3.2	0.5	1.27
15.1	r	101	0.0020428	5	8.39	0.46	0.282729	26	0.00309	-2.0	0.0	0.9	1.07
17.1	c	103	0.0020449	4	9.42	0.45	0.282643	14	0.00266	-5.0	-2.9	0.5	1.26
17.2	r	355	0.0020434	5	8.69	0.47	0.282512	16	0.00121	-9.7	-2.0	0.6	1.40
Bird Bluff	***K6-Bb47***	Granite			*144.58°S, 76.501°W*								
3.1	r	104	0.0020464	4	10.15	0.44	0.282544	20	0.00197	-8.5	-6.4	0.7	1.48
7.1	r	101	0.0020463	5	10.13	0.48	0.282503	13	0.00179	-10.0	-7.9	0.5	1.57
8.1	r	101	0.0020459	4	9.91	0.44	0.282496	12	0.00154	-10.2	-8.1	0.4	1.58
9.1	r	102	0.0020469	4	10.40	0.43	0.282522	13	0.00145	-9.3	-7.1	0.5	1.52
9.2	c	102	0.0020474	4	10.68	0.45	0.282478	9	0.00097	-10.8	-8.6	0.3	1.62
10.1	c	106	0.0020466	4	*10.27*	*0.44*	0.282518	12	0.00144	-9.4	-7.2	0.4	1.53
12.1	r	102	0.0020466	4	10.28	0.45	0.282501	9	0.00139	-10.0	-7.9	0.3	1.57
13.1	r	102	0.0020465	5	10.23	0.46	0.282497	9	0.00134	-10.2	-8.0	0.3	1.58
14.1	c	104	0.0020465	4	10.23	0.44	0.282459	10	0.00096	-11.5	-9.3	0.4	1.66
16.1	r	106	0.0020416	5	7.84	0.47	0.282492	15	0.00185	-10.4	-8.2	0.5	1.59
17.1	r	104	0.0020463	4	10.13	0.45	0.282576	25	0.00175	-7.4	-5.2	0.9	1.40
18.1	r	104	0.0020435	5	8.75	0.45	0.282555	16	0.00221	-8.1	-6.0	0.6	1.45
19.1	r	98	0.0020446	6	9.30	0.49	0.282507	10	0.00107	-9.8	-7.7	0.4	1.56
19.2	c	466	0.0020486	5	11.26	0.47	0.282149	22	0.00050	-22.5	-12.3	0.8	2.13
Thompson Ridge	***C6-T101***	Leucogranite			*145.047°S, 76.435°W*								
1.1	c	102	0.0020445	4	9.13	0.39	0.282603	13	0.00106	-6.4	-4.2	0.5	1.34
3.1	c	99	0.0020452	4	9.47	0.39	0.282632	15	0.00060	-5.4	-3.3	0.5	1.28
4.1	c	103	0.0020542	4	13.86	0.40	0.282631	17	0.00134	-5.5	-3.3	0.6	1.28
5.1	c	101	0.0020479	5	10.80	0.40	0.282697	25	0.00170	-3.1	-1.0	0.9	1.14
6.1	c	104	0.0020436	4	8.68	0.38	0.282591	14	0.00081	-6.9	-4.6	0.5	1.37
7.2	r	102	0.0020447	5	*9.20*	*0.40*	0.282604	13	0.00109	-6.4	-4.2	0.5	1.34
8.1	c	100	0.0020444	4	9.05	0.38	0.282631	13	0.00099	-5.5	-3.3	0.5	1.28
9.1	c	102	0.0020440	4	8.85	0.39	0.282624	12	0.00107	-5.7	-3.5	0.4	1.29
10.1	c	100	0.0020438	4	8.80	0.38	0.282668	24	0.00080	-4.1	-2.0	0.8	1.20
11.1	c	101	0.0020439	5	8.82	0.40	0.282652	17	0.00091	-4.7	-2.5	0.6	1.23
12.1	c	102	0.0020439	4	8.83	0.38	0.282629	14	0.00083	-5.5	-3.3	0.5	1.28
13.1	r	101	0.0020435	4	8.60	0.38	0.282643	15	0.00146	-5.0	-2.9	0.5	1.26
14.1	c	373	0.0020449	4	9.29	0.38	0.282477	16	0.00129	-10.9	-2.9	0.6	1.47
15.1	/	102	0.0020444	5	9.07	0.40	0.282616	15	0.00131	-6.0	-3.8	0.5	1.31
Mt Avers	***C6Aw87.3***	Leucogranite			*145.464°S, 76.466°W*								
1.1	r	100	0.0020456	5	9.64	0.40	0.282592	12	0.00087	-6.8	-4.7	0.4	1.37
2.1	r	350	0.0020462	4	9.95	0.39	0.282555	19	0.00093	-8.1	-0.6	0.7	1.31
2.2	c	103	0.0020464	4	10.06	0.39	0.282583	17	0.00089	-7.2	-4.9	0.6	1.39
5.1	c	101	0.0020458	4	9.76	0.39	0.282562	10	0.00069	-7.9	-5.7	0.4	1.43
6.1	r	100	0.0020445	4	9.12	0.39	0.282571	10	0.00088	-7.6	-5.4	0.4	1.41
7.1	r	100	0.0020460	4	*9.85*	*0.38*	0.282610	17	0.00094	-6.2	-4.0	0.6	1.33
8.1	r	103	0.0020446	4	9.18	0.38	0.282579	12	0.00088	-7.3	-5.0	0.4	1.39
10.1	c	100	0.0020456	4	9.66	0.39	0.282577	12	0.00086	-7.4	-5.2	0.4	1.40
11.1	r	100	0.0020455	4	9.61	0.38	0.282596	19	0.00099	-6.7	-4.5	0.7	1.36
12.1	r	100	0.0020460	5	9.86	0.40	0.282567	9	0.00084	-7.7	-5.5	0.3	1.42
13.1	c	103	0.0020449	4	9.32	0.38	0.282565	11	0.00117	-7.8	-5.6	0.4	1.43
15.1	r	102	0.0020447	4	9.21	0.38							
16.1	r	336	0.0020477	5	10.68	0.40	0.282494	36	0.00067	-10.3	-3.0	1.3	1.45
17.1	r	119	0.0020458	4	9.76	0.38	0.282512	15	0.00057	-9.6	-7.1	0.5	1.53
18.1	c	102	0.0020447	4	9.23	0.38	0.282604	26	0.00111	-6.4	-4.2	0.9	1.34

Table 8.3 continued. Oxygen and Hafnium isotope data from zircon spot analyses.

Analysis spot ID	spot	Age (Ma)	$^{18}O/^{16}O$	± (10^{-7})	$\delta^{18}O$ ‰	± 2 se	$^{176}Hf/^{177}Hf$	± (10^{-6})	$^{176}Lu/^{177}Hf$	e Hf (i)	eHf (p)	± 2σ	t_{DM} (Ga)*
Richardson ***C5-R60B***			Leucogranite		*145.69°S, 76.549°W*								
1.1	r	99	0.0020383	2	6.67	0.39	0.282699	20	0.00106	-3.0	-0.9	0.7	1.13
5.1	r	105	0.0020389	2	7.01	0.38	0.282690	17	0.00255	-3.4	-1.2	0.6	1.15
6.1	c	98	0.0020405	3	7.75	0.40	0.282663	21	0.00091	-4.3	-2.2	0.7	1.21
7.1	r	344	0.0020444	2	9.70	0.38	0.282500	15	0.00228	-10.1	-2.9	0.5	1.45
9.1	r	95	0.0020388	2	6.94	0.38	0.282688	14	0.00125	-3.4	-1.4	0.5	1.16
10.1	r	105	0.0020398	2	7.44	0.38	0.282704	20	0.00157	-2.9	-0.7	0.7	1.12
11.1	r	100	0.0020381	2	6.59	0.39	0.282689	27	0.00128	-3.4	-1.3	0.9	1.15
14.1	r	101	0.0020401	3	7.58	0.39	0.282652	28	0.00089	-4.7	-2.5	1.0	1.23
15.1	r	103	0.0020386	3	6.83	0.39	0.282832	47	0.00190	1.7	3.8	1.7	0.83
17.1	r	349	0.0020414	7	8.20	0.49	0.282539	20	0.00125	-8.7	-1.2	0.7	1.35
18.1	r	603	0.0020413	2	8.14	0.39	0.282555	65	0.00135	-8.1	4.8	2.3	1.17
19.1	r	103	0.0020379	3	6.48	0.40	0.282794	33	0.00193	0.3	2.5	1.2	0.92
20.1	r	107	0.0020395	2	7.28	0.38	0.282675	15	0.00109	-3.9	-1.6	0.5	1.18
Mt Woodwa	***8D27-10***												
1.1	/	577	0.0020390	3	6.44	0.17	0.282301	28	0.00039	-17.1	-4.4	1.0	1.73
3.1	/	682	0.0020469	4	10.29	0.18	0.282265	12	0.00070	-18.4	-3.5	0.4	1.75
4.1	/	595	0.0020396	4	6.74	0.18	0.282427	17	0.00077	-12.7	0.3	0.6	1.45
5.1	/	583	0.0020449	5	9.33	0.22	0.282340	10	0.00004	-15.7	-2.8	0.3	1.63
6.1	/	875	0.0020598	4	16.59	0.18	0.282370	17	0.00138	-14.7	4.1	0.6	1.43
8.1	/	644	0.0020462	5	9.93	0.22	0.282469	12	0.00045	-11.2	3.0	0.4	1.31
9.1	/	1048	0.0020467	3	10.18	0.17	0.282254	18	0.00121	-18.8	3.9	0.6	1.58
10.1	/	1091	0.0020442	4	8.99	0.18	0.282349	13	0.00119	-15.4	8.2	0.5	1.34
11.1	/	784	0.0020395	4	6.67	0.20	0.282430	12	0.00036	-12.6	4.8	0.4	1.31
12.1	/	1150	0.0020425	5	8.11	0.22	0.282133	13	0.00110	-23.1	1.9	0.5	1.78
15.1	/	966	0.0020414	4	7.61	0.22	0.282349	17	0.00150	-15.4	5.2	0.6	1.43
16.1	/	777	0.0020446	4	9.15	0.18	0.282184	11	0.00073	-21.3	-4.3	0.4	1.88
17.1	/	993	0.0020410	4	7.42	0.19	0.282254	13	0.00067	-18.8	3.0	0.5	1.59
19.1	/	623	0.0020443	4	9.00	0.20	0.282420	16	0.00062	-12.9	0.7	0.6	1.44
21.1	/	598	0.0020413	5	7.54	0.24	0.282067	12	0.00026	-25.4	-12.2	0.4	2.23
22.1	/	593	0.0020474	4	10.55	0.22	0.282359	13	0.00005	-15.1	-1.9	0.4	1.58
23.1	/	725	0.0020478	4	10.76	0.21	0.282368	12	0.00032	-14.7	1.3	0.4	1.49
24.1	/	553	0.0020435	4	8.62	0.19	0.282440	28	0.00011	-12.2	0.1	1.0	1.43
Mt Getz	***M5-G174***		Two-mica granite		*145.22°S, 76.553°W*								
6	/	101	0.0020490	4	8.77	0.45	0.282482	40	0.00107	-10.7	-8.5	1.4	1.61
7	/	106	0.0020487	5	8.61	0.46	*0.282316*	*300*	*0.00042*	*-16.6*	*-14.3*	*10.6*	*1.97*
9	/	95	0.0020471	5	7.85	0.46							
10	/	108	0.0020458	5	7.19	0.45	*0.282556*	*200*	*0.00074*	*-8.1*	*-5.7*	*7.1*	*1.44*
12	/	340	0.0020481	5	8.31	0.46	0.282516	45	0.00141	-9.5	-2.3	1.6	1.41
15	/	107	0.0020490	5	8.76	0.47	0.282265	42	0.00149	-18.4	-16.1	1.5	2.09
18	/	95	0.0020459	4	7.22	0.45	0.282576	110	0.00288	-7.4	-5.5	3.9	1.41
22	/	344	0.0020470	5	7.77	0.47	0.282542	50	0.00165	-8.6	-1.3	1.8	1.35
24	/	97	0.0020447	4	6.63	0.44	0.282599	93	0.00280	-6.6	-4.6	3.3	1.36
25	/	95	0.0020450	4	6.80	0.44	0.282566	130	0.00204	-7.7	-5.7	4.6	1.43
26	/	100	0.0020457	4	7.12	0.45	0.282673	76	0.00254	-4.0	-1.9	2.7	1.19
27	/	97	0.0020445	5	6.57	0.48	0.282536	77	0.00165	-8.8	-6.7	2.7	1.50

NOTES: r = rim, c = core, / = unknown

^{176}Lu decay constant of 1.865 x 10^{-11} (Soderlund *et al.*, 2004)

$^{176}Hf/^{177}Hf$ and $^{176}Lu/^{177}Hf$ of CHUR values of 0.282785 and 0.0336 (Bouvier *et al.*, 2008)

Present day depleted mantle values of $^{176}Hf/^{177}Hf$ and $^{176}Lu/^{177}Hf$ of 0.283225 and 0.0385 (Vervoort & Blichert-Toft,1999) and the bulk earth 176Lu/177Hf value of 0.015 (Goodge & Vervoort, 2006).

*Uncertainties on t_{DM} are ± 0.1 Ga, at minimum, and may approach 1 Ga in cases of old inherited grains with younger ages (Vervoort *et al.*, 2011), so the tDM are not here given in Ma.

Weighted mean $^{176}Hf/^{177}Hf$ ratios for reference zircons are as follows:

91500	0.282306 ± 6	for 23 of 25 completed analyses
Mud Tank	0.282512 ± 4	27 of 28 analyses
FC1	0.282185 ± 5	39 of 41 analyses
Temora 2	0.282680 ± 7	on basis of 16 grains.

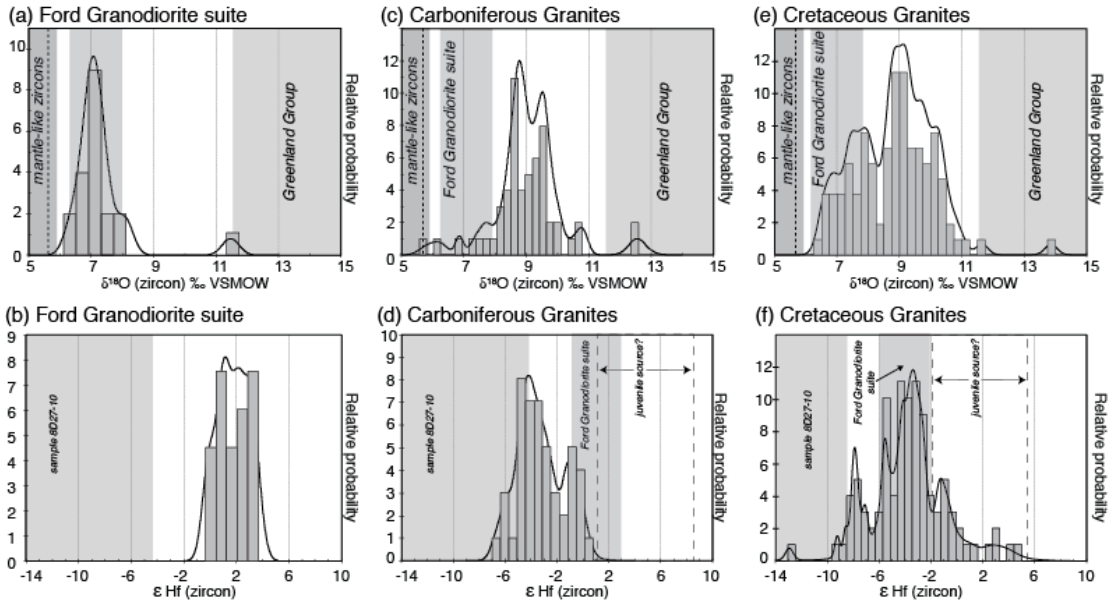

Fig. 8.6. Histograms and probability density plots of $\delta^{18}O$(zircon) and zircon εHf_t results from the Ford Granodiorite suite (a, b) from the Ford Ranges and from Devonian–Carboniferous (c, d) and Cretaceous granites (e, f) from the Fosdick complex.

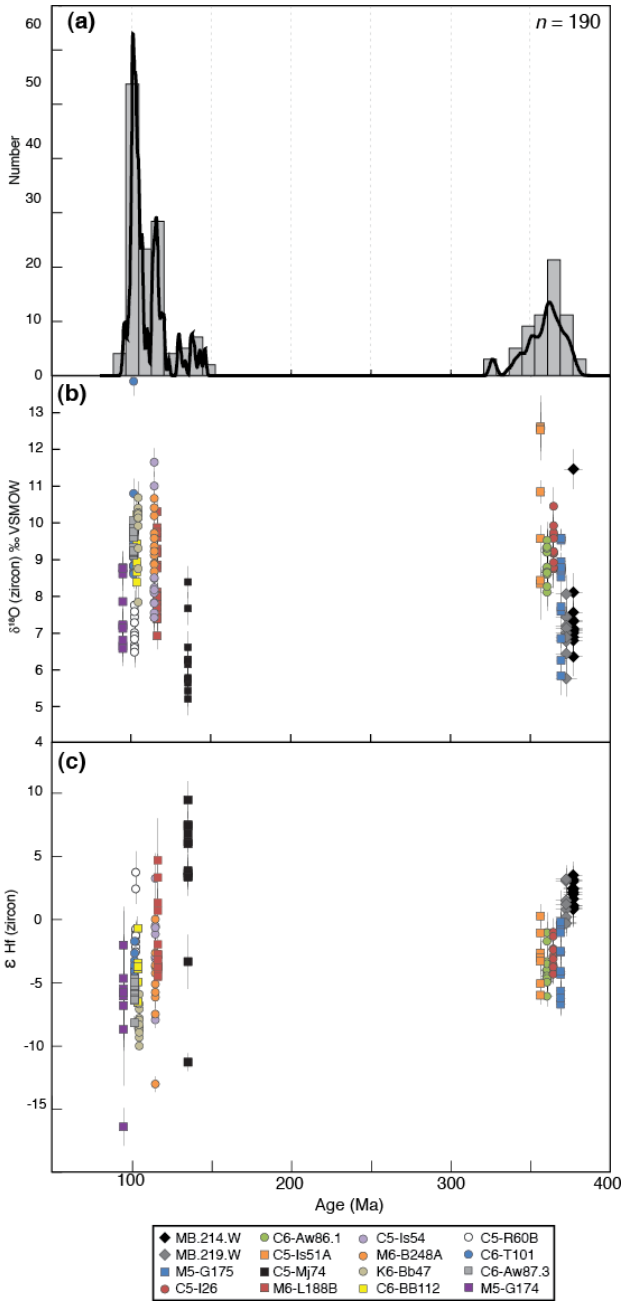

Fig. 8.7. Summary of $^{206}Pb/^{238}U$ ages (a), $\delta^{18}O$ (b) and εHf_t (c) values for zircon from Fosdick complex granite samples and $\delta^{18}O$ (b) and εHf_t (c) values from the Ford Granodiorite suite samples. $^{206}Pb/^{238}U$ data are from Siddoway and Fanning (2009), Korhonen et al. (2010b), and McFadden et al. (2010a, b), in addition to those reported herein. (a) Histogram and probability density plots of $^{206}Pb/^{238}U$ ages. (b) $\delta^{18}O$ versus the respective SHRIMP U–Pb age. Uncertainties are ±2σ. (c) εHf_t versus the respective SHRIMP U–Pb age. Uncertainties are ±2σ.

13.9‰ (Figs 8.6, 8.7). An older group of Cretaceous granites (116–115 Ma; M6-L188B, M6-B248A, C5-Is54) show a wider variation in εHf_t and $\delta^{18}O$ values in zircon compared to four younger granites emplaced in the interval c. 105 Ma to c. 96 Ma (Fig. 8.7); the younger group (K6-Bb47, C6-BB112, C6-T101, C6-Aw87.3) also shows a trend toward higher $\delta^{18}O$ with decreasing age (Fig. 8.7). Two additional younger granite samples C5-R60B (c. 102 Ma) and M5-G174 (c. 96 Ma) have the lowest $\delta^{18}O$ values (6.5 to 8.8‰; Fig. 8.7) of any granites from the Fosdick complex. The mafic gneiss sample C5-Mj74 is generally radiogenic with respect to εHf_t, with values from +3 to +10, except for two values of -3 and -11, and contains relatively low zircon $\delta^{18}O$ values of 5.2–8.4‰ (Fig. 8.7). Detrital zircons from sample 8D27-10 yield nonradiogenic εHf (350) values ranging from -3 to -18 and high $\delta^{18}O$ values of 6–11‰, with one value of 17‰ (Table 3).

8.8 Discussion

The new U–Pb zircon ages for granites reported here are representative of the two pulses of magmatism recorded in the Fosdick complex at c. 115 Ma and 100 Ma, associated with Cretaceous anatexis and magmatism in the Ross province during the change from oblique plate convergence to divergence (e.g. Siddoway 2008). Hf and O isotopes in zircon have been used to characterize the putative sources of granites in the Tasmanides and the Western Province of New Zealand (Hawkesworth and Kemp 2006; Kemp et al. 2006a, 2007; Bolhar et al. 2008; Tulloch et al. 2009), and the new data presented here allow a similar evaluation to be made for the Ross province of West Antarctica.

In western Marie Byrd Land, zircons from Ford Granodiorite suite samples have a restricted range of radiogenic εHf_t values and low $\delta^{18}O$ values (Table 8.3, Fig. 8.6a, b), suggesting derivation from a relatively uniform igneous source. In contrast, most granites in the Fosdick complex contain zircons with less radiogenic εHf_t and higher $\delta^{18}O$ values that are more characteristic of continental realms. For the Devonian–Carboniferous granites, there is no requirement for input from a more juvenile source, for example as a result of underplating during Paleozoic convergence. However, input from a more juvenile source is required to explain the wider range of εHf_t values for the Cretaceous granites, and in particular to explain the low $\delta^{18}O$ values for samples C5-R60B and M5-G174. This juvenile source may reflect mafic magmatism associated with attenuation of the sub-continental lithospheric mantle during Mesozoic intracontinental extension (Siddoway 2008), due to ridge-trench interaction (Luyendyk 1995; Weaver et al. 1994) or arising from other causes (Saito et al. 2012).

8.8.1 Infracrustal versus supracrustal source

Previous work based on the Nd–Sr whole-rock isotope composition of a relatively small number of samples proposed that the granites exposed in the Fosdick complex were derived by partial melting of a mixed source comprising Ford Granodiorite suite and Swanson Formation protoliths (Fig. 8.2; Korhonen et al. 2010b). In the present study, this petrogenetic model is tested using Hf and O isotope ratios in zircons from granites, which should provide a higher resolution record of mixing between the putative supracrustal and infracrustal sources and may provide information about any additional juvenile source requirement (Hawkesworth and Kemp 2006).

Both the Devonian–Carboniferous and the Cretaceous granites are inhomogeneous with respect to $\delta^{18}O$ in zircon and both have relatively high $\delta^{18}O$ values for most samples indicative of predominantly crustal derivation (Fig. 8.6). In addition to primary igneous zircon, a majority of the inherited Paleozoic cores from zircon within Cretaceous granites (5 samples) are significantly more crust-like, with higher $\delta^{18}O$ values than those obtained from Ford Granodiorite samples (Fig. G.2 in Appendix G). However, it is ambiguous whether the inherited cores were sampled from the source of the magma or incorporated from the wall rock during magma ascent and emplacement. Hf isotope ratios in zircons from the Devonian–Carboniferous and the Cretaceous granites are less radiogenic than zircons from the Ford Granodiorite suite, and zircons from Cretaceous granites in particular show a comparatively large spread in εHf_t values in comparison with the Devonian–Carboniferous granites (Figs 8.6, 8.7). These features suggest that both the Devonian–Carboniferous and Cretaceous granites were derived from more than one isotopically distinct source, and may in addition implicate a more juvenile source component for the Cretaceous granites.

The Hf–O isotope ratios of zircons from two Ford Granodiorite suite samples and the Hf isotope values of zircons from sample 8D27-10, a calcareous argillite that has a similar population of detrital zircons to those from the Swanson Formation metaclastic rocks, are taken to be representative of these source rocks at depth. There are currently no whole-rock $\delta^{18}O$ values available for the Swanson Formation. As a substitute the whole-rock $\delta^{18}O$ values of the correlative Greenland Group in New Zealand (13.7–16.2‰; Tulloch et al. 2009), with a $\Delta^{18}O_{Zrc\text{-}WR}$ correction of -2‰ for oxygen isotope fractionation between zircon and granitic magma (Valley et al. 1994; Valley 2003), are

taken to be representative of the Swanson Formation in general. This is justified because whole rock $\delta^{18}O$ values reported from the Greenland Group are similar to values expected for most sedimentary rocks (12‰; O'Neil and Chappell 1977). Although there are εHf_t zircon data from the Proterozoic basement rocks that crop out at the Haag Nunataks in West Antarctica (Flowerdew et al. 2007), in the absence of $\delta^{18}O$ data this representative of a potential Proterozoic source cannot be evaluated adequately in this study.

Zircons from Devonian–Carboniferous granites preserve εHf_t values intermediate between values expected for zircons that would have crystallised from anatectic melt derived solely from either the Swanson Formation or the Ford Granodiorite suite (Fig. 8.6d). In contrast, zircons from the Cretaceous granites preserve a wider range of εHf_t values than those from the Devonian–Carboniferous granites, although the pooled average εHf_t value of all zircons from Cretaceous granites is statistically indistinguishable from the εHf_t value of zircons from the Ford Granodiorite suite samples recalculated to 100 Ma (Fig. 8.6f). Similarly, the majority of $\delta^{18}O$ zircon values from Devonian–Carboniferous granites are intermediate between values expected for zircons that would have crystallised from anatectic melt derived solely from either the Ford Granodiorite suite or the Greenland Group, a proxy for the Swanson Formation (Fig. 8.6c). A majority of zircon $\delta^{18}O$ values from the Cretaceous granites also lie between the zircon $\delta^{18}O$ values of these two putative sources, but the range extends to lower values and overlaps the zircon $\delta^{18}O$ data from zircons of the Ford Granodiorite suite (Fig. 8.6e). Therefore, the Hf and O isotope signatures of zircons from both the Devonian–Carboniferous and the Cretaceous granites requires the input of material derived from both supracrustal and infracrustal sources.

The large spread in isotope ratios of the magmatic zircon populations, particularly for the Cretaceous granites, which is greater than the range of values for inherited zircon grains, suggests open system behavior and involvement of hafnium and oxygen from an external source (Kemp et al. 2005, 2007; Lackey et al. 2005; Yang et al. 2007; Zheng et al. 2007; Bolhar et al. 2008). That is to say that the Hf and O isotope characteristics are not indicative of closed system dissolution and precipitation within the Fosdick complex (cf. Flowerdew et al. 2006; Villaros et al. 2012). Also, the lack of homogeneous Hf and O isotope signatures for zircons from the granites is another indication of open system melting of deeper fertile crust, with extraction of the melt to higher crustal levels, which is an effective process of crustal differentiation (Brown 1994, 2007; Solar et al. 1998).

8.8.2 Binary mixing: The nature of the end-members

The Hf and O isotope signatures of granites from the Fosdick complex, which indicate open-system behavior and more than one source, potentially provide constraints on the amount and nature of crustal reworking in the Ross province of Marie Byrd Land. The Hf–O isotope composition of an anatectic granite can be modified from that of its source by: (1) hybridization with granite that has a different isotope composition, and/or (2) incorporation of suprasolidus or subsolidus material with a different isotope composition.

These alternative scenarios are investigated for both Devonian–Carboniferous and Cretaceous granites using binary mixture modelling between the two putative end-member sources, as identified based on the Nd and Sr isotope characteristics of similar granites from the Fosdick complex (Fig. 8.2; Korhonen et al. 2010b), but with an

additional juvenile source in the case of the Cretaceous granites. We build upon the approach of Kemp et al. (2006a, 2007) by integrating the Hf–O data from zircons with the results from phase equilibria modelling (Korhonen et al. 2010a). The exposed Ford Granodiorite end-member represents a relatively juvenile source that contains zircons with relatively radiogenic εHf_t values and relatively low $\delta^{18}O$ values, whereas the Swanson Formation end-member represents a supracrustal source with relatively nonradiogenic εHf_t and higher $\delta^{18}O$. The additional juvenile source is inferred to have more radiogenic εHf_t and lower $\delta^{18}O$ values than the Ford Granodiorite end-member.

Phase equilibria modelling predicts that both the Swanson Formation and the Ford Granodiorite would have reached *P–T* conditions above their solidi during both the Devonian–Carboniferous and the Cretaceous events, with high-grade metamorphism causing two separate episodes of partial melting of the Swanson Formation and Ford Granodiorite end-members (Korhonen et al. 2010a, 2012). Modelling of seven Swanson Formation and four Ford Granodiorite compositions indicates that Devonian–Carboniferous metamorphism could have yielded 4–40 mol.% melt from the Swanson Formation and 2–7 mol.% melt from Ford Granodiorite suite at the level exposed in the Fosdick complex (Korhonen et al. 2010a, Yakymchuk unpublished data; mol.% in the modelling is approximately equal to vol.% in nature). Modelling further suggests that the subsequent Cretaceous metamorphism could have produced 8–48 mol.% melt from fertile Swanson Formation compositions and 3–17 mol.% melt from fertile Ford Granodiorite suite compositions at the level exposed in the Fosdick complex, but less from protoliths melt-depleted from the Devonian–Carboniferous event (Korhonen et al. 2010a, Yakymchuk unpublished data). Thus, on the one hand, the amount of melt produced by

anatexis of the Swanson Formation at the level exposed in the Fosdick complex generally exceeded the melt connectivity transition (~7 vol.%, Rosenberg and Handy, 2005) and was probably mostly lost to shallower crustal levels (Korhonen et al. 2010a, b, 2012), whereas the amount of melt produced by anatexis of the Ford Granodiorite suite at the level exposed in the Fosdick complex may not have exceeded the melt connectivity transition and most likely was trapped in source. However, on the other hand, the volumetric proportion of granite exposed in the Fosdick complex demonstrates that melt derived from deeper in the crust was trapped locally during ascent to shallower crustal levels (cf. Brown, 2010).

Alternative mechanisms investigated using binary mixture modelling are: mixing between liquids derived from the partial melting of Swanson Formation and Ford Granodiorite suite, and mixing between liquid derived from one source and solid material from the other source. The latter process is interpreted to represent the incorporation of suprasolidus source rock or solid or suprasolidus wall rock into migrating melt. In addition, for the Cretaceous granites mixing between liquids derived from the partial melting of Swanson Formation or Ford Granodiorite and a more juvenile source, and mixing between liquid derived from the juvenile source and solid Swanson Formation or Ford Granodiorite are considered.

In this study, the Hf concentrations of Ford Granodiorite and Swanson Formation are averages taken from bulk rock values from the low-grade protoliths exposed outside the Fosdick complex (Korhonen et al. 2010b). The D_{Hf} values between silicate phases and melt are calculated from the mineral mole proportions obtained by phase equilibria modelling of both Ford Granodiorite suite and Swanson Formation end-member sources

for a pressure of 0.7 GPa and a temperature of 820°C (Korhonen et al. 2010a). At these conditions, a representative Swanson Formation composition is predicted to yield 27 mol.% melt and a representative Ford Granodiorite composition is expected to produce 3 mol.% melt. These melt proportions are combined with Hf distribution coefficients taken from Rubatto and Hermann (2007) for garnet and zircon and from the GERM database (http://www.earthref.org/GERM) for other phases to estimate the concentrations of Hf in the model melt. Zircon modes are estimated using Zr and Hf concentrations (e.g. Wark and Miller 1993) from the bulk rock analyses of Swanson Formation and Ford Granodiorite suite (Korhonen et al. 2010b). This zircon modal estimate represents an upper limit because some Zr may have been partitioned into major phases, such as garnet (Villaseca et al. 2003), during high-grade metamorphism. The concentration of Hf in melt derived from deeper in the Fosdick complex will be different since the melt volume produced is expected to have been larger. However, the mixing envelopes shown in Figures 8.8 and 8.9 are relatively insensitive to changes in the amount of melt considered in the calculations.

The $\delta^{18}O$ value of the two end-members used in the binary mixing calculations represent the range of measured isotope values of zircon from the Ford Granodiorite samples and a fictive range of isotope values for zircon from the Swanson Formation adjusted for oxygen isotope fractionation. Because no $\delta^{18}O$ whole rock values from the Swanson Formation are available, the range of whole rock $\delta^{18}O$ values of the correlative Greenland Group in New Zealand of 13.7–16.2‰ is used (Tulloch et al. 2009). These values are within the range documented for siliciclastic sediments (10–20‰; Eiler 2001). Due to zircon/melt oxygen isotope fractionation, the $\delta^{18}O$ value of zircon that has

crystallised from a granitic melt will be 1–2‰ less than that of the melt (Valley et al. 1994; Valley 2003). Using a zircon/melt $\delta^{18}O$ fractionation factor ($\Delta^{18}O_{Zrc\text{-}WR}$) of -2‰, zircons that have crystallised from a melt derived from partial melting of the Greenland Group (assumed to be similar to the Swanson Formation) are expected to yield $\delta^{18}O$ values of 11.7–14.2‰ with an average value of 12.9‰. In addition, a potential juvenile source is added as a third end-member. The εHf_t range of a potential juvenile source is constrained by the εNd values for mafic dykes from Marie Byrd Land (Saito et al. 2012) using the correlation for juvenile mantle-derived rocks of Vervoort and Blichert-Toft (1999). The potential juvenile source is inferred to have an average $\delta^{18}O$ value similar to that for zircons from mantle-derived magmas (5.7 ± 0.3‰; Hawkesworth and Kemp 2006) and a Hf concentration of 4.6 ppm—the average concentration for Cretaceous mafic rocks in Marie Byrd Land (Storey et al. 1999).

The ranges of $\delta^{18}O$ and εHf values for zircon from the end-members are plotted together with individual zircon analyses from the Devonian–Carboniferous granites (Fig. 8.8) and the Cretaceous granites (Fig. 8.9). A high and low εHf value for each end-member, considered to be representative of the spread in values, is connected with the calculated mixing curves for the scenarios discussed above. This procedure takes into account the spread of $\delta^{18}O$ and εHf values of each end-member, and, in principle, mixing may occur between batches of melt derived from sources with $\delta^{18}O$ and εHf values that vary between the mixing curves shown on Figures 8.8 and 8.9.

8.8.3 Binary mixture modelling: results

The approach presented above is a necessary simplification of a naturally complex anatectic system; however, it does provide important insights into the nature and relative proportions of source components and the mechanisms of mixing. Points along the model curves in Figures 8.8 and 8.9 represent the isotope signature of zircon that would crystallise from magma that records mixing between two end-members in various proportions. The sets of mixing curves between the Swanson Formation and the Ford Granodiorite suite calculated for the scenarios discussed above yield similar results and

---

Fig. 8.8. Results of binary mixture modelling between Swanson Formation and Ford Granodiorite suite (FGS) end-member sources for the Devonian–Carboniferous granites. Individual zircon Hf and O isotope analyses are plotted in (a) and representative fields are shown in (b) to illustrate the variability in Hf and O values of zircons within each sample. The $\delta^{18}O$ value of zircon in the Swanson Formation was approximated from that of the whole-rock $\delta^{18}O$ composition for the correlative Greenland Group in New Zealand and has been adjusted for oxygen isotope fractionation between granitic melt and zircon by a factor of -2‰. Hf-isotope values for zircons from sample 8D27-10, a calcareous argillite rock that contains detrital zircons with a U–Pb age distribution similar to that of Swanson Formation metaclastic rocks (Fig. 8.3a) are plotted, as a means to bracket the range of εHf_t values for the Swanson Formation. Crosses on the mixing curves are 10 vol.% increments and represent the isotope signature of zircon that would crystallise from magma that records mixing between the two putative end-members in various proportions. All zircon εHf_t values have been recalculated to 350 Ma. The cross in the upper right of each diagram shows approximate $\pm 2\sigma$ uncertainties for Hf and O isotope values. Three sets of curves are calculated to evaluate: (1) mixing between melts derived by anatexis of the Swanson Formation (Hf = 3.9 ppm) and the Ford Granodiorite suite (Hf = 5.0 ppm), (2) mixing of melt derived by anatexis of the Ford Granodiorite suite with solid or suprasolidus Swanson Formation (Hf = 3.2 ppm), and (3) mixing of melt derived by anatexis of the Swanson Formation with solid or suprasolidus Ford Granodiorite suite (Hf = 3.4 ppm). A εHf range of a potential juvenile source is constrained by the εNd signature of mafic dykes from Marie Byrd Land (Saito et al. 2012) using the correlation for juvenile mantle-derived rocks of Vervoort and Blichert-Toft (1999). The potential juvenile source is assigned an average $\delta^{18}O$ value of zircons from mantle-derived magmas (5.7 ± 0.3‰; Hawkesworth and Kemp 2006). No whole-rock or zircon $\delta^{18}O$ values are so far available for the Swanson Formation.

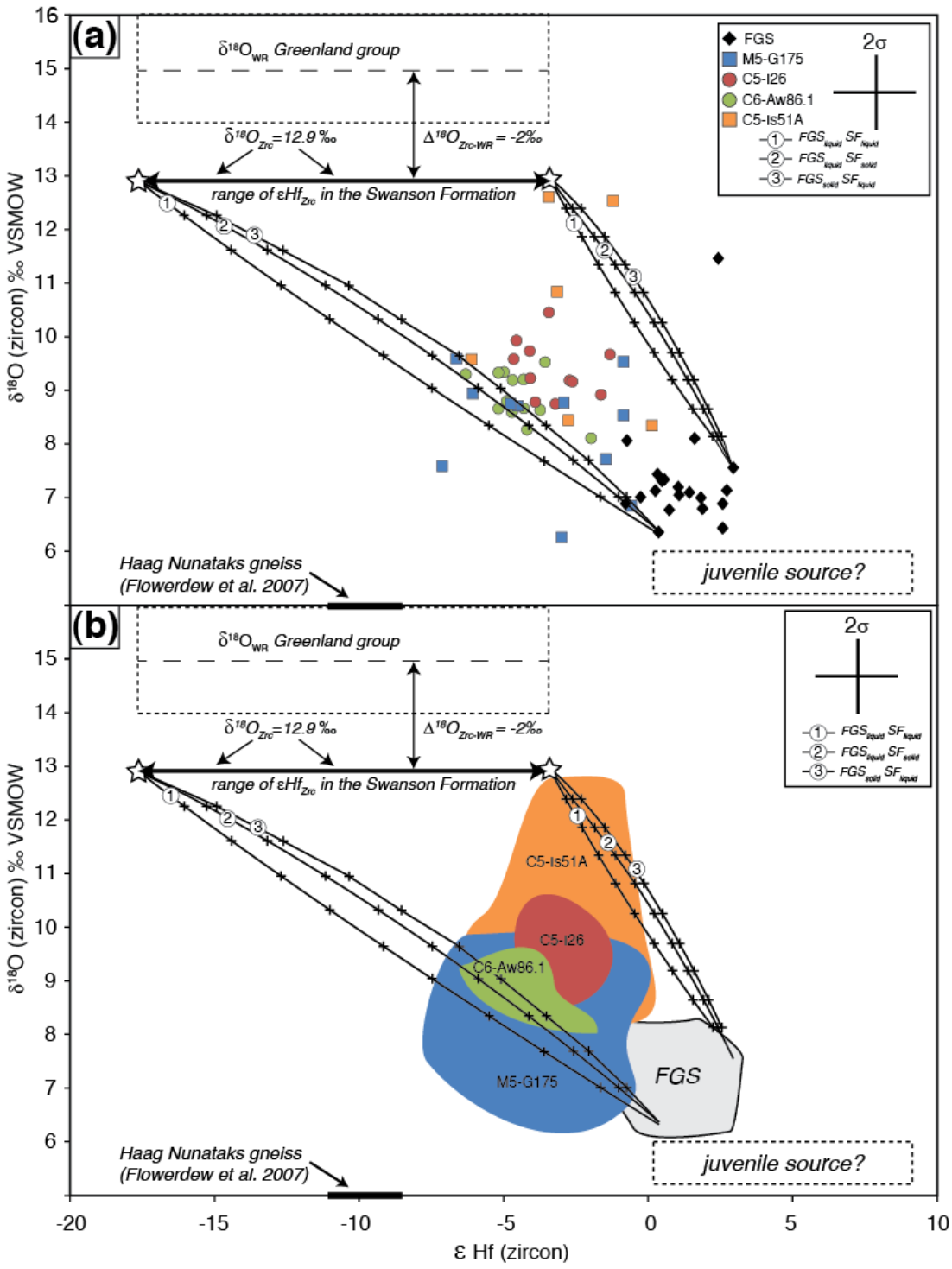
(a)
δ18OWR Greenland group
δ18OZrc=12.9 ‰
Δ18OZrc-WR = -2‰
range of εHfZrc in the Swanson Formation
FGS
M5-G175
C5-I26
C6-Aw86.1
C5-Is51A
2σ
① FGSliquid SFliquid
② FGSliquid SFsolid
③ FGSsolid SFliquid
Haag Nunataks gneiss
(Flowerdew et al. 2007)
juvenile source?
(b)
C5-Is51A
C5-I26
C6-Aw86.1
M5-G175
FGS
δ18O (zircon) ‰ VSMOW
ε Hf (zircon)

are separated from one another by less than three εHf units. Less than three εHf units also separate the calculated binary mixing curves between liquid derived from the juvenile source and material derived from either the Swanson Formation or the Ford Granodiorite suite. The close spatial association of these mixing curves on the Hf–O plot does not allow us to determine the physical process by which mixing occurred (Figs 8.8, 8.9), but these curves may be used to evaluate the relative contribution of each source to the isotope signature of the zircons from granites in the Fosdick complex.

For the Devonian–Carboniferous granites, most individual zircon εHf_t and $\delta^{18}O$ values plot within the calculated mixing envelope. Exceptions include two analyses from M5-G175 and one from C5-Is51A. Samples C5-I26 and C6-Aw86.1 define tightly

---

Fig. 8.9. Results of binary mixture modelling between Swanson Formation, Ford Granodiorite suite (FGS), and juvenile end-member sources for the Cretaceous granites. The SF and FGS sources are the same as described for Figure 8.8, but recalculated to 100 Ma. Individual zircon Hf and O isotope analyses are plotted in (a) and (c) and representative fields are shown in (b) and (d) to illustrate the variability in Hf and O values of zircons within each sample. Crosses on the mixing curves are 10 vol.% increments and represent the isotope signature of zircon that would crystallise from magma that records mixing between two of the putative end-members in various proportions. All zircon εHf_t values have been recalculated to 100 Ma. Seven sets of curves are calculated to evaluate: (1) mixing between melts derived from partial melting of the Swanson Formation (Hf = 3.9 ppm) and the Ford Granodiorite suite (Hf = 5.0), (2) mixing of melt derived by anatexis of the Ford Granodiorite suite with solid or suprasolidus Swanson Formation (Hf = 3.2 ppm), (3) mixing of melt derived by anatexis of the Swanson Formation with solid or suprasolidus Ford Granodiorite suite (Hf = 3.4 ppm), (4) mixing of melt derived from a juvenile source (Hf = 4.6 ppm) mixing with solid or suprasolidus Swanson Formation, (5) mixing of melt derived from a juvenile source mixing melt derived from anatexis of the Swanson Formation, (6) mixing of melt derived from a juvenile source mixing with solid or suprasolidus Ford Granodiorite suite, and (7) mixing of melt derived from a juvenile source mixing melt derived from anatexis of the Ford Granodiorite suite. Also plotted are the isotope values for zircons from sample 8D27-10, an argillaceous rock that contains detrital zircons with a U–Pb age distribution similar to that of Swanson Formation metaclastic rocks (Fig. 8.3a) that may be used to bracket the range of εHf_t values for the Swanson Formation. No whole-rock or zircon $\delta^{18}O$ values are so far available for the Swanson Formation.

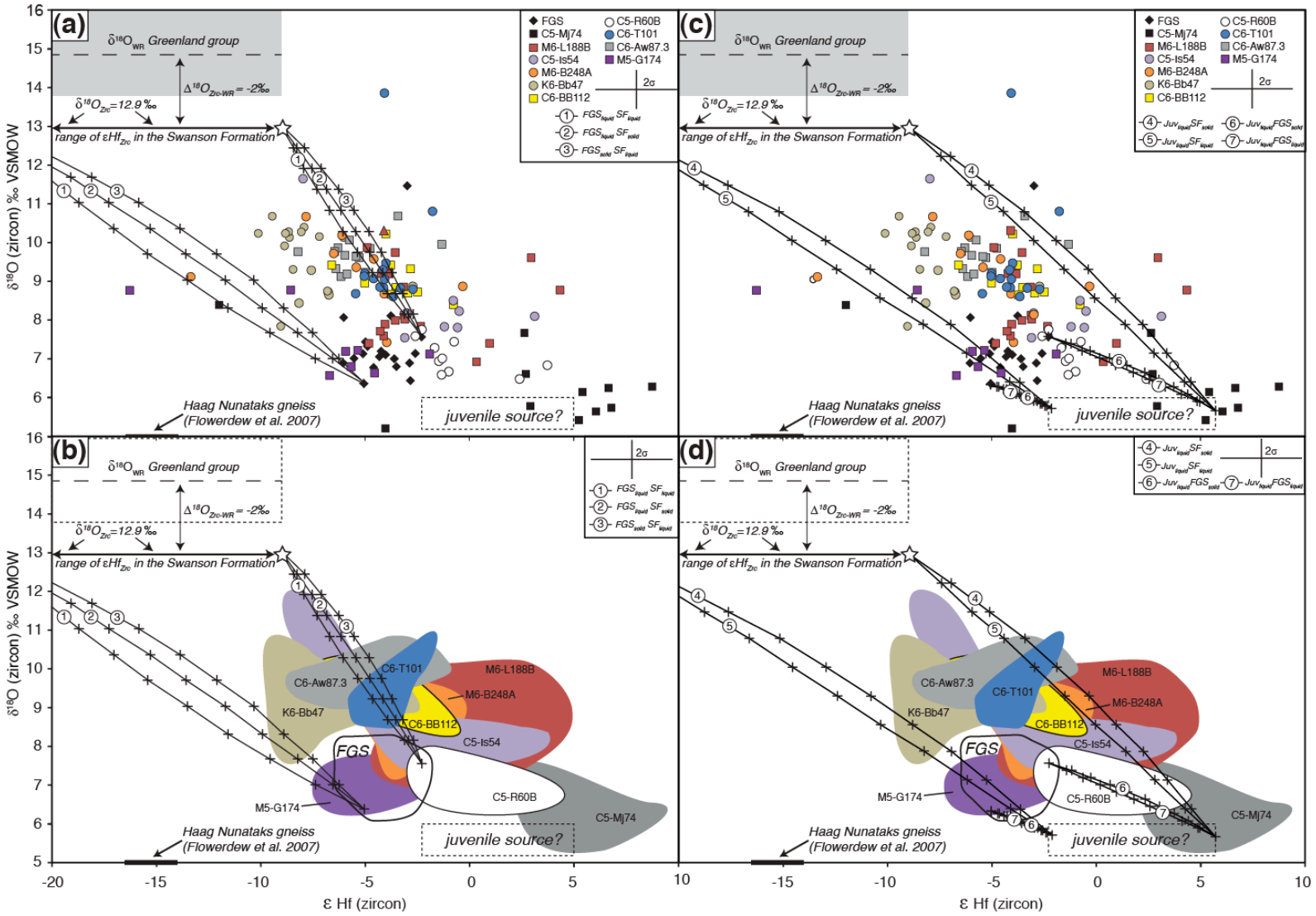
(a)
(b)
(c)
(d)
δ18O WR Greenland group
Δ18OZrc-WR = -2‰
δ18OZrc=12.9 ‰
range of εHfZrc in the Swanson Formation
FGS
C5-Mj74
M6-L188B
C5-Is54
M6-B248A
K6-Bb47
C6-BB112
C5-R60B
C6-T101
C6-Aw87.3
M5-G174
2σ
Haag Nunataks gneiss
(Flowerdew et al. 2007)
juvenile source?
δ18O (zircon) ‰ VSMOW
ε Hf (zircon)

clustered groups whereas samples C5-Is51A and M5-G175 contain comparatively large spreads in $\delta^{18}O$ and εHf_t zircon values (Fig. 8.8a). The zircon $\delta^{18}O$ values from samples C5-I26 and C6-Aw86.1 plot closer to the Ford Granodiorite source whereas the εHf_t values of zircons from these samples are similar to the most radiogenic values from detrital zircons in the Swanson Formation (Fig. 8.8a, b). The majority of zircon data from the Devonian–Carboniferous samples are consistent with the earlier Sr–Nd isotope results that suggest these granites were derived from a two-component mixture of material from the Swanson Formation and the Ford Granodiorite suite, with the latter representing the dominant component (Fig. 8.2; Korhonen et al. 2010a). These results are also consistent with phase equilibria modelling, which suggests that much of the melt derived from anatexis of the Swanson Formation was likely to have been lost to shallower crustal levels than exposed in the Fosdick complex whereas the Devonian–Carboniferous granites within the Fosdick complex were likely to have been dominated by melts derived from the Ford Granodiorite suite trapped during ascent from deeper in the crust where this protolith is expected to occur in greater abundance than the supracrustal rocks (Korhonen et al. 2010a). Zircon analyses for samples C5-I26 and C6-Aw86.1 plot in a region of the mixing envelope consistent with 30–50% involvement of Swanson Formation material (Fig. 8a, b). The large spread in values for samples C5-Is51A and M5-G175, including some outside the mixing envelope, may suggest that there was significant isotope heterogeneity within the magma and for this reason the zircon analyses from these samples were not used to evaluate the proportional contribution of each putative end-member component.

Binary mixing curves for various mixing scenarios for zircons from the Cretaceous granites are shown in Figure 8.9. A majority of zircon data from samples C6-Aw87.3, C6-T101, C6-BB112 and M6-B248A lie within or along the radiogenic εHf boundary of the mixing envelope and again data plot closer to the Ford Granodiorite source, which suggests that it provided the dominant contribution to many of the granites (Fig. 8.9a, b). Zircons from these samples plot in a region of the mixing envelope consistent with incorporation of 20–60% Swanson Formation material in melt derived from a Ford Granodiorite source. Zircons from sample K6-Bb47 also plot within the mixing envelope but they contain less radiogenic εHf_t values than the majority of zircons from other granites. This suggests a larger proportion of supracrustal material contributed to the isotope composition of this granite compared to other samples, which corroborates the interpretation by Korhonen et al. (2010b) that this granite was derived predominantly by partial melting of the Swanson Formation.

Samples C5-Is54, M6-L188B, C5-R60B and M5-G174 contain zircons with similar or more radiogenic εHf_t values than zircons from the Ford Granodiorite suite, which points to the involvement of a more juvenile source that is not exposed at the surface. With the exception of two zircon analyses from sample C5-Is54 the remaining zircons in this sample and zircons from sample C5-R60B define a spread in εHf_t values from +4 to -3 but a limited range in $\delta^{18}O$ from 6.5 to 8.5‰, which suggests a much smaller contribution of supracrustal material compared with the other granites analyzed from the Fosdick complex. This may indicate mixing between the Ford Granodiorite suite and melt derived from a deep-seated juvenile source (Fig. 8.9) not exposed in the Ford Ranges. Sample M6-L188B contains zircons that yield Hf and O isotope values within

the range expected for the Ford Granodiorite suite, but also contains several analyses with higher $\delta^{18}O$ values and some with more radiogenic εHf_t values. The spread in values recorded by this sample suggests the involvement of the Ford Granodiorite suite, the Swanson Formation, and an unexposed juvenile source. The addition of a relatively juvenile source to the mixing models for the Cretaceous granites constrains most of the data that display more radiogenic values than zircons from the Ford Granodiorite suite, including those of sample M5-G174, representing the array of felsic dikes that crosscut all migmatite structures (Siddoway et al. 2005) and the South Fosdick detachment zone. Binary mixing between the juvenile source and the Ford Granodiorite suite encompasses most of the data for sample C5-R60B, whereas a ternary mix of all three putative sources is required to constrain the majority of data from samples C5-Is54 and M6-L188B (Fig. 8.9c, d).

8.8.4 What are the petrogenetic implications?

The Hf isotope signature of zircons from most Devonian–Carboniferous and Cretaceous granites in the Fosdick complex require a large component derived from the Ford Granodiorite source or for some of the Cretaceous granites from a more juvenile source, but many of the granites also have relatively high $\delta^{18}O$ values, indicating the involvement of supracrustal material. This could reflect magma mixing and/or the incorporation of supracrustal material into migrating melt. The results of the binary mixture modelling suggest that a magma derived by partial melting of the Ford Granodiorite source and/or a more juvenile source must incorporate 20–60 vol.% solid or suprasolidus Swanson Formation material to comply with the isotope constraints (Figs

8.8, 8.9). Similar studies from the Lachlan Belt of Australia suggest that 40–85 vol.% crustal material was incorporated into granites derived from more juvenile sources to produce the observed Hf–O isotope signatures (Kemp et al. 2006a, 2007). However, whether felsic magma can incorporate this much material by processes such as melting and disaggregation is uncertain.

The incorporation of subsolidus or suprasolidus material into magma is an energy-intensive process that may be self-limiting (e.g. Bowen 1922; Koyaguchi 1986; Glazner 2007). Thermodynamic modelling of xenolith assimilation suggests that mafic magma can only incorporate a few tens of percent of warm (400°C) granite (Glazner 2007). The upper limit of this estimate is suppressed for more felsic melts due to their lower temperatures compared with basaltic melts. Granites now exposed in the Fosdick complex were emplaced at mid-crustal levels where ambient temperatures were up to ~870°C in the Carboniferous and the Cretaceous (Korhonen et al. 2010a), and both the Swanson Formation and the Ford Granodiorite suite are inferred to have been partially molten at the time of granite emplacement.

The Ford Granodiorite suite is predicted to have produced ~2–7 mol.% melt at the crustal level exposed (Korhonen et al. 2010a). However, at slightly deeper structural levels, the Ford Granodiorite suite could have produced significantly more melt through hydrate-breakdown melting, sufficient to be extracted and emplaced higher in the crust, including the present exposure level of the Fosdick complex (Korhonen et al. 2010a, b). The temperatures beneath the Fosdick complex are interpreted to have exceeded the stability of biotite (Korhonen et al. 2010a) and the Swanson Formation at depth was likely to be limited in volume and residual in nature and is not expected to have

contributed much melt from deeper structural levels. Geophysical models based on airborne magnetic and gravity surveys across the Ford Ranges indicate that the rocks underlying the Fosdick complex are similar to plutonic rocks exposed elsewhere in the Ford Ranges (Ferraccioli et al. 2000; Luyendyk et al. 2003). Therefore, the putative plutonic crust beneath Fosdick complex, which is likely to be dominated by the Ford Granodiorite suite, is interpreted to represent the primary source of melts making up the Devonian–Carboniferous and many of the Cretaceous granites now exposed in the Fosdick complex.

Isentropic ascent of melt sourced from the Ford Granodiorite suite would allow it to become superheated (Stolper and Asimow, 2007) and capable of incorporating more material than would be possible in the source. At the level of emplacement for this melt, most of the melt generated from the Swanson Formation is inferred to have been lost to higher structural levels to allow preservation of the high-grade mineral assemblages in the paragneisses (Korhonen et al. 2010a). However, some residual melt would have been retained along grain boundaries (Holness and Sawyer 2008), with the amount being dependent on the percolation threshold for the microstructure of the melt-bearing rock (Cheadle et al. 2004). Thus, migrating more-deeply sourced melt has the potential to incorporate suprasolidus Swanson Formation rocks by disaggregation.

Melt produced through anatexis may be extracted as a single pulse (batch melting) or more likely it may be extracted as several smaller pulses (fractional melting). A consequence of this process is that melt pulses extracted from an initially isotopically homogenous source may evolve different isotope compositions due to isotope fractionation of Lu from Hf. The Lu/Hf ratios are expected to change if melt is extracted

from a source that contains garnet or zircon (Vervoort and Patchett 1996; Hawkesworth and Kemp 2006). This process is particularly important in high-grade polymetamorphic terranes, such as the Fosdick complex, where multiple episodes of melt production and extraction have been suggested (Korhonen et al. 2010a, b, 2012). Modelling of melting in the lower crust suggests that residual rocks can develop an anomalously high $^{176}Hf/^{177}Hf$ signature within 300–400 million years (Vervoort and Patchett 1996). This time frame is too long for significant differences in the Hf-isotope signature to develop in residual material in the Fosdick complex. Although fractional melting may have played an important role in producing the granites in the Fosdick complex, the effects cannot be resolved using Hf-isotopes and any modification of the $^{176}Hf/^{177}Hf$ values recorded in zircon due to fractional melting is likely insignificant when compared with the Hf-isotope heterogeneity of zircons in the putative protoliths.

8.8.5 Temporal trends in the zircon Hf and O isotope characteristics

Devonian–Carboniferous granites contain zircons that display less radiogenic εHf_t and higher $\delta^{18}O$ values than zircons from the Ford Granodiorite suite (Fig. 8.10a, b), which is consistent with the previously proposed two-component mixing model (Korhonen et al. 2010b). The lowest $\delta^{18}O$ values come from sample M5-G175—the oldest of the Devonian–Carboniferous granites collected from the Fosdick complex—in which zircons have highly variable Hf and O values suggesting that the melts were not well homogenized (Fig. 8.10a). Zircons from the three younger Devonian–Carboniferous granites contain significantly elevated $\delta^{18}O$ values that not only exceed those of the Ford Granodiorite suite zircons but also show a tendency towards higher $\delta^{18}O$ values with

decreasing age (Fig. 8.10a). This is interpreted as an indication of an increasing contribution of Swanson Formation supracrustal material in the granite magmas during the evolution of the Devonian–Carboniferous melting event.

Excluding samples C5-R60B and M5-G174 (discussed below), the data from Cretaceous granites also show a slight tendency towards higher $\delta^{18}O$ values with decreasing age (Fig. 8.10c). Results from zircon in granites emplaced during wrench deformation (c. 116–115 Ma; C5-Is54, M6-L188B, and M6-B248) are slightly more variable, with a wide range of $\delta^{18}O$ values (6.2 to 11.6‰, with most ≥ 7.5‰), and the lowest $\delta^{18}O$ values for zircons from Cretaceous granites excluding samples C5-R60B and M5-G174 (Fig. 8.10c). Zircons from younger granites emplaced during transtension (c. 109–102 Ma; K6-Bb47, C6-BB112, C6-T101, and C6-Aw87.3) have more elevated $\delta^{18}O$ on average and less radiogenic εHf_t values (Fig. 8.10c, d), reflecting a greater contribution of supracrustal Swanson Formation. This generally supports the petrogenetic modelling of Korhonen et al. (2010a, 2012), which postulated that the younger, detachment-controlled sheeted leucogranite complex was derived primarily from a Swanson Formation source.

The Cretaceous granites were emplaced during a transition in tectonic regimes (McFadden et al. 2010a, b), which may have affected the ability of melt to escape the source region as now exposed in the Fosdick complex. On the one hand, granites emplaced during wrench deformation form steeply dipping to vertical sheets (McFadden et al. 2010a, b) that would have provided conduits for melt migration from and through the exposed level of the Fosdick complex to shallower crustal levels with only a low probability of entrapment. The εHf_t and $\delta^{18}O$ values of zircons from these granites

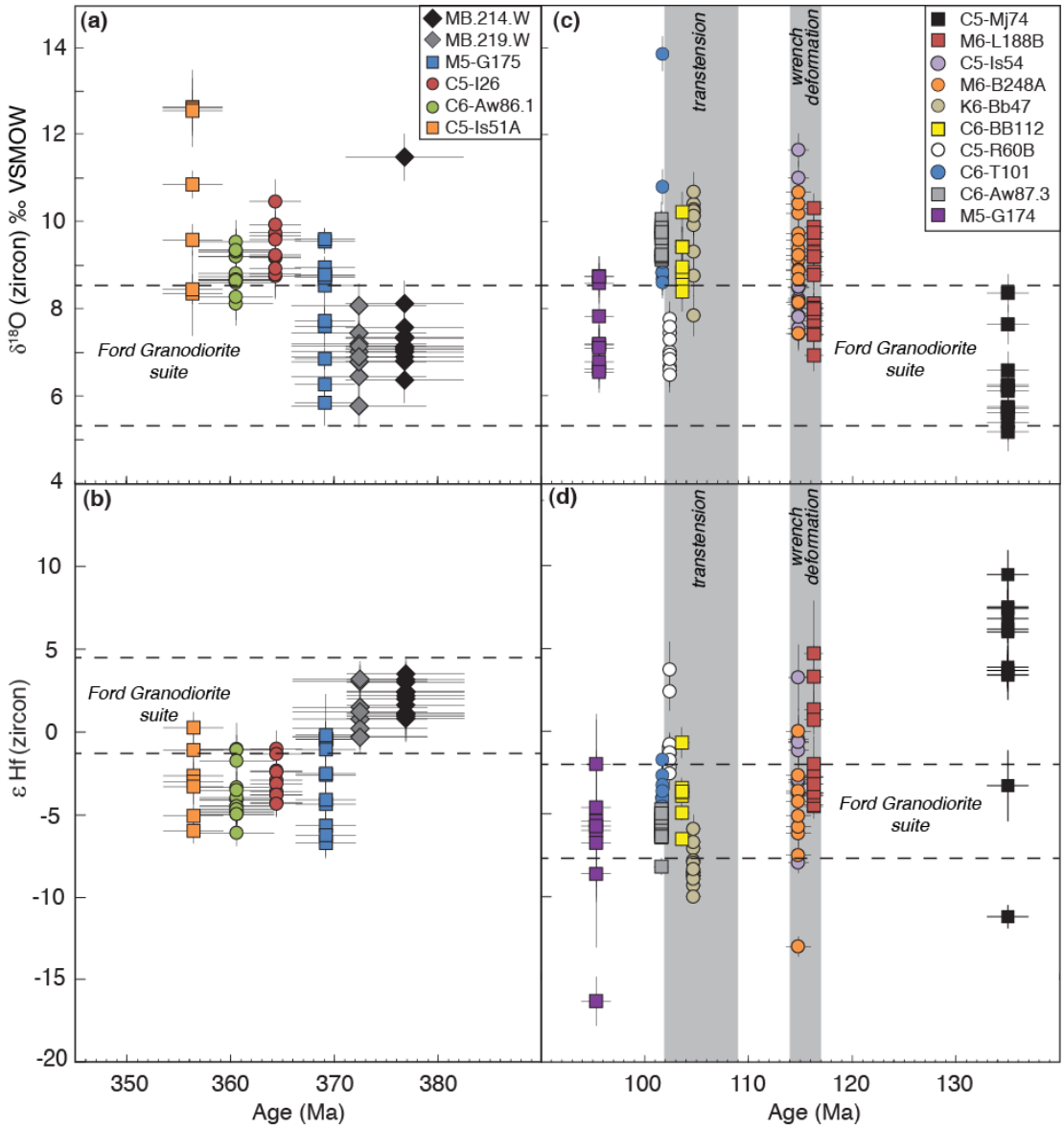

Fig. 8.10. Plots of $\delta^{18}O$ and εHf_t versus $^{206}Pb/^{238}U$ age for Devonian–Carboniferous (a, b) and Cretaceous (c, d) zircon datasets. Uncertainties are ±2σ for $\delta^{18}O$ and εHf_t. $^{206}Pb/^{238}U$ data are from Siddoway and Fanning (2009), Korhonen et al. (2010b), and McFadden et al. (2010a, b), as well as those reported herein.

suggest that a high proportion of the melt from which they crystallized was derived from plutonic rocks, which may include an unexposed juvenile source responsible for the relatively radiogenic εHf_t values in these older Cretaceous granites (Fig. 8.10d), consistent with a deeper source with only a limited Swanson Formation component. On the other hand, granites emplaced during transtension form sub-horizontal sheets (McFadden et al. 2010a, b). The less radiogenic εHf_t and high $\delta^{18}O$ values of zircons in these granites suggest they include a larger proportion of melt derived from the Swanson Formation, consistent with a higher degree of retention of locally-derived melt due to the change from steep to shallow transport channels. Therefore, one explanation for the secular trend away from more juvenile εHf_t and lower $\delta^{18}O$ values in the older Cretaceous granites to less radiogenic εHf_t and high $\delta^{18}O$ values in the younger Cretaceous granites is the change from wrench to transtensional tectonics and the consequent affect on trapping versus escape of melt (McFadden et al. 2010b; cf. Scott and Cooper 2006).

The isotope compositions of granites C5-R60B and M5-G174 are distinctly different from the other Cretaceous granites. C5-R60B was emplaced directly into the South Fosdick detachment zone at 102.4 ± 0.7 Ma and records the most radiogenic εHf_t values obtained from any granite studied and has low $\delta^{18}O$ values (Fig. 8.10c, d). M5-G174, one in an array of leucocratic dykes that crosscut the gneissic foliation in the central Fosdick complex, exhibits low $\delta^{18}O$ values, overlapping those from the Ford Granodiorite suite, and heterogeneous εHf_t values ranging from -16 to -1 with most between -8 and -1 (Fig. 8.10c, d). The appearance of a granites with lower $\delta^{18}O$ zircon values and, in one case, with juvenile εHf_t values within the South Fosdick detachment

zone may record a more radiogenic, mantle-like source brought in by lithospheric thinning induced by the change from wrench to transtensional tectonics in the region (McFadden et al. 2010a, b). A change in chemistry is also documented for older versus younger mafic dykes intruded over approximately the same time interval as the Cretaceous granites (c. 113 to c. 98 Ma, based on LA–ICP–MS U–Pb zircon ages for the dykes; Saito et al. 2012). The mafic dykes have positive εSr and negative to slightly positive εNd values (calculated at 100 Ma), consistent with derivation from a more enriched mantle source that is interpreted to be metasomatized sub-arc mantle that underwent decompression melting during intracontinental extension (Saito et al. 2013).

8.8.6 Comparison with the Antarctic Peninsula, the Tasmanides of Australia and the Western Province of New Zealand

Convergent continental margins represent the primary locus for the production of juvenile crust and its differentiation into stable continental crust (Brown and Rushmer 2006). The Fosdick complex within the Ross province represents a segment of one of the most extensive and long-lived convergent plate margins of the Phanerozoic, the active margin of Gondwana. The landmasses of Australia, New Zealand (Zealandia) and West Antarctica (Fig. 8.1a; Gibson and Ireland 1996) were contiguous during the Lachlan phase (c. 485–340 Ma) of Tasmanide orogenesis.

In eastern Australia, the Tasmanide orogen is attributed to alternating extensional and contractional tectonics associated with a west-dipping subduction zone that migrated oceanward from the Cambrian to the Permian (Foster and Gray 2000; Collins 2002; Gray and Foster 2004; Glen 2005; Cawood 2005; Foster et al. 2005). The Tasmanides of

eastern Australia occupied a relatively inboard position along the active margin from the Devonian to the Cretaceous. Two to three thousand kilometers east (present co-ordinates) of the Tasmanides along the active margin of Gondwana, the Western Province of New Zealand and the Ross province of West Antarctica occupied more outboard and more inboard positions, respectively, and both record Devonian–Carboniferous calc-alkaline and Cretaceous alkaline plutonism (Tulloch et al. 2009, 2011). A protracted period of Silurian to Devonian silicic magmatism is recorded in the Tasmanides with minor episodes of Carboniferous magmatism. In contrast, granites from the Western Province of New Zealand and the Ross province were emplaced over relatively short periods in the Devonian–Carboniferous and the Cretaceous (Adams 1987; Siddoway and Fanning 2009).

Because all three regions record silicic magmatism in the Phanerozoic and they are spatially distributed along the Gondwana margin (Fig. 8.1a), a comparison of the Nd and Hf isotope signatures of granites from the three regions may be used to evaluate variations in the extent of juvenile and evolved crustal sources along and across the strike of the former active margin of Gondwana. Figure 8.11 is an evolution diagram comparing whole rock εNd and zircon εHf data for igneous rocks from the three regions during the Paleozoic and Mesozoic.

Granites from the Ross province show nonradiogenic εHf (Fig. 8.11) and elevated $\delta^{18}O$ isotope signatures (Fig. 8.10a,c) within a setting dominated by crustal reworking, as can be expected for the more inboard location of this province in comparison with the Western Province of New Zealand (Fig. 8.1a). The Western Province of New Zealand

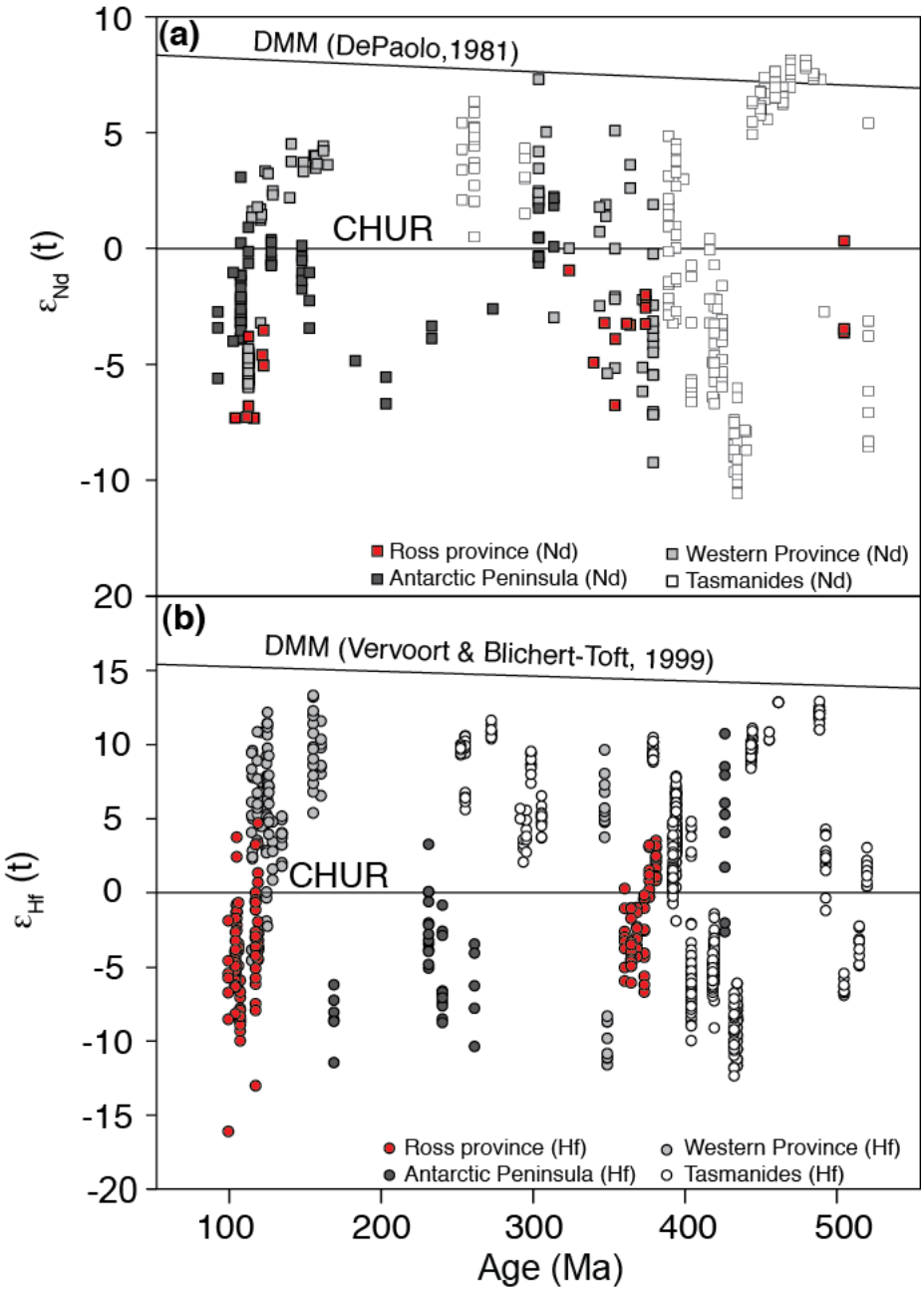

Fig. 8.11. Compilation of whole rock Nd (a) and zircon Hf (b) isotope data for igneous rocks from the eastern Gondwana margin. Sources of Nd data include McCulloch et al. (1987), Pankhurst et al. (1993, 1998), Muir et al. (1995, 1996, 1998), Flowerdew et al. (2005), Kemp et al. (2009), Tulloch et al. (2009, 2011), Korhonen et al. (2010b) and references therein. Hf values are from this study and Flowerdew et al. (2006), Kemp et al. (2007, 2009), Bolhar et al. (2008), Scott et al. (2009), Tulloch et al. (2011) and references therein. Reference evolution lines are for Hf (Vervoort and Blichert-Toft 1999) and Nd (DePaolo 1981).

includes Devonian–Carboniferous and Cretaceous granites with εNd signatures indicative of both a more juvenile source and a source similar to the Ross province granites (Tulloch et al. 2009), although granites with positive εNd and εHf values dominate in strong contrast to those from the Ross province (Fig. 8.11). These isotope signatures are consistent with significant Phanerozoic crustal growth of Zealandia, which was located further outboard in an active continental arc setting, with significant differences in the source and style of contemporaneous magmatism. The zircon Hf isotope and whole-rock Nd signatures in the Western Province reflect partial melts derived from a more juvenile source (e.g. a basaltic underplate) that incorporated lesser volumes of crustal materials than did partial melts in the Ross province.

In contrast to the episodic history of granite emplacement in the Ross province and the Western Province of New Zealand, granites from the Antarctic Peninsula and Thurston Island record protracted magmatism from the Carboniferous through the Cretaceous with relatively nonradiogenic whole rock εNd and zircon εHf signatures. An exception is a Late Silurian orthogneiss from Mount Eissenger on the Antarctica Peninsula, a sample that contains zircon cores with juvenile εHf values (Fig. 8.11; Flowerdew et al. 2006). The Tasmanides contain relatively few Paleozoic igneous rocks of comparable age to those in the Ross province and the Western Province of New Zealand, and Devonian granites in the Tasmanides generally have more juvenile εHf and εNd values than the Devonian–Carboniferous granites in the Ross province.

Hafnium isotope–time trends for igneous rocks from the Tasmanides show several linear arrays that indicate a progression from relatively nonradiogenic to radiogenic sources that are corroborated by whole-rock Nd isotope data (Kemp et al. 2009).

Relatively high $\delta^{18}O$ zircon values from several suites of granites show that they contain a supracrustal component, whereas Hf–O binary mixture modelling suggests assimilation of 40–85 vol.% crustally-derived material into a melts derived from a more juvenile source (Kemp et al. 2006a, b). Thus, the c. 300 million year span of magmatism in the Tasmanides involved both crustal reworking and the addition of new crustal material from juvenile sources. The significant contributions from more juvenile sources are attributed to periodic extension phases punctuated by short intervals of contraction in Paleozoic time (e.g. Collins 2002; Kemp et al. 2009). Only very subtle secular trends over short time intervals (c. 20 myr) are observed in the granites from Ross province, with a possible progression towards a greater contribution of supracrustal material with decreasing age in both the Devonian–Carboniferous and the Cretaceous granites (Fig. 8.10).

These results highlight the significant differences in crustal production and reworking that may occur both along (Antarctic Peninsula, Ross province and the Tasmanides) and across (Ross province and Western Province) a former active continental margin arc system. It is therefore important to evaluate the relative position and tectonic style of different segments of extensive ancient continental margin arc systems in order to test tectonic reconstructions and models of supercontinent evolution.

8.9 Conclusions

Hf and O isotope data from zircon separates from samples from the Fosdick complex are used to investigate the petrogenesis of granites within the complex. Devonian–Carboniferous granites (370–355 Ma) were formed by crustal melting and

mixing of either melts or melts and residual materials derived from the calc-alkaline Ford Granodiorite suite and the metasedimentary rocks of the Swanson Formation. In contrast, most Cretaceous granites (116–115 Ma and 105–96 Ma) require an unexposed more juvenile source in addition to the same crustal sources as the Devonian–Carboniferous granites. These results demonstrate that Devonian–Carboniferous granites in the Fosdick complex essentially record crustal reworking, whereas Cretaceous granites require a component of recent crustal growth to provide the more juvenile source in addition to crustal reworking. The most juvenile εHf_t and the lowest $\delta^{18}O$ zircon values come from the youngest granites emplaced during and after detachment faulting, a possible indication of input from a more radiogenic, mantle-like source. The substantial intrasample variations of Hf and O isotope values in zircon are consistent with the involvement of material derived from isotopically heterogeneous supracrustal and infracrustal sources, as well as a mantle source for the Cretaceous granites, during partial melting and differentiation of the continental crust.

The dominance of crustal reworking suggested by the isotope characteristics of zircons from granites in the Ross province of West Antarctica contrasts with correlative granite suites across the former active margin of Gondwana, such as those of the Western Province of New Zealand, which occupied a more outboard position with respect to the trench, where more radiogenic εHf isotope signatures in zircon from granites suggest derivation from more juvenile sources and less crustal reworking. The Devonian–Carboniferous granites in the Fosdick complex do not exhibit evidence for protracted magmatism nor for the temporal trends in source evolution that are present in granites from the Tasmanides, which were generated in a similar inboard position from the

subduction front during the Devonian–Carboniferous. The results of this study indicate significant variations in the petrogenetic processes producing granite magma along and across the former active margin of Gondwana.

Chapter 9. Conclusions and directions for future research

9.1 Summary

9.1.1 Overview

This dissertation has focused on the roles of high-temperature metamorphism, anatexis and granite petrogenesis that contribute to the chemical differentiation of the continental crust. Chapters 5 and 6 used phase equilibria modeling of open-system melting and accessory mineral dissolution to provide a theoretical framework to interpret high-temperature mineral assemblages and the U–Pb ages of monazite and zircon. Chapters 2–4, and, 7 and 8 reported the results of field mapping, phase equilibria modeling, accessory mineral and garnet geochronology and isotope geochemistry of migmatites and granites in the Fosdick complex in West Antarctica. The insights gained from both the theoretical modeling, and the field-based and laboratory-based components are widely applicable to other migmatite–granite complexes and high-grade metamorphic rocks. Below I summarize the main results and conclusions of each chapter of this dissertation and discuss some potential avenues of future research.

9.1.2 Chapter 2

Linking estimates of metamorphic pressures (P) and temperatures (T) with ages obtained from accessory minerals (t) provides a powerful tool to elucidate the P–T–t evolution of metamorphic rocks during the buildup and collapse of mountain belts. Ages obtained from U–Pb geochronology of accessory minerals are commonly very precise, yet the geological significance of these ages may be ambiguous unless they can be linked to the growth and consumption of major metamorphic minerals that record the P–T

conditions. This chapter reported the results of an integrated approach using Lu–Hf garnet geochronology, *in situ* U–Pb monazite geochronology and phase equilibria modeling to unravel the *P–T–t* evolution of polyphase migmatitic paragneisses and orthogneisses from the Fosdick migmatite–granite complex in West Antarctica. Lu–Hf garnet geochronology dates the peak of metamorphism at *c.* 116–111 Ma and Y-enriched domains in monazite record garnet breakdown to cordierite and biotite in the presence of melt during the initial stages of decompression and cooling at *c.* 106–100 Ma. This time frame coincides with the exhumation of high-grade rocks in the Western Province of New Zealand and indicates that regional extension preceded the final breakup of Zealandia from West Antarctica by *c.* 25 Myr.

9.1.3 Chapter 3

The compositions of primary melts generated through anatexis of the deep crust have been determined by experimental studies, from measurements of former melt inclusions in migmatites and granulites, and using phase equilibria modeling. However, the composition of melt extracted from the deep crust may differ from these primary melt compositions due to processes associated with melt–residuum separation and that occur during transport, including: peritectic mineral entrainment, the variable dissolution of accessory minerals, and fractional crystallization. In this chapter, the microstructures and geochemistry of Cretaceous anatectic granites from the Fosdick migmatite–granite complex were used to argue that they are cumulates rather than primary melt compositions. The complementary enriched liquid was extracted during filter pressing

associated with exhumation and doming of the complex and is expected to contain elevated concentrations of incompatible elements.

9.1.4 Chapter 4

The history of crustal evolution and reworking during Paleozoic subduction along the former East Gondwanan plate margin was investigated using age and isotope characteristics of zircons from Cambrian–Ordovician sedimentary rocks, and whole-rock and zircon geochemistry from the Devonian–Carboniferous Ford Granodiorite suite and associated granites from the Fosdick migmatite–granite complex in western Marie Byrd Land. Detrital zircons yielded U–Pb ages and Hf isotope compositions consistent with derivation from a Neoproterozoic–Cambrian source associated with the Ross Orogen and from a Mesoproterozoic source that may represent a Grenville-aged orogenic belt that lies beneath the East Antarctic ice sheet.

The Swanson Formation was intruded by the calc-alkaline Ford Granodiorite suite at *c.* 375–345 Ma that was associated with widespread active arc magmatism along the East Gondwana margin. Hf and O isotope values of zircon from the Ford Granodiorite suite and coeval granites within the Fosdick migmatite–granite complex are consistent with a greater proportion of crustal reworking to crustal growth. Younger samples of the Ford Granodiorite suite yield zircon Hf and O isotope values that suggest involvement of a larger (meta-) sedimentary component compared to the older samples. By contrast, contemporaneous granites in the Western Province of New Zealand and the Tasmanides yield more juvenile isotope values, consistent with a greater proportion of crustal growth, and temporal trends towards more juvenile isotope values over time. These differences

are interpreted to represent an along-arc change from the typical extensional accretionary mode in eastern Australia to a neutral or an advancing mode in West Antarctica, and to an across-arc difference in distance from the trench between West Antarctica and the Western Province of New Zealand.

9.1.5 Chapter 5

U–Pb geochronology of zircon and monazite in high-grade metamorphic rocks can yield highly precise ages, but our ability to tie these ages to the timing of tectonometamorphic processes operating in the deep crust is hindered by our limited understanding of the behavior of these minerals during crustal melting. In this chapter, the stability of these minerals during suprasolidus metamorphism was evaluated using phase equilibria modeling of open-system melting coupled with experimental data on zircon and monazite solubility. During heating above the solidus, zircon and monazite are expected to be partially to completely consumed up to peak *P–T*, the final outcome depending on the bulk rock compositions of Zr and LREE and rates of melting versus melt segregation and extraction. In melanosome, new zircon and monazite growth is expected to be limited during cooling from peak *P–T* to the solidus. By contrast, leucosome and anatectic granites in migmatites are predicted to contain newly formed zircon and monazite.

9.1.6 Chapter 6

The episodic drainage of melt during prograde metamorphism above the solidus reduces the fertility of source rocks for the remainder of the metamorphic evolution and

during any later overprinting orogenic event. Anatexis of progressively more residual rocks is not expected to generate the quantities of melt or the drastic decrease in density during decompression that is suggested by some tectonic models of migmatite–gneiss dome exhumation. Melt transfer through the suprasolidus crust and melt accumulation at shallow levels in the anatectic zone are postulated to be more important factors than decompression melting during the exhumation of migmatite–gneiss domes and metamorphic core complexes.

9.1.7 Chapter 7

The chemical differentiation of the continental crust and the preservation of high-grade mineral assemblages in migmatites and granulites require melt extraction from the deep crust to shallower crustal levels. For crustal differentiation to be effective, an interconnected melt-flow network must be activated in the deeper suprasolidus crust to enable the extraction and ascent of anatectic melt to shallower subsolidus crust where it may accumulate in plutons. This chapter evaluated the spatial arrangement of the initial sites of melt segregation and extraction in migmatitic paragneiss and orthogneiss using measurements of leucosome width and spacing collected along one-dimensional transects in the Fosdick migmatite–granite complex. The results demonstrate that the thickness and spacing of leucosomes are scale-invariant and part of a self-organized critical system, and the interaction of this critical system with the anisotropy in the host rocks accounts for the three-dimensional distribution of leucosome in high-grade metamorphic rocks.

9.1.8 Chapter 8

The relative proportions of crustal growth versus crustal reworking at active convergent margins have implications for the long-term stability and evolution of the continental crust. In this chapter, U–Pb and Hf and O isotope ratios of zircon from Devonian–Carboniferous and Cretaceous granites in West Antarctica are compared with those from correlative granite suites along and across the former active margin of East Gondwana. Granites from West Antarctica record a larger proportion of crustal reworking versus crustal growth when compared with correlative granite suites from the Tasmanides of East Australia, the Western Province of New Zealand and the Antarctic Peninsula. The results highlight prominent arc-parallel and arc-normal variations in the mechanisms and timing of crustal reworking versus crustal growth along the former active margin of East Gondwana.

9.2 Some outstanding issues and directions for future work

9.2.1 The P–T–t evolution of high-temperature metamorphic rocks

Unraveling the *P–T–t* history of high-grade metamorphic terrains requires an integrated approach combining phase equilibria modeling and detailed geochronology. Complications in constraining *P–T* conditions of formerly suprasolidus rocks include open system behavior during partial melting (e.g. Brown and Korhonen, 2009) and the diffusional resetting of mineral chemistry (e.g. Caddick et al., 2010). Open system behavior such as melt loss limits the use of pseudosections constructed for residual bulk chemical compositions to constraining the solidus phase assemblages and perhaps portions of the high-temperature subsolidus retrograde *P–T* path. Diffusional resetting of

mineral chemistry at high temperature makes it difficult to obtain reliable estimates of peak *P–T* conditions using conventional thermobarometry (e.g. Frost and Chacko, 1989) or mineral composition isopleths in pseudosections (e.g. Korhonen et al., 2012). To constrain the prograde path and melt loss history of such rocks, melt reintegration may yield a plausible protolith composition (Chapter 2). Finally, modeling of suprasolidus metamorphic assemblages requires careful consideration of the concentration of H_2O (e.g. White et al., 2004) and ratio of ferric to ferrous iron (Diener and Powell, 2010; Boger et al., 2012) in the bulk composition. The release of a new internally consistent dataset (Holland and Powell, 2011) and the continuing improvement of mineral activity–composition models (White et al., 2014a, b) will provide a new level of sophistication in phase equilibria modeling in more complex chemical systems and for a wider variety of rock types. In particular, the ongoing development of an activity–composition model for melt appropriate for use with mafic compositions offers fruitful avenues for research into the generation of Archean tonalite–trondhjemite–granodiorite suites.

Linking the ages of accessory minerals to the *P–T* path experienced by high-temperature metamorphic rocks provides a potentially powerful tool to constrain the timescales of tectonometamorphic processes operating in the deep crust. However, our understanding of the behavior of zircon and monazite during partial melting is still limited (Kelsey et al., 2008; Chapter 5). Complex zoning patterns in monazite make linking the ages obtained from different chemical zones to points or segments along *P–T* paths difficult (Gibson et al., 2004; Reno et al., 2011; Korhonen et al., 2012). As pointed out by Catlos (2013), the Y contents of monazite may show clear correlation with ages in

some cases but not in others and caution needs to be exercised when inferring distinct tectonic events and crystallization environments from chemistry alone.

Monazite from migmatites in the Fosdick complex show a variety of zoning patterns, but in general, ages obtained from Y-enriched rims can be linked to garnet breakdown during decompression based on: microstructural evidence of garnet breakdown, phase equilibria modeling that predicts garnet breakdown in the presence of melt, and the concomitant crystallization of associated anatectic granites. For these migmatites, my geological interpretation of the Y-enriched rims in monazite is consistent with the geological evolution of the complex. However, Y-enriched rims in monazite from other rocks may not related to garnet breakdown during decompression, but may, for example, relate to the breakdown of allanite and xenotime during subsolidus prograde growth (e.g. Giére et al., 2011). Interpreting the geological significance of Y-enriched and Y-depleted rims in monazite needs to be done on a case-by-case basis while considering the range of possible sources of Y available in metamorphic rocks (e.g. Kohn and Malloy, 2004; Spear and Pyle, 2010; Kelly et al., 2012).

9.2.2 Granite petrogenesis

Hf and O isotope measurements in zircon have provided new insights into the petrogenesis of granites over the last decade. For example, Kemp et al. (2007) report Hf and O isotope values from the classic 'I-type' granites of the Lachlan Fold Belt and suggest that their petrogenesis involved a significant metasedimentary component. These authors propose a model whereby I-type granites are the product of juvenile mantle-derived magma being emplaced into the lower crust and reworking by partial melting

metasedimentary material in a deep crustal hot zone (e.g. Annen et al., 2006). The resulting granitic magma is a hybrid comprising both crustal and mantle components. By contrast, Clemens et al. (2011) posit that I-type granites are purely crustal in origin generated during anatexis of intermediate source rocks with their final chemical compositions being controlled by the entrainment and dissolution of peritectic minerals.

For Cretaceous granites exposed in the Ford Ranges outside the Fosdick complex, Hf and O isotope values of two samples are consistent with derivation solely from the Devonian–Carboniferous Ford Granodiorite suite (Chapter 3). However, the Hf and O isotope values of zircon and whole-rock geochemistry are also compatible with a juvenile mantle-derived magma mixing with the Swanson Formation. Distinguishing between these two models is complicated by the significant geochemical heterogeneity of the potential source rocks (Chapters 2, 8).

An important aspect of these contrasting models for I-type granite genesis is the extent that isotope heterogeneity of granites reflects that of their sources. While this has been explored for S-type granites (Villaros et al., 2012), a detailed assessment of the heterogeneity of intermediate sources (e.g. Clemens et al., 2011) of I-type granites has yet to be conducted. Differentiating between the two models described above for the origin of I-type granites is of critical importance for constraining models of the growth of the continental crust (e.g. Dhuime et al., 2012; Cawood et al., 2013).

Appendix A.

Table A.1 Element concentrations of garnet (ppm)

Element	Mg	Si	P	Ca	Ti	Mn	Fe	Fe	Y	Zr	La	Ce	Pr	Nd	Sm	Sm	Eu	Eu	Gd	Gd	Tb	Dy	Dy	Ho	Er	Er	Tm	Tm	Yb	Yb	Lu	Lu	Hf	Hf
Mass	24	29	31	43	49	55	56	57	89	90	139	140	141	146	147	149	151	153	155	157	159	161	163	165	166	167	169	172	173	175	178	180
10CY-021-G1-1.d	30710	1.72E+05	n.d.	6790	27.0	24.1	8170	2.06E+05	2954.8	4	bdl	bdl	bdl	0.091	0.113	0.41	0.44	0.135	0.52	0.260	4.33	4.39	2.56	31.1	31.0	8.7	27.7	28.6	3.63	24.2	24.6	2.98	0.08	0.05
10CY-021-G1-2.d	30710	1.72E+05	n.d.	6790	25.6	21.6	8170	1.72E+05	2497.7	3	bdl	bdl	bdl	0.111	0.103	0.41	0.41	0.098	0.59	0.092	4.40	4.47	2.70	29.6	29.1	9.1	27.5	28.6	3.23	20.1	24.1	4.09	0.06	0.06
10CY-021-G1-3.d	30710	1.72E+05	n.d.	6820	25.9	20.9	8270	1.70E+05	2743.3	3	bdl	bdl	bdl	0.015	0.010	0.40	0.34	0.066	0.59	0.092	3.74	3.78	2.27	30.4	32.2	9.1	34.0	33.2	5.40	34.6	34.9	5.02	0.05	0.05
10CY-021-G1-4.d	30590	1.69E+05	n.d.	6730	27.2	23.6	8240	2.13E+05	2952.5	3	bdl	bdl	bdl	0.078	0.094	0.41	0.58	0.28	0.109	3.74	3.74	2.00	29.3	29.2	9.1	31.6	30.4	4.90	32.3	31.8	4.97	0.05	0.03	0.06
10CY-021-G1-5.d	30790	1.71E+05	n.d.	6910	27.2	33.0	8360	2.16E+05	2954.5	3	bdl	bdl	0.00	0.074	0.096	0.40	0.43	0.111	0.43	0.093	3.78	3.69	2.02	27.9	28.1	8.7	29.0	29.0	4.68	31.7	32.0	4.65	0.01	0.09
10CY-021-G1-6.d	30740	1.70E+05	n.d.	6910	25.6	35.4	8160	2.13E+05	2952.7	5	bdl	bdl	0.00	bdl	0.090	0.39	0.49	0.125	0.46	0.101	3.28	3.42	1.95	26.5	28.6	8.6	29.2	29.1	4.54	30.0	29.6	4.32	0.11	0.10
10CY-021-G2-1.d	28960	1.69E+05	n.d.	6740	25.6	18.5	10970	1.75E+05	3667.5	12	bdl	bdl	bdl	0.044	bdl	0.30	0.40	0.054	0.42	0.022	4.98	5.08	2.92	40.7	41.2	14.3	49.7	49.6	7.64	52.0	50.5	6.82	0.31	0.20
10CY-021-G2-2.d	29270	1.69E+05	n.d.	6780	27.0	20.5	10990	2.10E+05	4171.3	13	bdl	bdl	bdl	0.047	0.053	0.27	0.39	0.008	0.38	0.041	4.85	5.58	3.14	45.3	46.1	15.6	55.2	55.7	8.62	59.5	56.6	8.28	0.27	0.25
10CY-021-G2-3.d	29130	1.68E+05	n.d.	6180	6850	29.1	25.5	11000	4456	12	bdl	bdl	0.007	0.015	0.011	0.41	0.27	0.053	0.40	0.062	4.65	4.88	3.45	50.9	49.0	17.1	59.5	60.2	9.74	63.2	67.4	9.19	0.25	0.28
10CY-021-G2-4.d	30310	1.70E+05	n.d.	7300	31.7	28.1	11300	2.20E+05	4719	15	bdl	bdl	bdl	0.013	0.010	0.63	0.55	0.056	0.63	0.062	6.54	5.94	3.71	54.7	54.8	18.9	67.5	68.6	10.39	69.9	70.4	10.13	0.29	0.25
10CY-021-G2-5.d	29960	1.68E+05	n.d.	7100	7030	32.1	28.5	11100	4812	15	bdl	bdl	0.002	bdl	0.010	0.36	0.50	0.041	0.52	0.044	6.16	6.09	3.80	57.7	55.7	20.2	68.7	67.1	10.99	73.3	75.1	10.79	0.22	0.29
10CY-021-G2-6.d	29850	1.68E+05	n.d.	6700	7000	31.8	29.0	11160	4945	15	bdl	bdl	bdl	bdl	0.060	0.57	0.30	0.042	0.50	0.032	6.32	6.02	3.90	58.2	56.9	20.9	71.4	71.9	11.06	75.4	77.2	10.83	0.24	0.29
10CY-021-G2-7.d	29760	1.72E+05	n.d.	6660	7120	31.9	30.0	11240	5133	15	bdl	bdl	bdl	0.013	0.008	0.61	0.53	0.051	0.68	0.048	6.57	6.42	3.93	60.1	61.2	21.2	77.3	75.6	11.92	80.4	81.2	11.82	0.27	0.26
10CY-021-G2-8.d	29560	1.69E+05	n.d.	6740	6950	31.8	28.4	11090	5316	15	bdl	bdl	bdl	0.026	bdl	0.49	0.45	0.048	0.37	0.043	6.22	6.54	4.05	62.4	60.3	21.2	79.6	80.9	12.47	87.5	88.6	12.70	0.34	0.26
Y1-IG062-G1-1.d	19130	1.71E+05	n.d.	6780	7400	33.0	27.3	23160	7760	8	bdl	bdl	0.008	0.004	0.053	0.26	1.28	0.027	1.10	0.069	12.00	11.63	6.36	83.5	85.5	29.2	119.0	117.3	21.86	177.4	180.4	31.02	0.26	0.27
Y1-IG062-G1-10.d	23540	1.69E+05	n.d.	7340	7700	25.9	17.6	16350	4206	1	bdl	bdl	bdl	0.034	0.023	0.47	0.46	0.039	0.57	0.026	3.88	4.10	3.20	47.3	48.3	16.6	62.8	63.7	12.30	100.0	101.6	14.57	0.01	0.03
Y1-IG062-G1-11.d	23320	1.71E+05	n.d.	7310	7710	24.3	18.1	17510	4062	2	bdl	bdl	bdl	0.069	0.046	0.22	bdl	bdl	0.36	0.003	3.83	4.18	2.93	43.6	43.7	15.7	66.3	66.8	13.65	116.6	118.5	17.78	0.02	0.09
Y1-IG062-G1-12.d	21400	1.68E+05	n.d.	7510	7200	24.2	16.2	19430	3852	2	bdl	bdl	bdl	bdl	0.063	0.33	0.28	0.008	0.56	0.052	3.65	3.08	2.46	40.4	39.5	15.4	67.5	67.0	14.72	138.1	140.3	24.23	0.02	0.02
Y1-IG062-G1-13.d	20490	1.72E+05	n.d.	6630	7040	26.0	20.7	22470	5788	2	bdl	bdl	0.002	bdl	0.033	0.45	0.46	0.021	0.54	0.028	5.71	6.02	3.71	55.8	56.7	21.0	88.7	88.1	16.89	136.7	139.4	21.92	0.09	0.05
Y1-IG062-G2-1.d	30170	1.69E+05	n.d.	7050	7230	31.2	30.0	20550	5034	4	bdl	bdl	0.003	bdl	0.070	0.24	0.43	0.070	0.49	bdl	4.40	4.49	3.07	48.3	48.3	18.1	75.6	75.5	14.77	118.4	118.3	19.53	0.12	0.10
Y1-IG062-G1-3.d	22310	1.68E+05	n.d.	7170	7590	27.4	24.4	18040	4467	2	0.003	bdl	bdl	0.071	0.051	0.24	0.52	0.009	0.51	0.032	3.91	5.09	2.77	44.7	44.0	15.6	65.0	66.4	13.93	124.5	120.0	19.94	0.02	0.03
Y1-IG062-G1-4.d	24010	1.71E+05	n.d.	7380	7930	26.6	18.4	16990	4149	2	bdl	bdl	0.002	0.005	bdl	0.070	0.19	0.36	0.013	0.38	0.035	4.99	4.59	2.93	44.9	44.6	16.8	72.9	73.8	16.01	141.3	139.2	24.20	0.01	0.02
Y1-IG062-G1-5.d	25230	1.69E+05	n.d.	7480	7930	22.8	14.5	16280	4007	2	bdl	bdl	bdl	0.034	0.026	0.31	0.68	bdl	0.45	0.021	3.89	4.09	2.89	43.0	42.6	15.4	62.3	64.6	12.67	102.5	102.9	15.24	0.01	0.03
Y1-IG062-G1-6.d	26340	1.70E+05	n.d.	7450	7960	26.4	16.5	16520	4526	2	bdl	bdl	bdl	0.004	0.086	0.024	0.34	0.25	0.058	0.033	5.16	4.61	3.15	50.5	51.3	17.6	66.1	70.9	13.67	120.7	113.8	18.47	0.04	0.01
Y1-IG062-G1-7.d	26330	1.70E+05	n.d.	7760	7920	28.5	23.0	16420	4193	5	bdl	bdl	bdl	bdl	0.061	0.47	0.34	0.019	0.35	bdl	3.99	3.96	3.03	48.6	49.3	16.2	59.9	61.2	10.64	90.4	86.5	12.88	0.29	0.17
Y1-IG062-G1-8.d	26870	1.73E+05	n.d.	7540	8120	29.9	23.0	16700	4817	2	bdl	bdl	bdl	0.056	0.051	0.40	0.016	0.034	0.22	0.019	4.96	3.71	3.02	44.6	42.4	15.9	64.7	65.6	13.27	120.6	117.6	18.87	0.03	0.07
Y1-IG062-G1-9.d	25910	1.70E+05	n.d.	7240	7610	27.6	20.2	15990	4508	2	bdl	bdl	bdl	bdl	0.054	0.54	0.54	0.004	0.51	0.011	5.03	4.83	3.38	52.5	53.4	17.3	63.8	65.2	11.89	100.5	100.3	15.08	0.04	bdl
Y1-IG062-G2-1.d	16350	1.72E+05	n.d.	6720	6960	31.2	32.8	24500	5920	3	bdl	bdl	bdl	0.054	0.200	0.59	0.51	0.050	0.66	0.008	5.11	6.14	3.69	57.7	57.1	21.2	87.7	91.1	17.15	141.2	142.0	22.28	0.10	0.03
Y1-IG062-G2-2.d	20830	1.69E+05	n.d.	6570	6920	30.4	27.6	18320	4633	1	bdl	bdl	bdl	0.066	0.054	0.38	0.67	0.025	0.56	0.027	5.28	4.49	3.33	49.8	48.4	17.7	69.8	70.9	14.07	125.4	124.6	19.39	bdl	0.01
Y1-IG062-G2-3.d	23250	1.72E+05	n.d.	7250	7400	30.3	27.4	17330	5177	2	bdl	bdl	bdl	0.016	0.022	0.36	0.57	0.033	0.59	0.022	5.16	5.91	3.74	54.8	52.7	19.8	80.6	81.8	15.80	130.3	133.0	19.54	0.02	0.02
Y1-IG062-G2-4.d	23520	1.72E+05	n.d.	7650	7990	28.6	24.1	16990	5754	9	bdl	bdl	bdl	bdl	0.044	0.46	0.40	0.017	0.39	0.011	6.07	5.14	3.84	63.2	63.5	24.3	89.4	90.0	14.79	103.7	108.5	14.48	0.31	0.24
Y1-IG062-G2-5.d	23360	1.70E+05	n.d.	7060	7580	27.3	21.3	17120	5198	2	bdl	bdl	bdl	0.138	0.17	0.48	0.031	0.59	0.021	5.54	4.40	3.44	53.7	56.2	21.2	78.8	80.0	13.86	107.9	106.2	14.03	0.07	0.09
Y1-IG062-G2-6.d	22360	1.69E+05	n.d.	6980	7270	28.9	22.0	17520	4472	2	0.017	bdl	0.024	0.021	0.150	0.80	0.42	0.015	0.54	0.057	5.54	4.76	3.16	49.8	46.1	18.1	73.0	71.8	14.22	116.4	118.6	18.13	0.01	0.00
Y1-IG062-G2-7.d	21340	1.68E+05	n.d.	6730	7520	27.9	24.4	20060	4243	3	bdl	bdl	bdl	0.045	0.034	0.23	0.035	0.53	0.017	4.35	4.78	3.02	44.6	42.4	15.9	64.7	65.6	13.27	120.6	117.6	18.87	0.03	0.07
Y1-IG062-G2-8.d	19080	1.70E+05	n.d.	6280	6940	25.9	21.5	22320	5320	3	bdl	bdl	0.006	0.005	bdl	0.022	0.42	0.49	0.027	0.47	0.040	4.38	4.90	3.15	48.4	51.8	19.2	81.1	81.5	15.62	130.6	126.0	20.29	bdl	0.04
K6-A24-G1-10.d	17910	1.69E+05	n.d.	6840	7460	26.0	18.9	11680	3180	3	bdl	bdl	bdl	0.019	0.013	0.51	0.24	0.063	0.33	0.024	3.86	3.42	2.28	31.8	32.6	10.8	36.1	38.3	5.83	36.6	35.5	4.65	0.06	0.06
K6-A24-G1-11.d	22970	1.69E+05	n.d.	6480	6960	28.7	29.2	10610	4122	14	bdl	bdl	bdl	0.034	0.032	0.40	0.50	0.087	0.39	0.069	3.97	4.22	2.74	42.8	41.3	16.4	64.6	63.5	10.64	80.3	78.0	11.61	0.19	0.28
K6-A24-G1-12.d	22980	1.71E+05	n.d.	6740	7100	28.0	22.9	11550	4295	13	bdl	bdl	bdl	bdl	0.031	0.012	0.25	0.124	0.59	0.025	0.063	3.70	3.66	2.32	33.0	34.0	12.6	50.2	49.8	8.93	61.6	57.8	8.25	0.37	0.25
K6-A24-G1-13.d	24470	1.70E+05	n.d.	6840	7220	29.3	26.1	9450	3725	14	bdl	bdl	bdl	bdl	bdl	bdl	0.28	0.026	0.28	0.070	0.26	0.054	2.78	3.02	2.28	37.6	38.5	15.3	65.5	70.4	14.13	106.3	96.6	16.72	0.43	0.35
K6-A24-G1-2.d	20170	1.69E+05	n.d.	6990	7350	31.5	31.7	10230	4456	4	bdl	bdl	bdl	0.040	0.035	0.15	0.17	0.030	0.20	0.044	3.02	2.83	1.93	30.2	29.8	10.3	35.7	34.8	5.64	36.1	34.8	4.81	0.12	0.10
K6-A24-G1-3.d	21790	1.69E+05	n.d.	6930	7240	27.8	22.7	9830	4288	4	bdl	bdl	bdl	bdl	0.022	0.30	0.26	0.039	0.33	0.076	2.94	3.05	1.94	27.3	29.1	9.6	33.1	34.6	5.13	33.1	33.8	4.27	0.03	0.05
K6-A24-G1-4.d	22980	1.71E+05	n.d.	6560	7080	25.1	22.3	9470	4293	7	bdl	bdl	bdl	0.048	bdl	0.19	0.25	0.062	0.31	0.075	2.86	3.05	2.05	29.9	30.0	9.9	37.0	35.1	5.31	34.1	33.9	4.02	0.12	0.20
K6-A24-G1-5.d	23500	1.71E+05	n.d.	6720	7070	26.9	19.7	9550	4293	10	bdl	bdl	bdl	bdl	0.055	0.20	0.30	0.076	0.40	0.057	3.86	3.83	2.22	35.4	34.6	12.6	46.7	47.1	7.53	48.7	48.1	6.08	0.16	0.21
K6-A24-G1-6.d	19200	1.70E+05	n.d.	6600	7040	27.5	18.8	12930	3716	13	bdl	bdl	bdl	bdl	0.024	0.21	0.34	0.073	0.36	0.028	4.33	3.57	2.70	38.9	39.6	14.3	52.9	54.2	8.20	55.0	53.1	7.27	0.21	0.24
K6-A24-G1-7.d	20580	1.69E+05	n.d.	6770	6830	23.8	16.7	10950	3641	13	bdl	bdl	bdl	bdl	bdl	0.29	0.28	0.036	0.33	0.061	3.66	3.75	2.41	38.4	38.1	14.4	54.7	57.0	9.41	59.7	61.6	8.06	0.20	0.24
K6-A24-G1-8.d	22930	1.67E+05	n.d.	6240	6790	27.0	23.1	9720	3779	13	bdl	bdl	0.002	bdl	0.061	0.011	0.29	0.20	0.117	0.36	0.36	0.120	3.43	3.33	2.42	38.3	39.5	15.2	58.7	58.8	9.81	69.0	67.1	9.30	0.22	0.25
K6-A24-G1-9.d	23740	1.71E+05	n.d.	6660	7060	25.6	17.2	9480	3833	13	bdl	bdl	bdl	bdl	0.016	bdl	0.22	0.29	0.082	0.35	0.35	0.065	3.22	3.65	2.36	39.3	38.6	14.8	59.3	58.6	10.10	71.6	74.2	10.37	0.25	0.48
K6-A24-G2-1.d	26160	1.70E+05	n.d.	7090	7150	23.0	14.8	9330	3150	3	bdl	bdl	bdl	bdl	bdl	0.35	0.45	0.063	0.43	0.047	4.42	4.21	2.60	33.0	33.5	11.4	39.7	37.6	6.18	39.2	40.0	5.49	0.02	0.04
K6-A24-G2-2.d	26430	1.70E+05	n.d.	7090	7250	25.7	17.6	9250	3233	5	bdl	bdl	0.002	0.057	0.031	0.22	0.21	0.075	0.26	0.091	3.49	3.19	2.18	32.1	31.7	10.7	39.2	39.3	6.24	38.9	37.8	5.12	0.08	0.12
K6-A24-G2-3.d	25850	1.70E+05	n.d.	6850	7120	28.3	22.8	9200	3543	12	bdl	bdl	bdl	bdl	0.017	0.029	0.41	0.081	0.53	0.061	3.80	3.35	2.26	34.4	35.1	13.3	51.7	50.0	8.81	64.1	60.9	8.38	0.20	0.34
K6-A24-G2-4.d	25810	1.71E+05	n.d.	6980	7060	29.2	25.3	10400	3636	15	bdl	bdl	bdl	bdl	bdl	0.011	0.14	0.071	0.34	0.057	3.71	3.58	2.44	34.7	37.9	14.1	55.8	55.0	9.75	66.7	65.8	8.75	0.36	0.31
K6-A24-G2-5.d	26830	1.71E+05	n.d.	6620	7110	29.2	29.1	9370	3737	15	bdl	bdl	bdl	bdl	0.039	0.28	0.38	0.066	0.37	0.071	3.55	3.90	2.31	38.6	38.5	14.6	59.7	56.3	9.87	67.4	65.7	9.02	0.31	0.38
K6-A24-G2-6.d	26460	1.70E+05	n.d.	6920	7210	31.2	28.5	9300	3845	16	bdl	bdl	bdl	bdl	0.046	0.34	0.43	0.047	0.49	0.072	4.12	4.31	2.46	40.1	40.0	15.4	62.5	58.1	10.55	70.8	72.3	9.70	0.27	0.32
K6-A24-G2-7.d	26820	1.69E+05	n.d.	7010	7070	30.5	25.6	9320	3897	15	bdl	bdl	bdl	bdl	bdl	0.44	0.27	0.093	0.36	0.077	4.04	4.19	2.65	39.4	40.0	16.4	65.5	64.4	11.40	78.1	79.4	10.83	0.25	0.33
K6-A24-G2-8.d	26910	1.71E+05	n.d.	7020	7310	30.9	28.5	9330	4261	14	bdl	bdl	bdl	bdl	bdl	0.49	0.38	0.131	0.33	0.035	3.48	4.54	2.61	40.4	39.4	15.6	64.9	63.8	11.47	82.2	81.1	11.66	0.33	0.27
K6-A24-G2-9.d	26880	1.70E+05	n.d.	7040	7260	27.7	21.4	9480	3713	15	bdl	bdl	bdl	bdl	bdl	0.31	0.31	0.112	0.28	0.086	3.74	3.72	2.36	36.1	39.6	15.1	63.5	61.0	11.11	80.9	77.8	11.42	0.42	0.35
K6-B26-G1-1.d	21050	1.72E+05	n.d.	6300	6510	50.4	57.3	13140	3824	12	bdl	bdl	0.006	bdl	0.030	0.183	0.64	0.55	0.036	0.83	0.063	3.94	3.59	1.30	11.1	10.7	2.0	5.4	5.4	0.80	4.9	5.8	0.75	0.29	0.17
K6-B26-G1-10.d	24090	1.74E+05	n.d.	5060	5160	31.8	32.7	12790	70.0	8	bdl	bdl	bdl	bdl	0.027	0.009	0.11	0.21	0.017	0.23	0.029	1.80	1.91	0.98	10.4	9.9	2.3	6.6	7.0	0.90	5.3	5.5	0.71	0.17	0.21
K6-B26-G1-11.d	24010	1.71E+05	n.d.	5120	5370	34.4	35.3	12810	79.6	9	bdl	bdl	0.002	bdl	0.026	0.20	0.09	0.010	0.26	0.026	2.12	1.76	0.94	10.6	10.6	2.8	7.7	7.6	1.09	6.9	6.6	0.76	0.29	0.19
K6-B26-G1-12.d	23780	1.70E+05	n.d.	5560	5530	32.6	36.5	12630	86.3	11	bdl	bdl	bdl	bdl	0.037	0.082	0.22	0.23	0.057	0.26	0.036	1.85	1.86	1.00	11.0	11.4	3.1	9.2	9.3	1.37	7.9	7.8	1.05	0.29	0.24
K6-B26-G1-13.d	23640	1.72E+05	n.d.	5780	6150	40.0	43.7	12920	117.4	5	bdl	bdl	0.003	bdl	0.170	0.042	0.57	0.33	0.046	0.57	0.058	3.15	3.10	1.30	15.4	15.8	3.7	10.0	10.8	1.38	8.8	8.2	0.85	0.11	0.13
K6-B26-G1-14.d	23110	1.70E+05	n.d.	5340	5410	31.7	35.4	12640	91.1	4	bdl	bdl	bdl	bdl	0.013	0.026	0.46	0.27	0.024	0.44	0.014	2.39	2.52	1.23	12.3	12.1	2.8	8.1	7.6	1.04	5.3	5.3	0.55	0.07	0.07
K6-B26-G1-15.d	22360	1.70E+05	n.d.	5680	5690	42.2	52.8	13290	118.9	6	bdl	bdl	bdl	bdl	0.001	0.150	0.044	0.42	0.59	0.014	0.49	0.032	2.89	2.52	1.37	14.7	15.5	3.9	11.8	11.7	1.78	12.3	12.3	1.36	0.07	0.05
K6-B26-G1-2.d	22960	1.71E+05	n.d.	6000	6090	52.6	63.5	12570	85.2	10	0.017	bdl	0.141	0.008	0.148	0.230	0.50	0.44	0.033	0.65	0.061	3.50	3.88	1.31	10.5	9.9	1.6	4.2	4.2	0.51	3.8	4.4	0.53	0.20	0.16
K6-B26-G1-3.d	22930	1.69E+05	n.d.	5090	5410	28.7	29.8	12840	85.3	4	bdl	bdl	bdl	bdl	0.006	0.042	0.045	0.23	0.020	0.34	0.006	2.03	2.33	1.00	11.1	12.3	2.7	8.1	7.6	1.12	8.0	7.8	1.01	0.10	0.12
K6-B26-G1-4.d	23350	1.71E+05	n.d.	5430	5340	28.0	27.2	13090	65.1	6	bdl	bdl	0.004	bdl	0.029	0.065	0.21	0.21	0.007	0.23	0.012	1.72	1.90	0.91	9.5	9.9	2.1	5.5	5.2	0.71	4.3	4.6	0.45	0.14	0.20
K6-B26-G1-5.d	24480	1.69E+05	n.d.	5640	5840	28.6	25.6	13070	95.1	6	bdl	bdl	0.010	bdl	0.039	0.010	0.42	0.42	0.052	0.40	0.033	2.65	2.76	1.30	13.1	13.0	2.9	7.1	8.5	1.09	6.9	6.9	0.75	0.17	0.16
K6-B26-G1-6.d	23330	1.71E+05	n.d.	6310	6450	41.1	45.8	13190	139.3	9	bdl	bdl	0.004	bdl	0.064	0.144	0.73	0.92	0.087	0.71	0.100	4.54	4.71	2.12	20.6	19.9	4.1	10.8	11.2	1.79	9.7	10.6	1.15	0.17	0.13
K6-B26-G1-7.d	24030	1.70E+05	n.d.	5430	5690	33.0	38.2	13380	114.7	4	bdl	bdl	0.002	bdl	0.091	0.028	0.61	0.44	0.037	0.47	0.018	2.63	2.77	1.33	15.8	14.6	3.9	11.7	11.2	1.56	11.0	10.7	1.14	0.08	0.06
K6-B26-G1-8.d	24160	1.70E+05	n.d.	5370	5410	36.3	44.2	12900	94.4	4	bdl	bdl	bdl	bdl	0.035	bdl	0.37	0.20	0.010	0.44	0.015	2.63	2.71	1.28	13.4	12.5	3.0	8.2	8.7	1.23	6.8	6.8	0.77	0.04	0.00
K6-B26-G1-9.d	24100	1.70E+05	n.d.	5190	5190	31.0	36.4	12660	87.1	4	bdl	bdl	bdl	bdl	0.025	bdl	0.22	0.29	0.053	0.18	0.003	0.14	0.021	1.73	1.27	0.86	8.8	9.9	2.2	6.2	5.9	0.81	4.8	4.8	0.60	0.24	0.16
K6-B26-G2-1.d	23330	1.69E+05	n.d.	6980	7550	98.0	72.9	13270	324.2	11	bdl	bdl	0.012	0.005	0.300	0.240	0.77	0.75	0.095	1.03	0.107	6.98	5.67	2.85	31.9	31.6	9.1	33.0	32.4	5.02	41.0	41.5	6.25	0.20	0.18
K6-B26-G2-10.d	24180	1.70E+05	n.d.	7630	7920	53.5	52.3	12560	220.5	7	bdl	bdl	0.005	0.002	0.160	0.260	0.71	0.62	0.095	0.81	0.092	4.44	4.56	1.94	24.5	24.6	6.3	18.3	18.9	3.01	21.4	22.1	3.45	0.12	0.29
K6-B26-G2-11.d	24360	1.70E+05	n.d.	7130	7400	61.3	71.7	12480	272.1	9	bdl	bdl	0.005	0.001	0.214	0.210	0.92	1.02	0.122	0.98	0.164	6.16	6.45	2.46	29.3	27.9	8.0	25.4	24.1	3.97	27.9	27.4	4.98	0.19	0.23
K6-B26-G2-12.d	24000	1.70E+

Table A.1 continued

Element	Mg	Si	P	Ca	Ca	Ti	Ti	Mn	Fe	Fe	Y	Zr	La	Ce	Pr	Nd	Nd	Sm	Sm	Eu	Sm	Eu	Gd	Gd	Tb	Dy	Dy	Ho	Er	Er	Tm	Yb	Yb	Lu	Hf	Hf
Mass	24	29	31	43	44	48	49	55	56	57	89	90	139	140	141	143	146	147	149	151	152	153	155	157	159	161	163	165	166	167	169	172	173	175	178	180
K6-B26-G2-2.d	23620	1.71E+05	n.d.	7390	7540	62.1	79.6	12930	2.25E+05	2.04E+05	239.3	13	0.005	0.005	0.015	0.240	0.148	1.04	0.97	0.074	0.90	0.133	6.38	6.17	2.72	30.3	30.6	8.8	28.6	29.5	4.91	35.7	35.8	5.30	0.34	0.22
K6-B26-G2-3.d	23950	1.72E+05	n.d.	7430	7890	67.6	86.5	13020	2.27E+05	2.05E+05	249.1	14	bdl	bdl	0.002	0.150	0.190	1.17	1.11	0.088	1.24	0.100	6.55	6.36	2.70	30.1	31.9	9.5	30.6	31.2	5.11	37.0	36.1	5.17	0.28	0.35
K6-B26-G2-4.d	24170	1.69E+05	n.d.	7280	7570	72.5	94.3	12750	2.25E+05	2.01E+05	272.6	18	bdl	0.019	0.008	0.360	0.200	1.13	1.17	0.070	1.09	0.085	7.13	6.81	3.33	38.0	37.1	10.9	33.7	35.0	5.47	38.1	36.2	4.74	0.36	0.29
K6-B26-G2-5.d	15200	1.69E+05	n.d.	10290	11150	64.9	72.2	8270	1.41E+05	1.27E+05	136.0	13	0.608	1.000	0.107	0.330	0.660	0.78	0.83	0.189	0.62	0.199	4.12	3.88	1.68	18.3	19.0	5.1	14.9	14.5	2.36	15.4	14.8	1.91	0.30	0.29
K6-B26-G2-6.d	19170	1.70E+05	n.d.	5790	6110	50.1	57.7	11260	1.96E+05	1.75E+05	188.5	12	bdl	0.047	0.003	0.210	0.182	0.67	0.80	0.104	0.75	0.067	4.72	5.61	2.41	25.4	25.2	7.0	21.9	22.3	3.50	23.8	23.4	3.35	0.28	0.22
K6-B26-G2-7.d	13770	1.69E+05	n.d.	15200	15900	66.3	55.4	3450	6.20E+04	5.30E+04	73.0	27	0.500	0.720	0.081	0.450	0.280	0.29	0.22	0.060	0.28	0.107	1.85	1.85	0.77	8.9	8.7	2.5	9.1	8.0	1.25	8.9	9.2	1.00	0.62	0.63
K6-B26-G2-8.d	24100	1.71E+05	n.d.	7110	7310	69.3	85.0	12490	2.26E+05	2.06E+05	190.1	25	bdl	0.014	0.005	0.220	0.370	1.05	1.01	0.040	0.75	0.062	7.18	6.44	2.97	26.6	27.7	7.2	23.0	23.1	3.83	26.7	26.9	3.98	0.38	0.36
K6-B26-G2-9.d	15500	1.72E+05	n.d.	16400	17000	66.1	55.7	4300	7.70E+04	6.70E+04	67.0	29	0.520	0.890	0.107	0.310	0.330	0.18	0.12	0.085	0.24	0.025	1.67	1.28	0.65	8.3	8.4	2.0	5.9	5.4	0.82	6.1	6.0	0.66	0.69	0.75
K6-B51-G2-1.d	21370	1.71E+05	n.d.	4360	4620	30.3	36.7	12640	2.33E+05	2.17E+05	218.6	6	bdl	0.005	0.007	0.032	0.062	0.84	0.68	0.052	0.77	0.121	5.54	5.42	2.55	28.3	27.7	7.7	26.3	27.4	4.53	29.4	31.6	4.17	0.11	0.15
K6-B51-G2-10.d	26800	1.70E+05	n.d.	4560	4781	25.8	27.5	10300	2.29E+05	2.15E+05	57.1	13	bdl	0.004	0.002	bdl	0.105	0.28	0.40	0.054	0.42	0.098	2.80	2.73	1.15	9.7	8.6	1.6	3.8	4.2	0.45	3.2	3.1	0.26	0.18	0.33
K6-B51-G2-11.d	26870	1.72E+05	n.d.	4570	4850	30.7	35.5	10320	2.30E+05	2.20E+05	189.6	9	bdl	bdl	bdl	0.089	0.129	0.56	0.24	0.069	0.59	0.134	3.29	3.68	1.76	23.2	21.4	7.0	28.6	27.4	5.19	37.9	38.4	5.84	0.25	0.19
K6-B51-G2-12.d	26390	1.71E+05	n.d.	4600	4699	31.0	36.4	10220	2.28E+05	2.16E+05	197.6	22	bdl	bdl	bdl	0.012	0.054	0.53	0.43	0.102	0.45	0.105	3.34	3.75	1.73	23.6	22.4	8.2	31.4	31.5	5.52	42.0	41.8	6.44	0.41	0.43
K6-B51-G2-13.d	26570	1.71E+05	n.d.	4390	4680	31.1	31.4	10280	2.29E+05	2.13E+05	221.9	23	bdl	bdl	bdl	0.040	0.063	0.39	0.54	0.055	0.61	0.044	3.84	3.34	1.77	24.3	24.5	8.8	36.7	39.6	7.10	52.7	53.2	8.41	0.42	0.41
K6-B51-G2-14.d	26410	1.72E+05	n.d.	4580	4627	36.3	42.1	10050	2.26E+05	2.12E+05	272.4	10	bdl	0.003	0.002	0.025	0.034	0.74	0.63	0.059	0.71	0.112	5.74	5.69	2.60	32.0	32.9	10.6	40.1	39.6	7.19	55.0	55.8	8.34	0.24	0.20
K6-B51-G2-15.d	26610	1.68E+05	n.d.	4490	4503	35.1	42.8	9890	2.19E+05	2.05E+05	197.4	8	bdl	0.007	bdl	0.091	0.054	0.51	0.49	0.062	0.64	0.082	5.53	5.30	2.36	27.4	26.2	6.8	20.9	20.7	3.27	22.3	22.9	2.63	0.07	0.19
K6-B51-G2-2.d	19780	1.70E+05	n.d.	4130	4370	30.2	37.0	12270	2.26E+05	2.07E+05	199.6	10	bdl	bdl	bdl	bdl	0.011	0.44	0.44	0.123	0.44	0.041	4.83	5.00	2.18	24.1	25.0	7.5	27.9	28.0	5.37	37.7	37.6	5.76	0.24	0.20
K6-B51-G2-3.d	23770	1.72E+05	n.d.	4570	4698	26.6	29.4	11420	2.34E+05	2.12E+05	75.1	16	bdl	bdl	bdl	0.076	0.048	0.44	0.59	0.066	0.46	0.036	2.73	3.04	1.23	12.5	11.5	2.6	6.5	6.2	0.93	6.6	6.0	0.66	0.32	0.37
K6-B51-G2-4.d	24930	1.72E+05	n.d.	4650	4721	22.4	26.0	10840	2.32E+05	2.11E+05	77.0	12	bdl	0.002	bdl	0.016	0.019	0.40	0.38	0.048	0.41	0.051	2.92	2.55	1.31	12.2	12.4	2.3	6.5	6.9	0.86	6.0	6.1	0.65	0.30	0.27
K6-B51-G2-5.d	25520	1.71E+05	n.d.	4500	4700	21.0	18.6	10720	2.31E+05	2.10E+05	96.0	5	bdl	bdl	0.003	0.044	0.086	0.30	0.30	0.059	0.55	0.054	2.86	2.85	1.32	12.4	13.3	2.9	7.5	8.3	1.22	9.5	9.5	1.05	0.06	0.14
K6-B51-G2-6.d	26930	1.71E+05	n.d.	4400	4370	397	600	10280	2.28E+05	2.10E+05	142.4	5	bdl	bdl	bdl	0.013	0.035	0.61	0.58	0.082	0.49	0.137	4.23	4.35	1.89	19.6	21.5	5.0	15.6	15.4	2.32	14.6	15.3	1.83	0.08	0.08
K6-B51-G2-7.d	26500	1.71E+05	n.d.	4290	4730	84.0	126.0	10490	2.28E+05	2.14E+05	44.3	11	bdl	bdl	bdl	0.013	0.030	0.38	0.48	0.058	0.49	0.042	2.90	3.14	1.03	7.9	7.7	1.4	3.2	2.9	0.38	2.2	2.1	0.18	0.31	0.24
K6-B51-G2-8.d	26560	1.71E+05	n.d.	4610	4650	32.1	39.2	10370	2.29E+05	2.12E+05	60.3	5	bdl	bdl	bdl	0.104	0.027	0.45	0.42	0.078	0.35	0.112	3.37	3.13	1.26	9.9	10.4	1.8	3.5	3.4	0.47	2.7	2.4	0.22	0.10	0.07
K6-B51-G2-9.d	26410	1.71E+05	n.d.	4590	4640	22.6	20.2	10200	2.27E+05	2.15E+05	39.6	10	bdl	bdl	bdl	0.039	0.028	0.42	0.25	0.105	0.42	0.107	2.15	2.96	0.87	7.7	7.0	1.0	2.1	2.2	0.27	1.6	1.3	0.10	0.23	0.27
K6-B51-G7-1.d	17550	1.70E+05	n.d.	4400	4610	26.7	25.6	16640	2.43E+05	2.27E+05	192.4	8	bdl	0.002	bdl	0.033	0.143	0.41	0.43	0.133	0.44	0.093	3.98	4.67	2.02	21.5	22.5	6.9	22.1	22.6	3.82	30.2	29.5	3.93	0.17	0.19
K6-B51-G7-10.d	23200	1.72E+05	n.d.	4460	4478	22.5	20.6	12230	2.33E+05	2.19E+05	91.0	7	bdl	bdl	bdl	0.014	0.158	0.21	0.35	0.079	0.32	0.044	2.01	2.53	1.05	11.7	11.2	3.1	11.3	11.3	2.15	17.9	19.0	2.88	0.18	0.17
K6-B51-G7-11.d	23130	1.71E+05	n.d.	4420	4501	25.7	25.7	11940	2.32E+05	2.16E+05	99.6	7	bdl	0.004	bdl	0.013	0.066	0.25	0.18	0.070	0.39	0.049	3.33	2.49	1.30	13.4	12.8	3.1	9.1	9.2	1.37	10.2	9.7	1.35	0.16	0.16
K6-B51-G7-12.d	21480	1.71E+05	n.d.	4720	4663	24.8	24.7	13220	2.38E+05	2.24E+05	154.4	24	bdl	bdl	bdl	0.042	0.019	0.30	0.24	0.076	0.31	0.094	2.50	2.59	1.68	20.0	19.8	7.0	26.4	25.7	4.54	32.6	30.3	5.40	0.69	0.53
K6-B51-G7-2.d	23080	1.71E+05	n.d.	4720	4585	22.0	20.7	11930	2.32E+05	2.15E+05	101.0	15	bdl	bdl	bdl	0.150	bdl	0.22	0.26	0.011	0.25	0.020	2.72	2.68	1.17	12.0	12.2	3.3	11.4	11.1	2.26	18.1	18.0	2.77	0.34	0.33
K6-B51-G7-3.d	24320	1.71E+05	n.d.	4400	4539	24.8	27.5	11510	2.33E+05	2.14E+05	76.9	14	bdl	bdl	bdl	0.043	0.031	0.08	0.13	0.043	0.19	0.030	2.86	2.68	1.13	11.5	10.8	2.4	6.8	5.8	1.09	8.0	8.0	0.99	0.30	0.30
K6-B51-G7-4.d	24400	1.70E+05	n.d.	4170	4452	24.5	23.9	11140	2.31E+05	2.13E+05	68.8	10	0.002	bdl	bdl	0.030	0.019	0.30	0.23	0.080	0.29	0.060	2.28	2.24	0.96	8.6	9.4	2.0	5.8	5.7	0.96	6.1	6.7	0.83	0.26	0.24
K6-B51-G7-5.d	24910	1.72E+05	n.d.	4580	4557	23.0	20.4	11210	2.32E+05	2.13E+05	56.4	12	bdl	bdl	bdl	bdl	0.022	0.32	0.23	0.027	0.31	0.048	2.43	2.31	0.88	7.8	7.2	1.6	4.6	4.5	0.75	6.0	6.3	0.88	0.36	0.16
K6-B51-G7-6.d	24220	1.71E+05	n.d.	4650	4579	24.4	27.1	11100	2.29E+05	2.11E+05	60.3	10	bdl	0.004	bdl	0.140	0.038	0.24	0.23	0.096	0.32	0.013	2.34	2.63	0.96	9.2	8.5	1.9	4.4	4.6	0.75	5.5	5.0	0.76	0.17	0.22
K6-B51-G7-7.d	23960	1.72E+05	n.d.	4550	4677	34.2	37.4	11450	2.33E+05	2.14E+05	66.7	8	bdl	bdl	bdl	0.058	0.073	0.58	0.39	0.099	0.54	0.096	3.93	3.52	1.38	10.3	10.4	2.1	4.8	5.1	0.68	4.4	4.5	0.78	0.22	0.18
K6-B51-G7-8.d	23120	1.70E+05	n.d.	4220	4329	23.4	24.7	11840	2.31E+05	2.14E+05	38.1	9	bdl	0.002	bdl	0.015	0.068	0.37	0.25	0.089	0.44	0.120	2.48	2.69	0.84	5.8	5.4	1.1	3.5	3.1	0.60	6.0	5.6	1.15	0.19	0.15
K6-B51-G7-9.d	23170	1.73E+05	n.d.	4450	4620	24.4	25.4	12350	2.35E+05	2.18E+05	78.1	8	bdl	bdl	0.005	0.015	0.142	0.28	0.44	0.015	0.28	0.030	3.24	2.91	1.17	11.0	10.7	2.3	7.5	8.4	1.40	12.7	11.4	1.61	0.20	0.16
Y1-IG053-G1-1.d	15760	1.70E+05	n.d.	6760	7380	31.0	28.3	21840	2.29E+05	2.01E+05	238.2	16	bdl	bdl	bdl	0.002	bdl	0.028	0.78	0.046	0.044	0.66	0.049	7.16	6.59	3.51	36.9	37.4	8.4	20.2	20.2	2.07	11.8	11.8	1.12	0.27	0.21
Y1-IG053-G1-10.d	23980	1.70E+05	n.d.	8750	9200	45.0	43.5	12470	2.23E+05	1.98E+05	108.5	7	bdl	bdl	0.004	0.115	0.095	0.99	1.12	0.083	1.11	0.082	6.30	6.08	2.42	20.0	19.7	3.7	7.0	7.4	0.64	2.9	2.9	0.21	0.13	0.14
Y1-IG053-G1-11.d	22690	1.69E+05	n.d.	8680	9320	44.7	45.8	13210	2.27E+05	2.00E+05	108.2	7	bdl	0.004	bdl	0.085	0.069	0.91	0.64	0.109	0.86	0.098	5.93	5.66	2.14	18.9	18.5	3.8	8.2	8.8	0.87	4.5	4.3	0.45	0.14	0.14
Y1-IG053-G1-12.d	23600	1.71E+05	n.d.	8360	8720	39.9	42.1	12680	2.24E+05	1.99E+05	126.3	9	bdl	bdl	0.005	0.190	0.107	0.86	0.77	0.103	0.96	0.057	5.92	5.97	2.51	21.9	21.7	4.6	9.8	8.4	0.91	4.1	4.1	0.43	0.21	0.17
Y1-IG053-G1-13.d	24090	1.71E+05	n.d.	8030	8710	46.4	48.9	12810	2.29E+05	2.03E+05	121.0	6	0.020	0.136	0.004	0.130	0.220	0.82	0.88	0.064	0.87	0.092	5.19	5.80	2.10	19.4	19.5	4.3	9.6	9.5	1.10	5.1	4.8	0.51	0.12	0.20
Y1-IG053-G1-14.d	23310	1.69E+05	n.d.	8190	8440	47.3	48.5	12990	2.23E+05	1.98E+05	130.0	5	bdl	0.005	0.002	0.250	0.140	0.45	0.82	0.093	0.78	0.068	5.49	5.70	1.99	19.5	19.6	4.4	11.1	11.0	1.27	7.3	7.7	0.92	0.09	0.16
Y1-IG053-G1-15.d	23070	1.70E+05	n.d.	8230	8520	42.8	46.1	13840	2.24E+05	2.00E+05	147.0	6	0.035	0.114	0.009	0.250	0.190	0.51	0.74	0.081	0.97	0.050	5.57	5.78	2.24	22.3	21.6	5.5	14.3	13.5	1.85	10.3	10.1	1.13	0.15	0.20
Y1-IG053-G1-2.d	20940	1.69E+05	n.d.	7530	7630	38.0	33.9	13900	2.26E+05	1.99E+05	301.0	23	0.070	0.093	0.004	0.017	0.120	0.81	0.78	0.050	0.88	0.084	12.43	10.30	5.09	50.7	49.3	10.5	23.3	23.0	2.85	13.4	13.9	1.32	0.42	0.47
Y1-IG053-G1-3.d	22840	1.68E+05	n.d.	7550	7640	35.7	37.6	13210	2.26E+05	2.00E+05	295.6	13	bdl	bdl	0.004	0.060	0.034	0.53	0.46	0.067	0.65	0.072	9.50	9.20	4.60	45.1	45.3	10.4	25.0	24.7	2.99	15.6	15.5	1.41	0.26	0.34
Y1-IG053-G1-4.d	22870	1.68E+05	n.d.	7730	8010	42.7	46.3	13020	2.23E+05	1.95E+05	289.2	22	bdl	bdl	bdl	0.048	bdl	0.72	1.01	0.050	0.59	0.073	10.79	10.14	5.02	49.5	48.1	10.6	24.9	25.1	2.91	15.1	14.2	1.45	0.48	0.51
Y1-IG053-G1-5.d	18650	1.70E+05	n.d.	5440	5460	27.1	28.9	10590	1.80E+05	1.57E+05	215.0	16	bdl	0.008	0.002	bdl	bdl	0.36	0.39	0.051	0.45	0.064	5.79	5.23	2.67	32.9	30.1	7.8	21.3	21.5	2.73	14.9	15.7	1.77	0.30	0.40
Y1-IG053-G1-6.d	23260	1.69E+05	n.d.	6880	7010	31.3	29.3	13030	2.25E+05	1.96E+05	210.6	10	bdl	bdl	bdl	0.046	0.032	0.50	0.58	0.035	0.50	0.047	5.55	5.51	3.19	31.5	32.4	8.0	19.3	18.9	2.29	11.6	11.9	1.32	0.23	0.16
Y1-IG053-G1-7.d	23500	1.72E+05	n.d.	7740	8580	47.0	50.1	12750	2.26E+05	1.97E+05	159.9	7	bdl	0.007	bdl	0.051	0.046	1.02	0.66	0.058	0.92	0.072	9.20	9.47	3.39	28.1	28.5	5.1	11.0	11.4	1.19	6.7	6.6	0.58	0.16	0.14
Y1-IG053-G1-8.d	23510	1.72E+05	n.d.	8700	9340	62.0	71.2	12580	2.26E+05	1.99E+05	106.8	15	bdl	bdl	bdl	0.080	0.041	1.08	1.29	0.108	1.32	0.118	9.89	10.15	3.24	22.1	21.3	3.4	6.4	6.5	0.65	3.3	3.2	0.28	0.30	0.43
Y1-IG053-G1-9.d	23460	1.70E+05	n.d.	8390	8650	43.9	41.2	12300	2.20E+05	1.96E+05	111.2	6	bdl	0.002	bdl	0.046	0.174	0.82	0.51	0.050	1.11	0.102	7.20	7.22	2.52	19.5	20.3	3.6	7.1	7.1	0.73	3.3	3.8	0.27	0.02	0.15
Y1-IG057-G1-1.d	17230	1.71E+05	n.d.	6410	6610	36.1	35.6	21590	2.29E+05	2.03E+05	454.2	19	bdl	bdl	bdl	bdl	bdl	0.33	0.25	0.012	0.39	0.011	5.72	5.74	3.87	57.7	58.0	18.0	62.0	61.4	9.45	66.0	64.9	9.49	0.36	0.51
Y1-IG057-G1-10.d	26700	1.72E+05	n.d.	6470	6910	46.1	55.3	12550	2.17E+05	1.95E+05	557.0	24	bdl	bdl	bdl	bdl	0.029	0.35	0.45	bdl	0.54	0.017	9.30	9.19	5.33	72.4	71.7	23.0	80.6	77.0	12.83	93.1	93.1	15.17	0.38	0.43
Y1-IG057-G1-11.d	29330	1.71E+05	n.d.	6510	7010	48.5	56.2	11040	2.09E+05	1.89E+05	559.4	29	bdl	bdl	bdl	bdl	0.042	0.55	0.83	0.051	0.75	0.084	9.76	10.61	5.44	71.9	75.2	23.0	78.1	79.0	11.70	86.0	83.4	13.31	0.45	0.53
Y1-IG057-G1-12.d	29140	1.69E+05	n.d.	6880	7010	50.3	56.4	10930	2.10E+05	1.87E+05	525.0	30	bdl	bdl	bdl	0.073	0.143	0.54	0.83	0.108	0.82	0.097	8.56	10.28	5.22	67.9	68.3	20.7	67.2	67.4	9.99	62.8	62.5	9.23	0.53	0.59
Y1-IG057-G1-13.d	28290	1.67E+05	n.d.	6440	7040	43.7	48.1	10610	2.10E+05	1.87E+05	398.6	25	bdl	bdl	bdl	0.064	0.039	0.58	0.45	0.018	0.63	0.058	6.27	6.33	3.68	50.1	53.5	16.3	56.4	58.7	9.16	64.0	61.5	10.00	0.53	0.49
Y1-IG057-G1-14.d	19470	1.71E+05	n.d.	6830	6860	33.9	31.2	17260	2.33E+05	2.10E+05	370.2	21	bdl	bdl	bdl	bdl	0.010	0.38	0.30	0.029	0.50	0.043	5.23	4.61	3.11	46.0	43.9	15.0	52.8	53.1	8.29	56.9	54.6	8.43	0.47	0.39
Y1-IG057-G1-2.d	27680	1.71E+05	n.d.	6790	7110	45.7	51.7	10840	2.18E+05	1.94E+05	500.5	26	bdl	bdl	bdl	0.063	bdl	0.71	0.54	0.008	0.49	0.063	7.84	8.48	5.09	67.9	66.5	21.1	69.5	68.1	10.36	75.1	73.1	11.02	0.54	0.64
Y1-IG057-G1-3.d	24410	1.72E+05	n.d.	6980	7260	39.5	38.7	11940	2.27E+05	2.01E+05	498.0	26	bdl	bdl	bdl	bdl	bdl	0.24	0.46	0.032	0.36	0.104	7.43	8.50	4.97	68.4	65.9	20.2	65.3	64.9	9.77	66.3	64.6	9.57	0.56	0.53
Y1-IG057-G1-4.d	18660	1.70E+05	n.d.	6450	7290	37.0	36.6	17320	2.35E+05	2.08E+05	602.0	28	bdl	bdl	bdl	0.073	0.011	0.29	0.36	0.025	0.59	0.064	8.89	9.14	5.62	77.8	77.0	24.0	78.9	79.3	12.32	85.1	84.0	12.27	0.58	0.43
Y1-IG057-G1-5.d	20710	1.69E+05	n.d.	6580	6740	33.9	35.5	14730	2.30E+05	2.05E+05	335.2	14	0.046	0.206	0.029	bdl	0.136	0.37	0.47	0.093	0.64	0.039	6.95	6.41	3.72	46.4	46.1	13.2	38.7	40.1	5.95	41.9	42.3	6.45	0.32	0.26
Y1-IG057-G1-6.d	26660	1.71E+05	n.d.	7160	7110	42.8	51.6	11480	2.22E+05	1.97E+05	556.2	27	bdl	0.007	bdl	bdl	0.020	0.53	0.84	0.091	0.51	0.071	10.34	9.52	5.58	75.4	72.6	21.7	68.6	69.5	10.50	69.2	68.5	10.00	0.59	0.55
Y1-IG057-G1-7.d	29020	1.71E+05	n.d.	6930	7070	45.6	52.4	11200	2.17E+05	1.91E+05	549.0	27	bdl	bdl	bdl	bdl	0.021	0.89	0.84	0.135	0.83	0.085	9.14	10.34	5.73	75.7	73.8	21.5	66.9	66.3	9.82	66.4	63.9	9.44	0.33	0.52
Y1-IG057-G1-8.d	29240	1.71E+05	n.d.	6560	7050	40.7	45.6	11320	2.14E+05	1.92E+05	497.9	27	bdl	bdl	bdl	bdl	0.012	0.62	0.49	0.108	0.79	0.063	9.18	8.68	4.92	67.9	67.8	19.6	62.5	64.6	8.97	65.5	64.4	9.37	0.51	0.37
Y1-IG057-G1-9.d	28910	1.69E+05	n.d.	6510	6920	41.7	45.8	10900	2.07E+05	1.85E+05	524.5	28	bdl	bdl	bdl	0.030	0.020	0.55	0.60	0.074	0.72	0.048	9.53	9.38	5.45	70.5	70.1	22.4	72.4	71.2	10.95	77.3	77.7	12.09	0.59	0.66

Table A.1 continued

Element	Mg	Si	P	Ca	Ca	Ti	Ti	Mn	Fe	Fe	Y	Zr	La	Ce	Pr	Nd	Nd	Sm	Sm	Eu	Sm	Eu	Gd	Gd	Tb	Dy	Dy	Ho	Er	Er	Tm	Yb	Yb	Lu	Hf	Hf
Mass	24	29	31	43	44	48	49	55	56	57	89	90	139	140	141	143	146	147	149	151	152	153	155	157	159	161	163	165	166	167	169	172	173	175	178	180
Y1-IG061-G1-1.d	21320	1.69E+05	599	6270	6020	48.3	56.6	12790	2.54E+05	2.10E+05	272.9	44	bdl	bdl	bdl	0.096	0.097	0.62	0.77	0.139	0.67	0.151	7.48	7.85	3.35	37.2	36.8	9.5	30.4	29.2	4.45	29.0	28.5	3.69	0.70	0.68
Y1-IG061-G1-2.d	22230	1.68E+05	531	6280	5620	43.7	50.4	11220	2.48E+05	2.07E+05	406.4	27	bdl	bdl	bdl	0.040	0.050	0.52	0.84	0.131	0.8	0.142	7.86	8.11	4.30	56.0	57.7	16.6	53.6	54.0	6.45	36.5	36.6	4.25	0.57	0.51
Y1-IG061-G1-3.d	23610	1.68E+05	344	6730	6430	35.4	35.7	9860	2.41E+05	2.03E+05	223.6	5.3	bdl	bdl	bdl	0.028	0.008	0.22	0.32	0.048	0.45	0.061	2.89	3.00	1.68	23.1	25.1	8.0	33.2	33.3	5.63	41.9	40.9	5.68	0.11	0.11
Y1-IG061-G1-4.d	24130	1.67E+05	254	7000	6430	42.1	51.3	9610	2.45E+05	2.07E+05	177.9	5.4	bdl	bdl	bdl	0.055	bdl	0.60	0.36	0.102	0.38	0.073	3.34	3.31	1.59	20.2	20.6	6.1	23.1	23.3	3.76	29.0	27.9	3.36	0.16	0.12
Y1-IG061-G1-5.d	25000	1.69E+05	329	6050	6350	74.4	103.3	9570	2.43E+05	2.09E+05	171.9	16	bdl	bdl	bdl	0.120	0.087	0.84	0.99	0.194	1.11	0.228	6.00	6.39	2.57	24.6	26.1	5.7	21.1	20.4	3.80	29.4	29.3	4.27	0.32	0.26
Y1-IG061-G1-6.d	25430	1.70E+05	766	6770	6610	106	139	9590	2.46E+05	2.11E+05	362.0	51	bdl	bdl	bdl	0.068	0.039	0.76	0.72	0.181	0.91	0.171	9.06	8.92	4.13	50.7	50.3	13.4	46.2	45.6	7.44	58.0	58.2	7.61	0.93	0.85
Y1-IG061-G1-7.d	25680	1.74E+05	783	6140	6450	101	135	9690	2.48E+05	2.16E+05	393.7	67	bdl	bdl	bdl	0.041	0.135	0.68	0.65	0.170	0.84	0.151	9.82	9.27	4.70	54.6	57.2	14.2	48.8	48.9	8.09	61.2	59.6	7.83	1.19	1.20
Y1-IG061-G1-8.d	25880	1.69E+05	781	6230	6660	65.7	84.2	9640	2.41E+05	2.12E+05	267.8	53	bdl	bdl	bdl	0.014	0.078	0.72	0.65	0.192	0.72	0.120	7.49	8.36	3.81	38.6	39.0	9.0	27.1	27.9	4.43	29.4	29.3	3.52	0.85	1.06
Y1-IG061-G1-9.d	25640	1.74E+05	645	6120	6530	51.0	58.5	9790	2.46E+05	2.17E+05	210.5	42	bdl	bdl	bdl	bdl	0.027	0.54	0.31	0.137	0.46	0.090	5.92	5.98	2.64	30.1	30.7	6.9	20.8	21.1	3.34	22.8	23.3	2.73	0.79	0.81
Y1-IG061-G1-0.d	25690	1.75E+05	441	6510	6530	47.0	53.7	9720	2.42E+05	2.15E+05	304.6	29	bdl	bdl	bdl	0.067	0.018	0.51	0.58	0.149	0.63	0.110	5.92	5.98	3.12	38.2	39.2	11.0	39.3	40.8	6.95	52.6	52.7	6.72	0.61	0.48
Y1-IG061-G1-1.d	25670	1.76E+05	478	6440	6450	43.8	45.6	9770	2.42E+05	2.19E+05	320.3	33	bdl	bdl	bdl	0.014	0.060	0.59	0.55	0.123	0.55	0.142	5.19	5.95	3.09	40.6	40.3	12.1	48.1	46.9	8.40	64.0	66.6	9.46	0.60	0.52
Y1-IG061-G1-2.d	24010	1.75E+05	566	6060	6270	38.4	39.6	8860	2.25E+05	1.95E+05	200.2	38	bdl	bdl	bdl	0.014	0.030	0.31	0.31	0.081	0.36	0.046	3.14	3.24	1.65	22.8	23.4	7.2	29.1	29.7	5.42	39.1	37.8	5.97	0.82	0.72
Y1-IG061-G1-3.d	25670	1.72E+05	271	6160	6430	38.7	42.6	9650	2.42E+05	2.18E+05	314.7	6.1	bdl	bdl	bdl	0.040	0.133	0.64	0.50	0.082	0.65	0.112	5.35	5.59	2.78	35.9	36.4	11.1	43.2	43.9	7.77	59.8	58.5	8.51	0.04	0.10
Y1-IG061-G1-4.d	25540	1.72E+05	350	6390	6200	40.1	41.0	9650	2.47E+05	2.23E+05	268.5	14	bdl	bdl	bdl	bdl	0.067	0.50	0.35	0.114	0.63	0.103	3.82	3.93	2.14	29.4	29.1	9.6	38.1	38.0	6.55	49.1	51.1	6.77	0.26	0.23
Y1-IG061-G1-5.d	25850	1.71E+05	490	6700	6290	32.8	28.4	9580	2.48E+05	2.25E+05	187.7	25	bdl	bdl	bdl	0.012	0.042	0.41	0.24	0.086	0.41	0.036	2.76	2.98	1.52	21.0	21.4	6.4	24.5	23.8	4.05	31.6	32.9	4.09	0.62	0.51
Y1-IG061-G1-6.d	26510	1.69E+05	432	6070	6100	34.9	34.5	8950	2.39E+05	2.19E+05	211.0	20	bdl	bdl	bdl	bdl	0.063	0.46	0.19	0.057	0.306	0.065	3.08	3.06	1.81	24.6	24.9	8.4	33.4	33.7	5.69	46.5	44.9	6.85	0.41	0.46
Y1-IG061-G1-7.d	25820	1.67E+05	361	6440	6400	34.5	28.7	9410	2.44E+05	2.24E+05	191.2	11	bdl	bdl	bdl	0.013	0.048	0.24	0.25	0.092	0.422	0.068	2.96	2.36	1.79	22.0	22.1	6.5	24.9	26.9	4.34	32.6	32.7	4.83	0.33	0.23
Y1-IG061-G1-8.d	25650	1.69E+05	242	6350	6450	33.4	33.4	9390	2.47E+05	2.27E+05	269.1	4.3	bdl	bdl	bdl	0.013	0.008	0.34	0.29	0.125	0.304	0.107	3.24	3.09	1.89	27.8	28.8	10.0	40.0	39.8	6.48	47.9	45.8	6.41	0.13	0.10
Y1-IG061-G1-9.d	25720	1.71E+05	284	5890	6240	30.5	25.2	9410	2.45E+05	2.24E+05	225.8	6.2	bdl	bdl	bdl	0.039	0.039	0.28	0.35	0.105	0.381	0.049	3.27	3.09	1.87	25.9	26.3	8.1	27.3	26.9	3.88	24.4	25.3	2.99	0.13	0.08
Y1-IG061-G2-1.d	26440	1.70E+05	167	6990	7130	43.6	54.1	9560	2.40E+05	2.21E+05	245.2	3.9	bdl	bdl	bdl	0.081	0.136	0.48	0.57	0.094	0.44	0.131	3.40	3.71	2.00	27.4	27.0	8.8	34.9	34.7	6.18	45.9	45.4	6.72	0.02	0.04
Y1-IG061-G2-2.d	26010	1.70E+05	250	6600	6880	33.2	28.8	9590	2.41E+05	2.22E+05	231.0	3.2	bdl	bdl	bdl	0.025	0.009	0.31	0.35	0.129	0.366	0.134	3.05	3.12	1.76	26.0	25.5	8.2	32.0	32.6	5.59	40.0	42.5	6.07	0.04	0.07
Y1-IG061-G2-3.d	26480	1.69E+05	283	6660	6660	34.1	31.1	9770	2.45E+05	2.24E+05	202.8	6	bdl	bdl	bdl	0.028	0.026	0.32	0.31	0.081	0.46	0.099	2.79	2.85	1.59	23.0	22.2	7.3	28.8	28.9	4.99	34.8	36.2	5.12	0.14	0.15
Y1-IG061-G2-4.d	27150	1.67E+05	276	6950	6810	32.6	31.3	9750	2.43E+05	2.25E+05	206.0	7.5	bdl	bdl	bdl	0.027	0.051	0.32	0.33	0.062	0.337	0.084	2.66	2.61	1.52	21.9	23.0	7.2	29.7	28.8	5.04	36.5	36.4	5.02	0.18	0.12
Y1-IG061-G2-5.d	26970	1.73E+05	237	7190	6830	33.3	33.0	9740	2.46E+05	2.28E+05	229.5	6.4	bdl	bdl	bdl	0.012	bdl	0.46	0.40	0.067	0.32	0.118	3.17	3.45	1.85	25.7	26.6	8.6	33.7	32.7	5.81	39.5	40.6	5.24	0.16	0.12
Y1-IG061-G2-6.d	26140	1.73E+05	171	6670	6720	33.7	30.3	9720	2.42E+05	2.23E+05	249.0	3	bdl	bdl	bdl	0.038	bdl	0.29	0.33	0.153	0.308	0.112	3.58	3.04	1.99	26.6	28.5	8.7	33.7	34.6	5.66	41.2	39.5	5.38	0.02	0.10
Y1-IG061-G2-7.d	26590	1.74E+05	170	6910	6660	35.4	31.0	9780	2.44E+05	2.24E+05	262.5	2.8	bdl	bdl	bdl	0.068	0.018	0.45	0.42	0.154	0.339	0.157	3.78	3.33	2.01	29.1	27.9	9.6	36.4	36.5	6.25	47.5	46.9	6.87	0.06	0.06
Y1-IG061-G2-8.d	26010	1.75E+05	197	6680	6490	33.1	25.6	9710	2.40E+05	2.20E+05	229.8	4.1	bdl	bdl	bdl	0.013	0.019	0.44	0.38	0.062	0.39	0.098	3.16	3.88	1.94	24.4	26.9	8.1	29.9	31.1	5.14	35.4	35.9	4.64	0.11	0.09
Y1-IG061-G2-9.d	26200	1.78E+05	304	5890	5950	40.4	41.4	10010	2.45E+05	2.23E+05	254.2	15	bdl	bdl	bdl	bdl	0.021	0.54	0.29	0.065	0.53	0.076	4.31	4.12	2.51	30.9	30.2	9.0	34.8	34.9	5.75	42.7	42.5	5.88	0.32	0.35
Y1-IG061-G2-0.d	26570	1.72E+05	361	6160	6490	44.1	43.6	10120	2.44E+05	2.25E+05	272.7	13	bdl	bdl	bdl	0.071	0.066	0.54	0.74	0.103	0.63	0.089	4.97	5.08	2.52	34.5	33.9	9.6	33.5	32.6	5.53	39.4	37.2	4.93	0.25	0.28
Y1-IG061-G2-1.d	26250	1.73E+05	514	6970	6590	43.9	55.0	10120	2.43E+05	2.24E+05	291.4	33	bdl	bdl	bdl	bdl	0.068	0.75	0.60	0.215	0.62	0.153	7.79	8.26	3.62	42.3	41.1	10.9	35.6	35.7	5.78	40.4	39.2	5.12	0.56	0.62
Y1-IG061-G2-2.d	26500	1.72E+05	607	6800	6540	46.5	52.3	10210	2.45E+05	2.27E+05	215.5	30	bdl	bdl	bdl	0.068	0.150	0.34	0.43	0.032	0.51	0.088	3.37	2.98	1.88	26.1	26.2	8.7	35.6	37.6	6.26	47.6	46.6	7.75	0.50	0.58
Y1-IG061-G2-3.d	26880	1.69E+05	466	6000	6390	41.1	42.1	10230	2.46E+05	2.28E+05	245.1	30	bdl	bdl	bdl	0.037	0.035	0.33	0.22	0.081	0.304	0.049	3.68	3.99	2.05	29.5	29.3	10.0	41.5	40.6	7.02	53.3	53.8	8.16	0.58	0.52
Y1-IG061-G2-4.d	26270	1.73E+05	494	6390	6340	43.9	45.7	10140	2.44E+05	2.27E+05	281.2	30	bdl	bdl	bdl	0.059	0.017	0.55	0.42	0.129	0.43	0.080	4.89	5.16	2.86	35.5	35.3	10.7	40.9	41.5	6.78	51.7	51.8	7.46	0.59	0.62
Y1-IG061-G2-5.d	25900	1.72E+05	549	6300	6320	45.5	49.0	9930	2.44E+05	2.27E+05	312.6	40	bdl	bdl	bdl	bdl	0.087	0.39	0.48	0.095	0.5	0.095	5.58	5.65	2.91	39.8	40.5	13.2	48.6	48.3	7.81	56.7	56.7	8.02	0.72	0.83
Y1-IG061-G2-6.d	25860	1.69E+05	398	6160	6180	40.3	42.3	9780	2.43E+05	2.27E+05	268.9	28	bdl	bdl	bdl	0.050	0.016	0.33	0.35	0.092	0.41	0.067	5.17	4.34	2.44	32.3	33.5	10.2	38.3	37.6	6.05	45.7	44.5	6.21	0.49	0.59
Y1-IG061-G2-7.d	26120	1.63E+05	330	6540	6300	35.8	30.7	9640	2.43E+05	2.28E+05	261.9	9.4	bdl	bdl	bdl	0.024	0.034	0.41	0.41	0.099	0.45	0.105	4.26	4.59	2.13	30.0	30.5	9.5	35.7	35.7	5.74	42.3	41.6	5.54	0.17	0.24
Y1-IG061-G2-8.d	26200	1.64E+05	244	6390	6670	37.9	35.5	9830	2.47E+05	2.32E+05	238.5	2.9	bdl	bdl	bdl	0.054	0.037	0.36	0.39	0.140	0.39	0.120	2.91	3.18	1.77	25.6	25.9	8.1	32.9	31.7	5.23	39.6	40.2	5.77	0.06	0.11
Y1-IG061-G2-9.d	25780	1.74E+05	296	6460	6210	29.8	25.0	10370	2.45E+05	2.33E+05	177.3	4.8	bdl	bdl	bdl	0.037	0.008	0.45	0.35	0.111	0.48	0.087	3.28	3.25	1.84	23.2	22.7	5.9	19.0	18.3	2.71	15.9	15.5	1.77	0.12	0.08

Table A.2. Monazite U–Pb isotope and chemical analyses

		SHRIMP											Electron Microprobe Microanalysis (wt%)														
Spot	Session	Micro-structure	$^{238}U/^{206}Pb^*$	±1σ (%)	$^{207}Pb^*/^{206}Pb^*$	±1σ (%)	$^{207}Pb^*/^{235}U$	±1σ (%)	$^{238}U/^{206}Pb$ Age	±1σ	$^{207}Pb/^{235}U$ Age	±1σ	% Disc	Y_2O_3	ThO_2	UO_2	PbO	CaO	SiO_2	P_2O_5	La_2O_3	Ce_2O_3	Pr_2O_3	Nd_2O_3	Sm_2O_3	Gd_2O_3	Dy_2O_3	Lu_2O_3	Total
Paragneiss																													
Y1-BB006 (Bird Bluff)																													
06A-2.1	2013	Int.	64.36	2.0	0.0475	1.2	0.102	2.4	99.4	2	98.5	2	-1	3.38	4.91	1.12	0.067	1.76	0.13	29.71	12.92	26.74	2.60	10.67	2.10	1.58	0.64	0.14	98.46
06A-2.2	2013	Int.	57.61	2.0	0.0489	1.5	0.117	2.5	111	2	112	2	1	2.24	4.73	0.74	0.049	1.55	0.28	29.60	13.48	28.00	2.82	11.26	2.22	1.64	0.51	0.09	99.19
06A.3-1	2013	(Grt)	61.70	2.1	0.0482	0.7	0.108	2.2	104	2	104	2	0	2.70	5.37	1.66	0.075	1.76	0.27	29.94	13.04	27.25	2.68	10.52	2.06	1.40	0.53	0.09	99.33
06A.3-2	2013	(Grt)	62.61	3.1	0.0482	1.1	0.106	3.3	102	3	102	3	0	1.15	5.75	3.02	0.082	1.88	0.26	29.53	13.35	27.25	2.63	10.06	1.90	1.24	0.25	0.09	98.45
006B-3.1	2013	(Bt)	62.17	2.0	0.0489	1.3	0.108	2.4	103	2	104	2	2	1.42	5.65	0.92	0.049	2.37	0.12	29.72	14.06	28.83	2.81	10.39	1.91	1.31	0.42	0.03	100.01
006B-3.2	2013	(Bt)	62.81	2.4	0.0483	1.1	0.106	2.7	102	2	102	2	1	3.34	5.29	1.08	0.060	2.31	0.12	29.92	12.68	26.82	2.64	10.46	2.00	1.69	0.60	0.09	99.11
10CY-010 (Mt Bitgood)																													
10CY-10B_1.1	2011	Int.	61.80	3.37	0.0474	1.1	0.1057	4.20	103	3	102.1	4	-1	3.19	4.04	4.61	0.115	1.92	0.07	30.05	12.21	25.34	2.41	9.99	2.32	1.04	0.77	0.16	98.22
10CY-10B_1.2	2011	Int.	66.18	4.02	0.0486	2.6	0.1013	4.75	96.7	4	98.0	5	1	2.57	5.05	0.86	0.057	1.29	0.12	29.73	12.38	27.41	2.89	11.12	2.49	0.96	0.69	0.13	97.77
10CY-10B_1.3	2011	Int.	65.30	3.43	0.0478	1.1	0.1010	4.16	98.0	3	97.7	4	0	3.20	4.21	4.68	0.089	1.92	0.10	29.92	12.04	25.49	2.51	9.84	2.45	0.95	0.74	0.17	98.30
10CY-10B_1.4	2011	Int.	69.09	3.69	0.0486	1.7	0.0970	4.21	92.6	3	94.0	4	1	3.66	4.41	2.19	0.073	1.44	0.08	30.13	12.63	26.54	2.75	10.64	2.37	0.85	0.85	0.10	98.72
10CY-10B_12.1	2011	(Qtz)	62.87	3.60	0.0478	0.9	0.1048	4.37	102	4	101.2	4	-1	3.64	4.74	2.15	0.074	1.51	0.13	29.97	12.48	26.26	2.52	10.34	2.31	0.97	0.91	0.16	98.16
10CY-10B_12.2	2011	(Qtz)	65.56	3.39	0.0486	1.9	0.1023	3.90	97.6	3	98.9	4	1	2.29	4.84	0.71	0.048	1.00	0.29	29.49	13.36	28.03	2.70	11.61	2.28	0.76	0.53	0.15	98.10
10CY-10B.12.3	2011	(Qtz)	65.79	3.98	0.0482	2.3	0.1011	4.61	97.3	4	97.8	5	1	3.09	5.12	0.94	0.056	1.24	0.18	29.97	12.48	27.33	2.80	11.10	2.10	1.12	0.80	0.13	98.45
Y1-BB013 (Bird Bluff)																													
13A.9-1	2012	(Crd)	56.09	2.3	0.0526	2.2	0.129	3.2	114	3	123	4	8	1.61	8.34	0.72	0.060	1.21	0.49	29.02	13.71	25.97	2.79	10.19	1.84	1.44	0.34	0.09	97.82
13A.9-2	2012	(Crd)	63.54	2.2	0.0470	2.9	0.102	3.7	101	2	98.7	4	-2	2.62	5.05	1.78	0.066	1.13	0.13	29.72	14.25	27.00	2.92	9.41	1.86	1.25	0.44	0.11	97.74
13A.9-3	2012	(Crd)	60.46	2.5	0.0468	2.0	0.107	3.2	106	3	103	3	-3	2.96	4.55	1.58	0.067	1.06	0.11	29.55	14.08	26.63	2.85	9.85	1.86	1.46	0.52	0.13	97.26
13B.1-1	2012	(Bt)	61.19	2.3	0.0456	1.4	0.103	2.7	104	2	99.2	3	-5	2.94	5.08	2.45	0.077	1.04	0.15	29.84	13.58	26.42	2.89	9.68	1.99	1.62	0.48	0.15	98.37
13B.1-2	2012	(Bt)	62.88	2.5	0.0472	1.8	0.104	3.1	102	3	100	3	-2	3.56	4.81	0.89	0.061	0.85	0.09	30.06	13.43	26.64	2.82	10.83	2.04	1.70	0.65	0.18	98.61
13B.1-3	2012	(Bt)	60.94	2.2	0.0465	1.2	0.105	2.5	105	2	102	3	-3	3.23	4.76	1.57	0.062	0.90	0.10	29.92	13.74	26.74	2.80	10.39	1.84	1.59	0.51	0.19	98.33
13B.1-4	2012	(Bt)	61.95	2.2	0.0472	1.6	0.105	2.7	103	2	102	3	-2	3.56	4.75	0.86	0.051	0.87	0.10	29.86	13.29	26.37	3.00	10.77	2.05	1.77	0.63	0.15	98.10
13B.4-1	2012	Int.	63.43	2.2	0.0476	2.0	0.103	3.0	101	2	100.0	3	-1	3.81	5.10	0.99	0.061	1.11	0.11	30.06	12.58	25.94	2.95	10.75	2.18	1.84	0.87	0.17	98.52
13B.4-2	2012	Int.	62.54	2.3	0.0461	2.3	0.102	3.2	102	2	98.3	3	-4	2.94	5.02	0.78	0.053	0.89	0.11	29.57	13.90	26.46	2.83	10.20	2.02	1.60	0.64	0.18	97.19
13B.4-3	2012	Int.	61.10	2.3	0.0467	3.4	0.105	4.1	105	2	102	4	-3	3.33	5.25	0.79	0.060	0.92	0.11	29.38	13.35	25.41	2.89	10.11	2.31	1.71	0.76	0.11	96.48
13B.7-1	2012	Int.	63.36	2.2	0.0476	3.8	0.104	4.4	101	2	100	4	-1	3.28	4.51	1.08	0.048	0.89	0.12	29.90	14.03	27.23	2.96	10.46	1.95	1.50	0.65	0.13	98.76
13B.7-2	2012	Int.	53.43	2.3	0.0545	3.4	0.141	4.1	120	3	134	5	12	1.76	3.52	0.52	0.035	0.64	0.56	29.53	15.60	29.56	3.09	11.05	1.86	1.15	0.39	0.09	99.37
13B.7-3	2012	Int.	53.74	2.3	0.0515	3.3	0.132	4.0	119	3	126	5	6	1.89	6.21	0.72	0.062	0.95	0.27	29.35	14.25	27.23	3.03	10.75	2.00	1.44	0.54	0.13	98.83
10CY-015 (Mt Bitgood)																													
10CY-15A.22.1	2011	Int.	19.82	3.40	0.0544	1.2	0.3784	6.30	317	11	325.8	19	3	2.01	4.98	1.01	0.139	1.39	0.05	29.40	12.75	26.82	2.75	10.32	2.25	0.80	0.57	0.11	95.33
10CY-15A.22.2	2011	Int.	18.93	3.40	0.0549	1.2	0.4000	13.15	332	11	341.6	42	3	2.04	4.89	1.05	0.137	1.37	0.07	29.08	12.44	26.86	2.53	10.88	2.27	0.83	0.56	0.08	95.11
10CY-15A.22.3	2011	Int.	58.70	3.38	0.0476	1.6	0.1119	3.99	109	4	107.7	4	-1	2.91	3.30	0.86	0.046	0.39	0.58	28.66	12.79	27.71	2.84	11.55	2.47	0.75	0.58	0.15	95.60
10CY-15B_11.1	2011	(Bt)	65.81	3.46	0.0472	1.6	0.0990	4.08	97.2	3	95.8	4	-1	3.72	3.56	1.96	0.073	1.25	0.05	30.33	12.15	26.69	2.73	11.53	2.67	1.02	0.77	0.18	98.68
10CY-15B_11.2	2011	(Bt)	60.45	3.37	0.0479	1.0	0.1093	3.98	106	4	105.3	4	0	2.70	4.28	3.68	0.104	1.79	0.08	29.88	12.79	26.65	2.54	9.75	2.13	0.84	0.53	0.11	97.84
10CY-15B_11.3	2011	(Bt)	19.08	3.40	0.0526	1.2	0.3804	3.96	329	11	327.3	12	-1	2.22	4.53	1.01	0.132	1.30	0.06	30.08	13.45	28.39	2.84	11.27	2.30	0.80	0.50	0.08	98.94
10CY-15B_15.2	2011	(Kfs)	65.46	3.38	0.0475	1.4	0.0999	4.37	97.7	3	96.7	4	-1	3.81	3.38	2.75	0.071	1.34	0.09	30.17	11.95	26.48	2.57	11.17	2.51	1.01	0.80	0.12	98.23
10CY-15B_15.3	2011	(Kfs)	67.43	3.58	0.0489	1.5	0.1000	4.15	94.9	3	96.8	4	2	1.88	4.46	2.50	0.067	1.38	0.20	29.86	11.63	26.77	2.81	12.45	2.88	0.92	0.48	0.10	98.37
10CY-15B_15.4	2011	(Kfs)	64.89	3.38	0.0488	1.3	0.1037	4.27	98.6	3	100.1	4	2	3.63	2.63	3.33	0.083	1.36	0.05	30.35	12.32	26.59	2.80	11.04	2.57	0.98	0.79	0.20	98.72
10CY-15B_25.1	2011	(Kfs)	67.38	3.46	0.0495	1.4	0.1014	4.13	95.0	3	98.1	4	3	2.04	3.86	2.89	0.068	1.40	0.14	29.63	11.91	27.47	2.64	11.22	2.79	0.99	0.63	0.15	97.83
10CY-15B_25.2	2011	(Kfs)	63.70	3.49	0.0487	1.1	0.1054	4.71	100	3	101.8	4	1	4.07	2.62	4.37	0.098	1.45	0.14	30.01	11.13	25.68	2.53	10.67	2.92	1.24	1.00	0.18	98.11
10CY-15B_25.3	2011	(Kfs)	66.35	3.57	0.0490	1.4	0.1019	4.18	96.4	3	98.5	4	2	1.60	3.90	2.77	0.062	1.37	0.15	29.89	12.23	27.82	2.71	11.63	2.55	1.00	0.44	0.08	98.19
10CY-15B_25.4	2011	(Kfs)	61.47	3.71	0.0471	1.4	0.1056	4.37	104	4	102.0	4	-2	1.60	4.06	3.05	0.072	1.45	0.17	29.65	11.93	27.62	2.71	11.53	2.89	0.92	0.42	0.06	98.14

Table A.2 continued. Monazite U–Pb isotope and chemical analyses

		SHRIMP											Electron Microprobe Microanalysis (wt%)															
Spot	Session	Micro-structure	$^{238}U/^{206}Pb^*$	±1σ (%)	$^{207}Pb^*/^{206}Pb^*$	±1σ (%)	$^{207}Pb^*/^{235}U$	±1σ (%)	$^{238}U/^{206}Pb$ Age	±1σ	$^{207}Pb/^{235}U$ Age	±1σ	% Disc	Y_2O_3	ThO_2	UO_2	PbO	CaO	SiO_2	P_2O_5	La_2O_3	Ce_2O_3	Pr_2O_3	Nd_2O_3	Sm_2O_3	Gd_2O_3	Dy_2O_3	Lu_2O_3	Total
Paragneiss																													
10CY-021 (Mt Iphigene)																													
10CY-21A_14.1	2011	(Qtz)	64.19	3.50	0.0496	1.7	0.1065	3.93	99.7	3	102.7	4	3	1.41	4.80	1.24	0.047	1.35	0.11	29.45	13.12	28.16	2.96	11.65	2.64	0.90	0.45	0.08	98.37
10CY-21A_14.2	2011	(Qtz)	21.07	3.40	0.0535	1.3	0.3501	3.99	299	10	304.8	12	2	1.58	3.51	0.81	0.100	0.93	0.08	30.04	13.84	29.81	2.72	11.84	2.71	0.51	0.40	0.08	98.94
10CY-21A_14.3	2011	(Qtz)	68.66	3.52	0.0487	3.7	0.0978	5.14	93.2	3	94.7	5	2	2.57	4.65	1.52	0.060	1.39	0.12	30.17	13.06	27.58	2.67	10.75	2.35	0.77	0.55	0.15	98.37
10CY-21A_19.1	2011	(Qtz)	22.35	3.80	0.0545	2.0	0.3360	4.48	282	11	294.1	13	4	1.31	4.09	0.65	0.102	0.95	0.15	29.68	14.21	29.46	2.98	11.56	2.50	0.64	0.42	0.10	98.81
10CY-21A_19.2	2011	(Qtz)	86.96	6.97	0.0490	2.7	0.0776	7.53	73.7	5	75.9	6	3	0.90	4.46	0.91	0.043	1.25	0.08	29.70	13.73	29.18	2.82	11.92	2.56	0.62	0.39	0.07	98.65
10CY-21A_19.3	2011	(Qtz)	18.95	3.39	0.0548	3.4	0.3987	4.80	331	11	340.7	16	3	1.59	4.45	0.91	0.130	1.24	0.07	29.73	13.50	28.49	2.80	11.81	2.52	0.60	0.41	0.10	98.35
10CY-21A_19.4	2011	(Qtz)	62.30	3.61	0.0499	1.8	0.1104	4.12	103	4	106.3	4	4	2.96	5.42	1.48	0.059	1.53	0.08	30.09	13.47	27.47	2.49	10.13	1.99	0.54	0.52	0.19	98.40
10CY-21A_19.5	2011	(Qtz)	18.49	3.44	0.0531	1.7	0.3962	4.27	340	11	338.9	14	0	2.48	3.99	0.59	0.114	1.10	0.07	29.92	13.34	28.42	2.68	11.16	2.31	0.89	0.51	0.14	97.71
10CY-21B_12.1	2011	(Pl)	20.51	3.40	0.0524	1.3	0.3523	4.41	307	10	306.4	13	0	–	–	–	–	–	–	–	–	–	–	–	–	–	–	–	–
10CY-21B_12.2	2011	(Pl)	18.61	3.40	0.0519	1.2	0.3842	3.98	337	11	330.2	12	-2	–	–	–	–	–	–	–	–	–	–	–	–	–	–	–	–
10CY-21B_12.3	2011	(Pl)	53.07	3.91	0.0512	4.4	0.1329	23.98	120	5	126.7	27	5	–	–	–	–	–	–	–	–	–	–	–	–	–	–	–	–
10CY-21B_12.4	2011	(Pl)	18.78	3.40	0.0521	1.2	0.3826	4.18	334	11	329.0	13	-2	–	–	–	–	–	–	–	–	–	–	–	–	–	–	–	–
10CY-21B_12.5	2011	(Pl)	19.01	3.64	0.0529	1.2	0.3838	4.25	330	12	329.8	13	0	–	–	–	–	–	–	–	–	–	–	–	–	–	–	–	–
10CY-21B_13.1	2011	Int.	19.84	3.67	0.0542	1.3	0.3765	4.19	317	11	324.5	13	2	2.59	4.45	0.91	0.122	1.20	0.09	30.02	13.43	28.10	2.94	11.43	2.22	0.72	0.52	0.10	98.86
10CY-21B_13.2	2011	Int.	26.22	3.38	0.0526	2.0	0.2768	4.28	241	8	248.1	10	3	2.10	3.94	0.83	0.101	1.02	0.09	29.90	13.37	28.78	2.77	11.76	2.48	0.99	0.60	0.11	98.83
10CY-21B_13.3	2011	Int.	65.78	3.40	0.0471	1.3	0.0987	3.67	97.3	3	95.6	4	-2	3.83	4.46	0.61	0.058	1.16	0.07	30.58	12.86	27.53	2.57	11.25	2.43	1.00	0.81	0.17	99.39
10CY-023 (Mt Iphigene)																													
10CY-23A_7.1	2011	(Bt)	61.74	3.38	0.0473	2.5	0.1057	4.17	104	4	102.0	4	-2	3.43	4.43	1.02	0.056	1.22	0.08	30.42	12.86	26.95	2.61	10.87	2.37	1.09	0.66	0.08	98.17
10CY-23A_7.2	2011	(Bt)	62.28	3.39	0.0490	2.0	0.1085	3.95	103	3	104.6	4	2	2.80	5.38	1.26	0.062	1.51	0.09	30.23	12.24	26.53	2.82	10.85	2.81	1.11	0.79	0.16	98.64
10CY-23A_7.3	2011	(Bt)	61.06	3.40	0.0498	2.3	0.1124	4.24	105	4	108.2	5	3	3.54	4.64	1.08	0.059	1.26	0.08	30.26	12.77	27.02	2.81	11.41	2.53	1.01	0.69	0.21	99.39
10CY-23A_7.4	2011	(Bt)	61.94	3.68	0.0496	2.2	0.1105	4.30	103	4	106.4	5	3	3.37	4.63	0.98	0.055	1.24	0.07	30.23	12.66	27.24	2.79	11.25	2.17	0.74	0.67	0.11	98.21
10CY-23A_7.5	2011	(Bt)	60.85	3.57	0.0494	2.2	0.1120	4.19	105	4	107.8	5	3	2.91	5.12	1.22	0.058	1.40	0.08	30.18	11.87	26.46	2.70	11.11	2.90	1.12	0.87	0.16	98.15
10CY-23A_7.6	2011	(Bt)	63.37	3.51	0.0487	2.1	0.1059	4.13	101	4	102.2	4	1	3.43	4.68	1.08	0.064	1.27	0.08	30.31	12.76	27.22	2.86	11.04	2.39	0.83	0.61	0.14	98.76
10CY-23A_10.1	2011	(Qtz)	60.78	3.50	0.0472	1.7	0.1072	4.32	105	4	103.4	4	-2	3.70	3.20	1.81	0.067	1.14	0.05	30.26	12.45	27.07	2.73	10.91	2.63	1.21	1.31	0.20	98.73
10CY-23A_10.2	2011	(Qtz)	61.22	3.37	0.0492	2.1	0.1108	4.02	104	4	106.7	4	2	2.92	4.79	1.26	0.061	1.35	0.09	30.10	12.40	26.27	2.81	10.94	2.91	1.09	0.85	0.15	97.98
10CY-23A_10.3	2011	(Qtz)	63.88	3.50	0.0483	2.3	0.1043	4.16	100	4	100.8	4	1	2.51	4.75	1.15	0.058	1.32	0.07	29.73	12.53	27.82	2.63	10.91	2.53	0.81	0.83	0.15	97.80
10CY-23B_12.2	2011	(Pl)	62.33	3.40	0.0512	2.0	0.1132	4.00	103	3	108.9	4	6	0.92	4.48	1.02	0.049	1.24	0.07	29.79	13.65	29.13	2.78	11.75	2.71	0.78	0.43	0.06	98.87
10CY-23B_12.3	2011	(Pl)	62.49	3.50	0.0485	2.1	0.1070	4.10	102	4	103.2	4	1	1.62	5.07	1.06	0.051	1.35	0.09	29.72	13.19	27.71	2.67	11.41	2.51	0.88	0.52	0.11	97.96
10CY-23B_12.4	2011	(Pl)	62.18	3.40	0.0502	2.2	0.1112	4.14	103	3	107.1	4	4	1.54	4.98	1.03	0.038	1.37	0.11	29.64	13.23	28.21	2.77	11.71	2.54	0.91	0.58	0.08	98.73
10CY-23B_13.1	2011	(Pl)	62.08	3.45	0.0470	1.9	0.1043	4.05	103	4	100.8	4	-2	–	–	–	–	–	–	–	–	–	–	–	–	–	–	–	–
10CY-23B_13.2	2011	(Pl)	64.26	3.85	0.0483	1.9	0.1037	4.31	99.5	4	100.2	4	1	2.83	4.36	0.94	0.062	1.23	0.05	30.03	13.34	27.95	2.73	11.13	2.26	0.77	0.56	0.15	98.38
10CY-23B_13.3	2011	(Pl)	63.56	3.37	0.0489	1.8	0.1062	3.97	101	3	102.4	4	2	3.33	4.27	1.10	0.063	1.26	0.06	29.95	12.94	27.13	2.77	10.86	2.48	0.97	0.68	0.15	98.01
10CY-23B_20.1	2011	Int.	29.25	3.50	0.0526	1.8	0.2478	18.70	217	7	224.8	39	4	1.91	4.38	0.87	0.058	1.11	0.14	30.06	13.82	28.66	2.79	11.78	2.22	0.57	0.51	0.15	99.01
10CY-23B_20.2	2011	Int.	62.72	3.61	0.0490	5.3	0.1078	6.35	102	4	104.0	7	2	3.07	4.25	0.75	0.045	1.12	0.07	30.36	13.34	28.40	2.86	11.36	2.37	0.56	0.64	0.14	99.33
10CY-23B_20.3	2011	Int.	58.99	3.43	0.0494	2.9	0.1154	4.50	108	4	110.9	5	2	2.38	4.35	0.64	0.046	1.14	0.09	30.19	13.14	28.22	2.89	11.20	2.70	1.20	0.69	0.14	99.01
10CY-033 (Mt Avers)																													
10CY-33A_19.1	2011	Int.	65.70	3.40	0.0491	1.1	0.1031	3.56	97.4	3	99.7	4	2	2.47	5.14	0.99	0.063	1.39	0.09	30.13	13.18	27.43	2.90	10.91	2.09	0.60	0.50	0.07	97.96
10CY-33A_19.2	2011	Int.	19.64	3.69	0.0533	1.3	0.3739	4.27	320	12	322.5	13	1	2.04	3.88	0.84	0.110	1.05	0.09	29.73	13.96	29.06	2.95	10.95	1.95	0.56	0.47	0.14	97.79
10CY-33A_19.3	2011	Int.	56.30	3.55	0.0484	1.9	0.1185	4.10	114	4	113.7	5	0	2.55	4.44	1.49	0.058	1.30	0.11	29.80	13.18	27.33	2.79	11.11	2.39	0.73	0.51	0.12	97.91
10CY-33B_8.1	2011	Int.	19.79	3.42	0.0529	1.4	0.3685	4.09	318	11	318.6	12	0	2.32	4.40	0.77	0.104	1.11	0.13	29.59	13.62	28.53	2.77	11.08	2.13	0.60	0.49	0.08	97.72
10CY-33B_8.2	2011	Int.	63.25	3.39	0.0480	2.0	0.1046	4.00	101	3	101.1	4	0	3.27	4.88	1.03	0.058	1.37	0.07	30.34	13.34	27.77	2.41	10.46	2.53	0.57	0.61	0.13	98.83
10CY-33B_8.3	2011	Int.	58.38	3.65	0.0476	1.9	0.1124	4.12	109	4	108.2	4	-1	3.05	5.11	1.00	0.056	1.39	0.09	30.32	13.09	27.52	2.73	10.85	2.26	0.72	0.58	0.15	98.89
10CY-33B_10.1	2011	(Bt)	19.06	3.50	0.0551	2.9	0.3989	5.08	330	11	340.8	16	3	3.04	5.09	0.69	0.118	1.24	0.13	30.04	13.30	28.23	2.73	10.64	2.11	0.85	0.57	0.13	98.90
10CY-33B_10.2	2011	(Bt)	65.01	3.66	0.0497	2.5	0.1054	4.71	98.4	4	101.8	5	3	0.65	5.95	0.96	0.044	1.53	0.09	29.75	14.18	29.48	2.88	10.91	2.01	0.50	0.14	0.05	99.14
10CY-33B_10.3	2011	(Bt)	19.21	3.54	0.0518	1.7	0.3719	4.48	327	11	321.0	14	-2	1.99	2.02	0.76	0.062	0.56	0.09	29.68	15.61	31.77	3.04	9.80	1.75	0.63	0.33	0.12	98.21
10CY-33B_13.1	2011	(Crd)	61.86	3.40	0.0470	2.2	0.1047	4.09	103	4	101.1	4	-2	2.50	4.54	1.78	0.057	1.06	0.19	29.52	13.69	28.27	2.55	11.11	2.28	0.85	0.46	0.10	98.95
10CY-33B_13.2	2011	(Crd)	20.46	3.63	0.0525	1.5	0.3536	4.17	308	11	307.4	12	0	2.45	4.43	1.35	0.099	1.13	0.10	29.48	13.44	27.94	3.10	11.12	2.32	0.77	0.54	0.12	98.38
10CY-33B_13.3	2011	(Crd)	61.67	3.64	0.0475	1.9	0.1063	4.13	104	4	102.6	4	-1	2.75	4.65	1.65	0.084	1.41	0.10	29.40	13.49	27.39	2.61	10.47	2.25	0.85	0.52	0.13	97.75
10CY-33B_13.4	2011	(Crd)	72.49	3.60	0.0501	2.2	0.0953	4.36	88.3	3	92.4	4	5	2.54	4.91	1.82	0.077	1.58	0.10	28.52	12.97	26.68	2.60	10.54	2.36	0.74	0.53	0.13	96.11

Table A.2 continued. Monazite U–Pb isotope and chemical analyses

		SHRIMP												Electron Microprobe Microanalysis (wt%)															
Spot	Session	Micro-structure	$^{238}U/^{206}Pb^*$	±1σ (%)	$^{207}Pb^*/^{206}Pb^*$	±1σ (%)	$^{207}Pb^*/^{235}U$	±1σ (%)	$^{238}U/^{206}Pb$ Age	±1σ	$^{207}Pb/^{235}U$ Age	±1σ	% Disc	Y_2O_3	ThO_2	UO_2	PbO	CaO	SiO_2	P_2O_5	La_2O_3	Ce_2O_3	Pr_2O_3	Nd_2O_3	Sm_2O_3	Gd_2O_3	Dy_2O_3	Lu_2O_3	Total
Paragneiss																													
10CY-041 (Mt Avers)																													
10CY-41A_6.1	2011	Int.	18.21	3.39	0.0553	0.9	0.4189	6.49	345	11	355.2	21	3	–	–	–	–	–	–	–	–	–	–	–	–	–	–	–	–
10CY-41A_6.2	2011	Int.	18.97	3.42	0.0524	0.7	0.3812	4.16	331	11	327.9	13	-1	2.92	4.69	2.86	0.226	1.64	0.10	29.68	12.74	25.84	2.49	10.32	1.91	0.83	0.55	0.12	96.91
10CY-41A_6.3	2011	Int.	32.26	3.37	0.0493	1.3	0.2108	3.95	197	7	194.2	7	-1	2.88	4.29	2.63	0.202	1.52	0.10	29.74	12.74	26.97	2.52	10.48	1.92	0.95	0.55	0.14	97.62
10CY-41A_6.4	2011	Int.	19.09	3.46	0.0518	1.0	0.3742	4.12	329	11	322.8	12	-2	2.59	4.30	1.08	0.131	1.16	0.08	29.72	12.79	27.63	2.67	11.11	2.25	0.69	0.54	0.14	96.86
10CY-41A_6.5	2011	Int.	21.06	3.37	0.0581	0.7	0.3803	4.63	299	10	327.3	13	9	–	–	–	–	–	–	–	–	–	–	–	–	–	–	–	–
10CY-41A_6.6	2011	Int.	64.08	4.33	0.0483	1.8	0.1038	5.10	99.8	4	100.3	6	0	2.63	3.78	2.29	0.170	1.29	0.09	23.48	11.85	24.49	2.11	9.40	1.98	0.64	0.47	0.12	84.79
10CY-41A_19.1	2011	Int.	62.35	3.39	0.0487	1.9	0.1077	3.92	103	3	103.9	4	1	3.21	4.33	0.91	0.056	1.15	0.09	30.03	12.69	27.12	2.70	10.87	2.32	0.92	0.68	0.14	97.21
10CY-41A_19.2	2011	Int.	24.97	3.37	0.0528	1.7	0.2917	4.24	253	8	259.9	10	3	3.22	4.23	1.89	0.083	1.35	0.09	29.97	12.77	27.57	2.60	10.85	2.38	0.55	0.55	0.11	98.21
10CY-41A_19.3	2011	Int.	63.86	3.73	0.0488	2.1	0.1053	4.35	100	4	101.7	5	1	3.44	4.61	0.95	0.067	1.20	0.10	30.07	12.97	27.63	2.48	10.67	2.46	0.94	0.66	0.09	98.34
10CY-41A_19.4	2011	Int.	62.64	4.12	0.0473	1.4	0.1041	4.43	102	4	100.6	4	-2	3.19	5.39	1.67	0.081	1.55	0.10	29.95	12.77	26.79	2.62	10.50	2.21	0.67	0.57	0.08	98.12
10CY-41A-29.1	2011	(Qtz)	19.00	3.43	0.0546	1.6	0.3960	4.04	331	11	338.7	13	2	1.49	3.14	0.37	0.075	0.70	0.15	29.52	14.17	29.64	2.91	11.84	2.53	0.76	0.38	0.06	97.73
10CY-41A-29.2	2011	(Qtz)	26.28	3.37	0.0520	0.4	0.2729	3.88	241	8	245.0	9	2	2.83	4.62	1.88	0.068	1.41	0.13	29.62	12.94	27.54	2.59	10.73	2.39	0.72	0.54	0.14	98.13
10CY-41A-29.3	2011	(Qtz)	66.55	3.37	0.0475	2.0	0.0984	3.92	96.1	3	95.3	4	-1	3.53	4.95	1.06	0.069	1.30	0.15	29.31	12.46	26.64	2.76	10.61	2.31	0.96	0.78	0.16	97.07
Y1-IG057 (Mt Iphigene)																													
57A.3-1	2012	(Bt)	21.78	2.5	0.0526	4.0	0.333	4.7	289	7	292	14	1	2.32	5.10	0.87	0.049	0.95	0.10	29.32	14.40	27.20	3.05	10.17	1.80	1.52	0.40	0.13	97.36
57A.3-2	2012	(Bt)	64.29	2.3	0.0459	1.4	0.098	2.7	99.5	2	95.4	3	-4	2.57	5.44	1.99	0.064	1.15	0.12	29.41	13.18	25.70	2.78	9.87	2.07	1.76	0.80	0.19	97.09
57A.3-3	2012	(Bt)	62.61	2.4	0.0474	1.6	0.104	2.9	102	2	101	3	-1	2.29	5.20	2.36	0.079	1.19	0.13	29.43	13.42	25.68	2.75	9.69	2.13	1.85	0.76	0.16	97.10
57A.9-1	2012	(Grt)	61.65	2.3	0.0461	1.5	0.103	2.7	104	2	99.6	3	-4	2.11	5.07	1.25	0.055	0.96	0.13	29.57	14.66	27.46	2.85	10.28	1.81	1.30	0.42	0.12	98.04
57A.9-2	2012	(Grt)	19.39	2.2	0.0520	1.9	0.370	3.0	324	7	320	9	-1	2.47	4.61	0.28	0.092	0.78	0.11	28.89	14.87	27.59	2.97	10.64	1.99	1.53	0.57	0.13	97.52
57A.9-3	2012	(Grt)	63.66	2.3	0.0481	1.8	0.104	2.9	100	2	101	3	0	0.71	5.77	1.12	0.052	1.21	0.11	28.16	15.11	28.14	2.82	10.29	1.84	0.99	0.21	0.03	96.54
57A.9-4	2012	(Grt)	18.86	2.2	0.0530	2.6	0.387	3.4	333	7	332	11	0	1.33	6.93	0.36	0.136	0.90	0.42	28.25	14.73	27.22	3.03	10.27	1.80	1.55	0.42	0.08	97.42
57A.10-1	2012	(Grt)	60.24	2.2	0.0475	1.6	0.109	2.8	106	2	105	3	-1	1.36	5.14	0.83	0.100	0.89	0.11	28.78	14.92	27.08	2.86	10.40	2.06	1.26	0.49	0.14	96.42
57A.10-2	2012	(Grt)	20.04	2.3	0.0529	4.2	0.364	4.8	314	7	315	15	0	1.43	4.54	0.66	0.107	0.88	0.15	28.43	15.37	27.78	2.93	10.32	1.94	1.19	0.47	0.13	96.32
57A.10-3	2012	(Grt)	20.29	2.3	0.0529	2.1	0.359	3.1	310	7	312	10	1	2.32	4.62	0.83	0.123	0.89	0.11	28.46	14.48	27.20	3.08	10.30	1.80	1.45	0.46	0.11	96.23
57A.11-1	2012	(Grt)	25.83	2.4	0.0521	1.7	0.278	2.9	245	6	249	7	2	2.47	4.88	0.76	0.114	0.90	0.13	28.71	14.06	27.07	2.90	10.24	1.86	1.15	0.41	0.09	95.77
57A.11-2	2012	(Grt)	62.75	2.3	0.0478	1.4	0.105	2.7	102	2	101	3	0	1.83	5.85	1.37	0.060	1.09	0.11	28.63	13.05	26.05	2.93	10.40	2.30	1.77	0.61	0.12	96.19
57A.11-3	2012	(Grt)	65.27	2.7	0.0479	2.5	0.101	3.6	98.0	3	97.8	4	0	1.17	5.82	1.55	0.052	1.07	0.11	28.54	14.50	27.31	2.87	10.04	1.90	1.04	0.26	0.09	96.33
57B.2-1	2012	(Bt)	24.80	2.3	0.0528	3.0	0.293	3.8	255	6	261	10	3	1.06	5.66	1.52	0.048	1.02	0.13	29.22	14.22	27.53	2.95	10.15	1.90	1.43	0.48	0.05	97.37
57B.2-2	2012	(Bt)	55.15	8.6	0.0486	5.1	0.121	10.0	116	10	116	12	0	0.95	5.34	1.57	0.064	1.01	0.13	29.53	14.64	27.08	2.86	10.21	2.02	1.50	0.58	0.11	97.59
57B.2-3	2012	(Bt)	61.14	2.2	0.0479	1.7	0.108	2.8	105	2	104	3	0	1.08	5.80	1.53	0.057	1.07	0.12	29.26	14.36	27.22	2.95	10.12	1.93	1.41	0.40	0.06	97.34
Y1-IG061 (Mt Iphigene)																													
61A.3-1	2012	Int.	18.30	2.3	0.0548	2.1	0.413	3.1	343	8	351	11	2	1.08	4.94	0.26	0.078	0.65	0.31	29.37	14.73	28.78	3.05	11.23	2.32	1.81	0.41	0.08	99.08
61A.3-2	2012	Int.	63.35	2.3	0.0471	1.8	0.103	2.9	101	2	99.1	3	-2	3.02	4.28	0.86	0.052	0.82	0.07	30.02	14.43	27.24	2.98	10.36	1.94	1.25	0.56	0.14	98.04
61A.3-3	2012	Int.	25.38	2.3	0.0514	1.9	0.279	3.0	249	6	250	7	0	3.43	4.15	0.61	0.055	0.78	0.10	29.94	13.76	26.98	3.03	10.55	2.09	1.54	0.67	0.17	97.85
61A.5-1	2012	(Grt)	20.26	2.3	0.0523	1.8	0.356	3.0	311	7	309	9	0	2.46	4.51	1.61	0.151	0.94	0.08	28.70	13.77	26.16	2.96	10.06	1.91	1.51	0.52	0.20	95.54
61A.5-2	2012	(Grt)	19.06	2.6	0.0525	2.8	0.380	3.8	330	8	327	12	-1	2.41	4.75	0.87	0.115	0.85	0.06	28.69	14.28	26.85	2.88	10.30	1.86	1.20	0.46	0.08	95.65
61A.5-3	2012	(Grt)	19.72	2.2	0.0511	2.0	0.357	3.0	319	7	310	9	-3	2.06	4.06	0.83	0.110	0.80	0.06	28.57	15.06	27.29	2.95	10.24	1.82	1.34	0.45	0.09	95.71
61B.1-1	2012	Int.	19.66	2.2	0.0538	6.2	0.378	6.6	320	7	325	21	2	0.97	3.91	0.19	0.079	0.66	0.24	28.24	15.14	29.29	3.26	10.80	2.18	1.41	0.44	0.08	96.87
61B.1-2	2012	Int.	60.98	2.5	0.0480	2.8	0.108	3.7	105	3	105	4	0	3.46	4.13	0.87	0.046	1.05	0.05	29.27	13.77	26.51	2.94	10.46	2.33	1.63	0.71	0.18	97.41
61B.1-3	2012	Int.	62.84	2.3	0.0488	3.1	0.107	3.8	102	2	103	4	1	3.35	4.46	1.03	0.058	0.96	0.06	28.97	13.88	26.75	2.80	10.04	1.89	1.35	0.63	0.12	96.34
61B.4-1	2012	(Crd)	19.42	2.3	0.0520	1.9	0.370	3.0	324	7	319	10	-1	2.49	3.10	0.92	0.101	0.78	0.04	29.57	14.62	27.82	2.87	10.77	2.18	1.75	0.49	0.14	97.64
61B.4-2	2012	(Crd)	50.51	3.7	0.0486	2.7	0.133	4.5	126	5	127	6	0	2.17	3.29	0.97	0.050	0.79	0.06	29.59	14.95	28.00	3.07	10.81	1.95	1.57	0.53	0.14	97.94
61B.4-3	2012	(Crd)	24.19	2.8	0.0507	3.4	0.289	4.4	261	7	258	11	-1	2.04	2.97	0.82	0.046	0.72	0.06	29.55	14.58	28.45	3.09	11.19	2.23	1.45	0.48	0.05	97.72

Table A.2 continued. Monazite U–Pb isotope and chemical analyses

		SHRIMP												Electron Microprobe Microanalysis (wt%)														
Spot	Session	Micro-structure	$^{238}U/^{206}Pb^*$	±1σ (%)	$^{207}Pb^*/^{206}Pb^*$	±1σ (%)	$^{207}Pb^*/^{235}U$	±1σ (%)	$^{238}U/^{206}Pb$ Age	±1σ	$^{207}Pb/^{235}U$ Age	±1σ	% Disc	Y_2O_3	ThO_2	UO_2	PbO	CaO	SiO_2	P_2O_5	La_2O_3	Ce_2O_3	Pr_2O_3	Nd_2O_3	Sm_2O_3	Gd_2O_3	Dy_2O_3	Lu_2O_3	Total
Paragneiss																												
Y1-MJ074 (Marujupu Pk)																												
74A.1-1	2012	(Bt)	54.68	2.5	0.0509	3.3	0.128	4.1	117	3	123	5	5	2.73	4.31	0.72	0.047	0.81	0.04	29.95	14.30	27.74	2.86	10.60	1.94	1.38	0.63	0.06	98.14
74A.1-2	2012	(Bt)	61.61	2.2	0.0475	2.8	0.106	3.6	104	2	103	4	-1	3.05	4.18	0.70	0.055	0.97	0.06	29.97	13.77	27.40	3.04	10.71	1.96	1.29	0.57	0.15	97.89
74A.5-1	2012	Int.	62.82	2.4	0.0490	2.4	0.108	3.4	102	2	104	4	2	1.42	2.85	0.44	0.031	0.56	0.12	29.66	14.87	29.12	3.06	11.32	2.38	1.38	0.45	0.07	97.74
74A.5-2	2012	Int.	53.80	2.3	0.0511	2.3	0.131	3.2	119	3	125	4	5	1.43	6.69	0.56	0.046	1.01	0.36	29.39	14.56	27.55	2.85	10.45	1.83	1.12	0.48	0.08	98.42
74A.5-3	2012	Int.	56.16	2.4	0.0502	2.3	0.123	3.3	114	3	118	4	4	1.70	3.70	0.91	0.044	0.74	0.13	29.70	14.68	28.77	2.88	11.15	2.10	1.24	0.48	0.09	98.31
74A.7-1	2012	(Qtz)	67.60	2.5	0.0486	14.6	0.099	14.8	94.7	2	96.1	14	1	2.94	4.48	1.18	0.054	0.90	0.06	29.16	14.27	27.27	2.85	9.92	1.92	1.28	0.54	0.20	97.01
74A.7-2	2012	(Qtz)	62.05	2.4	0.0485	3.2	0.108	4.0	103	2	104	4	1	3.17	4.01	1.46	0.060	0.88	0.06	29.19	14.19	27.03	2.94	9.96	2.06	1.46	0.57	0.15	97.21
74B.14-1	2012	Int.	66.76	2.6	0.0461	1.9	0.095	3.2	95.8	2	92.3	3	-4	3.07	3.36	1.48	0.057	0.82	0.05	29.69	14.43	27.84	2.90	9.91	1.90	1.38	0.57	0.13	97.58
74B.14-2	2012	Int.	63.68	2.3	0.0465	2.1	0.101	3.1	100	2	97.4	3	-3	2.67	3.65	1.32	0.051	0.86	0.04	29.47	14.67	27.90	2.95	9.98	1.85	1.21	0.43	0.11	97.15
74B.14-3	2012	Int.	68.63	2.3	0.0467	6.0	0.094	6.4	93.3	2	91.1	6	-2	3.08	3.70	1.53	0.056	0.86	0.05	29.70	14.18	27.19	2.92	10.04	2.07	1.58	0.56	0.13	97.64
74B.17-1	2012	Int.	66.82	2.5	0.0474	2.3	0.098	3.4	95.8	2	94.7	3	-1	3.30	4.18	1.06	0.057	0.88	0.31	30.04	13.55	27.20	2.83	10.37	2.09	1.70	0.55	0.14	98.26
74B.17-2	2012	Int.	66.05	2.4	0.0476	11.0	0.099	11.3	96.9	2	96.2	11	-1	3.14	4.76	1.11	0.055	0.90	0.05	29.95	13.73	27.29	2.94	10.31	2.06	1.45	0.57	0.15	98.46
74B.17-3	2012	Int.	63.33	2.2	0.0477	2.8	0.104	3.5	101	2	100	4	-1	2.98	4.11	1.02	0.050	0.83	0.05	30.11	14.13	27.80	2.98	10.21	1.93	1.40	0.51	0.14	98.24
Y1-LH077 (Mt Lockhart)																												
77A.9-1	2012	(Bt)	66.10	2.2	0.0478	7.9	0.100	8.2	96.8	2	96.4	8	0	3.03	5.08	0.59	0.052	0.92	0.14	28.23	13.65	27.01	2.88	10.19	1.98	1.38	0.38	0.15	95.67
77A.9-2	2012	(Bt)	59.51	2.4	0.0479	2.3	0.111	3.3	107	3	107	4	-1	1.78	4.93	0.51	0.042	0.74	0.28	27.90	14.36	27.85	3.03	10.46	2.14	1.45	0.52	0.10	96.07
77A.9-3	2012	(Bt)	66.42	2.2	0.0471	2.3	0.098	3.2	96.3	2	94.8	3	-2	3.13	4.97	0.82	0.059	0.94	0.11	28.41	13.48	26.36	2.94	10.22	1.95	1.37	0.47	0.13	95.35
77A.11-1	2012	Int.	64.82	2.4	0.0480	2.8	0.102	3.7	98.7	2	98.7	4	0	3.41	4.64	0.85	0.053	0.91	0.13	30.10	13.25	27.16	2.98	10.59	2.03	1.83	0.64	0.14	98.72
77A.11-2	2012	Int.	58.25	2.5	0.0498	4.9	0.118	5.5	110	3	113	6	3	2.05	3.45	0.58	0.025	0.74	0.23	29.63	15.61	29.12	2.99	10.49	1.81	1.27	0.47	0.16	98.62
77A.11-3	2012	Int.	57.65	2.5	0.0490	2.3	0.117	3.4	111	3	113	4	2	1.82	3.77	0.49	0.033	0.76	0.25	29.38	14.77	29.03	3.13	11.00	1.99	1.33	0.51	0.06	98.31
77B.3-1	2012	(Bt)	63.56	2.3	0.0481	2.1	0.104	3.1	101	2	101	3	0	3.13	5.05	0.88	0.063	1.06	0.12	28.55	13.35	26.33	3.04	10.01	2.00	1.64	0.63	0.18	96.03
77B.3-2	2012	(Bt)	63.31	2.3	0.0471	2.1	0.103	3.2	101	2	99.1	3	-2	3.21	4.66	0.78	0.055	0.82	0.14	29.78	13.73	26.47	3.03	10.52	2.06	1.60	0.56	0.18	97.58
77B.5-1	2012	Int.	64.13	2.4	0.0473	6.9	0.102	7.3	99.7	2	98.3	7	-1	2.93	4.15	0.93	0.049	0.97	0.11	29.31	14.39	27.37	2.82	9.98	1.84	1.31	0.47	0.15	96.76
77B.5-2	2012	Int.	62.52	2.3	0.0465	2.2	0.103	3.2	102	2	99.2	3	-3	1.36	5.50	0.77	0.034	0.87	0.17	29.28	14.63	27.51	3.07	9.92	1.93	1.06	0.28	0.07	96.44
77B.5-3	2012	Int.	64.17	2.5	0.0483	2.1	0.104	3.3	99.7	3	100	3	1	2.34	5.22	0.85	0.059	0.85	0.12	28.72	14.25	26.75	2.88	9.71	1.81	1.20	0.52	0.14	95.44
Y1-CB080 (Mt Colombo)																												
80A.3-1	2012	(Bt)	55.08	2.2	0.0495	3.9	0.124	4.5	116	3	119	5	2	1.72	4.21	0.65	0.037	0.64	0.16	28.65	15.34	28.45	3.09	10.88	1.90	1.11	0.43	0.04	97.29
80A.3-2	2012	(Bt)	62.99	2.3	0.0468	1.7	0.103	2.8	102	2	99.1	3	-2	2.26	4.75	1.15	0.055	0.89	0.10	29.55	14.47	28.11	2.85	10.56	1.92	1.34	0.54	0.09	98.64
80B.1-1	2012	Int.	64.26	2.2	0.0497	2.2	0.107	3.1	99.6	2	103	3	3	1.79	4.03	0.70	0.043	0.84	0.18	29.42	14.68	27.90	3.10	10.71	1.95	1.37	0.42	0.07	97.20
80B.1-2	2012	Int.	58.60	2.3	0.0495	1.7	0.117	2.9	109	3	112	3	3	1.83	4.36	1.00	0.047	0.75	0.18	28.94	14.94	27.20	2.86	10.34	2.15	1.19	0.47	0.14	96.41
80B.1-3	2012	Int.	65.33	2.5	0.0468	1.5	0.099	2.9	97.9	2	95.7	3	-2	2.82	5.54	1.94	0.077	1.23	0.16	29.88	13.78	26.58	2.84	9.94	1.73	1.32	0.45	0.12	98.38
80B.5-1	2012	(Bt)	56.05	2.4	0.0496	1.9	0.122	3.0	114	3	117	4	3	2.34	4.94	1.23	0.051	0.95	0.14	29.23	13.91	26.44	2.86	10.18	1.71	1.27	0.38	0.13	95.77
80B.5-2	2012	(Bt)	58.31	2.4	0.0489	1.8	0.116	3.0	110	3	111	3	1	2.32	5.24	0.72	0.051	0.92	0.34	28.94	14.34	27.30	2.80	10.21	1.82	1.19	0.50	0.13	96.82
80B.5-3	2012	(Bt)	61.67	2.5	0.0472	2.5	0.106	3.5	104	3	102	4	-2	2.35	5.12	1.01	0.071	0.82	0.25	28.90	14.31	26.21	2.69	9.82	1.75	1.40	0.57	0.13	95.39
80B.6-1	2012	Int.	57.29	2.4	0.0470	5.3	0.113	5.8	112	3	109	6	-2	2.24	3.80	0.53	0.039	0.57	0.33	29.26	15.19	28.70	3.10	10.91	2.00	1.44	0.45	0.13	98.67
80B.6-2	2012	Int.	61.12	2.3	0.0459	1.4	0.103	2.7	105	2	100.0	3	-4	2.22	4.67	1.28	0.056	1.96	0.15	29.45	13.87	27.23	2.92	10.62	2.06	1.31	0.59	0.11	98.50
80B.6-3	2012	Int.	57.86	2.4	0.0470	1.5	0.112	2.8	110	3	108	3	-2	2.25	3.86	0.52	0.043	0.60	0.34	29.31	14.73	29.10	3.19	10.80	1.99	1.35	0.55	0.12	98.75
80B.7-1	2012	(Grt)	66.47	2.3	0.0472	1.8	0.098	2.9	96.3	2	94.8	3	-1	1.43	4.88	1.03	0.049	0.96	0.10	28.56	14.58	28.11	3.06	10.14	1.90	1.06	0.38	0.12	96.36
80B.7-2	2012	(Grt)	64.20	2.4	0.0477	1.8	0.102	3.0	99.6	2	99.0	3	-1	1.08	5.54	0.71	0.041	0.99	0.15	28.45	14.81	28.33	2.99	10.41	1.62	0.89	0.33	0.06	96.38
80B.7-3	2012	(Grt)	61.63	2.5	0.0476	1.6	0.106	3.0	104	3	103	3	-1	1.42	5.03	1.06	0.049	1.02	0.11	28.41	14.42	28.11	2.87	10.36	1.83	1.21	0.39	0.05	96.34

Table A.2 continued. Monazite U–Pb isotope and chemical analyses

		SHRIMP											Electron Microprobe Microanalysis (wt%)															
Spot	Session	Micro-structure	$^{238}U/^{206}Pb^*$	±1σ (%)	$^{207}Pb^*/^{206}Pb^*$	±1σ (%)	$^{207}Pb^*/^{235}U$	±1σ (%)	$^{238}U/^{206}Pb$ Age	±1σ	$^{207}Pb/^{235}U$ Age	±1σ	% Disc	Y_2O_3	ThO_2	UO_2	PbO	CaO	SiO_2	P_2O_5	La_2O_3	Ce_2O_3	Pr_2O_3	Nd_2O_3	Sm_2O_3	Gd_2O_3	Dy_2O_3	Lu_2O_3	Total
Orthogneiss																												
Y1-BB003 (Bird Bluff)																												
003A-1.1	2013	(Qtz)	53.93	2.6	0.0488	2.0	0.125	3.3	118	3	119	3	1	1.71	6.19	1.12	0.081	2.64	0.17	29.79	13.35	27.89	2.69	9.89	1.84	1.09	0.37	0.02	98.84
003A-1.2	2013	(Qtz)	60.49	2.2	0.0480	1.2	0.109	2.5	106	2	106	2	0	3.23	5.82	0.79	0.061	2.42	0.11	30.07	12.32	26.67	2.68	10.60	2.22	1.82	0.70	0.08	99.57
003A-1.3	2013	(Qtz)	61.91	2.2	0.0494	2.2	0.110	3.1	103	2	106	2	3	2.37	*1.71*	0.34	0.020	0.76	0.18	30.12	14.22	30.42	3.12	11.94	2.59	1.77	0.60	0.07	100.25
003B-1.1	2013	Int.	55.85	2.1	0.0498	1.7	0.123	2.7	114	2	118	2	3	2.51	1.92	0.34	0.043	1.13	0.26	28.37	13.51	29.48	3.09	11.91	2.28	1.61	0.60	0.10	97.16
003B-1.3	2013	Int.	60.95	2.2	0.0475	1.6	0.108	2.7	105	2	104	2	-1	2.49	4.57	0.74	0.077	1.92	0.12	28.75	12.09	26.75	2.67	11.02	2.43	1.74	0.67	0.15	96.19
003B-1.4	2013	Int.	57.56	2.2	0.0484	1.0	0.116	2.4	111	2	111	2	0	2.25	6.19	1.01	0.076	1.93	0.20	28.74	13.08	27.62	2.73	10.86	1.85	1.23	0.40	0.07	98.24
003B-2.1	2013	Int.	60.70	2.2	0.0480	0.8	0.109	2.3	105	2	105	2	0	2.91	6.08	1.32	0.083	1.61	0.19	29.94	12.31	26.54	2.69	10.28	2.08	1.45	0.44	0.13	98.05
003B-2.2	2013	Int.	62.09	2.1	0.0484	1.6	0.107	2.6	103	2	104	2	1	1.98	5.40	1.18	0.078	2.64	0.20	29.99	13.20	27.18	2.62	9.73	1.97	1.14	0.39	0.10	97.81
003B-2.3	2013	Int.	54.20	2.4	0.0485	1.4	0.123	2.8	118	3	118	3	0	2.20	2.97	0.32	0.027	1.09	0.32	29.55	13.91	29.85	3.19	11.63	2.21	1.50	0.51	0.12	99.39
10CY-029 (Mt Iphigene)																												
029A-4.1	2013	(Bt)	59.18	2.0	0.0496	1.7	0.115	2.6	108	2	111	2	3	1.05	6.53	0.54	0.039	1.83	0.20	29.32	13.72	28.60	2.94	10.30	2.09	1.24	0.25	0.04	98.69
029A-4.2	2013	(Bt)	17.97	2.2	0.0528	0.5	0.405	2.3	349	8	345	8	-1	3.06	6.84	0.43	0.064	1.71	0.26	29.50	12.29	26.18	2.77	10.44	2.26	1.68	0.65	0.14	98.28
029A-4.3	2013	(Bt)	59.90	2.1	0.0484	1.0	0.112	2.3	107	2	107	2	1	1.65	6.01	1.19	0.052	1.84	0.18	29.40	12.42	26.95	2.77	10.63	2.52	2.01	0.59	0.05	98.26
10CY-036 (Mt Avers)																												
036A-5.1	2013	(Grt)	17.34	2.3	0.0551	0.9	0.438	2.5	361	8	369	8	2	2.11	3.86	0.44	0.097	0.97	0.44	29.52	12.31	29.12	3.26	12.19	2.95	1.54	0.49	0.07	99.36
036A-5.2	2013	(Grt)	17.62	2.3	0.0537	1.1	0.421	2.6	356	8	356	8	0	2.99	5.79	0.34	0.120	0.95	0.87	29.12	12.22	27.29	2.87	11.48	2.64	1.99	0.68	0.09	99.44
036A-5.3	2013	(Grt)	17.12	2.0	0.0556	1.2	0.448	2.4	366	7	376	7	3	2.54	4.45	0.26	0.103	0.81	0.67	29.00	13.17	28.82	3.06	11.29	2.36	1.64	0.55	0.08	98.82
036B-3.1	2013	Int.	18.30	2.2	0.0544	1.0	0.410	2.4	343	7	349	7	2	2.27	6.53	0.46	0.134	1.50	0.98	28.07	12.41	26.41	2.72	11.32	2.71	1.78	0.53	0.12	97.97
036B-3.2	2013	Int.	27.91	2.1	0.0522	0.9	0.258	2.3	227	5	233	5	3	3.25	6.43	0.57	0.064	1.90	0.21	29.89	11.80	26.00	2.59	10.83	2.59	1.94	0.72	0.16	98.95
036B-3.3	2013	Int.	18.08	2.0	0.0537	1.0	0.410	2.2	347	7	349	7	0	2.27	6.57	0.45	0.141	1.50	0.84	28.79	12.49	27.03	2.93	11.36	2.60	1.83	0.54	0.15	99.49
036B-4.1	2013	(Pl)	19.14	2.2	0.0536	0.7	0.386	2.3	328	7	332	7	1	2.14	10.36	0.46	0.204	1.50	1.89	27.25	11.99	26.50	2.76	10.79	2.13	1.34	0.42	0.11	99.85
036B-4.2	2013	(Pl)	56.48	2.2	0.0485	1.1	0.118	2.4	113	2	114	2	0	3.40	5.13	1.07	0.062	1.90	0.17	29.91	12.22	26.63	2.73	10.71	2.53	1.94	0.81	0.14	99.35
036B-4.3	2013	(Pl)	43.06	2.1	0.0497	1.2	0.159	2.4	148	3	150	3	1	1.75	5.38	0.35	0.062	1.57	0.44	29.28	13.17	28.32	3.02	11.31	2.35	1.85	0.57	0.05	99.49
Y1-BG040 (Mt Bitgood)																												
040A-3.1	2013	Int.	17.96	2.5	0.0553	1.1	0.425	2.8	349	9	359	9	3	1.88	3.39	1.82	0.140	1.65	0.10	28.88	13.80	29.10	2.96	11.08	1.90	1.56	0.42	0.11	98.79
040A-3.2	2013	Int.	59.11	2.0	0.0482	0.8	0.113	2.2	108	2	108	2	0	2.48	5.16	2.26	0.068	1.82	0.18	28.92	12.91	27.63	2.91	10.52	2.09	1.56	0.60	0.11	99.20
040A-3.3	2013	Int.	18.08	2.0	0.0532	0.3	0.406	2.1	347	7	346	7	0	3.07	5.69	2.73	0.244	2.05	0.22	29.97	11.77	25.45	2.60	10.00	2.46	1.96	0.76	0.12	99.10
040A-5.1	2013	Int.	19.20	2.4	0.0530	0.7	0.381	2.5	327	8	328	8	0	2.68	5.56	2.67	0.224	1.86	0.20	29.74	12.59	26.58	2.55	10.01	2.15	1.63	0.59	0.13	99.16
040A-5.2	2013	Int.	18.46	2.1	0.0527	0.5	0.394	2.1	340	7	337	7	-1	2.10	5.01	1.53	0.154	1.68	0.16	29.69	13.30	28.40	2.84	10.71	2.04	1.16	0.44	0.08	99.31
040A-5.3	2013	Int.	63.31	2.1	0.0487	1.3	0.106	2.4	101	2	102	2	1	1.07	6.05	0.97	0.040	1.65	0.38	29.20	13.23	28.56	2.89	10.30	2.39	1.70	0.35	0.07	98.83
040B-2.1	2013	Int.	24.60	2.4	0.0598	0.9	0.335	2.6	257	6	294	6	14	1.99	4.53	0.52	0.098	0.71	0.25	29.59	13.85	28.50	2.97	10.74	2.12	1.69	0.54	0.04	98.16
040B-2.2	2013	Int.	33.60	2.6	0.0515	1.4	0.211	2.9	189	5	195	5	3	1.04	6.40	0.98	0.043	0.89	0.35	29.25	12.26	27.33	3.13	11.43	2.70	1.83	0.44	0.04	98.10
040B-2.3	2013	Int.	18.88	2.5	0.0530	0.4	0.387	2.5	333	8	332	8	0	2.65	4.06	2.45	0.184	0.94	0.17	29.78	13.26	27.28	2.67	10.44	2.15	1.50	0.59	0.13	98.26
040B-3.1	2013	Int.	46.19	2.4	0.0510	1.4	0.152	2.7	138	3	144	3	4	1.70	4.39	1.22	0.080	0.93	0.22	29.38	13.25	28.00	3.04	10.97	2.50	1.73	0.54	0.03	97.98
040B-3.2	2013	Int.	57.01	1.9	0.0492	0.8	0.119	2.1	112	2	114	2	2	1.21	3.89	1.90	0.062	0.98	0.20	29.45	13.37	28.28	2.91	11.36	2.63	1.82	0.42	0.03	98.50

Table A.2 continued. Monazite U–Pb isotope and chemical analyses

		SHRIMP												Electron Microprobe Microanalysis (wt%)														
Spot	Session	Micro-structure	$^{238}U/^{206}Pb^*$	±1σ (%)	$^{207}Pb^*/^{206}Pb^*$	±1σ (%)	$^{207}Pb^*/^{235}U$	±1σ (%)	$^{238}U/^{206}Pb$ Age	±1σ	$^{207}Pb/^{235}U$ Age	±1σ	% Disc	Y_2O_3	ThO_2	UO_2	PbO	CaO	SiO_2	P_2O_5	La_2O_3	Ce_2O_3	Pr_2O_3	Nd_2O_3	Sm_2O_3	Gd_2O_3	Dy_2O_3	Lu_2O_3	Total
Orthogneiss																												
Y1-IG053 (Mt Iphigene)																												
053A1.1	2013	(Bt)	56.81	2.0	0.0507	1.7	0.123	2.7	112	2	118	2	5	0.58	7.32	0.90	0.054	0.88	0.26	29.42	14.38	28.20	2.76	10.84	1.80	1.11	0.13	0.01	98.65
053A1.2	2013	(Bt)	60.26	2.5	0.0486	1.1	0.111	2.7	106	3	107	3	1	2.47	6.95	0.54	0.067	0.46	1.22	28.40	13.76	26.66	2.68	10.71	2.04	1.17	0.36	0.09	97.59
053A1.4	2013	(Bt)	59.50	2.3	0.0501	1.7	0.116	2.9	107	3	112	2	4	2.48	7.39	0.46	0.061	0.53	0.87	28.68	13.28	26.66	2.76	10.70	2.19	1.33	0.49	0.07	97.95
053A-7.1	2013	Int.	61.48	2.1	0.0498	1.6	0.112	2.7	104	2	107	2	3	2.13	6.92	0.62	0.058	0.44	0.80	28.46	14.10	28.01	2.69	10.65	1.77	1.32	0.39	0.13	98.49
053A-7.2	2013	Int.	60.02	2.5	0.0494	1.6	0.114	3.0	107	3	109	3	3	0.91	6.92	0.57	0.051	0.64	0.31	29.01	14.47	28.57	2.85	10.87	1.78	1.10	0.27	0.03	98.37
053A-7.3	2013	Int.	60.01	2.0	0.0510	1.4	0.117	2.4	107	2	113	2	6	2.23	7.09	0.68	0.057	0.47	0.88	28.03	13.85	27.59	2.82	10.57	2.04	1.28	0.37	0.07	98.01
053A-8.1	2013	Int.	58.59	2.2	0.0488	1.8	0.115	2.8	109	2	110	2	1	2.57	4.31	0.40	0.041	0.30	0.48	28.64	14.00	28.35	2.88	11.22	2.19	1.29	0.50	0.11	97.27
053A-8.2	2013	Int.	62.00	2.1	0.0493	1.1	0.110	2.4	103	2	106	2	2	0.72	6.62	1.06	0.054	0.75	0.21	29.03	14.18	28.13	2.99	10.97	1.96	1.05	0.28	0.03	98.04
053A-8.3	2013	Int.	62.44	2.6	0.0516	2.1	0.114	3.4	102	3	109	3	7	2.64	4.05	0.39	0.042	0.34	0.44	28.84	13.65	28.20	3.01	11.55	2.21	1.67	0.58	0.09	97.69
Y1-LH066 (Mt Lockhart)																												
066B-2.1	2013	Int.	54.35	2.2	0.0487	1.4	0.123	2.6	118	3	118	3	1	2.32	3.45	0.50	0.042	1.07	0.64	29.41	13.36	28.56	2.98	11.54	2.60	1.75	0.56	0.10	98.86
066B-2.2	2013	Int.	64.82	2.1	0.0481	0.9	0.102	2.3	98.7	2	98.9	2	0	2.75	4.97	1.71	0.056	1.52	0.11	30.02	13.17	26.94	2.77	10.57	2.25	1.48	0.50	0.10	98.91
066B-2.3	2013	Int.	58.11	2.1	0.0482	1.5	0.114	2.6	110	2	110	2	0	2.04	1.51	0.45	0.032	0.69	0.13	29.92	14.27	30.18	3.12	12.00	2.42	1.53	0.53	0.10	98.92
066B-5.1	2013	(Bt)	53.99	2.2	0.0471	1.5	0.120	2.6	118	3	115	3	-2	2.17	2.01	0.35	0.032	0.86	0.20	29.92	13.66	29.73	3.03	12.07	2.62	1.88	0.67	0.11	99.32
066B-5.2	2013	(Bt)	63.32	2.7	0.0475	2.0	0.104	3.4	101	3	100	3	-1	3.47	5.68	1.72	0.069	1.58	0.11	29.87	11.91	25.99	2.65	10.52	2.06	1.57	0.57	0.13	97.91
066B-8.1	2013	(Grt)	61.28	2.3	0.0493	1.2	0.111	2.6	104	2	107	2	2	2.12	7.02	1.09	0.068	1.44	0.49	28.84	12.71	27.44	2.78	10.86	2.10	1.46	0.53	0.11	99.08
066B-8.2	2013	(Grt)	62.69	2.1	0.0485	0.8	0.107	2.2	102	2	103	2	1	2.68	6.18	2.05	0.075	1.59	0.15	29.65	12.40	26.31	2.60	10.43	2.04	1.59	0.65	0.11	98.51
066B-8.3	2013	(Grt)	55.46	2.2	0.0496	1.2	0.123	2.5	115	3	118	3	2	2.06	6.83	1.03	0.077	1.44	0.49	28.96	12.50	27.57	2.76	10.89	2.09	1.37	0.50	0.09	98.65
Diatexite																												
Y1-IG071 (Mt Iphigene)																												
071A-1.1	2013	(Pl)	21.63	2.2	0.0519	0.5	0.331	2.2	291	6	290	6	0	2.87	6.25	1.46	0.156	1.48	0.25	29.80	13.07	26.68	2.54	9.86	2.01	1.63	0.51	0.15	98.71
071A-1.2	2013	(Pl)	18.03	2.2	0.0534	0.9	0.408	2.3	348	7	348	7	0	2.45	5.78	1.59	0.173	1.50	0.25	29.73	12.94	26.76	2.64	10.03	2.10	1.51	0.49	0.11	98.05
071A-7.1	2013	(Bt)	53.03	2.2	0.0488	0.6	0.127	2.3	120	3	121	3	1	3.08	4.95	3.92	0.113	1.65	0.20	30.18	12.45	25.75	2.61	9.51	2.19	1.44	0.66	0.15	98.87
071A-7.2	2013	(Bt)	55.47	2.2	0.0488	0.8	0.121	2.3	115	2	116	2	1	2.76	4.38	2.70	0.086	1.41	0.17	30.03	13.19	27.44	2.63	10.01	2.25	1.60	0.60	0.12	99.38
071A-7.3	2013	(Bt)	61.77	2.0	0.0487	1.6	0.109	2.6	104	2	105	2	1	3.29	5.91	1.40	0.074	1.47	0.19	30.25	12.49	26.40	2.63	9.96	2.28	1.63	0.64	0.08	98.67
071B-3.1	2013	Int.	19.63	2.3	0.0530	0.9	0.372	2.5	320	7	321	7	0	3.12	5.39	1.63	0.061	0.23	0.16	28.23	11.82	25.20	2.54	10.54	2.45	1.71	0.74	0.11	93.93
071B-3.3	2013	Int.	17.23	2.4	0.0543	0.9	0.434	2.5	364	8	366	8	1	2.68	5.40	2.04	0.074	0.28	0.20	28.91	13.01	25.98	2.63	10.12	1.98	1.49	0.58	0.10	95.48
071B.3.2	2013	Int.	57.51	2.2	0.0478	0.8	0.115	2.4	111	2	110	2	-1	2.77	4.87	1.39	0.144	0.24	0.14	28.98	12.93	26.69	2.67	10.63	1.94	1.43	0.62	0.11	95.55

Errors are 1-sigma; Pb_c and Pb^* indicate the common and radiogenic portions, respectively.
Error in Standard calibration by session: 2.0% (2011), 0.15% (2012) 0.49% (2013) (not included in above errors but required when comparing data from different mounts).
(1) Common Pb corrected using measured 204Pb.
(2) Int.: interstital between two or more minerals, (Bt): inclusion in biotite, (Crd): inclusion in cordierite, (Grt): inclusion in garnet, (Kfs): inclusion in K-feldspar, (Pl): inclusion in plagioclase, (Qtz): inclusion in Quartz
(3) '–' not analysed

Appendix B

B.1 Major oxide, trace element and REE chemistry

Major oxide and select trace elements were analysed by X-ray fluorescence spectrometry at Franklin and Marshall College. A PANanalytical 2404 X-ray fluorescence vacuum spectrometer equipped with a PW2540 X-Y sample handler was used following the procedures described by Boyd and Mertzman (1987). FeO was analysed by Fe^{2+} titration and the Fe_2O_3 was calculated by difference.

Rare earth elements were analysed by inductively coupled plasma mass spectrometry at the University of Maryland. Twenty milligrams of powdered sample was dissolved in closed Savillex® Teflon beakers using 0.5 ml of 14M HNO_3 and 3 ml of 29M HF. Samples were digested for 24 hours, dried down and subjected to a second dissolution in 0.25 ml 12M $HClO_4$, 0.5 ml of 14M HNO_3 and 3 ml of 29M HF for 72 hours. The solution was dried down, brought up in 6M HCl and dissolved for a further 24 hours; this last procedure was repeated until the sample was fully dissolved. Samples were diluted by a factor of 100. One ml of a 20 ppb ^{115}In solution was added to the diluted sample to enable correction for instrumental drift.

The following isotopes ^{115}In, ^{139}La, ^{140}Ce, ^{141}Pr, ^{143}Nd, ^{147}Sm, ^{153}Eu, ^{158}Gd, ^{159}Tb, ^{163}Dy, ^{165}Ho, ^{167}Er, ^{169}Tm, ^{173}Yb and ^{175}Lu were analysed using a Finnigan Element 2 single collector ICP-MS; solutions were introduced into the plasma using an APEX desolvating nebulizer. USGS standards G-2, a granite, and MAG-1, a marine sediment, were used to calculate sample concentrations. Signals were corrected for instrumental drift, by normalizing all data to the ^{115}In signal in the G-2 standard, and the blank, which was <0.1% of the signal for standards and <0.7% of the signal for unknowns. Granites

and orthogneisses were corrected using USGS standard G-2, while metasedimentary and paragneiss samples were corrected using USGS standard MAG-1. Uncertainties from counting statistics ranged from 1% to 6%, and propagated uncertainties for concentrations ranged from 4% to 12%.

B.2 Whole-rock Rb, Sr, Sm, and Nd isotope compositions (University of Maryland)

Rb, Sr, Sm and Nd isotope compositions were determined in the Isotope Geochemistry Laboratory at the University of Maryland. The rocks were prepared in a manner similar to that of Korhonen et al. (2010). Fifty milligrams of powder were dissolved in Savillex® Teflon beakers using 3 ml of 29M HF and 0.5 ml of 14M HNO_3, together with isotopic spikes enriched in ^{87}Rb, ^{84}Sr, ^{149}Sm, and ^{150}Nd, using a closed digestion at 180–190ºC for 24 hours. Samples were dried and re-dissolved in 3 ml of 29M HF, 0.5 ml of 14M HNO_3, and 0.25 ml of 12M $HClO_4$, and digested for a further 72 hours at 180–190ºC, then dried. To finish, 2 ml of 6M HCl was added to the samples, which were digested at 180ºC for 24 hours and dried again; this last procedure was repeated until the resulting solution was clear, after which samples were finally dried and brought up in 2 ml of 2.5M HCl.

Rubidium, Sr and REEs were separated from each other using a primary cation exchange column filled with AG50Wx4 (200–400 mesh) resin. Samples were loaded in chloride form. Rubidium and Sr were eluted in 2.5M HCl, while the REE were eluted from the column in 6M HCl. Rubidium cuts were dried and diluted in 2% HNO_3. Strontium cuts were passed through a cleanup column filled with Eichrom™ Sr-spec resin and eluted in 0.05M HNO_3. The REE cuts from the primary column were passed

through a secondary column filled with 0.225M 2-methyllactic acid (MLA). Samarium and Nd were eluted in 0.225M MLA (pH = 4.67).

Strontium, Nd and Sm ratios were analysed using a VG Sector 54 TIMS. Strontium cuts were loaded onto a single Re filament with a Ta-oxide activator, and analysed in a multi-dynamic mode. Strontium isotopes were corrected for mass fractionation by normalizing the measured $^{87}Sr/^{86}Sr$ ratio to an $^{86}Sr/^{88}Sr$ ratio = 0.1194. Repeated analysis of SRM 987 during the course of this study yielded an average $^{87}Sr/^{86}Sr$ value of 0.710238 (n = 30). The mass fractionation corrected and spike corrected $^{87}Sr/^{86}Sr$ ratio was normalized the average SRM 987 $^{87}Sr/^{86}Sr$ value to correct for instrumental bias. Strontium blank concentrations averaged 14.0 ng (n = 4), <1% of sample Sr concentrations. Samples 10CY-03, Y1-AW039, Y1-CB080, Y1-IG070, and Y1-LH077 were analyzed for Nd using a Nu Plasma multi-collector (MC) ICP-MS. Sample 10CY-039 was analysed for Sm also using the NU Plasma ICP-MS.

Rubidium ratios were measured using a Nu Plasma MC-ICP-MS at the University of Maryland. Samples were diluted by a factor of 100 and were introduced into the plasma using an Aridus I desolvating nebulizer. A 50 ppb Rb SpecPure® plasma standard was introduced after every three sample analyses and was used to correct for instrumental fractionation and drift. Rubidium blanks averaged 8.04 ppm (n = 4), <1% of the sample Rb concentrations.

Neodymium and Sm were loaded on two Re filaments with phosphoric acid and loaded into the machine in a triple filament arrangement. Neodymium ratios were measured in dynamic mode and corrected for mass fractionation by normalizing the measured $^{143}Nd/^{144}Nd$ ratio to $^{146}Nd/^{144}Nd = 0.7219$. Repeated analysis of the Ames

standard during the course of this study yielded an average $^{143}Nd/^{144}Nd$ value of 0.512126 (n = 33). The fractionation and spiked corrected $^{143}Nd/^{144}Nd$ ratio was normalized to the average Ames $^{143}Nd/^{144}Nd$ value to correct for instrumental bias. Samarium was measured in static mode. Samarium blanks averaged 0.311 ng (n = 3) while Nd blanks averaged 2.28 ng (n = 3); both <1% of sample Sm and Nd concentrations.

The USGS G-2 granite was analysed 7 times over a period of 12 months. Repeat analyses yielded an average $^{87}Sr/^{86}Sr$ of 0.709767 ± 0.000038 (n = 7) and an average $^{143}Nd/^{144}Nd$ of 0.512243 ± 0.000010 (n = 7). Rubidium concentrations averaged 167.6 ppm (range 162.9–174.2 ppm), Sr concentrations 488.8 ppm (range 482.1–496.2 ppm), and Rb/Sr ratios ranged from 0.3367 to 0.3511. Samarium concentrations averaged 7.1 ppm (range 7.0–7.3 ppm), Nd concentrations 52.6 ppm (range 52.2–53.2 ppm), and Sm/Nd ratios ranged from 0.1344 to 0.1372.

B.3 U–Pb analysis of zircon (SHRIMP: Australian National University)

U–Pb zircon age determinations were made using SHRIMP II and SHRIMP-RG at the Australian National University Research School of Earth Sciences (ANU-RSES) following the procedures described in Williams (1998 and references therein). Data were reduced using the SQUID Excel Macro (Ludwig, 2001). The zircon U/Pb ratios have been normalized relative to a value of 0.0668 for the Temora reference zircon, equivalent to an age of 417 Ma (Black et al. 2003); analytical uncertainties for the respective analytical sessions are given in the footnotes to the data tables. Uncertainties reported for individual analyses (ratios and ages) are given at the 1σ level. Tera–Wasserburg (Tera and Wasserburg, 1972) concordia plots, probability density plots with stacked

histograms, and weighted mean $^{206}Pb/^{238}U$ age calculations were calculated using ISOPLOT/EX (Ludwig, 2003). Where appropriate the "Mixture Modelling" algorithm of Sambridge and Compston (1994) via ISOPLOT/EX has been used to un-mix statistical age populations or groupings. From such groupings weighted mean $^{206}Pb/^{238}U$ ages have been calculated and the uncertainties reported as 95% confidence limits, including incorporation, in quadrature, of the uncertainty in the reference zircon calibration.

B.4 U–Pb analyses of zircon (LA-ICP-MS: University of Arizona)

Zircon grains (generally 50–100) were incorporated into a 1" epoxy mount together with fragments of the Sri Lanka standard zircon at the University of Arizona. The mounts were sanded down to a depth of ~20 microns, polished, imaged, and cleaned prior to isotopic analysis.

U–Pb geochronology of zircons was conducted by laser ablation multicollector inductively coupled plasma mass spectrometry (LA-MC-ICPMS) at the Arizona LaserChron Center (Gehrels et al., 2006, 2008). The analyses involve ablation of zircon with a New Wave DUV193 Excimer laser (operating at a wavelength of 193 nm) using a spot diameter of 35 μm. The ablated material is carried in helium into the plasma source of a GVI Isoprobe, which is equipped with a flight tube of sufficient width that U, Th, and Pb isotopes are measured simultaneously. All measurements are made in static mode, using Faraday detectors with 10^{11} ohm resistors for ^{238}U, ^{232}Th, ^{208}Pb, and ^{206}Pb, a Faraday detector with a 10e12 ohm resistor for ^{207}Pb, and an ion-counting channel for ^{204}Pb. Ion yields are ~1.0 mv per ppm. Each analysis consists of one 12-second integration on peaks with the laser off (for backgrounds), 12 one-second integrations with

the laser firing, and a 30 second delay to purge the previous sample and prepare for the next analysis. The ablation pit is ~12 microns in depth.

For each analysis, the errors in determining $^{206}Pb/^{238}U$ and $^{206}Pb/^{204}Pb$ result in a measurement error of ~1-2% (at 2-sigma level) in the $^{206}Pb/^{238}U$ age. The errors in measurement of $^{206}Pb/^{207}Pb$ and $^{206}Pb/^{204}Pb$ also result in ~1-2% (at 2-sigma level) uncertainty in age for grains that are >1.0 Ga, but are substantially larger for younger grains due to low intensity of the ^{207}Pb signal. For most analyses, the cross-over in precision of $^{206}Pb/^{238}U$ and $^{206}Pb/^{207}Pb$ ages occurs at ~1.0 Ga.

Common Pb correction is accomplished by using the measured ^{204}Pb and assuming an initial Pb composition from Stacey and Kramers (1975) (with uncertainties of 1.0 for $^{206}Pb/^{204}Pb$ and 0.3 for $^{207}Pb/^{204}Pb$). Our measurement of ^{204}Pb is unaffected by the presence of ^{204}Hg because backgrounds are measured on peaks (thereby subtracting any background ^{204}Hg and ^{204}Pb), and because very little Hg is present in the argon gas (background ^{204}Hg = ~300 CPS).

Inter-element fractionation of Pb/U is generally ~20%, whereas apparent fractionation of Pb isotopes is generally <1%. In-run analysis of fragments of a large zircon crystal (generally every fifth measurement) with known age of 563.5 ± 3.2 Ma (2-sigma error) is used to correct for this fractionation. The uncertainty resulting from the calibration correction is generally 1-2% (2-sigma) for both $^{206}Pb/^{207}Pb$ and $^{206}Pb/^{238}U$ ages.

Concentrations of U and Th are calibrated relative to our Sri Lanka zircon, which contains ~518 ppm of U and 68 ppm Th. Uncertainties shown in the data tables are at the 1-sigma level, and include only measurement errors. Analyses that are >30% discordant

(by comparison of $^{206}Pb/^{238}U$ and $^{206}Pb/^{207}Pb$ ages) or >5% reverse discordant are not considered further.

B.5 Lu–Hf and O analysis of zircon (Australian National University)

Following the U–Pb analyses, the SHRIMP 1–2 μm deep U–Pb pits were lightly polished away and oxygen isotope analyses made in the same location using SHRIMP II fitted with a Cs ion source and electron gun for charge compensation as described by Ickert et al. (2008). Oxygen isotope ratios were determined in multiple collector mode using an axial continuous electron multiplier (CEM) triplet collector, and two floating heads with interchangeable CEM–Faraday Cups. The Temora 2 and FC1 reference zircons were analysed to monitor and correct for isotope fractionation. The measured $^{18}O/^{16}O$ ratios and calculated $\delta^{18}O$ values have been normalised relative to an FC1 weighted mean $\delta^{18}O$ value of +5.4 ‰ (Ickert et al. 2008). Reproducibility in the Duluth Gabbro FC1 reference zircon $\delta^{18}O$ value ranged from ± 0.30‰ to 0.37‰ (2σ uncertainty) for the analytical sessions. As a secondary reference, the Temora 2 zircon was analysed in the same sessions, which gave $\delta^{18}O$ values of +8.2‰ in agreement with data reported by Ickert et al. (2008).

Lu–Hf isotope measurements were conducted by laser ablation multicollector inductively coupled plasma mass spectroscopy (LA–MC–ICPMS) using the ANU-RSES Neptune MC–ICPMS coupled with a 193 nm ArF Excimer laser, following procedures similar to those described in Munizaga et al. (2008). For all analyses of unknowns or secondary standards, the laser spot size was ~47 μm in diameter. Laser ablation analyses targeted the same locations within single zircon grains used for both the U–Pb and

oxygen isotope analyses described above. The mass spectrometer was first tuned to optimal sensitivity using a large grain of zircon from the Mud Tank carbonatite. Isotopic masses were measured simultaneously in static-collection mode. A gas blank was acquired at regular intervals throughout the analytical session (every 12 analyses). Typically the laser was fired with a 5–8 Hz repetition rate and 50–60 mJ energy. Data were acquired for 100 seconds, but in many cases only a selected interval from the total acquisition was used in data reduction.

Throughout the analytical session several widely used reference zircons (FC-1 and Temora 2) were analysed to monitor data quality and reproducibility. Signal intensity was typically ~5–6 V for total Hf at the beginning of ablation, and decreased over the acquisition time to 2 V or less. Isobaric interferences of ^{176}Lu and ^{176}Yb on the ^{176}Hf signal were corrected by monitoring signal intensities of ^{175}Lu and ^{173}Yb, ^{172}Yb and ^{171}Yb. The calculation of signal intensity for ^{176}Hf also involved independent mass bias corrections for Lu and Yb (see Munizaga et al. 2008 for further details). During the course of this data collection the reference zircons gave the following weighted mean ^{176}Hf/^{177}Hf ratios: 915000 = 0.282310 ± 14 (±2s) for 23 analyses, Mud Tank = 0.282516 ± 11 for 8 analyses, FC1 = 0.282173 ± 9 for 22 of 23 analyses, Plesovice = 0.282486 ± 11 for 16 of 17 analyses, and Monastery = 0.282744 ± 12 for 8 analyses. These are within analytical uncertainty of the values reported by Woodhead and Hergt (2005).

Table B.1. Sample Locations

Sample	Rock Type	Location	Latitude	Longitude
10CY-010	Paragneiss	Bird Bluff	76°27.757' S	144°53.870' W
10CY-015	Paragneiss	Bird Bluff	76°27.757' S	144°53.870' W
10CY-021	Paragneiss	Maigetter Peak	76°26.420' S	146°29.029' W
10CY-023	Paragneiss	Maigetter Peak	76°26.420' S	146°29.029' W
10CY-033	Paragneiss	Mount Avers	76°28.049' S	145°17.417' W
10CY-041	Paragneiss	Mount Avers	76°28.049' S	145°17.417' W
Y1-BB013	Paragneiss	Bird Bluff	76°29.507' S	144°33.442' W
Y1-CB080	Paragneiss	Mount Colombo	76°29.313' S	144°46.633' W
Y1-IG057	Paragneiss	Mount Iphigene	76°29.024' S	146°06.372' W
Y1-IG061	Paragneiss	Mount Iphigene	76°29.266' S	145°50.603' W
Y1-LH077	Paragneiss	Mount Lockhart	76°26.909' S	145°07.188' W
Y1-MJ074	Paragneiss	Marujupu Peak	76°31.009' S	145°38.625' W
10CY-035	Orthogneiss	Maigetter Peak	76°28.049' S	145°17.417' W
Y1-IG053	Orthogneiss	Mount Iphigene	76°29.024' S	146°06.372' W
Y1-IG071	Orthogneiss	Mount Iphigene	76°30.676' S	145°48.368' W
Y1-IG073	Orthogneiss	Mount Iphigene	76°30.676' S	145°48.368' W
Y1-MJ075	Orthogneiss	Marujupu Peak	76°30.989' S	145°38.572' W
Y1-IG062	Cretaceous Granite	Mount Iphigene	76°29.266' S	145°50.603' W
C6-AW86-1	Cretaceous Granite	Mount Avers	76°27.600' S	145°25.440' W
10CY-039	Cretaceous Granite	Mount Avers	76°28.049' S	145°17.417' W
Y1-AE033	Cretaceous Granite	Mount Avers	76°27.678' S	144°20.195' W
Y1-AE064	Cretaceous Granite	Mount Avers	76°28.028' S	145°14.525' W
Y1-AW038	Cretaceous Granite	Mount Avers	76°27.895' S	145°27.689' W
Y1-AW039	Cretaceous Granite	Mount Avers	76°27.736' S	145°22.031' W
Y1-AW049	Cretaceous Granite	Mount Avers	76°27.895' S	145°27.689' W
Y1-AW051	Cretaceous Granite	Mount Avers	76°27.736' S	145°22.031' W
Y1-IG052	Cretaceous Granite	Mount Iphigene	76°29.024' S	146°06.372' W
Y1-IG070	Cretaceous Granite	Mount Iphigene	76°30.676' S	145°48.368' W
10CY-024	Microgranite	Maigetter Peak	76°26.420' S	146°29.029' W
Billey Bluff	Other Granite	Ickes Mountains	75°32.000’ S	140°02.000' W
21220-3	Other Granite	Scott Nunataks	77°14.000' S	154°12.000' W
Y2-BR087	Other Granite	Sarnoff Mountains	77°09.703' S	145°16.739' W
Y2-MP083	Other Granite	McKinley Peak	77°53.606' S	148°19.422' W

Table B.2. Major element, trace element and REE concentrations

Rock Type	Paragneiss								
Sample no.	10CY-010	10CY-015	10CY-021	10CY-023	10CY-033	10CY-041	Y1-BB013	Y1-CB080	Y1-IG057
wt %									
SiO_2	61.55	68.82	67.4	66.51	67.85	67.32	60.89	70.39	42.01
TiO_2	0.94	0.81	0.94	1.05	0.76	0.77	0.85	0.76	1.57
Al_2O_3	17.54	14.67	14.56	14.76	14.39	14.26	19.04	13.15	23.1
Fe_2O_3	1.32	1.24	0.76	1.06	1.36	1.08	1.21	0.67	3.89
FeO	6.05	4.55	5.5	5.87	4.21	4.61	5.87	5.04	12.78
MnO	0.09	0.05	0.07	0.08	0.08	0.05	0.07	0.08	0.44
MgO	3.71	2.76	3.26	3.59	2.74	2.89	3.9	3	7.74
CaO	0.91	0.82	1.31	0.71	1.37	1.75	0.93	1.75	0.43
Na_2O	1.91	1.64	1.81	0.99	2.03	2.55	1.33	1.85	0.37
K_2O	3.98	3.05	3.31	3.52	3.6	3.69	5.23	2.61	5.54
P_2O_5	0.13	0.06	0.14	0.08	0.13	0.14	0.15	0.19	0.15
LOI	2.21	1.77	1.5	1.9	1.85	1.18	2.65	1.69	3.49
Total	100.34	100.24	100.56	100.12	100.37	100.29	100.12	100.05	99.44
ppm (XRF)									
Rb	275.5	246.8	197.7	228.3	200.9	187.6	299.1	140.6	394.1
Sr	106	66	133	80	126	161	135	152	18
Y	39.9	28.6	33.8	36.8	32.5	33	34.7	28.5	90.9
Zr	218	245	253	232	200	193	140	214	155
V	138	113	127	135	110	110	121	115	222
Ni	76	50	51	61	51	51	54	53	90
Cr	188	139	141	159	141	129	120	118	166
Nb	22.1	32	19.3	27.8	21.5	15.3	22	16.5	38.6
Ga	26.2	28	21.9	27.2	22.5	20	29	20.4	38.8
Cu	43	15	13	5	18	10	11	14	69
Zn	138	141	114	138	107	110	129	100	296
Co	28	21	22	27	20	20	23	22	51
Ba	682	306	399	373	428	456	901	427	262
La	28	28	28	32	22	26	28	26	16
Ce	74	57	65	75	54	54	72	68	53
U	3.4	5.6	1.2	2.6	3.8	2.3	2.3	2.1	1.2
Th	21	24.6	18.6	23.9	16.3	14.5	13.7	18.3	34.3
Sc	18	15	17	13	16	14	16	15	41
Pb	<1	<1	<1	<1	<1	<1	18	14	<1
ppm (ICP-MS)									
Sc	18.37	13.77	–	16.66	13.63	14.19	16.55	13.37	58.17
Y	40.51	34.36	–	45.17	27.97	34.41	23.86	25.85	99.24
La	57.07	47.77	–	68.67	43.88	35.6	41.47	48.63	67.98
Ce	114.43	96.99	–	140.03	91.1	72.74	83.69	98.39	137.65
Pr	13.45	11.27	–	16.46	10.71	8.72	9.58	11.45	16.23
Nd	51.61	43.12	–	63.15	40.6	33.1	37.54	44.01	60.72
Sm	10.33	8.72	–	12.75	7.96	6.89	7.61	8.56	11.96
Eu	1.6	0.98	–	1.09	1.13	1.22	1.41	1.31	0.63
Gd	8.07	6.66	–	9.31	5.79	5.65	5.75	6.35	10.06
Tb	1.33	1.11	–	1.45	0.94	0.99	0.9	0.98	2.16
Dy	7.36	6.11	–	8.19	5.21	5.9	4.76	5.19	16.04
Ho	1.47	1.17	–	1.66	0.99	1.23	0.87	0.93	3.58
Er	3.9	3.07	–	4.7	2.56	3.43	2.12	2.24	9.84
Tm	0.55	0.43	–	0.7	0.36	0.5	0.27	0.29	1.4
Yb	3.31	2.64	–	4.47	2.17	3.14	1.56	1.73	8.36
Lu	0.43	0.35	–	0.62	0.28	0.43	0.2	0.23	1.09

Table B.2 continued. Major element, trace element and REE concentrations

Rock Type	Paragneiss			Orthogneiss				
Sample no.	Y1-IG061	Y1-LH077	Y1-MJ074	10CY-035	Y1-AW039	Y1-AW049	Y1-IG053	Y1-MJ075
wt %								
SiO_2	71	69.59	68.37	74.19	67.82	64.19	65.51	72.84
TiO_2	0.68	0.76	0.74	0.08	0.76	0.92	0.89	0.29
Al_2O_3	14.34	13.58	15.71	14.29	15.85	16.48	16.6	14.8
Fe_2O_3	0.94	1.06	1	0.06	0.91	1.65	1.03	0.28
FeO	4.34	4.17	4.53	0.5	3.42	3.7	3.86	1.49
MnO	0.09	0.04	0.09	0.01	0.08	0.07	0.07	0.03
MgO	2.45	2.9	2.75	0.23	1.71	1.95	2.02	0.63
CaO	1.17	2.22	0.85	0.89	2.86	3.62	3.95	1.3
Na_2O	1.43	2.21	1.69	2.43	4.17	4.09	3.4	3.44
K_2O	3.42	2.89	3.92	7.22	2.23	2.17	2.2	5.03
P_2O_5	0.19	0.18	0.14	0.08	0.31	0.29	0.3	0.16
LOI	2.22	1.42	2.3	0.43	1.18	1.08	1.01	0.69
Total	100.53	100.06	100.29	100.04	100.5	99.54	100.26	100.46
ppm (XRF)								
Rb	176	157.5	201.1	201.2	148.6	131.3	127.9	236.1
Sr	157	147	151	264	186	291	280	158
Y	38	32	31.2	5.9	31.1	16	24.5	13
Zr	177	215	166	93	198	260	191	261
V	95	103	105	15	93	101	102	26
Ni	55	49	55	4	14	12	12	6
Cr	98	128	107	24	59	61	65	28
Nb	13.1	15	16.5	3	19.6	17.2	14.3	17.2
Ga	19.2	19	22.4	14.9	23.8	22.7	22.6	20.8
Cu	16	5	7	3	10	5	17	4
Zn	81	102	100	14	74	88	78	41
Co	18	18	19	<1	14	17	16	1
Ba	822	459	875	963	267	388	486	945
La	25	23	26	19	23	28	18	51
Ce	60	59	63	32	49	60	38	122
U	2.6	2.2	4.3	1.9	3.9	2.1	2.9	8.4
Th	14.4	16.8	11	6.8	8	6.7	1.5	17.1
Sc	11	14	14	<1	14	16	16	5
Pb	14	20	22	47	2	14	15	38
ppm (ICP-MS)								
Sc	12.59	12.49	10.88	1.46	13.92	14.8	14.76	5.03
Y	34.28	31.46	21.8	7.83	33.69	15.69	26.03	14.42
La	28.11	45.05	35.89	14.71	33.44	43.52	24.5	93.41
Ce	57.94	91.9	72.69	30.07	70.29	89.23	52.46	169.39
Pr	6.87	10.76	8.57	3.74	8.94	10.61	6.89	18.25
Nd	26.57	41.6	33.15	13.77	34.79	38.26	27.7	60.28
Sm	5.54	8.38	6.66	2.95	7.56	6.55	5.82	8.73
Eu	1.53	1.58	1.34	1.35	1.28	1.28	1.63	1.1
Gd	4.62	6.54	4.97	2.45	7.09	5.44	5.52	5.97
Tb	0.84	1.06	0.78	0.37	1.23	0.77	0.95	0.83
Dy	5.41	5.84	4.21	1.71	6.76	3.67	5.33	3.61
Ho	1.2	1.11	0.79	0.28	1.22	0.61	0.98	0.5
Er	3.55	2.82	2.04	0.73	3.38	1.46	2.63	1.04
Tm	0.54	0.37	0.29	0.11	0.52	0.19	0.36	0.12
Yb	3.48	2.18	1.74	0.73	3.1	1.07	2.01	0.63
Lu	0.46	0.28	0.23	0.12	0.45	0.17	0.29	0.08

Table B.2 continued. Major element, trace element and REE concentrations

Rock Type	Cretaceous granite								
Sample no.	10CY-039	Y1-IG062	C6-AW86-1	Y1-AE051	Y1-AE064	Y1-IG052	Y1-IG070	Y1-AW038	Y1-AE033
wt %									
SiO_2	73.95	75.6	75.85	76.08	75.01	75.33	77.5	71.16	74.06
TiO_2	0.04	0.01	0.08	0.02	0.04	0.02	0.01	0.03	0.1
Al_2O_3	14.85	13.97	13.47	14.62	14.64	14.17	13.85	16.02	15.58
Fe_2O_3	0.08	0.03	0.05	0.11	0.22	0.11	0.03	0.04	0.09
FeO	0.22	0.76	0.43	0.39	0.4	0.83	0.08	0.54	0.14
MnO	0.01	0.06	0.01	0.03	0.05	0.07	0.01	0.08	0.01
MgO	0.15	0.17	0.22	0.14	0.18	0.2	0	0.11	0.1
CaO	0.89	1.05	1.02	2.5	1.65	1.22	1.98	0.44	1.37
Na_2O	2.8	2.77	2.6	3.6	3.13	2.74	3.66	2.8	2.74
K_2O	6.81	5.8	5.93	2.84	5.15	5.43	3.21	8.89	5.91
P_2O_5	0.11	0.09	0.05	0.1	0.06	0.09	0.08	0.07	0.11
LOI	0.61	0.58	0.39	0.65	0.48	0.48	0.33	0.47	0.62
Total	99.93	100.39	99.76	100.47	100.57	100.3	100.42	100.24	100.23
ppm (XRF)									
Rb	181.6	167.1	182.9	79.6	147.4	136.8	91.6	284.3	177.6
Sr	236	225	321	209	210	250	224	167	194
Y	4.8	27.4	3	14.7	10.3	15.5	4	14.6	8.9
Zr	39	76	122	56	73	57	28	76	23
V	5	<1	12	1	6	6	1	5	8
Ni	6	2	2	2	3	2	1	1	1
Cr	35	21	11	33	21	18	19	14	8
Nb	2	1.2	2	1	2.1	0.9	0.8	2.4	2.2
Ga	14.9	14.2	15	17.4	15.9	14.1	15.8	14.9	18.5
Cu	4	7	3	2	4	7	25	4	3
Zn	11	11	13	9	13	10	7	13	10
Co	<1	<1	<1	<1	<1	<1	<1	<1	<1
Ba	895	632	803	402	515	1073	434	457	640
La	11	19	25	19	26	17	13	15	21
Ce	13	37	53	23	39	20	17	13	28
U	1.1	3.1	2	3	1.7	<0.5	1.1	1.4	1.4
Th	<0.5	3.2	7.4	<0.5	5.9	<0.5	<0.5	<0.5	<0.5
Sc	<1	4	<1	4	2	3	1	3	1
Pb	65	52	36	46	47	62	43	64	58
ppm (ICP-MS)									
Sc	0.79	7.32	1.11	4.51	3.96	6.4	0.51	3.57	1.04
Y	5.63	24.87	3.5	12.74	11.89	17.82	2.95	10.86	9.77
La	6.12	14.35	27.55	7.79	20.12	11.12	4.34	1.87	15.21
Ce	11.08	30.03	55.41	13.18	40.71	20.06	7.14	2.45	31.27
Pr	1.28	3.79	6.87	1.48	4.86	2.32	0.76	0.24	3.9
Nd	4.54	13.83	24.89	5.06	17.33	8.13	2.43	0.75	14.39
Sm	0.99	3.2	4.54	1.04	3.33	1.48	0.45	0.23	3.26
Eu	1.32	1.13	0.98	1.44	1.16	1.58	1.13	0.6	1.49
Gd	0.94	2.77	3.25	0.99	2.54	1.33	0.41	0.41	2.93
Tb	0.18	0.52	0.34	0.22	0.39	0.31	0.08	0.13	0.47
Dy	1	3.51	1.12	1.7	2.1	2.51	0.47	1.21	2.17
Ho	0.19	0.86	0.13	0.45	0.41	0.61	0.1	0.35	0.33
Er	0.52	3.31	0.26	1.73	1.43	2.3	0.33	1.51	0.79
Tm	0.08	0.65	0.03	0.33	0.3	0.48	0.06	0.34	0.1
Yb	0.45	4.95	0.21	2.36	2.51	3.8	0.45	2.87	0.57
Lu	0.07	0.84	0.03	0.39	0.46	0.62	0.08	0.53	0.08

Table B.2 continued. Major element, trace element and REE concentrations

Rock Type	Microgranite	Other granite			
Sample no.	10CY-024	21220-3	Billey Bluff	Y2-MP083	Y2-BR087
wt %					
SiO_2	74.25	74.96	75.53	75.44	74.63
TiO_2	0.28	0.14	0.21	0.21	0.16
Al_2O_3	13.99	13.26	13.28	12.59	13.51
Fe_2O_3	0.12	0.17	0.55	0.60	0.15
FeO	1.31	0.55	0.58	1.16	1.20
MnO	0.03	0.01	0.05	0.04	0.04
MgO	0.31	0.34	0.23	0.20	0.19
CaO	1.2	1.10	0.63	0.86	1.14
Na_2O	2.82	2.29	4.28	3.55	3.23
K_2O	5.34	6.31	4.58	4.55	4.93
P_2O_5	0.07	0.15	0.05	0.05	0.07
LOI	0.78	0.40	0.43	0.63	0.70
Total	99.87	99.34	100.03	99.38	99.38
ppm (XRF)					
Rb	194.5	238.7	228.3	358.1	266.7
Sr	222	191	119	86	121
Y	33.7	6.6	23.1	27.4	35.7
Zr	227	130	189	126	145
V	23	17	17	18	19
Ni	1	1	1	1	2
Cr	4	26	15	31	65
Nb	14.8	7.2	32.6	32.9	27.7
Ga	20	17.3	24.1	24.8	23.3
Cu	7	1	4	1	2
Zn	27	24	31	41	45
Co	2	<1	<1	<1	1
Ba	834	427	461	252	557
La	48	25	56	39	37
Ce	108	52	109	72	80
U	2.4	2.6	5.3	5.8	3.7
Th	35.7	13	34.6	33.6	13.5
Sc	3	3	2	7	8
Pb	29	48	12	26	17
ppm (ICP-MS)					
Sc	3.8	–	–	–	–
Y	35.39	–	–	–	–
La	66.24	45.26	59.79	39.73	74.85
Ce	140.77	56.37	79.19	44.36	92.17
Pr	17.14	9.46	10.22	7.63	16.14
Nd	62.71	33.01	32.42	26.11	54.95
Sm	10.99	5.67	4.65	4.85	9.05
Eu	1.22	0.79	0.55	0.43	0.74
Gd	8.33	3.96	3.41	4.10	6.59
Tb	1.25	0.48	0.51	0.70	0.92
Dy	6.65	2.00	3.04	4.27	4.91
Ho	1.26	0.26	0.59	0.81	0.84
Er	3.68	0.52	1.81	2.43	2.31
Tm	0.56	0.06	0.32	0.42	0.38
Yb	3.38	0.32	2.13	2.77	2.56
Lu	0.52	0.05	0.35	0.43	0.40

Table B.3. Sr–Nd isotope compositions

Rock Type	Paragneiss							Orthogneiss			
Sample no.	10CY-010	10CY-015	10CY-023	10CY-033	Y1-CB080	Y1-IG057	Y1-LH077	10CY-035	Y1-AW039	Y1-AW049	Y1-IG053
Rb	205.5	284.9	232.4	206.5	147.3	453.1	164.7	196.2	131.3	133.2	114.4
Sr	147.6	104.4	99.6	98.3	144.3	11.9	139.3	269.8	181	288.3	285.9
Rb/Sr	1.39	2.73	2.33	2.1	1.02	38.02	1.18	0.73	0.73	0.46	0.4
$^{87}Rb/^{86}Sr$	4.04	7.92	6.76	6.09	2.96	111.79	3.43	2.11	2.1	1.34	1.16
$^{87}Sr/^{86}Sr$	0.732242	0.739512	0.729157	0.73412	0.731493	0.876604	0.738139	0.718183	0.721511	0.714164	0.716095
$^{87}Sr/^{86}Sr_{(100Ma)}$	0.726599	0.728444	0.719704	0.725607	0.727356	0.720353	0.733346	0.715240	0.718575	0.712295	0.714476
$^{87}Sr/^{86}Sr_{(360Ma)}$	0.71189	0.699593	0.695066	0.703418	0.716573	0.313076	0.720852	0.707570	0.710921	0.707423	0.710255
Sm	13.2	9.8	10.5	7.2	7.6	12.5	7.5	2.5	7	6.5	6.5
Nd	69.9	51.4	46.6	35.6	38.6	65.7	38.2	11.5	34	38.4	34.5
Sm/Nd	0.19	0.19	0.23	0.2	0.2	0.19	0.2	0.22	0.21	0.17	0.19
$^{147}Sm/^{144}Nd$	0.114417	0.115205	0.121042	0.122924	0.119023	0.114522	0.11865	0.130924	0.13244	0.102905	0.11328
$^{143}Nd/^{144}Nd$	0.512098	0.512203	0.512253	0.51209	0.512187	0.512044	0.512027	0.512253	0.512022	0.512229	0.512252
$\varepsilon Nd_{(0Ma)}$	-10.5	-8.5	-7.5	-10.7	-8.8	-11.6	-11.9	-7.5	-12	-8	-7.5
$\varepsilon Nd_{(100Ma)}$	-9.5	-7.5	-6.6	-9.8	-7.8	-10.5	-10.9	-6.7	-11.2	-6.8	-6.5
$\varepsilon Nd_{(360Ma)}$	-6.8	-4.7	-4.0	-7.3	-5.2	-7.8	-8.3	-4.5	-9.1	-3.7	-3.7

Rock Type		Cretaceous Granite								Microgranite
Sample no.	Y1-MJ075	10CY-039	Y1-IG062	C6-AW86-1	Y1-AE064	Y1-IG052	Y1-IG070	Y1-AW038	Y1-AE033	10CY-024
Rb	224.8	164.9	154.4	167.2	130.7	131	84.6	255.2	154.9	192.1
Sr	156.5	240.1	225.8	328.8	210.7	252.9	219.1	172.3	195.2	225.6
Rb/Sr	1.44	0.69	0.68	0.51	0.62	0.52	0.39	1.48	0.79	0.85
$^{87}Rb/^{86}Sr$	4.16	1.9	1.99	1.47	1.74	1.53	1.12	4.24	2.13	2.3
$^{87}Sr/^{86}Sr$	0.730733	0.723183	0.719813	0.713661	0.721024	0.725517	0.72151	0.725957	0.728763	0.712208
$^{87}Sr/^{86}Sr_{(100Ma)}$	0.724913	0.720526	0.717036	0.711604	0.718598	0.723376	0.71994	0.720025	0.725792	0.708989
$^{87}Sr/^{86}Sr_{(360Ma)}$	0.709743	0.713598	0.709795	0.706242	0.712273	0.717794	0.71587	0.704562	0.718048	0.7006
Sm	7	0.4	3.5	5	2.6	1.1	0.4	0.3	2.9	10.1
Nd	46.8	2	15.02	25.8	13.4	5.7	3	1.1	12.3	54.9
Sm/Nd	0.15	0.22	0.23	0.19	0.2	0.19	0.15	0.31	0.24	0.18
$^{147}Sm/^{144}Nd$	0.090416	0.133665	0.136068	0.116648	0.11328	0.139991	0.09194	0.184829	0.143991	0.124266
$^{143}Nd/^{144}Nd$	0.512378	0.512338	0.512256	0.512281	0.512251	0.512277	0.51215	0.512346	0.51219	0.512079
$\varepsilon Nd_{(0Ma)}$	-5.1	-5.9	-7.5	-7	-7.6	-7	-9.5	-5.7	-8.7	-10.9
$\varepsilon Nd_{(100Ma)}$	-3.7	-5.1	-6.7	-5.9	-6.5	-6.3	-8.2	-5.5	-8.1	-10.0
$\varepsilon Nd_{(360Ma)}$	-0.2	-3	-4.7	-3.3	-3.7	-4.4	-4.7	-5.2	-6.3	-7.6

Notes:
$\lambda_{Rb} = 1.3968 \times 10^{-11}$
$\lambda_{Sm} = 6.54 \times 10^{-12}$
$^{143}Nd/^{144}Nd_{CHUR\,(0)} = 0.512638$
$^{147}Sm/^{144}Nd_{CHUR(0)} = 0.1967$

Table B.4. Summary of LA-ICP-MS U-Pb results for zircon

					Radiogenic Ratios						Age (Ma)	
	Spot Size (μm)	U (ppm)	Th (ppm)	U/ Th	$^{206}Pb/^{238}U$	2σ	$^{207}Pb/^{235}U$	2σ	$^{206}Pb/^{207}Pb$	2σ	$^{206}Pb/^{238}U$	2σ
Y1-AW039 – Orthogneiss												
Y1-AW039_11	30	172	61	3	0.0429	0.0024	0.3158	0.027	270.7	40.6	350.5	22.9
Y1-AW039_14	30	617	59	11	0.0441	0.0073	0.3162	0.055	278.3	125.2	351.3	20.8
Y1-AW039_25	30	509	110	5	0.0512	0.0026	0.3801	0.021	322.2	51.8	395.4	29.1
Y1-AW039_1	30	404	85	5	0.0559	0.0037	0.4180	0.030	350.5	80.2	363.5	9.9
Y1-AW039_2	30	139	82	2	0.0560	0.0034	0.4179	0.039	351.3	73.2	377.0	8.9
Y1-AW039_10	30	351	98	4	0.0577	0.0025	0.4326	0.022	361.5	55.5	370.5	13.0
Y1-AW039_24	30	154	127	1	0.0579	0.0019	0.4337	0.026	363.0	42.8	365.2	13.6
Y1-AW039_4	30	396	96	4	0.0580	0.0016	0.4328	0.017	363.5	36.0	372.6	10.0
Y1-AW039_18	30	282	117	2	0.0581	0.0029	0.4377	0.037	364.1	64.1	382.0	17.7
Y1-AW039_7	30	107	65	2	0.0583	0.0022	0.4353	0.039	365.2	49.5	361.5	15.3
Y1-AW039_21	30	163	64	3	0.0587	0.0028	0.4389	0.033	367.4	62.4	270.7	15.0
Y1-AW039_23	30	459	120	4	0.0587	0.0026	0.4372	0.021	367.6	58.5	429.9	49.8
Y1-AW039_13	30	113	76	1	0.0591	0.0019	0.4361	0.044	370.0	41.8	370.0	11.3
Y1-AW039_6	30	442	160	3	0.0592	0.0021	0.4431	0.018	370.5	48.2	415.3	62.0
Y1-AW039_8	30	426	234	2	0.0595	0.0016	0.4453	0.021	372.6	37.1	278.3	45.0
Y1-AW039_17	30	174	123	1	0.0597	0.0031	0.4450	0.037	373.7	71.2	373.7	19.0
Y1-AW039_5	30	444	105	4	0.0602	0.0015	0.4506	0.014	377.0	33.5	364.1	17.6
Y1-AW039_9	30	84	55	2	0.0611	0.0029	0.4440	0.064	382.0	67.7	367.4	17.0
Y1-AW039_22	30	260	107	2	0.0630	0.0038	0.4650	0.036	393.6	90.9	393.6	23.1
Y1-AW039_3	30	198	84	2	0.0633	0.0048	0.4738	0.042	395.4	115.1	367.6	15.9
Y1-AW039_14	30	293	101	3	0.0665	0.0103	0.4892	0.077	415.3	257.4	363.0	11.8
Y1-AW039_12	30	356	93	4	0.0690	0.0083	0.5126	0.062	429.9	214.0	322.2	16.1
*1.1=Systematic error of $^{206}Pb/^{238}U$ age based on Sri Lankan standard												
Y1-IG053 – Orthogneiss												
Y1-IG053_23	30	214	92	2	0.0536	0.0088	0.3982	0.095	336.8	180.8	349.7	16.9
Y1-IG053_17	30	246	180	1	0.0547	0.0023	0.4122	0.034	343.1	47.4	368.1	9.2
Y1-IG053_20	30	170	67	3	0.0548	0.0041	0.4364	0.061	343.8	85.6	365.5	11.9
Y1-IG053_22	30	293	151	2	0.0556	0.0031	0.4232	0.041	348.9	65.5	391.2	15.4
Y1-IG053_1	30	170	76	2	0.0557	0.0028	0.4107	0.042	349.7	58.9	382.7	8.8
Y1-IG053_10	30	152	127	1	0.0562	0.0048	0.4250	0.053	352.5	103.2	367.1	7.2
Y1-IG053_18	30	189	118	2	0.0568	0.0022	0.4258	0.034	356.3	48.1	373.8	28.8
Y1-IG053_21	30	235	184	1	0.0570	0.0022	0.4254	0.038	357.4	47.2	382.4	21.7
Y1-IG053_14	30	242	126	2	0.0570	0.0025	0.4184	0.022	357.6	54.0	358.6	30.9
Y1-IG053_9	30	353	196	2	0.0572	0.0051	0.4247	0.039	358.6	110.7	352.5	29.3
Y1-IG053_12	30	110	56	2	0.0577	0.0025	0.4069	0.087	361.4	55.9	375.3	15.1
Y1-IG053_16	30	329	159	2	0.0581	0.0044	0.4384	0.044	364.1	97.2	361.4	15.5
Y1-IG053_3	30	473	291	2	0.0583	0.0020	0.4330	0.020	365.5	43.5	427.9	17.6
Y1-IG053_6	30	367	333	1	0.0586	0.0012	0.4226	0.025	367.1	26.6	357.6	15.1
Y1-IG053_15	30	245	160	2	0.0586	0.0029	0.4366	0.030	367.1	65.4	367.1	17.8
Y1-IG053_2	30	241	213	1	0.0588	0.0015	0.4311	0.022	368.1	33.8	364.1	26.7
Y1-IG053_19	30	271	103	3	0.0588	0.0017	0.4338	0.024	368.5	38.2	343.1	13.8
Y1-IG053_7	30	489	323	2	0.0597	0.0047	0.4482	0.038	373.8	107.8	356.3	13.5
Y1-IG053_11	30	136	74	2	0.0599	0.0025	0.4518	0.052	375.3	56.7	368.5	10.4
Y1-IG053_8	30	428	268	2	0.0611	0.0036	0.4554	0.035	382.4	83.0	343.8	24.9
Y1-IG053_5	30	282	130	2	0.0612	0.0015	0.4632	0.034	382.7	33.8	357.4	13.2
Y1-IG053_24	30	378	273	1	0.0615	0.0025	0.4475	0.029	385.0	59.6	348.9	18.8
Y1-IG053_4	30	374	148	3	0.0626	0.0025	0.4636	0.024	391.2	60.2	336.8	53.7
Y1-IG053_13	30	249	140	2	0.0686	0.0029	0.5066	0.036	427.9	75.4	385.0	15.5
*0.9=Systematic error of $^{206}Pb/^{238}U$ age based on Sri Lankan standard												

Table B.4 continued. Summary of LA-ICP-MS U-Pb results for zircon

					Radiogenic Ratios						Age (Ma)	
	Spot Size (μm)	U (ppm)	Th (ppm)	U/ Th	$^{206}Pb/^{238}U$	2σ	$^{207}Pb/^{235}U$	2σ	$^{206}Pb/^{207}Pb$	2σ	$^{206}Pb/^{238}U$	2σ
Y1-AW049 – Orthogneiss												
Y1-AW049_8	30	441	272	2	0.0550	0.0049	0.4191	0.050	344.9	103.2	371.6	12.0
Y1-AW049_15	30	721	421	2	0.0556	0.0014	0.4140	0.013	348.5	29.0	367.6	15.0
Y1-AW049_23	30	436	277	2	0.0556	0.0022	0.4126	0.024	349.1	47.7	371.6	32.7
Y1-AW049_18	30	171	114	2	0.0558	0.0035	0.3980	0.042	349.8	75.1	369.3	8.4
Y1-AW049_12	30	247	238	1	0.0562	0.0046	0.4158	0.046	352.3	98.0	392.9	44.0
Y1-AW049_9	30	241	120	2	0.0569	0.0036	0.4254	0.038	357.0	78.8	344.9	29.9
Y1-AW049_11	30	183	95	2	0.0570	0.0028	0.4308	0.045	357.2	61.0	357.0	22.1
Y1-AW049_13	30	682	221	3	0.0571	0.0025	0.4284	0.021	358.0	54.2	360.1	22.5
Y1-AW049_25	30	254	111	2	0.0572	0.0060	0.4173	0.068	358.5	132.2	357.2	17.1
Y1-AW049_10	30	549	164	3	0.0575	0.0037	0.4239	0.029	360.1	81.0	352.3	27.8
Y1-AW049_4	30	182	130	1	0.0587	0.0025	0.4345	0.052	367.6	55.2	358.0	15.1
Y1-AW049_6	30	637	199	3	0.0590	0.0014	0.4392	0.012	369.3	31.1	348.5	8.3
Y1-AW049_5	30	310	127	2	0.0593	0.0054	0.4409	0.050	371.6	121.6	374.6	21.8
Y1-AW049_1	30	243	182	1	0.0593	0.0020	0.4382	0.027	371.6	44.5	349.8	21.5
Y1-AW049_17	30	753	290	3	0.0598	0.0036	0.4459	0.030	374.6	81.5	411.5	30.1
Y1-AW049_24	30	159	92	2	0.0602	0.0033	0.4484	0.049	376.6	75.9	378.0	25.6
Y1-AW049_20	30	85	51	2	0.0604	0.0042	0.4612	0.077	378.0	96.6	382.7	48.9
Y1-AW049_21	30	830	153	5	0.0612	0.0081	0.4421	0.061	382.7	187.2	349.1	13.7
Y1-AW049_7	30	208	90	2	0.0628	0.0073	0.4835	0.074	392.9	172.8	376.6	20.2
Y1-AW049_19	30	164	128	1	0.0659	0.0050	0.5000	0.064	411.5	124.0	358.5	36.9
*0.9=Systematic error of $^{206}Pb/^{238}U$ age based on Sri Lankan standard												
10CY-035 – Orthogneiss												
10CY-035_23	30	917	63	15	0.0174	0.0011	0.1158	0.009	111.2	7.9	296.4	9.1
10CY-035_14	30	1948	191	10	0.0177	0.0006	0.1193	0.004	113.1	4.0	294.0	10.3
10CY-035_10	30	1205	107	11	0.0183	0.0005	0.1224	0.005	117.0	3.9	287.5	17.9
10CY-035_20	30	582	8	71	0.0183	0.0008	0.1214	0.007	117.0	6.1	366.6	16.4
10CY-035_21	30	771	17	47	0.0281	0.0012	0.1950	0.010	178.6	13.6	367.3	23.8
10CY-035_4	30	647	204	3	0.0456	0.0029	0.3354	0.023	287.5	51.5	348.5	16.6
10CY-035_3	30	483	109	4	0.0467	0.0017	0.3440	0.018	294.0	30.2	304.0	12.2
10CY-035_1	30	929	111	8	0.0470	0.0015	0.3430	0.011	296.4	26.8	117.0	3.3
10CY-035_9	30	851	114	8	0.0483	0.0020	0.3553	0.016	304.0	37.0	386.4	33.3
10CY-035_25	30	841	18	47	0.0484	0.0041	0.3590	0.030	304.9	76.7	359.2	39.0
10CY-035_19	30	544	55	10	0.0495	0.0013	0.3670	0.018	311.5	24.7	363.2	14.4
10CY-035_8	30	152	77	2	0.0555	0.0027	0.4078	0.046	348.5	57.9	113.1	3.5
10CY-035_12	30	635	310	2	0.0573	0.0064	0.4286	0.049	359.2	140.0	379.9	8.6
10CY-035_24	30	2518	437	6	0.0574	0.0011	0.4311	0.011	360.0	24.6	311.5	7.9
10CY-035_13	30	92	66	1	0.0580	0.0024	0.4252	0.047	363.2	52.2	117.0	5.2
10CY-035_5	30	530	249	2	0.0585	0.0027	0.4371	0.022	366.6	60.0	178.6	7.6
10CY-035_7	30	1210	391	3	0.0586	0.0039	0.4340	0.029	367.3	87.6	111.2	7.1
10CY-035_18	30	1513	514	3	0.0607	0.0014	0.4522	0.011	379.9	32.7	360.0	6.8
10CY-035_11	30	527	289	2	0.0618	0.0055	0.4625	0.043	386.4	128.6	304.9	25.2
*1.1=Systematic error of $^{206}Pb/^{238}U$ age based on Sri Lankan standard												

Table B.4 continued. Summary of LA-ICP-MS U-Pb results for zircon

	Spot Size (μm)	U (ppm)	Th (ppm)	U/ Th	Radiogenic Ratios $^{206}Pb/^{238}U$	2σ	$^{207}Pb/^{235}U$	2σ	$^{206}Pb/^{207}Pb$	2σ	Age (Ma) $^{206}Pb/^{238}U$	2σ
Y1-MJ075 – Orthogneiss												
Y1-MJ075_15	30	388	319	1	0.0172	0.0012	0.1177	0.013	110.0	8.2	110.0	7.5
Y1-MJ075_9	30	712	665	1	0.0176	0.0006	0.1159	0.007	112.4	4.6	112.4	4.1
Y1-MJ075_7	30	587	351	2	0.0177	0.0015	0.1227	0.019	112.8	10.7	112.8	9.5
Y1-MJ075_5	30	555	346	2	0.0180	0.0005	0.1280	0.015	114.9	3.5	114.9	3.0
Y1-MJ075_18	30	668	789	1	0.0180	0.0019	0.1227	0.020	115.2	13.9	115.2	12.1
Y1-MJ075_13	30	472	307	2	0.0189	0.0007	0.1268	0.014	120.9	5.1	120.9	4.2
Y1-MJ075_20	30	475	190	3	0.0191	0.0015	0.1303	0.014	122.1	11.6	122.1	9.5
Y1-MJ075_12	30	574	342	2	0.0233	0.0013	0.1575	0.012	148.4	11.9	148.4	8.0
Y1-MJ075_19	30	1088	90	12	0.0375	0.0042	0.2756	0.032	237.2	61.5	237.2	25.9
Y1-MJ075_6	30	491	68	7	0.0509	0.0060	0.4132	0.050	320.2	117.5	320.2	36.7
Y1-MJ075_1	30	306	183	2	0.0561	0.0018	0.4229	0.021	351.6	39.3	351.6	11.2
Y1-MJ075_14	30	163	99	2	0.0565	0.0024	0.4133	0.029	354.0	50.2	354.0	14.2
Y1-MJ075_17	30	295	128	2	0.0576	0.0045	0.4275	0.045	361.2	99.8	361.2	27.6
Y1-MJ075_8	30	211	121	2	0.0751	0.0020	0.5913	0.038	466.7	54.7	466.7	11.7
Y1-MJ075_2	30	384	38	10	0.2401	0.0149	3.1317	0.208	1387.2	1066.6	1520.1	46.1
*1.0=Systematic error of $^{206}Pb/^{238}U$ age based on Sri Lankan standard												
Y1-IG062 – Cretaceous granite												
Y1-IG062_1	30	643	7.3	88	0.0159	0.0014	0.1060	0.014	102.0	8.9	102.0	8.8
Y1-IG062_16	30	1213	6.9	175	0.0205	0.0017	0.1389	0.012	130.6	13.7	352.8	7.2
Y1-IG062_11	30	1074	10	103	0.0229	0.0008	0.1566	0.008	145.7	7.4	356.8	14.6
Y1-IG062_24	30	1184	8	144	0.0476	0.0023	0.3482	0.019	299.5	41.5	386.1	23.1
Y1-IG062_14	30	167	48	4	0.0479	0.0046	0.3462	0.049	301.9	84.9	369.1	6.5
Y1-IG062_4	30	130	27	5	0.0563	0.0012	0.4223	0.058	352.8	25.4	369.5	20.7
Y1-IG062_5	30	788	61	13	0.0569	0.0024	0.4246	0.019	356.8	51.9	359.7	13.8
Y1-IG062_15	30	1054	41	25	0.0571	0.0012	0.4220	0.011	357.8	26.5	145.7	5.0
Y1-IG062_10	30	1284	67	19	0.0574	0.0023	0.4244	0.017	359.7	49.5	371.1	11.4
Y1-IG062_23	30	1865	119	16	0.0580	0.0014	0.4331	0.011	363.3	31.1	365.3	6.6
Y1-IG062_25	30	1221	52	24	0.0582	0.0011	0.4321	0.012	364.4	25.0	301.9	28.1
Y1-IG062_13	30	1635	97	17	0.0583	0.0011	0.4340	0.011	365.3	24.3	357.8	7.4
Y1-IG062_21	30	122	31	4	0.0584	0.0031	0.4308	0.067	365.6	69.1	130.6	10.5
Y1-IG062_7	30	1382	67	21	0.0589	0.0011	0.4390	0.009	369.1	23.9	370.9	12.2
Y1-IG062_9	30	113	52	2	0.0590	0.0034	0.4434	0.059	369.5	76.4	365.6	18.9
Y1-IG062_17	30	1219	54	23	0.0592	0.0020	0.4398	0.017	370.9	45.4	363.3	8.5
Y1-IG062_12	30	1395	63	22	0.0593	0.0019	0.4426	0.017	371.1	42.4	299.5	13.9
Y1-IG062_6	30	240	51	5	0.0617	0.0038	0.4628	0.039	386.1	89.4	364.4	6.9
*0.9=Systematic error of $^{206}Pb/^{238}U$ age based on Sri Lankan standard												

Table B.4 continued. Summary of LA-ICP-MS U-Pb results for zircon

	Spot Size (μm)	U (ppm)	Th (ppm)	U/ Th	Radiogenic Ratios $^{206}Pb/^{238}U$	2σ	$^{207}Pb/^{235}U$	2σ	$^{206}Pb/^{207}Pb$	2σ	Age (Ma) $^{206}Pb/^{238}U$	2σ
Y1-AW038 – Cretaceous Granite												
Y1-AW038_14	10	1386	29	48	0.0163	0.0005	0.1085	0.004	104.4	3.4	104.4	3.2
Y1-AW038_6	10	933	27	34	0.0174	0.0009	0.1169	0.006	111.1	6.3	111.1	5.6
Y1-AW038_2	10	1014	28	36	0.0158	0.0009	0.1051	0.006	100.8	6.0	100.8	5.9
Y1-AW038_8	10	923	24	39	0.0164	0.0009	0.1090	0.006	104.8	6.3	104.8	6.0
Y1-AW038_24	10	1091	29	38	0.0181	0.0010	0.1211	0.007	115.5	7.0	115.5	6.1
Y1-AW038_21	10	526	23	23	0.0161	0.0010	0.1083	0.007	102.7	6.6	102.7	6.4
Y1-AW038_26	10	1342	31	43	0.0174	0.0011	0.1165	0.007	111.0	7.5	111.0	6.8
Y1-AW038_22	10	1340	23	59	0.0185	0.0011	0.1234	0.008	117.9	7.9	117.9	6.7
Y1-AW038_23	10	929	23	40	0.0176	0.0011	0.1176	0.007	112.2	7.8	112.2	6.9
Y1-AW038_13	10	1013	23	45	0.0180	0.0011	0.1200	0.008	114.7	7.9	114.7	6.9
Y1-AW038_17	10	1259	30	42	0.0180	0.0012	0.1206	0.008	114.7	8.8	114.7	7.7
Y1-AW038_9	10	662	15	44	0.0171	0.0015	0.1145	0.010	109.2	10.2	109.2	9.3
Y1-AW038_1	10	587	28	21	0.0156	0.0022	0.1061	0.015	99.8	14.2	99.8	14.2
Y1-AW038_25	10	987	28	36	0.0165	0.0007	0.1219	0.036	105.3	4.7	105.3	4.5
Y1-AW038_12	10	635	27	24	0.0168	0.0006	0.1247	0.038	107.6	4.2	107.6	3.9
Y1-AW038_18	10	1117	39	28	0.0158	0.0022	0.1450	0.134	100.9	13.9	100.9	13.8
*1.3=Systematic error of $^{206}Pb/^{238}U$ age based on Sri Lankan standard												
Y1-IG070 – Cretaceous Granite												
Y1-IG070_25	30	711	8	91	0.0160	0.0006	0.1052	0.010	102.4	3.7	108.0	4.0
Y1-IG070_2	30	1868	81	23	0.0164	0.0005	0.1099	0.004	104.9	3.5	104.9	3.4
Y1-IG070_22	30	483	17	28	0.0165	0.0008	0.1054	0.011	105.5	5.6	107.0	3.3
Y1-IG070_7	30	795	17	48	0.0165	0.0004	0.1154	0.011	105.8	2.9	108.3	2.3
Y1-IG070_24	30	1091	38	29	0.0166	0.0005	0.1111	0.007	105.9	3.6	111.5	3.5
Y1-IG070_8	30	1089	44	25	0.0166	0.0007	0.1085	0.010	106.0	4.9	105.8	2.7
Y1-IG070_16	30	553	16	34	0.0166	0.0006	0.1079	0.009	106.1	4.2	106.0	4.6
Y1-IG070_9	30	440	17	26	0.0166	0.0004	0.1131	0.016	106.2	2.6	106.2	2.4
Y1-IG070_18	30	1119	45	25	0.0167	0.0005	0.1105	0.006	106.5	3.5	108.8	3.1
Y1-IG070_15	30	849	22	39	0.0167	0.0005	0.1099	0.009	106.5	3.3	106.5	3.1
Y1-IG070_21	30	1900	83	23	0.0167	0.0005	0.1130	0.006	106.7	3.5	106.1	3.9
Y1-IG070_3	30	976	37	27	0.0167	0.0005	0.1120	0.006	107.0	3.5	106.5	3.3
Y1-IG070_1	30	1306	40	33	0.0169	0.0006	0.1131	0.007	108.0	4.3	108.1	4.1
Y1-IG070_20	30	684	25	27	0.0169	0.0007	0.1115	0.009	108.1	4.5	106.7	3.3
Y1-IG070_5	30	1425	23	62	0.0169	0.0004	0.1190	0.009	108.3	2.4	105.5	5.3
Y1-IG070_23	30	1167	33	35	0.0169	0.0008	0.1136	0.008	108.3	5.6	108.3	5.2
Y1-IG070_11	30	1232	41	30	0.0170	0.0005	0.1157	0.005	108.8	3.4	105.9	3.4
Y1-IG070_6	30	1224	16	76	0.0174	0.0006	0.1159	0.006	111.5	3.9	102.4	3.6
*0.9=Systematic error of $^{206}Pb/^{238}U$ age based on Sri Lankan standard												

Table B.4 continued. Summary of LA-ICP-MS U-Pb results for zircon

	Spot Size (μm)	U (ppm)	Th (ppm)	U/ Th	Radiogenic Ratios $^{206}Pb/^{238}U$	2σ	$^{207}Pb/^{235}U$	2σ	$^{206}Pb/^{207}Pb$	2σ	Age (Ma) $^{206}Pb/^{238}U$	2σ
Y1-AE033 – Cretaceous Granite												
Y1-AEO33-5R	10	2050	16	129	0.0157	0.0007	0.1048	0.005	20.7	0.6	100.5	4.3
Y1-AEO33-10R	10	1922	14	136	0.0159	0.0003	0.1059	0.004	20.7	0.7	101.7	1.8
Y1-AEO33-11C	10	832	8	100	0.0159	0.0014	0.1065	0.010	20.6	0.4	101.8	8.9
Y1-AEO33-12R	10	1869	12	154	0.0160	0.0005	0.1063	0.004	20.7	0.5	102.2	3.4
Y1-AEO33-3C	10	1423	10	142	0.0160	0.0006	0.1054	0.005	20.9	0.5	102.3	4.0
Y1-AEO33-15R	10	2121	11	189	0.0160	0.0005	0.1068	0.005	20.7	0.6	102.3	2.9
Y1-AEO33-2R	10	1865	11	166	0.0161	0.0008	0.1066	0.006	20.8	0.5	102.8	4.8
Y1-AEO33-13R	10	1940	11	180	0.0162	0.0005	0.1087	0.005	20.5	0.6	103.5	3.2
Y1-AEO33-3R	10	1803	14	127	0.0162	0.0006	0.1076	0.004	20.7	0.5	103.6	3.5
Y1-AEO33-16R	10	2128	10	204	0.0162	0.0006	0.1071	0.006	20.9	0.8	103.7	3.6
Y1-AEO33-8R	10	810	27	30	0.0162	0.0003	0.1068	0.003	20.9	0.4	103.8	2.0
Y1-AEO33-22R	10	515	10	53	0.0168	0.0006	0.1139	0.006	20.3	0.7	107.3	3.6
Y1-AEO33-7C	10	550	12	44	0.0171	0.0002	0.1134	0.002	20.7	0.4	109.1	1.1
Y1-AEO33-4R	10	572	5	126	0.0172	0.0009	0.1252	0.019	18.9	2.8	110.0	5.5
Y1-AEO33-18R	10	851	6	148	0.0173	0.0012	0.1468	0.080	16.3	8.8	110.8	7.7
Y1-AEO33-19R	10	640	7	90	0.0174	0.0005	0.1746	0.009	13.7	0.6	111.1	3.3
Y1-AEO33-21R	10	710	5	134	0.0176	0.0006	0.1187	0.007	20.4	1.0	112.2	4.0
Y1-AEO33-14R	10	857	14	61	0.0179	0.0019	0.1488	0.043	16.6	4.5	114.3	12.2
Y1-AEO33-17R	10	1463	39	38	0.0185	0.0008	0.2745	0.048	9.3	1.6	118.1	5.3
*0.9=Systematic error of $^{206}Pb/^{238}U$ age based on Sri Lankan standard												
10CY-039 – Cretaceous Granite												
10CY039_120	10	1028	14	71	0.0160	0.0004	0.1066	0.003	102.0	2.5	106.2	4.9
10CY039_18	10	575	12	49	0.0163	0.0007	0.1084	0.005	104.2	4.8	104.4	3.4
10CY039_2	10	568	25	23	0.0163	0.0005	0.1091	0.004	104.4	3.5	106.3	7.1
10CY039_8	10	500	7.4	67	0.0164	0.0007	0.1100	0.005	105.0	4.5	108.7	11.5
10CY039_15	10	1500	11	135	0.0165	0.0008	0.1095	0.006	105.2	5.4	106.5	9.1
10CY039_13	10	582	16	36	0.0165	0.0009	0.1109	0.006	105.8	5.9	107.5	4.2
10CY039_25	10	521	10	54	0.0166	0.0008	0.1124	0.006	106.1	5.2	106.5	4.9
10CY039_1	10	541	8.9	61	0.0166	0.0008	0.1105	0.006	106.2	5.2	105.0	4.3
10CY039_3	10	397	7.6	52	0.0166	0.0011	0.1121	0.008	106.3	7.5	106.7	7.7
10CY039_5	10	724	16	44	0.0167	0.0014	0.1112	0.010	106.5	9.6	110.0	5.5
10CY039_7	10	748	11	69	0.0167	0.0008	0.1111	0.006	106.5	5.2	107.9	4.0
10CY039_9	10	611	15	41	0.0167	0.0012	0.1118	0.008	106.7	8.2	114.5	4.4
10CY039_6	10	671	14	47	0.0168	0.0007	0.1125	0.005	107.5	4.5	105.8	5.6
10CY039_11	10	727	17	42	0.0169	0.0006	0.1126	0.005	107.9	4.3	110.5	5.8
10CY039_4	10	498	14	37	0.0170	0.0018	0.1133	0.012	108.7	12.5	105.2	5.1
10CY039_19	10	510	19	26	0.0170	0.0008	0.1177	0.009	109.0	5.5	104.2	4.6
10CY039_23	10	482	20	24	0.0172	0.0010	0.1153	0.007	110.0	6.9	109.0	5.0
10CY039_10	10	446	6	77	0.0172	0.0009	0.1151	0.006	110.0	6.1	102.0	2.5
10CY039_14	10	651	14	45	0.0173	0.0009	0.1641	0.025	110.5	6.4	110.8	6.6
10CY039_24	10	458	9	53	0.0173	0.0010	0.1156	0.007	110.7	7.2	110.0	6.3
10CY039_22	10	554	10	55	0.0173	0.0010	0.1161	0.007	110.8	7.4	110.7	6.5
10CY039_12	10	586	10	61	0.0179	0.0007	0.1196	0.005	114.5	5.1	106.1	4.9
*2.2=Systematic error of $^{206}Pb/^{238}U$ age based on Sri Lankan standard												

Table B.4 continued. Summary of LA-ICP-MS U-Pb results for zircon

	Spot Size (μm)	U (ppm)	Th (ppm)	U/ Th	Radiogenic Ratios $^{206}Pb/^{238}U$	2σ	$^{207}Pb/^{235}U$	2σ	$^{206}Pb/^{207}Pb$	2σ	Age (Ma) $^{206}Pb/^{238}U$	2σ
Y1-AE051 – Cretaceous Granite												
Y1AE051_14	10	703	25	28	0.0149	0.0006	0.0998	0.004	95.6	3.5	106.4	1.6
Y1AE051_1	10	946	52	18	0.0155	0.0006	0.1182	0.006	99.3	3.5	95.6	3.7
Y1AE051_12	10	913	57	16	0.0156	0.0007	0.1037	0.005	100.0	4.7	110.7	4.0
Y1AE051_18	10	718	23	31	0.0157	0.0009	0.1052	0.006	100.4	5.5	108.6	4.4
Y1AE051_8	10	375	7	51	0.0157	0.0009	0.1205	0.058	100.6	5.7	100.0	4.7
Y1AE051_13	10	961	56	17	0.0159	0.0009	0.1062	0.006	101.5	5.9	101.8	4.6
Y1AE051_16	10	1113	43	26	0.0159	0.0007	0.1066	0.005	101.8	4.7	101.9	5.1
Y1AE051_10	10	612	17	35	0.0159	0.0008	0.1082	0.006	101.9	5.2	110.3	5.2
Y1AE051_25	10	583	25	23	0.0160	0.0013	0.1094	0.010	102.1	8.4	100.4	5.5
Y1AE051_4	10	843	50	17	0.0162	0.0008	0.1117	0.008	103.7	5.6	108.4	5.4
Y1AE051_11	10	548	17	32	0.0163	0.0011	0.1081	0.008	104.4	7.2	104.8	5.0
Y1AE051_5	10	983	51	19	0.0164	0.0008	0.1091	0.006	104.8	5.2	99.3	3.6
Y1AE051_21	10	424	12	36	0.0164	0.0009	0.1086	0.007	104.9	6.2	101.5	5.8
Y1AE051_24	10	755	34	22	0.0166	0.0003	0.1115	0.003	106.4	1.7	104.9	6.0
Y1AE051_19	10	604	5	131	0.0169	0.0022	0.1132	0.015	107.7	14.7	103.7	5.4
Y1AE051_3	10	1170	68	17	0.0170	0.0009	0.1140	0.006	108.4	5.9	104.4	6.9
Y1AE051_22	10	557	10	58	0.0170	0.0007	0.1129	0.005	108.6	4.8	102.1	8.2
Y1AE051_7	10	746	37	20	0.0171	0.0010	0.1290	0.037	109.1	6.6	112.7	12.3
Y1AE051_23	10	691	30	23	0.0172	0.0007	0.1210	0.019	109.9	5.2	107.7	13.6
Y1AE051_15	10	1102	7	168	0.0173	0.0011	0.1221	0.020	110.3	7.7	109.9	4.7
Y1AE051_20	10	563	18	32	0.0173	0.0008	0.1146	0.006	110.3	5.8	110.3	7.0
Y1AE051_2	10	1033	44	23	0.0173	0.0006	0.1157	0.004	110.7	4.4	109.1	6.1
Y1AE051_17	10	1150	9	125	0.0176	0.0019	0.1181	0.013	112.7	13.9	100.6	5.7
*1.2=Systematic error of $^{206}Pb/^{238}U$ age based on Sri Lankan standard												
Y1-AE064 – Cretaceous Granite												
Y1-AE064_25	10	649	19	35	0.0147	0.0007	0.0983	0.005	94.3	4.3	94.3	4.6
Y1-AE064_22	10	548	24	23	0.0151	0.0017	0.1017	0.012	96.9	10.5	96.9	10.9
Y1-AE064_3	10	717	28	26	0.0157	0.0006	0.1054	0.005	100.4	4.1	100.4	4.1
Y1-AE064_13	10	976	30	32	0.0157	0.0011	0.1041	0.007	100.6	6.9	100.6	6.8
Y1-AE064_7	10	441	21	21	0.0158	0.0006	0.1048	0.005	100.8	4.1	100.8	4.0
Y1-AE064_2	10	680	25	27	0.0159	0.0008	0.1056	0.005	101.9	4.9	101.9	4.8
Y1-AE064_1	10	692	26	26	0.0160	0.0008	0.1056	0.006	102.0	5.4	102.0	5.3
Y1-AE064_14	10	599	31	19	0.0161	0.0009	0.1072	0.006	103.2	5.9	103.2	5.7
Y1-AE064_4	10	354	25	14	0.0161	0.0006	0.1078	0.006	103.2	3.8	103.2	3.7
Y1-AE064_16	10	411	18	23	0.0162	0.0012	0.1085	0.009	103.7	8.0	103.7	7.8
Y1-AE064_19	10	497	22	23	0.0162	0.0010	0.1070	0.007	103.7	6.9	103.7	6.6
Y1-AE064_24	10	680	33	20	0.0163	0.0007	0.1122	0.009	104.2	4.4	104.2	4.3
Y1-AE064_6	10	814	33	25	0.0163	0.0008	0.1089	0.006	104.5	5.4	104.5	5.2
Y1-AE064_18	10	423	35	12	0.0164	0.0010	0.1221	0.008	105.1	6.7	105.1	6.3
Y1-AE064_21	10	601	32	19	0.0165	0.0008	0.1102	0.006	105.2	5.4	105.2	5.2
Y1-AE064_15	10	803	33	25	0.0165	0.0006	0.1100	0.004	105.6	4.1	105.6	3.9
Y1-AE064_8	10	610	12	52	0.0165	0.0008	0.1108	0.006	105.6	5.5	105.6	5.2
Y1-AE064_10	10	428	32	13	0.0165	0.0009	0.1124	0.013	105.7	6.3	105.7	6.0
Y1-AE064_5	10	449	28	16	0.0165	0.0004	0.1101	0.004	105.8	3.0	105.8	2.8
Y1-AE064_12	10	359	23	16	0.0168	0.0009	0.1117	0.007	107.2	6.3	107.2	5.9
Y1-AE064_23	10	942	16	58	0.0177	0.0020	0.1467	0.096	113.3	14.6	113.3	12.9
Y1-AE064_9	10	625	34	18	0.0164	0.0023	0.1518	0.100	104.9	15.2	104.9	14.5
Y1-AE064_20	10	900	12	78	0.0191	0.0007	0.1287	0.005	122.1	5.2	122.1	4.2
Y1-AE064_17	10	1338	30	45	0.0453	0.0018	0.4035	0.285	285.9	32.6	285.9	11.4
*0.7=Systematic error of $^{206}Pb/^{238}U$ age based on Sri Lankan standard												

Table B.4 continued. Summary of LA-ICP-MS U-Pb results for zircon

	Spot Size (μm)	U (ppm)	Th (ppm)	U/ Th	Radiogenic Ratios $^{206}Pb/^{238}U$	2σ	$^{207}Pb/^{235}U$	2σ	$^{206}Pb/^{207}Pb$	2σ	Age (Ma) $^{206}Pb/^{238}U$	2σ
Y1-IG052 – Cretaceous Granite												
Y1-IG052_24	10	496	20	25	0.0149	0.0009	0.0986	0.006	95.5	5.2	95.5	5.4
Y1-IG052_13	10	489	17	30	0.0153	0.0007	0.1031	0.006	97.8	4.3	97.8	4.4
Y1-IG052_20	10	298	9	33	0.0155	0.0007	0.1032	0.005	99.1	4.6	99.1	4.7
Y1-IG052_23	10	448	22	21	0.0156	0.0011	0.1134	0.029	100.0	7.3	100.0	7.3
Y1-IG052_9	10	432	16	26	0.0158	0.0011	0.1057	0.007	101.2	6.8	101.2	6.7
Y1-IG052_16	10	409	23	18	0.0158	0.0005	0.1054	0.004	101.3	3.4	101.3	3.4
Y1-IG052_4	10	387	17	23	0.0159	0.0006	0.1077	0.004	101.6	3.8	101.6	3.7
Y1-IG052_6	10	401	19	21	0.0159	0.0009	0.1049	0.006	101.6	5.8	101.6	5.7
Y1-IG052_10	10	402	17	24	0.0161	0.0010	0.1065	0.007	102.9	6.5	102.9	6.3
Y1-IG052_7	10	614	11	57	0.0162	0.0006	0.1146	0.006	103.7	4.0	103.7	3.9
Y1-IG052_5	10	434	19	23	0.0163	0.0007	0.1093	0.006	104.0	4.7	104.0	4.5
Y1-IG052_18	10	359	17	21	0.0164	0.0011	0.1093	0.008	104.8	7.2	104.8	6.9
Y1-IG052_19	10	538	11	49	0.0167	0.0005	0.1105	0.005	106.5	3.6	106.5	3.4
Y1-IG052_11	10	240	7	33	0.0167	0.0010	0.1135	0.007	106.6	6.5	106.6	6.1
Y1-IG052_1	10	595	13	47	0.0181	0.0006	0.1210	0.004	115.9	4.4	115.9	3.8
Y1-IG052_2	10	966	6	151	0.0224	0.0044	0.1555	0.030	143.0	39.3	143.0	27.5
Y1-IG052_21	10	328	118	3	0.0865	0.0046	0.7025	0.039	534.9	146.5	534.9	27.4
*1.1=Systematic error of $^{206}Pb/^{238}U$ age based on Sri Lankan standard												
10CY-024 – Microgranite												
10CY024_4	30	416	517	1	0.0143	0.0010	0.1032	0.035	19.3	5.1	101.9	5.6
10CY024_6	30	321	431	1	0.0158	0.0005	0.1020	0.024	21.4	2.9	102.0	3.9
10CY024_1	30	339	415	1	0.0159	0.0009	0.1141	0.031	21.3	2.7	105.6	8.1
10CY024_2	30	351	458	1	0.0159	0.0006	0.1026	0.014	19.1	6.3	91.3	6.3
10CY024_7	30	510	350	1	0.0159	0.0006	0.1171	0.026	21.4	4.3	108.3	4.4
10CY024_17	30	106	159	1	0.0160	0.0013	0.1080	0.055	21.3	4.9	100.9	3.4
10CY024_25	30	282	790	0	0.0163	0.0010	0.1080	0.021	18.8	4.1	102.0	3.8
10CY024_15	30	157	248	1	0.0164	0.0016	0.1273	0.042	20.9	4.6	106.2	4.0
10CY024_3	30	337	496	1	0.0165	0.0013	0.1070	0.016	19.0	4.7	106.1	4.7
10CY024_14	30	391	537	1	0.0166	0.0009	0.1072	0.020	24.1	18.2	107.2	12.8
10CY024_24	30	155	179	1	0.0166	0.0019	0.0947	0.051	19.4	3.1	117.2	21.0
10CY024_9	30	257	371	1	0.0166	0.0007	0.1203	0.030	18.4	13.7	108.0	12.5
10CY024_8	30	403	537	1	0.0166	0.0006	0.1095	0.025	18.6	5.2	110.7	7.1
10CY024_10	30	137	114	1	0.0168	0.0020	0.0957	0.073	21.3	3.9	105.9	5.8
10CY024_18	30	153	369	0	0.0168	0.0018	0.0879	0.041	17.8	5.6	104.9	9.9
10CY024_12	30	105	35	3	0.0169	0.0020	0.1263	0.095	20.5	3.2	108.1	8.9
10CY024_16	30	238	655	0	0.0169	0.0014	0.1138	0.020	20.5	10.3	102.6	8.2
10CY024_5	30	372	823	0	0.0169	0.0007	0.1091	0.023	26.3	12.0	107.2	11.2
10CY024_13	30	214	141	2	0.0173	0.0011	0.1281	0.037	20.9	8.6	120.4	11.0
10CY024_11	30	437	516	1	0.0183	0.0033	0.1307	0.032	24.2	12.6	106.1	11.8
10CY024_22	30	109	167	1	0.0189	0.0017	0.1245	0.052	20.8	3.8	104.1	6.2
*1.2=Systematic error of $^{206}Pb/^{238}U$ age based on Sri Lankan standard												

Notes

[1]Analyses with >10% uncertainty (1-sigma) in $^{206}Pb/^{238}U$ age are not included.

[2]Analyses with >10% uncertainty (1-sigma) in $^{206}Pb/^{207}Pb$ age are not included, unless $^{206}Pb/^{238}U$ age is <500 Ma.

[3]Best age is determined from $^{206}Pb/^{238}U$ age for analyses with $^{206}Pb/^{238}U$ age <1000 Ma and from $^{206}Pb/^{207}Pb$ age for analyses with $^{206}Pb/^{238}U$ age > 1000 Ma.

[4]Concordance is based on $^{206}Pb/^{238}U$ age / $^{206}Pb/^{207}Pb$ age. Value is not reported for $^{206}Pb/^{238}U$ ages <500 Ma because of large uncertainty in $^{206}Pb/^{207}Pb$ age.

[5]Analyses with $^{206}Pb/^{238}U$ age > 500 Ma and with >20% discordance (<80% concordance) are not included.

[6]Analyses with $^{206}Pb/^{238}U$ age > 500 Ma and with >5% reverse discordance (<105% concordance) are not included.

[7]Analyses conducted by LA-MC-ICPMS, as described by Gehrels et al. (2008).

[8]U concentration and U/Th are calibrated relative to Sri Lanka zircon standard and are accurate to ~20%.

[9]Common Pb correction is from measured ^{204}Pb with common Pb composition interpreted from Stacey and Kramers (1975).

[10]Common Pb composition assigned uncertainties of 1.5 for $^{206}Pb/^{204}Pb$, 0.3 for $^{207}Pb/^{204}Pb$, and 2.0 for $^{208}Pb/^{204}Pb$.

[11]U/Pb and $^{206}Pb/^{207}Pb$ fractionation is calibrated relative to fragments of a large Sri Lanka zircon of 563.5 ± 3.2 Ma (2-sigma).

[12]U decay constants and composition as follows: ^{238}U = 9.8485 x 10-10, 235U = 1.55125 x 10-10, $^{238}U/^{235}U$ = 137.88.

Table B.5. Summary of SHRIMP U-Pb results for zircon

Grain. spot	U (ppm)	Th (ppm)	Th/U	$^{206}Pb^*$ (ppm)	$^{204}Pb/^{206}Pb$	f_{206} %	Total $^{238}U/^{206}Pb$	±	Total $^{207}Pb/^{206}Pb$	±	Radiogenic $^{206}Pb/^{238}U$	±	Age (Ma) $^{206}Pb/^{238}U$	±
Y1-IG053 – Orthogneiss														
1.1	259	67	0.26	12.2	0.000058	0.16	18.15	0.22	0.0547	0.0008	0.0550	0.0007	345.3	4.2
1.2	151	59	0.39	7.8	-	0.16	16.63	0.21	0.0529	0.0010	0.0602	0.0008	377.0	4.7
2.1	268	73	0.27	12.8	0.000153	0.16	17.94	0.22	0.0533	0.0008	0.0557	0.0007	349.7	4.2
2.2	161	162	1.01	11.9	0.000084	0.16	11.58	0.15	0.0589	0.0009	0.0863	0.0011	533.5	6.7
3.1	336	66	0.20	18.0	0.000085	0.16	16.02	0.19	0.0550	0.0009	0.0624	0.0007	390.0	4.5
3.2	1288	651	0.51	65.9	0.000031	0.16	16.80	0.18	0.0541	0.0004	0.0595	0.0006	372.8	3.9
4.1	509	172	0.34	26.4	0.000049	0.16	16.56	0.19	0.0546	0.0006	0.0604	0.0007	377.8	4.2
4.2	218	119	0.55	11.0	0.000178	0.16	17.09	0.22	0.0539	0.0009	0.0585	0.0008	366.7	4.6
5.1	237	97	0.41	11.9	0.000110	0.16	17.15	0.21	0.0555	0.0009	0.0582	0.0007	364.5	4.4
5.2	1298	12	0.01	51.0	-	0.16	21.86	0.26	0.0555	0.0008	0.0455	0.0005	287.1	3.3
6.1	350	58	0.17	17.0	0.000078	0.16	17.63	0.20	0.0535	0.0007	0.0567	0.0007	355.6	4.0
6.2	204	66	0.32	10.4	0.000088	0.16	16.84	0.34	0.0546	0.0009	0.0593	0.0012	371.5	7.4
7.1	279	100	0.36	13.9	-	0.16	17.22	0.21	0.0543	0.0011	0.0580	0.0007	363.7	4.3
8.1	475	163	0.34	23.6	0.000080	0.16	17.33	0.19	0.0535	0.0008	0.0577	0.0006	361.8	4.0
9.1	326	63	0.19	15.4	0.000068	0.16	18.13	0.26	0.0538	0.0008	0.0551	0.0008	346.0	4.9
10.1	431	118	0.27	21.6	0.000052	0.16	17.16	0.25	0.0545	0.0006	0.0582	0.0009	364.9	5.2
11.1	390	144	0.37	19.7	0.000023	0.16	16.99	0.19	0.0543	0.0007	0.0588	0.0007	368.4	4.1
12.1	929	45	0.05	38.1	-	0.16	20.94	0.34	0.0544	0.0014	0.0476	0.0008	300.0	4.9
12.2	188	67	0.36	9.8	0.000117	0.16	16.44	0.21	0.0518	0.0009	0.0610	0.0008	381.7	4.8
13.1	647	278	0.43	32.8	0.000014	0.16	16.94	0.18	0.0544	0.0005	0.0590	0.0006	369.4	4.0
14.1	257	82	0.32	12.3	-	0.16	17.91	0.22	0.0538	0.0008	0.0558	0.0007	350.2	4.2
15.1	1261	350	0.28	63.9	0.000018	0.16	16.97	0.18	0.0545	0.0004	0.0589	0.0006	368.9	3.9
16.1	1188	466	0.39	59.4	0.000008	0.16	17.18	0.18	0.0536	0.0005	0.0582	0.0006	364.8	3.8
17.1	238	54	0.23	11.8	-	0.16	17.23	0.21	0.0526	0.0011	0.0581	0.0007	364.1	4.3
18.1	344	105	0.31	16.7	-	0.16	17.67	0.32	0.0542	0.0007	0.0566	0.0010	354.7	6.2
18.2	405	18	0.05	20.5	0.000083	0.16	17.00	0.20	0.0545	0.0006	0.0588	0.0007	368.2	4.2
19.1	342	115	0.34	16.6	0.000114	0.16	17.65	0.20	0.0538	0.0007	0.0566	0.0007	355.1	4.0
19.2	222	45	0.20	11.5	-	0.16	16.57	0.21	0.0539	0.0010	0.0604	0.0008	377.8	4.6
20.1	404	206	0.51	20.2	0.000034	0.16	17.18	0.19	0.0546	0.0006	0.0581	0.0007	364.3	4.0

Error in Temora reference zircon calibration was 0.33% for the analytical session.

Table B.5 continued. Summary of SHRIMP U-Pb results for zircon

Grain. spot	U (ppm)	Th (ppm)	Th/U	$^{206}Pb^*$ (ppm)	$^{204}Pb/^{206}Pb$	f_{206} %	Total $^{238}U/^{206}Pb$	±	Total $^{207}Pb/^{206}Pb$	±	Radiogenic $^{206}Pb/^{238}U$	±	Age (Ma) $^{206}Pb/^{238}U$	±
K6-B26 – Orthogneiss														
1.1	1331	501	0.38	65.3	-	0.01	17.51	0.27	0.0538	0.0004	0.0571	0.0009	358.0	5.4
2.1	474	154	0.32	22.0	0.000238	0.25	18.55	0.25	0.0552	0.0006	0.0538	0.0007	337.7	4.4
3.1	1474	610	0.41	68.1	0.000173	0.38	18.59	0.21	0.0562	0.0004	0.0536	0.0006	336.4	3.8
4.1	470	84	0.18	18.3	0.000086	0.37	22.05	0.25	0.0550	0.0007	0.0452	0.0005	284.9	3.2
4.2	261	124	0.48	12.6	0.000253	0.10	17.77	0.23	0.0544	0.0008	0.0562	0.0007	352.7	4.4
5.1	146	58	0.39	6.3	0.000193	0.15	19.83	0.27	0.0539	0.0011	0.0503	0.0007	316.6	4.3
6.1	545	165	0.30	27.8	0.000022	<0.01	16.86	0.21	0.0532	0.0006	0.0594	0.0007	371.9	4.5
7.1	1024	271	0.26	52.1	0.000015	<0.01	16.88	0.18	0.0540	0.0004	0.0592	0.0006	371.0	3.9
8.1	389	180	0.46	20.0	-	<0.01	16.67	0.19	0.0534	0.0007	0.0600	0.0007	375.8	4.3
9.1	573	183	0.32	27.7	0.000031	<0.01	17.75	0.19	0.0535	0.0006	0.0563	0.0006	353.3	3.8
10.1	926	169	0.18	46.0	0.000009	0.14	17.29	0.19	0.0549	0.0004	0.0578	0.0006	362.0	3.8
10.2	150	36	0.24	7.5	-	<0.01	17.12	0.22	0.0532	0.0011	0.0585	0.0008	366.3	4.6
11.1	676	129	0.19	33.1	0.000097	0.20	17.57	0.19	0.0552	0.0005	0.0568	0.0006	356.1	3.8
12.1	250	86	0.34	12.6	0.000067	<0.01	17.02	0.21	0.0527	0.0009	0.0588	0.0007	368.6	4.4
13.1	403	163	0.40	20.3	-	<0.01	17.08	0.19	0.0538	0.0006	0.0585	0.0007	366.8	4.1
14.1	375	107	0.29	19.1	-	<0.01	16.84	0.19	0.0532	0.0007	0.0594	0.0007	372.2	4.1
15.1	1190	246	0.21	61.0	0.000024	<0.01	16.76	0.19	0.0539	0.0004	0.0597	0.0007	373.6	4.2
15.2	136	77	0.56	6.8	0.000063	0.04	17.12	0.22	0.0542	0.0012	0.0584	0.0008	365.9	4.7
16.1	100	43	0.43	4.6	-	<0.01	18.80	0.28	0.0520	0.0013	0.0533	0.0008	334.6	4.9
17.1	112	44	0.40	5.6	-	<0.01	17.08	0.42	0.0514	0.0012	0.0587	0.0015	367.9	8.9
18.1	1080	375	0.35	55.7	0.000019	<0.01	16.67	0.18	0.0535	0.0004	0.0600	0.0006	375.9	3.9
19.1	323	116	0.36	16.0	-	0.05	17.38	0.20	0.0542	0.0007	0.0575	0.0007	360.4	4.1
20.1	2710	18	0.01	38.4	-	0.12	60.71	0.64	0.0491	0.0004	0.0165	0.0002	105.2	1.1

Error in Temora reference zircon calibration was 0.33% for the analytical session.

Table B.5 continued. Summary of SHRIMP U-Pb results for zircon

Grain. spot	U (ppm)	Th (ppm)	Th/U	$^{206}Pb^*$ (ppm)	$^{204}Pb/^{206}Pb$	f_{206} %	Total $^{238}U/^{206}Pb$	±	Total $^{207}Pb/^{206}Pb$	±	Radiogenic $^{206}Pb/^{238}U$	±	Age (Ma) $^{206}Pb/^{238}U$	±
Y1-IG070 – Granite														
1.1	1528	42	0.027	21.9	-	<0.01	59.91	0.65	0.0473	0.0006	0.0167	0.0002	106.8	1.2
2.1	1683	10	0.006	23.5	0.000058	0.08	61.56	0.67	0.0487	0.0006	0.0162	0.0002	103.8	1.1
3.1	1668	38	0.023	24.4	-	<0.01	58.65	0.75	0.0482	0.0007	0.0171	0.0002	109.0	1.4
4.1	1825	15	0.008	27.4	-	<0.01	57.29	0.61	0.0481	0.0005	0.0175	0.0002	111.6	1.2
5.1	1996	63	0.032	28.4	-	0.08	60.36	0.70	0.0488	0.0005	0.0166	0.0002	105.8	1.2
6.1	1194	42	0.035	17.2	0.000054	<0.01	59.77	0.66	0.0477	0.0007	0.0167	0.0002	107.0	1.2
7.1	1684	49	0.029	24.1	0.000023	0.03	60.08	0.69	0.0484	0.0005	0.0166	0.0002	106.4	1.2
8.1	3887	109	0.028	59.1	0.000329	0.41	56.54	0.60	0.0516	0.0006	0.0176	0.0002	112.6	1.2
8.2	2937	35	0.012	44.9	0.000076	0.04	56.15	0.59	0.0486	0.0004	0.0178	0.0002	113.7	1.2
9.1	2302	43	0.019	34.2	0.000278	0.79	57.77	0.61	0.0545	0.0016	0.0172	0.0002	109.8	1.2
10.1	3883	24	0.006	82.6	0.011033	20.13	40.37	0.45	0.2087	0.0104	0.0198	0.0004	126.3	2.6
11.1	1149	18	0.015	16.2	-	0.19	60.78	0.67	0.0496	0.0007	0.0164	0.0002	105.0	1.2
12.1	2896	84	0.029	42.3	0.000050	0.05	58.77	0.62	0.0486	0.0004	0.0170	0.0002	108.7	1.1
12.2	3023	96	0.032	43.6	0.000147	0.34	59.59	0.63	0.0509	0.0005	0.0167	0.0002	106.9	1.1
13.1	2044	47	0.023	29.5	-	0.03	59.55	0.64	0.0484	0.0005	0.0168	0.0002	107.3	1.1
14.1	2579	23	0.009	39.2	0.000073	0.12	56.45	0.70	0.0492	0.0004	0.0177	0.0002	113.1	1.4
15.1	2569	14	0.006	39.8	0.000043	<0.01	55.43	0.59	0.0483	0.0004	0.0180	0.0002	115.3	1.2

Error in Temora reference zircon calibration was 0.30% for the analytical session.

Table B.5 continued. Summary of SHRIMP U-Pb results for zircon

Grain. spot	U (ppm)	Th (ppm)	Th/U	$^{206}Pb^*$ (ppm)	$^{204}Pb/^{206}Pb$	f_{206} %	Total $^{238}U/^{206}Pb$	±	Total $^{207}Pb/^{206}Pb$	±	Radiogenic $^{206}Pb/^{238}U$	±	Age (Ma) $^{206}Pb/^{238}U$	±
Y1-IG062 – Granite														
1.1	1120	46	0.04	14.7	0.000000	0.03	65.39	0.72	0.0482	0.0007	0.0153	0.0002	97.8	1.1
1.2	513	360	0.70	128.0	0.000009	1.50	3.445	0.036	0.1128	0.0004	0.2859	0.0033	1621	17
2.1	1216	8	0.01	17.9	0.000001	<0.01	58.28	0.63	0.0473	0.0006	0.0172	0.0002	109.8	1.2
2.2	1544	46	0.03	72.8	0.000045	0.06	18.22	0.22	0.0538	0.0004	0.0548	0.0007	344.2	4.0
3.1	830	15	0.02	10.9	0.000027	0.06	65.46	0.75	0.0484	0.0008	0.0153	0.0002	97.7	1.1
3.2	967	127	0.13	51.1	0.002474	4.34	16.26	0.17	0.0889	0.0026	0.0588	0.0007	368.6	4.0
4.1	1910	8	0.00	86.9	0.000366	0.56	18.89	0.23	0.0575	0.0005	0.0526	0.0007	330.7	4.0
5.1	2736	6	0.00	128.8	0.000001	<0.01	18.25	0.19	0.0530	0.0003	0.0548	0.0006	344.1	3.5
6.1	2236	68	0.03	111.1	0.000478	0.99	17.30	0.18	0.0617	0.0003	0.0572	0.0006	358.8	3.6
6.2	196	48	0.24	9.9	0.000175	<0.01	17.02	0.22	0.0536	0.0009	0.0588	0.0008	368.2	4.6
6.3	1255	9	0.01	21.4	0.000082	0.15	50.44	0.55	0.0497	0.0006	0.0198	0.0002	126.4	1.4
7.1	307	183	0.60	15.8	-	0.10	16.66	0.20	0.0549	0.0008	0.0600	0.0007	375.3	4.4
8.1	2235	10	0.00	99.2	0.000076	0.20	19.34	0.20	0.0545	0.0005	0.0516	0.0005	324.3	3.3
9.1	2577	10	0.00	114.0	0.000026	<0.01	19.42	0.20	0.0524	0.0003	0.0515	0.0005	323.8	3.3
10.1	1210	248	0.21	65.0	0.000229	0.32	15.98	0.17	0.0571	0.0004	0.0624	0.0007	390.1	4.0
10.2	186	71	0.38	9.2	0.000080	0.01	17.38	0.24	0.0538	0.0012	0.0575	0.0008	360.6	4.8
11.1	1218	19	0.02	19.6	0.000112	0.27	53.44	0.60	0.0505	0.0009	0.0187	0.0002	119.2	1.3
11.2	293	113	0.39	15.2	0.000134	<0.01	16.61	0.21	0.0533	0.0008	0.0603	0.0008	377.2	4.7
12.1	2341	9	0.00	36.0	0.000032	0.01	55.80	0.59	0.0484	0.0005	0.0179	0.0002	114.5	1.2
12.2	482	34	0.07	26.0	0.000050	<0.01	15.92	0.18	0.0536	0.0006	0.0629	0.0007	393.3	4.3
12.3	3136	34	0.01	151.8	0.003210	5.92	17.75	0.18	0.1007	0.0041	0.0530	0.0006	332.9	3.8
13.1	3024	115	0.04	158.2	0.002723	5.19	16.42	0.17	0.0956	0.0005	0.0577	0.0006	361.8	3.7
14.1	1379	6	0.00	20.2	-	<0.01	58.80	0.65	0.0479	0.0007	0.0170	0.0002	108.8	1.2
15.1	1904	11	0.01	68.3	0.000004	0.15	23.95	0.25	0.0527	0.0003	0.0417	0.0004	263.3	2.7
16.1	276	190	0.69	14.2	-	<0.01	16.65	0.20	0.0540	0.0010	0.0601	0.0007	376.1	4.4
17.1	1168	4	0.00	16.7	0.000000	<0.01	60.01	0.67	0.0476	0.0007	0.0167	0.0002	106.6	1.2
18.1	1582	7	0.00	23.0	0.000181	0.07	58.96	0.64	0.0488	0.0006	0.0169	0.0002	108.3	1.2
18.2	262	124	0.47	12.9	0.000099	0.06	17.47	0.22	0.0542	0.0009	0.0572	0.0007	358.5	4.5
19.1	1792	86	0.05	92.3	0.000007	<0.01	16.68	0.17	0.0538	0.0003	0.0600	0.0006	375.4	3.8
20.1	2258	50	0.02	117.6	0.000078	0.20	16.49	0.17	0.0558	0.0003	0.0605	0.0006	378.8	3.8
21.1	962	3	0.00	13.8	0.000084	<0.01	59.74	0.66	0.0476	0.0007	0.0168	0.0002	107.1	1.2
21.2	2747	99	0.04	106.2	0.018363	33.06	22.23	0.23	0.3140	0.0092	0.0301	0.0007	191.3	4.2

Error in Temora reference zircon calibration was 0.33% for the analytical session.

Table B.5 continued. Summary of SHRIMP U-Pb results for zircon

Grain. spot	U (ppm)	Th (ppm)	Th/U	$^{206}Pb^*$ (ppm)	$^{204}Pb/^{206}Pb$	f_{206} %	Total $^{238}U/^{206}Pb$	±	Total $^{207}Pb/^{206}Pb$	±	Radiogenic $^{206}Pb/^{238}U$	±	Age (Ma) $^{206}Pb/^{238}U$	±
Y1-AW038 – Granite														
1.1	885	32	0.037	12.2	0.000048	0.10	62.14	0.70	0.0489	0.0008	0.0161	0.0002	102.8	1.2
2.1	938	29	0.031	13.5	0.000829	1.77	59.48	0.66	0.0622	0.0014	0.0165	0.0002	105.6	1.2
2.2	2811	59	0.021	43.3	0.000057	0.11	55.77	0.68	0.0492	0.0004	0.0179	0.0002	114.4	1.4
1.2	2044	34	0.016	31.2	0.000032	0.17	56.28	0.60	0.0497	0.0005	0.0177	0.0002	113.3	1.2
3.1	1738	34	0.019	26.6	0.000332	0.74	56.07	0.61	0.0542	0.0006	0.0177	0.0002	113.1	1.2
4.1	1474	42	0.028	27.2	0.016020	30.83	46.54	0.51	0.2928	0.0015	0.0149	0.0002	95.1	1.3
4.2	1549	31	0.020	22.8	-	0.08	58.30	0.64	0.0489	0.0006	0.0171	0.0002	109.6	1.2
5.1	1040	40	0.039	14.5	0.000111	0.02	61.64	0.68	0.0482	0.0007	0.0162	0.0002	103.7	1.1
6.1	1243	25	0.020	18.8	0.000022	<0.01	56.90	0.62	0.0482	0.0006	0.0176	0.0002	112.3	1.2
6.2	1615	27	0.016	23.3	0.000029	0.08	59.56	0.72	0.0488	0.0006	0.0168	0.0002	107.3	1.3
7.1	1497	34	0.023	22.6	0.000058	0.02	56.95	0.61	0.0484	0.0006	0.0176	0.0002	112.2	1.2
8.1	561	20	0.036	7.7	0.000241	0.15	62.78	0.74	0.0493	0.0010	0.0159	0.0002	101.7	1.2
9.1	1175	31	0.026	27.8	0.019187	34.99	36.27	0.40	0.3265	0.0260	0.0179	0.0009	114.5	6.0
10.1	1976	44	0.022	29.2	-	0.02	58.18	0.63	0.0484	0.0008	0.0172	0.0002	109.8	1.2
11.1	2344	29	0.012	46.3	0.001391	2.70	43.50	0.46	0.0704	0.0005	0.0224	0.0002	142.6	1.5
12.1	1395	58	0.042	19.5	-	0.03	61.59	0.68	0.0483	0.0006	0.0162	0.0002	103.8	1.1
13.1	1952	36	0.018	30.7	-	0.13	54.59	0.58	0.0494	0.0005	0.0183	0.0002	116.9	1.2
14.1	1782	32	0.018	26.4	-	<0.01	57.90	0.62	0.0467	0.0005	0.0173	0.0002	110.6	1.2
15.1	2238	41	0.018	34.8	0.000085	0.13	55.29	0.59	0.0494	0.0005	0.0181	0.0002	115.4	1.2
16.1	1564	39	0.025	22.8	0.000076	0.15	58.84	0.63	0.0494	0.0006	0.0170	0.0002	108.5	1.2
16.2	4660	30	0.006	233.4	0.006029	10.98	17.15	0.18	0.1413	0.0010	0.0519	0.0006	326.2	3.4
17.1	2145	35	0.017	33.3	0.000006	0.01	55.13	0.58	0.0484	0.0005	0.0181	0.0002	115.9	1.2
18.1	2000	31	0.016	30.7	0.000003	0.03	55.99	0.59	0.0486	0.0005	0.0179	0.0002	114.1	1.2
19.1	1683	29	0.017	25.7	0.000066	0.11	56.29	0.66	0.0492	0.0005	0.0177	0.0002	113.4	1.3
20.1	3303	36	0.011	52.0	0.000017	<0.01	54.55	0.57	0.0482	0.0004	0.0183	0.0002	117.1	1.2

Error in Temora reference zircon calibration was 0.30% for the analytical session.

Table B.5 continued. Summary of SHRIMP U-Pb results for zircon

Grain. spot	U (ppm)	Th (ppm)	Th/U	$^{206}Pb^*$ (ppm)	$^{204}Pb/^{206}Pb$	f_{206} %	Total $^{238}U/^{206}Pb$	±	Total $^{207}Pb/^{206}Pb$	±	Radiogenic $^{206}Pb/^{238}U$	±	Age (Ma) $^{206}Pb/^{238}U$	±
10CY-24 – Microgranite														
1.1	312	399	1.28	4.0	-	0.14	66.33	0.87	0.0491	0.0014	0.0151	0.0002	96.3	1.3
2.1	672	518	0.77	8.8	-	0.03	65.56	0.77	0.0482	0.0010	0.0152	0.0002	97.5	1.2
3.1	805	445	0.55	10.6	0.000023	<0.01	65.15	0.98	0.0478	0.0008	0.0154	0.0002	98.2	1.5
4.1	64	175	2.73	0.9	-	0.11	62.83	1.29	0.0490	0.0030	0.0159	0.0003	101.7	2.1
5.1	673	252	0.37	8.9	-	<0.01	64.67	0.75	0.0478	0.0009	0.0155	0.0002	98.9	1.2
6.1	278	201	0.72	3.9	0.000179	<0.01	61.58	0.82	0.0470	0.0014	0.0163	0.0002	104.0	1.4
7.1	288	81	0.28	14.2	0.000112	<0.01	17.47	0.21	0.0536	0.0007	0.0572	0.0007	358.8	4.2
8.1	138	365	2.63	1.8	-	0.49	66.37	1.13	0.0518	0.0021	0.0150	0.0003	95.9	1.6
9.1	114	197	1.72	1.5	-	<0.01	65.50	1.10	0.0476	0.0022	0.0153	0.0003	97.7	1.7
10.1	108	78	0.72	1.5	0.001163	0.31	61.74	1.04	0.0505	0.0022	0.0161	0.0003	103.3	1.8
11.1	134	116	0.87	9.3	0.000113	<0.01	12.36	0.16	0.0553	0.0009	0.0811	0.0011	502.9	6.5
12.1	55	117	2.13	0.7	0.004057	0.92	66.28	1.46	0.0552	0.0035	0.0149	0.0003	95.7	2.1
13.1	121	114	0.94	1.7	0.000242	0.16	61.01	0.99	0.0494	0.0021	0.0164	0.0003	104.6	1.7
14.1	131	81	0.61	1.9	0.000210	0.35	60.60	0.96	0.0509	0.0020	0.0164	0.0003	105.1	1.7
15.1	195	108	0.55	2.7	0.000349	<0.01	61.03	1.11	0.0467	0.0016	0.0164	0.0003	105.0	1.9
16.1	631	214	0.34	15.6	0.000042	0.16	34.72	0.47	0.0510	0.0007	0.0288	0.0004	182.8	2.5
16.2	854	193	0.23	44.3	-	<0.01	16.55	0.18	0.0536	0.0004	0.0605	0.0007	378.4	4.0
17.1	351	313	0.89	4.9	0.000317	0.08	61.13	0.77	0.0487	0.0017	0.0163	0.0002	104.5	1.3
18.1	80	107	1.34	1.0	-	0.16	67.03	1.29	0.0492	0.0028	0.0149	0.0003	95.3	1.9
19.1	820	115	0.14	11.3	0.000092	<0.01	62.10	0.70	0.0467	0.0008	0.0161	0.0002	103.2	1.2
20.1	102	64	0.63	1.4	0.001523	5.88	61.28	1.15	0.0947	0.0087	0.0154	0.0003	98.3	2.2

Error in Temora reference zircon calibration was 0.30% for the analytical session.

Table B.5 continued. Summary of SHRIMP U-Pb results for zircon

Grain.spot	U (ppm)	Th (ppm)	Th/U	$^{206}Pb^*$ (ppm)	$^{204}Pb/^{206}Pb$	f_{206} %	Total $^{238}U/^{206}Pb$	±	Total $^{207}Pb/^{206}Pb$	±	Radiogenic $^{206}Pb/^{238}U$	±	Age (Ma) $^{206}Pb/^{238}U$	±
21220-3 – Other Granite														
1.1	2235	99	0.04	30.7	0.000105	<0.01	62.54	0.67	0.0479	0.0006	0.0160	0.0002	102.3	1.1
1.2	215	65	0.30	35.4	0.000037	3.07	5.219	0.122	0.1019	0.0008	0.1857	0.0046	1098	25
2.1	3730	218	0.06	49.6	0.000008	<0.01	64.66	0.84	0.0476	0.0005	0.0155	0.0002	99.0	1.3
3.1	3636	176	0.05	51.7	0.000134	0.05	60.39	0.65	0.0485	0.0004	0.0166	0.0002	105.8	1.1
4.1	2420	152	0.06	34.8	0.000033	0.12	59.78	0.65	0.0491	0.0005	0.0167	0.0002	106.8	1.2
5.1	2080	90	0.04	29.2	0.000034	<0.01	61.12	0.66	0.0479	0.0006	0.0164	0.0002	104.6	1.1
6.1	1691	70	0.04	23.1	0.000053	0.02	62.87	0.68	0.0482	0.0006	0.0159	0.0002	101.7	1.1
7.1	901	46	0.05	12.3	-	<0.01	62.87	0.73	0.0470	0.0008	0.0159	0.0002	101.9	1.2
8.1	1456	73	0.05	20.4	0.000124	0.08	61.44	0.68	0.0487	0.0007	0.0163	0.0002	104.0	1.1
9.1	833	203	0.24	42.6	0.000039	<0.01	16.80	0.23	0.0540	0.0009	0.0595	0.0008	373	5
10.1	1222	96	0.08	17.3	-	0.04	60.59	0.68	0.0484	0.0007	0.0165	0.0002	105.5	1.2
10.2	338	67	0.20	4.8	0.000264	0.13	60.25	0.80	0.0492	0.0013	0.0166	0.0002	106.0	1.4
11.1	2447	112	0.05	34.5	-	0.04	60.93	0.65	0.0484	0.0006	0.0164	0.0002	104.9	1.1
12.1	2425	121	0.05	34.3	0.000044	0.03	60.69	0.65	0.0483	0.0005	0.0165	0.0002	105.3	1.1
13.1	2064	98	0.05	29.7	0.000050	0.03	59.68	0.65	0.0484	0.0005	0.0168	0.0002	107.1	1.2
14.1	1638	81	0.05	22.8	0.000069	0.02	61.82	0.68	0.0482	0.0006	0.0162	0.0002	103.4	1.1
15.1	3271	216	0.07	46.4	-	<0.01	60.56	0.68	0.0481	0.0004	0.0165	0.0002	105.6	1.2
16.1	2026	102	0.05	28.2	-	0.01	61.69	0.67	0.0482	0.0005	0.0162	0.0002	103.6	1.1
17.1	1232	51	0.04	17.2	-	0.15	61.54	0.69	0.0493	0.0007	0.0162	0.0002	103.8	1.2
18.1	996	44	0.04	14.2	0.000181	0.07	60.37	0.70	0.0487	0.0009	0.0166	0.0002	105.8	1.2
18.2	61	235	3.86	20.3	0.000001	7.59	2.581	0.043	0.1877	0.0024	0.3581	0.0070	1973	33
19.1	2322	107	0.05	32.7	0.000028	0.08	61.07	0.67	0.0488	0.0006	0.0164	0.0002	104.6	1.1
20.1	3167	173	0.05	45.6	0.000022	<0.01	59.61	0.64	0.0480	0.0005	0.0168	0.0002	107.3	1.2

Error in Temora reference zircon calibration was 0.49% for the analytical session.

Table B.5 continued. Summary of SHRIMP U-Pb results for zircon

Grain. spot	U (ppm)	Th (ppm)	Th/U	$^{206}Pb^*$ (ppm)	$^{204}Pb/^{206}Pb$	f_{206} %	Total $^{238}U/^{206}Pb$	±	Total $^{207}Pb/^{206}Pb$	±	Radiogenic $^{206}Pb/^{238}U$	±	Age (Ma) $^{206}Pb/^{238}U$	±
Billey Bluff – Other Granite														
1.1	1950	2505	1.28	28.2	0.000075	<0.01	59.50	0.65	0.0481	0.0006	0.0168	0.0002	107.4	1.2
2.1	61	117	1.91	0.8	0.002992	0.91	63.19	1.46	0.0553	0.0037	0.0157	0.0004	100.3	2.4
3.1	1088	1614	1.48	15.0	0.000088	0.10	62.38	0.71	0.0489	0.0008	0.0160	0.0002	102.4	1.2
4.1	1147	613	0.53	16.1	-	0.01	61.29	0.69	0.0482	0.0007	0.0163	0.0002	104.3	1.2
5.1	100	161	1.62	1.4	0.002109	0.71	62.90	1.20	0.0537	0.0031	0.0158	0.0003	101.0	2.0
6.1	313	352	1.13	4.3	-	0.44	62.01	0.85	0.0516	0.0015	0.0161	0.0002	102.7	1.4
7.1	88	145	1.64	1.2	0.003374	1.31	63.25	1.26	0.0584	0.0030	0.0156	0.0003	99.8	2.0
8.1	64	104	1.62	0.9	0.001275	1.62	61.94	1.52	0.0609	0.0053	0.0159	0.0004	101.6	2.6
9.1	226	331	1.47	3.1	-	0.24	63.47	0.99	0.0499	0.0018	0.0157	0.0002	100.5	1.6
10.1	509	417	0.82	7.0	0.000082	0.12	62.44	0.78	0.0490	0.0012	0.0160	0.0002	102.3	1.3
11.1	53	66	1.23	0.8	-	2.85	59.89	1.43	0.0707	0.0046	0.0162	0.0004	103.7	2.5
12.1	298	304	1.02	4.1	0.000457	0.37	62.00	0.86	0.0510	0.0015	0.0161	0.0002	102.8	1.4
13.1	277	246	0.89	3.9	-	0.04	61.06	0.87	0.0485	0.0016	0.0164	0.0002	104.7	1.5
14.1	996	877	0.88	14.4	-	0.19	59.60	0.68	0.0496	0.0008	0.0167	0.0002	107.1	1.2
14.2	90	149	1.66	1.2	-	1.48	61.79	1.25	0.0598	0.0031	0.0159	0.0003	102.0	2.1
15.1	300	350	1.17	4.2	0.000676	0.20	61.96	0.86	0.0496	0.0015	0.0161	0.0002	103.0	1.4
16.1	538	674	1.25	7.6	0.000062	0.10	61.14	0.76	0.0489	0.0011	0.0163	0.0002	104.5	1.3
16.2	290	269	0.93	4.0	0.000888	0.13	62.96	0.89	0.0491	0.0016	0.0159	0.0002	101.5	1.4
17.1	476	374	0.79	6.6	0.000056	0.08	61.67	0.79	0.0487	0.0012	0.0162	0.0002	103.6	1.3
18.1	1039	867	0.83	14.2	0.000191	0.13	62.93	0.72	0.0491	0.0008	0.0159	0.0002	101.5	1.2
19.1	999	1091	1.09	14.1	-	0.15	60.94	0.70	0.0493	0.0008	0.0164	0.0002	104.8	1.2
20.1	583	575	0.99	8.2	0.000160	0.34	60.93	0.75	0.0508	0.0011	0.0164	0.0002	104.6	1.3

Error in Temora reference zircon calibration was 0.49% for the analytical session.

Table B.5 continued. Summary of SHRIMP U-Pb results for zircon

Grain. spot	U (ppm)	Th (ppm)	Th/U	$^{206}Pb^*$ (ppm)	$^{204}Pb/^{206}Pb$	f_{206} %	Total $^{238}U/^{206}Pb$	±	Total $^{207}Pb/^{206}Pb$	±	Radiogenic $^{206}Pb/^{238}U$	±	Age (Ma) $^{206}Pb/^{238}U$	±
Y2-BR087 – Other Granite														
1.1	270	71	0.26	3.6	0.000868	0.12	65.18	1.00	0.0489	0.0017	0.0153	0.0002	98.0	1.5
2.1	322	60	0.19	4.4	0.000391	0.46	62.29	0.89	0.0517	0.0015	0.0160	0.0002	102.2	1.5
3.1	113	42	0.37	1.5	-	0.68	63.92	1.27	0.0534	0.0030	0.0155	0.0003	99.4	2.0
4.1	243	71	0.29	3.3	0.000025	0.45	63.27	0.99	0.0516	0.0018	0.0157	0.0002	100.6	1.6
5.1	272	132	0.49	3.8	0.000688	0.44	61.84	0.93	0.0516	0.0017	0.0161	0.0002	103.0	1.6
6.1	185	74	0.40	2.5	0.001046	0.20	62.32	1.04	0.0497	0.0020	0.0160	0.0003	102.4	1.7
7.1	183	73	0.40	2.5	0.001331	0.88	64.04	1.08	0.0550	0.0021	0.0155	0.0003	99.0	1.7
8.1	178	71	0.40	2.4	0.000524	0.07	62.68	1.02	0.0486	0.0020	0.0159	0.0003	102.0	1.7
9.1	140	52	0.37	1.9	0.000127	0.87	64.37	1.14	0.0549	0.0025	0.0154	0.0003	98.5	1.8
10.1	173	76	0.44	2.4	0.002012	0.35	61.87	1.02	0.0508	0.0021	0.0161	0.0003	103.0	1.7
11.1	99	35	0.36	1.3	0.000276	1.27	63.57	1.36	0.0581	0.0030	0.0155	0.0003	99.4	2.2
12.1	885	128	0.14	12.1	0.000249	0.05	62.90	0.75	0.0484	0.0009	0.0159	0.0002	101.6	1.2
13.1	95	44	0.46	1.3	0.003957	0.78	64.24	1.41	0.0542	0.0030	0.0154	0.0003	98.8	2.2
14.1	678	105	0.15	9.4	0.000550	0.16	62.09	0.76	0.0494	0.0010	0.0161	0.0002	102.8	1.3
15.1	174	62	0.36	2.4	0.000489	0.76	62.48	1.04	0.0541	0.0022	0.0159	0.0003	101.6	1.7
16.1	153	63	0.41	2.1	0.000824	0.38	62.48	1.08	0.0511	0.0023	0.0159	0.0003	102.0	1.8
17.1	150	60	0.40	2.1	0.000414	0.82	61.17	1.05	0.0546	0.0034	0.0162	0.0003	103.7	1.8
18.1	88	46	0.53	1.3	0.000108	0.84	57.69	1.21	0.0549	0.0031	0.0172	0.0004	109.9	2.3
19.1	310	160	0.52	4.4	0.000589	0.55	60.49	0.88	0.0525	0.0016	0.0164	0.0002	105.1	1.5
20.1	175	102	0.58	2.4	0.000776	0.90	63.30	1.06	0.0552	0.0022	0.0157	0.0003	100.1	1.7

Error in Temora reference zircon calibration was 0.49% for the analytical session.

Table B.5 continued. Summary of SHRIMP U-Pb results for zircon

Grain.spot	U (ppm)	Th (ppm)	Th/U	$^{206}Pb^*$ (ppm)	$^{204}Pb/^{206}Pb$	f_{206} %	Total $^{238}U/^{206}Pb$	±	Total $^{207}Pb/^{206}Pb$	±	Radiogenic $^{206}Pb/^{238}U$	±	Age (Ma) $^{206}Pb/^{238}U$	±
Y2-MP083 – Other Granite														
1.1	856	296	0.35	11.5	-	0.38	63.73	0.77	0.0510	0.0010	0.0156	0.0002	100.0	1.2
2.1	1217	348	0.29	16.6	-	0.16	63.03	0.72	0.0493	0.0008	0.0158	0.0002	101.3	1.2
3.1	436	133	0.30	5.9	0.000290	<0.01	63.69	0.85	0.0476	0.0013	0.0157	0.0002	100.5	1.3
4.1	401	176	0.44	5.5	0.000057	0.19	62.77	0.85	0.0495	0.0015	0.0159	0.0002	101.7	1.4
5.1	582	217	0.37	7.9	-	0.45	63.05	0.80	0.0516	0.0012	0.0158	0.0002	101.0	1.3
6.1	643	332	0.52	8.6	-	0.18	64.13	0.80	0.0495	0.0013	0.0156	0.0002	99.6	1.2
7.1	272	153	0.56	3.7	0.000902	0.53	63.49	0.94	0.0522	0.0017	0.0157	0.0002	100.2	1.5
8.1	600	252	0.42	8.1	-	0.46	63.27	0.79	0.0517	0.0011	0.0157	0.0002	100.6	1.3
9.1	425	200	0.47	5.9	0.000412	<0.01	62.43	0.83	0.0465	0.0013	0.0160	0.0002	102.6	1.4
10.1	503	205	0.41	6.9	0.000104	0.21	62.44	0.81	0.0497	0.0012	0.0160	0.0002	102.2	1.3
11.1	233	114	0.49	3.1	0.000050	0.36	63.52	0.99	0.0509	0.0019	0.0157	0.0002	100.3	1.6
12.1	519	198	0.38	7.1	0.000000	0.36	62.79	0.81	0.0509	0.0012	0.0159	0.0002	101.5	1.3
13.1	510	197	0.39	7.0	0.000656	0.44	62.56	0.82	0.0515	0.0013	0.0159	0.0002	101.8	1.3
14.1	344	160	0.46	4.7	0.000600	0.41	63.12	0.90	0.0513	0.0016	0.0158	0.0002	100.9	1.4
15.1	110	51	0.46	1.5	0.000847	0.53	63.61	1.27	0.0522	0.0028	0.0156	0.0003	100.0	2.0
16.1	3089	610	0.20	43.5	0.000046	<0.01	61.00	0.66	0.0481	0.0005	0.0164	0.0002	104.8	1.1
17.1	220	90	0.41	3.1	0.000595	0.55	61.98	0.92	0.0524	0.0026	0.0160	0.0002	102.6	1.6
18.1	158	100	0.63	2.1	-	1.15	63.97	1.11	0.0571	0.0023	0.0155	0.0003	98.9	1.7
19.1	486	188	0.39	6.6	-	0.02	63.23	0.80	0.0482	0.0011	0.0158	0.0002	101.1	1.3
20.1	408	178	0.44	5.7	0.000528	0.27	61.89	0.81	0.0502	0.0013	0.0161	0.0002	103.0	1.4

Error in Temora reference zircon calibration was 0.49% for the analytical session.

Notes:

1. Uncertainties given at the one s level.
2. f_{206} % denotes the percentage of ^{206}Pb that is common Pb.
3. Correction for common Pb for the U/Pb data has been made using the measured $^{238}U/^{206}Pb$ and $^{207}Pb/^{206}Pb$ ratios following Tera and Wasserburg (1972) as outlined in Williams (1998).

Table B.6. Zircon Hf and O isotope analyses

spot	assigned age (Ma)	$^{18}O/^{16}O$	$\pm10^{-7}$	$\delta^{18}O$ ‰	± 2 S.E.	$^{176}Hf/^{177}Hf$	$\pm10^{-6}$	$^{176}Lu/^{177}Hf$	$\pm10^{-5}$	$\varepsilon_{Hf(0)}$	$^{176}Hf/^{177}Hf_{(t)}$	$\varepsilon_{Hf(t)}$	± 2 S.E.	$\varepsilon_{Hf(360)}$	$\varepsilon_{Hf(100)}$
Y1-IG053 – orthogneiss															
IG053-1.1	345	0.0020439	1	8.67	0.35	0.282485	34	0.00050	1	-10.6	0.282482	-3.0	1.2	-2.7	–
IG053-1.2	377	0.0020448	2	9.11	0.36	0.282503	41	0.00121	7	-10.0	0.282495	-1.9	1.5	-2.2	–
IG053-2.1	350	0.0020449	1	9.14	0.36	0.282488	34	0.00045	1	-10.5	0.282486	-2.8	1.2	-2.6	–
IG053-2.2	533	0.0020400	1	6.75	0.35	0.282328	41	0.00116	12	-16.1	0.282317	-4.7	1.5	-8.4	–
IG053-3.2	367	0.0020441	2	8.74	0.36	0.282480	40	0.00131	5	-10.8	0.282471	-2.9	1.4	-3.1	–
IG053-4.2	367	0.0020448	1	9.11	0.35	0.282465	40	0.00110	2	-11.3	0.282458	-3.4	1.4	-3.6	–
IG053-5.1	367	0.0020439	1	8.67	0.35	0.282560	40	0.00101	4	-7.9	0.282554	0.0	1.4	-0.2	–
IG053-5.2	287	0.0020439	1	8.68	0.35	0.282460	38	0.00101	3	-11.5	0.282455	-5.3	1.3	–	–
IG053-6.1	356	0.0020442	1	8.82	0.35	0.282475	35	0.00041	1	-10.9	0.282473	-3.1	1.2	-3.0	–
IG053-6.2	367	0.0020433	1	8.36	0.35	0.282492	32	0.00055	5	-10.3	0.282489	-2.3	1.1	-2.5	–
IG053-7.1	367	0.0020438	2	8.61	0.37	0.282497	35	0.00077	1	-10.2	0.282492	-2.2	1.2	-2.4	–
IG053-8.1	367	0.0020441	2	8.76	0.36	0.282441	31	0.00059	2	-12.1	0.282437	-4.1	1.1	-4.3	–
IG053-9.1	346	0.0020440	2	8.73	0.36	0.282503	37	0.00079	3	-10.0	0.282498	-2.4	1.3	-2.1	–
IG053-13.1	367	0.0020438	2	8.61	0.36	0.282509	38	0.00136	3	-9.7	0.282500	-1.9	1.3	-2.1	–
IG053-14.1	350	0.0020445	2	8.96	0.36	0.282476	40	0.00104	3	-10.9	0.282470	-3.4	1.4	-3.2	–
IG053-16.1	367	0.0020445	1	8.96	0.35	0.282477	35	0.00070	1	-10.9	0.282473	-2.9	1.2	-3.0	–
IG053-17.1	367	0.0020452	1	9.30	0.35	0.282501	30	0.00146	4	-10.0	0.282491	-2.2	1.1	-2.4	–
IG053-18.1	355	0.0020443	3	8.87	0.38	0.282447	37	0.00045	1	-11.9	0.282444	-4.2	1.3	-4.1	–
IG053-18.2	367	0.0020446	0	8.99	0.35	0.282497	41	0.00037	1	-10.2	0.282495	-2.1	1.5	-2.3	–
IG053-19.1	355	0.0020445	1	8.98	0.35	0.282484	28	0.00072	1	-10.6	0.282480	-2.9	1.0	-2.8	–
IG053-19.2	378	0.0020431	2	8.27	0.37	0.282526	35	0.00071	2	-9.1	0.282521	-0.9	1.2	-1.3	–
K6-B26 – Orthogneiss															
K6B26-1.1	366	0.0020437	3	8.56	0.37	0.282494	42	0.00110	2	-10.0	0.282487	-2.4	1.5	-2.5	–
K6B26-2.1	338	0.0020435	0	8.47	0.35	0.282448	34	0.00125	4	-11.9	0.282441	-4.7	1.2	-4.2	–
K6B26-3.1	336	0.0020447	2	9.04	0.36	0.282479	42	0.00093	3	-10.2	0.282474	-3.5	1.5	-3.0	–
K6B26-4.2	366	0.0020429	5	8.20	0.42	0.282536	48	0.00090	3	-10.6	0.282530	-0.9	1.7	-1.0	–
K6B26-6.1	366	0.0020429	2	8.16	0.36	0.282485	36	0.00073	3	-9.1	0.282481	-2.6	1.3	-2.8	–
K6B26-7.1	366	0.0020432	1	8.34	0.35	0.282505	34	0.00095	7	-9.5	0.282499	-2.0	1.2	-2.1	–
K6B26-8.1	366	0.0020435	1	8.46	0.35	0.282527	40	0.00113	3	-9.1	0.282520	-1.2	1.4	-1.4	–
K6B26-9.1	366	0.0020443	1	8.88	0.35	0.282510	38	0.00164	6	-8.8	0.282499	-2.0	1.3	-2.1	–
K6B26-10.1	366	0.0020433	2	8.37	0.36	0.282505	36	0.00127	5	-8.5	0.282497	-2.0	1.3	-2.2	–
K6B26-10.2	366	0.0020426	3	8.03	0.39	0.282509	52	0.00113	14	-8.2	0.282502	-1.9	1.8	-2.0	–
K6B26-11.1	366	0.0020430	1	8.25	0.35	0.282475	59	0.00312	5	-7.9	0.282454	-3.6	2.1	-3.7	–
K6B26-12.1	366	0.0020433	2	8.40	0.36	0.282526	46	0.00089	3	-7.6	0.282520	-1.2	1.6	-1.4	–
K6B26-13.1	366	0.0020441	2	8.79	0.36	0.282464	38	0.00088	2	-7.3	0.282458	-3.4	1.3	-3.6	–
K6B26-14.1	366	0.0020442	1	8.84	0.35	0.282490	41	0.00075	3	-7.0	0.282485	-2.5	1.5	-2.6	–
K6B26-15.2	366	0.0020436	1	8.54	0.36	0.282549	45	0.00096	0	-6.7	0.282543	-0.4	1.6	-0.6	–
K6B26-16.1	335	0.0020459	1	9.67	0.35	0.282486	81	0.00091	4	-6.4	0.282481	-3.3	2.9	-2.8	–
K6B26-17.1	366	0.0020440	2	8.71	0.36	0.282542	43	0.00080	5	-6.1	0.282537	-0.6	1.5	-0.8	–
K6B26-18.1	366	0.0020440	1	8.73	0.35	0.282521	33	0.00076	4	-5.7	0.282516	-1.4	1.2	-1.5	–
K6B26-19.1	366	0.0020449	1	9.16	0.35	0.282511	47	0.00108	1	-5.4	0.282504	-1.8	1.7	-1.9	–
K6B26-20.1	105	0.0020461	2	9.77	0.36	0.282549	26	0.00039	0	-5.1	0.282549	-6.0	0.9	–	-6.2

Table B.6 continued. Zircon Hf and O isotope analyses

spot	assigned age (Ma)	$^{18}O/^{16}O$	$\pm10^{-7}$	$\delta^{18}O$ ‰	± 2 S.E.	$^{176}Hf/^{177}Hf$	$\pm10^{-6}$	$^{176}Lu/^{177}Hf$	$\pm10^{-5}$	$\varepsilon_{Hf(0)}$	$^{176}Hf/^{177}Hf_{(t)}$	$\varepsilon_{Hf(t)}$	± 2 S.E.	$\varepsilon_{Hf(360)}$	$\varepsilon_{Hf(100)}$
Y1-IG062– granite															
IG062-1.1	98	0.0020470	2	10.21	0.36	0.282582	32	0.00047	1	-7.2	0.282582	-5.0	1.1	–	-5.0
IG062-1.2	1621	0.0020386	1	6.05	0.35	0.282082	77	0.00131	3	-24.8	0.282042	10.3	2.7	–	–
IG062-2.1	110	0.0020456	2	9.51	0.37	0.282675	31	0.00048	0	-3.9	0.282675	-1.5	1.1	–	-1.7
IG062-2.2	344	0.0020458	1	9.58	0.35	0.282492	26	0.00064	1	-10.3	0.282488	-2.8	0.9	-2.5	–
IG062-3.1	98	0.0020465	1	9.94	0.35	0.282530	38	0.00057	2	-9.0	0.282529	-6.9	1.3	–	-6.8
IG062-4.1	331	0.0020469	1	10.16	0.35	0.282457	26	0.00111	1	-11.6	0.282451	-4.5	0.9	-3.9	–
IG062-6.1	359	0.0020448	1	9.12	0.35	0.282504	39	0.00128	3	-9.9	0.282496	-2.2	1.4	-2.2	–
IG062-6.2	368	0.0020456	0	9.50	0.35	0.282513	29	0.00105	1	-9.6	0.282506	-1.7	1.0	-1.9	–
IG062-6.3	126	0.0020455	1	9.47	0.36	0.282557	31	0.00073	2	-8.0	0.282556	-5.3	1.1	–	-5.9
IG062-10.1	390	0.0020456	2	9.51	0.36	0.282397	83	0.00087	9	-13.7	0.282391	-5.2	2.9	-5.9	–
IG062-10.2	361	0.0020446	1	9.02	0.35	0.282497	48	0.00103	9	-10.2	0.282491	-2.4	1.7	-2.4	–
IG062-11.1	119	0.0020466	2	9.99	0.36	0.282608	50	0.00123	9	-6.2	0.282606	-3.7	1.8	–	-4.1
IG062-11.2	377	0.0020454	2	9.39	0.36	0.282483	38	0.00101	3	-10.7	0.282476	-2.5	1.3	-2.9	–
IG062-12.1	114	0.0020462	2	9.78	0.36	0.282638	28	0.00082	2	-5.2	0.282637	-2.7	1.0	–	-3.0
IG062-12.2	393	0.0020467	3	10.06	0.37	0.282413	40	0.00033	2	-13.1	0.282411	-4.5	1.4	-5.2	–
IG062-12.3	333	0.0020442	2	8.81	0.37	0.282507	42	0.00053	2	-9.8	0.282504	-2.5	1.5	-1.9	–
IG062-14.1	109	0.0020465	2	9.94	0.36	0.282618	36	0.00060	2	-5.9	0.282617	-3.5	1.3	–	-3.7
IG062-17.1	107	0.0020457	2	9.53	0.37	0.282602	30	0.00054	1	-6.5	0.282601	-4.1	1.1	–	-4.3
IG062-18.1	108	0.0020463	1	9.84	0.35	0.282622	39	0.00070	3	-5.7	0.282621	-3.4	1.4	–	-3.6
IG062-18.2	359	0.0020455	1	9.45	0.35	0.282480	34	0.00124	5	-10.8	0.282472	-3.1	1.2	-3.1	–
IG062-19.1	375	0.0020451	1	9.25	0.35	0.282462	28	0.00079	5	-11.4	0.282457	-3.2	1.0	-3.6	–
IG062-20.1	379	0.0020448	1	9.13	0.35	0.282459	33	0.00107	7	-11.5	0.282452	-3.3	1.2	-3.8	–
IG062-21.1	107	0.0020461	2	9.76	0.36	0.282518	36	0.00057	5	-9.4	0.282517	-7.1	1.3	–	-7.3
Y1-AW038 – Granite															
AW038-1.1	103	0.0020461	2	9.35	0.31	0.282575	31	0.00106	1	-10.0	0.282573	-5.2	1.1	–	-5.3
AW038-1.2	113	0.0020471	1	9.85	0.30	0.282585	29	0.00098	1	-11.9	0.282583	-4.6	1.0	–	-4.9
AW038-3.1	113	0.0020462	1	9.40	0.30	0.282601	37	0.00131	0	-10.2	0.282599	-4.1	1.3	–	-4.4
AW038-4.2	110	0.0020460	1	9.32	0.30	0.282583	30	0.00135	3	-10.6	0.282581	-4.8	1.1	–	-5.0
AW038-5.1	103	0.0020451	1	8.87	0.30	0.282551	37	0.00155	7	-9.1	0.282549	-6.1	1.3	–	-6.2
AW038-6.1	112	0.0020466	1	9.60	0.30	0.282608	29	0.00103	1	-9.5	0.282606	-3.8	1.0	–	-4.1
AW038-6.2	107	0.0020460	1	9.33	0.30	0.282580	27	0.00088	1	-9.1	0.282579	-4.9	1.0	–	-5.1
AW038-7.1	112	0.0020460	0	9.33	0.30	0.282574	43	0.00148	4	-8.8	0.282571	-5.1	1.5	–	-5.3
AW038-8.1	103	0.0020457	2	9.18	0.31	0.282573	53	0.00046	0	-8.5	0.282573	-5.2	1.9	–	-5.3
AW038-10.1	110	0.0020467	2	9.65	0.31	0.282583	24	0.00116	2	-8.2	0.282581	-4.8	0.8	–	-5.0
AW038-12.1	103	0.0020452	1	8.94	0.30	0.282538	68	0.00178	4	-7.9	0.282535	-6.6	2.4	–	-6.6
AW038-14.1	111	0.0020472	2	9.92	0.31	0.282565	24	0.00085	2	-7.6	0.282564	-5.4	0.8	–	-5.6
AW038-15.1	115	0.0020459	2	9.30	0.30	0.282576	38	0.00102	2	-7.3	0.282574	-4.9	1.3	–	-5.2
AW038-16.1	108	0.0020450	2	8.83	0.31	0.282565	39	0.00123	2	-7.0	0.282563	-5.4	1.4	–	-5.6
AW038-17.1	116	0.0020465	2	9.59	0.31	0.282604	34	0.00108	1	-6.7	0.282602	-3.9	1.2	–	-4.3
AW038-18.1	114	0.0020451	2	8.88	0.31	0.282583	25	0.00071	0	-6.4	0.282582	-4.6	0.9	–	-5.0
AW038-19.1	113	0.0020457	2	9.20	0.32	0.282622	77	0.00096	1	-6.1	0.282620	-3.3	2.7	–	-3.6
AW038-20.1	117	0.0020459	1	9.29	0.30	0.282632	35	0.00127	4	-5.7	0.282630	-2.9	1.2	–	-3.3

Table B.6 continued. Zircon Hf and O isotope analyses

spot	assigned age (Ma)	$^{18}O/^{16}O$	$\pm10^{-7}$	$\delta^{18}O$ ‰	± 2 S.E.	$^{176}Hf/^{177}Hf$	$\pm10^{-6}$	$^{176}Lu/^{177}Hf$	$\pm10^{-5}$	$\varepsilon_{Hf(0)}$	$^{176}Hf/^{177}Hf_{(t)}$	$\varepsilon_{Hf(t)}$	± 2 S.E.	$\varepsilon_{Hf(360)}$	$\varepsilon_{Hf(100)}$
Y1-IG070 – Granite															
IG070-1.1	107	0.0020447	1	8.69	0.30	0.282582	32	0.00177	2	-10.0	0.282579	-4.9	1.1	–	-5.1
IG070-2.1	107	0.0020466	1	9.63	0.30	0.282528	37	0.00287	12	-11.9	0.282523	-6.9	1.3	–	-7.1
IG070-3.1	107	0.0020455	1	9.06	0.30	0.282574	39	0.00164	2	-10.2	0.282571	-5.2	1.4	–	-5.4
IG070-4.1	107	0.0020458	2	9.23	0.31	0.282583	34	0.00148	1	-10.6	0.282581	-4.9	1.2	–	-5.0
IG070-5.1	107	0.0020467	1	9.67	0.30	0.282586	43	0.00152	1	-9.1	0.282583	-4.8	1.5	–	-4.9
IG070-6.1	107	0.0020457	1	9.19	0.30	0.282561	33	0.00136	2	-9.5	0.282559	-5.6	1.2	–	-5.8
IG070-7.1	107	0.0020451	1	8.90	0.30	0.282608	36	0.00192	9	-9.1	0.282605	-4.0	1.3	–	-4.2
IG070-8.1	107	0.0020467	2	9.67	0.31	0.282575	37	0.00123	4	-8.8	0.282573	-5.1	1.3	–	-5.3
IG070-9.1	107	0.0020473	1	9.97	0.30	0.282576	41	0.00223	10	-8.5	0.282572	-5.2	1.5	–	-5.3
IG070-11.1	110	0.0020471	0	9.86	0.30	0.282555	35	0.00125	4	-8.2	0.282553	-5.8	1.2	–	-6.0
IG070-12.1	112	0.0020453	1	8.96	0.30	0.282613	44	0.00170	2	-7.9	0.282610	-3.7	1.6	–	-4.0
IG070-13.1	113	0.0020479	1	10.27	0.30	0.282551	36	0.00144	1	-7.6	0.282548	-5.9	1.3	–	-6.2
IG070-15.1	115	0.0020471	2	9.84	0.31	0.282587	40	0.00112	2	-7.3	0.282585	-4.5	1.4	–	-4.9
10CY-24 – Microgranite															
10CY-24-1.1	96	0.0020453	2	9.00	0.31	–	–	–	–	–	–	–	–	–	–
10CY-24-2.1	97	0.0020445	1	8.59	0.30	0.282629	97	0.00153	9	-10.0	0.282627	-3.4	3.4	–	-3.4
10CY-24-3.1	97	0.0020458	2	9.23	0.31	0.282618	71	0.00168	8	-11.9	0.282615	-3.8	2.5	–	-3.8
10CY-24-5.1	97	0.0020431	1	7.89	0.30	0.282596	45	0.00115	6	-10.2	0.282594	-4.6	1.6	–	-4.5
10CY-24-6.1	104	0.0020444	1	8.52	0.30	0.282642	50	0.00088	11	-10.6	0.282641	-2.8	1.8	–	-2.9
10CY-24-7.1	359	0.0020446	2	8.65	0.31	0.282469	48	0.00096	5	-9.1	0.282463	-3.4	1.7	–	-3.4
10CY-24-8.1	97	0.0020459	3	9.26	0.32	0.282596	42	0.00189	2	-9.5	0.282593	-4.6	1.5	–	-4.6
10CY-24-9.1	97	0.0020453	1	8.98	0.30	0.282607	41	0.00062	3	-9.1	0.282606	-4.2	1.5	–	-4.1
10CY-24-10.1	104	0.0020410	1	6.89	0.30	0.282670	35	0.00030	0	-8.8	0.282670	-1.8	1.2	–	-1.9
10CY-24-11.1	503	0.0020414	2	7.05	0.31	0.282223	58	0.00045	1	-8.5	0.282219	-8.8	2.1	–	-8.8
10CY-24-13.1	104	0.0020414	1	7.08	0.30	0.282692	45	0.00047	1	-8.2	0.282692	-1.0	1.6	–	-1.1
10CY-24-14.1	104	0.0020422	1	7.46	0.30	0.282653	35	0.00027	1	-7.9	0.282653	-2.4	1.2	–	-2.5
10CY-24-15.1	104	0.0020433	1	8.00	0.30	0.282605	41	0.00032	1	-7.6	0.282605	-4.1	1.5	–	-4.2
10CY-24-16.2	378	0.0020447	1	8.67	0.30	0.282480	37	0.00140	8	-7.3	0.282471	-2.7	1.3	–	-2.7
10CY-24-17.1	104	0.0020425	1	7.62	0.30	0.282574	40	0.00097	8	-7.0	0.282573	-5.2	1.4	–	-5.3
10CY-24-18.1	97	0.0020437	1	8.19	0.30	0.282625	70	0.00116	4	-6.7	0.282623	-3.6	2.5	–	-3.5
10CY-24-19.1	104	0.0020452	1	8.95	0.30	0.282578	25	0.00087	1	-6.4	0.282577	-5.1	0.9	–	-5.2

Table B.6 continued. Zircon Hf and O isotope analyses

spot	assigned age (Ma)	$^{18}O/^{16}O$	$\pm10^{-7}$	$\delta^{18}O$ ‰	± 2 S.E.	$^{176}Hf/^{177}Hf$	$\pm10^{-6}$	$^{176}Lu/^{177}Hf$	$\pm10^{-5}$	$\varepsilon_{Hf(0)}$	$^{176}Hf/^{177}Hf_{(t)}$	$\varepsilon_{Hf(t)}$	± 2 S.E.	$\varepsilon_{Hf(360)}$	$\varepsilon_{Hf(100)}$
21220-3 – Other granite															
21220-3_3	105	0.0020501	6	10.54	0.46	0.282362	40	0.00222	12	-15.0	0.282358	-12.8	1.4	–	-12.9
21220-3_4	105	0.0020503	5	10.61	0.44	0.282249	83	0.00159	4	-19.0	0.282246	-16.7	2.9	–	-16.8
21220-3_5	105	0.0020501	4	10.53	0.42	0.282356	27	0.00185	4	-15.2	0.282352	-13.0	1.0	–	-13.1
21220-3_8	105	0.0020494	5	10.16	0.44	0.282373	27	0.00144	3	-14.6	0.282370	-12.3	1.0	–	-12.4
21220-3_10	105	0.0020486	5	9.79	0.46	0.282387	36	0.00107	2	-14.1	0.282385	-11.8	1.3	–	-11.9
21220-3_11	105	0.0020514	5	11.14	0.44	0.282304	42	0.00224	10	-17.0	0.282300	-14.8	1.5	–	-14.9
21220-3_12	105	0.0020515	5	11.20	0.43	0.282409	30	0.00148	4	-13.3	0.282406	-11.1	1.1	–	-11.2
21220-3_13	105	0.0020499	6	10.43	0.46	0.282438	36	0.00145	5	-12.3	0.282435	-10.0	1.3	–	-10.1
21220-3_14	105	0.0020503	5	10.62	0.44	0.282392	31	0.00180	6	-13.9	0.282389	-11.7	1.1	–	-11.8
21220-3_15	105	0.0020505	6	10.73	0.46	0.282332	56	0.00206	10	-16.0	0.282328	-13.8	2.0	–	-13.9
21220-3_16	105	0.0020498	5	10.35	0.44	0.282450	27	0.00117	11	-11.8	0.282448	-9.6	1.0	–	-9.7
21220-3_17	105	0.0020503	5	10.61	0.44	0.282430	25	0.00123	6	-12.5	0.282428	-10.3	0.9	–	-10.4
21220-3_18	105	0.0020509	5	10.91	0.44	0.280893	29	0.00035	1	-66.9	0.280893	-64.6	1.0	–	-64.7
21220-3_19	105	0.0020504	5	10.66	0.44	0.282308	33	0.00215	4	-16.9	0.282304	-14.7	1.2	–	-14.8
21220-3_20	105	0.0020507	5	10.81	0.45	0.282426	36	0.00104	8	-12.7	0.282424	-10.4	1.3	–	-10.5
Billey Bluff –Other granite															
Billey_2	103	0.0020407	5	5.94	0.45	0.282790	44	0.00105	2	0.2	0.282788	2.4	1.6	–	2.3
Billey_3	103	0.0020392	5	5.21	0.44	0.282726	50	0.00271	30	-2.1	0.282720	0.0	1.8	–	-0.1
Billey_4	103	0.0020389	5	5.04	0.45	0.282723	42	0.00219	3	-2.2	0.282718	-0.1	1.5	–	-0.1
Billey_5	103	0.0020394	5	5.29	0.43	0.282764	34	0.00152	4	-0.8	0.282761	1.4	1.2	–	1.4
Billey_6	103	0.0020370	6	4.09	0.48	0.282677	45	0.00210	4	-3.8	0.282673	-1.7	1.6	–	-1.7
Billey_8	103	0.0020391	6	5.16	0.46	0.282767	33	0.00122	2	-0.7	0.282764	1.6	1.2	–	1.5
Billey_9	103	0.0020394	5	5.30	0.45	0.282744	32	0.00138	1	-1.5	0.282741	0.7	1.1	–	0.7
Billey_10	103	0.0020386	4	4.88	0.43	0.282741	32	0.00133	8	-1.6	0.282738	0.6	1.1	–	0.6
Billey_11	103	0.0020394	4	5.28	0.42	0.282776	36	0.00100	2	-0.3	0.282774	1.9	1.3	–	1.8
Billey_12	103	0.0020380	5	4.59	0.45	0.282651	55	0.00133	5	-4.7	0.282649	-2.5	1.9	–	-2.6
Billey_13	103	0.0020382	6	4.72	0.46	0.282727	30	0.00139	4	-2.1	0.282724	0.1	1.1	–	0.1
Billey_15	103	0.0020380	6	4.63	0.47	0.282734	28	0.00131	3	-1.8	0.282731	0.4	1.0	–	0.3
Billey_17	103	0.0020368	5	4.02	0.44	0.282745	34	0.00130	6	-1.4	0.282742	0.8	1.2	–	0.7
Billey_18	103	0.0020370	5	4.14	0.46	0.282726	41	0.00151	4	-2.1	0.282723	0.1	1.5	–	0.0
Billey_19	103	0.0020362	5	3.72	0.43	0.282731	40	0.00204	6	-1.9	0.282727	0.2	1.4	–	0.2
Billey_20	103	0.0020360	4	3.62	0.42	0.282713	35	0.00121	5	-2.6	0.282710	-0.4	1.2	–	-0.4

Table B.6 continued. Zircon Hf and O isotope analyses

spot	assigned age (Ma)	$^{18}O/^{16}O$	$\pm10^{-7}$	$\delta^{18}O$ ‰	± 2 S.E.	$^{176}Hf/^{177}Hf$	$\pm10^{-6}$	$^{176}Lu/^{177}Hf$	$\pm10^{-5}$	$\varepsilon_{Hf(0)}$	$^{176}Hf/^{177}Hf_{(t)}$	$\varepsilon_{Hf(t)}$	± 2 S.E.	$\varepsilon_{Hf(360)}$	$\varepsilon_{Hf(100)}$
Y2-BR087 –Other granite															
Y2-BR087_1	101	0.0020476	5	9.28	0.44	0.282570	37	0.00088	3	-7.6	0.282569	-5.4	1.3	–	-5.4
Y2-BR087_2	101	0.0020480	5	9.48	0.43	0.282564	44	0.00106	5	-7.8	0.282562	-5.6	1.6	–	-5.7
Y2-BR087_3	101	0.0020470	5	9.00	0.44	0.282604	30	0.00067	1	-6.4	0.282603	-4.2	1.1	–	-4.2
Y2-BR087_4	101	0.0020487	6	9.86	0.47	0.282595	39	0.00076	3	-6.7	0.282594	-4.5	1.4	–	-4.5
Y2-BR087_5	101	0.0020493	5	10.12	0.43	0.282574	36	0.00098	2	-7.5	0.282572	-5.3	1.3	–	-5.3
Y2-BR087_6	101	0.0020484	5	9.67	0.45	0.282621	37	0.00083	1	-5.8	0.282620	-3.6	1.3	–	-3.6
Y2-BR087_7	101	0.0020474	6	9.18	0.48	0.282547	48	0.00101	7	-8.4	0.282545	-6.2	1.7	–	-6.3
Y2-BR087_8	101	0.0020466	5	8.82	0.44	0.282596	50	0.00083	4	-6.7	0.282595	-4.5	1.8	–	-4.5
Y2-BR087_9	101	0.0020496	5	10.28	0.45	0.282591	30	0.00056	1	-6.9	0.282590	-4.6	1.1	–	-4.7
Y2-BR087_10	101	0.0020474	4	9.21	0.43	0.282594	46	0.00113	7	-6.7	0.282592	-4.6	1.6	–	-4.6
Y2-BR087_11	101	0.0020474	6	9.19	0.47	0.282586	34	0.00079	1	-7.0	0.282585	-4.8	1.2	–	-4.9
Y2-BR087_12	101	0.0020478	5	9.38	0.45	0.282467	34	0.00036	6	-11.2	0.282466	-9.0	1.2	–	-9.0
Y2-BR087_13	101	0.0020474	6	9.20	0.46	0.282646	32	0.00074	2	-4.9	0.282645	-2.7	1.1	–	-2.7
Y2-BR087_14	101	0.0020477	6	9.33	0.46	0.282596	32	0.00113	6	-6.7	0.282594	-4.5	1.1	–	-4.5
Y2-BR087_15	101	0.0020474	5	9.19	0.44	0.282606	28	0.00077	0	-6.3	0.282605	-4.1	1.0	–	-4.2
Y2-MP083 – Other granite															
Y2-MP083_3	101	0.0020442	5	7.63	0.45	0.282656	24	0.00053	2	-4.6	0.282655	-2.3	0.8	–	-2.4
Y2-MP083_4	101	0.0020441	6	7.60	0.46	0.282631	29	0.00057	2	-5.4	0.282630	-3.2	1.0	–	-3.3
Y2-MP083_5	101	0.0020456	6	8.33	0.47	0.282632	32	0.00046	1	-5.4	0.282631	-3.2	1.1	–	-3.2
Y2-MP083_6	101	0.0020458	6	8.40	0.47	0.282610	25	0.00063	2	-6.2	0.282609	-4.0	0.9	–	-4.0
Y2-MP083_7	101	0.0020447	5	7.87	0.44	0.282667	31	0.00062	0	-4.2	0.282666	-2.0	1.1	–	-2.0
Y2-MP083_8	101	0.0020450	6	8.03	0.46	0.282678	79	0.00069	3	-3.8	0.282677	-1.6	2.8	–	-1.6
Y2-MP083_9	101	0.0020452	6	8.10	0.47	0.282711	30	0.00057	2	-2.6	0.282710	-0.4	1.1	–	-0.4
Y2-MP083_10	101	0.0020452	6	8.10	0.48	0.282711	30	0.00062	1	-2.6	0.282710	-0.4	1.1	–	-0.4
Y2-MP083_11	101	0.0020451	5	8.07	0.44	0.282696	31	0.00080	1	-3.1	0.282695	-0.9	1.1	–	-1.0
Y2-MP083_12	101	0.0020447	5	7.88	0.45	0.282617	47	0.00073	1	-5.9	0.282616	-3.7	1.7	–	-3.8
Y2-MP083_13	101	0.0020449	6	7.98	0.46	0.282639	38	0.00056	1	-5.2	0.282638	-2.9	1.3	–	-3.0
Y2-MP083_14	101	0.0020456	5	8.33	0.44	0.282649	46	0.00068	0	-4.8	0.282648	-2.6	1.6	–	-2.6
Y2-MP083_15	101	0.0020446	5	7.83	0.43	0.282707	35	0.00051	4	-2.7	0.282706	-0.5	1.2	–	-0.6
Y2-MP083_16	101	0.0020443	5	7.67	0.44	0.282668	29	0.00095	0	-4.1	0.282666	-1.9	1.0	–	-2.0
Y2-MP083_17	101	0.0020424	5	6.73	0.45	0.282730	24	0.00066	2	-1.9	0.282729	0.3	0.8	–	0.2

Notes;
^{176}Lu decay constant of 1.865×10^{-11} (Soderlund *et al.* 2004).
$^{176}Hf/^{177}Hf$ and $^{176}Lu/^{177}Hf$ CHUR values of 0.282785 and 0.0336 (Bouvier *et al.* 2008).

Appendix C

C.1 Analytical Methods

C.1.1 Major oxide, trace element and REE chemistry

Major oxide and select trace elements were analyzed by X-ray fluorescence spectrometry at Franklin and Marshall College. A PANanalytical 2404 X-ray fluorescence vacuum spectrometer equipped with a PW2540 X-Y sample handler was used following the procedures described by Boyd and Mertzman (1987). FeO was analyzed by Fe^{2+} titration and the Fe_2O_3 was calculated by difference.

Rare earth elements were analyzed by inductively coupled plasma mass spectrometry at the University of Maryland. Twenty milligrams of powdered sample was dissolved in closed Savillex® Teflon beakers using 0.5 ml of 14M HNO_3 and 3 ml of 29M HF. Samples were digested for 24 hours, dried down and subjected to a second dissolution in 0.25 ml 12M $HClO_4$, 0.5 ml of 14M HNO_3 and 3 ml of 29M HF for 72 hours. The solution was dried down, brought up in 6M HCl and dissolved for a further 24 hours; this last procedure was repeated until the sample was fully dissolved. Samples were diluted by a factor of 100. One ml of a 20 ppb ^{115}In solution was added to the diluted sample to enable correction for instrumental drift.

The following isotopes ^{115}In, ^{139}La, ^{140}Ce, ^{141}Pr, ^{143}Nd, ^{147}Sm, ^{153}Eu, ^{158}Gd, ^{159}Tb, ^{163}Dy, ^{165}Ho, ^{167}Er, ^{169}Tm, ^{173}Yb and ^{175}Lu were analyzed using a Finnigan Element 2 single collector ICP-MS; solutions were introduced into the plasma using an APEX desolvating nebulizer. USGS standards G-2, a granite, and MAG-1, a marine sediment, were used to calculate sample concentrations. Signals were corrected for instrumental drift, by normalizing all data to the ^{115}In signal in the G-2 standard, and the blank, which

was <0.1% of the signal for standards and <0.7% of the signal for unknowns. Granites and orthogneisses were corrected using USGS standard G-2, while metasedimentary and paragneiss samples were corrected using USGS standard MAG-1. Uncertainties from counting statistics ranged from 1% to 6%, and propagated uncertainties for concentrations ranged from 4% to 12%. The analytical data are reported in Table C.2.

C.1.2 Whole-rock compositions (University of Maryland)

Sr and Nd isotope compositions were determined in the Isotope Geochemistry Laboratory at the University of Maryland. The rocks were prepared in a manner similar to that of Korhonen et al. (2010). Fifty milligrams of powder were dissolved in Savillex® Teflon beakers using 3 ml of 29M HF and 0.5 ml of 14M HNO_3, together with isotopic spikes enriched in ^{87}Rb, ^{84}Sr, ^{149}Sm, and ^{150}Nd, using a closed digestion at 180–190ºC for 24 hours. Samples were dried and re-dissolved in 3 ml of 29M HF, 0.5 ml of 14M HNO_3, and 0.25 ml of 12M $HClO_4$, and digested for a further 72 hours at 180–190ºC, then dried. To finish, 2 ml of 6M HCl was added to the samples, which were digested at 180ºC for 24 hours and dried again; this last procedure was repeated until the resulting solution was clear, after which samples were finally dried and brought up in 2 ml of 2.5M HCl.

Rubidium, Sr and REEs were separated from each other using a primary cation exchange column filled with AG50Wx4 (200–400 mesh) resin. Samples were loaded in chloride form. Rubidium and Sr were eluted in 2.5M HCl, while the REE were eluted from the column in 6M HCl. Rubidium cuts were dried and diluted in 2% HNO_3. Strontium cuts were passed through a cleanup column filled with Eichrom™ Sr-spec resin and eluted in 0.05M HNO_3. The REE cuts from the primary column were passed

through a secondary column filled with 0.225M 2-methyllactic acid (MLA). Samarium and Nd were eluted in 0.225M MLA (pH = 4.67).

Strontium, Nd and Sm ratios were analyzed using a VG Sector 54 TIMS. Strontium cuts were loaded onto a single Re filament with a Ta-oxide activator, and analyzed in a multi-dynamic mode. Strontium isotopes were corrected for mass fractionation by normalizing the measured $^{87}Sr/^{86}Sr$ ratio to an $^{86}Sr/^{88}Sr$ ratio = 0.1194. Repeated analysis of SRM 987 during the course of this study yielded an average $^{87}Sr/^{86}Sr$ value of 0.710238 (n = 30). The mass fractionation corrected and spike corrected $^{87}Sr/^{86}Sr$ ratio was normalized the average SRM 987 $^{87}Sr/^{86}Sr$ value to correct for instrumental bias. Strontium blank concentrations averaged 14.0 ng (n = 4), <1% of sample Sr concentrations.

Rubidium ratios were measured using a Nu Plasma multi-collector (MC) ICP-MS at the University of Maryland. Samples were diluted by a factor of 100 and were introduced into the plasma using an Aridus I desolvating nebulizer. A 50 ppb Rb SpecPure® plasma standard was introduced after every three sample analyses and was used to correct for instrumental fractionation and drift. Rubidium blanks averaged 8.04 ppm (n = 4), <1% of the sample Rb concentrations.

Neodymium and Sm were loaded on two Re filaments with phosphoric acid and loaded into the machine in a triple filament arrangement. Neodymium ratios were measured in dynamic mode and corrected for mass fractionation by normalizing the measured $^{143}Nd/^{144}Nd$ ratio to $^{146}Nd/^{144}Nd = 0.7219$. Repeated analysis of the Ames standard during the course of this study yielded an average $^{143}Nd/^{144}Nd$ value of 0.512126 (n = 33). The fractionation and spiked corrected $^{143}Nd/^{144}Nd$ ratio was normalized to the

average Ames $^{143}Nd/^{144}Nd$ value to correct for instrumental bias. Samarium was measured in static mode. Samarium blanks averaged 0.311 ng (n = 3) while Nd blanks averaged 2.28 ng (n = 3); both <1% of sample Sm and Nd concentrations.

The USGS G-2 granite was analyzed 7 times over a period of 12 months. Repeat analyses yielded an average $^{87}Sr/^{86}Sr$ of 0.709767 ± 0.000038 (n = 7) and an average $^{143}Nd/^{144}Nd$ of 0.512243 ± 0.000010 (n = 7). Rubidium concentrations averaged 167.6 ppm (range 162.9–174.2 ppm), Sr concentrations 488.8 ppm (range 482.1–496.2 ppm), and Rb/Sr ratios ranged from 0.3367 to 0.3511. Samarium concentrations averaged 7.1 ppm (range 7.0–7.3 ppm), Nd concentrations 52.6 ppm (range 52.2–53.2 ppm), and Sm/Nd ratios ranged from 0.1344 to 0.1372. The analytical data are reported in Table C.3.

C.1.3 U–Pb analysis of igneous zircon (SHRIMP: Australian National University)

U–Pb zircon age determinations were made using SHRIMP II and SHRIMP-RG at the Australian National University Research School of Earth Sciences (ANU-RSES) following the procedures described in Williams (1998 and references therein). Data were reduced using the SQUID Excel Macro (Ludwig, 2001). The zircon U/Pb ratios have been normalized relative to a value of 0.0668 for the Temora reference zircon, equivalent to an age of 417 Ma (Black et al. 2003); analytical uncertainties for the respective analytical sessions are given in the footnotes to Table C.4. Uncertainties reported in Table C.4 for individual analyses (ratios and ages) are given at the 1σ level. Tera–Wasserburg (Tera and Wasserburg, 1972) concordia plots, probability density plots with stacked histograms, and weighted mean $^{206}Pb/^{238}U$ age calculations were calculated using

ISOPLOT/EX (Ludwig, 2003). Where appropriate the "Mixture Modelling" algorithm of Sambridge and Compston (1994) via ISOPLOT/EX has been used to un-mix statistical age populations or groupings. From such groupings weighted mean $^{206}Pb/^{238}U$ ages have been calculated and the uncertainties reported as 95% confidence limits, including incorporation, in quadrature, of the uncertainty in the reference zircon calibration. The analytical data are reported in Table C.4.

C.1.4 U–Pb analyses of zircon (LA-ICP-MS: University of Arizona)

Zircon grains (generally 500–1000 for sedimentary rocks and 50–100 for igneous rocks) were incorporated into a 1" epoxy mount together with fragments of the Sri Lanka standard zircon at the University of Arizona. The mounts were sanded down to a depth of ~20 microns, polished, imaged, and cleaned prior to isotopic analysis.

U–Pb geochronology of zircons was conducted by laser ablation multicollector inductively coupled plasma mass spectrometry (LA-MC-ICPMS) at the Arizona LaserChron Center (Gehrels et al., 2006, 2008). The analyses involve ablation of zircon with a New Wave DUV193 Excimer laser (operating at a wavelength of 193 nm) using a spot diameter of 35 μm. The ablated material is carried in helium into the plasma source of a GVI Isoprobe, which is equipped with a flight tube of sufficient width that U, Th, and Pb isotopes are measured simultaneously. All measurements are made in static mode, using Faraday detectors with 10^{11} ohm resistors for ^{238}U, ^{232}Th, ^{208}Pb, and ^{206}Pb, a Faraday detector with a 10e12 ohm resistor for ^{207}Pb, and an ion-counting channel for ^{204}Pb. Ion yields are ~1.0 mv per ppm. Each analysis consists of one 12-second integration on peaks with the laser off (for backgrounds), 12 one-second integrations with

the laser firing, and a 30 second delay to purge the previous sample and prepare for the next analysis. The ablation pit is ~12 microns in depth.

For each analysis, the errors in determining $^{206}Pb/^{238}U$ and $^{206}Pb/^{204}Pb$ result in a measurement error of ~1-2% (at 2-sigma level) in the $^{206}Pb/^{238}U$ age. The errors in measurement of $^{206}Pb/^{207}Pb$ and $^{206}Pb/^{204}Pb$ also result in ~1-2% (at 2-sigma level) uncertainty in age for grains that are >1.0 Ga, but are substantially larger for younger grains due to low intensity of the ^{207}Pb signal. For most analyses, the cross-over in precision of $^{206}Pb/^{238}U$ and $^{206}Pb/^{207}Pb$ ages occurs at ~1.0 Ga.

Common Pb correction is accomplished by using the measured ^{204}Pb and assuming an initial Pb composition from Stacey and Kramers (1975) (with uncertainties of 1.0 for $^{206}Pb/^{204}Pb$ and 0.3 for $^{207}Pb/^{204}Pb$). Our measurement of ^{204}Pb is unaffected by the presence of ^{204}Hg because backgrounds are measured on peaks (thereby subtracting any background ^{204}Hg and ^{204}Pb), and because very little Hg is present in the argon gas (background ^{204}Hg = ~300 CPS).

Inter-element fractionation of Pb/U is generally ~20%, whereas apparent fractionation of Pb isotopes is generally <1%. In-run analysis of fragments of a large zircon crystal (generally every fifth measurement) with known age of 563.5 ± 3.2 Ma (2-sigma error) is used to correct for this fractionation. The uncertainty resulting from the calibration correction is generally 1-2% (2-sigma) for both $^{206}Pb/^{207}Pb$ and $^{206}Pb/^{238}U$ ages.

Concentrations of U and Th are calibrated relative to our Sri Lanka zircon, which contains ~518 ppm of U and 68 ppm Th. The analytical data for zircon from igneous rocks are reported in Table C.5 and for detrital zircon in Table C.6. Uncertainties shown

in these tables are at the 1-sigma level, and include only measurement errors. Analyses that are >30% discordant (by comparison of $^{206}Pb/^{238}U$ and $^{206}Pb/^{207}Pb$ ages) or >5% reverse discordant are not considered further.

C.1.6 Whole-rock oxygen isotope compositions (University of Wisconsin, Madison)

Whole-rock powders were analyzed in the University of Wisconsin Stable Isotope Laboratory by laser fluorination following the procedure described in Lackey et al. (2011). Isotope ratios were measured on a dual inlet gas source Finnigan MAT 251 mass spectrometer. Oxygen was extracted from 2–3 mg samples with BrF_5 using a 30W CO_2 laser (l = 10.6 mm), then purified cryogenically, passed through hot Hg to remove any residual F_2, and finally converted to CO_2 with a hot carbon rod (Valley et al., 1995). Analyses were standardized by running five analyses of UWG–2, the Gore Mountain garnet standard; $\delta^{18}O$ values were corrected to the long-term accepted value of 5.80‰ for UWG–2. The average raw $\delta^{18}O$ of UWG–2 for five analyses is 5.76 ± 0.08‰, one standard deviation. The analytical data are reported in Table C.7.

C.1.7 Lu–Hf isotope analyses of detrital zircons (University of Arizona)

Hf isotope analyses are conducted with a Nu HR ICPMS connected to a Photon Machines Analyte G2 excimer laser at the University of Arizona following the procedure outlined in Cecil et al. (2011). Instrument settings are established first by analysis of 10 ppb solutions of JMC475 and a Spex Hf solution, and then by analysis of 10 ppb solutions containing Spex Hf, Yb, and Lu. The mixtures range in concentration of Yb and Lu, with ^{176}(Yb+Lu) up to 70% of the ^{176}Hf. When all solutions yield $^{176}Hf/^{177}Hf$ of ~0.28216,

instrument settings are optimized for laser ablation analyses and seven different standard zircons (Mud Tank, 91500, Temora, R33, FC52, Plesovice, and Sri Lanka) are analyzed. These standards are included with unknowns on the same epoxy mounts. When precision and accuracy are acceptable, unknowns are analyzed using exactly the same acquisition parameters.

Laser ablation analyses are conducted with a laser beam diameter of 40 microns, with the ablation pits located on top of the U–Pb analysis pits. CL images are used to ensure that the ablation pits do not overlap multiple age domains or inclusions. Each acquisition consists of one 40-second integration on backgrounds (on peaks with no laser firing) followed by 60 one-second integrations with the laser firing. Using a typical laser fluence of ~5 J/cm2 and pulse rate of 7 hz, the ablation rate is ~0.8 microns per second. Each standard is analyzed once for every ~20 unknowns.

Isotope fractionation is accounted for using the method of Woodhead et al. (2004): βHf is determined from the measured $^{179}Hf/^{177}Hf$; βYb is determined from the measured $^{173}Yb/^{171}Yb$ (except for very low Yb signals); βLu is assumed to be the same as βYb; and an exponential formula is used for fractionation correction. Yb and Lu interferences are corrected by measurement of $^{176}Yb/^{171}Yb$ and $^{176}Lu/^{175}Lu$ (respectively), as advocated by Woodhead et al. (2004). Critical isotope ratios are $^{179}Hf/^{177}Hf$ =0.73250 (Patchett and Tatsumoto, 1980); $^{173}Yb/^{171}Yb$ = 1.132338 (Vervoort et al. 2004); $^{176}Yb/^{171}Yb$ =0.901691 (Vervoort et al., 2004; Amelin and Davis, 2005); $^{176}Lu/^{175}Lu$ = 0.02653 (Patchett, 1983). All corrections are done line-by-line. For very low Yb signals, βHf is used for fractionation of Yb isotopes. The corrected $^{176}Hf/^{177}Hf$ values are filtered for outliers (2-sigma filter), and the average and standard error are calculated from the

resulting ~58 integrations. There is no capability to use only a portion of the acquired data.

All solutions, standards, and unknowns analyzed during a session are reduced together. The cutoff for using βHf versus βYb is determined by monitoring the average offset of the standards from their known values, and the cutoff is set at the minimum offset. For most data sets, this is achieved at ~6 mv of ^{171}Yb. For sessions in which the standards yield ^{176}Hf/^{177}Hf values that are shifted consistently from the know values, a correction factor is applied to the ^{176}Hf/^{177}Hf of all standards and unknowns. This correction factor, which is not necessary for most sessions, averages 1 epsilon unit.

The ^{176}Hf/^{177}Hf at time of crystallization is calculated from measurement of present-day ^{176}Hf/^{177}Hf and ^{176}Lu/^{177}Hf, using the decay constant of ^{176}Lu ($\lambda = 1.867 \times 10^{-11}$) from Scherer et al. (2001) and Söderlund et al. (2004). No capability is provided for calculating Hf Depleted Mantle model ages because the ^{176}Hf/^{177}Hf and ^{176}Lu/^{177}Hf of the source material(s) from which the zircon crystallized is not known. The analytical data are reported in Table C.8.

C.1.8 Lu–Hf and O analysis of igneous zircon (Australian National University)

Following the U–Pb analyses, the SHRIMP 1–2 μm deep U–Pb pits were lightly polished away and oxygen isotope analyses made in same location using SHRIMP II fitted with a Cs ion source and electron gun for charge compensation as described by Ickert et al. (2008). Oxygen isotope ratios were determined in multiple collector mode using an axial continuous electron multiplier (CEM) triplet collector, and two floating heads with interchangeable CEM–Faraday Cups. The Temora 2 and FC1 reference

zircons were analysed to monitor and correct for isotope fractionation. The measured $^{18}O/^{16}O$ ratios and calculated $\delta^{18}O$ values have been normalised relative to an FC1 weighted mean $\delta^{18}O$ value of +5.4 ‰ (Ickert et al. 2008). Reproducibility in the Duluth Gabbro FC1 reference zircon $\delta^{18}O$ value ranged from ± 0.30‰ to 0.44‰ (2σ uncertainty) for the analytical sessions. As a secondary reference, the Temora 2 zircon was analysed in the same sessions, which gave $\delta^{18}O$ values of +8.2‰ in agreement with data reported by Ickert et al. (2008).

Lu–Hf isotope measurements were conducted by laser ablation multicollector inductively coupled plasma mass spectroscopy (LA–MC–ICPMS) using the ANU-RSES Neptune MC–ICPMS coupled with a 193 nm ArF Excimer laser, following procedures similar to those described in Munizaga et al. (2008). For all analyses of unknowns or secondary standards, the laser spot size was ~47 μm in diameter. Laser ablation analyses targeted the same locations within single zircon grains used for both the U–Pb and oxygen isotope analyses described above. The mass spectrometer was first tuned to optimal sensitivity using a large grain of zircon from the Mud Tank carbonatite. Isotopic masses were measured simultaneously in static-collection mode. A gas blank was acquired at regular intervals throughout the analytical session (every 12 analyses). Typically the laser was fired with a 5–8 Hz repetition rate and 50–60 mJ energy. Data were acquired for 100 seconds, but in many cases only a selected interval from the total acquisition was used in data reduction.

Throughout the analytical session several widely used reference zircons (FC-1 and Temora 2) were analysed to monitor data quality and reproducibility. Signal intensity was typically ~5–6 V for total Hf at the beginning of ablation, and decreased over the

acquisition time to 2 V or less. Isobaric interferences of ^{176}Lu and ^{176}Yb on the ^{176}Hf signal were corrected by monitoring signal intensities of ^{175}Lu and ^{173}Yb, ^{172}Yb and ^{171}Yb. The calculation of signal intensity for ^{176}Hf also involved independent mass bias corrections for Lu and Yb (see Munizaga et al. 2008 for further details). During the course of this data collection the reference zircons gave the following weighted mean ^{176}Hf/^{177}Hf ratios: 915000 = 0.282310 ± 14 (±2s) for 23 analyses, Mud Tank = 0.282516 ± 11 for 8 analyses, FC1 = 0.282173 ± 9 for 22 of 23 analyses, Plesovice = 0.282486 ± 11 for 16 of 17 analyses, and Monastery = 0.282744 ± 12 for 8 analyses. These are within analytical uncertainty of the values reported by Woodhead and Hergt (2005). The analytical data are reported in Table C.9.

Table C.1. Sample Locations

Sample	Rock Type	Location	Latitude	Longitude
10CY-001	Swanson Formation	Clark Mountains	77°16.729' S	142°09.726' W
10CY-002	Swanson Formation	Clark Mountains	77°16.729' S	142°09.726' W
Y2-BR086	Swanson Formation	Bailey Ridge	77°09.679' S	145°16.739' W
Y2-MD092	Swanson Formation	Mount Dolber	77°04.219' S	145°45.077' W
Y2-MP098	Swanson Formation	Mount Passel	76°53.851' S	144°52.003' W
318-M9	Metasedimentary gneiss	Mitchell Peak	76°25.000' S	147°22.000' W
21223-3	Metasedimentary gneiss	Scott Nunataks	77°14.000' S	154°12.000' W
21223-8	Metasedimentary gneiss	Scott Nunataks	77°14.000' S	154°12.000' W
8D27-10	Metasedimentary gneiss	Mt Woodward	77°18.000' S	145°47.000' W
912-2A	Ford Granodiorite Suite	Asman Ridge	77°10.000’ S	144°48.000’ W
9N27-4	Ford Granodiorite Suite	Mount Ralph	76°58.000’ S	144°32.000’ W
51225-1	Ford Granodiorite Suite	Chester Mountains	76°40.000' S	145°35.000' W
51225-2	Ford Granodiorite Suite	Chester Mountains	76°40.000' S	145°35.000' W
Y2-GP091	Ford Granodiorite Suite	Greer Peak	76°46.570' S	144°25.644' W
Y2-HN097	Ford Granodiorite Suite	Herman Nunatak	76°13.377' S	143°52.879' W
Y2-JU096	Ford Granodiorite Suite	Mount June	76°15.109' S	145°16.515' W
Y2-SM095	Ford Granodiorite Suite	Saunders Mountain	76°51.104' S	145°41.644' W
Y1-AE035	Devonian–Carboniferous Granite	Mount Avers	76°27.950' S	145°16.324' W
M5-G175	Devonian–Carboniferous Granite	Mount Getz	76°33.180' S	145°13.200' W
Y1-IG071	Diatexite	Mount Iphigene	76°30.676' S	145°48.368' W
Y1-IG073	Diatexite	Mount Iphigene	76°30.676' S	145°48.368' W

Table C.2. Major element, trace element and REE concentrations

Rock Type	Swanson Formation					Ford Granodiorite Suite		
Sample no	10CY-001	10CY-002	Y2-BR086	Y2-MD092	Y2-MP098	51225-1	51225-2	Y2-GP091
wt %								
SiO_2	64.33	63.92	71.59	73.92	74.06	68.24	66.43	67.50
TiO_2	0.68	0.70	0.73	0.57	0.68	0.70	0.78	0.59
Al_2O_3	15.86	16.52	14.02	11.54	12.00	15.13	15.37	15.35
Fe_2O_3	0.70	0.74	0.58	0.21	0.57	0.39	0.56	0.89
FeO	5.70	5.82	4.08	4.03	4.06	3.61	4.01	2.47
MnO	0.11	0.11	0.08	0.11	0.11	0.07	0.07	0.06
MgO	3.69	3.76	2.41	2.97	2.78	1.42	1.62	2.02
CaO	3.01	1.25	0.94	2.31	1.47	2.67	2.59	3.20
Na_2O	2.20	2.44	1.70	1.57	1.93	3.19	3.03	3.83
K_2O	3.02	4.24	3.36	2.33	2.15	3.70	4.19	3.05
P_2O_5	0.18	0.17	0.19	0.17	0.18	0.22	0.24	0.18
LOI	1.50	1.86	2.05	0.98	1.97	1.06	1.05	1.62
Total	100.11	100.32	100.13	100.18	100.44	99.74	99.34	99.42
ppm (XRF)								
Rb	140	195.9	162.8	98.9	95.9	189.2	208.7	143.8
Sr	207	149	137	196	155	223	218	378
Y	32	33.6	39.4	33.4	38.8	32.4	34.8	23
Zr	123	121	172	166	233	228	240	146
V	131	112	89	80	84	73	82	77
Ni	110	118	43	106	112	9	10	37
Cr	110	118	84	123	151	33	36	60
Nb	11.6	13.4	15.2	11.7	13.5	19.7	21.3	13.2
Ga	20.6	21.2	18.9	15.7	17.1	21.5	21.7	18.7
Cu	39	41	6	8	30	12	23	9
Zn	120	152	85	74	78	66	73	48
Co	26	28	18	17	17	11	14	12
Ba	483	658	727	426	438	514	565	483
La	26	29	32	30	37	34	44	24
Ce	69	75	82	65	83	75	105	51
U	3.1	1.4	3.8	1.9	3.8	5.1	5.3	2.1
Th	14.2	17.2	14.3	13.7	13.3	14.8	24.5	14.5
Sc	18	16	12	12	12	11	12	11
Pb	8	12	15	11	3	15	28	<1
ppm (ICP-MS)								
Sc	18.2	17.31	11.19	9.8	10.44	10.92	11.28	8.64
Y	28.59	30.36	38.89	27.05	31.32	34.49	33.81	20.93
La	32.26	37.35	42.9	32.66	36.72	47.96	53.18	25.03
Ce	66.58	76.4	90.12	66.73	75.01	103.16	114.31	50.07
Pr	7.83	8.84	10.6	7.92	8.97	12.8	14.07	6.16
Nd	30.03	34.16	40.27	30.29	34.16	48.3	52.72	23.34
Sm	6.25	6.96	8.43	6.1	6.92	8.97	9.47	4.65
Eu	1.34	1.44	1.65	1.18	1.29	1.38	1.34	1.06
Gd	5.05	5.52	6.95	4.89	5.47	7.53	7.59	4.21
Tb	0.85	0.91	1.2	0.81	0.93	1.17	1.18	0.69
Dy	5.03	5.26	7.03	4.75	5.5	6.31	6.48	3.9
Ho	1.03	1.07	1.41	0.96	1.14	1.19	1.22	0.74
Er	2.89	3.01	3.83	2.65	3.17	3.51	3.63	2.21
Tm	0.43	0.43	0.55	0.39	0.47	0.55	0.58	0.36
Yb	2.81	2.86	3.45	2.43	3.03	3.39	3.59	2.38
Lu	0.39	0.4	0.45	0.33	0.42	0.52	0.56	0.39

Table C.2. Major element, trace element and REE concentrations

	Ford Granodiorite Suite			Diatexite		Carboniferous granite	
	Y2-HN097	Y2-JU096	Y2-SM095	Y1-IG071	Y1-IG073	Y1-AE035	M5-G175
wt %							
SiO_2	69.08	69.10	67.38	72.88	71.63	66.59	67.54
TiO_2	0.53	0.54	0.68	0.46	0.48	0.87	0.70
Al_2O_3	14.98	15.00	15.29	13.91	14.62	16.04	15.23
Fe_2O_3	0.83	0.53	1.06	0.49	0.26	1.15	0.92
FeO	2.43	2.68	3.14	2.51	2.39	3.71	3.76
MnO	0.06	0.05	0.07	0.04	0.02	0.06	0.06
MgO	1.77	1.66	2.35	1.36	1.04	1.63	1.96
CaO	3.15	2.74	3.92	1.63	2.08	3.52	1.72
Na_2O	3.97	3.48	3.40	2.72	2.96	3.68	3.11
K_2O	2.52	3.35	2.63	4.16	4.00	2.26	4.14
P_2O_5	0.17	0.16	0.17	0.08	0.17	0.27	0.09
LOI	0.94	1.71	1.36	1.06	0.98	1.05	1.10
Total	99.76	99.59	100.44	100.52	99.92	100.19	99.65
ppm (XRF)							
Rb	88.1	116.9	98.5	173	150.7	146.4	201
Sr	354	418	346	191	259	281	249
Y	23.7	35.2	27	26.1	22.4	23	39.1
Zr	143	173	155	169	255	256	233
V	72	73	97	57	51	100	85
Ni	35	34	35	15	10	10	23
Cr	80	64	78	75	34	58	77
Nb	15.1	14.5	10.1	13.5	11.7	16.6	19.2
Ga	19.5	19.2	19	19.1	18.5	22	22.1
Cu	9	9	9	7	7	8	23
Zn	46	53	59	58	50	80	81
Co	11	11	15	8	6	14	15
Ba	472	628	525	551	1109	690	1119
La	23	38	29	24	40	23	36
Ce	44	80	55	53	100	50	87
U	4.9	4.7	2.3	3.7	3.6	2.2	6.2
Th	5.4	16.2	9.4	12.2	22.4	5.7	16.8
Sc	9	11	11	8	8	16	12
Pb	10	189	22	28	33	21	27
ppm (ICP-MS)							
Sc	8.72	9.59	11.42	10.32	7.97	15.77	13.95
Y	19	30.66	22.45	17.74	22.49	25.8	35.88
La	21.02	40.53	22.35	31.52	63.83	43.65	58.01
Ce	41.61	82.65	48.97	65.68	131.69	91.8	115.07
Pr	5.04	10.03	6.05	8.16	16	11.32	13.67
Nd	19.32	37.43	23.07	29.77	60.97	44.48	50.09
Sm	3.93	6.91	4.63	6.04	11.12	8.37	8.94
Eu	0.94	1.39	1.16	1.18	1.74	1.76	1.53
Gd	3.65	6.02	4.3	4.92	8.65	6.83	7.82
Tb	0.61	0.97	0.7	0.79	1.24	1.05	1.19
Dy	3.45	5.34	3.94	3.88	5.83	5.38	6.25
Ho	0.67	1.03	0.77	0.64	0.87	0.95	1.19
Er	1.99	3.06	2.27	1.56	1.91	2.54	3.5
Tm	0.32	0.49	0.36	0.2	0.21	0.37	0.53
Yb	2.03	3.09	2.29	1.1	0.96	2.19	3.1
Lu	0.32	0.49	0.37	0.15	0.12	0.33	0.48

Table C.3. Sr–Nd isotope compositions

Rock Type	Swanson Formation		Ford Granodiorite suite					
Sample no.	10CY-001	10CY-002	Y2-BR086	Y2-MD092	Y2-MP098	51225-1	51225-2	Y2-GP091
Rb	131.3	205.5	155.2	99.9	95.5	194.2	220.7	142.5
Sr	201.1	147.6	128.7	194.8	150.7	223	220.4	375.9
Rb/Sr	0.65	1.39	1.21	0.51	0.63	0.87	1.00	0.38
$^{87}Rb/^{86}Sr$	2.09	4.04	3.50	1.49	1.84	2.29	2.90	1.10
$^{87}Sr/^{86}Sr$	0.726291	0.732242	0.738139	0.727782	0.72801	0.720773	0.72163	0.71077
$^{87}Sr/^{86}Sr_{(100M}$	0.723375	0.726599	0.733244	0.725704	0.725442	0.717575	0.717575	0.709237
$^{87}Sr/^{86}Sr_{(360M}$	0.715775	0.71189	0.720484	0.720285	0.718746	0.709237	0.707005	0.705241
Sm	6.6	6.7	8	6	6.9	9.2	11.2	4.3
Nd	35.3	32.8	38.8	30.3	34.3	45.9	59.6	21.5
Sm/Nd	0.19	0.2	0.21	0.2	0.2	0.2	0.19	0.2
$^{147}Sm/^{144}Nd$	0.113254	0.122727	0.124266	0.120037	0.120772	0.090416	0.113363	0.121087
$^{143}Nd/^{144}Nd$	0.512117	0.512084	0.512079	0.511979	0.512061	0.512378	0.512292	0.512432
$\varepsilon Nd_{(0Ma)}$	-10.2	-10.8	-10.9	-12.8	-11.3	-5.1	-6.7	-4
$\varepsilon Nd_{(100Ma)}$	-9.1	-9.9	-10	-11.9	-10.3	-3.7	-5.7	-3.1
$\varepsilon Nd_{(360Ma)}$	-6.3	-7.4	-7.6	-9.3	-7.8	-0.2	-2.9	-0.5

Rock Type	Ford Granodiorite suite			Carboniferous granite		Diatexites	
Sample no.	Y2-HN097	Y2-JU096	Y2-SM095	Y1-AE035	M5-G175	Y1-IG071	Y2-IG073
Rb	85.3	122.2	100.4	128.6	213.8	171.17	146.55
Sr	357.2	422.8	345.6	271.1	248.5	190.47	279.69
Rb/Sr	0.24	0.29	0.29	0.47	0.86	0.90	0.52
$^{87}Rb/^{86}Sr$	0.69	0.84	0.84	1.37	2.49	2.60	1.64
$^{87}Sr/^{86}Sr$	0.708715	0.71085	0.710204	0.715979	0.720081	0.7176359	0.717636
$^{87}Sr/^{86}Sr_{(100M}$	0.707749	0.709681	0.709028	0.714059	0.716597	0.7139972	0.715341
$^{87}Sr/^{86}Sr_{(360M}$	0.705231	0.706634	0.705965	0.709056	0.707518	0.7045129	0.70936
Sm	3.8	8.6	4.8	6.1	10.2	8.5	11.5
Nd	18.2	46.6	23	31.4	53.6	41.3	61.6
Sm/Nd	0.21	0.18	0.21	0.19	0.19	0.2	0.2
$^{147}Sm/^{144}Nd$	0.110934	0.126897	0.127007	0.116782	0.114473	0.123871	0.112547
$^{143}Nd/^{144}Nd$	0.512276	0.512438	0.512368	0.512254	0.512225	0.5121746	0.512217
$\varepsilon Nd_{(0Ma)}$	-7.1	-3.9	-5.3	-7.5	-8.1	-9.0	-8.2
$\varepsilon Nd_{(100Ma)}$	-6	-3.0	-4.4	-6.5	-7.0	-8.1	-7.1
$\varepsilon Nd_{(360Ma)}$	-3.1	-0.7	-2.1	-3.8	-4.3	-5.7	-4.3

Notes: $\lambda_{Rb} = 1.3968 \times 10^{-11}$

$\lambda_{Sm} = 6.54 \times 10^{-12}$

$^{143}Nd/^{144}Nd_{CHUR\ (0)} = 0.512638$

$^{147}Sm/^{144}Nd_{CHUR(0)} = 0.1967$

Table C.4. Summary of SHRIMP U–Pb results for zircon.

Grain spot	U (ppm)	Th (ppm)	Th/U	$^{206}Pb^*$ (ppm)	$^{204}Pb/^{206}Pb$	f_{206} %	Total $^{238}U/^{206}Pb$	±	Total $^{207}Pb/^{206}Pb$	±	Radiogenic $^{206}Pb/^{238}U$	±	Age (Ma) $^{206}Pb/^{238}U$	±
Y2-JU096														
1.1	1055	64	0.06	52.4	-	<0.01	17.29	0.18	0.0536	0.0004	0.0578	0.0006	362.5	3.8
2.1	185	98	0.53	9.3	0.000068	0.03	17.00	0.21	0.0542	0.0009	0.0588	0.0007	368.5	4.4
3.1	166	132	0.79	8.3	-	<0.01	17.15	0.21	0.0536	0.0010	0.0583	0.0007	365.4	4.5
4.1	239	38	0.16	12.4	-	<0.01	16.66	0.20	0.0540	0.0008	0.0600	0.0007	375.9	4.4
5.1	386	168	0.44	19.4	-	<0.01	17.06	0.26	0.0533	0.0006	0.0587	0.0009	367.5	5.6
6.1	278	106	0.38	14.3	0.000027	0.03	16.69	0.19	0.0544	0.0007	0.0599	0.0007	374.9	4.3
6.2	163	89	0.55	8.2	0.000196	0.10	17.16	0.21	0.0547	0.0010	0.0582	0.0007	364.8	4.5
7.1	258	100	0.39	12.5	-	0.00	17.75	0.21	0.0536	0.0010	0.0563	0.0007	353.4	4.1
7.2	248	81	0.33	11.6	0.000113	0.12	18.44	0.22	0.0543	0.0009	0.0542	0.0007	340.1	4.0
8.1	1014	212	0.21	52.6	0.000025	0.09	16.56	0.19	0.0549	0.0006	0.0603	0.0007	377.7	4.2
9.1	439	119	0.27	22.1	-	-0.06	17.07	0.19	0.0534	0.0006	0.0586	0.0007	367.2	4.0
10.1	704	194	0.28	35.5	0.000010	-0.14	17.03	0.18	0.0528	0.0005	0.0588	0.0006	368.3	3.9
11.1	566	125	0.22	28.5	0.000080	0.02	17.02	0.19	0.0541	0.0005	0.0587	0.0007	367.9	4.0
12.1	143	63	0.44	7.5	-	-0.07	16.44	0.21	0.0537	0.0011	0.0609	0.0008	380.9	4.9
13.1	260	106	0.41	13.1	-	-0.01	17.08	0.20	0.0538	0.0008	0.0586	0.0007	366.8	4.2
14.1	636	139	0.22	32.9	-	-0.06	16.62	0.18	0.0537	0.0005	0.0602	0.0007	376.9	4.1
15.1	318	71	0.22	16.1	-	-0.06	16.98	0.20	0.0535	0.0007	0.0589	0.0007	369.1	4.2
16.1	791	188	0.24	38.9	0.000042	0.07	17.48	0.19	0.0542	0.0005	0.0572	0.0006	358.4	3.9
17.1	385	148	0.39	19.6	0.000021	0.02	16.90	0.19	0.0542	0.0007	0.0592	0.0007	370.5	4.1
18.1	163	33	0.20	8.2	0.000119	0.03	17.07	0.21	0.0541	0.0010	0.0586	0.0007	366.9	4.5
19.1	223	112	0.50	11.2	0.000103	0.08	17.13	0.20	0.0545	0.0008	0.0583	0.0007	365.5	4.3
20.1	152	110	0.72	7.6	-	0.11	17.15	0.23	0.0548	0.0010	0.0582	0.0008	364.8	4.8
Error in Temora reference zircon calibration was 0.30% for the analytical session.														
51225-2														
1.1	1524	202	0.13	76.5	0.000014	0.09	17.12	0.18	0.0546	0.0003	0.0584	0.0006	365.6	3.7
2.1	316	65	0.21	15.6	0.000030	0.04	17.35	0.20	0.0541	0.0008	0.0576	0.0007	361.0	4.2
3.1	246	219	0.89	12.3	-	<0.01	17.24	0.21	0.0536	0.0009	0.0580	0.0007	363.5	4.4
4.1	2742	398	0.14	137.6	-	<0.01	17.12	0.18	0.0536	0.0003	0.0584	0.0006	366.0	3.7
5.1	1278	247	0.19	63.2	0.000023	0.01	17.38	0.18	0.0538	0.0004	0.0575	0.0006	360.6	3.7
6.1	686	144	0.21	37.0	0.000013	0.02	15.95	0.17	0.0547	0.0007	0.0627	0.0007	392.0	4.2
7.1	2114	211	0.10	107.6	0.000011	0.01	16.87	0.18	0.0541	0.0003	0.0593	0.0007	371.2	4.0
7.2	709	117	0.17	35.5	-	<0.01	17.15	0.19	0.0538	0.0006	0.0583	0.0007	365.4	4.0
8.1	807	211	0.26	39.8	0.000019	0.03	17.42	0.19	0.0540	0.0005	0.0574	0.0006	359.8	3.8
9.1	382	52	0.14	18.9	-	0.01	17.38	0.20	0.0539	0.0008	0.0575	0.0007	360.6	4.1
9.2	403	8	0.02	30.6	0.000031	0.06	11.29	0.13	0.0589	0.0006	0.0885	0.0010	546.8	6.0
10.1	492	465	0.94	24.3	0.000031	0.16	17.44	0.20	0.0550	0.0006	0.0573	0.0007	359.0	4.1
11.1	683	131	0.19	34.2	0.000033	0.05	17.18	0.19	0.0542	0.0005	0.0582	0.0006	364.6	3.9
11.2	204	155	0.76	10.3	-	0.04	17.07	0.22	0.0542	0.0010	0.0586	0.0008	366.9	4.6
12.1	787	143	0.18	39.7	0.000041	0.08	17.02	0.18	0.0546	0.0005	0.0587	0.0006	367.7	3.9
13.1	834	107	0.13	42.3	0.000053	0.04	16.95	0.18	0.0543	0.0005	0.0590	0.0006	369.4	3.9
14.1	832	230	0.28	42.4	0.000045	<0.01	16.85	0.18	0.0538	0.0005	0.0594	0.0006	371.8	3.9
15.1	990	279	0.28	50.6	0.000039	<0.01	16.82	0.18	0.0537	0.0004	0.0595	0.0006	372.5	3.9
15.2	432	168	0.39	57.4	0.000004	<0.01	6.470	0.073	0.0682	0.0005	0.1549	0.0018	928.3	10.1
16.1	401	49	0.12	19.7	-	<0.01	17.45	0.21	0.0531	0.0007	0.0573	0.0007	359.5	4.2
17.1	442	450	1.02	22.1	-	<0.01	17.17	0.19	0.0534	0.0006	0.0583	0.0007	365.1	4.1
18.1	582	137	0.23	28.8	0.000017	0.09	17.35	0.19	0.0544	0.0006	0.0576	0.0006	360.8	3.9
19.1	606	152	0.25	29.9	0.000044	0.11	17.43	0.20	0.0546	0.0006	0.0573	0.0007	359.1	4.0
20.1	421	117	0.28	20.8	0.000021	<0.01	17.37	0.20	0.0537	0.0007	0.0576	0.0007	360.9	4.2
Error in Temora reference zircon calibration was 0.33% for the analytical session.														
9N27-4														
1.1	807	609	0.76	39.2	0.000045	0.06	17.66	0.19	0.0541	0.0004	0.0566	0.0006	354.9	3.7
2.1	510	180	0.35	24.5	0.000028	0.12	17.91	0.19	0.0545	0.0005	0.0558	0.0006	349.7	3.7
3.1	127	39	0.31	6.3	0.000235	<0.01	17.30	0.22	0.0538	0.0010	0.0578	0.0008	362.3	4.6
4.1	1321	667	0.51	65.2	0.000163	0.08	17.41	0.18	0.0544	0.0003	0.0574	0.0006	359.7	3.6
5.1	384	112	0.29	18.3	0.000000	0.08	18.06	0.20	0.0541	0.0006	0.0553	0.0006	347.2	3.9
6.1	671	192	0.29	34.5	0.000145	0.09	16.68	0.18	0.0549	0.0005	0.0599	0.0007	374.9	4.0
7.1	653	366	0.56	31.5	-	0.08	17.81	0.19	0.0542	0.0004	0.0561	0.0006	351.8	3.7
8.1	496	276	0.56	23.8	-	0.06	17.93	0.19	0.0540	0.0005	0.0557	0.0006	349.7	3.7
9.1	494	127	0.26	24.3	-	<0.01	17.44	0.19	0.0531	0.0005	0.0574	0.0006	359.7	3.8
10.1	848	345	0.41	41.0	0.000026	0.01	17.76	0.19	0.0537	0.0004	0.0563	0.0006	353.2	3.6
11.1	202	73	0.36	9.9	0.000139	0.04	17.56	0.21	0.0540	0.0008	0.0569	0.0007	356.8	4.2
12.1	343	131	0.38	17.1	0.001536	2.80	17.23	0.19	0.0762	0.0014	0.0564	0.0006	353.8	3.9
13.1	817	584	0.71	40.5	0.000076	<0.01	17.31	0.18	0.0538	0.0004	0.0578	0.0006	362.0	3.8
14.1	139	38	0.27	6.6	-	0.22	18.20	0.23	0.0552	0.0009	0.0548	0.0007	344.1	4.3
15.1	789	290	0.37	38.6	0.000024	0.03	17.59	0.19	0.0539	0.0004	0.0568	0.0006	356.4	3.7
16.1	481	242	0.50	23.1	0.000197	0.42	17.89	0.19	0.0568	0.0005	0.0557	0.0006	349.3	3.7
17.1	1487	1234	0.83	71.6	0.000021	0.05	17.84	0.18	0.0539	0.0003	0.0560	0.0006	351.4	3.5
18.1	311	81	0.26	15.2	0.000008	<0.01	17.55	0.20	0.0537	0.0006	0.0570	0.0006	357.3	3.9
19.1	699	211	0.30	33.2	0.000014	0.11	18.10	0.19	0.0543	0.0004	0.0552	0.0006	346.3	3.6
20.1	306	156	0.51	14.8	-	0.08	17.79	0.20	0.0542	0.0007	0.0562	0.0007	352.3	4.0
Error in Temora reference zircon calibration was 0.29% for the analytical session.														

Notes

1. Uncertainties given at the one s level.
2. f_{206} % denotes the percentage of ^{206}Pb that is common Pb.
3. Correction for common Pb for the U/Pb data has been made using the measured $^{238}U/^{206}Pb$ and $^{207}Pb/^{206}Pb$ ratios following Tera and Wasserburg (1972) as outlined in Williams (1998).

Table C.4. Summary of SHRIMP U–Pb results for zircon.

Grain spot	U (ppm)	Th (ppm)	Th/U	$^{206}Pb^*$ (ppm)	$^{204}Pb/^{206}Pb$	f_{206} %	Total $^{238}U/^{206}Pb$	±	Total $^{207}Pb/^{206}Pb$	±	Radiogenic $^{206}Pb/^{238}U$	±	Age (Ma) $^{206}Pb/^{238}U$	±
912-2A														
1.1	281	222	0.79	13.3	0.000022	<0.01	18.19	0.21	0.0531	0.0007	0.0550	0.0006	345.2	3.9
2.1	267	192	0.72	12.6	0.000213	0.30	18.16	0.21	0.0558	0.0007	0.0549	0.0006	344.4	3.9
3.1	159	69	0.43	7.4	-	0.03	18.39	0.23	0.0535	0.0009	0.0544	0.0007	341.2	4.1
4.1	252	102	0.40	11.9	0.000020	0.08	18.16	0.21	0.0540	0.0007	0.0550	0.0006	345.3	3.9
5.1	230	199	0.86	10.8	0.000113	0.19	18.25	0.21	0.0548	0.0007	0.0547	0.0006	343.2	3.9
6.1	684	386	0.56	30.8	0.001843	3.40	19.08	0.33	0.0801	0.0008	0.0506	0.0009	318.4	5.5
6.2	547	168	0.31	25.7	-	0.02	18.31	0.20	0.0535	0.0005	0.0546	0.0006	342.8	3.6
7.1	495	223	0.45	23.6	0.000025	<0.01	18.03	0.19	0.0531	0.0005	0.0555	0.0006	348.1	3.7
8.1	103	66	0.64	4.8	-	0.14	18.45	0.24	0.0544	0.0011	0.0541	0.0007	339.8	4.5
9.1	383	318	0.83	18.0	0.000207	0.48	18.24	0.20	0.0572	0.0007	0.0545	0.0006	342.4	3.7
10.1	1500	448	0.30	111.2	0.001021	2.04	11.59	0.12	0.0744	0.0003	0.0845	0.0009	523.0	5.2
11.1	165	113	0.69	7.8	-	<0.01	18.22	0.22	0.0529	0.0008	0.0549	0.0007	344.6	4.1
12.1	73	42	0.58	5.1	0.001798	2.45	12.13	0.17	0.0771	0.0077	0.0804	0.0014	498.6	8.3
13.1	350	146	0.42	16.5	0.000099	<0.01	18.27	0.20	0.0531	0.0006	0.0547	0.0006	343.6	3.8
13.2	388	137	0.35	18.6	0.000122	0.31	17.92	0.20	0.0559	0.0006	0.0556	0.0006	349.0	3.8
14.1	205	143	0.70	9.7	0.000058	0.14	18.12	0.21	0.0545	0.0008	0.0551	0.0007	345.8	4.0
15.1	391	191	0.49	18.7	0.000120	<0.01	17.97	0.20	0.0528	0.0006	0.0557	0.0006	349.4	3.8
16.1	470	316	0.67	22.4	0.000034	0.06	18.05	0.20	0.0539	0.0005	0.0554	0.0006	347.4	3.7
17.1	256	129	0.50	12.0	-	0.05	18.24	0.21	0.0538	0.0007	0.0548	0.0006	343.8	3.9
18.1	242	108	0.44	11.5	0.000056	<0.01	18.06	0.21	0.0531	0.0007	0.0554	0.0006	347.5	3.9
19.1	222	110	0.50	10.5	0.000150	0.05	18.08	0.21	0.0538	0.0007	0.0553	0.0007	346.8	4.0
20.1	240	221	0.92	11.5	0.000531	0.45	17.91	0.21	0.0571	0.0012	0.0556	0.0007	348.7	4.0
21.1	211	93	0.44	10.1	-	0.19	17.94	0.21	0.0550	0.0008	0.0556	0.0007	349.1	4.1
22.1	916	334	0.36	43.0	0.000079	0.12	18.33	0.19	0.0543	0.0004	0.0545	0.0006	342.0	3.5
Error in Temora reference zircon calibration was 0.29% for the analytical session.														
Y1-IG073 – Homogeneous diatexite														
1.1	342	24	0.07	16.8	0.000194	<0.01	17.48	0.21	0.0535	0.0008	0.0572	0.0007	358.7	4.3
1.2	505	78	0.15	25.7	-	0.10	16.89	0.19	0.0548	0.0006	0.0592	0.0007	370.5	4.2
4.1	677	93	0.14	30.2	0.000050	0.13	19.25	0.21	0.0540	0.0006	0.0519	0.0006	326.0	3.5
2.1	684	24	0.04	34.9	0.000035	<0.01	16.84	0.18	0.0538	0.0005	0.0594	0.0007	372.0	4.0
3.1	435	50	0.11	22.4	-	<0.01	16.70	0.19	0.0540	0.0006	0.0599	0.0007	375.0	4.1
5.1	397	49	0.12	20.4	0.000042	<0.01	16.69	0.19	0.0533	0.0006	0.0600	0.0007	375.4	4.2
6.1	1623	7	0.00	75.7	-	<0.01	18.42	0.19	0.0533	0.0003	0.0543	0.0006	340.8	3.5
7.1	275	43	0.16	13.9	-	0.12	17.02	0.21	0.0549	0.0008	0.0587	0.0007	367.7	4.5
8.1	419	71	0.17	21.2	-	0.05	16.97	0.19	0.0544	0.0008	0.0589	0.0007	368.8	4.1
9.1	480	42	0.09	23.3	0.000059	<0.01	17.68	0.20	0.0536	0.0009	0.0566	0.0006	354.7	3.9
10.1	315	60	0.19	16.0	-	0.11	16.90	0.20	0.0549	0.0008	0.0591	0.0007	370.3	4.3
11.1	387	73	0.19	19.9	0.000123	0.08	16.73	0.19	0.0547	0.0007	0.0597	0.0007	374.0	4.2
12.1	656	104	0.16	34.1	0.000069	<0.01	16.53	0.18	0.0539	0.0005	0.0605	0.0007	378.7	4.1
13.1	1408	240	0.17	73.2	0.000018	0.03	16.53	0.18	0.0544	0.0004	0.0605	0.0006	378.5	3.9
14.1	178	57	0.32	8.6	0.000115	0.16	17.70	0.23	0.0549	0.0012	0.0564	0.0007	353.8	4.5
15.1	610	26	0.04	31.3	0.000034	0.07	16.74	0.18	0.0546	0.0006	0.0597	0.0007	373.9	4.0
15.2	419	61	0.15	20.9	0.000029	0.01	17.20	0.19	0.0539	0.0007	0.0581	0.0007	364.2	4.1
16.1	629	26	0.04	27.7	0.000046	<0.01	19.28	0.21	0.0526	0.0005	0.0519	0.0006	326.2	3.6
17.1	362	67	0.19	17.0	0.000085	0.11	17.96	0.21	0.0544	0.0007	0.0556	0.0007	348.9	4.0
18.1	344	74	0.22	17.0	-	0.03	17.18	0.20	0.0541	0.0007	0.0582	0.0007	364.7	4.1
19.1	1842	9	0.01	85.7	0.000069	0.08	18.19	0.19	0.0540	0.0003	0.0549	0.0006	344.6	3.5
20.1	180	29	0.16	8.8	-	0.12	17.33	0.22	0.0547	0.0010	0.0576	0.0007	361.2	4.5
Error in Temora reference zircon calibration was 0.33% for the analytical session.														

Notes
1. Uncertainties given at the one s level.
2. f_{206} % denotes the percentage of ^{206}Pb that is common Pb.
3. Correction for common Pb for the U/Pb data has been made using the measured $^{238}U/^{206}Pb$ and $^{207}Pb/^{206}Pb$ ratios following Tera and Wasserburg (1972) as outlined in Williams (1998).

Table C.4. Summary of SHRIMP U–Pb results for zircon.

							Total Ratios				Radiogenic Ratios						
Grain.	U	Th	Th/U	$^{206}Pb^*$	$^{204}Pb/$	f_{206}	$^{238}U/$		$^{207}Pb/$		$^{207}Pb/$		$^{206}Pb/$		$^{207}Pb/$		
spot	(ppm)	(ppm)		(ppm)	^{206}Pb	%	^{206}Pb	±	^{206}Pb	±	^{235}U	±	^{238}U	±	^{206}Pb	±	r
Y1-IG071 – Inhomogeneous diatexite																	
1.1	586	42	0.071	29.2	0.000028	0.01	17.279	0.188	0.0539	0.0005	0.0579	0.0006					
2.1	1439	259	0.180	61.2	0.001003	2.12	20.206	0.214	0.0695	0.0013	0.0484	0.0005					
3.1	389	173	0.445	19.3	0.000090	<0.01	17.318	0.195	0.0538	0.0007	0.0577	0.0007					
4.1	1346	27	0.020	19.3	-	0.16	59.956	0.654	0.0494	0.0006	0.0167	0.0002					
4.2	267	102	0.383	25.8	0.000042	<0.01	8.873	0.103	0.0622	0.0006	0.1127	0.0013					
4.3	638	68	0.107	33.0	0.000027	<0.01	16.639	0.180	0.0539	0.0005	0.0601	0.0007					
5.1	1715	39	0.023	24.7	0.000016	0.03	59.661	0.652	0.0484	0.0005	0.0168	0.0002					
6.1	1092	14	0.013	15.6	0.000134	0.01	59.988	0.678	0.0482	0.0007	0.0167	0.0002					
6.2	345	33	0.097	55.3	0.000007	0.01	5.362	0.060	0.1039	0.0028	0.1865	0.0021	2.668	0.078	0.1038	0.0028	0.382
7.1	926	138	0.149	83.9	-	<0.01	9.482	0.101	0.0609	0.0004	0.1055	0.0011					
7.2	520	113	0.217	58.2	0.000179	0.31	7.664	0.083	0.0688	0.0009	0.1301	0.0014	1.188	0.023	0.0662	0.0011	0.549
8.1	1737	37	0.021	25.1	-	0.05	59.489	0.639	0.0486	0.0005	0.0168	0.0002					
8.2	193	109	0.565	50.0	0.000007	0.01	3.322	0.038	0.1120	0.0009	0.3010	0.0035	4.643	0.066	0.1119	0.0009	0.815
9.1	1317	35	0.027	18.6	-	0.01	60.986	0.666	0.0482	0.0006	0.0164	0.0002					
10.1	1298	7	0.005	56.5	0.000045	0.06	19.757	0.255	0.0533	0.0004	0.0506	0.0007					
10.2	138	77	0.562	12.0	-	<0.01	9.825	0.121	0.0604	0.0009	0.1018	0.0013					
11.1	1325	22	0.016	37.1	-	0.12	30.703	0.334	0.0512	0.0005	0.0325	0.0004					
11.1	260	25	0.097	39.6	0.000026	0.04	5.636	0.065	0.0732	0.0008	0.1775	0.0021	1.795	0.032	0.0734	0.0009	0.754
12.1	1343	6	0.004	57.6	-	<0.01	20.026	0.295	0.0507	0.0014	0.0501	0.0007					
12.2	450	59	0.131	33.9	-	<0.01	11.413	0.128	0.0574	0.0006	0.0877	0.0010					
13.1	1518	42	0.028	44.8	0.000016	0.24	29.081	0.312	0.0524	0.0005	0.0343	0.0004					
14.1	1174	7	0.006	35.4	-	0.03	28.445	0.308	0.0509	0.0005	0.0351	0.0004					
14.2	732	363	0.496	266.3	-	<0.01	2.361	0.025	0.1426	0.0003	0.4236	0.0045	8.327	0.090	0.1426	0.0003	0.978
15.1	2554	75	0.029	37.4	0.000011	0.08	58.694	0.628	0.0488	0.0004	0.0170	0.0002					
16.1	1378	50	0.036	19.5	-	<0.01	60.565	0.657	0.0473	0.0006	0.0165	0.0002					
17.1	1404	53	0.038	20.1	0.000040	<0.01	60.106	0.665	0.0478	0.0006	0.0166	0.0002					
18.1	1540	5	0.003	75.3	0.000029	<0.01	17.579	0.186	0.0534	0.0004	0.0569	0.0006					
19.1	1449	33	0.023	20.3	0.000050	<0.01	61.442	0.666	0.0475	0.0006	0.0163	0.0002					
19.2	324	130	0.401	42.8	0.000038	0.06	6.495	0.072	0.0671	0.0005	0.1539	0.0018	1.416	0.041	0.0667	0.0014	0.762
20.1	1365	5	0.003	19.5	-	0.05	60.172	0.670	0.0485	0.0006	0.0166	0.0002					
20.2	82	47	0.573	6.5	-	0.09	10.854	0.152	0.0598	0.0014	0.0920	0.0013					

Notes:

1. Uncertainties given at the one s level.
2. Error in Temora reference zircon calibration was 0.304% for the analytical session.
   (not included in above errors but required when comparing $^{206}Pb/^{238}U$ data from different mounts).
3. f_{206} % denotes the percentage of ^{206}Pb that is common Pb.
4. For areas older than ~800 Ma correction for common Pb made using the measured $^{204}Pb/^{206}Pb$ ratio.
5. For areas younger than ~800 Ma correction for common Pb made using the measured $^{238}U/^{206}Pb$ and $^{207}Pb/^{206}Pb$ ratios following Tera and Wasserburg (1972) as outlined in Williams (1998).
6. For % Disc, 0% denotes a concordant analysis.

Table C.5. Summary of LA-ICP-MSP U-Pb results for zircon

					Radiogenic Ratios				Age (Ma)			
	Spot Size (μm)	U (ppm)	Th (ppm)	U/Th	$^{206}Pb/^{238}U$	2σ	$^{207}Pb/^{235}U$	2σ	$^{206}/^{207}$ Pb	2σ	$^{206}Pb/^{238}U$	2σ
Y2-GP091 – Ford Granodiorite suite												
Y2-GP091_24	30	460	120	3.8	0.0611	0.0035	0.4571	0.030	382.5	81.4	359.4	9.9
Y2-GP091_17	30	110	78	1.4	0.0591	0.0035	0.4488	0.051	370.4	78.4	361.2	15.5
Y2-GP091_5	30	329	364	0.91	0.0596	0.0018	0.4423	0.019	373.2	40.4	363.0	10.9
Y2-GP091_4	30	109	57	1.9	0.0580	0.0058	0.4297	0.045	363.7	127.6	363.7	35.1
Y2-GP091_10	30	480	183	2.6	0.0595	0.0017	0.4466	0.016	372.7	38.9	363.8	10.2
Y2-GP091_8	30	125	126	1	0.0587	0.0038	0.4356	0.038	367.7	85.8	364.0	11.9
Y2-GP091_6	30	229	76	3	0.0602	0.0018	0.4472	0.020	377.1	41.1	365.0	18.1
Y2-GP091_3	30	265	78	3.4	0.0600	0.0028	0.4425	0.025	375.6	63.1	366.0	18.6
Y2-GP091_21	30	102	68	1.5	0.0600	0.0044	0.4575	0.046	375.9	101.3	367.1	26.1
Y2-GP091_7	30	344	110	3.1	0.0590	0.0024	0.4377	0.022	369.5	53.7	367.6	11.7
Y2-GP091_18	30	65	45	1.4	0.0584	0.0031	0.4333	0.090	366.0	68.2	367.7	23.3
Y2-GP091_20	30	104	69	1.5	0.0583	0.0030	0.4363	0.037	365.0	65.9	369.5	14.5
Y2-GP091_22	30	225	163	1.4	0.0598	0.0043	0.4488	0.033	374.1	97.8	370.4	21.2
Y2-GP091_12	30	96	76	1.3	0.0587	0.0019	0.4475	0.047	367.6	43.2	372.7	10.4
Y2-GP091_14	30	100	76	1.3	0.0581	0.0017	0.4139	0.054	363.8	37.0	373.2	10.8
Y2-GP091_23	30	156	96	1.6	0.0573	0.0016	0.4297	0.038	359.4	35.5	373.6	15.4
Y2-GP091_25	30	648	127	5.1	0.0610	0.0013	0.4549	0.010	381.8	29.4	374.1	26.2
Y2-GP091_15	30	195	93	2.1	0.0579	0.0018	0.4247	0.020	363.0	39.6	375.6	16.8
Y2-GP091_16	30	233	111	2.1	0.0608	0.0040	0.4447	0.037	380.8	92.7	375.9	27.0
Y2-GP091_11	30	193	54	3.6	0.0581	0.0020	0.4225	0.033	364.0	43.3	377.1	10.9
Y2-GP091_1	30	126	59	2.1	0.0597	0.0025	0.4499	0.043	373.6	57.5	380.8	24.3
Y2-GP091_2	30	160	39	4.1	0.0742	0.0046	0.6055	0.050	461.6	128.0	381.8	7.7
Y2-GP091_9	30	147	50	2.9	0.0626	0.0036	0.4793	0.045	391.4	85.1	382.5	21.3
Y2-GP091_19	30	105	39	2.7	0.0586	0.0043	0.4580	0.060	367.1	95.7	391.4	21.7
Y2-GP091_13	30	326	260	1.3	0.0576	0.0025	0.4309	0.023	361.2	56.0	461.6	27.7
*1.0=Systematic error of $^{206}Pb/^{238}U$ age based on Sri Lankan standard												
51225-1 – Ford Granodiorite suite												
51225-1_2	30	337	218	1.5	0.0562	0.0046	0.4205	0.040	352.5	98.9	352.5	28.1
51225-1_6	30	1295	265	4.9	0.0563	0.0013	0.4209	0.010	352.8	28.7	352.8	8.1
51225-1_7	30	693	192	3.6	0.0573	0.0029	0.4276	0.022	359.3	63.5	359.3	17.7
51225-1_4	30	381	147	2.6	0.0575	0.0034	0.4315	0.027	360.2	75.7	360.2	21.0
51225-1_10	30	279	173	1.6	0.0581	0.0017	0.4346	0.022	363.9	37.8	363.9	10.4
51225-1_1	30	520	123	4.2	0.0581	0.0024	0.4333	0.022	364.0	53.8	364.0	14.8
51225-1_17	30	158	150	1	0.0581	0.0013	0.4298	0.037	364.2	28.0	364.2	7.7
51225-1_22	30	430	258	1.7	0.0582	0.0019	0.4340	0.018	364.7	42.8	364.7	11.7
51225-1_9	30	330	121	2.7	0.0589	0.0021	0.4398	0.020	368.9	46.6	368.9	12.6
51225-1_12	30	482	166	2.9	0.0590	0.0016	0.4375	0.018	369.6	36.1	369.6	9.8
51225-1_13	30	487	204	2.4	0.0593	0.0036	0.4427	0.029	371.1	82.2	371.1	22.2
51225-1_8	30	339	150	2.3	0.0596	0.0038	0.4412	0.031	373.3	86.9	373.3	23.3
51225-1_11	30	810	260	3.1	0.0597	0.0014	0.4473	0.011	373.6	32.6	373.6	8.7
51225-1_24	30	497	196	2.5	0.0597	0.0032	0.4435	0.025	373.8	71.8	373.8	19.2
51225-1_18	30	400	203	2	0.0600	0.0011	0.4426	0.012	375.5	24.0	375.5	6.4
51225-1_25	30	423	158	2.7	0.0602	0.0017	0.4452	0.016	377.1	39.2	377.1	10.4
51225-1_14	30	1045	158	6.6	0.0603	0.0016	0.4489	0.013	377.4	36.4	377.4	9.7
51225-1_21	30	278	112	2.5	0.0604	0.0015	0.4514	0.025	378.2	33.6	378.2	8.9
51225-1_19	30	324	111	2.9	0.0605	0.0016	0.4489	0.021	378.6	37.4	378.6	9.9
51225-1_20	30	768	194	4	0.0612	0.0023	0.4562	0.019	382.6	53.6	382.6	14.0
51225-1_15	30	263	94	2.8	0.0634	0.0054	0.4738	0.046	396.4	128.9	396.4	32.5
51225-1_23	30	443	124	3.6	0.0665	0.0024	0.4984	0.025	415.0	60.4	415.0	14.5
51225-1_16	30	224	166	1.4	0.0667	0.0086	0.5213	0.092	416.2	216.8	416.2	52.1
51225-1_3	30	78	53	1.5	0.1810	0.0060	1.8772	0.074	1072.4	350.2	1074.4	42.8
*1.3=Systematic error of $^{206}Pb/^{238}U$ age based on Sri Lankan standard												
51225-2 – Ford Granodiorite suite												
51225-2_2	30	778	163	4.8	0.0559	0.0032	0.4158	0.024	350.7	67.9	358.6	12.7
51225-2_4	30	641	125	5.1	0.0572	0.0011	0.4286	0.011	358.4	24.4	350.7	19.4
51225-2_1	30	505	147	3.4	0.0572	0.0021	0.4270	0.019	358.6	45.5	371.9	7.2
51225-2_5	30	537	129	4.2	0.0577	0.0013	0.4253	0.014	361.6	28.3	358.4	6.8
51225-2_6	30	452	318	1.4	0.0579	0.0016	0.4304	0.015	362.9	36.2	361.6	7.8
51225-2_18	30	645	159	4.1	0.0580	0.0011	0.4323	0.012	363.2	24.9	362.9	10.0
51225-2_21	30	766	133	5.8	0.0580	0.0015	0.4309	0.014	363.4	32.6	380.2	13.4
51225-2_13	30	368	115	3.2	0.0580	0.0018	0.4345	0.019	363.7	40.6	369.8	7.5
51225-2_11	30	639	105	6.1	0.0584	0.0012	0.4365	0.011	366.0	27.4	373.5	10.0
51225-2_19	30	1143	174	6.6	0.0585	0.0007	0.4343	0.008	366.2	16.2	368.9	10.0
51225-2_10	30	792	96	8.2	0.0589	0.0016	0.4378	0.013	368.9	36.9	366.0	7.5
51225-2_8	30	401	124	3.2	0.0590	0.0012	0.4374	0.017	369.8	27.6	378.7	7.9
51225-2_15	30	209	71	2.9	0.0594	0.0011	0.4399	0.025	371.7	24.8	363.7	11.2
51225-2_3	30	589	217	2.7	0.0594	0.0012	0.4444	0.012	371.9	26.8	383.3	25.9
51225-2_9	30	161	135	1.2	0.0597	0.0016	0.4456	0.028	373.5	37.3	371.7	6.7
51225-2_17	30	683	140	4.9	0.0597	0.0014	0.4441	0.015	374.1	32.3	377.1	7.9
51225-2_24	30	561	206	2.7	0.0602	0.0019	0.4485	0.015	376.7	42.7	374.1	8.6
51225-2_16	30	484	137	3.5	0.0602	0.0013	0.4494	0.014	377.1	29.8	363.2	6.9
51225-2_12	30	572	157	3.6	0.0605	0.0013	0.4466	0.016	378.7	29.8	366.2	4.4
51225-2_23	30	676	208	3.2	0.0606	0.0012	0.4529	0.013	379.0	28.0	385.4	25.5
51225-2_7	30	472	169	2.8	0.0608	0.0022	0.4533	0.023	380.2	50.9	363.4	9.0
51225-2_14	30	213	140	1.5	0.0613	0.0043	0.4529	0.044	383.3	99.2	379.0	7.4
51225-2_20	30	911	244	3.7	0.0616	0.0042	0.4615	0.032	385.4	98.3	376.7	11.3
51225-2_22	30	326	167	2	0.0818	0.0036	0.6462	0.031	506.6	109.1	506.6	21.5
51225-2_25	30	547	131	4.2	0.1254	0.0058	1.2081	0.057	761.6	253.0	761.6	33.2
*1.3=Systematic error of $^{206}Pb/^{238}U$ age based on Sri Lankan standard												

Table C.5. Summary of LA-ICP-MSP U-Pb results for zircon

					Radiogenic Ratios				Age (Ma)			
	Spot Size (μm)	U (ppm)	Th (ppm)	U/Th	$^{206}Pb/^{238}U$	2σ	$^{207}Pb/^{235}U$	2σ	$^{206}/^{207}$ Pb	2σ	$^{206}Pb/^{238}U$	2σ
Y2-JU096 – Ford Granodiorite suite												
Y2-JU096_14	30	771	428	1.8	0.0499	0.0039	0.3737	0.032	313.9	75.7	364.7	15.8
Y2-JU096_7	30	582	315	1.8	0.0523	0.0048	0.3917	0.039	328.8	96.2	354.1	16.8
Y2-JU096_8	30	626	303	2.1	0.0530	0.0017	0.3967	0.016	332.7	35.1	370.2	10.6
Y2-JU096_11	30	391	264	1.5	0.0532	0.0084	0.4034	0.066	334.2	172.7	362.1	10.6
Y2-JU096_13	30	297	137	2.2	0.0542	0.0036	0.4004	0.029	340.3	74.7	369.5	12.9
Y2-JU096_24	30	264	159	1.7	0.0563	0.0051	0.4253	0.041	353.1	110.3	328.8	29.2
Y2-JU096_2	30	467	218	2.1	0.0565	0.0028	0.4234	0.026	354.1	59.5	332.7	10.6
Y2-JU096_10	30	721	444	1.6	0.0575	0.0017	0.4263	0.014	360.1	37.4	366.7	6.6
Y2-JU096_25	30	382	320	1.2	0.0577	0.0043	0.4314	0.036	361.7	94.2	360.1	10.4
Y2-JU096_22	30	475	315	1.5	0.0577	0.0019	0.4295	0.019	361.8	42.2	334.2	51.7
Y2-JU096_23	30	472	271	1.7	0.0578	0.0011	0.4284	0.012	362.0	25.2	371.2	17.8
Y2-JU096_4	30	360	205	1.8	0.0578	0.0017	0.4370	0.021	362.1	38.2	340.3	21.9
Y2-JU096_15	30	335	187	1.8	0.0581	0.0020	0.4318	0.018	364.2	45.4	313.9	24.1
Y2-JU096_21	30	650	372	1.8	0.0582	0.0032	0.4320	0.025	364.7	70.2	364.2	12.5
Y2-JU096_1	30	617	414	1.5	0.0582	0.0026	0.4310	0.023	364.7	57.7	368.1	9.9
Y2-JU096_9	30	407	190	2.1	0.0585	0.0011	0.4327	0.015	366.7	24.2	389.0	15.5
Y2-JU096_16	30	209	145	1.4	0.0588	0.0016	0.4381	0.024	368.1	36.6	364.7	19.2
Y2-JU096_6	30	258	98	2.6	0.0590	0.0021	0.4412	0.020	369.5	47.8	361.8	11.7
Y2-JU096_3	30	342	186	1.8	0.0591	0.0017	0.4466	0.021	370.2	39.3	362.0	7.0
Y2-JU096_12	30	288	131	2.2	0.0593	0.0029	0.4346	0.025	371.2	66.2	353.1	31.2
Y2-JU096_20	30	394	187	2.1	0.0622	0.0026	0.4836	0.029	389.0	60.3	361.7	26.1
*1.0=Systematic error of $^{206}Pb/^{238}U$ age based on Sri Lankan standard												
Y1-IG073 – Homogeneous diatexite												
Y1-IG073_20	30	268	20	13.1	0.0516	0.0094	0.3865	0.077	324.5	187.6	376.2	13.9
Y1-IG073_09	30	375	36	10.4	0.0534	0.0027	0.3994	0.029	335.2	54.3	359.3	20.4
Y1-IG073_05	30	128	64	2	0.0554	0.0034	0.3979	0.046	347.7	73.7	379.4	12.1
Y1-IG073_11	30	249	59	4.2	0.0558	0.0029	0.4122	0.036	350.3	62.4	369.9	12.0
Y1-IG073_08	30	317	38	8.3	0.0559	0.0048	0.4062	0.040	350.5	101.6	347.7	21.2
Y1-IG073_24	30	77	48	1.6	0.0565	0.0041	0.4045	0.085	354.1	87.1	371.5	15.4
Y1-IG073_14	30	276	197	1.4	0.0566	0.0025	0.4232	0.028	354.7	53.2	356.4	13.6
Y1-IG073_13	30	525	81	6.5	0.0566	0.0010	0.4208	0.015	355.1	22.7	350.5	29.0
Y1-IG073_07	30	274	53	5.2	0.0568	0.0023	0.4197	0.028	356.4	48.5	335.2	16.3
Y1-IG073_22	30	242	65	3.7	0.0571	0.0010	0.4242	0.039	358.0	22.2	371.3	19.8
Y1-IG073_02	30	127	49	2.6	0.0573	0.0033	0.4208	0.065	359.3	73.3	350.3	17.7
Y1-IG073_12	30	197	42	4.7	0.0574	0.0018	0.4236	0.034	359.7	40.3	359.7	11.2
Y1-IG073_19	30	311	58	5.4	0.0574	0.0011	0.4267	0.023	360.0	25.2	355.1	6.3
Y1-IG073_18	30	112	70	1.6	0.0580	0.0020	0.4361	0.072	363.6	42.9	354.7	15.0
Y1-IG073_16	30	115	88	1.3	0.0581	0.0023	0.4271	0.044	364.3	52.5	365.7	7.7
Y1-IG073_15	30	525	75	7	0.0584	0.0013	0.4331	0.016	365.7	28.5	364.3	14.4
Y1-IG073_04	30	173	192	0.9	0.0591	0.0020	0.4532	0.035	369.9	44.4	413.7	38.1
Y1-IG073_10	30	168	40	4.2	0.0593	0.0032	0.4324	0.053	371.3	73.5	363.6	11.7
Y1-IG073_06	30	180	39	4.6	0.0593	0.0025	0.4334	0.032	371.5	57.2	360.0	6.9
Y1-IG073_23	30	111	69	1.6	0.0599	0.0018	0.4276	0.063	374.8	39.7	324.5	57.8
Y1-IG073_01	30	332	63	5.3	0.0601	0.0023	0.4508	0.032	376.2	51.9	358.0	6.3
Y1-IG073_03	30	331	24	13.6	0.0606	0.0019	0.4456	0.022	379.4	45.5	374.8	10.6
Y1-IG073_25	30	818	210	3.9	0.0614	0.0033	0.4581	0.026	383.9	76.8	354.1	24.6
Y1-IG073_17	30	226	61	3.7	0.0663	0.0064	0.4891	0.059	413.7	158.0	383.9	20.0
*1.2=Systematic error of $^{206}Pb/^{238}U$ age based on Sri Lankan standard												
Y1-IG071 – Inhomogeneous diatexite												
Y1-IG071_11	30	1032	42	24	0.0165	0.0003	0.1106	0.005	105.5	2.3	425.7	18.2
Y1-IG071_11	30	1491	57	26	0.0165	0.0004	0.1096	0.004	105.8	2.5	766.1	19.8
Y1-IG071_3	30	756	17	44	0.0223	0.0024	0.1528	0.020	142.3	21.9	142.3	15.4
Y1-IG071_9	30	765	7	108	0.0233	0.0009	0.1632	0.008	148.7	8.3	439.2	9.6
Y1-IG071_25	30	1084	31	35	0.0275	0.0006	0.1918	0.007	175.0	6.7	212.0	9.0
Y1-IG071_5	30	1142	28	41	0.0334	0.0014	0.2377	0.011	212.0	19.1	358.4	15.9
Y1-IG071_17	30	624	5	123	0.0410	0.0016	0.2980	0.013	259.3	24.9	321.6	7.2
Y1-IG071_14	30	673	243	2.8	0.0442	0.0035	0.3238	0.027	279.1	61.4	411.9	19.2
Y1-IG071_19	30	951	5	194	0.0502	0.0015	0.3686	0.012	315.5	28.4	148.7	5.5
Y1-IG071_7	30	1068	7	151	0.0512	0.0012	0.3831	0.010	321.6	23.2	334.5	7.7
Y1-IG071_12	30	933	8	113	0.0514	0.0018	0.3838	0.015	323.1	34.9	105.5	2.2
Y1-IG071_10	30	1123	12	93	0.0533	0.0013	0.3944	0.010	334.5	25.4	105.8	2.3
Y1-IG071_16	30	1225	5	272	0.0552	0.0016	0.4084	0.013	346.5	34.7	323.1	10.8
Y1-IG071_21	30	1139	4	308	0.0556	0.0016	0.4124	0.013	349.1	32.8	364.1	10.8
Y1-IG071_18	30	911	231	3.9	0.0564	0.0016	0.4248	0.015	353.9	34.7	279.1	21.9
Y1-IG071_6	30	1032	24	44	0.0572	0.0026	0.4227	0.020	358.4	57.3	579.6	29.2
Y1-IG071_20	30	406	40	10	0.0580	0.0015	0.4368	0.018	363.4	34.2	346.5	10.0
Y1-IG071_13	30	421	149	2.8	0.0581	0.0018	0.4269	0.016	364.1	39.3	259.3	9.7
Y1-IG071_23	30	216	183	1.2	0.0618	0.0027	0.4583	0.031	386.8	64.2	353.9	9.8
Y1-IG071_8	30	573	13	45	0.0660	0.0032	0.5206	0.026	411.9	79.1	315.5	9.0
Y1-IG071_1	30	629	59	11	0.0683	0.0030	0.5345	0.024	425.7	77.5	363.4	9.4
Y1-IG071_4	30	693	45	15	0.0705	0.0016	0.5528	0.015	439.2	42.2	349.1	9.5
Y1-IG071_15	30	685	143	4.8	0.0941	0.0050	0.7802	0.042	579.6	169.2	386.8	16.6
Y1-IG071_2	30	235	14	17	0.1262	0.0035	1.1937	0.041	766.1	151.7	175.0	3.7
*1.0=Systematic error of $^{206}Pb/^{238}U$ age based on Sri Lankan standard												

Table C.5. Summary of LA-ICP-MSP U-Pb results for zircon

					Radiogenic Ratios				Age (Ma)			
	Spot Size (μm)	U (ppm)	Th (ppm)	U/Th	$^{206}Pb/^{238}U$	2σ	$^{207}Pb/^{235}U$	2σ	$^{206}/^{207}$ Pb	2σ	$^{206}Pb/^{238}U$	2σ
Y1-AE035 – Devonian–Carboniferous granite												
Y1-AE035_16	30	114	52	2.2	0.0537	0.0030	0.4022	0.093	337.2	62.3	337.2	18.4
Y1-AE035_1	30	180	93	1.9	0.0623	0.0018	0.4659	0.049	389.3	42.6	389.3	11.0
Y1-AE035_2	30	261	172	1.5	0.0567	0.0020	0.4182	0.026	355.8	43.1	355.8	12.2
Y1-AE035_3	30	258	119	2.2	0.0578	0.0035	0.4223	0.035	362.4	76.2	362.4	21.0
Y1-AE035_3	30	242	114	2.1	0.0588	0.0009	0.4397	0.036	368.3	20.3	368.3	5.6
Y1-AE035_5	30	207	167	1.2	0.0585	0.0013	0.4453	0.025	366.4	28.1	366.4	7.6
Y1-AE035_6	30	251	84	3	0.0572	0.0021	0.4187	0.039	358.6	46.0	358.6	12.8
Y1-AE035_7	30	472	481	1	0.0598	0.0012	0.4414	0.014	374.5	27.9	374.5	7.4
Y1-AE035_8	30	135	56	2.4	0.0599	0.0025	0.4365	0.046	374.7	57.3	374.7	15.2
Y1-AE035_9	30	310	115	2.7	0.0597	0.0022	0.4427	0.032	374.0	49.7	374.0	13.2
Y1-AE035_9	30	385	200	1.9	0.0583	0.0030	0.4402	0.033	365.1	66.3	365.1	18.2
Y1-AE035_11	30	368	99	3.7	0.0592	0.0027	0.4372	0.026	370.5	60.0	370.5	16.2
Y1-AE035_12	30	259	105	2.5	0.0613	0.0016	0.4546	0.026	383.5	37.4	383.5	9.8
Y1-AE035_13	30	149	60	2.5	0.0605	0.0031	0.4456	0.032	378.8	70.8	378.8	18.6
Y1-AE035_14	30	138	61	2.3	0.0575	0.0018	0.4334	0.046	360.6	40.2	360.6	11.2
Y1-AE035_17	30	145	63	2.3	0.0601	0.0016	0.4342	0.045	376.0	37.6	376.0	10.0
Y1-AE035_18	30	206	127	1.6	0.0593	0.0015	0.4441	0.032	371.4	34.4	371.4	9.2
Y1-AE035_19	30	137	62	2.2	0.0583	0.0020	0.4276	0.046	365.1	43.8	365.1	12.0
Y1-AE035_20	30	140	53	2.7	0.0606	0.0037	0.4395	0.062	379.4	84.9	379.4	22.4
Y1-AE035_21	30	227	107	2.1	0.0609	0.0009	0.4469	0.023	381.1	21.7	381.1	5.6
Y1-AE035_22	30	106	44	2.4	0.0584	0.0021	0.4411	0.063	365.9	46.4	365.9	12.6
Y1-AE035_23	30	240	101	2.4	0.0608	0.0020	0.4415	0.036	380.2	47.3	380.2	12.4
Y1-AE035_24	30	138	64	2.1	0.0598	0.0019	0.4446	0.064	374.2	43.3	374.2	11.6
Y1-AE035_25	30	207	168	1.2	0.0586	0.0017	0.4294	0.035	367.1	37.9	367.1	10.4

*1.3=Systematic error of $^{206}Pb/^{238}U$ age based on Sri Lankan standard

Notes:

[1] Analyses with >10% uncertainty (1-sigma) in 206Pb/238U age are not included.

[2] Analyses with >10% uncertainty (1-sigma) in 206Pb/207Pb age are not included, unless 206Pb/238U age is <500 Ma.

[3] Best age is determined from 206Pb/238U age for analyses with 206Pb/238U age <1000 Ma and from 206Pb/207Pb age for analyses with 206Pb/238Uage > 1000 Ma.

[4] Concordance is based on 206Pb/238U age / 206Pb/207Pb age. Value is not reported for 206Pb/238U ages <500 Ma because of large uncertainty in 206Pb/207Pb age.

[5] Analyses with 206Pb/238U age > 500 Ma and with >20% discordance (<80% concordance) are not included.

[6] Analyses with 206Pb/238U age > 500 Ma and with >5% reverse discordance (<105% concordance) are not included.

[7] Analyses conducted by LA-MC-ICPMS, as described by Gehrels et al. (2008).

[8] U concentration and U/Th are calibrated relative to Sri Lanka zircon standard and are accurate to ~20%.

[9] Common Pb correction is from measured 204Pb with common Pb composition interpreted from Stacey and Kramers (1975).

[10] Common Pb composition assigned uncertainties of 1.5 for 206Pb/204Pb, 0.3 for 207Pb/204Pb, and 2.0 for 208Pb/204Pb.

[11] U/Pb and 206Pb/207Pb fractionation is calibrated relative to fragments of a large Sri Lanka zircon of 563.5 ± 3.2 Ma (2-sigma).

[12] U decay constants and composition as follows: 238U = 9.8485 x 10-10, 235U = 1.55125 x 10-10, 238U/235U = 137.88.

Table C.6. U–Pb data for detrital zircon analyses

				Isotope ratios							Apparent ages (Ma)								
Spot	U	206Pb	U/Th	206Pb*	±	207Pb*	±	206Pb*	±	error	206Pb*	±	207Pb*	±	206Pb*	±	Best age	±	Conc
	(ppm)	204Pb		207Pb*	(%)	235U*	(%)	238U	(%)	corr.	238U*	(Ma)	235U	(Ma)	207Pb*	(Ma)	(Ma)	(Ma)	(%)
Y2-MD092																			
29	172	9789	1.2	17.3897	5.0	0.5538	5.8	0.0698	3.0	0.51	435.2	12.6	447.5	21.0	511.0	109.5	435.2	12.6	85.2
27	174	13158	1.1	17.7489	5.7	0.6006	7.1	0.0773	4.2	0.60	480.1	19.5	477.6	26.9	465.9	125.6	480.1	19.5	103.0
85	253	22863	1.8	16.9718	4.4	0.6385	5.0	0.0786	2.4	0.49	487.7	11.4	501.4	19.8	564.2	95.5	487.7	11.4	86.5
34	56	3646	0.7	18.6314	13.4	0.5862	14.1	0.0792	4.6	0.33	491.4	21.9	468.5	53.1	357.3	302.8	491.4	21.9	137.5
7	117	9456	1.5	18.1793	7.8	0.6014	8.2	0.0793	2.6	0.32	491.9	12.4	478.1	31.5	412.5	175.0	491.9	12.4	119.3
66	69	7890	2.8	16.7894	6.1	0.6633	7.7	0.0808	4.8	0.62	500.7	22.9	516.7	31.3	587.7	132.1	500.7	22.9	85.2
89	59	5445	1.8	16.9861	20.8	0.6676	21.3	0.0822	4.4	0.21	509.5	21.6	519.2	86.7	562.3	458.0	509.5	21.6	90.6
101	188	26497	1.1	16.7859	4.0	0.6846	4.3	0.0833	1.5	0.34	516.1	7.2	529.6	17.7	588.1	87.5	516.1	7.2	87.8
21	305	29070	1.8	17.3081	3.1	0.6753	3.3	0.0848	1.3	0.38	524.6	6.4	523.9	13.6	521.3	67.6	524.6	6.4	100.6
1	294	32147	1.7	17.6573	4.1	0.6629	4.4	0.0849	1.5	0.34	525.3	7.4	516.4	17.8	477.3	91.7	525.3	7.4	110.1
96	405	38243	1.2	17.2761	2.7	0.6800	2.9	0.0852	1.1	0.38	527.1	5.7	526.8	12.1	525.3	59.4	527.1	5.7	100.3
33	120	8458	1.2	18.5008	9.0	0.6449	9.5	0.0865	2.8	0.30	535.0	14.6	505.3	37.7	373.2	203.9	535.0	14.6	143.4
83	70	8299	0.6	16.0025	13.5	0.7536	13.9	0.0875	3.0	0.22	540.6	15.5	570.3	60.5	690.9	289.8	540.6	15.5	78.2
25	315	50924	1.4	17.0127	2.9	0.7153	3.2	0.0883	1.3	0.40	545.2	6.7	547.9	13.5	558.9	63.6	545.2	6.7	97.6
15	49	3404	2.2	17.3747	22.8	0.7023	23.3	0.0885	5.0	0.21	546.7	26.2	540.2	98.1	512.8	507.1	546.7	26.2	106.6
63	364	39480	10.5	16.9796	2.7	0.7249	3.0	0.0893	1.3	0.42	551.2	6.8	553.6	12.9	563.2	59.7	551.2	6.8	97.9
6	213	22710	1.0	17.3947	2.6	0.7092	3.0	0.0895	1.5	0.51	552.4	8.1	544.3	12.5	510.3	56.1	552.4	8.1	108.2
68	282	22547	2.4	17.2238	2.6	0.7173	3.0	0.0896	1.5	0.50	553.2	7.9	549.1	12.6	532.0	56.5	553.2	7.9	104.0
78	491	59117	4.7	17.1039	1.7	0.7269	2.2	0.0902	1.3	0.61	556.6	7.1	554.8	9.3	547.3	37.6	556.6	7.1	101.7
62	182	25822	1.1	16.8969	6.8	0.7368	7.0	0.0903	1.8	0.26	557.3	9.7	560.5	30.2	573.8	147.5	557.3	9.7	97.1
16	117	10229	6.0	18.6877	7.9	0.6696	8.1	0.0908	2.0	0.25	560.0	10.8	520.5	33.1	350.5	178.4	560.0	10.8	159.8
64	85	5655	0.6	17.5517	10.4	0.7134	10.7	0.0908	2.3	0.22	560.3	12.3	546.7	45.1	490.6	230.1	560.3	12.3	114.2
90	74	7853	0.7	18.0053	8.6	0.7004	9.0	0.0915	2.7	0.30	564.2	14.4	539.0	37.6	434.0	191.3	564.2	14.4	130.0
44	71	5553	1.9	18.4905	11.2	0.6837	11.6	0.0917	3.0	0.26	565.5	16.0	529.0	47.7	374.4	252.4	565.5	16.0	151.0
38	102	9673	1.7	17.2198	10.1	0.7402	10.7	0.0924	3.5	0.33	570.0	19.0	562.5	46.1	532.5	221.1	570.0	19.0	107.0
40	81	10389	1.7	17.4874	18.0	0.7323	18.5	0.0929	4.3	0.23	572.5	23.6	557.9	79.5	498.6	398.7	572.5	23.6	114.8
102	95	10495	1.9	18.0255	6.9	0.7123	7.4	0.0931	2.5	0.34	574.0	13.7	546.1	31.2	431.5	154.9	574.0	13.7	133.0
47	98	8636	1.5	17.5210	7.5	0.7329	8.3	0.0931	3.5	0.43	574.0	19.4	558.2	35.7	494.4	166.1	574.0	19.4	116.1
50	116	14153	0.6	17.6704	5.7	0.7274	6.4	0.0932	3.0	0.46	574.5	16.3	555.0	27.6	475.6	126.5	574.5	16.3	120.8
17	364	44413	15.5	16.8419	2.3	0.7678	2.8	0.0938	1.6	0.57	577.9	8.9	578.5	12.4	580.9	50.1	577.9	8.9	99.5
37	130	15674	1.6	16.9948	6.7	0.7690	7.0	0.0948	2.2	0.31	583.8	12.1	579.2	30.9	561.2	145.3	583.8	12.1	104.0
80	1050	139735	4.3	16.6495	0.9	0.7853	1.3	0.0948	0.9	0.69	584.0	5.0	588.5	5.8	605.8	20.2	584.0	5.0	96.4
32	181	31642	3.5	16.5187	4.2	0.7931	4.5	0.0950	1.3	0.30	585.1	7.5	592.9	20.0	622.8	91.6	585.1	7.5	93.9
35	672	23722	1.2	16.1397	7.5	0.8185	11.1	0.0958	8.2	0.74	589.8	46.0	607.2	50.7	672.7	160.8	589.8	46.0	87.7
59	436	52017	23.1	16.6609	2.1	0.7946	2.3	0.0960	1.0	0.44	591.0	5.8	593.8	10.5	604.3	45.2	591.0	5.8	97.8
93	112	21390	0.8	17.7764	6.3	0.7495	7.2	0.0966	3.5	0.48	594.6	19.7	567.9	31.2	462.4	139.0	594.6	19.7	128.6
26	122	13474	1.8	17.3203	9.8	0.7708	9.9	0.0968	1.6	0.16	595.8	9.2	580.2	43.9	519.7	215.1	595.8	9.2	114.6
81	92	13842	22.8	16.6480	6.2	0.8067	6.5	0.0974	1.8	0.28	599.2	10.5	600.6	29.4	606.0	134.7	599.2	10.5	98.9
77	244	26423	3.6	16.5584	3.7	0.8123	6.9	0.0975	5.8	0.84	600.0	33.3	603.7	31.3	617.6	79.6	600.0	33.3	97.1
86	197	37531	1.8	16.7057	2.4	0.8354	3.2	0.1012	2.1	0.65	621.5	12.2	616.6	14.6	598.5	51.8	621.5	12.2	103.8
22	157	16702	0.8	16.5497	4.6	0.8595	4.8	0.1032	1.3	0.27	632.9	7.7	629.8	22.3	618.8	98.9	632.9	7.7	102.3
87	298	31892	2.3	16.5651	1.9	0.8694	2.5	0.1045	1.6	0.63	640.5	9.7	635.3	11.9	616.8	42.0	640.5	9.7	103.8
8	997	146827	29.7	16.3058	0.8	0.9012	1.8	0.1066	1.6	0.91	652.9	10.2	652.4	8.7	650.8	16.1	652.9	10.2	100.3
3	81	8061	2.2	16.1384	5.6	0.9113	6.2	0.1067	2.8	0.45	653.3	17.3	657.7	30.2	672.9	119.7	653.3	17.3	97.1
84	479	48340	6.4	15.2597	1.6	0.9670	2.2	0.1070	1.6	0.70	655.4	9.8	686.9	11.1	791.4	33.2	655.4	9.8	82.8
71	211	21896	6.6	15.9781	2.0	0.9506	3.6	0.1102	3.0	0.83	673.7	19.1	678.4	17.9	694.2	43.5	673.7	19.1	97.0
24	378	39794	1.0	15.4178	1.7	1.0408	6.8	0.1164	6.6	0.97	709.7	44.6	724.3	35.5	769.8	35.5	709.7	44.6	92.2
45	682	55552	3.5	15.2492	1.8	1.0543	5.1	0.1166	4.7	0.94	711.0	31.8	731.0	26.3	792.9	37.6	711.0	31.8	89.7
51	348	37374	169.2	15.6179	1.4	1.0733	4.9	0.1216	4.7	0.96	739.6	33.2	740.4	26.0	742.6	28.9	739.6	33.2	99.6
70	189	27949	2.3	15.2858	2.4	1.1357	3.1	0.1259	1.9	0.62	764.5	14.0	770.5	16.8	787.9	51.2	764.5	14.0	97.0
2	358	41392	3.8	14.7054	2.0	1.2370	2.7	0.1319	1.9	0.70	798.9	14.3	817.5	15.4	868.6	40.9	798.9	14.3	92.0
100	157	31116	2.4	14.7628	3.2	1.3621	9.9	0.1458	9.3	0.94	877.6	76.6	872.8	57.9	860.5	67.2	877.6	76.6	102.0
12	132	35489	1.7	14.2240	2.8	1.5786	3.4	0.1629	1.8	0.53	972.6	16.0	961.8	20.9	937.2	58.4	937.2	58.4	103.8
4	103	32245	3.9	14.1884	4.9	1.3991	6.2	0.1440	3.7	0.60	867.1	30.3	888.6	36.7	942.4	101.5	942.4	101.5	92.0
67	67	16232	1.5	14.1121	7.4	1.5847	7.6	0.1622	1.7	0.23	969.0	15.6	964.2	47.4	953.4	151.6	953.4	151.6	101.6
92	289	84295	2.0	13.9389	1.5	1.6082	1.8	0.1626	1.0	0.58	971.1	9.5	973.4	11.4	978.6	30.4	978.6	30.4	99.2
52	256	87196	3.7	13.7684	1.6	1.7002	2.5	0.1698	1.9	0.76	1010.9	17.5	1008.6	15.7	1003.6	32.4	1003.6	32.4	100.7
60	343	97994	1.4	13.6433	1.7	1.7109	2.4	0.1693	1.7	0.71	1008.2	16.0	1012.6	15.5	1022.1	34.7	1022.1	34.7	98.6
95	78	27928	2.4	13.6122	5.9	1.6563	6.4	0.1635	2.5	0.39	976.3	22.6	992.0	40.7	1026.8	119.8	1026.8	119.8	95.1
75	81	15210	1.1	13.6061	4.3	1.7889	5.0	0.1765	2.4	0.48	1048.0	23.1	1041.4	32.3	1027.7	87.8	1027.7	87.8	102.0
11	120	29422	2.8	13.5863	5.6	1.6405	8.3	0.1616	6.1	0.74	965.9	55.0	985.9	52.3	1030.6	112.5	1030.6	112.5	93.7
46	83	34777	1.5	13.5241	4.0	1.7963	4.2	0.1762	1.2	0.28	1046.2	11.3	1044.1	27.4	1039.9	81.3	1039.9	81.3	100.6
103	120	36676	2.3	13.5214	3.3	1.8109	5.1	0.1776	3.9	0.77	1053.8	38.4	1049.4	33.6	1040.3	66.4	1040.3	66.4	101.3
30	132	21508	1.5	13.4674	2.5	1.7634	2.7	0.1722	1.2	0.44	1024.4	11.5	1032.1	17.7	1048.4	49.5	1048.4	49.5	97.7
9	302	73236	1.9	13.4630	0.9	1.8020	1.4	0.1759	1.1	0.76	1044.8	10.6	1046.2	9.4	1049.0	18.8	1049.0	18.8	99.6
48	161	42860	1.9	13.4113	2.2	1.7539	2.8	0.1706	1.8	0.64	1015.4	17.1	1028.6	18.4	1056.8	44.0	1056.8	44.0	96.1
41	253	90275	1.4	13.3537	1.0	1.9093	1.6	0.1849	1.1	0.74	1093.8	11.6	1084.3	10.3	1065.5	20.9	1065.5	20.9	102.7
20	189	52682	3.0	13.2015	2.9	1.9982	3.9	0.1913	2.6	0.67	1128.5	27.2	1114.9	26.6	1088.4	58.8	1088.4	58.8	103.7
57	171	39668	2.7	13.1272	1.7	1.8874	2.4	0.1797	1.7	0.70	1065.3	16.6	1076.7	15.9	1099.8	34.1	1099.8	34.1	96.9
79	138	66331	2.7	13.0249	3.3	1.9074	3.5	0.1802	1.4	0.38	1068.0	13.3	1083.7	23.5	1115.4	65.2	1115.4	65.2	95.8
36	399	116114	1.4	12.9269	1.1	2.0249	5.2	0.1898	5.1	0.98	1120.5	52.7	1123.9	35.7	1130.4	22.6	1130.4	22.6	99.1
28	468	122503	3.7	12.8228	0.6	2.0756	2.3	0.1930	2.2	0.96	1137.7	23.4	1140.8	16.0	1146.5	12.8	1146.5	12.8	99.2
23	149	89140	3.2	12.7962	2.3	2.0550	2.8	0.1907	1.6	0.58	1125.3	16.5	1134.0	18.9	1150.7	44.9	1150.7	44.9	97.8
39	100	7324	1.7	12.7740	6.6	1.7050	8.2	0.1580	4.9	0.60	945.5	43.3	1010.4	52.6	1154.1	130.6	1154.1	130.6	81.9
105	74	20248	1.5	12.1414	2.8	2.4062	3.2	0.2119	1.7	0.52	1238.9	18.9	1244.5	23.1	1254.1	53.9	1254.1	53.9	98.8
18	133	35383	1.3	10.9397	2.2	3.0757	2.9	0.2440	1.8	0.64	1407.6	23.3	1426.7	22.1	1455.1	42.1	1455.1	42.1	96.7
74	305	78208	4.3	9.4646	0.9	3.7974	1.9	0.2607	1.7	0.90	1493.3	23.2	1592.2	15.6	1725.7	15.8	1725.7	15.8	86.5
99	68	33126	1.5	9.3585	2.0	4.7016	2.4	0.3191	1.4	0.56	1785.4	21.1	1767.5	20.2	1746.4	36.7	1746.4	36.7	102.2
72	298	138434	1.2	9.2749	0.2	4.5408	1.5	0.3054	1.5	0.99	1718.3	22.2	1738.5	12.4	1762.8	3.9	1762.8	3.9	97.5
104	140	50366	2.9	9.2113	1.6	4.8114	1.8	0.3214	0.8	0.47	1796.7	13.2	1786.9	15.1	1775.4	29.0	1775.4	29.0	101.2
43	226	72463	3.7	9.0792	0.5	5.0552	1.7	0.3329	1.7	0.96	1852.3	26.7	1828.6	14.6	1801.7	8.5	1801.7	8.5	102.8
82	98	49893	0.9	9.0065	1.3	4.5545	1.7	0.2975	1.2	0.68	1678.9	17.2	1741.0	14.3	1816.3	22.9	1816.3	22.9	92.4
10	53	27672	0.7	8.7728	2.2	5.1909	2.8	0.3303	1.8	0.64	1839.7	28.6	1851.1	24.0	1863.9	39.2	1863.9	39.2	98.7
55	234	137499	4.5	8.0458	1.9	6.3685	8.2	0.3716	8.0	0.97	2037.1	140.1	2027.9	72.4	2018.7	33.5	2018.7	33.5	100.9
14	110	82638	4.8	5.8552	0.7	11.1267	3.2	0.4725	3.1	0.97	2494.5	64.4	2533.8	29.8	2565.4	12.1	2565.4	12.1	97.2
73	69	25129	1.3	5.5998	1.1	11.7982	2.0	0.4792	1.7	0.85	2523.6	35.2	2588.5	18.7	2639.7	17.6	2639.7	17.6	95.6
5	248	157673	3.7	5.2690	0.4	13.7257	1.3	0.5245	1.2	0.96	2718.3	27.7	2731.0	12.3	2740.3	5.9	2740.3	5.9	99.2
31	366	126014	1.4	4.9891	0.3	14.9972	1.4	0.5427	1.4	0.98	2794.6	31.0	2815.1	13.3	2829.8	4.4	2829.8	4.4	98.8
94	20	13830	1.7	4.3973	2.0	15.8764	4.3	0.5063	3.8	0.89	2640.9	82.0	2869.4	40.8	3033.9	31.8	3033.9	31.8	87.0

Table C.6 continued. U–Pb data for detrital zircon analyses

				Isotope ratios							Apparent ages (Ma)								
Spot	U (ppm)	206Pb 204Pb	U/Th	206Pb* 207Pb*	± (%)	207Pb* 235U*	± (%)	206Pb* 238U	± (%)	error corr.	206Pb* 238U*	± (Ma)	207Pb* 235U	± (Ma)	206Pb* 207Pb*	± (Ma)	Best age (Ma)	± (Ma)	Conc (%)
Y2-MP098																			
33	121	16299	4.3	17.2803	4.7	0.6535	4.8	0.0819	1.1	0.23	507.5	5.4	510.6	19.4	524.8	103.4	507.5	5.4	96.7
97	778	84595	4.1	17.3709	0.8	0.6594	1.0	0.0831	0.6	0.59	514.5	2.9	514.3	4.0	513.3	17.6	514.5	2.9	100.2
24	131	21372	1.7	15.5838	7.3	0.7504	10.0	0.0848	6.8	0.68	524.8	34.1	568.5	43.5	747.2	155.3	524.8	34.1	70.2
50	207	25148	0.7	17.5397	3.0	0.6684	3.4	0.0850	1.8	0.51	526.1	8.9	519.7	14.0	492.1	65.2	526.1	8.9	106.9
81	75	10331	2.0	18.0953	6.1	0.6539	7.3	0.0858	3.9	0.54	530.8	19.9	510.9	29.3	422.9	137.3	530.8	19.9	125.5
68	73	8143	2.0	16.7650	10.9	0.7176	11.2	0.0873	2.6	0.23	539.3	13.2	549.3	47.4	590.8	236.5	539.3	13.2	91.3
9	93	17555	0.8	16.3769	5.3	0.7368	6.4	0.0875	3.5	0.55	540.8	18.3	560.5	27.6	641.4	114.7	540.8	18.3	84.3
29	138	18315	1.3	17.2137	6.6	0.7039	7.0	0.0879	2.2	0.32	542.9	11.6	541.1	29.2	533.3	144.6	542.9	11.6	101.8
34	82	7725	2.0	19.0563	8.9	0.6392	9.1	0.0883	2.1	0.23	545.7	10.9	501.8	36.0	306.2	202.0	545.7	10.9	178.2
63	189	27234	1.8	16.7798	2.1	0.7309	2.5	0.0889	1.4	0.54	549.3	7.2	557.1	10.9	588.9	46.3	549.3	7.2	93.3
23	41	6216	0.9	16.9041	11.7	0.7265	12.5	0.0891	4.3	0.34	550.0	22.5	554.5	53.4	572.9	256.2	550.0	22.5	96.0
22	124	40416	1.5	16.7385	4.8	0.7345	5.5	0.0892	2.8	0.51	550.6	14.8	559.2	23.7	594.3	103.1	550.6	14.8	92.7
82	70	10693	1.2	17.8069	14.9	0.6919	15.3	0.0894	3.6	0.24	551.7	19.0	533.9	63.6	458.6	331.1	551.7	19.0	120.3
5	79	13039	0.7	17.5902	12.3	0.7004	13.4	0.0894	5.5	0.41	551.7	28.9	539.1	56.3	485.7	272.2	551.7	28.9	113.6
28	70	7451	1.8	18.1448	7.8	0.6822	8.7	0.0898	3.9	0.45	554.2	20.8	528.1	36.0	416.8	175.0	554.2	20.8	133.0
77	165	10456	3.9	16.8669	6.4	0.7363	6.5	0.0901	1.1	0.17	556.0	6.1	560.2	28.1	577.7	139.7	556.0	6.1	96.2
32	887	101402	2.8	16.9924	0.6	0.7319	1.4	0.0902	1.3	0.89	556.7	6.7	557.7	6.1	561.5	13.8	556.7	6.7	99.1
84	200	15319	2.2	16.7536	5.1	0.7507	6.2	0.0912	3.4	0.55	562.7	18.4	568.6	26.8	592.3	111.4	562.7	18.4	95.0
18	247	62075	1.2	17.0025	2.8	0.7417	3.2	0.0915	1.6	0.50	564.2	8.6	563.4	13.8	560.2	60.3	564.2	8.6	100.7
46	100	16580	0.8	17.4576	10.2	0.7264	10.4	0.0920	2.1	0.21	567.2	11.7	554.5	44.4	502.4	224.4	567.2	11.7	112.9
47	128	15797	1.4	16.8913	5.8	0.7518	6.7	0.0921	3.4	0.51	567.9	18.8	569.2	29.3	574.5	125.5	567.9	18.8	98.9
69	107	10128	1.5	17.2503	7.5	0.7414	7.8	0.0928	2.2	0.29	571.8	12.3	563.2	33.8	528.6	164.4	571.8	12.3	108.2
76	493	41901	72.5	17.1738	1.8	0.7464	2.3	0.0930	1.4	0.62	573.1	7.8	566.1	10.0	538.4	39.5	573.1	7.8	106.5
36	289	41911	9.0	16.7925	2.7	0.7651	3.5	0.0932	2.2	0.63	574.3	12.0	576.9	15.3	587.3	58.3	574.3	12.0	97.8
95	231	18219	15.5	17.1890	2.2	0.7488	2.7	0.0934	1.6	0.60	575.3	9.0	567.5	11.9	536.4	47.9	575.3	9.0	107.3
94	197	28976	8.1	17.3044	3.7	0.7443	4.0	0.0934	1.3	0.33	575.7	7.3	564.9	17.2	521.7	82.0	575.7	7.3	110.3
44	74	4445	1.2	18.3333	10.6	0.7033	11.1	0.0935	3.2	0.29	576.3	17.9	540.8	46.7	393.6	239.4	576.3	17.9	146.4
86	240	25138	6.5	17.4125	3.5	0.7430	3.8	0.0938	1.5	0.40	578.1	8.4	564.1	16.4	508.1	76.3	578.1	8.4	113.8
52	109	15950	1.2	16.9419	5.2	0.7689	5.6	0.0945	2.1	0.38	582.0	11.9	579.1	24.7	568.0	112.3	582.0	11.9	102.5
73	310	50014	1.0	17.0120	1.5	0.7724	2.5	0.0953	2.0	0.80	586.8	11.3	581.1	11.1	559.1	32.5	586.8	11.3	105.0
43	297	31116	1.7	17.0520	1.9	0.7731	2.8	0.0956	2.1	0.73	588.6	11.5	581.5	12.5	553.9	42.2	588.6	11.5	106.3
74	187	13659	1.3	17.0765	3.6	0.7738	4.5	0.0958	2.7	0.60	590.0	15.1	582.0	19.9	550.8	79.0	590.0	15.1	107.1
6	419	120385	21.0	16.2828	2.9	0.8183	4.5	0.0966	3.4	0.76	594.7	19.1	607.1	20.4	653.8	62.5	594.7	19.1	91.0
20	116	11900	2.6	16.8469	4.5	0.7922	4.9	0.0968	1.9	0.39	595.6	10.9	592.4	21.9	580.3	97.5	595.6	10.9	102.6
101	175	14157	3.3	17.4015	5.1	0.7714	6.2	0.0974	3.4	0.55	598.9	19.5	580.6	27.3	509.5	112.9	598.9	19.5	117.6
31	218	36571	1.7	16.4325	3.0	0.8270	4.6	0.0986	3.5	0.76	606.0	20.3	612.0	21.3	634.1	65.3	606.0	20.3	95.6
102	142	21241	1.1	16.5492	4.7	0.8228	5.1	0.0988	1.9	0.38	607.1	11.2	609.6	23.5	618.8	102.4	607.1	11.2	98.1
62	160	26020	8.9	15.8542	3.6	0.8677	6.0	0.0998	4.9	0.80	613.1	28.4	634.3	28.5	710.7	76.5	613.1	28.4	86.3
8	228	28498	1.4	16.5174	2.7	0.8400	5.8	0.1006	5.1	0.88	618.1	30.2	619.2	26.9	623.0	58.5	618.1	30.2	99.2
4	56	11059	1.2	16.4612	9.3	0.8468	9.7	0.1011	2.9	0.30	620.8	17.1	622.9	45.3	630.4	200.3	620.8	17.1	98.5
103	306	27239	2.9	16.3908	1.2	0.8847	1.8	0.1052	1.3	0.73	644.6	8.1	643.5	8.5	639.6	26.1	644.6	8.1	100.8
75	275	30428	1.6	16.5175	1.6	0.8814	2.2	0.1056	1.5	0.67	647.1	9.1	641.7	10.5	623.0	35.0	647.1	9.1	103.9
79	308	40375	4.8	16.4668	1.6	0.8869	1.8	0.1059	0.9	0.49	649.0	5.5	644.7	8.6	629.6	33.6	649.0	5.5	103.1
7	197	27799	2.2	16.0577	1.7	0.9330	2.9	0.1087	2.4	0.81	665.0	14.9	669.2	14.2	683.6	35.9	665.0	14.9	97.3
71	83	8686	1.2	15.7218	7.1	0.9846	7.5	0.1123	2.3	0.31	685.9	15.1	696.0	37.6	728.6	150.6	685.9	15.1	94.1
98	129	31995	2.8	15.9040	4.7	0.9920	5.0	0.1144	1.5	0.31	698.4	10.2	699.7	25.1	704.1	100.5	698.4	10.2	99.2
85	448	75349	2.6	16.0213	1.6	0.9857	1.9	0.1145	1.1	0.56	699.0	7.0	696.5	9.5	688.5	33.3	699.0	7.0	101.5
26	338	74732	4.2	15.9466	2.2	1.0324	3.2	0.1194	2.3	0.73	727.1	16.1	720.1	16.6	698.4	47.0	727.1	16.1	104.1
19	223	22884	3.0	15.1845	1.9	1.1520	3.7	0.1269	3.2	0.86	770.0	23.4	778.2	20.4	801.8	40.2	770.0	23.4	96.0
105	220	57229	7.5	15.2724	1.8	1.1590	5.5	0.1284	5.2	0.95	778.6	38.3	781.5	30.0	789.7	36.8	778.6	38.3	98.6
2	365	57584	1.5	15.3371	1.4	1.1614	2.4	0.1292	1.9	0.79	783.2	13.7	782.6	12.8	780.8	30.3	783.2	13.7	100.3
61	696	29943	2.2	15.3294	0.8	1.1828	1.6	0.1315	1.3	0.84	796.4	9.8	792.6	8.6	781.9	17.7	796.4	9.8	101.9
17	67	15995	2.8	14.1574	6.2	1.3954	7.0	0.1433	3.3	0.47	863.2	26.4	887.0	41.2	946.8	126.1	946.8	126.1	91.2
48	120	52047	3.0	14.1031	2.2	1.4870	5.1	0.1521	4.6	0.90	912.7	38.9	925.1	30.7	954.7	44.3	954.7	44.3	95.6
15	304	71778	2.2	14.0629	1.2	1.6058	3.5	0.1638	3.3	0.94	977.7	30.1	972.5	22.2	960.6	25.3	960.6	25.3	101.8
70	357	73254	5.9	14.0334	1.3	1.5673	3.7	0.1595	3.4	0.93	954.1	30.4	957.4	22.8	964.9	27.3	964.9	27.3	98.9
11	199	42773	2.5	13.9464	1.2	1.4546	7.4	0.1471	7.3	0.99	884.9	60.1	911.8	44.4	977.5	24.8	977.5	24.8	90.5
35	268	48632	1.5	13.9137	1.7	1.6192	2.6	0.1634	2.0	0.77	975.6	17.8	977.7	16.2	982.3	33.7	982.3	33.7	99.3
39	43	8210	2.0	13.9051	8.9	1.4702	12.0	0.1483	8.1	0.68	891.2	67.6	918.2	72.8	983.6	180.8	983.6	180.8	90.6
40	51	10753	1.3	13.8706	7.0	1.7078	7.4	0.1718	2.5	0.33	1022.0	23.4	1011.5	47.5	988.6	142.1	988.6	142.1	103.4
37	37	5890	2.2	13.7244	6.6	1.6720	8.3	0.1664	5.0	0.60	992.4	45.7	998.0	52.7	1010.1	134.6	1010.1	134.6	98.2
16	92	35428	5.5	13.6386	2.9	1.7599	5.6	0.1741	4.8	0.85	1034.6	45.5	1030.8	36.1	1022.8	58.6	1022.8	58.6	101.1
41	438	78471	3.8	13.6230	1.1	1.5932	2.0	0.1574	1.6	0.82	942.4	14.2	967.6	12.4	1025.1	23.0	1025.1	23.0	91.9
88	310	161322	7.8	13.5096	1.4	1.7963	4.2	0.1760	3.9	0.94	1045.1	38.0	1044.1	27.3	1042.0	28.3	1042.0	28.3	100.3
27	84	21454	1.6	13.4846	4.9	1.8061	5.3	0.1766	2.0	0.38	1048.5	19.6	1047.7	34.9	1045.8	99.6	1045.8	99.6	100.3
60	213	84693	2.8	13.4779	1.4	1.7897	2.5	0.1749	2.0	0.81	1039.3	19.5	1041.7	16.3	1046.8	29.2	1046.8	29.2	99.3
21	75	31505	2.3	13.4280	4.0	1.7575	4.8	0.1712	2.6	0.54	1018.5	24.0	1029.9	30.9	1054.3	81.1	1054.3	81.1	96.6
56	285	75216	1.4	13.4174	1.2	1.7925	1.8	0.1744	1.3	0.74	1036.5	12.8	1042.7	11.8	1055.9	24.5	1055.9	24.5	98.2
54	72	17966	1.9	13.4087	4.5	1.9110	4.9	0.1858	1.8	0.36	1098.8	18.0	1084.9	32.6	1057.2	91.6	1057.2	91.6	103.9
53	226	40150	1.7	13.3388	2.2	1.7894	2.5	0.1731	1.1	0.43	1029.2	10.3	1041.6	16.2	1067.7	45.0	1067.7	45.0	96.4
1	128	26488	2.1	13.3274	2.2	1.8672	3.0	0.1805	2.0	0.68	1069.6	19.8	1069.5	19.7	1069.4	44.2	1069.4	44.2	100.0
80	121	54302	1.0	13.2384	2.4	1.8581	2.7	0.1784	1.3	0.48	1058.2	12.5	1066.3	17.7	1082.8	47.5	1082.8	47.5	97.7
83	174	50182	1.9	13.2168	2.1	1.9233	7.0	0.1844	6.7	0.96	1090.8	67.4	1089.2	47.0	1086.1	41.3	1086.1	41.3	100.4
65	202	102806	2.0	13.1834	1.9	1.8575	2.4	0.1776	1.5	0.61	1053.9	14.3	1066.1	16.0	1091.2	38.7	1091.2	38.7	96.6
100	101	17969	1.3	13.1417	2.6	1.9724	5.1	0.1880	4.4	0.86	1110.5	44.5	1106.1	34.1	1097.5	51.5	1097.5	51.5	101.2
12	85	48848	1.7	13.0118	3.1	2.0075	5.5	0.1895	4.5	0.83	1118.4	46.6	1118.1	37.2	1117.4	61.7	1117.4	61.7	100.1
64	202	44792	1.8	12.6991	1.3	2.1292	3.4	0.1961	3.1	0.92	1154.3	33.0	1158.3	23.5	1165.7	26.4	1165.7	26.4	99.0
13	656	124221	3.2	12.6836	0.6	2.1364	2.2	0.1965	2.2	0.97	1156.6	23.0	1160.6	15.5	1168.2	11.1	1168.2	11.1	99.0
96	132	28037	1.3	11.2563	2.1	2.8376	9.7	0.2317	9.5	0.98	1343.2	115.3	1365.5	73.3	1400.7	41.0	1400.7	41.0	95.9
72	124	56487	1.4	9.6974	1.4	4.1607	1.7	0.2926	0.9	0.57	1654.7	13.7	1666.3	13.6	1681.0	25.2	1681.0	25.2	98.4
67	169	55746	5.8	9.5776	1.8	4.0204	6.4	0.2793	6.2	0.96	1587.7	86.7	1638.3	52.3	1703.9	33.3	1703.9	33.3	93.2
90	225	80340	1.5	9.4822	0.4	4.6795	1.9	0.3218	1.9	0.98	1798.6	29.6	1763.6	16.1	1722.3	7.2	1722.3	7.2	104.4
58	261	113839	1.6	9.4290	0.5	4.5972	6.7	0.3144	6.7	1.00	1762.2	102.9	1748.8	55.9	1732.7	8.9	1732.7	8.9	101.7
78	194	92239	1.8	9.3334	0.5	4.1979	2.3	0.2842	2.2	0.97	1612.3	31.5	1673.6	18.7	1751.3	9.9	1751.3	9.9	92.1
91	238	105208	1.8	9.1398	0.3	4.9652	1.2	0.3291	1.2	0.97	1834.2	18.9	1813.4	10.3	1789.6	5.7	1789.6	5.7	102.5
10	179	51977	0.7	8.9938	0.8	5.1244	3.8	0.3343	3.7	0.98	1859.0	59.7	1840.2	32.1	1818.9	13.6	1818.9	13.6	102.2
49	177	73311	2.1	8.7446	0.8	5.3258	1.7	0.3378	1.6	0.90	1875.9	25.6	1873.0	14.9	1869.8	13.6	1869.8	13.6	100.3
87	117	91248	3.2	8.0341	0.8	6.3819	1.9	0.3719	1.7	0.89	2038.2	29.1	2029.8	16.3	2021.2	14.7	2021.2	14.7	100.8
14	105	195681	1.7	5.1369	0.3	14.2031	1.7	0.5292	1.7	0.98	2737.9	37.2	2763.4	16.1	2782.0	5.5	2782.0	5.5	98.4
3	245	97152	0.4	5.0903	0.1	14.1968	2.3	0.5241	2.3	1.00	2716.6	50.0	2762.9	21.4	2796.9	2.3	2796.9	2.3	97.1

Table C.6 continued. U–Pb data for detrital zircon analyses

				Isotope ratios							Apparent ages (Ma)								
Spot	U	206Pb	U/Th	206Pb*	±	207Pb*	±	206Pb*	±	error	206Pb*	±	207Pb*	±	206Pb*	±	Best age	±	Conc
	(ppm)	204Pb		207Pb*	(%)	235U*	(%)	238U	(%)	corr.	238U*	(Ma)	235U	(Ma)	207Pb*	(Ma)	(Ma)	(Ma)	(%)
318-M9																			
67	267	80122	2.0	17.9398	2.3	0.4012	3.7	0.0522	2.9	0.78	328.0	9.2	342.5	10.8	442.1	51.8	328.0	9.2	NA
33	506	111794	1.2	17.7906	0.8	0.4751	1.5	0.0613	1.3	0.87	383.5	4.8	394.7	4.9	460.6	16.7	383.5	4.8	NA
90	333	78529	2.5	17.3691	1.5	0.5563	2.2	0.0701	1.6	0.73	436.6	7.0	449.1	8.1	513.6	33.4	436.6	7.0	85.0
69b	399	106244	3.5	17.4958	1.3	0.5622	1.8	0.0713	1.2	0.68	444.2	5.2	453.0	6.5	497.6	28.5	444.2	5.2	89.3
66	241	64553	2.7	16.6451	2.8	0.6340	3.5	0.0765	2.0	0.58	475.4	9.3	498.6	13.8	606.4	61.4	475.4	9.3	78.4
61	425	153731	124.6	17.3579	1.3	0.6416	1.5	0.0808	0.9	0.56	500.7	4.2	503.3	6.1	515.0	28.0	500.7	4.2	97.2
29	225	69754	1.4	17.0668	1.6	0.6738	1.9	0.0834	1.0	0.55	516.4	5.2	523.0	7.8	552.0	35.0	516.4	5.2	93.6
68b	409	91772	3.3	17.2016	1.2	0.6748	2.1	0.0842	1.8	0.84	521.1	9.0	523.6	8.7	534.8	25.3	521.1	9.0	97.4
47	670	161760	8.5	16.7159	0.5	0.7059	3.4	0.0856	3.3	0.99	529.3	16.9	542.3	14.1	597.2	9.8	529.3	16.9	88.6
97	432	95308	2.2	16.8803	0.8	0.7051	6.2	0.0863	6.1	0.99	533.7	31.3	541.8	25.9	575.9	18.3	533.7	31.3	92.7
38	264	94882	7.4	17.1081	1.5	0.7001	2.4	0.0869	1.8	0.77	537.0	9.3	538.9	9.8	546.7	32.9	537.0	9.3	98.2
30	208	57209	2.2	17.1791	2.0	0.7002	3.6	0.0872	2.9	0.82	539.2	15.1	538.9	14.9	537.7	44.5	539.2	15.1	100.3
75	359	162785	3.5	17.0491	0.9	0.7058	3.1	0.0873	2.9	0.95	539.4	15.1	542.3	12.9	554.3	20.3	539.4	15.1	97.3
27	230	72265	2.2	17.1208	1.5	0.7071	2.1	0.0878	1.5	0.70	542.5	7.7	543.0	8.9	545.1	33.1	542.5	7.7	99.5
35	118	68108	1.8	17.0134	3.9	0.7144	4.1	0.0881	1.3	0.31	544.6	6.6	547.3	17.4	558.8	85.3	544.6	6.6	97.4
55	655	140774	16.7	17.0232	0.7	0.7193	1.8	0.0888	1.6	0.92	548.5	8.5	550.2	7.5	557.6	15.5	548.5	8.5	98.4
22	107	57960	0.6	16.9195	4.7	0.7273	5.1	0.0893	1.9	0.38	551.1	10.3	555.0	21.9	570.9	103.1	551.1	10.3	96.5
79	98	47306	0.9	16.8267	2.3	0.7318	2.7	0.0893	1.3	0.49	551.4	6.9	557.6	11.5	582.9	50.7	551.4	6.9	94.6
100	995	365941	8.1	16.6572	0.4	0.7464	3.0	0.0902	3.0	0.99	556.6	16.0	566.1	13.1	604.8	8.8	556.6	16.0	92.0
39	208	64190	1.2	17.1950	1.2	0.7279	2.1	0.0908	1.8	0.83	560.1	9.5	555.3	9.1	535.7	26.0	560.1	9.5	104.6
52	754	286126	7.6	16.9501	0.5	0.7461	1.8	0.0917	1.7	0.96	565.7	9.3	566.0	7.8	567.0	10.8	565.7	9.3	99.8
84	182	66123	1.0	16.9928	1.7	0.7468	2.1	0.0920	1.2	0.58	567.6	6.6	566.3	9.2	561.5	37.6	567.6	6.6	101.1
48	335	100178	5.6	16.0027	1.4	0.7997	5.3	0.0928	5.1	0.96	572.2	27.9	596.7	23.9	690.9	30.9	572.2	27.9	82.8
85	426	178033	19.0	16.8339	1.0	0.7677	1.7	0.0937	1.4	0.80	577.6	7.7	578.4	7.6	581.9	22.4	577.6	7.7	99.2
21	62	18331	1.8	16.7835	3.7	0.7815	5.6	0.0951	4.2	0.75	585.8	23.6	586.3	24.9	588.5	79.7	585.8	23.6	99.5
36	39	15062	2.0	16.3166	9.2	0.8063	9.4	0.0954	2.2	0.23	587.5	12.3	600.3	42.8	649.3	197.4	587.5	12.3	90.5
19	114	66491	1.7	16.4518	4.1	0.8136	4.1	0.0971	0.9	0.21	597.3	5.0	604.5	18.9	631.6	87.3	597.3	5.0	94.6
91	130	37134	2.0	15.8959	3.6	0.8433	3.8	0.0972	1.1	0.29	598.1	6.2	621.0	17.6	705.2	77.4	598.1	6.2	84.8
76	1557	618894	13.7	16.4793	0.4	0.8214	0.7	0.0982	0.6	0.84	603.7	3.4	608.8	3.2	628.0	8.1	603.7	3.4	96.1
37	181	146321	2.3	15.9833	2.1	0.8656	4.1	0.1003	3.5	0.86	616.4	20.8	633.2	19.4	693.5	44.9	616.4	20.8	88.9
41	396	112119	5.0	15.3050	1.0	1.0047	3.2	0.1115	3.0	0.95	681.6	19.6	706.2	16.2	785.2	20.9	681.6	19.6	86.8
46	86	34426	2.6	15.1835	4.6	1.0274	6.6	0.1131	4.8	0.72	691.0	31.2	717.6	34.1	801.9	96.6	691.0	31.2	86.2
50	138	56705	2.5	15.7990	2.1	0.9986	2.7	0.1144	1.8	0.65	698.4	11.7	703.1	13.8	718.1	44.2	698.4	11.7	97.3
49	231	98508	2.5	15.3241	1.1	1.0473	2.2	0.1164	2.0	0.88	709.8	13.2	727.5	11.6	782.6	22.1	709.8	13.2	90.7
17	960	337018	3.7	15.4442	0.4	1.0592	2.3	0.1186	2.2	0.99	722.7	15.3	733.4	11.8	766.2	7.9	722.7	15.3	94.3
16	350	149175	2.5	15.4650	0.8	1.0762	1.4	0.1207	1.1	0.80	734.6	7.6	741.8	7.2	763.3	17.3	734.6	7.6	96.2
43	1037	615522	15.7	15.6639	0.6	1.0914	3.4	0.1240	3.3	0.98	753.5	23.8	749.2	18.1	736.4	13.1	753.5	23.8	102.3
95	489	80796	5.9	14.4360	0.8	1.2086	7.7	0.1265	7.7	0.99	768.1	55.7	804.6	43.0	906.8	17.5	768.1	55.7	84.7
44	309	122113	3.6	14.6507	0.8	1.2166	2.2	0.1293	2.0	0.94	783.7	14.9	808.2	12.0	876.3	15.7	783.7	14.9	89.4
42	393	266967	4.1	14.6608	1.0	1.2240	1.9	0.1301	1.5	0.83	788.7	11.4	811.6	10.4	874.9	21.7	788.7	11.4	90.1
81	97	35350	3.9	14.9438	2.1	1.2024	10.1	0.1303	9.9	0.98	789.7	73.7	801.7	56.2	835.2	42.7	789.7	73.7	94.5
94	391	193150	1.7	15.1164	0.6	1.2037	4.6	0.1320	4.6	0.99	799.1	34.4	802.3	25.6	811.3	12.4	799.1	34.4	98.5
62	171	117457	2.6	13.8069	1.8	1.3207	4.9	0.1323	4.5	0.93	800.7	34.1	854.8	28.3	998.0	37.4	800.7	34.1	80.2
80	228	88514	9.9	14.4650	0.9	1.2739	2.9	0.1336	2.7	0.94	808.7	20.6	834.2	16.3	902.7	19.5	808.7	20.6	89.6
53	281	87657	2.9	14.5742	0.6	1.4022	3.6	0.1482	3.5	0.99	891.0	29.5	889.9	21.3	887.2	12.0	891.0	29.5	100.4
63a	111	62856	2.7	13.7237	1.3	1.7455	3.4	0.1737	3.2	0.92	1032.6	30.2	1025.5	22.2	1010.2	27.1	1010.2	27.1	102.2
59	490	185459	4.6	13.6887	0.7	1.5546	2.2	0.1543	2.0	0.95	925.3	17.7	952.3	13.3	1015.4	13.6	1015.4	13.6	91.1
28	206	148971	3.2	13.6521	0.7	1.6963	2.0	0.1680	1.8	0.93	1000.8	17.0	1007.1	12.5	1020.8	14.3	1020.8	14.3	98.0
89	220	51191	3.4	13.5264	0.7	1.6877	1.1	0.1656	0.8	0.77	987.7	7.5	1003.9	6.7	1039.5	13.6	1039.5	13.6	95.0
87	271	166136	2.8	13.5024	0.7	1.7405	2.8	0.1704	2.7	0.96	1014.6	25.1	1023.6	17.9	1043.1	14.9	1043.1	14.9	97.3
34	83	54718	1.4	13.4956	2.0	1.7427	2.2	0.1706	1.0	0.45	1015.3	9.3	1024.5	14.3	1044.1	40.0	1044.1	40.0	97.2
64a	90	24840	2.4	13.4903	1.2	1.7788	2.8	0.1740	2.6	0.91	1034.3	24.5	1037.7	18.3	1044.9	23.4	1044.9	23.4	99.0
20	118	69923	1.6	13.4627	1.4	1.8301	3.3	0.1787	3.0	0.91	1059.8	29.0	1056.3	21.4	1049.1	27.4	1049.1	27.4	101.0
15	96	75687	2.5	13.4536	2.5	1.7569	2.7	0.1714	0.9	0.35	1020.0	8.9	1029.7	17.4	1050.5	50.9	1050.5	50.9	97.1
70	284	201113	4.9	13.3459	0.6	1.8915	5.2	0.1831	5.2	0.99	1083.8	51.6	1078.1	34.6	1066.6	13.0	1066.6	13.0	101.6
71	274	168191	3.0	13.3150	0.8	1.8141	1.3	0.1752	1.1	0.82	1040.6	10.4	1050.6	8.6	1071.3	15.2	1071.3	15.2	97.1
25	193	174323	1.9	13.2561	0.7	1.9087	2.3	0.1835	2.2	0.95	1086.1	22.2	1084.1	15.6	1080.2	14.7	1080.2	14.7	100.6
98	726	332417	32.3	13.2365	0.3	1.7852	1.7	0.1714	1.6	0.98	1019.7	15.4	1040.1	10.8	1083.1	6.2	1083.1	6.2	94.1
88	85	34967	1.8	13.2250	1.7	1.9160	2.8	0.1838	2.2	0.79	1087.6	21.8	1086.7	18.5	1084.9	34.3	1084.9	34.3	100.2
86	135	49828	3.7	13.1999	1.6	1.8846	2.2	0.1804	1.5	0.69	1069.3	14.9	1075.7	14.5	1088.7	31.9	1088.7	31.9	98.2
78	251	177784	2.6	13.1538	0.5	1.8081	0.8	0.1725	0.6	0.74	1025.8	5.3	1048.4	4.9	1095.7	10.1	1095.7	10.1	93.6
26	177	202340	3.0	13.1522	0.7	1.8949	2.7	0.1808	2.6	0.97	1071.1	25.3	1079.3	17.7	1096.0	13.7	1096.0	13.7	97.7
83	275	143861	4.2	13.1075	0.7	1.9218	1.7	0.1827	1.6	0.92	1081.7	16.0	1088.7	11.7	1102.8	13.9	1102.8	13.9	98.1
51	117	86556	3.2	13.0387	1.1	1.9649	1.8	0.1858	1.5	0.80	1098.6	14.9	1103.6	12.3	1113.3	21.7	1113.3	21.7	98.7
74	573	232622	1.9	12.9830	0.5	1.9290	1.4	0.1816	1.3	0.94	1075.9	12.8	1091.2	9.2	1121.8	9.6	1121.8	9.6	95.9
54	144	364338	0.9	12.3228	1.1	2.2712	1.4	0.2030	0.9	0.65	1191.3	10.0	1203.4	9.9	1225.1	21.1	1225.1	21.1	97.2
96	660	222250	2.5	11.3334	0.2	2.7109	1.4	0.2228	1.3	0.99	1296.8	15.8	1331.5	10.1	1387.6	3.9	1387.6	3.9	93.5
93	68	63779	0.8	11.0200	1.1	2.9714	1.3	0.2375	0.7	0.56	1373.6	9.2	1400.3	10.1	1441.2	20.8	1441.2	20.8	95.3
24	447	24770	4.2	9.5826	0.3	4.2457	2.0	0.2951	2.0	0.99	1666.8	28.8	1682.9	16.3	1703.0	5.3	1703.0	5.3	97.9
45	132	86076	2.5	9.2253	0.5	3.6776	6.1	0.2461	6.1	1.00	1418.1	77.8	1566.5	49.0	1772.6	9.3	1772.6	9.3	80.0
32	128	133203	1.0	8.7796	0.6	5.1074	2.2	0.3252	2.1	0.97	1815.2	33.5	1837.3	18.6	1862.5	10.1	1862.5	10.1	97.5
73	564	195055	3.7	8.5164	0.3	5.2346	2.6	0.3233	2.6	0.99	1806.0	40.2	1858.3	21.9	1917.3	5.2	1917.3	5.2	94.2
40	389	363488	2.9	8.0960	2.8	4.9921	6.5	0.2931	5.9	0.90	1657.1	85.8	1818.0	55.2	2007.6	50.4	2007.6	50.4	82.5
31	729	490009	2.3	6.4267	0.2	8.7167	2.2	0.4063	2.2	1.00	2197.9	40.3	2308.8	19.8	2408.4	2.6	2408.4	2.6	91.3
56	178	269460	2.6	6.3467	0.4	8.8795	1.7	0.4087	1.7	0.97	2209.1	31.6	2325.7	15.8	2429.7	6.7	2429.7	6.7	90.9
77	380	516685	1.0	6.2454	0.1	9.7471	1.0	0.4415	1.0	0.99	2357.4	20.3	2411.2	9.6	2456.9	2.5	2456.9	2.5	95.9

Table C.6 continued. U–Pb data for detrital zircon analyses

				Isotope ratios							Apparent ages (Ma)								
Spot	U	206Pb	U/Th	206Pb*	±	207Pb*	±	206Pb*	±	error	206Pb*	±	207Pb*	±	206Pb*	±	Best age	±	Conc
	(ppm)	204Pb		207Pb*	(%)	235U*	(%)	238U	(%)	corr.	238U*	(Ma)	235U	(Ma)	207Pb*	(Ma)	(Ma)	(Ma)	(%)
21223-3																			
39	424	23390	9.9	19.1374	4.8	0.1279	6.8	0.0178	4.8	0.71	113.5	5.4	122.2	7.9	296.5	110.0	113.5	5.4	NA
27	450	32853	4.6	17.8730	2.5	0.3057	7.2	0.0396	6.8	0.94	250.5	16.7	270.9	17.2	450.4	55.7	250.5	16.7	NA
8	267	17021	2.6	17.1597	3.2	0.3351	8.3	0.0417	7.7	0.92	263.4	19.9	293.5	21.3	540.2	70.0	263.4	19.9	NA
26	141	23871	4.6	17.7116	3.8	0.3983	4.6	0.0512	2.6	0.56	321.7	8.0	340.4	13.2	470.5	83.8	321.7	8.0	NA
7	333	40261	3.0	17.2414	1.1	0.4792	6.5	0.0599	6.4	0.99	375.2	23.5	397.5	21.5	529.8	24.3	375.2	23.5	NA
43	136	38567	1.6	16.2729	1.7	0.5547	6.1	0.0655	5.8	0.96	408.8	23.1	448.1	22.0	655.1	36.8	408.8	23.1	62.4
40	647	101154	1.2	17.6809	1.0	0.5180	5.8	0.0664	5.7	0.99	414.6	23.0	423.8	20.2	474.4	21.4	414.6	23.0	87.4
32	360	55794	9.2	17.1413	1.3	0.5475	6.4	0.0681	6.2	0.98	424.5	25.6	443.4	22.8	542.5	28.1	424.5	25.6	78.2
9	387	74058	1.9	17.6971	1.4	0.5528	8.5	0.0709	8.3	0.99	441.9	35.6	446.8	30.6	472.3	31.5	441.9	35.6	93.5
33	275	51644	3.0	17.2563	0.9	0.5887	3.1	0.0737	2.9	0.96	458.3	13.0	470.0	11.6	527.9	19.1	458.3	13.0	86.8
20	390	62566	2.2	17.4282	1.6	0.5991	7.7	0.0757	7.5	0.98	470.6	34.2	476.7	29.3	506.1	34.8	470.6	34.2	93.0
19	298	104523	2.3	17.4097	1.0	0.6135	1.8	0.0775	1.6	0.85	481.0	7.2	485.8	7.1	508.5	21.5	481.0	7.2	94.6
18	248	51171	3.5	17.2510	1.5	0.6272	2.1	0.0785	1.4	0.69	487.0	6.8	494.4	8.2	528.6	32.9	487.0	6.8	92.1
24	423	93607	2.9	17.3954	1.3	0.6389	2.3	0.0806	1.9	0.84	499.8	9.2	501.6	9.0	510.2	27.5	499.8	9.2	98.0
16	516	180052	3.9	17.2224	1.0	0.6531	4.8	0.0816	4.6	0.98	505.5	22.6	510.4	19.1	532.2	22.6	505.5	22.6	95.0
34	440	59013	2.7	17.0623	0.9	0.6703	6.4	0.0829	6.3	0.99	513.7	31.3	520.9	26.1	552.6	19.0	513.7	31.3	93.0
14	270	132808	9.0	17.2599	1.5	0.6769	2.3	0.0847	1.7	0.74	524.3	8.6	524.9	9.5	527.4	33.9	524.3	8.6	99.4
45	957	145611	5.7	17.2036	0.5	0.6808	1.4	0.0849	1.4	0.95	525.6	6.9	527.3	5.9	534.6	10.3	525.6	6.9	98.3
4	489	296222	2.9	16.9521	1.0	0.7014	2.7	0.0862	2.4	0.92	533.3	12.5	539.6	11.1	566.7	22.8	533.3	12.5	94.1
30	360	89903	4.8	16.5888	1.2	0.7314	4.3	0.0880	4.2	0.96	543.7	21.7	557.4	18.6	613.7	26.8	543.7	21.7	88.6
15	220	99318	1.7	16.6175	2.5	0.7322	3.0	0.0882	1.7	0.55	545.2	8.7	557.9	12.9	609.9	54.3	545.2	8.7	89.4
11	1075	327638	3.3	17.1179	0.2	0.7241	4.0	0.0899	4.0	1.00	554.9	21.1	553.1	17.0	545.5	5.3	554.9	21.1	101.7
37	479	147969	25.9	17.0746	0.8	0.7339	3.3	0.0909	3.2	0.97	560.7	17.2	558.8	14.2	551.0	17.0	560.7	17.2	101.8
6	46	14697	1.9	16.6834	9.8	0.7516	10.0	0.0909	1.9	0.19	561.1	9.9	569.1	43.6	601.4	213.0	561.1	9.9	93.3
1	360	85500	5.0	15.8503	2.4	0.8093	7.0	0.0930	6.5	0.94	573.5	35.8	602.1	31.7	711.3	52.1	573.5	35.8	80.6
2	321	98837	4.4	15.9305	1.0	0.8106	4.6	0.0937	4.5	0.98	577.2	24.8	602.8	20.9	700.5	20.6	577.2	24.8	82.4
31	216	89301	3.0	15.4926	1.7	0.8595	6.6	0.0966	6.4	0.97	594.3	36.2	629.9	30.9	759.6	34.8	594.3	36.2	78.2
35	66	22978	3.0	13.8055	2.5	1.3317	6.6	0.1333	6.1	0.92	806.9	46.5	859.6	38.4	998.2	51.3	998.2	51.3	80.8
3	690	24432	1.5	13.7872	0.7	1.4899	2.9	0.1490	2.8	0.97	895.3	23.4	926.3	17.5	1000.9	13.3	1000.9	13.3	89.5
29	64	17212	1.3	13.7159	1.9	1.4896	2.9	0.1482	2.1	0.74	890.8	17.8	926.2	17.5	1011.4	39.1	1011.4	39.1	88.1
10	531	236229	2.1	13.6976	0.4	1.7343	1.2	0.1723	1.1	0.94	1024.7	10.6	1021.3	7.7	1014.1	8.4	1014.1	8.4	101.0
44	172	79131	1.2	13.6064	0.9	1.7365	2.7	0.1714	2.6	0.95	1019.6	24.3	1022.2	17.5	1027.6	17.6	1027.6	17.6	99.2
12	218	152454	2.7	13.5480	0.8	1.7104	3.0	0.1681	2.9	0.97	1001.4	27.2	1012.4	19.4	1036.3	15.4	1036.3	15.4	96.6
41	528	88290	15.5	12.8115	0.4	1.6753	2.4	0.1557	2.4	0.99	932.6	21.0	999.2	15.5	1148.3	7.3	1148.3	7.3	81.2
25	110	53407	2.3	10.2662	1.1	3.5464	5.3	0.2641	5.2	0.98	1510.6	69.8	1537.6	41.9	1575.0	19.7	1575.0	19.7	95.9
22	224	55009	1.8	8.9282	0.6	4.0431	2.7	0.2618	2.6	0.98	1499.1	35.4	1642.9	22.0	1832.2	10.0	1832.2	10.0	81.8
17	12	15123	1.0	8.1972	3.4	5.9585	4.2	0.3542	2.5	0.59	1954.8	41.7	1969.8	36.4	1985.6	60.0	1985.6	60.0	98.5

Table C.6 continued. U–Pb data for detrital zircon analyses

				Isotope ratios							Apparent ages (Ma)								
Spot	U	206Pb	U/Th	206Pb*	±	207Pb*	±	206Pb*	±	error	206Pb*	±	207Pb*	±	206Pb*	±	Best age	±	Conc
	(ppm)	204Pb		207Pb*	(%)	235U*	(%)	238U	(%)	corr.	238U*	(Ma)	235U	(Ma)	207Pb*	(Ma)	(Ma)	(Ma)	(%)
21223-8																			
R61	108	16498	1.8	16.9073	5.7	0.4570	10.1	0.0560	8.3	0.82	351.5	28.3	382.2	32.1	572.5	124.9	351.5	28.3	NA
54	30	3426	1.5	21.2912	14.7	0.4099	15.6	0.0633	5.3	0.34	395.6	20.3	348.8	46.1	47.6	352.3	395.6	20.3	NA
45	271	10781	2.5	14.6525	1.8	0.6137	5.7	0.0652	5.4	0.95	407.3	21.3	485.9	22.0	876.1	37.2	407.3	21.3	46.5
59	528	112627	11.4	17.0026	1.4	0.5289	8.7	0.0652	8.6	0.99	407.3	33.8	431.1	30.5	560.2	30.5	407.3	33.8	72.7
8 <	206	26264	5.6	17.2319	1.4	0.5255	3.0	0.0657	2.6	0.88	410.1	10.4	428.8	10.4	531.0	31.0	410.1	10.4	77.2
40	305	25086	3.2	17.4095	1.0	0.5882	5.6	0.0743	5.5	0.98	461.8	24.5	469.7	21.1	508.5	22.9	461.8	24.5	90.8
56	326	46011	1.6	17.3915	1.0	0.6120	4.9	0.0772	4.8	0.98	479.4	22.4	484.8	19.1	510.7	22.2	479.4	22.4	93.9
52	158	24537	1.6	17.6556	1.4	0.6168	3.8	0.0790	3.5	0.93	490.1	16.5	487.8	14.6	477.5	31.4	490.1	16.5	102.6
2	294	50700	1.7	17.1393	1.5	0.6371	2.2	0.0792	1.7	0.75	491.3	7.9	500.5	8.8	542.8	32.5	491.3	7.9	90.5
62	232	42404	1.3	17.6877	1.5	0.6281	2.1	0.0806	1.4	0.67	499.6	6.7	494.9	8.2	473.5	34.1	499.6	6.7	105.5
24	710	84997	1.5	17.1489	1.0	0.6544	1.2	0.0814	0.8	0.64	504.4	3.9	511.2	5.0	541.5	20.9	504.4	3.9	93.2
57	50	8799	1.0	17.7284	5.1	0.6439	5.4	0.0828	1.7	0.31	512.8	8.3	504.7	21.5	468.4	113.9	512.8	8.3	109.5
67	238	63908	1.4	17.1506	0.8	0.6723	3.4	0.0836	3.3	0.97	517.7	16.4	522.1	13.9	541.3	18.0	517.7	16.4	95.6
13	809	198589	6.5	17.1316	0.3	0.6764	1.5	0.0840	1.4	0.99	520.2	7.2	524.6	6.0	543.7	5.5	520.2	7.2	95.7
34	331	55249	2.0	17.2085	1.0	0.6795	2.4	0.0848	2.2	0.91	524.7	11.0	526.5	9.9	534.0	21.9	524.7	11.0	98.3
50	611	247337	2.9	17.1207	0.4	0.6856	1.2	0.0851	1.1	0.94	526.7	5.5	530.1	4.8	545.1	8.9	526.7	5.5	96.6
7	139	20612	1.9	17.2080	1.6	0.6877	6.6	0.0858	6.4	0.97	530.8	32.5	531.4	27.2	534.0	34.8	530.8	32.5	99.4
14	320	76145	4.2	16.8003	1.0	0.7048	9.6	0.0859	9.6	0.99	531.1	48.8	541.7	40.5	586.3	21.9	531.1	48.8	90.6
66	232	318557	1.2	17.3008	1.0	0.6851	1.7	0.0860	1.4	0.80	531.6	7.0	529.9	7.1	522.2	22.7	531.6	7.0	101.8
32	404	62511	6.7	16.9280	0.8	0.7030	6.1	0.0863	6.0	0.99	533.7	30.9	540.6	25.5	569.8	16.7	533.7	30.9	93.7
28	406	88145	1.6	17.4269	1.0	0.6842	1.2	0.0865	0.7	0.60	534.7	3.8	529.3	5.1	506.3	21.8	534.7	3.8	105.6
41	345	83876	1.5	17.0142	0.9	0.7123	1.5	0.0879	1.2	0.82	543.1	6.5	546.1	6.4	558.7	18.7	543.1	6.5	97.2
19	644	146512	1.9	17.0289	0.7	0.7196	2.2	0.0889	2.1	0.95	548.9	11.0	550.4	9.3	556.9	14.4	548.9	11.0	98.6
55	109	18249	1.8	17.2898	3.3	0.7092	5.3	0.0889	4.2	0.79	549.2	22.2	544.2	22.4	523.6	71.4	549.2	22.2	104.9
42	151	36274	0.5	16.9674	1.4	0.7380	3.0	0.0908	2.6	0.88	560.4	14.1	561.2	12.9	564.7	31.1	560.4	14.1	99.2
23	1180	57319	4.6	14.3670	0.3	0.9180	4.0	0.0957	4.0	1.00	588.9	22.5	661.3	19.5	916.7	6.4	588.9	22.5	64.2
35	689	120728	1.5	16.7062	0.5	0.8044	1.3	0.0975	1.2	0.93	599.5	6.8	599.3	5.8	598.4	10.3	599.5	6.8	100.2
15	171	40331	1.9	16.2684	1.1	0.8293	3.7	0.0979	3.5	0.95	601.8	20.3	613.3	17.1	655.7	24.4	601.8	20.3	91.8
11	497	92920	4.2	16.4949	0.8	0.8235	3.0	0.0985	2.9	0.97	605.7	16.8	610.0	13.8	625.9	16.5	605.7	16.8	96.8
1	693	112922	8.2	16.2985	0.3	0.8541	2.8	0.1010	2.8	0.99	620.1	16.7	626.9	13.3	651.7	7.0	620.1	16.7	95.1
20	193	34781	3.5	15.9183	1.6	0.9367	5.4	0.1081	5.1	0.95	661.9	32.3	671.1	26.5	702.2	34.7	661.9	32.3	94.3
30	67	14954	0.7	15.0298	3.2	1.0257	8.6	0.1118	8.0	0.93	683.3	51.7	716.8	44.2	823.3	66.4	683.3	51.7	83.0
33	426	227140	5.8	15.4988	0.9	1.0047	5.3	0.1129	5.2	0.99	689.8	34.3	706.2	27.1	758.7	18.9	689.8	34.3	90.9
22	486	138638	4.6	14.8602	0.6	1.0914	5.0	0.1176	4.9	0.99	716.9	33.4	749.2	26.3	846.9	12.0	716.9	33.4	84.7
46	267	50357	1.7	15.5143	0.5	1.0697	1.3	0.1204	1.2	0.92	732.6	8.4	738.6	6.9	756.6	11.0	732.6	8.4	96.8
39	339	103772	2.5	14.0807	0.7	1.3132	7.7	0.1341	7.7	1.00	811.3	58.8	851.5	44.7	958.0	14.7	811.3	58.8	84.7
60	292	48594	2.3	13.9675	0.7	1.6043	4.8	0.1625	4.8	0.99	970.7	43.0	971.9	30.2	974.4	13.5	974.4	13.5	99.6
29	396	70960	40.7	13.6744	0.5	1.3794	5.7	0.1368	5.7	1.00	826.6	44.1	880.2	33.6	1017.5	9.9	1017.5	9.9	81.2
44	286	153114	4.2	13.5668	0.8	1.7102	4.8	0.1683	4.7	0.98	1002.6	44.0	1012.4	30.9	1033.5	17.1	1033.5	17.1	97.0
21	171	42308	2.7	13.5377	1.1	1.5412	1.8	0.1513	1.3	0.76	908.4	11.4	947.0	10.8	1037.8	22.8	1037.8	22.8	87.5
53	258	79608	5.9	13.5159	0.4	1.8423	3.8	0.1806	3.8	0.99	1070.2	37.6	1060.7	25.2	1041.1	8.9	1041.1	8.9	102.8
51	588	135022	1.1	13.3237	0.3	1.6706	1.4	0.1614	1.4	0.97	964.8	12.5	997.4	9.1	1070.0	6.7	1070.0	6.7	90.2
4	285	123503	1.5	13.2891	0.6	1.9612	3.4	0.1890	3.4	0.98	1116.1	34.4	1102.3	22.9	1075.2	12.0	1075.2	12.0	103.8
26	220	58837	1.5	13.2870	0.6	1.8273	1.2	0.1761	1.0	0.87	1045.6	9.7	1055.3	7.6	1075.5	11.3	1075.5	11.3	97.2
49	289	187007	0.9	13.2237	0.1	1.8227	2.3	0.1748	2.3	1.00	1038.6	21.8	1053.7	14.9	1085.1	2.4	1085.1	2.4	95.7
25	418	189069	1.7	13.1424	0.2	1.7974	1.6	0.1713	1.6	0.99	1019.4	15.2	1044.5	10.7	1097.4	5.0	1097.4	5.0	92.9
65	170	96301	2.4	12.4524	0.8	2.1759	2.0	0.1965	1.8	0.92	1156.6	19.1	1173.4	13.6	1204.5	15.2	1204.5	15.2	96.0
5	288	127225	2.6	12.4088	0.4	2.2356	3.4	0.2012	3.3	0.99	1181.8	36.1	1192.3	23.6	1211.4	8.3	1211.4	8.3	97.6
58	102	76697	1.1	12.1409	1.0	2.2664	3.3	0.1996	3.2	0.96	1173.0	34.0	1201.9	23.3	1254.2	19.0	1254.2	19.0	93.5
68	18	8453	2.4	11.9507	5.1	2.4150	6.2	0.2093	3.6	0.58	1225.2	40.0	1247.1	44.6	1285.0	98.6	1285.0	98.6	95.3
36	152	72498	1.5	10.0681	0.2	3.4464	1.1	0.2517	1.1	0.98	1447.0	14.2	1515.0	8.8	1611.4	4.2	1611.4	4.2	89.8
16	351	169440	1.8	9.8682	0.3	3.9646	1.8	0.2837	1.8	0.98	1610.2	25.3	1627.0	14.6	1648.7	5.9	1648.7	5.9	97.7
64	191	70477	1.8	9.4690	0.6	4.2596	6.3	0.2925	6.3	1.00	1654.2	91.2	1685.6	51.7	1724.9	10.6	1724.9	10.6	95.9
31	322	169511	3.2	9.3391	0.4	4.0468	3.1	0.2741	3.0	0.99	1561.6	42.2	1643.6	25.0	1750.2	7.6	1750.2	7.6	89.2
17	254	133969	1.3	8.8422	0.3	4.1690	4.9	0.2674	4.9	1.00	1527.4	66.9	1668.0	40.4	1849.7	4.9	1849.7	4.9	82.6
43	131	180703	2.2	5.5289	0.2	11.1625	2.5	0.4476	2.5	1.00	2384.6	49.8	2536.8	23.4	2660.8	3.2	2660.8	3.2	89.6

Table C.6 continued. U–Pb data for detrital zircon analyses

				Isotope ratios							Apparent ages (Ma)								
Spot	U	206Pb	U/Th	206Pb*	±	207Pb*	±	206Pb*	±	error	206Pb*	±	207Pb*	±	206Pb*	±	Best age	±	Conc
	(ppm)	204Pb		207Pb*	(%)	235U*	(%)	238U	(%)	corr.	238U*	(Ma)	235U	(Ma)	207Pb*	(Ma)	(Ma)	(Ma)	(%)
8D27-10																			
1	116	23078	0.5	17.8046	2.2	0.6248	2.5	0.0807	1.1	0.47	500.2	5.5	492.9	9.6	458.9	48.3	500.2	5.5	109.0
73	517	201519	42.0	17.1791	1.0	0.6749	1.2	0.0841	0.8	0.62	520.5	3.8	523.7	5.1	537.7	21.3	520.5	3.8	96.8
60	740	434697	11.7	17.2390	0.6	0.6750	1.7	0.0844	1.6	0.93	522.3	8.0	523.7	7.0	530.1	13.9	522.3	8.0	98.5
4	352	358110	9.2	16.1286	3.3	0.7250	4.7	0.0848	3.3	0.70	524.8	16.4	553.6	19.9	674.2	71.5	524.8	16.4	77.8
62	757	213979	2.4	17.1759	0.5	0.6923	0.8	0.0862	0.6	0.77	533.3	3.2	534.2	3.3	538.1	11.2	533.3	3.2	99.1
13	190	31804	1.8	17.2333	2.3	0.6968	2.7	0.0871	1.4	0.52	538.3	7.2	536.9	11.1	530.8	49.9	538.3	7.2	101.4
37	70	32054	1.4	17.2906	6.1	0.6968	6.3	0.0874	1.4	0.22	540.0	7.3	536.9	26.2	523.5	134.6	540.0	7.3	103.2
75	353	80437	1.2	17.0952	1.7	0.7098	1.8	0.0880	0.7	0.37	543.7	3.6	544.6	7.7	548.4	36.9	543.7	3.6	99.1
24	128	24879	2.2	16.9638	2.7	0.7188	4.0	0.0884	3.0	0.74	546.3	15.6	550.0	17.1	565.2	59.0	546.3	15.6	96.7
51	123	42497	1.0	16.7343	2.5	0.7297	2.8	0.0886	1.3	0.47	547.0	7.0	556.4	12.1	594.8	54.0	547.0	7.0	92.0
46	134	60325	1.8	17.1311	2.3	0.7141	2.5	0.0887	1.1	0.43	548.0	5.7	547.2	10.6	543.8	49.4	548.0	5.7	100.8
6	560	129956	1.4	16.9786	0.7	0.7239	1.4	0.0891	1.3	0.88	550.5	6.7	553.0	6.1	563.3	14.8	550.5	6.7	97.7
8	238	74350	1.5	17.0424	1.3	0.7223	1.7	0.0893	1.1	0.62	551.3	5.6	552.0	7.3	555.1	29.4	551.3	5.6	99.3
87	136	32603	1.0	17.5450	4.0	0.7039	4.2	0.0896	1.2	0.28	553.0	6.1	541.1	17.4	491.4	87.9	553.0	6.1	112.5
26	89	33652	2.2	17.1518	4.3	0.7208	4.5	0.0897	1.2	0.28	553.5	6.6	551.1	19.0	541.2	94.1	553.5	6.6	102.3
40	320	101507	0.9	16.8722	1.1	0.7414	1.3	0.0907	0.8	0.58	559.9	4.1	563.2	5.8	577.0	23.8	559.9	4.1	97.0
78	573	131917	4.6	16.9591	0.8	0.7421	1.2	0.0913	0.9	0.76	563.1	4.7	563.6	5.0	565.8	16.5	563.1	4.7	99.5
16	481	172900	3.6	16.7833	0.7	0.7513	1.1	0.0914	0.9	0.78	564.1	4.6	569.0	4.8	588.5	15.0	564.1	4.6	95.9
28	442	94934	3.1	17.0242	1.0	0.7412	1.3	0.0915	0.9	0.65	564.5	4.6	563.1	5.7	557.4	22.1	564.5	4.6	101.3
30	107	23893	1.4	17.1314	5.2	0.7414	5.5	0.0921	1.6	0.29	568.1	8.7	563.2	23.6	543.7	114.1	568.1	8.7	104.5
52	284	89556	4.5	16.8872	1.0	0.7543	1.1	0.0924	0.5	0.46	569.6	2.7	570.7	4.8	575.1	21.3	569.6	2.7	99.1
72	229	84338	1.0	16.9672	1.1	0.7511	1.5	0.0924	1.0	0.70	569.9	5.6	568.8	6.4	564.8	22.9	569.9	5.6	100.9
71	227	23433	22.2	16.6565	1.7	0.7697	2.9	0.0930	2.3	0.81	573.1	12.7	579.6	12.6	604.9	36.1	573.1	12.7	94.8
2	807	189117	34.1	16.6904	0.6	0.7683	1.0	0.0930	0.7	0.78	573.3	4.1	578.8	4.2	600.5	12.9	573.3	4.1	95.5
85	52	18919	3.1	16.9805	5.6	0.7610	6.0	0.0937	2.0	0.34	577.5	11.1	574.6	26.2	563.1	122.6	577.5	11.1	102.6
44	221	174383	1.8	16.9445	2.4	0.7697	3.3	0.0946	2.2	0.68	582.6	12.4	579.6	14.5	567.7	52.7	582.6	12.4	102.6
35	325	61838	2.2	16.4576	0.7	0.7964	2.0	0.0951	1.9	0.94	585.4	10.7	594.8	9.2	630.8	15.5	585.4	10.7	92.8
67	524	296194	8.3	16.2674	1.0	0.8098	3.2	0.0955	3.1	0.95	588.3	17.3	602.4	14.7	655.8	21.4	588.3	17.3	89.7
20	162	63523	3.7	16.9052	3.0	0.7805	4.0	0.0957	2.7	0.67	589.1	15.2	585.8	17.8	572.7	64.5	589.1	15.2	102.9
99	361	138223	3.6	16.8816	0.9	0.7860	1.7	0.0962	1.5	0.85	592.3	8.4	588.9	7.8	575.8	19.6	592.3	8.4	102.9
10	318	163363	12.0	16.4684	1.0	0.8067	1.5	0.0964	1.1	0.74	593.0	6.3	600.6	6.8	629.4	21.5	593.0	6.3	94.2
11	538	195561	11.6	16.8888	0.8	0.7885	3.0	0.0966	2.9	0.96	594.3	16.3	590.3	13.4	574.8	17.3	594.3	16.3	103.4
31	130	27666	0.7	16.7543	2.4	0.7970	2.6	0.0968	0.9	0.35	595.9	5.1	595.1	11.5	592.2	51.8	595.9	5.1	100.6
18	298	228324	2.1	16.7944	1.5	0.8049	2.3	0.0980	1.7	0.75	602.9	10.0	599.6	10.5	587.0	33.3	602.9	10.0	102.7
42	71	32218	2.7	16.8063	3.7	0.8147	4.4	0.0993	2.4	0.54	610.3	13.8	605.1	20.2	585.5	81.3	610.3	13.8	104.2
84	2781	84690	45.6	16.7150	0.2	0.8257	1.9	0.1001	1.9	1.00	615.0	11.1	611.2	8.7	597.3	4.0	615.0	11.1	103.0
82	172	68348	4.9	15.6730	2.7	0.8882	3.1	0.1010	1.4	0.45	620.0	8.2	645.4	14.6	735.2	57.8	620.0	8.2	84.3
70	458	255559	6.5	16.2732	0.4	0.8808	5.5	0.1040	5.4	1.00	637.6	33.0	641.4	25.9	655.0	9.5	637.6	33.0	97.3
41	158	57649	2.0	16.4387	2.1	0.8742	2.4	0.1042	1.3	0.53	639.1	7.8	637.9	11.6	633.3	44.7	639.1	7.8	100.9
98	511	221110	1.4	16.3743	1.0	0.8797	2.5	0.1045	2.3	0.91	640.5	14.1	640.8	12.1	641.8	22.6	640.5	14.1	99.8
12	240	92799	3.0	16.0033	0.8	0.9426	1.8	0.1094	1.6	0.89	669.3	10.1	674.3	8.9	690.8	17.9	669.3	10.1	96.9
45	66	30584	1.3	16.1452	5.5	0.9619	6.6	0.1126	3.5	0.54	688.0	23.1	684.3	32.7	672.0	118.7	688.0	23.1	102.4
86	352	56075	1.3	15.0494	1.5	1.0905	1.9	0.1190	1.2	0.63	724.9	8.3	748.7	10.2	820.5	31.2	724.9	8.3	88.4
54	646	708132	7.0	15.2598	1.0	1.0985	2.5	0.1216	2.2	0.91	739.6	15.5	752.6	13.0	791.4	21.9	739.6	15.5	93.5
32	216	54614	1.6	15.0151	3.1	1.1491	5.5	0.1251	4.5	0.82	760.1	32.2	776.8	29.7	825.3	65.5	760.1	32.2	92.1
38	225	106757	2.4	14.5365	1.1	1.2920	2.4	0.1362	2.1	0.89	823.2	16.2	842.2	13.5	892.5	22.3	823.2	16.2	92.2
21	387	560075	1.6	14.1290	0.6	1.3730	1.8	0.1407	1.7	0.94	848.6	13.7	877.4	10.8	950.9	12.9	848.6	13.7	89.2
88	244	180641	1.7	14.6202	1.0	1.4000	1.4	0.1484	0.9	0.67	892.2	7.7	888.9	8.3	880.6	21.5	892.2	7.7	101.3
7	663	181475	2.3	14.4348	0.4	1.4186	1.0	0.1485	0.9	0.93	892.6	7.7	896.8	5.9	907.0	7.3	892.6	7.7	98.4
53	349	168135	5.3	14.2448	0.5	1.4693	2.8	0.1518	2.8	0.99	911.0	23.9	917.8	17.2	934.2	9.5	934.2	9.5	97.5
39	168	82961	2.8	13.9314	1.5	1.6312	1.7	0.1648	0.7	0.43	983.5	6.5	982.3	10.4	979.7	30.4	979.7	30.4	100.4
33	809	177542	2.5	13.8609	0.4	1.5531	1.8	0.1561	1.7	0.97	935.2	15.2	951.7	11.1	990.1	8.6	990.1	8.6	94.5
61	195	93970	5.7	13.8458	1.0	1.5985	3.3	0.1605	3.1	0.95	959.6	27.8	969.6	20.4	992.3	19.9	992.3	19.9	96.7
57	35	18837	1.5	13.8203	3.8	1.6400	4.8	0.1644	2.9	0.61	981.1	26.4	985.7	30.0	996.0	76.7	996.0	76.7	98.5
80	424	135515	1.7	13.8018	0.5	1.6325	0.8	0.1634	0.6	0.74	975.7	5.3	982.8	5.0	998.7	10.9	998.7	10.9	97.7
90	150	6033	2.4	13.7314	2.9	1.4965	3.1	0.1490	1.2	0.38	895.6	9.9	929.0	19.1	1009.1	58.9	1009.1	58.9	88.8
77	179	78539	2.3	13.7112	0.7	1.6585	3.0	0.1649	2.9	0.98	984.1	26.7	992.8	19.0	1012.1	13.4	1012.1	13.4	97.2
17	247	272277	1.3	13.6678	0.6	1.7498	3.9	0.1735	3.9	0.99	1031.1	37.0	1027.1	25.4	1018.5	12.3	1018.5	12.3	101.2
63	251	125597	1.0	13.6466	1.0	1.6926	1.1	0.1675	0.6	0.50	998.4	5.2	1005.7	7.3	1021.6	20.1	1021.6	20.1	97.7
22	73	57719	1.1	13.6133	2.2	1.7117	2.9	0.1690	1.8	0.63	1006.6	16.8	1012.9	18.3	1026.6	44.8	1026.6	44.8	98.1
74	163	95946	4.1	13.5856	1.1	1.7352	1.9	0.1710	1.5	0.82	1017.5	14.4	1021.7	12.0	1030.7	21.8	1030.7	21.8	98.7
92	263	170261	3.6	13.5533	0.7	1.7168	0.9	0.1688	0.5	0.63	1005.2	5.0	1014.8	5.5	1035.5	13.4	1035.5	13.4	97.1
69	357	132472	2.0	13.5298	0.7	1.8044	0.9	0.1771	0.7	0.71	1050.9	6.5	1047.0	6.1	1039.0	13.4	1039.0	13.4	101.1
79	409	543156	1.0	13.4865	0.5	1.7310	1.3	0.1693	1.2	0.92	1008.4	11.0	1020.1	8.3	1045.5	10.2	1045.5	10.2	96.4
96	177	72428	1.6	13.3517	1.2	1.6826	5.8	0.1629	5.7	0.98	973.0	51.2	1001.9	36.9	1065.7	24.0	1065.7	24.0	91.3
10	450	330767	2.2	13.2593	0.5	1.8126	2.3	0.1743	2.2	0.98	1035.8	21.3	1050.0	14.9	1079.7	9.4	1079.7	9.4	95.9
5	66	41758	1.8	13.2322	2.1	1.8441	2.2	0.1770	0.6	0.29	1050.4	6.2	1061.3	14.3	1083.8	41.7	1083.8	41.7	96.9

Table C.6 continued. U–Pb data for detrital zircon analyses

				Isotope ratios							Apparent ages (Ma)								
Spot	U	206Pb	U/Th	206Pb*	±	207Pb*	±	206Pb*	±	error	206Pb*	±	207Pb*	±	206Pb*	±	Best age	±	Conc
	(ppm)	204Pb		207Pb*	(%)	235U*	(%)	238U	(%)	corr.	238U*	(Ma)	235U	(Ma)	207Pb*	(Ma)	(Ma)	(Ma)	(%)
8D27-10 continued																			
65	301	136339	1.1	13.2223	0.7	1.9400	1.3	0.1860	1.0	0.82	1099.9	10.4	1095.0	8.4	1085.3	14.5	1085.3	14.5	101.3
3	218	141089	2.4	13.2014	0.7	1.7586	2.9	0.1684	2.8	0.97	1003.2	26.4	1030.3	19.0	1088.5	14.3	1088.5	14.3	92.2
59	362	184862	2.0	13.1922	0.5	1.9177	2.6	0.1835	2.6	0.98	1086.0	25.5	1087.3	17.4	1089.8	10.1	1089.8	10.1	99.6
89	97	51042	2.0	13.1467	1.4	1.9146	1.8	0.1826	1.2	0.65	1080.9	11.7	1086.2	12.0	1096.8	27.4	1096.8	27.4	98.6
95	565	186981	3.4	13.1380	0.3	1.9230	1.0	0.1832	0.9	0.96	1084.6	9.5	1089.1	6.6	1098.1	5.5	1098.1	5.5	98.8
34	185	78613	2.4	13.1370	1.3	1.8843	1.4	0.1795	0.4	0.26	1064.4	3.5	1075.6	9.2	1098.2	26.9	1098.2	26.9	96.9
58	48	37259	1.7	13.1083	2.3	1.8940	2.7	0.1801	1.3	0.48	1067.3	12.5	1079.0	17.6	1102.6	46.5	1102.6	46.5	96.8
93	352	378556	2.3	12.9412	0.6	1.8340	2.5	0.1721	2.4	0.97	1023.9	22.8	1057.7	16.4	1128.3	12.7	1128.3	12.7	90.7
50	66	40507	2.1	12.7247	2.1	2.1117	3.0	0.1949	2.1	0.69	1147.8	21.7	1152.6	20.4	1161.7	42.3	1161.7	42.3	98.8
25	280	159095	4.7	12.6101	0.4	2.1522	6.0	0.1968	6.0	1.00	1158.3	63.4	1165.8	41.6	1179.7	8.2	1179.7	8.2	98.2
43	183	133486	1.1	12.3924	0.9	2.3381	1.7	0.2101	1.5	0.86	1229.6	16.6	1224.0	12.3	1214.0	17.5	1214.0	17.5	101.3
55	194	88356	1.3	12.2323	0.5	2.3670	1.2	0.2100	1.1	0.92	1228.8	11.9	1232.7	8.3	1239.6	8.9	1239.6	8.9	99.1
15	144	140502	0.2	11.3159	0.6	2.9960	1.3	0.2459	1.2	0.90	1417.2	15.0	1406.6	10.1	1390.5	11.3	1390.5	11.3	101.9
91	133	175471	1.5	11.2402	0.6	2.9757	0.8	0.2426	0.5	0.67	1400.1	6.6	1401.4	5.9	1403.4	11.0	1403.4	11.0	99.8
81	163	153148	2.0	11.2106	0.5	2.8407	1.1	0.2310	1.0	0.90	1339.6	11.8	1366.4	8.1	1408.5	9.1	1408.5	9.1	95.1
27	49	37670	1.2	10.9831	2.3	3.1693	2.5	0.2525	1.0	0.40	1451.1	13.0	1449.7	19.2	1447.6	43.3	1447.6	43.3	100.2
94	164	108613	2.0	10.9592	4.8	3.2075	5.0	0.2549	1.1	0.21	1463.9	13.9	1459.0	38.4	1451.7	92.2	1451.7	92.2	100.8
76	81	113795	0.9	10.1760	1.1	3.7989	1.2	0.2804	0.4	0.36	1593.2	6.1	1592.5	9.7	1591.5	21.1	1591.5	21.1	100.1
36	473	166143	1.5	9.4124	0.2	4.0644	1.7	0.2775	1.6	0.99	1578.6	23.0	1647.2	13.5	1735.9	3.0	1735.9	3.0	90.9
47	113	59967	1.1	9.4022	0.5	4.5075	1.9	0.3074	1.8	0.96	1727.8	27.8	1732.4	15.9	1737.9	9.7	1737.9	9.7	99.4
56	247	97954	2.6	9.1688	0.2	4.5776	0.9	0.3044	0.9	0.96	1713.1	13.1	1745.2	7.5	1783.9	4.3	1783.9	4.3	96.0
66	1131	836799	4.1	8.9661	0.3	4.5807	4.7	0.2979	4.7	1.00	1680.8	69.7	1745.8	39.3	1824.5	4.6	1824.5	4.6	92.1
83	184	154792	2.2	6.8446	0.4	8.7318	3.0	0.4335	3.0	0.99	2321.3	58.5	2310.4	27.6	2300.8	7.4	2300.8	7.4	100.9
23	153	221734	1.1	5.3518	0.2	13.4395	0.6	0.5216	0.5	0.93	2706.2	12.1	2711.0	5.6	2714.7	3.4	2714.7	3.4	99.7
64	129	292508	2.1	3.2904	1.0	29.0661	1.9	0.6936	1.6	0.85	3396.5	43.4	3455.8	19.0	3490.3	15.7	3490.3	15.7	97.3

1. All uncertainties are reported at the 1-sigma level, and include only measurement errors.
2. U concentration and U/Th are calibrated relative to our Sri Lanka zircon and are accurate to ~20%.
3. Common Pb correction is from ^{204}Pb, with composition interpreted from Stacey and Kramers (1975) and uncertainties of 1.0 for 206Pb/204Pb, 0.3 for 207Pb/204Pb, and 2.0 for 208Pb/204Pb.
4. U/Pb and ^{206}Pb/^{207}Pb fractionation is calibrated relative to fragments of a large Sri Lanka zircon of 563.5 ± 3.2 Ma (2-sigma).
5. U decay constants and composition as follows: ^{238}U = 9.8485 x 10^{-10}, ^{235}U = 1.55125 x 10^{-10}, ^{238}U/^{235}U = 137.88

Table C.7. Whole-rock oxygen isotope results

Sample	Std/Unkn	mg	µml	µml/mg	$\delta^{18}O$ raw	$\delta^{18}O$ crrtd (smow)
UWG-2	std	2.50	32.1	12.8	5.68	
UWG-2	std	2.95	38.4	13.0	5.66	
UWG-2	std	3.36	41.3	12.3	5.83	
UWG-2	std	4.00	51.2	12.8	5.80	
K6-SR29a	WR	2.53	36.3	14.3	12.73	12.77
K6-SR30	WR	2.58	38.2	14.8	13.44	13.48
K6-SR32	WR	3.09	45.4	14.7	9.96	10.00
10CY-001	WR	2.41	35.4	14.7	-6.89	-6.85
10CY-002	WR	2.74	39.7	14.5	-9.16	-9.12
Y2-MP098	WR	2.77	40.4	14.6	11.98	12.02
Y2-BR086	WR	2.44	35.9	14.7	10.00	10.04
Y2-MD092	WR	2.97	42.3	14.2	13.29	13.33
UWG-2	std	3.06	39.7	13.0	5.81	

Notes:
UWG-2: n= 5, x = 5.76, ± 0.08, 1 St. Dev.

Table C.8. Hf isotope analyses for detrital zircons

Spot	Age (Ma)	(^{176}Yb + ^{176}Lu) /^{176}Hf (%)	Volts Hf	^{176}Hf/^{177}Hf	± (1s)	^{176}Lu/^{177}Hf	^{176}Hf/^{177}Hf $_{(t)}$	$\varepsilon_{Hf(0)}$	± 1s	$\varepsilon_{Hf(t)}$
Y2-MP098										
6	595	9.3	2.5	0.281726	0.000031	0.000689	0.281719	-37.4	1.1	-24.5
9	541	6.9	2.2	0.282313	0.000031	0.000407	0.282309	-16.7	1.1	-4.8
10	1819	17.6	2.3	0.281711	0.000041	0.001156	0.281671	-38.0	1.5	1.7
12	1117	18.4	2.2	0.282223	0.000030	0.001230	0.282197	-19.9	1.0	4.3
13	1168	57.6	1.5	0.282246	0.000048	0.003033	0.282179	-19.1	1.7	4.8
14	2782	13.4	1.9	0.280949	0.000030	0.000802	0.280906	-64.9	1.1	-3.1
16	1023	14.3	2.7	0.282312	0.000028	0.000787	0.282297	-16.7	1.0	5.7
17	947	17.9	1.7	0.282286	0.000041	0.001110	0.282266	-17.7	1.5	2.8
19	770	28.2	2.3	0.282312	0.000036	0.001681	0.282288	-16.7	1.3	-0.4
21	1054	8.1	2.2	0.282380	0.000038	0.000499	0.282370	-14.3	1.3	9.0
22	551	2.8	2.3	0.282295	0.000029	0.000167	0.282293	-17.3	1.0	-5.1
27	1046	11.6	2.1	0.282226	0.000028	0.000703	0.282212	-19.8	1.0	3.2
33	508	36.5	2.5	0.282236	0.000038	0.002256	0.282214	-19.4	1.4	-8.9
35	982	36.2	1.7	0.282273	0.000044	0.002210	0.282232	-18.1	1.6	2.4
40	998	9.3	1.6	0.282116	0.000037	0.000607	0.282105	-23.7	1.3	-1.7
43	589	2.2	2.1	0.282439	0.000029	0.000129	0.282437	-12.3	1.0	0.8
46	567	11.9	2.2	0.282375	0.000029	0.000714	0.282367	-14.5	1.0	-2.1
47	568	10.1	2.3	0.282281	0.000037	0.000601	0.282275	-17.8	1.3	-5.4
48	955	25.7	2.1	0.282187	0.000040	0.001441	0.282161	-21.2	1.4	-0.7
49	1868	9.7	2.3	0.281521	0.000031	0.000578	0.281500	-44.7	1.1	-3.3
50	525	5.4	2.1	0.282329	0.000044	0.000326	0.282326	-16.1	1.6	-4.5
53	1068	10.4	2.1	0.282209	0.000033	0.000613	0.282196	-20.4	1.2	3.1
54	1062	10.2	2.0	0.281984	0.000039	0.000611	0.281972	-28.3	1.4	-5.0
58	1731	17.3	2.0	0.281510	0.000038	0.001024	0.281476	-45.1	1.4	-7.3
61	797	12.5	2.2	0.282290	0.000031	0.000853	0.282277	-17.5	1.1	-0.2
62	613	30.6	2.6	0.282071	0.000034	0.001822	0.282050	-25.2	1.2	-12.3
64	1166	4.3	2.3	0.281896	0.000030	0.000212	0.281891	-31.4	1.1	-5.5
65	1090	18.0	2.0	0.282139	0.000035	0.001041	0.282118	-22.8	1.2	0.9
67	1704	15.4	2.0	0.281249	0.000039	0.000946	0.281218	-54.3	1.4	-17.1
70	965	34.5	2.3	0.282129	0.000035	0.001954	0.282093	-23.2	1.2	-2.9
71	686	19.1	1.8	0.282342	0.000038	0.001147	0.282328	-15.6	1.3	-0.9
72	1679	9.6	2.4	0.281849	0.000033	0.000555	0.281831	-33.1	1.2	4.1
75	644	8.0	2.6	0.282446	0.000036	0.000459	0.282440	-12.0	1.3	2.2
76	570	0.9	2.8	0.282492	0.000027	0.000052	0.282491	-10.4	1.0	2.3
90	1721	13.5	2.2	0.281921	0.000037	0.000869	0.281893	-30.5	1.3	7.3
102	607	12.0	2.5	0.282436	0.000035	0.000736	0.282428	-12.3	1.2	0.9
91	1788	28.1	2.6	0.281651	0.000032	0.001647	0.281596	-40.1	1.1	-1.7
87	2018	16.3	2.7	0.281202	0.000033	0.000893	0.281168	-56.0	1.2	-11.6
82	550	8.5	2.8	0.282295	0.000031	0.000475	0.282291	-17.3	1.1	-5.2
78	1749	12.8	2.5	0.281583	0.000033	0.000733	0.281559	-42.5	1.2	-3.9
80	1081	17.0	2.2	0.282401	0.000036	0.001386	0.282372	-13.6	1.3	9.7
95	576	1.3	3.1	0.282245	0.000038	0.000060	0.282244	-19.1	1.3	-6.3
96	1402	28.1	2.3	0.282070	0.000040	0.001567	0.282029	-25.3	1.4	4.8
97	515	18.7	2.7	0.282307	0.000024	0.001198	0.282295	-16.9	0.8	-5.9
98	699	14.7	2.0	0.282600	0.000027	0.000884	0.282589	-6.5	1.0	8.7

Table C.8 continued. Hf isotope analyses for detrital zircons

Spot	Age (Ma)	(^{176}Yb + ^{176}Lu) /^{176}Hf (%)	Volts Hf	^{176}Hf/^{177}Hf	± (1s)	^{176}Lu/^{177}Hf	^{176}Hf/^{177}Hf $_{(t)}$	$\varepsilon_{Hf(0)}$	± 1s	$\varepsilon_{Hf(t)}$
Y2-MD092										
41	1066	17.9	2.4	0.282305	0.000034	0.000960	0.282285	-17.0	1.2	6.2
43	1802	44.0	2.7	0.281579	0.000028	0.002587	0.281490	-42.7	1.0	-5.2
45	711	9.1	2.6	0.282246	0.000025	0.000554	0.282239	-19.1	0.9	-3.5
47	574	0.5	2.8	0.282367	0.000040	0.000029	0.282367	-14.8	1.4	-2.0
48	1057	29.2	2.4	0.282198	0.000028	0.001617	0.282166	-20.7	1.0	1.8
55	2019	22.9	2.8	0.281348	0.000030	0.001238	0.281301	-50.8	1.1	-6.9
57	1100	27.9	3.2	0.282255	0.000032	0.001542	0.282223	-18.7	1.1	4.8
60	1022	36.4	3.0	0.282248	0.000032	0.002066	0.282209	-19.0	1.1	2.5
62	557	1.1	2.7	0.282361	0.000026	0.000068	0.282360	-15.0	0.9	-2.6
63	551	34.4	2.7	0.282281	0.000037	0.001760	0.282262	-17.8	1.3	-6.2
45A	711	60.6	2.3	0.282474	0.000054	0.004084	0.282420	-11.0	1.9	3.0
67	953	20.5	1.9	0.282205	0.000047	0.001129	0.282185	-20.5	1.6	0.1
70	765	9.5	2.4	0.282242	0.000030	0.000541	0.282234	-19.2	1.1	-2.4
72	1763	8.4	3.0	0.281525	0.000029	0.000526	0.281507	-44.6	1.0	-5.4
73	2640	39.9	2.3	0.281190	0.000037	0.002263	0.281075	-56.4	1.3	-0.4
_2	799	19.3	3.0	0.282457	0.000032	0.001080	0.282441	-11.6	1.1	5.7
_5	2740	37.2	3.3	0.280989	0.000032	0.002148	0.280876	-63.5	1.1	-5.2
_9	1049	36.1	3.1	0.282386	0.000033	0.002198	0.282342	-14.1	1.2	7.9
10	1864	19.6	2.5	0.281583	0.000031	0.001227	0.281540	-42.5	1.1	-2.0
11	1031	13.6	2.7	0.282194	0.000031	0.000839	0.282178	-20.9	1.1	1.6
12	937	13.6	2.5	0.281880	0.000035	0.000826	0.281865	-32.0	1.2	-11.6
14	2565	4.1	3.3	0.281063	0.000026	0.000236	0.281052	-60.9	0.9	-3.0
18	1455	22.0	2.9	0.282025	0.000026	0.001347	0.281988	-26.9	0.9	4.5
21	525	10.7	3.2	0.282265	0.000030	0.000602	0.282259	-18.4	1.0	-6.9
23	1151	12.0	2.8	0.282245	0.000029	0.000712	0.282230	-19.1	1.0	6.2
27	480	35.8	2.3	0.282644	0.000035	0.002037	0.282626	-5.0	1.3	5.1
29	435	8.4	1.8	0.282135	0.000039	0.000476	0.282131	-23.0	1.4	-13.4
31	2830	17.6	3.6	0.280864	0.000032	0.000943	0.280813	-67.9	1.1	-5.3
32	585	7.6	2.6	0.282386	0.000030	0.000455	0.282381	-14.1	1.1	-1.2
38	570	2.9	2.9	0.282331	0.000035	0.000178	0.282329	-16.0	1.2	-3.4
74	1726	6.4	3.1	0.281736	0.000022	0.000482	0.281720	-37.1	0.8	1.3
75	1028	8.6	2.2	0.282306	0.000030	0.000540	0.282296	-16.9	1.1	5.7
78	557	76.3	2.2	0.282493	0.000036	0.004576	0.282445	-10.3	1.3	0.4
79	1115	15.8	2.7	0.282280	0.000029	0.000973	0.282259	-17.9	1.0	6.4
81	599	0.8	2.9	0.282542	0.000024	0.000045	0.282542	-8.6	0.9	4.8
82	1816	10.9	2.2	0.281482	0.000027	0.000735	0.281456	-46.1	1.0	-6.0
83	541	1.0	2.7	0.282399	0.000030	0.000077	0.282398	-13.7	1.0	-1.6
85	488	4.6	2.6	0.282440	0.000033	0.000307	0.282437	-12.2	1.2	-1.4
86	622	10.4	2.5	0.282424	0.000032	0.000613	0.282417	-12.8	1.1	0.9
90	564	20.9	2.1	0.282070	0.000045	0.001381	0.282055	-25.3	1.6	-13.2
92	979	23.6	2.1	0.282418	0.000039	0.001619	0.282388	-13.0	1.4	7.9
94	3034	16.3	1.9	0.280714	0.000039	0.001013	0.280655	-73.2	1.4	-6.1
95	1027	14.2	2.1	0.282384	0.000038	0.000915	0.282366	-14.2	1.3	8.2
96	527	83.8	1.8	0.282459	0.000060	0.004933	0.282411	-11.5	2.1	-1.5
99	1746	11.9	2.3	0.281781	0.000030	0.000815	0.281754	-35.5	1.1	2.9
100	878	12.6	1.9	0.282257	0.000040	0.000939	0.282242	-18.7	1.4	0.4
103	1040	8.6	2.3	0.282332	0.000024	0.000509	0.282322	-16.0	0.8	6.9
104	1775	1.2	2.9	0.281607	0.000020	0.000075	0.281604	-41.7	0.7	-1.7
105	1254	10.5	2.3	0.282219	0.000031	0.000668	0.282203	-20.0	1.1	7.6

Notes;
^{176}Lu decay constant of 1.867×10^{-11} (Soderlund et al. 2004).
^{176}Hf/^{177}Hf and ^{176}Lu/^{177}Hf CHUR values of 0.282785 and 0.0336 (Bouvier et al. 2008).

Table C.9. Hf and O isotope analyses of zircons from granites

spot	assigned age (Ma)	$^{18}O/^{16}O$	$\pm10^{-7}$	$\delta^{18}O$ (‰)	± 2 S.E.	$^{176}Hf/^{177}Hf$	$\pm10^{-6}$	$^{176}Lu/^{177}Hf$	$\pm10^{-5}$	$\varepsilon_{Hf(0)}$	$^{176}Hf/^{177}Hf_{(t)}$	$\varepsilon_{Hf(t)}$	± 2 S.E.
MB.214.1W (Yakymchuk et al., 2013)													
1	377	0.0020390	2	7.10	0.48	0.282626	22	0.000769	1	-5.6	0.282621	2.6	0.8
2	377	0.0020411	5	8.11	0.52	0.282634	28	0.001273	4	-5.3	0.282625	2.8	1.0
3	377	0.0020375	5	6.36	0.53	0.282597	23	0.000939	4	-6.6	0.282590	1.5	0.8
5	377	0.0020388	4	7.00	0.51	0.282638	24	0.000937	2	-5.2	0.282632	3.0	0.8
6	377	0.0020391	5	7.13	0.53	0.282597	29	0.001386	3	-6.7	0.282587	1.4	1.0
7	377	0.0020389	6	7.05	0.54	0.282619	27	0.001238	3	-5.9	0.282610	2.2	1.0
8	377	0.0020400	6	7.56	0.55	0.282678	30	0.002069	8	-3.8	0.282663	4.1	1.1
9	377	0.0020479	6	11.46	0.54	0.282656	24	0.000998	3	-4.6	0.282649	3.6	0.9
10	377	0.0020384	4	6.80	0.51	0.282642	31	0.001181	9	-5.1	0.282633	3.0	1.1
12	377	0.0020395	5	7.34	0.53	0.282602	46	0.000851	6	-6.5	0.282596	1.7	1.6
13	377	0.0020386	4	6.89	0.51	0.282659	31	0.000788	5	-4.5	0.282653	3.7	1.1
14	377	0.0020395	4	7.32	0.50	0.282603	47	0.001346	6	-6.4	0.282593	1.6	1.7
MB.219.1W (Yakymchuk et al., 2013)													
1	373	0.0020397	2	7.44	0.49	0.282601	28	0.001647	4	-6.5	0.282589	1.4	1.0
2	373	0.0020377	6	6.44	0.50	0.282660	27	0.001058	4	-4.4	0.282653	3.6	1.0
3	373	0.0020392	6	7.20	0.52	0.282622	31	0.001884	7	-5.8	0.282609	2.1	1.1
4	373	0.0020410	8	8.07	0.51	0.282571	22	0.001708	4	-7.6	0.282559	0.3	0.8
5	373	0.0020388	7	7.01	0.50	0.282585	25	0.001879	2	-7.1	0.282572	0.8	0.9
6	373	0.0020384	2	6.78	0.49	0.282611	26	0.001522	3	-6.1	0.282601	1.8	0.9
7	811	0.0020346	7	4.93	0.48	0.282179	26	0.001214	2	-21.4	0.282160	-4.0	0.9
9	373	0.0020391	1	7.14	0.48	0.282668	31	0.001623	7	-4.1	0.282657	3.8	1.1
10	373	0.0020386	9	6.89	0.49	0.282571	28	0.001863	6	-7.6	0.282558	0.3	1.0
11.1	599	0.0020369	9	6.07	0.50	0.282170	23	0.000624	2	-21.7	0.282163	-8.6	0.8
11.2	373	0.0020363	8	5.77	0.50	–	–	–	–	–	–	–	–
912-2A													
1	345	0.0020472	6	8.69	0.52	0.282471	36	0.00168	4	-11.1	0.282460	-3.8	1.3
2	345	0.0020480	5	9.12	0.49	0.282573	75	0.00161	8	-7.5	0.282563	-0.2	2.7
5	345	0.0020462	5	8.21	0.50	0.282605	88	0.00152	9	-6.4	0.282595	1.0	3.1
8	345	0.0020478	5	9.02	0.51	0.282577	80	0.00104	8	-7.3	0.282571	0.1	2.8
9	345	0.0020468	4	8.50	0.48	0.282569	57	0.00114	6	-7.6	0.282562	-0.2	2.0
11	345	0.0020458	5	8.02	0.50	0.282621	50	0.00120	5	-5.8	0.282614	1.6	1.8
13	345	0.0020464	5	8.32	0.51	0.282439	13	0.00131	1	-12.2	0.282431	-4.8	0.5
14	345	0.0020470	4	8.60	0.47	0.282509	56	0.00140	6	-9.8	0.282500	-2.4	2.0
15	345	0.0020472	4	8.73	0.48	–	–	–	–	–	–	–	–
17	345	0.0020483	5	9.26	0.50	0.282189	24	0.00187	2	-21.1	0.282177	-13.8	0.8
18	345	0.0020478	5	9.01	0.51	0.282543	38	0.00155	4	-8.5	0.282533	-1.2	1.3
19	345	0.0020472	5	8.73	0.49	0.282559	100	0.00186	10	-8.0	0.282547	-0.7	3.5
20	345	0.0020468	5	8.52	0.50	0.282628	140	0.00117	14	-5.5	0.282621	1.9	5.0
21	345	0.0020475	5	8.88	0.50	0.282469	63	0.00174	6	-11.2	0.282458	-3.9	2.2
22	345	0.0020446	4	7.44	0.49	0.282479	150	0.00182	15	-10.8	0.282467	-3.5	5.3
9N27-4													
1	354	0.0020441	5	7.20	0.51	0.282455	30	0.00097	3	-11.7	0.282449	-4.0	1.1
3	354	0.0020447	6	7.50	0.53	0.282453	16	0.00086	2	-11.7	0.282448	-4.1	0.6
4	354	0.0020443	5	7.32	0.50	0.282511	42	0.00141	4	-9.7	0.282502	-2.1	1.5
5	354	0.0020451	5	7.70	0.49	0.282569	94	0.00121	9	-7.6	0.282561	0.0	3.3
7	354	0.0020458	4	8.02	0.48	0.282578	41	0.00134	4	-7.3	0.282569	0.2	1.5
8	354	0.0020437	5	7.01	0.49	0.282573	55	0.00138	6	-7.5	0.282564	0.1	1.9
10	354	0.0020447	6	7.49	0.52	0.282549	38	0.00101	4	-8.3	0.282543	-0.7	1.3
11	354	0.0020492	5	9.69	0.51	0.282458	76	0.00098	8	-11.6	0.282452	-3.9	2.7
12	354	0.0020490	5	9.60	0.50	0.282421	64	0.00127	6	-12.9	0.282413	-5.3	2.3
13	354	0.0020461	5	8.20	0.50	0.282431	13	0.00097	1	-12.5	0.282425	-4.9	0.5
14	354	0.0020469	5	8.56	0.50	0.282509	88	0.00112	9	-9.8	0.282502	-2.1	3.1
15	354	0.0020446	6	7.47	0.52	0.282556	41	0.00097	4	-8.1	0.282550	-0.4	1.5
18	354	0.0020446	5	7.45	0.51	0.282554	84	0.00081	8	-8.2	0.282549	-0.5	3.0
19	354	0.0020445	5	7.40	0.50	0.282531	18	0.00158	2	-9.0	0.282521	-1.5	0.6
20	354	0.0020450	6	7.66	0.52	0.282471	150	0.00073	15	-11.1	0.282466	-3.4	5.3

Table C.9 continued. Hf and O isotope analyses of zircons from granites

spot	assigned age (Ma)	$^{18}O/^{16}O$	$\pm10^{-7}$	$\delta^{18}O$ (‰)	± 2 S.E.	$^{176}Hf/^{177}Hf$	$\pm10^{-6}$	$^{176}Lu/^{177}Hf$	$\pm10^{-5}$	$\varepsilon_{Hf(0)}$	$^{176}Hf/^{177}Hf_{(t)}$	$\varepsilon_{Hf(t)}$	± 2 S.E.
51225-2													
1	364	0.0020465	3	9.96	0.37	0.282472	36	0.00200	3	-11.1	0.282459	-3.4	1.3
2	364	0.0020462	2	9.80	0.36	0.282561	41	0.00106	2	-7.9	0.282554	0.0	1.5
3	364	0.0020433	0	8.38	0.35	0.282565	37	0.00196	7	-7.8	0.282552	-0.1	1.3
5	364	0.0020464	1	9.89	0.35	0.282534	43	0.00160	2	-8.9	0.282524	-1.1	1.5
7.2	364	0.0020356	2	4.61	0.36	0.282497	37	0.00185	4	-10.2	0.282485	-2.5	1.3
8	364	0.0020457	0	9.55	0.35	0.282553	39	0.00132	1	-8.2	0.282545	-0.4	1.4
9.1	364	0.0020457	2	9.55	0.36	0.282432	36	0.00058	4	-12.5	0.282429	-4.5	1.3
9.2	364	0.0020443	1	8.85	0.36	0.282312	36	0.00003	0	-16.7	0.282312	-8.6	1.3
10	364	0.0020470	1	10.20	0.36	0.282499	32	0.00099	12	-10.1	0.282493	-2.2	1.1
11.2	364	0.0020441	2	8.79	0.36	0.282535	51	0.00183	10	-8.8	0.282523	-1.2	1.8
12	364	0.0020460	2	9.70	0.36	0.282577	52	0.00121	4	-7.3	0.282569	0.5	1.8
13	364	0.0020458	2	9.61	0.36	0.282498	33	0.00202	4	-10.1	0.282485	-2.5	1.2
15	364	0.0020449	1	9.14	0.35	0.282506	39	0.00123	3	-9.8	0.282498	-2.0	1.4
15.2	364	0.0020414	1	7.47	0.36	0.282295	34	0.00135	6	-17.3	0.282286	-9.5	1.2
17	364	0.0020477	1	10.54	0.35	0.282450	29	0.00146	11	-11.8	0.282441	-4.1	1.0
18	364	0.0020453	0	9.37	0.35	0.282516	40	0.00138	2	-9.5	0.282507	-1.7	1.4
19	364	0.0020456	2	9.48	0.36	0.282529	34	0.00168	7	-9.0	0.282518	-1.3	1.2
Y2-JU096													
1	367	0.0020421	1	7.40	0.30	0.282501	32	0.00184	3	-10.0	0.282489	-2.3	1.1
2	367	0.0020429	2	7.82	0.32	0.282560	41	0.00060	1	-7.9	0.282556	0.1	1.5
3	367	0.0020465	3	9.56	0.34	0.282516	51	0.00122	3	-9.5	0.282508	-1.6	1.8
4	377	0.0020459	1	9.28	0.30	0.282528	54	0.00271	25	-9.1	0.282510	-1.6	1.9
5	367	0.0020444	1	8.56	0.30	0.282561	44	0.00071	2	-7.9	0.282557	0.1	1.6
6.1	377	0.0020471	1	9.86	0.30	0.282466	51	0.00191	8	-11.3	0.282453	-3.6	1.8
6.2	367	0.0020458	3	9.23	0.34	0.282441	40	0.00153	9	-12.1	0.282431	-4.4	1.4
8	377	0.0020433	1	8.02	0.30	0.282541	38	0.00086	1	-8.6	0.282536	-0.7	1.3
9	367	0.0020455	0	9.09	0.30	0.282500	41	0.00125	6	-10.1	0.282492	-2.2	1.5
10	367	0.0020438	1	8.26	0.30	0.282459	45	0.00181	5	-11.5	0.282447	-3.8	1.6
11	367	0.0020448	2	8.72	0.30	0.282580	87	0.00119	7	-7.2	0.282572	0.6	3.1
12	377	0.0020453	1	8.99	0.30	0.282455	37	0.00115	2	-11.7	0.282448	-3.8	1.3
13	367	0.0020466	2	9.62	0.32	0.282489	49	0.00139	3	-10.4	0.282480	-2.6	1.7
14	377	0.0020453	2	8.97	0.31	0.282500	42	0.00206	6	-10.1	0.282486	-2.4	1.5
17	367	0.0020438	1	8.24	0.30	0.282527	37	0.00103	5	-9.1	0.282520	-1.2	1.3
18	367	0.0020463	2	9.47	0.30	0.282480	44	0.00113	6	-10.8	0.282473	-2.9	1.6
19	367	0.0020437	1	8.19	0.30	0.282587	56	0.00054	0	-7.0	0.282584	1.0	2.0
20	367	0.0020441	1	8.39	0.30	0.282609	41	0.00119	4	-6.2	0.282601	1.7	1.5
Y1-IG073													
1.1	362	0.0020473	4	10.32	0.38	0.282456	36	0.00070	1	-10.0	0.282452	-3.7	1.3
1.2	362	0.0020469	3	10.13	0.35	0.282464	29	0.00072	2	-11.9	0.282460	-3.5	1.1
2.1	362	0.0020458	1	9.59	0.35	0.282458	27	0.00160	9	-10.2	0.282448	-3.9	1.0
3.1	362	0.0020451	6	9.26	0.36	0.282489	27	0.00050	0	-10.6	0.282486	-2.5	1.0
4.1	362	0.0020473	6	10.36	0.36	0.282488	37	0.00122	2	-9.1	0.282480	-2.7	1.4
5.1	362	0.0020474	6	10.39	0.37	0.282489	43	0.00100	3	-9.5	0.282483	-2.6	1.6
6.1	362	0.0020457	1	9.55	0.36	0.282472	32	0.00095	2	-9.1	0.282466	-3.2	1.2
7.1	362	0.0020457	8	9.54	0.36	0.282481	34	0.00102	5	-8.8	0.282475	-2.9	1.3
8.1	362	0.0020460	9	9.70	0.35	0.282502	38	0.00060	2	-8.5	0.282498	-2.1	1.5
9.1	362	0.0020465	6	9.96	0.35	0.282465	38	0.00063	1	-8.2	0.282461	-3.4	1.4
10.1	362	0.0020460	4	9.71	0.36	0.282460	37	0.00087	3	-7.9	0.282455	-3.6	1.4
11.1	362	0.0020450	6	9.21	0.36	0.282461	32	0.00055	1	-7.6	0.282458	-3.5	1.2
13.1	362	0.0020435	1	8.49	0.35	0.282496	27	0.00147	2	-7.3	0.282487	-2.5	1.0
14.1	362	0.0020463	2	9.82	0.35	0.282465	37	0.00097	3	-7.0	0.282459	-3.5	1.4
15.2	362	0.0020449	7	9.17	0.35	0.282487	34	0.00059	4	-6.7	0.282483	-2.6	1.3
16.1	362	0.0020459	2	9.67	0.36	0.282474	34	0.00074	1	-6.4	0.282469	-3.1	1.3
18.1	362	0.0020438	1	8.64	0.36	0.282462	46	0.00086	2	-6.1	0.282457	-3.6	1.7
19.1	362	0.0020457	8	9.55	0.36	0.282472	33	0.00074	3	-5.7	0.282467	-3.2	1.2
20.1	362	0.0020450	6	9.23	0.36	0.282490	43	0.00087	6	-5.4	0.282485	-2.6	1.6

Table C.9 continued. Hf and O isotope analyses of zircons from granites

spot	assigned age (Ma)	$^{18}O/^{16}O$	$\pm10^{-7}$	$\delta^{18}O$ (‰)	± 2 S.E.	$^{176}Hf/^{177}Hf$	$\pm10^{-6}$	$^{176}Lu/^{177}Hf$	$\pm10^{-5}$	$\varepsilon_{Hf(0)}$	$^{176}Hf/^{177}Hf_{(t)}$	$\varepsilon_{Hf(t)}$	± 2 S.E.
Y1-IG071													
1.1	360	0.0020461	2	9.37	0.31	0.282451	36	0.00103	12	-11.8	0.282445	-4.0	1.3
3.1	360	0.0020462	3	9.43	0.34	0.282483	45	0.00245	11	-10.7	0.282467	-3.2	1.6
4.1	100	0.0020478	1	10.19	0.30	0.282539	36	0.00144	1	-8.7	0.282537	-6.6	1.3
4.2	689	0.0020450	2	8.82	0.32	0.282340	45	0.00046	4	-15.7	0.282335	-0.6	1.6
4.3	360	0.0020481	2	10.36	0.30	0.282356	26	0.00084	2	-15.2	0.282351	-7.3	0.9
5.1	100	0.0020463	2	9.49	0.31	0.282540	28	0.00155	3	-8.6	0.282538	-6.5	1.0
6.1	100	0.0020474	2	10.00	0.31	0.282567	26	0.00126	2	-7.7	0.282565	-5.6	0.9
8.1	100	0.0020477	2	10.14	0.31	0.282565	50	0.00118	2	-7.8	0.282563	-5.6	1.8
8.2	1696	0.0020419	1	7.32	0.30	0.281601	37	0.00065	1	-41.9	0.281580	-4.4	1.3
9.1	100	0.0020470	1	9.83	0.30	0.282477	34	0.00095	4	-10.9	0.282476	-8.7	1.2
10.1	360	0.0020486	3	10.60	0.32	0.282365	29	0.00114	2	-14.8	0.282358	-7.1	1.0
12.1	360	0.0020482	1	10.42	0.30	0.282285	27	0.00042	9	-17.7	0.282283	-9.8	1.0
14.2	2277	0.0020418	2	7.27	0.31	0.281289	49	0.00052	2	-52.9	0.281266	-2.1	1.7
15.1	100	0.0020467	1	9.68	0.30	0.282596	55	0.00178	2	-6.7	0.282593	-4.6	1.9
16.1	100	0.0020462	4	9.43	0.35	0.282440	33	0.00105	6	-12.2	0.282439	-10.0	1.2
17.1	100	0.0020465	1	9.58	0.30	0.282498	33	0.00102	1	-10.1	0.282497	-8.0	1.2
18.1	360	0.0020474	2	10.01	0.32	0.282528	83	0.00106	2	-9.1	0.282521	-1.3	2.9
19.1	100	0.0020366	1	4.71	0.30	0.282343	46	0.00100	4	-15.6	0.282342	-13.5	1.6
19.2	923	0.0020372	1	4.98	0.30	0.282298	45	0.00096	4	-17.2	0.282282	2.9	1.6
20.1	100	0.0020469	1	9.79	0.30	0.282502	30	0.00088	1	-10.0	0.282501	-7.8	1.1
20.2	568	0.0020457	1	9.17	0.30	0.282320	39	0.00090	7	-16.4	0.282311	-4.1	1.4
C5-I51a (Yakymchuk et al., 2013)													
1	353	0.0020490	6	9.57	0.36	0.282415	21	0.00103	10	-13.1	0.282408	-5.5	0.7
3	353	0.0020465	19	8.34	0.97	0.282591	26	0.00093	9	-6.9	0.282584	0.8	0.9
4	353	0.0020467	5	8.44	0.34	0.282509	30	0.00096	10	-9.8	0.282502	-2.1	1.1
7	1055	0.0020436	6	6.92	0.35	0.282221	41	0.00191	20	-19.9	0.282183	2.4	1.4
8	353	0.0020516	5	10.84	0.32	0.282498	34	0.00098	10	-10.1	0.282492	-2.5	1.2
9	353	–	–	–	–	0.282441	23	0.00106	11	-12.2	0.282434	-4.6	0.8
10	353	0.0020567	11	12.61	0.67	0.282492	30	0.00125	12	-10.4	0.282484	-2.8	1.1
12	353	0.0020566	16	12.58	0.88	–	–	–	–	–	–	–	–
13	353	0.0020565	5	12.53	0.47	0.282550	36	0.00048	5	-8.3	0.282547	-0.6	1.3
14	353	–	–	–	–	0.282479	27	0.00129	13	-10.8	0.282470	-3.3	1.0
M5-G175 (Yakymchuk et al., 2013)													
1.1	369	0.0020483	4	8.53	0.45	0.282565	27	0.00130	4	-7.8	0.282556	0.1	0.9
2.1	369	0.0020464	5	7.59	0.47	0.282386	22	0.00093	2	-14.1	0.282379	-6.1	0.8
2.2	630	0.0020403	5	4.63	0.48	–	–	–	–	–	–	–	–
3	369	0.0020458	4	8.75	0.28	0.282457	28	0.00160	3	-11.6	0.282446	-3.8	1.0
4	369	0.0020458	4	8.71	0.29	0.282463	50	0.00146	4	-11.4	0.282453	-3.5	1.8
5	369	0.0020437	4	6.26	0.46	0.282504	30	0.00115	2	-9.9	0.282496	-2.0	1.1
6	369	0.0020474	4	9.53	0.28	0.282570	78	0.00206	6	-7.6	0.282556	0.1	2.7
7	369	0.0020428	7	5.84	0.52	0.282569	30	0.00185	6	-7.6	0.282557	0.1	1.1
9	369	0.0020437	5	7.72	0.32	0.282544	21	0.00077	4	-8.5	0.282539	-0.5	0.7
10	369	0.0020462	3	8.95	0.24	0.282416	21	0.00104	2	-13.0	0.282409	-5.1	0.7
11	369	0.0020476	4	9.59	0.26	0.282403	40	0.00140	3	-13.5	0.282393	-5.7	1.4
15	369	0.0020420	3	6.85	0.25	0.282571	23	0.00102	1	-7.6	0.282564	0.4	0.8
16	369	0.0020459	3	8.77	0.25	0.282506	27	0.00110	4	-9.9	0.282498	-1.9	0.9

Notes;
^{176}Lu decay constant of 1.865×10^{-11} (Soderlund et al. 2004).
$^{176}Hf/^{177}Hf$ and $^{176}Lu/^{177}Hf$ CHUR values of 0.282785 and 0.0336 (Bouvier et al. 2008).

Appendix D.

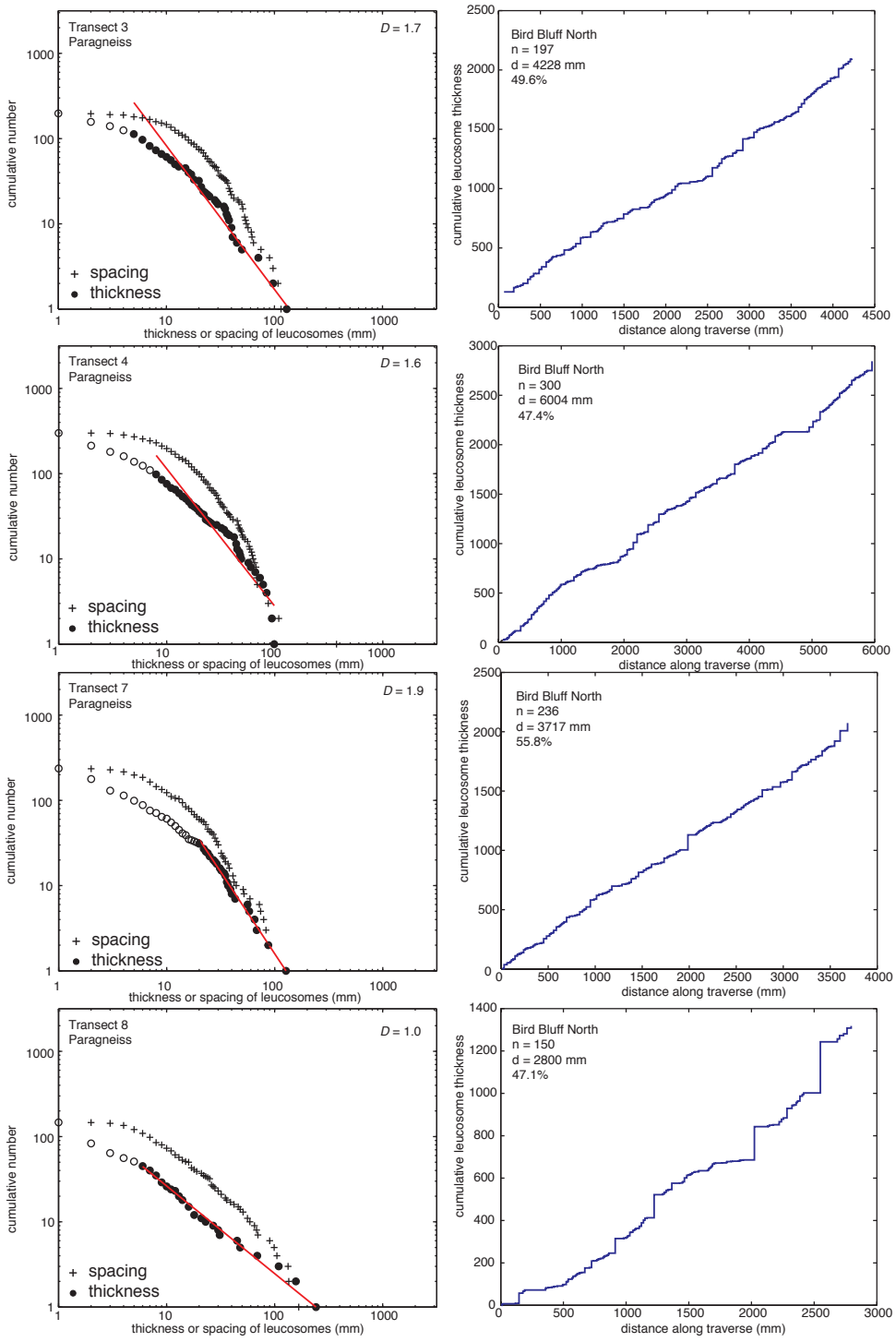

Fig. D.1. Cumulative thickness and log–log cumulative thickness–spacing plots for all transects.

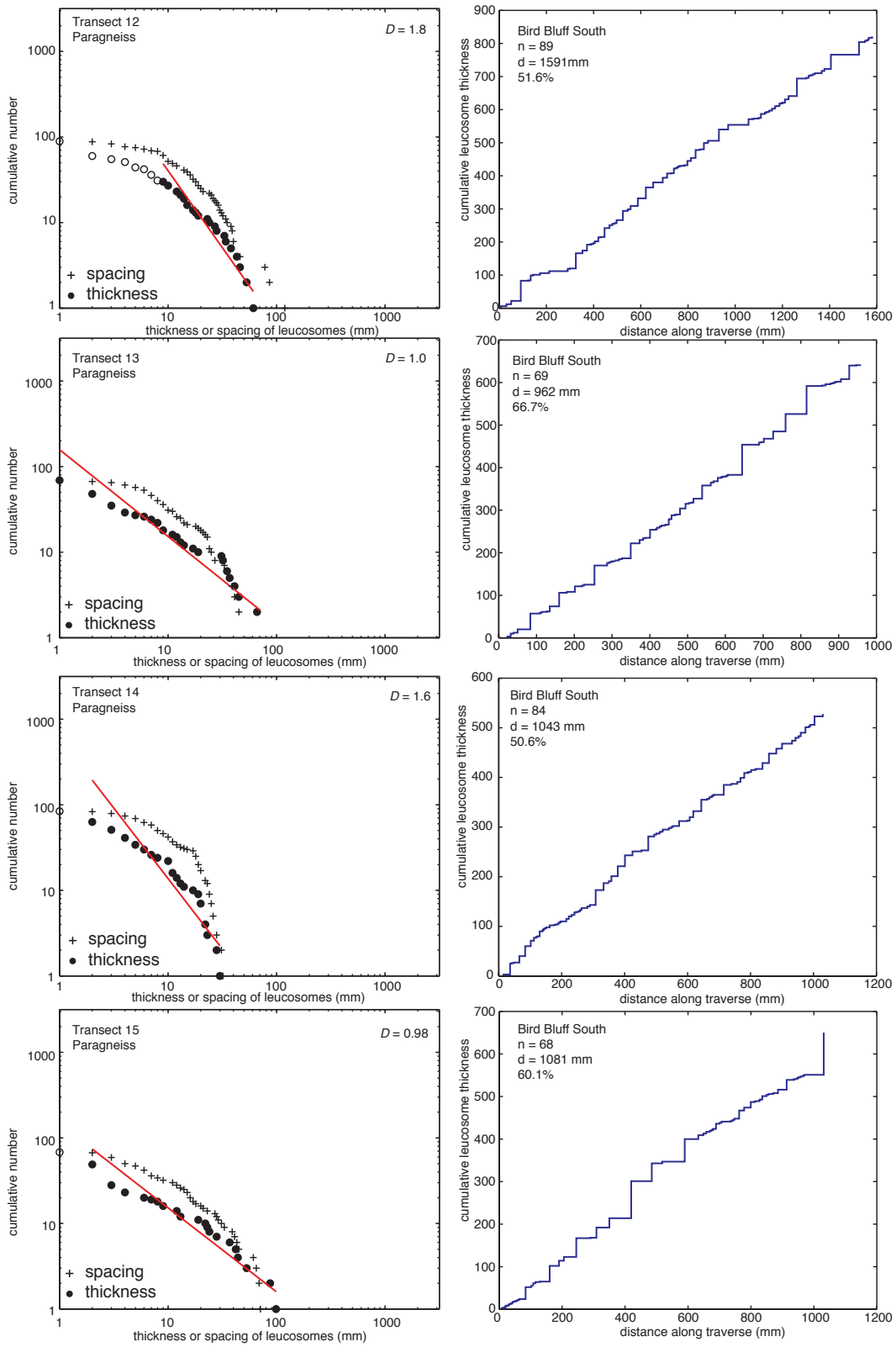

Fig. D.1 continued.

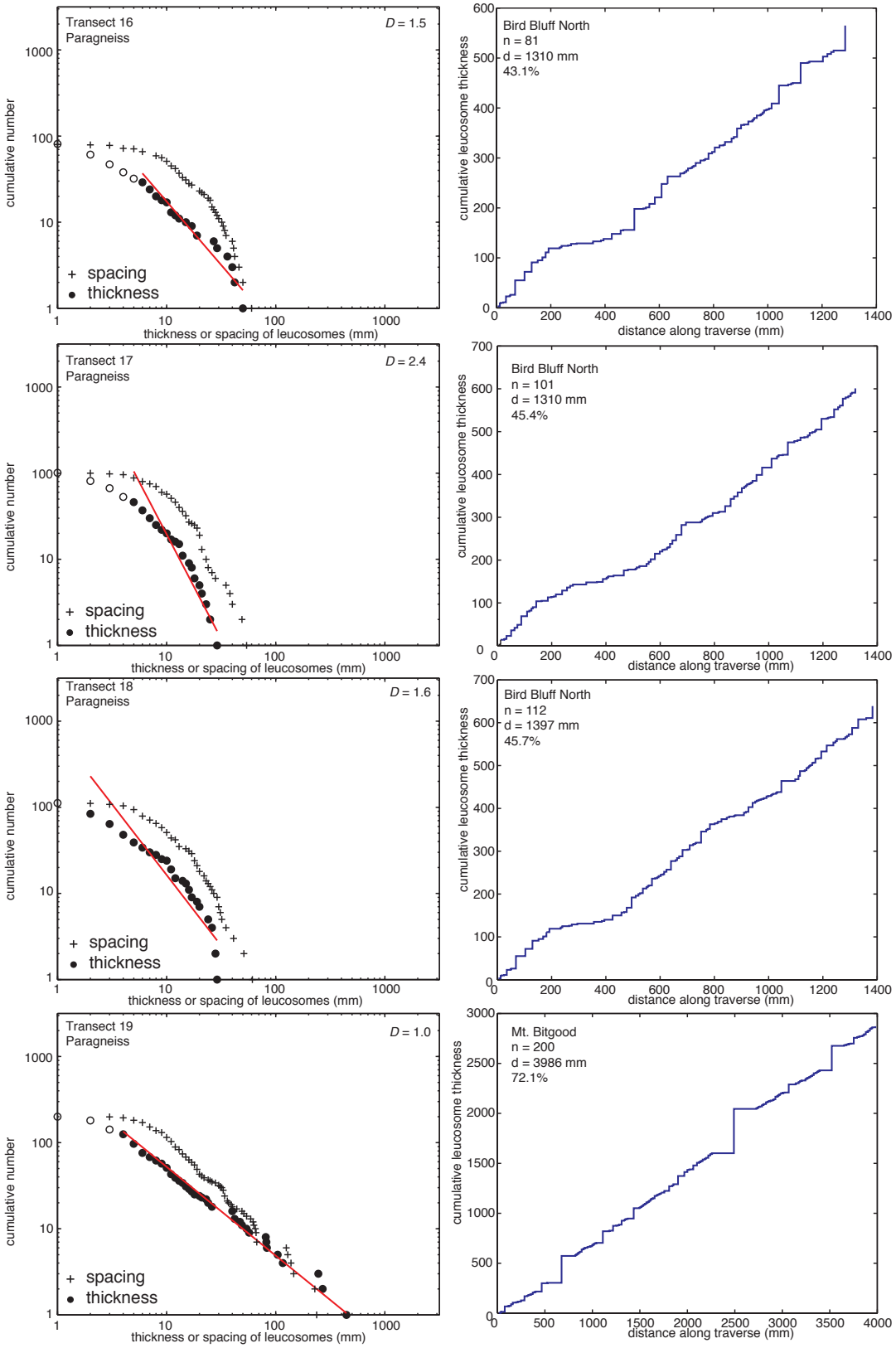

Fig. D.1 continued.

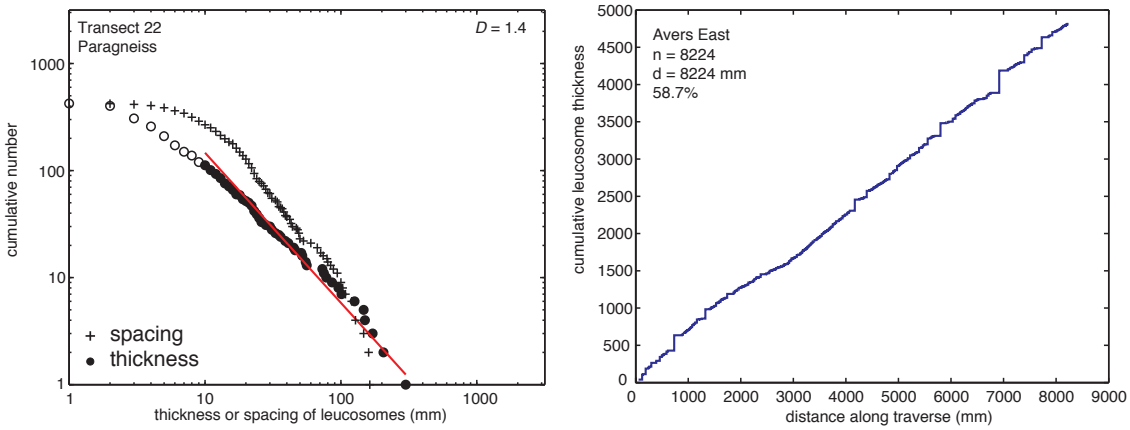

Fig. D.1 continued.

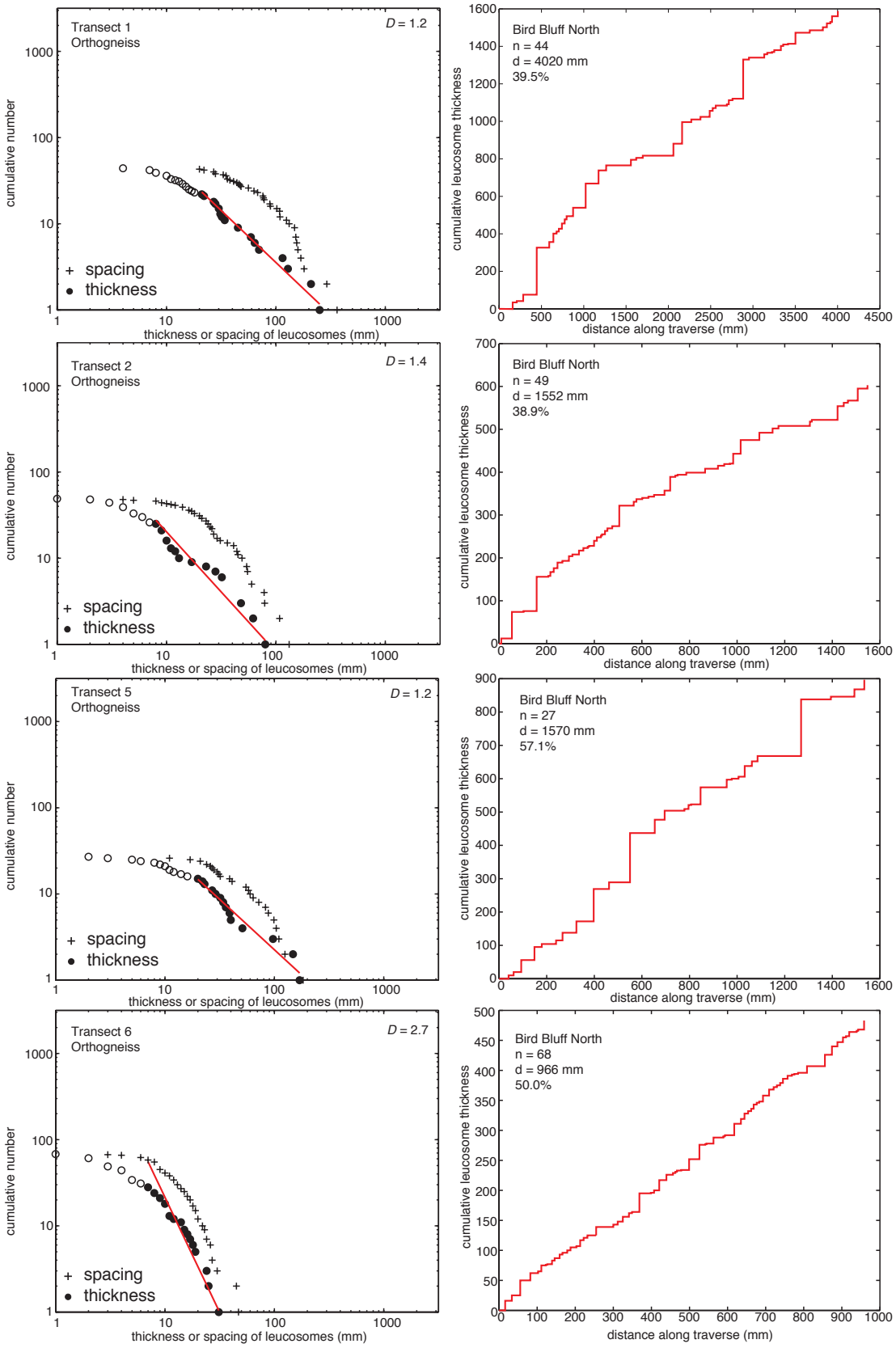

Fig. D.1 continued.

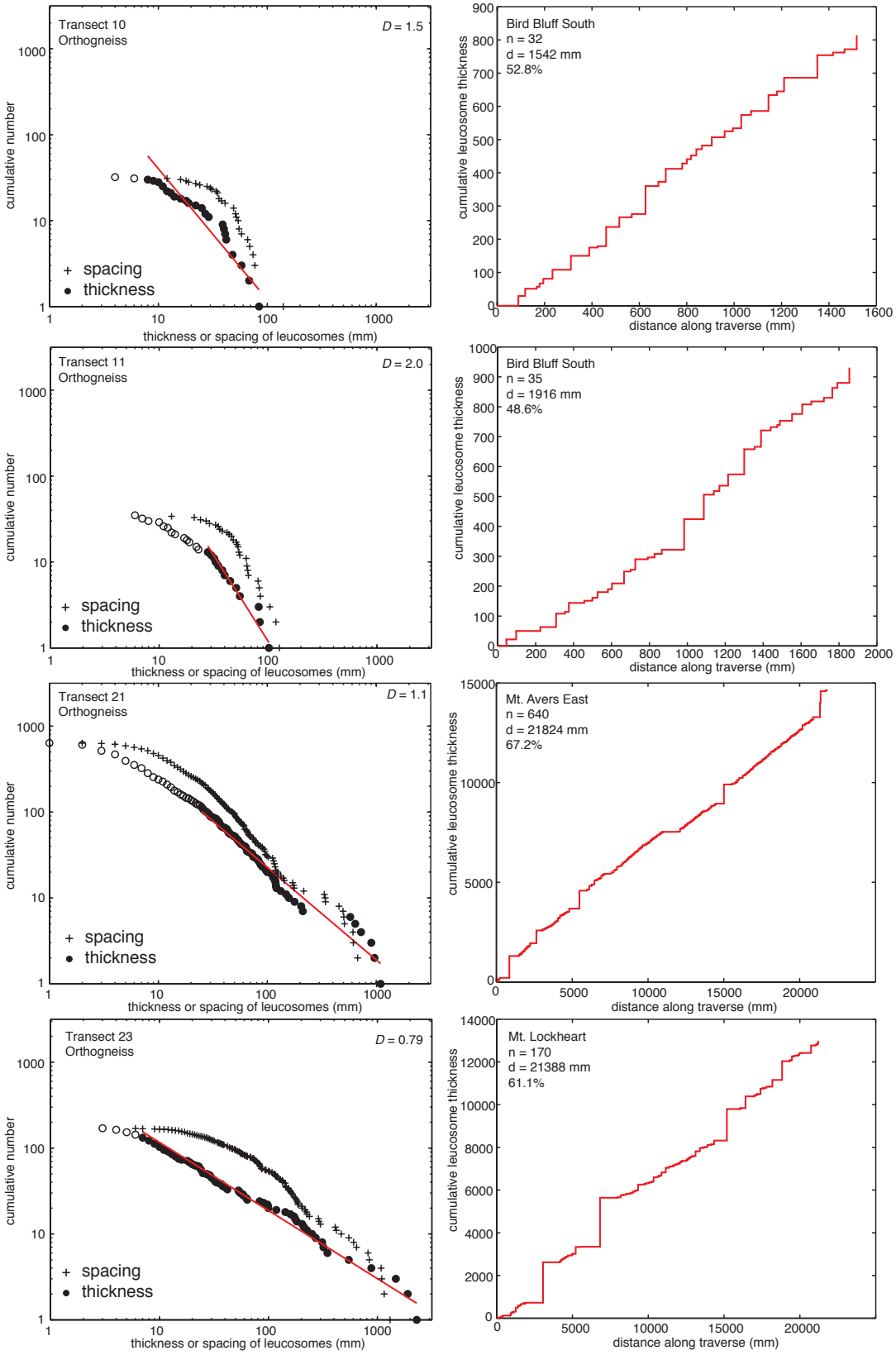

Fig. D.1 continued.

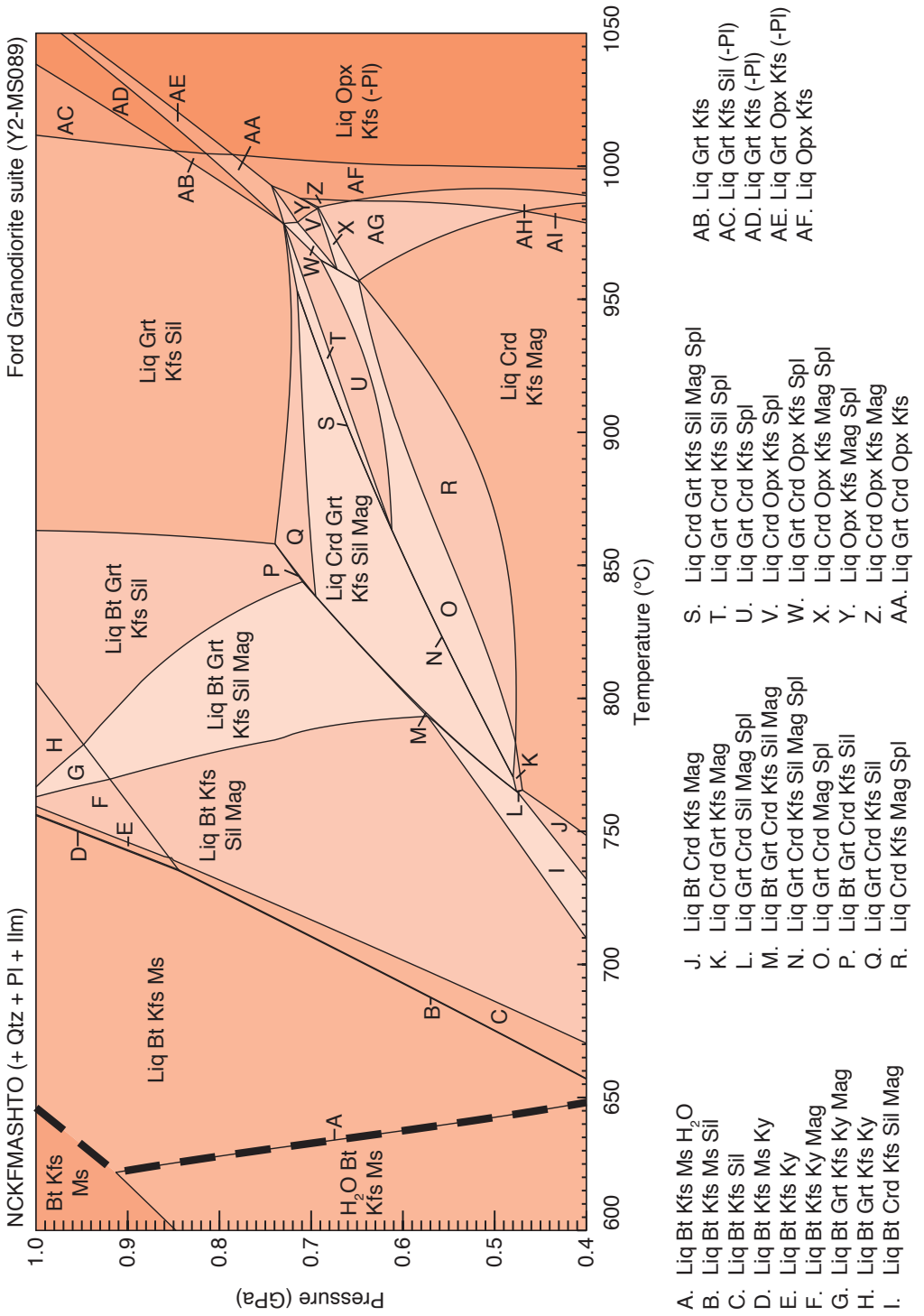

Fig. D.2 Fully labeled *P–T* pseudosections

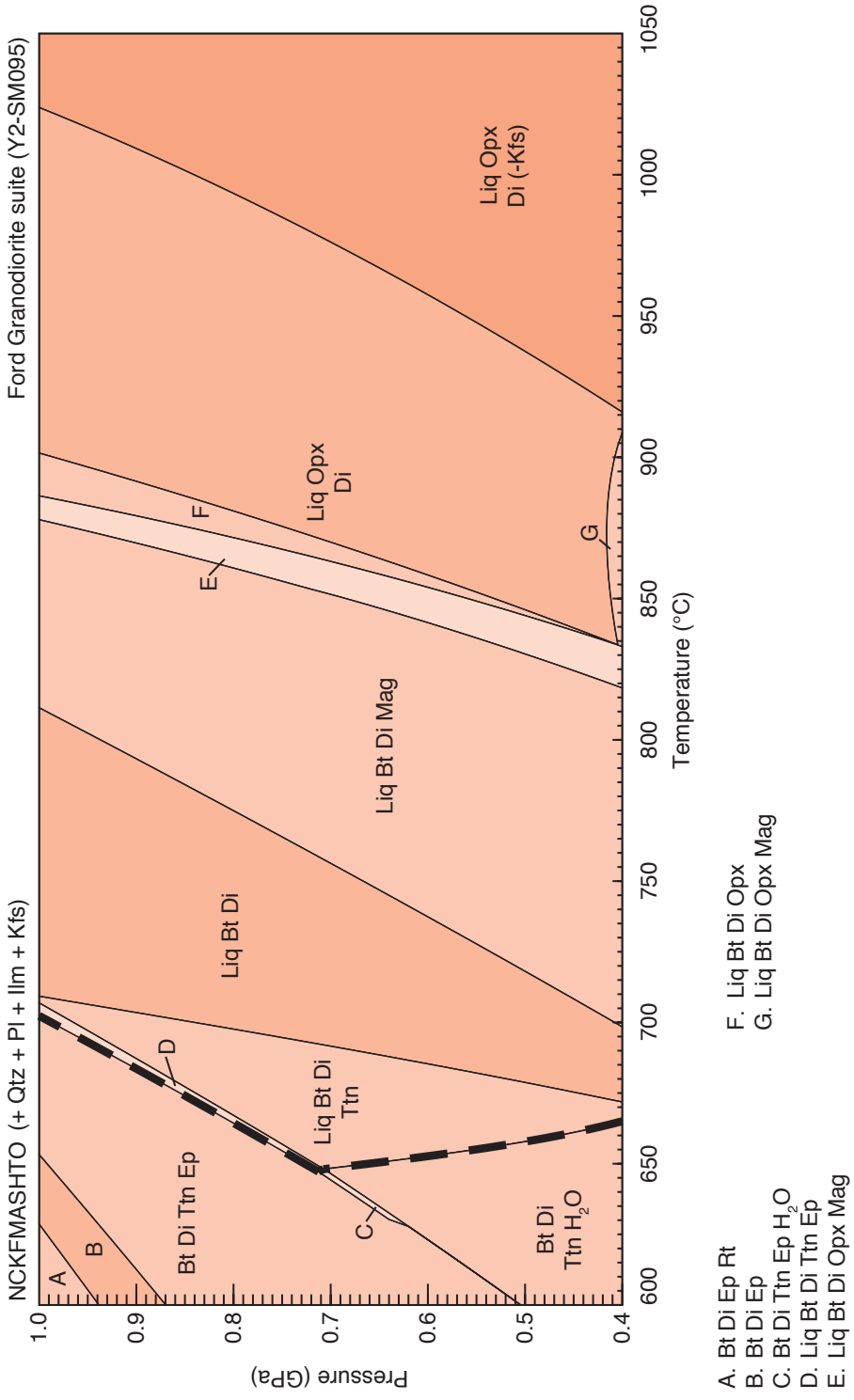

Fig. D.2 continued

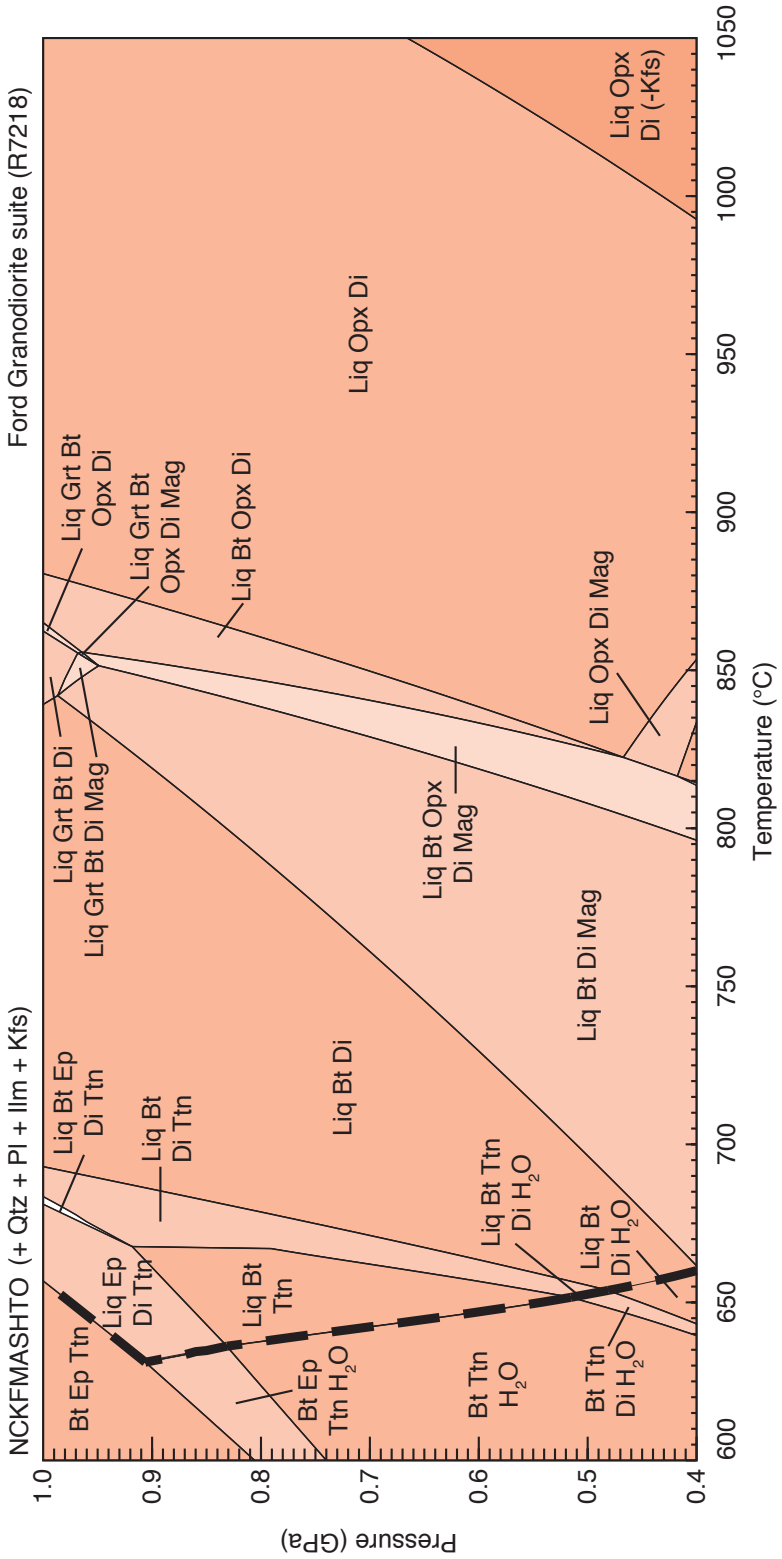

Fig. D.2 continued

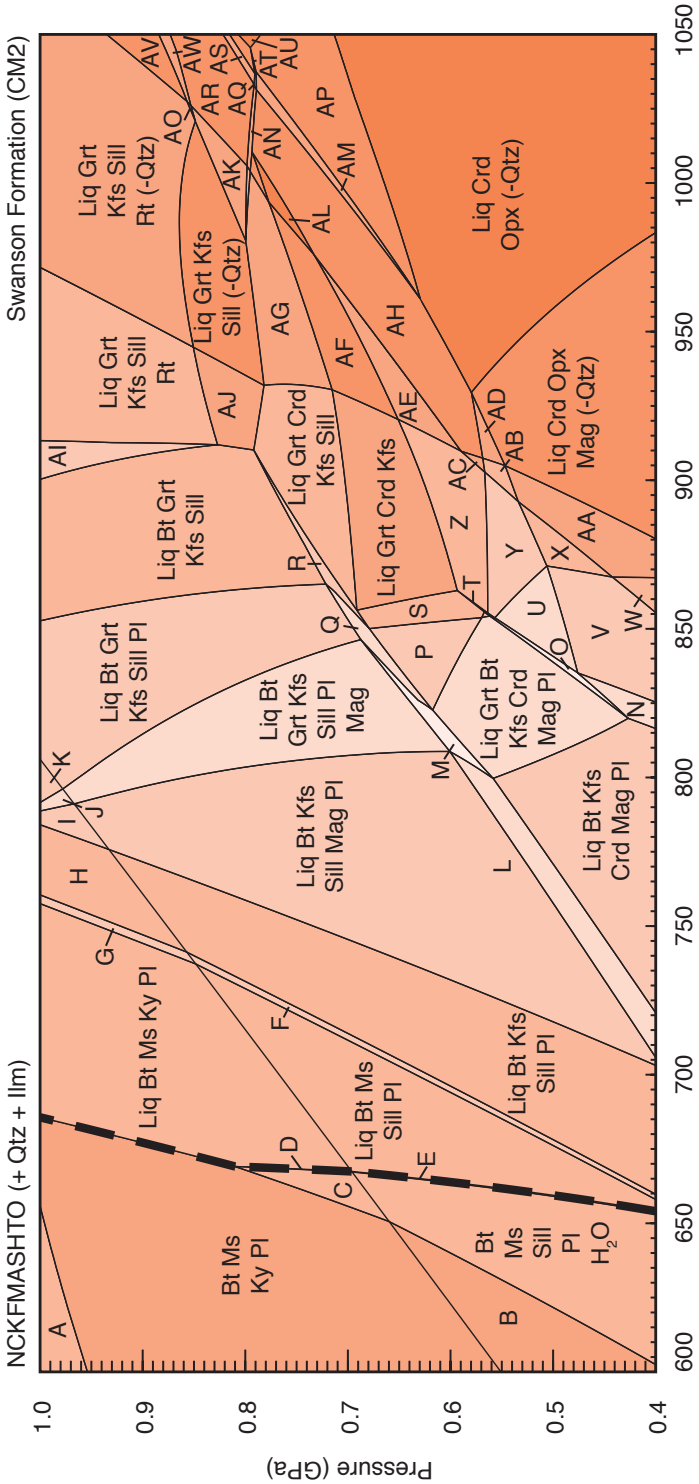

A. Grt Bt Ms Ky Pl
B. Bt Ms Sil Pl
C. Bt Ms Ky Pl H_2O
D. Liq Bt Ms Ky Pl H_2O
E. Liq Bt Ms Sil Pl H_2O
F. Liq Bt Ms Kfs Sil Pl
G. Liq Bt Ms Kfs Ky Pl
H. Liq Bt Kfs Ky Pl
I. Liq Bt Kfs Ky Pl Mag
J. Liq Bt Grt Kfs Sil Mag Pl
K. Liq Bt Grt Kfs Ky Pl
L. Liq Bt Crd Kfs Sil Mag Pl
M. Liq Bt Grt Crd Kfs Sil Pl Mag
N. Liq Bt Crd Opx Kfs Mag Pl
O. Liq Bt Grt Crd Opx Kfs Mag Pl
P. Liq Bt Grt Crd Kfs Pl
Q. Liq Bt Grt Crd Kfs Sil Pl
R. Liq Bt Grt Crd Kfs Sil
S. Liq Bt Grt Crd Kfs
T. Liq Bt Grt Crd Opx Kfs
U. Liq Grt Crd Opx Kfs Pl Mag
V. Liq Crd Opx Kfs Pl Mag
W. Liq Crd Opx Kfs Pl Mag (-Qtz)
X. Liq Crd Opx Kfs Mag
Y. Liq Grt Crd Opx Kfs Mag
Z. Liq Grt Crd Kfs Mag
AA. Liq Crd Opx Kfs Mag (-Qtz)
AB. Liq Grt Crd Opx Kfs Mag (-Qtz)
AC. Liq Grt Crd Kfs Mag (-Qtz)
AD. Liq Grt Crd Opx Mag (-Qtz)
AE. Liq Grt Crd Opx Kfs Mag (-Qtz)
AF. Liq Grt Crd Kfs (-Qtz)
AG. Liq Grt Crd Kfs Sill (-Qtz)
AH. Liq Grt Crd Opx (-Qtz)
AI. Liq Bt Grt fs Sil Rt
AJ. Liq Grt Kfs Sil
AK. Liq Grt Crd Kfs Sil (-Qtz)
AL. Liq Grt Crd (-Qtz)
AM. Liq Grt Crd Opx Spl (-Qtz)
AN. Liq Grt Crd Opx Sil (-Qtz)
AO. Liq Grt Opx Kfs Sil Rt (-Qtz)
AP. Liq Crd Opx Spl (-Qtz)
AQ. Liq Grt Crd Opx Sil Spl (-Qtz)
AR. Liq Grt Opx Sil (-Qtz)
AS. Liq Grt Opx Sil Spl (-Qtz)
AT. Liq Crd Opx Sil Spl (-Qtz)
AU. Liq Opx Spl (-Qtz)
AV. Liq Grt Sil Rt (-Qtz)

Fig. D.2 continued

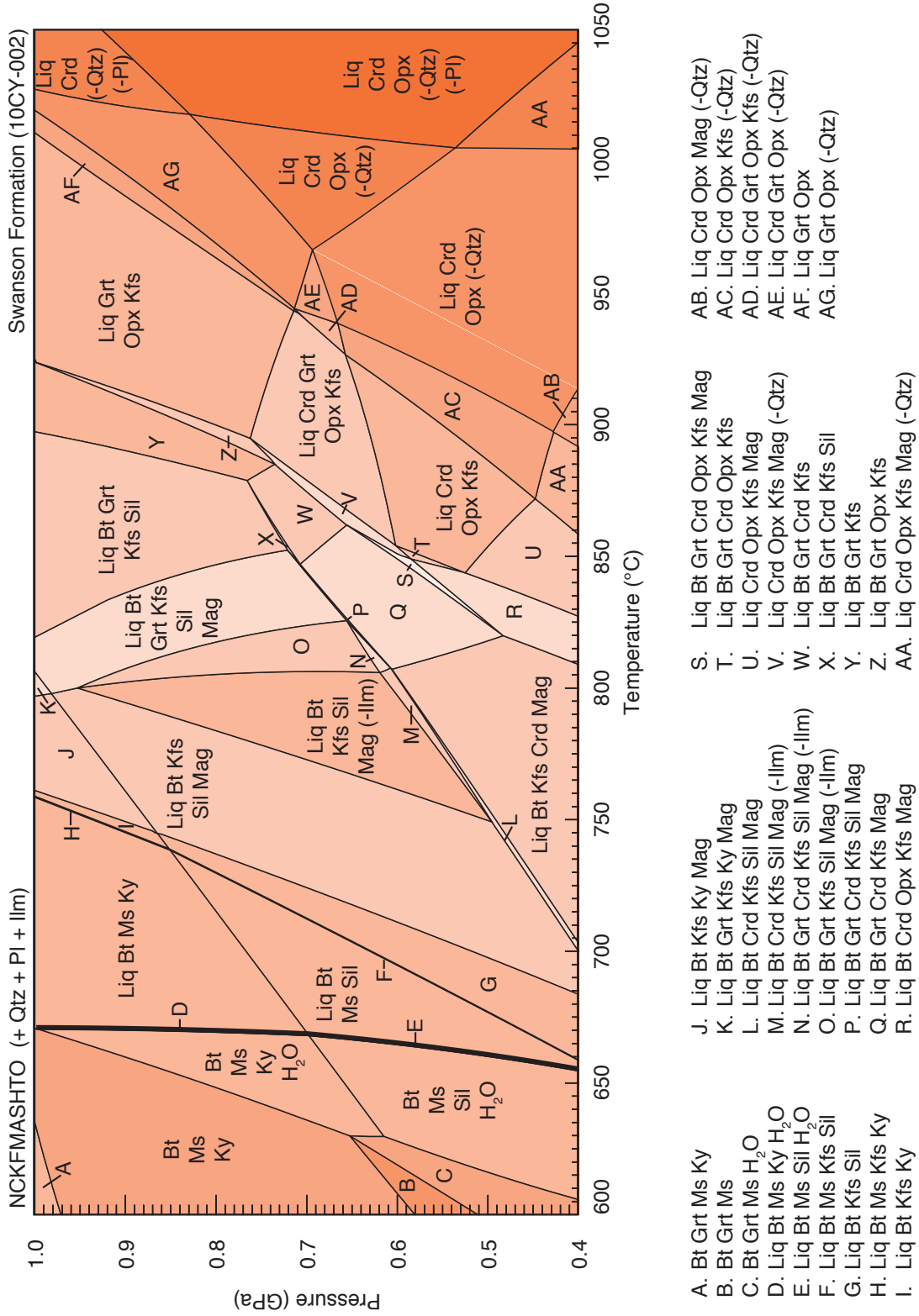

A. Bt Grt Ms Ky
B. Bt Grt Ms
C. Bt Grt Ms H_2O
D. Liq Bt Ms Ky H_2O
E. Liq Bt Ms Sil H_2O
F. Liq Bt Ms Kfs Sil
G. Liq Bt Kfs Sil
H. Liq Bt Ms Kfs Ky
I. Liq Bt Kfs Ky

J. Liq Bt Kfs Ky Mag
K. Liq Bt Grt Kfs Ky Mag
L. Liq Bt Crd Kfs Sil Mag
M. Liq Bt Crd Kfs Sil Mag (-Ilm)
N. Liq Bt Grt Crd Kfs Sil Mag (-Ilm)
O. Liq Bt Grt Kfs Sil Mag (-Ilm)
P. Liq Bt Grt Crd Kfs Sil Mag
Q. Liq Bt Grt Crd Kfs Mag
R. Liq Bt Crd Opx Kfs Mag

S. Liq Bt Grt Crd Opx Kfs Mag
T. Liq Bt Grt Crd Opx Kfs
U. Liq Crd Opx Kfs Mag
V. Liq Crd Opx Kfs Mag (-Qtz)
W. Liq Bt Grt Crd Kfs
X. Liq Bt Grt Crd Kfs Sil
Y. Liq Bt Grt Kfs
Z. Liq Bt Grt Opx Kfs
AA. Liq Crd Opx Kfs Mag (-Qtz)

AB. Liq Crd Opx Mag (-Qtz)
AC. Liq Crd Opx Kfs (-Qtz)
AD. Liq Crd Grt Opx Kfs (-Qtz)
AE. Liq Crd Grt Opx (-Qtz)
AF. Liq Grt Opx
AG. Liq Grt Opx (-Qtz)

Fig. D.2 continued

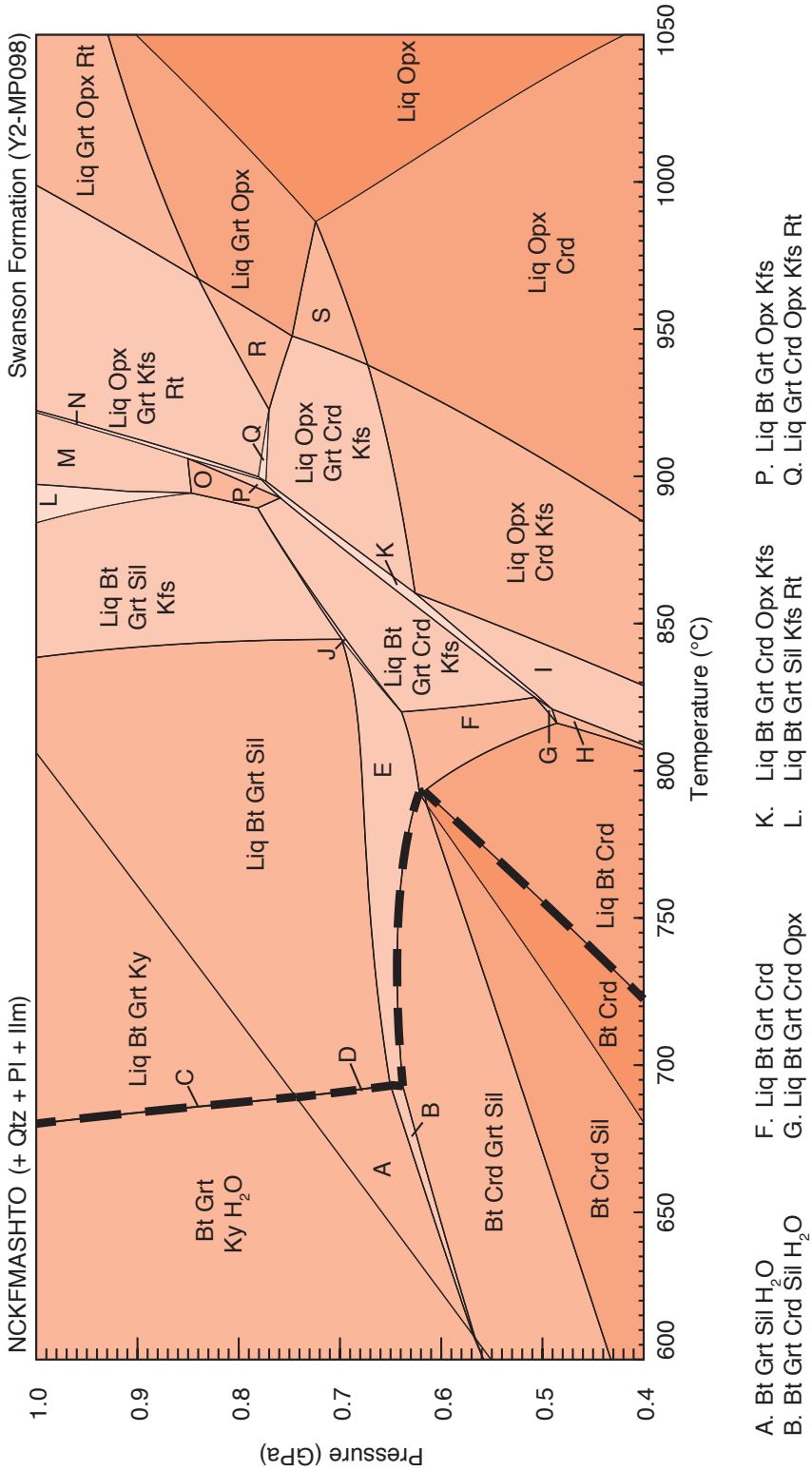

A. Bt Grt Sil H_2O
B. Bt Grt Crd Sil H_2O
C. Liq Bt Grt Ky H_2O
D. Liq Bt Grt Sil H_2O
E. Liq Bt Grt Crd Sil
F. Liq Bt Grt Crd
G. Liq Bt Grt Crd Opx
H. Liq Bt Crd Opx
I. Liq Bt Crd Opx Kfs
J. Liq Bt Grt Crd Sil Kfs
K. Liq Bt Grt Crd Opx Kfs
L. Liq Bt Grt Sil Kfs Rt
M. Liq Bt Grt Kfs Rt
N. Liq Bt Grt Opx Kfs Rt
O. Liq Bt Grt Kfs
P. Liq Bt Grt Opx Kfs
Q. Liq Grt Crd Opx Kfs Rt
R. Liq Grt Opx Kfs
S. Liq Grt Crd Opx

Fig. D.2 continued

Appendix E

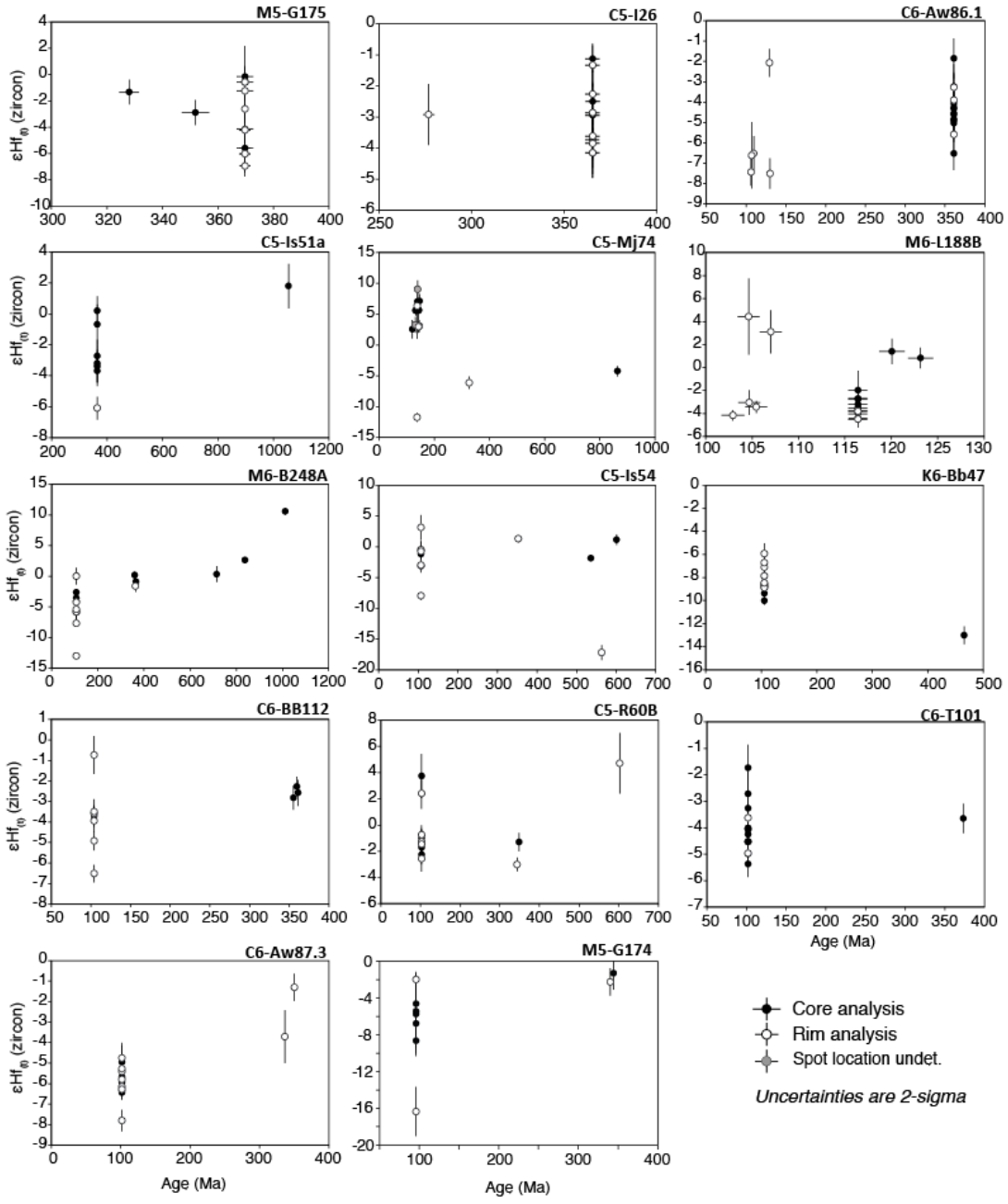

Fig. E.1. εHf_t versus $^{206}Pb/^{238}U$ age plots of zircons from granites in the Fosdick complex. Solid black circles represent core analyses and open circles represent rim analyses. One analysis annotated with a grey circle represents either a mixed zone analysis or an unassigned spot on an individual zircon. Vertical error bars represent two standard deviations from the mean. Cretaceous zircons display a greater spread of εHf_t values than older zircons.

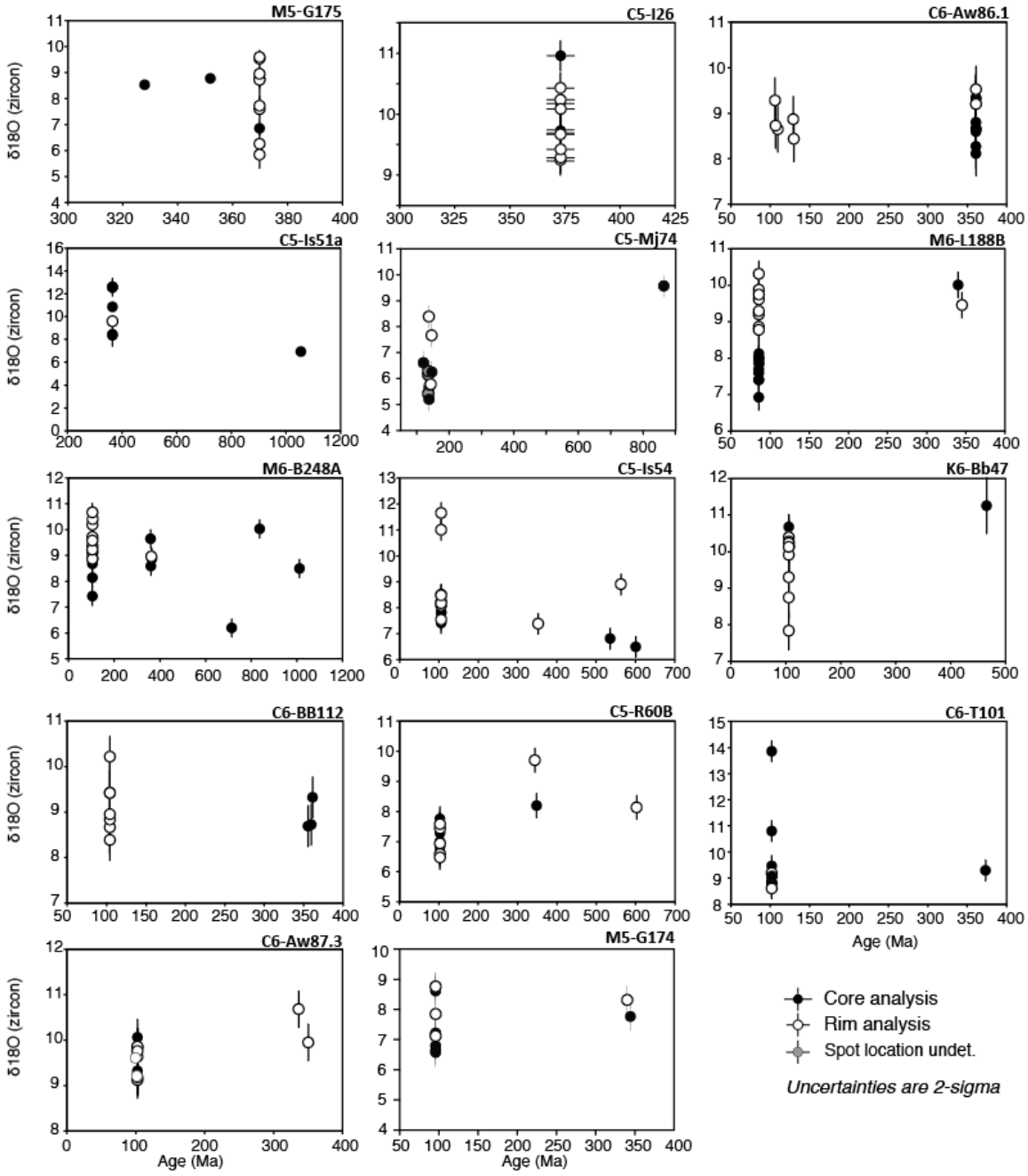

Fig. E.2. $\delta^{18}O_{(zircon)}$ versus $^{206}Pb/^{238}U$ age plots of zircons from granites in the Fosdick complex. Solid circles represent core analyses and open circles represent rim analyses. Vertical error bars represent two standard deviations from the mean. Cretaceous zircons display a greater spread of $\delta^{18}O_{(zircon)}$ values than older zircons.

Appendix F

Sample	Field Name	Date Collected	Location	Latitude	Longitude
2010–2011 Field season					
10CY-001	Swanson Formation	12/4/10	Clark Mtns.	77˚16.729' S	142˚09.726' W
10CY-002	Swanson Formation	12/4/10	Clark Mtns.	77°16.729' S	142°09.726' W
10CY-003	Microgranite	12/4/10	Clark Mtns.	77°16.729' S	142°09.726' W
10CY-004	Byrd Coast Granite	12/4/10	Clark Mtns.	77°16.729' S	142°09.726' W
10CY-005	Byrd Coast Granite	12/4/10	Clark Mtns.	77°16.729' S	142°09.726' W
10CY-006	Byrd Coast Granite	12/4/10	Clark Mtns.	77°16.729' S	142°09.726' W
10CY-007	Granite	12/4/10	Mt McClund (Sarnoff Mtns)	77°11.000' S*	144°26.000' W*
10CY-008	Granite	12/4/10	Mt McClund (Sarnoff Mtns)	77°11.000' S*	144°26.000' W*
10CY-009	Orthogneiss	12/5/10	Mt Bitgood	76°27.757' S	144°53.870' W
10CY-010	Paragnieiss	12/5/10	Mt Bitgood	76°27.757' S	144°53.870' W
10CY-011	Leucosome (Paragneiss)	12/5/10	Mt Bitgood	76°27.757' S	144°53.870' W
10CY-012	Paragneiss	12/5/10	Mt Bitgood	76°27.757' S	144°53.870' W
10CY-013	Microgranite	12/5/10	Mt Bitgood	76°27.757' S	144°53.870' W
10CY-014	Pegmatitic granite dyke	12/5/10	Mt Bitgood	76°27.757' S	144°53.870' W
10CY-015	Paragneiss	12/5/10	Mt Bitgood	76°27.757' S	144°53.870' W
10CY-016	Metaplutonic Schollen	12/5/10	Mt Bitgood	76°27.757' S	144°53.870' W
10CY-017	Granite	12/5/10	Mt Bitgood	76°27.757' S	144°53.870' W
10CY-018	Diorite	12/5/10	Mt Bitgood	76°27.757' S	144°53.870' W
10CY-019	Granite	12/5/10	Mt Bitgood	76°27.757' S	144°53.870' W
10CY-020	Leucosome	12/8/10	Mt Bitgood	76°27.757' S	144°53.870' W
10CY-021	Paragneiss	12/8/10	Maigetter Pk.	76°26.284' S	146°28.607' W
10CY-022	Leucogranite	12/8/10	Maigetter Pk.	76°26.284' S	146°28.607' W
10CY-023	Paragneiss	12/8/10	Maigetter Pk.	76°26.284' S	146°28.607' W
10CY-024	Microgranite	12/8/10	Maigetter Pk.	76°26.284' S	146°28.607' W
10CY-025	Granite (Leopard rock)	12/8/10	Maigetter Pk.	76°26.284' S	146°28.607' W
10CY-026	Orthongneiss	12/8/10	Maigetter Pk.	76°26.284' S	146°28.607' W
10CY-027	Paragneiss	12/8/10	Mt Iphigene (1070 Pk)	76°29.000' S*	146°04.210' W*
10CY-028	Leucosome	12/8/10	Mt Iphigene (1070 Pk)	76°29.000' S*	146°04.210' W*
10CY-029	Orthogneiss	12/8/10	Mt Iphigene (1070 Pk)	76°29.000' S*	146°04.210' W*
10CY-030	Orthogneiss	12/8/10	Mt Iphigene (1070 Pk)	76°29.000' S*	146°04.210' W*
10CY-031	Orthogneiss	12/8/10	Mt Iphigene (1070 Pk)	76°29.000' S*	146°04.210' W*
10CY-032	Diorite	12/8/10	Mt Iphigene (1070 Pk)	76°29.000' S*	146°04.210' W*
10CY-033	Paragneiss	12/17/10	Mt Avers East	76°28.049' S	145°17.417 W
10CY-034	Leucosome (Paragneiss)	12/17/10	Mt Avers East	76°28.049' S	145°17.417 W
10CY-035	Orthogneiss	12/17/10	Mt Avers East	76°28.049' S	145°17.417 W
10CY-036	Granite	12/17/10	Mt Avers East	76°28.049' S	145°17.417 W
10CY-037	Leucosome	12/17/10	Mt Avers East	76°28.049' S	145°17.417 W
10CY-038	Diorite	12/17/10	Mt Avers East	76°28.049' S	145°17.417 W
10CY-039	Granite	12/17/10	Mt Avers East	76°28.049' S	145°17.417 W
10CY-040	Granite (diatextie)	12/17/10	Mt Avers East	76°28.049' S	145°17.417 W
10CY-041	Paragneiss	12/17/10	Mt Avers East	76°28.049' S	145°17.417 W
2011–2012 Field season					
Y1-BB001	Orthogneiss	11/13/11	Bird Bluff	76°29.643' S	144°32.519' W
Y1-BB002	Leucosome (Orthogneiss)	11/13/11	Bird Bluff	76°29.643' S	144°32.519' W
Y1-BB003	Orthogneiss	11/13/11	Bird Bluff	76°29.643' S	144°32.519' W
Y1-BB004	Granite	11/13/11	Bird Bluff	76°29.643' S	144°32.519' W
Y1-BB005	Leucosome (Orthogneiss)	11/13/11	Bird Bluff	76°29.643' S	144°32.519' W
Y1-BB006	Paragneiss	11/14/11	Bird Bluff	76°29.507' S	144°33.442' W
Y1-BB007	Leucosome (Paragneiss)	11/14/11	Bird Bluff	76°29.507' S	144°33.442' W
Y1-BB008	Leucosome (Paragneiss)	11/14/11	Bird Bluff	76°29.507' S	144°33.442' W
Y1-BB009	Orthogneiss	11/14/11	Bird Bluff	76°29.507' S	144°33.442' W
Y1-BB010	Leucosome (Orthogneiss)	11/14/11	Bird Bluff	76°29.507' S	144°33.442' W
Y1-BB011	Amphibolite	11/14/11	Bird Bluff	76°29.507' S	144°33.442' W
Y1-BB012	Leucosome (Paragneiss)	11/14/11	Bird Bluff	76°29.507' S	144°33.442' W
Y1-BB013	Paragneiss	11/14/11	Bird Bluff	76°29.507' S	144°33.442' W
Y1-BB014	Paragneiss	11/14/11	Bird Bluff	76°29.507' S	144°33.442' W
Y1-BB015	Orthogneiss	11/15/11	Bird Bluff	76°29.501' S	144°33.328' W
Y1-BB016	Leucosome (Orthogneiss)	11/15/11	Bird Bluff	76°29.501' S	144°33.328' W
Y1-BB017	Leucosome (Orthogneiss)	11/15/11	Bird Bluff	76°29.501' S	144°33.328' W
Y1-BB018	Diorite	11/16/11	Bird Bluff	76°30.197' S	144°36.176' W
Y1-BB019	Amphibolite Dyke	11/16/11	Bird Bluff	76°30.314' S	144°36.140' W
Y1-BB020	Orthogneiss	11/16/11	Bird Bluff	76°30.430' S	144°36.076' W
Y1-BB021	Leucosome (Orthogneiss)	11/21/11	Bird Bluff	76°30.009' S	144°34.777' W
Y1-BB022	Leucosome (Orthogneiss)	11/21/11	Bird Bluff	76°30.009' S	144°34.777' W
Y1-BB023	Orthogneiss	11/21/11	Bird Bluff	76°30.009' S	144°34.777' W
Y1-BB024	Leucogabbro	11/24/11	Bird Bluff	76°29.484' S	144°33.827' W
Y1-BB025	Granite	11/24/11	Bird Bluff	76°29.484' S	144°33.827' W

* Approximate coordinates

Sample	Field Name	Date Collected	Location	Latitude	Longitude
Y1-AE026	Microgranite	12/2/11	Mt Avers East	76°27.491' S	144°20.803' W
Y1-AE027	Diorite	12/2/11	Mt Avers East	76°27.491' S	144°20.803' W
Y1-AE028	Granite (Pegmatite)	12/2/11	Mt Avers East	76°27.491' S	144°20.803' W
Y1-AE029	Microgranite	12/2/11	Mt Avers East	76°27.491' S	144°20.803' W
Y1-AE030	Paragneiss	12/2/11	Mt Avers East	76°27.491' S	144°20.803' W
Y1-AE031	Leucosome (Paragneiss)	12/2/11	Mt Avers East	76°27.491' S	144°20.803' W
Y1-AE032	Granite	12/3/11	Mt Avers East	76°27.678' S	144°20.195' W
Y1-AE033	Granite	12/3/11	Mt Avers East	76°27.678' S	144°20.195' W
Y1-AE034	Paragneiss	12/3/11	Mt Avers East	76°27.678' S	144°20.195' W
Y1-AE035	Granite (FGD)	12/3/11	Mt Avers East	76°27.950' S	145°16.324' W
Y1-AE036	Granite	12/3/11	Mt Avers East	76°27.950' S	145°16.324' W
Y1-AW037	Granite (2-mica)	12/4/11	Mt Avers West	76°27.420' S	145°30.240' W
Y1-AW038	Granite	12/4/11	Mt Avers West	76°27.420' S	145°30.240' W
Y1-AW039	Orthogneiss (dark grey)	12/4/11	Mt Avers West	76°27.420' S	145°30.240' W
Y1-BG040	Orthogneiss	12/5/11	Mt Bitgood	76°27.824' S	144°54.988' W
Y1-BG041	Leucosome (Orthogneiss)	12/5/11	Mt Bitgood	76°27.824' S	144°54.988' W
Y1-LN042	Diorite	12/8/11	Mt Lockhart North	76°26.360' S*	145°10.749' W*
Y1-LN043	Granite	12/8/11	Mt Lockhart North	76°26.360' S*	145°10.749' W*
Y1-AE044	Leucosome (Psammite)	12/10/11	Mt Avers East	76°27.443' S	145°21.398' W
Y1-AE045	Psammite	12/10/11	Mt Avers East	76°27.443' S	145°21.398' W
Y1-AE046	Paragneiss	12/10/11	Mt Avers East	76°27.443' S	145°21.398' W
Y1-AE047	Microgranite	12/12/11	Mt Avers East	76°27.624' S	145°20.871' W
Y1-AE048	Microgranite	12/12/11	Mt Avers East	76°27.624' S	145°20.871' W
Y1-AW049	Orthogneiss	12/13/2011	Mt Avers West	76°27.900' S	145°28.080' W
Y1-AW050	Orthogneiss	12/13/2011	Mt Avers West	76°27.900' S	145°28.080' W
Y1-AW051	Leucosome (Paragneiss)	12/13/2011	Mt Avers West	76°27.720' S	145°22.020' W
Y1-IG052	Granite	12/14/2011	Mt Iphigene (1070 Pk)	76°29.040' S	146°06.360' W
Y1-IG053	Orthogneiss	12/14/2011	Mt Iphigene (1070 Pk)	76°29.040' S	146°06.360' W
Y1-IG054	Paragneiss	12/14/2011	Mt Iphigene (1070 Pk)	76°29.040' S	146°06.360' W
Y1-IG055	Diorite	12/14/2011	Mt Iphigene (1070 Pk)	76°29.040' S	146°06.360' W
Y1-IG056	Leucosome	12/14/2011	Mt Iphigene (1070 Pk)	76°29.040' S	146°06.360' W
Y1-IG057	Paragneiss	12/14/2011	Mt Iphigene (1070 Pk)	76°29.040' S	146°06.360' W
Y1-IG058	Paragneiss	12/14/2011	Mt Iphigene (1070 Pk)	76°29.040' S	146°06.360' W
Y1-IG059	Diorite	12/14/2011	Mt Iphigene (1070 Pk)	76°29.040' S	146°06.360' W
Y1-AE060	Granite	12/15/2011	Mt Avers East	76°29.040' S	146°06.360' W
Y1-IG061	Paragneiss	12/16/2011	Mt Iphigene	76°29.266' S	145°50.603' W
Y1-IG062	Granite	12/16/2011	Mt Iphigene	76°29.280' S	145°50.580' W
Y1-AE063	Mafic/felsic dyke	12/17/2011	Mt Avers East	76°28.140' S	145°14.820' W
Y1-AE064	Granite	12/17/2011	Mt Avers East	76°28.140' S	145°14.820' W
Y1-AE065	Granite	12/17/2011	Mt Avers East	76°28.140' S	145°14.820' W
Y1-LH066	Orthogneiss	12/18/2011	Mt Lockhart	76°26.701' S	145°08.851' W
Y1-LH067	Granite	12/18/2011	Mt Lockhart	76°26.701' S	145°08.851' W
Y1-LH068	Granite	12/18/2011	Mt Lockhart	76°26.701' S	145°08.851' W
Y1-AE069	Paragneiss	12/22/2011	Mt Avers East	76°27.812' S*	145°23.906' W*
Y1-IG070	Granite	12/24/2011	Mt Iphigene	76°30.660' S	145°48.360' W
Y1-IG071	Diatexite	12/24/2011	Mt Iphigene	76°30.660' S	145°48.360' W
Y1-IG072	Paragneiss	12/24/2011	Mt Iphigene	76°30.660' S	145°48.360' W
Y1-IG073	Diatexite	12/24/2011	Mt Iphigene	76°30.660' S	145°48.360' W
Y1-MJ074	Paragneiss	12/25/2011	Marujupu Pk	76°31.023' S	145°39.046' W
Y1-MJ075	Orthogneiss	12/25/2011	Marujupu Pk	76°31.020' S	145°33.660' W
Y1-LH076	Orthogneiss	12/26/2011	Mt Lockhart	76°26.909' S	145°07.188' W
Y1-LH077	Paragneiss	12/26/2011	Mt Lockhart	76°26.909' S	145°07.188' W
Y1-LH078	Granite	12/26/2011	Mt Lockhart	76°26.808' S*	145°08.037' W*
Y1-LH079	Granite	12/28/2011	Mt Lockhart	76°27.524' S*	145°05.306' W*
Y1-CB080	Paragneiss	12/29/2011	Mt Colombo	76°29.389' S	144°46.460' W
Y1-CB081	Diorite	12/29/2011	Mt Colombo	76°29.389' S	144°46.460' W
Y1-CB082	Granite	12/29/2011	Mt Colombo	76°29.228' S*	144°44.888' W*
Y2-MP083	Byrd Coast Granite	1/18/12	McKinley Peak	77°53.606' S	148°19.422' W
Y2-MP084	Microgranite	1/18/12	McKinley Peak	77°53.606' S	148°19.422' W
Y2-MP085	Microgranite	1/18/12	McKinley Peak	77°53.606' S	148°19.422' W
Y2-BR086	Swanson Formation	1/19/12	Bailey Ridge	77°09.679' S	145°16.739' W
Y2-BR087	Byrd Coast Granite	1/19/12	Bailey Ridge	77°09.703' S	145°16.739' W
Y2-AG088	Ford Granodiorite suite	1/19/12	Mt. Darling (Allegheny)	77°15.226' S	143°25.302' W
Y2-MS089	Ford Granodiorite suite	1/19/12	Mt. Swan	76°57.806' S	143°50.486' W
Y2-MS090	Granite pophyry	1/19/12	Mt. Swan	76°57.806' S	143°50.486' W
Y2-GP091	Ford Granodiorite suite	1/19/12	Greer Peak (Weiner Peaks)	76°46.570' S	144°25.644' W
Y2-MD092	Swanson Formation	1/19/12	Mt. Dolber	77°04.219' S	145°45.077' W
Y2-MD093	Byrd Coast Granite	1/19/12	Mt. Dolber	77°04.219' S	145°45.077' W
Y2-SM094	Diorite pophyry	1/20/12	Saunders Mountain	76°51.099' S	145°16.515' W
Y2-SM095	Ford Granodiorite suite	1/20/12	Saunders Mountain	76°51.099' S	145°16.515' W
Y2-JU096	Ford Granodiorite suite	1/20/12	Mt. June	76°15.109' S	145°16.515 W
Y2-HN097	Ford Granodiorite suite	1/20/12	Hermann Nunatak	76°13.377' S	143°52.879' W
Y2-MP098	Swanson Formation	1/20/12	Mt. Passell	76°53.851' S	144°52.003' W

* Approximate coordinates

References

Acosta-Vigil, A., Cesare, B., London, D. & Morgan Vi, G. B., 2007. Microstructures and composition of melt inclusions in a crustal anatectic environment, represented by metapelitic enclaves within El Hoyazo dacites, SE Spain. *Chemical geology*, **237**, 450–465.

Adams, C. J., 1986. Geochronological studies of the Swanson Formation of Marie Byrd Land, West Antarctica, and the correlation with northern Victoria Land, East Antarctica and the South Island, New Zealand. *New Zealand Journal of Geology and Geophysics*, **29**, 345–358.

Adams, C. J., 1987. Geochronology and granite terrans in the Ford Ranges, Marie Byrd Land, West Antarctica. *New Zealand Journal of Geology and Geophysics*, **30**, 51–72.

Adams, C. J., 2004. Rb-Sr age and strontium isotope characteristics of the Greenland Group, Buller Terrane, New Zealand, and correlations at the Eastern Gondwanaland margin. *New Zealand Journal of Geology and Geophysics*, **47**, 189–200.

Adams, C. J., 2010. Lost Terranes of Zealandia: possible development of late Paleozoic and early Mesozoic sedimentary basins at the southwest Pacific margin of Gondwana. *Andean Geology*, **37**, 442–454.

Adams, C. J. & Griffin, W. L., 2012. Rodinian detrital zircons in Late Cretaceous sandstones indicate a possible Precambrian basement under southern Zealandia. *Precambrian Research*, **212–213**, 13–20.

Adams, C. J., Mortimer, N., Campbell, H. J. & Griffin, W. L., 2013. The mid-Cretaceous transition from basement to cover within sedimentary rocks in eastern New Zealand; evidence from detrital zircon age patterns. *Geological Magazine*, **150**, 455–478.

Ague, J. J., 1991. Evidence for Major Mass-Transfer and Volume Strain during Regional Metamorphism of Pelites. *Geology*, **19**, 855–858.

Albarède, F., 2003. The thermal history of leaky chronometers above their closure temperature. *Geophysical Research Letters*, **30**, 15-1–15-4.

Albertz, M., Paterson, S. R. & Okaya, D., 2005. Fast strain rates during pluton emplacement: Magmatically folded leucocratic dikes in aureoles of the Mount Stuart Batholith, Washington, and the Tuolumne Intrusive Suite, California. *Geological Society of America Bulletin*, **117**, 450–465.

Allibone, A. & Wysoczanski, R., 2002. Initiation of magmatism during the Cambrian-Ordovician Ross Orogeny in southern Victoria Land, Antarctica. *Geological Society of America Bulletin*, **114**, 1007–1018.

Annen, C., Blundy, J. D. & Sparks, R. S. J., 2006. The Genesis of Intermediate and Silicic Magmas in Deep Crustal Hot Zones. *Journal of Petrology*, **47**, 505–539.

Appleby, S. K., Gillespie, M. R., Graham, C. M., Hinton, R. W., Oliver, G. J. H. & Kelly, N. M., 2009. Do S-type granites commonly sample infracrustal sources? New results from an integrated O, U–Pb and Hf isotope study of zircon. *Contributions to Mineralogy and Petrology*, **160**, 115–132.

Arevalo Jr, R., McDonough, W. F. & Luong, M., 2009. The K/U ratio of the silicate Earth: Insights into mantle composition, structure and thermal evolution. *Earth and Planetary Science Letters*, **278**, 361–369.

Auzanneau, E., Vielzeuf, D. & Schmidt, M., 2006. Experimental evidence of decompression melting during exhumation of subducted continental crust. *Contributions to Mineralogy and Petrology*, **152**, 125–148.

Ayres, M. & Harris, N., 1997. REE fractionation and Nd-isotope disequilibrium during crustal anatexis: constraints from Himalayan leucogranites. *Chemical Geology*, **139**, 249–269.

Babeyko, A. Y., Sobolev, S. V., Trumbull, R., Oncken, O. & Lavier, L., 2002. Numerical models of crustal scale convection and partial melting beneath the Altiplano–Puna plateau. *Earth and Planetary Science Letters*, **199**, 373–388.

Bahlburg, H., Vervoort, J. D., Du Frane, S. A., Bock, B., Augustsson, C. & Reimann, C., 2009. Timing of crust formation and recycling in accretionary orogens: Insights learned from the western margin of South America. *Earth-Science Reviews*, **97**, 215–241.

Bak, P., Tang, C. & Wiesenfeld, K., 1988. Self-organized criticality. *Physical Review A*, **38**, 364–374.

Baldwin, J. A. & Brown, M., 2008. Age and duration of ultrahigh-temperature metamorphism in the Anápolis–Itauçu Complex, Southern Brasília Belt, central Brazil – constraints from U–Pb geochronology, mineral rare earth element chemistry and trace-element thermometry. *Journal of Metamorphic Geology*, **26**, 213–233.

Banerjee, D. & Bhattacharya, P., 1994. Petrology and geochemistry of greywackes from the Aravalli Supergroup, Rajasthan, India and the tectonic evolution of a Proterozoic sedimentary basin. *Precambrian Research*, **67**, 11–35.

Barboni, M. l., Schoene, B., Ovtcharova, M., Bussy, F. o., Schaltegger, U. & Gerdes, A., 2013. Timing of incremental pluton construction and magmatic activity in a back-arc setting revealed by ID-TIMS U/Pb and Hf isotopes on complex zircon grains. *Chemical Geology*, **342**, 76–93.

Barnes, P. M., 1990. Provenance of Cretaceous accretionary wedge sediments: The Mangapokia Formation, Wairarapa, New Zealand. *New Zealand Journal of Geology and Geophysics*, **33**, 125–135.

Bartoli, O., Cesare, B., Poli, S., Bodnar, R. J., Acosta-Vigil, A., Frezzotti, M. L. & Meli, S., 2013. Recovering the composition of melt and the fluid regime at the onset of crustal anatexis and S-type granite formation. *Geology*, **41**, 115–118.

Barton, C. C. & La Pointe, P. R., 1995. *Fractals in the earth sciences*. Plenum Press, New York ; London.

Baxter, E. F. & Scherer, E. E., 2013. Garnet Geochronology: Timekeeper of Tectonometamorphic Processes. *Elements*, **9**, 433–438.

Bea, F., 1996. Residence of REE, Y, Th and U in granites and crustal protoliths; implications for the chemistry of crustal melts. *Journal of Petrology*, **37**, 521–552.

Bea, F. & Montero, P., 1999. Behavior of accessory phases and redistribution of Zr, REE, Y, Th, and U during metamorphism and partial melting of metapelites in the lower crust: an example from the Kinzigite Formation of Ivrea-Verbano, NW Italy. *Geochimica et Cosmochimica Acta*, **63**, 1133–1153.

Bea, F., Montero, P. & Ortega, M., 2006. A LA–ICP–MS evaluation of Zr reservoirs in common crustal rocks: Implications for Zr and Hf geochemistry, and zircon-forming processes. *The Canadian Mineralogist*, **44**, 693–714.

Bea, F., Pereira, M. & Stroh, A., 1994. Mineral/leucosome trace-element partitioning in a peraluminous migmatite (a laser ablation-ICP-MS study). *Chemical Geology*, **117**, 291–312.

Beaumont, C., Jamieson, R. A., Nguyen, M. H. & Lee, B., 2001. Himalayan tectonics explained by extrusion of a low-viscosity crustal channel coupled to focused surface denudation. *Nature*, **414**, 738–742.

Berger, A., Burri, T., Alt-Epping, P. & Engi, M., 2008. Tectonically controlled fluid flow and water-assisted melting in the middle crust: An example from the Central Alps. *Lithos*, **102**, 598–615.

Black, L. P., Kamo, S. L., Allen, C. M., Aleinikoff, J. N., Davis, D. W., Korsch, R. J. & Foudoulis, C., 2003. TEMORA 1: a new zircon standard for Phanerozoic U–Pb geochronology. *Chemical geology*, **200**, 155–170.

Boehnke, P., Watson, E. B., Trail, D., Harrison, T. M. & Schmitt, A. K., 2013. Zircon saturation re-revisited. *Chemical Geology*, **351**, 324–334.

Boger, S., White, R. & Schulte, B., 2012. The importance of iron speciation (Fe+ 2/Fe+ 3) in determining mineral assemblages: an example from the high‚Äêgrade aluminous metapelites of southeastern Madagascar. *Journal of Metamorphic Geology*, **30**, 997–1018.

Boger, S. D., 2011. Antarctica – Before and after Gondwana. *Gondwana Research*, **19**, 335–371.

Bolhar, R., Weaver, S. D., Whitehouse, M. J., Palin, J. M., Woodhead, J. D. & Cole, J. W., 2008. Sources and evolution of arc magmas inferred from coupled O and Hf isotope systematics of plutonic zircons from the Cretaceous Separation Point Suite (New Zealand). *Earth and Planetary Science Letters*, **268**, 312–324.

Bonamici, C. E. & Duebendorfer, E. M., 2010. Scale-invariance and self-organized criticality in migmatites of the southern Hualapai Mountains, Arizona. *Journal of Structural Geology*, **32**, 1114–1124.

Bonnet, E., Bour, O., Odling, N. E., Davy, P., Main, I., Cowie, P. & Berkowitz, B., 2001. Scaling of fracture systems in geological media. *Reviews of Geophysics*, **39**, 347–383.

Bons, P. D., Arnold, J., Elburg, M. A., Kalda, J., Soesoo, A. & van Milligen, B. P., 2004. Melt extraction and accumulation from partially molten rocks. *Lithos*, **78**, 25–42.

Bons, P. D., Becker, J. K., Elburg, M. A. & Urtson, K., 2010. Granite formation: Stepwise accumulation of melt or connected networks? *Earth and Environmental Science Transactions of the Royal Society of Edinburgh*, **100**, 105–115.

Bons, P. D., Druguet, E., Castaño, L.-M. & Elburg, M. A., 2008. Finding what is now not there anymore: Recognizing missing fluid and magma volumes. *Geology*, **36**, 851–854.

Bons, P. D. & Elburg, M. A., 2001. Fractal size distribution of plutons: An example from the Lachlan Fold Belt, Australia. In: *S-type granites and related rocks* (eds Chappel, B. W. & Fleming, P. D.), 21–22, Australian Geological Survey.

Booth, A. L., Chamberlain, C. P., Kidd, W. S. & Zeitler, P. K., 2009. Constraints on the metamorphic evolution of the eastern Himalayan syntaxis from geochronologic and petrologic studies of Namche Barwa. *Geological Society of America Bulletin*, **121**, 385–407.

Booth, A. L., Zietler, P. K., Kidd, W. S. F., Wooden, J., Liu, Y., Idleman, B., Hren, M. & Chamberlaing, C. P., 2004. U-Pb zircon constraints on the tectonic evolution of southeastern Tibet, Namche Barwa Area. *American Journal of Science*, **304**, 889–929.

Borg, S., Stump, E. & Holloway, J., 1986. Granitoids of northern Victoria Land, Antarctica: A reconnaissance study of field relations, petrography, and geochemistry. *Antarctic Research Series*, **46**, 115–188.

Borg, S. G. & DePaolo, D. J., 1991. A tectonic model of the Antarctic Gondwana margin with implications for southeastern Australia: isotopic and geochemical evidence. *Tectonophysics*, **196**, 339–358.

Borg, S. G., Stump, E., Chappell, B. W., McCulloch, M. T., Wyborn, D., Armstrong, R. L. & Holloway, J. R., 1987. Granitoids of northern Victoria Land, Antarctica; implications of chemical and isotopic variations to regional crustal structure and tectonics. *American journal of science*, **287**, 127–169.

Bouvier, A., Vervoort, J. D. & Patchett, P. J., 2008. The Lu–Hf and Sm–Nd isotopic composition of CHUR: Constraints from unequilibrated chondrites and implications for the bulk composition of terrestrial planets. *Earth and Planetary Science Letters*, **273**, 48–57.

Bowen, N. L., 1922. The Behavior of Inclusions in Igneous Magmas. *The Journal of Geology*, **30**, 513–570.

Boyd, F. R. & Mertzman, S. A., 1987. Composition and structure of the Kaapvaal lithosphere, southern Africa. In: *Magmatic Processes: Physiochemical Principles.* (ed Mysen, B. O.) *Geochemical Society Special Publicaion*, 13–24.

Bradshaw, J. D., Andrews, P. B. & Field, B. D., 1983. Swanson Formation and related rocks of Marie Byrd Land and a comparison with the Robertson Bay Group of northern Victoria Land. In: *Antarctic Earth Science* (eds Oliver, R. L., James, P. R. & Jago, J. B.), 274–279, Cambridge University Press, Cambridge.

Bradshaw, J. D., Vaughan, A. P., Millar, I. L., Flowerdew, M. J., Trouw, R. A., Fanning, C. & Whitehouse, M. J., 2012. Permo-Carboniferous conglomerates in the Trinity Peninsula Group at View Point, Antarctic Peninsula: sedimentology, geochronology and isotope evidence for provenance and tectonic setting in Gondwana. *Geological Magazine*, **149**, 626–644.

Braun, M. G., 2002. Dunite distribution in the Oman Ophiolite: Implications for melt flux through porous dunite conduits. *Geochemistry Geophysics Geosystems*, **3**.

Brown, C. R., Yakymchuk, C., Brown, M., Fanning, C. M., Korhonen, F. J., Piccoli, P. M. & Siddoway, C. S., 2014. Are cumulate granites typical of migmatitic gneiss domes? An example from the Fosdick Mountains of Marie Byrd Land, West Antarctica. *Journal of Petrology*, **In review**.

Brown, M., 1973. The definition of metatexis, diatexis and migmatite. *Proceedings of the Geologists' Association*, **84**, 371–382.

Brown, M., 1994. The generation, segregation, ascent and emplacement of granite magma: the migmatite-to-crustally-derived granite connection in thickened orogens. *Earth-Science Reviews*, **36**, 83–130.

Brown, M., 2001a. Crustal melting and granite magmatism: Key issues. *Physics and Chemistry of the Earth Part a-Solid Earth and Geodesy*, **26**, 201–212.

Brown, M., 2001b. From microscope to mountain belt: 150 years of petrology and its contribution to understanding geodynamics, particularly the tectonics of orogens. *Journal of Geodynamics*, **32**, 115–164.

Brown, M., 2001c. Orogeny, migmatites and leucogranites: a review. *Journal of Earth System Science*, **110**, 313–336.

Brown, M., 2002. Retrograde processes in migmatites and granulites revisited. *Journal of Metamorphic Geology*, **20**, 25–40.

Brown, M., 2004. The mechanism of melt extraction from lower continental crust of orogens. *Earth and Environmental Science Transactions of the Royal Society of Edinburgh*, **95**, 35–48.

Brown, M., 2005. Synergistic effects of melting and deformation: an example from the Variscan belt, western France. *Geological Society, London, Special Publications*, **243**, 205–226.

Brown, M., 2007. Crustal melting and melt extraction, ascent and emplacement in orogens: mechanisms and consequences. *Journal of the Geological Society*, **164**, 709–730.

Brown, M., 2008. Granites, migmatites and residual granulites: Relationships and processes. *Working with migmatites. Edited by EW Sawyer and M. Brown. Mineralogical Association of Canada, Short Course Series*, **38**, 97–144.

Brown, M., 2010a. Melting of the continental crust during orogenesis: the thermal, rheological, and compositional consequences of melt transport from lower to upper continental crust. *Canadian Journal of Earth Sciences*, **47**, 655–694.

Brown, M., 2010b. The spatial and temporal patterning of the deep crust and implications for the process of melt extraction. *Philosophical Transactions of the Royal Society A: Mathematical, Physical and Engineering Sciences*, **368**, 11–51.

Brown, M., 2013. Granite: From genesis to emplacement. *Geological Society of America Bulletin*, **125**, 1079–1113.

Brown, M., Averkin, Y. A., McLellan, E. L. & Sawyer, E. W., 1995. Melt segregation in migmatites. *Journal of Geophysical Research: Solid Earth*, **100**, 15655–15679.

Brown, M. & Dallmeyer, R. D., 1996. Rapid Variscan exhumation and the role of magma in core complex formation: southern Brittany metamorphic belt, France. *Journal of Metamorphic Geology*, **14**, 361–379.

Brown, M. & Korhonen, F. J., 2009. Some remarks on melting and extreme metamorphism of crustal rocks. In: *Physics and Chemistry of the Earth's Interior* (eds Gupta, A. K. & Dasgupta, S.), 67–87, Indian National Science Academy, Springer (India) Private Limited, India.

Brown, M. & Solar, G. S., 1998. Granite ascent and emplacement during contractional deformation in convergent orogens. *Journal of Structural Geology*, **20**, 1365–1393.

Brown, M. & Solar, G. S., 1999. The mechanism of ascent and emplacement of granite magma during transpression: a syntectonic granite paradigm. *Tectonophysics*, **312**, 1–33.

Brown, M. M. & Rushmer, T., 2006. *Evolution and differentiation of the continental crust*. Cambridge University, Cambridge.

Brown, R. L. & Gibson, H. D., 2006. An argument for channel flow in the southern Canadian Cordillera and comparison with Himalayan tectonics. *Geological Society, London, Special Publications*, **268**, 543–559.

Burg, J.-P., Nievergelt, P., Oberli, F., Seward, D., Davy, P., Maurin, J.-C., Diao, Z. & Meier, M., 1998. The Namche Barwa syntaxis: evidence for exhumation related to compressional crustal folding. *Journal of Asian Earth Sciences*, **16**, 239–252.

Burg, J.-P. & Vanderhaeghe, O., 1993. Structures and way-up criteria in migmatites, with application to the Velay dome (French Massif Central). *Journal of Structural Geology*, **15**, 1293–1301.

Butler, J. P., Jamieson, R. A., Steenkamp, H. M. & Robinson, P., 2013. Discovery of coesite-eclogite from the Nordøyane UHP domain, Western Gneiss Region, Norway: field relations, metamorphic history, and tectonic significance. *Journal of Metamorphic Geology*, **31**, 147–163.

Cawood, P. A., 2005. Terra Australis Orogen: Rodinia breakup and development of the Pacific and Iapetus margins of Gondwana during the Neoproterozoic and Paleozoic. *Earth-Science Reviews*, **69**, 249–279.

Caddick, M. J., Konopásek, J. ô. & Thompson, A. B., 2010. Preservation of Garnet Growth Zoning and the Duration of Prograde Metamorphism. *Journal of Petrology*, **51**, 2327–2347.

Catlos, E. J., 2013. Versatile Monazite: resolving geological records and solving challenges in materials science: Generalizations about monazite: Implications for geochronologic studies. *American Mineralogist*, **98**, 819–832.

Cecil, M. R., Gehrels, G. E., Ducea, M. N. & Patchett, P. J., 2011. U-Pb-Hf characterization of the central Coast Mountains Batholith; implications for petrogenesis and crustal architecture. *Lithosphere*, **3**, 247–260.

Cesare, B., Maineri, C., Baron Toaldo, A., Pedron, D. & Acosta Vigil, A., 2007. Immiscibility between carbonic fluids and granitic melts during crustal anatexis: A fluid and melt inclusion study in the enclaves of the Neogene Volcanic Province of SE Spain. *Chemical geology*, **237**, 433–449.

Chappell, B. W., White, A. J. R. & Hine, R., 1988. Granite provinces and basement terranes in the Lachlan Fold Belt, southeastern Australia. *Australian Journal of Earth Sciences*, **35**, 505–521.

Cheadle, M. J., Elliott, M. T. & McKenzie, D., 2004. Percolation threshold and permeability of crystallizing igneous rocks: The importance of textural equilibrium. *Geology*, **32**, 757–760.

Chen, Y.-X., Zheng, Y.-F. & Hu, Z., 2013. Synexhumation anatexis of ultrahigh-pressure metamorphic rocks: Petrological evidence from granitic gneiss in the Sulu orogen. *Lithos*, **156–159**, 69–96.

Cheng, H., DuFrane, S. A., Vervoort, J. D., Nakamura, E., Zheng, Y.-F. & Zhou, Z., 2010. Protracted oceanic subduction prior to continental subduction: New Lu-Hf and Sm-Nd geochronology of oceanic-type high-pressure eclogite in the western Dabie orogen. *American Mineralogist*, **95**, 1214–1223.

Cheng, H., King, R. L., Nakamura, E., Vervoort, J. D. & Zhou, Z., 2008. Coupled Lu–Hf and Sm–Nd geochronology constrains garnet growth in ultra-high-pressure eclogites from the Dabie orogen. *Journal of Metamorphic Geology*, **26**, 741–758.

Cherniak, D. J., Watson, E. B., Grove, M. & Harrison, T. M., 2004. Pb diffusion in monazite: a combined RBS/SIMS study. *Geochimica et Cosmochimica Acta*, **68**, 829–840.

Clark, C., Collins, A. S., Santosh, M., Taylor, R. & Wade, B. P., 2009. The P-T-t architecture of a Gondwanan suture: REE, U–Pb and Ti-in-zircon thermometric constraints from the Palghat Cauvery shear system, South India. *Precambrian Research*, **174**, 129–144.

Clark, C., Fitzsimons, I. C., Healy, D. & Harley, S. L., 2011. How does the continental crust get really hot? *Elements*, **7**, 235–240.

Clarke, D. B. (2007). Assimilation of xenocrysts in granitic magmas: principles, processes, proxies, and problems. *The Canadian Mineralogist* **45**, 5–30.

Clauset, A., Shalizi, C. R. & Newman, M. E. J., 2009. Power-Law Distributions in Empirical Data. *SIAM Review*, **51**, 661–703.

Clemens, J. & Droop, G., 1998. Fluids, P–T paths and the fates of anatectic melts in the Earth's crust. *Lithos*, **44**, 21–36.

Clemens, J. D., 2006. Melting of the continental crust: fluid regimes, melting reactions, and source-rock fertility. In: *Evolution and Differentiation of the Continental Crust* (eds Brown, M. & Rushmer, T.), 297–331, Cambridge University Press, Cambridge.

Clemens, J. D. & Stevens, G., 2012. What controls chemical variation in granitic magmas? *Lithos*, **134-135**, 317–329.

Clemens, J. D., Stevens, G. & Farina, F., 2011. The enigmatic sources of I-type granites: The peritectic connexion. *Lithos*, **126**, 174–181.

Coggon, R. & Holland, T. J. B., 2002. Mixing properties of phengitic micas and revised garnet-phengite thermobarometers. *Journal of Metamorphic Geology*, **20**, 683–696.

Coleman, D. S., Gray, W. & Glazner, A. F., 2004. Rethinking the emplacement and evolution of zoned plutons: Geochronologic evidence for incremental assembly of the Tuolumne Intrusive Suite, California. *Geology*, **32**, 433–436.

Collins, W. J., 2002. Nature of extensional accretionary orogens. *Tectonics*, **21**, 6–1–6–12.

Collins, W. J., Belousova, E. A., Kemp, A. I. S. & Murphy, J. B., 2011. Two contrasting Phanerozoic orogenic systems revealed by hafnium isotope data. *Nature Geosci*, **4**, 333–337.

Collins, W. J. & Sawyer, E. W., 1996. Pervasive granitoid magma transfer through the lower-middle crust during non-coaxial compressional deformation. *Journal of Metamorphic Geology*, **14**, 565–579.

Craven, S. J., Daczko, N. R. & Halpin, J. A., 2012. Thermal gradient and timing of high-T–low-P metamorphism in the Wongwibinda Metamorphic Complex, southern New England Orogen, Australia. *Journal of Metamorphic Geology*, **30**, 3–20.

Cruden, A., 2006. Emplacement and growth of plutons: implications for rates of melting and mass transfer in continental crust. In: *Evolution and differentiation of the continental crust* (eds Brown, M. & Rushmer, T.), 455–519, Cambridge University Press, Cambridge.

Cruden, A. R. & McCaffrey, K. J. W., 2001. Growth of plutons by floor subsidence: implications for rates of emplacement, intrusion spacing and melt-extraction mechanisms. *Physics and Chemistry of the Earth, Part A: Solid Earth and Geodesy*, **26**, 303–315.

Cuney, M. & Barbey, P., 1982. Mise en evidence de phenomenes de cristallisation fractionnee dans les migmatites. *Comptes-Rendus des Seances de L'Academie des Sciences, Serie*, **2**, 37–42.

Dallai, L., Ghezzo, C. & Sharp, Z. D., 2003. Oxygen isotope evidence for crustal assimilation and magma mixing in the Granite Harbour Intrusives, northern Victoria Land, Antarctica. *Lithos*, **67**, 135–151.

Davidson, C., Schmid, S. M. & Hollister, L. S., 1994. Role of melt during deformation in the deep crust. *Terra Nova*, **6**, 133–142.

Davidson, J. P. & Arculus, R. J., 2006. The significance of Phanerozoic arc magmatism in generating continental crust. In: *Evolution and Differentiation of the Continental Crust* (eds Brown, M. & Rushmer, T.), 135–151, Cambridge University Press, New York.

de Saint Blanquat, M., Horsman, E., Habert, G., Morgan, S., Vanderhaeghe, O., Law, R. & Tikoff, B., 2011. Multiscale magmatic cyclicity, duration of pluton construction, and the paradoxical relationship between tectonism and plutonism in continental arcs. *Tectonophysics*, **500**, 20–33.

Degeling, H., Eggins, S. & Ellis, D., 2001. Zr budgets for metamorphic reactions, and the formation of zircon from garnet breakdown. *Mineralogical Magazine*, **65**, 749–758.

DePaolo, D. J., 1981a. Neodymium isotopes in the Colorado Front Range and crust–mantle evolution in the Proterozoic. *Nature*, **291**, 193–196.

DePaolo, D. J., 1981b. Trace element and isotopic effects of combined wallrock assimilation and fractional crystallization. *Earth and Planetary Science Letters*, **53**, 189–202.

Dhuime, B., Hawkesworth, C. & Cawood, P., 2011. When Continents Formed. *Science*, **331**, 154–155.

Dhuime, B., Hawkesworth, C. J., Cawood, P. A. & Storey, C. D., 2012. A Change in the Geodynamics of Continental Growth 3 Billion Years Ago. *Science*, **335**, 1334–1336.

Diener, J. & Powell, R., 2012. Revised activity–composition models for clinopyroxene and amphibole. *Journal of Metamorphic Geology*, **30**, 131–142.

Diener, J. F. A. & Powell, R., 2010. Influence of ferric iron on the stability of mineral assemblages. *Journal of Metamorphic Geology*, **28**, 599–613.

Diener, J. F. A., Powell, R., White, R. W. & Holland, T. J. B., 2007. A new thermodynamic model for clino- and orthoamphiboles in the system Na2O-CaO-FeO-MgO-Al2O3-SiO2-H2O-O. *Journal of Metamorphic Geology*, **25**, 631–656.

Diener, J. F. A., White, R. W. & Powell, R., 2008. Granulite facies metamorphism and subsolidus fluid-absent reworking, Strangways Range, Arunta Block, central Australia. *Journal of Metamorphic Geology*, **26**, 603–622.

DiVenere, V., Kent, D. V. & Dalziel, I. W. D., 1995. Early Cretaceous paleomagnetic results from Marie Byrd Land, West Antarctica: Implications for the Weddellia collage of crustal blocks. *Journal of Geophysical Research: Solid Earth*, **100**, 8133–8151.

DiVenere, V. J., Kent, D. V. & Dalziel, I. W. D., 1994. Mid-Cretaceous paleomagnetic results from Marie Byrd Land, West Antarctica; a test of post-100 Ma relative motion between East and West Antarctica. *Journal of Geophysical Research*, **99**, 15.

Dostal, J. & Keppie, J. D., 2009. Geochemistry of low-grade clastic rocks in the Acatlan Complex of southern Mexico: Evidence for local provenance in felsic-intermediate igneous rocks. *Sedimentary Geology*, **222**, 241–253.

Droop, G. T. R. & Brodie, K. H., 2012. Anatectic melt volumes in the thermal aureole of the Etive Complex, Scotland: the roles of fluid-present and fluid-absent melting. *Journal of Metamorphic Geology*, **30**, 843–864.

Druguet, E. & Carreras, J., 2006. Analogue modelling of syntectonic leucosomes in migmatitic schists. *Journal of Structural Geology*, **28**, 1734–1747.

Duller, P. R. & Floyd, J. D., 1995. Turbidite Geochemistry and Provenance Studies in the Southern Uplands of Scotland. *Geological Magazine*, **132**, 557–569.

Eagles, G., Gohl, K. & Larter, R. D., 2004. High-resolution animated tectonic reconstruction of the South Pacific and West Antarctic Margin. *Geochemistry, Geophysics, Geosystems*, **5**, Q07002.

Ebadi, A. & Johannes, W., 1991. Beginning of melting and composition of first melts in the system Qz-Ab-Or-H2O-CO2. *Contributions to Mineralogy and Petrology*, **106**, 286–295.

Eiler, J. M., 2001. Oxygen Isotope Variations of Basaltic Lavas and Upper Mantle Rocks. *Reviews in Mineralogy and Geochemistry*, **43**, 319–364.

Elburg, M. A., 1996. Evidence of isotopic equilibration between microgranitoid enclaves and host granodiorite, Warburton Granodiorite, Lachlan Fold Belt, Australia. *Lithos*, **38**, 1–22.

Elliot, D. H., 2013. The geological and tectonic evolution of the Transantarctic Mountains; a review. *Special Publication - Geological Society of London*, **381**, 7–35.

Elliot, D. H., Fanning, C. M. & Hulett, S. R. W., 2014. Age provinces in the Antarctic craton: Evidence from detrital zircons in Permian strata from the Beardmore Glacier region, Antarctica. *Gondwana Research*.

Epstein, B., 1947. The mathematical description of certain breakage mechanisms leading to the logarithmico-normal distribution. *Journal of the Franklin Institute*, **244**, 471–477.

Evans, K. A., Powell, R. & Holland, T. J. B., 2010. Internally consistent data for sulphur-bearing phases and application to the construction of pseudosections for mafic greenschist facies rocks in Na2O-CaO-K2O-FeO-MgO-Al2O3-SiO2-CO2-O-S-H2O. *Journal of Metamorphic Geology*, **28**, 667–687.

Ewing, T., Hermann, J. r. & Rubatto, D., 2013. The robustness of the Zr-in-rutile and Ti-in-zircon thermometers during high-temperature metamorphism (Ivrea-Verbano Zone, northern Italy). *Contributions to Mineralogy and Petrology*, **165**, 757–779.

Fagereng, Å., 2011. Fractal vein distributions within a fault-fracture mesh in an exhumed accretionary mélange, Chrystalls Beach Complex, New Zealand. *Journal of Structural Geology*, **33**, 918–927.

Ferraccioli, F., Damaske, D., Bozzo, E., Spano, M. & Chiappini, M., 2000. Magnetic anomaly patterns over crustal blocks of the King Edward VII Peninsula, Marie Byrd Land, West Antarctica. *Annali di Geofisica*, **43**, 229–241.

Ferraccioli, F., Bozzo, E. & Damaske, D., 2002. Aeromagnetic signatures over western Marie Byrd Land provide insight into magmatic arc basement, mafic magmatism and structure of the Eastern Ross Sea Rift flank. *Tectonophysics*, **347**, 139–165.

Ferrero, S., Bartoli, O., Cesare, B., Salvioli-Mariani, E., Acosta-Vigil, A., Cavallo, A., Groppo, C. & Battiston, S., 2012. Microstructures of melt inclusions in anatectic metasedimentary rocks. *Journal of Metamorphic Geology*, **30**, 303–322.

Ferrero, S., Bodnar, R. J., Cesare, B. & Viti, C., 2011. Re-equilibration of primary fluid inclusions in peritectic garnet from metapelitic enclaves, El Hoyazo, Spain. *Lithos*, **124**, 117–131.

Ferrero, S., Braga, R., Berkesi, M., Cesare, B. & Laridhi Ouazaa, N., 2014. Production of metaluminous melt during fluid-present anatexis: an example from the Maghrebian basement, La Galite Archipelago, central Mediterranean. *Journal of Metamorphic Geology*, **32**, 209–225.

Finn, C., Moore, D., Damaske, D. & Mackey, T., 1999. Aeromagnetic legacy of early Paleozoic subduction along the Pacific margin of Gondwana. *Geology*, **27**, 1087–1090.

Fioretti, A. M., Visona, D., Cavazzini, G. & Lombardo, B., 1997. Devonian magmatism; implications for the evolution of northern Victoria Land, Antarctica, and correlation with southeastern Australia and northeastern Tasmania. *International Symposium on Antarctic Earth Sciences*, **7**, 293–296.

Flowerdew, M. J., Millar, I. L., Curtis, M. L., Vaughan, A. P. M., Horstwood, M. S. A., Whitehouse, M. J. & Fanning, C. M., 2007. Combined U-Pb geochronology and Hf isotope geochemistry of detrital zircons from early Paleozoic sedimentary rocks, Ellsworth-Whitmore Mountains Block, Antarctica. *Geological Society of America Bulletin*, **119**, 275–288.

Flowerdew, M. J., Millar, I. L. & Vaughan, A. P. M., 2006a. Potential of Combined U-Pb Geochronology and Hf isotope Geochemical Studies on Zircon to Aid Sedimentary Provenance within Antarctica: Examples from West Antarctica. *Terra Antarctica Reports*, **12**, 57–64.

Flowerdew, M. J., Millar, I. L., Vaughan, A. P. M., Horstwood, M. S. A. & Fanning, C. M., 2006b. The source of granitic gneisses and migmatites in the Antarctic Peninsula: a combined U–Pb SHRIMP and laser ablation Hf isotope study of complex zircons. *Contributions to Mineralogy and Petrology*, **151**, 751–768.

Flowerdew, M. J., Millar, I. L., Vaughan, A. P. M. & Pankhurst, R. J., 2005. Age and tectonic significance of the Lassiter Coast Intrusive Suite, eastern Ellsworth Land, Antarctic Peninsula. *Antarctic Science*, **17**, 443–452.

Foster, D. A., Gray, D. R., Spaggiari, C., Kamenov, G. & Bierlein, F. P., 2009. Palaeozoic Lachlan orogen, Australia; accretion and construction of continental crust in a marginal ocean setting: isotopic evidence from Cambrian metavolcanic rocks. *Geological Society, London, Special Publications*, **318**, 329–349.

Foster, G., Kinny, P., Vance, D., Prince, C. & Harris, N., 2000. The significance of monazite U–Th–Pb age data in metamorphic assemblages; a combined study of monazite and garnet chronometry. *Earth and Planetary Science Letters*, **181**, 327–340.

Fraser, G., Ellis, D. & Eggins, S., 1997. Zirconium abundance in granulite-facies minerals, with implications for zircon geochronology in high-grade rocks. *Geology*, **25**, 607–610.

Frost, B. R. & Chacko, T. (1989). The Granulite Uncertainty Principle: Limitations on Thermobarometry in Granulites. *The Journal of Geology* **97**, 435–450.

Gehrels, G. E., Valencia, V. A. & Ruiz, J., 2008. Enhanced precision, accuracy, efficiency, and spatial resolution of U-Pb ages by laser ablation–multicollector–inductively coupled plasma–mass spectrometry. *Geochemistry, Geophysics, Geosystems*, **9**, Q03017.

Gibson, H. D., Carr, S. D., Brown, R. L. & Hamilton, M. A., 2004. Correlations between chemical and age domains in monazite, and metamorphic reactions involving major pelitic phases: an integration of ID-TIMS and SHRIMP geochronology with Y–Th–U X-ray mapping. *Chemical Geology*, **211**, 237–260.

Gieré, R., Rumble, D., Günther, D., Connolly, J. & Caddick, M. J., 2011. Correlation of Growth and Breakdown of Major and Accessory Minerals in Metapelites from Campolungo, Central Alps. *Journal of Petrology*, **52**, 2293–2334.

Gill, J. B., Hiscott, R. N. & Vidal, P., 1994. Turbidite Geochemistry and Evolution of the Izu-Bonin Arc and Continents. *Lithos*, **33**, 135–168.

Gillespie, P. A., Howard, C. B., Walsh, J. J. & Watterson, J., 1993. Measurement and characterisation of spatial distributions of fractures. *Tectonophysics*, **226**, 113–141.

Gillespie, P. A., Johnston, J. D., Loriga, M. A., McCaffrey, K. J. W., Walsh, J. J. & Watterson, J., 1999. Influence of layering on vein systematics in line samples. *Geological Society, London, Special Publications*, **155**, 35–56.

Glazner, A. F., 2007. Thermal limitations on incorporation of wall rock into magma. *Geology*, **35**, 319.

Glen, R. A., 2005. The Tasmanides of eastern Australia. *Geological Society, London, Special Publications*, **246**, 23–96.

Glen, R. A., 2013. Refining accretionary orogen models for the Tasmanides of eastern Australia. *Australian Journal of Earth Sciences*, **60**, 315–370.

Glen, R. A., Saeed, A., Quinn, C. D. & Griffin, W. L., 2011. U–Pb and Hf isotope data from zircons in the Macquarie Arc, Lachlan Orogen: Implications for arc

evolution and Ordovician palaeogeography along part of the east Gondwana margin. *Gondwana Research*, **19**, 670–685.

Goodge, J. & Fanning, C., 2002. Precambrian crustal history of the Nimrod Group, central Transantarctic Mountains. In: *Antarctica at the Close of a Millennium, Proceedings of the 8th International Symposium on Antarctic Earth Science. Royal Society of New Zealand Bulletin*, 43–50.

Goodge, J. W. & Vervoort, J. D., 2006. Origin of Mesoproterozoic A-type granites in Laurentia: Hf isotope evidence. *Earth and Planetary Science Letters*, **243**, 711–731.

Goodge, J. W. & Finn, C. A., 2010. Glimpses of East Antarctica: Aeromagnetic and satellite magnetic view from the central Transantarctic Mountains of East Antarctica. *Journal of Geophysical Research: Solid Earth*, **115**, B09103.

Goodge, J. W., Fanning, C. M. & Bennett, V. C., 2001. U–Pb evidence of ~1.7 Ga crustal tectonism during the Nimrod Orogeny in the Transantarctic Mountains, Antarctica: implications for Proterozoic plate reconstructions. *Precambrian Research*, **112**, 261–288.

Goodge, J. W., Fanning, C. M., Devon, M. B., Licht, K. J. & Emerson, F. P., 2010. Continuation of the Laurentian Grenville Province across the Ross Sea Margin of East Antarctica. *The Journal of Geology*, **118**, 601–619.

Goodge, J. W., Fanning, C. M., Norman, M. D. & Bennett, V. C., 2012. Temporal, Isotopic and Spatial Relations of Early Paleozoic Gondwana-Margin Arc Magmatism, Central Transantarctic Mountains, Antarctica. *Journal of Petrology*, **53**, 2027–2065.

Goodge, J. W., Fanning, C. M., Vervoort, J. D. & Fisher, C. M., 2013. Archean, Paleoproterozoic and Mesoproterozoic crust of cenral East Antarctica: New Insights on subglacial geology strengthen Rodian ties to Western Laurentia. *Geological Society of America Abstracts with Programs*, **45**, 8.

Gordon, S. M., Little, T. A., Hacker, B. R., Bowring, S. A., Korchinski, M., Baldwin, S. L. & Kylander-Clark, A. R. C., 2012. Multi-stage exhumation of young UHP–HP rocks: Timescales of melt crystallization in the D'Entrecasteaux Islands, southeastern Papua New Guinea. *Earth and Planetary Science Letters*, **351–352**, 237–246.

Gray, D. R. & Foster, D. A., 2004. Tectonic evolution of the Lachlan Orogen, southeast Australia: historical review, data synthesis and modern perspectives. *Australian Journal of Earth Sciences*, **51**, 773–817.

Green, E., Holland, T. & Powell, R., 2007. An order-disorder model for omphacitic pyroxenes in the system jadeite-diopside-hedenbergite-acmite, with applications to eclogitic rocks. *American Mineralogist*, **92**, 1181–1189.

Griffin, W. L., Pearson, N. J., Belousova, E., Jackson, S. E., van Achterbergh, E., O,ÄôReilly, S. Y. & Shee, S. R., 2000. The Hf isotope composition of cratonic mantle: LAM-MC-ICPMS analysis of zircon megacrysts in kimberlites. *Geochimica et Cosmochimica Acta*, **64**, 133–147.

Gu, X. X., 1994. Geochemical Characteristics of the Triassic Tethys-Turbidites in Northwestern Sichuan, China - Implications for Provenance and Interpretation of the Tectonic Setting. *Geochimica et Cosmochimica Acta*, **58**, 4615–4631.

Guernina, S. & Sawyer, E. W., 2003. Large-scale melt-depletion in granulite terranes: an example from the Archean Ashuanipi Subprovince of Quebec. *Journal of Metamorphic Geology*, **21**, 181–201.

Guilmette, C., Indares, A. & Hébert, R., 2011. High-pressure anatectic paragneisses from the Namche Barwa, Eastern Himalayan Syntaxis: Textural evidence for partial melting, phase equilibria modeling and tectonic implications. *Lithos*, **124**, 66–81.

Hacker, B. R., Andersen, T. B., Johnston, S., Kylander-Clark, A. R., Peterman, E. M., Walsh, E. O. & Young, D., 2010. High-temperature deformation during continental-margin subduction & exhumation: The ultrahigh-pressure Western Gneiss Region of Norway. *Tectonophysics*, **480**, 149–171.

Hall, D. & Kisters, A., 2012. The stabilization of self-organised leucogranite networks—Implications for melt segregation and far-field melt transfer in the continental crust. *Earth and Planetary Science Letters*, **355-356**, 1–12.

Handler, M. R., Wysoczanski, R. J. & Gamble, J. A., 2003. Proterozoic lithosphere in Marie Byrd Land, West Antarctica; Re-Os systematics of spinel peridotite xenoliths. *Chemical geology*, **196**, 131–145.

Handy, M., Mulch, A., Rosenau, M. & Rosenberg, C., 2001. The role of fault zones and melts as agents of weakening, hardening and differentiation of the continental crust: a synthesis. *Geological Society, London, Special Publications*, **186**, 305–332.

Harley, S. L., 1998. On the occurrence and characterization of ultrahigh-temperature crustal metamorphism. *Geological Society, London, Special Publications*, **138**, 81–107.

Harley, S. & Kelly, N., 2007. The impact of zircon–garnet REE distribution data on the interpretation of zircon U–Pb ages in complex high-grade terrains: an example from the Rauer Islands, East Antarctica. *Chemical Geology*, **241**, 62–87.

Harley, S. L., Kelly, N. M. & Möller, A., 2007. Zircon behaviour and the thermal histories of mountain chains. *Elements*, **3**, 25–30.

Harley, S. L., Fitzsimons, I. C. W. & Zhao, Y., 2013. Antarctica and supercontinent evolution: historical perspectives, recent advances and unresolved issues. *Geological Society, London, Special Publications*, **383**, 1–34.

Harlov, D., Wirth, R. & Hetherington, C., 2011. Fluid-mediated partial alteration in monazite: the role of coupled dissolution–reprecipitation in element redistribution and mass transfer. *Contributions to Mineralogy and Petrology*, **162**, 329–348.

Harlov, D. E. & Hetherington, C. J., 2010. Partial high-grade alteration of monazite using alkali-bearing fluids: Experiment and nature. *American Mineralogist*, **95**, 1105–1108.

Harris, N. & Massey, J., 1994. Decompression and anatexis of Himalayan metapelites. *Tectonics*, **13**, 1537–1546.

Harris, N. B. W., Caddick, M., Kosler, J., Goswami, S., Vance, D. & Tindle, A. G., 2004. The pressure-temperature-time path of migmatites from the Sikkim Himalaya. *Journal of Metamorphic Geology*, **22**, 249–264.

Harrison, T. M. & Watson, E. B., 1983. Kinetics of zircon dissolution and zirconium diffusion in granitic melts of variable water content. *Contributions to Mineralogy and Petrology*, **84**, 66–72.

Harrison, T. M., Watson, E. B. & Aikman, A. B., 2007. Temperature spectra of zircon crystallization in plutonic rocks. *Geology*, **35**, 635–638.

Hartel, T. H. D. & Pattison, D. R. M., 1996. Genesis of the Kapuskasing (Ontario) migmatitic mafic granulites by dehydration melting of amphibolite: the importance of quartz to reaction progress. *Journal of Metamorphic Geology*, **14**, 591–611.

Hatcher, R. D. & Merschat, A. J., 2006. The Appalachian Inner Piedmont: an exhumed strike-parallel, tectonically forced orogenic channel. *Geological Society, London, Special Publications*, **268**, 517–541.

Hawkesworth, C. J. & Kemp, A. I. S., 2006. Using hafnium and oxygen isotopes in zircons to unravel the record of crustal evolution. *Chemical geology*, **226**, 144–162.

Hayashi, K., Fujisawa, H., Holland, H. D. & Ohmoto, H., 1997. Geochemistry of similar to 1.9 Ga sedimentary rocks from northeastern Labrador, Canada. *Geochimica et Cosmochimica Acta*, **61**, 4115–4137.

Hegner, E., Gruler, M., Hann, H. P., Chen, F. & Guldenpfennig, M., 2005. Testing tectonic models with geochemical provenance parameters in greywacke. *Journal of the Geological Society*, **162**, 87–96.

Henjes-Kunst, F. & Kreuzer, H., 2003. Mid-Paleozoic igneous activity in northern Victoria Land, Antarctica: implications of new geochronological data. *Geologisches Jahrbuch B*, **85**, 271–302.

Hensen, J. & Osunai, Y., 1994. Experimental study of dehydration melting of F-bearing biotite in model pelitic compositions. *Mineralogical Magazine*, **58**, 410–411.

Hermann, J. & Rubatto, D., 2003. Relating zircon and monazite domains to garnet growth zones: age and duration of granulite facies metamorphism in the Val Malenco lower crust. *Journal of Metamorphic Geology*, **21**, 833–852.

Hippertt, J., 1999. Are S–C structures, duplexes and conjugate shear zones different manifestations of the same scale-invariant phenomenon? *Journal of Structural Geology*, **21**, 975–984.

Hobbs, B. E. & Ord, A., 2010. The mechanics of granitoid systems and maximum entropy production rates. *Philosophical Transactions of the Royal Society A: Mathematical, Physical and Engineering Sciences*, **368**, 53–93.

Högdahl, K., Majka, J., Sjöström, H., Nilsson, K., Claesson, S. & Konečný, P., 2012. Reactive monazite and robust zircon growth in diatexites and leucogranites from a hot, slowly cooled orogen: implications for the Palaeoproterozoic tectonic evolution of the central Fennoscandian Shield, Sweden. *Contributions to Mineralogy and Petrology*, **163**, 167–188.

Holail, H. M. & Moghazi, A. K. M., 1998. Provenance, tectonic setting and geochemistry of greywackes and siltstones of the late Precambrian Hammamat Group, Egypt. *Sedimentary Geology*, **116**, 227–250.

Holland, T. & Powell, R., 2003. Activity-composition relations for phases in petrological calculations: an asymmetric multicomponent formulation. *Contributions to Mineralogy and Petrology*, **145**, 492–501.

Holland, T. J. B. & Powell, R., 1998. An internally consistent thermodynamic data set for phases of petrological interest. *Journal of Metamorphic Geology*, **16**, 309–343.

Hollister, L. S., 1993. The Role of Melt in the Uplift and Exhumation of Orogenic Belts. *Chemical Geology*, **108**, 31–48.

Hollister, L. S. & Crawford, M. L., 1986. Melt-enhanced deformation: A major tectonic process. *Geology*, **14**, 558–561.

Holness, M. B. & Sawyer, E. W., 2008. On the Pseudomorphing of Melt-filled Pores During the Crystallization of Migmatites. *Journal of Petrology*, **49**, 1343–1363.

Hoskin, P. W. O. & Schaltegger, U., 2003. The composition of zircon and igneous and metamorphic petrogenesis. *Reviews in mineralogy and geochemistry*, **53**, 27–62.

Ickert, R. B., Hiess, J., Williams, I. S., Holden, P., Ireland, T. R., Lanc, P., Schram, N., Foster, J. J. & Clement, S. W., 2008. Determining high precision, in situ, oxygen isotope ratios with a SHRIMP II: Analyses of MPI-DING silicate-glass reference materials and zircon from contrasting granites. *Chemical geology*, **257**, 114–128.

Indares, A., White, R. W. & Powell, R., 2008. Phase equilibria modelling of kyanite-bearing anatectic paragneisses from the central Grenville Province. *Journal of Metamorphic Geology*, **26**, 815–836.

Ireland, T. R., Floettmann, T., Fanning, C. M., Gibson, G. M. & Preiss, W. V., 1998. Development of the early Paleozoic Pacific margin of Gondwana from detrital-zircon ages across the Delamerian Orogen. *Geology*, **26**, 243–246.

Jamieson, R. A., Unsworth, M. J., Harris, N. B. W., Rosenberg, C. L. & Schulmann, K., 2011. Crustal Melting and the Flow of Mountains. *Elements*, **7**, 253–260.

Jeon, H., Williams, I. S. & Chappell, B. W., 2012. Magma to mud to magma: rapid crustal recycling by Permian granite magmatism near the eastern Gondwana margin. *Earth and Planetary Science Letters*, **319**, 104–117.

Johannes, W., 1988. What controls partial melting in migmatites? *Journal of Metamorphic Geology*, **6**, 451–465.

Johannes, W., Ehlers, C., Kriegsman, L. M. & Mengel, K., 2003. The link between migmatites and S-type granites in the Turku area, southern Finland. *Lithos*, **68**, 69–90.

Johnson, S. E. & Vernon, R. H., 1995. Stepping stones and pitfalls in the determination of an anticlockwise P-T-t-deformation path: the low-P, high-T Cooma Complex, Australia. *Journal of Metamorphic Geology*, **13**, 165–183.

Johnson, T. & Brown, M., 2004. Quantitative constraints on metamorphism in the variscides of southern Brittany - a complementary pseudosection approach. *Journal of Petrology*, **45**, 1237–1259.

Johnson, T., Hudson, N. & Droop, G., 2001. Melt segregation structures within the Inzie Head gneisses of the northeastern Dalradian. *Scottish Journal of Geology*, **37**, 59–72.

Johnson, T. E., Brown, M. & Solar, G. S., 2003. Low-pressure subsolidus and suprasolidus phase equilibria in the MnNCKFMASH system: Constraints on conditions of regional metamorphism in western Maine, northern Appalachians. *American Mineralogist*, **88**, 624–638.

Johnson, T. E., White, R. W. & Powell, R., 2008. Partial melting of metagreywacke: a calculated mineral equilibria study. *J Metamorph Geol*, **26**, 837–853.

Kalsbeek, F., Pulvertaft, T. C. R. & Nutman, A. P., 1998. Geochemistry, age and origin of metagreywackes from the Palaeoproterozoic Karrat Group, Rinkian Belt, West Greenland. *Precambrian Research*, **91**, 383–399.

Kelemen, P. B., Braun, M. & Hirth, G., 2000. Spatial distribution of melt conduits in the mantle beneath oceanic spreading ridges: Observations from the Ingalls and Oman ophiolites. *Geochemistry Geophysics Geosystems*, **1**.

Kelly, E. D., Carlson, W. D. & Connelly, J. N., 2011. Implications of garnet resorption for the Lu–Hf garnet geochronometer: an example from the contact aureole of the Makhavinekh Lake Pluton, Labrador. *Journal of Metamorphic Geology*, **29**, 901–916.

Kelly, N. M., Harley, S. L. & Möller, A., 2012. Complexity in the behavior and recrystallization of monazite during high-T metamorphism and fluid infiltration. *Chemical Geology*, **322–323**, 192–208.

Kelsey, D. E., Clark, C. & Hand, M., 2008. Thermobarometric modelling of zircon and monazite growth in melt-bearing systems; examples using model metapelitic and metapsammitic granulites. *Journal of Metamorphic Geology*, **26**, 199–212.

Kelsey, D. E. & Powell, R., 2011. Progress in linking accessory mineral growth and breakdown to major mineral evolution in metamorphic rocks: a thermodynamic approach in the Na2O-CaO-K2O-FeO-MgO-Al2O3-SiO2-H2O-TiO2-ZrO2 system. *Journal of Metamorphic Geology*, **29**, 151–166.

Kemp, A. I. S., Wormald, R. J., Whitehouse, M. J. & Price, R. C., 2005. Hf isotopes in zircon reveal contrasting sources and crystallization histories for alkaline to peralkaline granites of Temora, southeastern Australia. *Geology*, **33**, 797–800.

Kemp, A. I. S., Hawkesworth, C. J., Paterson, B. A., Foster, G. L., Kinny, P. D., Whitehouse, M. J., Maas, R. & Eimf, 2006a. Exploring the plutonic-volcanic link: a zircon U-Pb, Lu-Hf and O isotope study of paired volcanic and granitic units from southeastern Australia. *Transactions of the Royal Society of Edinburgh-Earth Sciences*, **97**, 337–355.

Kemp, A. I. S., Hawkesworth, C. J., Paterson, B. A. & Kinny, P. D., 2006b. Episodic growth of the Gondwana supercontinent from hafnium and oxygen isotopes in zircon. *Nature*, **439**, 580–583.

Kemp, A. I. S., Hawkesworth, C. J., Foster, G. L., Paterson, B. A., Woodhead, J. D., Hergt, J. M., Gray, C. M. & Whitehouse, M. J., 2007. Magmatic and crustal differentiation history of granitic rocks from Hf-O isotopes in zircon. *Science*, **315**, 980–983.

Kemp, A. I. S., Hawkesworth, C. J., Collins, W. J., Gray, C. M., Blevin, P. L. & Eimf, 2009. Isotopic evidence for rapid continental growth in an extensional accretionary orogen: The Tasmanides, eastern Australia. *Earth and Planetary Science Letters*, **284**, 455–466.

Kiminami, K. & Fujii, K., 2007. The relationship between major element concentration and grain size within sandstones from four turbidite sequences in Japan. *Sedimentary Geology*, **195**, 203–215.

King, J., Harris, N., Argles, T., Parrish, R. & Zhang, H., 2011. Contribution of crustal anatexis to the tectonic evolution of Indian crust beneath southern Tibet. *Geological Society of America Bulletin*, **123**, 218–239.

Koester, E., Pawley, A. R., Fernandes, L. A., Porcher, C. C. & SOLIANI, E., 2002. Experimental melting of cordierite gneiss and the petrogenesis of syntranscurrent peraluminous granites in southern Brazil. *Journal of Petrology*, **43**, 1595–1616.

Kohn, M. J., 2009. Models of garnet differential geochronology. *Geochimica et Cosmochimica Acta*, **73**, 170–182.

Kohn, M. J. & Malloy, M. A., 2004. Formation of monazite via prograde metamorphic reactions among common silicates: implications for age determinations. *Geochimica et Cosmochimica Acta*, **68**, 101–113.

Korhonen, F. J., Saito, S., Brown, M. & Siddoway, C. S., 2010a. Modeling multiple melt loss events in the evolution of an active continental margin. *Lithos*, **116**, 230–248.

Korhonen, F. J., Saito, S., Brown, M., Siddoway, C. S. & Day, J. M. D., 2010b. Multiple generations of granite in the Fosdick Mountains, Marie Byrd Land, West Antarctica; implications for polyphase intracrustal differentiation in a continental margin setting. *Journal of Petrology*, **51**, 627–670.

Korhonen, F. J., Brown, M., Grove, M., Siddoway, C. S., Baxter, E. F. & Inglis, J. D., 2012. Separating metamorphic events in the Fosdick migmatite-granite complex, West Antarctica. *Journal of Metamorphic Geology*, **30**, 165–192.

Korhonen, F. J., Brown, M., Clark, C. & Bhattacharya, S., 2013a. Osumilite–melt interactions in ultrahigh temperature granulites: phase equilibria modelling and

implications for the P–T–t evolution of the Eastern Ghats Province, India. *Journal of Metamorphic Geology*, **31**, 881–907.

Korhonen, F. J., Clark, C., Brown, M., Bhattacharya, S. & Taylor, R., 2013b. How long-lived is ultrahigh temperature (UHT) metamorphism? Constraints from zircon and monazite geochronology in the Eastern Ghats orogenic belt, India. *Precambrian Research*, **234**, 322–350.

Kruckenberg, S. C., Ferré, E. C., Teyssier, C., Vanderhaeghe, O., Whitney, D. L., Seaton, N. C. & Skord, J. A., 2010. Viscoplastic flow in migmatites deduced from fabric anisotropy: An example from the Naxos dome, Greece. *Journal of Geophysical Research: Solid Earth*, **115**.

Kruckenberg, S. C., Vanderhaeghe, O., Ferré, E. C., Teyssier, C. & Whitney, D. L., 2011. Flow of partially molten crust and the internal dynamics of a migmatite dome, Naxos, Greece. *Tectonics*, **30**.

Kruhl, J. r. H., 2013. Fractal-geometry techniques in the quantification of complex rock structures: A special view on scaling regimes, inhomogeneity and anisotropy. *Journal of Structural Geology*, **46**, 2–21.

Kruhl, J. H. & Renftel, L.-O., 1994. *Fractals and dynamic systems in geoscience*. Springer-Verlag, Berlin; London.

Kruskal, W. H. & Wallis, W. A., 1952. Use of Ranks in One-Criterion Variance Analysis. *Journal of the American Statistical Association*, **47**, 583–621.

Kylander-Clark, A. R. C., Hacker, B. R., Johnson, C. M., Beard, B. L., Mahlen, N. J. & Lapen, T. J., 2007. Coupled Lu–Hf and Sm–Nd geochronology constrains prograde and exhumation histories of high- and ultrahigh-pressure eclogites from western Norway. *Chemical Geology*, **242**, 137–154.

Labrousse, L., Prouteau, G. & Ganzhorn, A. C., 2011. Continental exhumation triggered by partial melting at ultrahigh pressure. *Geology*, **39**, 1171–1174.

Lackey, J., Valley, J. & Saleeby, J., 2005. Supracrustal input to magmas in the deep crust of Sierra Nevada batholith: Evidence from high-O zircon. *Earth and Planetary Science Letters*, **235**, 315–330.

Lapen, T. J., Johnson, C. M., Baumgartner, L. P., Mahlen, N. J., Beard, B. L. & Amato, J. M., 2003. Burial rates during prograde metamorphism of an ultra-high-pressure terrane: an example from Lago di Cignana, western Alps, Italy. *Earth and Planetary Science Letters*, **215**, 57–72.

Laporte, D. & Watson, E. B., 1995. Experimental and theoretical constraints on melt distribution in crustal sources: the effect of crystalline anisotropy on melt interconnectivity. *Chemical Geology*, **124**, 161–184.

Laporte, D., Rapaille, C. d. & Provost, A., 1997. Wetting Angles, Equilibrium Melt Geometry, and the Permeability Threshold of Partially Molten Crustal Protoliths. In: *Granite: From Segregation of Melt to Emplacement Fabrics* (eds Bouchez, J. L., Hutton, D. H. W. & Stephens, W. E.) *Petrology and Structural Geology*, 31–54, Springer Netherlands.

Lasalle, S., Dunning, G. & Indares, A., 2014. In situ LA–ICP–MS dating of monazite from aluminous gneisses: insights on the tectono-metamorphic history of a granulite-facies domain in the central Grenville Province. *Canadian Journal of Earth Sciences*, **51**, 558–572.

Lesher, C. E., 1994. Kinetics of Sr and Nd exchange in silicate liquids: Theory, experiments, and applications to uphill diffusion, isotopic equilibration, and irreversible mixing of magmas. *Journal of Geophysical Research: Solid Earth*, **99**, 9585–9604.

Ludwig, K. R., 2001. User's guide to SQUID 2.2, Berkeley Geochronology Center, Berkeley.

Ludwig, K. R., 2003. User's manual for ISOPLOT 3, A Geochronological Toolkt for Microsoft Excel, Berkeley Geochronology Center, Special Publication No. 4, Berkeley.

Lupulescu, A. & Watson, E. B., 1999. Low melt fraction connectivity of granitic and tonalitic melts in a mafic crustal rock at 800 °C and 1 GPa. *Contributions to Mineralogy and Petrology*, **134**, 202–216.

Luyendyk, B. P., 1995. Hypothesis for Cretaceous rifting of East Gondwana caused by subducted slab capture. *Geology*, **23**, 373–376.

Luyendyk, B., Cisowski, S., Smith, C., Richard, S. & Kimbrough, D., 1996. Paleomagnetic study of the northern Ford Ranges, western Marie Byrd Land, West Antarctica: Motion between West and East Antarctica. *Tectonics*, **15**, 122–141.

Luyendyk, B. P., Wilson, D. S. & Siddoway, C. S., 2003. Eastern margin of the Ross Sea Rift in western Marie Byrd Land, Antarctica: Crustal structure and tectonic development. *Geochemistry, Geophysics, Geosystems*, **4**, 1090.

Maaløe, S., 1992. Melting and diffusion processes in closed-system migmatization. *Journal of Metamorphic Geology*, **10**, 503–516.

Mahan, K. H., Bartley, J. M., Coleman, D. S., Glazner, A. F. & Carl, B. S., 2003. Sheeted intrusion of the synkinematic McDoogle pluton, Sierra Nevada, California. *Geological Society of America Bulletin*, **115**, 1570–1582.

Marchildon, N. & Brown, M., 2002. Grain-scale melt distribution in two contact aureole rocks: implications for controls on melt localization and deformation. *Journal of Metamorphic Geology*, **20**, 381–396.

Marchildon, N. & Brown, M., 2003. Spatial distribution of melt-bearing structures in anatectic rocks from Southern Brittany, France: implications for melt transfer at grain- to orogen-scale. *Tectonophysics*, **364**, 215–235.

Martins, L., Vlach, S. R. F. & Janasi, V. d. A., 2009. Reaction microtextures of monazite: Correlation between chemical and age domains in the Nazaré Paulista migmatite, SE Brazil. *Chemical Geology*, **261**, 271–285.

McCaffrey, K. J. W. & Petford, N., 1997. Are granitic intrusions scale invariant? *Journal of the Geological Society*, **154**, 1–4.

McDaniel, D. K., Hemming, S. R., McLennan, S. M. & Hanson, G. N., 1994. Petrographic, Geochemical, and Isotopic Constraints on the Provenance of the Early Proterozoic Chelmsford Formation, Sudbury Basin, Ontario. *Journal of Sedimentary Research*, **64**, 362–372.

McDonough, W. F. & Sun, S. s., 1995. The composition of the Earth. *Chemical geology*, **120**, 223–253.

McFadden, R., Siddoway, C., Teyssier, C., Fanning, C. M. & Kruckenberg, S. C., 2007. Cretaceous oblique detachment tectonics int eh Fosdick Mountains, Marie Bryd Land, Antarctica. In: *Antarctica: a Keystone in a Changing World – Online Proceedings ont he 10th ISAES* (ed Raymond, C. R.), USGS Open-File Report 2007-1047.

McFadden, R. R., Siddoway, C. S., Teyssier, C. & Fanning, C. M., 2010a. Cretaceous oblique extensional deformation and magma accumulation in the Fosdick Mountains migmatite-cored gneiss dome, West Antarctica. *Tectonics*, **29**, TC4022.

McFadden, R. R., Teyssier, C., Siddoway, C. S., Whitney, D. L. & Fanning, C. M., 2010b. Oblique dilation, melt transfer, and gneiss dome emplacement. *Geology*, **38**, 375–378.

McLaren, S. & Powell, R., 2014. Magmatism, orogeny and the origin of high-heat-producing granites in Australian Proterozoic terranes. *Journal of the Geological Society*.

McLellan, E. L., 1988. Migmatite structures in the Central Gneiss Complex, Boca de Quadra, Alaska. *Journal of Metamorphic Geology*, **6**, 517–542.

Miles, A., Graham, C., Hawkesworth, C., Gillespie, M., Dhuime, B. & Hinton, R., 2014. Using Zircon Isotope Compositions to Constrain Crustal Structure and Pluton Evolution: the Iapetus Suture Zone Granites in Northern Britain. *Journal of Petrology*, **55**, 181–207.

Millar, I. L. & Pankhurst, R. J., 1987. Rb-Sr geochronology of the region between the Antarctic Peninsula and the Transantarctic Mountains; Haag Nunataks and Mesozoic granitoids. *Geophysical Monograph*, **40**, 151–160.

Miller, J. S., 2008. Assembling a pluton...one increment at a time. *Geology*, **36**, 511–512.

Milord, I., Sawyer, E. & Brown, M., 2001. Formation of diatexite migmatite and granite magma during anatexis of semi-pelitic metasedimentary rocks: an example from St. Malo, France. *Journal of Petrology*, **42**, 487–505.

Mišković, A. & Schaltegger, U., 2009. Crustal growth along a non-collisional cratonic margin: A Lu–Hf isotopic survey of the Eastern Cordilleran granitoids of Peru. *Earth and Planetary Science Letters*, **279**, 303–315.

Misra, S., Burg, J.-P. & Mainprice, D., 2011. Effect of finite deformation and deformation rate on partial melting and crystallization in metapelites. *Journal of Geophysical Research*, **116**, B02205.

Moecher, D. P., Samson, S. D. & Miller, C. F., 2004. Precise time and conditions of peak Taconian granulite facies metamorphism in the Southern Appalachian Orogen, USA, with implications for zircon behavior during crustal melting events. *The Journal of geology*, **112**, 289–304.

Montési, L. G. J., 2013. Fabric development as the key for forming ductile shear zones and enabling plate tectonics. *Journal of Structural Geology*, **50**, 254–266.

Morand, V. J., 1990. Low-pressure regional metamorphism in the Omeo Metamorphic Complex, Victoria, Australia. *Journal of Metamorphic Geology*, **8**, 1–12.

Morfin, S., Sawyer, E. W. & Bandyayera, D., 2013. Large volumes of anatectic melt retained in granulite facies migmatites: An injection complex in northern Quebec. *Lithos*, **168–169**, 200–218.

Morfin, S., Sawyer, E. W. & Bandyayera, D., 2014. The geochemical signature of a felsic injection complex in the continental crust: Opinaca Subprovince, Quebec. *Lithos*, **196–197**, 339–355.

Mortimer, N., 2004. New Zealand's geological foundations. *Gondwana Research*, **7**, 261–272.

Mortimer, N., Hoernle, K., Hauff, F., Palin, J. M., Dunlap, W. J., Werner, R. & Faure, K., 2006. New constraints on the age and evolution of the Wishbone Ridge, Southwest Pacific Cretaceous microplates, and Zealandia-West Antarctica breakup. *Geology*, **34**, 185–188.

Muir, R. J., Ireland, T. R., Weaver, S. D. & Bradshaw, J. D., 1994. Ion microprobe U-Pb zircon geochronology of granitic magmatism in the Western Province of the South Island, New Zealand. *Chemical geology*, **113**, 171–189.

Muir, R. J., Weaver, S. D., Bradshaw, J. D., Eby, G. N. & Evans, J. A., 1995. The Cretaceous Separation Point batholith, New Zealand: granitoid magmas formed by melting of mafic lithosphere. *Journal of the Geological Society*, **152**, 689–701.

Muir, R. J., Ireland, T. R., Weaver, S. D. & Bradshaw, J. D., 1996. Ion microprobe dating of Paleozoic granitoids; Devonian magmatism in New Zealand and correlations with Australia and Antarctica. *Chemical geology*, **127**, 191–210.

Muir, R. J., Ireland, T. R., Weaver, S. D., Bradshaw, J. D., Evans, J. A., Eby, G. N. & Shelley, D., 1998. Geochronology and geochemistry of a Mesozoic magmatic arc system, Fiordland, New Zealand. *Journal of the Geological Society*, **155**, 1037–1052.

Mukasa, S. B. & Dalziel, I. W. D., 2000. Marie Byrd Land, West Antarctica; evolution of Gondwana's Pacific margin constrained by zircon U-Pb geochronology and feldspar common-Pb isotopic compositions. *Geological Society of America Bulletin*, **112**, 611–627.

Munizaga, F., Maksaev, V., Fanning, C. M., Giglio, S., Yaxley, G. & Tassinari, C. C. G., 2008. Late Paleozoic–Early Triassic magmatism on the western margin of Gondwana: Collahuasi area, Northern Chile. *Gondwana Research*, **13**, 407–427.

Nash, W. & Crecraft, H., 1985. Partition coefficients for trace elements in silicic magmas. *Geochimica et Cosmochimica Acta*, **49**, 2309–2322.

Nebel-Jacobsen, Y., Münker, C., Nebel, O. & Mezger, K., 2011. Precambrian sources of Early Paleozoic SE Gondwana sediments as deduced from combined Lu–Hf and U–Pb systematics of detrital zircons, Takaka and Buller terrane, South Island, New Zealand. *Gondwana Research*, **20**, 427–442.

Nelson, K. D., Zhao, W., Brown, L. D., Kuo, J., Che, J., Liu, X., Klemperer, S. L., Makovsky, Y., Meissner, R., Mechie, J., Kind, R., Wenzel, F., Ni, J., Nabelek, J., Leshou, C., Tan, H., Wei, W., Jones, A. G., Booker, J., Unsworth, M., Kidd, W. S. F., Hauck, M., Alsdorf, D., Ross, A., Cogan, M., Wu, C., Sandvol, E. & Edwards, M., 1996. Partially Molten Middle Crust Beneath Southern Tibet: Synthesis of Project INDEPTH Results. *Science*, **274**, 1684–1688.

Nemchin, A. A. & Bodorkos, S., 2000. Zr and LREE concentrations in anatectic melt as a function of crystal size distributions of zircon and monazite in the source region. In: *Geological Society of America Abstracts and Programs*, abstract no. 52286.

Nemchin, A. A., Giannini, L. M., Bodorkos, S. & Oliver, N. H. S., 2001. Ostwald ripening as a possible mechanism for zircon overgrowth formation during anatexis: theoretical constraints, a numerical model, and its application to pelitic migmatites of the Tickalara Metamorphics, northwestern Australia. *Geochimica et Cosmochimica Acta*, **65**, 2771–2788.

Nichols, G. T., Berry, R. F. & Green, D. H., 1992. Internally consistent gahnitic spinel-cordierite-garnet equilibria in the FMASHZn system: geothermobarometry and applications. *Contributions to Mineralogy and Petrology*, **111**, 362–377.

Norlander, B. H., Whitney, D. L., Teyssier, C. & Vanderhaeghe, O., 2002. Partial melting and decompression of the Thor-Odin dome, Shuswap metamorphic core complex, Canadian Cordillera. *Lithos*, **61**, 103–125.

Norton, D. & Taylor, H. P., 1979. Quantitative Simulation of the Hydrothermal Systems of Crystallizing Magmas on the Basis of Transport Theory and Oxygen Isotope Data: An analysis of the Skaergaard Intrusion. *Journal of Petrology*, **20**, 421–486.

Nyman, M. W., Pattison, D. R. M. & Ghent, E. D., 1995. Melt Extraction during Formation of K-Feldspar + Sillimanite Migmatites, West of Revelstoke, British Columbia. *Journal of Petrology*, **36**, 351–372.

O' Neil, J. R. & Chappell, B. W., 1977. Oxygen and hydrogen isotope relations in the Berridale batholith. *Journal of the Geological Society*, **133**, 559–571.

O'Brien, P. J. & Rötzler, J., 2003. High-pressure granulites: formation, recovery of peak conditions and implications for tectonics. *Journal of Metamorphic Geology*, **21**, 3–20.

Pankhurst, R. J., Millar, I. L., Grunow, A. M. & Storey, B. C., 1993. The pre-Cenozoic magmatic history of the Thurston Island crustal block, West Antarctica. *Journal of Geophysical Research*, **98**, 11.

Pankhurst, R. J., Weaver, S. D., Bradshaw, J. D., Storey, B. C. & Ireland, T. R., 1998. Geochronology and geochemistry of pre-Jurassic superterranes in Marie Byrd Land, Antarctica. *Journal of Geophysical Research*, **103**, 2529–2547.

Patiño Douce, A. E. & Harris, N., 1998. Experimental Constraints on Himalayan Anatexis. *Journal of Petrology*, **39**, 689–710.

Paton, C., Hellstrom, J., Paul, B., Woodhead, J. & Hergt, J., 2011. Iolite: Freeware for the visualisation and processing of mass spectrometric data. *Journal of Analytical Atomic Spectrometry*, **26**, 2508–2518.

Pattison, D. R. M. & Harte, B., 1988. Evolution of structurally contrasting anatectic migmatites in the 3-kbar Ballachulish aureole, Scotland. *Journal of Metamorphic Geology*, **6**, 475–494.

Paulsen, T. S., Encarnación, J., Grunow, A. M., Valencia, V. A., Pecha, M., Layer, P. W. & Rasoazanamparany, C., 2013. Age and significance of "outboard" high-grade metamorphics and intrusives of the Ross orogen, Antarctica. *Gondwana Research*, **24**, 349–358.

Pereira, M. F., Chichorro, M., Fernández, C., Silva, J. B. o. & Matias, F. V., 2013. The role of strain localization in magma injection into a transtensional shear zone (Variscan belt, SW Iberia). *Journal of the Geological Society*, **170**, 93–105.

Peterson, J., Chacko, T. & Kuehner, S., 1991. The effects of fluorine on the vapor-absent melting of phlogopite+ quartz; implications for deep-crustal processes. *American Mineralogist*, **76**, 470–476.

Powell, R. & Holland, T. J. B., 1988. An Internally Consistent Dataset with Uncertainties and Correlations .3. Applications to Geobarometry, Worked Examples and a Computer-Program. *Journal of Metamorphic Geology*, **6**, 173–204.

Powell, R. & Holland, T. J. B., 2008. On thermobarometry. *Journal of Metamorphic Geology*, **26**, 155–179.

Powell, R., Guiraud, M. & White, R. W., 2005. Truth and beauty in metamorphic phase-equilibria: conjugate variables and phase diagrams. *The Canadian Mineralogist*, **43**, 21–33.

Pressley, R. A. & Brown, M., 1999. The Phillips pluton, Maine, USA: evidence of heterogeneous crustal sources and implications for granite ascent and emplacement mechanisms in convergent orogens. *Lithos*, **46**, 335–366.

Pyle, J. M. & Spear, F. S., 2003. Four generations of accessory-phase growth in low-pressure migmatites from SW New Hampshire. *American Mineralogist*, **88**, 338–351.

Rabinowicz, M. & Vigneresse, J. Ä., 2004. Melt segregation under compaction and shear channeling: Application to granitic magma segregation in a continental crust. *Journal of Geophysical Research: Solid Earth*, **109**.

Rapp, R. P. & Watson, E. B., 1986. Monazite solubility and dissolution kinetics: implications for the thorium and light rare earth chemistry of felsic magmas. *Contributions to Mineralogy and Petrology*, **94**, 304–316.

Rapp, R. P., Ryerson, F. & Miller, C. F., 1987. Experimental evidence bearing on the stability of monazite during crustal anaatexis. *Geophysical Research Letters*, **14**, 307–310.

Redler, C., White, R. W. & Johnson, T. E., 2013. Migmatites in the Ivrea Zone (NW Italy): Constraints on partial melting and melt loss in metasedimentary rocks from Val Strona di Omegna. *Lithos*, **175–176**, 40–53.

Reichardt, H. & Weinberg, R. F., 2012. Hornblende chemistry in meta-and diatexites and its retention in the source of leucogranites: an example from the Karakoram Shear Zone, NW India. *Journal of Petrology*, **53**, 1287–1318.

Reno, B. L., Piccoli, P. M., Brown, M. & Trouw, R. A. J., 2012. In situ monazite (U-Th)-Pb ages from the Southern Brasília Belt, Brazil: constraints on the high-temperature retrograde evolution of HP granulites. *Journal of Metamorphic Geology*, **30**, 81–112.

Rey, P. F., Teyssier, C., Kruckenberg, S. C. & Whitney, D. L., 2011. Viscous collision in channel explains double domes in metamorphic core complexes. *Geology*, **39**, 387–390.

Rey, P. F., Teyssier, C. & Whitney, D. L., 2009. The role of partial melting and extensional strain rates in the development of metamorphic core complexes. *Tectonophysics*, **477**, 135–144.

Richard, S. M., Smith, C. H., Kimbrough, D. L., Fitzgerald, P. G., Luyendyk, B. P. & McWilliams, M. O., 1994. Cooling history of the northern Ford Ranges, Marie Byrd Land, West Antarctica. *Tectonics*, **13**, 837–857.

Roberts, M. P. & Finger, F., 1997. Do U-Pb zircon ages from granulites reflect peak metamorphic conditions? *Geology*, **25**, 319–322.

Rosenberg, C. L. & Handy, M. R., 2005. Experimental deformation of partially melted granite revisited: implications for the continental crust. *Journal of Metamorphic Geology*, **23**, 19–28.

Roser, B. P., Cooper, R. A., Nathan, S. & Tulloch, A. J., 1996. Reconnaissance sandstone geochemistry, provenance, and tectonic setting of the lower paleozoic terranes of the West Coast and Nelson, New Zealand. *New Zealand Journal of Geology and Geophysics*, **39**, 1–16.

Rothstein, D. A. & Manning, C. E., 2003. Geothermal gradients in continental magmatic arcs; constraints from the eastern Peninsular Ranges Batholith, Baja California, Mexico. *Geological Society of America Special Papers*, **374**, 337–354.

Rowell, A. J., Rees, M. N., Duebendorfer, E. M., Wallin, E. T., Van Schmus, W. R. & Smith, E. I., 1993. An active Neoproterozoic margin: evidence from the Skelton Glacier area, Transantarctic Mountains. *Journal of the Geological Society*, **150**, 677–682.

Rubatto, D., 2002. Zircon trace element geochemistry: partitioning with garnet and the link between U–Pb ages and metamorphism. *Chemical Geology*, **184**, 123–138.

Rubatto, D. & Hermann, J., 2007. Experimental zircon/melt and zircon/garnet trace element partitioning and implications for the geochronology of crustal rocks. *Chemical Geology*, **241**, 38–61.

Rubatto, D., Williams, I. S. & Buick, I. S., 2001. Zircon and monazite response to prograde metamorphism in the Reynolds Range, central Australia. *Contributions to Mineralogy and Petrology*, **140**, 458–468.

Rubatto, D., Hermann, J. & Buick, I. S., 2006. Temperature and bulk composition control on the growth of monazite and zircon during low-pressure anatexis (Mount Stafford, central Australia). *Journal of Petrology*, **47**, 1973–1996.

Rubatto, D., Chakraborty, S. & Dasgupta, S., 2013. Timescales of crustal melting in the Higher Himalayan Crystallines (Sikkim, Eastern Himalaya) inferred from trace element-constrained monazite and zircon chronology. *Contributions to Mineralogy and Petrology*, **165**, 349–372.

Rudnick, R., 1995. Making continental crust. *Nature*, **378**, 571–578.

Rudnick, R. & Gao, S., 2003. Composition of the continental crust. *Treatise on geochemistry*, **3**, 1–64.

Rushmer, T., 2001. Volume change during partial melting reactions: implications for melt extraction, melt geochemistry and crustal rheology. *Tectonophysics*, **342**, 389–405.

Rutter, E. & Mecklenburgh, J., 2006. The extraction of melt from crustal protoliths and the flow behavior of partially molten crustal rocks: an experimental perspective. *Evolution and differentiation of the continental crust. Edited by M. Brown and T. Rushmer. Cambridge University Press, Cambridge, UK*, 386–429.

Sagar, M. W. & Palin, J. M., 2011. Emplacement, metamorphism, deformation and affiliation of mid-Cretaceous orthogneiss from the Paparoa Metamorphic Core Complex lower-plate, Charleston, New Zealand. *New Zealand Journal of Geology and Geophysics*, **54**, 273–289.

Sagar, M. W. & Palin, J. M., 2013. Carboniferous U–Pb zircon age for S-type Karamea Suite Redjacket Granite, Paparoa Metamorphic Core Complex lower plate, northern Westland. *New Zealand Journal of Geology and Geophysics*, **56**, 109–120.

Saito, S., Brown, M., Korhonen, F. J., McFadden, R. R. & Siddoway, C. S., 2013. Petrogenesis of Cretaceous mafic intrusive rocks, Fosdick Mountains, West Antarctica; melting of the sub-continental arc mantle along the Gondwana margin. *Gondwana Research*, **23**, 1567–1580.

Sambridge, M. S. & Compston, W., 1994. Mixture modeling of multi-component data sets with application to ion-probe zircon ages. *Earth and Planetary Science Letters*, **128**, 373–390.

Sandiford, M. & McLaren, S., 2002. Tectonic feedback and the ordering of heat producing elements within the continental lithosphere. *Earth and Planetary Science Letters*, **204**, 133–150.

Sandiford, M., McLaren, S. & Neumann, N., 2002. Long-term thermal consequences of the redistribution of heat-producing elements associated with large-scale granitic complexes. *Journal of Metamorphic Geology*, **20**, 87–98.

Sawyer, E., 1986. The influence of source rock type, chemical weathering and sorting on the geochemistry of clastic sediments from the Quetico metasedimentary belt, Superior Province, Canada. *Chemical Geology*, **55**, 77–95.

Sawyer, E. W., 1987. The Role of Partial Melting and Fractional Crystallization in Determining Discordant Migmatite Leucosome Compositions. *Journal of Petrology*, **28**, 445–473.

Sawyer, E. W., 1991. Disequilibrium Melting and the Rate of Melt–Residuum Separation During Migmatization of Mafic Rocks from the Grenville Front, Quebec. *Journal of Petrology*, **32**, 701–738.

Sawyer, E. W., 1994. Melt segregation in the continental crust. *Geology*, **22**, 1019.

Sawyer, E. W., 1998. Formation and Evolution of Granite Magmas During Crustal Reworking: the Significance of Diatexites. *Journal of Petrology*, **39**, 1147–1167.

Sawyer, E. W., 2001. Melt segregation in the continental crust: distribution and movement of melt in anatectic rocks. *Journal of Metamorphic Geology*, **19**, 291–309.

Sawyer, E. W., 2010. Migmatites formed by water-fluxed partial melting of a leucogranodiorite protolith: Microstructures in the residual rocks and source of the fluid. *Lithos*, **116**, 273–286.

Sawyer, E. W. & Barnes, S. J., 1988. Temporal and compositional differences between subsolidus and anatectic migmatite leucosomes from the Quetico metasedimentary belt, Canada. *Journal of Metamorphic Geology*, **6**, 437–450.

Sawyer, E. W., Cesare, B. & Brown, M., 2011. When the Continental Crust Melts. *Elements*, **7**, 229–234.

Scherer, E., Münker, C. & Mezger, K., 2001. Calibration of the Lutetium-Hafnium Clock. *Science*, **293**, 683–687.

Scherer, E. E., Cameron, K. L. & Blichert-Toft, J., 2000. Lu–hf garnet geochronology: closure temperature relative to the Sm–Nd system and the effects of trace mineral inclusions. *Geochimica et Cosmochimica Acta*, **64**, 3413–3432.

Schilling, F. & Partzsch, G., 2001. Quantifying partial melt fraction in the crust beneath the central Andes and the Tibetan Plateau. *Physics and Chemistry of the Earth, Part A: Solid Earth and Geodesy*, **26**, 239–246.

Schoene, B., Schaltegger, U., Brack, P., Latkoczy, C., Stracke, A. & Günther, D., 2012. Rates of magma differentiation and emplacement in a ballooning pluton recorded by U–Pb TIMS-TEA, Adamello batholith, Italy. *Earth and Planetary Science Letters*, **355**, 162–173.

Schulte, D. O., Ring, U., Thomson, S. N., Glodny, J. & Carrad, H., 2014. Two-stage development of the Paparoa Metamorphic Core Complex, West Coast, South

Island, New Zealand: Hot continental extension precedes sea-floor spreading by ~25 my. *Lithosphere*, **6**, 177–194.

Scott, J., Muhling, J. R., Fletcher, I., Billia, M., Palin, J. M., Elliot, T. & Guenter, C., 2011. The relationship of Palaeozoic metamorphism and S-type magmatism on the paleo-Pacific Gondwana margin. *Lithos*, **127**, 522–534.

Scott, J. M. & Cooper, A. F., 2006a. Early Cretaceous extensional exhumation of the lower crust of a magmatic arc: Evidence from the Mount Irene Shear Zone, Fiordland, New Zealand. *Tectonics*, **25**, TC3018.

Scott, J. M. & Cooper, A. F., 2006b. Early Cretaceous extensional exhumation of the lower crust of a magmatic arc: Evidence from the Mount Irene Shear Zone, Fiordland, New Zealand. *Tectonics*, **25**.

Scott, J. M., Cooper, A. F., Palin, J. M., Tulloch, A. J., Kula, J., Jongens, R., Spell, T. L. & Pearson, N. J., 2009. Tracking the influence of a continental margin on growth of a magmatic arc, Fiordland, New Zealand, using thermobarometry, thermochronology, and zircon U-Pb and Hf isotopes. *Tectonics*, **28**, TC6007.

Siddoway, C., 2008. Tectonics of the West Antarctic Rift System: new light on the history and dynamics of distributed intracontinental extension. *Antarctica: A Keystone in a Changing World*, 91–114.

Siddoway, C. S., Baldwin, S. L., Fitzgerald, P. G., Fanning, C. M. & Luyendyk, B. P., 2004a. Ross Sea mylonites and the timing of intracontinental extension within the West Antarctic rift system. *Geology*, **32**, 57–60.

Siddoway, C. S., Richard, S. M., Fanning, C. M. & Luyendyk, B. P., 2004b. Origin and emplacement of a Middle Cretaceous gneiss dome, Fosdick Mountains, West Antarctica. *Special Paper - Geological Society of America*, **380**, 267–294.

Siddoway, C. S., Sass, L. C., III & Esser, R. P., 2005. Kinematic history of western Marie Byrd Land, West Antarctica; direct evidence from Cretaceous mafic dykes. *Geological Society Special Publications*, **246**, 417–438.

Siddoway, C. S. & Fanning, C. M., 2009. Paleozoic tectonism on the East Gondwana margin: Evidence from SHRIMP U–Pb zircon geochronology of a migmatite–granite complex in West Antarctica. *Tectonophysics*, **477**, 262–277.

Simpson, G. D. H., 2000. Synmetamorphic vein spacing distributions: characterisation and origin of a distribution of veins from NW Sardinia, Italy. *Journal of Structural Geology*, **22**, 335–348.

Sizova, E., Gerya, T. & Brown, M., 2012. Exhumation mechanisms of melt-bearing ultrahigh pressure crustal rocks during collision of spontaneously moving plates. *Journal of Metamorphic Geology*, **30**, 927–955.

Skjerlie, K. P. & Johnston, A. D., 1993. Fluid-Absent Melting Behavior of an F-Rich Tonalitic Gneiss at Mid-Crustal Pressures: Implications for the Generation of Anorogenic Granites. *Journal of Petrology*, **34**, 785–815.

Skora, S., Baumgartner, L., Mahlen, N., Johnson, C., Pilet, S. b. & Hellebrand, E., 2006. Diffusion-limited REE uptake by eclogite garnets and its consequences for Lu–Hf

and Sm–Nd geochronology. *Contributions to Mineralogy and Petrology*, **152**, 703–720.

Skora, S., Lapen, T. J., Baumgartner, L. P., Johnson, C. M., Hellebrand, E. & Mahlen, N. J., 2009. The duration of prograde garnet crystallization in the UHP eclogites at Lago di Cignana, Italy. *Earth and Planetary Science Letters*, **287**, 402–411.

Slagstad, T., Jamieson, R. A. & Culshaw, N. G., 2005. Formation, crystallization, and migration of melt in the mid-orogenic crust: Muskoka domain migmatites, Grenville Province, Ontario. *Journal of Petrology*, **46**, 893–919.

Smit, M., Scherer, E., Bröcker, M. & van Roermund, H. M., 2010. Timing of eclogite facies metamorphism in the southernmost Scandinavian Caledonides by Lu–Hf and Sm–Nd geochronology. *Contributions to Mineralogy and Petrology*, **159**, 521–539.

Smit, M. A., Scherer, E. E. & Mezger, K., 2013. Lu–Hf and Sm–Nd garnet geochronology: Chronometric closure and implications for dating petrological processes. *Earth and Planetary Science Letters*, **381**, 222–233.

Smith, C. H., 1996. Migmatites of the Alexandra Mountains, West Antarctica: Pressure-Temperature conditions of formation and regional context. *Geologisches Jahrbuch*, **B52**, 169–178.

Söderlund, U., Patchett, J. P., Vervoort, J. D. & Isachsen, C. E., 2004. The Lu-176 decay constant determined by Lu-Hf and U-Pb isotope systematics of Precambrian mafic intrusions. *Earth and Planetary Science Letters*, **219**, 311–324.

Soesoo, A. & Urtson, K., 2009. Stepwise magma migration and accumulation processes and their effect on extracted melt chemistry. *Estonian Journal of Earth Sciences*, **58**, 246.

Soesoo, A., Kalda, J., Bons, P., Urtson, K. & Kalm, V., 2004. Fractality in geology: a possible use of fractals in the studies of partial melting processes. *Proceedings of the Estonian Acandemy of Sciences, Geology*, **53**, 13–27.

Solar, G. S. & Brown, M., 2001. Petrogenesis of Migmatites in Maine, USA: Possible Source of Peraluminous Leucogranite in Plutons? *Journal of Petrology*, **42**, 789–823.

Solar, G. S., Pressley, R. A., Brown, M. & Tucker, R. D., 1998. Granite ascent in convergent orogenic belts: Testing a model. *Geology*, **26**, 711–714.

Sousa, J., Kohn, M. J., Schmitz, M. D., Northrup, C. J. & Spear, F. S., 2013. Strontium isotope zoning in garnet: implications for metamorphic matrix equilibration, geochronology and phase equilibrium modelling. *Journal of Metamorphic Geology*, **31**, 437–452.

Spear, F. S. & Pyle, J. M., 2010. Theoretical modeling of monazite growth in a low-Ca metapelite. *Chemical Geology*, **273**, 111–119.

Spear, F. S., Kohn, M. J. & Cheney, J. T., 1999. P-T paths from anatectic pelites. *Contrib Mineral Petrol*, **134**, 17–32.

Spell, T. L., McDougall, I. & Tulloch, A. J., 2000. Thermochronologic constraints on the breakup of the Pacific Gondwana margin: The Paparoa metamorphic core complex, South Island, New Zealand. *Tectonics*, **19**, 433–451.

Stacey, J. S. & Kramers, J. D., 1975. Approximation of terrestrial lead isotope evolution by a two-stage model. *Earth and Planetary Science Letters*, **26**, 207–221.

Stepanov, A. S., Hermann, J., Rubatto, D. & Rapp, R. P., 2012. Experimental study of monazite/melt partitioning with implications for the REE, Th and U geochemistry of crustal rocks. *Chemical Geology*, **300**, 200–220.

Stolper, E. & Asimow, P., 2007. Insights into mantle melting from graphical analysis of one-component systems. *American Journal of Science*, **307**, 1051–1139.

Storey, B. C., Pankhurst, R. J. & Johnson, A. C., 1994. The Grenville Province within Antarctica; a test of the SWEAT hypothesis. *Journal of the Geological Society of London*, **151,** 1–4.

Storey, B. C., Leat, P. T., Weaver, S. D., Pankhurst, R. J., Bradshaw, J. D. & Kelley, S., 1999. Mantle plumes and Antarctica-New Zealand rifting; evidence from Mid-Cretaceous mafic dykes. *Journal of the Geological Society of London*, **156,** 659–671.

Stowell, H., Parker, K. O., Gatewood, M., Tulloch, A. & Koenig, A., 2014. Temporal links between pluton emplacement, garnet granulite metamorphism, partial melting and extensional collapse in the lower crust of a Cretaceous magmatic arc, Fiordland, New Zealand. *Journal of Metamorphic Geology*, **32**, 151–175.

Stüwe, K., 2007. *Geodynamics of the lithosphere*. Springer-Verlag, Berlin.

Tanner, D. C., 1999. The scale-invariant nature of migmatite from the Oberpfalz, NE Bavaria and its significance for melt transport. *Tectonophysics*, **302**, 297–305.

Taylor, H. P. & Sheppard, S. M. F., 1986. Igneous rocks; I, Processes of isotopic fractionation and isotope systematics. *Reviews in mineralogy and geochemistry*, **16**, 227–271.

Taylor, J. & Stevens, G., 2010. Selective entrainment of peritectic garnet into S-type granitic magmas: Evidence from Archaean mid-crustal anatectites. *Lithos*, **120**, 277–292.

Taylor, S., 1967. The origin and growth of continents. *Tectonophysics*, **4**, 17–34.

Taylor, S. R. & McLennan, S. M., 1985. *The continental crust: its composition and evolution*. Blackwell, Oxford.

Tera, F. & Wasserburg, G. J., 1972. U-Th-Pb systematics in three Apollo 14 basalts and the problem of initial Pb in lunar rocks. *Earth and Planetary Science Letters*, **14**, 281–304.

Teyssier, C. & Whitney, D. L., 2002. Gneiss domes and orogeny. *Geology*, **30**, 1139.

Tirel, C., Brun, J.-P. & Burov, E., 2008. Dynamics and structural development of metamorphic core complexes. *Journal of Geophysical Research: Solid Earth*, **113**, B04403.

Tirel, C. l., Brun, J.-P. & Burov, E., 2004. Thermomechanical modeling of extensional gneiss domes. *Geological Society of America Special Papers*, **380**, 67–78.

Tochilin, C. J., Reiners, P. W., Thomson, S. N., Gehrels, G. E., Hemming, S. R. & Pierce, E. L., 2012. Erosional history of the Prydz Bay sector of East Antarctica from detrital apatite and zircon geo- and thermochronology multidating. *Geochemistry, Geophysics, Geosystems*, **13**, Q11015.

Tomkins, H., Powell, R. & Ellis, D., 2007. The pressure dependence of the zirconium‚Äêin‚Äêrutile thermometer. *Journal of Metamorphic Geology*, **25**, 703–713.

Tukey, J. W., 1977. *Exploratory Data Analysis*. Addison-Wesley.

Tulloch, A. J., Beggs, M., Kula, J., Spell, T. & Mortimer, N., 2006. Cordillera Zealandia, the Sisters Shear Zone and their influence on the early development of the Great South Basin. In: *New Zealand Petroleum Conference Proceedings*, Ministry of Economic Development, Wellington.

Tulloch, A. J., Ramezani, J., Kimbrough, D. L., Faure, K. & Allibone, A. H., 2009a. U-Pb geochronology of mid-Paleozoic plutonism in western New Zealand: Implications for S-type granite generation and growth of the east Gondwana margin. *Geological Society of America Bulletin*, **121**, 1236–1261.

Tulloch, A. J., Ramezani, J., Mortimer, N., Mortensen, J., van den Bogaard, P. & Maas, R., 2009b. Cretaceous felsic volcanism in New Zealand and Lord Howe Rise (Zealandia) as a precursor to final Gondwana break-up. *Geological Society, London, Special Publications*, **321**, 89–118.

Tulloch, A. J., Ireland, T. R., Kimbrough, D. L., Griffin, W. L. & Ramezani, J., 2011. Autochthonous inheritance of zircon through Cretaceous partial melting of Carboniferous plutons: the Arthur River Complex, Fiordland, New Zealand. *Contributions to Mineralogy and Petrology*, **161**, 401–421.

Turcotte, D. L., 1997. *Fractals and chaos in geology and geophysics*. Cambridge University Press, Cambridge.

Turnbull, R. E., Tulloch, A. J. & Ramezani, J., 2013. Zetland Diorite, Karamea Batholith, west Nelson; field relationships, geochemistry and geochronology demonstrate links to the Carboniferous Tobin Suite. *New Zealand Journal of Geology and Geophysics*, **56**, 83–99.

Unsworth, M., Jones, A. G., Wei, W., Marquis, G., Gokarn, S., Spratt, J., Bedrosian, P., Booker, J., Leshou, C. & Clarke, G., 2005. Crustal rheology of the Himalaya and Southern Tibet inferred from magnetotelluric data. *Nature*, **438**, 78–81.

Valley, J. W., 2003. Oxygen Isotopes in Zircon. *Reviews in Mineralogy and Geochemistry*, **53**, 343–385.

Valley, J. W., Chiarenzelli, J. R. & McLelland, J. M., 1994. Oxygen isotope geochemistry of zircon. *Earth and Planetary Science Letters*, **126**, 187–206.

Valley, J. W., Kitchen, N., Kohn, M. J., Niendorf, C. R. & Spicuzza, M. J., 1995. UWG-2, a garnet standard for oxygen isotope ratios; strategies for high precision and accuracy with laser heating. *Geochimica et Cosmochimica Acta*, **59**, 5223–5231.

Valley, J. W., Kinny, P. D., Schulze, D. J. & Spicuzza, M. J., 1998. Zircon megacrysts from kimberlite: oxygen isotope variability among mantle melts. *Contributions to Mineralogy and Petrology*, **133**, 1–11.

Valley, J. W., Bindeman, I. N. & Peck, W. H., 2003. Empirical calibration of oxygen isotope fractionation in zircon. *Geochimica et Cosmochimica Acta*, **67**, 3257–3266.

van der Molen, I., 1985. Interlayer material transport during layer-normal shortening. Part II. Boudinage, pinch-and-swell and migmatite at Søndre Strømfjord Airport, West Greenland. *Tectonophysics*, **115**, 297–313.

Van Orman, J., Grove, T., Shimizu, N. & Layne, G., 2002. Rare earth element diffusion in a natural pyrope single crystal at 2.8 GPa. *Contributions to Mineralogy and Petrology*, **142**, 416–424.

Vanderhaeghe, O., 1999. Pervasive melt migration from migmatites to leucogranite in the Shuswap metamorphic core complex, Canada: control of regional deformation. *Tectonophysics*, **312**, 35–55.

Vanderhaeghe, O. & Teyssier, C., 2001. Partial melting and flow of orogens. *Tectonophysics*, **342**, 451–472.

Vavra, G., Gebauer, D., Schmid, R. & Compston, W., 1996. Multiple zircon growth and recrystallization during polyphase Late Carboniferous to Triassic metamorphism in granulites of the Ivrea Zone (Southern Alps): an ion microprobe (SHRIMP) study. *Contributions to Mineralogy and Petrology*, **122**, 337–358.

Veevers, J. J., 2012. Reconstructions before rifting and drifting reveal the geological connections between Antarctica and its conjugates in Gondwanaland. *Earth-Science Reviews*, **111**, 249–318.

Vernon, R. H., White, R. W. & Clarke, G. L., 2008. False metamorphic events inferred from misinterpretation of microstructural evidence and P–T data. *Journal of Metamorphic Geology*, **26**, 437–449.

Vervoort, J. D. & Jonathan Patchett, P., 1996. Behavior of hafnium and neodymium isotopes in the crust: Constraints from Precambrian crustally derived granites. *Geochimica et Cosmochimica Acta*, **60**, 3717–3733.

Vervoort, J. D. & Blichert-Toft, J., 1999. Evolution of the depleted mantle: Hf isotope evidence from juvenile rocks through time. *Geochimica et Cosmochimica Acta*, **63**, 533–556.

Vervoort, J. D., Patchett, P. J., Blichert-Toft, J. & Albarède, F., 1999. Relationships between Lu–Hf and Sm–Nd isotopic systems in the global sedimentary system. *Earth and Planetary Science Letters*, **168**, 79–99.

Vervoort, J. D., Patchett, P. J., Söderlund, U. & Baker, M., 2004. Isotopic composition of Yb and the determination of Lu concentrations and Lu/Hf ratios by isotope dilution using MC-ICPMS. *Geochemistry, Geophysics, Geosystems*, **5**, Q11002.

Vervoort, J. D., Plank, T. & Prytulak, J., 2011. The Hf–Nd isotopic composition of marine sediments. *Geochimica et Cosmochimica Acta*, **75**, 5903–5926.

Vetter, U. & Tessensohn, F., 1987. S- and I-Type granitoids of North Victoria Land, Antarctica, and their inferred geotectonic setting. *Geologische Rundschau*, **76**, 233–243.

Vielzeuf, D., Clemens, J. D., Pin, C. & Moinet, E., 1990. Granites, Granulites, and Crustal Differentiation. In: *Granulites and Crustal Evolution* (eds Vielzeuf, D. & Vidal, P.) *NATO ASI Series*, 59–85, Springer Netherlands.

Villaros, A., Stevens, G., Moyen, J.-F. o. & Buick, I., 2009. The trace element compositions of S-type granites: evidence for disequilibrium melting and accessory phase entrainment in the source. *Contributions to Mineralogy and Petrology*, **158**, 543–561.

Villaros, A., Buick, I. S. & Stevens, G., 2012. Isotopic variations in S-type granites: an inheritance from a heterogeneous source? *Contributions to Mineralogy and Petrology*, **163**, 243–257.

Villaseca, C., Martín Romera, C., De la Rosa, J. & Barbero, L., 2003. Residence and redistribution of REE, Y, Zr, Th and U during granulite-facies metamorphism: behaviour of accessory and major phases in peraluminous granulites of central Spain. *Chemical Geology*, **200**, 293–323.

Villaseca, C., Orejana, D. & Paterson, B. A., 2007. Zr–LREE rich minerals in residual peraluminous granulites, another factor in the origin of low Zr–LREE granitic melts? *Lithos*, **96**, 375–386.

Walsh, J. J. & Watterson, J., 1993. Fractal analysis of fracture patterns using the standard box-counting technique: valid and invalid methodologies. *Journal of Structural Geology*, **15**, 1509–1512.

Wanas, H. A. & Abdel-Maguid, N. M., 2006. Petrography and geochemistry of the Cambro-Ordovician Wajid Sandstone, southwest Saudi Arabia: Implications for provenance and tectonic setting. *Journal of Asian Earth Sciences*, **27**, 416–429.

Ward, R., Stevens, G. & Kisters, A., 2008. Fluid and deformation induced partial melting and melt volumes in low-temperature granulite-facies metasediments, Damara Belt, Namibia. *Lithos*, **105**, 253–271.

Wark, D. A. & Miller, C. F., 1993. Accessory Mineral Behavior during Differentiation of a Granite Suite - Monazite, Xenotime and Zircon in the Sweetwater Wash Pluton, Southeastern California, USA. *Chemical Geology*, **110**, 49–67.

Watson, E. B., 1996. Dissolution, growth and survival of zircons during crustal fusion: kinetic principals, geological models and implications for isotopic inheritance. *Transactions of the Royal Society of Edinburgh-Earth Sciences*, **87**, 43–56.

Watson, E. B. & Harrison, T. M., 1983. Zircon saturation revisited: temperature and composition effects in a variety of crustal magma types. *Earth and Planetary Science Letters*, **64**, 295–304.

Watson, E. B., Vicenzi, E. P. & Rapp, R. P., 1989. Inclusion/host relations involving accessory minerals in high-grade metamorphic and anatectic rocks. *Contributions to Mineralogy and Petrology*, **101**, 220–231.

Watt, G. R., Burns, I. M. & Graham, G. A., 1996. Chemical characteristics of migmatites: accessory phase distribution and evidence for fast melt segregation rates. *Contributions to Mineralogy and Petrology*, **125**, 100–111.

Watt, G. R. & Harley, S. L., 1993. Accessory phase controls on the geochemistry of crustal melts and restites produced during water-undersaturated partial melting. *Contributions to Mineralogy and Petrology*, **114**, 550–566.

Weaver, S. D., Bradshaw, J. D. & Adams, C. J., 1991. Granitoids of the Ford Ranges, Marie Byrd Land, Antarctica. In: *Geological Evolution of Antarctica*, 345–351, Cambridge University Press : Cambridge - New York, International, International.

Weaver, S. D., Adams, C. J., Pankhurst, R. J. & Gibson, I. L., 1992. Granites of Edward VII Peninsula, Marie Byrd Land; anorogenic magmatism related to Antarctic-New Zealand rifting. *Special Paper - Geological Society of America*, **272**, 281–290.

Weaver, S. D., Storey, B. C., Pankhurst, R. J., Mukasa, S. B., DiVenere, V. J. & Bradshaw, J. D., 1994. Antarctica-New Zealand rifting and Marie Byrd Land lithospheric magmatism linked to ridge subduction and mantle plume activity. *Geology*, **22**, 811–814.

White, R. W. & Powell, R., 2002. Melt loss and the preservation of granulite facies mineral assemblages. *Journal of Metamorphic Geology*, **20**, 621–632.

White, R. & Powell, R., 2010. Retrograde melt–residue interaction and the formation of near‚ÄêanhydrousÄê leucosomes in migmatites. *Journal of Metamorphic Geology*, **28**, 579–597.

White, R. W., Powell, R., Holland, T. J. B. & Worley, B. A., 2000. The effect of TiO2 and Fe2O3 on metapelitic assemblages at greenschist and amphibolite facies conditions: mineral equilibria calculations in the system K2O-FeO-MgO-Al2O3-SiO2-H2O-TiO2-Fe2O3. *Journal of Metamorphic Geology*, **18**, 497–511.

White, R. W., Powell, R. & Holland, T. J. B., 2001. Calculation of partial melting equilibria in the system Na2O-CaO-K2O-FeO-MgO-Al2O3-SiO2-H2O (NCKFMASH). *Journal of Metamorphic Geology*, **19**, 139–153.

White, R. W., Powell, R. & Clarke, G. L., 2003. Prograde Metamorphic Assemblage Evolution during Partial Melting of Metasedimentary Rocks at Low Pressures: Migmatites from Mt Stafford, Central Australia. *Journal of Petrology*, **44**, 1937–1960.

White, R. W., Powell, R. & Halpin, J. A., 2004. Spatially-focussed melt formation in aluminous metapelites from Broken Hill, Australia. *Journal of Metamorphic Geology*, **22**, 825–845.

White, R. W., Pomroy, N. E. & Powell, R., 2005. An in situ metatexite-diatexite transition in upper amphibolite facies rocks from Broken Hill, Australia. *J Metamorph Geol*, **23**, 579–602.

White, R. W., Powell, R. & Holland, T. J. B., 2007. Progress relating to calculation of partial melting equilibria for metapelites. *Journal of Metamorphic Geology*, **25**, 511–527.

White, R. W., Stevens, G. & Johnson, T. E., 2011. Is the Crucible Reproducible? Reconciling Melting Experiments with Thermodynamic Calculations. *Elements*, **7**, 241–246.

White, R. W., Powell, R., Holland, T. J. B., Johnson, T. E. & Green, E. C. R. (2014a). New mineral activity–composition relations for thermodynamic calculations in metapelitic systems. *Journal of Metamorphic Geology* **32**, 261–286.

White, R. W., Powell, R. & Johnson, T. E. (2014b. The effect of Mn on mineral stability in metapelites revisited:new a–x relations for manganese-bearing minerals. *Journal of Metamorphic Geology*, doi: 10.1111/jmg.12095.

Whitehouse, M. J. & Platt, J. P., 2003. Dating high-grade metamorphism--constraints from rare-earth elements in zircon and garnet. *Contributions to Mineralogy and Petrology*, **145**, 61–74.

Whitney, D. L., Teyssier, C. & Fayon, A. K., 2004. Isothermal decompression, partial melting and exhumation of deep continental crust. *Geological Society, London, Special Publications*, **227**, 313–326.

Whitney, D. L., Teyssier, C. & Rey, P. F., 2009. The consequences of crustal melting in continental subduction. *Lithosphere*, **1**, 323–327.

Whitney, D. L., Teyssier, C., Rey, P. & Buck, W. R., 2013. Continental and oceanic core complexes. *Geological Society of America Bulletin*, **125**, 273–298.

Whittington, A. & Treloar, P., 2002. Crustal anatexis and its relation to the exhumation of collisional orogenic belts, with particular reference to the Himalaya. *Mineralogical Magazine*, **66**, 53–91.

Wickham, S., 1987. The segregation and emplacement of granitic magmas. *Journal of the Geological Society*, **144**, 281–297.

Williams, I. S., 1998. U–Th–Pb geochronology by ion microprobe. In: *Applications of microanalytical techniques to understanding mineralizing processes* (eds McKibben, M. A., Shanks, W. C. & Ridley, W. I.), 1–25, Reviews in Economic Geology, Society of Economic Geologists, Socorro, New Mexico.

Williams, I., 2001. Response of detrital zircon and monazite, and their U–Pb isotopic systems, to regional metamorphism and host-rock partial melting, Cooma Complex, southeastern Australia. *Australian Journal of Earth Sciences*, **48**, 557–580.

Williams, M. L., Jercinovic, M. J., Harlov, D. E., Budzyń, B. & Hetherington, C. J., 2011. Resetting monazite ages during fluid-related alteration. *Chemical Geology*, **283**, 218–225.

Williams, M. L., Jercinovic, M. J. & Hetherington, C. J., 2007. Microprobe Monazite Geochronology: Understanding Geologic Processes by Integrating Composition and Chronology. *Annual Review of Earth and Planetary Sciences*, **35**, 137–175.

Woodhead, J., Hergt, J., Shelley, M., Eggins, S. & Kemp, R., 2004. Zircon Hf-isotope analysis with an excimer laser, depth profiling, ablation of complex geometries, and concomitant age estimation. *Chemical Geology*, **209**, 121–135.

Woodhead, J. D. & Hergt, J. M., 2005. A Preliminary Appraisal of Seven Natural Zircon Reference Materials for In Situ Hf Isotope Determination. *Geostandards and Geoanalytical Research*, **29**, 183–195.

Xu, H., Ye, K., Song, Y., Chen, Y., Zhang, J., Liu, Q. & Guo, S., 2013. Prograde metamorphism, decompressional partial melting and subsequent melt fractional crystallization in the Weihai migmatitic gneisses, Sulu UHP terrane, eastern China. *Chemical Geology*, **341**, 16–37.

Yakymchuk, C. & Brown, M., 2014a. Behaviour of zircon and monazite during crustal melting. *Journal of the Geological Society*.

Yakymchuk, C. & Brown, M., 2014b. Consequences of open-system melting in tectonics. *Journal of the Geological Society*, **171**, 21–40.

Yakymchuk, C., Siddoway, C. S., Fanning, C. M., McFadden, R., Korhonen, F. J. & Brown, M., 2013a. Anatectic reworking and differentiation of continental crust along the active margin of Gondwana; a zircon Hf-O perspective from West Antarctica. *Special Publication - Geological Society of London*, **383,** 169–210

Yakymchuk, C., Brown, M., Ivanic, T. J. & Korhonen, F. J., 2013b. Leucosome distribution in migmatitic paragneisses and orthogneisses: A record of self-organized melt migration and entrapment in a heterogeneous partially-molten crust. *Tectonophysics*, **603**, 136–154.

Yakymchuk, C., Brown, C. R., Brown, M., Siddoway, C. S., Fanning, C. M. & Korhonen, F. J., 2014. Paleozoic evolution of 1 western Marie Byrd Land, Antarctica. *Geological Society of America Bulletin*, **in review**.

Yang, J.-H., Wu, F.-Y., Wilde, S. A., Xie, L.-W., Yang, Y.-H. & Liu, X.-M., 2006. Tracing magma mixing in granite genesis: in situ U–Pb dating and Hf-isotope analysis of zircons. *Contributions to Mineralogy and Petrology*, **153**, 177–190.

Yardley, B. W. D., 2009. The role of water in the evolution of the continental crust. *Journal of the Geological Society of London*, **166**, 585–600.

Zack, T., Moraes, R. & Kronz, A., 2004. Temperature dependence of Zr in rutile: empirical calibration of a rutile thermometer. *Contributions to Mineralogy and Petrology*, **148**, 471–488.

Žák, J., Verner, K., Finger, F., Faryad, S. W., Chlupáčová, M. & Veselovský, F., 2011. The generation of voluminous S-type granites in the Moldanubian unit, Bohemian

Massif, by rapid isothermal exhumation of the metapelitic middle crust. *Lithos*, **121**, 25–40.

Zeitler, P. K. & Chamberlain, C. P., 1991. Petrogenetic and Tectonic Significance of Young Leukogranites from the Northwestern Himalaya, Pakistan. *Tectonics*, **10**, 729–741.

Zeitler, P. K., Chamberlain, C. P. & Smith, H. A., 1993. Synchronous Anatexis, Metamorphism, and Rapid Denudation at Nanga-Parbat (Pakistan Himalaya). *Geology*, **21**, 347–350.

Zeng, L., Asimow, P. D. & Saleeby, J. B., 2005a. Coupling of anatectic reactions and dissolution of accessory phases and the Sr and Nd isotope systematics of anatectic melts from a metasedimentary source. *Geochimica et Cosmochimica Acta*, **69**, 3671–3682.

Zeng, L., Saleeby, J. B. & Asimow, P., 2005b. Nd isotope disequilibrium during crustal anatexis: A record from the Goat Ranch migmatite complex, southern Sierra Nevada batholith, California. *Geology*, **33**, 53–56.

Zeng, L., Saleeby, J. B. & Ducea, M., 2005c. Geochemical characteristics of crustal anatexis during the formation of migmatite at the Southern Sierra Nevada, California. *Contributions to Mineralogy and Petrology*, **150**, 386–402.

Zheng, Y.-F., Zhang, S.-B., Zhao, Z.-F., Wu, Y.-B., Li, X., Li, Z. & Wu, F.-Y., 2007. Contrasting zircon Hf and O isotopes in the two episodes of Neoproterozoic granitoids in South China: Implications for growth and reworking of continental crust. *Lithos*, **96**, 127–150.

Zirakparvar, N. A., Vervoort, J. D., McClelland, W. & Lewis, R. S., 2010. Insights into the metamorphic evolution of the Belt-Purcell basin; evidence from Lu-Hf garnet geochronology. *Canadian Journal of Earth Sciences*, **47**, 161–179.

Zuluaga, C. A., Stowell, H. H. & Tinkham, D. K., 2005. The effect of zoned garnet on metapelite pseudosection topology and calculated metamorphic P-T paths. *American Mineralogist*, **90**, 1619–1628.